



Oceans '99 MTS/IEEE

Riding the Crest into
the 21st Century

CONFERENCE & EXHIBITION
13-16 September 1999
Seattle, Washington

*Conference
Proceedings
Volume 3*

DISTRIBUTION STATEMENT A
Approved for Public Release
Distribution Unlimited

20000317 033



REPORT DOCUMENTATION PAGE			Form Approved OMB No. 0704-0188	
Public reporting burden for this collection of information is estimated to average 1 hour per response, including the time for reviewing instructions, searching existing data sources, gathering and maintaining the data needed, and completing and reviewing the collection of information. Send comments regarding this burden estimate or any other aspect of this collection of information, including suggestions for reducing this burden, to Washington Headquarters Services, Directorate for Information Operations and Reports, 1215 Jefferson Davis Highway, Suite 1204, Arlington, VA 22202-4302, and to the Office of Management and Budget, Paperwork Reduction Project (0704-0188), Washington, DC 20503.				
1. AGENCY USE ONLY (Leave Blank)	2. REPORT DATE	3. REPORT TYPE AND DATES COVERED		
4. TITLE AND SUBTITLE Oceans 1999 MTS/IEEE		5. FUNDING NUMBERS G		
6. AUTHORS multiple				
7. PERFORMING ORGANIZATION NAME(S) AND ADDRESS(ES) Institute of Electrical and Electronics Engineers, Inc. 445 Hoes Lane PO Box 1331 Piscataway, NJ 08855-1331		8. PERFORMING ORGANIZATION REPORT NUMBER GG239		
9. SPONSORING / MONITORING AGENCY NAME(S) AND ADDRESS(ES) Office of Naval Research 800 North Quincy Street Arlington, VA 22217-5660		10. SPONSORING / MONITORING AGENCY REPORT NUMBER N00014-99-1-0242		
11. SUPPLEMENTARY NOTES Prepared in cooperation with Marine Technology Society				
12a. DISTRIBUTION / AVAILABILITY STATEMENT			12b. DISTRIBUTION CODE	
13. ABSTRACT (Maximum 200 words)				
14. SUBJECT TERMS Advanced Marine Technology, Communications & Navigation, Ocean Monitoring Systems, Marine Policy & Education, Marine Resources, Underwater Acoustics, Signal & Information Processing, Ocean & Coastal Engineering			15. NUMBER OF PAGES	
			16. PRICE CODE	
17. SECURITY CLASSIFICATION OF REPORT Unclassified	18. SECURITY CLASSIFICATION OF THIS PAGE Unclassified	19. SECURITY CLASSIFICATION OF ABSTRACT Unclassified	20. LIMITATION OF ABSTRACT UL	

VOLUME 3

Table of Contents/Sessions	viii-xxxi
----------------------------------	-----------

Authors Index	xxxii-xxxxiv
---------------------	--------------

Papers

Volume 1.....	1-547
---------------	-------

Volume 2.....	548-1080
---------------	----------

Volume 3.....	1081-1602
---------------	-----------

Seattle · 13 - 16 September 1999



Volume 1

Session 1A:

Undersea Cable Burial Plows

Co-Chairs:

D. Bloomquist, DTRC, MD
H.B. Ali, ONR IFO Asia, JAPAN

**Analysis of Plowing Forces for
a Finite-Width Plow Blade in
Dense Ocean-Bottom Sand** 1
J.C. Coyne & G.W. Lewis, General Dynamics, NJ

**Development of an Improved
Cable Trenching Plowshare** 11
J.A. Hill, Tyco Submarine Systems, MD and
R. Elliott, Perry Tritech, FL and
F.D. Messina, SeaTech Solutions, NJ

**A New Generation Undersea
Cable Burial Plow - A Review
of Operational Design Goals** 17
N. Leifer, General Dynamics, NJ and
E. Fihn, Perry Tritech, FL and
F.D. Messina, SeaTech Solutions, NJ

Session 2A:

Advanced Marine Technology

Co-Chairs:

K. Ferer, Neptune Sciences, VA
F. de Strobel, SACLANTCEN, ITALY

**The Advantages Challenges & Practical
Implementation of an Interferometric
Swath Bathymetry System** 23
A.D. Wilby, Ultra Electronics Ocean Systems, UK

**Characterization of the Seafloor
Using Normal Incidence Acoustic
Backscattered Time Domain Signals
from a Parametric Sonar** 30
B. Berntsen, J.M. Hovem, Norwegian University of
Science and Technology, NORWAY
O. Bergem, SACLANTCEN, ITALY

**Beyond Interferometry, Resolving
Multiple Angles-of-Arrival in
Swath Bathymetric Imaging** 37
P.H. Kraeutner & J.S. Bird,
Simon Fraser University, CANADA

**Robust Position and Heading Sensor
for High Speed Military Vessels** 46
J-M. Godhavn, Navia Maritime, NORWAY

Session 3A:

Underwater Imaging

Co-Chairs: T. Sakou, Tokai University, JAPAN
M. Olsson, Deepsea Power & Light, CA

**Quantitative Stereo Imaging from the
Autonomous Benthic Explorer (ABE)** 52
H. Singh, F. Weyer, J. Howland, A. Duester,
D. Yoerger & A. Bradley, WHOI, MA

**Design and Initial Results of High-
Resolution Shadowed Image Particle
Profiling and Evaluation Recorder** 58
S. Samson, L. Langebrake, C. Lembke & J.
Patten, University of South Florida, FL

**Building 3D Elevation Maps of Sea-Floor
Scenes from Underwater Stereo Images** 64
A. Khamene & S. Negahdaripour, Univ. Miami, FL

**Automatic Optical Station Keeping
and Navigation of an ROV; Sea
Trial Experiments** 71
X. Xu & S. Negahdaripour, Univ. of Miami, FL

Session 4A:

Tales from the Deep Ocean

Co-Chairs: T. Brockett, Sound Ocean Systems
T. Ginnis, Williamson & Assoc, WA

**The Hunt for STS-51L; Space Shuttle
Challenger: The Undersea Search
for the Cause of a Tragedy** 77
D.S. Schwartz, University of Washington, WA



Table of Contents

Conference Proceedings

Finding the Liberty Bell-7	
Mercury Spacecraft	*
C. Newport, Liberty Bell-7, MD	

MIDWAY - Search for the Japanese Fleet	*
D. Jourdan, T Bethge & J Burns, Nauticos, MD	

Session 5A:	
Marine Living Resources	
Co-Chairs:	J. Wiltshire, Univ. Hawaii, HURL, HI H. Nakahara, Res Inst for Ocean Econ, JAPAN

Development of an Advanced	
Whale Tracking System	*
H. Nakahara, Res Inst for Ocean Economics, S. Osumi, Institute of Cetacean Research, T. Hayashi, Chiba Institute of Technology and H. Hoshino, Kaiyo Systems, JAPAN	

Development of an Operational	
Repository of Coastal Hydraulics	
and Inlet Dynamics	99
R. Nichols, Marine Information Resources, MD S. Snyder, NC State University, NC	

Session 6A:	
Buoy and Moorings Engineering	
Co-Chairs:	W. Paul, WHOI, MA D. Milburn, USNOO, MS

Characterizing the Excitation and	
Response of a Spar Buoy	
in Random Seas	104
J.M. Niedzwecki & E.W. Sandt, Texas A&M University, TX	

The Dynamics of Shallow Water	
Oceanographic Moorings: Experimental	
and Numerical Results	107
J.I. Gobat & M A Grosenbaugh, WHOI, MA	

Advances in Buoy Technology for Wind/Wave	
Data Collection and Analysis	113
S.G.P. Skey, Axy's Environmental Systems and M.D. Miles, National Res. Council of CANADA	

Wave Generation Instrumentation	
in Hydraulic Models	119
B.W. McCleave, H. Greer & M. Briggs, US Army Engineers WES, MS	

Session 7A:	
SubBottom Mapping / Buried Objects	
Co-Chairs:	M.T. Kalcic, NRL, MS J. Potter, Nat'l Univ. of Singapore, SINGAPORE

Buried Object Detection by	
Auto-Regressive Prewhitening	126
A. Trucco & S. DiSerio, University of Genoa and V. Murino, University of Verona, ITALY	

Calculation of the Engineering Properties	
of Marine Sediments from Acoustic Reflection	
Data Using Biot Theory	133
R.G. McGee & J.A. Boughner, Evans-Hamilton, WA and P. Ogushwitz, Pro Scientific Consult. NJ	

Session 8A:	
Remote Sensing	
Co-Chairs:	B. Rogers, RHR and Associates, MI L.L. Utyakov, Shirshov Inst of Ocean, RUSSIA

Effects of Wind Variability on	
Scatterometry at Low Wind Speeds	134
W.J. Plant, University of Washington APL, WA	

Satellite Ocean Surface Stress	
Measurements Applied to Air-Sea	
Interaction and Circulation	138
D.E. Weissman, Hofstra University, NY	

The Possibility of Passive Whale	
Tracking with the Use of an	
Hyperspectral Sensor	141
C. Barnes, G. Gilbert, J. Schoonmaker & J. Rohr SPAWARSYSCEN, CA	

* Paper received too late for publishing



Flow Visualization in the Ocean— Implications of Laboratory

Bioluminescence Experiments 145

J. Rohr, J. Schoonmaker & J. Losee, SPAWAR
and M.I. Latz, Scripps Inst. of Oceanography, CA
and M. Hyman, NCSS, FL

Session 1B:

Planned Ocean Programs

Co-Chairs: H. Strong, Mitretek Systems, VA
C.D. MacDonald, State of Hawaii, HI

Independent Study of NOS Hydrographic

Survey Data Acquisition 157

E.J. Fields & T.I. Lillestolen, NOAA, DC and
D. Dunlop & C.V. Mauro, Mitretek Systems, VA

The Status and Future of Real-Time Tide and Current Data Systems

for United States Ports 169

R.M. Barazotto, NOAA/NOS, MD

Private Sector Opportunities in National Ocean Service

Hydrographic Surveying 176

N. Foster & D.B. MacFarland, NOAA NOS, MD

A Planned Underwater Dive

Attractions Program for Hawaii 180

C.D. MacDonald, C.A. Mitsuyasu & E. Corbin,
State of Hawaii, HI

Session 2B:

Autonomous Vehicle Technology

Co-Chairs: J. McFarlane, ISE, CANADA
J. Bunce, Neptune Sciences, MS

AUV's — The Maturity of the Technology 189

R.L. Wernli, SPAWAR Systems Center, CA

Autonomous Vehicle Programs and Applications at SPAWAR

Systems Center 196

B. Fletcher, SPAWARSYSCEN, CA

Multi Input-Multi Output System Identification of AUV Systems

by Neural Network 201

H. Sayyaadi & T. Ura, Univ. of Tokyo, JAPAN

Multi-Sensor Fusion for Autonomous

Underwater Cable Tracking 209

A. Balasuriya, Nanyang Tech. Univ.
SINGAPORE and T Ura, Univ. of Tokyo, JAPAN

Session 3B:

Underwater Communication

Chair: M. Moroney, Volpe Natl. Transp Ctr, MA

Doppler Compensation for Underwater

Acoustic Communications 216

B.S. Sharif, J. Neasham, O.R. Hinton &
A.E. Adams, University of Newcastle, ENGLAND

Chirp FSK Modem for High Reliability

Communication in Shallow Water 222

L.R. LeBlanc, P. Beaujean, M. Singer, C. Boubli &
G.T. Strutt FAU, FL

Direct Sequence Spread Spectrum

Based Modem for Under Water

Acoustic Communications and

Channel Measurements 228

E.M. Sozer & M. Stojanovic, Northeastern Univ. MA
J.G. Proakis, Delphi Communication Systems, MA,
J.A. Rice & M. Hatch, SPAWAR, CA, and
A. Benson, ONR, VA

Session 4B:

Tales from the Deep Ocean II

Co-Chair: T. Brockett, Sound Ocean Systems
M. Williamson, Williamson & Assoc., WA

The Role of Image Processing in the

Search for the I.N.S. DAKAR 234

D. Johnson, Williamson & Associates, WA

USS Yorktown *

K. Sadorf, U.S. Navy, CA

Derbyshire Search *

J. Holland, WHOI, MA

* Paper received too late for publishing



- I - 52 Japanese Submarine ***
P. Tidwell, Cape Verde Explorations, AFRICA

Session 5B:

Marine Mineral Resources

- Co-Chairs:** J. Na, Hanyang University, KOREA
J. Wiltshire, Univ. of Hawaii, HURL, HI

Marine Manganese Tailings Concrete:

- Advantages and Drawbacks 237**
J.C. Wiltshire & K.A. Moore, Univ. of Hawaii, HI

Sustainable Development of Tropical, Coastal, Urban Zones in an

- Archipelago Environment 245**
M. Santosa & D.M. Rosyid, Sepuluh Nopember
Insitute of Technology, INDONESIA

Remote Control Seafloor Coring

- in the West Mariana Basin 255**
T. McGinnis, Williamson & Associates, WA

Session 6B:

Buoy / Moorings Advances

- Co-Chairs:** W. Paul, WHOI, MA
D. Milburn, USNOO, MS

Use of Synthetic Ropes in Deepwater

- Moorings: ABS Guidance Notes 257**
M-Y. Lee & T. Grove,
American Bureau of Shipping, TX

Sea Lions and Buoys, a

- Battle of Wills and Wits 269**
K.C. O'Neil, J.M. Hemsley & L. Allison, NDBC, MS

Long-Term Moored Observations on Georges Bank as part of the U.S. GLOBEC Northwest

- Atlantic/Georges Bank Program 273**
J.D. Irish, R.C. Beardsley, W.J. Williams
& K.H. Brink, WHOI, MA

Session 7B:

Acoustic Noise and Reverberation

- Chair:** D. Ramsdale, Neptune Sciences, MS

Parameter Estimation for McDaniel's

- Non-Rayleigh Reverberation Model 279**

M. Gu & D. A Abraham, Univ. of Connecticut, CT

Choosing a non-Rayleigh

- Reverberation Model 284**
D.A. Abraham, University of Connecticut, CT

Advanced Technologies for Undersea Surveillance of

- Modern Threats 289**
D.J. Meggitt, Natural Resources Consultants,
D.K. Roderick & K.P. Cooke, Lockheed Martin VA

An Adaptive Signal Processing for Enhanced Target Detection

- in Active Sonar Systems 295**
K.M. Kim, Korea Maritime Univ, D.H. Youn, Yonsei
Univ, K.C. Doh & W.C. Oh, Agency Defense for
Development, KOREA

Session 8B:

Sonar Signal Processing

- Chair:** R. Dwyer, IEEE, CT

Coherent Source Direction Estimation for Three-Row

- Bathymetric Sidescan Sonars 299**
W. Xu, MIT/WHOI, MA and
W.K. Stewart, Virtual Marine Assoc. FL

A D-RLS Method for Estimating an Exponentially Complex Signal with Application to Scattering

- Centers Identification 305**
A. Hajjari & O. Eloutassi, Fes, MOROCCO

Noise Subtraction for Improving the Localization of an

- Underwater Mobile 310**
A. Quinquis & H. Thomas, ENSIETA, FRANCE
and C. Ioana, Military Tech. Academy, ROMANIA

* Paper received too late for publishing



An Array Aperture Synthesis Technique for Noisy Environment..... 315

S. Kim, C. Lee & D.H. Youn, Yonsei University,
W.C. Lee, Soongsil University and K.M. Kim,
Korea Maritime University, KOREA

Session 1C: Environmental Challenges

Co-Chairs: A. Mearns, NOAA OA, WA
L.F. Tsen, Univ. Tenaga Nasional, MALAYSIA

Pesticide Contamination in Lake Naivasha (Kenya) 319

S.M. Gitahi, Lake Naivasha Association, KENYA

Water Quality at a Major Ocean Outfall on the San Pedro Shelf, California: Summary of a Nine-Year Study 324

G. Robertson, Orange County Sanitation District,
A. Barnett, MEC Analytical Systems,
A. Lissner, SAIC, and D. Maurer,
California State University Long Beach, CA

Secondary Production Estimates from Benthic Biomass: Assessing Coastal Eutrophication 344

D. Maurer, California State Univ. Long Beach and
G. Robertson, Orange County Sanitation District, CA

Session 2C: Advanced Measurement Systems

Chair: K. Ferer, Neptune Sciences, VA

A 1.6 Gigabit/Second 25-85 kHz Acoustic Imaging Array - Novel Mechanical and Electronics Design Aspects 352

P. Venugopalan, P. Deshpande, S. Badiu,
S. Constantin, B. Lu, & J.R. Potter, National
University of Singapore ARL, SINGAPORE

Design of a Flow-Through Integrating Cavity for Measuring the Optical Absorption Coefficient 359

N.J. McCormick, University of Washington, WA

Mobile Underwater Debris Survey System (MUDSS) 363

D.C. Summey, J.F. McCormack, P.J. Carroll,
J.D. Lathrop, D.J. Overway, J.E. Fernandez,
J.S. Taylor, C.N. Pham, G.A. Bills, W.S. Howell,
P.M. Mount, & R.A. Leasko, Naval Surface
Warfare Center, FL

NASA Scatterometer Measurements of Ocean Surface Winds in Tropical Cyclones 373

W.L. Jones & J. Zec, Univ. of Central Florida, FL
V.J. Cardone, OceanWeather, CT and
W.J. Pierson, City College of CUNY, NY

Session 3C: Water Current Measurement

Co-Chairs: H. Shaotang, IOT, CHINA
T. Morrison, McLane Research Lab, MA

Upgraded Vector Measuring Current Meter 377

D. Hosom, R. Weller, G. Allsup,
S. Anderson & R. Trask WHOI, MA

Theoretical Model and Error Analysis of Acoustic Correlation Current Profiler (ACCP) 382

W. Zhu, C. Wang, Y. Huang & P. He,
Academia Sinica, CHINA

Reynolds Stress Resolution from a Modular Acoustic Velocity Sensor 386

A.J. Williams, WHOI, MA and
C. Beckford, Westtown School, PA

Design Enhancements to Improve Survivability of a Lightweight Trawl-Resistant Bottom Mount for the Workhorse Acoustic Doppler Current Profilers 391

S.C. Cumbee, J.M. Foley & R.J. Wahl, USNOO,
MS & P. Clay, Mooring Systems, MA



Table of Contents

Conference Proceedings

Session 4C:

Marine Civil Engineering

Chair: M.C. Murton, VSE, VA

A Case History of Offshore Disposal at the Port of

Los Angeles *

J. Foxworthy, Port of Los Angeles and
A. Alcom, Moffatt & Nichol Engineers, CA

Engineering Response to Shore Erosion Near Grays Harbor USA.....

396

V. Shepsis, D. Simpson & S. Phillips,
Pacific International Engineering, WA

Ettringite Distress in Concrete

Marine Structures *

T.E. Spencer, Blaylock Engineering Group, CA

Modeling and Analysis of a

Floating Breakwater *

E. Watchorn, CEFER Engineering, CANADA

Session 5C:

Restoration Planning & Implementation

Chair: J. Burgess, NOAA NMF, MD

A State Perspective on

Large Scale Urban Restoration 406

D.F. Jacobs, CA State Dept. of Fish & Game, CA

Community-Based Habitat

Restoration Program 409

C.D. Doley, NOAA Fisheries, MD

Strengthening the Response/Restoration Linkage - Lessons Learned from Recent

Oil Spills 410

D. Helton, NOAA Damage Assessment and
Restoration Center Northwest, WA

State Approach to Managing

Urban Embayments 414

M. Mauren & B. Bunning, WA Dept. of Natural
Resources, WA

Session 6C:

Buoy / Moorings Technology

Co-Chairs: D. Milburn, USNOO, MS
W. Paul, WHOI, MA

Measurement of Precipitation at

Sea by NDBC Moored Buoys 417

E. Michelena, R. Timko & D. Scally, NDBC, MS

Coastal Mooring Design: Taut Elastomeric and Chain Catenary

Surface Buoy Moorings 419

W. Paul, J. Irish, M. Grosenbaugh & J. Gobat,
Woods Hole Oceanographic Institution, MA

Field Evaluation of the Meteorological and Oceanographic

Articulating Platform 427

C.A. Kohler & C-C. Teng, USCG, NDBC, MS

Session 7C:

Acoustic Noise and Propagation

Chair: R. Farwell, Neptune Sciences, MS

Surface Wave Influence on Acoustic Propagation in

Very Shallow Water 434

O. Bergem, D. Dilorio & N.G. Pace,
SACLANTCEN, ITALY

Surface-Generated Noise in an Ocean Waveguide With an Inhomogeneous

Transition Layer 439

J-Y. Liu & C-F. Huang, National Sun Yat-sen
University, TAIWAN

Geoacoustic Inversion with

Artificial Neural Networks 446

J. Benson, N.R. Chapman & A. Antoniou,
University of Victoria, CANADA

* Paper received too late for publishing



Session 8C:

Data Access, Retrieval and Display

Co-Chairs: B. Porto, Natural Selection, CA
J.G. Balchen, Norwegian University, NORWAY

Providing Real-Time Data

Trajectory Access in Autonomous Underwater Vehicles 452
X. Yuan, M. Evett & S. Smith, FAU and
K. Ganesan, MicroSoft Corp, FL

Segmentation of Underwater 3D Acoustical Images for Augmented and Virtual Reality Applications 459
R. Giannitrapani, Univ. of Udine, A. Trucco, Univ. Genova and V. Murino, Univ. Verona, ITALY

Interactive Web Access to Real-Time El Niño/La Niña Data from the TAO Buoy Network in the Tropical Pacific 466
W.H. Zhu, E.F. Burger, D.C. McClurg &
D.W. Denbo, University of Washington, and
N.N. Soreide, NOAA/PMEL, WA

The Scientific Graphics Toolkit 470
D.W. Denbo, University of Washington, WA

TeleInVivo: A Volume Visualization Tool with Applications in Multiple Fields 474
S. Jarvis, R. Barton & J. Coleman, Fraunhofer Center for Research in Computer Graphics, RI

Session 9C:

Characterization of Discharges from Shipyards and Drydocks

Co-Chairs: M.A. Champ, ATRP, VA
T.J. Fox, CASRM, VA

Assessing the Degree of Appropriate Treatment of Shipyard and Drydock Wastewater Discharges and Stormwater Runoff 481
G.F. Lee & A.J.-Lee, G Fred Lee & Assoc, CA

Session 1D:

Ship Technology

Co-Chairs: J. Bash, UNOLS, RI
T. Achmadi, ITS Campus-Sukolilo, INDONESIA

Lamp Ray: Ship Hull Assessment for Value, Safety and Readiness 493
S.E. Harris & E.V. Slate, Imetrix, MA

R/V Western Flyer Operability and Hull-Strength Upgrade 501
S. Etchemendy & M. VandenBerg, MBARI, CA
and R. Van Slyke, J. Morgan & T. Leach,
The Glosten Associates, WA

Exeter II: Developing and Preparing for Santa Clara University's Second Underwater Research Vessel 519
C.A. Bulich, C.A. Kitts & J.M. Ota, Santa Clara University, CA and D. Davis, MBARI, CA

Design of a SWATH Coastal Research Vessel 526
J.L. Coburn, WHOI, MA, R.D. Gaul, Blue Sea, TX
and W.L. Hurley, The Glosten Associates, WA

U.S. Oceanographic Research Vessels and the International Safety Management Code (ISM) 543
J. M. Ringelberg, G.W. Beers & T.B. Powell,
JMS Naval Architects & Salvage Engineers, CT

Volume 2

Session 2D:

Remotely Operated Vehicles

Co-Chairs: D. Michel, Global Industries, TX
H. Maeda, Univ. of Tokyo IIS, JAPAN

A Basis for Closed Loop ROV Control 548
K. Smrcina, SonicWorks MA



IES An Open System for Underwater Inspection	549
A. Martins, F. Pereira, N. Cruz, A. Matos, S. Greelish & J. Sousa, FEUP-DEEC, PORTUGAL	

Performing Ship Hull Inspections Using a Remotely Operated Vehicle.....	555
D.C. Lynn & G.S. Bohlander, NSW, MD	

ROV Exploration of the Keel of the Campbell Ice Tongue in Antarctica	563
R. Bono, M. Caccia, E. Spirandelli & G. Veruggio C.N.R. - Istituto Automazione Navale, ITALIA	

A Specialized ROV for Cleaning Groundwater Recharge Basins.....	567
D.M. Kocak, J.W. Neely & J. Holt, HBOI, FL and M. Miyake, Orange County Water Dist, CA	

Session 3D:

Underwater Acoustic Telemetry

Co-Chairs:

P. Sabathe, Thompson Marconi Sonar, FRANCE
J. Illgen, Illgen Simulation Technologies, CA

Results Using an Alternative Approach to Channel Equalization Using a Pattern Classification Strategy	580
F.M. Caimi & G.A. Hassan, Florida Institute of Technology, FL	

An Time-Domain-Oriented Multiple Access Protocol for Underwater Acoustic Network Communications.....	585
B. Hou, O.R. Hinton, A.E. Adams & B.S. Sharif, University Of Newcastle, England	

Channel-Estimation-Based Adaptive Equalization of Underwater Acoustic Signals	590
M. Stojanovic, Northeastern University and L. Freitag & M. Johnson, WHOI, MA	

An Adaptive Array Direct-Sequence Code Division Multiple Access (DS-CDMA) Receiver for a Shallow-Water Asynchronous Multiuser Network	596
C.C. Tsimenidis, O.R. Hinton, B.S. Sharif & A.E. Adams, University of Newcastle, U.K.	

Ocean Acoustic IR Measurement and Characterization for ACOMMS Performance Prediction	601
F.M. Caimi, FIT/HBOI, M.C. Carroll, HBOI, FL and R. Tongta, Suranaree University of Technology, THAILAND	

Session 4D:

Real Time Measurement Systems

Co-Chairs:

C. Woody, NDBC, MS
S. Holt, Mitretek Systems, VA

Altimeter Data for Operational Use in the Marine Environment	605
S. Digby & T. Antczak, JPL, CA and R. Leben, G. Born & S. Barth, Univ. of Colorado, CO, and R. Cheney, NOAA/LASA, MD, and D. Foley, JIMAR, HI and G. Goni, NOAA/AOML, FL and G. Jacobs, NRL, MS, and N. Shay, Univ. of Miami, FL	

A Study on Potential Open Systems Compliant Processors for Oceanographic and Atmospheric Systems	614
S.M. Holt, Mitretek Systems, VA	

The Coastal Marine Demonstration of Forecast Information to Mariners Off the U.S. East Coast:

A Status Report	620
R.M. Barazotto & F. Aikman, NOAA NOS, L.C. Breaker, NOAA NWS, DC, L. Walstad, Univ. of Maryland, MD and F.C. Klein, Mitretek Systems, VA	

Implementation of a Hydroacoustic Monitoring System for the Comprehensive Nuclear-Test-Ban Treaty	624
P. Grenard, Comprehensive Nuclear-Test-Ban Treaty Organization, AUSTRIA	



**A Set of Acoustical Systems
for Environment Monitoring
on the Oceanic Shelf..... 630**

V.A. Akulichev, S.I. Kamenev, Y.N. Morgunov,
A.V. Nuzhdenko & S.I. Penkin, Pacific Ocean Inst.
Far East Branch, Russian Acad. of Sci., RUSSIA

**Session 5D:
Vessel Antifouling Paint**

Co-Chairs: A. Mearns, NOAA NMF, WA
G. Shelef, TECHNION-IIT, ISRAEL

**Aquatic Ecological Risks Posed
by Tributyltin in U.S. Surface Waters:
Pre-1989-1997 Data 631**

R. Cardwell, M.S. Brancato, J. Toll,
D. DeForest & L. Tear, Parametrix, WA

**An Evaluation of Risks to U.S.
Pacific Coast Sea Otters
Exposed to Tributyltin 642**

D. MacLellan, M.S. Brancato & D. DeForest &
J. Volosin, Parametrix, WA

**Impacts of Invasive Species Introduced
through the Shipping Industry 676**
M.S. Brancato & D. MacLellan, Parametrix, WA

**Session 6D:
Ropes and Tension Members**

Co-Chairs: F. Sloan, Allied Signal Performance
Fibers Technology VA
O. Lopez-Yanez, Coordinated Equipment, CA

**Use of High Modulus Fiber
Ropes in Large Scale Towed
Marine Applications 677**
P. Sack & K. Schuetzner, Veritas DGC, TX

**Creep-Rupture Models and
Experimental Results for
Polyester Rope 681**
E.W. Huntley & A.S. Whitehill, Whitehill Mfg, PA

**DeepStar Taut Leg Mooring
Polyester Test Program 690**
P. Devlin, Texaco and S. Homer, BHP Petro, TX
J. Flory, Tension Technology International, NJ

High Modulus Rope Designs 698
D. Ryan, Puget Sound Rope Works, WA

**The Evaluation of Long-Term
Marine Overfinish Stability
on Mooring Ropes 702**
S.M. Richard, W.A. Archie & F.E. Sloan,
AlliedSignal Performance Fibers Tech. VA

**Session 7D:
Noise, Reverberation and Propagation
Chair: D. Ramsdale, Neptune Sciences, MS**

**Adaptive and Mobile Biomimetic
Sonar Recognizes Objects
from Echoes 707**
R. Kuc, Yale University, CT,
M.F. Kirichenko, Nat'l Acad. of Sci. of Ukraine &
M.P. Lepekha, T. Shevchenko Univ. UKRAINE

**A Robust Automatic Gain Control
Technique for Serially Multiplexed
Underwater Acoustic Arrays 713**
J.M. Stevenson, S.G. Briest, A.D. Fronk,
V.K. McDonald, J.R. Olson & C. Fletcher,
SPAWAR, CA

**Measurements of Underwater
Sound Intensity Vector 717**
D.L. Hutt, P.C. Hines & A.J. Hamilton, Defence
Research Establishment Atlantic, CANADA

**Session 8D:
Matched Field Processing
Co-Chairs: D. Ramsdale, Neptune Sciences,
MS W. Fox, APL University of Washington, WA**

**Matched Field Processing by Using a
Short Vertical Array: Experimental
Results in Deep Water 723**
R.H. Zhang, L.R. Guo, S.H. Zhou & J. Yan,
Chinese Academy of Sciences, CHINA



3D Adaptive Matched Field Processing for a Moving Source in a Shallow Water Channel	728
L.M. Zurk, N. Lee & J. Ward, MIT Lincoln Lab, MA	

A Cross-Relation Based Matched Field Processor for Source Localization with Random Noise Sources	732
R.M. Dizaji, N.R. Chapman & R.L. Kirlin, University of Victoria, CANADA	

Session 1E:	
Virtual Ocean Data Systems	
Chair:	E. Gough, Univ. of Washington APL, WA

AUV Data Processing and Visualization Using GIS and Internet Techniques	738
A. Delarue, E. An & S. Smith, FAU, FL	

Multi-Channel Acoustic Simulator (MCAS) for Testing Multi-Hydrophone Sonar Systems	743
T. Peterson, SPAWAR, CA	

Telesonar Network Modeling and Simulation	747
K. Raysin, E. Dorman & S. Matheny & SAIC and J. Rice, SPAWARSYSCEN, CA	

Session 2E:	
ROV Applications	
Chair:	R.L. Wernli, SPAWARSYSCEN, CA

Successful Techniques for Supporting MultiDisciplinary Science Programs with ROPOS	753
J.F. Garrett & K. Shepherd, Canadian Scientific Submersible Facility, CANADA	

Dynamics Simulation of Low Tension Tethers	757
B. Buckham & M. Nahon, University of Victoria, CANADA	

From Mars to Marine Archaeology: A Report on the Jeremy Project	767
J.M. Ota, C.A. Kitts, A. Weast & J. Bates, Santa Clara University, CA	

Session 3E:	
Navigation	
Chair:	C. Richards, C A Richards, TX

Critical Elements in the Development of Modern Shipboard Electronic Aids to Navigation	*
D.A. Phinney, Volpe National Transportation Systems Center, MA	

Development and Implementation of a Low-Cost LBL Navigation System for an AUV	774
A. Martins, N. Cruz & F. L Pereira, FEUP-DEEC, PORTUGAL	

A Comparison of a Mechanically Stabilized Gyrocompass and a GPS-Aided Inertial Navigation System	780
W. Bradley & F. Van de Kop, USNOO, MS	

Session 4E:	
Real Time Monitoring	
Co-Chairs:	C. Woody, NDBC, MS S. Holt, Mitretek Systems, VA

Architecture and Development of an Environmental Acquisition and Reporting System	785
P.A. Lessing & B. Edwards, NDBC, MS	

Puget Sound Wind Speed Data Collection System	789
J. Nortz, Washington State Ferries and J. Creech, Meteor Communications, WA	

* Paper received too late for publishing



**Assessment of Environmental
Conditions Using Automatic
Monitoring Systems 796**

G. Zappalà & E. Crisafi, Istituto Sperimentale
Talassografico CNR - Messina, and
L. Alberotanza, Istituto per lo Studio della
Dinamica delle Grandi Masse CNR -VENEZIA

**Monitoring Program for the
First Steel Catenary Riser
Installed in a Floating
Platform in Deep Water 801**

R.Z. Machado, M. Mourelle, R. Franciss,
R.M. Silva & C.S. Lima, R. Eisemberg &
D. Oliveira, Petrobras R&D Center, BRASIL

**An Automated Sidescan Sonar
Pipeline Inspection System 811**

R.C. Gauer, A. McFadzean & C. Reid,
Coda Technologies, TX

Session 5E:

Northwest Coastal Restoration Success

Chair: R. Bellmer, NOAA Fisheries, MD

**Restoration of Habitat
Functions in an Urban
Estuary: Progress and
Lessons from Elliott Bay 817**

C.D. Tanner, Fish and Wildlife Service and
R.C. Clark, NOAA Fisheries NW Region, WA

**Restoration Case Study:
Commencement Bay Natural
Resource Damage Assessment
Restoration Actions 822**

J.K. Lantor, Fish and Wildlife Service and
R.C. Clark, NOAA Fisheries

**Blackbird Mine Natural Resource
Damage Assessment 827**

N.E. Iadanza, NOAA Fisheries and
D. Chapman & T. Penn, NOAA ORR, WA

**Habitat Restoration Program of the Army
Corps of Engineers: Recovering Our
Nation's Marine Resources 833**

P. Cagney, US Army Corps of Engineers, WA

**Session 6E:
Offshore Structures**

Chair: M. Atturio, NFESC, CA

**Hydroelastic Response of a
Mat-Type, Floating Runway near
a Breakwater in Irregular Seas 839**

R.C. Ertekin, J.W. Kim &
D. Xia Univ. of Hawaii, HI

**Planning and Design of Floating
Berths for Passenger-Only
Ferry Terminals 848**

D.T. Joque & F.L. Yang, BERGER/ABAM
Engineers and L.R. Demich, Sverdrup Civil, WA

**Experimental Study on a
Pile-Supported Structure
Built on a Reef Subjected
to Tsunamis 862**

K. Sekita, Tokai University, J. Maki, Tomoe and
A. Okamura and M. Hagiwara, Nippon Steel,
JAPAN

**Corroborative Research on the
Use of Mega-Float as Airport 868**

E. Isobe, Technological Research Association of
Mega-Float, JAPAN

**Session 7E:
Seafloor Mapping**

Chair: M.M. Harris, NRL, MS

**GeoAcoustic Echo Processor (GEP)
for High Resolution Mapping and
Bottom Classification 873**

J.T. Ambrose, Computer Sciences Corp, NJ;
M. O'Brien, T. Schmitt & H. Vanbrundt, SPAWAR,
CA and S. Zietz, Drexel University, PA

**Multibeam Sonar Image Matching
for Terrain-Based Underwater
Navigation 882**

O. Strauss, F. Comby & M.J. Aldon,
LIRMM, FRANCE



Seabed Segmentation Using a Combination of High Frequency Sensors	888
E. Pouliquen, B. Zerr, N.G. Pace & F. Spina, SACLANTCEN, ITALY	

Look-Ahead Bottom Profiling with a Small Acoustic Aperture	894
J.S. Bird & P. Kraeutner, Simon Fraser, CANADA	

A Decade of Isophase Swath Bathymetry	901
N. Lesnikowski, Williamson & Associates, WA	

Session 8E: Experimental Signal Processing	
Chair:	R. Dwyer, IEEE, CT

A Study of Enhanced Signal Processing on Multibeam Bathymetric Data	904
G. Shah & K. Talukdar, SeaBeam Instruments MA	

Interpolation Beamforming with a Bent Array	910
D.N. Swingler, Saint Mary's University and B.H. Maranda, DREA, CANADA	

Experimental Investigations into High Resolution Sonar Systems	916
M.A. Pinto, S. Fioravanti & A. Belletini, SACLANTCEN, ITALY, A. Hetet & Y. Perrot, GESMA, FRANCE. and S. Chapman, & D.R. Bugler, DERA, UK.	

High-Resolution Beamforming for Multibeam Echo Sounders Using Raw EM3000 Data	923
A. Ronhovde & S. Holm, University of Oslo and L. Yang, SINTEF-ECY, and T. Taxt, University of Bergen, NORWAY	

Joint Channel and Data Estimation Genetic Algorithm Based Blind Equalization	931
F.M. Caimi & D Wang, FIT, FL	

Session 9E: Treatment of Regulated Discharges from Drydocks and Shipyards I	
--	--

Session 1F: Data Visualization	
Co-Chairs:	E. Gough, Univ. of Wash. APL, WA C.D. Levings, West Vancouver Lab, CANADA

ISTV: Interactive Structured Time-Varying Visualizer	938
R.J. Moorhead, M.A. Chupa, K. Gaither & R. Vickery, Mississippi State Univ. and S. Nations & A. Johannsen, Engineering Animation, MS	

Simulation of Underwater Sensor Networks	945
S. McGirr, SPAWARSYSCEN, K. Raysin, SAIC, and C. Ivancic & C. Alspaugh, NC Consulting, CA	

Realtime 3D El Niño/La Niña Visualizations and Animation from the TAO Buoy Network in the Tropical Pacific	951
D.C. McClurg & C.W. Moore, UW/NOAA-PMEL and N.N. Soreide, NOAA/PMEL, WA	

Modeling Mantle Dynamics in the Banda Sea Triple Junction: Exploring a Possible Link to El Niño Southern Oscillation	955
B.A. Leybourne and M.B. Adams, NAVOCEANO, MS	

Session 2F: Unmanned Underwater Vehicles	
Co-Chairs:	C. Brancart, C S Draper Lab, MA R. Blidberg, AUSI, MA

HUGIN - Use of UUV Technology in Marine Applications	967
N. Størkersen & P.E. Hagen, Norwegian Defence Research Establishment and K. Vestgard, Kongsberg Simrad, NORWAY	



Conference Proceedings

Table of Contents

Depth Accuracy in Seabed Mapping with Underwater Vehicles 973

B. Jalving, Norwegian Defence Research
Establishment, NORWAY

Improving the Safety of AUVs 979

A. Ortiz, J. Proenza, & G. Oliver,
University of the Balearic Islands, SPAIN
and G. Bernat, University of York, UK

Session 3F:

Underwater Telemetry / Modems

Chair: V. McDonald, SPAWAR, CA

Channel-Estimation-Based

Adaptive Equalization of

Underwater Acoustic Signals 985

M. Stojanovic, Northeastern University, and
L. Freitag and M. Johnson, WHOI, MA

A Matched Field Processing

Approach to Underwater

Acoustic Communication 991

J. Gomes & V. Barroso,
Instituto Superior Tecnico, PORTUGAL

A DFE Coefficient Placement

Algorithm for Underwater Digital

Acoustic Communications 996

M.J. Lopez, MIT & A.C. Singer,
Univ. of Illinois and
S.L. Whitney & G.S. Edelson, Sanders, IL

Performance Measurements of a

Diverse Collection of Undersea

Acoustic Communications Signals 1002

V. McDonald, J. Rice, M. Porter, & P. Baxley,
SPAWAR, CA,

Session 4F:

Real Time Monitoring

Co-Chairs: S. Holt, Mitretek Systems, VA
C. Woody, NDBC, MS

Shallow Water Multiplexer

Development for the South Florida Ocean

Measurement Center (SFOMC) 1009

E. An, R. Coulson, J. Webb, D. Williams,
R. Reibman, & S. Dunn, FAU, FL

Dial-A-Buoy Reads NDBC

Observations 1017

D.B. Gilhousen, NDBC, MS

Session 5F:

Marine Living Resources

Co-Chairs: P. Hoagland, WHOI, MA
P.H. Viet, Vietnam National Univ, VIET NAM

The Deep Ocean Water Upwelling

Machine Using Density Current -

Creation of Fishing Ground

and Absorption of CO₂ 1019

K. Ouchi, Nakashima Propeller, and H. Nakahara,
Research Institute of Ocean Economics, JAPAN

Reef Degradation Following Mass

Coral Bleaching in Kenya 1025

R.M. Mdodo, Kenya Marine Fisheries, KENYA

Session 6F:

Electro/Optical Cables and Connectors

Chair: T. Coughlin, Vector Cable, TX

Finite Element Stress Analysis

of Cables 1026

R.H. Knapp & S. Das, Structural Solutions, HI

Cable Route Surveys From a

Surveyors Perspective 1034

A. St. Clair Wright, Williamson & Associates, WA



Session 7F:

Inversion Techniques

Co-Chairs: D. Rouseff, Univ. of Washington, WA
R. Zhang, Chinese Acad. Of Sciences, CHINA

Geoacoustic Inversion Via

Genetic Algorithm Using a

Broadband Signal and

Two Hydrophones 1038

W. Seong & C. Park, Seoul National University,
KOREA

Geo-Acoustic Inversion of

Experimental Data from Two

Shallow Water Sites 1046

M. Siderius, P.L. Nielsen & F.B. Jensen,
SACLANTCEN, ITALY

Broad-Band Acoustic Propagation

Through Moving Internal Solitary

Wave Packets in Shallow Water 1052

A. Turgut & S.N. Wolf, NRL, DC and
D. Rouseff, Univ. of Washington APL, WA

Session 8F:

Active Sonar Signal Processing

Chair: R. Dwyer, IEEE, CT

Diversity in Multistatic Active Sonar 1058

L. Mozzone, S. Bongi & F. Filocca,
SACLANTCEN, ITALY

Ocean Variability Effects on Sound

Propagation in Shallow Water 1064

P.L. Nielsen, M. Siderius & F.B. Jensen,
SACLANTCEN, ITALY

Mapping Seabed Acoustic Reflection

and Scattering Coefficients Using

Tactical Sonar Systems 1070

M. Sundvik, E. Rabe & M. Vaccaro, NUWC, RI

Session 9F:

Treatment of Regulated Discharges from Drydocks and Shipyards II

Session 1G:

Ocean Data for Dispersed

Collaborative Groups

Co-Chairs: E. Gough, Univ. of Wash. APL, WA
V. Akulichev, Pacific Oceanologic Inst. RUSSIA

Interactive Java Graphics of Network-

Distributed in-situ Data Sets in a

Collaborative Tool Environment 1076

D.W. Denbo, University of Washington and
C.R. Windsor, MacroStaff, WA

A Data-Centered Approach

to Hydrographic Processing 1080

D.A. Caswell & S. Cannon, Racal Pelagos, CA

Volume 3

Session 2G:

AUV Mission Control

Co-Chairs: J. Bunce, Neptune Sciences, LA
C. Brancart, C S Draper Lab, MA

Internet Mission Control of the

ROMEO Unmanned Underwater

Vehicle Using the CORAL

Mission Controller 1081

G. Bruzzone, M. Caccia, R. Bono & G. Veruggio,
CNR-Istituto Automazione Navale, ITALY and
C. Ferreira, C. Silvestre, P. Oliveira & A. Pascoal
Instituto Superior Técnico, PORTUGAL

A Reconfigurable Mission Control

System for Underwater Vehicles 1088

J.E. Silva, A. Martins & F.L. Pereira, Faculdade de
Engenharia da Universidade do Porto - DEEC,
PORTUGAL

* Paper received too late for publishing - see last pages of Volume 3



Session 3G:

Optics and Imaging

Chair: M. Olsson, Deepsea Power & Light, CA

High Resolution Underwater

Acoustic Imaging 1093

I.S.F. Jones, University of Sydney, AUSTRALIA

Development of Miniature

Head-Mounted, Virtual Image

Displays for Navy Divers 1098

D.G. Gallagher, NCSC, FL

A 3-D Laser Line Scanner for

Outcrop Scale Studies

of Seafloor Features 1105

D.M. Kocak & F.M. Caimi, HBOI, FL and

P.S. Das & J.A. Karson, Duke University, NC

Session 5G:

Regulating Vessel Antifouling Paint

Chair: A. Mearns, NOAA NMF, WA

Assessing the Impact of Antifouling Compounds in the Marine Environment - Lessons to be Learned from the Use

and Misuse of Biological Indicators of TBT Contamination 1115

S.M. Evans & G.J. Nicholson,
Dove Marine Laboratory, U.K.

Regulating Biocidal Antifoulants:

Creating a Level Playing Field *

J. Toll, M.S. Brancato and D. DeForest,
Parametrix, WA

The Effects of Regulating the Use of TBT-Based Antifouling Paints on

TBT Contamination 1119

S.M. Evans & R. Smith, Dove Marine Lab, U.K.

Session 6G:

Seafloor Properties and Engineering

Co-Chairs: H. Herrman, NFEFC, CA
J. Preston, Quester Tangent, CANADA

The Strength of Correlations

Between Geotechnical Variables

and Acoustic Classification 1123

J.M. Preston & W.T. Collins, Quester Tangent, and

D.C. Mosher, Geological Survey of Canada,

and R.H. Kuwahara, DREA, CANADA and

R.H. Poeckert, Racal-Pelagos, CA

Integration of Multibeam Bathymetry

and Sidescan Sonar Data for

Geological Surveys 1129

R. Parrott, G. Fader & J. Shaw, Geological Survey

of Canada and J. Hughes-Clarke & E. Kamerrer,

University of New Brunswick, CANADA

Acoustic Observations of a Fluid Mud

Layer Transporting Sediment on the

Northern California Shelf 1134

P. Traykovski, J.D. Irish & J.F. Lynch, WHOI, MA

Preliminary Relationships Between

Precision Acoustic Observations and Core

Geotechnical and Chemical Properties at

Contaminated Sites 1138

D.D. Caulfield, Caulfield Engineering, CANADA

Session 7G:

Inversion Techniques

Chair: A. Turgut, NRL, DC

Determination of Sound Velocity Profile

Errors Using Multibeam Data 1144

W.J. Capell, SeaBeam Instruments, MA

Multi-Sensor Surveillance with in-situ

Environmental Characterization 1149

W.M. Sanders, NRL, MS

* Paper received too late for publishing



Measurements and Analysis of Scattering from Proud and Buried Targets in a Shallow-Water Laboratory Environment	1154
H.J. Simpson & B.H. Houston , NRL, DC, and C.K. Frederickson, Univ of Central Arkansas, AR, and R. Lim, NSWC, FL	

Session 8G:

Marine Education

Chair: S.H. Walker, Univ. of S. Mississippi, MS

Identification of World Wide Web Educational Materials in Conjunction with the National Sea Grant College Programs Haznet Effort	1158
S.H. Walker, University of S. Mississippi, MS and H.D. Walters, Mississippi Gulf Coast Community College, MS	

NOPP Drifter Data in the Classroom	*
S. Schoedinger, CORE, DC	

The Need to Re-Engineer University-Level Marine Science Education	1165
F.W. Hughes, The Boeing Company, WA	

Session 1H:

Naval Oceanography in the 21st Century

Co-Chairs: J. Carroll & D. Durham, NMOC, MS

Naval Oceanography: Start of the Next Millennium	1169
D.L. Durham & K.D. Cooper, Naval Meteorology and Oceanography Command (NMOC), MS	

Workflow Management in an Oceanographic Information Processing Environment	1170
J.A. Lever, L.J. Bernard & R. Starek, J. Easton, C.M. Jarrett, M. Jugan, Naval Oceanographic Office, MS	

A Concept for the Naval Oceanographic Office Survey Operations Center	1176
J.A. Lever, S. Raffa, D. McCarren, A. Lewando & M. Carran, Naval Oceanographic Office, MS	

Using a MineHunting Sonar for Real-Time Environmental Characterization	1181
S.C. Lingsch & W.C. Lingsch, Naval Oceanographic Office, MS	

Session 2H:

AUV Activity

Co-Chairs: C. Brancart, C S Draper Lab, MA

Twelve Hour Operation of Cruising Type AUV "R-One Robot" Equipped with a Closed Cycle Diesel Engine System	1188
T. Obara, Mitsui Engr & Shipbuilding, JAPAN T. Ura, University of Tokyo, JAPAN	

A Fully Interactive Dynamic Simulation of a Semi-Submersible Towing a Large Towfish	1194
M.L. Seto, ISE Research and G.D. Watts & D. Hopkin, DREA, CANADA	

Estuarine Environment Studies with Isurus, a REMUS Class AUV	1205
N. Cruz, A. Matos, A. Martins, J. Silva, D. Santos, D. Boutov & D. Ferreira, Faculdade de Engenharia da Universidade do Porto - DEEC, PORTUGAL	

* Paper received too late for publishing



Session 3H:

Oceanographic Instrumentation

Co-Chairs: K. McCoy, Ocean Sensors, CA
H.U. Oebius, Technische Universitat, GERMANY

Laboratory Evaluation and Preliminary Field Trials of a New "WOCE Standard" Idronaut Mk 317 and OS316

CTD Probe 1211

F. Graziottin, Idronaut srl. ITALY, and
G.K. Morrison, GO Environmental Services, FL
R. Stoner & F. de Strobel, SACLANTCEN, ITALY

Expendable High Precision Micro Optical Sensors to be used in Automated Concerted Profilings for Large Area Density Contouring of the Deep Sea 1218

K-H. Mahrt, University of Kiel, GERMANY and
A. Hosseinioun, Goal International, CA

A Novel Approach for Obtaining Bubble Dissolution Measurements at Sea: Results 1223

R. Costa, NUWC, RI, R.A. Roy, Boston Univ. MA
and K.W. Commander, NSWC, FL

Shallow Water Expendable and Trawler Safe Environmental Profilers 1229

R. Tyce, Univ. of Rhode Island, RI, and
F. de Strobel, V. Grandi & L. Gualdesi,
SACLANTCEN, ITALY

Session 4H:

Remote Sensing of Biological and Chemical Processes

Chair: D. Weissman, Hofstra University, NY

Monitoring Algae Blooms in the Baltic Sea :

A Multi-Sensor Approach 1234

O. Rud Stockholm Universitet, SWEDEN and
M. Gade, Universitaet Hamburg, GERMANY

Marine Pollution in European

Coastal Waters Monitored by the ERS-2 SAR: A Comprehensive

Statistical Analysis 1239

M. Gade, Univ Hamburg, GERMANY and
J.M. Redondo, Univ Politecnica de Catalunya,
SPAIN

Biological Monitoring with the Western Canadian ODAS Marine

Buoy Network 1244

J. Gower, A. Pena & A. Gargett, IOS, CANADA

Mapping Nearshore and Intertidal Marine Habitats with Remote Sensing and GPS:

The Importance of Spatial
and Temporal Scales 1249

C.D. Levings, M.S. North, G.E. Piercey,
G. Jamieson, & B. Smiley, Fisheries and Oceans,
CANADA

Session 6H:

Oil Spill Trajectory Tools

Chair: A. Mearns, NOAA Marine Fisheries, WA

The NOAA Trajectory

Analysis Planner: TAP II 1256

C.H. Barker, NOAA/OR&R/HAZMAT, WA

GNOME: NOAA's Next Generation Spill

Trajectory Model 1262

C. Beegle-Krause, NOAA/OR&R/HAZMAT, WA

Session 8H:

Marine Education

Chair: S.H. Walker, Univ. of S. Mississippi, MS

Project Oceanography: Bringing Oceanography from the Ocean, the Laboratory, and space to Students in the Middle

School Classroom 1267

P.G. Coble, & J.A. Rasure,
University of South Florida, FL



Table of Contents

Conference Proceedings

Education for a Marine Technical Workforce: The Marine Advanced Technology Education Center 1270
N.L. Crane & D.E. Sullivan,
Monterey Peninsula College, CA

Session 9H:
Policy and Regulatory, R&D Programs Discussion Related to Discharges from Drydocks and Shipyards

Session 1I:
Naval Oceanography in the 21st Century
Co-Chairs: J. Carroll & D. Durham, NMOC, MS

Construction and Visualization of a Seafloor Backscatter Database Using Naval "Through the Sensor" Technology 1275
W.E. Brown, Naval Oceanographic Office, MS and
M.L. Barlett & J.F. England, The University of Texas at Austin, TX

Ship to Shore "Digital Status Report" Multimedia Communication 1281
S.C. Cash, NAVOCEANO, MS

Reconstruction of Sampled and Modeled Oceanographic Information Using an Exploratory Environment 1284
P. Gruzinkas & D. Cole, USNOO,
and A. Hass, Logicon, MS

Satellite Data and Naval Oceanography: A Growing Symbiosis *

R. Crout, PSI and J. Boatman, NMOC, MS

Airbourne Lidar: A Surveying Tool for the New Millenium 1290
R.A. Smith, Naval Oceanographic Office, MS
G.R. West, John Chance and Associates, LA and
J. Lillycrop, Army Corps of Engineers

Session 2I:
UUV Developments

Chair: J. Bunce, Neptune Sciences, LA

Beach and Near-Shore Crawling UUV for Oceanographic Measurements 1300
J.C. Evans, J.S. Smith, P. Martin & Y.S. Wong,
Univ. of Liverpool, U. K.

Development of Deep Sea Free Swimming ROV "UROV7K" 1307
T. Aoki, T. Murashima, S. Tsukioka, H. Nakajyoh &
M. Ida, JAMSTEC, JAPAN

Mission Command Macros for Autonomous Underwater Vehicle 1312
X. Yuan, S. Snowden, S. Smith & M. Evett, FAU
and K. Ganesan, MicroSoft Company, FL

Session 3I:
Navigation

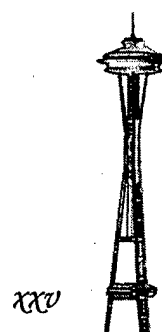
Chair: C. Richards, C A Richards, TX

Restoration of Maritime Navigation Systems in Central American Ports 1317
L. de Cáceres, COCATRAM, NICARAGU and
M.J. Moroney, Volpe National Transportation Systems Center, MA

ROV Actuator Fault Diagnosis through Servo-Amplifiers' Monitoring: An Operational Experience 1318
R. Bono, Ga Bruzzzone, Gi Bruzzzone & M. Caccia,
Istituto Automazione Navale, ITALY

* Paper received too late for publishing

Seattle · 13 - 16 September 1999



Session 4I:

Measurement of Ocean Dynamics with Radar and Radiometers

Chair: W.J. Plant, APL Univ. of Washington, WA

An Accuracy Assessment of Shoreline
Data for Castle Bay Alaska Compiled
from Synthetic Aperture Radar 1325
G.H. Tuell, J.R. Lucas & D.B. Graham
NOAA/NOS/NGS, MD

W-Band Radar Measurements of
Laboratory Water Waves 1333
G. Connan & R. Garello, ENST, FRANCE and
H.D. Griffiths & P.V. Brennan,
University College London, UK

Polarmetric Radiometer Sensing of
Sea Surface Friction Velocity 1338
D.E. Weissman, Hofstra University, NY and
V.G. Irisov, Envir. Research Labs/NOAA, CO
and W.J. Plant & W. Keller,
APL Univ. of WA, WA

Session 6I:

Physical Oceanography

Chair: P. Hoagland, WHOI, MA

Acoustical Remote Sensing
of Ocean Internal Waves: Progress
and Remaining Challenges 1341
D. Rouseff, T.E. Ewart & S.A. Reynolds,
APL University of Washington, WA

Double Diffusion in the Mode of "Salt Fingers"
in the Ocean: New In Methodology of
Laboratory Studies 1347
V.V. Koblyansky, L.S. Vilentchik, M.M. Domanov,
D.L. Lushnikov & I.G. Ahmetsafin,
Federal Research Center MCB, RUSSIA

Tidal Zoning and Vertical
Reference Measuring Cook
Inlet, Alaska 1999 1351
J. Oswald, LCMF and D. Lockhart & R. Richards,
Racal Pelagos, CA

Session 7I:

Transducers and Arrays

Chair: B. Maranda, DREA, CANADA

Simulation & Control Techniques Utilized
for Generic Assessment of a Fully
Reelable Submarine Towed Array
Handling System 1352
S.P. Tomlinson, D. Cowling & J.S. Baker,
DERA, U.K.

The Development of a Sonobuoy
Using Sparker Acoustic Sources
as an Alternative to Explosive
SUS Devices 1367
R.B. Schaefer, Phoenix Science & Technology and
D. Flynn, NAWC, MA

SIREM: An Instrument to
Evaluate Superdirective and
Intensity Receiver Arrays 1376
P.C. Hines & D.L. Hutt, DREA, CANADA

Session 8I:

Current Issues in Puget Sound

Chair: A. Mearns, NOAA Marine Fisheries, WA

The Puget Sound Basin and Salmon:
Developing a Scientific Basis
of Understanding *
R.C. Francis, A. Strom, J. Nelson,
L. Weitkamp & B. Tweit, University of
Washington, WA

The Puget Sound Ambient
Monitoring Program *
J. Newton, Puget Sound Water Quality Action
Team, WA

The Sound is Cleaner:
A Century of Contaminant Trends
Observed from Dated Cores 1381
E.A. Crecelius, L.F. Lefkovitz & V.I. Cullinan
Battelle Marine Science Lab, WA

* Paper received too late for publishing



Session 9I:

Panel Discussion on Treatment of Regulated Discharges from Shipyards and Drydocks

Session 1J:

Satellite Communication

Chair: D. Ramsdale, Neptune Sciences, MS

Oceanographic DataLink (ODL) 1395
K.A. Gamache & P.E. Fogel, ViaSat, MA

Performance Analysis of the Real-Time Motion Compensation System Controlling a Directional Antenna Aboard the OceanNet Buoy 1404
M.O. Mathewson, Seatex & W. Covell, Harris, WA

Bi-directional Communication into the Deep Ocean based on OrbComm Satellite Transmission and Acoustic Underwater Communication 1405
G. Meinecke, V. Ratmeyer & G. Wefer, University of Bremen, GERMANY

Session 2J:

AUV Developments

Chair: J. Bunce, Neptune Sciences, LA

Using Small AUVs for Oceanographic Measurements 1410
M. Dhanak, E. An, K. Holappa & S. Smith, FAU, FL

Application of Swimming Functions of Aquatic Animals to Autonomous Underwater Vehicles 1418
N. Kato, Tokai University, JAPAN

Session 3J:

Oceanographic Sensors

Co-Chairs: K. McCoy, Ocean Sensors, CA
N.C. Hoi, Vietnam Oceano Inst. VIET NAM

The Optical Refractometer Project OPRA - A Further Development of an in situ Going Optical Density Measuring Sensor 1425
C. Waldmann, Univ. of Bremen, GERMANY

Location and Recovery of Lost Instruments Using Acoustic Targets 1429
A.T. Morrison, McLane Research Lab. and
A.J. Williams, WHOI, MA

Precise Heading and DGPS Measurements of Vessel Motion Improve VM-ADCP Current Measurements Significantly 1435
J-M. Godhavn, Navia Maritime and
P. Jaccard, University of Bergen, NORWAY

Performance Data of a Buoyancy Driven Deep Sea YOYO- Profiler for Long Term Moored Deployment 1441
C. Waldmann, Univ. of Bremen, GERMANY

Session 4J:

Measurement of Ocean Dynamics with Radar and Radiometers

Chair: D. Weissman, Hofstra, NY

Signal Received by an Airborne Polarimetric Bistatic Radar Observing the Sea Surface 1446
O. Airiau & A. Khenchaf, Univ. Nantes, FRANCE

Sea Surface Scattering for Near-Grazing Incidence 1452
A. Khenchaf, University of Nantes, FRANCE



Session 5J:

Advances in Oil Spill Response

Chair: A. Mearns, NOAA NMF, WA

Use of In-Situ Burning as Part of the Oil Spill

Response Toolbox 1457
N. Barnea, Office of Response and Restoration,
NOAA, WA

Ballast Water Treatment During Emergency Response: The Case of the *M/T Igloo Moon* 1463

B. Benggio, NOAA HazMat, A. Mearns NOAA
Marine Fisheries and
T. Waite, University of Miami, FL

Resolving Alaska and West Coast Dispersant Issues 1469

A. Mearns, NOAA Marine Fisheries, WA

Session 6J:

Non-Acoustic Imaging

Chair: F.M. Caimi, HBOI, FL

Undersea Object Detection and Recognition: The Use of Spatially and Temporally Varying Coherent Illumination 1474

F.M. Caimi, J.H. Blatt & B.C. Bailey, FIT, FL

PI Controller for Visual Tracking: Further Results 1480

H. Tairi, B. Chaouke, L. Masmoudi & L. Radouane,
Faculty of Sciences, MOROCCO

Fanbeam Hyperspectral Acquisition for Underwater Applications 1486

E. Yafuso, R. Anderson & R. Seiple
Science and Technology International, HI

Session 7J:

Underwater Acoustic Sensors

Chair: W.M. Carey, NUWC, CT

A Digital Programmable High Resolution 200kHz Water Column Profiler 1490

W.W. Cartier & D.D. Lemon,
ASL Environmental Sciences, CANADA

Beamforming and Imaging with Acoustic Lenses in Small, High-Frequency Sonars 1495

E.O. Belcher, APL Univ. of Washington, WA
and H.Q. Dinh, NEOD & D.C. Lynn, NSWC, MD
and T.J. Laughlin, NSWC, IN

How to Succeed at Hydrographic Surveying and Related Services for Multiple Sheets in the Upper Cook Inlet, Alaska: Planning, Testing, Training and Attention to Detail 1500

R. Richards, D. Lockhart, W. Gilmour, C.
MacKenzie & E. Saade, Racal Pelagos, CA



POSTER SESSION

Exploring 3-Dimensional Oceanographic Data Sets on the Web Using Virtual Reality Modeling Language 1501
C.W. Moore & D.C. McClurg, Univ. of Washington and N.N. Soreide & A.J. Hermann, NOAA/PMEL, WA and C. Lascara & G. Wheless, Old Dominion University, VA

Acoustic Communication Channel Modeling for the Baltic Sea 1504
P.A. Baxley, H. Bucker & J.A. Rice, SPAWAR, CA
M.D. Green, Datasonics, MA and J. Woxstroem, Undusd, SWEDEN

FSK and PSK Performance of the Utility Acoustic Modem 1512
M. Johnson, J. Preisig & L. Freitag, WHOI, MA

Experience of Working Out and Modernization of Multibeam Echosounders 1513
S. Dremoutchev, V. Iourytsin, V. Kuznetsov, A. Nosov & G. Postnov, P.P. Shirshov, RUSSIA

An Integrated Approach to Improving Tsunami Warning and Mitigation 1514
F.I. Gonzalez, E.N. Bernard, H.B. Milburn, V.V. Titov, H.O. Mofjeld, M.C. Eble, J.C. Newman, R.A. Kamphaus & C.L. Hadden NOAA/PMEL, WA

Environment of Russian Margins - The Interplay Field of Oceanology and Industry Interests 1515
L.R. Merklin, L.I. Lobkovsky & S.A. Kovachev, Shirshov Institute of Oceanology and A.N. Dmitrievsky, Institute of Oil and Gas Technologies, RUSSIA

Seafloor Characterization and Mapping Pods (SCAMP): Submarine-Mounted Geophysical Mapping 1524
D.N. Chayes & J.L. Ardai, Lamont-Doherty, NY
R.M. Anderson, Arctic Sub. Lab, CA, S. Goemmer, Johns Hopkins APL, MD, B.J. Coakley, Tulane University, LA, and M.R. Rognstad, R.B. Davis & M. Edwards, Univ. of Hawaii, HI

Investigation of Hydroacoustic Parametric Sub-Bottom Profiler Characteristics 1525
V.A. Voroiun, S.S. Konovalova, T.N. Kutsenko, S.P. Tarasov & V.I. Tlmosheibbo, Taganrog State University of Radioengineering, RUSSIA

A Versatile, Portable and Low Cost Computerized Data Logging and Charting System Compatible with Electronic Charts 1526
P. Pirillo, FDA, CFSAN, DC

Design Considerations and Peculiarities for Hyperbaric Manned Submersibles Life Support Systems 1531
E.I. Trushliakov, Ukrainian State Maritime Technical University, UKRANE, visiting scientist at University of Michigan, MI

Application of Magnetic Signature Processing to Magnetic Center Pinpointing in Marine Vehicles 1532
A.V. Kildishev & J.A. Nyenhuis, Purdue Univ. IN
D.L. Boyko, P.N. Dobrodeyev & S.A. Volokhov, National Academy of Sciences, UKRAINE

Analysis of a Multi-Element Multi-User Receiver for a Shallow Water Acoustic Network (SWAN) Based on Recursive Successive Interference Cancellation (RSIC) Technique 1537
B. Hou, O. Hinton, B. Sharif & A.E. Adams, Univ of Newcastle Upon Tyne, U.K.



Micro ROV for Underwater Observations 1542

B.J. Rozman & L.L. Utyakov,
P P Shirshov Institute of Oceanology,
RAS, RUSSIA

New Generation of Technical Means and Methods for Ocean

Monitoring Systems 1544

L.L. Utyakov, D.G. Levchenko & I.S. Kovchin,
P P Shirshov Institute of Oceanology and
A.A. Paramonov, Experimental Design Bureau of .
Oceanology Technique and
M.A. Shakhramanian, Ministry of Extreme
Situations, RUSSIA

Acoustic Tomography of Eddy in the Western Mediterranean Sea 1548

Y.A. Chepurin, V.V. Goncharov & D.L. Aleynik,
P.P.Shirshov Institute of Oceanology, RUSSIA

Implementing a 4000 Meter HDTV Camera System 1551

M. Chaffey, MBARI, CA

Cultural Resources Investigation of the Monongahela River, Southwestern Pennsylvania, Using High-Resolution Side Scan Sonar and Magnetometer *

J.A. Boughner, Evans-Hamilton, WA

Student Poster Session

A New Way of Identifying

Buried Objects 1552

D. Boulinguez, & A. Quinquis, ENSIETA, Brest,
FRANCE

Santa Clara Remote Extreme Environmental Mechanisms (SCREAM) Laboratory:

Past, Present and Future *

C.A. Bulich, Santa Clara University, Santa Clara,
CA

Conversion of the Ocean Clipper to DPS-3 Classification 1557

J.D. Carter, C.P. Scott & H.M. Taylor, Texas A&M
University, College Station, TX

W-band Radar Measurement of Laboratory Waves *

G. Connan, ENST de Bretagne, Brest, FRANCE

Fast Interpolation, Segmentation and Visualization of 3D Sonar Seabottom Data by Using Tree Structures 1571

R.C. Loke & J.M.H. du Buf, University of Algarve,
Faro, PORTUGAL

Matched Arrival Processing for Efficient Inversion in Underwater Acoustics 1577

X. Ma, & Z. Michalopoulou, New Jersey Institute of
Technology, Newark, NJ

Diver Navigation and Tracking System 1581

D. Newborough, & B. Woodward, Loughborough
University, Loughborough, U.K.

Multipath TimeDelay Detection and Estimation for Ocean Acoustic Tomography 1587

F. Poree, ENST de Bretagne, Brest, FRANCE

* Paper received too late for publishing



Verification of a Vertical-Plane Simulation Model for the

REMUS AUV *

T. Prestero, MIT, Cambridge, MA

Interferometric Noise for

Sidescan Sonar 1591

C. Sintès, and B. Solaiman, GESMA, Brest,
France

Matched Field Processing:

Environmental Focusing
and Source Tracking with
Applications to North

Elba Data Set 1598

C. Soares, & S.M. Jesus, University of Algarve,
Faro, PORTUGAL and A. Waldhorst, University
Bochum, GERMANY

Acoustical Remote Sensing with Spatially Located Transducers

in the Surf Zone *

B. Strully, University of Washington,
Seattle, WA

* Paper received too late for publishing



A

Abraham, D.A.	Vol. 1 pg. 279
Abraham, D.A.	Vol. 1 pg. 284
Adams, A.E.	Vol. 1 pg. 216
Adams, A.E.	Vol. 2 pg. 585
Adams, A.E.	Vol. 2 pg. 596
Adams, A.E.	Vol. 3 pg. 1537
Adams, M.B.	Vol. 2 pg. 955
Ahmetsafin, I.G.	Vol. 3 pg. 1347
Aikman, F.	Vol. 2 pg. 620
Airiau, O.	Vol. 3 pg. 1446
Akulichev, V.A.	Vol. 2 pg. 630
Alberotanza, L.	Vol. 2 pg. 796
Alcom, A.	*
Aldon, M.J.	Vol. 2 pg. 882
Aleynik, D.L.	Vol. 3 pg. 1548
Allison, L.	Vol. 1 pg. 269
Allsup, G.	Vol. 1 pg. 377
Alspaugh, C.	Vol. 2 pg. 945
Ambrose, J.T.	Vol. 2 pg. 873
An, E.	Vol. 2 pg. 738
An, E.	Vol. 2 pg. 1009
An, E.	Vol. 3 pg. 1410
Anderson, S.	Vol. 1 pg. 377
Anderson, R.	Vol. 3 pg. 486
Anderson, R.M.	Vol. 3 pg. 1524
Antczak, T.	Vol. 2 pg. 605
Antonioui, A.	Vol. 1 pg. 446
Aoki, T.	Vol. 3 pg. 1307
Archie, W.A.	Vol. 2 pg. 702
Ardai, J.L.	Vol. 3 pg. 1524

B

Badiu, S.	Vol. 1 pg. 352
----------------	----------------

Bailey, B.C.	Vol. 3 pg. 1474
Baker, J.S.	Vol. 3 pg. 1352
Balasuriya, A.	Vol. 1 pg. 209
Barazotto, R.M.	Vol. 1 pg. 169
Barazotto, R.M.	Vol. 2 pg. 620
Barker, C.H.	Vol. 3 pg. 1256
Barlett, M.L.	Vol. 3 pg. 1275
Barnea, N.	Vol. 3 pg. 1457
Barnes, C.	Vol. 1 pg. 141
Barnett, A.	Vol. 1 pg. 324
Barroso, V.	Vol. 2 pg. 991
Barth, S.	Vol. 2 pg. 605
Barton, R.	Vol. 1 pg. 474
Bates, J.	Vol. 2 pg. 767
Baxley, P.A.	Vol. 2 pg. 1002
Baxley, P.A.	Vol. 3 pg. 1504
Beardsley, R.C.	Vol. 1 pg. 273
Beaujean, P.	Vol. 1 pg. 222
Beckford, C.	Vol. 1 pg. 386
Beegle-Krause, C.	Vol. 3 pg. 1262
Beers, G.W.	Vol. 1 pg. 543
Belcher, E.O.	Vol. 3 pg. 1495
Belletini, A.	Vol. 2 pg. 916
Benggio, B.	Vol. 3 pg. 1463
Benson, A.	Vol. 1 pg. 228
Benson, J.	Vol. 1 pg. 446
Bergem, O.	Vol. 1 pg. 30
Bergem, O.	Vol. 1 pg. 434
Bernard, E.N.	Vol. 3 pg. 1514
Bernard, L.J.	Vol. 3 pg. 1170
Bernat, G.	Vol. 2 pg. 979
Berntsen, B.	Vol. 1 pg. 30
Bethge, T.	*



Bills, G.A. Vol. 1 pg. 263
Bird, J.S. Vol. 1 pg. 37
Bird, J.S. Vol. 2 pg. 894
Blatt, J.H. Vol. 3 pg. 1474
Boatman, J. *

Bohlander, G.S. Vol. 2 pg. 555
Bongi, S. Vol. 2 pg. 1058
Bono, R. Vol. 2 pg. 563
Bono, R. Vol. 3 pg. 1081
Bono, R. Vol. 3 pg. 1318
Born, G. Vol. 2 pg. 605
Boubli, C. Vol. 1 pg. 222
Boughner, J.A. Vol. 1 pg. 133
Boughner, J.A. *

Boulinguez, D. Vol. 3 pg. 1552
Boutov, D. Vol. 3 pg. 1205
Boyko, D.L. Vol. 3 pg. 1532
Bradley, A. Vol. 1 pg. 52
Bradley, W. Vol. 2 pg. 780
Brancato, M.S. Vol. 2 pg. 631
Brancato, M.S. Vol. 2 pg. 642
Brancato, M.S. Vol. 2 pg. 676
Brancato, M.S. *

Breaker, L.C. Vol. 2 pg. 620
Brennan, P.V. Vol. 3 pg. 1333
Briest, S.G. Vol. 2 pg. 713
Briggs, M. Vol. 1 pg. 119
Brink, K.H. Vol. 1 pg. 273
Brown, W.E. Vol. 3 pg. 1275
Bruzzone, G. Vol. 3 pg. 1081
Bruzzone, Ga Vol. 3 pg. 1318
Bruzzone, Gi Vol. 3 pg. 1318
Bucker, H. Vol. 3 pg. 1504

Buckham, B. Vol. 2 pg. 757
Bulich, C.A. *

Bulich, C.A. Vol. 1 pg. 519
Bunning, B. Vol. 1 pg. 414
Burger, E.F. Vol. 1 pg. 466
Burns, J. *

C

Caccia, M. Vol. 2 pg. 563
Caccia, M. Vol. 3 pg. 1081
Caccia, M. Vol. 3 pg. 1318
Cagney, P. Vol. 2 pg. 883
Caimi, F.M. Vol. 2 pg. 580
Caimi, F.M. Vol. 2 pg. 601
Caimi, F.M. Vol. 2 pg. 931
Caimi, F.M. Vol. 3 pg. 1105
Caimi, F.M. Vol. 3 pg. 1474
Cannon, S. Vol. 2 pg. 1080
Capell, W.J. Vol. 3 pg. 1144
Cardone, V.J. Vol. 1 pg. 373
Cardwell, R. Vol. 2 pg. 631
Carran, M. Vol. 3 pg. 1176
Carroll, M.C. Vol. 2 pg. 601
Carroll, P.J. Vol. 1 pg. 363
Carter, J.B. Vol. 3 pg. 1557
Cartier, W.W. Vol. 3 pg. 1490
Cash, S.C. Vol. 3 pg. 1281
Caswell, D.A. Vol. 2 pg. 1080
Caulfield, D.D. Vol. 2 pg. 1138
Chaffey, M. Vol. 3 pg. 1551
Chaouki, B. Vol. 3 pg. 1480
Chapman, D. Vol. 2 pg. 82
Chapman, N.R. Vol. 1 pg. 446
Chapman, N.R. Vol. 2 pg. 732



Chapman, S. Vol. 2 pg. 916
 Chayes, D.N. Vol. 3 pg. 1524
 Cheney, R. Vol. 2 pg. 605
 Chepurin, Y.A. Vol. 3 pg. 1548
 Chupa, M.A. Vol. 2 pg. 938
 Clark, R.C. Vol. 2 pg. 817
 Clark, R.C. Vol. 2 pg. 822
 Clay, P. Vol. 1 pg. 391
 Coakley, B.J. Vol. 3 pg. 1524
 Coble, P.G. Vol. 3 pg. 1267
 Coburn, J.L. Vol. 1 pg. 526
 Cole, D. Vol. 3 pg. 1284
 Coleman, J. Vol. 1 pg. 474
 Collins, W.T. Vol. 3 pg. 1123
 Comby, F. Vol. 2 pg. 882
 Commander, K.W. Vol. 3 pg. 1223
 Connan, G. Vol. 3 pg. 1333
 Connan, G. *

Constantin, S. Vol. 1 pg. 352
 Cooke, K.P. Vol. 2 pg. 289
 Cooper, K.D. Vol. 3 pg. 1169
 Corbin, E. Vol. 1 pg. 180
 Costa, R. Vol. 3 pg. 1223
 Coulson, R. Vol. 2 pg. 1009
 Covell, W. Vol. 3 pg. 1404
 Cowling, D. Vol. 3 pg. 1352
 Coyne, J.C. Vol. 1 pg. 1
 Crane, N.L. Vol. 3 pg. 1270
 Crecelius, E.A. Vol. 3 pg. 1381
 Creech, J. Vol. 2 pg. 789
 Crisafi, E. Vol. 2 pg. 796
 Crout, R. *

Cruz, N. Vol. 2 pg. 549

Cruz, N. Vol. 2 pg. 774
 Cruz, N. Vol. 3 pg. 1205
 Cullinan, V.I. Vol. 3 pg. 1381
 Cumbee, S.C. Vol. 1 pg. 391

D

Das, P.S. Vol. 2 pg. 1026
 Das, S. Vol. 3 pg. 1105
 Davis, D. Vol. 1 pg. 519
 Davis, R.B. Vol. 3 pg. 1524
 de Strobel, F. Vol. 3 pg. 1211
 de Strobel, F. Vol. 3 pg. 1229
 de Cáceres, L. Vol. 3 pg. 1317
 DeForest, D. Vol. 2 pg. 631
 DeForest, D. Vol. 2 pg. 642
 DeForest, D. *

Delarue, A. Vol. 2 pg. 738
 Demich, L.R. Vol. 2 pg. 848
 Denbo, D.W. Vol. 1 pg. 466
 Denbo, D.W. Vol. 1 pg. 470
 Denbo, D.W. Vol. 2 pg. 1076
 Devlin, P. Vol. 2 pg. 690
 Dhanak, M. Vol. 3 pg. 1410
 Digby, S. Vol. 2 pg. 605
 Dilrio, D. Vol. 1 pg. 434
 Dinh, H.Q. Vol. 3 pg. 1495
 DiSerio, S. Vol. 1 pg. 126
 Dizaji, R.M. Vol. 2 pg. 732
 Dmitrievsky, A.N. Vol. 3 pg. 1515
 Dobrodeyev, P.N. Vol. 3 pg. 1532
 Doh, K.C. Vol. 1 pg. 295
 Doley, C.D. Vol. 1 pg. 409
 Domanov, M.M. Vol. 3 pg. 1347
 Dorman, E. Vol. 2 pg. 747



Authors Index

Conference Proceedings

Dremoutchev, S. Vol. 3 pg. 1513
 du Duf, J.M.H. Vol. 3 pg. 1571
 Duester, A. Vol. 1 pg. 52
 Dunlop, D. Vol. 1 pg. 157
 Dunn, S. Vol. 2 pg. 1009
 Durham, D.L. Vol. 3 pg. 1169

E

Easton, J. Vol. 3 pg. 1170
 Edelson, G.S. Vol. 2 pg. 996
 Edwards, B. Vol. 2 pg. 785
 Edwards, M. Vol. 3 pg. 1524
 Eisemberg, R. Vol. 2 pg. 801
 Elliot, R. Vol. 1 pg. 11
 Eloutassi, O. Vol. 1 pg. 305
 England, J.F. Vol. 3 pg. 1275
 Ertekin, R.C. Vol. 2 pg. 839
 Etchemendy, S. Vol. 1 pg. 501
 Evans, J.C. Vol. 3 pg. 1300
 Evans, S.M. Vol. 3 pg. 1115
 Evans, S.M. Vol. 3 pg. 1119
 Evett, M. Vol. 1 pg. 452
 Evett, M. Vol. 3 pg. 1312
 Ewart, T.E. Vol. 3 pg. 1341

F

Fader, G. Vol. 3 pg. 1129
 Fernandez, J.E. Vol. 1 pg. 363
 Ferreira, C. Vol. 3 pg. 1081
 Ferreira, D. Vol. 3 pg. 1205
 Fields, E.J. Vol. 1 pg. 157
 Fihn, E. Vol. 1 pg. 17
 Filocca, F. Vol. 2 pg. 1058
 Fioravanti, S. Vol. 2 pg. 916
 Fletcher, B. Vol. 1 pg. 196

Fletcher, C. Vol. 2 pg. 713
 Flory, J. Vol. 2 pg. 690
 Flynn, D. Vol. 3 pg. 1367
 Fogel, P. Vol. 3 pg. 1395
 Foley, J.M. Vol. 1 pg. 391
 Foley, D. Vol. 2 pg. 605
 Foster, N. Vol. 1 pg. 176
 Foxworthy, J. *

Francis, R.C. *

Franciss, R. Vol. 2 pg. 801
 Frederickson, C.K. Vol. 3 pg. 1154
 Freitag, L. Vol. 2 pg. 590
 Freitag, L. Vol. 2 pg. 985
 Freitag, L. Vol. 3 pg. 1512
 Fronk, A.D. Vol. 2 pg. 713

G

Gade, M. Vol. 3 pg. 1234
 Gade, M. Vol. 3 pg. 1239
 Gaither, K. Vol. 2 pg. 938
 Gallagher, D.G. Vol. 3 pg. 1098
 Gamache, K.A. Vol. 3 pg. 1395
 Ganesan, K. Vol. 1 pg. 452
 Ganesan, K. Vol. 3 pg. 1312
 Garelo, R. Vol. 3 pg. 1333
 Gargett, A. Vol. 3 pg. 1244
 Garrett, J.F. Vol. 2 pg. 753
 Gauer, R.C. Vol. 2 pg. 811
 Gaul, R.D. Vol. 1 pg. 526
 Giannitrapani, R. Vol. 1 pg. 459
 Gilbert, G. Vol. 1 pg. 141
 Gilhousen, D.B. Vol. 2 pg. 1017
 Gilmour, W. Vol. 3 pg. 1500
 Gitahi, S.M. Vol. 1 pg. 319



Gobat, J. Vol. 1 pg. 419
 Gobat, J.I. Vol. 1 pg. 107
 Godhavn, J-M. Vol. 1 pg. 46
 Godhavn, J-M. Vol. 3 pg. 1435
 Gomes, J. Vol. 2 pg. 991
 Gommer, S. Vol. 3 pg. 1524
 Goncharov, V.V. Vol. 3 pg. 1548
 Goni, G. Vol. 2 pg. 605
 Gonzalez, F.I. Vol. 3 pg. 1514
 Gower, J. Vol. 3 pg. 1244
 Graham, D.B. Vol. 3 pg. 1325
 Grandi, V. Vol. 3 pg. 1229
 Graziottin, F. Vol. 3 pg. 1211
 Green, M.D. Vol. 3 pg. 1504
 Greer, H. Vol. 1 pg. 119
 Grenard, P. Vol. 2 pg. 624
 Griffiths, H.D. Vol. 3 pg. 1333
 Grosenbaugh, M. Vol. 1 pg. 419
 Grosenbaugh, M.A. Vol. 1 pg. 107
 Grove, T. Vol. 1 pg. 257
 Gruzinskas, P. Vol. 3pg. 1284
 Gu, M. Vol. 1pg. 279
 Gualdesi, L. Vol. 3 pg. 1229
 Guo, L.R. Vol. 2 pg. 1273

H

Hadden, C.L. Vol. 3 pg. 1514
 Hagen, P.E. Vol. 2 pg. 967
 Hagiwara, M. Vol. 2 pg. 862
 Hajjari, A. Vol. 1 pg. 305
 Hamilton, A.J. Vol. 2 pg. 717
 Harris, S.E. Vol. 1 pg. 493
 Hass, A. Vol. 3 pg. 1284
 Hassan, G.A. Vol. 2 pg. 580

Hatch, M. Vol. 1 pg. 228
 Hayashi, T. *

He, P. Vol. 1 pg. 382
 Helton, D. Vol. 1 pg. 410
 Hemsley, J.M. Vol. 1 pg. 269
 Hermann, A.J. Vol. 3 pg. 1501
 Hetet, A. Vol. 2 pg. 916
 Hill, J.A. Vol. 1 pg. 11
 Hines, P.C. Vol. 2 pg. 717
 Hines, P.C. Vol. 3 pg. 1376
 Hinton, O.R. Vol. 1 pg. 216
 Hinton, O.R. Vol. 2 pg. 585
 Hinton, O.R. Vol. 2 pg. 596
 Hinton, O. Vol. 3 pg. 1537
 Holappa, K. Vol. 3 pg. 1410
 Holland, J. *

Holm, S. Vol. 2 pg. 923
 Holt, J. Vol. 2 pg. 614
 Holt, S.M. Vol. 2 pg. 567
 Homer, S. Vol. 2 pg. 690
 Hopkin, D. Vol. 3 pg. 1194
 Hoshino, H. *

Hosom, D. Vol. 1 pg. 377
 Hosseinioun, A. Vol. 3 pg. 1218
 Hou, B. Vol. 2 pg. 585
 Hou, B. Vol. 3 pg. 1537
 Houston, B.H. Vol. 3 pg. 1154
 Hovem, J.M. Vol. 1 pg. 30
 Howell, W.S. Vol. 1 pg. 363
 Howland, J. Vol. 1 pg. 52
 Huang, Y. Vol. 1 pg. 382
 Huang, C-F. Vol. 1 pg. 439
 Hughes, F.W. Vol. 3 pg. 1165



Hughes-Clarke, J. Vol. 3 pg. 1129
Huntley, E.W. Vol. 2 pg. 681
Hurley, W.L. Vol. 1 pg. 526
Hutt, D.L. Vol. 2 pg. 717
Hutt, D.L. Vol. 3 pg. 1376
Hyman, M. Vol. 1 pg. 145

I

Iadanza, N.E. Vol. 2 pg. 827
Ida, M. Vol. 3 pg. 1307
Ioana, C. Vol. 1 pg. 310
Iourytsin, V. Vol. 3 pg. 1513
Irish, J. Vol. 1 pg. 419
Irish, J.D. Vol. 1 pg. 273
Irish, J.D. Vol. 3 pg. 1134
Irisov, V.G. Vol. 3 pg. 1338
Isobe, E. Vol. 2 pg. 868
Ivancic, C. Vol. 2 pg. 945

J

Jaccard, P. Vol. 3 pg. 1435
Jacobs, D.F. Vol. 1 pg. 406
Jacobs, G. Vol. 2 pg. 605
Jalving, B. Vol. 2 pg. 973
Jamieson, G. Vol. 3 pg. 1249
Jarrett, C.M. Vol. 3 pg. 1170
Jarvis, S. Vol. 1 pg. 474
Jensen, F.B. Vol. 2 pg. 1046
Jensen, F.B. Vol. 2 pg. 1064
Jesus, S.M. Vol. 3 pg. 1598
Johannsen, A. Vol. 2 pg. 398
Johnson, D. Vol. 1 pg. 234
Johnson, M. Vol. 2 pg. 590
Johnson, M. Vol. 2 pg. 985
Johnson, M. Vol. 3 pg. 1512

Jones, I.S.F. Vol. 3 pg. 1093
Jones, W.L. Vol. 1 pg. 373
Joque, D.T. Vol. 2 pg. 848
Jourdan, D. *

Jugan, M. Vol. 3 pg. 1170

K

Kamenev, S.I. Vol. 2 pg. 630
Kamerrer, E. Vol. 3 pg. 1129
Kamphaus, R.A. Vol. 3 pg. 1514
Karson, J.A. Vol. 3 pg. 1105
Kato, N. Vol. 3 pg. 1418
Keller, W. Vol. 3 pg. 1338
Khamene, A. Vol. 1 pg. 64
Khenchaf, A. Vol. 3 pg. 1446
Khenchaf, A. Vol. 3 pg. 1452
Kildishev, A.V. Vol. 3 pg. 1532
Kim, J.W. Vol. 2 pg. 839
Kim, K.M. Vol. 1 pg. 295
Kim, K.M. Vol. 1 pg. 315
Kim, S. Vol. 1 pg. 315
Kirichenko, M.F. Vol. 2 pg. 707
Kirlin, R.L. Vol. 2 pg. 732
Kitts, C.A. Vol. 1 pg. 519
Kitts, C.A. Vol. 2 pg. 767
Klein, F.C. Vol. 2 pg. 620
Knapp, R.H. Vol. 2 pg. 1026
Kobylyansky, V.V. Vol. 3 pg. 1347
Kocak, D.M. Vol. 2 pg. 567
Kocak, D.M. Vol. 3 pg. 1105
Kohler, C.A. Vol. 1 pg. 427
Konovalova, S.S. Vol. 3 pg. 1525
Kovachev, S.A. Vol. 3 pg. 1515
Kovchin, I.S. Vol. 3 pg. 1544



Kraeutner, P. Vol. 2 pg. 894
 Kraeutner P.H. Vol. 1 pg. 37
 Kuc, R. Vol. 2 pg. 707
 Kutsenko, T.N. Vol. 3 pg. 1525
 Kuwahara, R.H. Vol. 3 pg. 1123
 Kuznetsov, V. Vol. 3 pg. 1513

L

Langebrake, L. Vol. 1 pg. 58
 Lantor, J.K. Vol. 2 pg. 822
 Lascara, C. Vol. 3 pg. 1501
 Lathrop, J.D. Vol. 1 pg. 363
 Latz, M.I. Vol. 1 pg. 145
 Laughlin, T.J. Vol. 3 pg. 1495
 Leach, T. Vol. 1 pg. 501
 Leasko, R.A. Vol. 1 pg. 363
 Leben, R. Vol. 2 pg. 605
 LeBlanc, L.R. Vol. 1 pg. 222
 Lee, A.J. Vol. 1 pg. 481
 Lee, C. Vol. 1 pg. 315
 Lee, G.F. Vol. 1 pg. 481
 Lee, M-Y. Vol. 1 pg. 257
 Lee, N. Vol. 2 pg. 728
 Lee, W.C. Vol. 1 pg. 315
 Lefkovitz, L.F. Vol. 3 pg. 1381
 Leifer, N. Vol. 1 pg. 17
 Lembke, C. Vol. 1 pg. 58
 Lemon, D.D. Vol. 3 pg. 1490
 Lepekha, M.P. Vol. 2 pg. 707
 Lesnikowski, N. Vol. 2 pg. 901
 Lessing, P.A. Vol. 2 pg. 785
 Levchenko, D.G. Vol. 3 pg. 1544
 Lever, J.A. Vol. 3 pg. 1170
 Lever, J.A. Vol. 3 pg. 1176

Levings, C.D. Vol. 3 pg. 1249
 Lewando, A. Vol. 3 pg. 1176
 Lewis, G.W. Vol. 1 pg. 1
 Leybourne, B.A. Vol. 2 pg. 955
 Lillestolen, T.I. Vol. 1 pg. 157
 Lillycrop, J. Vol. 3 pg. 1290
 Lim, R. Vol. 3 pg. 1154
 Lima, C.S. Vol. 3 pg. 801
 Lingsch, W.C. Vol. 3 pg. 1181
 Lingsch, S.C. Vol. 3 pg. 1181
 Lissner, A. Vol. 1 pg. 324
 Liu, J-Y. Vol. 1 pg. 439
 Lobkovsky, L.I. Vol. 3 pg. 1515
 Lockhart, D. Vol. 3 pg. 1351
 Lockhart, D. Vol. 3 pg. 1500
 Loke, R.C. Vol. 3 pg. 1571
 Lopez, M.J. Vol. 2 pg. 996
 Losee, J. Vol. 1 pg. 145
 Lu, B. Vol. 1 pg. 352
 Lucas, J.R. Vol. 3 pg. 1325
 Lushnikov, D.L. Vol. 3 pg. 1347
 Lynch, J.F. Vol. 3 pg. 1134
 Lynn, D.C. Vol. 2 pg. 555
 Lynn, D.C. Vol. 3 pg. 1495

M

Ma, X. Vol. 3 pg. 1577
 MacDonald, C.D. Vol. 1 pg. 180
 MacFarland, D.B. Vol. 1 pg. 176
 Machado, R.Z. Vol. 2 pg. 801
 MacKenzie, C. Vol. 3 pg. 1500
 MacLellan, D. Vol. 2 pg. 642
 MacLellan, D. Vol. 2 pg. 676
 Mahrt, K-H. Vol. 3 pg. 1218



Maki, J. Vol. 2 pg. 862
Maranda, B.H. Vol. 2 pg. 910
Martin, P. Vol. 3 pg. 1300
Martins, A. Vol. 2 pg. 549
Martins, A. Vol. 2 pg. 774
Martins, A. Vol. 3 pg. 1088
Martins, A. Vol. 3 pg. 1205
Masmoudi, L. Vol. 3 pg. 1480
Messina, F.D. Vol. 1 pg. 11
Messina, F.D. Vol. 1 pg. 17
Matheny, S. Vol. 2 pg. 747
Mathewson, M.O. Vol. 3 pg. 1404
Matos, A. Vol. 2 pg. 549
Matos, A. Vol. 3 pg. 1205
Mauren, M. Vol. 1 pg. 414
Maurer, D. Vol. 1 pg. 324
Maurer, D. Vol. 1 pg. 344
Mauro, C.V. Vol. 1 pg. 157
McCarren, D. Vol. 3 pg. 1176
McCleave, B.W. Vol. 1 pg. 119
McClurg, D.C. Vol. 1 pg. 466
McClurg, D.C. Vol. 2 pg. 951
McClurg, D.C. Vol. 3 pg. 1501
McCormick, J.F. Vol. 1 pg. 363
McCormick, N.J. Vol. 1 pg. 359
McDonald, V.K. Vol. 2 pg. 713
McDonald, V. Vol. 2 pg. 1002
McFadzean, A. Vol. 3 pg. 811
McGee, R.G. Vol. 1 pg. 133
McGinnis, T. Vol. 1 pg. 255
McGirr, S. Vol. 2 pg. 945
Mdodo, R.M. Vol. 2 pg. 1025
Mearns, A. Vol. 3 pg. 1463

Mearns, A. Vol. 3 pg. 1469
Meggett, D.J. Vol. 1 pg. 289
Meinecke, G. Vol. 3 pg. 1405
Merklin, L.R. Vol. 3 pg. 1515
Michalopoulou, Z. Vol. 3 pg. 1577
Michelena, E. Vol. 1 pg. 417
Milburn, H.B. Vol. 3 pg. 1514
Miles, M.D. Vol. 1 pg. 113
Mitsuyasu, C.A. Vol. 1 pg. 180
Miyake, M. Vol. 2 pg. 567
Mofjeld, H.O. Vol. 3 pg. 1514
Moore, K.A. Vol. 1 pg. 237
Moore, C.W. Vol. 2 pg. 951
Moore, C.W. Vol. 3 pg. 1501
Moorhead, R.J. Vol. 2 pg. 938
Morgan, J. Vol. 1 pg. 501
Morgunov, Y.N. Vol. 2 pg. 630
Moroney, M.J. Vol. 3 pg. 1317
Morrison, A.T. Vol. 3 pg. 1429
Morrison, G.K. Vol. 3 pg. 1211
Mosher, D.C. Vol. 3 pg. 1123
Mount, P.M. Vol. 1 pg. 363
Mourelle, M. Vol. 2pg. 801
Mozzone, L. Vol. 2 pg. 1058
Murashima, T. Vol. 3 pg. 1307
Murino, V. Vol. 1 pg. 126
Murino, V. Vol. 1 pg. 459

N

Nahon, M. Vol. 2 pg. 757
Nakahara, H. Vol. 2pg. 1019
Nakahara, H. Vol. 3pg. 1307
Nations, S. Vol. 2 pg. 938



Neasham, J.	Vol. 1 pg. 216
Neely, J.W.	Vol. 2 pg. 567
Negahdaripour, S.	Vol. 1 pg. 64
Negahdaripour, S.	Vol. 1 pg. 71
Nelson, J.	*
Newborough, H.D.	Vol. 3 pg. 581
Newman, J.C.	Vol. 3 pg. 1514
Newport, C.	*
Newton, J.	*
Nichols, R.	Vol. 1 pg. 99
Nicholson, G.J.	Vol. 3 pg. 1115
Niedzwecki, J.M.	Vol. 1 pg. 104
Nielsen, P.L.	Vol. 2 pg. 1046
Nielsen, P.L.	Vol. 2 pg. 1064
North, M.S.	Vol. 3 pg. 1249
Nortz, J.	Vol. 2 pg. 789
Nosov, A.	Vol. 3 pg. 1513
Nuzhdenko, A.V.	Vol. 2 pg. 630
Nyenhuis, J.A.	Vol. 3 pg. 1532

O

Obara, T.	Vol. 3 pg. 1188
Ogushwitz, P.	Vol. 1 pg. 133
Oh, W.C.	Vol. 1 pg. 295
Okamura, A.	Vol. 2 pg. 862
Oliveira, D.	Vol. 2 pg. 801
Oliveira, P.	Vol. 3 pg. 1081
Oliver, G.	Vol. 2 pg. 979
Olson, J.R.	Vol. 2 pg. 713
Ortiz, A.	Vol. 2 pg. 979
Osumi, S.	*
Oswald, J.	Vol. 3 pg. 1351
Ota, J.M.	Vol. 1 pg. 519
Ota, J.M.	Vol. 2 pg. 767

Ouchi, K.	Vol. 2 pg. 1019
Overway, D.J.	Vol. 1 pg. 363
O'Brien, M.	Vol. 2 pg. 873
O'Neil, K.C.	Vol. 1 pg. 269

P

Pace, N.G.	Vol. 1 pg. 434
Pace, N.G.	Vol. 2 pg. 888
Paramonov, A.A.	Vol. 3 pg. 1544
Park, C.	Vol. 2 pg. 1038
Parrott, R.	Vol. 3 pg. 1129
Pascoal, A.	Vol. 3 pg. 1081
Patten, J.	Vol. 1 pg. 58
Paul, W.	Vol. 1 pg. 419
Pena, A.	Vol. 3 pg. 1244
Penkin, S.I.	Vol. 2 pg. 630
Penn, T.	Vol. 2 pg. 829
Pereira, F.L.	Vol. 2 pg. 549
Pereira, F.L.	Vol. 2 pg. 774
Pereira, F.L.	Vol. 3 pg. 1088
Perrot, Y.	Vol. 2 pg. 916
Peterson, T.	Vol. 2 pg. 743
Pham, C.N.	Vol. 1 pg. 363
Phillips, S.	Vol. 1 pg. 396
Phinney, D.A.	*
Piercey, G.E.	Vol. 3 pg. 1249
Pierson, W.J.	Vol. 1 pg. 373
Pinto, M.A.	Vol. 2 pg. 916
Pirillo, P.	Vol. 3 pg. 1526
Plant, W.J.	Vol. 1 pg. 134
Plant, W.J.	Vol. 3 pg. 1338
Poeckert, R.H.	Vol. 3 pg. 1123
Poree, F.	Vol. 3 pg. 1587



Porter, M. Vol. 2 pg. 1002
Postnov, G. Vol. 3 pg. 1513
Potter, J.R. Vol. 1 pg. 352
Pouliquen, E. Vol. 2 pg. 888
Powell, T.B. Vol. 1 pg. 543
Preisig, J. Vol. 3 pg. 1512
Prestero, T. *Preston, J.M. Vol. 3 pg. 1123
Proakis, J.G. Vol. 1 pg. 228
Proenza, J. Vol. 2 pg. 979

Q

Quinquis, A. Vol. 1 pg. 310
Quinquis, A. Vol. 3 pg. 1552

R

Rabe, E. Vol. 2 pg. 1070
Radouane, L. Vol. 3 pg. 1480
Raffa, S. Vol. 3 pg. 1176
Rasure, J.A. Vol. 3 pg. 1267
Ratmeyer, V. Vol. 3 pg. 1405
Raysin, K. Vol. 2 pg. 747
Raysin, K. Vol. 2 pg. 945
Redondo, J.M. Vol. 3 pg. 1239
Reid, C. Vol. 2 pg. 811
Reibman, R. Vol. 2 pg. 1009
Reynolds, S.A. Vol. 3 pg. 1341
Rice, J. Vol. 2 pg. 747
Rice, J. Vol. 2 pg. 1002
Rice, J.A. Vol. 1 pg. 228
Rice, J.A. Vol. 3 pg. 1504
Richards, R. Vol. 3 pg. 1351
Richards, R. Vol. 3 pg. 1500
Richard, S.M. Vol. 2 pg. 702
Ringelberg, J.M. Vol. 1 pg. 543

Robertson, G. Vol. 1 pg. 324
Robertson, G. Vol. 1 pg. 344
Roderick, D.K. Vol. 1 pg. 289
Rognstad, M.R. Vol. 3 pg. 1524
Rohr, J. Vol. 1 pg. 141
Rohr, J. Vol. 1 pg. 145
Ronhovde, A. Vol. 2 pg. 923
Rosyid, D.M. Vol. 1 pg. 245
Rouseff, D. Vol. 2 pg. 1052
Rouseff, D. Vol. 3 pg. 1341
Roy, R.A. Vol. 3 pg. 1223
Rozman, B.J. Vol. 3 pg. 1542
Rud, O. Vol. 3 pg. 1234
Ryan, D. Vol. 2 pg. 698

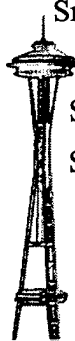
S

Saade, E. Vol. 3 pg. 1500
Sack, P. Vol. 2 pg. 677
Sadorf, K. *Samson, S. Vol. 1 pg. 58
Sanders, W.M. Vol. 3 pg. 1149
Sandt, E.W. Vol. 1 pg. 104
Santos, D. Vol. 3 pg. 1205
Santosa, M. Vol. 1 pg. 245
Sayyaadi, H. Vol. 1 pg. 201
Sally, D. Vol. 1 pg. 417
Schaefer, R.B. Vol. 3 pg. 1367
Schmitt, T. Vol. 2 pg. 873
Schoedinger, S. *Schoonmaker, J. Vol. 1 pg. 141
Schoonmaker, J. Vol. 1 pg. 145
Schuetzner, K. Vol. 2 pg. 677
Schwartz, D.S. Vol. 1 pg. 77
Seiple, R. Vol. 3 pg. 1486



Sekita, K.	Vol. 2 pg. 862
Seong, W.	Vol. 2 pg. 1038
Seto, M.L.	Vol. 3 pg. 1194
Shah, G.	Vol. 2 pg. 904
Shakhramanian, M.A.	Vol. 3 pg. 1544
Sharif, B.	Vol. 3 pg. 1532
Sharif, B.S.	Vol. 1 pg. 216
Sharif, B.S.	Vol. 2 pg. 585
Sharif, B.S.	Vol. 2 pg. 596
Shaw, J.	Vol. 3 pg. 1129
Shay, N.	Vol. 2 pg. 605
Shepherd, K.	Vol. 2 pg. 753
Shepsis, V.	Vol. 1 pg. 396
Siderius, M.	Vol. 2 pg. 1046
Siderius, M.	Vol. 2 pg. 1064
Silva, J.E.	Vol. 2 pg. 801
Silva, J.E.	Vol. 3 pg. 1088
Silva, R.M.	Vol. 3 pg. 1205
Silvestre, C.	Vol. 3 pg. 1081
Simpson, D.	Vol. 1 pg. 396
Simpson, H.J.	Vol. 3 pg. 1154
Singer, M.	Vol. 1 pg. 222
Singer, A.C.	Vol. 2 pg. 996
Singh, H.	Vol. 1 pg. 52
Sintes, C.	Vol. 3 pg. 1591
Skey, S.G.P.	Vol. 1 pg. 113
Slate, E.V.	Vol. 1 pg. 493
Sloan, F.E.	Vol. 2 pg. 702
Smiley, B.	Vol. 3 pg. 1249
Smith, J.S.	Vol. 3 pg. 1300
Smith, R.	Vol. 3 pg. 1119
Smith, R.A.	Vol. 3 pg. 1290
Smith, S.	Vol. 1 pg. 452

Smith, S.	Vol. 2 pg. 738
Smith, S.	Vol. 3 pg. 1312
Smith, S.	Vol. 3 pg. 1410
Smrcina, K.	Vol. 2 pg. 548
Snowden, S.	Vol. 3 pg. 1312
Snyder, S.	Vol. 1 pg. 99
Soares, C.	Vol. 3 pg. 1598
Solaiman, B.	Vol. 3 pg. 1591
Soreide, N.N.	Vol. 1 pg. 466
Soreide, N.N.	Vol. 2 pg. 951
Soreide, N.N.	Vol. 3 pg. 1501
Sousa, J.	Vol. 2 pg. 549
Sozer, E.M.	Vol. 1 pg. 228
Spencer, T.E.	*
Spina, F.	Vol. 2 pg. 888
Spirandelli, E.	Vol. 2 pg. 563
St. Clair Wright, A.	Vol. 2 pg. 1034
Starek, R.	Vol. 3 pg. 1170
Stevenson, J.M.	Vol. 2 pg. 713
Stewart, W.K.	Vol. 1 pg. 299
Stojanovic, M.	Vol. 1 pg. 228
Stojanovic, M.	Vol. 2 pg. 590
Stojaovic, M.	Vol. 2 pg. 985
Stoner, R.	Vol. 3 pg. 1211
Størkersen, N.	Vol. 2 pg. 967
Strauss, O.	Vol. 2 pg. 882
Strom, A.	*
Strully, B.	*
Sullivan, D.E.	Vol. 3 pg. 1270
Summey, D.C.	Vol. 1 pg. 363
Sundvik, M.	Vol. 2 pg. 1070
Swingler, D.N.	Vol. 2 pg. 910



T

Tairi, H.	Vol. 3 pg. 1480
Talukdar, K.	Vol. 2 pg. 904
Tanner, C.D.	Vol. 2 pg. 817
Tarasov, S.P.	Vol. 3 pg. 1525
Taxt, T.	Vol. 2 pg. 923
Taylor, H.M.	Vol. 3 pg. 1557
Taylor, J.S.	Vol. 1 pg. 363
Tear, L.	Vol. 2 pg. 631
Teng, C.C.	Vol. 1 pg. 427
Thomas, H.	Vol. 1 pg. 310
Tidwell, P.	*
Timko, R.	Vol. 1 pg. 417
Titov, V.V.	Vol. 3 pg. 1514
Tlmosheiibo, V.I.	Vol. 3 pg. 1525
Toll, J.	Vol. 2 pg. 631
Toll, J.	*
Tomlinson, S.P.	Vol. 3 pg. 352
Tongta, R.	Vol. 2 pg. 601
Trask, R.	Vol. 1 pg. 377
Traykovski, P.	Vol. 3 pg. 1134
Trucco, A.	Vol. 1 pg. 126
Trucco, A.	Vol. 1 pg. 459
Trushliakov, E.I.	Vol. 3 pg. 1531
Tsimenidis, C.C.	Vol. 2 pg. 596
Tsukioka, S.	Vol. 3 pg. 1307
Tuell, G.H.	Vol. 3 pg. 1325
Turgut, A.	Vol. 2 pg. 1052
Tweit, B.	*
Tyce, R.	Vol. 3 pg. 1229

U

Ura, T.	Vol. 1 pg. 201
Ura, T.	Vol. 1 pg. 209

Ura, T.	Vol. 3 pg. 1188
Utyakov, L.L.	Vol. 3 pg. 1542
Utyakov, L.L.	Vol. 3 pg. 1544

V

Vaccaro, M.	Vol. 2 pg. 1070
Van de Kop, F.	Vol. 2 pg. 780
Van Slyke, R.	Vol. 1 pg. 501
Vanbrundt, H.	Vol. 2 pg. 873
VandenBerg, M.	Vol. 1 pg. 501
Venugopalan, P.	Vol. 1 pg. 352
Veruggio, G.	Vol. 2 pg. 563
Veruggio, G.	Vol. 3 pg. 1081
Vestgard, K.	Vol. 2 pg. 967
Vickery, R.	Vol. 2 pg. 938
Vilentchik, L.S.	Vol. 3 pg. 1347
Volokhov, S.A.	Vol. 3 pg. 1532
Volosin, J.	Vol. 2 pg. 642
Voroium, V.A.	Vol. 3 pg. 1525

W

Wahl, R.J.	Vol. 1 pg. 391
Waite, T.	Vol. 3 pg. 1463
Waldmann, C.	Vol. 3 pg. 1425
Waldmann, C.	Vol. 3 pg. 1441
Walker, S.H.	Vol. 3 pg. 1158
Walstad, L.	Vol. 2 pg. 620
Walters, H.D.	Vol. 3 pg. 1158
Wang, C.	Vol. 1 pg. 382
Wang, D.	Vol. 2 pg. 931
Ward, J.	Vol. 2 pg. 728
Wachorn, E.	*
Watt, G.	Vol. 3 pg. 1194
Weast, A.	Vol. 2 pg. 767
Webb, J.	Vol. 2 pg. 1009



Wefer, G. Vol. 3 pg. 1405
Weissman, D.E. Vol. 1 pg. 138
Weissman, D.E. Vol. 2 pg. 1338
Weitkamp, L. *

Weller, R. Vol. 1 pg. 377
Wernli, R.L. Vol. 1 pg. 189
West, G.R. Vol. 3 pg. 1290
Weyer, F. Vol. 1 pg. 52
Wheless, G. Vol. 3 pg. 1501
Whitehill, A.S. Vol. 2 pg. 681
Whitney, S.L. Vol. 2 pg. 996
Wilby, A.D. Vol. 1 pg. 23
Williams, A.J. Vol. 1 pg. 386
Williams, A.J. Vol. 3 pg. 1429
Williams, D. Vol. 2 pg. 1009
Williams, W.J. Vol. 1 pg. 273
Wiltshire, J.C. Vol. 1 pg. 237
Windsor, C.R. Vol. 2 pg. 1076
Wolf, S.N. Vol. 2 pg. 1052
Wong, Y.S. Vol. 3 pg. 1300
Woodward, B. Vol. 3 pg. 1581
Woxstroem, J. Vol. 3 pg. 1504

X

Xia, D. Vol. 2 pg. 839
Xu, W. Vol. 1 pg. 299
Xu, X. Vol. 1 pg. 71

Y

Yafuso, E. Vol. 3 pg. 1486
Yan, J. Vol. 2 pg. 723
Yang, L. Vol. 2 pg. 923
Yang, F.L. Vol. 2 pg. 848
Yoerger, D. Vol. 1 pg. 52
Youn, D.H. Vol. 1 pg. 295

Youn, D.H. Vol. 1 pg. 315
Yuan, X. Vol. 1 pg. 452
Yuan, X. Vol. 3 pg. 1312

Z

Zappalà, G. Vol. 2 pg. 796
Zec, J. Vol. 1 pg. 373
Zerr, B. Vol. 2 pg. 888
Zhang, R.H. Vol. 2 pg. 723
Zhou, S.H. Vol. 2 pg. 723
Zhu, W.H. Vol. 1 pg. 466
Zhu, W. Vol. 1 pg. 382
Zietz, S. Vol. 2 pg. 873
Zurk, L.M. Vol. 2 pg. 728



Internet mission control of the ROMEO Unmanned Underwater Vehicle using the CORAL Mission Controller

Ga. Bruzzone, R. Bono, M. Caccia, G. Veruggio

Consiglio Nazionale delle Ricerche

Istituto Automazione Navale

Via De Marini, 6

16149 Genova, Italy

E-mail: {gabry, ric, max, gian} @ian.ge.cnr.it

C. Ferreira, C. Silvestre, P. Oliveira, A. Pascoal

Instituto Superior Técnico

Institute for Systems and Robotics

Av. Rovisco Pais

1096 Lisboa Codex, Portugal

E-mail: {cpdf, cjs, pjcro, antonio} @isr.ist.utl.pt

Abstract

This paper addresses the problem of mission control of Unmanned Underwater Vehicles (UUVs) through the Internet network. Its main focus is on the integration of a Petri Net based mission control system developed by the Instituto Superior Técnico using the CORAL environment, with the control system of ROMEO, a prototype ROV developed by the Robotics Department of CNR-IAN. The system has been evaluated controlling ROMEO's missions directly from Lisbon in the underwater virtual world (UVW) in the IAN lab and in a pool in Genoa. In particular, the reliability of the Internet connection has been verified and the constraints introduced by communication delays have been examined. This research and development effort aims at contributing to the development of reliable mission control systems for the operation of robotic ocean vehicles at distance, over communication channels that may experience considerable delays. This is a subject of great relevance, in view of the widespread interest in the development of systems to allow a scientific end-user to program, execute, and follow the state of progress of robotic vehicle missions at sea from the comfort of his/her laboratory.

1. Introduction

In the Nineties the requirements of unmanned underwater vehicles (UUVs) in terms of capabilities of managing uncertainty and possibility of reducing development and trial costs induced the development of hierarchical intelligent control architectures (Byrnes et al., 1993; Le Rest et al., 1994; Pascoal et al., 1997; Wang et al., 1993) and virtual environments for underwater robots (Bono et al., 1997; Brutzman, 1995; Leonard et al., 1995). The result was the implementation of open, flexible architectures for

developing robotic techniques and fostering co-operation between research groups, ultimately promoting vehicle exploitation (Healey et al., 1996; Coste-Manière et al., 1996).

At the same time, numerous novel robotics systems that employ the infrastructure of the Internet to extend current human abilities have been developed (Paulos and Goldberg, 1999), allowing remote interactions with actual mobile robots connected to the Web.

The high level of maturity achieved by this technology in space robotics applications (Backes et al., 1998), together with the resolution of basic problems in UUVs navigation, guidance and control (Fossen, 1994; Fryxell et al., 1996; Healey and Lienard, 1993; Whitcomb et al., 1999), has suggested its extension to the field of underwater robotics in order to allow a scientific end-user to program, execute, and follow the state of progress of robotic vehicle missions at sea from the comfort of his/her laboratory.

In order to allow Internet users to interact with places far away from their home or test control algorithms on a real robotic platform, mobile robots on the Web have to satisfy some basic specifications (Siegwart and Saucy, 1999): the robot system requires a high degree of autonomy to face any large time delay; a minimal data transfer should always indicate the instant status, events and robot position; the control strategy of the robot should be as intuitive as possible, and the update rate of the transmitted video images should be as high as possible to provide a good feeling to reality. It is worth noting that autonomous underwater vehicles, which can communicate with the human supervisor and/or the mission controller through a very narrow-band acoustic link satisfy the first three requirements, while good quality video feedback can be guaranteed by data compression techniques in the case of Internet control of a remotely operated vehicle.

In the research reported in this paper, a pool mission of Romeo, the prototype ROV developed by the CNR-IAN, has been controlled by a Petri Net based mission controller developed by the IST-ISR using CORAL, through an Internet link between Genoa and Lisbon. According to the hierarchical control architecture paradigms, the ROMEO's control system provides a set of basic navigation, guidance, and control task functions, which can be coordinated and activated by an automatic mission controller connected to the vehicle surface network. Task activation and coordination depend on the occurrence of external discrete-events such as operator commands and events triggered by sensor readings. This motivated the development of a methodology for mission control that builds on the theory of Petri nets, which are naturally oriented towards the modeling and analysis of asynchronous discrete-event systems with concurrency. Mission control is thus performed by specifying mission programs that are embodied in Petri net structures. A mission control development environment named CORAL, designed by IST, allows for graphically constructing the required Petri nets and executing them in real-time on a CORAL software Engine that runs on a PC. The operator can visualize the state of progress of the mission by observing the evolution of tokens in the corresponding Petri net structure. CORAL allows the execution of mission programs for general robotic vehicles. The only extra effort required for a specific application is the definition of the list of commands/replies to and from a given robotic system. This was done in the case of ROMEO by defining the packet format for commands/replies between CORAL and ROMEO on the basis of the basic tasks adopted. Furthermore, Romeo's original control system was adapted by adding a state machine capable of handling the command/reply mechanism and of triggering the execution of specific tasks in parallel, in order to exploit the Petri Net's capabilities in concurrency management.

Romeo networked architecture and basic task functions are described in section 2, while a short description of the Petri Net-based CORAL mission controller is given in section 3. The experimental setup, i.e. the physical integration of Romeo control system and CORAL mission controller, is described in section 4, where experimental results are reported and discussed.

II. ROMEO

Romeo's architecture basically consists of three Ethernet LANs (surface, on-board and lab LAN), which can be connected to the world-wide web for scientific cooperations. The surface LAN connects a net manager computer (IPER) and a multi-machine distributed Human Computer Interface (HCI), which allows a number of different operators to interact with the robot at various levels of the control system. The conventional HCI for scientific applications consists of three interfaces for the pilot, who tele-operates the vehicle, the supervisor, who supervises the plant behavior

and resources' allocation, and the marine scientist, who examines real-time images and sensors data to detect areas of interest. The IPER machine acquires all the vehicle surface sensors, as, for instance, acoustic positioning system, ship GPS and gyro-compass, and manages communications from the human interfaces and the robot control system on-board the vehicle, dispatching the telemetry data and collecting, by solving conflicts, the user commands. The surface LAN can also support the connection of an external supervisory/mission control module, which automatically manages a vehicle mission, as in the case of CORAL shown in Figure 1. In addition to the computer running the vehicle control system, the on-board LAN can also connect advanced end-user devices carried by the vehicle. Furthermore, the lab LAN supports the Underwater Virtual World simulation facilities (6 d.o.f. vehicle dynamics, environment and sensors) and graphics interfaces.

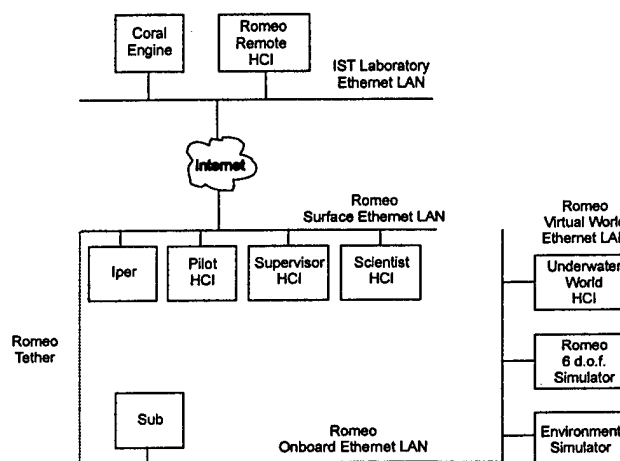


Fig. 1. CORAL-ROMEO networked architecture

Romeo control system is based on a hierarchical dual-loop architecture (Caccia et al., 1999) providing the human operator/mission controller with a set of basic guidance task functions performing auto-heading, auto-depth, auto-altitude and automatic maneuvering on the horizontal plane. The sub-set of commands handling the task functions used in the CORAL-ROMEO mission are reported in Table 1. Algorithmic details about depth, heading and horizontal maneuvering task functions can be found in (Caccia et al., 1999) and (Caccia et al., 1998) respectively. Here it is sufficient to remark the meaning of the basic horizontal maneuvering tasks:

- Short Range Maneuvering (SRM): the vehicle hovers the target with the desired orientation;
- Long Range Maneuvering (LRM): the vehicle heads the target;
- Go to (GOTO): the vehicle moves to the target point switching between LRM, medium range maneuvering, i.e. car driver-like guidance, and SRM according to the target range;

- Docking (DOCKING): go to the docking point, recorded executing the GET_DOCK command

```

Depth control:
  DEPTH(z*)
  DEPTH?(z*, TIME_OUT)
Heading control:
  HEADING( $\psi^*$ )
  HEADING?( $\psi^*$ , TIME_OUT)
Horizontal maneuvering:
  LRM(x*, y*)
  XY?(x*, y*, TIME_OUT)
  SRM(x*, y*,  $\psi^*$ )
  GOTO(x*, y*,  $\psi^*$ )
  XYPSI?(x*, y*,  $\psi^*$ , TIME_OUT)
  DOCKING
  DOCKING?(TIME_OUT)
Horizontal motion estimation:
  FIX_XY()
  GET_DOCK()

x, y, z: vehicle position
 $\psi$ : vehicle heading

```

Table 1. ROMEO task function commands

The ?-marked commands implement the *space-trap* queries, which evaluate if the corresponding task function has been executed by a specified time-out. A suitable evaluation criteria is the following: indicating by

$\underline{x}^{(k)}(t)$ the k-th time derivative of the generic signal $\underline{x}(t)$,
 « $\underline{x}(t)$ tracks $\underline{x}^*(t)$ of order n » if
 $\|\underline{x}^{(k)}(t) - \underline{x}^{*(k)}(t)\| < \varepsilon_k, \quad \forall t \in [t_0 - T, t_0], \quad 0 \leq k \leq n$, where
 $\|\cdot\|$ represents the Euclidean-norm. Tracking of order 1
 is usually adopted, except in the case of LRM tracking of order 0.

III. The CORAL Development Environment. Implementation issues

This section introduces CORAL as a software environment for the design and implementation of Petri net structures and explains its interfacing to the System Control level of the CNR-IAN ROMEO vehicle. We assume the reader is familiar with Petri Net theory; see (Cassandras, 1993) for a lucid presentation of the subject. See also (Oliveira et al., 1998) and the references therein for the development of CORAL as a tool for mission programming and execution tool for the MARIUS AUV.

The organization of CORAL can be explained in very simple terms with the help of Figure 2, which illustrates how the design of a subset of a generic Petri net is done, and how the equivalent CORAL language description is obtained. In order to understand the figure and the design methodology adopted, two basic concepts are required:

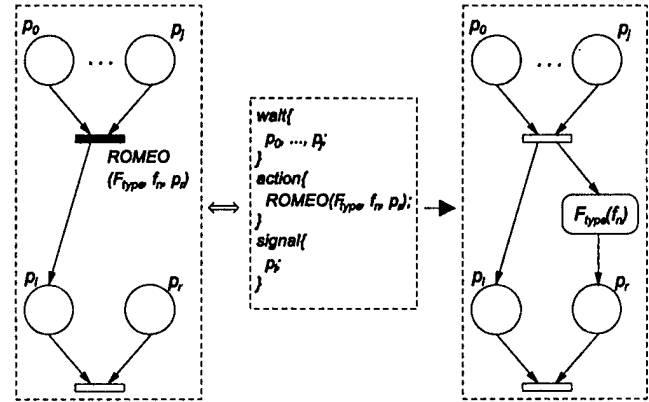


Figure 2: CORAL/System level Interface.

i) **System Control Level Calling Header** - The firing of a generic transition will start the execution of a System Control Level command, which is evoked through an header with the structure

ROMEO(F_{type}, f_n, P_r)

where ROMEO specifies a System Control Level function interface presented in the previous section, F_{type} identifies the type of function or particular algorithm to be executed, and f_n are the parameters of the function to be called. The last calling parameter set P_r indicates a finite set of places in the Petri Net that will be marked depending on the type of messages received from the ROMEO system control level.

ii) **Wait, Action and Signal keywords** - to describe a Petri net, the CORAL language uses three basic keywords: *wait*, *action*, and *signal*. The formal equivalence between the textual description of a Petri net using these keywords and its underlying Petri net graph can be easily understood by examining the input and output sets of a particular transition t_k . The following equivalence relationships follow immediately:

$$\begin{aligned}
 I(t_k) &\Leftrightarrow \text{wait}\{p_0, \dots, p_i\}, \\
 O(t_k) &\Leftrightarrow \text{action}\{\text{ROMEO}(F_{type}, f_n, p_r)\} \\
 &\quad \text{signal}\{p_r\}.
 \end{aligned}$$

where $I(t_k)$ and $O(t_k)$ are the input and output sets of places to and from the transition t_k , respectively. In this case, the function called has only one output event, and its occurrence will activate the marking of place p_r . The extension to more complex Petri Net structures is obvious.

A CORAL Engine has been developed that accepts Petri net descriptions and executes them in real-time. Figure 3 shows a schematic representation of the CORAL Engine data structure and the communication mechanisms that implement a Petri Net. The CORAL Engine accepts input messages corresponding to the markings of the Petri net being run, checks for the current set of enabled transitions, and issues output messages that correspond to the new markings determined by the firing of those transitions. In practice, this is done by executing a CORAL Engine synchronous loop described by the following sequence of actions:

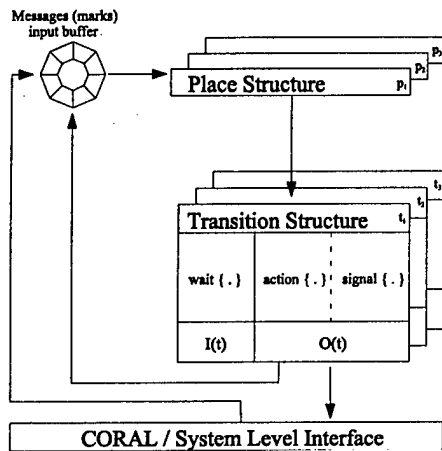


Figure 3: CORAL Implementation Structure.

for each message in the input buffer,
 (1) update the number of marks in the corresponding place.
 (2) for the current state, check for the set of enabled transitions.
 (3) choose one transition from the set of enabled transitions.
 (4) update the number of marks in the set of input places

$$I(t_k) \Leftrightarrow (\text{wait}\{\dots\}).$$

(5) issue messages in order to update the number of marks in the set of outputs places,

$$O(t_k) \Leftrightarrow (\text{action}\{\dots\} \text{ signal}\{\dots\}).$$

(6) repeat (2) through (5) until the set of enabled transitions has been exhausted.

This cycle is repeated until the input buffer is empty.

IV. Experimental setup and results

The integration of the CORAL mission controller and ROMEO control system has been carried out in the lab thanks to the IAN Underwater Virtual World facilities (Bono et al., 1999). The execution of a set of real-time hardware-in-the-loop virtual missions allowed to verify the communication protocol, and to check the correctness of the events' management in the actual experimental conditions, including the communication bandwidth constraints due to the 9600 bps mobile phone serial data link between the ROV operating site and the network in the IAN lab. Once the system set-up was completed in the lab, the same set of missions has been executed with the actual vehicle in a swimming pool in Genoa, located at about 5 km from the IAN lab. The research scientists in IST lab in Lisbon followed the mission in real-time by means of a graphics representation of the vehicle basic telemetry (position and heading) sent through Internet using datagram BSD sockets. It is worth noting that for mission control commands/acknowledges transmission, according to the sequence shown in Figure 4, the more reliable stream BSD sockets have been used.

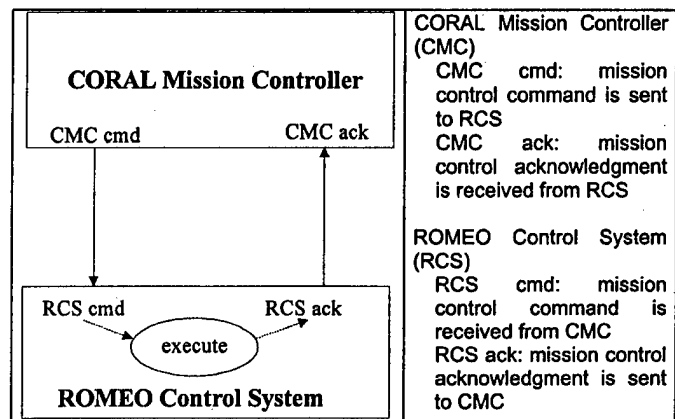


Figure 4. Right sequence of each mission control command/acknowledge.

The most significant mission consists of three phases:

1. go to operating site
 Romeo reaches the operating depth and a suitable orientation to initialize its horizontal position estimate by sonar ranges from the pool walls, records its position to dock there at the end of the mission and moves to the operating site;
2. way-point navigation
 Romeo navigates through four way-points, placed in the corners of a square, executing a long range maneuvering guidance task;
3. docking
 Romeo hovers the operating site, moves to the docking point and emerges.

The events' sequence, including the corresponding timestamps, has been recorded by both the Romeo Supervisor HCI and CORAL engine machines. The logged data have been merged off-line to analyze the system performance. The starting time has been fixed when the first command has been sent by CMC.

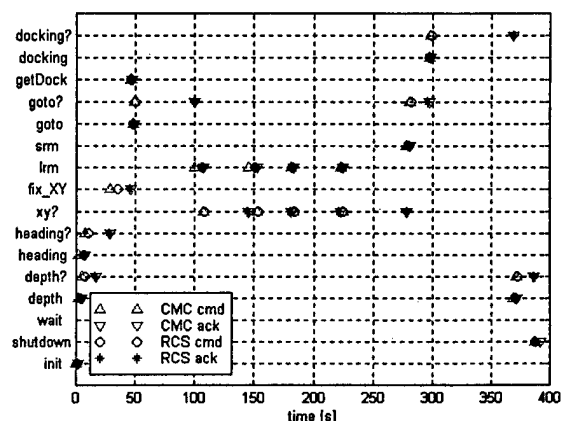


Figure 5. Romeo and CORAL pool mission events' sequence

Defining t_0^{cmc} and t_1^{cmc} the instants, in the CMC clock reference, when CMC sends and receives the «INIT»

command/ack, and t_0^{RCS} and t_1^{RCS} the instants, in the RCS clock reference, when RCS receives and sends the «INIT» command/ack, the time offset t_{offset} between the CMC and RCS recorded events' sequences has been

$$\text{approximated as } t_{offset} = \frac{t_1^{CMC} - t_0^{CMC}}{2} - \frac{t_1^{RCS} - t_0^{RCS}}{2}.$$

The resulting events' sequence is plotted in Figure 5. The Petri net corresponding to the «go to operating site» phase is depicted in Figure 6, while the system behavior is reported in Figure 7, where the parallel execution in the presence of non-deterministic and time-varying delays of auto-depth and auto-heading tasks before estimating the vehicle horizontal position is pointed out.

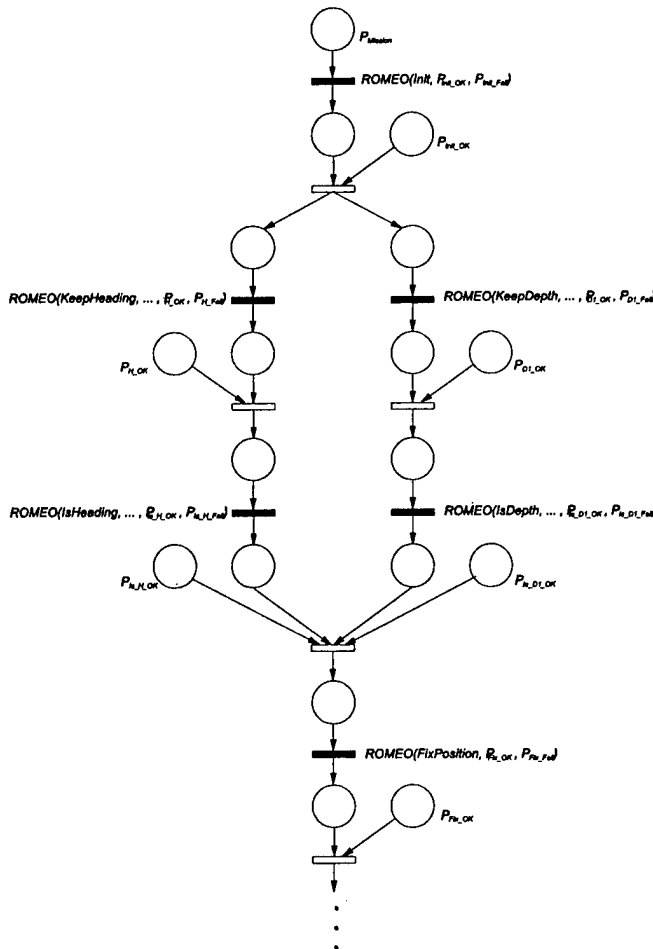


Figure 6: Petri Net Mission Control Program (first phase)

Although the DEPTH and HEADING commands are sent by CMC contemporaneously, the latter takes a longer time to reach RCS (see the time interval between 0 and 10 seconds in the top picture). Anyway, the CORAL engine waits for the successfully execution of both the tasks before sending the FIX_XY command, which takes 10 seconds to be executed in order to allow the correct initialization of the extended Kalman filter for motion estimation (see the time interval between 30 and 50 seconds in the top picture). At that time, the GET_DOCK command is executed in order to record the point where to dock at the end of the mission. It is worth

noting that, executing the GOTO task function, the ROV maneuvers on the horizontal plane in order to approach the target point with the desired orientation (see the bottom picture after about 50 seconds).

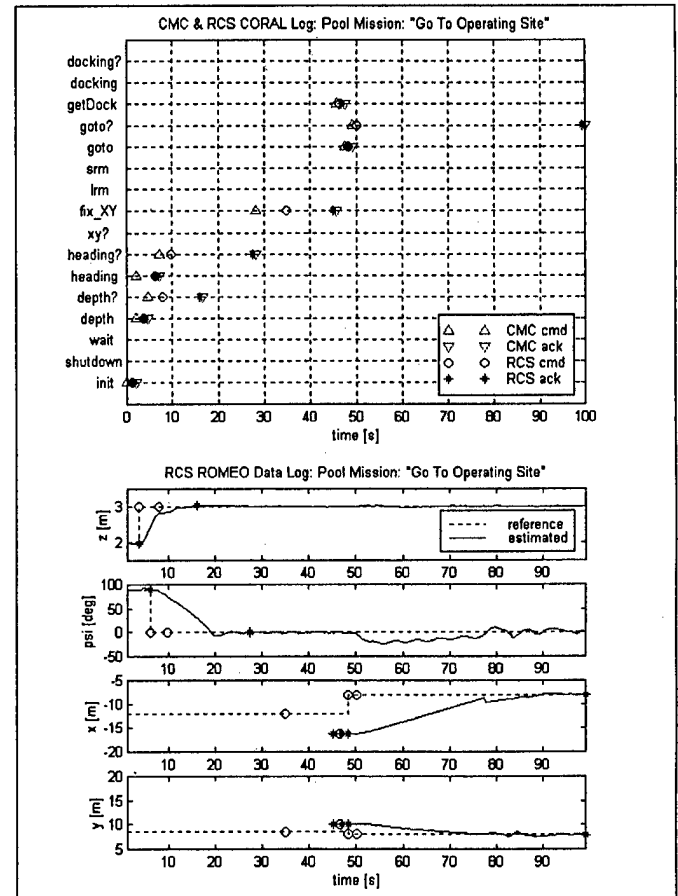


Figure 7: «go to operating site»: Romeo and CORAL events' sequence and ROV telemetry

The system behavior during the «way-point navigation» phase is reported in Figure 8, where remarkable network delays, i.e. of about 7 seconds, in the transmission of the first two LRM commands are visible. The maneuvering behavior consisting in heading the target is shown by the Romeo telemetry plots in the bottom picture.

Figure 9 shows the system behavior in the «docking» phase. After hovering the target with the desired orientation, the ROV reaches, with a complex maneuver, the docking position and emerges. The jump in the vehicle x position after more than 380 seconds (see the bottom picture) is due to bad sonar measurements obtained when the sonar was too close to the surface.

V. Conclusions

This paper described an experiment whereby a Petri Net based mission control developed by the Instituto Superior Técnico using CORAL, was integrated with the control system of ROMEO, a prototype ROV developed by the

Robotics Department of CNR-IAN. The system was evaluated controlling ROMEO's missions directly from Lisbon in the underwater virtual world (UVW), in the IAN lab, and in a pool in Genoa. The relative simplicity with which an example mission was jointly programmed and run demonstrates that true inter-group cooperation on the subject of underwater vehicle mission control is within reach. This example is but a small step in the process of developing systems that will allow scientific end-users to program, execute, and follow the state of progress of robotic vehicle missions at sea from the comfort of their laboratories.

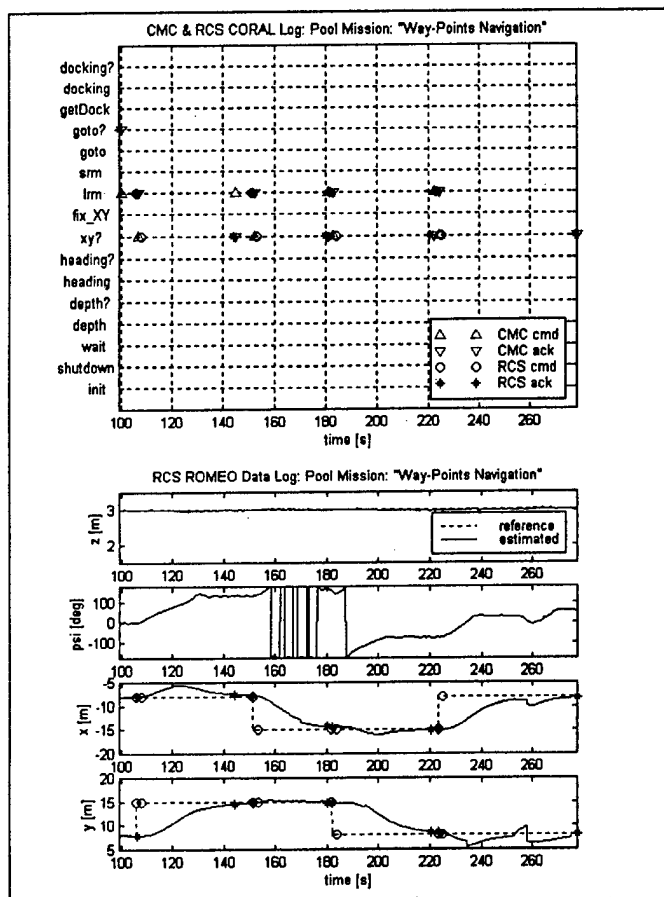


Figure 8. «way-point navigation»: Romeo and CORAL events' sequence and ROV telemetry

VI. Acknowledgments

This work has been performed in the framework of a bilateral agreement between the Italian Consiglio Nazionale delle Ricerche and the Portuguese Instituto de Cooperaçao Cientifica e Tecnológica Internacional.

VII. References

Backes, P.G., K.S. Tso, G.K. Tharp (1998). Mars Pathfinder mission Internet-based operations using WITS. Proc. of IEEE ICRA 98, pp. 284-291, Leuven, Belgium.
Byrnes, M.L. Nelson, S.H. Kwak, R.B. McGhee, A.J. Healey (1993). Rational Behavior Model: An Implemented Tri-Level

Multilingual Software Architecture for Control of Autonomous Underwater Vehicles, Proc. of 8th International Symposium on Unmanned Untethered Submersible Technology, pp. 160-178.

Bono R., G. Bruzzone, M. Caccia, G. Veruggio, P. Virgili (1997). A Real-time Architecture for Development and Control of Unmanned Underwater Vehicles, Proc. of 4th IFAC Workshop on Algorithms and Architectures for Real-Time Control, Vilamoura, Portugal, pp. 58-63.

Bono R., G. Bruzzone, M. Caccia, G. Veruggio (1999). A flexible networked architecture for scientific applications and robotics research, Proc. of 11th International

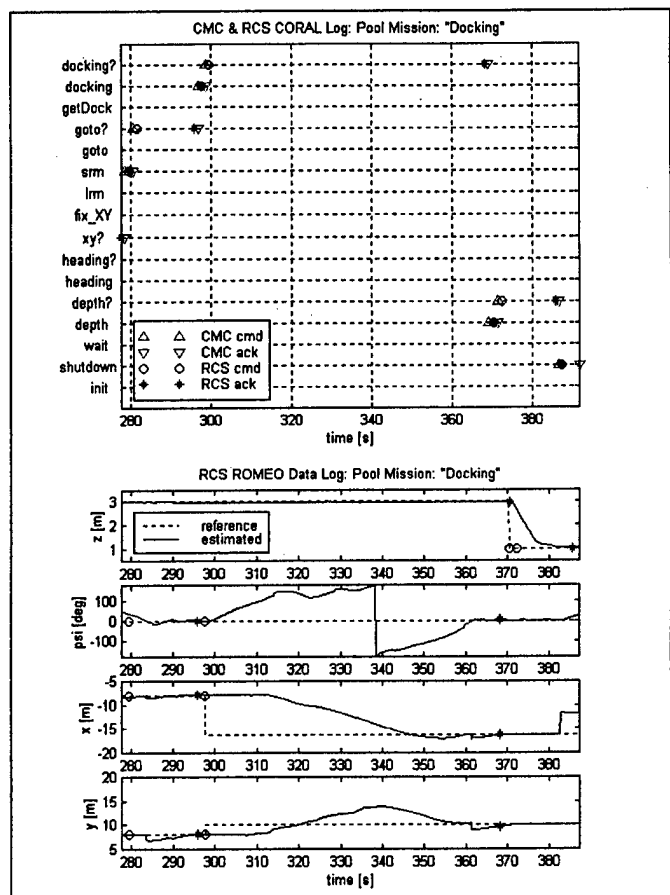


Figure 9. «docking»: Romeo and CORAL events' sequence and ROV telemetry

Symposium on Unmanned Untethered Submersible Technology, Durham, USA.

Brutzman, D. (1995). Virtual World Visualization for an Autonomous Underwater Vehicle, Proc. of Oceans '95 MTS/IEEE, San Diego, USA.

Caccia M., Casalino G., Cristi R., Veruggio G. (1998). Acoustic motion estimation and control for an unmanned underwater vehicle in a structured environment, IFAC Control Engineering Practice, Vol. 6, No. 5, September 1998, pp. 661-670, Elsevier Science Ltd., England.

Caccia M., G. Bruzzone, G. Veruggio (1999). Hovering and altitude control for open-frame UUVs. IEEE

- International Conference on Robotics and Automation, pp. 72-77. Detroit, USA.
- Cassandras C. (1993). Discrete Event Systems. Modeling and Performance Analysis, Aksen Associates Incorporated Publishers.
- Coste-Manière E., H.H. Wang, S.M. Rock, A. Peuch, M.Perrier, V.Rigaud, M.J.Lee (1996). Cooperative research in underwater robot programming. Proc. of the 6th IARP'96 Workshop on Underwater Robotics.
- Fossen, T.I. (1994). Guidance and Control of Ocean Vehicles, John Wiley & Sons, England.
- Fryxell, D., P. Oliveira, A. Pascoal, C. Silvestre and I. Kaminer (1996). Navigation, guidance and control of AUVs: an application to the MARIUS vehicle, IFAC Control Engineering Practice, Vol. 4, No. 3, pp. 401-409, Elsevier Science Ltd., England.
- Healey, A.J. and D. Lienard (1993). Multivariable slidingmode control for autonomous diving and steering of unmanned underwater vehicles. IEEE Journal of Oceanic Engineering, Vol. 18, No. 3, pp. 327-339.
- Healey, A., D. Marco, R.B. McGhee, P. Oliveira, A. Pascoal, V. Silva, C. Silvestre (1996). Implementation of a CORAL/Petri net strategic level on the NPS Phoenix vehicle, Proc. of the 6 th IARP'96 Workshop on Underwater Robotics.
- Leonard, J. J., S. T. Tuohy, J. G. Bellingham, B. A. Moran, J. H. Kim, H. Schmidt, N. M. Patrikalakis and C. Chrysostomidis (1995). Virtual Environments for AUV Development and Ocean Exploration. Proc. Int. Symp. on Unmanned Untethered Submersible Technology, pages 436-443, New Hampshire.
- Le Rest, L. Marce, V. Rigaud (1994). VORTEX-PILOT: a top-down approach for AUV's mission telerobotics language, Proc. of OCEANS'94, vol. 2, pp. 102-107.
- Oliveira, P., A. Pascoal, V. Silva, C. Silvestre (1998). The Mission Control System of the MARIUS AUV: System design, implementation, and tests at sea. International Journal of Systems Science, Special Issue on Underwater Robotics, Vol. 29, No 10, pp 1065-1080.
- Pascoal, A., C. Silvestre, P. Oliveira, A. Bjerrum, G. Ayela, J.-P. Pignon, S. Bruun, C. Petzelt (1997). MARIUS: An Autonomous Underwater Vehicle for Coastal Oceanography. IEEE Robotics and Automation Magazine, Special Issue on Robotics and Automation in Europe: Projects funded by the Commission of the European Union, pp. 46-59.
- Paulos, E., and K.Goldberg (organizers) (1999). Current challenges in Internet robotics. Workshop IEEE ICRA 1999. Detroit, USA.
- Siegwart, R. and P.Saucy (1999). Interacting mobile robots on the Web. Proc. of Workshop IEEE ICRA 1999, Detroit, USA.
- Wang, H.H. , R.L. Marks, S.M. Rock, M.J. Lee (1993). Task-Based Control Architecture for Untethered, Unmanned Submersible, Proc. of 8th International Symposium on Unmanned Untethered Submersible Technology, Durham, USA, pp. 137-148.
- Whitcomb, L., D. Yoerger, H. Singh (1999). Advances in Doppler-based navigation of underwater robotic vehicles. Proc. of IEEE ICRA 1999, pp. 399-406, Detroit, USA.

A RECONFIGURABLE MISSION CONTROL SYSTEM FOR UNDERWATER VEHICLES

Jorge Estrela Silva, Alfredo Martins*, Fernando Lobo Pereira

Faculdade de Engenharia da Universidade do Porto and
Instituto de Sistemas e Robótica
Rua dos Bragas, 4099 Porto Codex
Portugal

* Instituto Superior de Engenharia do Porto
Rua de S. Tomé 4200 Porto
Portugal

Abstract — This paper describes the mission control software used in the LSTS/FEUP underwater vehicles. This software follows the guidelines of the generalized vehicle architecture [1], adapts the original idea to encompass the current application requirements and constitutes a first implementation.

The work is focused on the design and implementation of an application that can be easily adapted to different vehicle configurations or even to different vehicles. One of the desired goals was to enhance software reusability and to establish a development environment that allows developers with a minimal knowledge of coding details to upgrade the application. To assist this purpose, a CASE tool, which provides modern software development techniques, was used.

A simulation environment was also developed whose purpose is to test the applications and to detect possible malfunctions before they occur during mission execution.

MOTIVATION

Porto University has been working on the ISURUS vehicle for two years. ISURUS is a REMUS vehicle created by the Woods Hole Oceanographic Institution (WHOI). Since the beginning we have been customizing the vehicle to fulfill our particular needs and interests. We upgrade the vehicle in order to minimize power consumption, increase data logging capacity, install new oceanographic sensors and increase vehicle operational capabilities. A new navigation system was developed for this vehicle using *Kalman* filtering techniques [2]. Soon we felt the need to adapt the original software to accommodate the new features.

Furthermore, as the research interests of this group encompasses topics in advanced control theory, we aimed at a framework allowing the implementation of several control algorithms and test them in a real environment. For that purpose, the software should provide capabilities for testing

several control laws during the same mission, with minimum human interaction. It should be possible to schedule the same control law with different parameters and log the vehicle performance.

The original WHOI control software [3] used on ISURUS was targeted to DOS. It was decided to abandon this line of development since in a medium term it would be impractical to guarantee the static scheduling provided by the WHOI software. Using DOS would imply the need to divide carefully our longer tasks in chunks of processing, in order to provide pseudo multi-tasking. The multi-tasking would have to be explicitly coded leading to software harder to understand. We would be dealing with several tasks with different priorities and scheduling rates. Furthermore, it is desirable to have parallel development of several tasks what would be difficult and more error prone in such an environment.

Developing a multi-tasking OS or adapting DOS to that purpose was out of question given the time vs. usability/reliability trade-off and given the great variety of available products on the market. For those reasons it was decided to choose a commercial multi-tasking real time operating system.

Furthermore, since new related projects were started, demand for new software applications would justify the decision made.

Since the whole software would be rewritten, it was decided to specify an architecture that would promote software reutilization. We identified the processes, data flows, system events, communications, reactions to special events and maneuvers that would be common to a great majority of vehicles (as hardware independent as possible). The software and underlying control laws was organized in several layers and modules.

We adopted a commercial tool (TEJA) [4] to support the development of a first instance of the software, mainly on the simulation layer. This tool allowed us to graphically model the dynamic behavior of the application using the hybrid state

machine paradigm. The interaction (data flow and event triggering) between different tasks is also graphically modeled by using the OMT methodology. In the end, it generates C++ code that must be built to the target OS.

ARCHITECTURE

The application organization follows a hierarchical layered model, with well defined interfaces and access points. This organization allows the development team to rapidly locate the desired changes or upgrades and to assign those tasks.

Several agents, running concurrently, are defined at each layer. Each agent will manage a specific subsystem encompassing the relevant information. This approach ensures functional separation, thus reducing the side effects of future upgrades.

Libraries of device drivers for sensors and actuators and algorithms for control, guidance and fault management will be created as new situations arise. These algorithms can be developed for a specific vehicle configuration or can be designed in such a way that its behavior is a function of the vehicle model parameters, thus permitting code reusability. The TEJA CASE tool allows the developer to graphically choose the set of components that will constitute the application for each vehicle configuration.

The architecture is intended to be operating system independent. However, the implementation depends on the capabilities of the operating system. We assumed that any operating system we will use will have multi-tasking capabilities. The remaining desired features (scheduling, priorities, message passing, communications, service identification via names) are encapsulated in classes whose implementation can be adapted to different operating systems. The application tasks rely on those classes instead of direct system calls. The overhead of this methodology was shown to be negligible on the ISURUS 486DX computer.

1 – Abstraction Layer

In the first layer, we can distinguish two different sub-levels:

- The tasks which deal with interrupts and low level routines (device drivers). Normally the OS shall provide these modules: drivers for the serial ports, network adapter, disk drive and console, and access to memory mapped devices. These tasks, as also the bulk of the OS kernel, have the highest priority. A communications stack like TCP/IP or some real time protocol is also needed (on ISURUS we used a TCP/IP stack for PPP connections).
- The tasks provide the high-level protocol to interface with the specified device: knowledge of messages formats and timings, message parsing, processing and handling, information gathering and fault tolerance.

We adopted a distributed and hierarchical fault-tolerance scheme. For a given abstraction level, the identities ensures

robustness by interpreting lower term fault detection data and either by undertaking the pertinent error recovery or by forwarding it to a higher abstraction level. For instance, occasionally, the vehicle serial ports stop responding. The task associated with each serial port has the duty of checking the time since the last character was received. The knowledge required to infer whether the serial port is dead or not is embedded in that task, since that is intrinsically related to the device protocol.

Every task on the system can log their messages. Besides the normal data gathering performed by the oceanographic sensors, the log file also behaves as the vehicle "black box". To log all the available information concerning vehicle status (temperature, voltage, power consumption, etc.), whenever possible, has proved, in the course of field missions, to be very useful. We have already discovered and modeled a conflict between two devices only by inspecting the log files. For this reason we think AUVs should be provided with enough data storage capability (several hundreds of MB). For ROVs, the information can be logged via data link on a remote computer.

Data communication between the first and second layers is done via shared memory. The application processes use a library whose aim is to provide abstraction of the set of system devices. Layer 1 processes broadcast their data calling the functions provided by this library.

By using this approach, when changing or adding an instrument, we only have to create a new process. There is no need of rebuilding the remaining software.

2 - Functional Layer

The components of this layer are virtual sensors and groups of functions that basically provide the motion and navigation operators. This layer controls redundancy and supports fault-tolerance procedures so that alternative modes of operation are available for dynamic reconfiguration.

Layer 2 processes send commands by invoking a function which puts the data on the shared memory and signals the target process. The details of process identification are hidden by this library, which behaves like a device database. For instance, on layer 2, the navigation process can ask "give me attitude data" or "give me range to a position" with no priori knowledge of the sensors installed. On the other hand, they can also query the set of installed devices and test whether a given device (which can be identified by its name) is present.

Positioning takes place at the function layer. A positioning algorithm must be implemented for each set of installed sensors. Normally, during one mission, each vehicle uses only one navigation algorithm, with several modes, that will try to extract the best result from the installed sensors. However, it can of interest to select different algorithms in order to compare results during a given mission. Eventually, two modes

(for instance, due a total failure of a special sensor) might be so different that both algorithms have to be specified separately.

Another block of the functional layer is the virtual world. Its function is to map the real world objects and important phenomena. It can be used by the coordination level in order to provide mission re-planning due to detected obstacles. In a multi-vehicle environment, provided communication with the vehicle takes place, this virtual world can be updated with data collected from each vehicle. We're also planning to estimate sound speed along a given segment based on distributed data.

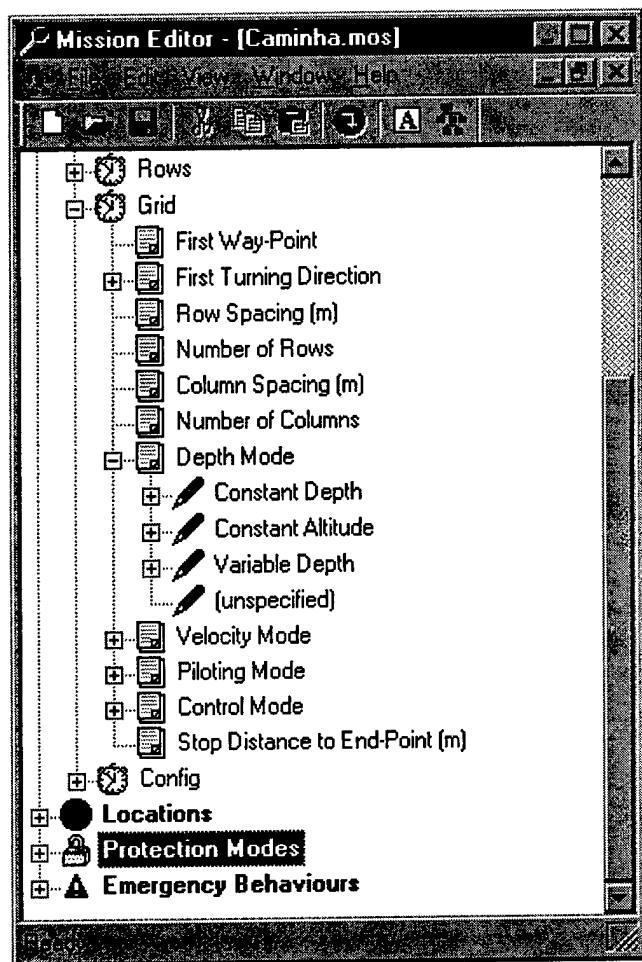


Figure 1 - The template for the Grid maneuver in the mission editor.

3 - Coordination Layer

The function of the coordination layer is to accomplish correct mission execution and tolerance to unexpected events. Tasks are scheduled according to vehicle state and received events, having in view the mission correct execution. A mission is organized in a set of several tasks picked from the functional layer ("Objectives" on the WHOI nomenclature or "behaviours") which are loaded either from a file at vehicle power-on or dynamically via a remote data link. A behaviour

can be an atomic command (like triggering a device) or a maneuver. A maneuver has hooks for trajectory generation algorithms, guidance algorithms and motion control. The desired algorithms can be chosen from the available set on the functional layer. The choice is made via mission file.

Other tasks can be made active asynchronously, mainly due to fault detection or user interaction. Besides event signaling, the coordination layer is fed by the functional layer with additional data and conditions that can be scheduled for verification (for instance, "no deeper than ...", "keep vehicle in a given geographic zone"). When the condition is violated an event is triggered. The response of the coordination layer to each event is defined in the mission file and can be set different for each individual mission stage. Those responses are implemented by recruiting resources from the functional. A small set of emergency behaviors is specially hard-coded in order to guarantee the ultimate robustness.

Whenever a faulty situation is detected, the current mission is either paused or aborted, depending on the seriousness of the situation, followed by mission or vehicle recovery.

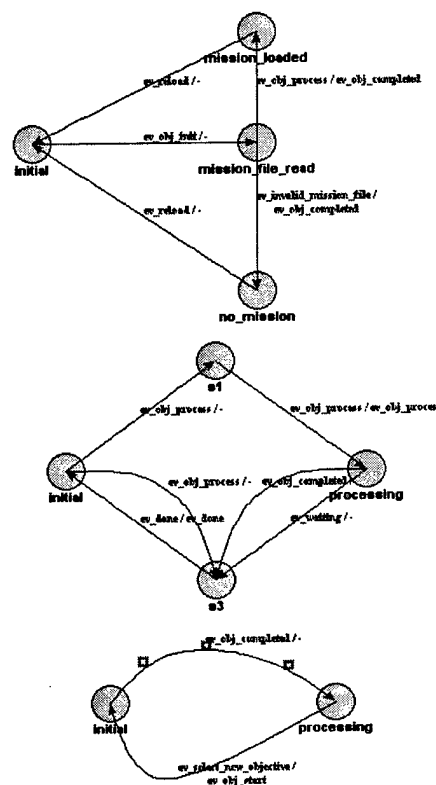


Figure 2 - State diagrams of the mission coordinator

IMPLEMENTATION

As stated previously, the described architecture was followed in the implementation of the software for the ISURUS AUV.

After a market survey, we chose QNX to be the operating system. QNX is a real-time, extensible POSIX-certified OS with a small microkernel and a set of optional cooperating processes. This architecture allows us to scale QNX to the particular needs of the vehicle. Although, the memory requirements were much bigger than we expected.

Although its deficiencies on thread support (multitasking is UNIX-like with processes running on separated addressing space), QNX provided most of the required function: process prioritisation, FIFO scheduling, message passing system, traditional Unix IPC mechanisms, standard real-time timer functions (up to 0.5 ms precision) and total access to the underlying hardware.

The most natural way of designing application on QNX is using the blocking-mode paradigm. The processes stay blocked until receiving a message or a proxy. A proxy is a kind of signal that can be attached to special events (timers, data arrival, etc). The message passing system used by QNX is very powerful, providing inherently mutual exclusion: when a process A sends a message, it stays blocked (if we do not want the processes to block we must use a message queue) until the destination process B issues a receive call. When a process issues a receive call, it also stays blocked until it has some pending message. When process B receives the message, process A remains blocked until process B replies. The send-receive-reply sequence can be seen as invoking a function which is resident on another process.

On the abstraction layer, we implemented processes to deal with each of the following components:

- Compass and inclinometers
- Altimeter
- CTD
- Acoustic system
- Motors
- AD, counters, and parallel interfaces.

This layer also include the data logger process. The priority of the data logger process is client driven. We do not want a higher priority to block because it is dependent of the execution of a lower priority process. The same behaviour could not be achieved even if we set the data logger with the highest priority. In that case, a process could be preempted by the data logger which eventually could be doing processing to a lower priority process.

Although, formally, the functional layer and the coordinator layer are distinct, in the current implementation the simplicity of the later suggested a tight coupling between them. Thus we decided to keep them in the same process.

SIMULATION

When writing new modules or adding new maneuvers it is essential to have a straightforward way of performing some tests "on the bench". For testing purposes, the first software

layer can be replaced by a simulation layer that mimics the normal operating mode of the vehicle. This architecture allows the developer to test new tasks with no need to build the usual test stubs. Furthermore, the new task will run integrated with the remaining application, providing an environment as similar as possible to the real operating mode of the vehicle. This way it is easy to find unexpected interactions with the remaining tasks.

The simulation layer is composed by the task which performs the simulation calculations and several other tasks which model the physical devices. The physical devices are divided into sensors and actuators. This tasks interact with the above layer using the same interface (functions that access a shared memory segment for data communication, sending messages to the data logger or triggering events using the event manager) and with the simulation task through local variables. We modeled the actuators dynamics and power consumption and added noise to sensor measurements. One interesting achievement was the modeling of the acoustic system: the navigation task was tested in a virtual environment by simulating the presence of two transponders (lockout times and delays were accounted for), currents and constant sound speed. The behavior of the vehicle was also simulated with the implemented PID controllers and guidance algorithms.

The model uses the decoupled equations of motion from Fossen [5]. The parameters were obtained from water tests. The integration of these equations is made at a fixed frequency using a simple integration technique [4].

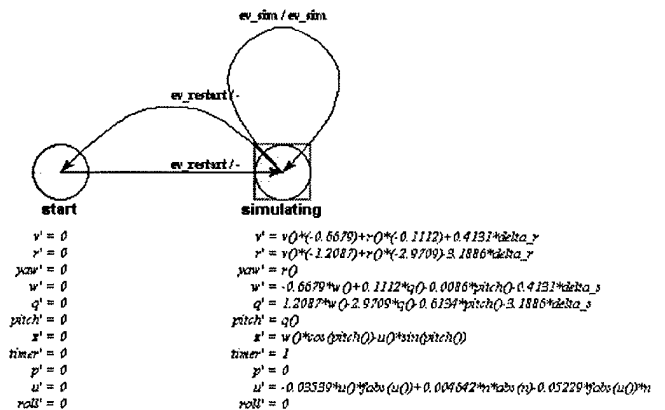


Figure 3 – Dynamic model of the ISURUS vehicle

The main constraint of this implementation is to keep the capability of running the simulation process on the target (the vehicle computer) keeping real-time operation. This was achieved because the vehicle models, although realistic, were kept simple as also the integration algorithm. It is not possible to have simulations running faster (or slower) than physical time but the system was not intended to do so anyway.

The model equations used were here strongly customized to the ISURUS vehicle but our goal is to implement a 6DOF model having the parameters read from some configuration file. Obviously, with a different vehicle we will have different

physical devices whose models can be easily implemented according to this architecture.

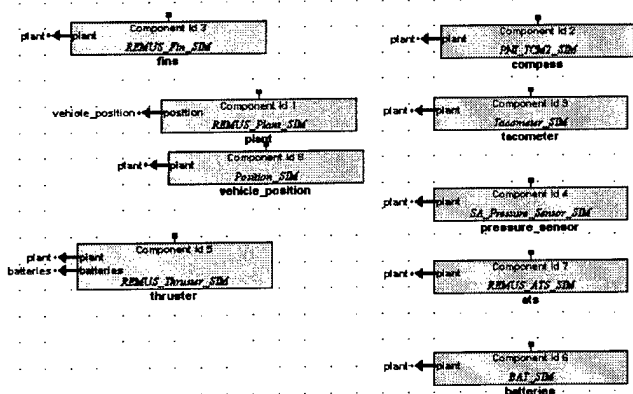


Figure 4 – Block Diagram of the Simulation Layer for the ISURUS AUV

MISSIONS

The vehicle has already executed several missions using the new software. Since the beginning, the only software difficulty we experimented was related with disk consistency. QNX file-system is not very tolerant to system reboots.

We use a Point-to-Point Protocol (PPP) connection to download the mission objectives to the vehicle or upload the log files. This approach allows us to use standard applications (FTP, telnet) to perform the routine operations. It is even possible to change the code and rebuild it on the vehicle in execution time, although we only used this feature a very few times in test missions.

Missions have been specified with the help of an application (Figure 1) with graphical interface that simplifies the whole process. The mouse is used to insert the desired mission tasks. The user must only fill the presented input boxes with the desired parameters values. In the end, the application generates the mission file (which can also be manually edited). This is a improvement when compared to writing text files.

CONCLUSIONS AND FUTURE WORK

The control architecture has proved to be useful on helping to point out the most important aspects of the software organization and establishing a solid framework. The relevant modules for the current application were identified and implemented.

The current implementation allowed us to improve our REMUS vehicle by upgrading the navigation subsystem, adding new maneuvers and actions and changing vehicle operation from a end-user perspective. We consider it to be a major improvement to the original WHOI software. The combination of the QNX operating system and our application revealed satisfactory.

We are concluding several lateral applications (mission editor and applications for data warehousing, visualization and retrieval) which will improve our operational capacity.

In a near future, this framework will be used in related projects, as also great part of the implemented software.

REFERENCES

- [1] J. Borges de Sousa and F. Lobo Pereira. A Generalized Vehicle Control Architecture for Multiple Autonomous Vehicles. In *Proceedings of the IEEE AUV'96 Conference*, Monterey, CA, USA, June 1996, 223-30.
- [2] Anibal Matos, Nuno Cruz, and Fernando Lobo Pereira. Development and Implementation of a Low-cost LBL Navigation System for an AUV.
- [3] B. Allen, R. Stokey, T. Austin, N. Forrester, R. Goldsborough, C. Alt. REMUS: a small, low cost UV; System description, field trials and performance results. In *Proceedings of Oceans 97 Conference*, Halifax, Canada, October 1997.
- [4] A. Deshpande and Joao Borges de Sousa. "Real-time Multi-agent Coordination using DIADEM: Applications to Automobile and Submarine Control." 1997 IEEE Conference on Systems, Man and Cybernetics
- [5] T. Fossen, Guidance and control ocean vehicles, New York, John Wiley & Sons Hall, 1994.

HIGH RESOLUTION UNDERWATER ACOUSTIC IMAGING

Ian S F Jones
Ocean Technology Group
University of Sydney,
Australia
ian.jones@otg.usyd.edu.au

ABSTRACT

A high resolution underwater imaging system using sparse array technology has been developed and tested in turbid waters around Australia. High resolution three dimensional imaging implies many voxels. The present system can image $10^3 \times 10^3 \times 4 \times 10^3$ voxels although faster images can be obtained by zooming to a smaller volume of interest. With three dimensional images, precise dimensions of complex shapes such as pipe joints can be obtained. Potential applications in offshore platform inspection are discussed.

The longer wavelengths of Megahertz acoustic signals produces less scattering than light while array technology allows the imager to take advantage of pulsed ensonification to further reduce backscatter fogging of the image. The advantage of acoustics is most pronounced in very turbid waters.

The megahertz frequencies allow millimeter resolution with array sizes compatible with ROVs. Digitization takes place on the acoustics tile that make up the array and the signals are then passed by fiber optical cable to the above surface processor to reduce the volume and underwater weight of the system

There are a number of obstacles to producing an innovation in underwater imaging. Worries about adequate coherence lengths to support arrays capable of adequate resolution were found to be groundless. One impediment to success was the computing loads implied by multi-element arrays and large voxel numbers. To attack this problem international groups were funded to provide potential solutions and a decreasingly smaller number of groups supported at each review point. This technique has produced a lower cost approach for the underwater acoustic camera design.

1. INTRODUCTION

Finding objects in turbid waters with underwater video is a problem due to the lack of visibility. High frequency acoustic signals suffer less scattering in turbid waters, so an attempt has been made to produce an innovation in high resolution underwater acoustic imaging. The innovation team needed to solve three problems before the "underwater camera" could produce resolutions of

millimetres at ranges of meters. It needed to model sparse arrays to determine the number of sensing elements (thousands), to produce an economical acoustic sensor tile that could be used to form such large element arrays and finally to simplify the data processing to be within the capabilities of today's computers.

These problems have been solved and the successful testing of the prototype has cleared the way for commercialisation and possibly wide diffusion of the technology to produce an innovation. Uses for the technology range from counting fish in aquaculture farms to finding bodies in dams and rivers. The production of dimensioned engineering drawings of damaged underwater structures by exploiting the three dimensional nature of the information is a novel use of the technology.

BACKGROUND

The perceived need for high resolution underwater imaging drove the Australian DSTO to attempt to produce an innovation. An initial decision to use ultrasonic and multi-element arrays set the parameters of the early work. An alternative strategy of using an acoustic lens to form the beams rather than delay and addition of array elements was considered. Belcher (1998) has described the lens approach and he has found a suitable application for this technology in a diver hand held sonar. The current version is used as a side scan sonar with 64 beams, limiting later resolution to about $r/200$, where r is the distance from the camera to the object. However systems are being developed with 2D arrays of many elements that can be placed in the focal plane of an acoustic lens. It is not easy to obtain a large depth of field with a fixed acoustic lens. Subsequent work has shown that other approaches such as gated laser detectors have limits that restrict their ability to revolutionise underwater imaging.

DSTO recognised that the potential commercialiser of the R&D for underwater imaging needed to be involved early in the program and so the Defence Acquisitions Organisation was approached to fund the two most promising groupings of firms to play a part in the research phase. This was a result of the philosophy that innovation will be more often achieved if the cultural

difference between R&D providers and the production engineer, sales and marketing people is addressed early in the program and time and familiarity allowed to smooth away some of the initial prejudices. "Partnering" meetings were used to expose each party's aspirations and find how they could be satisfied within the goal of producing an innovation. The technology developed in the R&D phase needs to be vested in the commercialiser if he is to be successful. In many cases much of the technology is not easily transferred by formal documentation. Thus involvement of the potential commercialiser from the start of the program not only allows production engineering issues to be kept sight of but allows this diffusion of the specialised knowledge needed to support the innovation.

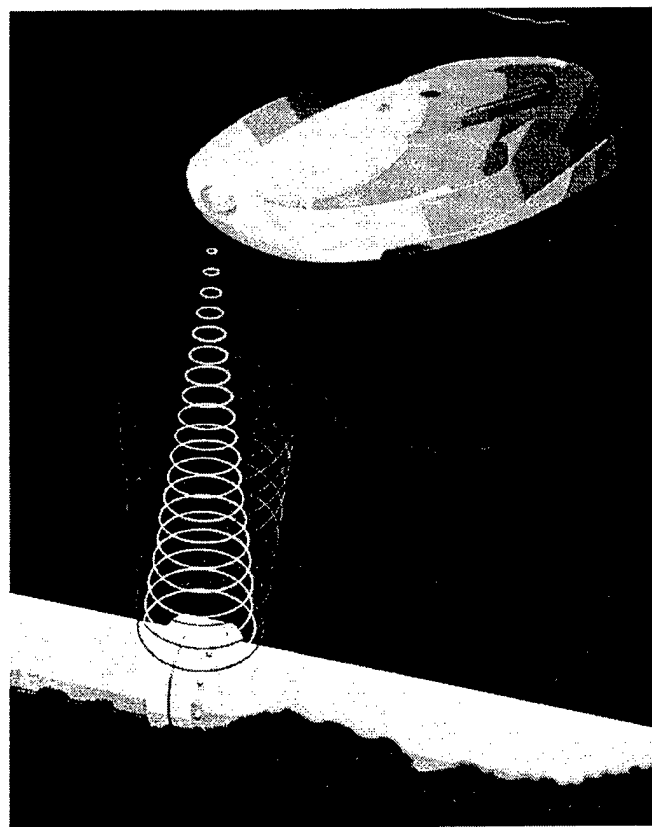


Figure 1. An artist's impression of the UAI technology employed on a ROV to image a sub sea pipeline.

While it was in principle possible to provide a 4,000,000 element acoustic array to image items with millimeter resolution at ranges of a few meters, there was no prospect that such a device could be produced within a reasonable cost or that the weight and size would make such a device able to be deployed in many situations needing underwater imaging. The computational power needed also seemed to make the goal of millimeter resolution in three dimensions impossible when the project was started in 1992.

A ten year plan was drawn up at the start of the program before a solution to the technical problems was in sight.

The plan was important because it kept in mind that commercialisation was the goal. It gave an indication of the resources needed and that these resources were substantially more than the R&D costs. An important feature of the project was the production of a vision or plan even before an engineering solution could be foreseen. This plan looked at a way of mitigating the risks inherent in attempted innovations

The research and development phases set out to resolve the three principal technical impediments to success by constructing an engineering prototype. These were the number of elements needed in a conventional array, the economical production of acoustic sensors and rapid processing of the image from the array signals.

DESCRIPTION OF UAI

Underwater imaging of objects in ports and rivers and lakes using light is often rendered ineffective in turbid conditions. The longer wavelength of acoustic waves, over that of light, gives it an inherent advantage of lower scattering by the suspended particles in turbid waters. This was demonstrated theoretically by Thuraisingham (1994). These particles in natural situations are usually either suspended sediments or phytoplankton. In situations such a waste water flows, the scatterers that restrict vision are industrial and domestic waste products.

Acoustic radiation is produced in the current prototype by a piezoelectric device which illuminates a region in front of the acoustic receiving array of hydrophones with a "flash" of sound. This sound is of the nature of a chirp around a centre frequency of about 3.5 MHz. There is no lens in the system as the equivalent to focusing in the video camera is achieved by delaying the received signals by different amounts to steer acoustic beams in particular directions. By keeping track of the time and knowing the speed of sound in water the range of each item in the image made up of many beams can be determined. This is in contrast to a video camera which presents the light scattered along the beam as a single brightness without regard to range.

When the plan was drawn up in 1993 the envelope of possible performance features of UAI was not known. The obvious parameters of performance, measured by resolution, range and field of view, all of which should be as large as possible, are in conflict with high refreshment rate which is faster the less extensive the image. While cost was important, performance that justified the purchase by specialised users was considered more important in defining the parameter space studied. The UAI was not envisaged as leading to consumer items.

The sparse array technology was decided upon after a study of the theoretical performance of random sparse arrays by Blair and Anstee (1999). Careful study by both

the CSIRO and DSTO showed that about a twelve hundred fold reduction in the number of elements could be achieved while retaining adequate performance of "image to sidelobe clutter". Such a ratio increases as the number of elements in the array increases until the limit of a fully populated array is reached. Some randomly generated patterns were found to be noisier than others and so the modelling results for the pattern finally chosen were carefully studied.

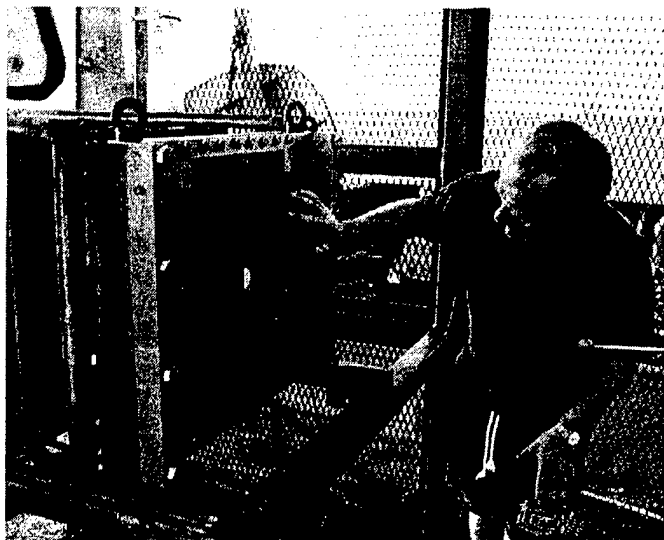


Figure 2. Mike Bell examining the partially completed sparse acoustic array mounted on the test case of the engineering prototype of the underwater acoustic imaging sonar.

The design and construction of multi sensor sparse array tiles and associated electronics were undertaken by Thomson Marconi Sonar. The 50 mm square tile contains 32 receiver elements 0.42 mm diameter which are ultrasonically milled from a sheet of piezoelectric ceramic. The ceramic sheet is then sandwiched between two precision printed circuit boards, the outer one of which has holes drilled aligned with the pegs to act as acoustic windows. These are subsequently filled with polyurethane as a waterproofing material. Underneath the sensors are bonded directly to buffering field effect transistors and amplifier printed circuit boards. Ribbon cable connects the tiles to the "wet-end" electronics where the signals are conditioned and digitized. The digitised signals are then sent to the "dry end" electronics by fiber optical cable. As some hundred acoustic tiles will be needed in the most capable applications of underwater acoustic imaging systems, the ability to be able to manufacture these devices economically is very important if this project is to lead to a significant innovation. This goal has been met.

The tiles which can be seen in Fig 2 incorporate a one bit digitisation system. Such a system reduces the bandwidth requirements of the cable taking the information to the processor mounted on the support vessel. In 1995 the

team showed that representation of each sensor signal by one bit stream of data had the potential to reduce the cost while largely preserving the quality of the image. The system was subsequently adopted.

The digital signals from the sparse array were processed in the "dry end" electronics. First the signal received by each sensor was dechirped. This process produces a signal that is equivalent to the acoustic backscatter that would be expected from an illuminating transducer if it had sent out a single sharp pulse. Next the signals from all the elements in the array were combined with appropriate delay from the transmitted chirp to produce the backscatter level from a single voxel (three dimensional pixel) in the field of view. This process was repeated for other voxels until the region to be imaged was completed. This process can be very computer intensive and the opportunities to speed up the process were discussed in Blair and Jones (1998). A process of stimulating an invention to exploit these opportunities was undertaken by using groups outside the innovation team.

Specifications of prototype

imaging mode	
resolution	r/1000
range	1-5m
transmitted signal	chirp
frequency	~ 3.5 Mhz
signal/ clutter	1/N
size	1000λ

λ = wavelength of sound

N = number of acoustic elements in the array

The optimal presentation of the image has been left to the commercialisation stage. At present a single chirp is stored and the image can be viewed as a three dimensional object and rotated. The next chirp can then be viewed. Acoustic backscatter images are not the same as an optical colour image with which we are very familiar. The acoustic image is more akin to a black and white image except that it depends upon the acoustic nature of the surface of the object rather than its optical backscattering properties. In addition the illumination is from a single point much as in a flash picture and the resulting images are different from diffuse light images. In particular there are bright reflections much like those seen in some flash images of people with glasses. Rendering of the image of backscatter will in many applications prove beneficial in human interpretation of the acoustic image.

The successful demonstration of the technology at sea in Darwin Harbour, Australia was used as the indication that the R&D phase was complete and

commercialisation could begin. In addition to the Darwin tests further tests were carried out in Sydney Harbour to extend the range of parameter space by examining larger arrays.

REVIEWS

As the project moved from research to development of the engineering prototype the documentation and review became more extensive. The effort by Thomson Marconi Sonar Pty Ltd increased as the project advanced from research to development. A risk management committee was established to assess the technical risks during development and to monitor the reduction of uncertainty as the project advanced. It is argued in Madry and Jones (1999) that risk management of innovation needs to address a number of issues that are not the usual focus of project review. In the later stages three monthly project management review was provided by the Defence Acquisition Organisation.

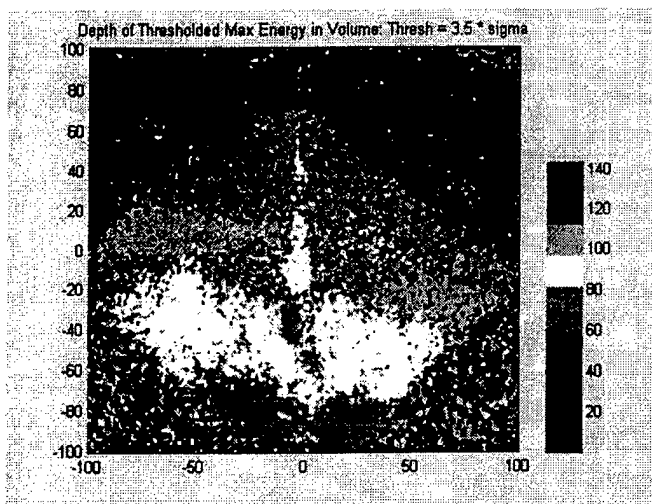


Figure 3. The dimensions of a diamond shaped plate imaged underwater. The ranges were smoothed by 3x3 median filter and points at different range to the body in the upper part of the diagram not shown.

RESOURCES

The three organisations undertook this project in the spirit of "partnering". Thomson Marconi Sonar (TMS Pty) and the CSIRO were bound together by contractual relationships, while DSTO acted as a technical adviser to the Defence Acquisitions Organisation who provided the contractual documents and managed the flow of the majority of the funds.

The TMS team was managed by Dr Andrew Madry in the planning of the developmental phase and by Graham Mountford in the prototyping phase. Ian Bedwell designed the acoustic tile which is at the heart of the economic success of this project. The CSIRO team was initially lead by two very successful engineers, Dr George

Kossoff and Dr David Robinson. Dr Don McLean, an astrophysist directed the final CSIRO component of the program. The DSTO team involved Dr Ian S F Jones, who wrote the innovation plan (see Jones (1996)) and acted as champion of the project thru out its lifetime. Jim Thompson, Dr David Blair and Mike Bell playing prominent roles over the decade.

The RAN in the component of the Force Development Division, representing the lead customer played an important part in defining their operational concept. This allow the R&D to include solutions consistent with the projected requirements of the RAN mine hunting activities.

APPLICATIONS

Underwater acoustic imaging can be applied to a number of problems. While designed to overcome the problem of low visibility in harbors and rivers, the three dimensional nature of our information allows measurement in the same sense as stereo camera can provide dimensional information. We particularly have in mind imaging damaged underwater structures. With this as a goal we have started looking at the dimensions of metal plates.

Our first study was of a diamond shaped metal plate with differing acoustic texture over its surface using the criteria of the maximum energy in a voxel. The plate is shown in Fig 3 with the top point inclined away from the camera and the right hand point being closer than the left. The dimensions are in millimeters. Regions of low acoustic backscatter are masked by the sidelobe clutter of regions of the plate closer to the camera when the maximum energy technique is used without more intelligent processing. The colour boundaries (shown as gray scales here) are lines of constant distance from the plane of the camera. In the centre of the plate is an Allen screw which is higher than its surroundings and it casts a shadow behind it. Three holes in the plate are not well recognised in this dimensional representation and need to be identified by an acoustic brightness image.

Considerable potential exists to distinguish the clutter from a plausible continuous surface but already an engineer could recognise those ranges that lie near the expected position of a plate and those which appear far from the surrounding surface .

CONCLUSIONS

The Engineering R&D Phase of this attempted innovation has produced a new underwater acoustic technology with potentially wide application.

High resolution underwater acoustic imaging has been shown to be possible and a design developed that can

be produced economically. An engineering prototype has produced range determinations that would be useful for the inspection of underwater engineering structures. More work is needed to tailor the technology to particular applications. In particular those with turbid water or with the need for precise measurement of components will find the present technology more suitable than the underwater video camera.

REFERENCES

- Belcher, E (1998) Hand-held sonar displays, near photographic images, *Sea Technology*, **39**, pt 12, 19-23.
- Blair, D G and S. D. Anstee (1999) Underwater Acoustic Imaging: A Simulation Program and Related Theory. DSTO Tech Note (under review).
- Blair, D. G. and I. S. F. Jones (1997) Underwater Acoustic Imaging: Rapid Signal Processing. DSTO Tech. Note TN-0098.
- Erikson, K. et al. (1997) A 128x128 (16k) Ultrasonic Transducer Hybrid Array. *Acoustical Imaging*, **23**, 485-494.
- Jones, I S F (1996) Underwater acoustic imaging innovation program. DSTO Tech. Note TN-0065.
- Madry, A and I. S. F. Jones (1999) Risk reduction in Government sponsored innovation. *Technology Business Review*. Aust. Grad. Sch. Eng. Innovation, Sydney ISSN 1329-3214(Aug/Sept submitted).
- Thuraisingham, R. A. (1994) Theoretical estimates of high frequency acoustic attenuation and backscattering from suspended sand particles in the ocean and in an estuary. DSTO Tech. Report TR 0078.

DEVELOPMENT OF MINIATURE, HEAD-MOUNTED, VIRTUAL IMAGE DISPLAYS FOR NAVY DIVERS

D.G. Gallagher
United States Navy Coastal Systems Station
Diving & Life Support Systems Division
6703 West Hwy 98-Code A52
Panama City, FL 32407 USA
Tel: (850) 235-5417
FAX: (850) 234-4671
Email: GallagherDG@NCSC.NAVY.MIL

ABSTRACT

Much of navy diving is conducted in regions where the visibility is extremely limited, such as the very shallow water/surf zone (VSW/SZ) region. Special sensor, imaging, navigation, and communication technologies are required to enhance a diver's ability to "see", navigate, and communicate in these regions. These include hand-held sonars, GPS (global positioning system) units, acoustic navigation systems, and low-light-level cameras.

A visual interface technology is required for the diver to interpret and make use of this enhanced information, which often is a combination of video images, graphical displays, and alphanumeric data. One such technology is a simple underwater display screen. Unfortunately, in many cases underwater display screens can not be seen at all due to the extremely adverse conditions, rendering an enhanced diver sensor system useless. It remains a considerable technical challenge to provide a diver display system that can be clearly viewed underwater in regions with extremely poor visibility and lighting.

The United States Navy's Coastal Systems Station (CSS), Panama City, Florida has been developing diver display systems, specifically virtual image head-mounted display (HMD) systems, for navy divers since 1992. These systems incorporate state-of-the-industry microdisplay technology. This paper will discuss the development of these systems, current status of the technology, and the future outlook for the navy's diver HMDs.

II. INTRODUCTION

Underwater displays have been used in both military and civilian applications for many years. Small alphanumeric, and simple graphic displays are used on diver equipment consoles, digital watches, and dive computers. While these displays are very reliable, they can be difficult to see (in some cases impossible) under conditions of extremely poor water visibility, such as in the VSW/SZ region, even with efficient backlight and illumination technology.

Video display screens have the capability of displaying full video images (black & white, and color) in addition to graphics and text. Typically, they are used to view the output from underwater imaging devices, such as handheld cameras or sonars. These displays have historically been mounted directly to the piece of equipment in operation. Unfortunately, viewing them has also been difficult. Aside from the problems with poor water visibility, they are very sensitive to viewing angle. As a result, a diver must be as close as possible to the screen to see it clearly. Often a large "viewing hood" is attached to the display screen to facilitate better viewing.

To remedy these problems some video displays have been mounted directly to diving helmets, or in some cases integrated into them. This approach can work very well in applications where a diving helmet is used; particularly if the display is integrated into the helmet. However, this presents a serious problem for the navy diver operating in the VSW/SZ region. Missions in this region necessitate the use of a rebreather. Consequently, divers are using lightweight

scuba masks, or full facemasks. The bulky and heavy video display systems designed for diving helmets are completely untenable for VSW/SZ mission scenarios.

III. US NAVY DIVER DISPLAYS

Operations in the VSW/SZ region of the ocean present unique challenges that have not been effectively addressed by technologies developed for deeper water applications. This is particularly true in the case of diver HMDs. Smaller, lighter systems with better viewing optics are needed for the growing number of operations conducted in this critical region.

Through funding from the US Navy's Office of Special Technology, and the EOD (Explosive Ordnance Disposal) Program Office, the Coastal Systems Station embarked on a series of projects to develop a small, lightweight diver's HMD. The HMD would be employed by navy divers wearing a full facemask (US Navy MK-20/commercial AGA-type mask), or scuba mask, conducting a variety of missions in the VSW/SZ region. It would be capable of displaying text, graphics, and full video images to a diver regardless of water visibility and ambient lighting conditions. Based on the nature of navy diving missions, and as a safety concern, the diver's HMD was required to be monocular, vice binocular. In this way the diver would always have at least one eye completely unobstructed should an emergency arise. To provide maximum flexibility during testing and evaluation the display system was required to be a separate "add-on" piece of equipment, allowing each diver to continue using his own facemask. (Dorch and Gallagher, 1994)

Much engineering and human factors data was available for the design of military cockpit HUDs (head-up displays) and HMDs (head-mounted displays). Also for HMDs used for industrial and VR (virtual reality) entertainment applications.

While some of this information was applicable for our application, we found that much of it was not. A lightweight HMD for use underwater by a diver wearing a facemask is a unique application of this technology with very specific design concerns not addressed in cockpit, industrial, or entertainment applications.

A. Microdisplay Technology

To build such a system required using video displays much smaller in size than had previously been used in diver helmet-mounted systems. In those

systems, display screens 2.5 inches to 4 inches (63.5mm to 101.6mm) diagonally in size were typical. The new navy HMD system would require the use of an ultra-miniature class of displays known as microdisplays. These are displays with a viewing area less than 1.0 inch (25.4mm) diagonally in size. (Gallagher, 1998) Microdisplays are typically classified according to the specific technology employed to generate the display image itself. Some of these technologies, like cathode ray tube (CRT), have been used in military HMD systems for over 30 years. Others, like virtual retinal displays (VRD) that "scan" an image directly into the eye with a micro-laser, are on the cutting edge of the state-of-the-art.

Microdisplay technologies considered for our application were cathode ray tube (CRT), liquid crystal (LCD), electroluminescent (EL), field emission (FED), and light emitting diode (LED). CRT and LCD-based microdisplays were industry standards, already used in video camcorders as viewfinder displays. FED and EL-based microdisplays were under serious consideration for use in other military HMD applications. LED-based microdisplays had already seen limited use in some military and industrial HMD applications. Based on their technological maturity, availability, resolution, cost, reliability, power requirement, and physical size; we selected the CRT, LCD, and FED-based microdisplays from which to produce prototype systems for further evaluation.

B. Optics: Virtual Images

In some of the previous helmet-mounted systems the diver's eye was physically several inches from the display itself. This long eye relief distance, and fairly large display size, necessitated using large diameter magnifying lenses to provide a field-of-view (FOV) sufficient to allow the diver to see the entire magnified display screen. In most cases, the diver was also viewing the screen through a few inches of water as well. Since water acts as an additional lens in the system, distortion was introduced. (Dorch and Gallagher, 1994) To resolve this, most of the helmet-mounted systems also used "water-corrected" optics. This resulted in diver display units that were large, heavy, and expensive.

Obviously, a different optical approach was needed since our new system would be attached to a lightweight facemask. Our goal was to provide the best magnification in the smallest and

lightest possible package. Each prototype was designed to fit directly against the diver's facemask (or just a few millimeters away) during operation. For the MK-20 full facemask this was an eye-relief of approximately 2.0 inches (50mm); for the scuba mask approximately 1.375 inches (35mm). This would allow a much smaller diameter lens to provide the field-of-view (FOV) necessary to see the entire magnified display screen. This also minimized the effect of optical distortion from the water to the point that it was negligible. The magnified image of the display screen is referred to as a *virtual image* since it appears to be located at some "apparent" distance in front of the viewer's eye. (Dorch and Gallagher, 1994) (Fig. 1)

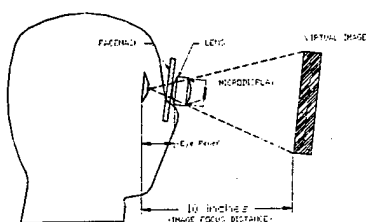


Figure 1: Virtual Image System For Navy Diver HMD

Four separate optical systems were developed and used in the prototype diver HMDs. Three of the systems employed off-the-shelf glass achromatic lenses. An achromatic lens is comprised of two different optical elements cemented together to form a lens doublet. This typically provides better polychromatic imaging (for color displays), corrects optical aberrations, and has brighter images than a single simple magnifying lens. (Dorch and Gallagher, 1994) The fourth system used a set of modified plastic lens elements from a commercial HMD used in industrial and entertainment applications.

C. Diver HMD Prototypes

Four prototype configurations were built to evaluate the selected microdisplay technologies and optical systems.

1) Prototype # 1: J-Tube HMD

Prototype #1 used a monochrome CRT-based microdisplay with a viewing screen 0.54 inches (13.7mm) diagonally in size, and provided 360 x 280 pixels (100,800) of resolution. It used a single glass achromatic lens 0.98 inches (25mm) in diameter with a 1.96 inch (50mm) focal length in an adjustable focus eyepiece. To make the system more compact, the

optical path was folded 90-degrees using a glass amici prism. Used with the full facemask this provides a fairly narrow 14-degree horizontal field-of-view (FOV) with a magnification approximating a 3.75 inch (95.25mm) diagonal screen at a distance of 10 inches (254mm). (Dorch and Gallagher, 1994)

The specially designed housing is a folded J-Tube arrangement designed to mount to the right side of the MK-20 full facemask and be worn in a fixed position during operation. The J-Tube housing was produced from acetal plastic (Delrin) and used standard o-ring seals. It is rated to a depth of 150FSW. Power (from a 12-volt DC source) and test information is sent directly to the unit via an umbilical from the surface. This prototype performed fairly well but had limited brightness, low resolution, and the smallest magnification. (Dorch and Gallagher, 1994) (Fig. 2)

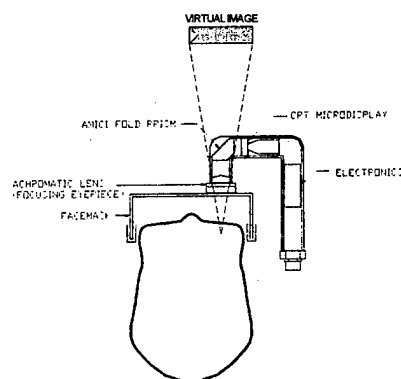


Figure 2: Prototype #1 - J-Tube HMD

2) Prototype #2: Cylindrical HMD

This prototype was tested with both the MK-20 full facemask and standard scuba mask. It used low resolution LCD and FED-based microdisplays. Both microdisplays provided color, and had viewing screens 0.7 inches (17.8mm) diagonally in size. The LCD provided 420 x 230 (96,600) pixels of resolution, while the FED provided 420 x 240 (100,800) pixels of resolution. The optical system was slightly larger with a single glass achromatic lens 1.18 inches (30mm) in diameter with a 1.96 inch (50mm) focal length in an adjustable focus eyepiece. To make the system more compact, the optical path was folded 90-degrees using a glass amici prism. Used with the full facemask this provided a 16-degree horizontal field-of-view (FOV), with the scuba mask it is closer to 22-degrees. The magnification approximates a 5

inch (127mm) diagonal screen at a distance of 10 inches (254mm).

The cylinder-shaped housing was also produced from acetal plastic (Delrin), made use of standard o-ring seals, and is rated to a depth of 150FSW. It was designed to mount to the right side of the MK-20 full facemask, or a standard scuba mask. It was provided with an additional linkage to allow the wearing position to be adjusted during operation, including being flipped-up out of the way when not needed. Power (from a 12-volt DC source) and test information is sent directly to the unit via an umbilical from the surface. Other versions of this prototype connect directly to diver portable equipment. (Dorch and Gallagher, 1994) This prototype performed well, providing low resolution color with good brightness and magnification. This particular prototype was the most extensively field tested version of the diver HMD (Fig. 3).



Figure 3: Prototype #2 - Cylindrical HMD

3) Prototype #3: Advanced (High Strength) HMD

Prototype #3 used a high resolution color LCD microdisplay 0.7 inches (17.8mm) diagonally in size that provided 800 x 225 (180,000) pixels of resolution. This system was tested with both the MK-20 full facemask and scuba mask. It uses four plastic lens elements 1.0 inches (25.4mm) in diameter with a combined focal length of 1.75 inches (44.45mm) in a fixed focus system. The optical path was folded 90-degrees to make the unit more compact. This was

accomplished using a thin optical grade mirror instead of a glass prism. (Alexander, 1996) The use of plastic lenses and a fold mirror greatly reduced the weight of the system. With the full facemask this provides a narrower 14-degree FOV, and a 20-degree FOV with the scuba mask. The magnification approximates a 5.75 inch (146mm) diagonal screen at a distance of 10 inches (254mm).

The custom housing was produced from high strength, injection-molded, reinforced nylon; made use of standard o-ring seals, and carries a depth rating of 300FSW. It was designed to mount to the right side of the MK-20 full facemask or a standard scuba mask. It was provided with a ball-in-socket linkage that allows finer adjustments to the wearing position during a dive, and also allows the unit to be flipped-up out of the way when not needed. Test information is sent via an umbilical from the surface routed through a diver's belt-worn, 12-volt DC rechargeable battery pack. (Alexander, 1996). Other versions of this prototype connect directly to diver portable equipment. This prototype performed well, providing high resolution color with good brightness and magnification, albeit a narrower field-of-view (FOV). The rugged housing design has helped make this prototype the "workhorse" navy diver HMD to date. (Fig. 4)

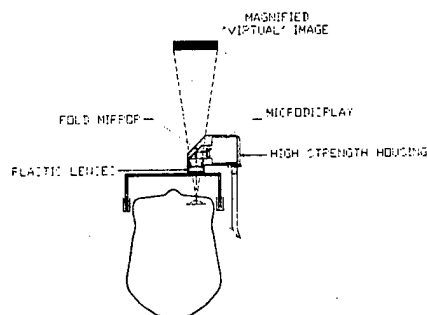


Figure 4: Prototype #3 - Advanced (High Strength) HMD

4) Prototype #4: Wide FOV Diver HMD

Prototype #4 also used the high resolution color LCD microdisplay with two glass achromatic lenses approximately 2.0 inches (50mm) in diameter with a combined focal length of approximately 1.57 inches (40mm) in a fixed focus system. The short focal length combined with the larger lens size prohibited folding the optical path 90-degrees. This yielded a much heavier and longer unit. The LCD microdisplay was used in both landscape (horizontal) and portrait (vertical) viewing orientations. This prototype was

configured for, and tested with, the scuba mask only. Magnification approximates a 6.25 inch (158.75mm) diagonal screen at 10 inches (254 mm) in front of the diver's eye at a 35-degree field-of-view (FOV).

The custom housing was produced from UV (ultraviolet) light curable epoxy resin using a stereolithography process and carries a depth rating of 150FSW. It mounts to the top center of a scuba mask over either the right, or left eye. A flexible linkage allows minor adjustments during operation. This prototype performed well, providing high resolution color with good brightness, excellent magnification, and a very wide field-of-view (FOV). It is the largest and heaviest of the prototypes built. This particular prototype was designed for use with a diver's handheld imaging sonar, and connects directly to that system. (Fig. 5)



Figure 5: Prototype #4-Enhanced Diver Display (Wide FOV)

D. Testing and Evaluation

Tests were conducted in swimming pools, bays, lagoons, and the open ocean under a variety of water visibility and ambient lighting conditions. To evaluate each system we sent text, graphics (maps, compass symbols, schematics), and video images to the diver HMDs via an umbilical directly from the surface. (Dorch and Gallagher, 1994) In later testing, the diver HMDs were connected directly to various handheld diver equipment (imaging sonars, cameras, navigation systems).

Divers from a variety of military and civilian backgrounds helped in evaluating the systems. These included military divers from the navy's EOD and SEAL communities, the army's Special Operations Force (SOF); and civilian divers from police departments,

search /rescue/recovery units, and even recreational scuba divers. (Dorch and Gallagher, 1994) (Alexander, 1996) The divers provided feedback on every aspect of system design and performance.

Magnetic signature testing (in accordance with MIL-M-19595C) was conducted on each microdisplay, and each prototype system in anticipation of their possible use in support of EOD mine countermeasures (MCM) operations.

E. Results and Conclusions

1) Microdisplays

While each microdisplay technology tested performed adequately; the higher resolution (800 x 225 pixels) color LCDs were by far the preferred technology due to the best combination of resolution, brightness, color, low power requirement, and thin packaging.

2) Optics

We concluded that a fixed focus system is best suited for a lightweight underwater HMD. Two of our prototypes made use of an adjustable focusing eyepiece with a sliding o-ring seal (refer to Fig. 2 and 3). During testing we found that the actual amount the eyepiece was moved during the focusing process was negligible. Once the eyepiece was set at the optimum focus point for one diver, each subsequent diver's adjustment placed the eyepiece essentially back to the original location. We found this to be acceptable for the vast majority of military and civilian divers who tested the systems.

3) Brightness Control

All of our prototypes had a fixed brightness level. We arbitrarily set the brightness level prior to final assembly using various video, sonar, and text data screens in an attempt to optimize the brightness. This optimized brightness level was to be used whether the diver operated in murky water at night, or clear water during daylight. In the area of brightness we found that "one size does not fit all". Based on many evaluation dives we concluded that each diver needs the capability to adjust his display brightness level during the dive as different ambient conditions or mission scenarios dictate. It was impossible to set an optimum brightness level for all types of data and all ambient conditions.

4) Magnification and Field-Of-View (FOV)

Obviously, the magnification should enable the diver to read alphanumeric text and graphic symbols clearly. Based on our testing, we found that a minimum alphanumeric character size of 0.5 inches (12.7mm) at a focus distance of 10 inches (254mm) could be comfortably read by more than 90% of all the test divers.

The best field-of-view (FOV) is one that provides maximum viewing of the magnified image at the appropriate eye relief distance. We found that different divers tended to vary the eye relief distance slightly. Also, the same diver would vary the eye relief distance slightly depending on the specific type of data presented (text, video, sonar graphic). We found that a field-of-view (FOV) that provided a viewing area slightly larger than the magnified display image (at the prescribed eye relief distance) was optimum. Not only does this allow some flexibility in eye relief distance, but gives the general impression of a brighter image.

5) Eye Dominance, Eye Strain, and Eye Fatigue

During our tests we found that when a diver used the system to occasionally glance at displayed information; such as to check depth, bottle pressure, or a compass heading; it did not matter on which side of the mask the display was worn, or which eye was dominant. No significant eye strain or fatigue was experienced. However, when information or imagery (camera, sonar, maps) required focused attention for an extended period of time (greater than 10 minutes), eye dominance became much more important. Attempting to concentrate on a display screen with the non-dominant eye was extremely difficult and fatiguing, nearly always requiring the diver to close the uncovered eye in order to view the screen for any length of time. If the same information was being viewed with the dominant eye, eye strain and fatigue were reduced tremendously. Fifty percent of divers (military and civilian) wearing the system over their dominant eye could leave the display fixed in front of that eye during the entire dive with minimal eye strain and fatigue. They developed a technique for alternately looking "at" the display with their dominant eye, or "through" the display with their non-dominant (uncovered) eye.

Even so, any extended use of the system (greater than about 30 minutes) did cause a fairly high level of

eye strain and fatigue. This is typical for monocular HMD systems. All test divers agreed that any final version of the diver HMD should incorporate a mechanism that allows the unit to be flipped-up out of the way periodically to allow the diver to take a "HUD break" (as they came to be known) during a mission. The mechanism should also allow the diver to make minor adjustments to the wearing position and eye relief distance during the dive. By slightly shifting the wearing position of the display, different eye muscles come into use. This can greatly reduce eye strain and fatigue over the course of a dive mission, much like shifting feet or seat positions does during a long driving trip.

6) Other Human Factors Issues

Most divers (especially the military divers) suggested that the method of attaching the HMD to the mask should incorporate a quick-release mechanism. This would allow the entire display system to be quickly attached or removed from the mask during the dive. This would not only provide good operational flexibility, but also be an essential safety feature in case of entanglement.

IV. CONCLUSIONS

Military HMD applications have historically been the technology drivers for microdisplay development. The Defense Advanced Research Projects Agency (DARPA) alone has invested millions of dollars in the development of microdisplay technology and low-weight optical systems over the last decade. Increasingly however, commercial applications such as digital cameras, cellular phones, and virtual reality entertainment products are becoming the new technology drivers. Higher resolution in smaller display screens is the continuing trend. (Gallagher, 1998)

The US Navy is currently developing a "next generation" color diver HMD that will incorporate new higher resolution (800 x 600 pixel, SVGA) microdisplay technology. Other efforts include work on a fully integrated diver display mask system, and integrating virtual display systems into atmospheric diving suits. Navy divers in the 21st century will be using highly sophisticated underwater sensor systems that incorporate some of the most advanced imaging and navigation technologies available, and virtual image displays will certainly be an integral part of those systems.

REFERENCES

1. Alexander, J., Advanced Diver Display Project-Final Report, Coastal Systems Station, Panama City, FL, 1996.
2. Dorch, R., Gallagher, D., Diver's Head-Mounted Display, Coastal Systems Station, Panama City, FL, 1994.
3. Gallagher, D., Microdisplay Technology State-of-the-Industry, Coastal Systems Station, Panama City, FL, 1998.

ACKNOWLEDGMENTS

Larry Tierney from the Office of Special Technology's EOD/LIC Program (Ft. Washington, VA), LCDR Randy Getman from Naval Sea Systems Command EOD PMO-2 Program Office (Washington, DC), and Dr. Ed Belcher of the University of Washington's Applied Physics Laboratory (Seattle, WA) helped sponsor these projects. John Dudinsky, Jesse Alexander, and Frank Downs of the Coastal Systems Station (Panama City, FL) were integral in local project/program management. OPTICS-1, Inc. (Westlake Village, CA) was instrumental in optical system development and in providing invaluable guidance in optical design.

A 3-D LASER LINE SCANNER FOR OUTCROP SCALE STUDIES OF SEAFLOOR FEATURES

Donna M. Kocak¹, Frank M. Caimi^{1,2}, Partha S. Das¹, Jeffery A. Karson³

kocak@hboi.edu, caimi@ee.fit.edu, psdas@hboi.edu, jkarson@geo.duke.edu

¹Harbor Branch Oceanographic Institution, Inc.
Engineering Division
Ft. Pierce, Florida

²Florida Institute of Technology
Department of Electrical & Computer Science and Engineering
Melbourne, Florida

³Duke University
Division of Earth & Ocean Sciences
Durham, North Carolina

ABSTRACT

Manned submersibles and remotely operated vehicles make it possible to use many of the techniques of land geology on the seafloor. For example, making geological maps of seafloor exposures along mid-ocean spreading centers as well as other settings is now feasible. A fundamental aspect of geological maps is the documentation of the orientation of various planes and lines in space. *Strike* and *dip* typically characterize planes, and *trend* and *plunge* characterize lines. Sedimentary bedding, lava flow tops, dike margins, igneous layering, metamorphic foliations, joints and faults are just a few examples of planar structures observed along spreading centers. Land geologists determine the orientation of outcrop-scale features with various types of hand-held compasses and inclinometers, like the Brunton Compass used widely in North America. However, this type of instrument is not appropriate for use on the seafloor and different approaches are required to obtain orientation data.

A 3-D laser scanning system currently being developed by the Harbor Branch Oceanographic Institution Engineering Division, under National Science Foundation

and Duke University sponsorship, affords a method of collecting orientation data. Similar to previously designed HBOI systems, surfaces of interest are rapidly scanned to produce high-resolution digital maps. The 3-D map coordinates combined with the measured roll and pitch angles of the instrument are used to accurately determine orientation of the scanned geologically relevant planes and lines on seafloor outcrops. Unlike other techniques currently in use, this instrument does not need to be carefully positioned or placed on the rock surface and is not affected by magnetic fields. Furthermore, due to the high scan rate, the instrument need not be held stationary while scanning. During a single seafloor traverse of several hours, thousands of measurements can potentially be made.

A discussion of the application, method of operation, and initial design parameters of the new 3-D laser line scanner is provided in this paper, as well as comparative design parameters and an example image from similar systems developed previously for different applications. Preliminary Finite Element Analysis results are presented for the laser and detector housings suited for deep-ocean operation. Initial deployment is expected on

Woods Hole Oceanographic Institution's *Alvin* submersible next year.

I. Introduction

The underwater 3-D mapping system currently under development will be capable of making quantitative measurements relevant to studies of slope morphology, sedimentology, hydrothermal vents, biology, structural geology, and rock magnetism. When mounted on a manned submersible or remotely operated vehicle (ROV), image coordinate maps of seafloor exposures can be produced. Information inherent in the images can be derived to aid geologists in producing geological maps that can be analyzed for gaining insight into the geological formation process. Particularly important is the documentation of strike, dip, trend and plunge on features such as sedimentary bedding, lava flow tops, dike margins, igneous layering, metamorphic foliations, joints and faults. Fig. 1 shows a typical seafloor rock outcrop. The image shown is a digital mosaic of a cliff face approximately 50 meters high and 30 meters wide. The slope facing the viewer is approximately 50°. The rocks contain slab-like basaltic formations called "dikes" that were formed as molten rock was injected into cracks [1]. Measurement of the orientations of the edges of the dikes is one objective of the geological study. Some edges can be vertical, but in this image they are inclined to angles of approximately 40°. Using various methods, geologists are interested in determining if the dikes were once vertical and later tilted or if they were injected into inclined cracks. Obtaining accurate estimates of the orientations of the flat planar surfaces are also objectives of the geological study.

With current approaches, geologists are using Woods Hole Oceanographic Institution's "Geocompass" to make orientation measurements. The Geocompass measures orientation relative to the earth's magnetic

poles and inclination relative to the gravitational field.

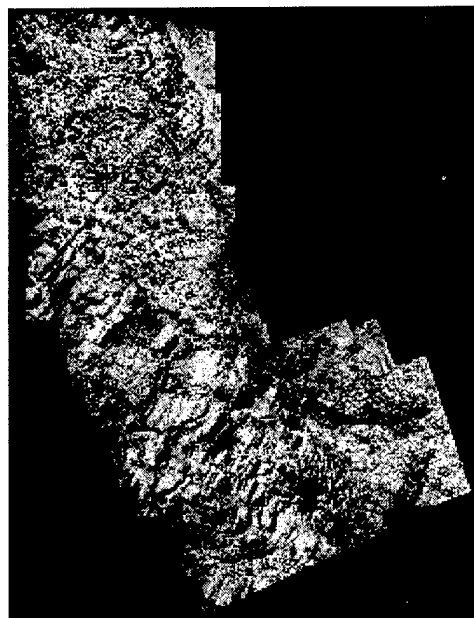


Fig. 1. Typical seafloor rock outcrop.

Data are recorded to an internal computer and are routed to the submersible's data logging system as the device is held against an outcrop surface. This simple approach has provided the first direct measurements of strike and dip on the seafloor and has made it possible to collect fully oriented samples for paleomagnetic and microstructural studies. Measurements from the Geocompass have been compared to estimates of orientation provided by divers, and results demonstrate that there is a wide range of accuracy and reliability among divers. Using the instrument insures consistent, objective results.

Additional testing by repeated measurements showed that the precision of the instrument was very good, but greatly influenced by the roughness of the outcrops measured. Despite its advantages of being simple, inexpensive (about \$11k) and having little maintenance costs, the Geocompass has some distinct disadvantages. Its magnetic compass requires calibration for the magnetic field of the submersible and is affected by strongly magnetized rocks in seafloor outcrops

(e.g., Fe-Ti basalts, ferrogabbros, serpentinites, etc.). The device must be physically placed against the rock surface requiring good piloting skills but often consuming valuable bottom time. This latter requirement makes it difficult to use from an ROV. The instrument is also cumbersome, taking up space in the sample basket and requiring an attached cable. Perhaps one of the worst problems is that it is difficult for observers in the submersible to observe the test surface. The observer is often forced to describe a particular type of surface to the pilot without observation. Video cameras aid the process and, assuming the submersible is in stable location, it is also possible for observers to view the surface from the pilot's window. Generally, guess work is involved in locating the measurements. It is commonly found upon reviewing video or hull-mounted cameras that the Geocompass could have been better positioned.

Although, this first-generation tool has demonstrated the feasibility and applications of collecting structural data from seafloor outcrops at spreading centers, transform faults, and subduction zones, the new laser technology approach described in the following sections offers the possibility of greatly improved efficiency and accuracy in collection.

II. RELATED WORK

Over the past decade, HBOI has developed three high-speed laser line scanners capable of providing 3-D surface maps and operating at near video frame rates. The first laser triangulation system was developed for the U.S. Navy as an experimental ROV-based test bed for robotic inspection [2-4]. The system was designed to map surface features at close range, approximately 0.5-2 m, with a positional accuracy of 1 mm at image acquisition rates of several seconds per

complete scan. The next generation of laser line scanners utilized patented image intensifier technology to produce a lower power implementation. This approach resulted in an increase of the image acquisition rate to 20 scans per second and a reduction of laser power from 150 to 10 mW. One of the two systems built was developed for the University of Southern Mississippi Department of Marine Science to view amorphous aggregates referred to as "marine snow" [5]. Resolution of the images is approximately 1 mm in (x, y, z) dimensions at distances less than 10 cm. The image acquisition rate was chosen to eliminate blurring of the moving particles and to capture sequential frames for motion studies. A similar HBOI system has been developed and is capable of operating at 1-2 m range with identical frame scan rates and laser power. Design specifications for each of these laser line scanners, as well as the Duke University system, are shown in Table 1. Fig. 2 illustrates an example test scan of a dome and step wedge object recorded in clear water at a nominal range of 1 m (NCEL, 400x400 pixel resolution).

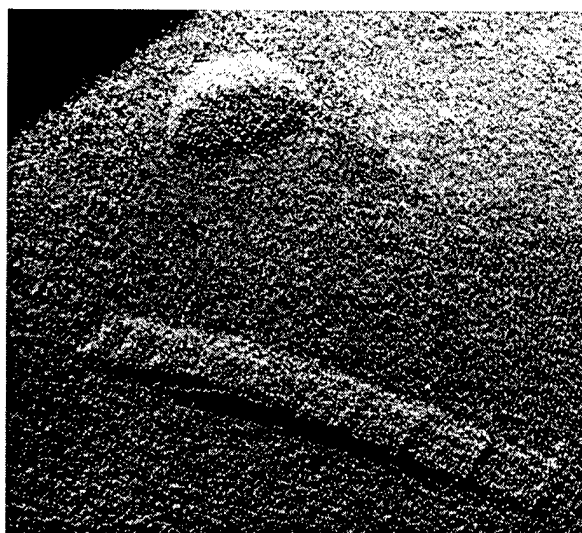


Fig. 2. Laser line scanned image of dome and step wedge test objects.

	NCEL	USM	HBOI	Duke
Application	ROV inspection	Biological mapping	Biological mapping	Geological mapping
Range	0.5-2.0 m	10 cm	0.5 m	2.0-3.0 m
Angular Field	40° x 40° (air) 30° x 30° (water)	28° x 28° (air) 21° x 21° (water)	28° x 28° (air) 21° x 21° (water)	30° x 30° (air) 22° x 22° (water)
Accuracy	1 in 1000	1 in 200	1 in 200	1 in 100
Pixel Resolution	134 ² , 200 ² , 400 ² , 800 ²	200 ²	200 ²	100 ²
Scan Rate	< 4 s	0.05 s	0.05 s	0.20 s
Laser Power	150 mW	10 mW	10 mW	75 mW
Laser Wavelength	532 nm	670 nm	670 nm	532 nm
Power Source	115 VAC	150±50 or 28 VDC	150±50 or 28 VDC	120 VDC
Depth Rating	914 m (3,000 ft)	914 m (3,000 ft)	914 m (3,000 ft)	4,500 m (14,764 ft)
Viewports	Acrylic, dome	Acrylic, flat	Acrylic, flat	Acrylic, flat
Housing Size	57"L x 9" OD	28"L x 8" OD	29"L x 8" OD	12"&20"L x 9" ¹ OD
Housing Material	Anodized AL	Anodized AL	Anodized AL	Titanium

Table 1. Design specifications for laser line scanners developed by HBOI

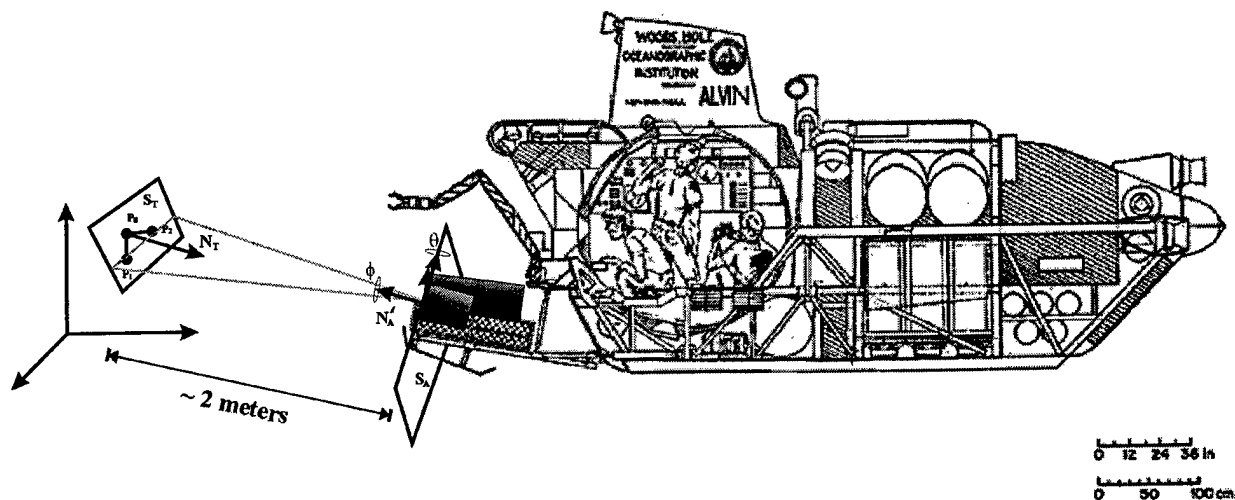


Fig. 3. 3-D laser line scanner shown on *Alvin* submersible.

¹ Based on preliminary design prior to final FEA modeling and analysis.

III. THEORY OF OPERATION

The laser line scanner currently under development will be mounted on WHOI's *Alvin* submersible, possibly as shown in Fig. 3. The vehicle will be maneuvered to position the scanner approximately 2 m from the surface of interest² (S_T). Once in position, as visually confirmed by the observers (via viewport or video camera), the observer can command the instrument to acquire an image using a laptop computer. On command the instrument performs a scan, storing the data locally on the hard disk and transmitting the data to the laptop computer display allowing the observers to react to the measurements. A high scan rate of 0.2 seconds per image allows vehicle drift or movement up to approximately 0.5 knots with acceptable degradation or "blurring" of the data. Additional scans can be acquired in less than a second delay, and the maximum number of scans per dive is limited only by the size of the storage device. The current configuration contains a 4 GB hard drive capable of storing over 20,000 range maps -- more than 66 minutes of data. Incorporated in the instrument housing is a roll and pitch sensor, fiber optic gyro (FOG) and magnetic compass. Each of the stored image files contains the date, time, roll, pitch, heading, and 3-D image coordinates. Rock outcrop orientation is determined accurately by combining the 3-D coordinates with the measured roll (ϕ) and pitch (θ) angles of the instrument during the scan. Heading (ψ or yaw) information provided by the FOG can be used to reference the data to a known datum (north heading, fault line location, etc.). Drift in the FOG, common over hours of use, can be automatically corrected using the magnetic compass reading, provided that the compass is away from rock induced magnetic fields.

² Positioning may be simplified by mounting a low-powered laser (HeNe) on the scanner and detector housing such that the two beams converge at a distance of 2 meters.

Used in this manner, the scanner does not need to be carefully positioned or placed on the rock surface and the orientation output is not influenced by magnetic field anomalies. The following sections describe how the range coordinates and rock outcrop orientations are computed.

A. Capturing Range Coordinates

A triangulation method is used to determine 3-D range coordinates. The geometric configuration of the instrument is shown in Fig. 4. The horizontal scan angles of the laser (θ) are pre-calibrated, and the separation of the laser scan center and PSD detector axis center is fixed at $k_1 + k_2 = BL$. During operation, the laser is scanned through angles θ_x and θ_y in a raster fashion to create a continuous reflection map at the detector surface. The detector produces a measure of the reflected light position along the x-axis in the image plane. For each point in the scan, the z-axis position can be estimated by:

$$Z(t) = \frac{BL}{\frac{x(t)}{f} + \frac{1}{\tan \theta(t)}}, \quad (1)$$

$$X(t) = Z(t) \frac{x(t)}{f} = Z(t) \tan \varphi,$$

where f is the equivalent focal length of the lens forming an image at the detector, BL is the baseline length, and θ is the horizontal projection angle. Capital and lower case symbols refer to the object and image plane coordinate systems, respectively.

For this geological application, a baseline of 1.11 m is chosen to scan at a nominal distance of 2 m from the instrument housing. The projection angle of the laser is approximately $\pm 11^\circ$ in water. In order to determine the magnitude of the z-coordinate, accurate estimates for x and θ should be obtained. Although $\theta(t)$ may be easily derived from the scanner, estimates of $x(t)$ are

subject to errors from noise from the detector and scan geometry.

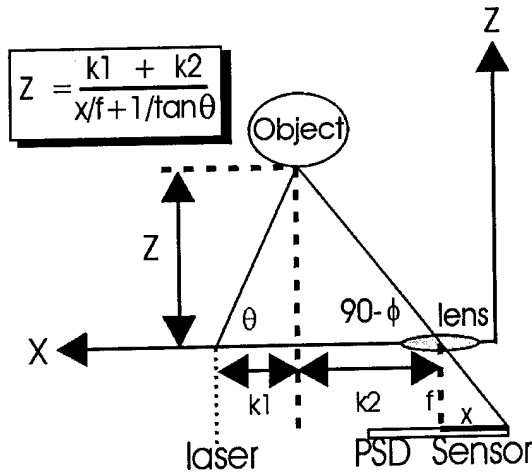


Fig. 4. Geometric configuration of the laser scanning system.

B. Computing Orientation

Scanning the laser and applying the triangulation method described above for each pixel location produces a 100x100 (x, y, z) coordinate map of the imaged surface. The orientation of the rock outcrop surface is determined accurately by computing the angle between the normal vector to the instrument plane and the normal vector to the outcrop (target) plane (refer to Fig. 3).

The first step is to find the vector normal to the instrument reference plane on *Alvin* (S_A). Assuming that no transformations are applied ($\phi = 0$ and $\theta = 0$), we can select $V_1 = [1 \ 0 \ 0 \ 1]$ and $V_2 = [0 \ 1 \ 0 \ 1]$ as unit vectors along the x- and y- axis in S_A , respectively. (Note that a homogeneous coordinate representation is being used). The normal vector N_A can be computed as:

$$N_A = V_1 \times V_2 = [x, y, z, 1] \quad (2)$$

Now, taking into account the *measured* ϕ and θ , the $Rz(\phi)$ and $Rx(\theta)$ transformation

matrices can be applied to get the normal vector relative to the current *Alvin* position:

$$N_A' = Rz(\phi) Rx(\theta) [x, y, z, 1] \quad (3)$$

$$= \begin{bmatrix} \cos \phi & \sin \phi & 0 & 0 \\ -\sin \phi & \cos \phi & 0 & 0 \\ 0 & 0 & 0 & 0 \\ 0 & 0 & 0 & 1 \end{bmatrix} \begin{bmatrix} 1 & 0 & 0 & 0 \\ 0 & \cos \theta & \sin \theta & 0 \\ 0 & -\sin \theta & \cos \theta & 0 \\ 0 & 0 & 0 & 1 \end{bmatrix} \begin{bmatrix} x \\ y \\ z \\ 1 \end{bmatrix} \quad (4)$$

The second step is to compute the vector normal to the target plane (S_T). Utilizing various post-processing methods (histogram localization, averaging, etc.), three points (P_0 , P_1 , and P_2) can be derived from the coordinate data and used to determine the normal vector S_T by:

$$N_T = \overline{P_0 P_1} \times \overline{P_0 P_2} \quad (5)$$

Having both the normal vectors, the orientation of the target surface can be defined as the angle (α) between N_A' and N_T computed by:

$$\cos \alpha = \frac{N_A' \cdot N_T}{|N_A'| |N_T|} \quad (6)$$

The total information required for referencing the location of the rock outcrop surface (S_T) can be described by the angle coordinate pair (α, ψ), where ψ is referenced to the vehicle heading (rotational angle).

IV. FEA ANALYSIS OF DEEP-OCEAN HOUSING

Unlike previous laser scanner housings designed for operation at a maximum depth of 3,000 ft (914 m), the current design must withstand operation at 14,764 ft (4,500 m) for use on the *Alvin* submersible. The maximum pressure expected during operation in the mid-Pacific is about 6,800 psi (46.88 MPa) and the design pressure (or test pressure) is 10,200 psi

Aluminum Endplate

Titanium Cylinder

Acrylic Viewport

A. Development of FEA Model

A full-scale nonlinear 2-D axisymmetric FEA model, similar to the proposed housing shown in Fig. 5, was developed using the ANSYS FEA software [8]. The arbitrary quadrilateral 8-noded 2-D structural solid element, PLANE82 [9], has been adopted in the solid body, whereas, at each interface, a lower version of this element, PLANE42 [9] has been used. Both the elements have large deformation and large strain capabilities as well as compatible displacement shapes. A special 3-noded 2-D element, CONTAC48 [9], has been used to model the contact and sliding between the acrylic window and aluminum (Al) endplate, as well as between the

aluminum endplate and titanium (Ti) cylinder. The elements PLANE42 are used at the interfaces instead of elements PLANE82, since the elements with mid-side nodes do not generate valid contact elements to capture the true behavior of the contact/sliding mechanism [10].

A typical discretized FEA model with external loading and boundary conditions is shown in Fig. 7, whereas material properties of the different components of the laser scanner housing are shown in Table 2. For the present analysis, only the top half of the housing is considered because of its close symmetry about the Z-axis.

B. FEA Results

The main emphasis of the FEA analysis is two-fold: (1) develop a housing for underwater application with the goal of withstanding 10,200 psi (70.33 MPa) test pressure without developing stress beyond yield limits within separate components, and (2) keep the deflection of the acrylic viewport within a reasonable limit to avoid any distortion of the laser beam. As an initial validation of the FEA model, the radial (S_R) and circumferential (S_θ) stress distribution through the titanium cylinder at $Y(Z)=0$ (away from any interface) is compared to the Lamé's theory for thick cylinder, and are found to be very close, as expected. Moreover, the stress distribution (axial, radial and circumferential stresses, i.e. S_z , S_R and S_θ) through the acrylic window matches closely with the results, as presented by Stachiw [6].

Studies of different stress components indicate that the design of interface area will be dominated by the stress component S_3 (third principal stress) since this component has the maximum value; whereas, the equivalent stress (S_{eqv}) will guide the design criteria for other parts away from the interface. On that basis, the overall maximum stress distributions throughout the different

components of the housing were found as shown in Table 3. Fig. 7 shows the FEA model with 10,200 psi external loading, as indicated by the arrows along the outer edges.

The results in Table 3 show that the stresses within the acrylic window (S_3) and Al endplate (S_{eqv}) are higher than their corresponding material yield limit shown in Table 2. Following these initial findings for induced stress distribution various new FEA models are being developed to reduce the overall stresses -- mainly in the acrylic window and Al endplate. A detailed discussion on the variation of different parameters and their effect on the overall stress distribution are not presented here. Only the major modifications presently being incorporated into the initial design are listed. These modifications include:

- a) Potentially increase Ti cylinder outer diameter (DO),
- b) Add gasket of 0.5 in. (0.0127 m) thick Ti between Al endplate and Ti cylinder,
- c) Modify acrylic window as follows:
 - i. Increase thickness-to-minor diameter ratio (t/D_i) from 1.0 to 1.587,
 - ii. Reduce seat overhang ratio (D_i/D_f) from 1.17 to 1.0746,
 - iii. Keep α as 90° , and
 - iv. Modify Al endplate accordingly.

As a result, the overall stresses within the acrylic window, Al endplate, and Ti cylinder of laser scanner housing fall below their respective yield limits. Additional modifications are still under review and will be followed by a full 3-D analysis for verification. However, the proposed modified design clearly indicates its ability withstand the maximum test pressure without permanent damage.

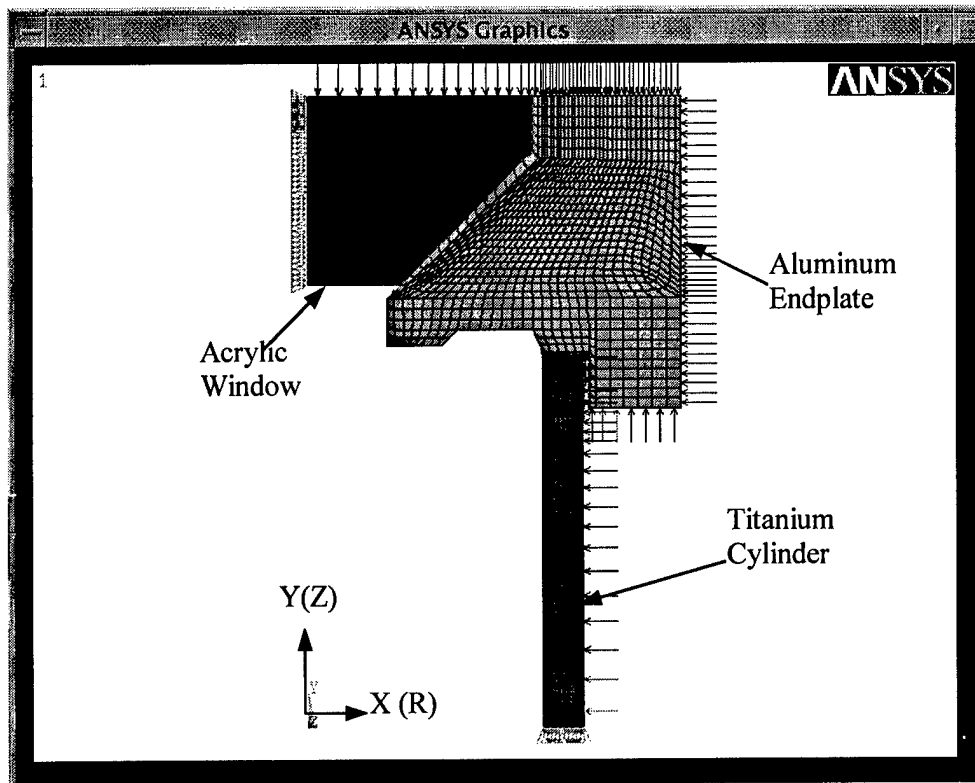


Fig. 7: Discretized FEA model of initial housing design with external loading and boundary conditions.

Material	Compressive Modulus of Elasticity in psi (MPa)	Poisson's Ratio	Compressive Yield Strength in psi (MPa)
Aluminum	9,550E+3 (65.845+3)	0.3	35,000 (241.317)
Titanium	16,500E+3 (113.763E+3)	0.3	80,000 (551.581)
Acrylic	420E+3 (28.96E+3)	0.3	16,530 (113.970) Short Term 7,000 (48.263) Long Term

Table 2. Material properties of different components.

Component	Maximum Stress in psi (MPa)
Acrylic Viewport	$S_3 = -22,029$ (151.88) $S_{eqv} = 13,068$ (90.10)
Aluminum Endplate	$S_3 = -32,000$ (220.63) at interface $S_{eqv} = 45,033$ (310.49)
Titanium Cylinder	$S_3 = -72,000$ (496.44) $S_{eqv} = 64,698$ (446.08)

Table 3. Maximum stress distributions throughout components of initial housing design.

V. CONCLUSION

The 3-D laser line scanner technology described herein has the potential to improve current techniques by affording quick, accurate, and unambiguous data for determining orientation of geologically relevant planes and lines on seafloor outcrops. It also offers quantitative measurement capability relevant to studies of slope morphology, sedimentology, hydrothermal vents, biology, volcanology, structural geology, and rock magnetism. Repeated measurements of active features (e.g., sessile organisms or hydrothermal vent structures) is expected to provide growth and decay estimates for these features. The rapid surface mapping capability of 5 images per second will allow thousands of measurements to be made during a single seafloor traverse compared to 10 or so with current techniques. The modular design, deep-ocean rating, and low power consumption of the system ensure compatibility with almost any underwater platform.

VI. ACKNOWLEDGEMENTS

The authors wish to acknowledge the support of the National Science Foundation under grants OCE9318399 and OCE09814147 for advanced system development, as well as the U.S. Navy under contract N47408-91-C-1209 for initial prototype development and the Atlantic Foundation for additional support. They would also like to thank Coy Colquitt for preliminary mechanical design and 3-D SolidWorks™ modeling of the underwater housing, Sarah Biamonte for technical assistance, and Mike Cheney for additional modeling support. This is HBOI contribution number 1307.

VII. REFERENCES

- [1] Lawrence, R.M., J.A. Karson, S.D. Hurst, "Dike Orientations and Fault-Block Rotations in Slow-Spread Oceanic Crust at the SMARK Area, Mid-Atlantic Ridge at 22°40'N," J. Geophysical Research, v. 103, pp. 663-676, 1998.
- [2] Caimi, F.M., D.C. Smith, D.M. Kocak, "Undersea 3-D Imaging and Mapping for Inspection and Research," Advanced Imaging, pp. 32-36, July 1992.
- [3] Caimi, F., and D. Smith, "Three Dimensional Mapping Systems and Methods," U.S. Patent 5,418,608, 1995.
- [4] Massey, J., "Underwater Laser Mapping for Ship Husbandry," Proc. Mar. Tech. Soc., Underwater Intervention '94, pp. 312-318, San Diego, February 1994.
- [5] Caimi, F.M., D.M. Kocak, "Developments in Laser-Line Scanned Undersea Surface Mapping and Image Analysis Systems for Scientific Applications," Proc. IEEE OCEANS '96, pp. 929-936, Fort Lauderdale, FL, September 1996.
- [6] Stachiw, J.D., *Acrylic Plastic Viewports: Ocean Engineering and Other Hyperbaric Applications*, Marcel Dekker, Inc., New York, 1982.
- [7] Cook, R. D. and Young, W. C., *Advanced Mechanics of Materials*, Macmillan Publishing Company, New York, 1985.
- [8] ANSYS User's Manuals, September 1997.
- [9] ANSYS Elements Reference, Release 5.4, September 1997.
- [10] ANSYS Modeling and Meshing Guide, Release 5.4, September 1997.

ASSESSING THE IMPACT OF ANTIFOULING COMPOUNDS IN THE MARINE ENVIRONMENT. LESSONS TO BE LEARNED FROM THE USE AND MISUSE OF BIOLOGICAL INDICATORS OF TBT CONTAMINATION

S.M. Evans and G.J. Nicholson

Dove Marine Laboratory
Department of Marine Sciences and Coastal Management
Newcastle University
Cullercoats
Tyne and Wear, NE30 4PZ
UK

e-mail: s.m.evans@ncl.ac.uk

Abstract. The condition known as imposex in whelks has been used widely as a biological indicator of tributyltin (TBT) contamination in the marine environment. It has provided valuable information on the extent and impact of contamination. It has also been used successfully in monitoring changes in levels of contamination since regulations, limiting the use of TBT-based antifoulants to vessels >25 m in length, were introduced. However, its misuse has also generated misleading information. There have been at least four reasons for this. First, sampling has been biased on 'hot-spots' of contamination, giving a false impression of the severity of the problem. Second, imposex is not, as has often been assumed, a specific response to TBT. Third, insufficient attention has been given to the longevity and habits of indicator species. Fourth, predictions of extinctions of species, which have been based on assessments of imposex, have not been fulfilled. It is argued that, while biological indicators should play key roles in assessing the impacts of pollutants, rigorous protocols are needed.

1. Introduction

It is generally accepted the tributyltin (TBT) is the most effective biocide ever used in antifouling paints. TBT-

based coatings have been used widely on yachts, mariculture structures and ocean-going vessels. They improve a ship's performance by preventing the growth of fouling organisms on the hull, thereby reducing drag and concomitantly decreasing fuel consumption. This brings, not only enormous savings to the shipping industry, but also environmental benefits. Lower fuel consumption means reduced emissions of 'acid rain' and 'greenhouse' gases. An additional benefit is that effective antifouling prevents the transport of invasive (non-native) organisms on ship hulls. Such organisms can have enormous ecological and economic impacts, and pose major threats to marine ecosystems.

However, the use of TBT also has environmental costs. It leaches from the antifoulants into the water column and can cause damage to non-target organisms. It was, for example, held responsible for the near collapse of oyster farming in west France and for the demise of populations of dogwhelks in areas of high boating activity in southwest England during the 1980s. Not surprisingly, the use of these TBT-based paints was regulated in a number of countries, including Europe, USA, Canada, Australia and New Zealand. Several governments reacted by banning the use of TBT-based coatings on vessels <25m in length.

There is an obvious need to monitor the success of the regulations in reducing levels of TBT. However, there

are difficulties in making, and interpreting the results of, chemical measures of TBT in the environment. This is for three reasons. First, TBT can be effective at concentrations which are close to the limits of detection. Second, there are sometimes large spatial and temporal variations in concentrations of TBT at fixed locations because it may be released into the environment in pulses (e.g. from dry docks) which may be biologically harmful but may be missed by regular sampling. Third, the distribution of TBT in the environment is complex. It occurs at much higher levels in the surface microlayer and sediment than in the water column.

As a result of these difficulties, bioassays have been developed as indicators of TBT contamination. Imposex has been one of these. TBT causes imposex, in which male genitalia, a penis and vas deferens, become superimposed on the female's system. Gibbs *et al.* (1987) recommended two quantitative measures of imposex: (i) the relative penis size index (RPSI) which compares the size of the penis of the female with that of the male as a standard; and (ii) the vas deferens sequence index (VDSI), which recognises six stages primarily in the development of the vas deferens. Females at stages 1 - 4 of the vas deferens sequence (VDSI) are capable of breeding, but those at stages 5 and 6 are rendered sterile. Additional measures of the health and/or reproductive status of populations, suffering from imposex, have been made in some studies. They include assessments of abundance of whelks on the shore, adult sex ratios (populations with male-biased ratios are likely to have suffered from high female mortality) and the proportions of juveniles in populations (as indicators of juvenile recruitment and therefore breeding performance).

II. The Use of Imposex as a Biological Indicator of TBT Contamination

The first detailed survey of imposex was of the dogwhelk *Nucella lapillus* in southwest England in the mid-1980s. Bryan *et al.* (1986) found that the condition, and presumably therefore TBT contamination, was severe in areas of high boating activity. In the most severe cases, there was female sterility and premature death. There was an absence of juveniles in some populations and, in the worst affected areas, the species became locally extinct. Further surveys showed that the condition was widespread. It was reported in surveys of *N. lapillus* in northeast England, Scotland, the British coast including the Isle of Man, the Netherlands, and the entire coastline of the North Sea. In other whelk species, it occurred in Canada, USA, Malaysia, Singapore, Indonesia, West

Africa, New Zealand and Australia (Evans *et al.* 1995).

However, although TBT contamination was severe in the 1980s, regulations which prohibited the use of TBT-based antifoulants on small boats, have been highly successful in reducing ambient concentrations of TBT in the marine environment. Evidence has come from a number of different sources. These include the recovery of populations of oysters and reduced concentrations of TBT in the water column, sediments and tissues of molluscs. Populations of whelks have shown three clear signs of recovery: reduced symptoms of imposex, increased abundance and fecundity and the recolonisation of some areas where they had become locally extinct.

The current situation is that commercial harbours, especially those with dry-docking and repair facilities, are still hot-spots of TBT contamination. However, the impacts of these remaining hot-spots are surprisingly localised. Gradients of sharply decreasing contamination have been described from dockyards, marinas and commercial harbours in Hong Kong, ports and fishing harbours in Iceland, marinas in Israel and a boatyard on the Isle of Cumbrae, Scotland (Table 1).

Table 1. Gradients of TBT in tissue and imposex (RPSI) in samples of dogwhelks *N. lapillus* across a boatyard entrance at Millport, Scotland.

Distance from boatyard entrance (metres)	TBT (ng/g dry weight)	RPSI
100	65	1.3
75	66	0.5
50	85	0.7
25	109	0.4
entrance (north)	369	12.9
entrance (south)	217	12.1
25	88	0.7
50	59	0.4
75	58	1.1
100	46	0.9

III. The Misuse of Imposex as a Biological Indicator of TBT Contamination.

However, there is not full accord. There have been some claims, based on surveys of imposex in whelks, that, despite the regulations, TBT contamination has continued to worsen. According to the North Sea Quality Status Report (1993), TBT pollution of the North Sea is

so bad that it is likely to have catastrophic effects on the survival of sensitive species such as the dogwhelk. This assessment is based on an account of a survey by Harding *et al.* (1992) of imposex in *N. lapillus* in coastal areas of the North Sea and English Channel. An additional concern is that the open North Sea is contaminated. Ten Hatters-Tjabbes *et al.* (1994) found imposex in some common whelks *Buccinum undatum* from central and southern parts of the North Sea, and report that its severity correlated with the intensity of shipping in adjacent areas. Cadée *et al.* (1995) predicted that *B. undatum* would eventually become extinct in the North Sea with the continued use of TBT-based antifoulants.

The results of these studies have been contradicted by more recent work. The predicted catastrophes have not occurred. Both *N. lapillus* and *B. undatum* are still abundant in the North Sea, and symptoms of imposex are generally mild (Evans *et al.* 1996; Nicholson & Evans 1997). However, these findings raise questions about the value of imposex as an indicator of TBT contamination. There appear to be at least four areas of concern:

(i) *Biased Sampling.* Sampling programmes have concentrated on hot-spots of contamination, such as drydocks, marinas and ports, giving a false impression of global contamination of the open seas and oceans. Where programmes have included areas of open coast adjacent to hot-spots, the impact has been local. Imposex-free populations, or those with mild symptoms, have been described within a few km of pollution at Loch Sween, Scotland, Wellington Harbour and Porirua Inlet, New Zealand, Port Philip Bay, Melbourne and Ambon Bay, Indonesia.

(ii) *The Causes of Imposex.* Imposex is not, as has often been assumed, entirely specific to TBT. Extensive studies by Bryan *et al.* (1986) appeared to establish that, apart from two related organotins, tri-*n*-propyltin and tetrabutyltin, TBT was the only compound to cause it in *N. lapillus*. The finding that copper, and even environmental stress, could induce it imposex in *Lepsiella vinosa* was therefore unexpected. Subsequently, it has been shown that triphenyltin, nonylphenol and exposure to faeces of seabirds can induce it in different species of whelks (Table 2).

(iii) *The Habits of Indicator Species.* Since imposex is irreversible, it tends to reflect conditions which have prevailed in the past rather than ambient ones. It is particularly difficult to interpret its significance in *B. undatum*, which is a long-lived, mobile species. It is

sensitive to TBT during its juvenile development only. Since it can survive for 15 or more years, imposex may reflect conditions which prevailed a decade and a half previously, at some unknown location.

(iv) *The Use of Imposex to Indicate Fecundity.* Harding *et al.* (1992) reported that many populations of *N. lapillus* at sampling sites on the coast of Norway were sterile based on assessments of imposex. However, the expected extinctions have not occurred. The species is still common or abundant, and fecund, at these sites (Evans *et al.* 1996).

Table 2. The development of imposex in dogwhelks *N. lapillus* exposed to TBT and nonylphenol in the laboratory.

	Group			
	TBT controls	TBT	Nonyl-phenol controls	Nonyl-phenol
Sample size	40	40	40	40
Mean VDSI	1.7	3.7	1.9	3.1
Mean RPSI	4.2	15.7	1.4	14.1

IV. Conclusions

(i) Imposex in whelks is a useful biological indicator of TBT contamination. It can indicate the extent of contamination, its biological impact and can also be used for long-term monitoring of populations of whelks.

(ii) The condition must be used with caution. It can be caused by agents other than TBT so that confirmatory chemical measures are always needed. Care is needed in the design of sampling programmes and in the interpretation of imposex scores.

(iii) While biological indicators should play key roles in assessing the impacts of pollutants, rigorous protocols are needed.

V. References

Bryan, G.W., Gibbs, P.E., Burt, G.R. and Hummerstone, L.G. (1986) The decline of the gastropod *Nucella lapillus* around southwest England: evidence for the effects of

tributyltin from anti-fouling paints. *Journal of the Marine Biological Association of the United Kingdom* **66**, 611-640.

Bryan, G.W., Gibbs, P.E. and Burt, G.R. (1988) A comparison of the effectiveness of tri-*n*-butyltin chloride and five other organotin compounds in promoting the development of imposex in the dogwhelk, *Nucella lapillus*. *Journal of the Marine Biological Association of the United Kingdom*, **68** 733-744.

Cadée, G.C., Boon, J.P., Fischer, C.V., Mensink, B.P., and ten Hallers-Tjabbes, C.C. (1995) Why the whelk (*Buccinum undatum*) has become extinct in the Dutch Wadden Sea. *Netherlands Journal of Sea Research* **34**, 337-339.

Evans, S.M., Leksono, T. and McKinnell, P.D. (1995) Tributyltin pollution: a diminishing problem following legislation limiting the use of TBT-based antifouling paints. *Marine Pollution Bulletin* **30**, 14-21.

Evans, S.M., Evans, P.M. and Leksono, T. (1996) Widespread recovery of dogwhelks, *Nucella lapillus* (L.) from tributyltin contamination in the North Sea and Clyde Sea. *Marine Pollution Bulletin* **32**, 263-269.

Gibbs, P.E., Bryan, G.W., Pascoe, P.L. and Burt, G.R. (1987) The use of the dogwhelk (*Nucella lapillus*) as an indicator of TBT contamination. *Journal of the Marine Biological Association of the United Kingdom* **67**, 507-524.

Harding, M.J.C., Bailey, S.K. and Davies, I.M. (1992) TBT imposex survey of the North Sea. UK Department of the Environment. Contract PECD 7/8214.

Nicholson, G.J. and Evans, S.M. (1997) Anthropogenic impacts on the stocks of the common whelk *Buccinum undatum* (L.). *Marine Environmental Research* **44**, 305-314.

North Sea Quality Report (1993) Man's impact on ecosystems. In: *North Sea Quality Status Report*, North Sea Task Force, Oslo and Paris, Olsen & Olsen, Fredensborg, pp. 80-98.

Ten Hallers-Tjabbes, C.C., Kemp, J.F. and Boon, J.P. (1984) Imposex in whelks (*Buccinum undatum*) from the open North Sea: relation to shipping traffic intensities. *Marine Pollution Bulletin* **28**, 311-313.

THE EFFECTS OF REGULATING THE USE OF TBT-BASED ANTIFOULING PAINTS ON TBT CONTAMINATION

S.M. Evans and R. Smith

Dove Marine Laboratory
Department of Marine Sciences and Coastal Management
Newcastle University
Cullercoats
Tyne and Wear, NE30 4PZ
UK

e-mail: s.m.evans@ncl.ac.uk

Abstract. There was severe TBT pollution in coastal waters in the mid-1980s, particularly in areas of high shipping and mariculture activity. Organotin concentrations were high in water samples, sediments and tissues of marine molluscs. Responses, such as imposex in whelks and shell growth abnormalities in oysters, which can be caused by TBT, were also well-developed. They were associated with reproductive failure, and even local extinction of species, in the most severe cases. However, several governments have regulated the use of TBT-based antifouling paints, prohibiting their application to vessels <25m in length. These regulations have been highly successful in reducing TBT pollution. Environmental concentrations of TBT have decreased, and there has been substantial recovery of populations of whelks and oysters. Serious TBT contamination is now restricted largely to ports and harbours, especially those with dry-docking facilities.

1. Introduction

Tributyltin (TBT) leaches into the marine environment from the antifouling paints which are used on the hulls of boats and mariculture cages. It is potentially highly toxic at low concentrations. This is reflected in low lethal dose (LD) concentrations to TBT in sea water, especially in the case of larvae of invertebrates. For example, the 15day LC50 for larvae of the common mussel *Mytilus edulis* is 0.1 µg/l. However, sub-lethal impacts occur at even lower concentrations. No Observed Effect Concentrations (NOEC) for the growth and reproduction of plankton are 0.4 ng/l, and for shell calcification in oysters and normal development of the genital system in female dogwhelks, 2 ng/l.

TBT has a short residence time of days only in the water column but it becomes adsorbed on to particles and aggregates in sediments, where its half-life may be a matter of years.

There was widespread use of TBT-based antifoulants by the 1980s, and the worst contaminated areas were semi-enclosed bodies of water, which have poor flushing characteristics and in which there was intensive shipping (or ship-related) activity or mariculture. The concentrations recorded in 'hot-spots', such as harbours, marinas, dry docks, estuaries, sealochs and bays, were often well above NOECs. For example, concentrations in the water column were mostly >100 ng/l but occasionally exceeded 300 ng/l (Batley 1996).

Not surprisingly, TBT pollution had impacts on marine biota. The best documented example is from Arcachon Bay (west France), which is a centre for both yachting and oyster culture. TBT leaching from the antifouling paints used on yachts was held responsible for abnormal shell growth and reproductive failure of oysters. Production of oysters fell to about 33-50 % of the normal harvest (Table 1). A similar collapse of oyster farming was reported in estuaries in southern England, and TBT was the probable cause of declines in populations of other bivalve molluscs.

TBT was also linked to declines in populations of dogwhelks *Nucella lapillus* in areas of high boating activity in southwest England (Bryan *et al.* 1986). Female *N. lapillus* developed the condition known as imposex in which male characteristics, including a penis and vas deferens, become superimposed on the female's own genitalia. It can cause sterility because the vas deferens

becomes convoluted and forms a nodule which blocks the genital pore. As a consequence, the species became locally extinct in Plymouth Sound and in the estuaries of the rivers Dart and Fal. Subsequently, advanced symptoms of imposex were recorded in *N. lapillus* at other North Atlantic sites, and in other whelk species in Canada, New Zealand, Australia, Japan, Indonesia, Malaysia, Hong Kong, Singapore, the Malacca Strait, Thailand, Israel, Malta, the Mediterranean Sea, Ghana and the Canary Islands. TBT contamination was a widespread problem (Ellis and Pattisina 1980).

Table 1. Production of oysters in Arcachon Bay, France.

Period	Production (tons)
1978-79	10000
1979-80	6000
1980-81	3000
1981-82	5000
1982-83	8000
1983-84	12000
1984-85	12000

II. Managing TBT Pollution: The Effectiveness of Regulations.

Basically two approaches have been used to reduce TBT pollution. One of these was to ban the use of TBT-based antifoulants on small pleasure craft which were believed to be the main source of contamination in coastal waters. The other approach was to regulate the paints themselves. This was done by, for example, encouraging the use of new copolymer self-polishing paints, which have relatively slow TBT release rates, and discouraging the use of the original free association paints, from which TBT leaches more rapidly. France was the first to introduce regulations. It did so in 1982, very much in response to the oyster farming problem in Arcachon Bay. The use of TBT-based antifoulants was prohibited on vessels <25m in length. Similar regulations followed in the UK, USA, Canada, New Zealand, Australia, South Africa, Hong Kong and most European countries.

There is substantial evidence that these regulations have been effective in reducing TBT contamination and the adverse effects of pollution. Reductions are due primarily to lower inputs from small boats, and declining levels of pollution have therefore been most marked in estuaries and areas where there are marinas. This has almost certainly been the cause of declining levels in water samples, sediments and the tissues of molluscs. They

have been reported in studies worldwide (Table 2).

Table 2. Examples of studies in which reductions in TBT contamination have been described, based on chemical measures.

Location	Reference
UK	Dixon 1989 Cleary 1991 Bryan & Gibbs 1996
Gulf of Mexico	Wade <i>et al.</i> 1991
Australia	Batley <i>et al.</i> 1992
USA	Wuertz <i>et al.</i> 1991
France	Alzieu 1996
Japan, Europe and USA	CEFIC 1994

Concomitantly, there have been recoveries of many of the populations of molluscs which were severely impacted in the 1980s. These have sometimes been dramatic. Oyster farming in France recovered almost immediately after the introduction of regulations in 1982 (Table 1), and oyster farming in England and Australia also improved rapidly following the regulations in these countries. In addition, there has been widespread recovery of populations of other bivalves and gastropods (Table 3).

Table 3. Examples of studies in which recoveries of populations of molluscs have been described, since the introduction of regulations limiting the use of TBT-based antifoulants.

Species	Location	Reference
Dogwhelks	Clyde Sea North Sea	Evans <i>et al.</i> 1996
Dogwhelks	Canada	Tester <i>et al.</i> 1996
Dogwhelks	New Zealand	Smith 1996
Mud snails	USA	Curtis 1998
Oysters	France	Alzieu 1996
Oysters	Australia	Batley <i>et al.</i> 1992
Scallops	Ireland	Minchin <i>et al.</i> 1987
Flame shells	Ireland	Minchin 1995

A recent (1998) survey of imposex in dogwhelks *N. lapillus* along North Sea coastlines illustrates the extent to which recovery has occurred. It was reported that in 1991 there was either total or partial sterility in two thirds of the populations surveyed from Norway, Denmark, the Netherlands, France and the UK (Harding *et al.* 1992). Widespread extinctions might have been predicted. However, the species was present on all of the shores which were revisited in 1998, and it was common or abundant on most of them. Symptoms of imposex had declined, and they were reproducing successfully (Table 4).

Table 4. Measures of imposex (RPSI and VDSI) in North Sea dogwhelks sampled in 1991 and 1998.

	Survey	
	1991	1998
Norway and Denmark		
Number sites	21	12
Mean RPSI	38	19
Mean VDSI	4.5	3.6
France		
Number sites	16	18
Mean RPSI	18	6
Mean VDSI	3.9	3.3
United Kingdom		
Number sites	20	15
Mean RPSI	16	8
Mean VDSI	3.7	3.3

Commercial harbours, especially those with shipyards and dry docks, remain contaminated by TBT. This is because ocean-going vessels continue to use TBT-based antifoulants, and consequently it continues to accumulate in harbour sediments. However, there is evidence of recovery of populations of dogwhelks *N. lapillus* in Sullom Voe (Scotland) where the only source of TBT is from tankers which visit the oil terminal there. It can probably be attributed to the widespread use of copolymer coatings, replacing free association paints.

III. The Future of TBT-based Antifoulants: Management or Ban ?

It is unfortunate that a full understanding of the effectiveness of regulations in managing environmental levels of TBT is becoming apparent only at a time when the International Maritime Organisation (IMO) is

considering the introduction of a total ban on TBT-based antifoulants. It is currently considering draft regulations whereby the application of TBT-based coatings will be banned from 2003, and TBT paints (from previous applications) will not be allowed on hulls from 2008.

TBT-based paints have achieved a notoriety which is not justified by the scientific evidence. Furthermore, there is no doubt that additional regulations could reduce ambient levels of TBT still further. There could, for example, be stricter controls for paint application and removal procedures, dockyard waste disposal and the use and availability of paints. Research is also needed to create new technologies for the treatment of TBT-contaminated waste water, more efficient and less toxic paints and offshore ports where the dilution of open waters will reduce pollution.

The ultimate objective must be to veto the use of all toxins in the marine environment and the use of TBT, or other biocides, should eventually be outlawed. However, there are increasing concerns that the proposed ban on TBT-based antifoulants is premature. A ban will mean the immediate introduction of alternatives. However, the long-term biocidal properties of alternatives are largely untested, and it is difficult to predict either the economic or environmental consequences of using them. Poor antifouling performance will certainly be costly for the shipping industry because it will result in higher fuel consumption and the need to slip and repaint vessels more often. There may also be environmental consequences. Increased fuel consumption will lead to an increase in emissions of 'greenhouse' and 'acid rain' gases. In addition, the increased spread of those 'invasive' (non-native) species, which are carried on the hulls of fouled ships, is likely to become a major problem. They already cause enormous ecological and economic damage, and could become the cause of an environmental disaster. There is a need, furthermore, to demonstrate the alternatives are actually more 'environmentally friendly' than TBT. It is claimed that one alternative, the herbicide booster Irgarol 1051, which is already in use, is at environmental levels which are sufficient to damage phytoplankton communities. Several alternatives contain high levels of copper, and increased copper content of oysters in Arcachon Bay has been linked with the increased use of such paints, following the ban of TBT-based paints on small boats.

IV. References.

Alzieu, C. (1996) Biological effects of tributyltin on marine organisms. In *Tributyltin: Case Study of an Environmental*

Contaminant, ed. S.J. de Mora. Cambridge University Press, pp. 167-211.

Batley, G. (1996) The distribution and fate of tributyltin in the marine environment. In *Tributyltin: Case Study of an Environmental Contaminant*, ed. S.J. de Mora. Cambridge University Press, pp. 139-166.

Batley, G.E., Scammell, M.S. and Vrockbank, C.I. (1992) The impact of the banning of tributyltin-based antifouling paints on the Sydney rock oyster *Saccostrea commercialis*. *Science of the Total Environment* **122**, 301-314.

Bryan, G.W., Gibbs, P.E., Burt, G.R. and Hummerstone, L.G. (1986) The decline of the gastropod *Nucella lapillus* around southwest England: evidence for the effects of tributyltin from anti-fouling paints. *Journal of the Marine Biological Association of the United Kingdom* **66**, 611-640.

CEFIC (1994) Use of triorganotin compounds in anti-fouling paints. results of TBT monitoring studies. Paper submitted to International Maritime Organisation Marine Environment Protection Committee 35th Session: Agenda 17.

Cleary, J.J. (1991) Organotin in the marine surface microlayer and subsurface waters off southwest England: relation to toxicity thresholds and the UK environmental quality standard. *Marine Environmental Research* **32**, 65-73.

Dixon, T. (1989) Early response to TBT ban. *Marine Pollution Bulletin* **20**, 2.

Ellis, D.V. and Pattisina, L.A. (1990) Widespread neogastropod imposex: a biological indicator of global TBT contamination. *Marine Pollution Bulletin* **21**, 248-253.

Evans, S.M., Evans, P.M. and Leksono, T. (1996) Widespread recovery of dogwhelks, *Nucella lapillus* (L.) from tributyltin contamination in the North Sea and Clyde Sea. *Marine Pollution Bulletin* **32**, 263-269.

Harding, M.J.C., Bailey, S.K. and Davies, I.M. (1992) TBT imposex survey of the North Sea. UK Department of the Environment. Contract PECD 7/8214.

Minchin, D. (1995) Recovery of a population of the flame shell *Lima hians* in an Irish bay previously contaminated with TBT. *Environmental Pollution* **90**, 259-262.

Minchin, D., Oehlmann, J., Duggan, C.B., Stroben, E. and Kaetinge, M. (1995) Marine TBT antifouling contamination in Ireland, following legislation in 1987. *Marine Pollution Bulletin*, **30**, 633-639.

Smith, P.J. (1996) Selective decline in imposex levels in the dogwhelk *Lepsiella scobina* following a ban on the use of TBT antifoulants in New Zealand. *Marine Pollution Bulletin* **32**, 362-365.

Tester, M., Ellis, D.V. and Thompson, J.A.J. (1996) Neogastropod imposex for monitoring recovery from marine TBT contamination. *Environmental Toxicology and Chemistry* **15**, 560-567.

Wade, T.L., Garcia-Romero, B. and Brohns, J.M. (1991) Oysters as biomonitors of butyltins in the Gulf of Mexico. *Marine Environmental Research* **32**, 233-341.

Wuertz, S., Miller, C.E., Doolittle, M.M., Brennan, J.F. and Cooney, J.J. (1991) Butyltins in estuarine sediments two years after tributyltin was restricted. *Chemosphere* **22**, 1113-1120.

THE STRENGTH OF CORRELATIONS BETWEEN GEOTECHNICAL VARIABLES AND ACOUSTIC CLASSIFICATIONS

Jon M. Preston* and William T. Collins

Quester Tangent Corp., 99 - 9865 West Saanich Road, Sidney, BC V8L 5Y8 Canada

David C. Mosher

Geological Survey of Canada-Pacific, Institute of Ocean Sciences, Sidney, BC V8L 4B2 Canada

Roland H. Poeckert*

Racal-Pelagos, Inc., 5434 Ruffin Rd., San Diego, CA, 92123

Ron H. Kuwahara*

Defence Research Establishment Atlantic, 9 Grove St, PO Box 1012, Dartmouth, NS B2Y 3Z7 Canada

Abstract – Seabed grain size, shear strength, bearing strength, and porosity were measured at 15 sites, all in bays and harbours around southern Vancouver Island. Sounder echoes at 38 and 200 kHz from the same sites were classified using the QTC VIEW™ technology. This approach uses a feature set generated from the direct echoes by a set of algorithms and then reduced by multivariate analysis, with similar acoustic responses put into the same class. Canonical correlation analysis was used to uncover correlations between two data sets: the frequency of occurrence of each acoustic class, and the four geotechnical variables. Bearing strength was found to be the major contributor to the first geotechnical canonical variable, which correlated with classes from the 38-kHz echoes with a coefficient of 0.94.

I. INTRODUCTION

Estimating shear strength, grain size, and other geotechnical variables of the seabed from a vessel underway could give much better coverage, and be quicker and cheaper, than using seabed probes or collecting samples. Calculating geotechnical variables from acoustic data is practically impossible, because there are no direct theoretical or empirical connections between acoustic vibrations and large-scale inelastic concepts such as bearing strength. In the absence of direct acoustic-geotechnical connections, these relationships can only be statistical.

This paper explores the strength of correlations between sediment geotechnical properties and characteristics of acoustic signatures in soft seabeds. Our motivation is that if correlations are strong, they could be used to estimate geotechnical variables in areas that have been surveyed only acoustically. While the estimates would have only a statistical basis, this may be a useful empirical technique for area surveys.

The acoustic data for this paper had higher signal-to-noise ratios than that used in a previous study [1], and stronger correlations were found. The basic theory of canonical analysis is summarized in [1], and is not repeated here.

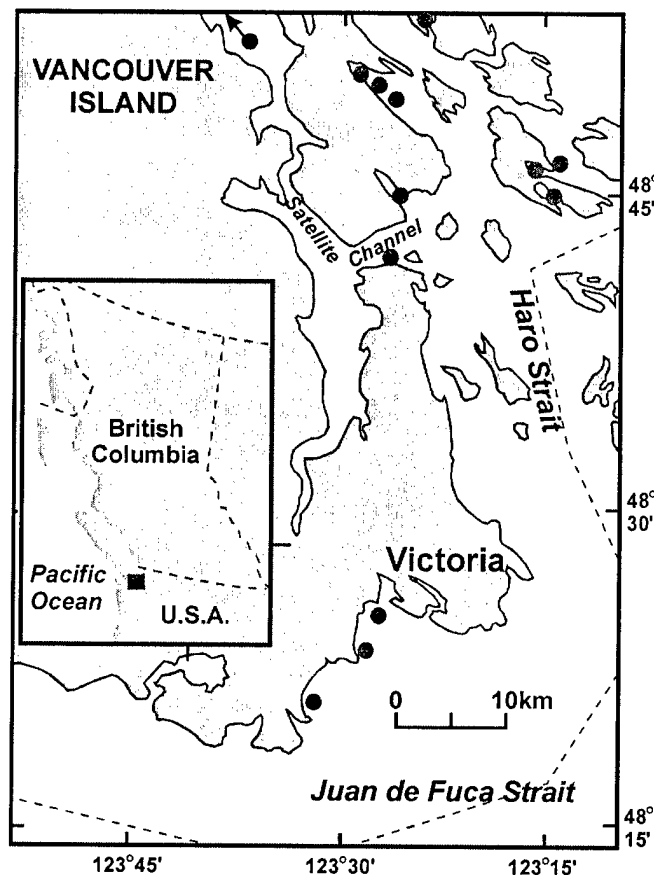


Fig. 1. Locations of 13 of the 15 sites, indicated by circles. The other two were in Nanoose Bay, 41 km north of the northwest corner of this chart.

* JMP, RHP and RHK were with the Esquimalt Defence Research Detachment of Defence Research Establishment Atlantic when this work was done.

II. LOCATION

The 15 sites were in bays and harbours on the east (sheltered) side of Vancouver Island, as shown in Fig. 1. The sediments were generally non-cohesive and composed primarily of different classes of sand with varying amounts of silt and clay. All sites had soft sediments; the highest shear strength observed was only 10 kPa. Hard substrates were excluded because the overall aim was to study the ability of the bottom to support a naval mine dropped onto it.

III. GEOTECHNICAL DATA

The geotechnical variables used in this statistical work were mean grain size at the surface and at 10–15 cm depth, shear strength and porosity at the same depth, and dynamic bearing strength as measured by a free-fall penetrometer. There are some strong correlations among these data, particularly between the two grain size measurements, and between porosity and bearing strength.

Seabed grain-size distributions were measured using ASTM Procedure D422. Surface data are from grab samples. Core samples were analyzed to determine the grain-size distribution, porosity, and shear strength, at 5-cm depth intervals in the top 20 cm and at 10-cm intervals below that. Mean specific gravity for dried sediment, following ASTM D854, was found to be 2.721 ± 0.017 , and this value was used to convert aliquot weights and volumes to porosity [2]. Shear strength was measured on the intact core with a laboratory Torvane [3]. The choice of a 7.5-cm gravity core lowered rapidly into the bottom caused some sample disturbance, particularly near the sediment-water interface.

A free-fall penetrometer, STING [4, 5] was used to measure dynamic bearing strength. STING consists of a 1-m long, 19-mm shaft with a replaceable foot wider than the shaft (typically 25 or 35 mm), topped by an instrument housing and tail fins. The foot diameter can be changed to match the anticipated bearing strength. The only important sensor was an accelerometer to record the deceleration as the shaft enters the bottom. STING's mass was 9.5 kg, and it weighed 69 N in water. Dragging a thin recovery line, its terminal velocity was 5–6 m/s in the water depths at these sites. Since data were logged for up to 2 min, as many as six impacts could be recorded in sequence by pulling STING up a few meters and releasing. For each impact, the deceleration was compared with the buoyancy, body drag, and tether drag to extract the sediment force. The dynamic bearing strength is the sediment force per unit area of the foot divided by the strain rate, which is the 0.15 power of the inverse of the time to penetrate a distance equal to the diameter of the foot. Bearing strength was calculated at 5-cm depth intervals.

As shown in Table 1, there were strong correlations among the geotechnical variables, particularly between grain size, bearing strength, and porosity. Fig. 2

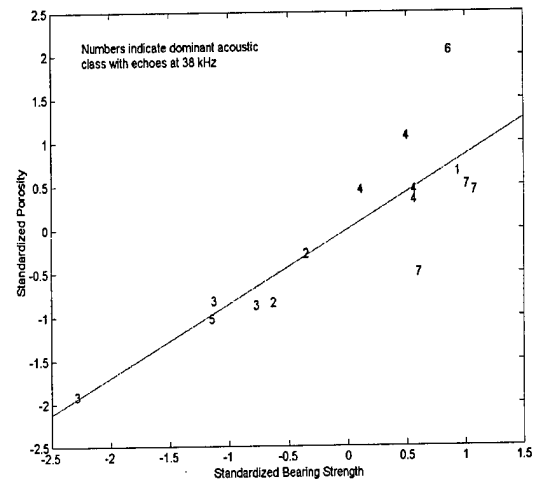


Fig. 2. Porosity and bearing strength, both reduced to zero mean and unit variance, for the 15 sites. Symbols indicate the acoustic class from the 38-kHz data set.

illustrates one of these correlations. In a sand-to-silt transition (increasing bearing strength implies decreasing mean grain size) bearing strength and porosity both increase, and the acoustic classes appear to reflect a combination of these variables plus some additional details. Results such as these suggest that there are indeed underlying correlations to be found by canonical analysis.

In preparation for canonical correlation analysis, it is important to prune the set of geotechnical variables to those that are largely independent of each other. Grain size at depth is redundant beside surface grain size, so was not used. This left four geotechnical variables. All were used, since a prime purpose of this work was to investigate which of these variables correlated with acoustic classes in various situations.

Table 1. Correlations of the initial geotechnical data set.

	Mean Grain Size		Shear Strength	Bearing Strength	Porosity
	Surface	10 – 15 cm			
MGS surf	1	0.97	0.08	-0.78	-0.67
MGS deep	0.97	1	-0.06	-0.70	-0.59
Shear Str.	0.08	-0.06	1	-0.24	-0.39
Bear. Str.	-0.78	-0.70	-0.24	1	0.85
Porosity	-0.67	-0.59	-0.39	0.85	1

IV. ACOUSTIC DATA ACQUISITION AND PROCESSING

A hull-mounted Knudsen 38/200 Echo Sounder, operating at both frequencies at 250 W with a pulse length of 0.25 ms, was used to produce the echoes. Beam widths were 6° at 200 kHz and 19° at 38 kHz. The echo envelopes, after TVG, bandpass filtering, and sampling at 20 kHz, were stored on Exabyte tapes.

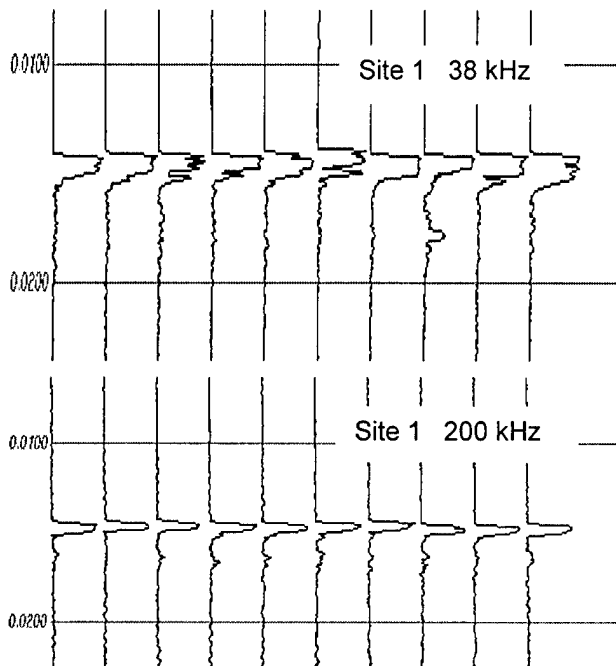


Fig 3. Echoes from site 1. The vertical axis is two-way travel time in seconds. At 38 kHz this site was classified as 89% class 2 and 9% class 7. The 200-kHz classes are a distinct set, and at 200 kHz this site was 99% class 1 of that set.

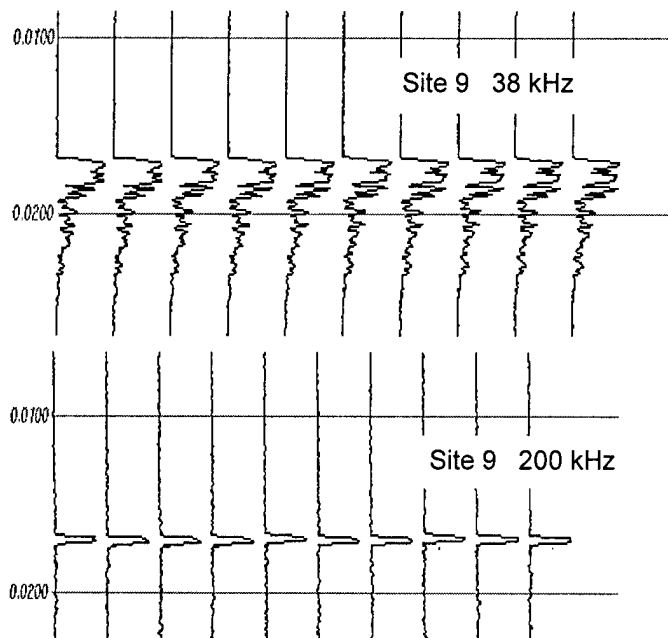


Fig. 4. Echoes from site 9. At 38 kHz this site was classified as 100% class 1, while at 200 kHz it was 57% class 4, 25% class 7, 11% class 8, and 5% class 5.

The QTC VIEW™ technique for bottom classification is based on the shape of the direct echo (no multipath echo is used). Figs. 3 and 4 show stacks of echoes from sites 1 and 9. Site 1 has twice the mean grain size and about one-half the shear strength and bearing strength of site 9.

The echoes were processed using QTC VIEW™ technology [6]. After picking the bottom, aligning with respect to the bottom pick, and stacking to reduce noise, a suite of algorithms was employed to extract features from the echoes. The many features are descriptors of echo shape, including the distribution of energy between the specular and scattered portions. Each feature value was normalized across all the echoes to zero mean and unity variance. Multivariate statistics were used to reduce the large number of features to the three linear combinations responsible for as much variance as possible. These three values, called Q-coordinates, were used to cluster the echoes into classes. In this unsupervised approach, the 38-kHz echoes formed seven classes (Fig. 5) and the 200-kHz echoes eight classes (Fig. 6). Most of the sites were acoustically uniform at both frequencies, which is one indication of successful and useful classification. These figures indicate classes and composition at each site, for example, at 38 kHz, site 7 was 85% class 6, 13% class 7, and 2% other classes.

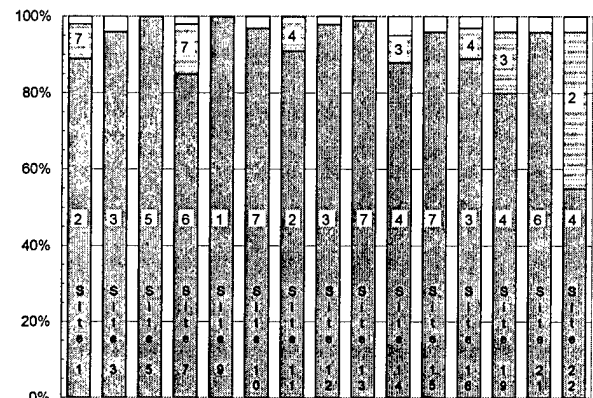


Fig. 5. Acoustic classes and proportional composition of the test sites at 38 kHz. Classes representing less than 4% have been suppressed.

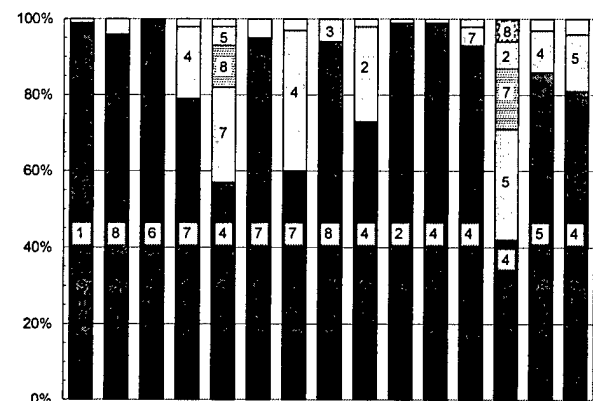


Fig. 6. Acoustic classes and proportional composition of the test sites at 200 kHz. Classes representing less than 4% have been suppressed.

V. MULTIVARIATE CORRELATION ANALYSIS OF ACOUSTIC AND GEOTECHNICAL DATA

If the variables in a multivariate data set divide naturally into two groups, canonical correlations indicate the relationships among the groups of variables [1,7]. Here, one group of variables is the frequency of occurrence of each acoustic class at each site, and the other is the four geotechnical variables at each site. Canonical correlation analysis finds the linear combinations of variables from each set that have the highest correlations with each other (second and lower combinations being uncorrelated with higher). Each linear combination is characterized by an eigenvalue, which is the square of the canonical correlation. The corresponding eigenvector is the coefficients of each variable in the pair of linear combinations of variables, that is, in the canonical variables. Loading of each original variable into the canonical variable is a measure of the prominence of that variable in the correlation and is available from the analysis. The eigenvalues can be tested for statistical significance; here we use Bartlett's original test [8], although others exist.

In preparation, each set of values, such as porosity or composition of classes at a site, was standardized to zero mean and unit variance. Standardized variables are plotted in Figs. 2 and 7.

Canonical correlation analysis was performed on the 38-kHz data set, with four variables in the geotechnical data set and six in the acoustic data set (not seven since the seventh is one minus the sum of the first six – note that as the classifications originate from principal component analysis they are by nature uncorrelated). The eigenvalues were 0.942, 0.684, 0.620, and 0.121 (the number of eigenvalues equals the lesser number of variables in a data set). Bartlett's test first uses all the eigenvalues, then all but the largest, and so on. The first two results were 0.998 and 0.87, indicating that there is only a 0.2% chance that a random data set would give one canonical correlation as good or better, and a 13% chance that a random set would give two. The corresponding results using the 200-kHz set were eigenvalues of 0.861, 0.817, 0.597, and 0.234, giving Bartlett results of 0.9996 and 0.996.

Knowing that there are statistically significant correlations at both frequencies, we can interpret the coefficients to find which variables are heavily involved in the canonical variables. Table 2 shows the loadings of each geotechnical variable into the first and second canonical variables for each frequency. Because the lower frequency penetrates deeper, one would expect volume properties to be emphasized at 38 kHz, and bearing strength, a volume property, was most heavily loaded in the first geophysical canonical variable. At the higher frequency, the echo is dominated by surface scattering. None of the four geotechnical variables adequately describes just the surface, but porosity and grain size are important to the surface acoustic

Table 2. Loadings for the geotechnical variables in the first and second canonical variables for each frequency.

	38 kHz		200 kHz	
	Root 1	Root 2	Root 1	Root 2
Mean Grain Size	-0.60	-0.18	-0.41	0.89
Shear Strength	-0.34	-0.66	-0.47	-0.00
Bearing Strength	0.95	0.12	0.57	-0.49
Porosity	0.72	0.59	0.91	-0.28

characteristics. The major contributor to the first geotechnical canonical variable at 200 kHz was found to be the porosity.

The final result of one of the canonical correlations is shown in Fig. 7, namely the first canonical variables for each site, at 38 kHz. The regression line could be used to estimate geotechnical data for a new site based on its proportional composition of acoustic classes. The steps would be: express the proportional compositions with unit variance and zero mean, multiply that row vector by the column vector of acoustic canonical weights, and use the regression line to get the corresponding geotechnical value. This yields an estimate of a weighted sum of geotechnical variables, not individual values. For this data set, the accuracy is indicated by the spread about the regression line of Fig. 7.

Canonical correlation analysis requires a large number of samples and assumes normal distributions. Our data sets did not meet these criteria. An emerging approach to this common situation is a bootstrap analysis in which the experimental data points are

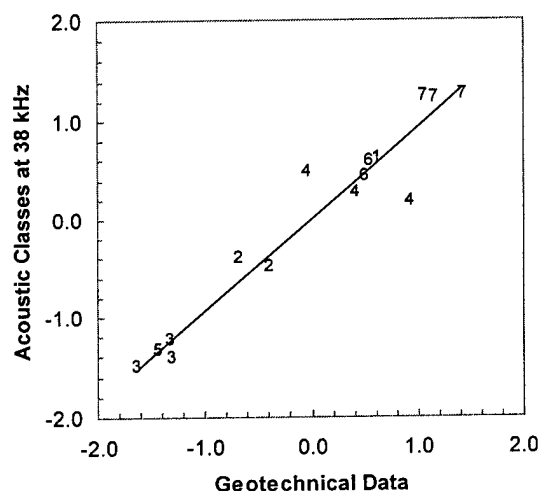


Fig. 7. The first canonical variables for the geotechnical data set and the frequencies of occurrence at 38 kHz. Values plotted are the sum of the standardized variables at each site, each multiplied by its canonical weight. Symbols indicate the acoustic class.

resampled, with replacement, to generate many data sets [9]. Bootstrap is particularly useful for estimating confidence intervals of parameter (e.g. mean or variance) estimates. Here, it was used to estimate errors in the correlation coefficients among the variables of the data sets. Using standardized (zero mean, unit variance) values, the correlation coefficients calculated assuming Gaussian distributions and by bootstrap differed by no more than 0.02, small compared to their range of values: 0.60 to -0.73. Also, the bootstrap analysis gave small errors in these coefficients, typically 0.04 to 0.07. These results suggest that treating these data sets as if they were Gaussian had small effects on the correlation results, a conclusion that is supported by the strong canonical correlations and the Bartlett test.

VI. CONCLUSIONS

Acoustic classifications and geotechnical data were obtained for 15 sites in sheltered embayments near Vancouver Island. The seabeds in all sites had low shear strengths and grain sizes from silts to sands. The acoustic data were high quality and clustering was good, as shown by nearly homogeneous classification results at each site. Four geotechnical variables were selected: surface grain size, porosity, shear strength, and bearing strength. Some of these were strongly correlated, and acoustic classifications appeared to fit sensibly with these correlations.

Canonical correlation analysis was used to quantify the extent of the correlation between the acoustic and geotechnical data sets, and to identify the geotechnical variables most responsible. At least one canonical correlation was statistically significant at each sonar frequency. At 38 kHz, the strength-related variables had the highest factor loadings, that is, contributed most heavily to the linear combinations of geophysical variables that correlated with the acoustic set. Sonar at 200 kHz penetrates less, and the highest loading factors in this case were for porosity and grain size. Of the four geotechnical variables, porosity and grain size are the better descriptors of surface properties.

All 15 sites had soft substrates because they had been selected for studies of mine burial on impact. Whether or not mines would bury at each site is not the subject of this paper, but hard sites at which impact was clearly precluded were not studied. Of all our measurements of shear strength at all depths, only a few were over 10 kPa, which is below the range of most literature studies of correlations involving shear strength (an exception is [10]). In spite of using such a limited range, the classifications and correlation results were convincing. Extending this work to stiffer substrates would be of considerable interest.

Canonical analysis does not lead to estimates of a particular geophysical variable, but rather to estimates of linear combinations. For these data sets, it has been shown that combinations of geotechnical variables are

strongly correlated with combinations of acoustic classifications. In particular, strength-related variables are highly correlated with classes from 38 kHz data, while 200-kHz echoes seem to relate more to surface character.

With the strength of these correlations established and with guidance as to which geotechnical variables are the more pertinent, a basis has been established for predicting geotechnical variables from acoustic classifications, using other correlation techniques such as multivariate analysis.

ACKNOWLEDGMENTS

The Canadian Department of National Defence supported this work by running a series of experiments aboard CCGS Vector and by a contract to Quester Tangent Corporation. CCGS Vector is a small research ship of the Canadian Coast Guard.

REFERENCES

1. A.S. Tsemahman, W.T. Collins, and B.T. Prager, "Correlation analysis of acoustic seabed classification and sediment properties near Vancouver Island", *Proceedings of Oceans '97*.
2. T.W. Lambe, *Soil Testing for Engineers*, John Wiley & Sons, New York (1951).
3. S. Serota and A. Jangle, "A direct-reading pocket shear vane", *Civ. Eng. ASCE* **42** 73-76 (1972).
4. D.F. Lott and R.H. Poecket, "Extending cooperative research", *Sea Technology*, **37** 56-61 (1996).
5. R.H. Poeckert, J.M. Preston, T. Miller, R. Religa, and A. Eastgaard, "A seabed penetrometer", Defence Research Establishment Atlantic Technical Memorandum 97/233 (1997).
6. J.L. Galloway and W.T. Collins, "Dual frequency acoustic classification of seafloor habitat using the QTC VIEW™", *Proceedings of Oceans '98*.
7. B.F. Manly, *Multivariate statistical methods: a primer*, Chapman and Hall (1994); also *Statistica user manual*, StatSoft Inc., Tulsa, OK (1995).
8. M.S. Bartlett, "The general canonical correlation distribution", *Annals of Mathematical Statistics* (1947).
9. A.M. Zoubir and B. Boashash, "The bootstrap and its application in signal processing", *IEEE Signal Proc. Magazine* **15** 56-76 (1998).
10. Theilen, F.R. and Percher, I.A., "Assessment of shear strength of the sea bottom from shear wave velocity measurements of box cores and *in situ*", in *Shear waves in marine sediments*, Hovem, Richardson, and Stoll (eds.), Kluwer Academic Pub, Netherlands, pp 76-74.

Dr. Jon Preston, Senior Scientist, Quester Tangent Corporation, has twelve years experience as a research scientist with the Department of National Defence, Canada. At Defence Research Establishment Pacific, Victoria, BC, he developed mine countermeasures technology, particularly processing of high-frequency imagery, and towfish altitude and position measurement and control. Much of the work done by the DREP mine countermeasures group can be seen in the route survey payload of the 12 Maritime Coastal Defence Vessels recently acquired by the Canadian Navy. Starting about 1996, his research interests broadened to include both acoustic and invasive sensing of sediments, and he lead several multi-faceted research cruises focussing on sediments. During his years at DREP he published over 20 internal reports and 10 papers in conference proceedings. He was technical chairman of the IEEE Oceans '93 conference.

Dr. Preston's BSc is from McMaster University, 1970. His PhD work, in the plasma physics group at the University of British Columbia, dealt mostly with sensors, diagnostic equipment, and signal processing. Between graduation from UBC in 1974 and moving to DREP, he was responsible for Canada's R&D program in automatic detection of chemical warfare compounds. This work lead to a family of new detectors used in many NATO armies, 25 internal reports, 4 journal papers, and 2 patents.

INTEGRATION OF MULTIBEAM BATHYMETRY AND SIDESCAN SONAR DATA FOR GEOLOGICAL SURVEYS

Russell Parrott^{1*}, John Hughes Clarke², Gordon Fader¹, John Shaw¹ and Edouard Kamerrer²

¹Geological Survey of Canada (Atlantic), Box 1006, Dartmouth, NS, Canada B2Y 4A2

²University of New Brunswick, Box 4400, Fredericton, NB, Canada, E3B 5A3

*Corresponding Author

I. ABSTRACT

A geophysical survey conducted off Liverpool, Nova Scotia, Canada in November 1998 collected data using multibeam bathymetric, sidescan sonar, high-resolution sub-bottom profiler, and acoustic seafloor classification systems. During the survey, multibeam bathymetric and sidescan sonar data were processed on-site and imported into a Geographical Information System for further analysis and display. Shaded relief images derived from the multibeam bathymetric data and sidescan sonar mosaics were combined with data from maps and aerial photographs of the area. These maps and images formed the basis for a preliminary interpretation of geological processes and features on the seabed. Post-processing of the multibeam bathymetric data using newly-developed algorithms improved the resolution of seafloor features and provided acoustic backscatter intensity measurements. These data were used to define the distribution of coarse and fine-grained sediments and seabed features and to compare and contrast various system resolutions. Seafloor samples and photographs were also taken to provide information for the interpretation of the various acoustic data sets. A variety of seafloor features are presented, using both sidescan sonar and multibeam bathymetric data for illustration.

The seafloor is dominated by glacial features deposited during the recession of the last glaciers across the area (ca. 14,000-12,000 years BP). These include a large curvilinear moraine, smaller ribbed moraines and glaciomarine sediment. Bedrock crops out in many areas forming shoals. The glacial features were slightly modified, largely by shore-face processes, during a subsequent rise of post-glacial sea level from a low stand of approximately 65 m below present-day sea level to its present position. During the marine transgression, several coastal sand bodies were deposited at the northern flank of bedrock outcrops. Ribbed or lift-off moraines, which are normally thought to be destroyed in transgressed zones on the inner shelf, dominate the topography of the study area. Their distribution, in depths as shallow as 15 m, suggests that they survived the effects of the marine transgression largely intact. Bottom photographs confirm that the moraines are erosional remnants, armoured by boulders and cobbles. Existing models of marine transgression and sea level history must therefore consider the idea that some glacial features can survive shoreface erosion during marine transgression.

II. INTRODUCTION

Digital multibeam bathymetric surveys have evolved to become a primary offshore geological mapping tool used by the Geological Survey of Canada for marine geological surveys. Multibeam bathymetry and backscatter intensity data, collected as the first stage of a multiparameter geophysical survey in Liverpool, Nova Scotia (Fig. 1), provided a rapid means of determining the regional morphology and nature of the sediments on the seafloor. Multi-element transducers provide individual soundings of the water depth and echo strength for each ping, and enable a wide swath to be surveyed in a single pass through an area. Survey lines were spaced to provide overlapping coverage of the seafloor. The water depths and echo strengths calculated for each transducer element were integrated with precise navigation to provide a geographically referenced data set. The multibeam bathymetric data were used to create shaded relief images that depict seafloor morphology which help identify additional features such as channels, areas of bedrock outcrop, small and large scale bedforms, boulders and anthropogenic debris [1,2].

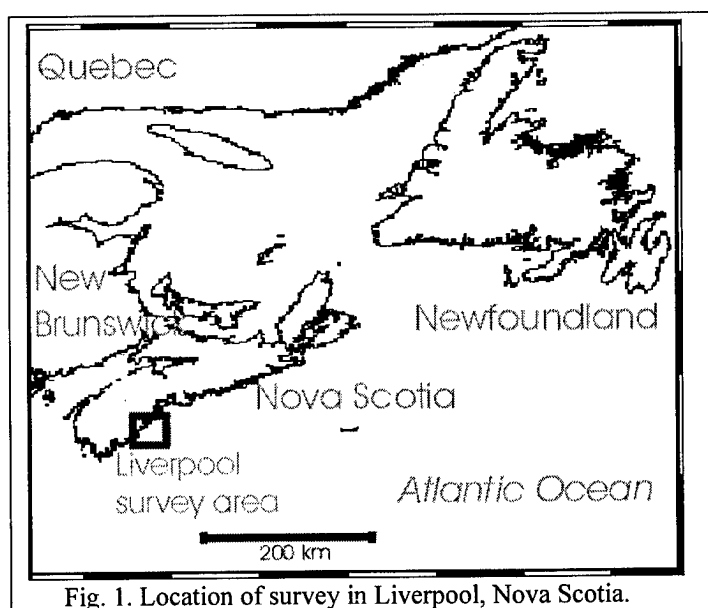


Fig. 1. Location of survey in Liverpool, Nova Scotia.

Differentiation of bedrock lithologies in other inner shelf areas is made possible based on the fine structure and morphological characterization capabilities of the systems. Acoustic backscatter intensity measurements help determine the general distribution of coarse and fine-grained sediments. Features identified on the multibeam data were investigated during subsequent surveys using higher resolution sidescan

sonar systems and sub-bottom profilers for information on sub-surface structure, material and thickness.

III. SURVEY AREA AND METHODS

A. Multibeam bathymetry system

Multibeam bathymetry data were collected in the approach to Liverpool, (Fig. 1) using a Simrad EM3000 multibeam bathymetry system mounted in a 10 metre hydrographic survey launch with an Applied Analytics POS-MV attitude sensing system, and a differential GPS navigation system. Survey lines were run at a 75 metre spacing throughout the study area to provide 100 percent coverage of the seafloor in depths greater than about 20 metres. During the survey, data were imported into a Unix workstation, and processed using the HIPS data cleaning program (by Universal Systems Limited, Fredericton, NB) to remove spurious soundings and clean navigation data and to correct for tidal variations. The processed data were imported into a GRASS GIS system where shaded colour relief images were generated and overlaid on scanned bathymetry maps of the area as shown in Fig. 2.

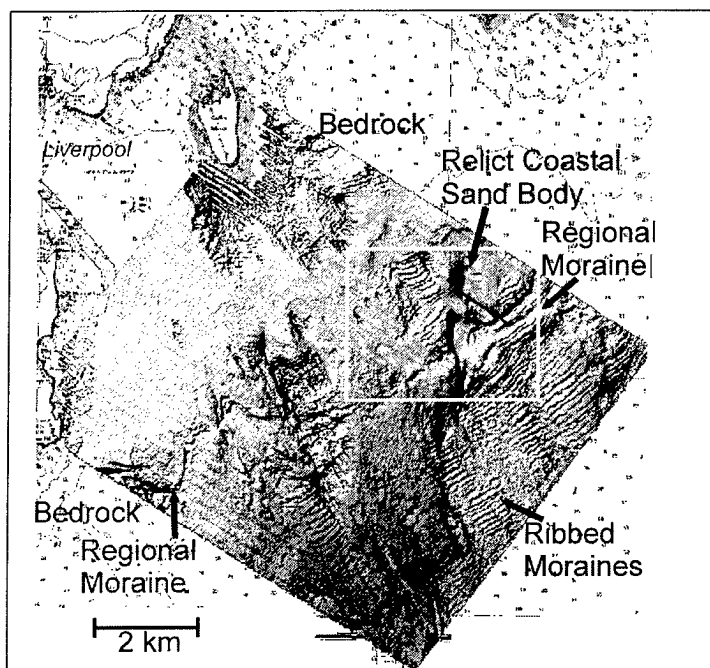


Fig. 2. Shaded relief image generated from Simrad EM3000 multibeam bathymetry data collected in October 1998. The white rectangle indicates the location of data shown in Fig. 3. The location of the seismic profile shown in Fig. 8 is indicated by the line within the white rectangle.

After the survey, the multibeam bathymetry data were re-processed by the Ocean Mapping Group at the University of New Brunswick (OMG/UNB) to enhance and maximize the resolution.

B. Multibeam backscatter

Acoustic backscatter intensity values are controlled by the physical properties of seafloor sediments, seafloor relief and roughness. The character and intensity of the backscatter provides valuable information on the nature and distribution of sediments within an area. The multibeam bathymetry data were

processed by the OMG/UNB to extract backscatter information from which a 2 metre resolution backscatter was produced.

C. Sidescan sonar system

High-resolution, acoustic images of the seabed were produced with a Simrad MS992 dual frequency (120 and 330 kHz) sidescan sonar system equipped with a neutrally buoyant towbody deployed behind a dead weight depressor. This configuration was chosen to reduce motion and artifacts on the sidescan sonar records due to vessel induced heave and thereby increase resolution and clarity of presentation. The sidescan sonar system was capable of resolving objects of 0.15 metres and larger. The sidescan sonar data were collected at 100 metre range for lines in the centre of the survey area and at 200 metre range for the outer lines. Sidescan sonar data were imported into a Unix workstation where slant range and beam corrections were applied, integrated with navigation and imported into a GRASS GIS system. Individual lines were combined to form a digital sidescan sonar mosaic, at 2 metre resolution.

D. Sub-bottom Profiler

High-resolution, sub-bottom profiler data were collected throughout the survey area with either a Huntec DTS system or an IKB Seistec system. Both systems use an electrodynamic (boomer) source to produce a repeatable impulse-like output which provides a resolution of about 0.25 metres. The DTS system, equipped with two external streamers, was towed about 10-30 metres above the seafloor. The Seistec system, equipped with an internal line-and-cone array and an external streamer, was towed at the surface. The systems were fired 2 times per second and graphic records displayed on a thermal graphic recorder.

IV. RESULTS

A. Multibeam Bathymetry

Multibeam bathymetry surveys in the approaches to Liverpool demonstrate the usefulness of multibeam bathymetry data as an initial step in the regional assessment of marine geology. Earlier geophysical surveys had allowed a preliminary interpretation of the geology and morphology [3]. The earlier surveys recognized a broad, eroded till plain off Liverpool and the presence of a buried channel extending seaward, but did not have the resolution to identify or determine the morphology or character of the various moraines and other features. Multibeam bathymetry data collected in the area provided considerably more detail about the morphology and genesis of the seafloor than available from existing hydrographic charts (Fig. 2). The sea floor is dominated by glacial features that were deposited during the recession of the last glaciers across the area (ca. 14,000-12,000 years BP). These include a large regional curvilinear moraine, smaller ribbed moraines and glaciomarine sediment. Bedrock outcrops in many areas to form shoals. The glacial features were slightly modified, largely by shore-face processes, during the subsequent rise of post-glacial sea level to its present position from a low stand of approximately 65 metres below present-day sea level [4]. During the marine transgression, several coastal sand bodies were deposited at the northern flank of bedrock outcrops. Ribbed or lift-off moraines, which were previously considered to be absent from transgressed zones, are seen to dominate the

study area. Their distribution across this inner shelf, in depths as shallow as 15 m, suggests that they survived the effects of the transgression largely intact.

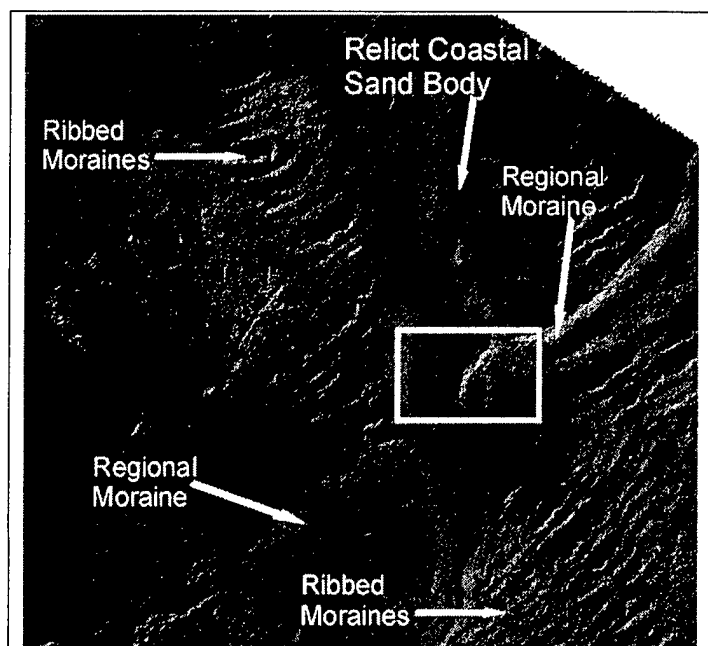


Fig. 3. Shaded relief image created from reprocessed multibeam bathymetry data. The location of the data is shown by the white rectangle in Fig. 2. The small white rectangle indicates the location of data shown in Fig. 3.

The image in Fig. 3 shows data after reprocessing by OMG/UNB. Note the presence of bedrock outcrops, a regional terminal moraine, ribbed moraines and a relict coastal sand body.

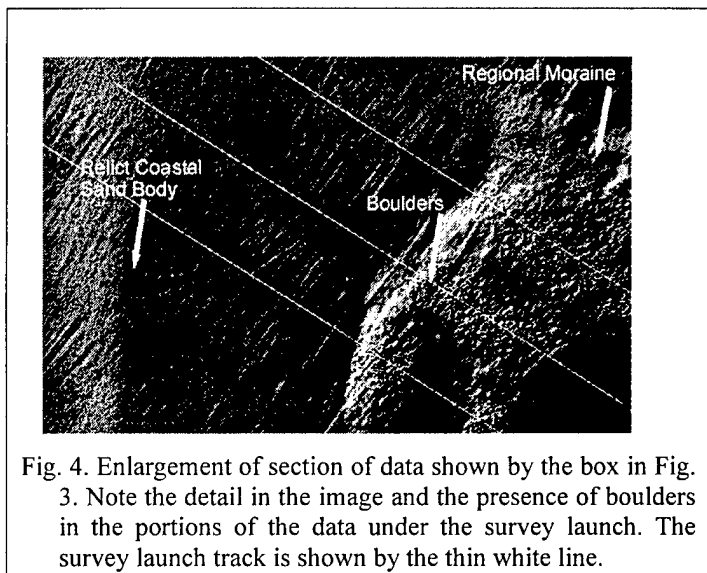


Fig. 4. Enlargement of section of data shown by the box in Fig. 3. Note the detail in the image and the presence of boulders in the portions of the data under the survey launch. The survey launch track is shown by the thin white line.

Fig. 4 shows the degree of detail that can be obtained from the multibeam bathymetry data. This allows detection of the presence of 1.5-2.0 metre boulders in the near-nadir portions of the data (under and slightly off to the side of the survey launch), for water depths to 50 metres. The boulders appear in track parallel bands across the moraines in these data. However, in the outer portions of the swath boulders of these

sizes are not detected. Sidescan sonar data indicate that the moraines are entirely covered by boulders. This example illustrates the resolution limits on the Simrad EM3000 multibeam bathymetry system in water depths to 50 metres, collected at a survey speed of 20 m/s (11 knots) and wave condition of less than 2 metres. The highest resolution is obtained from near-nadir portion of the swath. Data from the outer portions of the swath insonify a larger area on the seafloor, are more sensitive to the vessel motion and consequently provide less resolution. Such calibrations are very important for proper interpretation of seabed geology and features.

B. Multibeam backscatter

The mosaic of backscatter data produced from the multibeam system (Fig. 5) enables interpretation of the distribution of different types of sediments and large-scale bedforms within the area. The muds and sands (characterized by the lighter colours) can be seen adjacent to the coarser gravels and bedrock (characterized by the darker colours). The resolution of the mosaic produced from multibeam backscatter data has comparable resolution to the mosaic of sidescan sonar data.

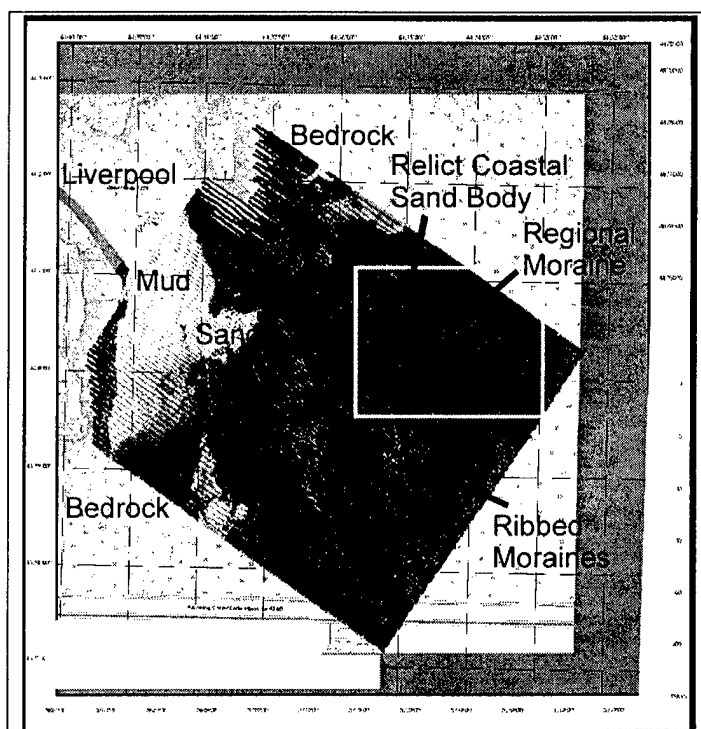


Fig. 5. Backscatter intensity generated from Simrad EM3000 multibeam bathymetry data.

C. Sidescan sonar

The sidescan sonar mosaic data provided a comparable display to the multibeam backscatter data. Sediment type and distribution are quite evident on both data sets. The presence of the bedrock, regional moraines and ribbed moraines is less distinct, but nonetheless visible. Very little evidence is seen for the presence of small scale bedforms or boulders. A major advantage of the sidescan sonar data is the much higher resolution (0.15 metres) available in the raw sidescan sonograms affording a clear image of small boulders and bedrock outcrop. This is evident in a section of data showing

the relict coastal sand body, regional moraine and portions of ribbed moraines are shown in Fig. 7. Boulder cover on the regional and ribbed moraines is continuous, whereas boulders are absent on the sand body.

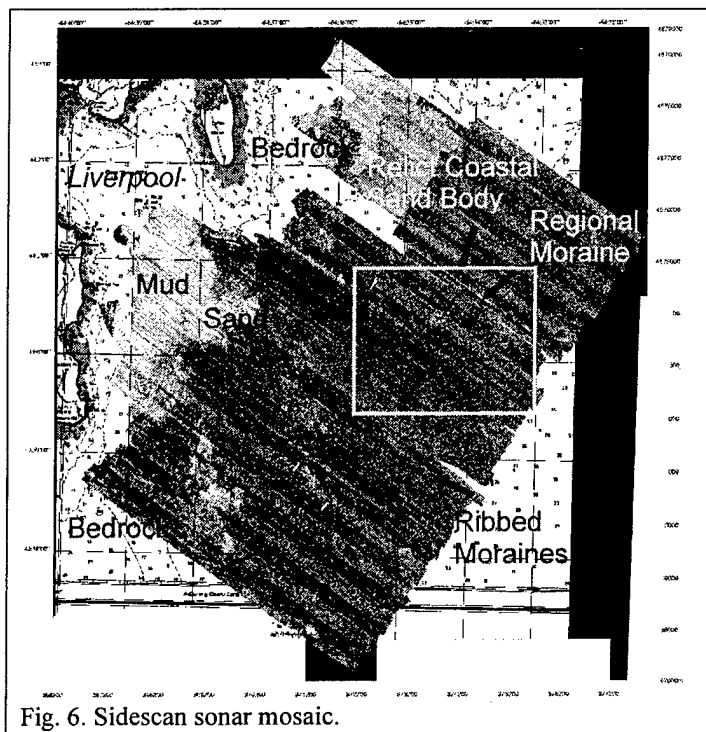


Fig. 6. Sidescan sonar mosaic.

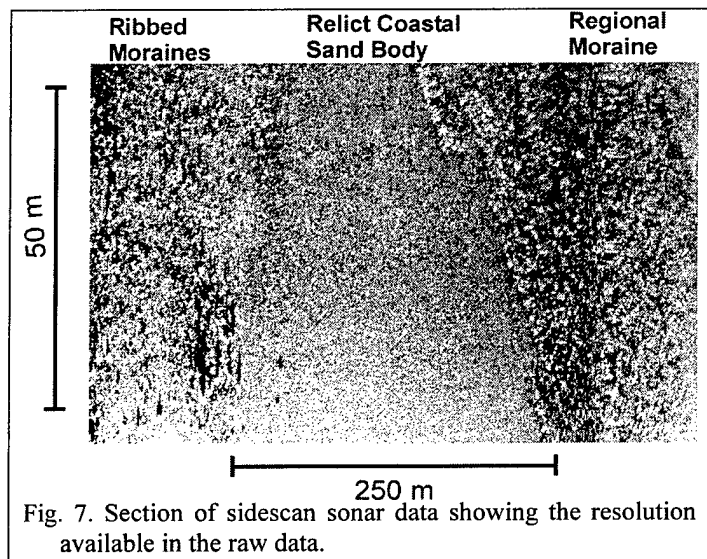


Fig. 7. Section of sidescan sonar data showing the resolution available in the raw data.

D. Sub-bottom Profiler

High-resolution, sub-bottom profiler data were used to map the thickness and structure of materials below the seafloor, and provide information on the genesis of the sediments. Huntect DTS sub-bottom profiler data, displayed in Fig. 8, shows a boulder-covered glacial moraine cropping out at the seafloor. Sand sized sediment, which we speculate was winnowed from this and other glacial features in the area during a time of lower

sea level, has been reworked into a broad liner, stratified sand body, shown in all figures and to the left in Fig. 8.

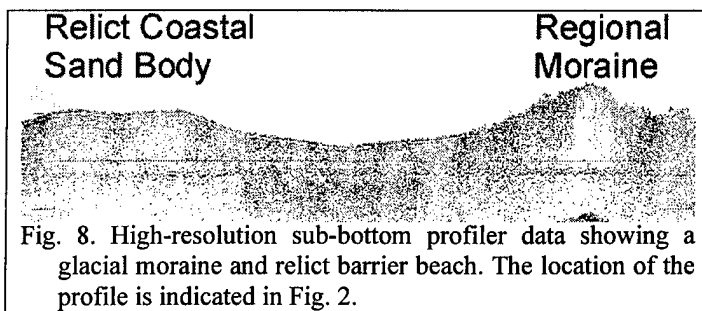


Fig. 8. High-resolution sub-bottom profiler data showing a glacial moraine and relict barrier beach. The location of the profile is indicated in Fig. 2.

V. CONCLUSIONS

Multibeam bathymetry has become an essential component of multiparameter marine geophysical surveys. Images generated from multibeam bathymetric data allow optimal design of subsequent surveys with sidescan sonar, seismic systems and sampling programs. Subtle aspects of sedimentation and erosion can be enhanced by digital processing of the data. Multibeam bathymetry is particularly useful for providing high-resolution images of seafloor morphology at a level of detail and speed previously unattainable. Interpretation of fine-scale geology and identification of small (<2 m) targets requires use of more traditional techniques such as sidescan-sonar surveys and photography. Multibeam bathymetry provides the framework for defining environmental conditions of a dynamic geological setting and is the recommended first approach in marine geological studies.

REFERENCES

- [1] Courtney, R.C. and Fader, G.B.J., 1994, A new understanding of the ocean floor through multibeam mapping. *In*: Anna Fiander [ed.] Science Review of the Bedford Institute of Oceanography, the Halifax Fisheries Research Laboratory, and the St. Andrews Biological Station (1992&'93) Canada Department of Fisheries and Oceans, Scotia-Fundy Region: 9-14.
- [2] Shaw, J., Parrott, D.R., and Hughes Clark, J., 1996, Use of Multibeam bathymetry to determine seabed impacts at the Argentia Naval Base, Newfoundland, *In*: Partnership in Coastal Zone Management, J. Taussik and J. Mitchel [eds.] 1996, Samara Publishing Limited, Cardigan.
- [3] Piper, D.J.W., Mudie, P.J., Letson, J.R.J., Barnes, N.E., and Iulicucci, R.J., 1986, The marine geology of the inner Scotian Shelf off the south shore, Nova Scotia, Geological Survey of Canada Paper 85-19, 65p. + 1 chart.
- [4] Stea, R.R., Boyd, R., Fader, G.B.J., Courtney, R.C., Scott, D.B., and Pecore, S.S., 1994, Morphology and seismic stratigraphy of the inner continental shelf off Nova Scotia, Canada: Evidence for a -65 m lowstand between 11,650 and 11,250 C¹⁴ yr B.P. *Marine Geology*, 117, pp 135-154.

Bibliographies

D. Russell Parrott,

Marine Geophysicist, Address: Geological Survey of Canada - Atlantic (GSCA), Bedford Institute of Oceanography, Box 1006, Dartmouth, Nova Scotia, Canada, B2Y4A2, Email: parrott@agc.bio.ns.ca, Work: 1984 - present GSCA, 1975-84 Huntex ('70) Ltd., School: BEng Mining 1972, MEng Geophysics 1975, McGill University, Membership: APENS Interests: Multibeam bathymetry, high resolution, seismic reflection and sidescan sonar, environmental geology.

Gordon B. J. Fader,

Marine Geologist, Address: Geological Survey of Canada - Atlantic (GSCA), Bedford Institute of Oceanography, Box 1006, Dartmouth, Nova Scotia, Canada, B2Y4A2, Email: fader@agc.bio.ns.ca, Work: 1969 - present, GSCA, School: BS Geology 1969, St. Marys University, Membership: GAC Interests: Marine geological

mapping, Quaternary geology, glaciation, seismic reflection and sidescan sonar interpretation, marine minerals, environmental geology.

John Shaw

Research Scientist at the Geological Survey of Canada - Atlantic (GSCA). Address: Geological Survey of Canada (Atlantic), P.O. Box 1006, Bedford Institute of Oceanography, Dartmouth, N.S., Canada, B2Y 4A2. Work: 1985-1986 Fellow, Instit. Irish Studies, Queen's University of Belfast; 1986-present GSCA School: BSc Queen's Univ. Belfast; MSc and PhD The New University of Ulster Interests: Quaternary sea-level change, multibeam bathymetry.

John Hughes Clarke

Research Associate Work: 1991-present UNB, 1989-91, Research Fellow, James Cook Univ, Australia, 1988-89 PDF Geological Survey of Canada, School: BA geology Oxford 1983, MSc oceanography Southampton, 1984. PhD Dalhousie 1988, Interests: acoustic imaging techniques, marine sediment transport, multibeam bathymetry and backscatter

Edouard Kamerrer

Graduate Student, Ocean Mapping Group, Department of Survey Engineering, University of New Brunswick, Address: Department of Survey Engineering, University of New Brunswick, Fredericton, N.B. Canada, Email kamerrer@omg.unb.ca

Acoustic Observations of a Fluid Mud Layer Transporting Sediment on the Northern California Shelf.

James D. Irish, Peter Traykovski, and James F. Lynch,
Dept. Applied Ocean Physics and Engineering,
Woods Hole Oceanographic Institution

Abstract

During the past few years, STRATAFORM field efforts off Eureka, CA have involved numerous investigators studying the source, deposition and movement of sediment brought to the sea by the Eel River. During the winter of 1997-98, WHOI investigators deployed tripods and moorings across the shelf to observe the sediment movement. The 60-m tripod had an acoustic backscattering sensor (ABS) that profiled the bottom meter of the water column at 1-cm intervals. In late January 1998 a series of high river discharge events coupled with high waves produced a series of ~30 g/l suspended sediment layers, ~20 cm thick that propagated past the tripod. The optical backscattering sensor at 0.5 m saw only a maximum of 3-g/l peak and so missed these thin "fluid mud" layers. Such fluid mud layers can be a major source of sediment transport, and are often not well resolved by traditional optical techniques, but are observed with remote acoustic profiling techniques.

I. Introduction

The continental shelf off the Eel River in Northern California is a highly energetic environment with large winter storm waves and a large supply of sediment carried to the sea during runoff events. This system has been studied extensively during the past few years as part of the ONR sponsored STRATAFORM (Strata Formation on Continental Margins) program.

Initial coring surveys of the region revealed that the flood deposits were located seaward of the 50-m isobath (Wheatcroft et al., 1997), while the river plume, as observed by later helicopter-based hydrographic surveys, was generally located within the 40-m isobath (Geyer, personal communication). Therefore, the direct deposition of sediments by the plume is not the process occurring here, and additional observations were required to study the processes transporting the sediment across the shelf. The transport processes which can redistribute the sediments range from resuspension of sediment

by waves and/or strong currents and the subsequent transport by the mean currents and/or density driven flows of high sediment concentration fluids. The observation of this latter process requires continuous profiling technology since the flow is confined to a thin layer at the bottom. To do this during the winter of 1997-98, WHOI investigators deployed a cross-shelf array of sensors designed to observe the cross-shelf sediment transport. This array consisted of three instrumented surface moorings with sensors located along the mooring cable in the water column and three instrumented bottom boundary layer tripods.

II. Observational Techniques

A. Instrumentation

The cross-shelf array of tripods and moorings was deployed from November, 1997 to March, 1998 along the STRATAFORM K-line, approximately 12 km north of the Eel River mouth. The tripods and surface mooring were paired together and located on the 20, 40 and 60-m isobaths. The bottom-mounted tripod at 20-m contained a 300 kHz RD instruments Workhorse Acoustic Doppler Current Profiler. The 40 m tripod contained a large number of acoustical and optical sensors; but was tipped over, broken apart (perhaps by fishing activities), and partially buried. Most of the instrumentation could not be recovered.

The tripod at 60 m contained a 2-frequency (2.5 and 5.0 MHz) downward looking, Acoustic Backscattering Sensor (ABS) which recorded profiles of backscattered acoustic intensity with 128 m range bins with 1 cm vertical resolution. A vertical array of Marsh-McBirney ElectroMagnetic Current Meters (EMCM) on this tripod were located at 0.5, 1.1 and 2.1 meters above bottom (mab) to measure the bottom boundary layer velocity profiles. A Downing and Associates Optical Backscattering Sensor (OBS) was located next to each EMCM sensor the same depth. These instruments burst sampled at 2 Hz for 8 minutes each hour. This sampling allowed us to adequately sample the variability on the time scales of the surface waves as well as the lower frequency variability, and yet stay within the constraints of the instruments' battery and data storage capacity.

B. Calibrations

Because the ABS and OBS sensors used do not directly measure particle concentration in grams per liter, calibrations were done with sediments from grab samples taken at the 60-m site. The samples were mostly fine grain mud (size $< 63 \mu\text{m}$), but also contained very little fine sand ($> 63 \mu\text{m}$). The maximum concentrations possible during the calibration were limited to several grams per liter because a limited supply of sediment was available and the tank size.

Both optical and acoustic sensors are sensitive to particle size. Optical sensors scatter light geometrically, so that the backscattered signal is proportional to the cross sectional area of the particles. Thus, the OBS sensors have a radius⁻¹ relationship of sediment concentration to backscattered intensity and are therefore more sensitive to the finer particles.

Acoustic sensors in the MHz frequency range operate in the Rayleigh scattering regime for the fine particle sizes seen here. Thus, the ABS sensors have a radius³ size per unit concentration dependence for particles that are smaller than the inverse acoustic wavenumber. As particle size increases, the scattering intensity increases until the wavenumber times particle size is of the order one, after which the acoustic also scatters geometrically, so the acoustic sensors are most sensitive to the larger, sand particles (e.g. ~ 150 to $300 \mu\text{m}$.) This size dependence can allow rough particle size determinations to be made *in situ* (for example, see Shang and Hay, 1988, Thorne, et al., 1993, and Lynch, et al., 1994). Interpretation of the observations in terms of grams of sediment from optical and acoustic sensors is therefore more difficult, and the multi-frequency approach can be used to better predict the concentrations.

Sediment aggregates can also affect both the calibrations and observations. Smaller particles can form larger aggregates that optically appear like large particles, and would thus cause overprediction of the sediment concentrations. During periods of high stress in the bottom boundary layer, these aggregates can be broken into their smaller components. To simulate this during the sensor calibrations, the tank was vigorously stirred before making the measurements. Also, high frequency acoustic backscattering sensors, while sensitive to disaggregated particle size, are not sensitive to the larger aggregates (Schaafsma, personal communication). Therefore, although not as sensitive to fine particles, the acoustic sensors should give a better measurement of concentrations which are not falsely augmented by the aggregation of particles as are optical sensors.

III. Sediment Profile Observations

The Eel River did not have the large flood events during the winter of 1997-98 that it did in 1994-95 and 1996-97. However, several flood events had discharges in excess of $3,000 \text{ m}^3/\text{s}$ and carried significant sediment into the shelf region. The major storm events occurred from January 12 to February 11, 1998. During this time, the downward looking ABS on the 60-m depth tripod recorded time series variations of the vertical profiles of sediment concentration. The hourly averaged bursts from the last three weeks of January 1998 (Fig. 1) show the high temporal variability of the suspended sediment concentrations.

Two kinds of signatures are seen in the record. First and most evident are the vertical banding, where sediment is mixed upward from the bottom or advected through the region with high sediment concentrations that extend above the height observed by the ABS profile records. These suspended sediment events are observed with both the ABS and OBS sensors on the tripod. The unique feature of the ABS observations and the second type of signature seen, is the thin (10-20 cm thick) high concentration ($> 10 \text{ g/l}$) layer seen during periods of high wave velocity during January 14 through 21. These concentrations are well above the commonly accepted 10 g/l lower limit for the definition of fluid mud, and are the most outstanding new quantitative observation of sediment transport seen during the deployment.

The high concentration layer often shows a sharp interface between the fluid mud and the water above. The concentrations in the water are typically an order of magnitude less than in the fluid mud layer. This sharp density gradient (lutocline) is a characteristic feature of fluid mud suspensions and well resolved by the ABS.

Also, the acoustic reflection from the bottom provided a record of the bottom elevation changes during the storm events. The elevation changes show a small depositional event on January 13, a larger depositional event on January 20 and an erosional event during January 24 and 25. All of the depositional events are observed to occur only when the fluid mud signature is seen.

The 8-minute, 2 Hz sampled bursts also resolve the wave-forced dynamics of the fluid mud layers (Fig. 2). The thickness of the fluid mud layer is seen to be modulated up and down, with an interfacial wave, with period that is usually equal to the surface wave velocity forcing. There appears very little mixing at the interface in this time, and is typical of the fluid mud layer when there are not high, low-frequency currents. Each hourly burst, such as seen in Fig. 2, help resolve the dynamic processes creating and affecting the fluid mud layer.

The two OBS records (Fig. 1) show decreasing suspended sediment concentrations with height above bottom. The sensor located 0.5 mab (before the depositional events) recorded peaks in suspended sediment concentration of $\sim 3 \text{ g/l}$. These peaks in concentration at 0.5

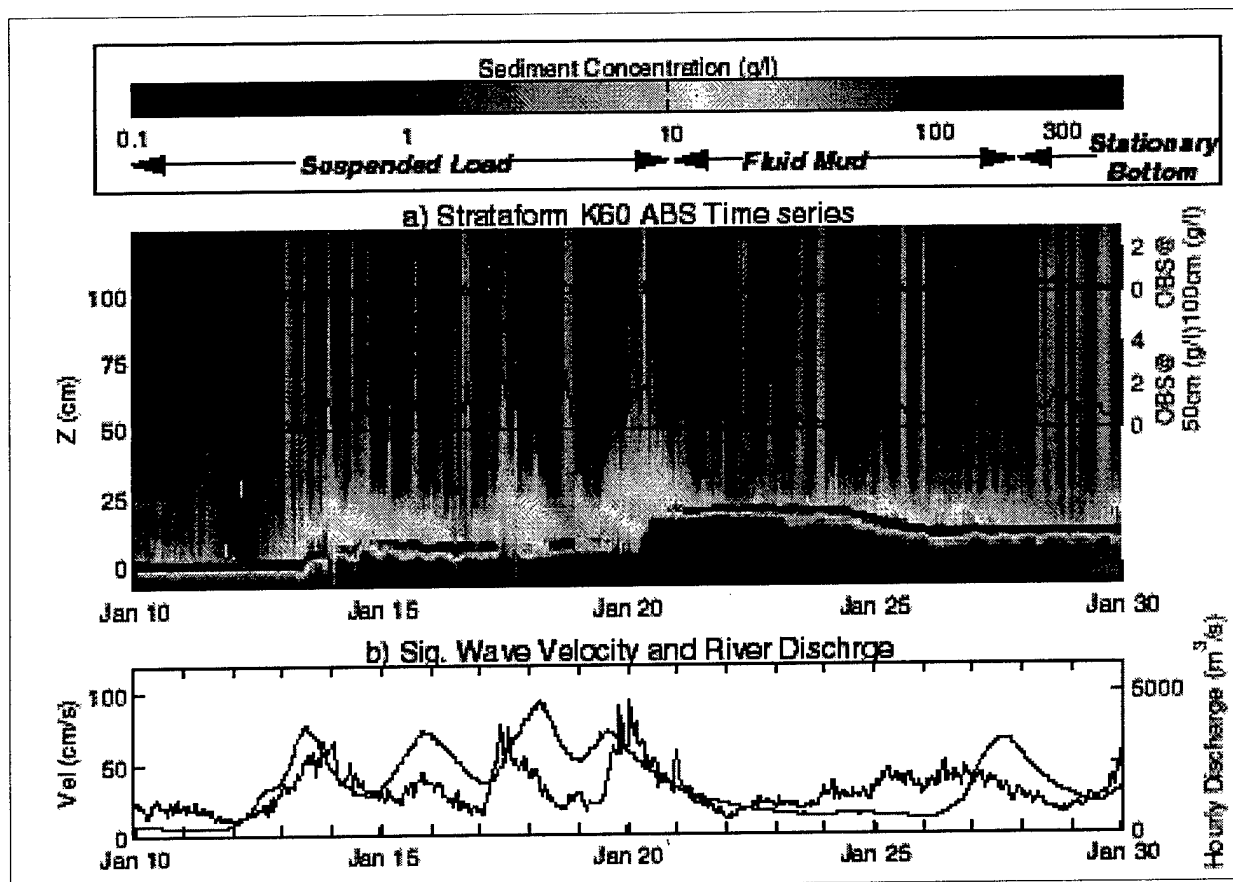


Fig. 1. Acoustic Backscattering Profiles. The main central panel shows the time series of acoustic backscattered intensity from January 10 to 30, 1998. The sediment concentrations are indicated on the color scale at the top. The bottom panel shows the significant wave velocity and river discharge for the same period. During January 14 to 20 a thin (10 to 20 cm thick), high concentration (30 g/l), fluid mud layer (yellow) is observed. The bottom return (bright red) shows the elevation changes associated with depositional and erosional events. Also, superimposed on the ABS profiles, are the times series of OBS observations with peak concentrations of 3 g/l at 0.5 mab and 1 g/l at 1.1 mab.

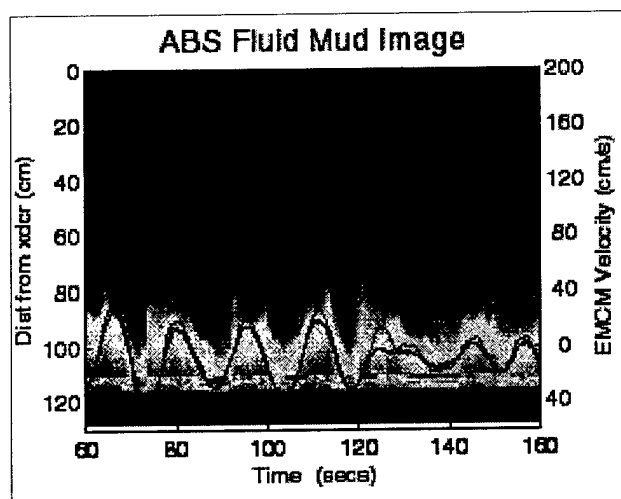


Fig. 2. High frequency ABS burst profiles of the fluid mud layer interface. The EMCM current meter observations are superimposed to illustrate the coherence of the wave forcing and fluid mud waves.

is typical of that used in bottom boundary layer sediment mab are also seen in the ABS records with similar concentration levels. The height of the OBS sensors transport studies, and is obviously too high to observe the fluid mud layer. The few OBS point measurements are unable to resolve the variability in waves on the fluid mud layer shown in Fig. 2 and illustrates the power of acoustic profiling and weakness of optical point measurements.

The exact sediment concentration within the fluid mud layer is difficult to estimate since the acoustic energy is attenuated as it propagates through the layer. During periods of maximum concentration, the attenuation is strong enough that the acoustic return from the seafloor disappears. This results in reduced backscattered intensities and underestimates the sediment concentration within the fluid mud layer. The results shown in Fig. 1 do not correct for this attenuation. However, the maximum concentration estimates of greater than 30 g/l at the top of the fluid mud layer are not strongly affected by attenuation and should be good estimates. Any error due to attenuation

of the acoustic signal will cause the fluid mud concentration to be underestimated.

III. Conclusions

Observations made with ABS instrumentation show the existence of a high concentration fluid mud layer at the bottom which is observed at times of high wave activity and may play an important role in the formation of mid-shelf mud deposits. Previous observations relied mostly on optical backscattering sensors and transmissometers as a means of measuring sediment concentration. These instruments make a point measurement at one depth, and thus are not well-suited for observing the vertical structure associated with thin fluid mud layers. However, the ABS profiler resolved profiles of sediment in the bottom meter of the boundary layer and was able to observe the detailed concentration structure and temporal variability of these thin fluid mud layers. Preliminary estimates show that they were responsible for the majority of the sediment transport during the winter of 1997-98. A detailed discussion of the sediment transport due to these fluid mud transport events is given in Traykovski, et al., 1999. For studying processes related to strata formation, the fluid mud flow events are far more important than suspended transport since all of the observed depositional events in the winter of 1997-98 were associated with the fluid mud flow events.

Acknowledgements

We would like to thank Dr. Joe Kravitz and the Office of Naval Research (ONR) for his support of

our efforts in the STRATAFORM program. This work was funded under ONR Code 1125GG grant N00014-94-10331. We would like to thank Nick Witzell, Craig Marquette, Steve Cross and the Captain and Crew of the R/V POINT SUR for their assistance in instrument preparation, deployment and recovery. We also thank our STRATAFORM colleagues who have contributed their data and understanding to the program. This is Woods Hole Oceanographic Institution Contribution Number 9956.

References

- Lynch, J.F., J.D. Irish, C.R. Sherwood and Y.C. Agrawal, "Determining Suspended Sediment Particle Size Information from Acoustic and Optical Backscatter Measurements, *Cont. Shelf Res.*, 14 (10/11), 1139-1165, 1994.
- Sheng, J. and A.E. Hay, An Examination of the Spherical Approximation in Aqueous Suspensions of Sand, *Jour. Acoustic. Soc. Am.*, 83, 598-610, 1988.
- Thorne, P.D., P.J. Hardcastle, R.L. Soulsby, An Analysis of Acoustic Measurements of Suspended Sediments, *Jour. Geophys. Res.*, 98, 899-910, 1993.
- Traykovski, P., W.R. Geyer, J.D. Irish and J.F. Lynch, The Role of Density Driven Fluid Mud Flows for Cross-shelf Transport on the Eel River Continental Shelf, submitted to *Cont. Shelf Res.*, 1999.
- Wheatcroft, R.W., C.K. Sommerfield, D.E. Drake, J.C. Borgeld and C.A. Nittrouer, Rapid and Widespread Dispersal of Flood Sediment on the Northern California Margin, *Geology*, 25, 163-166, 1997.

PRELIMINARY RELATIONSHIPS BETWEEN PRECISION ACOUSTIC OBSERVATIONS AND CORE GEOTECHNICAL AND CHEMICAL PROPERTIES AT CONTAMINATED SITES

David D. Caulfield
Caulfield Engineering, Stony Plain, Alberta
T7Z 1X2

ABSTRACT

Two major precision acoustic marine surveys have been carried out over the last four years with the USEPA at two contaminated sites. Each site had available extensive geotechnical and chemical core data to allow the establishment of initial statistical relationships between the acoustic data and the core information. Using historical data for expected acoustic response of clean and gas free sediments, it was found that deviations in the acoustic parameters of bottom loss, velocity, and absorption occurred in the contaminated sediments when compared to the expected clean sediment response. Initial results indicated that the deviations in acoustic properties from normal sediments were found to be related to gross gas and contaminate content of these sediments. The initial statistical models relating the acoustic properties to the core data are presented with illustrations of the use of this technique for contaminated sediment distribution mapping. It is critical to note that these relationships appear to be site specific and the success of the program resulted from the proper mix of core and micro-spaced acoustic survey lines.

INTRODUCTION

Analysis of shallow subbottom acoustic data has taken two historical paths, optimized graphical displays for visual interpretation with local core data, and signal processing analytical procedures to relate the acoustic parameters to the actual physical parameters in the bottom and subbottom layers. The success of the analytical procedures is based on the extensive work of many researchers.

The original theoretical and experimental work of Officer (1958) and Biot (1956) led Breslau (1965) to present one of the first acoustic classification results for mapping the water bottom interface. This paper confirmed relationships between the physical properties of the sediment and the acoustic reflection coefficient. These concepts were expanded into a

large national program, with the first statistical data base of relationships between acoustic variables and the physical properties of the sediments reported by Hamilton (1970). Continued data gathering and modeling of interrelationships of acoustic parameters with the physical properties of the sediments, Sheriff (1975) and Robinson and Treitel (1980), led to an initial acoustic engineering model for mapping shallow marine sediments, Caulfield and Yim (1983). This early 1983 engineering model indicated that for general marine dredging needs, a statistical model relating acoustic variables to bottom physical properties might be adequate. This work was integrated into the 8 year U.S. Army Corps of Engineer Dredging Research Program. The database acquired through the surveying and sampling of dozens of harbors confirmed this hypothesis, McGee, Ballard, and Caulfield (1996), and led to procedures for classifying standard (gas and contaminate free) marine sediments with acoustic variables. This work also showed the importance of obtaining fully calibrated acoustic data. Procedures and software were developed to insure the absolute repeatability of the acoustic data

ACOUSTIC PROPERTIES OF STANDARD MARINE SEDIMENTS

Standard marine sediments are defined for the purposes of this work as sediments that are gas and contaminant free. Table 1 is a mean average of typical subbottom physical properties for these 'standard sediments' and their associated observed acoustic parameters. Local core data provides updates on the region's specific gravity (bulk density). For these sediments it is assumed that they are fully saturated sediments and that a linear relationship between density and porosity exists.

Table I - Clean Material Vs. Density (gm/cm³), Reflection Coefficient, and Bottom Loss (db).

Material Type	Bulk Density	Reflection Coef. R	Bottom Loss(db)
Coarse Sand	2.05	0.41	7.8
Medium Sand	2.01	0.385	8.3
Fine Sand	1.98	0.375	8.5
Silty Sand	1.83	0.32	9.9
Sandy Silt	1.6	0.214	13.5
Silty Clay	1.4	0.159	16.1
Clay	1.26	0.09	20.6

Typical water-bottom interface reflection coefficients (R) for these clean sediments are provided. The reflection coefficient is the ratio of the incident wave amplitude divided by the reflection amplitude. The term bottom loss (BL) can be defined as:

$$BL = 20 \cdot \log_{10} (R) \quad (1)$$

The bottom loss is a negative number but for the purposes of this report will be shown as positive numbers for the convenience of analytical processing. If the acquisition

system is fully calibrated the absolute bottom loss (BL) for the site can be computed. Table I also provides the bottom loss for the clean sediments.

The large database available for standard marine sediments indicates that the summary data in Table I is a good approximation for relating the acoustic parameters to the physical properties for clean gas free sediments. It will be shown in the next sections that the deviations of these acoustic parameters for sediments containing gas and contaminants is so large, that though desirable, a closer model is not necessary when considering using the resultant data for contaminant mapping.

ACQUISITION METHODS AND CALIBRATION MODELING

An earlier paper (Caulfield, Filkins 1999) details the acoustic data acquisition procedures and calibration details. The sound sources used are pingers, chirp, or boomers in order to provide data coverage over a wide frequency range of 400 Hz to 12 KHz. Various receiver types are available and are selected to optimize the beam pattern and to match the sound source utilized. The data from the receiving arrays is amplified using calibrated amplifiers and digitized for future processing. Field color-coded displays insure digitizing levels are correct. An important addition to the acquisition procedure is the use of a calibration hydrophone of known bandwidth and sensitivity. This calibration phone allows absolute calibration of the source level and the receiver sensitivities allowing absolute computation of the bottom reflection coefficients. In addition, the calibration hydrophone allows recording of the source wavelet, which enables the computation of the reflection sign (phase) and allows the implementation of spiking filters (chirp procedures) to optimize resolution.

Because of the importance of the calibration procedure, Fig. 1 is provided to illustrate the ray paths for the first bottom reflection and for the calibration hydrophone. The symbols on each ray path indicate various terms associated with each ray path of a sonar model that can be constructed for calibration of the system elements and the absolute computation of the bottom reflection (Bottom Loss (BL)). Each term will be described in the following discussion.

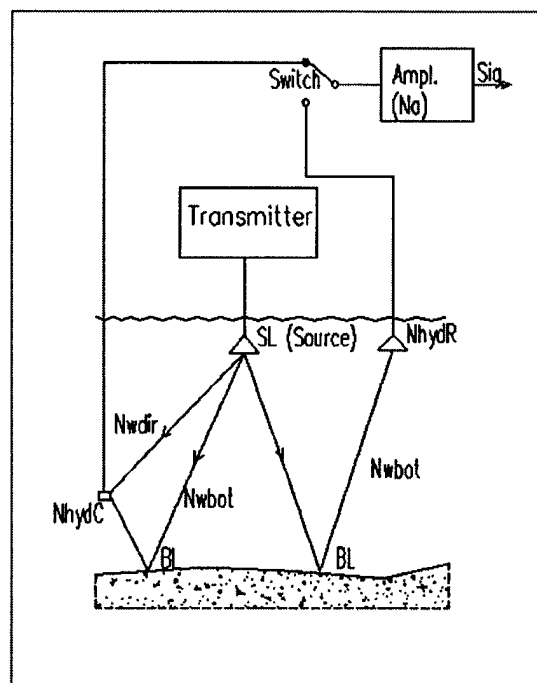


Fig. 1. Calibration and bottom loss (BL) ray path diagram.

The general sonar equation, with each term expressed in decibels (db), for Bottom Loss is:

$$BL = SL - S_R - N_w - N_{hyd} + N_A + DI \quad (1)$$

where

BL = Bottom Loss (db)

SL = Source Level (db)

S_R = Signal output from the calibrated receiver (db)

$N_w = 20 * \log (\text{Range, meters})$ (db), transmission loss due to spherical spreading along the path of sound propagation.

N_{hyd} = receiving hydrophone sensitivity (db)

N_A = calibrated receiving amplifier gain (db)

DI = directivity index (db)

This equation can be solved for each of the ray paths shown in Fig. 1 by the insertion of the proper ray paths and terms. For example, the calibration of the sound source is performed by noting that the Bottom Loss term is zero, and the transmission loss term would be N_{wdir} . The calibration hydrophone therefore enables continuous spot-checking of the complete system during the course of the survey allowing the generation and verification of quality control objectives. The importance of this calibration is that a fully calibrated system allows confirmation of anomalies detected during the course of the survey. It will be shown that these anomalies allowed the mapping of the contaminated sediments. Software programs are available to allow automated computation of these calibration parameters both in the field and during data processing.

ANOMALY DETERMINATION

The determination of the acoustic anomalies from standard sediments for each site were obtained by anchoring the survey vessel over each of the previously obtained core sites (or where a new core was to be taken). Then detailed physical and chemical core analysis was carried out. Based on the core physical properties an expected Bottom Loss for the site was predicted based on clean sediments. Then the acoustic data was taken with all of the sound sources being utilized for the survey with repeated calibration steps. Data processing generated absolute values for the Bottom Loss, the gross absorption, and the reflection sign (phase) from the bottom-water interface.

For rapid contaminate distribution mapping the Bottom Loss measurements over contaminated core sites were found to deviate as a gross function of the total contamination in the sediment. Fig. 2 is a plot of the deviation in observed Bottom Loss from expected values versus a Pollution Factor.

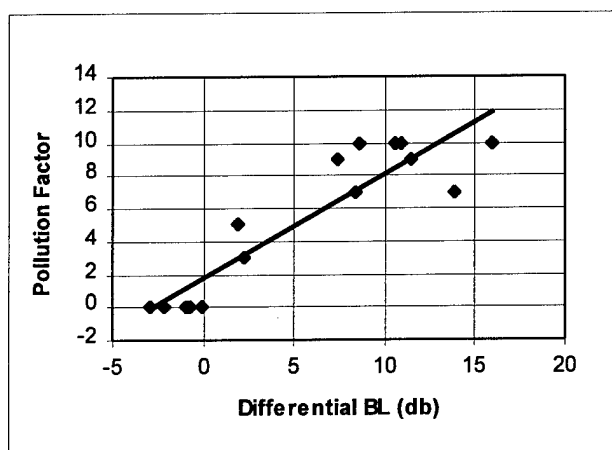


Fig. 2. Pollution Factor Versus Differential BL (Observed BL - Clean BL).

The Pollution Factor was determined by assigning the highest chemical content cores a value of 10, and then proportionally assigning smaller factors in a linear manner based on the proportion of contaminated material in each core relative to the most contaminated core. A Pollution Factor of zero was given to the clean sediments. For the initial site, the cores with the highest chemical contaminant content also had the highest gas content. Reference to standard engineering manuals such as Baumeister, Avallone, and Baumeister III (1957) shows that mercury, petroleum products, etc. all have different bulk moduli and sound velocities which will effect the observed bottom loss. This reference also shows that dissolved chemicals in water also affect the sound velocity of the water.

In sediments with high gas content the reflected signal is phase reversed. Figure 5 illustrates the averaged reflection sign reversal (Negative Percentage) versus deviation in Bottom Loss. A zero (0) percent Plus Percentage would mean

no sign reversal and a one hundred (100) percent Negative Percentage represents complete sign reversal.

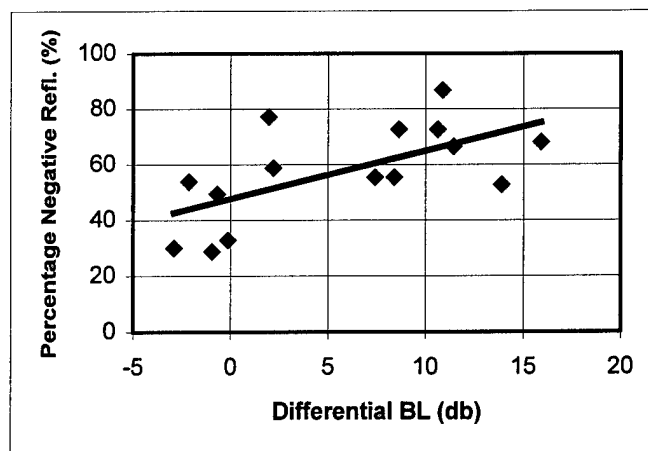


Fig. 3. Percentage Negative Reflection Sign Vs. Differential BL.

The wide scatter resulted from the use of wide beam pattern sound sources and the high spatial variance of the distribution of the sediments. The reflection sign is derived by computing the cross-correlation of the source wavelet with the bottom reflection and then recording the sign of the peak correlation. All contaminated sediments exhibited a high variance in Bottom Loss and this reflection sign measurement. This high variance was used as a possible indicator of contaminated sediments.

The gross absorption was not analyzed in detail at the initial site, as the above two parameters were sufficient to map the sediments for this project. However, the contaminated sediments did have a relatively high absorption compared to the non-contaminated sediments.

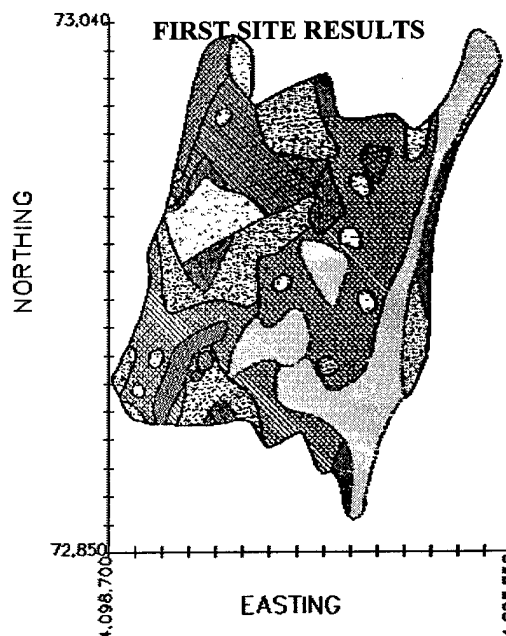


Fig. 4. Site 1 bottom surface sediment distribution map.

SITE 1 RESULTS

For site 1 the analysis proceeded by identifying the vertical layer distribution and constructing the standard layer cross-sections from the seismic records and through automated processing algorithms. Each seismic data set was then analyzed for Bottom Loss and Negative Percentage (reflection sign) to determine if that data set was contaminated or not. An annotated survey line cross-section was then generated with the contaminate layers indicated. A summary spatial distribution surface material map was then generated for each test area as shown in Fig. 4. Fig. 5 provides soil description symbol codes for the data in Fig.4.

LEGEND		
NORMAL SEDIMENT	BASIC SOIL DESCRIPTION	POLLUTED SEDIMENT
	FOAM/FLUFF	
	CLAY/SILTY CLAY	
	CLAY ON SILT/SILTY SAND	
	SILT	
	SILTY SAND TO SANDY SILT	
	SAND	
	HARD/COMPACT	
	SILTY SAND ON SILTY SAND	
	SURFACE ROCK	
	SAND ON SILTY SAND	

Fig. 5. Display codes for material type and condition.

Note the very high spatial variation in contaminate distribution shown in Fig.4. The combination of this sediment distribution data and the layer thickness maps allowed generation of estimated dredging volumes for the sites.

SITE 2 ANALYSES

The same acquisition, calibration, and analysis procedures discussed above were applied to the Site 2 data. Similar contaminate distribution maps and contaminated sediment volumes were generated. An added program during field activities was immediate core geotechnical analysis to determine if the gas content affected the results. The bulk densities were a fractional portion less than for a core analyzed at a latter time. The gas had escaped in this delayed processed core.

Because of the availability of both the calibrated acoustic data and the field calibrated core geotechnical and chemical data general statistical analysis between these measurements were carried out. To make these analyses a summary number had to be assigned to the chemical pollution and the organic content. The present USEPA procedure of establishing a percentage of a particular core section chemical (organic, metal, etc.) observation to the maximum observation at the entire survey site for that chemical was adopted. This

procedure is not a standard as the publication of this paper, but is presently the established recommendation. Therefore, all of the following discussion must be considered as site specific only.

The first comparison was to examine the relationship between the differential (Delta) Bottom Loss and the density. It is generally accepted that low-density sediments (clays) tend to retain contaminates and organics. Fig. 6 illustrates the observed relationships between Bottom Loss and density.

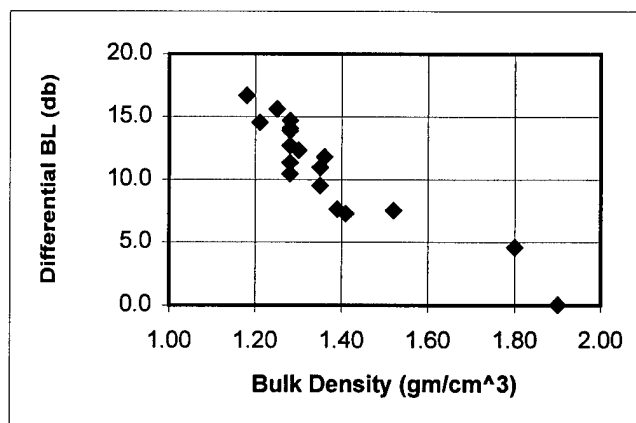


Fig. 6. Differential BL Vs. Bulk Density.

The Bottom Loss anomalies are greater in the softer materials; indicating that contaminates, organics, and gas are retained in these materials. Note that in the higher density materials there is no observed deviation indicating that the sands are clean.

It was assumed that the gas in the sediments is generated by the total organic content and the chemical PAH's and PCB's (PAH_PCB). Various analyses were carried out examining the relationship of the differential Bottom Loss to these physical items. The highest correlation between variables occurred when the Bottom loss deviation was proportioned between the TOC and the PAH-PCB's. Fig. 7 is a comparison of the corrected Percentage (%) TOC and the Differential Bottom Loss.

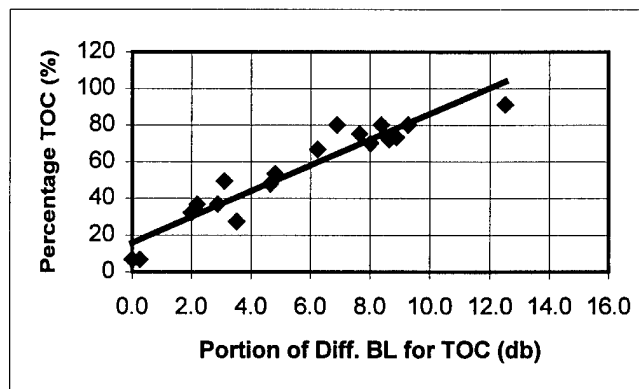


Fig. 7. Percentage TOC Vs. Portion of Diff. BL for TOC.

The highest correlation (0.9485) was obtained with the data pairing shown in Fig. 7, the corrected differential Bottom Loss versus the percentage TOC. The corrected differential Bottom Loss being the total differential Bottom Loss corrected for the ratio of TOC% over the TOC's and PAH_PCB's for the site.

Fig. 8 is a plot of the residue differential Bottom Loss versus the Percentage of PAH_PCB's.

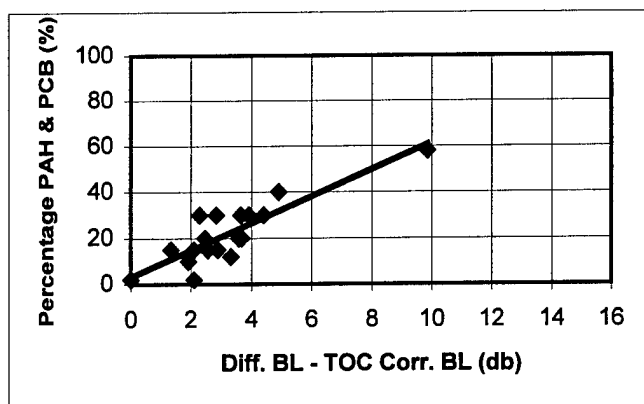
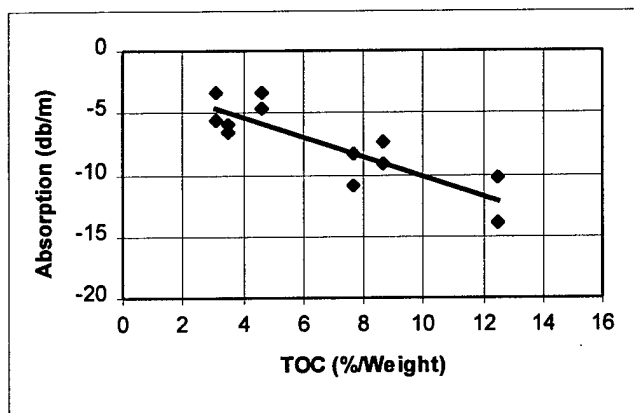


Fig. 8. Percentage PAH & PCB Versus Diff. Bottom Loss less Total Organic Content Corrected Bottom Loss.

The correlation coefficient for the data in Fig. 8 was 0.8623.

Since the Bottom Loss deviation is related to core data TOC at this site, the other acoustic variables were also tested. The absorption (db/meter) had relationship with a correlation coefficient of 0.884. Fig. 9 shows the statistical relationship between observed absorption between 600 Hz and 1500 Hz versus TOC.



The above set of analysis was site specific. However, the effort proved worthwhile, as it enables the identification of two major clay layers that had the same densities, but different levels of contamination.

CONCLUSIONS

The ability to use acoustic deviation analysis for the mapping of contaminants resulted from the use of fully calibrated survey equipment and procedures. This set of fully calibrated data allowed the determination of site-specific parameters for classification of the acoustic parameters of the contaminated sediments at each core site. These parameters could then be used to allow the detailed mapping of the entire site. The general acoustic relationships versus the physical and chemical properties of the sediments developed here are site specific. Each new site requires selected coring and physical and chemical analysis to allow determination of parameters and procedures to be used at that site.

ACKNOWLEDGEMENTS

The work reported on herein was supported in part by the U.S. Army Engineers Waterways Experimental Station and the US Environmental Protection Agency. The success of the mapping project at these two sites resulted from the contribution of many individuals. In particular, at the USACE facility Dr. Bob Ballard, Jr., Darla McVan, and Tim Fagerburg and their supporting staff; at the USEPA facilities John Filkins, Mark Tuchman and their supporting staffs. In addition, Allen Lowrie at the U.S. Naval Oceanographic facility provided geological interpretation guidance.

REFERENCES

- BRESLAU, L.R., 1965, Classification of Sea-Floor Sediments with a Ship-borne Acoustical System, *Proc. Symp. 'Le Petrole et la Mer'* Sect I, No. 132, pp 1-9, Monaco, 1995.
- BAUMEISTER, T., AVALLONE, E.A., and BAUMEISTER III, T., 1957, Marks' Standard Handbook of Mechanical Engineers, Eighth Edition, McGraw-Hill Book Company, N.Y, N.Y.
- BIOT, M.A., 1956, Theory of Propagation of Elastic Waves in a Fluid-saturated Porous Solid; I, Low Frequency Range, *Journal of the Acoustical Society of America*, v.28, pp. 168-178.
- CAULFIELD, D.D. and FILKINS, J.C., 1996, Final Report Micro Survey - Acoustic Core and Physical Core Inter-relations with Spatial Variation, Trenton Channel of the Detroit River, Caulfield Engineering/USEPA, Report No. 2060.
- CAULFIELD, D.D. and FILKINS, J.C., 1999, Acoustic Techniques for the Mapping of Distribution of Contaminated Sediments, *Northeastern Geology and Environmental Sciences*, v. 21, nos. ½, p. 130-135.
- CAULFIELD, D.D. and YIM, Y.C., 1983, Predictions of Shallow Subbottom Sediment Acoustic Impedance while

Estimating Absorption and Other Losses, *Journal of the Canadian Society of Exploration Geophysicists*, v. 19(1), pp 44-50.

HAMILTON, E.L., 1970, Reflection Coefficients and Bottom Losses at Normal Incidence Computed from Pacific Sediment Properties, *Geophysics*, v.35, 995-1004.

MCGEE, R.G., BALLARD, R.F., and CAULFIELD, D.D., 1995, A Technique to Assess the Characteristics of Bottom and Subbottom Sediments, Technical Report DRP-95-3, U.S. Army Engineers, Waterways Experimental Station, Vicksburg, MS.

OFFICER, C.B., 1958, Introduction to the Theory of Sound Transmission, McGraw-Hill, N.Y., N.Y.

ROBINSON, E.A., and TREITEL, S., 1980, Geophysical Signal Analysis, Prentice-Hall, N.J.

SHERIFF, R.E., 1975, Factors Affecting Seismic Amplitudes, *Geophysical Prospecting*, v. 23, pp. 125-138.

Authors Note: Complete reprints of the three volumes for site 1 is available from the author on CD's. The complete volumes for site 2 will be available in a few months. For copies contact the author at davec@cauleng.com

DETERMINATION OF SOUND VELOCITY PROFILE ERRORS USING MULTIBEAM DATA

William J. Capell, Sr.
L-3 Communications SeaBeam Instruments
141 Washington Street
East Walpole, MA 02032 USA

Abstract

A sounding on the vertical beam will be in error by precisely the proportional error in the mean sound velocity of the water column. However, a beam launched at $\pm 45^\circ$ will not have such an error. The time required for this beam to reach a specific depth has very low sensitivity to sound velocity profile (SVP) errors. Although such errors do induce a small perturbation of the athwart ship location of such a sounding point, the computed depth will be correct for that sounding point. This results in survey tracks at approximately $\pm 45^\circ$ with correct depth data to serve as reference data for the nearly vertical beams of crossing swaths. These crossing swaths may come from *checklines* used in most hydrographic surveys.

The sounding data of multibeam echo sounder (MBES) systems are a result of processing information from many sources. These include ship's heading and navigation data, vertical reference data and sound velocity data in addition to the basic MBES itself. Data from each of these sources is subject to individualized errors contributing to the overall data quality – or the lack thereof. To limit these errors, system planners often have established error budgets for various components of the system.

With the advent of new technologies, the last remaining obstacles to absolute depth precision may soon be SVP errors and roll bias. (Roll bias as used herein means that uncompensated portion of the difference between the receive array and the vertical reference unit.) This paper describes a post processing solution that can significantly reduce errors related to both SVP and roll bias. This process is specific for swaths that include beams at $\pm 45^\circ$ and is suitable for all such multibeam data derived from a Mills Cross type of MBES.

I. General

In reviewing the error sources for multibeam bathymetry data, two dominant error sources stand out which are not correctable by better sonar detection processes. These are the SVP errors including any error in the surface sound velocity (SSV) and the roll bias error.

The SVP is subject to significant errors caused by rapid changes in temperature or salinity over short periods of time. These changes are especially troublesome in littoral waters. They may come as the result of rapid heating and cooling of the water column over the day, outflows from estuaries, or by significant distances traveled along survey lines. Temperature and aging effects may induce offsets into the roll data of a vertical reference unit (a roll bias).

Fig. 1 (a) shows an acoustic wavefront as it passes over 2 sensors of a hydrophone array. α is the instantaneous angle of the receive array to the earth's horizontal, λ_o is the wavelength at the receive array and λ_a is means wavelength in the water column. Fig. 1 (b) shows the water path taken as the wavefront approaches, and passes through, the surface sound velocity layer. If an error exists in the sound velocity data, there will be an error related to the proportional sound velocity error and the beam angle. Equation 1 gives the proportional depth error versus beam angle for given errors in the SSV (C_o) and the mean water column velocity (C_a) for the conditions of Fig. 1. Since innumerable combinations of SVP exist, it is necessary here to represent the velocity within the water column with its mean value.

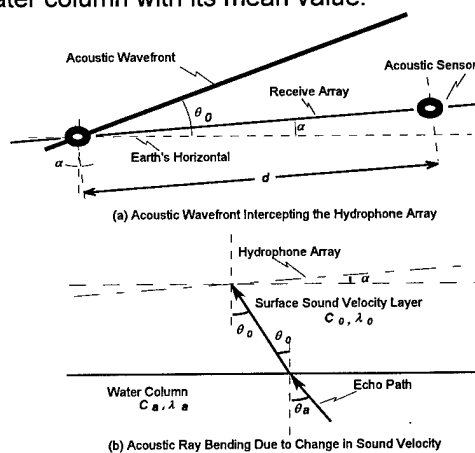


Fig. 1. Schematic of Acoustic Signals

Equation 1 shows that the proportional depth error is related to the mean sound velocity (C_a), the error in the

mean sound velocity (dC_a), the surface sound velocity (C_0), and the error in the surface sound velocity (dC_0). Angles θ_a , θ_0 and α are defined in Fig. 1 (b).

$$\frac{dZ}{Z} = \left(1 - \tan(\theta_a)^2\right) * \frac{dC_a}{C_a} \dots + \left(1 - \frac{\tan(\theta_0 - \alpha)}{\tan(\theta_0)}\right) * \tan(\theta_a)^2 * \frac{dC_0}{C_0} \quad (1)$$

Equation 1 also shows that certain beams can provide correct depths regardless of unknown errors in the SVP as long as the SSV is correctly known ($dC_a = 0$) or the hydrophone array is horizontal to the earth's surface ($\alpha = 0$). Also shown here is that the beams which provide the correct depth are at angles of approximately $\pm 45^\circ$. The first term defines the depth error resulting from SVP while the second term defines the depth error resulting specifically from erroneous SSV data. When the error of the second term is minimized as outlined above, equation 1 can be reduced to

$$\frac{dZ}{Z} = \left(1 - \tan(\theta_a)^2\right) * \frac{dC_a}{C_a} \quad (2)$$

Comparison of the soundings of the data from these $\pm 45^\circ$ beams of crossing survey lines with data from the vertical beams of the tracks which they cross provides sufficient information to compute the proportional SVP error of each of the crossing tracks. Additionally, comparison of the soundings of the data from these $\pm 45^\circ$ beams crossing the $\pm 45^\circ$ beams of other survey lines provides sufficient information to compute roll biases and differential changes in tide (including draft) between the crossing tracks.

The data from the survey lines can be modified using the newly computed roll bias data and SVP to provide better merged bathymetry data sets nearly devoid of roll bias and SVP errors.

Fig. 2 is a plot of equation 2. It shows that dZ goes through zero when θ_a goes through 45° . That means that the beam at 45° has minimal error regardless of nominal errors in the SVP. This provides a means of

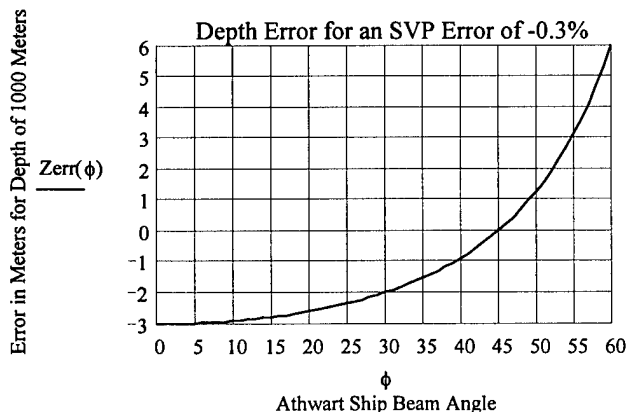


Fig. 2. Depth Error versus Angle

establishing some 'ground truth' for depths within the survey area even when there are errors in the SVP. It is further seen that the proportional depth error on the vertical is equal to the proportional error in the SVP, but at 60° the depth error is twice as large.

A zero depth error for the beam at 45° does not mean that the athwart ship sounding point for this beam is unaffected. In fact, the sounding point is displaced by an amount proportional to twice the relative error in the SVP as given in equation 3. For example, with a 0.3% error in SVP at a depth of 1000 meters, the sounding point at 45° would be displaced by 0.6%, or 6 meters, from its expected distance of 1000 meters. This amounts to an angular offset of 0.17° (0.3% of a radian) which is small compared to typical beam spacings. Therefore, the survey lines within $\pm 45^\circ$ are very well known – even for an SVP error of 0.3%.

$$\frac{dX}{X} = 2 * \frac{dC_a}{C_a} \quad (3)$$

II. The Survey Process

It is routine practice to run roll bias tests over relatively flat terrain on occasion and make adjustments as required. However, this process is time consuming and expensive. It would be useful to monitor the roll bias during normal survey operations so that small adjustments can be made for drift during the survey process.

In addition to the normal survey lines which usually provide at least 100% coverage (the 'primary survey') with some degree of overlap, survey checklines (with total coverage of perhaps 10% of the area) run at nearly right angles to the primary survey lines provide a verification of the total data gathering process. Rather than running the checklines at the end of the primary survey, these tracks may have been run as a 'pre-survey' to gather planning data for the region.

Fig. 3 is an example depicting four crossing areas of the primary survey lines and the checklines. These four crossing areas will be used to compute roll bias, tidal differences and SVP error. Typically, the actual tidal differences in littoral waters are statistically larger than

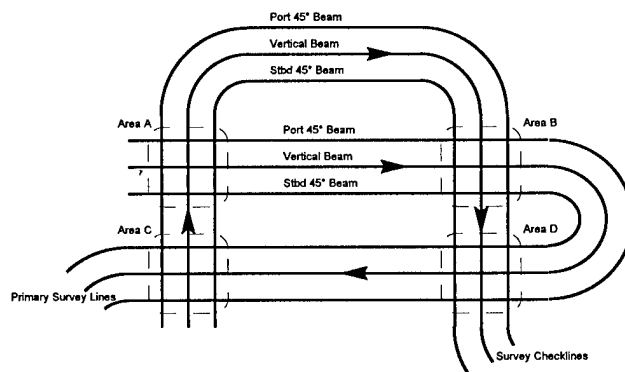


Fig. 3. Two Survey Lines showing Tracks of the Vertical and the $\pm 45^\circ$ Beams

the depth errors due to roll biases. In deep ocean areas, tidal differences can be ignored. After determining the roll biases, tidal differences and SVP errors for these areas, the results can be extrapolated over time and location throughout the survey area to provide a filtered correction. Thus a nearly continuous correction of these errors is available.

Since there is no depth error associated with the $\pm 45^\circ$ beams and little athwart ship error, then the only depth bias associated with these beams is the roll bias in the VRU data and tidal differences in shoal waters. Roll bias is considered a long term effect and will be relatively constant for a period of at least several weeks. Tidal effects, of course, occur over a much shorter time frame.

III. Computing Tidal Offset

Fig. 4 is an expanded view Area A of Fig. 3. One might expect the data of TRACK 1 and TRACK 2 at Intersection 1 to agree since they are both starboard 45° beams and there is no error related to the SVP. Similarly, one might expect the data of TRACK 1 and TRACK 2 at Intersection 2 to agree since they are both port 45° beams and there is no error related to the SVP. However, there may have been both roll bias changes and significant tidal shifts between these two tracks since there may have been a significant time delay between these two tracks. The data even may have been taken by two different multibeam systems.

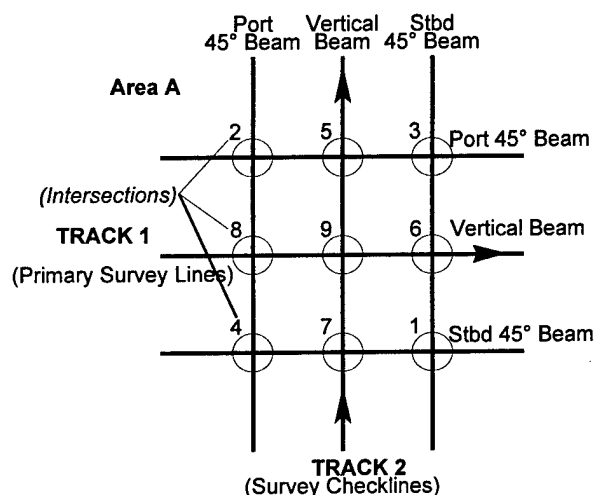


Fig. 4. Expanded View of Area A Details

The first thing to do for surveys in littoral waters is determine the tidal difference between the 2 tracks and remove it from the data. This is done by evaluating the measured depths at the intersections of the $\pm 45^\circ$ beams - Intersections 1, 2, 3 and 4.

In the following equations for Intersections 1, 2, 3 and 4, Z_j is defined as the actual depth at the j^{th} intersection. Similarly, $RB_{i,j}$ is the depth error related to roll bias for the i^{th} track at the j^{th} intersection and T_i is the tide offset between the two tracks.

Roll bias is defined here as positive when its value causes the measured starboard depth to be greater and the measured port depth to be shallower than their actual values.

$Z_{meas_{i,j}} = Z_j \pm RB_{i,j} + T_i$ (use '+' for starboard beams and '-' for port beams) defines the measured depth for track i at intersection j . Since only the tidal difference, not absolute tides, for the intersecting tracks can be determined, the total tidal offset will be assigned to Track 2, i.e., $T_1 = 0$ and $T_2 = T$. After determining the actual tidal difference, this value can be assigned to either track or in some reasonable proportion to each based on any other input available to the surveyor.

Averaging the measured depths for Intersections 1 and 2 for Track 1 gives

$$Avg1_{1\&2} = 0.5 * (Z_1 + RB_{1,1} + Z_2 - RB_{1,2}).$$

Averaging the measured depths for Intersections 1 and 2 for Track 2 gives

$$Avg2_{1\&2} = 0.5 * (Z_1 + RB_{2,1} + Z_2 - RB_{2,2}) + T.$$

Subtracting these average depth for intersections 1 & 2 for Track 1 from the average depth for intersections 1 & 2 for Track 2 gives

$$Avg2_{1\&2} - Avg1_{1\&2} = T + \dots$$

$$0.5 * ((RB_{2,1} - RB_{2,2}) - (RB_{1,1} - RB_{1,2})) \quad (4)$$

Equation 4 gives the value of the tidal difference for Area A plus a residual value which is a very small percent of the actual roll bias offsets. In shoal waters, this roll bias residual may be ignored for this equation and tidal offset can be defined as

$$T \approx Avg2_{1\&2} - Avg1_{1\&2}. \quad (5)$$

The data of Tracks 1 and 2 can now be normalized by removing the tidal offset. The process is continued for all crossing areas of interest to remove tidal offsets. Again, the tidal correction cannot determine the absolute values of the tides, but it can define differential tide offsets in shoal data so that the remainder of the process can proceed normally.

IV. Computing Roll Bias

After removing tidal offsets from the bathymetry data, roll bias can be determined next using the modified data set. In most deep water sites, tide can be neglected and roll bias computed without regard to tidal effects. The depth difference of the modified data at each intersection for the two tracks is (using '+' for starboard beams and '-' for port beams)

$$\Delta Z_i = (Z_i \pm RB_{1,i}) - (Z_i \pm RB_{2,i}). \quad (6)$$

Looking now at equation 6 applied to the intersections where the $\pm 45^\circ$ beams cross each other and dividing by Z_i for $i = 1 \dots 4$ gives the ratios

$$\frac{\Delta Z_1}{Z_1} = \frac{RB_{1,1}}{Z_1} - \frac{RB_{2,1}}{Z_1} \quad (7)$$

$$\frac{\Delta Z_2}{Z_2} = -\frac{RB_{1,2}}{Z_2} + \frac{RB_{2,2}}{Z_2} \quad (8)$$

$$\frac{\Delta Z_3}{Z_3} = -\frac{RB_{1,3}}{Z_3} - \frac{RB_{2,3}}{Z_3} \quad (9)$$

$$\frac{\Delta Z_4}{Z_4} = \frac{RB_{1,4}}{Z_4} + \frac{RB_{2,4}}{Z_4} \quad (10)$$

For angles as small as typical roll biases, this gives roll bias values in radians because the values for cross track distances is the same as the depth for the $\pm 45^\circ$ beams. For these $\pm 45^\circ$ beams, the angular roll bias (β) is defined as $\beta_i = \frac{RB_{i,j}}{Z_j}$ and equations 7 - 10 become

$$\frac{\Delta Z_1}{Z_1} = \beta_1 - \beta_2 \quad (11)$$

$$\frac{\Delta Z_2}{Z_2} = -\beta_1 + \beta_2 \quad (12)$$

$$\frac{\Delta Z_3}{Z_3} = -\beta_1 - \beta_2 \quad (13)$$

$$\frac{\Delta Z_4}{Z_4} = \beta_1 + \beta_2 \quad (14)$$

Taking the difference of equations 11 and 13, and the difference of equations 14 and 12 gives

$$\frac{\Delta Z_1}{Z_1} - \frac{\Delta Z_3}{Z_3} = \frac{\Delta Z_4}{Z_4} - \frac{\Delta Z_2}{Z_2} = 2 * \beta_1 \quad (15)$$

Taking the sum of equations 11 and 13, and the sum of equations 12 and 14 gives

$$\frac{\Delta Z_1}{Z_1} + \frac{\Delta Z_3}{Z_3} = \frac{\Delta Z_4}{Z_4} + \frac{\Delta Z_2}{Z_2} = -2 * \beta_2 \quad (16)$$

Equations 16 and 16 give two calculations of the roll bias angles for each track at each crossing. Since the roll bias does not change at a rapid rate, many additional calculations of these values may be made over the course of the survey at each crossing of the tracks and a reasonable average found. This separates roll bias from instantaneous roll errors.

V. Computing SVP Errors

After accounting for the latest roll bias correction, evaluate all of the track crossings to ensure that tidal offsets and roll biases in fact are not present in the newly modified data set. Then define the depths in this modified bathymetry data for track i and intersection j as

$$Z_{mod_{i,j}} = Z_j + Z_j * (1 - \tan^2(\theta_{i,j})) * \frac{dCa_{i,j}}{Ca_{i,j}}$$

where $Z_{mod_{i,j}}$ is the measured depth at the j^{th} intersection for the i^{th} track; Z_j is the true depth at the j^{th} intersection; $dZ_{i,j}$ is the error in measured depth at the j^{th}

intersection for the i^{th} track; $\theta_{i,j}$ is the beam angle sounding the j^{th} intersection for the i^{th} track; $Ca_{i,j}$ is the average sound velocity of the water column at the j^{th} intersection for the i^{th} track; and $dCa_{i,j}$ is the error in the average sound velocity of the water column at the j^{th} intersection for the i^{th} track.

The modified depths for Intersections 5, 6, 7 and 8 for track 1 can be shown to be

$$Z_{mod_{1,5}} = Z_5 \quad (17)$$

$$Z_{mod_{1,6}} = Z_6 * \left(1 + \frac{dCa_{1,6}}{Ca_{1,6}}\right) \quad (18)$$

$$Z_{mod_{1,7}} = Z_7 \quad (19)$$

$$Z_{mod_{1,8}} = Z_8 * \left(1 + \frac{dCa_{1,8}}{Ca_{1,8}}\right) \quad (20)$$

Similarly, the modified depths for track 1 at Intersections 5, 6, 7 and 8 can be shown to be

$$Z_{mod_{2,5}} = Z_5 * \left(1 + \frac{dCa_{2,5}}{Ca_{2,5}}\right) \quad (21)$$

$$Z_{mod_{2,6}} = Z_6 \quad (22)$$

$$Z_{mod_{2,7}} = Z_7 * \left(1 + \frac{dCa_{2,7}}{Ca_{2,7}}\right) \quad (23)$$

$$Z_{mod_{2,8}} = Z_8 \quad (24)$$

Next, take the differences of the 2 tracks at each of these 4 sounding points such that

$$\frac{dCa_{2,5}}{Ca_{2,5}} = Z_{mod_{2,5}} - Z_{mod_{1,5}} \quad (25)$$

$$\frac{dCa_{2,7}}{Ca_{2,7}} = Z_{mod_{2,7}} - Z_{mod_{1,7}} \quad (26)$$

$$\frac{dCa_{1,6}}{Ca_{1,6}} = Z_{mod_{1,6}} - Z_{mod_{2,6}} \quad (27)$$

$$\frac{dCa_{1,8}}{Ca_{1,8}} = Z_{mod_{1,8}} - Z_{mod_{2,8}} \quad (28)$$

These equations give 2 values for proportional SVP error for each track. If the SVP was slowly changing, then the 2 values for each track can be averaged. Otherwise, these values should be fitted to a trend for final computation.

A final check of the tidal and SVP corrections is to compare the crossing depths at Intersection 9.

VI. Conclusions

The process described here shows how to determine the size of the SVP error, monitor the roll bias for variations, and compute tidal differences of crossing survey lines to provide a better merged data set. As multibeam sonar sensors become more precise and random errors from the VRU and navigation become negligible, the surveyor will still have to contend with the unexpected,

and often unmeasured, changes in the SVP and roll bias drift.

The equations are based on the preciseness of the 45° beams as described and presumes that short term errors in roll and depth induced by acoustic noise and sensor jitter will average out over multiple soundings and multiple crossings. A review of the error curve of Fig. 2 shows that is practical to use data from the 45° beam averaged with nearby beams on each side to aid in the computations. Similarly, is reasonable to use data from the vertical beam averaged with the nearby beams on each side since the SVP error is nearly constant over the central beams. It is also reasonable to include 1 or 2 pings before and after each precise crossing point. Such averaging will detract from the process only in areas of severe slopes.

It is no longer necessary to guess the SVP error to attempt correction of the topography. It can be com

puted. But there must be some few crossing lines to provide the basis for the computations.

Acknowledgments

The author wishes to thank Ron Allen, Ken Kiesel and Kushal Talukdar for their support and encouragement for this work which resulted in 2 patents for SeaBeam Instruments.

References

1. U.S. Patent 5,608,689 Issued March 4, 1997 entitled Sound Velocity Profile Signal Processing System And Method For Use In Sonar Systems
2. U.S. Patent 5,640,369 Issued June 17, 1997 entitled Signal Processing System And Technique For Calculating Roll Bias Data

MULTI-SENSOR SURVEILLANCE WITH *IN-SITU* ENVIRONMENTAL CHARACTERIZATION

William M. Sanders
Naval Research Laboratory, Code 7180
Stennis Space Center, MS 39529

Abstract - It has been speculated that the performance of surveillance systems can be enhanced by the capability to sense and adapt to the environment in which it is deployed. Moreover, the use of multiple sensors, which observe the same surroundings using different physics, should provide more information and greater accuracy in characterizing an operational environment. However, it is not often easy or straightforward to predict the accuracy or validity of environmentally derived data from inverse methods, even when using a single sensor type.

This presentation describes a methodology for predicting the parameter estimation errors achieved by a hypothetical system comprising an acoustic and an electromagnetic (EM) sensor. Simple models of the acoustic and electromagnetic environments involving a minimal set of parameters are employed. Some parameters are unique to one sensor, but many are common to both types. Therein lies the potential for gain. Simultaneous observation of the same physical mechanisms using different signals should result in a reduction of errors and therefore more useful and reliable information.

This hypothesis is tested by investigating a shallow water environment with mostly known parameters. Observations of towed acoustic and electric dipole sources in the Strataform experiment are used to predict inversion performance. The predicted inversion errors in the two-sensor case are compared with those for individual sensors.

Estimation of errors is made possible by assuming:

- 1) Errors in measurements and theoretical/model parameters are Gaussian,
- 2) The forward equation can be linearized about some true set of values.
- 3) Parameters are not strongly correlated.

Under these assumptions, the variance of the *A Posteriori* errors can be formulated in terms of Cramer-Rao bounds on experimental errors, the variance of *A Priori* uncertainties and signal propagation characteristics, the latter quantities being the derivatives of the acoustic and EM field with respect to the model parameters. A split-step Fourier parabolic equation (PE) model is used for the acoustic signal. Derivatives of the field are derived in terms of the PE kinetic and potential

energy operators. The EM signal is modeled using a multi-layer integral transform solution.

I. INTRODUCTION

In-situ environmental characterization allows a surveillance system to sense and adapt to a particular operational setting. This may occur during initial deployment, as periodic updates or as a response to sudden changes, such as the passing of a thermal front. Whereas environmental data may be available in the form of archived sound speed profiles or geoacoustic databases, they may not be accurate or up-to-date. It may be possible to improve system performance using timely local observations.

Of course, the value of refined environmental data varies depending on the nature and functionality of a surveillance system. For the detection problem, active systems and passive arrays capable of matched-field processing are more sensitive to mismatch than an isolated static hydrophone. Even in the latter case, uncertainty in the environment leads to errors in localization and classification. Hence, the notion that acquisition of environmental data leads to enhanced system performance has driven multi-sensor *in-situ* environmental characterization. However, beyond showing the effects of specific mismatch, the improvement in performance due to refined observations and inversion has not been quantified.

This analysis investigates uncertainties in environmental parameters when the surroundings are probed using two disparate signals. These uncertainties are taken to be the errors resulting from inverse methods. Using inverse method terminology, they are the biases and covariance of *A Posteriori* information in model space, for which the elements are the environmental parameters. This analysis assumes an unbiased solution to the inverse problem can be found. The goal here is to estimate the variances in the individual parameters, which can thereby be used as error bounds.

In general, the probability density functions describing *A Posteriori* information can be difficult to describe analytically, so some assumptions are imposed. If all errors are assumed Gaussian, and if the

measured data are linearly related to the parameters, then *A Posteriori* errors can be derived. The latter condition of linearity may seem to make this analysis inapplicable to most acoustic surveillance, as acoustic inversion has been observed to involve highly nonlinear relationships. It is assumed here that there is some small region in the parameter space about the true state, for which a roughly linear relationship exists. This constrains this analysis to the case of refinement of errors given relatively accurate *A Priori* knowledge. It would not accurately predict the magnitude of errors when little is initially known and one wishes to parameterize a totally unfamiliar environment. Given these assumptions, the covariance of *A Posteriori* errors can be expressed, as in Equation (1) [1].

$$C'_m \approx \left[G_0^t (C_d + C_t)^{-1} G_0 + C_m^{-1} \right]^{-1} \quad (1)$$

Here, C'_m is the covariance of the *A Posteriori* parameter errors, C_m is the covariance of the *A Priori* parameter errors, C_d is the covariance of measurement errors, C_t is the covariance of theoretical errors and G_0 is the linearization of the model. The acoustic model calculates a vector of magnitudes of the acoustic pressure. Hence, G_0 is a matrix of partial derivatives of the magnitudes with respect to the environmental parameters. Similarly, the EM model calculates a vector of electric field strengths, and G_0 contains the partial derivatives of these strengths with respect to the environmental parameters.

Note the three sources of error in Equation (1). The *A Priori* errors (C_m) are predetermined by the extent of knowledge available prior to observation. The measurement errors (C_d) are a result of imperfect observations of signal magnitude. Estimates of these are usually given as Cramer-Rao bounds and are primarily determined by signal-to-noise ratio (SNR). Lastly, theoretical errors, sometimes called modelization errors, (C_t) are caused by a difference between the actual environment and that assumed by the model used in the inversion process. These errors, which may occur even when the model uses accurate parameters, are the result of incompleteness on the part of the model in accounting for all physical processes that affect signal propagation. It is interesting to note that in many analyses, it is assumed that modelization errors are negligible (the model perfectly represents reality) and uncertainty is bounded by measurement errors. This may be due to the difficulty in estimating the magnitude of C_t . However, in this analysis, it is assumed that this hypothetical surveillance system will be designed to effectively probe the environment using high SNR signals and observation errors are relatively small. Hence, the uncertainty is primarily a factor of modelization errors. Various degrees of model inaccuracies will be tested to evaluate this effect on

parameter estimation errors.

II. APPROACH

The objective of this analysis is to evaluate the reduction in uncertainty achieved by probing the environment. It is hypothesized that the variances of some of the parameter estimates are decreased by utilization of two sensors (acoustic and EM) as opposed to an acoustic only measurement. This should be possible, not just because there is redundant information, but because some physical phenomena affect the propagation of both signals in different ways. For instance, most variability in both the acoustic sound speed and EM conductivity of seawater is due to thermal effects. Therefore, propagation of both signals through the water column effectively senses its thermal structure.

In order to test this hypothesis, errors are analyzed for a well-parameterized environment, which was probed using both signal types. This uses data from the 1997-98 Strataform experiment in which low frequency towed acoustic and EM sources were used to probe the Eel River region, off the coast of northern California. Environmental data were gathered using sediment cores and conductivity-temperature-depth profiles.

One key to this process is to reduce the parameter set to a minimum. Choosing a small set of uncorrelated parameters not only makes the problem computationally tractable, but makes the required linearization (G_0) simpler. The greatest technical challenge here is to design EM and acoustic models that not only realistically model propagation, but can also produce derivatives of the fields, with respect to the environmental parameters. Further, although this initial effort uses a minimal set of parameters, the models must be capable of being extended to more complicated environments for future research. Hence, the parabolic equation (PE) model was used for acoustic propagation, and an integral transform solution for EM propagation. Both models were previously used to accurately model the Eel River setting, as is shown in Figures 1 and 2.

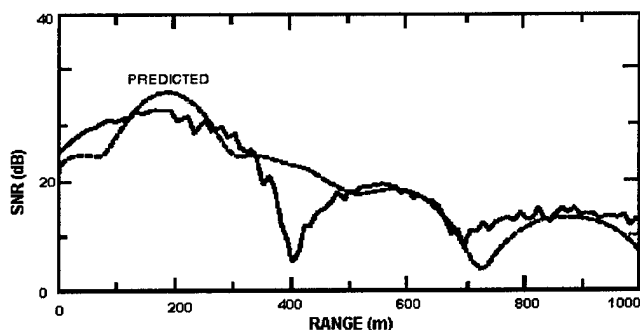


Figure 1. Actual and modeled acoustic signal for Eel River experiment.

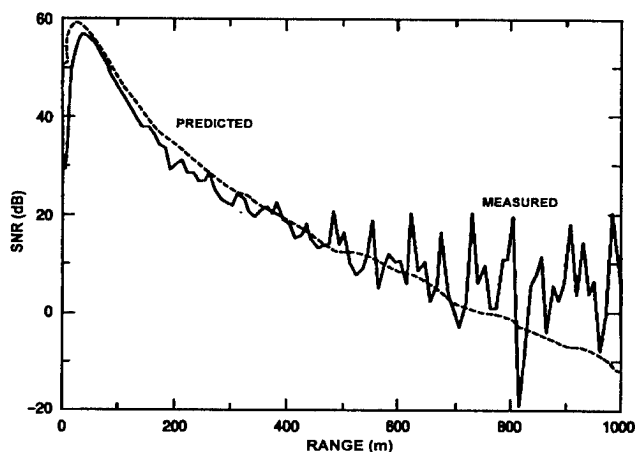


Figure 2. Actual and modeled electromagnetic signal for Eel River experiment.

The EM signal used in this experiment was a continuous five Hz narrowband tone emitted from a horizontally oriented dipole at 10 m depth. Due to the conductivity of seawater, solutions to the wave equation are not harmonic, but diffusive. So rather than being characterized by a wavelength, low frequency EM propagation in the ocean is characterized by a skin depth, which would be on the order of 100 m for a 5 Hz signal.

The range independent environment used by the models, shown in Figure 3, comprises four layers. The upper layer is the atmosphere, an infinite half-space which is slightly conductive. The air-sea interface is treated as an acoustically flat pressure-release surface. The mixed layer of the ocean has constant temperature and therefore, both constant sound speed and conductivity. In the third layer, the thermocline, the temperature, and therefore, both sound speed and conductivity decrease linearly with depth to the bottom at 62 m. The final layer, the sediment, is taken to be an infinite half-space in which the acoustic and EM propagation is characterized by a constant temperature, porosity and density.

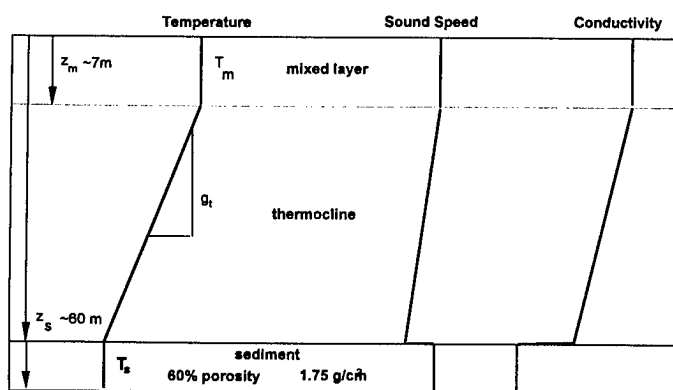


Figure 3. Environmental model for acoustic and EM propagation.

The list of parameters used in this analysis, their assumed true values, and variances of *A Priori* errors are listed in Table I.

Parameter	Value	Variance
Mixed-layer depth	7 m	1 m ²
Mixed-layer temperature	11.8 °C	.04 °C ²
Thermocline temperature gradient	-0.59 °C/m	10 ⁻³ °C ² /m ²
Water depth	62 m	.25 m ²
Sediment porosity	0.6	.0025
Sediment density	1.75 g/cm ³	.01 g ² /cm ⁶
Sediment grain sound speed	1911 m/s	10 ⁻⁵ m ² /s ²
Pore fluid temperature	8.5 °C	.04 °C ²

Table II. Environmental parameters

III. ACOUSTIC PROPAGATION

In order to derive the required linearization of the acoustic field, the parabolic equation [2], which is used to model propagation, is analyzed:

$$\frac{i}{k_0} \frac{\partial \Psi(r, z)}{\partial r} = H_{op} \Psi(r, z). \quad (2)$$

Here r is horizontal range, z is depth, and k_0 is an acoustic wave number. $\Psi(r, z)$ is the slowly varying envelope of the acoustic pressure:

$$p(r, z) = P_0 \sqrt{\frac{R_0 \rho(z)}{r \rho_0}} \Psi(r, z) e^{ik_0 r}. \quad (3)$$

P_0 is a source pressure level specified at a range R_0 , ρ_0 is a reference density and $\rho(z)$ is the depth varying ambient density. The operator $H_{op} = U_{op} + T_{op}$ is a combination of potential and kinetic energy operators. The solution to Equation (2) is achieved by propagating a solution over a small range step, Δr .

$$\Psi(r + \Delta r, z) = \Phi(r, z) \Psi(r, z) \quad (4)$$

The propagator $\Phi(r, z)$ is approximated by:

$$\Phi(r, z) \approx e^{-ik_0 H_{op} \Delta r}. \quad (5)$$

Here, $H_{op} = U_{op} + T_{op}$ is a numerical approximation of the ideal operator $H_{op} = U_{op} + T_{op}$. The kinetic energy operator T_{op} is independent of environmental

parameters, while the potential energy operator U_{op} can be factored into operators that are functions of different parameters:

$$U_{op} = U_1(c(z)) + U_2(\rho(z)) + U_3(\alpha(z)) . \quad (6)$$

Here, $c(z)$ is the acoustic sound speed and $\alpha(z)$ is the acoustic attenuation.

IV. ELECTROMAGNETIC PROPAGATION

As with acoustic propagation, the required linearization of the EM field, must be derived. The following model describes the electric field due to a horizontally oriented electric dipole in a stratified medium. In each layer, the solution to the depth-separated wave equation in cylindrical coordinates (r, θ, z) is given by the superposition of modes in the waveguide. Modes with no electric field in the z direction are said to be transverse electric (TE) waves and those with no magnetic field in the z direction are transverse magnetic (TM) waves. Any field in this waveguide can be described by the sum of its TE and TM components.

$$E_l^z = \int_{-\infty}^{\infty} [A_l \phi_l^+(v, z) + B_l \phi_l^-(v, z)] H_1^{(1)}(vr) \cos \theta dv$$

$$H_l^z = \int_{-\infty}^{\infty} [C_l \phi_l^+(v, z) + D_l \phi_l^-(v, z)] H_1^{(1)}(vr) \sin \theta dv \quad (7)$$

In the above, E_l^z is the electric field in layer number l , H_l^z is the magnetic field, v is a horizontal wave number, $\phi_l^+(v, z)$ and $\phi_l^-(v, z)$ are field functions satisfying the wave equations in each layer. Assuming time dependence of the form $e^{-i\omega t}$, $\phi_l^-(v, z)$ is an upward moving (decreasing z) wave and $\phi_l^+(v, z)$ is downward (increasing z) moving. A_l and B_l are amplitudes for the upward and downward moving TE waves, respectively, and will be determined from boundary conditions. Similarly, C_l and D_l are amplitudes for upward and downward moving TM waves. $H_1^{(1)}(vr)$ is the first order Hankel function of the first kind. For a layer in which the conductivity is constant (atmosphere, mixed layer and sediment), the exponential function is used for the field functions. However, in the thermocline, in which the conductivity decreases linearly with depth, the Airy function is the solution to the wave equation.

The solutions to Equation (7) are determined by matching boundary conditions, given by Maxwell's equations, at the interfaces [3]. These give amplitudes (A_l , B_l , C_l and D_l) in terms of reflection coefficients that are functions of the environmental parameters.

V. ACOUSTIC-ONLY INVERSION ERRORS

The errors resulting from use of the acoustic sensor alone form a baseline for comparison of multi-sensor results. In the Eel River experiment, in which a 25 Hz acoustic source was towed at 10 m depth past a bottom-mounted hydrophone, inversion of the range independent environment resulted in resolution of only two bottom parameters, while revealing nothing new of the water column. However, a more revealing result occurs if a source is dropped from the surface to the bottom, thereby "sampling" the entire water column. In this case, several parameters are refined. The degree to which errors are reduced depends on the magnitude of modeling errors assumed. In the following, the reduction in the variance of the errors of a parameter is plotted as a function of model error magnitude. The reduction is shown as the ratio of the variance of *A Posteriori* errors to that of *A Priori* errors in that parameter. The maximum magnitude of modelization error considered is on the order of the magnitude of the actual acoustic pressure. This is representative of a poor acoustic model. At the other extreme is the case in which the model error is 1/1000 the magnitude of the actual acoustic pressure - an accuracy that is unlikely to be achieved in actuality.

It is shown in figure 4(a) that a reduction in the variance of the error in estimating bottom depth is easily achieved, even with large modelization errors. Meanwhile, estimation of mixed layer temperature is only refined by using an accurate model as shown in figure 4(b). Lastly, the estimate of the mixed layer depth remains almost unaffected, even when using an extremely accurate model, as shown in figure 4(c).

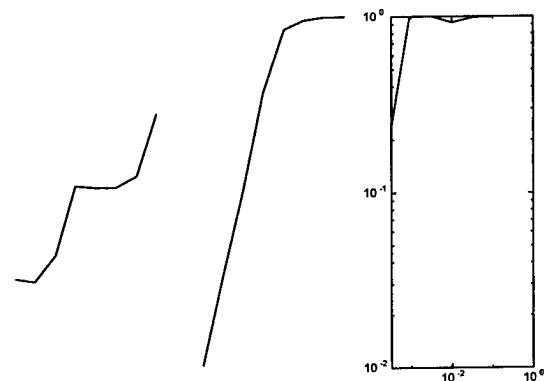


Figure 4. Effect of modelization error on inverting (a) bottom depth, (b) mixed layer temperature and (c) mixed layer depth.

VI. DISCUSSION

This analysis has devised a methodology for predicting the magnitude of errors resulting from inversion of environmental parameters using observations from two sensors. Unfortunately, results using the EM model are not available. Although this

project has not progressed enough to present final results, some observations are worth noting.

First, source-receiver geometry and the type of observations may determine the feasibility of environmental inversion. These factors determine how the environment is sampled. Not all parameters are observable at all times. Hence, configuration of the observations may preclude the estimation of some parameters. That not all parameters can be observed may obviate the need for different sensor types. For example, buried seismic sensors provide more information on sediment parameters than hydrophones. Indeed, this methodology can be extended to analyze the use of more than two sensor types with no real added complication or cost.

Secondly, it is likely that uncertainties will be bounded by the accuracy of the model used by inversion. Although it may be theoretically possible to invert a parameter, this practical restriction may make any refinement of errors unlikely.

However, this methodology has been used to analyze a single inversion situation. It must be applied to different configurations in order to make general conclusions.

VII. ACKNOWLEDGEMENTS

This work is supported by the Naval Research Laboratory through the CORE/NRL post-doctoral fellowship program.

VIII. REFERENCES

- [1] Albert Tarantola, *Inverse Problem Theory*, Elsevier, 1987
- [2] Kevin B. Smith and Frederick D. Tappert, "UMPE: The University of Miami Parabolic Equation Model Version 1.1," Scripps MPL Technical Memorandum 432, (1993)
- [3] J. A. Kong, *Theory of Electromagnetic Waves*, Wiley-Interscience, New York, 1975.

MEASUREMENTS AND ANALYSIS OF SCATTERING FROM PROUD AND BURIED TARGETS IN A SHALLOW-WATER LABORATORY ENVIRONMENT

Harry J. Simpson and Brian H. Houston
Naval Research Laboratory: Code 7136
4555 Overlook Ave., Washington DC, 20375

Carl K. Frederickson
University of Central Arkansas
Conway AR, 72035

Raymond Lim
Coastal Systems Station Dahlgren Division/Naval Surface Warfare Center, Code R22
6703 W. Highway 98, Panama City, FL 32407-7001

ABSTRACT

Finding and identifying objects in littoral waters is of growing interest. Although current acoustic based systems can readily detect objects sitting proud, identification is considerably more difficult [1]. For a buried target, even detection may prove difficult especially using higher frequency systems. These higher frequency systems are limited in range and sound penetration, which makes imaging buried targets extremely difficult. The research presented here is concerned with the use of relatively low frequency acoustics (1 kHz to 50 kHz) to overcome transmission and penetration limitations. Further, we are interested in employing the structural acoustics response of the target for identification purposes.

This research includes sound penetration above and below the critical angle, evanescent field interactions with buried targets [2], roughened interface enhanced scattering from buried targets [3], and the identification of wave-types propagating within the bottom [4,5]. Measurements of proud, partially, and completely buried targets have been conducted. The targets discussed here include a 60 cm diameter stainless steel sphere and a 30 cm diameter Aluminum retro-reflector. Of particular interest is the scattering from buried targets for ensonification angles below the critical angle. Also of interest is quantifying the enhancements of scattering for below critical angle ensonification due to interface roughness [6], and evanescent waves.

The measurements of the sphere are also used to validate scattering models. It has been possible to model the scattering from a proud and buried sphere using a T-Matrix method [7]. The results of these measurements along with analysis using scattering and sound propagation models will be discussed.

I Introduction

Using lower frequency, 5 kHz to 50 kHz and 1 kHz to 20 kHz acoustical systems for detection has several key advantages over higher frequency systems. The advantages include long range detection capability and increased penetration into the bottom. Imaging targets at these longer wavelengths is more difficult, however, it may be possible to use structural acoustical signatures to identify proud and buried objects in littoral waters.



Figure 1. The NRL Shallow Water Laboratory is a 500 cubic meter deionized water tank with a 3 m deep sandy bottom. Suspended above the pool is threedimensional robotics system used to position sources and hydrophones within the water column and in the sandy bottom.

To this end, a shallow water laboratory, shown in Fig. 1, with a high degree of environmental stability was constructed at NRL DC. The shallow water laboratory is a 8 m wide by 10 m long by 7 m deep rectangular

deionized water tank. A 3 meter deep, 212 micrometer mean diameter washed and filtered sand was installed in the bottom of the tank. Further, a three dimensional robotics system is supported above the tank that provides positioning of hydrophones and sources over a 5 m by 5 m work space with a 13 micrometer repeatability. The sand-water interface can be roughened to a desired contour or smoothed and leveled to a ~ 0.4 mm rms roughness.

Using this laboratory's unique capabilities, scattering measurements of proud, partially, and completely buried targets have been conducted. The targets discussed here are a 60 cm diameter hollow stainless steel sphere with a 5% wall thickness, and an 30 cm diameter conical Aluminum retro-reflector. Using the sphere in these scattering measurements addresses the influence of the bottom on the targets since the structural acoustics of the spherical shell are well understood and can be modeled. The retro-reflector was utilized to provide a large backscattered signal while its compact size made burial easy. Of particular interest is the scattering from buried targets for ensonification angles below the critical angle. Also of interest is quantifying the enhancements of scattering for below critical angle ensonification due to interface roughness [6] and evanescent waves.

The measurements of the sphere are also used to validate scattering models. For this, the physical parameters of the water-saturated sandy bottom must be known [5]. Thus, bottom characterization measurements have been conducted to obtain the sound speeds, permeability, porosity and density for the installed bottom. It has been possible to model the scattering from a proud and buried sphere using a T-Matrix method [7]. The results of these measurements along with analysis using scattering and sound propagation models will be discussed.

II Sphere Measurements

The first set of scattering measurements off the 60 cm diameter sphere included freefield, proud, half buried and several fully buried sphere placements. A 3 m horizontal line source and a small omnidirectional hydrophone were used to ensonify the sphere and measure the scattered acoustical field respectively. For these measurements, the source was stationary and the hydrophone was mounted to the two-dimensional horizontal robotics system to measure the bistatic acoustical scattering response of the sphere at the different target locations.

A second set of measurements using a spherical omni-directional source and the same small omnidirectional hydrophone were also made. Figure 2 shows the measurement configuration used during these latter buried sphere measurements. The fully buried sphere was 2.5 cm and 11.4 cm below the sand-water interface, measured

from the sand-water interface to the top of the sphere. The hydrophone was mounted 51 cm above the sand-water interface and a spherical source was mounted 61 cm above the sand-water interface. The source and hydrophone were mounted on a horizontal robotics system that was used to position the source and hydrophone around the buried and half buried targets. This source-hydrophone configuration provides a quasi-monostatic acoustical scattering response from the fully or partially buried sphere.

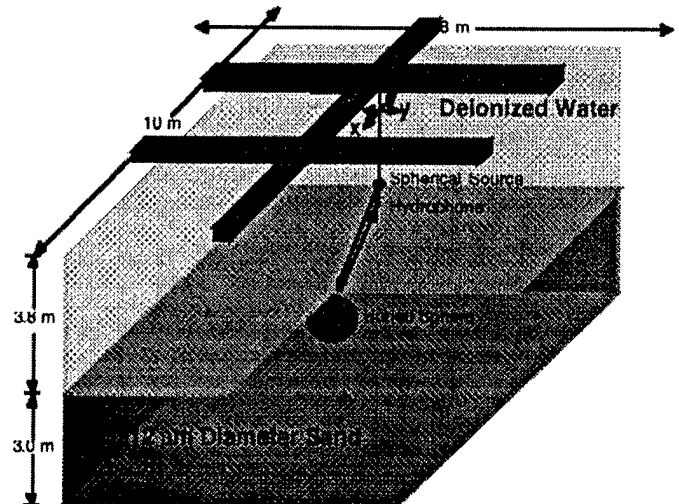


Figure 2. Diagram of a buried sphere measurement. A spherical source ensonifies the buried sphere and a hydrophone mounted 10 cm below the source measures the scattered signal. Both are attached to the horizontal scanner that positions the source-hydrophone pair around the buried sphere.

Figure 3 shows the frequency response, with the source and hydrophone 1 m from the sphere buried 2.5 cm below the sand-water interface. Also shown in Fig. 3 is the noise floor for the measurement. At this source-hydrophone location the measurement had a nominal 10 dB to 20 dB signal to noise ratio and an ensonification angle of approximately 38 degrees, measured up from the sand-water interface. This ensonification angle is well above the 28 degree critical angle. As the source-hydrophone is moved horizontally further from the buried sphere, it passes through the critical angle and a sharp decrease in the target strength is noted. Below a 10 degree ensonification angle, no scattered signal is observed above the noise floor of these measurement.

For the same source-hydrophone location, 1 m from the 2.5 cm buried sphere, a numerical model using a T-matrix based calculation was performed. Figure 4 shows the comparison between the measured acoustical response of the sphere and the calculated acoustical response of the sphere. Note that the comparison is done on a linear vertical scale. The agreement between the numerical model and the measurement is generally good. In order to perform

this calculation several environmental measurements of this laboratory's sandy bottom were necessary.

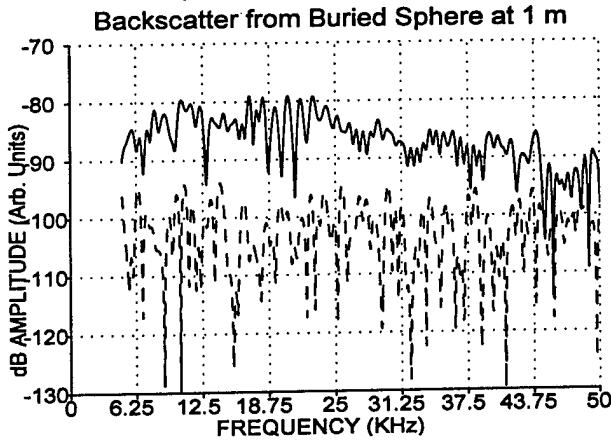


Figure 3. Acoustical frequency response from a sphere buried 2.5 cm below the sand-water. The solid line is the scattered response and the dashed line is the noise floor for this measurement.

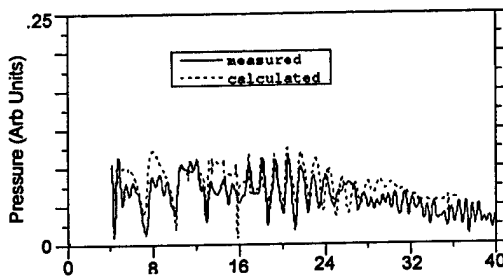


Figure 4. Comparison of measured acoustical response to a T-matrix based calculation. The solid line is the measured acoustical frequency response and the dashed line is the T-matrix prediction for this measurement configuration. Note that the vertical scale is linear in amplitude and not a dB scale.

Many of these environmental measurements were conducted prior to this set of measurements. The relevant environmental parameters included the water and saturated sand wavespeeds, 1482 m/s and 1680 m/s respectively. The wavespeeds and attenuation as a function of frequency were measured using a buried two-dimensional syntheticarray hydrophone technique [5].

III Buried Retro-Reflector Measurements

Reasonable agreement was obtained between the numerical model and the measurement for the 5 kHz to 50 kHz range. However, for ensonification angles significantly below the critical angle of 28 degrees, the target strength of the buried sphere falls below the noise floor of the measurement. Also for roughened interface measurement, the scattering return from the roughened interface dominated any signal from the buried target above 5 kHz. It was decided to investigate the evanescent wave scattering

using a slightly lower frequency. A second line source with a nominal response between 1 kHz and 20 kHz was employed to study evanescent wave scattering from buried objects in this frequency band.

This lower frequency 3 m line source, can be suspended in the water column from just the two ends. This allowed the positioning of the line source at ensonification angles of 10°, 15°, 20°, 25° and 0°, as measured down from the normal to the sand-water interface, shown in Fig. 5. This configuration has a distinct advantage over a horizontal line source or the spherical source in that there is a single ensonification angle, or quasi-plane wave, ensonifying the sandy bottom around the buried target. Thus there should be a minimum of acoustical energy ensonifying the sand-water interface and the buried target other than at the desired ensonification angle.

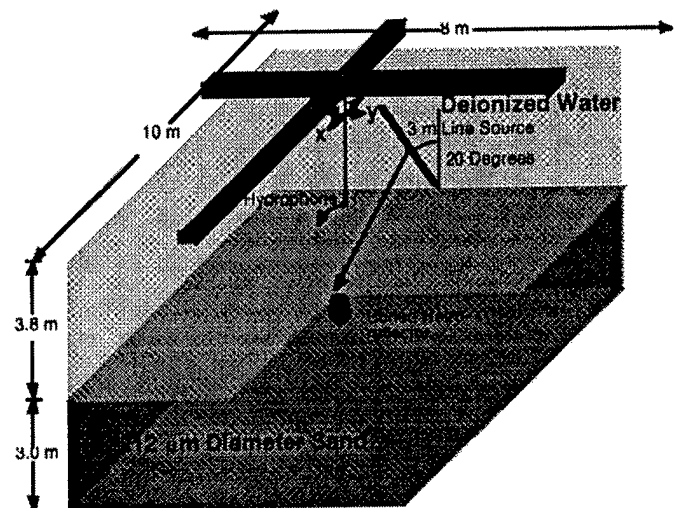


Figure 5. Diagram of the measurement configuration for a 20 degree ensonification angle. The source is suspended in the water 20 degrees down from the interface normal. The retro-reflector is buried just under the sand-water interface. A hydrophone mounted to a two-dimensional robotics system measures the bistatic scattered signal.

For these five ensonification configurations several measurements of the scattered acoustical response of the buried sphere were made around the target. For these measurements, an aluminum conical retroreflector was used. The retro-reflector is a 30 cm diameter cylinder that is 20 cm long. A 45 degree cone was machined out of one end to form the conical retro-reflector. The authors note that at the lower frequencies of the measurement that this target does not function as a retro-reflector, but rather as a complex shaped target. However, a freefield measurement of this "quasi" retro-reflector has been made for the 1. kHz to 20 kHz frequency band of the measurements. Using this lower frequency source and retro-reflector it was possible to measure the target strength of the buried retro-reflector for ensonification angles below the critical angle.

Figure 6 shows a side view of the 20 degree ensonification of the buried retro-reflector. A 20 degree ensonification angle is below the critical angle of 28 degrees and the wave penetrating into the bottom should be evanescent. The target is buried just beneath the sand-water interface and is tilted at about a 30 degree angle.

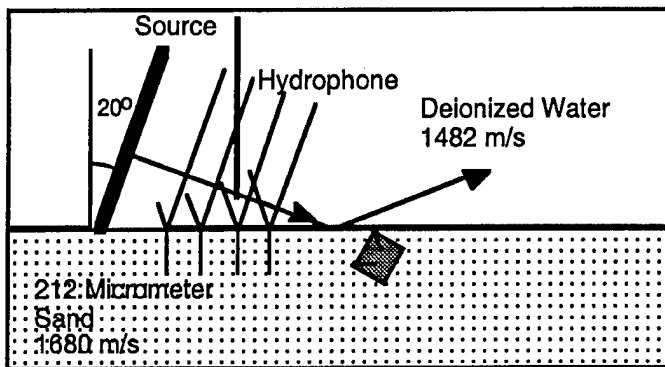


Figure 6 shows the buried retro-reflector ensonified at a 20 degree angle.

Figure 7 shows the frequency response of the buried retro-reflector for a 20 degree ensonification at the 20 degree backscattered direction. The dashed curve in Fig. 7 is the noise floor for this measurement. At 3 kHz there is nominally 30 dB of SNR and as expected the signal rolls off with frequency.

The effect of a roughened interface on the scattered signal as a function of frequency was also investigated. Several measurements of the buried retro-reflector with different roughened interfaces were measured with and without a buried retroreflector. These measurements were made for 10 degree and 20 degree ensonification angles.

IV Remarks

We have presented some of the recent results obtained from carefully controlled laboratory studies directed towards enhancing our understanding of acoustic penetration and scattering from buried objects. Preliminary analysis shows encouraging agreement between theoretical calculations using a T-matrix formulation and our measurements of the scattering cross-section of a sphere buried at a shallow depth below a smooth interface. Further, our preliminary analysis also shows strong evidence of significant low frequency evanescent bottom penetration with subsequent scattering. Moreover, as a practical matter, we were unable to obtain useful scattering cross-section measurements at frequencies above - 5 kHz when the bottom was roughened. This is a result of high back-scattering levels off of the roughened interface at these frequencies, evanescent field decay, and attenuation.

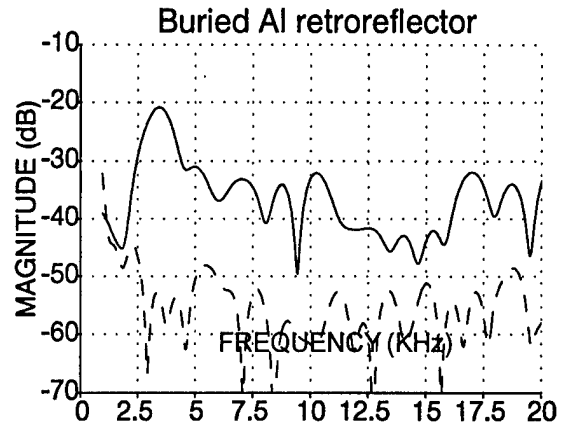


Figure 7. The measured backscattered acoustic frequency response of a buried retro-reflector for a 20 degree ensonification angle. The solid curve is the frequency response of the buried retro-reflector. The dashed line is the frequency response of the noise for this measurement.

Acknowledgments

This work was supported by ONR

References

- [1] T. J. Yoder, J. A. Bucaro, B. H. Houston, and H. J. Simpson, "Long range detection and identification of underwater mines using very low frequencies (1-10 kHz)," Proceedings of the 1998 SPIE Detection and Remediation Technologies for Mines and Mine-like Targets 111, International Society for Optical Engineering Technical Publications, 3392, 1998
- [2] W. L. J. Fox, A. Maguer, A. Tesei and H. Schmidt, "Measurements of acoustic scattering from partially and completely buried thin-shelled targets," J. Acoust. Soc. Am., Vol. 105, No. 2, Pt. 2, 1999
- [3] K.L. Williams and D.R. Jackson, "A model for bistatic scattering into ocean sediments for frequencies from 10-100 kHz," J. Underwater Acoust. (Accepted for Publication Oct. 1997)
- [4] N. P. Chotiros, "Biot model of sound propagation in water-saturated sand," J. Acoust. Soc. Am. 97, 199-214 (1995)
- [5] H. J. Simpson and B. H. Houston, "Synthetic array measurements of acoustic waves propagating into a water-saturated sandy bottom for a smoothed and a roughened interface," J. Acoust. Soc. Am. in review
- [6] E.I. Thorsos, D.R. Jackson, J.E. Moe and K.L. Williams, "Modeling of subcritical penetration into sediments due to interface roughness," Conference Proceedings "High Frequency acoustics in shallow water," N.G. Pace et al, NATO Saclant (1997)
- [7] R. Lim and H. J. Simpson, "A comparison of benchmark acoustic scattering solutions with tank experiments on buried and partially buried spheres," J. Acoust. Soc. Am., Vol. 105, No. 2, Pt. 2, 1999

IDENTIFICATION OF WORLD WIDE WEB EDUCATIONAL MATERIALS IN CONJUNCTION WITH THE NATIONAL SEA GRANT COLLEGE PROGRAMS HAZNET EFFORT

Sharon H. Walker, Ph.D., Program Director for Education
NOAA-Sea Grant College Program

And

Associate Director for Outreach, Institute of Marine Sciences and
Professor, IMS-Department of Coastal Sciences,
The University of Southern Mississippi

And

Howard D. Walters
Instructor, Mississippi Gulf Coast Community College

I. Abstract

In 1997, the Southeast and Gulf state's Sea Grant programs implemented the Sea Grant HazNet program with funding from the National Sea Grant College Program and local Sea Grant programs and affiliated institutions. This effort was undertaken realizing that research, education, and outreach programs were needed to assist states in enhancing and empowering a citizenry who is capable of employing the most effective means to reduce loss of life and to mitigate the economic impacts of various coastal hazards.

This effort is currently in its second year of funding, with the following infrastructure components either in place or in the process of being implemented: design and produce a HazNet Website; assess hazards research needs; establish a listserver with members of industry, and

government offices and other interested users; and plan and develop educational programs for the general public and precollege students and their teachers. The long-term success of this effort can be measured by: increased communications; the adoption and effective use of hazard mitigation measures throughout the private and public domains; the establishment of a coherent plan to guide future hazards research; the development and/or revision and complementary infusion of coastal hazards activities by precollege classroom teachers; and enhanced programs relative to coastal hazards to increase public awareness. Lastly, this study has the potential to serve as a national model for natural hazards and it should also result in a reduction in the potential catastrophic effects of natural hazards by having a more knowledgeable populace.

The research presented in this report will summarize efforts to utilize

the educational capacity and potential of the World Wide Web through the transfer of educational materials and lesson plans for classroom teachers. Under the umbrella of the Sea Grant HazNet program, researchers identified and organized materials available at a variety of URLs on the World Wide Web and have made them available at the national HazNet Web site.

II. Background

Citizens in the southeast Atlantic and Gulf of Mexico coastal states are at risk from a variety of natural hazards, most notably the winds, waves and floods generated by seasonal storms and hurricanes. Other coastal states face these same threats as well as others including tsunami flooding, non-storm related riverine flooding and coastal erosion. Risks to life and property from these recurring natural hazards will increase with the anticipated growth of coastal populations. According to National Geographic, the U.S. South and West are expected to grow by 32 and 51 percent respectively by the year 2025. "Half the U.S. population lives in coastal states, with some 34 million in Texas and Florida, two favorite hurricane targets" (National Geographic Society, 1998).

According to the Insurance Institute for Property Loss Reduction, an estimated \$58 billion in insured losses from catastrophic events over the last ten years is attributable to wind events alone. Total insured losses produced by Hurricanes Hugo, Andrew, Iniki, and the winter storms of 1993 and 1994 were \$24.7 billion. The value of insured coastal property has increased 69 percent between 1993 and 1998 (from

\$1.86 to \$3.15 trillion) and the frequency and severity of coastal hazards are predicted to increase. The increasing human population in the coastal areas is directly contributing to increases in development and, thus, economic risk. These observations underscore the need for a dedicated national effort to reduce the economic and social costs of natural hazards.

Hazards associated with storms are compounded by other factors, including but not limited to: increases in sea level rise; land subsidence; the inexperience of coastal populations to properly prepare for a major hazard event or to deal with its aftermath; and increasingly valuable development along the nation's coastline. Research, education and outreach programs are needed to assist states in creating an aware and prepared citizenry capable of employing the most effective means to reduce loss of life and to mitigate economic impacts.

The Federal Emergency Management Agency (FEMA) has taken the lead in this effort with the publication in 1995 of the "National Hazard Mitigation Strategy: Partnerships for Building Safer Communities." Its foundation is the creation and strengthening of partnerships to address the five major elements outlined in the strategy: hazard identification and risk assessment; applied research and technology transfer; public awareness, training and education; incentives and resources; and leadership and coordination. These elements are also addressed in the NOAA Strategic Plan: A Vision for

2005 as an element of its "Environmental Stewardship Mission: Sustain Healthy Coasts" and within the "Public Safety" section of the Sea Grant Network Plan: 1995-2005.

All of these elements are addressed by the Sea Grant HazNet program. In addition, the establishment of Sea Grant HazNet represents the kind of strategic investment at the national level which allows Sea Grant to address critical issues of national importance in a synergistic fashion. This synergy emanates from the combined efforts and resources of the Sea Grant program network interacting in partnership with outside entities from the public and private sectors. Sea Grant HazNet incorporates the strengths of all the individual Sea Grant programs in addressing local hazards issues according to local needs and constraints, while promoting the entire Sea Grant network as a unified program to outside partners participating in the implementation of the National Hazard Mitigation Strategy.

Based on the previous, current, and planned research, extension and communications activities within the individual Sea Grant programs, it is clear the Sea Grant network can help to address the many challenges faced in the national effort to reduce losses of all kinds due to natural and man-made hazards. Some of these include:

1. To initiate, coordinate and sustain effective partnerships to attack the multiplicity of associated natural coastal hazards problems.

2. To identify and assess hazards related risk.
3. To develop and implement effective mitigation policies, incentives, methods and resources.
4. To substantially increase public awareness of coastal hazards, their associated risks and what can be done to reduce public and private losses of all kinds.

The need to address natural coastal hazards was one of the four priorities established at a 1997 meeting of the Southeast and Gulf states Sea Grant Regional meeting (SEGUL). The idea for a cooperative network of Sea Grant programs interacting among themselves and in partnership with others in the National Hazard Mitigation Strategy was conceived at that meeting. The creation of Sea Grant HazNet was proposed as a mechanism to help achieve that goal.

While Sea Grant HazNet was initiated by the SEGUL programs, it will nevertheless link all the Sea Grant programs in a web of information exchange. Building on its initial successes and learning from its failures, it is anticipated that, through active program participation, Sea Grant HazNet will increase substantially. As conceived, Sea Grant HazNet is a truly national Sea Grant program, addressing local and national issues, and is being undertaken as a network in the national arena of hazard mitigation.

The major features of HazNet include: the creation of a World Wide Web site on which to post Sea Grant

research, extension and education information and provide linkages to other related entities; the establishment of a listserver to facilitate dialogue among the Sea Grant programs and enable information exchange between Sea Grant and outside partners; and the convening of a pilot Southeast Hazards Research Needs Assessment Workshop to include all elements of Sea Grant programs, as well as representatives from user groups and potential collaborators. Through these and other elements, the proposed Sea Grant HazNet program will address the several purposes listed for proposals in the National Outreach Competition RFP as follows:

- improve hazards related technology transfer to user groups;
- increase public awareness and understanding of hazards and hazards mitigation;
- strengthen the natural coastal hazards element of the Sea Grant Outreach network;
- enhance regional, national and multi-institutional (network) natural coastal hazards outreach;
- address the national need to reduce the loss of lives and property due to natural hazards;
- bring Sea Grant resources to the national hazards mitigation effort; and
- utilize innovative communications technologies to reach constituent groups with needed information

and technology to address hazards mitigation problems.

Through HazNet, all of the programs of Sea Grant, acting as a network---with the research capabilities of the affiliated institutions, the "grassroots" extension network of the Marine Advisory Services, the school access of the K-12 education programs, and the expertise found within the communications network---offer a unique resource to the nation in meeting the challenges presented by natural hazards.

III. Procedure

Under the overall HazNet structure, researchers at the University of Southern Mississippi's Institute of Marine Sciences were funded through the MississippiAlabama Sea Grant College Program to identify and develop educational materials for middle school teachers. These materials would incorporate reviewed concepts and activities already developed and available through the internet, but reorganized into a more readily accessible format utilizing the national HazNet Web site. Increasingly, the internet and the World Wide Web have been identified as a valuable medium for the exchange of information and scientific data. The expansion of this technology is perceived as driven by "the relatively low cost, widespread access, and flexibility, with advances in technology and standards playing a key role" (Passin, 1998). Further, as reported by NOAA researchers, the "advent of the World Wide Web as a means of providing universal access to a vast spectrum of information has revolutionized data

and information dissemination and management. The easy availability of information on the Web to a large and diverse audience has generated a literal explosion in use of the internet and the Web, making the Web a logical and effective way for NOAA to provide information....” (Soreide, et.al., 1998).

An extensive search of the internet was undertaken with commercial browser software using each of the identified coastal hazards and related terminology as search descriptors, i.e. hurricane, tsunami, erosion, flooding, tornado, volcano, and earthquake. Further, a general category for related Earth processes and general science information was also established. This initial search produced an unworkable “hodgepodge” of materials which reflected both the massive scope of the World Wide Web and its basic lack of organization. This finding points out two facts: 1) the World Wide Web, as it currently exists, has limited assess and utility as a purveyor of materials for teachers who do not have the time to invest in searching and reviewing materials given the limitations of their work days and the amount of content posted to the Web; 2) efforts to better manage and organize the content of the World Wide Web can potentially be of great value to improving access to quality materials for classroom teachers by reducing search time and pre-reviewing educational materials.

The educational materials search was refined by selectively limiting the search to those URLs associated with government agencies and/or universities. The researchers believe that such a limitation was

more likely to avoid the commercialism inherent to many Web sites encountered in the initial search. Further, government and university materials are more likely to be available free of charge and/or easily downloadable for no charge, which would make the materials more immediately useful for teachers.

This newly refined search enabled the researchers to identify a list of 200 URLs associated with the coastal hazards identified for this project. This initial list was reduced to 92 active Web sites associated with either government agencies or university research or education centers. All of these sites contain educational materials, lesson plans, databases appropriate to classroom use, and/or links to other related Web sites. Further, all of these sites are free for classroom teachers and can be printed locally.

These 92 active sites were read for content and appropriateness for use by classroom teachers and then keyed by content or overall subject area. A key and the list of sites were reviewed by the HazNet project director and then posted to the HazNet Web site which is maintained at NOAA's Coastal Services Center in South Carolina. A link to these educational materials was established on the site directory page for HazNet at the URL: www.haznet.org. This site is currently active, but contains a disclaimer that the site remains under development. A review paragraph for each of the 92 Web sites is being developed to assist teachers in quickly finding educational materials appropriate for their individual classes. These paragraphs will identify the

host/sponsor of the Web site, the general content category, i.e. which coastal hazard is the focus of each site, the types of educational materials and/or lesson plans, the appropriate instructional grade levels of the lessons, and links to other related materials. It is anticipated that these paragraphs will be online in early Fall 1999.

A potential extension for the HazNet educational materials was identified in the review of materials. NOAA's Weather Services Area in conjunction with the United States Geologic Survey and the National Geographic Society developed a teaching poster on natural hazards which was published as a supplement to the National Geographic in July 1998. This poster is now out of print, but the maps and charts which comprised the poster remain in the archives of the National Geographic Society. A conversation between HazNet researchers and the National Geographic Society has been initiated with a view toward making some version of the natural hazards maps available through the HazNet Web site.

IV. Summary

Both the need to increase the knowledge base of the coastal populace in regard to coastal hazards and the relative value of the World Wide Web as a tool to increase the exchange and transmission of information to that populace have been identified in research and planning efforts among federal and state agencies. The Sea Grant HazNet effort, and the complementary and coordinated efforts of local researchers as reported here, are addressing both the critical need for

education and information transmission concerning coastal hazards and the utilization of the World Wide Web as a mechanism to facilitate the transfer of that information.

The value of this educational research effort is that it addresses classroom teachers who have the most control over the content of scientific information and lessons presented in their individual classrooms. Further, it incorporates the World Wide Web into a readily accessible and useful tool for these classroom teachers by organizing a set of previously developed materials into a concise set based on precise content areas--the coastal hazards identified by the national Sea Grant HazNet effort. This effort effectively leverages the funds expended in developing the educational materials originally by reincorporating these existing materials based upon newly identified research, planning, and outreach goals.

By systematically compiling and organizing the educational materials and lesson plans available through the various agency and university Web sites, these lesson plans are more readily usable by classroom teachers who can access and print these materials in their own classrooms. These lesson plans, estimated at several thousand in number, typically represent the "best of the best" lessons which federally funded programs have developed. Additionally, the identified materials are also comprised of several dozen "computer interactive" lessons-lessons which students complete in the classroom on general science and coastal hazards topics, but

which integrate the databases, realtime monitoring systems, and government and university resources available through the World Wide Web into meaningful learning experiences. This evolving instructional methodology--computer interactive and Web-based instruction--offers the promise of a substantive transformation of science teaching and of teacherstudent interaction in the science classroom.

V. Acknowledgments

This research has been funded by the Mississippi-Alabama Sea Grant Consortium, Project #E/0-61, Grant #NA86RG0039, and by the University of Southern Mississippi's Institute of Marine Sciences/Gulf Coast Research Laboratory.

The Background section of this paper has been excerpted from the National Sea Grant HazNet proposal. The Principal Investigator for that effort is Bob Bacon of the South Carolina Sea Grant Consortium/ Sea Grant Extension Program.

VI. References

Bacon, Robert, et.al. (1997). *Sea Grant HazNet. A Proposal from the Southeast and Gulf (SEGUL) Region Sea Grant Programs to the National Sea Grant College Program.*

National Geographic Society (1998). *Natural Hazards of North America. A supplemental map produced by National Geographic Maps for National Geographic Magazine, July, 1998.*

Passin, Thomas B. (1998). *Data Interchange Using Web Sites.* Ocean Community Conference 1998, The Marine Technology Society Annual Conference, Proceedings Volume 1, p.45.

Soreide, Nancy N. et.al. (1998). *NOAA Strategic Goals Presented As Theme Pages on the World Wide Web.* Ocean Community Conference 1998, The Marine Technology Society Annual Conference, Proceedings Volume 1, p. 64.

THE NEED TO RE-ENGINEER UNIVERSITY-LEVEL MARINE SCIENCE EDUCATION

Frank W. Hughes, Ph.D.
The Boeing Company

I. ABSTRACT

The capability and quality of graduates from marine science education programs is important because ocean issues are of widespread national and societal interest and concern. Major drivers for this interest and concern include the important uses of the oceans for the national and societal needs of national defense, economic growth and utilization, and human health. The significant needs for environmental assessment and prediction and for environmental stewardship (the protection and management of the environment and natural resources) are also major drivers.

Producing graduates who have the proper capabilities and quality requires the re-engineering of the contents of marine science education programs. Graduates must possess not only the proper set of attributes to be able to satisfy the requirements of jobs in the marine workplace but must also be prepared for continuing, lifelong learning.

Specific recommendations for re-engineering marine science education programs are provided. These include increasing cooperation with colleges of engineering, business, and education, as well as increasing emphasis on master's level graduates. Marine science education programs within colleges and universities, due to their inherently multi-disciplinary nature, can be used as models to help improve the quality of cross-disciplinary educational programs throughout the entire university. Such cross-disciplinary activities can make significant contributions to the needed improvements of overall undergraduate science, mathematics, engineering, and technology (SME&T) education recommended in several recent major national reports. Teaching across disciplines on a university-wide basis can provide opportunities both for educating the public in general about the major environmental issues associated with the oceans as well as for educating technical and scientific specialists. Marine science education programs should begin

teaching graduates how to advise policy and management decisions. Additionally, these programs should begin teaching graduates how to deal with the outcomes of the multiplicity of major ocean research programs including how to manage them and how to coordinate them.

II. INTRODUCTION

Current college and university-level marine science education programs are focused too narrowly to meet the demands and expectations which society places on their graduates. These programs should be producing graduates who have not only a solid foundation of science and technology but who also have basic business and interpersonal skills.

If the above statements sound overly critical, they should be considered in the context of the continuous improvement of quality. Although we have in this country the best system of college and university education in the world, that does not mean that our education system cannot, or should not, be made even better. It is in the spirit of identifying the need for such improvements that this paper is written.

For this paper, the term marine science should be interpreted broadly in order to make the term "marine science education" be as all-inclusive as possible. Note that environmental education is a term broader than marine science education and is not directly addressed in this paper. This paper is not just limited to, or focused on, oceanography programs, however, but is meant to include a broad range of college and university-based programs and disciplines. Among those included are fisheries, atmospheric sciences, ocean engineering, as well as ocean and marine technician training programs. The paper addresses all educational programs past the K-12 level, in both traditional two-year and four-year schools, up to and including all graduate levels. If the college or university-based educational program or activity may seem marginal for inclusion by this paper, let's include it for purposes of this discussion. We must

also not overlook the fact that the study of marine science and of the seas addresses an area with international dimensions, not just regional or national dimensions.

Thus, the capabilities and quality of graduates from marine science education programs are important because ocean issues themselves are of such widespread national and international interest and concern. Major drivers for interest and concern about ocean issues include the important uses of the oceans for the national and broader societal needs of national defense, for economic growth and utilization, and for human health. Additional major drivers for interest and concern are the significant societal needs for environmental assessment and prediction as well as for environmental stewardship (i.e., the protection and management of the environment and natural resources).

The major drivers cited above summarize a long list of specific concerns and needs. Some of these specific concerns and needs are: managing the coasts for economic and environmental prosperity; protecting and restoring fisheries and other living marine resources; advancing and applying ocean science and technology; detecting and forecasting oceanic components of climate variability; facilitating safe and efficient marine operations; managing living marine resources and fisheries for sustainable use; the consequences of global warming; preserving healthy, and restoring degraded, marine ecosystems; mitigating the human impacts of natural disaster; and ensuring public health.

Signs of trouble in the oceans are myriad and typically include declines in natural systems and populations, increases in harmful or negative events, pollution and chemical contamination, and global warming and sea level rise. Many reports cite these signs. One recent example is *Danger at Sea: Our Changing Ocean*.

III. DESIRED ATTRIBUTES OF GRADUATES

The Heinz Center report, *Our Ocean Future*, (1998) states it well when it says that the vigor of the national ocean science and technology program depends directly on the availability of a well-educated and trained pool of talent, ranging from technicians to Ph.D. The report also asks the following two meaningful questions: Is the present institutional framework adequate to educate and retain the necessary talent? Are the resources available to those institutions to meet the broader educational needs of the country?

Graduates are needed that can address the specific needs and concerns which are identified in the introduction to this paper. In addition to having the technical expertise to address these issues, graduates must also be able to advise policy and management decisions. This particularly capability is arguably as important as research. Graduates must also be able to integrate across disciplines, or at least serve as a positive example for interdisciplinary cooperation, and must possess the essential qualities and skills of a graduate needed to survive in the workplace of the future.

The essential qualities and skills a graduate must have to achieve success in all sectors of the marine sciences workplace of the future include a solid, foundational technological proficiency in a core discipline; broad training to address interdisciplinary problems; skills in critical thinking; adaptability (or flexibility); and excellent communication skills which include not only reading and writing but also listening as well as the ability to communicate with a variety of nonpeers including the public. Some additional qualities and skills which will be needed by successful practitioners include basic business skills, interpersonal skills, project management skills, an understanding of continuous improvement, and a recognition of the need for continuous learning.

IV. NEED FOR EDUCATIONAL SYSTEM CHANGES

To meet these education needs requires changes not only in the contents of the existing curriculum but changes in the education system and the educational delivery system themselves. A detailed discussion of some of these needed changes goes well beyond the scope of this paper, but they will be mentioned in passing.

There is a need for the educational delivery system to both complement and supplement the traditional M.S. and Ph.D. programs. As a start, traditional graduate education programs need to avoid the "cloning paradox". This graduate educational paradox has the following elements: focusing the training on preparing graduates for careers in academia, not industry; the Ph.D. is the preferred degree with the master's degree treated as a consolation prize; and the graduation rate usually involves overproduction as it is not done in response to market demand.

Marine science education programs should both encourage and accommodate the lifelong learning process. This must involve addressing the issues of

accreditation, which is needed primarily for quality control, and of articulation so that we can stop penalizing students who don't take all of their credits at one institution by creating waste for them through making them retake many courses. Marine science education programs also need to address work-based learning. This must involve resolving issues of how to award credit for work experience, articulation of these credits, and establishing standards in order to control the quality of this type of learning.

Many of the needed changes will not occur until educational institutions and the individual programs within those institutions better recognize and reward the full spectrum of the elements of scholarship. The best known elements of scholarship are the discovery of knowledge (also known as research) and the transfer of knowledge (also known as teaching). The additional elements of the integration of knowledge, the application of knowledge, and the archiving of knowledge should also be recognized and rewarded, and specialists should be developed in each of these areas. Currently, a single faculty member is supposed to be equally proficient in all elements of scholarship, but their success and promotion are most directly connected only to research and teaching proficiencies.

Marine science education also involves much more than just traditional colleges and universities. Good coverage of the range of informal marine education activities is given in one of the International Year of the Ocean Discussion Papers which were coordinated by NOAA. A list of the categories in informal education providers with a few representative examples of each is as follows: public and private institutions (museums, science centers, aquaria, parks, sanctuaries, maritime centers); World Wide Web (SeaWeb sponsored by the Pew Charitable Trusts, Environmental News Network which sponsored the Year of the Ocean page); media (television, books, newspapers and magazines); government agencies - federal, state, local (NOAA, Corps of Engineers, state departments of ecology, local public libraries); and professional societies (MTS and AAAS). Education institutions need to address how to integrate across, interface with, and incorporate the results of learning attained through this informal network.

V. SPECIFIC RECOMMENDATIONS

Specific recommendations for re-engineering marine science education programs are directed at two major types of activity. The first is increasing cooperation and collaboration on the campus of the institution. The second involves increasing the outreach of the institution to the community where community is used

in the broadest sense of the term.

Under increasing cooperation and collaboration at the campus of the institution are the following recommended two principal areas of focus: 1) improving the teaching of the graduates of the particular marine science education program itself, and 2) improving the teaching of students from other programs throughout the campus. The highest priority for teaching students from other programs should be given to the teaching of K-12 teachers in the schools of education. Marine science programs should be actively involved in the education of K-12 teachers both while the teachers are undergraduates as well as during the continuing education programs in which these teachers participate throughout their careers.

The next highest priority for teaching students from other programs should be given to using major environmental issues, exemplified by ones related to the oceans, as educational integrating themes across disciplines to teach technically-based service courses on a university-wide basis. Because marine science education programs are inherently multi-disciplinary programs, their expertise in teaching material of this nature can be used to teach other departments and schools how to teach, grade, and test across disciplines which should help improve the quality of crossdisciplinary educational programs throughout the entire university. Teaching across disciplines on a universitywide basis can provide opportunities both for educating the public in general about the major environmental issues associated with the oceans as well as for educating a variety of technical and scientific specialists. By doing this, marine science education programs would be contributing (and possibly even taking the lead) to broadening and improving the teaching of science, mathematics, engineering, and technology (SMET) across the institutional curriculum. This broadening of SMET instruction has been recommended by several recent major national reports including the Ehlers Report (1998).

For improving the education of the graduates of one's own program, the offering of an undergraduate degree (B.S.) in marine science programs should be dropped wherever it is offered. The undergraduates would be better served spending their time improving their foundational technological proficiency in a core discipline. Programs should increase their cooperation with colleges of engineering, business, and education. This will help obtain for one's own graduates the attributes they need. In addition, this collaboration will reciprocally strengthen the graduates of these other programs. Increased emphasis should also be placed on master's level graduates and master's degrees

should be introduced into programs where only the Ph.D. degree option exists. The master's degree should not be considered a booby prize awarded to those incapable of obtaining a Ph.D. but should be considered as proper preparation for graduates who want to accept opportunities for nontraditional careers in business and industry instead of the more traditional careers of public (government) service or academia. Helping students get summer job experience and internships will improve both their opportunities for jobs in business and industry but will also contribute to their acquiring the basic set of essential qualities and skills needed for career success.

One of the more important skills that marine science education programs should begin teaching their own graduates is how to advise policy and management decisions. Another important skill that should be taught to graduates is how to deal with the outcomes of the multiplicity of major ocean research programs. The study, *Oceanography in the Next Decade*, predicts that many ocean scientists will work in jobs in which they will benefit from a knowledge of how to manage major ocean research programs and how to coordinate them. Because most faculty members are not experienced with either the advising of policy or the management of major programs, there are two alternatives for them to acquire this knowledge and skill. One is to collaborate with other schools and colleges to get access to those who have this expertise. The second is to outreach to the community in order to gain this experience through direct involvement.

Community outreach activities which could address the above include having industry and government representatives on advisory boards for the education program as well as getting government and industry representatives on campus and in the classrooms as teachers, as presenters of talks or seminars, or as panelists. Students could, as part of the curriculum, work on projects which address policy issues. Faculty and students both can increase their involvement with the informal education process. This could be done in a number of ways including the studying and critiquing of books, TV documentaries, and web sites. The latter two would permit exploration of the importance of television and of the World Wide Web as media for conveying information while demonstrating both their capabilities and limitations. Becoming involved with professional societies and both encouraging and assisting these professional societies to become involved with education is another possible activity. This active involvement would also set an example for the students to emulate. Societies whose memberships are primarily from other areas than academia should be targeted for these efforts.

VI. SUMMARY

The statement in The Heinz Center report, *Our Ocean Future*, cited earlier, bears repeating here because it should help serve as an excellent motivator for implementing changes based on the ideas expressed in this paper. The report states that the vigor of the national ocean science and technology program depends directly on the availability of a well-educated and trained pool of talent, ranging from technicians to Ph.D. and goes on to ask the following two meaningful questions: Is the present institutional framework adequate to educate and retain the necessary talent? Are the resources available to those institutions to meet the broader educational needs of the country?

VII. LIST OF REFERENCES

1998, Bruce McKay, Kieran Mulvaney, and Boyce Thorne-Miller, *Danger At Sea: Our Changing Ocean*, (unpublished, <http://www.seaweb.org/danger/>)

1998, *Our Ocean Future*, The H. John Heinz Center for Science, Economics, and the Environment, Washington, D.C., (unpublished, <http://www.heinzctr.org/publications/>)

1998 International Year of the Ocean - Discussion Papers (unpublished, <http://www.yoto98.noaa.gov/papers.htm>)

1998 Unlocking Our Future: Toward a New National Science Policy. A Report to Congress by the House Committee on Science. September 24, 1998. (The Ehlers Report)

Oceanography in the Next Decade: Building New Partnerships. National Research Council. 1992. 202 pp. National Academy Press.

"Naval Oceanography: Start of the Next Millennium"

Dr. Donald L. Durham
Technical/Deputy Director,
Naval Meteorology and Oceanography Command
and
Mr. Kenneth D. Cooper
Deputy Technical Director,
Naval Meteorology and Oceanography Command

ABSTRACT

On the eve of the 20th Century, the United States was in the midst of a physical science renaissance as internationally renowned scientists measured and analyzed the natural world, and explorers stretched its geographic boundaries to yield new frontiers for science.

Naval Oceanography entered the 20th Century with chronometers, sextants, lead lines, log books, logarithm tables and pilot charts. On the eve of the 21st Century, Naval Oceanography is equipped with precise time and time interval, the Global Positioning System, multi-beam echosounder systems, global data warehouses, supercomputing, and softcopy products transmitted globally.

The paper, "Naval Oceanography: Start of the Next Millennium", describes the course upon which the United States Navy is embarked at the outset of the 21st Century to meet the continuing challenge of ensuring Navy's ability to fight effectively under all weather or ocean conditions.

Navy's needs challenge the advancement of basic and applied ocean sciences in the world's littorals. The natural littoral environment is a complex ecosystem, inter-relating meteorology, oceanography, and related marine sciences.

Monographic descriptive oceanography, which dominated much of the past century, is now expanding to embrace a fully integrated systems interaction approach. This applies to measurement systems, resultant geospatially referenced data and coupled air-ocean modeling. Measurement and observation sensors and techniques are moving toward smaller, more capable sensors deployed from more cost-efficient, unmanned platforms. Remotely sensed data are continuously being refined to detect increasingly more detailed ocean features. Vast streams of collected information - well beyond the terabyte a day range of today's advanced sensors - will be fused from multiple data sources and viewed in three- and four-dimensional data assimilation. Massive parallel processing and visualization will be the commonplace tools used to communicate complex answers tailored to the specific needs of a wide range of users - even in remote locations.

Navy Oceanography is poised to embrace true rapid environmental assessment on location as an integral part of operational primacy through harnessing the latest, rapidly advancing, high-technology information and ocean science.

Workflow Management in an Oceanographic Information Processing Environment

John A. Lever, Landry J. Bernard III,
Robert Starek, John Easton,
Christine M. Jarrett, Michael Jugan

Naval Oceanographic Office
Stennis Space Center, MS
39522-5001

I. Background

A. Organizational

The mission of the Naval Oceanographic Office (NAVOCEANO) is *"to conduct multidisciplinary military ocean surveys; to collect and analyze all-source oceanographic data; and to generate operationally significant strategic and tactical products and services which address U.S. Navy and DoD oceanographic needs for effective weapon and sensor system performance and safe, accurate navigation."* In this framework, NAVOCEANO constitutes a production environment, assimilating oceanographic measurements and producing products for operational customers. The products can take the form of oceanographic databases, tactical charts, analyzed imagery, textual reports, real-time products such as Multi-Channel Sea Surface Temperature or altimetry-derived wave heights, or any of a number of other operationally significant products. Virtually all production at NAVOCEANO operates on information, normally oceanographic data or products. Production can consist of automated processing, databasing, or operator intelligent analysis. In any case, it is generally possible to construct detailed process flows that capture the form of the production.

B. Definition

Workflow Management (WfM)¹ refers to software methodology that provides a framework for tracking the production of work products. A WfM implementation would typically include mechanisms for recording and maintaining records of the work items, assigning a work item to an individual or process, recording pending/in-work/completed tasks against the work item, maintaining the suspense date for the work item, and recording completion of the item. The WfM implementation (also Workflow Management System (WfMS)²) would also provide mechanisms for the supervisor to obtain information such as number of items recorded for processing, suspense dates/times, status of progress against the work items, completion of the work items, amount of work recorded per individual, and so on. In other words, the WfM tool can maintain a dynamic database of most types of information that describe the totality of work at any given point in time. Typical uses for WfM include office type functions such as the processing of any type of transactions; e.g., insurance claims. This paper concerns Workflow Management as defined by the Workflow Management Coalition (WfMC).³

C. Derived Benefits

- Awareness – WfM provides a mechanism by which management can determine the status of each work item; i.e., how much work has been performed on a product, how much remains, estimated delivery, etc.
- Accountability – In a workflow-managed environment, it is possible to determine

¹ Workflow Handbook, Workflow Management Coalition, 1997

² Workflow Management Coalition Terminology and Glossary, Document Number WfMC-TC-1011, Workflow Management Coalition, June 1996

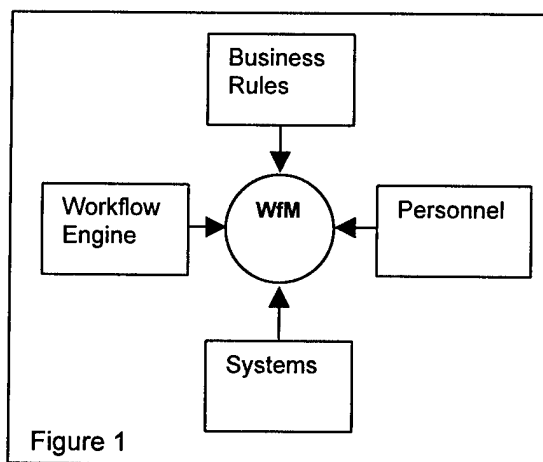
³ *ibid.*

levels of production at personal, departmental, and organizational scales.

- **Measurability** – WfM provides a natural way to collect metrics that are useful to determine organizational performance.
- **Productivity** – WfM lets the manager balance workloads, correct production problems, and take other actions to improve productivity from an informed position.

D. Key Components

The key components required to implement Workflow Management are: (1) business rules that capture the production activities of the organization; (2) the personnel who are the foundation and enduring element of production, (3) the systems that are used to generate the products, and (4) a workflow engine that tracks, monitors, routes, and schedules the work activities (see Figure 1).



II. Implementation

A. Prior Implementation Areas

NAVOCEANO has implemented Workflow Management in two separate areas to date; both implementations have been referred to as the Production Management Tool (PMT). The PMT can be described as an implementation of

WfM that is customized to specific production areas at NAVOCEANO. PMT consists of a Commercial off-the-Shelf software package augmented with NAVOCEANO production rules, a custom user interface, and custom-built modules for receiving Requests for Product (RFPs) and maintaining a historical source package of references and imagery used for each request.

- **WSC** – The Warfighting Support Center (WSC) Special Products Division implementation of the PMT provides a means to track work against RFPs. An approved RFP causes the generation of a custom product in support of a specific customer requirement; the product normally takes the form of a report or analyzed image. As the Fleet Interaction Branch receives an RFP, it is entered into the RFP database or RFP Application Module, a part of the PMT. The PMT then maintains status information on the RFP, including such items as suspense date, customer name, customer Area of Responsibility (AOR), product type, product spatial location and extent, and mission supported. It also maintains a source package for each RFP, which carries information about the sources of materials used in the preparation of the product. The branch supervisor uses PMT to track the numbers and types of RFPs that are pending with the associated suspense dates and which RFPs are assigned to which analysts. In this way, the workload can be managed and balanced. PMT allows the supervisor to generate production reports detailing metrics on status (completed, new, approved, waiting, rejected, cancelled), RFP by customer, request date, request due date, completed RFPs, RFPs due today, overdue RFPs, and RFPs completed after due date. In addition, an auxiliary report writer is available which allows for more complex queries such as how many priority one requests were made within a date range, what customer asks for a particular product,

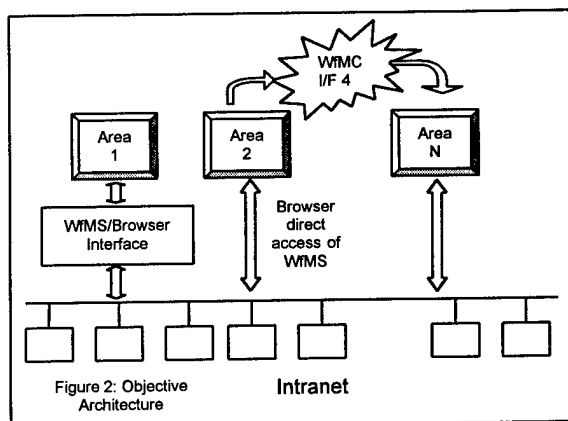
how many RFPs were produced by a particular branch, etc. The latter reports are particularly useful in answering *ad hoc* management queries.

- **STOIC** – The Special Tactical Oceanographic Information Chart (STOIC) is a customized tactical environmental support tool that combines hydrographic and oceanographic information together in one product. STOICs are used by the Fleet for operational, exercise, and mission planning support. They are produced in paper and digital format for littoral regions, typically to a 1:25000 scale (8x8 nautical mile area), for a specific time frame or by season. The center portion of the chart consists of the hydrographic soundings, contours, coastal features, and other hydrographic information. Around the perimeter of the STOIC are the oceanographic Essential Elements of Information (EELs), which consist of graphs, tables, or text for the area. These EELs can include currents, physical properties of seawater (temperature, salinity and sound speed), bottom composition, fishing, shipping, dangerous marine life, and underwater visibility. These varieties of hydrographic and oceanographic information are produced by several NAVOCEANO organizational elements. PMT will be used for RFP tracking and work assignments throughout the various divisions and used to generate product metrics and reports.

B. Architecture

The current implementation of workflow at NAVOCEANO is limited to the two production areas mentioned above. Also, these areas function independently, so there is no interface between them. Each area operates in a client-server configuration using single-vendor commercial software and a tailored user interface. The objective architecture (Figure 2)

would include multiple process areas, operating on multiple servers (with a nominal correspondence between process and server). The architecture would include an interface between the server and a Web-type browser, so that (1) multiple instantiations of the client are not required, and (2) more workers have access to the server (and process). WfM servers which directly support access by Web browsers are also desired. In the objective architecture, servers (and processes) would be linked to form a more inclusive end-to-end process flow. This could be accomplished by implementing WfM applications on vendor packages that are compliant with the WfMC Reference Model Interface 4 for Workflow Interoperability.⁴ Conceivably, the entire production could be implemented in this way, providing access at any point by a manager at any location through a Web browser.



The description above presents a high level representation of the objective system architecture across the enterprise. One specific process area is of interest for its particular extension to the traditional workflow model. The WSC operates a real-time satellite processing center for Multi-Channel Sea Surface Temperature (MCSST) and Altimetry Data Fusion. The WSC also operates ocean models for waves, tides, and three-dimensional temperatures in the Department of Defense

⁴ "Workflow Standard – Interoperability Internet e-mail MIME Binding," Document Number WfMC-TC-1018, Workflow Management Coalition, 25 September 1998

High Performance Computing (HPC) Major Shared Resource Center (MSRC) at NAVOCEANO. These real-time and time-critical dynamic processes generate products that are combined with imagery, bathymetry, and atmospheric data in response to RFPs. The monitoring of the automated processing is a natural extension of the original PMT.

Workflow management in automated production systems decomposes into multiple batch executions with relatively short time-steps compared to interactive analytical processing, the domain of the traditional workflow model. In a given computer process, there are several independent variables that influence process flow. The underlying components of network availability, data availability, process status, and system status constitute the building blocks for a comprehensive workflow management system. Workflow statistics that are not supported by information technology availability statistics do not yield accurate information about the process flow.

The workflow sub-components being developed to support the PMT extensions include an event-driven monitoring system for collecting status about data and processes. When completed, the Millennium Concentrator System (MCS) will provide visibility into critical path connectivity, parent and child process status, system availability, and data availability. These process variables will be tracked end-to-end from product initiation to the final Web posting and customer data pull. A time-correlated error-mapping function will augment the production status. The MCS will use Hypertext Markup Language (HTML), Secure Socket Layers (SSL), and JAVA to develop custom interfaces to existing process monitors and use a Web client to display concentrated status information. The process concentrator engine will be a Relational Database Management System (RDBMS).

The MCS will not be designed as a monolithic application, but will use agents designed to work in specific domains. These agents will gather information in their respective domain and pass the information to the concentrator; in this way the system operates much like a hub-and-spoke distribution. Having a set of independent spokes will reduce the costs of development by allowing the integration of existing applications into the MCS. The hub-and-spoke design will also permit an incremental development path. Spoke agents can be tailored for process and domain-specific criteria. For example, the MSRC agents will have different reporting functions than the agents designed for the WSC computer center. The agents will also have a dual role to allow agents to report on the status of other agents. This dual reporting will ensure that reported system failures are not simply reporting errors. The notional process/data flow using this implementation is characterized in Figure 3.

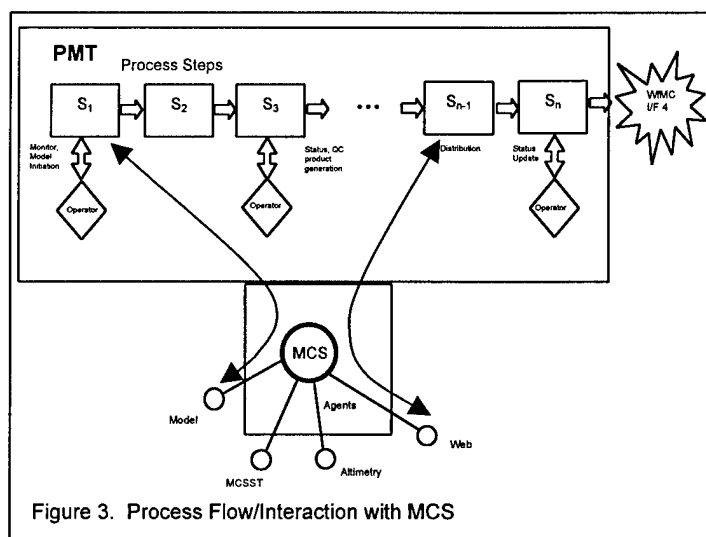


Figure 3. Process Flow/Interaction with MCS

C. Required Technology

The PMT uses a commercial workflow engine and a commercial relational database system. A tailored interface for the PMT was designed to customize the application for specific NAVOCEANO requirements. This

application operates in a client/server mode using vendor client software. The MCS will employ a Web-based application using JAVA applets and HTTP protocols in addition to a relational database engine. Unique security concerns will limit the direct query of processes by the concentrator. The agent software design will require a persistent application profile with the ability to automatically restart an agent process. The agent-to-agent communication will permit this self-start feature. The application design will weigh the advantages of SSL, Virtual Private Network (VPN), and encryption as design criteria. The PMT application will function at a higher level application layer in the system architecture. The information stored by the PMT will be available to the MCS through the RDBMS Application Programmer Interface. This server/browser architecture will utilize PMT information without the additional cost of client licenses.

III. Future Direction

The NAVOCEANO enterprise forms a production environment which encompasses

multiple diverse production areas, as shown in Figure 4. A process flow for a particular product line can be envisioned as a thread through the production areas, beginning with Collection Management through Product Dissemination. For example, a process thread could be constructed for a hydrographic database as follows:

- Collection Management – survey planning
- Data Collection – post-processing of soundings, single and multibeam sonars
- Information Warehousing – storing collected values in the NAVOCEANO Data Warehouse
- Product Generation – build and quality control the database
- Product Dissemination – distribute database as a standard product

Further levels of decomposition are both possible and necessary, down to a discrete work unit that can be managed. Even at the top level, the progress status provides useful information to senior management.

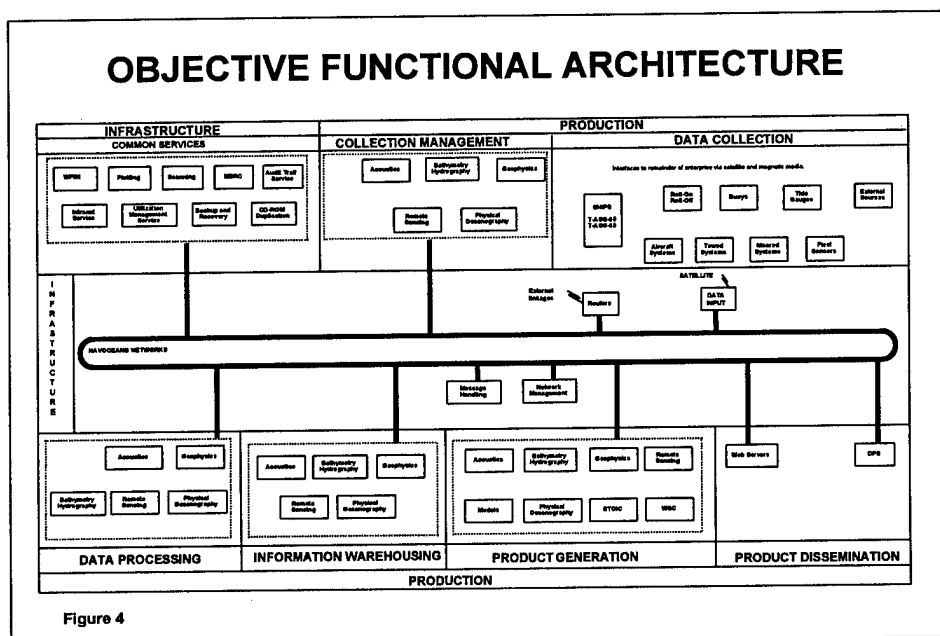


Figure 4

This level of visibility into the Office-wide production process remains a goal, however. Process flow throughout the Office is not as well circumscribed as the two cases mentioned earlier. Production rules are "in people's heads," following *ad hoc* procedures to some extent. Tracking is done either on paper or in process-unique databases. At present, there is no automated way to track production from end to end. To get to the desired state of Workflow Management will require a thorough understanding of the processes. Process modeling is required; the preferred method would consist of formal documentation using IDEF-0 methods. A few process areas have been documented to that level of detail. The Mine Warfare production area has a full set of process documentation and is well suited for WfM implementation. That implementation is under consideration for FY00.

It is envisioned that we will continue to evolve the Workflow Management capability at NAVOCEANO through the staged implementation of singular applications.

Ultimately, a more generalized approach could be undertaken which would provide full generality throughout the production environment. This approach would involve the decomposition of the environment into "processing categories," similar to those in Figure 4, and "functional processing units" (FPU) as subsets of the categories. A functional processing unit would consist of the formalization of a work unit, and could comprise a combination of entities such as human-executed tasks or software processes; in other words, the functional capabilities to accomplish a discrete task of limited scope. A workflow would consist of the FPUs "snapped on" a workflow backbone. Ultimately, a "Workflow Architect" could be commissioned with full access to tools designed to combine FPUs into processes in a near-dynamic fashion. A by-product of this approach is that rather than building workflow engines for existing work environments, the processes would be constructed using workflow tools, and be immediately ready for workflow monitoring.

A Concept for the Naval Oceanographic Office Survey Operations Center

John A. Lever, Stanley Raffa,
CDR David McCarren,
Alfred Lewando,
Dr. Michael Carron

Naval Oceanographic Office
Stennis Space Center, MS
39522-5001

I. Background

The Commander, Naval Meteorology and Oceanography Command, operating under the Oceanographer of the Navy in the Office of the Chief of Naval Operations (OP-096), collects vital information about the ocean through its field activity, the Naval Oceanographic Office (NAVOCEANO).

NAVOCEANO, located at the John C. Stennis Space Center in Mississippi, exercises technical control over a fleet of eight permanently forward-deployed survey ships, collecting oceanographic, geophysical, and hydrographic data in, on, and above all the world's oceans. These survey ships are operated by the Military Sealift Command and are manned by civilian contract mariners and civilian oceanographers and technicians. After analysis and processing at NAVOCEANO's facility at Stennis Space Center, the data are delivered to fleet operational units or the National Imagery and Mapping Agency (NIMA).

NAVOCEANO collects bathymetry data and provides this information to NIMA for processing and printing of nautical charts. Geophysical data, such as gravity, are collected and processed to support a

variety of Department of Defense (DOD) weapons systems and performance prediction models.

Military surveys are conducted all over the world, and survey missions are determined using a stringent requirements process. (When operating in-theater, the appropriate Naval Component Commander assigns the ships a Task Force Element designation.) While equipment used for data collection during military surveys is similar to that used in marine scientific research, information from military surveys, regardless of security classification, is not for general use by the scientific community.

II. Introduction

A. Current Process

NAVOCEANO ships operate for 10, 26-day surveys per year, with scientists traveling to the ships for two survey legs, or about 60 days deployed at a time. These survey teams are manned with the skills to provide the necessary knowledge to support the specific data collection efforts of each survey. Our survey ships collect data from a minimum of 15 different systems during each survey and often carry additional sensors aboard. The data collected are checked onboard for completeness and quality, stored, and shipped back to NAVOCEANO during in-port periods. Post-processing at NAVOCEANO often takes as long or longer than the collection effort. If problems due to sensor calibration, deterioration of sensor performance, or software malfunction are discovered in the data during this post processing, hundreds of thousands of dollars worth of collection efforts can be invalidated. In-port periods are used for updating and testing software and hardware improvements and upgrades. Often survey days are lost to support the sea trial periods of these upgrades.

B. Need for Change

New digital sensors are collecting ever-increasing quantities of data. In many cases these data are even more sensitive to small changes in environmental conditions or sensor performance. With the goal being total bottom coverage with many of these sensors, the concern over holes or "holidays" in the data requires much more careful monitoring of survey progress. In this world of downsizing of budgets and manpower it is essential we leverage technology to optimize our skills and deal with the rapidly increasing data flows from these new sensor technologies. To provide for the necessary talents to support this multidisciplinary effort, a substantial and expensive training effort is required to ensure that each team has the necessary skills to support and monitor all these systems. With a greater emphasis on simulation and modeling to rehearse impending conflicts, the fleet has an ever-increasing need for data in near-real time. Accordingly, NAVOCEANO has a need for an ever-increasing data communications/processing bandwidth.

C. Need

We need to optimize our precious and skilled labor force over more than one ship at a time and leverage a shrinking budget to do this. We need to use improved connectivity to the ships to allow many of these functions to become "cyber" functions. Specific areas we hope to affect include:

- Better planning and survey support
- Better use of highly skilled manpower
- Upgrade, monitor, and troubleshoot systems and sensors
- Increase data flow throughput
- Provide near-real-time support to models and products

III. Operational Concept

A. General

The NAVOCEANO Survey Operations Center (SOC) will enable scientists, engineers, and analysts ashore to evaluate the status and performance of shipboard systems and the quality of data collected from ships deployed around the world. Watchstanders will also remotely manage software configuration control, initiate shipboard software upgrades, troubleshoot onboard data collection systems, and monitor survey progress and coverage to assist with on-scene decisions. Oceanographic and hydrographic data and associated quality control information will be transmitted to shore from each ship several times each day, via a high-speed satellite link, based on the operational need of the end user. A series of protocols, referred to as "*data tiers*," will be established to determine the precedence of data types and associated metadata for transfer, when bandwidth or some other constraint limits the amount of data that can be transmitted from each ship. A discussion of data tiers during various operational scenarios follows in the next section.

Data received and processed in the SOC will immediately be warehoused for ready access in the DOD Major Shared Resource Center. Data that are returned to NAVOCEANO by more conventional means (i.e., hand-carried or mailed) will continue to be processed and warehoused at NAVOCEANO's data ingest facility using the same methods as in the past.

The costs associated with the SOC will be quickly amortized for several reasons. Fewer people will be required to post-process data at sea. There will no longer be a need for major post-processing system hardware upgrades for each of the eight ships. Survey operations and data quality control, post-processing, and warehousing will be much more efficient.

B. Data Tier Definitions

1) Monitoring and Perishable - bundles of data in near-real time to monitor Operations and to support quality control, modeling, and operation of shipboard systems. These are perishable data and include such elements as: water profiles, light attenuation, sea surface temperature, weather, navigation, meta-data on collection efforts, and quality control data.

2) Special Product Data - nonperishable data for rapid turn-around, single beam, Acoustic Doppler Current Profiler, and special data sets being collected without onboard experts. These are smaller data sets that are of a reasonable size for electronic transmission. These data are needed for rapid turnaround in support of exercises and operations.

3) Mega Data - raw data, backups, and data sets that are too large to be transmitted to the office electronically.

C. Operational Modes

1) Normal Mode - would have tier one data coming back at intervals throughout the day. The data coverage displays would be continually updated with sample sites indicated. These data would be catalogued and stored on receipt for access through the data warehouse and online data servers. This would make the data available to modelers and the Warfighting Support Center (WSC) in near-real time. The two watchstanders monitoring the eight ships from the SOC would be watching the progress and contacting various NAVOCEANO codes when they observe problems or any issues arise. They would have access to the Integrated Survey System operator screens aboard the ships and conduct daily video-teleconference (VTC) sessions with the senior scientists

aboard each ship for the coordination of supporting actions throughout the office. Engineers and software administrators would be able to log on to the shipboard systems and evaluate performance of systems and conduct troubleshooting and software support from the SOC. Not only would the watchstanders in the SOC be available to support the teams on the various ships, but the ship teams themselves could assist teams on other ships. For example, if a system on the USNS HENSON was malfunctioning and the most experienced technician for that system was on the USNS BOWDITCH they could VTC and collaborate on the way to proceed. Similarly it might be possible for the physical oceanographer on the USNS PATHFINDER to monitor the performance of the systems on the USNS SUMNER and perform as a "cyber" member of the team.

2) Special Product Mode - would see the same operation as discussed above for Normal Mode and additional time to support the real-time or near-real-time transmission for one or more data types to support a need for a special product. This might be bathymetry, sidescan sonar imagery, or backscatter imagery to support a special product. This mode would be used when the size of the area of interest was relatively small compared to the data collected in a day. Again, these special data could be watched more closely during the collection process for quality and be almost immediately available for products.

3) Rapid Assessment Mode - in addition to normal mode support this would involve continuous connectivity to the ship for the transmission of tier 1, 2, and 3 data back to NAVOCEANO for the building of products. It will be more effective to transmit these data back to NAVOCEANO vice passing them in-theater to a user since much of the data to be merged with these collected data sets are held here and the manpower to build the products is available to the WSC.

The communications pipes are in place to push those products from here.

IV. Systems Integration

A. Integration Strategy

The SOC will be deployed using a low-risk phased integration strategy. It is envisioned that integration will be effected using phased capabilities to provide proofs of concept early on. The initial phase will consist of the following activities:

- Requirements Definition
- Equipment Acquisition
 - Shipboard
 - In-house computers
- Communications Leases
 - Space
 - Terrestrial
- Equipment Installation on T-AGS 62
- Initial Software integration

The completion of those activities will result in an Initial Operational Capability consisting of data connectivity and limited monitoring capability on one platform, T-AGS 62.

The next phase would be the completion of integration for one platform, including the following:

- Completion of in-house computer hardware integration
- Software modifications to allow access to the Integrated Survey System
- Visualization Software
- An Operational Evaluation
- The result of these activities will be a Full Operational Capability for one platform.

Successive activities will consist of communications installation aboard the other platforms, and concurrent upgrades of the in-house capability:

- T-AGS 60/61/51
- T-AGS 63/64/65/52

B. Data Communications

To date, the SOC integration efforts have concentrated on data communications, since the definition and acquisition of communications capabilities to support the required bandwidth was viewed as perhaps the most difficult challenge.

The commercial C-Band satellite system has been selected because of the high bandwidth data communications and worldwide coverage. NAVOCEANO survey ships operate on a global basis and the C-Band satellites can provide two-way T1 (1.544 MBps) communications between ships and the SOC. Table 1 shows the required transmission times for tiered data at T1 rates.

Type	Volume for 1998	Volume for 1999	Volume for 2000	Volume for 2001	Volume for 2002	Volume for 2003
T-AGS 51						
TOTAL	12.5 GB	1172.5 GB	1245 GB	1245 GB	1845 GB	1845 GB
Air Time per day @ E1 rate (Hrs)	0.05	5.05	5.36	5.36	7.94	7.94
T-AGS 52						
TOTAL	12.5 GB	12.5 GB	1165 GB	1245 GB	1845 GB	1845 GB
Air Time per day @ E1 rate (Hrs)	0.05	0.05	5.02	5.36	7.94	7.94
T-AGS 60						
TOTAL	105 GB	1338 GB	1338 GB	2218 GB	2218 GB	2218 GB
Air Time per day @ E1 rate (Hrs)	0.45	5.76	5.76	9.55	9.55	9.55
T-AGS 61						
TOTAL	105 GB	1338 GB	1338 GB	1938 GB	2218 GB	2218 GB
Air Time per day @ E1 rate (Hrs)	0.45	5.76	5.76	8.34	9.55	9.55
T-AGS 62						
TOTAL	505 GB	1618 GB	2218 GB	2218 GB	2218 GB	2218 GB
Air Time per day @ E1 rate (Hrs)	2.17	6.97	9.55	9.55	9.55	9.55
T-AGS 63						
TOTAL		1418 GB	2218 GB	2218 GB	2218 GB	2218 GB
Air Time per day @ E1 rate (Hrs)	0.00	6.11	9.55	9.55	9.55	9.55
T-AGS 64						
TOTAL		0 GB	0 GB	2218 GB	2218 GB	2218 GB
Air Time per day @ E1 rate (Hrs)	0.00	0.00	0.00	9.55	9.55	9.55
T-AGS 65						
TOTAL		0 GB	0 GB	0 GB	2218 GB	2218 GB
Air Time per day @ E1 rate (Hrs)	0.00	0.00	0.00	0.00	9.55	9.55
Summary						
Year	FY 98	FY 99	FY 00	FY 01	FY 02	FY 03
	740 GB	6897 GB	8522 GB	13300 GB	16998 GB	16998 GB

Table 1. Data Volumes/Transmission Time

The shipboard configuration will include a 10-foot satellite dish with control electronics for satellite tracking. A stabilizing platform is necessary to compensate for ship motion. The entire satellite tracking system weighs less than 1000 lbs. Navigation inputs will be provided from the Global Positioning System to allow for acquisition of the C-Band satellites.

NAVOCEANO survey data collected from the Integrated Survey System (ISS-60) will be transmitted daily back to the SOC. System configuration will allow for voice, real-time video and Internet access. Ship to shore data rates require the highest bandwidth, and data rates up to 2048 KBps can be achieved.

All data transmitted from NAVOCEANO survey ships will be received at a gateway terminal on the east or west coast. Data will be routed through the Defense Research Engineering Network to the DOD Major Shared Resource Center at Stennis Space Center and finally passed to the SOC at NAVOCEANO. All data will be monitored in the SOC, and continuous feedback will be provided to all survey ships on the quality of the survey data. Shore to ship data rates will allow for up to 384 KBps.

V. Summary

The SOC represents a major paradigm shift towards a network-centric mode of operations for U. S. Naval oceanography. The virtualization of the oceanographer's functions will serve as a force multiplier; in this way the Naval Oceanographic Office will participate in the evolution toward the DOD's Joint Vision 2010.

USING A MINEHUNTING SONAR FOR REAL-TIME ENVIRONMENTAL CHARACTERIZATION

Stephen C. Lingsch
William C. Lingsch

Naval Oceanographic Office
1002 Balch Blvd.
Stennis Space Center, MS 39522

Abstract

The Naval Oceanographic Office (NAVOCEANO) provides environmental support to Mine Warfare (MIW) in digital form for characterizing the environment. These data include bathymetry, sediments, mine burial probability, and climatology for currents, temperature, and salinity prior to an exercise or operation. In most cases high-resolution databases needed by MIW are on the order of centimeter spatial resolution, much higher than available databases. The minehunting phase of the operation using AN/AQS-14 minehunting side-scan sonar provides this information. Data are processed using the Unified Sonar Image Processing System for the processing and databasing of the AN/AQS-14 sonar imagery. The Comprehensive Environmental Assessment System (CEAS), a Geographic Information System (GIS), is used for the integration of historical and in-situ environmental data. The AN/AQS-14 sonar imagery is processed in near-real time (12 hours), providing the Mine Countermeasures (MCM) Commander with the current environmental picture, used for tactical planning. The MCM Commander can direct his assets, which include side-scan sonar, forward-looking search sonar, and Explosive Ordnance Demolition (EOD) divers efficiently, or avoid areas which are not huntable.

The AN/AQS-14 side-scan sonar data are georeferenced, allowing for bottom characterization and identification of provinces in accordance with current MIW doctrine. In addition to bottom characterization, georeferencing can show sonar system artifacts not apparent in the standard waterfall display. Change detection is also performed, with historical data or data collected during the operation.

In addition to sonar imagery, environmental data from the EOD divers (e.g., temperature, bottom grabs, and visibility), temperature and salinity collected using Expendable Bathythermographs (XBT), and contact information are all entered into CEAS for comparison with climatology.

Presented are the GIS and image processing software, data-basing, and techniques used for MIW environmental support. Results will be presented from MIW exercises from the past two years.

I. Introduction

A major influence on Mine Countermeasures (MCM) operations is the environment. For the MCM Commander, detailed knowledge of his operating environment is essential to accurately predict Mine Warfare (MIW) sensor performance for both minehunting and minesweeping. The problem is that the littoral battlespace where these operations take place is dynamic in both time and space. Databases do not always exist in these "hot areas," and where they do they may be based on few real observations, necessitating extensive interpolation and/or interpretation. While these databases are very valuable for pre-mission planning, it is imperative to collect in-situ measurements to validate and build them, rather than assuming a single bottom type and sound velocity for an entire operating/exercise area.

Under the MIW Campaign Plan, sponsored by Expeditionary Warfare (N85), the Naval Oceanographic Office (NAVOCEANO) is tasked to develop high-resolution digital bottom-mapping (acoustic imagery) databases; environmental databases which include bathymetry, sediments, bottom roughness, clutter density, sound velocity, currents, visibility; and a master minelike contacts database. This effort leveraged off the current infrastructure of NAVOCEANO's Integrated Database Management System (IDBMS), the Comprehensive Environmental Assessment System¹ (CEAS), the Unified Sonar Image Processing System² (UNISIPS), and the scientific expertise within NAVOCEANO. IDBMS is the data warehouse at NAVOCEANO where all worldwide observed and derived databases (gridded and provinced) are stored. CEAS is a Geographic Information System (GIS) based system which fuses environmental data for display, overlay, and analysis. UNISIPS is used for processing side-scan sonar data and outputting full-resolution, georeferenced acoustic imagery mosaics at selected grid intervals. Outputs of these systems can be directly ingested into the MIW Environmental Decision Aids Library (MEDAL). MEDAL, the MIW Tactical Decision Aid (TDA) used by MCM forces, is a Joint Maritime Command Information System (JMCIS) software

segment that supports MIW mission planning, evaluation, and command and control.

A large effort of the MIW Campaign Plan at NAVOCEANO involves processing and databasing the MIW minehunting side-scan sonar data, AN/AQS-14 (AQS-14), at NAVOCEANO. These data are used to derive fleet products, such as bottom type (with additional ground truth data), bottom roughness, and clutter density, relating directly to MIW doctrine. In addition, the full-resolution data provide a picture of historical minelike contacts along Q-Routes and in other operational areas. Historical data can be compared during MIW operations with current data to determine if a bottom object is new, referred to as "Change Detection." Historical minelike contacts can be ignored, thereby increasing timeliness of the mission.

II. In-Situ Environmental Characterization

A. AQS-14 Sonar

The primary source for in-situ environmental characterization is the AN/AQS-14 side-scan sonar. The AQS-14 is a multibeam side-scan sonar towed from the Airborne Mine Countermeasures helicopter MH-53E. The AQS-14 system consists of an active, stabilized underwater vehicle that is towed by an electromechanical cable and winch. Multiple beams are formed along-track, allowing it to be towed at speeds up to 18 knots while maintaining full along-track coverage. Adaptive signal processing allows for "hands-off" operation through varying bottom reverberation environments. The towed vehicle maintains an operator-selected altitude above the bottom or depth below the surface by means of an active control system and sensors.

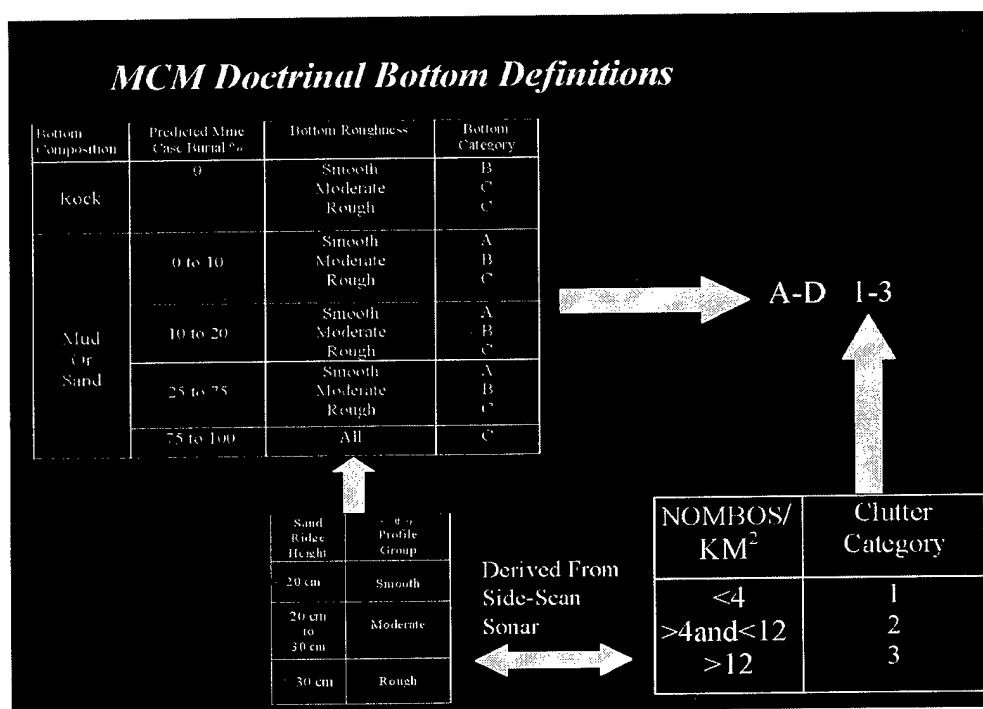
B. AN/AQS-14 Processing

Multiple missions or sorties are flown to search the operational area for mines, reviewing the data in a "waterfall" display for the detection of minelike contacts. The data are then passed to UNISIPS for standard side-scan processing and databasing, including navigation, radiometric, and geotectic corrections, and final mapping to a geodetic grid.

Once georeferenced, the bottom is characterized and provisioned according to MIW doctrine. Bottoms are categorized into four types (A-D) based on composition (mud, sand, and rock), mine burial, and roughness (sand ridge height), with clutter density being defined as the number of NOn-Mine-like-Bottom-ObjectS (NOMBOS) per km² (Fig. 1). Historical data and in-situ diver reports are used with the AQS-14 side-scan records to determine in-situ bottom types. These provinces are digitized in UNISIPS and imported into CEAS along with the geodetically corrected side-scan mosaics. These bottom types are provided to the MCM Commander, allowing him to alter routes to bypass unhuntable areas, redirect assets, and provide more accurate mine clearance estimates.

C. Change Detection

"Change Detection" compares high-resolution baseline databases against mission or in-situ data to determine whether an object is new. Prosecuting only new objects save valuable time and assets during an MCM operation. Issues currently being addressed are temporal perishability of databases, navigational accuracy required, and attitude/grazing angle dependency. These issues must be resolved in order to confidently assess whether or not a minelike object should be prosecuted. NAVOCEANO is building databases in exercise areas to test these issues.



D. Acoustic Imagery Data Structure

Once the side-scan imagery is entered into UNISIPS, rapid retrieval of the side-scan imagery for a given position is required for the comparison of historical vs. in-situ data. Due to the volume of data, both historical (50 – 100 Gb) and in-situ (25-50 Gb), an efficient data structure for rapid retrieval is necessary. The imagery data structure described allows for rapid access to the file and position within the file.

The region is divided into tiles, with each tile containing the geodetic grid. The data structure of the geodetic grid stores all the contributing "scanline" file polygonal boundaries, and relative pathname locations. When a position is entered, each tile is searched to determine the proper tile. Once the correct tile is chosen, the polygonal boundaries for each of the contributing files are searched; if the position lies within the boundary of the file, the file is displayed at the requested position. Fig. 5 shows the output of a search for both the historical and mission data.

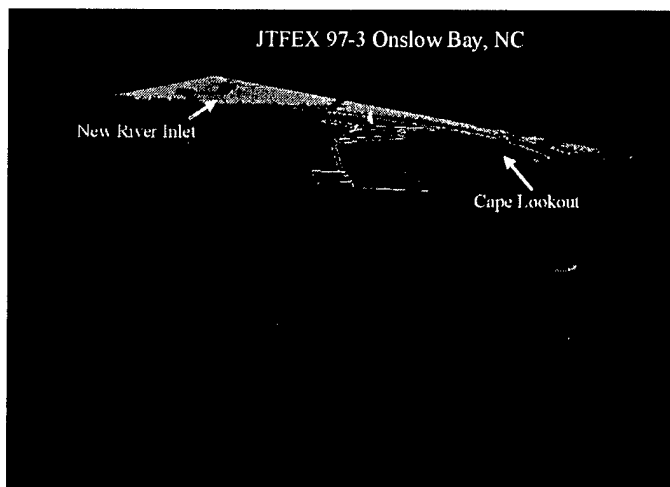


Fig. 2. JTFEX 97-3 Geometry.

III. Bottom-Mapping Examples

Two fleet exercises are used as examples of what is known as "Real-Time Bottom Mapping." The first example is the Joint Fleet EXercise (JTFEX) 97-3 held off Onslow Bay, North Carolina in September 1997. The second example is MARCOT/Unified Spirit 98, which occurred off Stephenville, Newfoundland in July 1998.

A. JTFEX 97-3

1. Overview

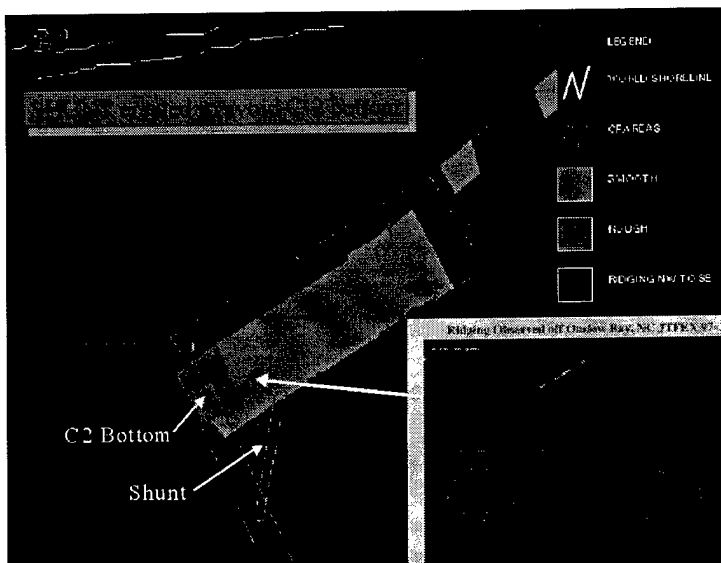
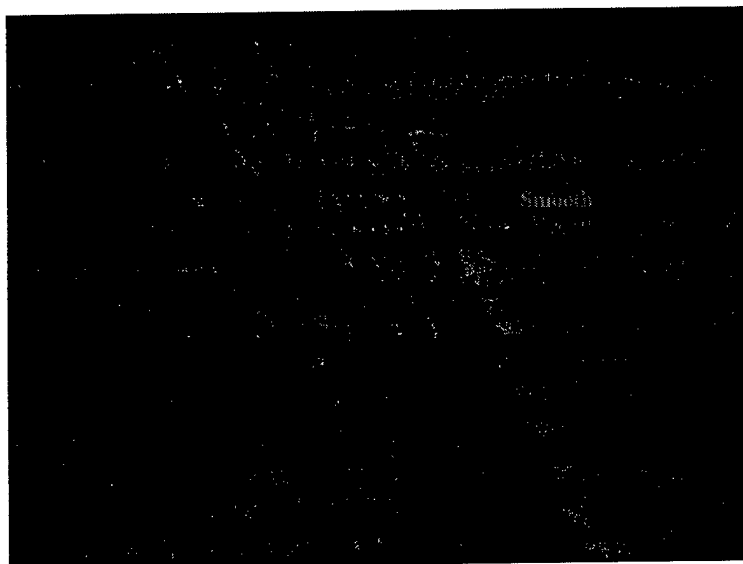
Digital historical data were provided by NAVOCEANO, including surface sediments, sound speed profiles (SSPs), bathymetry (gridded and soundings), currents, and high-resolution bottom imagery. Surface sediments, bathymetry, and SSPs were ingested into the MEDAL system. These historical

data were used for pre-mission planning and as input to the sonar performance prediction model. The sonar performance prediction model uses historical SSPs, depth, bottom type, and wind speed. In addition, bathymetry is used for mine threat, and bottom types are used for mine burial prediction. The software systems CEAS and UNISIPS were brought onboard the MIW Command Ship USS INCHON during JTFEX 97-3 to ingest data from MIW systems, update historical databases, and providing near-real-time products to the MCM Commander. The data included AQS-14 side-scan sonar, environmental dive reports from the Explosive Ordinance Disposal (EOD) Team, and Conductivity, Temperature, and Depth (CTD) data from the Battle Space Profiler (BSP). During the first three days of JTFEX 97-3, reconnaissance missions were flown with the AQS-14. The sonar was flown at an altitude that protected it from moored mines but ensonified the bottom for environmental provincing and initial minehunting. The geometry for JTFEX 97-3 is given in Fig. 2.

2. In-Situ Bottom Characterization

Eight to ten missions were flown daily. This generated about 4 Gb of raw data per day. Aboard the aircraft, a "first pass" review of the data was performed by sonar operators to detect minelike contacts on the Post Mission Analysis (PMA) system as the data were being recorded to a high-density analog tape. Onboard the USS INCHON, a more detailed "second pass" was performed for minelike contacts on the PMA system. The data were then passed to UNISIPS, processed, and further reviewed. Once all missions were flown for the day, a digital mosaic was created at a 2-m resolution. A sample mosaic of a day's mission is shown in Fig. 3. Although minelike objects are lost at this resolution, bottom trends showing areas of ridging and homogeneity are apparent. The UNISIPS software allows the operator to recall the full-resolution data from the mosaic in areas of interest.

The digital acoustic imagery mosaics were brought into CEAS and merged with other environmental data. Bottom provinces were digitized interactively in UNISIPS according to MIW doctrinal A through D categories. The clutter density also was calculated according to MIW doctrine assigning a value 1 through 3. Additionally, the ridging direction was reported for mission-planning purposes. Ridging can cause bottom mines to be hidden at specific aspect angles. These provinces were presented to the MCM Commander during morning briefs. The inset in Fig. 4 shows the full-resolution data and digital mosaic indicating ridging and medium clutter. This area was classified as a "C2" bottom that led to a decision by the MCM Commander to avoid it, and a shunt was created in CEAS and passed to MEDAL. Fig. 4 shows the bottom provinces and the Q-Route modified with a shunt to bypass the "C2" area.



EXERCISE MINE			
Datatype: UNISIPS		Datatype: UNISIPS	
Latitude : N 34 35.7323195	Width :	Latitude : N 34 35.7937663	Width :
Longitude : W 76 54.8816928	Height :	Longitude : W 76 54.8328576	Height :
Bearing : 274.6032	Run : 13679	Heading : 239.0112	Run : 11776
Pixel Value: 6	Column : 296	Pixel Value: 34	Column : 790
Query Lat/Lon	Target Width	Target Height	Max error line (m): 0.0
Close	Clear Text Fields	Close	Clear Text Fields
		s/014-12-3/052_053.u	

3. JTFEX 97-3 Change Detection

Historical AQS-14 imagery data over the area were provided from the previous year's exercise. This allowed the opportunity to perform "change detection." Fig. 5 shows two images, JTFEX 97-3 with the historical data, indicating that a new minelike object was on the bottom. After prosecuting this object it turned out to be an exercise mine. This concept worked well over homogenous bottoms, but in an area of clutter it could be difficult. Other limiting factors include navigation position errors and the dynamics of the oceanographic and meteorological conditions in the area.

B. MARCOT/Unified Spirit 98

1. Overview

MARCOT 98 occurred in St. George's Bay off Stephenville, Newfoundland. The geometry of the exercise is shown in Fig. 6. Digital historical data were provided by the Canadian Hydrographic Office, including bathymetry, surface sediments, acoustic imagery derived from Simrad EM1000, roughness, and mine burial prediction. Based on these data sets, doctrinal bottom type were derived (Fig. 7). Climatological data included SSPs and currents. As with JTFEX 97-3 bathymetry, bottom type and SSPs were used for the sonar performance prediction model.

2. Bottom Provincing

Based on historical data most of the sea floor in the exercise area was designated as B1 (left side of Fig. 7). However, through analysis of the AQS-14 imagery, a large portion of the area was designated as A1, with isolated rock gardens designated as B3 (right side of Fig. 7). Many of the false contacts in Fig. 7 lie within the rock gardens. Previous imagery from the EM1000 hull-mounted multibeam sonar was not of high enough resolution to detect the isolated rock gardens.

3. MARCOT Change Detection

Approximately 8 days into the exercise, a re-mining operation took place. AQS-14 missions were flown over areas previously covered during the exercise. Fig. 8 shows a georeferenced image collected on 8 July with the same patch of seafloor collected 12 July after the re-mining operation, clearly showing a mine laid during the reseeding operation.

IV. Conclusions

The use of in-situ environmental data collected by the fleet has been proven to be tactically useful. JTFEX 97-3 was the first time near-real-time digital mosaicing and bottom provincing were performed in a full production mode that has become standard during MCM exercises which employ the AQS-14 sonar. AQS-14 data along with EOD dive reports and BSP data provided the MCM Commander a detailed picture of the environment that allowed the MCM Commander to avoid high clutter areas, predict sonar coverage accurately, and operate the MIW sensors at the optimal aspect to avoid shading of objects. This directly affected the completeness and timeliness of the MCM exercise.

"Change detection" proved effective in homogenous and low-clutter bottom environments. The applicability of this method to other bottom types and clutter density areas still needs validating. Furthermore, the half-life of the historical contacts still remains to be determined. This will vary in different areas, depending on the dynamics and type of environment.

Although the MIW Campaign Plan effort at NAVOCEANO is focused on post processing these data and building large regional environmental databases, the benefits of near-real-time acoustic imagery bottom mapping proved extremely valuable to the MCM mission.

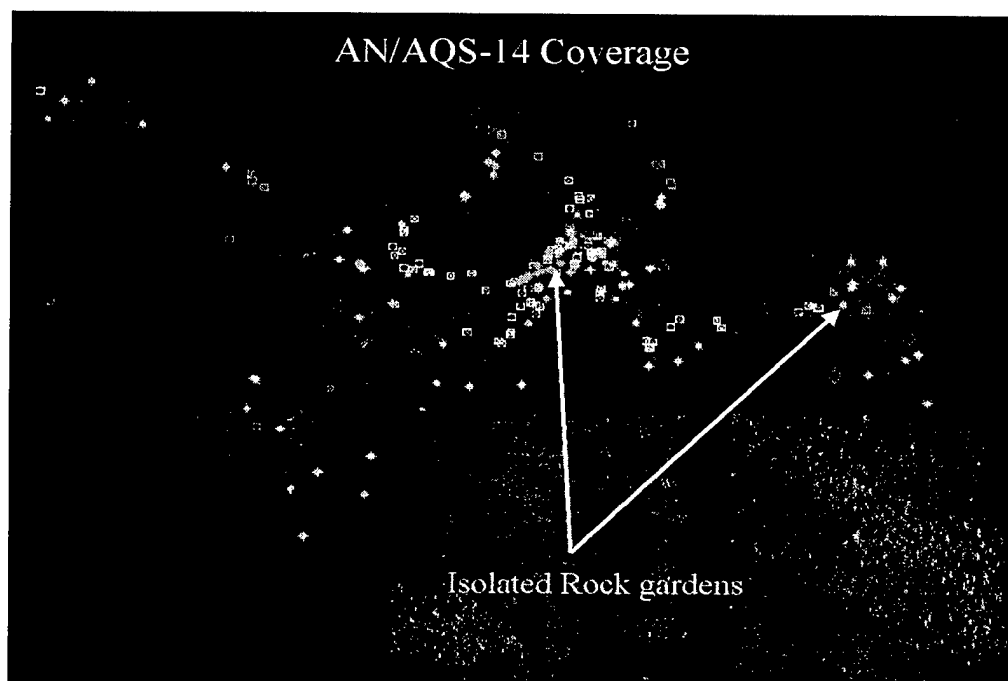
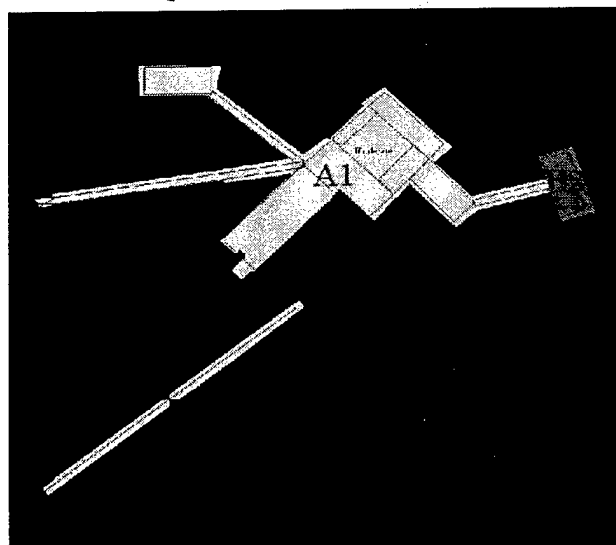


Fig. 6. MARCOT 98 Geometry and AQS-14 Coverage. The Inset Shows Typical Clutter Within Rock Garden.

Assumed Bottom Types Prior to
AN/AQS-14 Data Acquisition



Bottom Types Using In-situ
AN/AQS14 Data

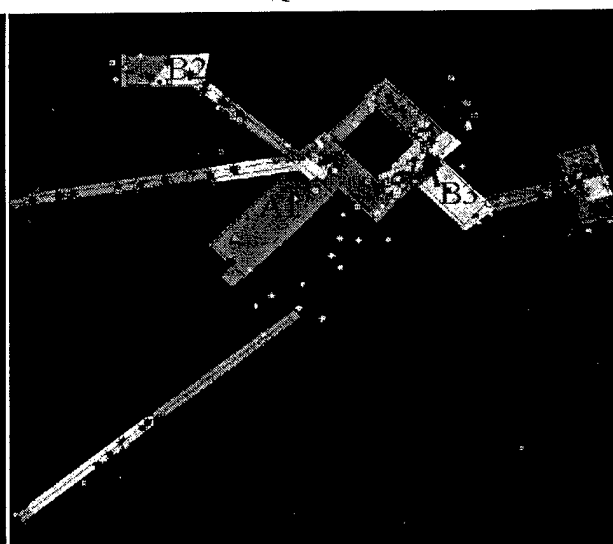
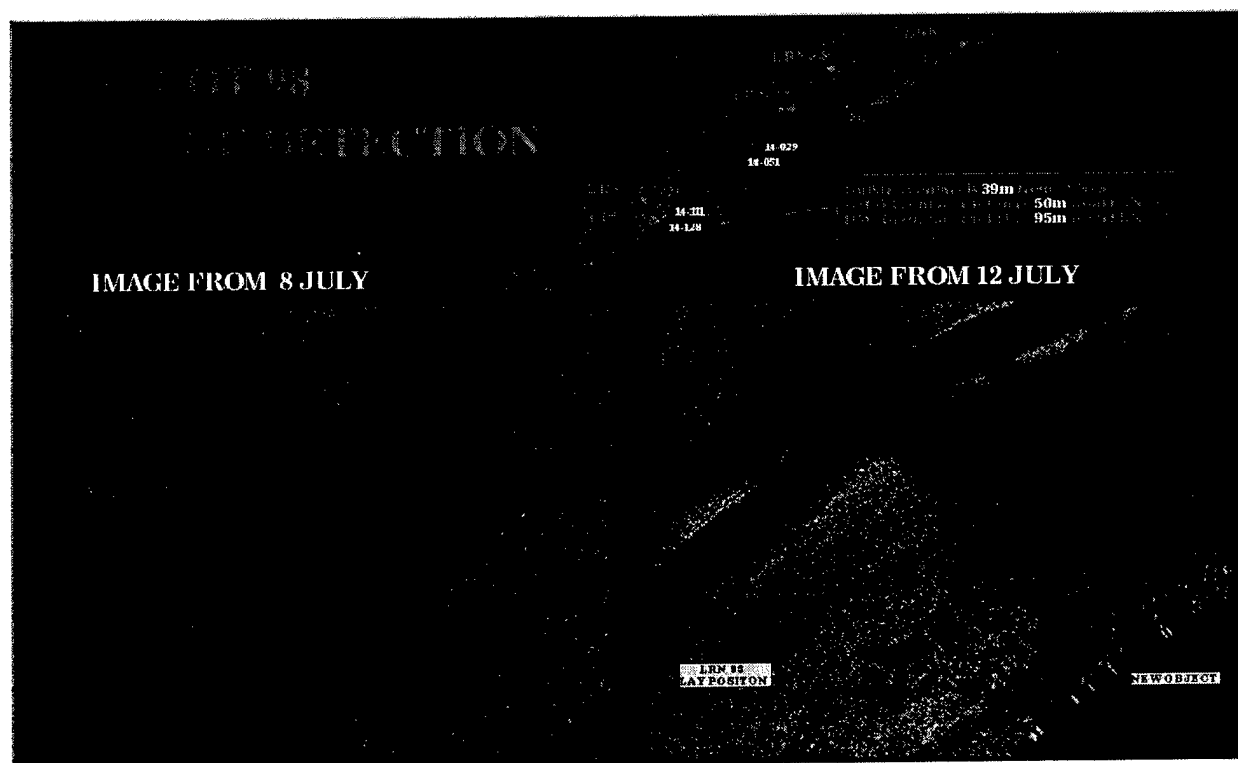


Fig. 7. Pre-Exercise Bottom Types are Shown on the Left with the Right Showing Bottom Types Using the In-Situ AQS-14 Data.



V. Acknowledgements

Without the coordinated efforts of the following programs, the success of the work presented in this paper would not be possible: the Office of Naval Research (ONR), MEDAL Program Manager, Code 322TE; Director, Expeditionary Warfare, N85, MIW Campaign Plan Sponsor; the Naval Oceanographic Office, and IDBMS, CEAS and UNISIPS Systems developers; MCM Commander Squadron Two; and the authors of the Mine Countermeasures Planning and Procedures, NWP27 Series, Commander Mine Warfare Command.

The authors would also like to acknowledge Mr. Mike Sandler (NAVOCEANO Code N351), Mr. Ken Grossman (NAVOCEANO Code N951), LCDR Mark Null (COMINEWARCOM) and LT Terry Hinkle (OA Division USS INCHON), and the entire OA Division onboard the USS INCHON during JTFEX 97-3 and MARCOT 98. Without the hard work and cooperation from this staff, this work would not have been possible.

References

1. Lingsch, S. C., K. Grossman and S. Mesick. 1996. *The Integration of Tools and Data Bases for Geophysical and Oceanographic Application in a GIS Environment*, Proceedings for 1996 ESRI Users Conference, Palm Springs, CA, 20-24 May 1996.
2. Lingsch, S.C., and C.S. Robinson. 1995. *Processing, Presentation, and Data Basing of Acoustic Imagery*, Oceans '95 MTS/IEEE Conference Proceedings, pp. 1582-1591.

TWELVE HOUR OPERATION OF CRUISING TYPE AUV "R-ONE ROBOT" EQUIPPED WITH A CLOSED CYCLE DIESEL ENGINE SYSTEM

Tamaki Ura* and Takashi Obara**

*Underwater Technology Research Center, Institute of Industrial Science, the University of Tokyo

**Underwater Systems Department, Mitsui Engineering & Shipbuilding Co., Ltd.

Abstract :

Institute of Industrial Science of the University of Tokyo and Mitsui Engineering & Shipbuilding Co., Ltd. are jointly developing an autonomous underwater vehicle called "R-One Robot" which is equipped with an air-independent power (AIP) system of a Closed Cycle Diesel Engine System (CCDE) for long range survey. The vehicle is 8 m in length and 4 tons in weight, and its depth rating is 400 m. The CCDE produces 5 kW output and its capacity is about 60 kWh which depends on the capacity of tanks for fuel, liquid oxygen and carbon dioxide absorber. The first long range sea trial was conducted in 1996, which included 4 hour operation.

This paper presents the outline of long range operation of the R-One Robot conducted in June 1998 in the Pacific Ocean, off the shore of Tanabe, Wakayama Prefecture. In one trial, the robot was launched from the pier of the shipbuilding yard, operated on the surface for about 4 km, descended between 10

m to 50 m and cruised autonomously for 12 hours 37 minutes, for about 70 km. By this sea trial, it is confirmed that the R-One Robot will be a suitable platform for continuous measurement of various chemical and biological properties of water column over a long range taking advantage of a wide payload bay at the fore of the robot.

1. Introduction

The underwater environment where an AUV (Autonomous Underwater Vehicle) should pursue its given mission varies from site to site, and availability of support from surface may not be same in all cases. It is, therefore, natural that a great variety of AUVs should be developed in conformity with the large variety of missions.

Based on the above idea, Institute of Industrial Science (IIS) at the University of Tokyo developed AUVs listed in Table 1. Highly intelligent systems are being

Table 1 AUVs constructed by IIS, University of Tokyo

Name	Type	Objective	Construction	Trials	Current Status	Shape	Mass (kg)	CPU	Design Depth(m)
PTEROA150	Cruising	R&D	1989	Sea	Ended	Whale	220	Intel-80186	2,000
PW45	Cruising	R&D	1990	Pool	Ended	Whale	7	NEC-V50	3
ALBAC	Shuttle	PU	1992	Sea	Res.	Torpedo with Wings	45	2xNEC-V50	300
Twin-Burger 1	Testbed	R&D	1992	Pool	Ended	Multi-Hull	118	10xT800, 4xT425	50
Twin-Burger 2	Testbed	R&D	1994	Lake	Ope.	Multi-Hull	118	12xT800,3xT400	50
R-one Robot	Cruising	PU	1995	Sea	Ope.	Torpedo	4,000	MC68040, 25MHz 2xPEP-9000 VM40	400
Manta-Ceresia	Cruising	R&D	1996	Pool	Ope.	Manta	14	ACT-AT8502	10
Tri-Dog 1	Testbed	R&D	1999	-	Under Dev.	Multi-Hull	174	3xIntel-Pentium MMX,233MHz	100
Biwako Robot	Multi-Purpose	PU	2000	-	Under Dev.	Multi-Hull	160	-	150
Nakhodka Robot	Multi-Purpose	PU	-	-	Under Dev.	Multi-Hull	-	-	3,000

PU: for Practical Use, Ope. : Operational

investigated using Twin-Burger vehicles which are versatile testbeds and equipped with TV cameras and image recognition systems. Reconfiguration of their hardware system is easy for introducing new sensors and devices. A new testbed vehicle named "Tri-Dog 1" as the successor to the Twin-Burger vehicle will be constructed by the end of 1999. A glider vehicle named "ALBAC" was constructed and deployed as a handy platform for survey of water column up to 300 m depth. The "Pteroa150" is the first IIS AUV and was designed for bottom survey so as to get good pull-up maneuverability. The "Biwako Robot" (tentative name) will be completed in March 2000 as a practical AUV for environmental survey of fresh water of Lake Biwa, which is the largest lake of Japan and supplies fresh water for people in Osaka and Kyoto districts. This vehicle will be equipped with an underwater microscope for real time survey of plankton which can be a benchmark of eutrophication as they gather around a thermocline. The "Nakhodka Robot" (tentative name) will be designed to survey wrecks on the deep sea floor without being disturbed by fishing nets, tangled cable and wire, and distorted structures.

The R-One Robot whose energy is derived from an air independent Diesel engine generator was developed as a prototype for long-range cruising AUV that can cover a very wide area of ocean. The R-One Robot succeeded in 12 hour continuous dive on June 16th, 1998 in the Pacific Ocean off Tanabe City. In this paper, an outline of this long range operation will be presented and provide a perspective of the survey which is under planning.

11. R-One Project

Since 1990, the University of Tokyo and Mitsui Engineering & Shipbuilding Co., Ltd., have been jointly progressing a project for "Development of an unmanned untethered submersible equipped with an air-independent power system of a Closed Cycle Diesel Engine (CCDE) for one-day survey", in short, the "R-One Project" [1,2,3].

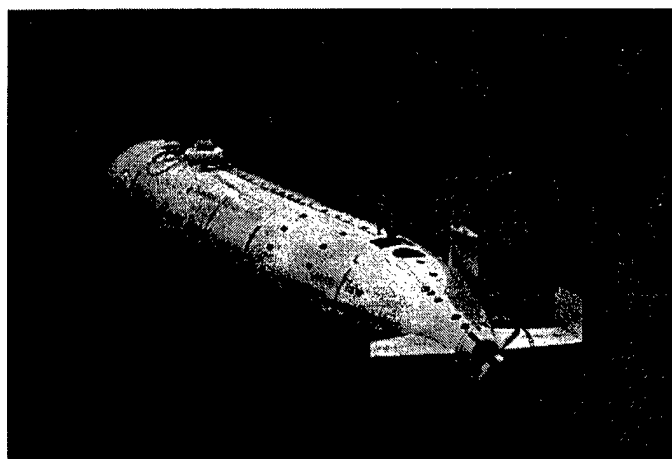


Fig. 1 R-One Robot

The target of the project is to realize a new platform for oceanographic and environmental observation in the sea.

Although a CCDE consists of a relatively bulky and weighty Diesel engine and a generator which can not be miniaturized below a specific size making it unsuitable for short term operation and for a small robot, it can be adopted for the large robot of more than 100 km cruising range. Robustness of the Diesel engine provides high reliability which is essential for continuous operation over a long period. The range of 100 km may not be long considering the extent of the ocean, but capacity of the energy system, i.e. maximum range, can be increased only by changing the volume of fuel, oxygen and absorber tanks.

A CCDE system with 5 kW output was developed by 1993 and tested in the laboratory. It was reconfigured to fit into a cylindrical pressure hull of the vehicle. Tanks were designed to get a 60 kWh capacity, which corresponds to 24 hour, 100 km range continuous dive, and fitted in the same pressure hull. Following the first autonomous dive session in shallow water in July 1996 off Tamano City (c.f. Fig. 3) in Okayama Prefecture, full-scale tests of hour duration and continuous autonomous dive for about 20 km were successfully conducted in Pacific Ocean off Tanabe City (c.f. Fig. 3) in Wakayama Prefecture on August 21 st, 1996. At the same area of sea, a 12 hour operation was carried out in June 16th, 1998.

III. R-One Robot

A) Hardware

Structure and Configuration

The R-One Robot shown in Figs. 1 and 2 and Table 1 has a torpedo-shaped hull, which consists of a main pressure vessel, a fore payload bay, and an aft

Table 2 Principal Dimensions and Equipment of R -One Robot

Length Overall :	8.27 m
Diameter of Body :	1.15 m
Height Overall :	2.02 m
Full Span of Horizontal Wing :	1.80 m
Weight in Air :	4.35 ton
(including fuel, liquefied oxygen, absorbent and ballast)	
Wet Payload Space :	600 litre
Computer :	PEP-9000, 25 MHz
2 x MC68040, VM40	
CCDE : 60 kWh, DC280 V	
Base Engine :	YANMAR 3TN66E
Maximum Output :	5 kW
INS : Ring Laser Gyro	
Dopplar Sonar :	1 MHz, 2-30 m
Forward Looking Sonar :	275 kHz
Down Looking Sonar :	375 kHz
Acoustic Link :	20 kHz

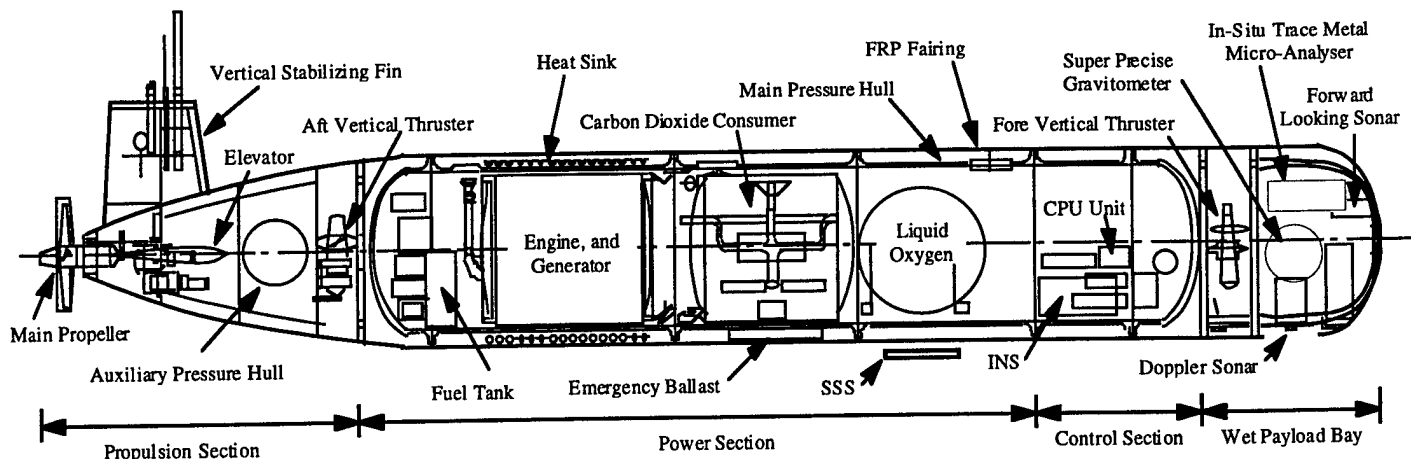


Fig. 2 General Arrangement of R-One Robot

propulsion system. The main pressure vessel made of A5083 aluminum houses a power system and a robot control system, and provides the major buoyancy for the robot. The fore and aft frames, which support all external sensors, research payload, thrusters and actuators, are attached to either end of the vessel. These components are enveloped in flooded fairings made of FRP to provide a torpedo-shape. The fore and aft fairing has a smooth transition to straight line using polynomial curve for good hydrodynamic performance.

A CTDO data logger, a color video camera and recorder, two halogen lamps for the video and a still camera with a strobe light are arranged in the forward fairing as a research payload bay (0.6 M³). A ballast of 20 kg is attached to the lower part of the midship of the hull, and it can be discharged by sending a signal from the main computer or in case of blackout of the system. A radio antenna is installed on the top of the vertical tail fin to locate out the robot and to establish a link when it floats on the sea surface.

CCDE System [3]

Figure 3 shows a flow diagram of the CCDE system. The combustion products of hydrocarbon fuel are mainly carbon dioxide, water vapor and soot. The water vapor contained in the exhaust can be removed by condensing in the cooler, and the soot can be considerably reduced by slightly increasing the oxygen concentration in the recirculated gas at the engine inlet. Thus, the CCDE system is mainly characterized by disposal process of carbon dioxide. While there are various methods [4,5], the "carbon dioxide absorption by chemical solution" exhaust gas processing method was selected with non-regenerative absorbent, i.e. solution of potassium hydroxide (KOH). This method was selected because the CCDE can be operated fully independently from its surroundings. This will enable the AUV to dive thousands of meters which is going to have wide application in the future.

Control System

The main computer is a PEP-9000 with two Motorola 68040 processors which runs under the VxWorks real time operating system. As the CCDE system is controlled by a dedicated computer, the main computer deals with the CCDE as a black box with a battery.

Motion Control

Movement of the robot is controlled by using six actuators:

- 1) A main thruster (1.5 kW);
- 2) An= horizontal direction controller for the main thruster (+/- 15 deg)

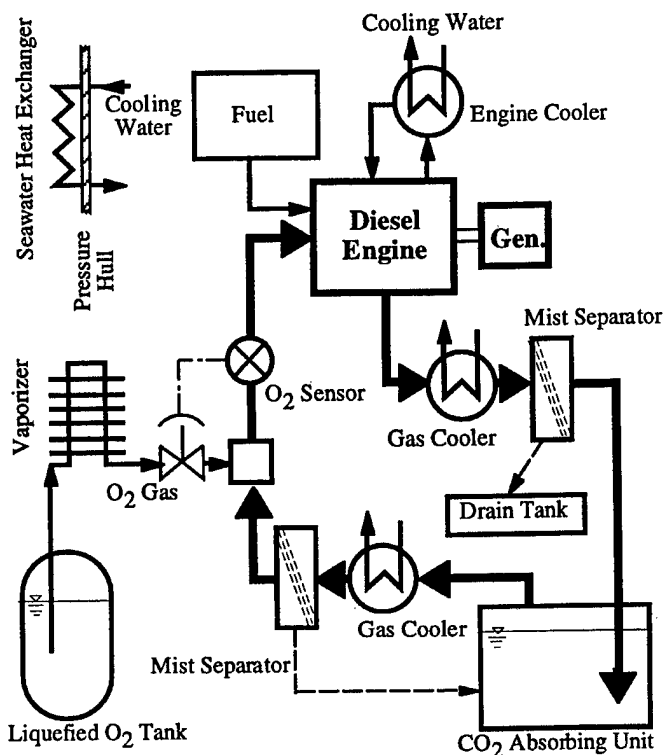


Fig. 3 CCDE System

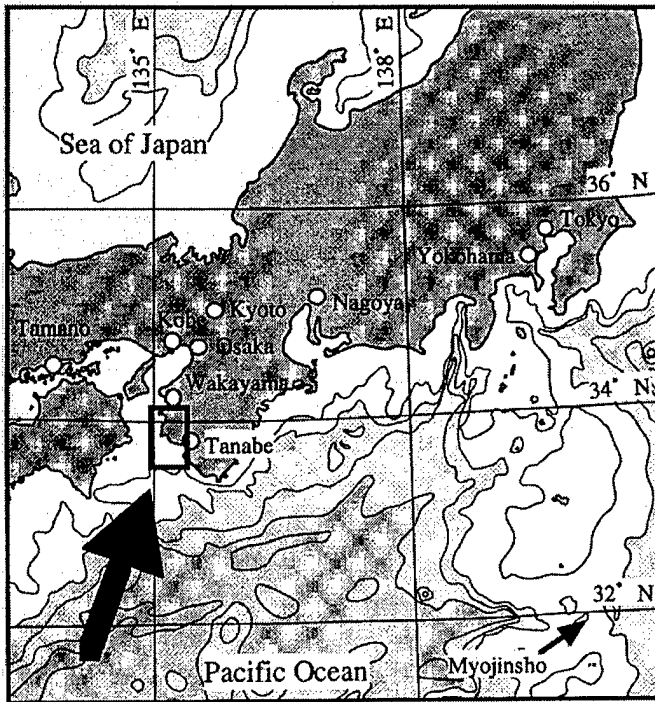


Fig. 4 Trial Site

3) A pair of elevators; and

4) Two vertical thrusters (fore/aft, 2 x 0.75 kW).

The vertical thrusters are used for up and down control during hovering. The elevators are used for pitch control in forward movement. The robot does not have a rudder, but the yaw movement is obtained by controlling the horizontal direction of the main thruster.

B) Software

Software Architecture

Following tasks run under the VxWorks operating system:

- 1) Supervise task group;
- 2) Maneuvering device control task group;
- 3) Navigation device control task group;
- 4) Communication device management task group; and
- 5) Diagnosis and treatment task group.

Although the CCDE is dealt with as a black box as mentioned above, its running data is stored in a file in the main computer.

Autonomous Dive

By the 1998 dive, 4 basic dive modes as shown below had been developed. A mission is accomplished by combining a series of these modes:

- 1) Vertical dive mode using vertical thrusters;
- 2) Direction keeping mode;
- 3) Depth keeping mode; and
- 4) Waypoint navigation mode (Target points are given in latitude, longitude and depth data).

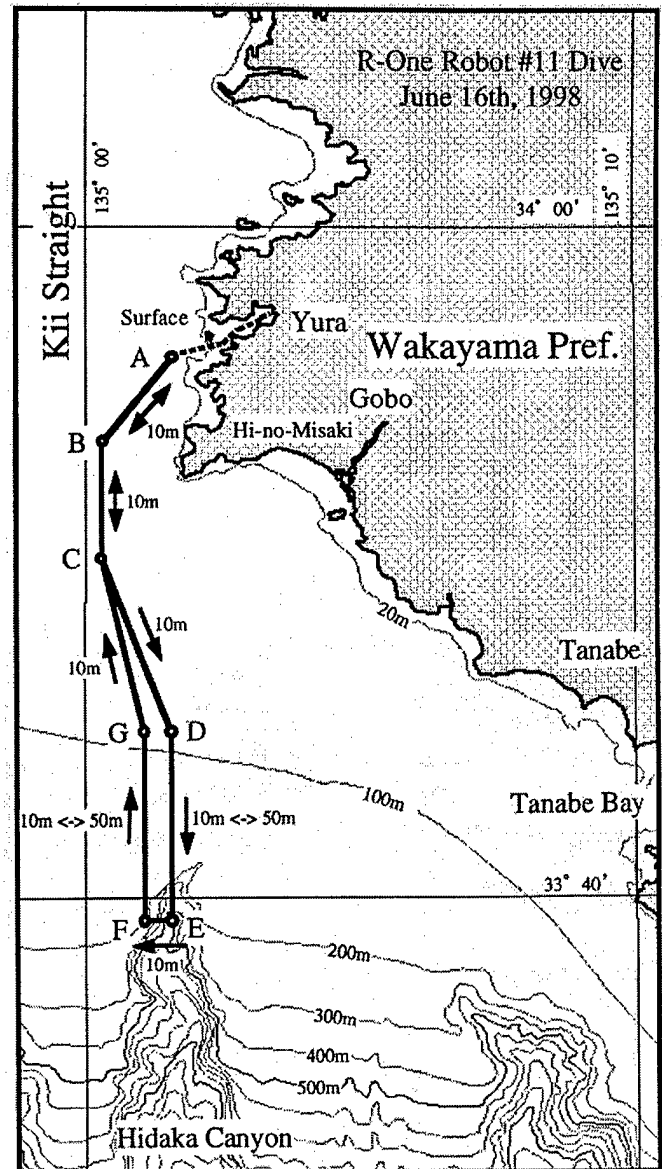


Fig. 5 Trajectory of Dive #11

These basic modes are accomplished by operating each actuator. During the sea trials conducted so far, the sea bed is not perceived by the robot because it cruises in water keeping high altitude from the bed. Thus, altitude keeping mode and obstacle avoidance mode were omitted. Such kinds of modes are appended by adding appropriate software packages for a future expedition.

IV. Twelve Hour Diving

An autonomous dive test of the R-One Robot (dive #11) was carried out on June 16th, 1998 in the Pacific Ocean about 30 km off Tanabe City, Wakayama Prefecture. Figures 4 and 5 show the trial location and the waypoints, where the current from the Kii straight transports Osaka Bay's sea water and a branch of

Table3 Time Table of Dive #11 (WP: Waypoint)

Time h:min	Elapsed Time h:min	Time Between WPs h:min	WPs and Events	Latitude N	Longitude E	Range Overall m	Distance between WPs m	Average Speed km/h
05:30	(0)		Start CCDE					
07:07	0		Descent	33:55:48	135:03:20	0		-
08:13	1:06	1:06	B	53:00	00:30	6,619	6,619	5.6
09:12	2:05	59	C	50:00	00:30	12,175	5,556	5.4
10:50	3:43	1:38	D	45:00	03:00	22,201	10,026	6.7
12:36	5:29	1:46	E	39:30	03:00	32,358	10,157	5.4
13:02	5:55	26	F	39:30	02:00	33,899	1,541	3.6
15:35	8:28	2:33	G	45:00	02:00	44,056	10,157	3.5
17:42	10:35	2:07	C	50:00	00:30	53,600	9,577	5.2
18:48	11:40	1:05	B	53:00	00:30	59,156	5,556	4.9
19:44	12:37	57	Ascent	54:56	01:58	63,826	4,670	5.1
21:33	(16:03)		Stop CCDE					

Kuroshio current comes from the south. Figure 6 shows that the robot was operating on the surface from the pier to the first waypoint "A", where the session of autonomous dive started. The major objectives of the test by making the robot pass through multiple waypoints by using an inertial navigation system (INS) are to confirm the total system performance as a long range cruising type AUV and to find out deficiencies which should be overcome. During the dive, INS's position data is updated at intervals by acoustic communication link based on the acoustic-tracking system on board the support vessel, that consists of a super short base-line (SSBL) acoustic positioning system and a global positioning system (GPS). The position update signal from the support vessel can be sent at appropriate timing, and its interval is decided considering required accuracy of the robot trajectory. This system will be replaced by an onboard (on robot)

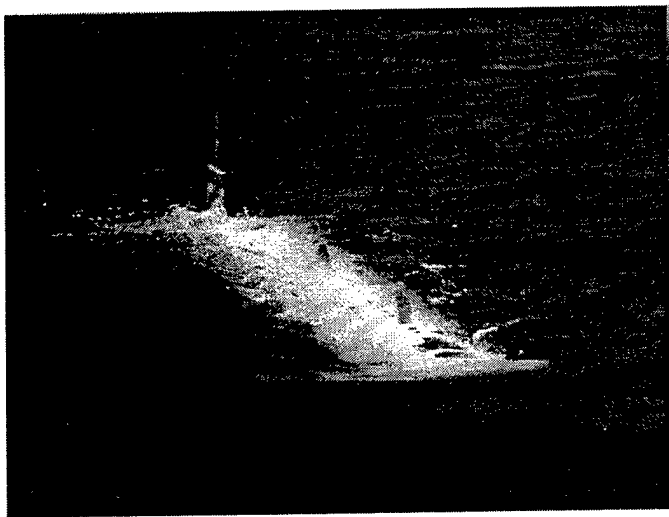


Fig. 6 R-One Robot goes on the surface

GPS system, which becomes available when the robot ascends to the surface in order to get accurate position data by itself and to communicate with the support vessel.

When the robot is within a specified cylindrical space around the waypoint, currently 100 m radius and ± 4 m height, the robot changes the course to a next destination waypoint. As cruising speed is about 3 knots, it was anticipated that the robot could come back to the initial destination point "A" in approximately 12 hours. Table 3 shows the timetable and average speed between each waypoint. The robot passed through waypoints one by one, and turned to the west at E, then went to the north from F. Since a current flowed to the southeast through the dive and rotation rate of the main thruster was fixed, speed of the vehicle to the south was faster than that to the north.

Between D and G, the robot automatically repeated descent and ascent between 10 m and 50 m depth. By this action, it is possible to determine three dimensional distribution of the properties of water column.

It should be noted that the CCDE was operated for 16 hours without any trouble.

V. Next Step

Based on the results of the trial #11, reliability of the ROne Robot was proven and it was shown that the R-One Robot can carry out a long range expedition which requires more than 12 hour operation without support from the surface vessel by improving some sensors and installing some software programs.

There is an active underwater volcano named "Myojinsho [6]" (c.f. Figs. 4 and 7) 420 km south of Tokyo along the Izu-Ogasawara arc. Due to the eruption in 1952, the survey ship No.5 Kaiyo-maru was destroyed

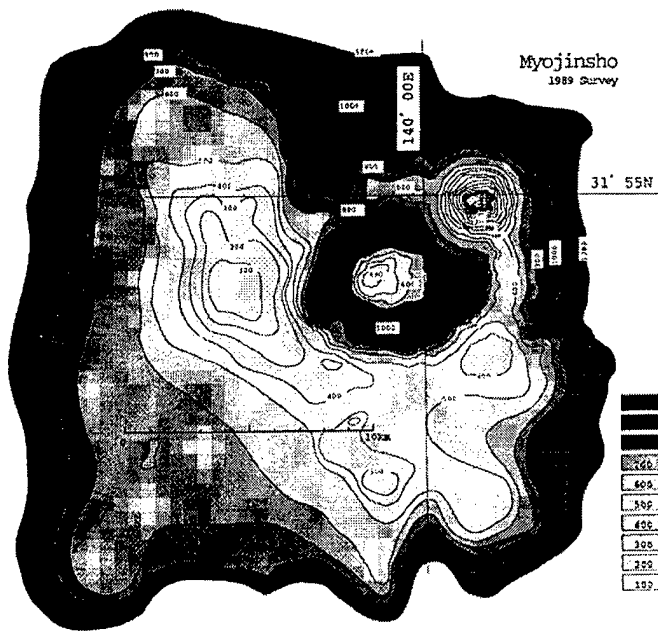


Fig. 7 Underwater Volcano Myojinsho

and 31 people were lost. Taking advantage of autonomy and long endurance, the R-One Robot is scheduled for an expedition to Myojinsho volcano in December, 1999. New measurement apparatus to be installed include a side scan SONAR, a super precise gravitometer, an in-situ trace metal micro-analyzer for observation, a satellite communication system (c.f. Fig. 8) which were developed for such special missions, and a D-GPS system whose data are transmitted to the support vessel via the satellite communication system when the robot occasionally ascends to the surface. This large and extensive installation is possible because of the large wet payload bay of the robot.

There are many active underwater volcanos around the Japan Islands. Since it is quite difficult to survey their underwater environment by conventional methods, the versatile AUV could be the unique observation platform.

References

- [1] Ura, T., et al, "R1 project of an autonomous vehicle equipped closed cycle Diesel engine for one-day investigation of mid-ocean ridge", *Proc. Oceanology Intn.*, (1992)

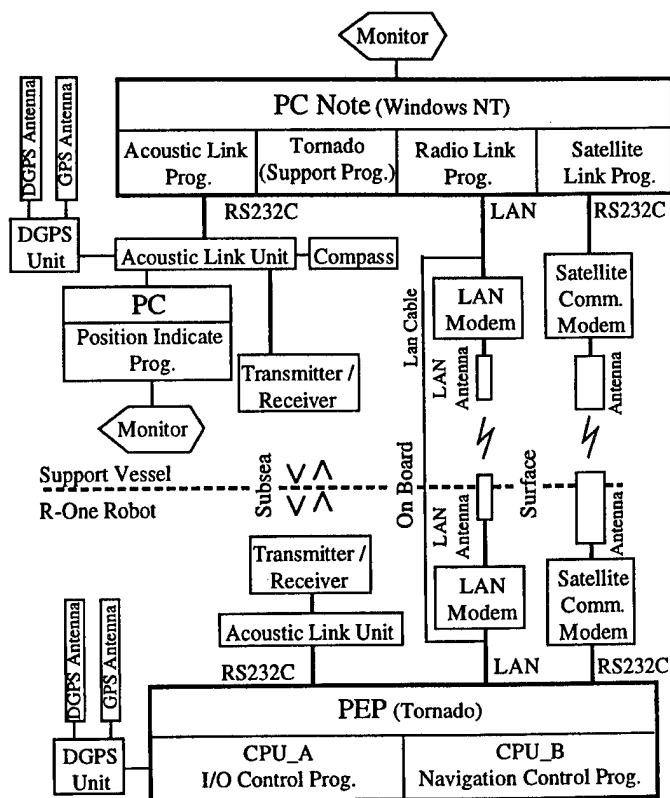


Fig. 8 Communication System between Robot and Surface Support System for Myojinsho Expedition

- [2] Obara, T., et al, "Basic design of an unmanned untethered submersible with a closed cycle Diesel engine", *Proc. Unmanned Untethered Submersible Tech.*, (1993), pp.411-419.
- [31] Obara, T, et al, "Development of depth independent closed cycle Diesel engine for an autonomous underwater vehicle", *Proc. Unmanned Untethered Submersible Tech.*, (1991), pp.1 -9.
- [4] Obara, 1, et al,"A new closed circuit Diesel engine for underwater power", *Proc. Intervention89*, (1989), pp.276-282.
- [5] Gay, J., "The results of an experimental investigation on a non-air-breathing Diesel engine system", *Proc. Unmanned Untethered Submersible Tech.*, (1993), pp.420-426.
- [6] Fiske, R.S. et al "Tephra Dispersal from Myojinsho, Japan, during its shallow submarine eruption of 1952/1953", *Bull Volcanol*, 59, (1998), pp.262-275.

A FULLY INTERACTIVE DYNAMIC SIMULATION OF A SEMI-SUBMERSIBLE TOWING A LARGE TOWFISH

Mae L. Seto
ISE Research Ltd.
Port Coquitlam, Canada

George D. Watt
Defence Research Establishment Atlantic
Dartmouth, Canada

David Hopkin
Defence Research Establishment Atlantic
Dartmouth, Canada

ABSTRACT

ISER and DREA are collaborating on the development of SIMRMS, a fully interactive nonlinear submersible /cable /towfish six degree-of-freedom (DOF) time domain simulation. This capability is not found in standard tow system codes. SIMRMS is a meshing of the DREA Submersible Simulation Program (DSSP) and the DYNTOCABS tow cable/towfish simulator. DSSP is a nonlinear 6 DOF vehicle simulator that models control, propulsion, and ballasting. DYNTOCABS provides a three-dimensional, nonlinear, 3 DOF, finite segment simulation of the cable and includes a nonlinear 6 DOF model of an active towfish. The two programs have been merged so that the equations of motion for all system components are simultaneously integrated in time. New features and capabilities have also been developed.

SIMRMS is used as a test bed to minimize technical risk for further development of a remote minehunting system. This paper discusses, and presents full scale sea trials data validating, the program's capabilities.

ACRONYMS

BG	Distance from center of buoyancy to center of gravity
CG	Center of gravity
DSSP	DREA Submarine Simulation Program
DYNTOCABS	Dynamics of Towed Cable Systems
RMS	Remote Minehunting System
RMV	Remote Minehunting Vehicle
SIMRMS	Simulating Remote Minehunting System
VDT	Variable Depth Towbody

1. INTRODUCTION

ISE Research Ltd. (ISER) and Defence Research Establishment Atlantic (DREA) are supporting development of a Remote Minehunting System (RMS) for the Canadian Navy. The RMS includes a Remote Minehunting Vehicle (RMV) towing a deployable, active,

Variable Depth Towbody (VDT) housing a side scan sonar for route surveying and mine location (see, for example, Fig. 1). In route surveying, sonar images are obtained for an area where minehunting is anticipated, in order to provide a reference against which future minehunting images are compared. A high degree of VDT stability is required to get good images, and its absolute location is needed for differencing images with those from subsequent minehunting surveys. RMV motions, whether from waves or necessary maneuvers, cause VDT (sonar) disturbances. These disturbances degrade the sonar image and make mine detection difficult.

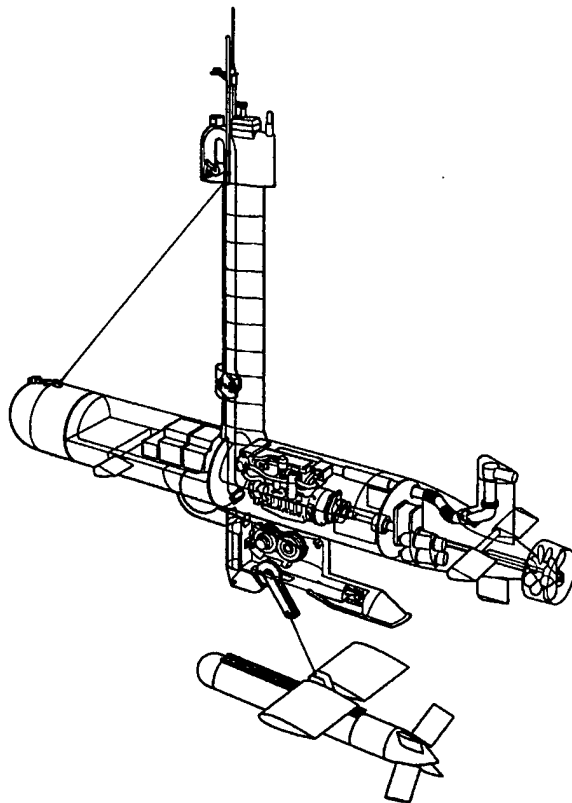


Fig. 1 DOLPHIN Mk 2 and Aurora VDT

Using a semi-submersible RMV has personnel safety and cost advantages over a minehunting surface ship. A semi-submersible retains the larger surface ship's stability in waves, its air breathing endurance, high data rate real time communications link, and accurate global positioning. However, a semi-submersible is still subject to surge motions in high sea states which cause cyclic tow cable tensions and, potentially, towfish positioning variations. Also, the lower inertia of the smaller semi-submersible results in increased interactions with the VDT.

The semi-submersible DOLPHIN vehicles, developed by ISER, are stable, proven, remote platforms capable of operations in up to sea state 5 [1]. They have been used for hydrographic surveys and have towed large towfish at 10 knot speeds down to depths of 120 m. DOLPHIN Mk 2 is 8.5 m long with a 1 m hull diameter, has a dry mass of 4500 kg, and is propelled by a 350 HP engine driving contra-rotating propellers. The Aurora VDT, also developed by ISER, is 3.2 m long with a 0.5 m diameter hull and incorporates an active depressor with a 2.4 m long span and four, symmetrical, independently actuated tail fins. Aurora has a dry weight of 400 kg.

Preliminary simulation work [2], confirmed by subsequent sea trials, has shown that interactions between the DOLPHIN Mk 2 RMV and its VDT are significant. Tow cable tension, for example, with the VDT at 130 m depth and 300 m scope can be a sizeable fraction of the available RMV thrust and buoyancy. It is necessary to assess the impact of RMV motions on the tow system and tow system effects on RMV maneuverability in order to understand, predict, and operate with these interactions.

This motivated the development of SIMRMS (SIMulating Remote Minehunting System), a fully interactive RMV/cable/VDT simulation program. Standard tow cable analysis codes like BCABLE [3] and DYNTOCABS [4,5,6] are intended to model cable systems towed by large ships. They model the tow system only, requiring the tow vehicle tow point kinematics as a boundary condition. This approach is satisfactory only if the tow vehicle is large enough that it does not interact with the tow.

Some work had been done previously on tow vehicle/towfish interactions, but at low speeds [7]. ISER and DREA chose to tackle the problem by integrating two programs which were both proven and familiar: the DREA Submarine Simulation Program (DSSP) and the Coastal Systems Station (Panama City) DYNAMics of Towed CABLE Systems (DYNTOCABS) program. DSSP is a nonlinear 6 DOF vehicle simulator that also models control, propulsion, and ballasting. DYNTOCABS provides a three-dimensional, nonlinear, 3 DOF, finite segment

simulation of the cable, and includes a nonlinear 6 DOF model of a towfish with active control.

Initially, the merging of DSSP and DYNTOCABS was iterative [2]. That is, the programs were repeatedly run alternately, with results from one becoming the boundary conditions for the other, and vice versa. These results showed both that interactions were substantial and that the programs could predict them well.

DSSP and DYNTOCABS were then fully merged, eliminating any iteration in the simulation. The fully interactive SIMRMS program simultaneously integrates in time the equations of motion for all system components (the RMV, the VDT, and the cable segments).

RMV, cable, and VDT hydrodynamic characteristics are determined in SIMRMS through input files. For the current work, these characteristics describe the DOLPHIN Mk 2 RMV and the Aurora VDT, as shown in Fig. 1.

SIMRMS has become a valuable test bed for further development of the RMS. It provides RMV and VDT performance predictions for untried maneuvers and an environment for tuning RMV/VDT control systems. Presently, SIMRMS does not model sea state effects, altitude following, or cable winching. Work is underway to include these features.

This paper describes the current features of SIMRMS, validates its predictions against full scale sea trials data, and discusses on-going development.

II. SIMRMS RMV, VDT AND CABLE MODELS

The RMV and VDT dynamics are each modelled with six, second order, nonlinear ordinary differential equations of motion, one for each degree-of-freedom, in body fixed coordinate systems. Control surface deflection, propulsion, tow cable, variable ballast, and steady and unsteady hydrodynamic effects are all modelled in the applied force terms on the right hand sides of these equations. The hydrodynamic forces are described using derivatives based on in-house DREA empirical and theoretical methods [8, 9,10].

The tow cable is modelled as a series of rigid links connected by frictionless spherical joints. Cable hydrodynamics is modelled using normal and tangential drag, side force, and added mass loading functions. Mass and hydrodynamic loads are uniformly distributed over each link, halved, and then lumped at the connecting joints. The cable links do not stretch and do not support moments; they are two-force members supporting only longitudinal loads. Hence, cable dynamics are described by a set of three, second order, nonlinear, ordinary differential equations of translational motion for each joint.

Proportional, integral, differential, and feed forward controllers for the RMV and VDT roll, pitch, yaw, and depth are implemented to emulate RMV algorithms that determine control surface deflection set points. These set points are based on feedback vehicle attitudes and vehicle set points. The control surface time responses are modelled by linear, second order, ordinary differential equations. Control surface response damping, frequency, and maximum rate inputs, together with initial conditions, determine a unique response [11].

The distribution of RMV control authority is quite flexible. Input file information determines whether a pair of planes deflects differentially or as a locked set. Roll, pitch, and depth authority can similarly be switched between the bow and stern planes. Plane control law algorithms can also be changed via input files.

The RMV navigates by three possible modes, emulating DOLPHIN Mk 2 capabilities. In 'rudder' mode, rudder deflection commands are given to the RMV via an input file. SIMRMS integrates the equations of motion from one command implementation to the next. This is similar to flying the RMV from a console. In 'heading' mode, the RMV is given a heading angle set point to maintain. In 'waypoint' mode, the RMV follows a series of lines through inertial-reference-frame waypoint specifications that define its flight path.

The waypoints can be chosen from a list of existing maneuvers or they can be generated by 'preview' mode. Here, waypoints defining a standard minehunting maneuver (Fig. 2) are automatically generated as a function of user specified lane spacing, minimum turn diameter, swath length, nominal RMV speed, waypoint spacing, and number of sweeps.

The RMV propulsion model simulates the power delivered to the contra-rotating propellers as a function of RMV speed, cross flow angle, tow load, and the engine set point and achieved (feedback) rpms. Thrust and power levels are obtained from propeller open water thrust and torque characteristics, wake fraction, thrust deduction, and shaft and transmission loss parameters. Cross-flow effects on propulsion are estimated from wind tunnel experiments with a powered submarine model [12]. The maximum engine power is modelled as a function of rpm using the manufacturers performance specifications.

The RMV has variable ballast tanks at its bow and stern. These tanks vent or flood at a given rate for a controlled duration, all of which can be modelled in SIMRMS and controlled via an input file.

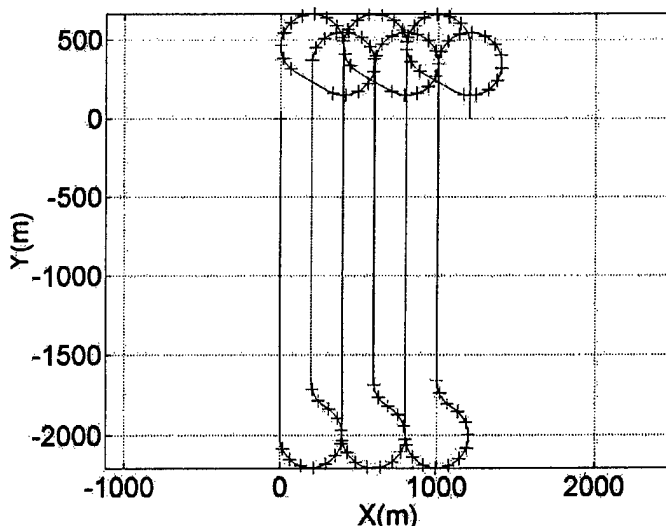


Fig. 2: A minehunting maneuver defined by waypoints (+) generated in preview mode.

III. VALIDATION

The SIMRMS validation began by ensuring that the program reproduced the already validated behaviors of DSSP and DYNTOCABS at the limiting extremes where cable scope is zero (the VDT is docked: the DSSP limit) and the RMV is infinitely large and powerful (the DYNTOCABS limit). This was done satisfactorily.

The validation of primary interest compares the SIMRMS predictions of RMV/tow interactions with sea trials data, and this is presented here. The data is from 1998 trials of the DOLPHIN Mk 2 towing the Aurora VDT through figure 8 turns in which turn diameter, cable scope, and VDT depth varied. Tables 1a through 1c summarize results from 12 of the runs in which the turns were tightest and the interactions strongest. Fig. 3 plots several quantities of interest as a function of time for case 8.

Table 1 compares trials data and SIMRMS predictions of both level flight and critical turn values. Engine speed, cable tension at the RMV towpoint, RMV depth, pitch and roll, and VDT speed through the water are examined. The absolute trials measurements are listed and the SIMRMS prediction is presented as either a ratio or an absolute measurement. Table 1 style comparisons were made for all quantities shown in Fig. 3 for all cases. This analysis for the case in Fig. 3 is shown in Table 2.

Table 1a: Comparison of SIMRMS predictions and trials data RMV engine speed and cable tension
(RMV ~ 10 knots)

case	inputs				achieved RMV engine speed (set point as shown in inputs)				RMV cable tension			
	depth (m)	scope (m)	turn dia (m)	rpm set point	level flight		turn max		level flight		turn min	
					trials (rpm)	SIMRMS/ trials	trials (rpm)	SIMRMS/ trials	trials (lb)	SIMRMS/ trials	trials (lb)	SIMRMS/ trials
1	20	50	250	1895	1890	1.003	1934	0.980	597	0.873	547	0.945
2	40	100	250	1837	1855	0.990	1858	0.989	787	1.107	709	1.081
3	60	120	250	2102	2119	0.992	2148	0.979	1758	0.948	1313	1.017
4	80	160	250	2215	2200	1.007	2222	1.007	2145	1.038	1383	1.159
5	80	240	250	2290	2314	0.990	2352	0.974	2019	1.022	960	1.049
6	100	200	250	2335	2342	1.006	2457	0.950	2848	0.99	2101	1.302
7	100	200	300	2437	2428	1.004	2484	0.981	3069	1.001	1932	1.055
8	100	250	250	2437	2427	1.004	2495	0.977	2785	1.008	1137	1.131
9	100	250	300	2437	2417	1.008	2458	0.991	2726	1.030	1722	0.906
10	120	260	250	2637	2487	1.015	2606	1.009	3289	1.068	2060	0.814
11	120	300	300	2582	2487	1.018	2612	0.987	3210	1.040	2008	0.789
12	120	300	400	2475	2484	0.996	2504	0.996	3149	1.010	1701	1.120

Table 1b: Comparison of SIMRMS predictions and trials data RMV depth and pitch
(RMV ~ 10 knots)

case	inputs				RMV depth (set point = 3.0 m)				RMV pitch (+ve nose-up) (set point = 0.0 deg)			
	depth (m)	scope (m)	turn dia (m)	rpm set point	level flight		turn min		level flight		turn max	
					trials (m)	SIMRMS/ trials	trials (m)	SIMRMS/ trials	trials (deg)	SIMRMS (deg)	trials (deg)	SIMRMS (deg)
1	20	50	250	1895	3.100	0.957	3.096	0.958	-0.62	1.43	-0.70	1.47
2	40	100	250	1837	3.100	0.976	3.086	0.971	-0.56	-0.26	-0.60	0.69
3	60	120	250	2102	3.300	0.948	3.292	0.929	-1.29	-4.10	-1.09	-1.79
4	80	160	250	2215	3.400	0.934	2.925	1.043	-1.23	-5.96	1.10	-1.72
5	80	240	250	2290	3.357	0.911	3.184	0.927	-1.52	-1.92	-0.68	1.70
6	100	200	250	2335	3.300	0.976	3.108	0.973	-1.43	-7.60	-0.82	-0.75
7	100	200	300	2437	3.506	0.917	3.284	0.928	-0.68	-7.60	-0.49	-1.73
8	100	250	250	2437	3.490	0.899	3.178	0.925	-1.25	-4.89	0.26	1.12
9	100	250	300	2437	3.498	0.897	3.202	0.925	-1.26	-4.89	0.53	1.12
10	120	260	250	2637	3.590	0.897	3.413	0.902	-3.06	-7.98	-2.36	-2.85
11	120	300	300	2582	3.602	0.880	3.278	0.903	-1.49	-6.25	0.96	1.07
12	120	300	400	2475	3.645	0.872	3.388	0.872	-1.50	-6.40	0.08	1.33

Table 1c: Comparison of SIMRMS predictions and trials data VDT speed and RMV roll
(RMV ~ 10 knots)

case	inputs				RMV roll (+ve out of turn) (set point = 0.0 deg)				VDT speed through water			
	depth (m)	scope (m)	turn dia (m)	rpm set point	level flight		turn extrema		level flight		turn min	
					trials (deg)	SIMRMS (deg)	trials (deg)	SIMRMS (deg)	trials (m/s)	SIMRMS/ trials	trials (m/s)	SIMRMS/ trials
1	20	50	250	1895	-0.45	0.00	2.04	-0.15	5.21	1.035	5.04	1.052
2	40	100	250	1837	1.62	-0.10	2.83	0.62	4.69	1.021	4.24	1.038
3	60	120	250	2102	1.46	0.00	1.87	1.59	5.08	0.988	4.45	0.982
4	80	160	250	2215	0.74	0.01	14.44	2.23	5.09	0.974	3.37	1.187
5	80	240	250	2290	0.71	-0.02	4.30	1.25	5.67	0.935	3.26	1.012
6	100	200	250	2335	-0.03	-0.03	10.61	2.64	4.81	1.035	4.11	0.844
7	100	200	300	2437	-0.82	0.08	6.17	3.46	5.00	1.040	3.42	1.149
8	100	250	250	2437	-0.26	-0.04	18.87	2.11	5.35	0.989	2.82	1.128
9	100	250	300	2437	-0.74	-0.04	22.00	2.26	5.18	1.021	3.62	0.967
10	120	260	250	2637	-0.74	-0.06	20.87	3.75	4.79	1.081	3.28	0.976
11	120	300	300	2582	-0.41	-0.15	26.80	2.78	4.89	1.080	3.55	0.885
12	120	300	400	2475	0.11	-0.15	24.60	3.63	4.99	1.038	3.21	1.112

Table 2: SIMRMS and trials data comparison for case 8 (Figure 3 - 250 m scope, 100 m depth, 250 m turn diameter)

SIMRMS / trials	quantity	level flight	turn
	RMV tension	1.008	1.131
	VDT depth	1.000	1.003
	RMV speed	1.025	0.987
	VDT speed	0.986	1.128
	engine rpm	1.004	0.977
	RMV depth	0.899	0.925
diff (deg)	VDT roll	0.67	-3.33
	VDT pitch	0.32	0.51
	RMV roll	-0.22	-16.75
	RMV pitch	3.64	-0.86

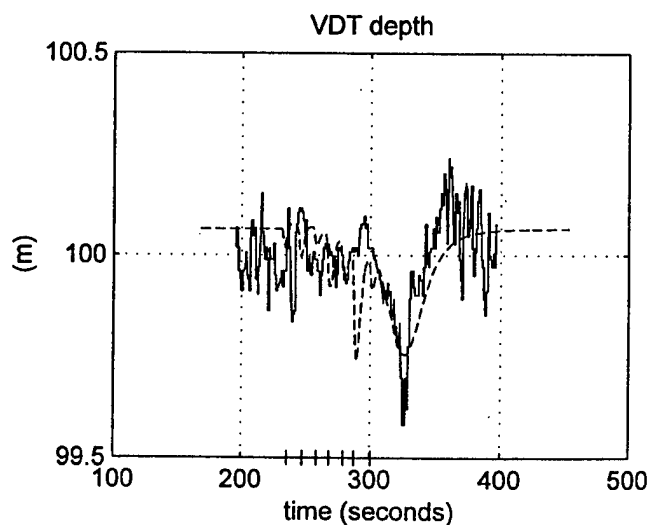
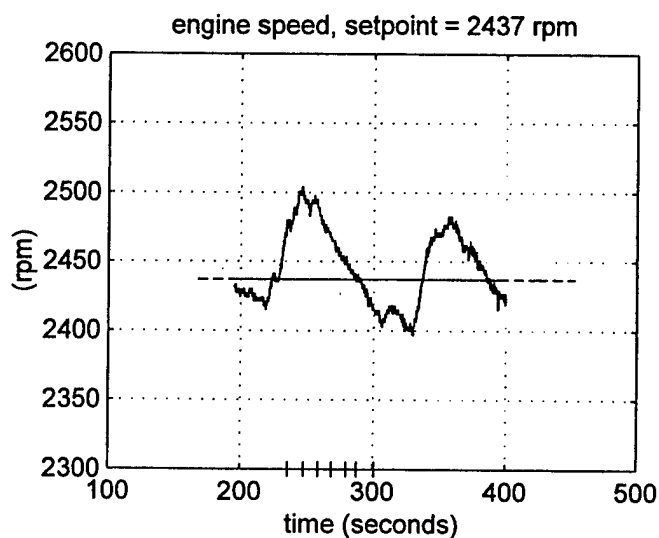
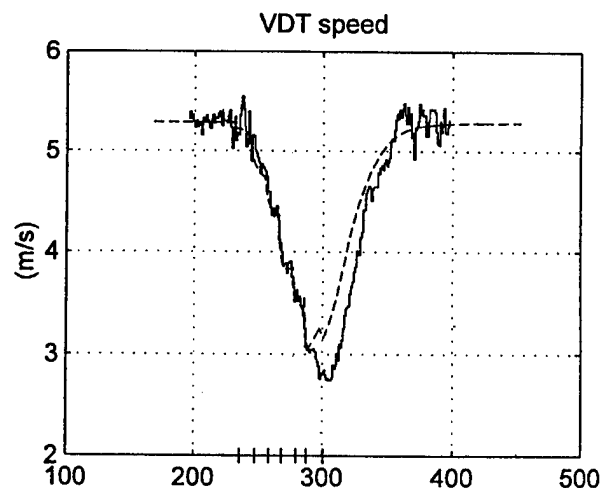
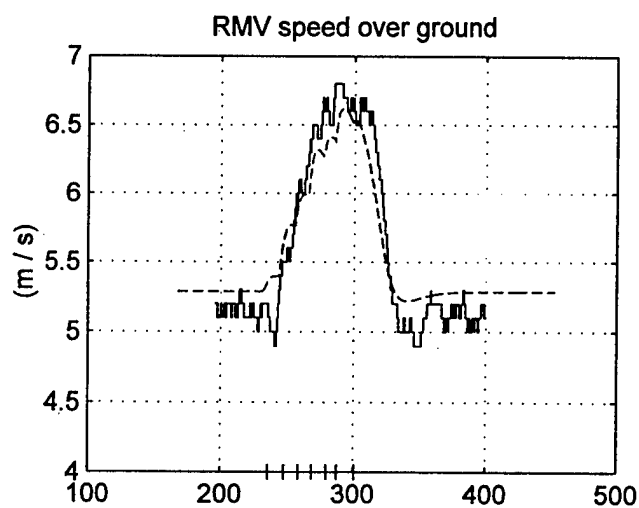
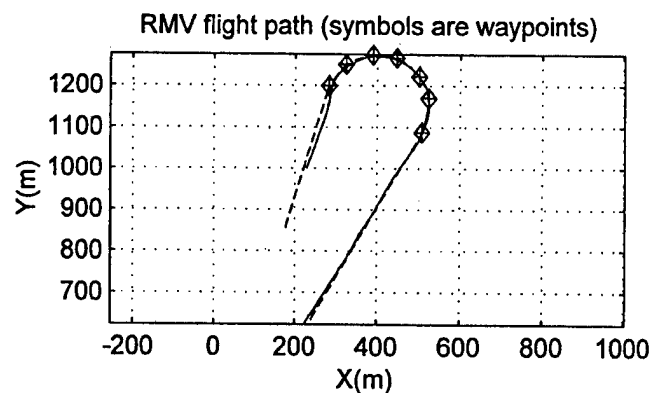
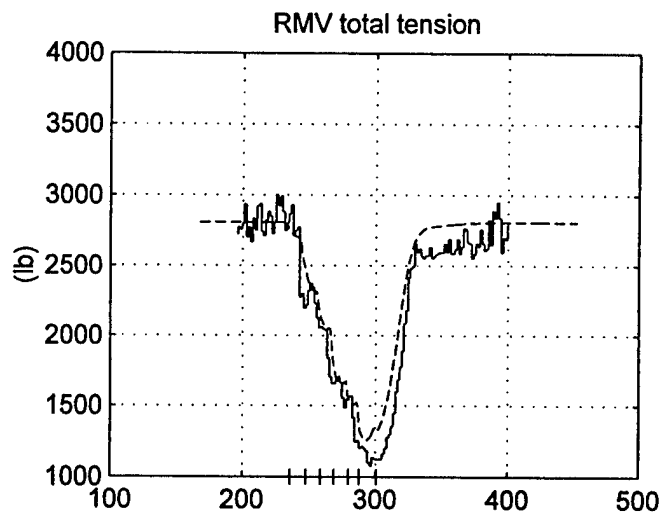


Fig. 3a: SIMRMS predictions (dashed line) superimposed on trials data (solid line) for cable scope = 251 , VDT depth = 100 m, and RMV turn diameter = 250m (figure 1 / 3). RMV waypoint crossings are '+' on time axes. Waypoints are shown in 'RMV flight path'.

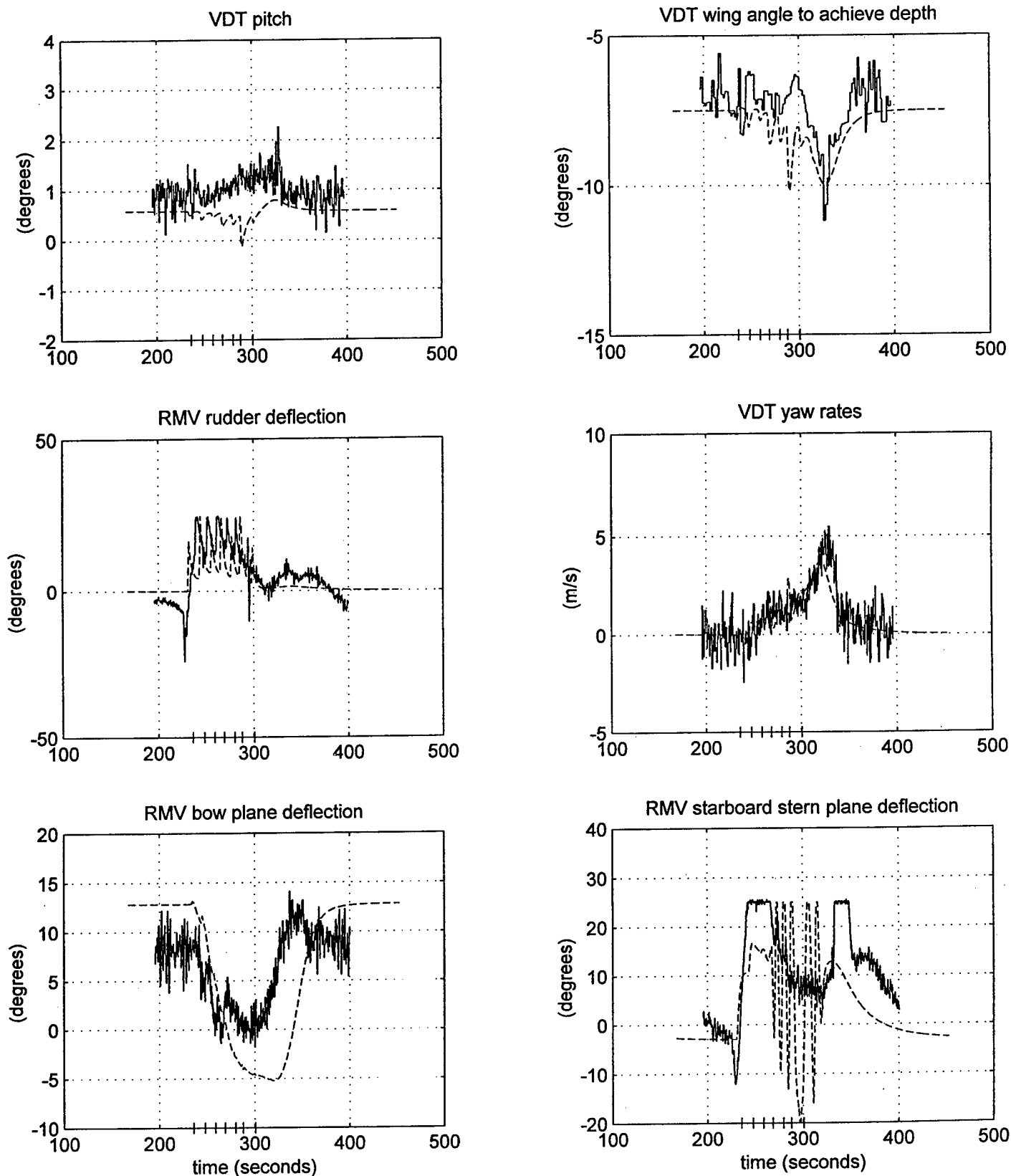


Fig. 3b: SIMRMS predictions (dashed line) superimposed on trials data (solid line) for cable scope = 251 , VDT depth = 100 m, and RMV turn diameter = 250m (figure 2/ 3). RMV waypoint crossings are '+' on time axes. Waypoints are shown in 'RMV flight path'.

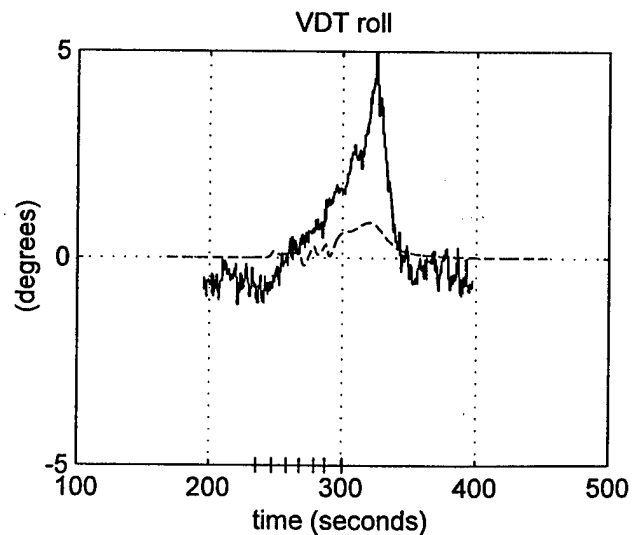
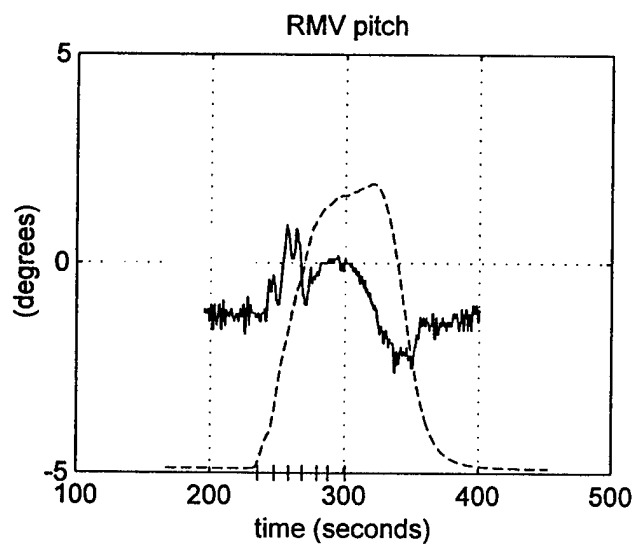
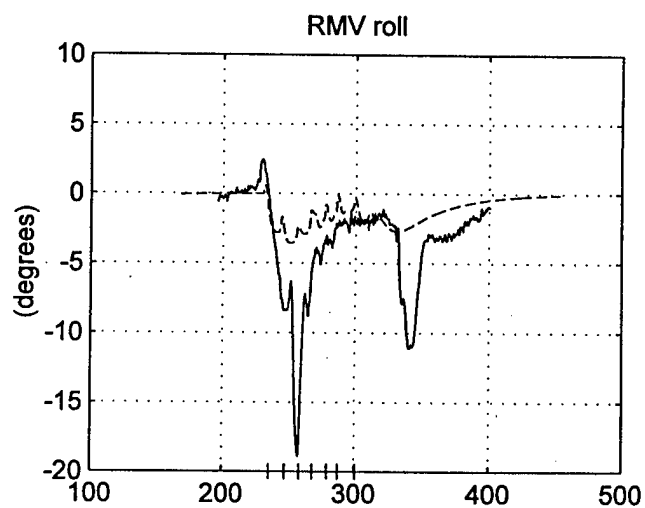
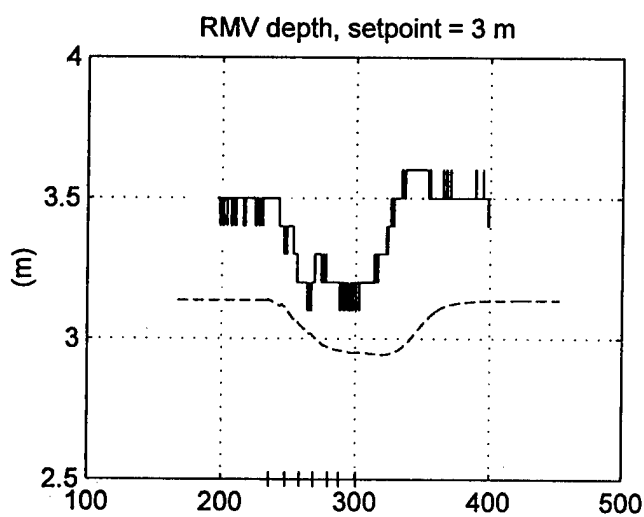
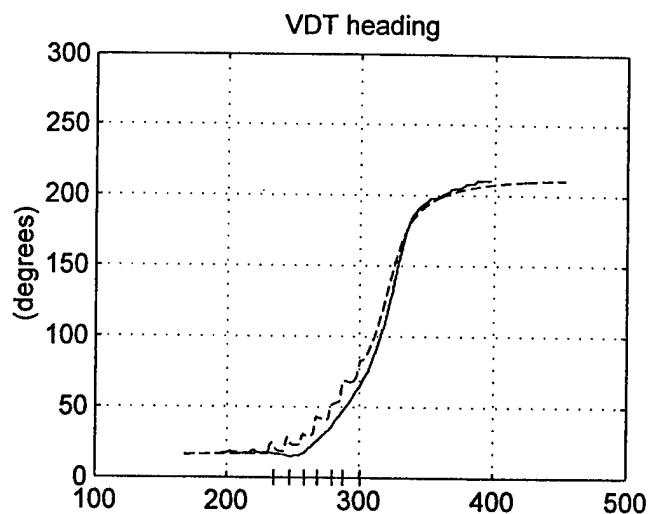
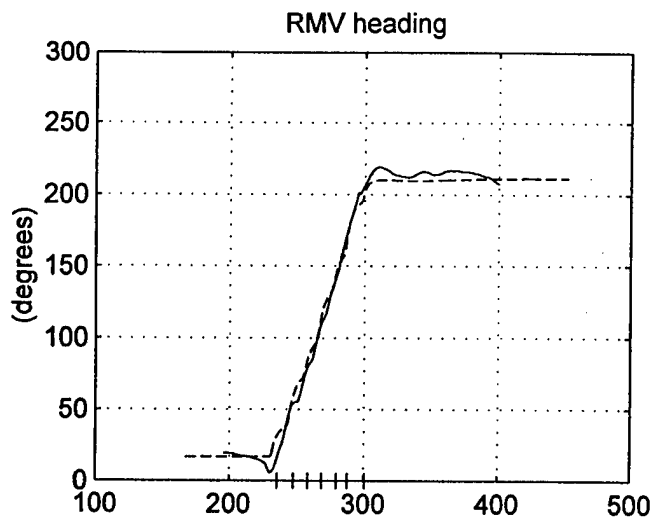


Fig. 3c: SIMRMS predictions (dashed line) superimposed on trials data (solid line) for cable scope = 251 , VDT depth = 100 m, and RMV turn diameter = 250m (figure 3/ 3). RMV waypoint crossings are '+' on time axes. Waypoints are shown in 'RMV flight path'.

A. RMV Propulsion, Speed, and Cable Tension DOLPHIN speed control is effected through closed loop control on engine rpm. The rpm set point cannot be met if doing so requires more power than the engine can generate at that rpm (the engine is then 'power limited'). SIMRMS models these phenomena. Cases 10, 11, and 12 in Table 1 represent the deepest tows and, hence, the greatest power requirements. In cases 10 and 11 the RMV is power limited. Case 12 has the same level flight tow condition as case 11 but is not power limited since the rpm set point is achievable.

SIMRMS models the trends in the engine rpm well, with the worst discrepancy being less than 3%. SIMRMS correctly predicts that case 10 and 11 are power limited and that case 12 is not. For these power limited cases, it is interesting that SIMRMS achieved rpms are higher than those measured in trials. SIMRMS consistently over predicts available power by 2%.

An important measure of the validity of the propulsion model, as well as of the hydrodynamic models, is the accuracy of the SIMRMS RMV speed prediction. This prediction is compared with trials data (an average of 11 runs) in Table 3 for a 300 m scope tow with the VDT at a depth of 120 m, the most demanding set of conditions trialed. The SIMRMS prediction is within the speed variation of the measured data.

Table 3: Propulsion performance from SIMRMS predictions and trials data (300 m scope, 120 m VDT depth, rpm set point = 2582)			
	SIMRMS	trials range (11 runs)	% diff from trials avg
achieved level flight engine rpm	2534	2461-2500	2.2
RMV tow tension (lb)	3327	3188-3350	1.8
RMV speed (m / s)	5.26	4.73-5.32	4.7

The tension logged in trials is the total RMV tow point tension, of which nominally 90% is in the axial direction directly affecting propulsion performance and speed. Tension predictions in level flight are generally good, usually being less than 5% but occasionally 10 to 15% in error. Minimum tension predictions in a turn can be in error by as much as 30%, particularly when the turn diameter/scope and scope/depth ratios are small. This latter, transient, quantity is probably less important than the ability of the code to predict the overall shape of the tension variation with time, as shown in Fig. 3a.

B. RMV Depth, Pitch, and Roll Discrepancies Unfortunately, RMV buoyancy was not precisely

measured during the sea trials. The variable ballast, and other ballast, was manually adjusted for each run, and sometimes during the run, to achieve desired pitch and depth settings; these adjustments were not logged. In addition, the amount of onboard fuel (specific gravity 0.8) in the collapsible fuel bags was not logged; the vehicle BG can vary by 12% between the fully fueled and empty conditions. These unknowns affect RMV trim and vertical plane dynamics.

SIMRMS predictions assume the ballast tanks and fuel bags are always half full. This results in systematic differences between RMV depth and pitch predictions and measurements, as seen in Table 1.

The greatest discrepancies in the validation are for RMV roll angles in turns with deep tows. Roll angles of over 20 degrees are observed but SIMRMS does not predict anything higher than 4 degrees (Table 1c). The cases in Table 1 were rerun in SIMRMS with a smaller BG (assuming full fuel bags) but only a further 4 degrees of roll was obtained. A possible reason for the low roll angle predictions is a large trials BG reduction from systematic operator reduction of ballast in response to increasing tow depth (down force). A complicating factor is a predicted side force on the mast self-aligning fairings generated by curvature in the onset streamlines during turns [9], something not accounted for in the current RMV roll derivatives.

Although SIMRMS under predicts the critical RMV roll angles, it does predict well the time at which roll occurs and the roll 'cusps' from sudden turns as the RMV passes through a waypoint.

C. RMV Horizontal Plane Validation The SIMRMS RMV flight path is predicted using the same input waypoint file as used in the trials. A portion of the Figure 3 case 8 'RMV Flight Path' plot is reproduced below in Fig. 4.

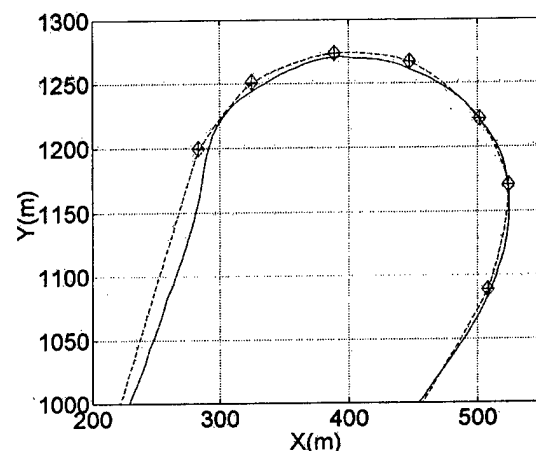


Fig. 4: RMV flight path for a tow of 250 m scope, 100 m VDT depth, and 250 m turn diameter (symbols indicate waypoints)

Generally, SIMRMS predictions of horizontal plane characteristics (yaw rates, heading, and flight path data) agree satisfactorily with sea trials data. The agreement deteriorates when the lateral RMV cable tension is maximum, when the RMV tends to turn outside the predicted trajectory. This happens when RMV heading changes occur and results in the largest errors in RMV heading predictions. The discrepancy grows with decreasing turn diameter/scope ratio to a maximum of 5 m in a 250 m diameter turn once in the turn.

D. VDT Comparisons

SIMRMS predictions and sea trials data for the VDT depth, pitch, roll, and speed are generally in good agreement. During level flight and in turns the depth agreement is within 2.3% for a range of 20 m to 120 m. Similarly, pitch is within 2 degrees and roll about 3 degrees. Discrepancies in the VDT speed are less than 10% in level flight while the transitory minimum speed prediction is within 20%, and usually much better.

IV. RMV/TOW INTERACTIONS

Evidence of strong interactions between the DOLPHIN Mk 2 RMV and Aurora VDT is apparent from:

- increased RMV speed in a turn as the tow load decreases,
- RMV depth and pitch variations (when variable ballast is inactive) due to tow load variations,
- RMV roll in response to increased lateral cable tension in a turn.

The first of these is well predicted by SIMRMS. The second interaction is predicted to be large by SIMRMS but validation could not take place because of unlogged ballast changes during the trials. The last interaction is not well modelled though the trials data show it to be large.

V. CONCLUDING REMARKS

SIMRMS simulates the 6 DOF dynamics of a fully coupled RMV/cable/VDT minehunting system, including [5] dynamic interactions. Hydrodynamic loads and control algorithms can be customized through input files. SIMRMS has been validated against full scale sea trials data. With the exception of RMV roll and pitch, the agreement between SIMRMS and the trials data is acceptable. SIMRMS appears to capture RMV/tow interactions well, but requires better ballast and fuel data, and a better roll hydrodynamic model, to complete the validation.

VI. ON-GOING WORK

ISER and DREA are continuing to develop and improve SIMRMS. Work is divided into two types of activities, problems to solve and new features.

A new RMV hydrodynamic roll model will be implemented shortly. ISER is using SIMRMS to devise an active control strategy for managing RMV variable ballast to maintain optimal buoyancy and trim for various fuel and tow cable tension loads. When complete, new trials will be required to validate the SIMRMS pitch interaction.

New SIMRMS features currently under development include:

- a sea state simulation modelling the effects of sea state on the RMV and, hence, the VDT.
- a variable cable scope model, since it is desirable to incorporate active winching and deploying of the VDT into maneuvering strategies.
- VDT altitude keeping relative to three-dimensional sea floor profiles.

REFERENCES

- [1] J. Preston and L. Shupe, "Remote Mine-Hunting Systems - Vehicle Stability Trials," *Proceedings on the Knowledge-based Systems and Robotics Workshop*, Fisheries and Oceans Canada, pp. 115-121, 1993.
- [2] M.L. Seto. and G.D. Watt, "The Interaction Dynamics of a Semi-Submersible Towing a Large Towfish," *Proceedings of the Eighth International Offshore and Polar Engineering Conference*, Montreal, Canada, Vol. II, pp. 263-270, 1998.
- [3] S. Latchman, "Effect of Cable and Towbody Parameters on Tension and Cable Length when towing at 200 m Depths and 10 Knots," *Proceedings of Oceans '93*, Vol. III, pp. 491-496, 1993.
- [4] J.W. Kamman, T.C. Nguyen, and J.W. Crane, "Modelling Towed Cable System Dynamics," *Proceedings of the IEEEIMTS Oceans 1989 International Conference on Methods for Understanding the Global Ocean*, IEEE, New York, pp. 1484-1489, 1989.
- [5] J.W. Kamman and T.C. Nguyen, "User's Manual for DYNTOCABS," Technical Memorandum NCSC TM 550-90, 1990.
- [6] J.W. Kamman, "Application of Multivariable Linear Control Design to Marine Towed System," *Journal of Guidance, Control and Dynamics*, Vol. 19, No. 6, pp. 1246-1251, 1996.
- [7] K. Zhu. and W. Li, "Coupled Motion Simulation of Underwater Towed and Self-Propulsive Vehicle," *Proceedings of the Seventh International Offshore and Polar Engineering Conference*, Honolulu, USA, Vol. II, pp. 38-43, 1997.
- [8] G.D. Watt, M.L. Seto, and T.E. Brockett, "Hydrodynamic Considerations for Semi Submersible Minehunting Vehicles," *Proceedings of the 4th Canadian Marine Hydromechanics and Structures Conference*, Ottawa, Canada, 1997.

- [9] G.D. Watt, "Two Underwater Vehicle Projects at DREA: 1) Estimating Underwater Vehicle Stability and Control Derivatives and 2) Lift on Self Aligning Fairings in Turns," *Proceedings of the Workshop on Control and Simulation Systems for Underwater Vehicles*, Institute for Marine Dynamics, St. John's, Canada, 1998.
- [10] G.D. Watt, "Estimates for the Added Mass of a Multi-Component, Deeply Submerged Vehicle," *RINA Warship 88 International Symposium on Conventional Naval Submarines*, paper no. 14, 1988.
- [11] G.D. Watt, "Modelling Submarine Control Surface Deflection Dynamics," DREA Technical Memorandum 90/203, 1990.
- [12] G.D. Watt, "On the Necessity for Modelling Submarine Propeller Transverse Forces During Simulations of High Speed Maneuvers," *Proceedings of the Second Canadian Marine Dynamics Conference*, Vancouver, 1993.

ESTUARINE ENVIRONMENT STUDIES WITH ISURUS, A REMUS CLASS AUV

Nuno Cruz, Aníbal Matos, Alfredo Martins, Jorge Silva,
Domingos Santos, Dmitri Boutov, Diogo Ferreira and F. Lobo Pereira

Faculdade de Engenharia da Universidade do Porto and
Instituto de Sistemas e Robótica
Rua dos Bragas, 4050-123 Porto
Portugal

Abstract — In this paper, we address the current developments of the “PISCIS” project. We focus on the experimental results from recent operational missions with an AUV in a estuarine environment. Besides describing mission planning and logistic details, we also present tools for oceanographic data processing and visualization. This will be demonstrated with some examples of collected data.

I. INTRODUCTION

The Systems and Underwater Technology Lab (LSTS) of the University of Porto has been operating and customizing *Isurus*, a REMUS class AUV, for the past 2 years.

System capabilities and limitations have been identified and improvements have been incorporated. In particular, all the software has been redesigned, a new navigation system has been implemented and relevant sensors were installed whenever required and viable. Experiments designed to fulfil potential end-user requirements (trying to maximize the collected information about a given process), demonstrated the reliability and the operational effectiveness of this system.

The first operational missions were demonstrated by field tests conducted in the estuary of Minho river in the northern border between Portugal and Spain. During autonomous missions, typically longer than one hour, the vehicle continuously collected CTD and bathymetric data, while navigating on a LBL transponder network.

This paper is organized as follows. In Section II, we briefly describe the “PISCIS” project and the motivation for the use of AUVs in oceanographic missions. In Section III we give a short presentation of the *Isurus* AUV. Sections IV through VI deal with mission planning, describing the scenario, the mission requirements and the mission editor. We move on, in Section VII, to a discussion on mission logistics, focussing on vehicle tracking and on the steps involved in a typical mission with *Isurus*. Then, in Section VIII, we show some results of mission data processing. Finally, in Sections IX and X, we discuss the conclusions and future work.

II. MOTIVATION

“PISCIS – Prototype of an Integrated System for Coastal-waters Intensive Sampling” is an Eureka R&D project, supported by the PRAXIS XXI Program. This project envisages the development of a highly operational and low-cost AUV based system for scientific and environmental data collection in the Portuguese coastal waters.

Traditional sampling techniques for underwater observation are generally expensive and do not offer a comprehensive coverage, specially as the requirements of oceanographic and environmental field studies become more and more demanding. In fact, recent advances in ocean sciences and technology have been stressing the importance of efficient observation methods in order to fulfill the requirements of the so-called real-time oceanography [1,2].

AUVs may be efficiently used in a wide range of applications. They were first developed with military applications in mind, namely for mine hunting missions. Later on, scientists realized their true potential and started to use them as mobile sensors, taking samples in difficult scenarios at a reasonable cost. Currently, there is an increasing worldwide effort concerning the design and implementation of AUVs. This trend will result in the availability of fully operational vehicles that will make it possible to envisage the operation of AUVs in more complex applicational scenarios.

The development of a system such as the one devised has much to gain from the interaction with demanding potential end-users. The information gathered from the requirements of realistic missions is proving to be invaluable in the overall system design. The resulting system will emerge from a trade-off between this top-down perspective and a bottom-up approach driven by the constraints imposed by state-of-the-art technologies.

III. THE *ISURUS* AUV

Isurus (Fig. 1) is a REMUS (*Remote Environment Measuring UnitS*) class AUV, acquired from the Woods Hole Oceanographic Institution, MA, USA, in 1997. REMUS vehicles are low cost, lightweight AUVs specially designed for coastal waters monitoring (maximum depth of 200m) [3]. The reduced weight and dimensions makes them extremely easy to handle, not requiring special equipment for launching and recovering, such as winching systems.

Isurus has a diameter of 20 cm and is about 1.5 meters long, weighting about 30 kg in air. This vehicle can cruise at a maximum forward speed of 4 knots, however the best energy efficiency is achieved at about 2 knots. At this velocity, the energy provided by the rechargeable lead acid batteries last for over 10 hours (i.e., over 20 nautical miles). We are currently evaluating other options for the batteries, based on technologies that allow for higher energy densities, namely Nickel Metal Hydride and Lithium-Ion.



Figure 1 - The *Isurus* AUV

REMUS original acoustic navigation system could be used in either LBL or USBL mode. A dedicated DSP processed the signals received by the hydrophones. We have implemented a new navigation system, which only operates in LBL mode, but where the DSP based signal detection was replaced by analog filters tuned to the frequencies of the signals emitted by the transponders. An algorithm that fuses range measurements with dead-reckoning information was also implemented in the on-board computer.

Although small in size, it is possible to accommodate a wide range of oceanographic sensors, according to mission objectives. For the missions described in this paper, we have integrated a CTD (from Ocean Sensors, CA, USA) and an altimeter (from Imagenex, Canada) in a specially designed nose extension.

A wide range of sensors can be easily integrated on these vehicles. Successful tests have been performed in the past with sidescan sonars, ADCP (*Acoustic Doppler Current Profiler*), and Optical BackScatter.

IV. MISSION SCENARIO

Cooperation with oceanographers and marine biologists from Porto University were instrumental to produce a set of application scenarios in which AUV based systems are clearly advantageous compared to alternative existing methods [4]. One of these scenarios consists in the use of AUVs for the identification of relevant factors affecting the eel recruitment process in estuarine environments. Aspects of the dynamics of

the coastal ocean and the estuary, such as horizontal and vertical circulation are believed to play an important role.

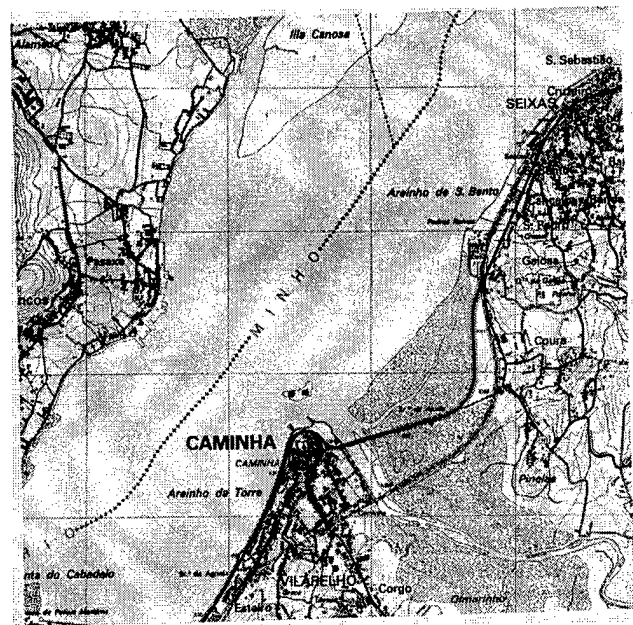
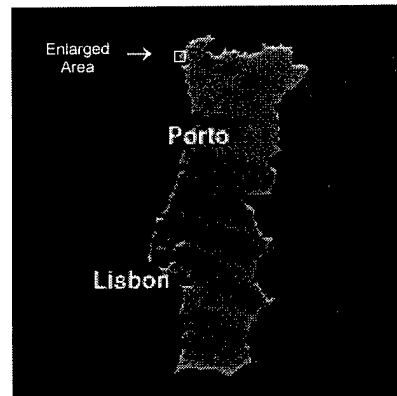


Figure 2 – Mission scenario overview (4km x 4km)

The scenario chosen for the first operational missions was the estuary of Minho river in the northern border between Portugal and Spain (Fig. 2), for 3 main reasons:

- **Logistics:** A marine station situated in this estuary provided the facilities required for field testing and development, including a small boat to support the missions.
- **Previous knowledge:** This river has been the subject of study and active research during the last 15 years. This has provided for some knowledge on the operational scenario, namely currents, depth profiles, tides, etc.
- **Scientific relevance:** Several studies, including 2 PhD thesis, have been recently conducted in this environment, particularly about the eel population. The hydrological aspects have been less studied, but it seems that the AUV measurements can provide information for a better understanding on the evolving ecological processes.

The estuary is about 5 km long, with a maximum width of about 2 km and a very narrow mouth. Due to the specific

characteristics of this estuarine region, the strong interaction between fresh and salt water causes circulation patterns with great variability in the values of temperature and salinity. Previous data also showed that typical currents can be over 1 knot, particularly during tidal changes.

As far as bathymetry is concerned, there are a few old charts, but the riverbed is continuously changing due to the strong dynamics. Typical depth values indicate depths around 3/5 meters, although there is a deeper channel well known to fishermen.

V. MISSION DESIGN

Estuarine circulation is usually very complex and horizontal sampling with the AUV at different depths may show circulation patterns very difficult to observe with any other technique. In order to achieve this, several cross sections (about 500 meters apart) should be performed, with the depth varying from the surface to the bottom. This should be repeated for different tides. Data to be collected included temperature and salinity. Other interesting data would be Dissolved Oxygen, but this sensor was not yet installed when the missions started. Later on, atmospheric parameters such as air temperature, luminosity and wind should also be analyzed.

The availability of an onboard altimeter allowed to test another type of mission: autonomous bathymetry. The idea was to evaluate the possibility of using the AUV to map the bottom of the river and construct its 3D map. If viable, the vehicle could be deployed in consecutive sections of the river, in order to build an updated map of the bottom. Besides demonstrating the vehicle as a tool for underwater mapping, these charts would also allow for a safer navigation. In the longer term, they may also be used to detect changes in the topography, map the ferry-boat channel, help in the construction of oceanographic models and the construction of 3D virtual environments for mission simulation.

VI. MISSION EDITING

An AUV mission starts with the vehicle programming, by editing a mission file with the objectives that need to be successively accomplished.

In the original implementation, a text file would have to be edited, which would result in a hard to debug file. Furthermore, the new QNX software architecture allows for the design of new mission objectives, as required, for example, in adaptive sampling missions (in which case, the mission goals may not be fully defined a priori).

For these reasons, we have redesigned the mission structure and we have developed a graphic mission editor to facilitate mission edition [6]. The new set of objectives encompasses all the previous ones and includes a few others, where the most important changes are related to adaptive sampling objectives. A different approach was taken as far as vehicle protection modes are concerned. We now have a set of protection modes for each objective. Each mode may be enabled or disabled, and for each enabled protection, there is

an emergency behavior associated (i.e., tells the vehicle what to do if the protection is triggered).

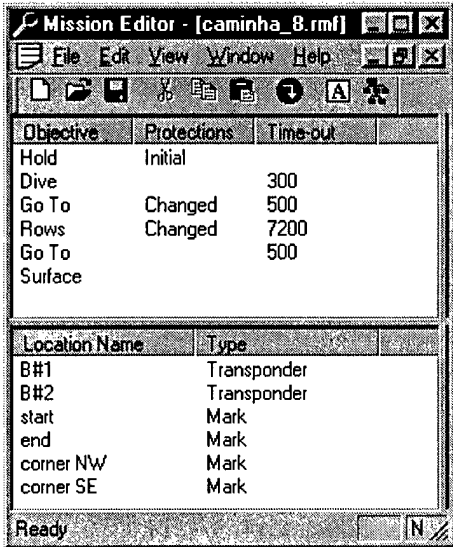


Figure 3 – A typical mission window

Figure 3 shows a simple mission window, where the vehicle is sent to a starting point, from where it swims in a lawnmower pattern ("Rows"). At the end, it is sent to the end point, where it surfaces to be recovered.

By selecting an objective, the user may edit the specific details. Figure 4 shows details of the "Rows" objective. In this case, the rows are 500 meters long and the objective would be completed after 5 consecutive rows, with 50 meters spacing between them.

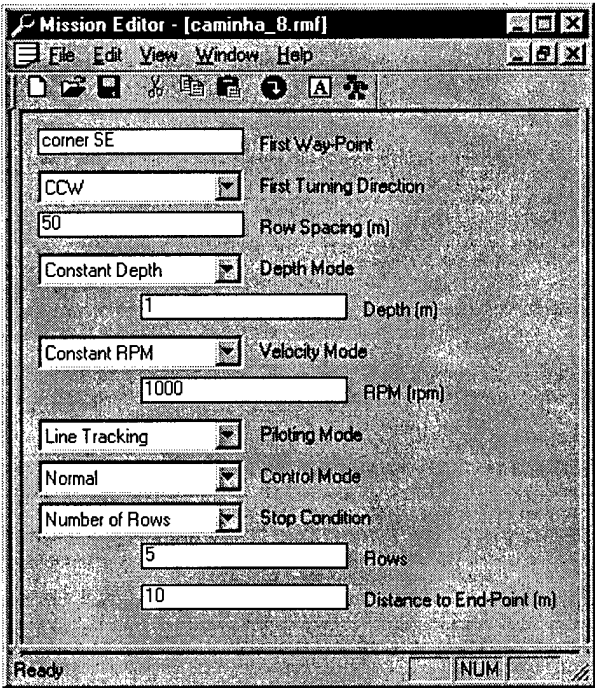


Figure 4 - Parameters for the "Rows" objective

VII. LOGISTICS

A. The PAL System

There is a significant risk of losing an AUV while performing autonomous operations. However, *Isurus* has an automatic responder that sends a specific acoustic signal whenever an interrogation is received. This system has a backup battery that keeps it working in the event of a failure in the main power system.

When the first field trials started, we developed PAL (*Portable Acoustic Locator*), a simple device with 2 purposes: to be able to generate a series of acoustic signals, interpreted by the vehicle as an abort command, and to measure distance to the vehicle by measuring the time elapsed between the interrogation signal and the vehicle's response.

PAL has been quite helpful during operations and it has been successively upgraded to measure ranges to different devices. Now, it is also possible to use it to know the position of the vehicle with respect to the baseline. We integrated new filters for the transponder receiver frequencies, so that it is possible to detect when the vehicle interrogates each of the transponders. Since the vehicle is consecutively switching from one transponder to the other, we can measure the time between interrogations and, so, determine the range to each of the transponders. This is only possible with the new LBL navigation system [5] and the new vehicle software [6], implemented on the QNX real time operating system. These two systems ensure that the vehicle switches to the other transponder *immediately* after detecting a response (the uncertainty in this switching time is kept below 1 ms). The best feature about this mode of operation is that it is completely passive, that is, it is possible to know the vehicle position just by *listening* to its normal operation. Furthermore, it does not depend on the location of the PAL transducer, since it only deals with time differences.

B. A Typical Mission

During this mission, the AUV would be navigating on an LBL transponder network. The estuarine scenario is characterised by having poor acoustics, so we had to increase the threshold levels for acoustic detection, reducing the maximum length allowed for the baseline. For this mission, we only used 2 transponders, defining a baseline not larger than 1 km.

It is difficult to work on the boat, even in a relatively calm day, so we tried to have the mission ready before leaving the marina. The only information missing before leaving was the *exact* transponder location.

After editing the mission objectives in the laptop, the final diagnostics were made, during which the various subsystems were verified (Figure 5). The pressure sensor was reset to compensate for changes in the atmospheric pressure and the compass was calibrated to compensate for local variation in the magnetic field.



Figure 5 - Final diagnostics by the riverside

Isurus was then placed on the boat, along with the few things required for mission support: 2 transponders with anchors and surface expressions, GPS receiver, KVH Datascope, PAL, and a laptop.

The first navigation transponder was deployed with the aid of a portable GPS receiver. Since there are no DGPS reference stations in the region, the position error was about 50 meters. We then used a KVH Datascope to provide precision bearings to natural references (whose positions were already stored in the laptop). Triangulation of these bearings allowed for an overall accuracy of about 10 to 20 meters.

For the second transponder, we went to the indicative GPS position and repeated the above process. However, at this time, we were also able to use Datascope to determine the bearing from the first transponder, and, with PAL, we measured range between both transponders. This way, we had enough information for a precise positioning (in fact, a lot better than required for this mission).

With the determination of the *exact* transponder location, the mission file was completed and transferred to the vehicle. PAL was then connected to the laptop serial port and the transducer was placed in the water. When the laptop tracking program started running, the vehicle was ready to start the mission.

At the end of the mission, the vehicle surfaced and stopped pinging the transponders, so the tracking program could not locate the vehicle any longer. We then moved the boat to the last known position and use the range utility (with PAL) to find it.

The mission operations ended with the recovery of the transponders (PAL was also used when they were hard to find) and the download of all the collected information.

VIII. MISSION DATA PROCESSING

There are two data sets collected during a typical mission. The first set is related to the vehicle internal data, which is only analyzed in the lab. This allows to evaluate the performance of the various subsystems (navigation, control, power consumption, etc) and provide useful information for

potential improvements. The other data set comprise all the information from the oceanographic sensors.

The oceanographic data requires time and position information. This is done by post-mission filtering of the navigation information, in order to correct for eventual positioning errors that may have occurred during the mission.

Measurements can be delivered to the end-users as raw data or they can be processed to allow for a rapid validation. In order to reduce this validation time, and also to help us troubleshooting any vehicle problem, we designed a Matlab application for data processing and visualization.

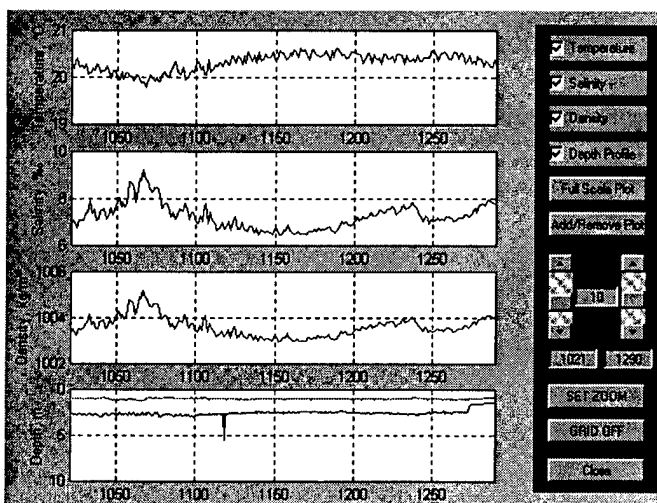


Figure 6 - Matlab application window with ocean data

Once the program starts, mission data needs to be loaded (by clicking a "Load Data" button). The user can then select the type of information to plot: ocean data, vehicle data, or custom. This last option allows to select any variables and is specially useful for troubleshooting. Figure 6 shows a plot of the ocean data for a part of the mission.

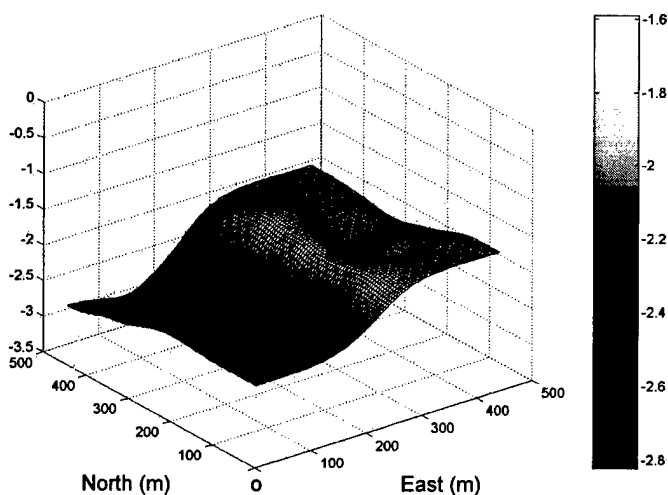


Figure 7 - Bathymetry of the sampled area

Oceanographic data can also be displayed in 2D or 3D maps, after filtering. Figure 7 shows the result of filtering

bathymetry data and interpolating where there was no data available. It should be pointed out that in this particular mission, the row spacing was 50 meters, which only allows for a low-pass interpolation. This is the reason why the shape of the bottom is smoother than in reality. In order to obtain a more accurate description of the bottom, we would need to process data from a mission with less row-spacing.

In Figure 8, we can see temperature values for the same region as above, at 1 meter of depth. In this case, we plotted isotherms and a temperature distribution map.

In both figures, the plot reference (0,0) corresponds to coordinates (N 41°53'33",0; W 8°49'53",4).

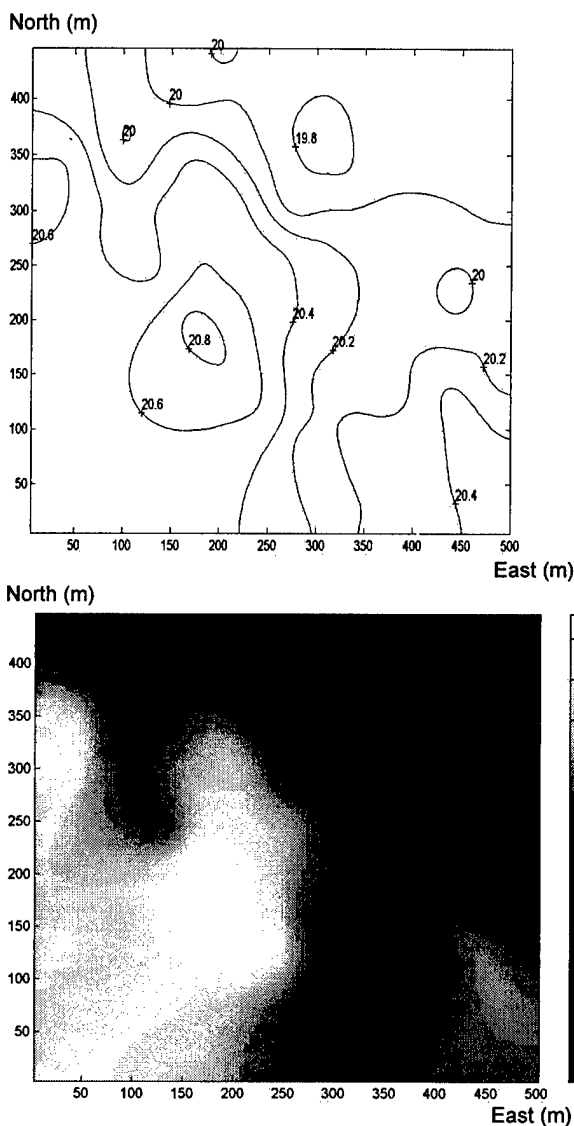


Figure 8 - Isotherms and temperature map

IX. CONCLUSIONS

The autonomous operation of the AUV, collecting relevant CTD and bathymetry data during over an hour with no operator intervention, was a pioneer experience in Portugal. In fact, the *Isurus* AUV succeeded in performing the programmed missions, even in adverse operational conditions, both weather-related (some of the sections were conducted with heavy rain and strong winds) and underwater environment (very shallow water).

The estuary of the Minho river is a challenging environment for AUV operations, since it is very shallow, with typical depths varying from 2 to 5 meters, and highly significant water currents during tide changes.

The high variability of the environment and also the need to collect the samples rapidly, before tide changing, contribute for the importance of the AUV as the most efficient way of mapping the underwater environment, as could be realized by the quasi-synoptic image of the river characteristics.

The shallowness of the environment and the variability of the bottom topography pose serious problems for depth control. In fact, the errors typically accepted as irrelevant when operating in tens or hundreds of meters, become very important in underwater environments as shallow as this one. At the end, we achieved a standard deviation of 7 cm from the required depth, which is a good measure of performance for the depth controllers.

The acoustic conditions at this scenario are about the worst than can be found in an underwater environment. Acoustic navigation has to deal with multipath for the sound waves, which means that the distance between the vehicle and each of the transponders had to be reduced. Furthermore, the high variability of the hydrological values significantly affects the sound speed, also increasing positioning errors. In this case, we had to operate with baselines about 1 km, in order to have reliable navigation. Even at this small distance, the vehicle would often experience difficulties in detecting transponder replies, probably due to channeling of the acoustic waves. However, overall vehicle navigation proved to be smooth.

The whole system is becoming more complete, but remains highly operational. The estuarine environment was first used as a testbed for new subsystems test and integration and most of the laboratory equipment required for development was easily transported to the station. The small boat available for operational support was sufficient for the estuarine mission. Data visualization immediately after mission completion is very useful to validate mission.

Operational missions have been facilitated by the PAL system, which has provided for a high degree of confidence when the vehicle is performing long autonomous missions.

X. FUTURE DEVELOPMENT

We are now in the process of installing an underwater video camera in the vehicle. This will be particularly important for an environmental monitoring mission to be performed in the near future. This mission will take place in a sewage outfall region off the Portuguese coast, where regular

inspection is required, comprising *in situ* water analysis and visual inspection of the underwater pipeline. The vehicle will travel about 2 km while maintaining the pipeline in the camera field of view. Later on, water monitoring sensors will be added in order to accomplish the whole monitoring plan.

Other planned missions include precise bathymetry of a large river dam (to study bottom erosion) and visual inspection of artificial reefs installed off the Portuguese coast.

As far as software is concerned, the mission editor is being upgraded, in order to include a tool for mission validation. Even though the objectives are already individually validated, the idea is to test overall mission integrity.

The fact that the position of PAL transducer is irrelevant to track the vehicle (as long as it is kept within maximum range), allows for the implementation of a new system for remote tracking. The idea is to place a passive device in the operation area and transmit data to the shore station through a radio link.

The laboratory will maintain the present strategy for the longer term. New partners and end users will be sought. New sensors will be added as required by their requirements.

These activities constitute the basis to achieve the ultimate goals of the project, namely performing autonomous environmental monitoring missions off the Portuguese coast with single and multiple vehicles, performing autonomous underwater docking and, finally, contribute for the establishment of a permanent underwater observatory.

REFERENCES

- [1] T. Curtin, J. Bellingham, J. Catipovic and D. Webb. Autonomous Oceanographic Sampling Networks. In *Oceanography*, Vol. 6, No. 3, 1993, pp. 86-94.
- [2] F. Lobo Pereira, J. Borges de Sousa, C. Gil Martins, E. Pereira da Silva. AUV System Requirements for Coastal Oceanography. In *Proceedings of the IEEE AUV'96 Conference*, Monterey, CA, USA, June 1996, 399-406.
- [3] C. Alt, B. Allen, T. Austin and R. Stokey. Remote Environmental Measuring Units. In *Proceedings of the Autonomous Underwater Vehicle's 94 Conference*, Cambridge, MA, USA, July 1994, pp. 13-19.
- [4] J. Borges de Sousa, N. Cruz, A. Matos and F. Lobo Pereira. Multiple AUVs for Coastal Oceanography. In *Proceedings of the MTS/IEEE Oceans'97 Conference*, Halifax, Nova Scotia, Canada, October 1997.
- [5] A. Matos, N. Cruz and F. Lobo Pereira. Development and Implementation of a Low-Cost LBL Navigation System for an AUV. To appear in the *Proceedings of the MTS/IEEE Oceans'99 Conference*, Seattle, WA, USA, September 1999.
- [6] J. Silva, A. Matos and F. Lobo Pereira. A Reconfigurable Mission Control System for Underwater Vehicles. To appear in the *Proceedings of the MTS/IEEE Oceans'99 Conference*, Seattle, WA, USA, September 1999.

LABORATORY EVALUATION AND PRELIMINARY FIELD TRIALS OF NEW " WOCE STANDARD " IDRONAUT MK317 AND OS316 CTD PROBES.

F. Graziottin, Idronaut Srl., Italy; G K Morrison, GO Environmental Services Inc., Florida; R. Stoner & F. de Strobel, SACLANTCENT, Italy.

The MK 317 is a multi-parameter Conductivity, Temperature and Depth profiling unit (CTD) with a fast (50mS) Platinum resistance thermometer and a free flushing 3cm ceramic, four electrode, conductivity cell. (as used in the Neil Brown Instrument Systems, Inc. MKIII CTD) one of the units tested had redundant temperature and conductivity probes installed. Laboratory evaluations including shock tests on the pressure sensor, and both noise and calibration stability tests on conductivity and temperature sensors have been conducted at the SACLANT Underwater Research Center, oceanographic calibration facility. This facility has for three decades generated CTD calibrations that exceed WOCE standards in order to satisfy both NATO Navies and the Southern European Oceanographic Research community requirements Results are presented and compared from casts made with both the Mk 317 and OS 316 (in self recording mode) and SBE 911 plus or SBE 25 operating from the same deployment frame.

I Introduction

For many years the European community has, by means of funding instrumentation development and promoting the use of such equipment in Community funded Research projects, been encouraging European manufacturers to challenge the supremacy of North American oceanographic equipment manufacturers. This policy has made the incumbent North American companies both nervous and willing to participate in joint manufacturing ventures. This paper will review the evaluation of products from one such collaborative venture between Idronaut Srl of Milano Italy and General Oceanics Inc. of Miami, Florida. Equipment has been deployed during cruises from the R/V Alliance, February 1999 and B/O Garcia del Cid, May 1999. The performance of several different manufacturers' conductivity, temperature and depth profiling systems have been compared.

II Equipment

There are several different Idronaut CTDs involved in this evaluation. During the first

cruise there were two instruments, a MK317 which had been adapted to handle data from an old Meerestechnik Elektronik sound velocimeter and an OS316. The comparison instrument was a SBE 911 plus. During the second cruise there were three Idronaut instruments, a MK317 with a

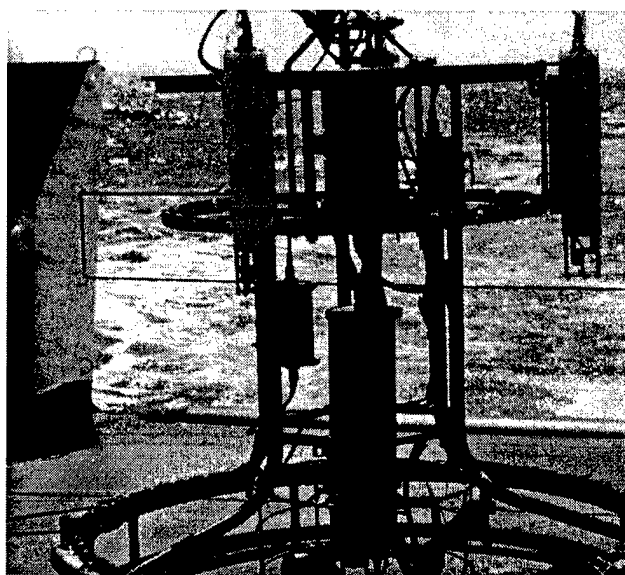


Figure 1: CTD array on board B/O Garcia del Cid

single temperature and conductivity sensor, a 316 with dual temperature and conductivity sensors and a MK318 with three conductivity sensors and one temperature sensor. The comparison instruments were a MKIIIC and an SBE 25. The instruments that were evaluated are tabulated in Table 1.

Table 1 Instruments reviewed

Instrument	Description
911 plus	Standard model SeaBird CTD
316	Idronaut internal recording Environmental CTD
317sv	Idronaut internal recording CTD, with GO MKIIIC conductivity cell and a Pt100 thermometer, modified to accommodate ME Sound Velocimeter
MKIIIC	Standard MKIIIC CTD
SBE 25	Standard internal recording SBE Model 25 CTD
317	Idronaut internal recording CTD with two GO MKIIIC conductivity cells and two Pt100 thermometers
318	Idronaut internal recording CTD with three GO MKIIIC conductivity cells and one Pt100 thermometer, unfortunately damaged prior to data collection
319	Idronaut internal recording Environmental CTD modified to accommodate dual conductivity and temperature sensors

On the second cruise a new MK 318 CTD with three conductivity sensors was physically damaged, beyond repair, without collecting any data.

All raw data collected have been presented unprocessed with the exception of the SeaBird data which has been processed according to the recommendation of SeaBird. See APPENDIX A for a description of the

processing applied to the SeaBird instruments' data sets.

III Laboratory tests

Prior to the January cruise the CTDs were subjected to a routine calibration and also a

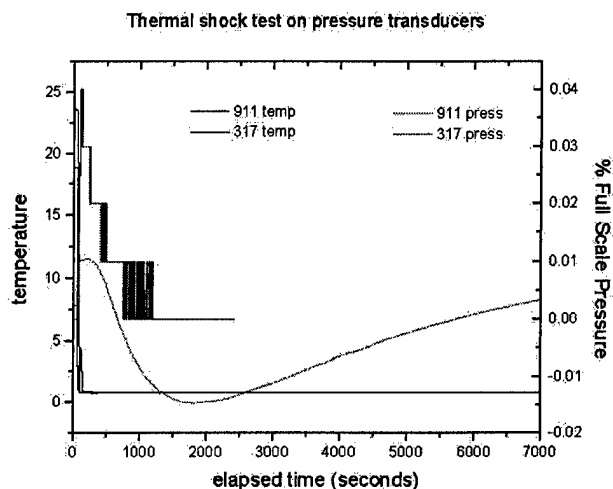


Figure 2 Thermal shock response

thermal shock test on the pressure transducers. The results of the thermal shock tests are presented as figure 2. The MK317 evaluated had an amplitude response that was initially greater than that of the 911 but the recovery time of the MK317 was less than 1,500 seconds compared to the 911 which was still not fully recovered after 7,000 seconds. The observed amplitude responses were equivalent to ± 1.2 decibar and 0.75 decibar for the MK317 and 911+ respectively. The apparent poor resolution of the 317 pressure sensor is a function of the data having been truncated at 0.1 decibar with a full scale of 1,000 decibar. The actual resolution of the instrument is 16 bit or 0.1 in 7,000.

Attempts at examining the noise and stability of sensors in the laboratory calibration tanks were inconclusive as the noise levels of the sensors were less than the noise created during the cycling of the baths. The authors have therefore attempted to compare the temperature and salinity signals during an actual cast. Figures 3 and 4 are graphic

presentations of temperature and salinity over a 100 meter section of ocean.. The Idronaut two headed environmental probe, model 319, has noise equivalent to it's digitizing increment of 0.001 degrees, four of the sensors agree to within ± 0.005 degrees over the 100 meter section plotted the fifth sensor is displaced by about 35 milli-degrees but has the identical form of the other sensors.

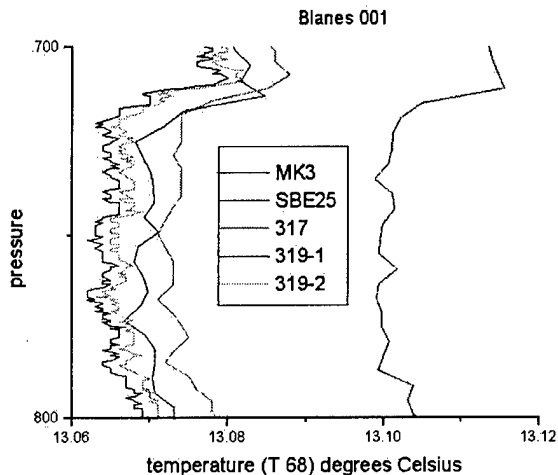


Figure 3 Temperature noise comparison

A comparison of salinity sensor performance was inferred from the salinity plot for the same section of the water column. Figure 4 illustrates the same digitizing noise in the

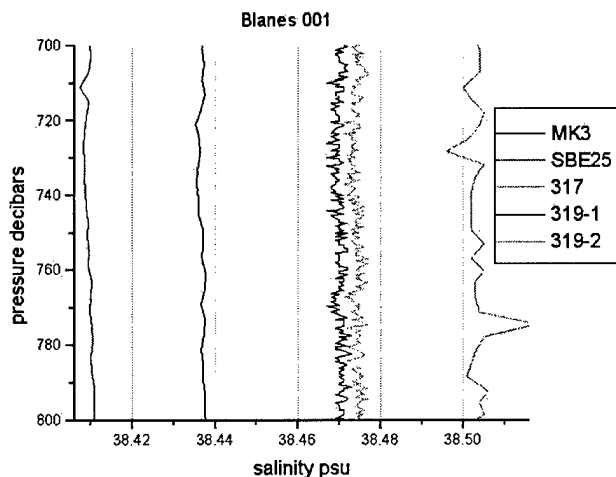


Figure 4 Salinity noise comparison model 319 salinity sensors that was apparent in the temperature signals. The 319, MKIIC and SBE 25 exhibit almost no evidence of,

time constant mismatch, generated "salinity spiking" the excursions in the salinity profile of the 317 at 730 and 780 meters are however almost certainly generated by this phenomenon. A procedure will need to be developed to correct this problem.

IV Field results from R/V Alliance

The first two stations were conducted from the R/V Alliance on each of the two casts two water samples were taken and later analysed Tables 2 and 3 show the result of these calibration checks. Cast 1 intercompared a 316 and the 911 and cast 4 the second data set presented intercompared the 317sv and the 911.

Table 2 Water bottle comparison at Lerici #1

Instrument	Salinity psu	Pressure decibars	Salinity difference
Bottle 1	38.524	964	
Bottle 2	38.524	964	
911	38.520	964	- 0.004
316	38.526	964	+0.002

Figures 5, 6, and 7 show the inter-comparison of temperature, salinity and oxygen respectively.

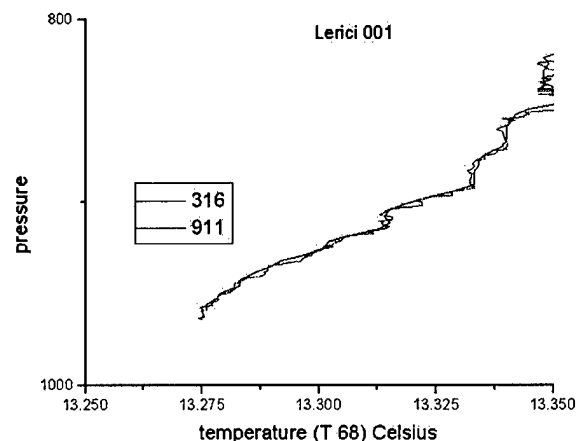


Figure 5 Temperature comparison

The temperature traces of the two probes are intertwined and show neither significant offsets nor gradients. Figure 6 is the equivalent presentation for salinity, the bottle data has already shown us that the instruments are in good absolute agreement.

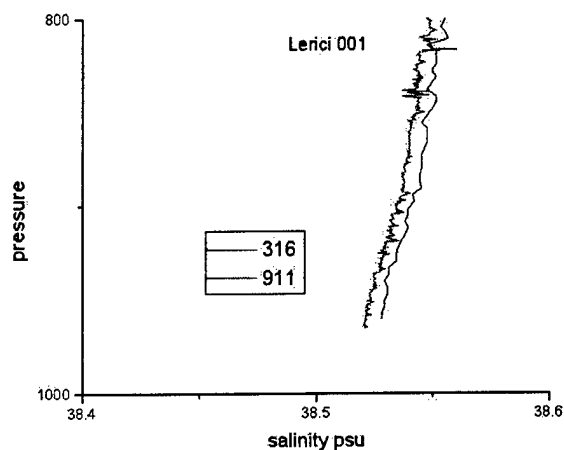


Figure 6 Deep salinity inter-comparison

It is interesting to note that there is a lot more noise or maybe structure in the 911 signal than is apparent in the 316 signal. There is an offset which the bottle data has shown to be of the order of 0.006 psu. Figure 7 shows the differences in measured dissolved Oxygen displayed as percent of saturation.

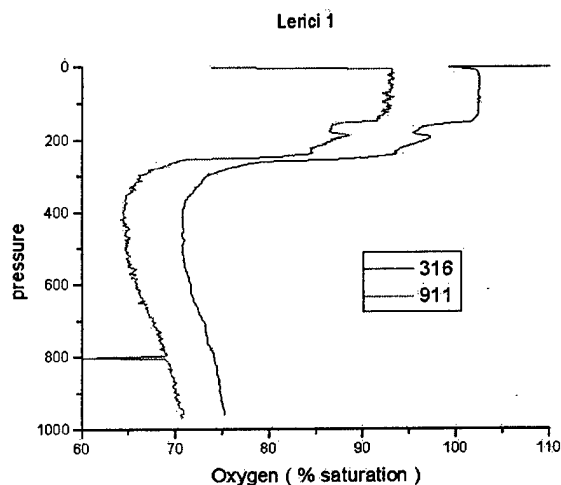


Figure 7 Differences in percent saturation of dissolved Oxygen.

The Oxygen data displays both an offset and a marked pressure dependence both of which may be readily corrected with data from a Winkler titration.

The second R/V Alliance station is described by Figures 8, 9 and 10 and the water bottle comparison is outlined in table 3 below.

Table 3 Water bottle comparison at Lerici #4

Instrument	Salinity psu	Pressure Decibars	Salinity difference
Bottle 1	38.573	608	+ 0.001
Bottle 2	38.571	608	- 0.001
911	38.578	608	+ 0.006
317sv	38.577	608	+ 0.005

Table 3 clearly illustrates that the salinity measurements are consistent and repeatable between the two instruments that are being compared, at least in the upper 1,000 meters of the water column.

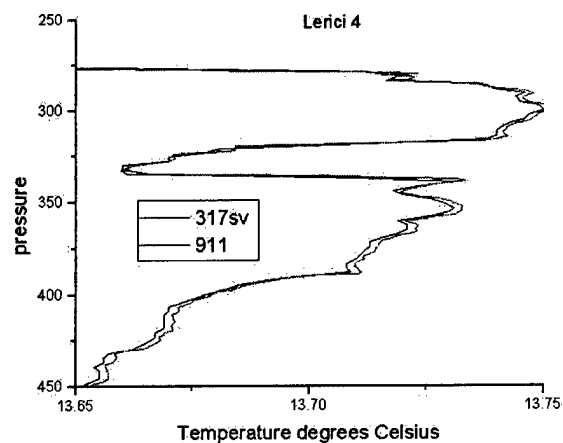


Figure 8 Temperature comparison Lerici #4

There is a small offset between the two temperatures of the order of 0.006 degrees, it appears to be uniform over the pressure range that was measured. Figure 9 illustrates the difference between salinities as measured by the two instruments.

The salinity indicated by the 911, Figure 9, appears to be about .002 to .003 psu higher than that measured by the 317sv.

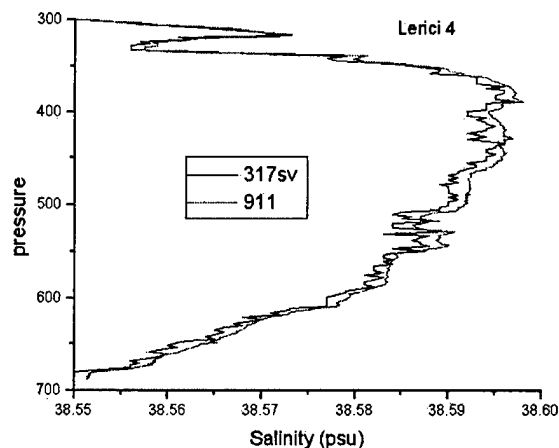


Figure 9 Salinity comparison Lerici #4

The calculated sound velocities, Figure 10, from both the 911 and the 317sv are indistinguishable from one another, and the value measured by the Merestechnik Elektronik probe differs only by a few tenths of

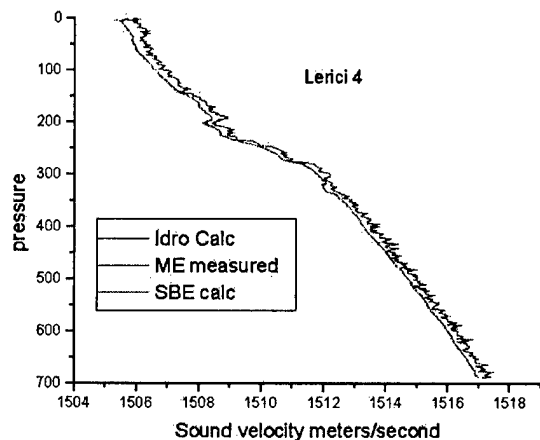


Figure 10 Sound velocity comparison

a meter per second from their common value. There is also a little more noise associated with the direct measured value.

V Field results from B/O Garcia del Cid

In May 1999 during a short cruise from Barcelona to the Blanes canyon we had a second opportunity to inter-compare Idronaut and other manufacturers CTDs. Figures 11, 12, 13 and 14 illustrate the results from this second cruise.

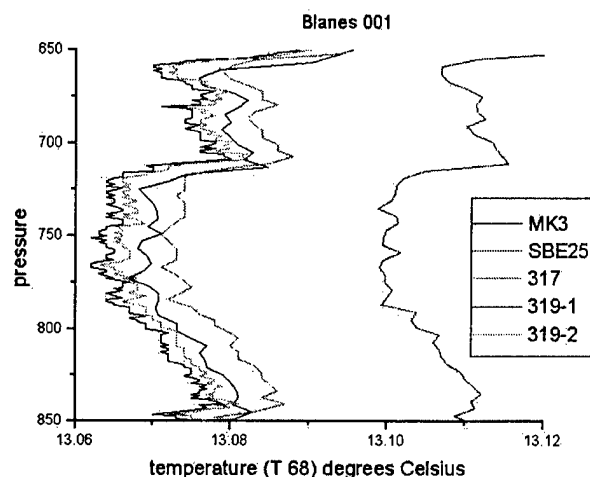


Figure 11 Temperature comparison Blanes #1

MKIIIC and Idronaut temperatures are grouped to the left of the graph with a total scatter of ± 0.005 degrees. The SBE 25 temperatures are offset by 35 milli degrees. The form of all of the profiles is however very similar except that the digitizer noise is noticeable in the 319 data.

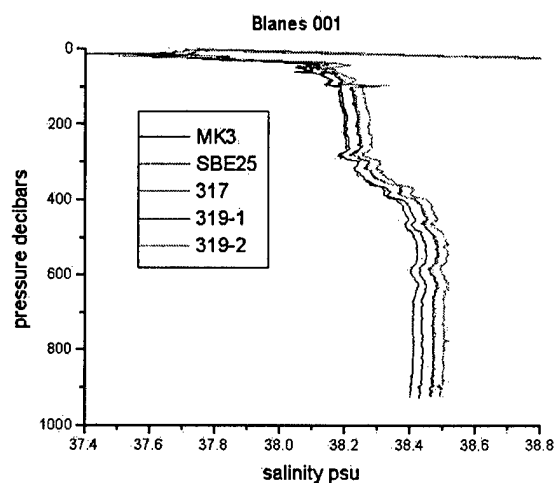


Figure 12 Salinity comparison Blanes #1

With the exception of the MKIIIC and SBE 25 all of the traces in Figure 12 are parallel with a fixed offset from top to bottom. Careful calibration against water bottles would make all of the profiles useful.

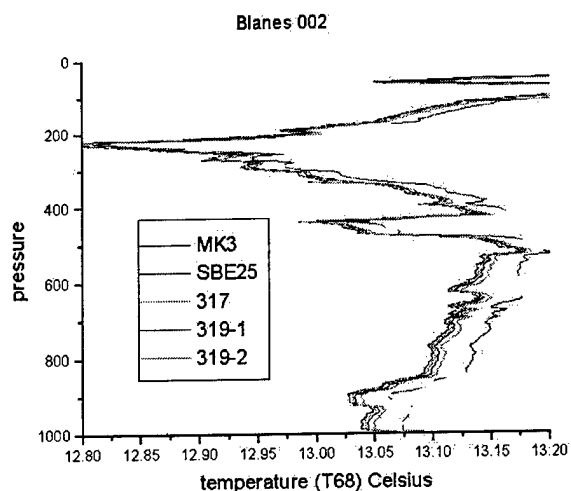


Figure 13 Temperature comparison Blanes #2

The curves from Figure 13 indicate that the SBE 25 temperature may have a significantly greater offset at depth than at the surface, this is probably the reason for the observed differences in the previous station's salinity offsets.

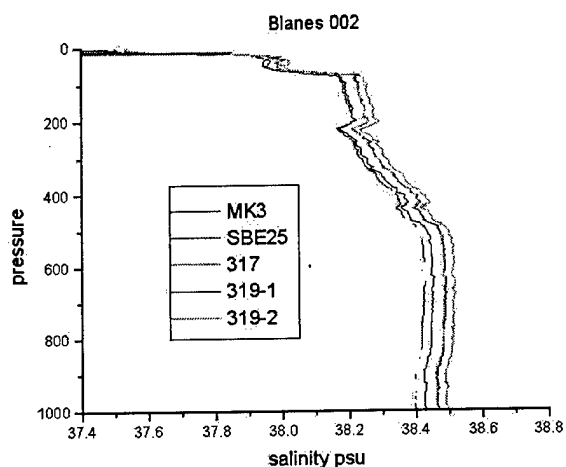


Figure 14 Salinity comparison Blanes #2

As in the first Blanes station the MKIIIC and SBE25 salinity signals appear to diverge with

increasing depth the other traces are again parallel.

VI Conclusions

It is of course extremely unfortunate that one of the instruments that was to have been evaluated was inadvertently destroyed prior to producing any usable field data. It would have been very interesting to have inter-compared the new 24 bit Idronaut Mk 318 and the traditional MKIIIC and SBE 911.

The balance of the data collected has held few surprises. The 316 and 319 CTDs from Idronaut that are designed for environmental applications rather than oceanographic use have shown their limitation with digitizer noise at the 0.001 level. Their Pt100 thermometers and robust conductivity cells have certainly performed well providing correctable performance across the entire pressure field measured. It would be interesting to repeat the experiment with rigorous water sampling to compute both salinities and dissolved oxygen values. The MK317 sensors have compared favorably with the reference instruments in both of the field trials and also in the laboratory tests.

VII Acknowledgements

The authors are very pleased to acknowledge the Officers and crew of both the R/V Alliance and the B/O Garcia del Cid without whose expertise and cooperation the project would not have been possible. We also would like to recognize Dr Jose Ignacio Diaz and Mr Mario Manriques of the Institut de Ciencias del Mar of Barcelona, Spain and their technical team onboard of the Garcia del Cid.

APPENDIX A

The following is copied verbatim from a SeaBird Electronics Inc. 911 plus manual, these instructions were followed carefully in processing the 911 data. [Capitalized names are programs that are run on the data as described.]

Standard processing of SBE 9/11 CTD Data

With oxygen

1. SEASAVE acquire the data at 24 hz.
2. DATCNV Convert the raw data to pressure, temperature, conductivity and parameters obtained from auxillary sensors such as dissolved oxygen current, dissolved oxygen temperature, and light transmission.
3. ALIGNCTD Advance oxygen 1 to 5 seconds relative to pressure
4. WILDEDIT check for and mark "wild" data points
5. CELLTM Conductivity cell thermal mass correction. Typical values are $\alpha = 0.03$ and $1/\beta = 7.0$
6. FILTER Low pass filter pressure with a time constant of 0.15 seconds to increase pressure resolution for LOOPEDIT
7. LOOPEDIT Mark scans where the CTD is moving less than the minimum velocity or travelling backwards due to ship roll.
8. DERIVE Compute oxygen
9. BINAVG Average data into the desired pressure or depth bins
10. DERIVE Compute salinity, density, and other oceanographic parameters.

EXPENDABLE HIGH PRECISION MICRO OPTICAL SENSORS TO BE USED IN AUTOMATED CONCERTED PROFILINGS FOR LARGE AREA DENSITY CONTOURING OF THE DEEP SEA

by

Karl-H. Mahrt

Institute of Experimental and Applied Physics
University of Kiel, Germany

Abolfath Hosseinioun

Goal International, San Francisco, USA

Abstract — This paper deals with a newly developed miniature optical density probe of better than ppm precision on the basis of the measurement of the angle of refraction of a tiny collimated light beam when passing through the interface plane between the sea water under test and an optical index of refraction standard reference material. For the first time the problems of designing and building of an extremely stable optical bulk head in combination with a particularly compact micro optical bench module were solved. These findings were the prerequisites to achieve the required high stability of the instrument. The central opto-electronical parts are few and consist mainly of a well defined single mode laser diode as a light source and a high precision lateral effect photo diode as beam position measuring device of the goniometer. The realized prototypes measure in all Neptunian waters down to 6000 meters.

These high precision micro optical density measuring devices for buoyancy driven expendable pop-up profilers are to be released in concerted actions from numerous bottom stationed autonomous multiple shot releasers properly distributed over a large area in the deep sea in order to observe the variability of the density field in space and time with high precision.

I. Introduction

In view of the continuously increasing demand of high performance Ocean instruments in general and more especially in search of better density measuring sensor systems particularly suitable for the use in permanent operational observation networks in larger Ocean areas we focused again on the study of optical index of refraction sensors that follow the principle of measuring the angle of refraction of a light beam entering from sea water into a glass prism. This prism serves as an index standard reference material and at the same time as a high pressure bulk head feed through of the light into the vacuum optical bench module of the

sensor, containing the refraction measuring photo pick-up at its end. From previous studies in the laboratory and at sea [1], [2], we learnt about the practical feasibility of such a concept for high accuracy applications and in the progress of our work we became well aware of the possibility to develop very much smaller even expendable versions of outstanding ruggedness and very high accuracy. Miniature expendable devices of such brand e.g. in combination with the inspiring concept of J.-P. Guinard's «Échantillonneur de Masses d'eau MARines» EMMA system [3], [4] seem to us to be very challenging by opening a new powerful perspective to derive on a routine basis density contours of large Ocean areas by synoptically profiling from numerous EMMA platforms suitably distributed on the bottom of the Ocean region of interest.

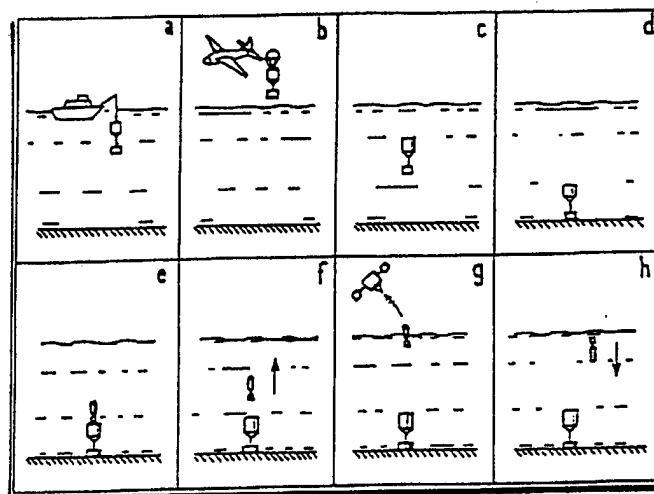


Fig. 1: (taken from [3]) The EMMA system: Storage of a bunch of probes, encapsulated in a conservation liquid in order to be protected against fou-

ling and to prevent sensor drift over a very long period of time. Released probes mount to the surface buoyancy driven.

II. Measuring density with the refractometer

The well known relationship between the density and the index of refraction n

$$\rho = k \cdot \frac{n^2 - 1}{n^2 + 1} \quad (1)$$

makes the optical index of refraction measurement inherently suitable for density determinations, with k being related to some molecular properties. From studying the empirical equation of state of sea water one learns, that one has to adjust for some residual influences of temperature and pressure and therefore these data must be provided with moderate accuracy when converting the n -measurements to ρ -results in the range of ppm accuracy.

III. The instrument principle

Figure 2 depicts the basic operation principle of the expendable sensor. 635 nm laser light from source 1 passes through the Y-coupler 2 and is guided through a fibre to the collimator 3 at the tip of the sensor head. From there a light beam with less than 0.5 mm diameter is launched into the sea water. The beam hits the index reference prism 4 at little less than grazing angle, enters the vacuum optical bench module and finally hits the lateral effect photo diode 5 at its end. Two trans-impedance amplifiers 6 and 7 convert both the photo currents I_1 and I_2 into the voltages U_1 and U_2 . In order to correct for wavelength and light dispersion effects in the optical media a small amount of the laser light is taken via coupler 2 to measure the wavelength by the spectrometer module 10 and convert it to the voltage U_λ . In addition to this one has to account for influences of the temperature which is measured by temperature sensor 8 and associated electronics 9 delivering the voltage U_T .

The four simultaneously measured signals U_1 , U_2 , U_λ , U_T of the sensor are taken to finally calculate the index of refraction value n .

$$n = n_0 + f(U_1, U_2) + \Delta f(U_\lambda, U_T) \quad (2)$$

The sum $U_1 + U_2$ represents the total light intensity and may be used to detect particles traversing the measuring volume and to eliminate the spikes they cause in the refractive index profiles.

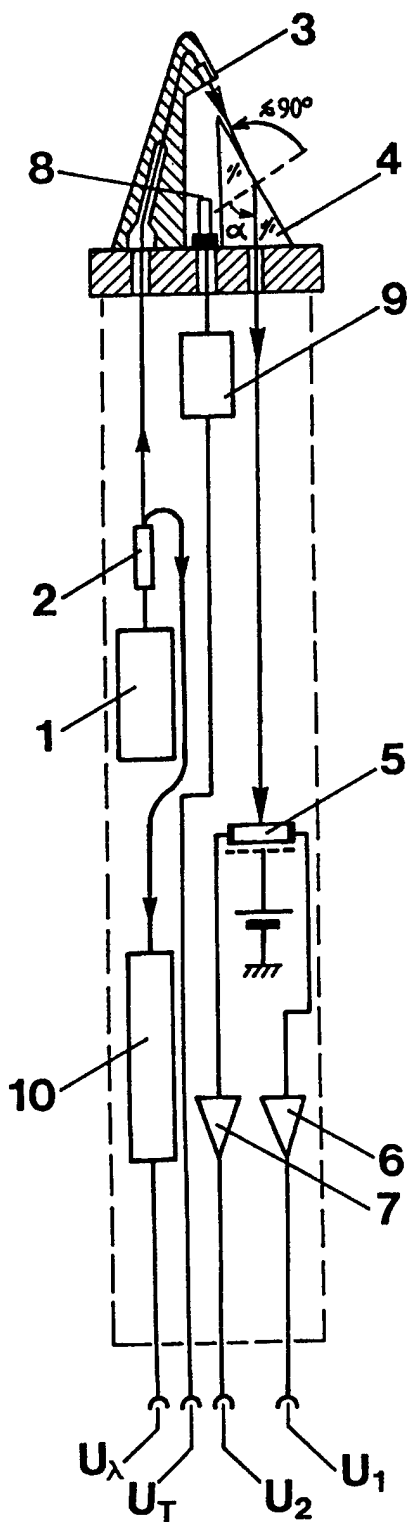


Fig. 2: The refractometer principle.

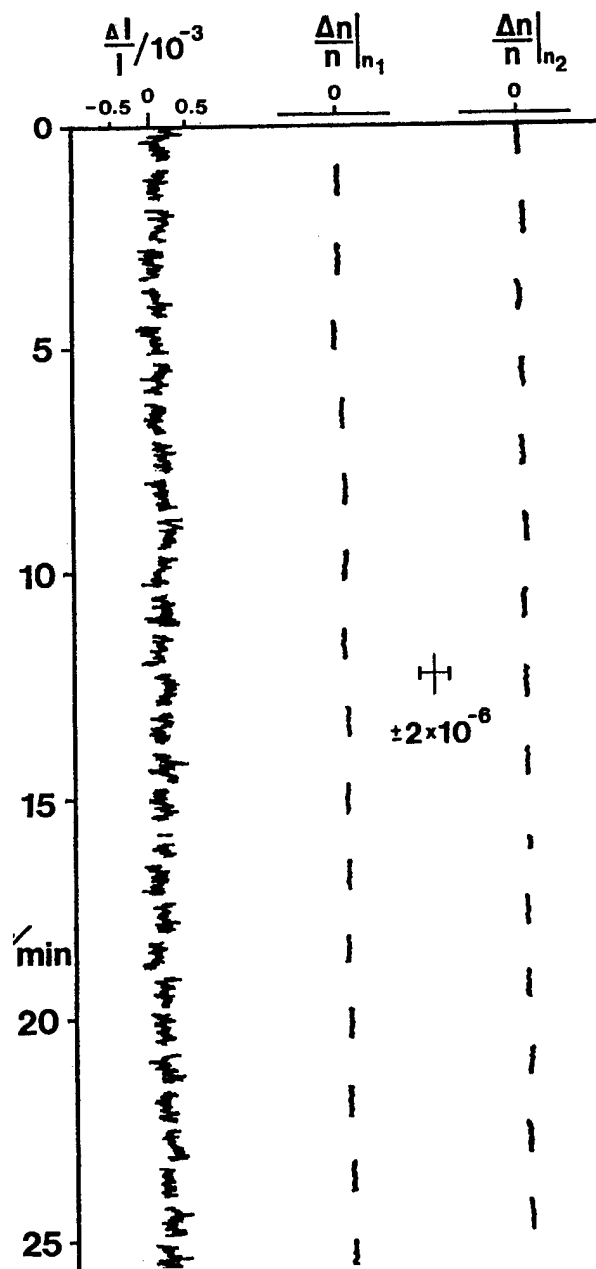


Fig. 3: Typical fluctuations of total light intensity and refractive index signals at two different index values.

IV. The instrument prototype

To arrive at light weight and small prototype instruments we used specially developed micro optical components, fibre optics and miniature electronics using mostly surface mounted devices. All sensor parts exposed to sea water are made of glass and titanium. A lithium battery power pack is included into the sensor with a capacity of at least 8

hours of continuous operation of the device. This is to prepare for a deep sea demonstration experiment with several probes following the concept of the EMMA system.

The major specifications are as follows:

light wavelength	: 635 nm
range	: ca. 1.331 ... 1.355
resolution	: $\leq 10^{-7}$
reproducibility	: 2×10^{-7}
accuracy	: still to be determined, expected to be $\leq 5 \times 10^{-7}$
refraction area	: 1,9 mm ²
measuring volume	: 1,1 mm ³
max. sampling frequency	: 1 kHz
total length	: 31 cm
max. diameter	: 4 cm
max. operating depth	: 6000 m
total mass (including batteries)	: 460 g

Figure 3 shows a typical plot from a test run of the instrument, when introducing an artificial deflection of the light beam simulating a switching between the two pre-selected index values n_1 and n_2 within the measuring range of the sensor. In this case the sampling frequency was 25 Hz, the same value we anticipate to use in our first field trial with bottom released pop-up probes at low ascending speeds. On the left hand side in figure 3 one can see the fluctuations of the relative total intensity of the light as measured at the receiver.

Finally, figure 4 shows a photograph of the first prototype instrument and its protective container for transport.

V. Remarks

In order to meet the practical requirements of the oceanographical community one has to calibrate the sensor according to the presently generally adopted empirical equation of state of sea water. This is obviously necessary in order to ensure homogeneity between data sets gathered with different data collecting sensor systems. So our program is to calibrate and study the sensor

tho

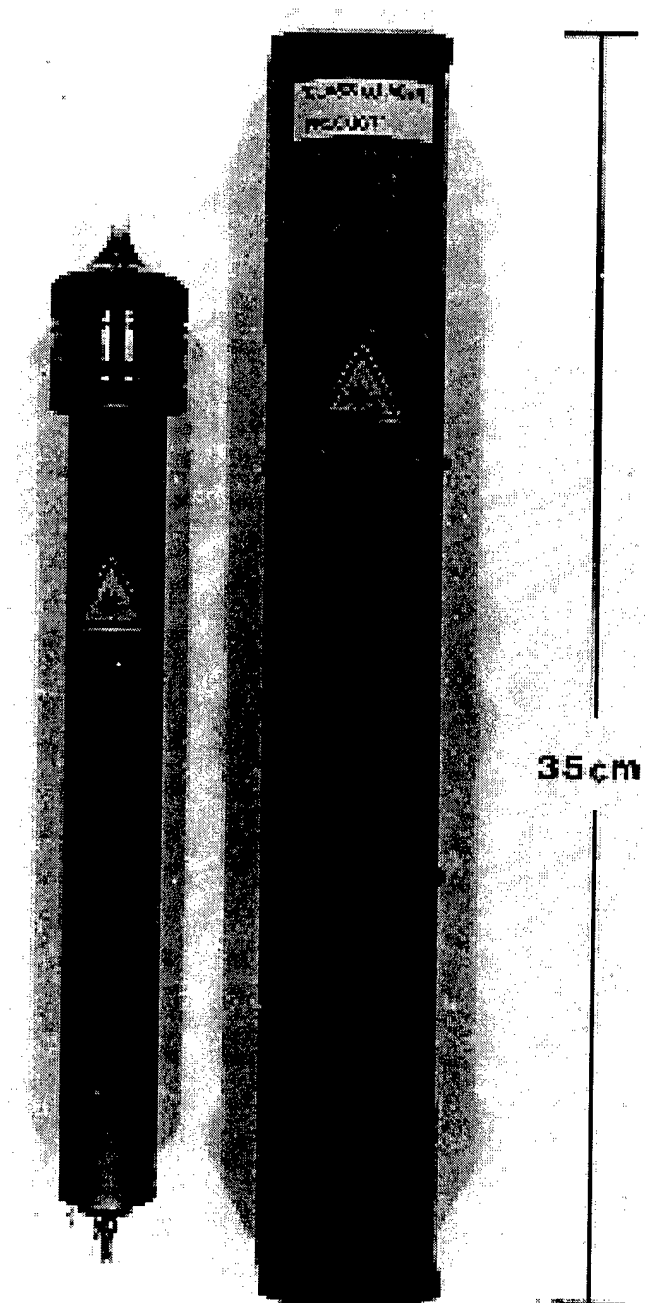


Fig. 4: The instrument prototype and its protective case.

roughly by use of temperature, conductivity, and pressure instruments with better than WOCE specifications, to finally come up with a statement on the experimentally determined sensor accuracy under practical conditions. At this place we would like to mention that in the course of our development work we used many times and with great advantage our very well defined sound speed

research facilities for reproducibility determinations of the optical sensor by monitoring the sound speed with stabilities down to 1 mm/s allowing e.g. to judge on refractive index stabilities down to about 5×10^{-8} . From this measuring experience and in view of the still compelling sound speed equation

$$v = \sqrt{\frac{1}{\kappa \rho}} \quad (3)$$

we feel very much tempted to spend some effort and concentrate more on a fundamental study of the DENSITY - REFRACTIVE INDEX - SOUND VELOCITY - relationship in water and sea water, in the lab as well as at sea.

Acknowledgements

The authors would like to thank J. P. Guinard, «Société Bretonne d'Instrumentation Océanographique», BriO, Concarneau, France and P. Marchand, «Institut Français de recherche pour l'exploitation de la mer», IFREMER, Brest, France, for all their powerful and personal engagement and work to have us go together in a joint European Community MAST III project „EMMA-DO“. We deeply regret, that due to a longer paralyzing severe crisis of our Kiel University all this was in vain and caused terrible delays and losses and we apologize for all the painful inconveniences. We are confident that nevertheless our common goals will still be reached in not so far a future.

References

- [1] Mahrt, K.-H. and Waldmann, H.-C.: „Field proven high speed micro optical density profiler sampling 1000 times per second with 10^{-6} precision“
OCEANS '88, IEEE Publ. No. 88-CH 2585- 8, Baltimore, MD, USA, Volume 2 (4), 497 ... 504, (1988)
- [2] Kroebe, W. und Mahrt, K.-H.: „Neuartiges Punktrefraktometer als räumlich und zeitlich extrem hochauflösender faseroptischer Mikrostruktursensor zur höchstpräzisen Bestimmung der Dichte- und Salzgehaltsfluktuationen in situ im Meer bei nur 0,1 Mikroliter Meßvolumen und bis zu 10 000 Messungen pro Sekunde“
Abschlußbericht EUREKA Projekt 1246, Euromar MICSOS 03 F 0136 C, 37 Seiten, Kiel, Feb. (1997).
- [3] Guinard, J.-P.: „EMMA: A new system for sampling marine water masses physical characteristics“
Oceanology International 96
Brighton, UK, Volume 2 (3), 191 ... 197, (1996)
ISBN: 0900254149
- [4] Conogan, R. and Guinard, J.-P.: „Observing operationally in situ Ocean water parameters: the EMMA system“

A Novel Approach for Obtaining Bubble Dissolution Measurements at Sea: Results

Russell Costa¹, Ronald A. Roy², and Kerry W. Commander³

Abstract-- A hybrid system for measuring the dissolution of gas bubbles in an oceanic environment was developed utilizing the Coastal Systems Station's Light Scattering Bubble Counter (LSBC). The LSBC independently measures flow velocity and bubble size, and is capable of distinguishing bubbles from particulate matter. In the hybrid system, the dynamic range of the LSBC measurements is 50 microns to about 300 microns in radius. The system is filled at depth in the sea, purged of all gas, and then closed from the outside environment. A steady flow is established and clean air is forced through a porous ceramic disk to create the initial bubble population. This bubbly mixture is re-circulated through the system at a constant flow rate of 22 liters per minute (LPM), or 33 LPM, corresponding to velocities of 30 cm/s and 45 cm/s through the LSBC aperture, respectively. The bubble radii are measured continuously using the LSBC, resulting in time-dependent bubble-size distributions. A numerical technique has been developed to estimate the dissolution rate from the bubble distribution time series.

Index Terms—bubble dissolution, light scattering

I. INTRODUCTION

The formation of gas bubbles beneath breaking waves and within surface ship wakes is an important factor in the design and operation of many sonar systems. Bubbles act as strong acoustic scatterers and attenuators, particularly in the vicinity of their resonant frequencies. Moreover, assemblages of bubbles can alter bulk acoustical properties in a profound way, leading to extreme levels of dispersion and non-linearity on the two-phase medium. The dynamics of these oceanic bubbles must be understood in order to factor them into models to be used in the design and analysis of various sonar systems. One key parameter is the dissolution rate (dR/dt), where R is the instantaneous bubble radius. This parameter, when coupled with the bubble terminal rise velocity, determines the longevity, and thus the acoustical significance of a bubble plume or ship wake.

Previous investigations to determine dissolution rates have been laboratory based, employing artificial or filtered seawater. Wyman *et al.* [1] measured the dissolution rates of bubbles introduced into stirred seawater under pressure. The work showed the dissolution rate to be independent of temperature, and that this rate did not deviate significantly with changing initial bubble radius (1.5-2.5 mm). Wyman did find, however, that the dissolution rate increases with increasing hydrostatic pressure until the external pressure reaches between 3 and 4 atmospheres. More recently, Detsch [2] found that for bubbles ranging from 50 μm to 500 μm in radius, bubble dissolution rates are highly dependent on the dissolved gas concentration and independent of both the temperature and the initial bubble size. This work was all done at atmospheric pressure.

For bubbles large enough to ignore surface tension and clean enough to ignore surface layers, the most important parameter governing mass transfer is the dissolved gas concentration (DGC), expressed as a percentage of saturation for the local thermodynamic conditions. For a liquid with a DGC of, say, 50% of saturation implies that the partial pressure of dissolved gas is approximately $\frac{1}{2}$ of the ambient gas pressure. By Henry's law, this imbalance leads to a mass transfer in the direction of lower partial pressure at a rate that is proportional to the partial pressure imbalance. Oceanic bubbles may behave differently, owing to the presence of surface-active impurities that can inhibit mass transfer. These two factors suggest that accurate dissolution rate measurements are best done *in situ*, thus the motivation for this instrument.

II. SYSTEM DESCRIPTION

The Bubble Dissolution Measurement System (BDMS) is a hybrid system built around the Light Scattering Bubble Counter (LSBC). The objective was a system that could be deployed from a research vessel, at remote sites, to measure *in situ* bubble dissolution rates at varying depths. The BDMS consists of a submerged, isolated, re-circulating flow system driven by a large-orifice peristaltic pump. The apparatus is deployed to depth, filled with seawater, purged of all gas, and then sealed. An initial bubble

1. Naval Undersea Warfare Center, Division Newport, Newport RI 02841

2. Department of Aerospace and Mechanical Engineering, Boston University, Boston, MA 02215

3. Coastal Systems Station, Naval Surface Warfare Center, Dahlgren Division, Panama City, FL 32407

population is created using air forced through a porous disk, and repeatedly convected through the sensing volume of the LSBC, which provides a running record of the evolving bubble size distribution.

A. Light Scattering Bubble Counter

The LSBC is an instrument developed by S.C. Ling of Catholic University for the Coastal Systems Station (CSS) in Panama City, FL [3]. The instrument shown in fig. 1 estimates bubble size *in situ* from a bubbly flow by collecting the light scattered at 125 degrees forward (no glory or diffracted components) where the scattered returns are dominated by the specular component. At this angle, the peak of the scattering amplitude is a monotonic function over the size range of interest. Thus the peak amplitude scattered from a single bubble crossing the sample volume corresponds to a specific bubble radius.

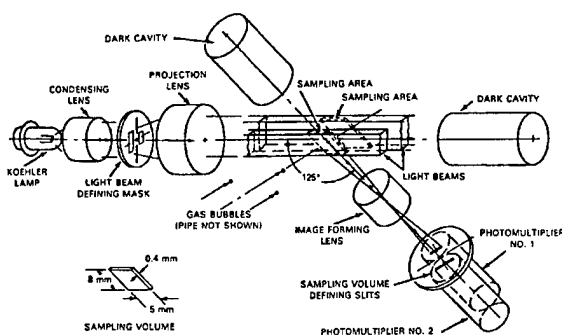


Fig. 1. Schematic of light scattering bubble detector.

Fig. 1. Light Scattering Bubble Counter

The instrument has two sample volumes in the center of a cylindrical orifice through which a flow containing entrained microbubbles is guided. A white light source is condensed, masked, and projected out into two sample volumes. The sample volumes are spaced 7 mm apart in the direction of the flow. The geometry of the sample volumes is a result of the collection lens used to image the two volumes onto two separate photo-multipliers, which convert the scattered light to voltage continuously. Dark cavities are built into the orifice to prevent reflections of light at the angle of projection and scattering. The output of each photo-multiplier is sampled at a 10kHz sampling rate and saved in binary files, with a tape backup recorded simultaneously.

The system is calibrated by generating single bubbles, beneath the two sample volumes, and allowing them to rise freely through the volume. An estimate of the rise velocity is thus obtained and from the theory of Stokes (with corrections from Langmuir and Blodgett) the corresponding bubble radius is estimated [4]. A correlation then exists between the bubble radius and the peak-scattered amplitude from the bubble crossing the sample volume. A polynomial fit to the

calibration data is shown below bounded by the 95% confidence limits with the residuals also shown.

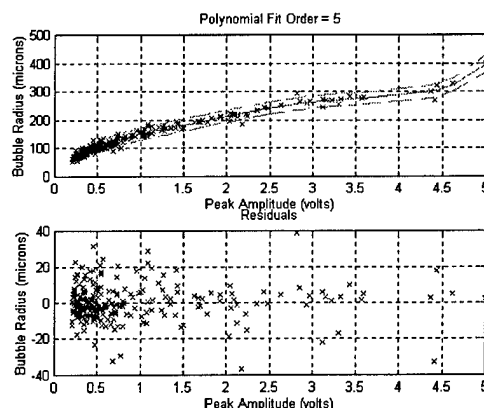


Fig. 2. LSBC Calibration Curve

B. Hybrid System Design and Operation

To measure dissolution rates *in situ* using the LSBC several design requirements had to be met. Initially, a bubble-free water sample at depth had to be obtained and a closed system had to be created. Next, a bubble population, in the size range measurable by the LSBC, had to be generated and circulated through the LSBC orifice to measure the evolution of the bubble size distribution (BSD). Finally, the system had to be refilled with fresh seawater and purged of all remaining air before the next run. These runs also had to be repeatable in a reasonable amount of time (minimal time between runs).

Figure 3 shows a block description of the system and its components. The red lines signify the control connections to the valves. Since the LSBC orifice is 1.5 inches in diameter, relatively large volumetric flow rates are required to ensure sufficient flow velocity to entrain all bubbles in the size range of interest. Furthermore, the pump could not be intrusive to the bubble population. For these reasons a large capacity peristaltic pump was used, with 1-inch internal diameter (ID) tygon tubing, capable of volumetric flow rates of up to 45 liters per minute (LPM). Another attractive feature of the peristaltic pump was that it could pump in either direction, which helps in purging the system of air between runs.

The system is filled and purged through the normally open, pneumatically controlled ball valves that are mounted above and below the LSBC orifice. The valves are actuated using nitrogen regulated at 85-psi pressure and are used to close the system prior to a given run. The connections are all made with schedule 40 PVC pipe, tygon tubing, and necessary fittings. The system internal volume (ocean water sample) is 2 liters.

The air delivery system for generating bubble populations consists of a porous ceramic disk mounted in a schedule 80 PVC threaded tee, a 3-way pneumatic ball valve, a check valve, and an air pressure regulator attached to a high pressure clean air tank. A bubble population is created, by forcing air through the ceramic disk. The ceramic is pressure rated and requires an over pressure of 7-9 psi for air to flow through it. The flow rate through the disk is a function of the input over pressure and was measured in the laboratory using a mass flowmeter.

The 3-way valve controls the air delivery system in the following manner. The valve's normally open path connects the ceramic disk to the check valve. Its actuated path connects the air regulator to the ceramic disk for generation of a population. The input over pressure is controlled manually at the air regulator. While the system is being lowered to the measurement depth the valve is actuated and the input over pressure is set high at the regulator to keep water from seeping through the disk into the air system. Once the system is at the measurement

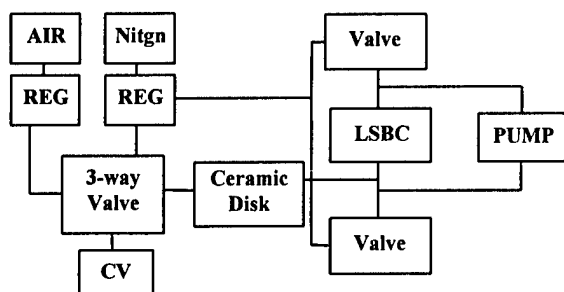


Fig. 3. BDMS Functional Description

Depth, the valve is released to its normal path and the check valve keeps the pressure at the face of the ceramic at 5 psi above the ambient pressure. This serves two purposes: it keeps the disk clear of water and it allows the void from the valve output to the disk to be raised to the pressure selected at the air regulator faster, thus minimizing the time delay for the air to be forced through the disk.

In a typical run, once the air delivery system has been initialized as described above, the system is closed and the pump is started. The pump maintains a constant flow rate in a counter clockwise direction (downward through the LSBC orifice). With the pump operating at a constant rate and the real time displays cleared of bubble events, the air delivery valve is actuated for 5 seconds, creating an initial bubble population. The data is then recorded from both LSBC channels for a typical run length of 5 minutes. After each run the fill valves are released (opened) and the pump is cycled in both directions, at various speeds, to clear the system of any remaining air and to refresh the sample volume. The procedure is repeated for several repeat runs at a given depth. The typical time

from the start of one run to the next is approximately 15 minutes (conservatively).

III. EXPERIMENT AND DATA PROCESSING

An experiment was performed at the Nanoose test range just off the coast of Vancouver Island, BC, Canada in September, 1998. The BDMS was lowered by crane from a research vessel and bubble dissolution data was obtained at depths from 5-25 feet at two different flow rates. The conditions for the test were calm and the weather had been clear for several weeks. The water temperature was relatively constant down to 20 feet depth varying slightly from 15.5 to 14.5 °C. From 20-30 feet the temperature decreased to approximately 13 °C. The salinity was approximately 27 ppm at the depths of interest.

The data from the test consists of 39 runs. Each run is a time series of light scattering data from the bubbly flow as it evolves from inception to full dissolution. As stated earlier, the LSBC is calibrated for single bubble events. A matched filtering scheme was implemented to exclude any detection that results from scattering from multiple bubbles or particulate matter. This is accomplished by matching the pulse, from each detection, in amplitude and duration. Scattering from particulate matter typically results in a flatter and more elongated pulse. Scattering from multiple bubbles can have double peaks (from interference) or are elongated in duration, thus are also distinguishable.

The data from each run, after processing (thresholding and filtering), consists of a time-dependent estimate of BSD that shows an evolution that is the result of some given dissolution rate. Figure 4 shows the results taken at a depth of five feet. The plot represents the BSD for 6-second intervals in the time series. The color bar is a log scale whose maximum is 100 (10^2) and minimum is 1 (10^0) and represents the number of bubble estimates at a given size in the time window that is represented. A clear evolution from the larger bubbles to the smaller ones can be seen and shows qualitatively the effect of dissolution on the population as a function of time.

The next part of the problem is extracting a rate of dissolution from the measured time-dependent BSD. One must first establish the statistical significance of our sample volume. The sample volume represents 3% of the total volume and, to be considered statistically significant should be representative of the overall population statistics of the systemic BSD at a given point in time. The desired way to establish this would be to estimate the BSD independent of the LSBC sample volume, a task that would best be done *in situ* during a run while sampling another part of the flow. Since this was not feasible, we had to assume that the sample volume was sufficient. This assumption is not entirely baseless. From previous

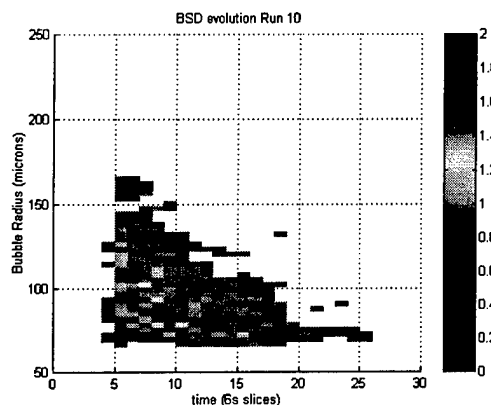


Fig. 4. BSD evolution at 5 feet (Run 10)

experimental data the repeatability of runs were found to be very good. This, coupled with the random nature of the bubble trajectories in the turbulent flow, gives us a strong basis for assuming our sample volume size to be sufficient.

Figure 5 shows total histograms of repeat runs taken at a 5-foot depth. The histograms are taken in 1-micron bins and illustrate the repeatability of the system. The experimental mean and standard deviation of these runs were nearly identical. Visually, the plot on the left has some bins with more counts, giving it a spikier, sparser look. The small bin size accentuates this feature.

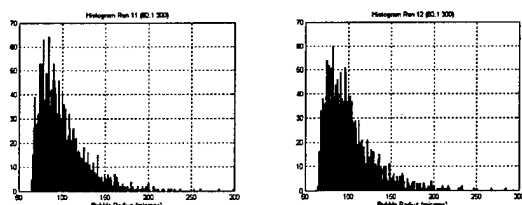


Fig. 5. Repeat runs at 5 feet

As a start to estimating bubble dissolution rates from the BSD time series we begin with the work of Detsch. In his experiments he found that the rate of dissolution was independent of initial bubble radius. If we start with this assumption, then a simple numerical approach can be applied to the data for the use of estimating the dissolution rate. Figure 6 outlines a numerical approach, which takes an initial distribution (sampled from the data) and then calculates a total BSD time series using a constant dissolution rate.

The dissolution rate is varied from $.25 \mu\text{m}/\text{sec}$ to $15 \mu\text{m}/\text{sec}$ in $.01$ micron increments. For each iteration of the dissolution rate, the total BSD of the model data (in $1 \mu\text{m}$ bins) is compared with the actual data from which the initial BSD was derived, and the mean squared error is calculated. The dissolution rate estimate is then taken as the minimum of this curve.

Figure 7 shows the mean square error curves for four runs at a depth of five feet. The mean dissolution rate from these runs is $1.2 \mu\text{m}/\text{sec}$.

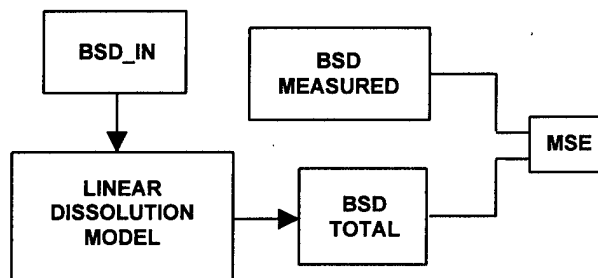


Fig. 6. Numerical Approach to Linear Dissolution

The mean square error plots for the repeat runs compare favorably and the minimums are very close. As an additional check for model accuracy the total histograms for the measured and the modeled BSD time series are shown in fig. 8 for one of the runs from fig. 7. Clearly the histograms compare favorably adding confidence to the model accuracy and thus confidence in the dissolution rate estimates.

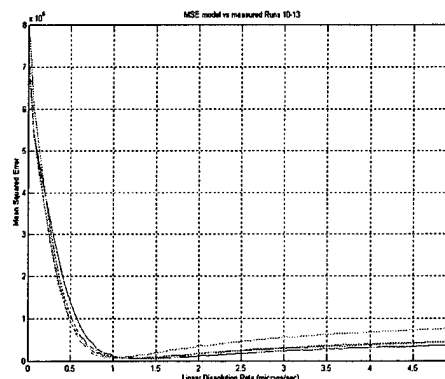


Fig. 7. Mean Square Error of Modeled vs. Measured BSD (depth = 5ft)

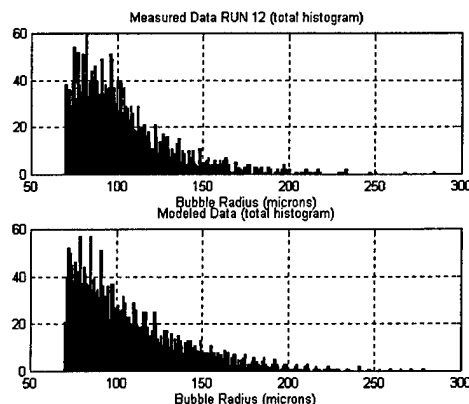


Fig. 8. Modeled vs Measure BSD at 5 feet (Run 12)

The procedure outlined above was performed for all pertinent runs, and the optimum dissolution rates estimated for each run. Figure 9 shows the estimated dissolution rates as a function of depth at the two different flow rates for our experiment.

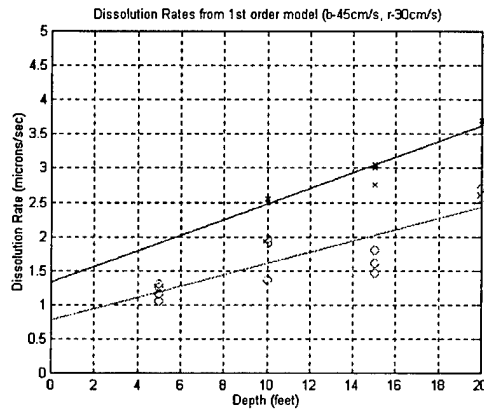


Fig. 9. Dissolution Rate Estimates

For all the repeat runs the dissolution rate estimates are reasonably close and it is clear that the dissolution rate increases with depth and the flow rate. The slopes of the dissolution rate with depth for the two flow rates are very close showing a clear depth dependence.

IV. ANALYSIS AND CONCLUSIONS

As part of the field experiment, at the Nanoose test range, salinity and temperature were measured, however, the DGC could not be measured (as a function of depth) - a parameter key to explaining the results from this first experiment. In particular, to effectively compare the estimates derived from this system to existing bubble dissolution models; one must know the local relative dissolved gas concentration with precision. In lieu of such gas concentration measurements, the authors make the assumption: the absolute dissolved gas concentration, and thus the partial pressure of dissolved gas, is constant down to 20 feet in depth and that it is equal to the saturation level calculated at the sea surface. The relative dissolved gas concentration thus (as stated earlier) decreases linearly from 100% at the surface to 50% at 10 meters depth, at which point the partial pressure of dissolved gas is equal 1/2 the internal pressure of the bubble (ignoring vapor pressure).

In an attempt to bracket the experimental results with model predictions, two models were chosen for comparison with the experimental data. The first model is taken from Detsch [2], and is known as the "Dirty Bubble Equation" [6]. The expression in (1) is applicable to freely rising bubbles where the rise velocity has been calculated using the theory from Stokes [4].

$$\dot{r} = \frac{2RT}{\pi} \left(\frac{\Delta C}{P} \right) \kappa^{2/3} \left(\frac{2\rho g}{9\mu} \right)^{1/3} \quad (1)$$

In (1), g is the acceleration due to gravity, R is the gas constant for air and P and T are the absolute pressure and temperature, respectively. The parameter ΔC equals $C_s - C$, where C_s is the saturation concentration (at depth) calculated from Henry's law, and C is the concentration at the sea surface (assumed constant at depth), κ is the diffusion constant, μ is the viscosity, and ρ is the density. All these parameters were found for air-seawater as a function of temperature and pressure.

This equation should act as a lower bound estimate of the bubble dissolution rate since it is reasonable to assume that added convection associated with the recirculating flow in our system only serves to enhance the dissolution rate. Figure 10 shows the dissolution rate at $T=15^\circ\text{C}$ and Salinity of 27ppm, as a function of the percentage of dissolved gas.

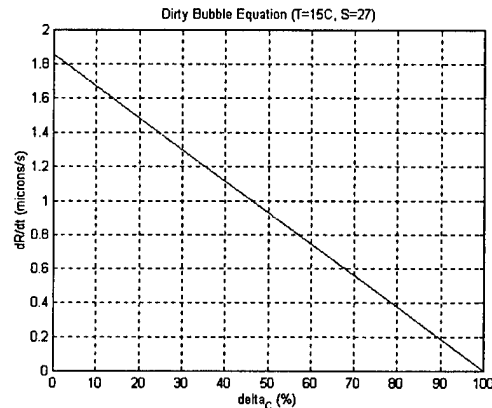


Fig. 10. Dirty Bubble Equation

In comparing figures 9 and 10 it is clear that the dissolution rates measured with BDMS far exceed those predicted by (1). For example a depth of twenty feet corresponds to a gas concentration of approximately 62%, which from fig. 10 corresponds to a dissolution rate of $0.7 \mu\text{m/sec}$, well below that plotted in fig. 9.

The next approach was derived from [5] and is shown in (2) below

$$\dot{r} = \frac{2RT}{P} \left(\frac{U}{2\pi} \right)^{1/2} r^{-1/2} \left(\kappa^{1/2} \Delta C \right) \quad (2)$$

where $U = \|v - V\|$ is the absolute value of the difference of the bubble rise velocity and the average flow velocity, respectively. This is a worse case

estimate of the velocity of the liquid flow relative to the bubble surface (maximum), and as such should provide an upper bound to the predicted bubble dissolution rate. This equation is a result of neglecting contributions due to surface tension and pressure fluctuations, and grouping the contributions of the individual constituent gases so that they possess a combined diffusion constant, and gas concentration for air in seawater [ref. 5, see eq. 14]. The effect of surface tension, as embodied in the Laplace pressure, is negligible for bubbles in our size range. Also, pressure fluctuations associated with the flow and with small changes in depth are deemed insignificant.

Figure 11 shows the dissolution rate, as a function of depth, calculated from (2) and averaged over the radius range of 70 μm to 300 μm .

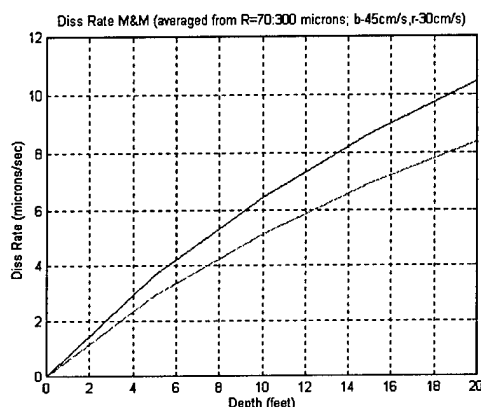


Fig. 11. Mean Dissolution Rates from equation (2)

This plot shows a clear dependence on flow velocity and depth, for the rate of dissolution similar to that shown in the data. The absolute values of dR/dt are significantly higher for this model, however, than for those estimated from our experiments. The difference is approximately a factor of 2-3 times higher. Although many factors could contribute to this difference, we believe the largest error comes from overestimating the liquid flow velocity relative to the bubble surface. Future experiments must account for the details of the bubble trajectories within the system. It might be possible to do this in the lab using particle image velocimetry to track the relative motion of the fluid and the bubbles.

In the course of this work we designed and built an instrument for a novel approach to obtaining bubble dissolution estimates *in situ* at sea, and developed a numerical technique for estimating the mean dissolution rates for a population of bubbles. The motivation for this work came from observations of variability in acoustical measurements of surface ship wakes and ambient bubble populations. The variations appear extreme, in so far as the lifetimes of micro-bubbles in the sea are concerned. Of particular interest is variability seen for different oceanic

environments, which made an *in situ* measurement approach attractive. At this point in the work, we are confident that the system itself is viable and that with additional instrumentation and more sophisticated modeling, *in situ* dissolution rates could be extracted accurately and consistently.

V. ACKNOWLEDGEMENTS

This work was supported by ONR code 333 and code 3210A.

VI. REFERENCES

- [1] Wyman, J. Jr., Scholander, P.F., Edwards, G.A., and Irving, L., "On the Stability of Gas Bubbles in Seawater", *J. Mar. Res.*, **11**, pp. 47-62, 1952.
- [2] Detsch, R.M., "Dissolution of 100 to 1000 μm Diameter Air Bubbles in Reagent Grade Water and Seawater", *J. Geo. Res.*, **95** (C6), pp. 9765-9773, 1990.
- [3] Ling, S.C., and Pao, H.P., "Study of Microbubbles in the North Sea", *Sea Surface Sound*, B.R. Kerman, Ed., Kluwer Academic Publishers, pp. 197-210, 1988.
- [4] Crum, L.A. and Eller, A.I., "Motion of Bubbles in a Stationary Sound Field", *JASA*, **48**, pp. 181-189, 1970.
- [5] Merlivat, L. and Memery, L., "Gas Exchange Across an Air-Water Interface: Experimental Results and Modeling of Bubble Contribution to Transfer", *J. Geo. Res.*, **88** (C1), pp. 707-724, 1983.
- [6] Levich, V.G., *Physicochemical Hydrodynamics*, Prentice-Hall, Englewood Cliffs, NJ, 1962.

SHALLOW WATER EXPENDABLE AND TRAWLER SAFE ENVIRONMENTAL PROFILERS

Robert Tyce**, Federico de Strobel*, Vittorio
Grandi*, Lavinio Gualdesi*

** Department of Ocean Engineering,
University of Rhode Island,
Narragansett, RI, 02882 USA

*SACLANT Undersea Research Centre,
Viale San Bartolomeo, 400,
19138 San Bartolomeo (SP), Italy

Abstract

A prototype Shallow Water Expendable Environmental Profiler (SWEEP) for rapid environment assessment has been developed and tested by SACLANT Undersea Research Centre in collaboration with the University of Rhode Island Department of Ocean Engineering. The SWEEP system is intended for autonomous vertical profiling of acoustic, optical and physical properties of the water column and seafloor in depths down to 100m. It is designed for data return and control via cellular phone or worldwide satellite packet communication while on the surface. The first prototype is an anchored profiler that uses an integral buoyant winch and sensor package to profile from the bottom up to the surface. The system is modular in design, allowing modules to be reused in new deployment alternatives. Already being planned is a Shallow water Environmental Profiler, in Trawl safe, Real time configuration (SEPTR). SEPTR is a bottom-up profiler with added ADCP, tide/wave gage and extended duration battery packages in a recoverable trawler safe housing. The design duration for the SWEEP is one month or 100 profiles in 100m water depth. The design duration for SEPTR is 3 months or 360 profiles in 100m. The profilers make use of new low cost, high performance sensors that include the following:

- 3-axis acceleration and magnetic field sensors
- Conductivity, temperature and pressure sensors
- Ambient light / optical attenuation sensors
- Ambient noise and current sensors
- Seafloor acoustic sensors
- DGPS navigation sensors

Two way communication of data, position and control allows profile results to be returned in real time, and operational commands, profile schedules, and DGPS correctors to be sent to multiple profiler instruments. Complete profiles will also be stored on board for recoverable units.

I. Background

Recent years have seen the development of a number of autonomous profilers to improve our ability to remotely observe the ocean (Rosby *et al.*, 1986; Davis *et al.*, 1991; Downing *et al.*, 1992; McCoy 1994, and Stevenson 1997). The Shallow Water Expendable Environmental Profiler (SWEEP) is a new winch driven autonomous profiler being developed as part of the NATO SACLANT Undersea Research Centre's program in Rapid Environmental Assessment (REA). Begun in 1997, the design includes the following modules: 1) Winch with line, motor, and battery subsystems; 2) physical, acoustical and optical sensor subsystems; 3) Cellular / satellite packet communication subsystems, together with DGPS navigation and antennas; and 4) Microprocessor computer system for control, communication and data logging. The system uses two way communication of data, position and control; allowing profile results to be viewed in geographic context, and new operational commands and profiling schedules to be sent to multiple SWEEP instruments. The first prototype uses cellular phone communication, with testing of new Low Earth Orbit Satellite systems for future profilers (Tyce *et al.*, 1998). Figure 1 illustrates the operational scenario for an air-launched SWEEP buoy.

II. Measurement Requirements

A set of requirements was developed for the SWEEP system consistent with the Rapid Environmental Assessment project at SACLANTCEN for NATO. The requirements include an expendable package deployable from ship or aircraft platforms with low cost sensors, accurate navigation, and communications systems able to send data and receive commands worldwide in near real time once surfaced. A month of autonomy with up to 100 profiles at rates to 0.5 m/sec in 100 m maximum water depth was deemed necessary. Measurements required in addition to traditional oceanographic measurements of temperature, conductivity, currents and depth include optical, acoustical, and physical properties of the water column and sea surface. Table 1 details the present list of required and desired characteristics of the SWEEP system. This project is intended to produce a production prototype with all of the required characteristics. Both required and desired characteristics are included in the recoverable, trawler safe version now being planned.

III. Design Concepts

The primary design concept for this project is an expendable autonomous instrument with a single set of sensors profiling the water column at programmed intervals and reporting water column, seafloor and sea surface parameters at controlled times via wireless communication. The vertical profiler concept includes both expendable anchored instruments that profile water column properties up from the bottom, and recoverable trawler safe bottom up profilers. These instruments might be deployed either from an aircraft in sonobuoy size format, or from a ship in larger, trawl safe format. They have a modest set of inexpensive sensors at very low cost, or can include more expensive sensors such as

SWEEP

Shallow Water Expendable Environmental Profiler

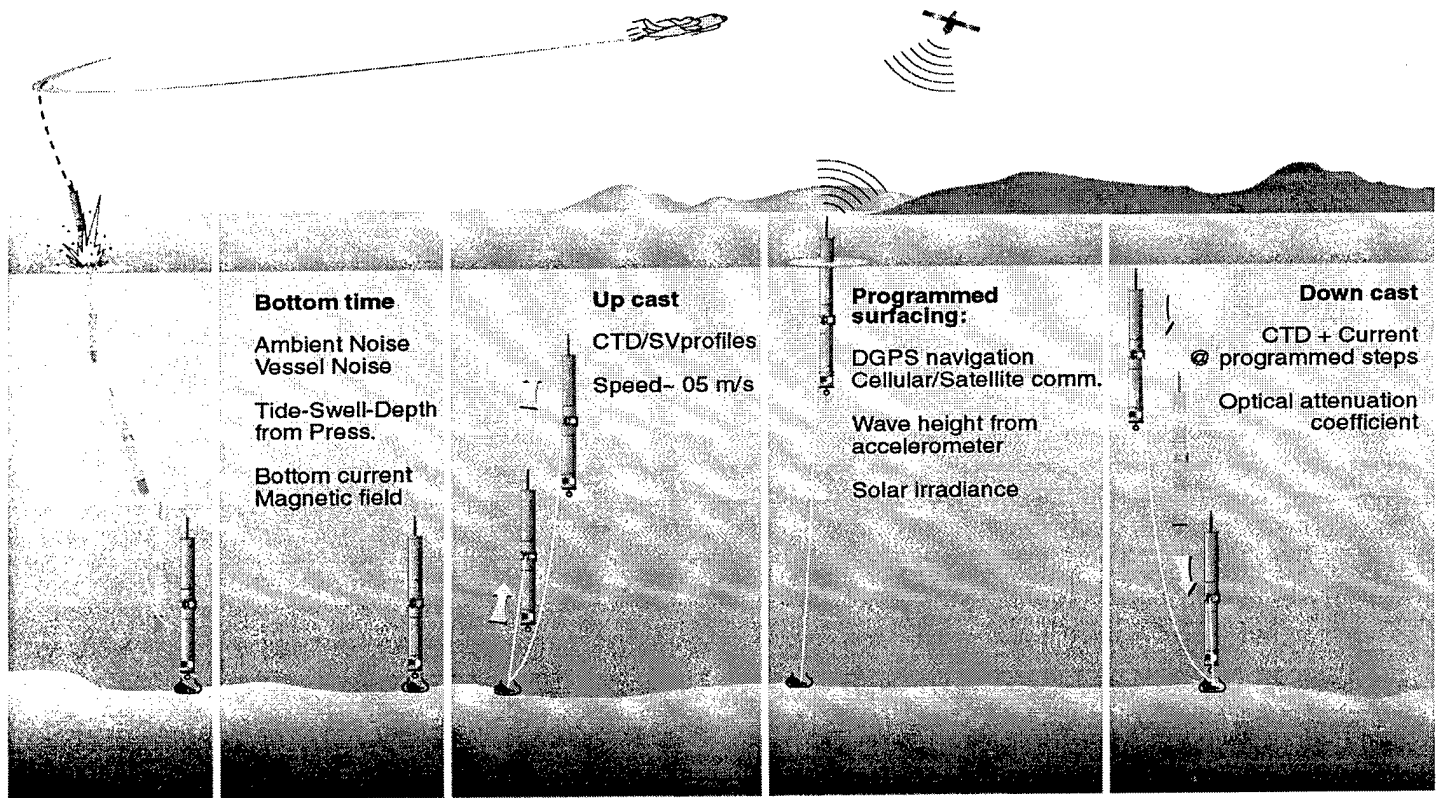


Figure 1: SWEEP Operational Scenario

ADCP sonars and tide/wave gages when required by the mission. This overall design concept is feasible at this time as the result of several recent developments: 1) New low cost environmental sensors developed in Europe and the US. 2) New Low Earth Orbit 2-way satellite communication networks such as ORBCOMM (Griffith et al. 1996). 3) New small submersible winches. Sensors have been obtained for all of the required measurement systems which cost between \$5 and \$100, with the exception of the 3 axis magnetometer at \$200, and the new current and ambient noise sensor systems which are being built at SACLANTCEN with production costs to be determined. Integration of very inexpensive sensors is essential to achieving an expendable system. Our target cost is \$6-10k US per system in production, excluding the trawler safe configuration, which includes an Acoustic Doppler Current Profilers (ADCP) and a tide/wave gage. Use of very inexpensive sensors is made possible partly by advances in sensor technology and partly by the operational nature of the measurements required for this system, which are generally not as demanding as scientific research requirements. The first SWEEP prototype is an anchored profiler that uses an integral buoyant winch and sensor package to profile from the bottom up to the surface.

IV. SWEEP Modules Included

Two-way communications modules (COM): Choice of GSM cellular telephone or ORBCOMM two way satellite communication options with submersible antennas. A recently developed GSM communicator with integral modem from TELITAL Italy is being used for cellular phone communications. An ORBCOMM LEOS mobile satellite communications system is also being tested for integration with the SWEEP prototype. These modules include flexible antennas custom built at SACLANTCEN.

GPS/DGPS Navigation module (NAV): A DGPS capable receiver, with differential corrections from fixed reference stations provided by the 2-way communications module when possible. This module uses NMEA and RTCM 104 standard messages at 4800 baud and an internal GPS antenna which receives through the fiberglass pressure case.

Oceanographic sensor modules (CTD): Low cost pressure, temperature, and conductivity sensors for determining water density, sound speed, swell, tides. Based upon existing Idronaut CTD profiler sensors. Provides interface, control and signal conditioning for strain gage pressure, PT100

temperature and 7 element conductivity sensors. Includes a 4 channel, 24 bit A/D with serial interface to the CPU module.

Acoustics Module (CUR): The acoustic current meter is based upon a commercial "sing around" sound velocimeter design. This system interfaces to the frequency/period measurement channels in the CPU module and measures current and sound velocity. Orientation for current and ambient noise is provided by the 3-axes magneto resistive and accelerometer modules, which serve as compass and roll/pitch (tilt) sensors. There is also an optional CPU interface for RS232 data from separate ADCP and tide/wave gage systems for more detailed current and surface elevation measurements in the trawler safe configuration.

Ambient noise is derived from conventional hydrophones using low frequency preamplifiers based upon a previous SACLANTCEN development for towed array applications. Noise intensity is used to prevent surfacing during ship passage. We also plan to use the phase relationships amongst several transducers to determine noise directionality in SEPTR. Preamplifier outputs are interfaced to the 12-bit A/D converter in the CPU module.

Light attenuation/irradiance sensor module (LITE): This is an internal low cost light to frequency converter module for solar irradiance measurements at the surface and diffuse attenuation coefficient profiles submerged (Dierssen *et al.*, 1997). This module interfaces to a time processor input on the CPU module.

3-Axis Accelerometer module (ACC): This internal low cost accelerometer module serves to measure sensor tilt and heave during current, ambient noise, and surface wave measurements. Its 3 DC outputs interface to the A/D converter on the CPU module.

3-Axis Magneto Resistive module (MAG): Internal low cost magneto resistive modules provide both magnetic field measurements and compass heading for other sensors. It uses 3 A/D converter channels

Central Processor Unit module (CPU): Manages all communications, sensor control, data acquisition, signal processing, storage and retrieval. Includes Motorola 68332 microprocessor and both analog, digital, and time processor interfaces sensing and control.

Winch Module (WCH): A low cost internal DC motor and gearbox coupled to a modified fishing reel with level wind through an enclosure end cap, makes up the winch module. The motor control electronics provides a digital interface to the CPU module. The winch is designed to accommodate 125m of 0.8mm electromechanical cable or longer high strength fishing line. A latching solenoid controls a low power brake.

Table 1: Measurement Performance Requirements

Function	Range		Resolution		Accuracy		Units
	Required	Desired	Required	Desired	Required	Desired	
Pressure	0-10		0.002		0.005		bars
Depth	1-100		0.02		0.05		m
Temperature	0-40		0.02		0.02		degrees C
Conductivity	0-60		0.02		0.05		mS/cm
Current speed	0-100		10		10		cm/sec
Current Direction	0-360		2		5		degrees
Noise Intensity	50-150		1		3		dB/uPa/Hz
Noise Direction		0-360		1		5	degrees
ADCP profiles		0-100m		1 hr		0.1 kt	
Swell Magnitude	0-20		0.1		0.5		m
Tide magnitude	0-20		0.1		0.5		m
Position (D)GPS	Global		1	0.1	100	2	m
Sound Velocity	1.4-1.6k		.1	.01	1	0.1	m/sec
Vehicle Buoyancy	x		x		x		From CTD
Communication	Coastal	Global	2.4 up	15 up	4.8 dwn	15 dwn	kbaud
Light attenuation	0-100		1		1		%/m
Solar irradiance		1-10 ⁵		0.1%		0.2%	uW/scm/nm
Wave height		0-20		0.1		0.5	m
Wave Direction		0-360		1		5	degrees
Acceleration-3 axes	4000		10		10		mg
Magnetic Field	+/-2		50u		100u		Gauss

Motor Control Module (MCM): A 68HC11 based motor controller developed at SACLANTCEN is interfaced to the CPU by serial RS232. A digital encoder enables absolute motor positioning and speed control. The system uses PWM motor speed control with a latching solenoid brake.

Battery and power supply modules (BATT): The SWEEP includes a combination of alkaline batteries for long life and rechargeable batteries for occasional high current requirements (winch and radio transmitter). The alkaline batteries are used to trickle charge the rechargeable batteries for optimum battery life. Voltage regulation and DC/DC conversion are provided to the electronics.

Enclosure modules (ENC): The integral anchored SWEEP configuration consists of two lightweight fiberglass cylinders with end caps joined by the open frame winch and current meter assembly. Designed for operation to 100m depth.

Anchor module (ANC): The anchor module includes both a heavy anchor released under winch control plus 2 meters of light weight chain to insure constant tension on the winch line while heaving on the surface.

Air launch module (AIR): Modifications to support sonobuoy type air launch are expected as part of a future effort.

V. Prototype Testing

During 1998 and 1999 the modules for the first SWEEP prototype were built and tested. Submerged field tests were also conducted of the assembled prototype. Figure 2 shows the SWEEP prototype buoy surfaced in the vicinity of a diver with underwater video camera. This camera was used to observe actual buoy dynamics. The tests included the following:

- Orbcomm Low Earth Orbit Satellite communicator tests
- GSM cellular phone communicator and antenna tests
- DGPS navigation system test using GSM correctors

- CTD calibration tests
- Battery system tests
- Accelerometer sensor tests
- Current meter and ambient noise sensor tests
- Echo sounder subsystem tests
- Pressure case overpressure and motor seals tests
- Motor driver and winch performance tests
- Submerged field tests June, July, Nov. '98 & Mar. '99

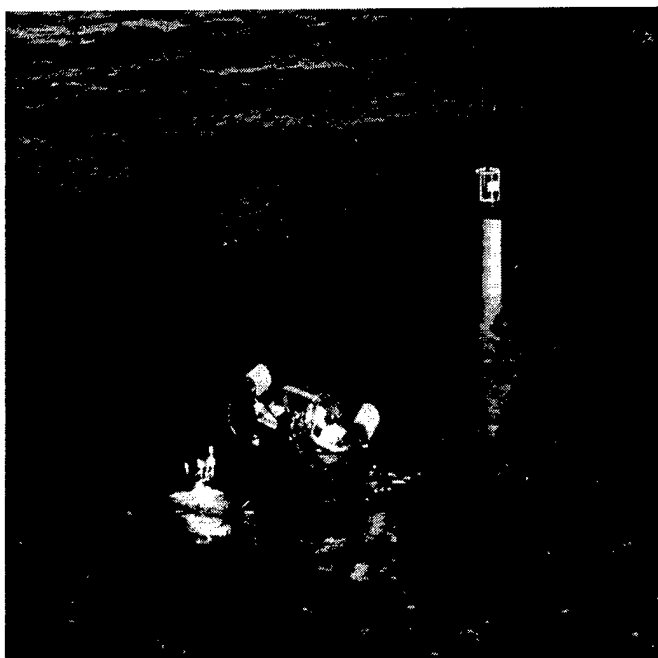


Figure 2: SWEEP buoy surfaced near diver

The first submerged field tests evaluated various prototype system modules. During July and November '98 submerged field tests, the first integrated prototype buoy conducted automated profiles. Figure 3a shows repeated SWEEP profiles for 15 minutes during November in 10 m water depth. In this figure the buoy began at just over 4 meters water depth and made 5 subsurface profiles. It then profiled to the surface, called the ship via GSM cellular phone and reported the data. After reporting the data it awaited new profiling instructions via the same phone link.

Figure 3b shows the temperature data for this series of profiles over only 15 minutes. Note the nearly 1 degree increase in temperature near the surface over this short period. This experiment was conducted outside of La Spezia bay near power plant and town outfalls in shallow water, so several causes for this rapid temperature change are possible. Note that the temperature is relatively constant at 4 m depth. These data demonstrate that environmental water column profilers are needed in order to monitor and model areas of rapid environmental change.

In addition to profiler data return, November field tests also evaluated novel Differential GPS navigation and remote control of the buoy by means of two-way cellular phone communications. After phoning "home" and delivering

profiler data, the buoy received new profiling instructions and executed additional profiles. The buoy also received standard RTCM differential correctors (computed by nearby SACLANTCEN shore equipment) via cellular phone and successfully used them to provide accurate buoy positioning

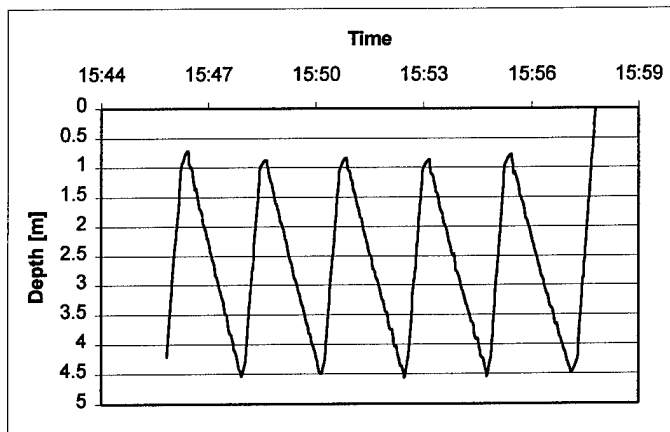


Figure 3a: Sea Test Depth Recording

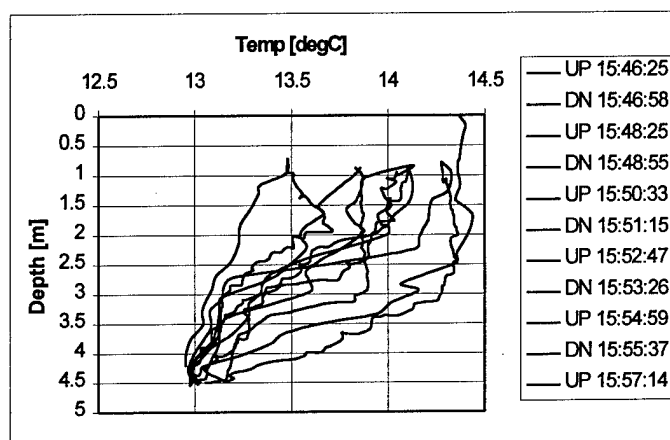


Figure 3b: Sea Test Temperature Profiles

without a separate radio receiver for commercial RTCM broadcast reception.

VI. Trawler Safe Development of SWEEP

In 1999 it was decided to develop a new profiler configuration which combines SWEEP environmental profiler capabilities with the trawler safe ADCP capabilities of the Barny instruments previously developed at SACLANTCEN (de Strobel *et al.*, 1994). It is referred to as SEPTR, for Shallow water Environmental Profiler in Trawler safe, Real time configuration. Figure 4 shows a trawler safe Barny ADCP platform just as it releases its pop-up recovery buoy, which contains the ADCP. The added capabilities of the SEPTR will permit real time reporting of ADCP and tide/wave gage data together with all the SWEEP water column profiler data. Complete data will also be stored on board. For recovery, the Barny uses a pop-up float to bring a strong line to the surface along with the ADCP (figure 6). The new configuration is expected to contain a smaller pop-up buoy for recovery as well as the winch driven profiler. Battery packs for 3 months endurance and 360 profiles will be contained in a standard

Barny size housing. Figure 5 is a conceptual diagram of the new trawler safe SEPTR design. . The present plan is to complete two SEPTR prototypes for use in support of oceanographic modeling efforts planned for September 2000.

VII. SWEEP Production

SACLANTCEN is now developing both standard SWEEP and trawler safe SEPTR profilers. By mid 2000 the pre-production SWEEP prototype should be complete, and commercial production will be undertaken to produce a small series of SWEEP buoys for Rapid Environmental Assessment demonstrations in 2001 and 2002. By September 2000, two SEPTR units will be complete, and field trials undertaken as part of other SACLANTCEN programs. At the end of 2000 plans for production of trawler safe profilers will be evaluated.

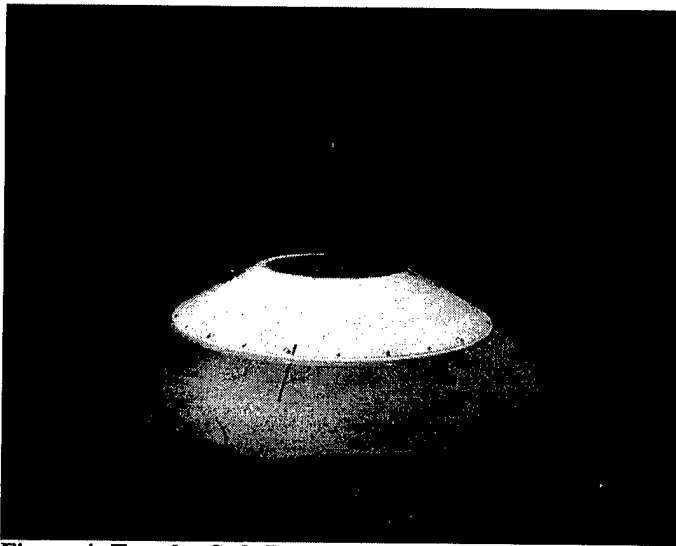


Figure 4: Trawler Safe BARNY Sentinel recovery

VIII. Conclusions

SACLANT Undersea Research Centre and the University of Rhode Island are well along in the development of low cost and trawler safe environmental profilers for rapid environmental assessment, with the potential for significant impact on our ability to observe and predict ocean environmental properties. During the next year these systems should be completed, extensive field tests undertaken, and production of a small series of SWEEP buoys contracted for future demonstrations.

References

Davis, R.E., Webb, D.C., Regier, L.A., and Dufour, J. (1991), "The Autonomous Lagrangian Circulation Explorer (ALACE)," *J. Atmospheric and Oceanic Technology*, Vol. 9, No. 3, pp. 264-285.

De Strobel, Federico, and Gualdesi, Lavinio (1997), "'Barny' - A trawler safe, bottom mounted, ADCP platform for Mediterranean, long term coastal water applications," *J. Marine Env. Engg.*, Vol. 4, pp. 175-187.

Dierssen, Heidi M., and Smith, Raymond C. (1997), "Estimation of irradiance just below the air-water interface," *Ocean Optics XIII*, Proc. SPIE 2963, pp. 204-209.

Downing, John, De Roos, B. G., and McCoy, Kim (1992), "An Autonomous Expendable Conductivity, Temperature, Depth Profiler for Ocean Data Collection," *1992 IEEE Oceans Proceedings*, Vol. 1, pp. 672-677

Griffith, Peter C., Potts, Dana C., and Morgan, Stephen Lee (1996), "Low-Earth-Orbit Satellite Systems in Ocean Science," *Oceans '96 MTS/IEEE Proceedings*, Vol. 1, pp. 277-281.

McCoy, Kim (1994), "The Autonomous Profiling Vehicle," *1994 IEEE Oceans Proceedings*, Vol. 1, pp. 419-423.

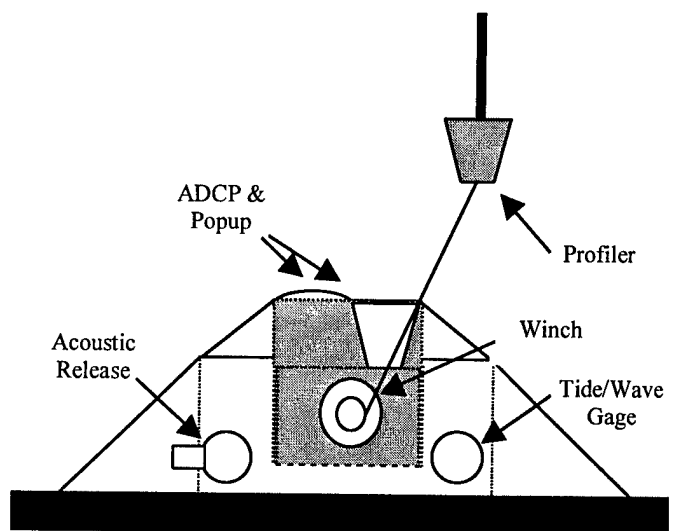


Figure 5: Trawler safe SEPTR concept

Rosby, T., Dorson, D., and Fontain, J. (1986), "The RAFOS System," *J. Atmospheric and Oceanic Technology*, Vol. 3, No. 4, pp. 672-679.

Stevenson, J. Mark (1997), "A Prototype Autonomous Buoyed Environmental Measurement System," *Conference Proceedings of the Rapid Environmental Assessment Conference*, SACLANT Undersea Research Centre, 1-14 March, 1997, La Spezia, Italy.

Tyce, Robert, Federico de Strobel, Vittorio Grandi, Lavinio Gualdesi (1998), "Shallow Water Expendable Environmental Profiler (SWEEP) design with control and data recovery via cellular phone and low earth orbit satellite networks," in *Proceedings of Oceanology International '98*, 10-13 March, Brighton, UK.

MONITORING ALGAE BLOOMS IN THE BALTIC SEA : A MULTI-SENSOR APPROACH

Ove Rud* and Martin Gade**

* Remote Sensing Laboratory - Department of Physical Geography, Stockholm University, 106 91 Stockholm, Sweden, Tel.: +46(0)8 164788, Fax: +46(0)8 164955, E-mail: ove.rud@natgeo.su.se

**Universität Hamburg, Institut für Meereskunde, Troplowitzstr. 7, 22529 Hamburg, Germany
Phone: +49(0)40 42838 5450 Fax: +49(0)40 42838 5713 E-mail: gade@ifm.uni-hamburg.de

Abstract – We present data from four different satellite sensors, which have been acquired over the same sea area during an algae bloom, within less than two hours. The data includes: the Thematic Mapper (TM) on Landsat-5, the synthetic aperture radar (SAR) aboard the Second European Remote Sensing Satellite (ERS-2), the Wide Field Scanner (WiFS) aboard the Indian IRS-1C satellite, and the Advanced Very High Resolution Radiometer (AVHRR) flown on the NOAA-14 satellite. Using this extensive data set, for the first time, an investigation of the usefulness of the fusion of different remote sensing data (particularly by incorporating radar data) for monitoring of an ongoing algae bloom has been performed. The results of our analysis show that the fusion of optical and microwave remote sensing data (even with different spatial resolutions) can yield more information about the biological and oceanic characteristics of sea surface areas.

I. INTRODUCTION

Regularly occurring blooms of nitrogen-fixing filamentous cyanobacteria (blue-green algae) in the Baltic Sea have given rise to an increasing interest and concern due to their environmental impact and health hazards. The summer (July - August) blooms in the open sea are often dominated by the species *Nodularia spumigena* and *Aphanizomenon sp.* Due to the high spatial and temporal variability, and the scarcity of data from the open sea, the extent of cyanobacteria blooms is very difficult to show using data from conventional shipboard monitoring. During the later phase of the bloom, algae start to flocculate and accumulate on the sea surface in large quantities, thereby becoming visible even with non-optimal satellite sensors. The possibility to detect the surface accumulations by a satellite sensor is most often limited to the visible spectral bands, but in areas of intensive surface accumulation, the near infrared band can also be used.

The use of satellite data, such as the Advanced Very High Resolution Radiometer (AVHRR), is limited to

cloudfree days because of the used optical and infrared bands, and to large-scale patterns due to its low spatial resolution. Moreover, the spectral resolution is also not optimal for algae detection and monitoring. Nevertheless, for long time-series comparison of the dynamics of algae blooms, and near real-time monitoring of ongoing blooms, AVHRR has proven to be a useful data source, due to its high temporal resolution.

Recently, a large variety of different sensors have been operational, thus allowing for synoptical studies concerning the monitoring of the same oceanic (and atmospheric) phenomena, such as ongoing algae blooms. We have therefore searched our archives in order to find a data set of satellite images acquired by different sensors within a short time period. Such data sets may give rise for better understanding of oceanic (and atmospheric) phenomena and their imaging by the different sensors working at different electromagnetic frequencies.

II. AVAILABLE DATA

On July 15, 1997, a day with extensive cyanobacterial blooms in large parts of the Baltic Sea, especially the northern Baltic Proper, data from four different satellite sensors have been acquired over the same sea surface area. The data includes: the AVHRR flown on the NOAA-14 satellite, the Wide Field Scanner (WiFS) aboard the Indian IRS-1C satellite, the Thematic Mapper (TM) on Landsat-5 and the synthetic aperture radar (SAR) aboard the Second European Remote Sensing Satellite (ERS-2). Details about the different sensors, the satellite platforms, spatial resolutions (pixel sizes), and acquisition times are given in Table 1.

All sensors working in the visual and infrared part of the spectrum are passive sensors. The TM with its seven wavelength bands (ranging from 450 nm to 12.5 μ m: three in the visible, one in the near infrared, two in the mid infrared, and one in the thermal infrared part of the spectrum) has good capabilities of detecting the different variations of algae accumulations. The high spatial

Table 1. Pixel sizes and acquisition times for the four different sensors on July 15, 1997.

Sensor	Satellite	Pixel size (m)	Time (UTC)
TM	Landsat-5	30 m	08:57
SAR	ERS-2	12.5 m	09:47
WiFS	IRS-1C	188 m	10:26
AVHRR	NOAA-14	1.1 km	11:01

resolution also helps to identify the surface patterns in great detail.

The WiFS sensor, with only two spectral bands (600-800 nm: one visible and one near infrared) also identifies most of the surface patterns in the area. The resolution of 188 meters makes it an interesting contribution between the high (TM) and low (AVHRR) resolution imagery.

The AVHRR/2 sensor uses five spectral bands (600 nm – 12.5 μ m), but because of its low spatial resolution (see Table 1) it is only capable of registering meso- and large-scale surface patterns. AVHRR data have been thoroughly used for monitoring algae blooms such as the cyanobacteria accumulations in the Baltic Sea [1].

ERS-SAR images are two-dimensional maps of the radar backscattering at 5.3 GHz (C-band, 5.7 cm), here from the ocean surface. This backscattering is caused by small-scale surface waves, which have wavelengths comparable to the radar wavelength (7.2 cm; Bragg waves). These waves are often damped by the surface films produced by the (blooming) algae, so that the natu-

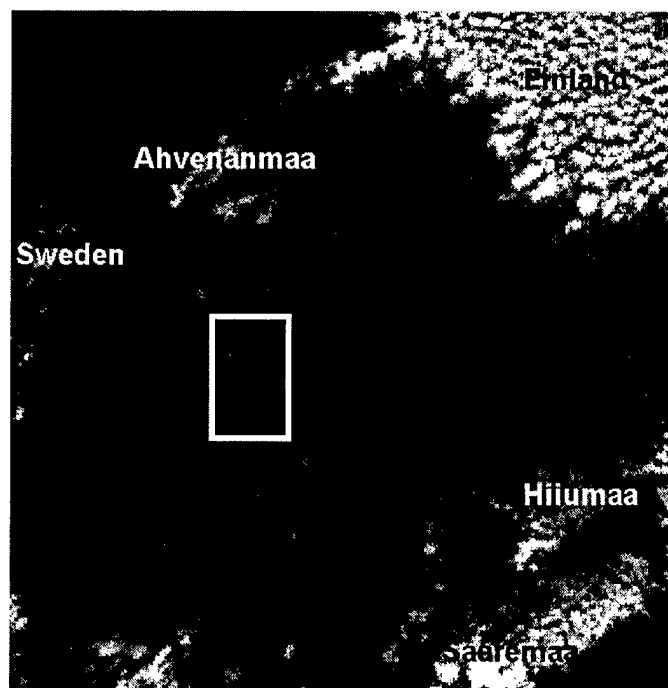


Fig. 1: Composite AVHRR image (visible, near and thermal infrared) taken on July 15, 1997 at 11:01 UTC over the northern Baltic Proper between Sweden (left) and Finland (upper right). The image dimensions are 300 km by 300 km and the rectangle denotes the location of the subsections shown in Fig. 2.

ral slicks, apart from other oceanic and atmospheric

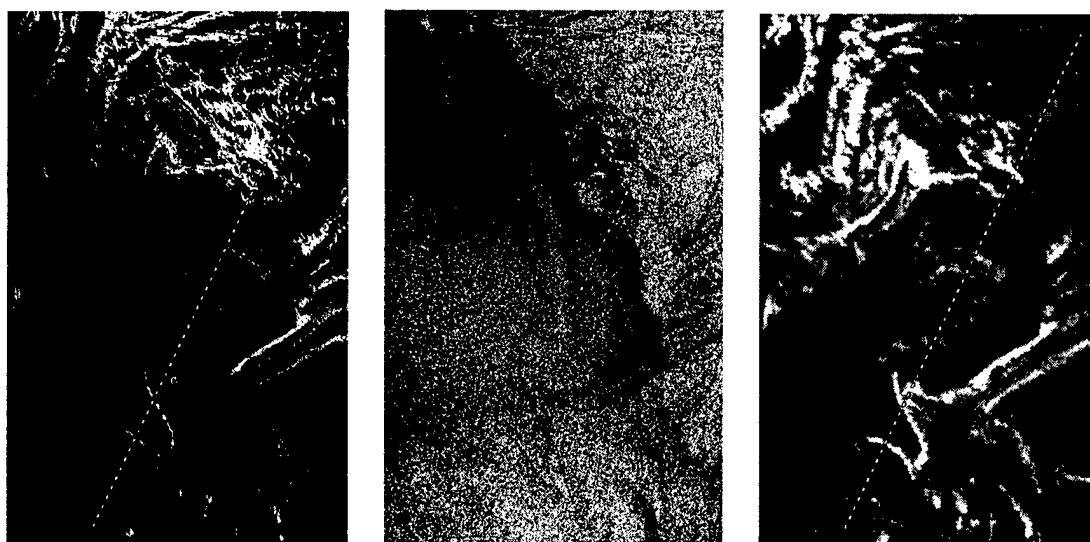


Fig. 2: Subsections (29 km x 45 km) of the TM band 4 (left), SAR (middle), and WiFS band 2 (left) images (the location is denoted in Fig. 1). All images were acquired within 2 hours on July 15, 1997, and were resampled to a pixel size of 50 m to allow better comparison. The algae bloom accumulations are visible in all images. The dashed line corresponds to the profiles shown in Fig. 3.

comparable to the radar wavelength (7.2 cm; Bragg waves). These waves are often damped by the surface films produced by the (blooming) algae, so that the natural slicks, apart from other oceanic and atmospheric phenomena, are visible on SAR images as dark irregular patches [2]. The advantages of SAR sensors are their independence of daytime and weather conditions and their high spatial resolution.

All satellite images were georeferenced to the same projection (UTM, zone 34) with the same corner coordinates as the TM scene, the smallest of the four satellite scenes. The total RMS error in the transformation between the images is about 0.5 pixels for the optical sensors and 1 pixel for the SAR scene.

Apart from satellite imagery, bathymetry data, wind, and modeled current data have also been available for our analyses; however, in this paper we concentrate on the comparison of the satellite imagery.

III. RESULTS AND DISCUSSION

The bright patches in the center of the AVHRR composite shown in Fig. 1 are due to algae accumulations, but also due to clouds and contrails (see the elongated lines). In order to study the imaging of the ongoing algae bloom by the different sensors we have chosen a subsection marked by the rectangle in Fig. 1. The corresponding parts of the WiFS band 2, SAR, and TM band 4 images are shown in Fig. 2.

Cyanobacteria accumulations occur in large quantities in most of the investigated area. The spatial variations that exist give rise to the typical patterns seen in each of the panels of Fig. 2. These patterns show up in all visible and near-infrared images, with the most obvious patterns in the visible bands (not shown herein). The reason for this is the ability of the TM 2 sensor (0.5–0.6 μm) to detect also sub-surface algae. However, the accumulations are also visible in the TM 4 near infrared band (0.8–0.9 μm), but to a smaller extent compared to the visible band (TM 2).

The widespread cyanobacterial accumulation that can be seen in the near infrared, indicates that in those areas the accumulations are very close to or at the sea surface. Most surface patterns are well visible in both the high-resolution (30 meters) TM scene (left panel of Fig. 2) and the medium-resolution (188 meters) WiFS scene (right panel). The densest accumulations are also visible in the AVHRR imagery (Fig. 1), but in less detail compared to imagery with higher spatial resolution. The dark signatures visible in the SAR image (middle panel of Fig. 2), which are usually attributed to the occurrence of slicks on the sea surface, are very well correlated with high reflectance areas seen in the band-4 scene of the TM (near infrared, 750 – 900 nm). This indicates that the

SAR sensor detects the presence of the cyanobacteria on the sea surface.

We have calculated profiles along the dashed lines included into each panel of Fig. 2. The results are shown in Fig. 3, where the upper (red) curve corresponds to the relative pixel values of the TM band 4 image, the middle (green) curve corresponds to the pixel values of the SAR image, and the bottom (blue) curve corresponds to the relative pixel values of the WiFS band 2 image. Note that the middle curve is plotted in logarithmic scales for better visualization.

As can be seen from the profiles in Fig. 3, we found an obvious correlation between low values in the SAR image and peaks in the TM band 4 and WiFS band 2: at a relative distance of about 15 km the single spike in the WiFS band 2 (bottom curve) corresponds very well with the singular drop of the SAR image intensity (middle curve) and with a respective peak in the TM band 4 (upper curve). A similar good correlation can be found at distances of about 18 km and about 40 km, where all sensors detected a triple spike. This good correlation is a strong indicator that both the SAR and the near infrared sensors detected cyanobacterial accumulations at the very surface of the sea.

Due to the surface current in the area there is a small displacement of the surface features identified in the various satellite images. From this displacement and from the time periods between the image acquisitions we calculated mean current velocities between 10 cm/s and 30 cm/s. From our results we infer that the mean surface current along the scan line in the southern

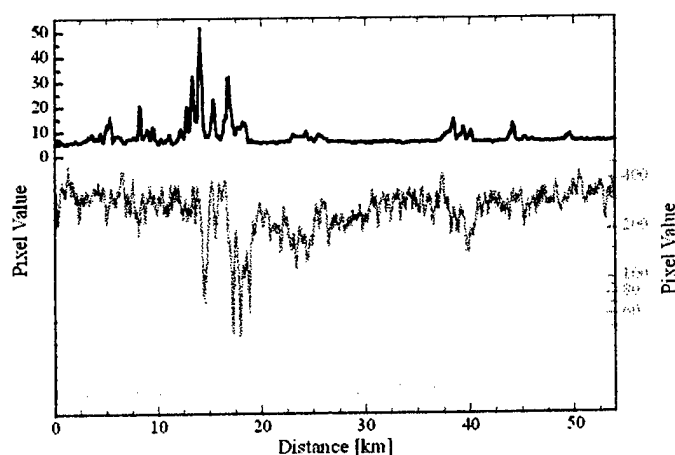


Fig. 3: The three graphs show the relative pixel values for the TM band 4 (top, red), SAR (center, green), and WiFS band 2 (bottom, blue graph) along the profiles indicated in Fig. 2. Low values in the SAR image, due to the dampening of the small-scale surface waves, correlate well with the peaks in the TM band 4 and WiFS band 2.

(20 cm/s, derived from SAR and WiFS data, respectively). However, by comparing the right-handed parts of the profiles shown in Fig. 3 (corresponding to the northern (top) parts of the panels in Fig. 2) we inferred that the mean surface current along the scan line in this particular area was changing from 10 cm/s in southerly direction (derived from TM and SAR data) to about 30 cm/s in northerly direction (derived from SAR and WiFS data). We attribute this finding to the fact that at the time of the image acquisitions an inflow of cold water from the Bothnian Sea in the north into the northern Baltic Proper in the south occurred. The front line of this inflow passes through the image subsections of Fig. 2, thus causing an overall turbulent current field in that particular area.

In order to better demonstrate the spatial displacement with time of the observed features, we have generated a three-color composite shown in Fig. 4 by using the TM band 4 (red channel), SAR (green channel), and WiFS band 2 (blue channel) images thereby denoting the time order of acquisition. The image dimension is 90 km x 90 km, and all data have been resampled to a pixel size of 50 m. Note that for a better visualization of the interesting features we have inverted the SAR image so that areas of reduced radar backscatter appear as bright green patches. The oceanic front is well visible in the SAR image (see the bright green line reaching towards the upper left image corner), and the observed displacements can best be seen in the image center, north of the oceanic front. Contrails visible in the WiFS band 2 image can be seen as elongated blue lines in the upper right image corner.

The obvious 'front' in the middle of the image (reaching from northwest to southeast) is visible in all investigated images and spectral bands. The homogeneous area to the left (west) of this front is due to somewhat colder and cyanobacteria-free water flowing from the Bothnian Sea southwards into the Baltic Proper.

An area of high surface concentration of algae, which is likely to coincide with a locally low wind field, causes strong reduction of the radar backscattering (visible as a bright green patch in the image center).

IV. SUMMARY AND CONCLUSIONS

We have presented first results of our synoptical studies of the imaging of an ongoing algae bloom by different optical and microwave sensors. It turned out that the subsurface algae accumulations were best detected by the visual TM band 2 (not shown herein), but that we found best correlation between the different imagery between the SAR and the near infrared images. We believe that this finding reflects the fact that both sensors (radar and near infrared) are influenced by phe-

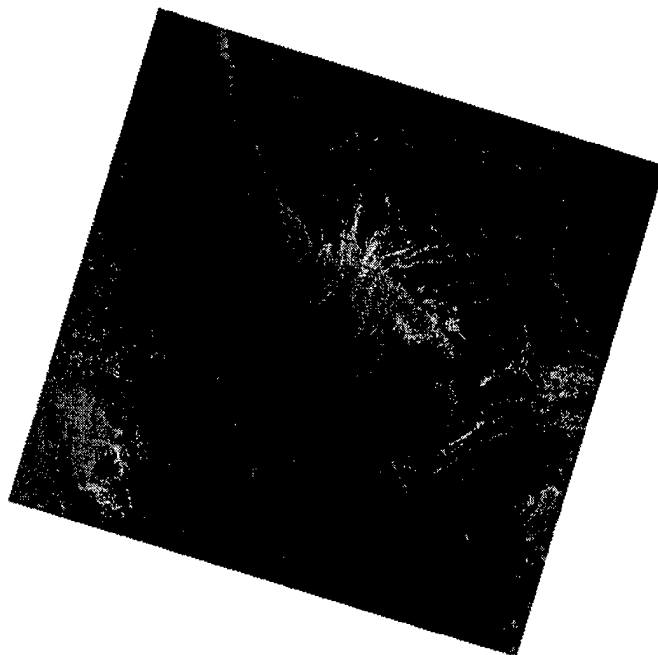


Fig. 4: Three-color georeferenced composite based on TM band 4 (red), SAR (green), and WiFS band 2 (blue) images. For better visibility the SAR data has been inverted so that areas of reduced radar backscatter appear in bright green. Image dimensions are 90 km x 90 km.

nomena occurring at the very sea surface, like the damping of the small-scale surface waves (seen by the SAR) and the accumulation of cyanobacteria at the sea surface (seen by the TM band 4 and by the WiFS band 2).

Whether the SAR detects the presence of any oily/fatty substances released by the algae and then concentrated along the observed patterns, or whether it detects the physical presence of the cyanobacteria accumulation on the sea surface is an issue to be investigated further.

Noteworthy is also the fact that the front line is displaced in the SAR image with respect to the other sensors, which cannot be explained by a different density of cyanobacteria on the water surface and which is still under investigation.

Summarizing, our investigation has shown that the combination of satellite imagery of different (optical and microwave) sensors may help better understanding and monitoring those phenomena which are often observed in satellite imagery, in particular, ongoing algae blooms.

monitoring those phenomena which are often observed in satellite imagery, in particular, ongoing algae blooms.

ACKNOWLEDGMENTS

The authors are grateful to Ms. Miho Ishii for the valuable help with all the figures and to Peter Land and Bertil Håkansson for support and valuable discussions. This work has been supported by the European Community (EC) under contract ENV4-CT96-0334, "Clean Seas".

REFERENCES

- [1] Kahru, M., U. Horstmann, and O. Rud, Increased cyanobacterial blooming in the Baltic Sea detected by satellites: Natural fluctuation or ecosystem change?, *Ambio* 23, 469-472, 1994.
- [2] Gade, M., W. Alpers, H. Hühnerfuss, H. Masuko, and T. Kobayashi, The imaging of biogenic and anthropogenic surface films by the multi-frequency multi-polarization SIR-C/X-SAR, *J. Geophys. Res.*, 18851-18866, 1998.

MARINE POLLUTION IN EUROPEAN COASTAL WATERS MONITORED BY THE ERS-2 SAR: A COMPREHENSIVE STATISTICAL ANALYSIS

Martin Gade* and José M. Redondo**

* Universität Hamburg, Institut für Meereskunde, Troplowitzstr. 7, 22529 Hamburg, Germany
Phone: +49(0)40 42838 5450 Fax: +49(0)40 42838 5713 E-mail: gade@ifm.uni-hamburg.de

** Departament de Física Aplicada, Universitat Politècnica de Catalunya, 08034 Barcelona, Spain
Phone: +343 401 79 84 Fax: +343 401 60 90 E-mail: redondo@etseccpb.upc.es

Abstract - The oil pollution of the southern Baltic Sea, the North Sea, and the northwestern Mediterranean Sea has been studied within a two-year period from December 1996 until November 1998. In total, we have analyzed more than 700 synthetic aperture radar (SAR) images, which have been acquired over the three test areas by the Second European Remote Sensing Satellite (ERS-2). In this paper, we present the results of our statistical analyses. Moreover, we introduce advanced image processing techniques for the classification of the observed radar signatures, namely the calculation of the fractal dimension, and discuss the possibility of identifying different types of oceanic phenomena.

I. INTRODUCTION

Within the project „Clean Seas“, which is funded by the European Commission, three test areas in European marginal waters, namely the southern Baltic Sea and North Sea and the northwestern Mediterranean (for details see [1]), were chosen for the remote sensing of marine pollution. The test areas include some main ship routes and the estuaries of the major rivers Oder (Baltic Sea), Thames, Rhine (North Sea), and Rhone (Mediterranean). In total a sea surface area of more than 250,000 km² has been monitored. From each of the three test areas 15 SAR frames [1] have routinely been acquired by the synthetic aperture radar (SAR) aboard the Second European Remote Sensing Satellite (ERS-2), so that a total of 709 SAR images could be used for our analyses. Since oil spills dampen the small-scale surface waves, which are responsible for the radar backscattering from the water surface, they are visible as dark patches in SAR imagery.

However, some oceanic and atmospheric phenomena may cause signatures similar to those of oil spills, so that any automated oil detection algorithm using radar imagery may cope with false alarms. For that reason, we analyzed the SAR images by eye, in order to ensure

maximum confidence of the statistics to be produced. The SAR images were processed at a resolution of 100 m and were provided by the Rapid Information Dissemination System (RAIDS) SAR processing facility in West Freugh, UK.

II. STATISTICAL RESULTS

During the two years of our studies, 220 SAR images have been acquired over the Baltic Sea test area, 207 SAR images over the North Sea test area, and 282 SAR images over the test area in the northwestern Mediterranean Sea. We have analyzed every SAR image with respect to the occurrence of marine oil pollution. The locations and sizes of the detected oil pollution have been calculated and catalogued. As a result, we included circles into the three maps shown in Fig. 1 at the locations of the detected oil spills. The sizes of the circles are proportional to those of the oil spills, ranging from 0.1 km² to 56 km².

The main pollution occurs along the main ship traffic routes, which is most obvious in the Baltic Sea (see the left panel in Fig. 1) going from southwest to northeast. This effect is less pronounced in the North Sea test area, because of the overall dense ship traffic. In the northwestern Mediterranean, however, main ship traffic routes may also be inferred from the locations of detected oil pollution. However, the highest occurrence of marine oil pollution was found in the northwestern Mediterranean, south of Barcelona, where the outflow of the river Llobregat seems to cause a high incidence of pollution in that particular area. In total, we detected 675 oil spills from which 122 covered a sea area of more than 5 km² [1]. We found more oil spills during summer time (bright, i.e. green, yellow, and orange, circles) than during winter time (dark, i.e. red, blue, and purple, circles).

In order to better demonstrate the spatial distribution of the detected marine oil pollution in the northwestern Mediterranean Sea we have calculated maps showing

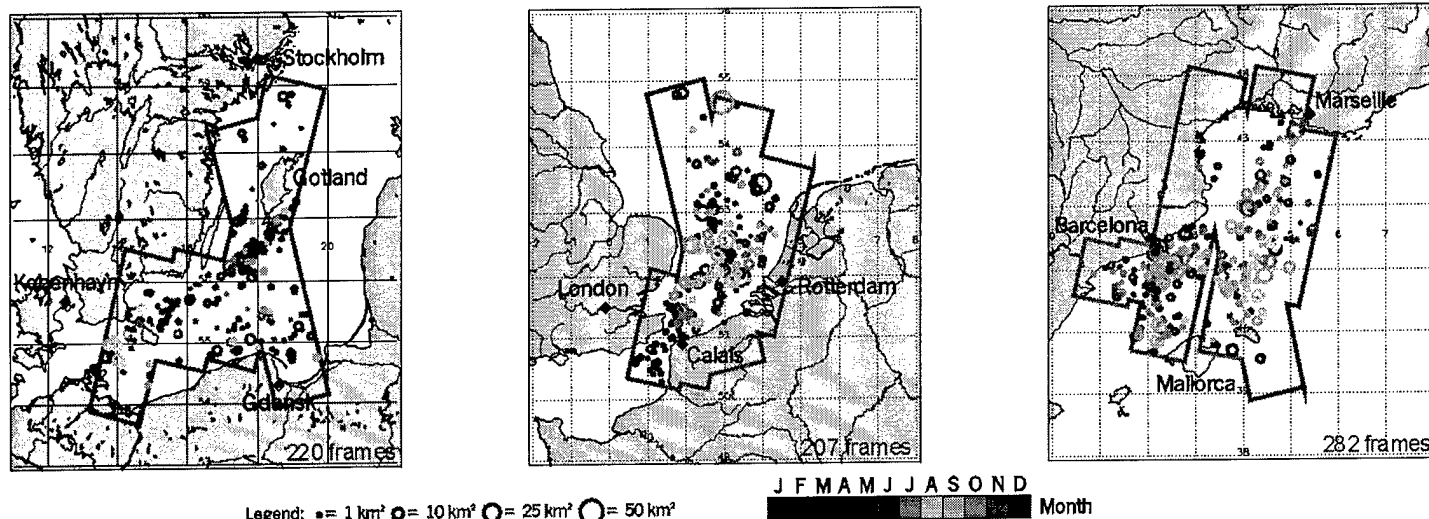


Fig. 1: Maps of the three test areas Baltic Sea (left), North Sea (middle), and Mediterranean (right). The circles denote the locations of the detected oil spills, the circle sizes are proportional to the respective sizes of the oil spills, and the color-coding gives the time of the year (namely the month) when the pollution has been detected. Note that the main pollution occurs along the main ship traffic routes and that we detected more oil spills during summer time (bright, i.e. green, yellow, and orange, circles) than during winter time (dark, i.e. red, blue, and purple, circles).

contour plots of the mean spill-covered area per SAR image. As an example, our results for the northwestern Mediterranean Sea are depicted in Fig. 2. For the upper panel only oil pollution detected during winter time (October through March) has been taken into account, and for the lower panel only pollution detected during summer time (April through September). Each plot has been generated by determining the local (normalized) percentage of the total spill-covered area (i.e., the sum of the sizes of all detected oil spills divided by the area of the grid cell, which was chosen to be 20' by 20'). As a maximum, we found mean polluted sea surface areas of more than 4000 m² per km² off the mouth of the river Llobregat near Barcelona.

It is noteworthy that the measured pollution is higher during summer time is higher than during winter time, which we attribute to the fact that the visibility of any marine pollution is higher in summer because of the overall lower (mean) wind speed and wave height. Thus, any oil pollution may be easier to detect because of the wind speed dependence of the visibility of oil spills on SAR images [1,2]. Especially during summer time (lower panel), the areas of highest pollution can easily be delineated: (1) south of Barcelona, where the outflow of the river Llobregat is driven southwards by the local currents, (2) along the main ship traffic routes going from Barcelona southwards and eastwards and from Marseille towards southwest, (3) around the harbor of Marseille, and (4) south of Tarragona, between Barcelona and the mouth of the river Ebro.

III. CALCULATION OF FRACTAL DIMENSIONS

Some of the theory relating fractal analysis to the turbulence is presented in [3]. Recently, fractal (image) analysis has become a rapidly evolving research field with various approaches, ranging from mathematical to experimental. In this paper we present a basic method for identifying different dynamical processes that might influence the radar backscattering from the ocean surface to demonstrate the capability of fractal analysis of improving existing oil pollution detection algorithms.

We used a box-counting algorithm to detect the self-similar characteristics for different SAR-image intensity levels. This purely geometrical description may be related to dynamical (oceanic and atmospheric) processes assuming that an energy transfer generated at a certain range of scales will affect the ocean surface at the same scales. The best geometrical characterization of a multifractal set showing different fractal dimensions D for different SAR-image intensities i is given by the maximum fractal dimension; however, relevant information may also be obtained from the complete function $D(i)$.

The fractal dimension $D(i)$ as a function of intensity i may be calculated using

$$D(i) = - \frac{\log N(i)}{\log e} \quad (1)$$

where $N(i)$ is the number of boxes of size e needed to cover the contour at a SAR intensity (i.e. radar backscattering) level i . The algorithm operates by dividing the

digitized (two-dimensional) surface into smaller and smaller square boxes and by counting the number of them which have values close to the respective SAR intensity i .

Let us assume a convoluted line, which is embedded in a plane (that is why it is usually referred to as D_2 , or

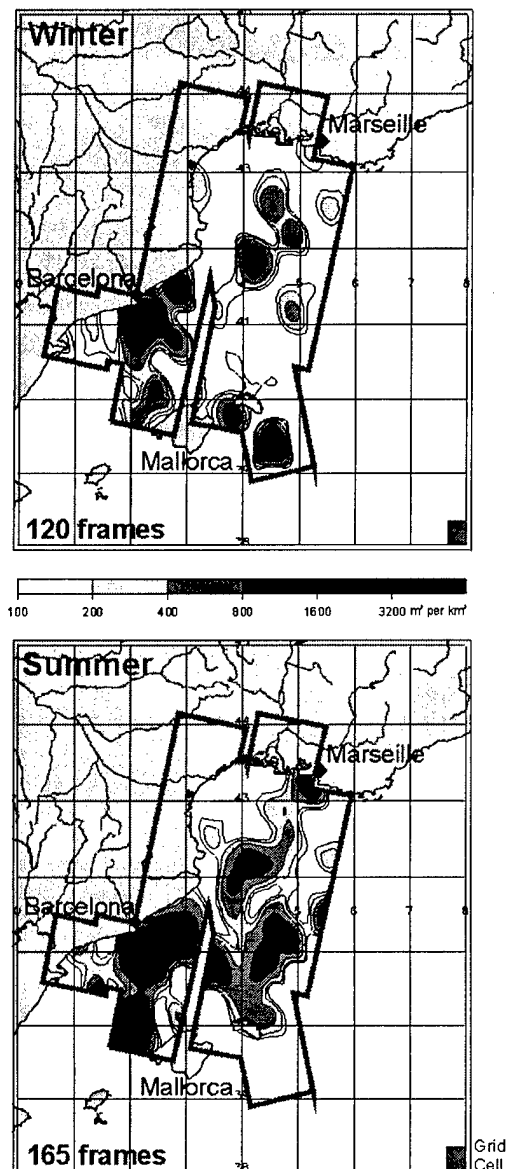


Fig.2: Contour plots denoting the mean spill-covered area in the northwestern Mediterranean Sea as retrieved from SAR images acquired between December '96 and November '98. The mean (detected) pollution is higher during summer time (lower panel: April through September) than during winter time (upper panel: October through March). For each grid cell (20' by 20') the total slick-covered area has been weighted with the number of acquired SAR frames.

fractal dimension within an Euclidean plane of dimension 2). If it is a single Euclidean line, its (non fractal) dimension will be one. If it fills the entire plane its dimension will be two. The box-counting algorithm divides the embedding Euclidean plane in smaller and smaller boxes (by dividing the initial length L_0 of the SAR image by n , which is the recurrence level of the iteration). For each box of size L_0/n it is then decided if the convoluted line, which is analyzed, is intersecting that box. The number $N(i)$ is the number of boxes which were intersected by the convoluted line (at intensity level i). Finally, we plot N versus L_0/n (i.e., the size e of the box) in a log-log plot, and the slope of that curve, within reasonable experimental limits, gives the fractal dimension. Note that the sign of the fractal dimension is not relevant. As a demonstration of the calculation of fractal dimensions Fig. 3 shows a log-log plot of the number of boxes $N(i)$ covering the convoluted line at a certain intensity level i as a function of the box size e (in pixels).

The calculation of $N(i)$ has to be done for different contour levels corresponding to different SAR intensity levels i . However, for practical purposes it is enough to check at the edges of the boxes whether there is any pixel with the desired intensity level, except in very fragmented convoluted lines.

We show in Fig. 4 five different sections of ERS-2 SAR images corresponding to different oceanic and atmospheric phenomena. Also plotted are the respective functions $D(i)$ without (dark, purple) and after applying a speckle-noise (Kuan) filter (bright, pink): a,b) anthropogenic oil spills of different shapes, c) atmospheric convective cells, d) biogenic sea slicks, and e) rain cells.

All curves shown in Fig. 4 exhibit a strong increase of

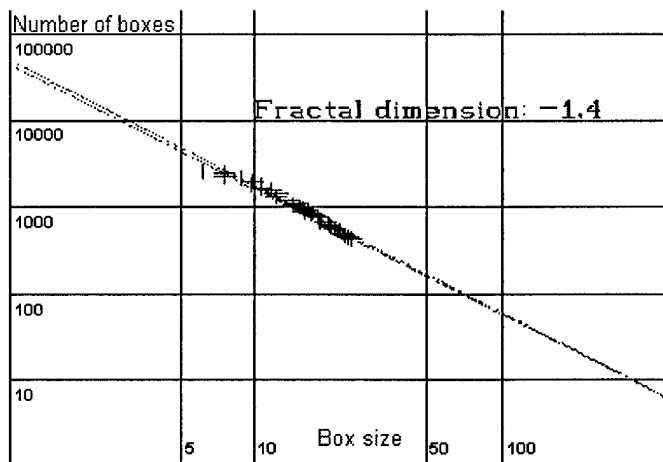


Fig. 3: Example for the calculation of the fractal dimension. In this log-log plot the number of boxes covering the convoluted line is plotted as a function of the box size (in pixels).

$D(i)$ at low SAR image intensities (or normalized radar cross sections, NRCS) between -30 dB and -20 dB and a strong decrease at larger backscatter values between -18 dB and -5 dB. Especially Panels a), b), and e) show a pronounced maximum at large NRCS values (i.e. at the right-handed side of the curve), which is due to the speckle noise, a typical characteristic of SAR images. However, the anthropogenic oil spills (Panels a) and b)) tend to exhibit a second peak at lower backscatter values. This second peak, which is best pronounced for the elongated spill shown in Panel a), has a smaller (maximum) fractal dimension. On the other hand, the wind-induced patterns and natural slicks (Panels c) and d), respectively) show a broad (and larger) maximum of $D(i)$. The irregular-shaped rain cells (Panel e)), again, seem to cause a second peak at lower backscatter values. The "tail" at the high-backscatter ends of the curves in Panels b) and c) are due to ships, which are visible as bright spots in the respective SAR subsections.

We are aware that this small set of examples may not be representative for the entire range of different kinds of signatures in SAR imagery caused by various oceanic and atmospheric phenomena. However, our analysis shows that there seems to be a basic difference in the curves of $D(i)$ dependent on the main spatial characteristics of the observed feature. That is, large- and meso-scale phenomena, such as the atmospheric convective cells and the large sea surface area covered by natural slicks, seem to exhibit a broader curve of $D(i)$ without a second maximum, whereas small-scale, more "patchy" features, like oil spills and rain cells, tend to give rise to a second maximum, which may be more or less pronounced, depending on the shape of the particular feature.

The application of an adaptive speckle filter (like the Kuan filter; see the bright, pink curves in Fig. 4) leads to a reduction of the second maximum of the $D(i)$ curves, especially for the "patchy" features, like oil spills and rain cells (Panels a), b), and e), respectively). It is also noteworthy that the speckle filter causes a smaller difference in the $D(i)$ curves of the large- and meso-scale phenomena (convective cells and slicks, Panels c) and d)). Finally, the differences in the maximum fractal dimension are better visible after having applied a speckle filter.

IV. SUMMARY AND CONCLUSIONS

In the framework of the joint European project "Clean Seas", the oil pollution of the southern Baltic Sea, the North Sea, and the northwestern Mediterranean Sea has been studied within a two-year period from December 1996 until November 1998. Our statistical analyses clearly show that satellite-borne SAR is an appropriate

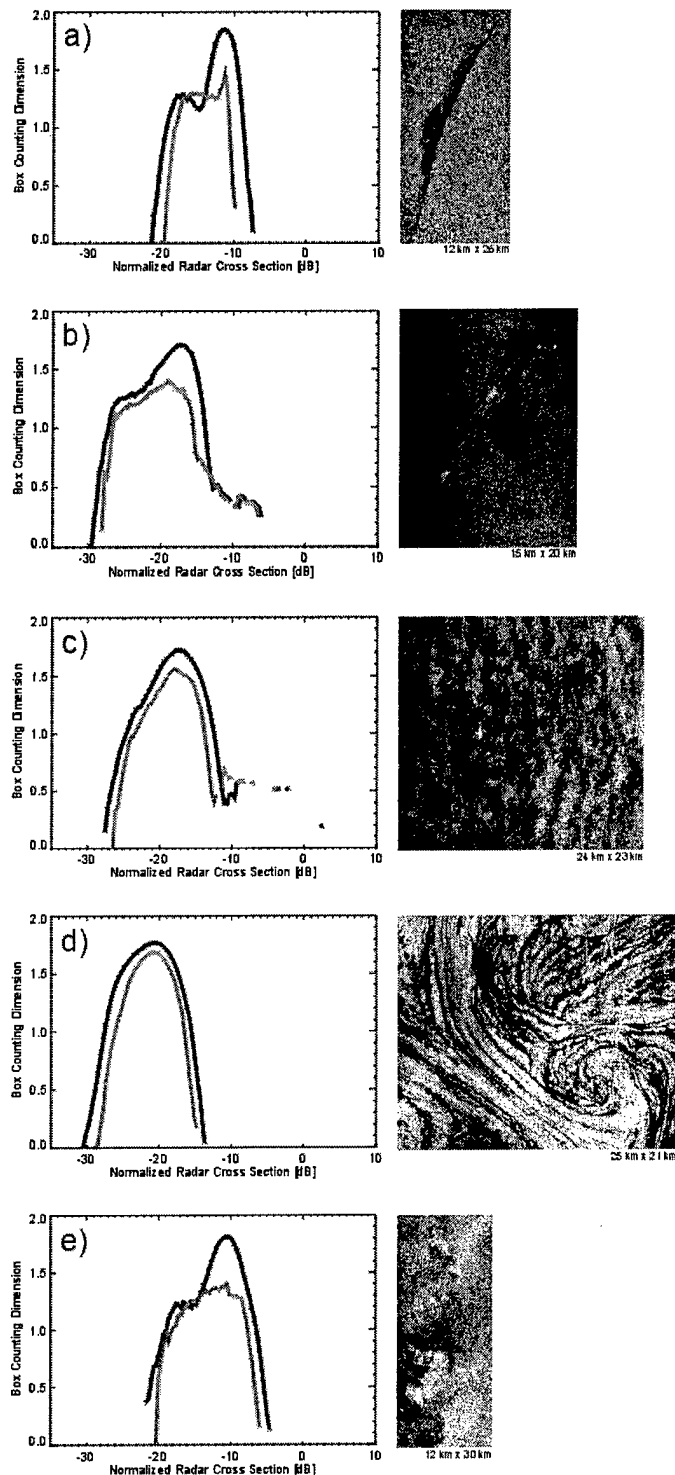


Fig. 4: Five different sections of ERS-2 SAR images corresponding to different oceanic and atmospheric phenomena. Also plotted are the respective functions $D(i)$ without (dark, purple) and after applying a speckle-noise (Kuan) filter (bright, pink): a,b) anthropogenic oil spills, c) atmospheric convective cells, d) biogenic sea slicks, and e) rain cells.

system for routine oil spill detection, both in coastal areas and along ship routes. However, due to the poor coverage in time we are still far from using satellite-borne SAR imagery as a sufficient tool for oil spill monitoring.

We have introduced an advanced image processing technique for the classification of the observed radar signatures, namely the calculation of the fractal dimension. There seem to be differences in the maximum fractal (box counting) dimension of oil spills compared to other types of oceanic phenomena, probably due to the short span of the spills. We believe that by using fractal analysis techniques existing oil spill detection algorithms may be significantly improved. Finally, our results show imply that even the presence of a ship (or any other small bright feature) within a given SAR subsection can be inferred from the high-backscatter "tail" of the calculated $D(i)$ curves.

ACKNOWLEDGMENTS

The authors are grateful to J. Scholz for his help in generating the figures and to G.W. Jolly for the coordination of the Clean Seas project. This work has been supported by the European Community (EC) under contract ENV4-CT96-0334, "Clean Seas".

REFERENCES

- [1] Gade, M., W. Alpers, H. Hühnerfuss, H. Masuko, and T. Kobayashi, The imaging of biogenic and anthropogenic surface films by the multi-frequency multi-polarization SIR-C/X-SAR, *J. Geophys. Res.*, 18851-18866, 1998.
- [2] Gade, M., and W. Alpers, "Using ERS-2 SAR images for routine observation of marine pollution in European coastal waters," *Sci. Total Environ.*, in press, 1999.
- [3] Redondo, J.M., "Fractal description of density interfaces," *Institute of Mathematics and its Applications*, vol. 56, 210-218, 1996.

BIOLOGICAL MONITORING WITH THE WESTERN CANADIAN ODAS MARINE BUOY NETWORK

Jim Gower, Angelica Peña and Ann Gargett

Institute of Ocean Sciences,
P.O. Box 6000, Sidney, BC, V8L 4B2
Tel: 250 363-6558, Fax: 363-6746, e-mail: gowerj@dfo-mpo.gc.ca

Abstract

Optical sensors are being added to some of the 17 meteorological ODAS (Ocean Data Acquisition System) buoys which provide weather and ocean data along and off the west coast of Canada for the Environment and the Fisheries departments of the Canadian federal government. The added sensors, installed on two 3-meter discus buoys so far, measure insolation, water colour, salinity and fluorescence. They are planned to provide time series of surface water properties that can be linked to ocean colour images from satellites such as Seawifs. These satellite images show coastal physical and biological patterns in space and time for fisheries management and climate-related studies. Buoy data are presented and discussed to show the progress that is being made towards a system for operational monitoring of coastal productivity patterns.

1. Introduction

Data on marine ecosystems have traditionally been limited by the space and time scales imposed by ship cruises. More recently "ocean colour" satellites are starting to provide large-area images of phytoplankton biomass and data on their spectral properties. To complement these data, time series of physical and biological parameters at fixed locations are required for calibration and validation, for interpolation between the cloud-free periods when satellite images are available, and for tracking changes over short (blooms, seasonal cycle) and long (interannual and climate) time scales. Related requirements for monitoring the newly-announced Marine Protected Areas on the west coast of Canada are also being evaluated.

To provide time series which are useful in these contexts, various sensors are being tested for addition to some of the 17 buoys along and off the west coast of Canada which provide weather and ocean data for the federal Environment (EC) and Fisheries and Oceans

(DFO) departments. A system for real-time display of the data on the web is under development at <http://www-sci.pac.dfo-mpo.gc.ca/ecobuoys>. Additional sensors (transmissometer, acoustic profiler, improved fluorometer) are planned.

The first 3 EC/DFO meteorological buoys were installed on the west coast of Canada in 1987, and the array was finally brought up to its full number of 16 in 1993, with an additional experimental buoy (46134) being added in 1998. Three of the buoys are deployed offshore, 6 are in exposed locations near shore, and 8 are in sheltered waters (Figure 1). The buoys are well located for monitoring coastal water as well as weather. They provide adequate power, data handling and hourly real time data relay for all data. The standard buoys measure wind speed and direction, wave height and spectrum, surface water and air temperature and atmospheric pressure, data which are very useful when interpreting the biological data, or when planning a service call to the buoy.

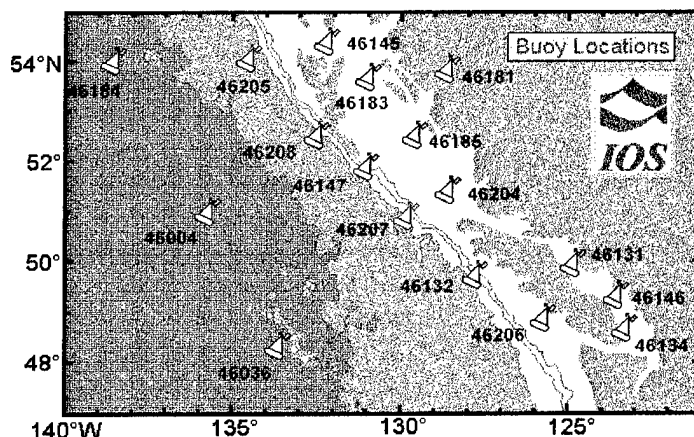


Fig. 1. Locations of the weather buoys in the west coast network. Biological sensors have been installed on buoys 46146 in southern Georgia Strait, and 46134 near the Institute of Ocean Sciences in Sidney, BC.

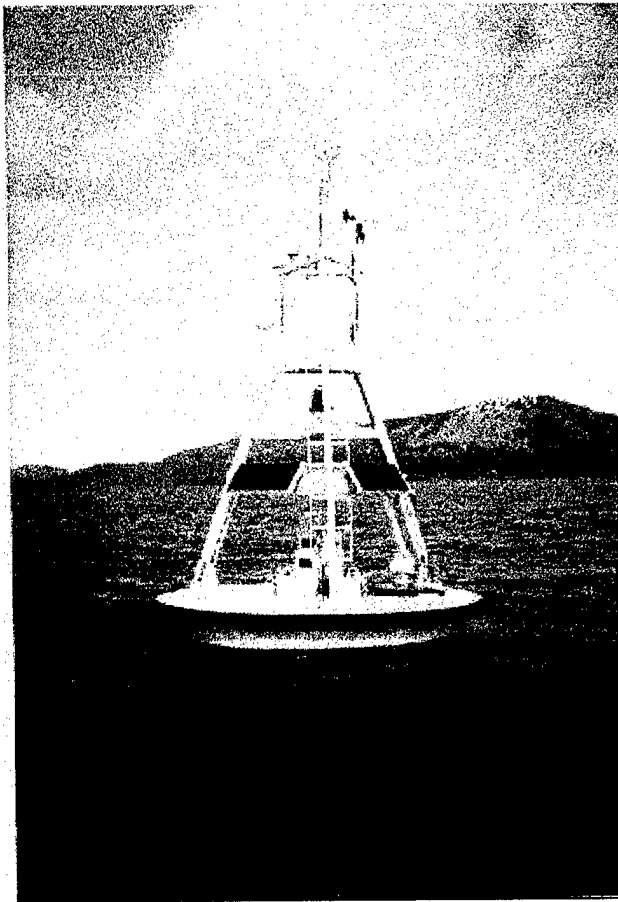


Fig. 2a. Weather buoy 46134 in Saanich Inlet near IOS. The buoy design is based on a standard 3-meter discus hull. Anemometers, radar reflector and satellite antennae are mounted at about 4 m above the sea surface. An automatic water sampler is mounted on the centre of the buoy deck. The top of the package holding the optical instruments can be seen on the deck at right.

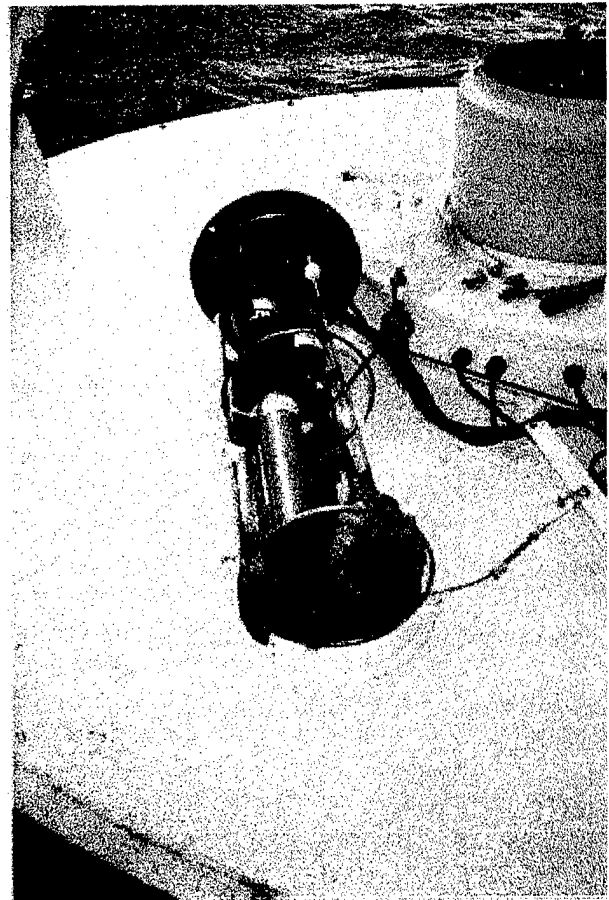


Fig. 2b. The "biological" instrument package withdrawn from the well in which it is mounted to look below the buoy. The lower end of the package is closer to the camera, over the well opening. Instruments presently include two fluorometers, a salinometer, and a 7-band optical radiometer. An optical PAR meter and a deep water inlet are hung 8 meters below the package.

As well as their intended use in weather forecasting, the data from the buoys have been used to validate COADS wind data (Cherniawsky and Crawford, 1996), wind and wave measurements from the Topex/Poseidon satellite (Gower, 1994), and to detect the long term sea surface temperature trends associated with El-Nino and climatic change. The need for biological time series of data is made especially urgent by the launch (in August 1997) of the Seawifs satellite, and the planned launch of other satellites with similar and more sophisticated sensors in the near future.

The buoys have sufficient sensor, data handling and communication bandwidth capacities to relay additional measurements. A project to install additional sensors was initiated in 1996 starting with a few test sensors on easily accessible buoys. The proposal is to eventually expand the system to a network of Marine Ecosystem Observatories, which would be based on the existing 3-m buoy or on an improved design.

II. Sensor Installation on Canadian West Coast ODAS Buoys

A minimally modified test buoy with externally mounted sensors was deployed on Constance Bank near Victoria on September 24, 1997. An irradiance PAR sensor was installed on the top of the buoy, and a similar underwater PAR sensor was deployed at 2.5 m depth under the centre of the buoy, looking up. A 7-channel radiometer designed to cover the Seawifs satellite spectral bands plus in-situ chlorophyll fluorescence at 685 nm was mounted under the buoy, looking down. Water was pumped to two fluorometers, mounted on the buoy, from depths of 0.5 and 2.5 m. Problems with the buoy electronics prevented data acquisition until December 17 after which measurements continued until April 18 1998, when the buoy was recovered. On May 13 1998, this same buoy was re-deployed on a standard ODAS location on Halibut Bank (46146), where it is still providing data.

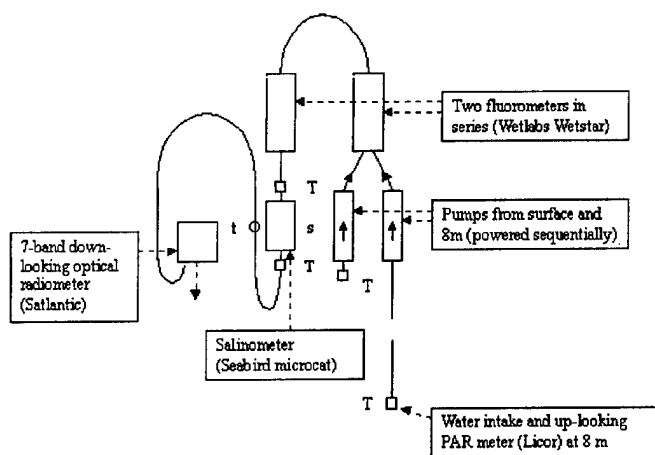


Fig 3. Pumped water flow in the sensing system used on buoy 46134. "T" indicates small flow-through anti-fouling modules. The outflow water is pumped onto the window of the radiometer to discourage growth.

Problems were quickly encountered with cleaning the optical sensors on this buoy. Their fixed locations under the buoy required use of divers or of a vessel large enough to lift the buoy out of the water. In addition, the use of separate fluorometers to measure at two depths, made it hard to separate spurious differences due to fouling, from real differences due to near-surface stratification. Also, a measurement depth deeper than 2.5 meters is required to sample below the summer pycnocline, but this was limited by the draft of the buoy.

In 1998 an improved sensor package was constructed, designed to be mounted in a well or "moon-pool" cut vertically through the hull of the buoy (Fig. 2). The underwater PAR sensor and a deep-water inlet were located 8 meters below this package at the end of a weighted line. In addition, water was pumped from the two depths through both fluorometers and a salinometer with small anti-fouling modules in the line (Fig. 3). This package was deployed on November 28, 1998 in a new buoy at a location in Saanich Inlet near the Institute of Ocean Sciences, and given the code 46134. The location is accessible and sheltered, and in an area known for its high spring and summer productivity.

III. Examples of buoy data

A. Solar Irradiance (PAR) time series

This appears to be the simplest and cheapest parameter to measure from a buoy, of those here attempted. The sensors are mounted in air and at both the Halibut Bank and the Saanich Inlet locations they appears to remain clean over long periods. The data are important as showing both the energy supply for

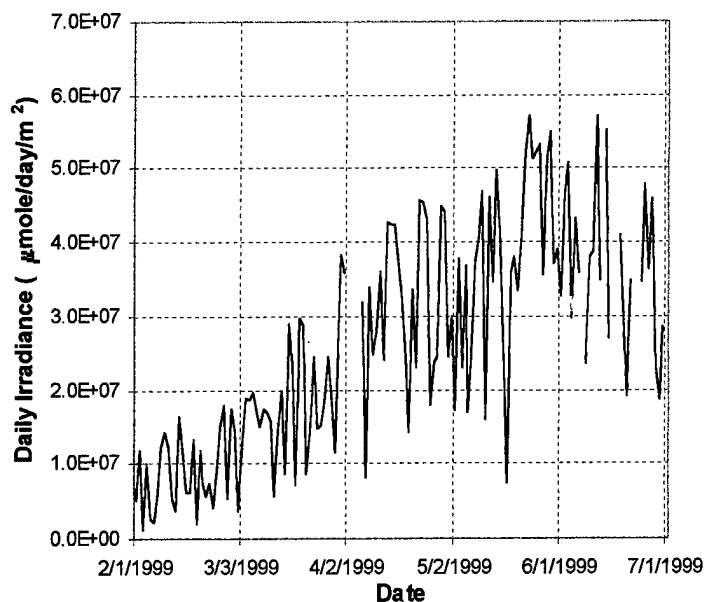


Fig. 4. PAR time series from buoy 46134 showing increased insolation during the spring. Real-time data collection is interrupted for brief periods due to trouble with networks at IOS. Hourly measurements are here converted to daily totals.

photosynthesis and the heat input to the ocean. Aerosol optical depth can also be deduced on relatively cloud-free days. An example of a PAR time series is shown in Fig 4.

B. Fluorometer time series

The two fluorometers on buoy 46134 provided consistent data over most months of 1999. Occasional periods of erratic disagreement were encountered which appeared to be due to the aggregation of phytoplankton into clumps of "marine snow." This gave different average readings for the one-minute periods (separated by one minute of flushing) over which the two instruments are read out.

Fig. 5 shows fluorometer measurements of the increase in chlorophyll pigment concentrations associated with the spring bloom in Saanich Inlet in late March 1999. Concentrations remain mostly low at 8-meters depth. Fig. 6 shows chlorophyll values measured by the fluorometer during April when the values were declining. PAR irradiance (insolation) measurements are plotted as a dotted line, showing the day/night cycle. The photoinhibiting effect of daylight on the fluorescence signal can be clearly seen as an apparent drop in chlorophyll pigment during the day. Times are in UT, so that daylight is approximately symmetrical about 20:00 hrs each day.

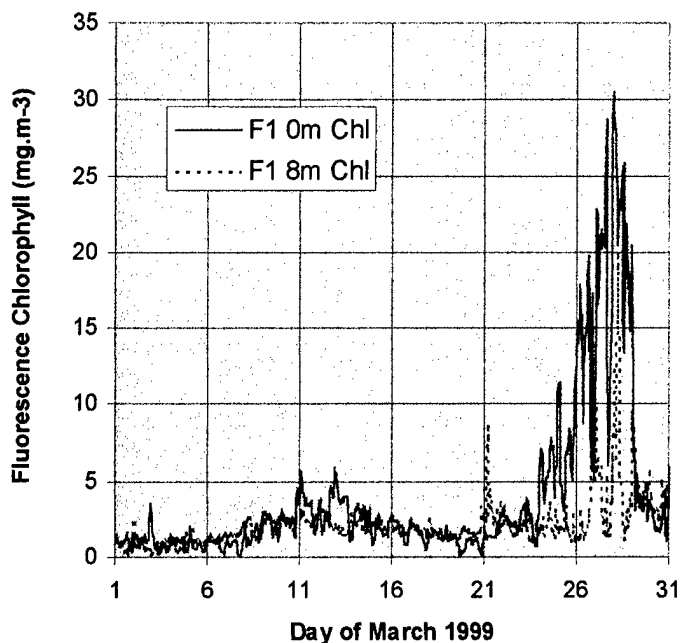


Fig.5. Time series of chlorophyll pigment concentrations deduced from fluorescence measurements on buoy 46134 at near-surface and 8 meters depth, showing the increase due to the spring bloom at the surface near the end of March.

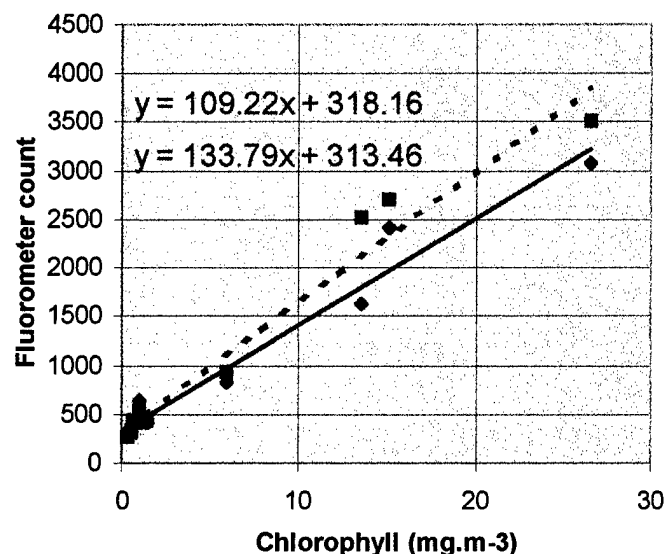


Fig. 7. Calibration of the two fluorimeters using results of analysis of water samples from 8-meters depth.

The fluorometer output is scaled to chlorophyll pigment concentrations in these two Figs. using analyses of water samples collected near-simultaneously with buoy measurements (interpolated between the two nearest hourly times) at 8-m depth, avoiding the photoinhibition at the surface.

C. Colour time series

Measurements of the up-welling radiance under the buoy show the changing colour (blue to green) of the water with increasing phytoplankton concentration. This increase in "greenness" can be expressed by the "green-to-blue" ratio of the radiance measurements at 555 and 443 nm (Fig 8). Measurements of radiance will need to be corrected for shadowing by the buoy before comparison with satellite data.

D. Effects of fouling

Over a long period, fouling of underwater optical sensors by growth of marine animals or plants will reduce measured optical signals, change their measured spectral properties, and eventually reduce the available signal to zero (Fig 9). Fluorometer data is also subject to errors when material lodges in the test volume.

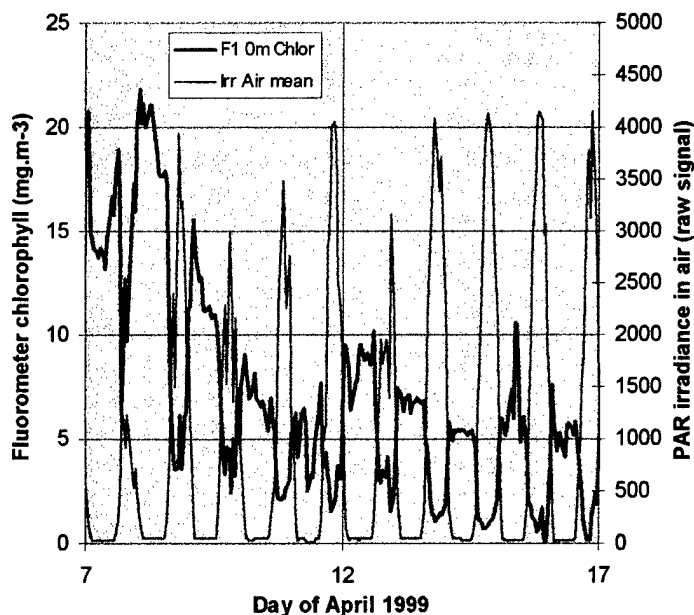


Fig 6. Chlorophyll pigment time series in April (heavy line) showing the effects of photoinhibition on the fluorescence signal. The light line shows the daily cycle of solar irradiance.

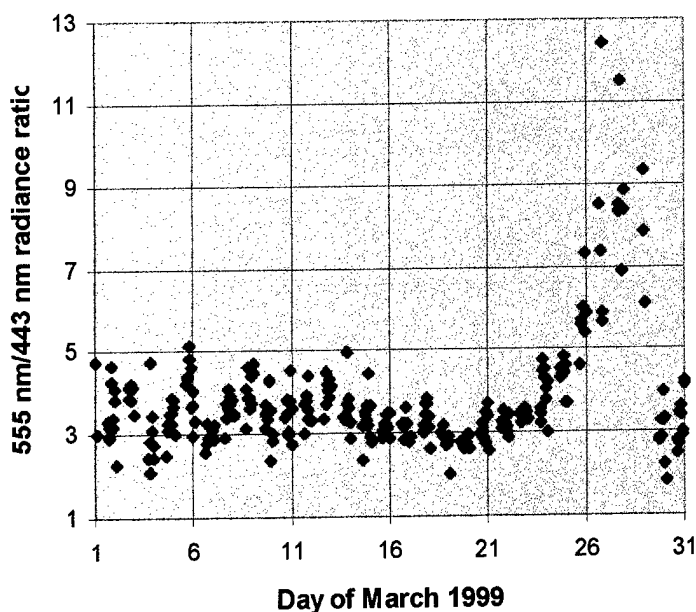


Figure 8. Time series of upwelling radiance colour ratio measured at the Saanich Inlet buoy during March 1999, showing the colour change (blue to green) caused by the start of the spring bloom of phytoplankton near the end of the month (compare to Fig 5).

IV. Conclusions

The project is making steady progress towards the goal of an operational Marine Ecosystem Observatory. Funds are now being sought to extend the sensor installation using the newer package design on buoys in Georgia Strait, off the west coast of Vancouver Island and in Hecate Strait. In addition, further instruments are being evaluated, including a transmissometer and an acoustic profiler for detecting zooplankton biomass and perhaps fish. In December 1998, the first of two new Marine Protected Areas on the west coast were announced. A suitably instrumented buoy may well have a role for marking and monitoring such areas.

V. References

- Cherniawsky, J.Y., and W.R. Crawford, 1996, "Comparison between weather buoy and Comprehensive Ocean-Atmosphere Data Set wind data for the west coast of Canada," *J. Geophys. Res.*, **101**, 18377-18389.
- Gower, J.F.R., 1996, "Intercalibration of wave and wind data from TOPEX/Poseidon and moored buoys off the west coast of Canada," *J. Geophys. Res.*, **101**, 3817-3829.

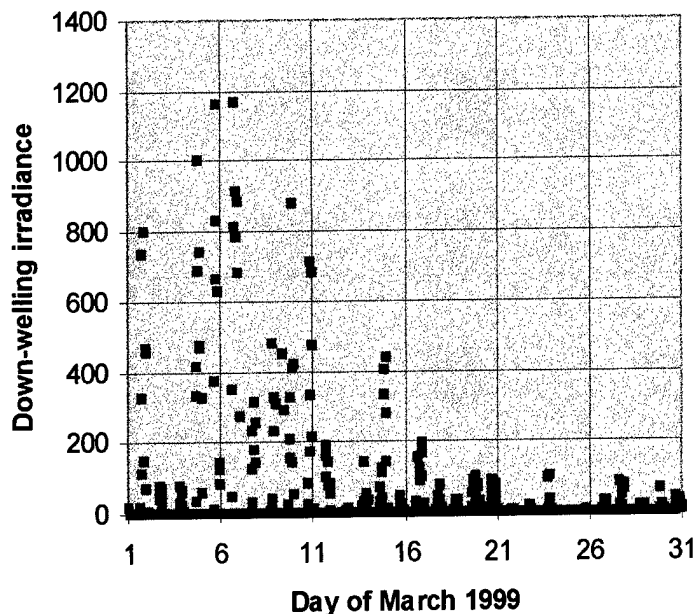


Figure 9. Reduction of the optical signal due to biological and physical fouling. This is most marked on the up-looking PAR sensor (shown here), since falling particles settle on it, and the high illumination of the up-facing surface encourages growth.

VI. Acknowledgements

We acknowledge the help and enthusiasm of many organizations and individuals who share our interest in monitoring and protecting coastal waters, especially the Data Buoy group of Environment Canada, the Hovercraft and Dive Unit of the Canadian Coast Guard, and John Wallace, Lizette Beauchemin, Isabel Beaudet, Phil Lloyd and Jerry Gurney of IOS

MAPPING NEARSHORE AND INTERTIDAL MARINE HABITATS WITH REMOTE SENSING AND GPS: THE IMPORTANCE OF SPATIAL AND TEMPORAL SCALES

C.D. LEVINGS¹, M.S. NORTH¹
G.E. PIERCEY¹, G. JAMIESON²,
AND B. SMILEY³

¹FISHERIES AND OCEANS CANADA,
SCIENCE BRANCH, WEST VANCOUVER
LABORATORY, 4160 MARINE DRIVE, WEST
VANCOUVER, B.C. V7V 1N6 CANADA

²FISHERIES AND OCEANS CANADA,
SCIENCE BRANCH, PACIFIC BIOLOGICAL
STATION, NANAIMO, B.C. V9R 5K6

³FISHERIES AND OCEANS CANADA,
SCIENCE BRANCH, INSTITUTE OF OCEAN
SCIENCE, SIDNEY, B.C. V8L 4B2

Abstract

Determining the position and surface area of critical fish habitats such as seagrass beds is an essential component of coastal zone management. Positional data is particularly important as the boundaries between habitats may determine the loss or maintenance of seascape units essential for ecosystem functioning. These data are also important for land or seabed owners or leasees, since property boundaries must also be considered. Surface area data are also vital to track temporal changes in the extent of habitats through time, and responses to natural and anthropogenic changes. Mapping scale is particularly important to surface area determinations and cumulative effect studies. Some resource managers are concerned with interacting habitat units as small as 100 m².

In this paper, we present results and experience of mapping and assessment of algae and seagrass beds in British Columbia (B.C.) using air photo interpretation, compact airborne spectrographic imager, ground surveys using a high precision GPS, and conventional survey techniques. Low-level colour air photography (1:5000 scale) was found to be an effective and accurate methodology, but only when accompanied by

thorough ground-truthing. Ground-truthing was conducted by foot surveys at low tide or by observations from a boat or hovercraft at high water. Results from CASI were more problematic, especially to determine the boundaries if similar plant or algae habitats, but could be improved with more spectral signature data of specific plant species as well as consideration of the seasonal change of those spectra. Mapping of algae beds using a GPS at 1:500 scale (est.) was tested by foot surveys to delineate the boundary of the habitat or by a grid system where the positions of vertical and horizontal transects were georeferenced using the instrument. The latter method was accurate and relatively efficient and enabled quick mapping of the habitat units into a GIS. There are very few data on the temporal change of the extent and position of specific habitats in our region. However by reviewing data in a land tenure data base maintained by the Government of B.C. obtained with conventional survey techniques (e.g. transits) we determined that the number of hectares of nearshore habitat used for industrial purposes (log storage) has declined over the past decade in the Strait of Georgia. As an indicator of trends in habitat use over the entire shoreline of the Strait, these data were sufficient. In an effort to increase the role of the public in habitat monitoring over time, we developed and tested methods for mapping by citizens. The methods in the "Shorekeeper's Guide" give citizens options for using conventional survey and/or GPS methods for mapping beaches in coastal communities. Scales for this work are about 1:500.

I. Introduction

The coast of British Columbia (B.C.), the west shore of Canada, encloses some of the most complex geophysical and ecological units around the Pacific Rim. Including all of the major islands and archipelagos, the total shoreline length is 27,000 km. A wide variety of marine and estuarine habitats are represented on this coast, including open ocean beaches, fjords, estuaries, rocky shores, and tidal channels. On the south portion of the coast, a brackish enclosed sea, the Strait of Georgia (SoG), is the home for the majority of B.C.'s people. Vancouver, Canada's major Pacific port, is located here, and is characterized by a rapid population growth rate of about 15 % in recent years. Industrial and urban development in the SoG has led to significant losses of environmentally sensitive fish habitat, especially marshes in estuaries and seagrass beds in nearshore areas (Levings and Thom 1994). On the north coast, the human population is much sparser, and habitats are generally less impacted by development. In this region, industrial forestry in river basins is the current major threat to coastal habitats, since logs removed from the forest are usually dumped into and transported through marine zones. The riparian habitats

along the coast, as well as the catchment basins of rivers entering estuaries, can be affected by these activities (Simenstad et al. 1997). Oil spills are a potential major threat to habitats on the west coasts of Vancouver and the Queen Charlotte Islands, since tankers from Alaska routinely transit the offshore waters, enroute to refineries in the State of Washington (Waldichuk 1990).

In this paper we describe some recent advances in methodology useful for integrated coastal zone management in B.C. Technical staff responsible for management of coastal environments and habitats need tools to assist them in their task to keep track of changes in coastal regions. In particular, quantitative data on habitat loss and gain are required when monitoring estuarine habitat restoration using vegetation transplants or other habitat recovery techniques (Levings 1995, 1996). Some of the most important techniques involve the rapidly evolving field of Geographic Information Systems (GIS). Although GIS has been used widely to assist in terrestrial habitat management for wildlife (Burrough 1986), its application to coastal zone management in our region has been limited. There is a great potential to use GIS to organize, analyze, and present basic data required by fish habitat managers under the fish habitat management policy of the Department of Fisheries and Oceans (DFO) (1986). These data include:

- a. What is the location of the habitat, usually in relation to planned industrial activity?
- b. What is the area of the habitat?
- c. What is the ecological value of the habitat?
- d. How much of this habitat will be lost if an industrial activity is permitted?
- e. If a habitat restoration or compensation project has been conducted, did it meet prescribed target in terms of area?

Habitat managers need to keep track of relatively small bits of habitat, particularly in the intertidal zone and in shallow water ($1 < 20$ m) since these nearshore areas are where most of the land use changes (diking, port development, urbanization) are occurring. Tracking the location and temporal change of small habitats is essential for cumulative effects analysis. For seagrass habitat, for example, as a general policy about 100 m² is the minimum area of concern in our region. This requires mapping at a much larger scale than needed for broad scale planning or oil spill contingency plans - other agencies in our region have developed habitat maps for the latter purposes (e.g. Howes and Wainwright 1993). It is necessary to keep track of the cumulative total of small habitats in particular areas, in order to avoid insidious losses of the estuarine environment that have occurred on many coastlines

(Odurn 1970). Now technology that enables rapid and accurate quantification of these habitat measurements, in a cost-effective manner, is of obvious direct use for integrated coastal zone managers.

II. Data Availability

In the past two decades there has been very rapid growth in data banks and technical report literature on coastal areas, especially reports written and maps produced by government agencies and private consultants. Many of these data are difficult to locate for use in decision making since they do not enter the usual scientific literature data bases such as the Aquatic Scientific and Fisheries Abstract service. In order to improve their availability it is necessary to launch specific searches for the information. Once found, the awareness of the information can be enhanced through publication of bibliographies listing reports, data, and maps. As an example, we have recently published an annotated bibliography for fish habitat maps in the Strait of Georgia (Lessard et al. 1996a). We have also created an Internet home page with this information (<http://www.ios.bc.ca/ios/mehsd/coast>).

There are very few data on temporal change of the extent and position of specific habitats in our region. We reviewed data in a land tenure data base maintained by the Government of B.C. obtained with conventional survey techniques (e.g. transits)(Glover and Levings 1998). We found that the number of hectares of nearshore habitat used for a specific industrial purpose (log storage) has remained fairly stable over the past decade in the Strait of Georgia (Table 1). As an indicator of trends in habitat use over the entire shoreline perimeter, of the Strait, these data were sufficient.

Table 1. Area (ha) leased for log storage in the Strait of Georgia, 1986 to 1996. Data compiled from Province of B.C. Crown Lands data base, using methods described in Glover and Levings (1998).

YEAR	NEWLY LEASED	RENEWALS
1986	49.9	345.8
1987	108	441.5
1988	296	302.8
1989	154.3	105.8
1990	24.9	142.2
1991	135.2	114.7
1992	29.2	144.6
1993	58.6	280.8
1994	17.3	253.2
1995	41.5	104.8
1996	43.1	119.9

III. Global Positioning Systems

Decisions on habitat are particularly sensitive to locations relative to legal, zoning, and ecological boundaries. Given the high economic and ecological values involved, it is important to make sure that positions are accurate. There are no published standards available on this matter for work in the coastal zone. Based on recommendations from the manufacturer and B.C. Surveys and Resource Mapping Branch, if at least 180 readings are taken with a Differential Global Positioning System (DGPS) instrument (Trimble Navigation, Pathfinder Basic Plus), point measurements have an error of < 5 m. This is probably sufficiently accurate for most decisions. We have not made comparisons of locating habitats using conventional surveying methods such as laser transits. However many habitat surveys are needed in relatively remote areas where benchmarks are scarce so that obtaining horizontal control points is difficult. There is a definite advantage in using DGPS under these circumstances.

DGPS can also be very useful for mapping habitats (e.g. algae beds at low tide) at large scales (e.g. 1:500). In Howe Sound B.C. we used GPS (Trimble TDC2) to delineate the boundaries of the algal habitats directly or with a grid system where the positions of vertical and horizontal transects; on the beach were georeferenced using the instrument. The latter method was accurate, relatively efficient, and enabled quick mapping of the habitat units into a GIS (Levings, unpublished data).

IV. Remote Sensing

A. Intertidal

Tides on the B.C. coast typically range between 3 and 5 m, but at the heads of some fjords the range is up to 8 m (Thomson 1981). In this region the lowest tides during daylight hours, when the water line is close to chart datum, occur for about a week in summer. Depending on the slope of the local shoreline, extensive areas of the intertidal habitat can be photographed or otherwise sensed from aircraft or satellites during this "window", contingent on sunlight and weather conditions. Protocols for aerial photography for mapping coastal habitat, particularly submerged aquatic vegetation, have been published by Dobson et al. (1995).

Because of large scale mapping requirements, lowlevel colour or infrared photos combined with

groundtruthing and DGPS have been used extensively in developing substrate and vegetation maps in our region. In a recent study of Saanich Inlet, on Vancouver Island, about 95 km of shoreline was mapped to compile a tabulation of the relative areas of two species of seagrass (Table 2). In this project colour air photos (scale 1:6000) were obtained on the lowest daytime tides in 1995. Fieldwork for ground-truthing required about 20 person-days and included foot surveys on beaches, video, 35-mm photos, and direct observations from a small boat. As required, point or boundary data on the seagrass beds were registered with DGPS (Lessard et al. 1996b). The polygons marked on the air photos were georeferenced, digitized, and overlain on standard terrestrial bass maps as described in Durance (1996). The data were finally imported into the GIS Arcinfo for further analyses as required. The Compact Airborne Spectrographic Imager (CASI) was investigated in Baynes Sound, Vancouver Island, as an alternate method to aerial photography. Although CASI is a more advanced technology it may not necessarily be more objective (North 1996). CASI records the reflectance of ground features and is able to distinguish different types of vegetation. The advantages of CASI over air photos include:

- a. Data are digital rather than analogue
- b. Greater spectral range and possibility of setting spectral bands specifically, which may allow better discrimination of vegetation types
- c. Possibility of detecting and discriminating submerged features (see below for possible application to subtidal surveys).

However, CASI data must always be "trained" with ground-truthing and spectral records from various vegetation types. The spectral data from the instrument then need to be analyzed and classified with various computer algorithms (including multivariate analyses), which are the choice of the investigator. To develop a meaningful classification of the data, the investigator must work with a computer at several stages, particularly to identify training sites and determine which of the pixels in the CASI image are most similar to those in the training sites. The classification process is therefore not completely automated and is in some degree as subjective as air photo interpretation

Table 2. Areas of polygons of eelgrass (*Zostera marina* and *Z. japonica*) in several reaches of Saanich Inlet, British Columbia, mapped from aerial photos and ground-truthing in July, 1995 (from Durrance 1996, and Lessard et al. 1996b).

LOCATION	SPECIES COMPOSITION OF POLYGONS			AREA (HECTARES)			
	pure Z.m.	Z.m.+Z.j.	pure Z.j.	pure Z.m.	Z.m.+Z.j.	pure Z.j.	total
EAST COAST							
Deep Cove	3	1	5	2.8	<0.1	1.3	4.1
Deep Cove to Patricia Bay	2	11	0	0.2	0.8	0.0	1.0
Patricia Bay	8	9	3	5.6	1.9	6.6	14.1
Patricia Bay to Coles Bay	0	1	0	0.0	0.2	0.0	0.2
Coles Bay	4	0	0	<0.1	5.2	1.3	6.5
Brentwood Bay	4	0	0	1.2	0.0	0.0	1.2
Sub-total	21	22	8	9.8	8.1	9.2	27.1
WEST COAST							
near Bamberton	1	0	0	0.0	0.3	0.0	0.3
Mill Bay	3	1	0	2.4	5.0	0.0	7.4
Hatch Point to Mill Bay	4	0	2	0.7	0.0	2.7	3.4
Sub-total	8	1	2	3.1	5.3	2.7	11.1
SOUTH END							
Goldstream Estuary	2	0	0	0.0	1.9	0.0	1.9
SAANICH INLET (TOTAL)	31	23	10	12.9	15.3	11.9	*40.9

Z.m. - *Z. marina* Z.j. - *Z. japonica* Z.m. + Z.j. - both species

* Value includes polygon areas of <0.1 ha that were not included in the table (0.8 ha)

B. Subtidal

Shallow water habitats, below the limit of lowest tide, can only be mapped with remote technology. There are some exceptions to this generalization. SCUBA can be used to make direct underwater observations and the diver's position can be plotted using DGPS in a surface vessel. This method was recently used to develop a habitat map for Vancouver Harbour. Kelp and seagrass habitats occur to the limit of light penetration into coastal waters, which in turn depends on local conditions such as turbidity. If the water is very clear it is possible to use aerial photos and CASI for sensing below the water's surface. For very large kelp (e.g. *Macrocystis pyrifera*) where the blades float on the surface, aerial photos and multispectral imagery can also be used. The former method has been developed for mapping biomass of kelp on the west coast of Vancouver Island by Foreman (1975).

A variety of acoustic methods have been used for mapping subtidal habitats. In an early application, a

200 kHz echosounder was used to map seagrass beds in San Francisco Bay (Echeverria and Fulton 1989). Water depth was shallow enough so that groundtruthing could be done from a helicopter and boat. In our region, depth and habitat type as defined by sediment type have been mapped using Acoustic Substrate Classification (ASC) ("RoxAnn" or "Quester Tangent" technologies), which also provides accurate positioning using DGPS (Curran 1995). Cripps (1996) reported that subtidal clam habitat, which is characterized by a particular combination of sand and mud, was successfully mapped with ASC. He also reported that eelgrass beds could be mapped with this technology. Bornold et al. (1996) found that sidescan sonar, another example of ASC, was an effective technique to investigate subtidal habitats off the Oregon coast. As with the other remote sensing techniques described above, ASC methods require considerable ground-truthing, using SCUBA, submersible, video or still camera, ROV, or core sampling.

V. Ecological Classifications

A basic principle in an ecological accounting system is the use of a standardized "currency" for keeping track of habitats. Alternatively if a standard currency is not available, data should be collected in comparable units that when aggregated will allow comparisons through time in monitoring programs. On the northeast Pacific coast, it is very difficult to compare habitat data because there is no agreed upon ecological classification system in use. In the Strait of Georgia-Puget Sound inland sea, for example, there are at least 8 systems in place (Levings and Thom 1994). In order to overcome this problem, and match with the capability of remote sensing systems, we have decided to use a relatively simple system that relies on relatively easily recognizable vegetation units (e.g. eelgrass beds) and sediment features (e.g. sand flats) as habitat units.

VI. Ground-truthing Surveys to Confirm Identification of Habitat and Estimates of Area

The effort expended on ground-truthing before, during, or after remote sensing surveys is obviously related to the complexity and extent of the study area. Site specific forestry surveys (scale 1:5000 to 1:20000) require that between 76 and 100 % of the polygons from air photo interpretation are checked by ground-truthing (Resources Inventory Committee 1995). We could not find similar criteria to use for coastal work in our region. Air photo interpreters can provide guidance for field verification by noting areas where they had difficulties (e.g. sun glare or shadow). Because the extent of vegetation can change rapidly owing to seasonal changes, the ground-truthing should be done at the same time as the remote sensing, if at all possible.

As noted above, habitat managers in our agency need to account for habitats $> 100 \text{ m}^2$ in area, which is quite similar to the 300 m^2 minimum specified in the protocol for submerged aquatic vegetation mapping given by Dobson et al. (1995). However Durance (1996) found that the minimum polygon size for seagrass observable in aerial photos from Saanich Inlet was 1000 m^2 . In addition to the obvious matters such as photo clarity, it is likely that biological factors, which determine the sharpness of the habitat boundaries, such as plant density and morphology, are factors, which influence the minimum size that an interpreter can detect. During ground-truthing on shorelines at low tide, the area of habitats with well-defined boundaries, such as seagrass beds, can be assessed with conventional surveying techniques but as mentioned above horizontal control can be a problem in remote areas. However DGPS can be used to delineate the perimeter of habitats, and algorithms are available to compute area. The position of the habitat can be georeferenced and

placed on a base map. Accuracy can be improved by taking a large number of readings at single points around the perimeter of the habitat or tracing the perimeter by walking around the boundaries. The accuracy of the latter method can be improved by placing small objects (e.g. ping pong balls) at short intervals around the perimeter.

In an effort to increase the role of the public in habitat monitoring over time, we developed and tested methods for mapping by citizens. The methods in the "Shorekeeper's Guide" (Jamieson et al. 1999) give citizens options for using conventional survey and/or GPS methods for mapping beaches in coastal communities. Scales for this work are about 1:500

VII. Error

There are several error issues that we have encountered in trying to quantify habitat boundaries and areas. Clearly defined boundaries between habitat types occur rarely in nature, and their occurrence is scale dependent. A boundary between water and adjacent land may be easily mapped at 1:250000 scale. But at 1:5000 scale, the visibility of details in the shoreline may make location of the boundary less certain, or may result in a more complex boundary being mapped. The problem is even more apparent for boundaries between vegetation types, where two communities of vegetation grade into each other. Identification and mapping of such a boundary will depend both on scale and on the classification system being used.

Identification of boundaries from remotely sensed images, such as air photos or CASI multispectral data, is a complex and somewhat subjective process, as mentioned above. In the case of air photo interpretation, identification of features based on the tone, texture, and colour of the photo is a skill that takes some time to develop. Classification of multispectral imagery involves identification of training sites (areas on the image for which the habitat type is known, and that the computer can use as a basis for classifying the rest of the image) and selection of the classification algorithm.

Determination of the area of habitat from remotely sensed images depends partly on image resolution. The area cannot be calculated to a precision of one square metre if the resolution of the image is only 10 m^2 . Furthermore, habitat boundary generalization that results at smaller scales will decrease the precision of area calculations. The resolution of the image depends partly on scale, which depends on flying height. For example, 1:6000 scale air photos are obtained at a flying height of 6000-ft (1829 m), and can give a

resolution of less than a metre. However, photos at this scale may not cover enough area to include recognizable features, such as roads and piers, which makes georeferencing more difficult and less accurate. CASI data collected for us at Baynes Sound at a flying height of 6700-ft (2042 m) have pixels of four by four metres. Decreasing the pixel size to obtain greater resolution may increase the data set to an unmanageable size, and will also mean that a longer flying window (time when tides, light angles, and weather conditions are suitable for flying) is required to cover the study area.

Georeferencing is required both for the imagery itself and for the field data used to help classify the imagery. GPS data and aircraft roll, pitch, and yaw data can be collected at the same time the imagery is collected, and used in processing, along with existing basemaps, to georeference the imagery. Even after this processing, there may be some inaccuracy in the georeferencing (e.g. a few metres). Corrections for aircraft motion cannot completely remove this source of error, and DGPS accuracy is limited, although GPS receivers used to georeference CASI imagery are more accurate (e.g. < 1 m). The accuracy of the GPS instruments used in our recent algal habitat surveys was also within this range.

VIII. Conclusions and Research Recommendations

The use of technological advances such as those described in this paper will improve the effectiveness of coastal zone managers but there are still several areas where applied research and development are needed before they can be fully implemented. An urgent need is for the development of standards for field checking of photo/multispectral data classification and for collection of training-site data for multispectral data classification, especially with respect to use of DGPS and large-scale mapping. There is also a requirement for refinements of CASI remote sensing techniques, particularly development of a more extensive spectral library and more detailed study of methods to distinguish key habitat and vegetation types. Similar refinements are needed for subtidal habitats and ASC methods. Coastal ecologists need to focus on development of habitat classification systems that enable the bridging of field biological data with remote sensing and GIS. It is unlikely that technology will ever replace the good judgment of an experienced ecologist, but remote sensing may remove the subjectivity of some traditional habitat mapping methods. The effectiveness of coastal habitat surveys can therefore be improved by deploying small teams involving specialists in remote sensing, GIS, and field ecology.

IX Acknowledgements

Much of the work described in this report was supported by the Department of Fisheries and Oceans Habitat Action Plan, Environmental Analysis component or by the Oceans Act Implementation Fund.

Disclaimer: Mention of specific instrument brands does not represent an endorsement or recommendation.

X. Literature cited

- Bornhold, B., R. Currie, D. Fox, J. Golden, H. Olynyk, and D. Johnson. 1996. Habitat mapping southern Oregon continental shelf, p. 27-33. *In*: T. Curran [ed.]. Proceedings of the Ocean Feature Classification Workshop, Institute of Ocean Sciences, Sidney, British Columbia, May 3, 1996.
- Burrough, P.A. 1986. Principles of Geographic Information Systems for Land Resources Assessment. Clarendon Press, Oxford. 194 p.
- Cripps, K. 1996. Geoduck and sea cucumber surveys using RoxAnn (1994-95 surveys), p. 9-15. *In*: T. Curran [ed.]. Proceedings of the Ocean Feature Classification Workshop, Institute of Ocean Sciences, Sidney, British Columbia, May 3 1996.
- Curran, T [ed.]. 1995. Remote sensing techniques for subtidal classification. Proceedings of a workshop organized by Kitasoo First Nations Fisheries Program, Resource Inventory Committee of B.C., Canadian Hydrographic Service. Institute of Ocean Sciences. March 17, 1995. Available on the World Wide Web at <http://www.jos.bc.ca/ios/chs>.
- Department of Fisheries and Oceans (DFO). 1986. Policy of the Management of Fish Habitat. Department of Fisheries and Oceans, Ottawa, Ontario. Cat. No. Fs23-23-98/1 986E. 28 p.
- Dobson, J.E., E.A. Bright, R.L. Ferguson, D.W. Field, L. L. Wood, K.D. Haddad, H. Iredale 111, J. R. Jensen, V.V. Klemas, R.J. Orth and J.P. Thomas. 1995. NOAA Coastal Change Analysis Program (C-CAP): Guidance for Regional Implementation. NOAA Tech. Rep. NMFS 123. 92 p.
- Durance, C. 1996. Eelgrass habitat assessment, p. 42-51. *In* W.C. Austin, S.P. Leyland, C. Durance, 1996. Saanich Inlet Study: Sensitive Habitats and Biota. B.C. Ministry of Environment, Lands and Parks, Victoria, B.C. (also available on the World Wide Web at <http://www.env.gov.bc.ca/epd/wqgb>).

- Echeverria, S.W., and P.J. Ruffen. 1989. Inventory of eelgrass (*Zostera marina* L.) in San Francisco/San Pablo Bay. NOAA Southwest Region, National Marine Fisheries Service, Terminal Island, California. Administrative Report October, 1989. 18 p.
- Foreman, R. E. 1975. KIM-1: a method for inventory of floating kelps and its application to selected areas of kelp license Area 12: final report. BERP Report 75-1. University of British Columbia Botany Department. 21 p.
- Glover, E.A., and C.D. Levings. 1998. Use of the British Columbia Provincial Tenure Administration (TAS) for Analysis of Marine Habitat Use in the Strait of Georgia, British Columbia. Proceedings of Coastal Zone'98, Victoria, B.C. August 30 - September 3, 1998. p. 153-154.
- Howes, D.E, P. Wainwright, J. Haggarty, J.H. Harper, E. Owens, D. Reimer, K Summers, J. Cooper, L. Berg, and R. Baird. 1993. *Coastal Resources and Oil Spill Response Atlas for the Southern Strait of Georgia*. B.C. Ministry of Environment, Lands and Parks, Environmental Emergencies Coordination Office, Victoria, B.C. 317P.
- Jamieson, G.S., C.D. Levings, B.C. Mason, and B.D. Smiley. 1999. Shorekeepers' Guide for Monitoring Intertidal Habitats of Canada's Pacific Waters. Manual Published by Department of Fisheries and Oceans, Pacific Region. (in press).
- Lessard, J., C.D. Levings, M.S. North, and D.J.H. Nishimura. 1996a. An annotated bibliography of fish habitat maps for the Strait of Georgia. Can. Manuscr. Rep. Fish. Aquat.Sci. 2350. 31 p + app.
- Lessard, J., M.S. North, C.D. Levings, and D.J.H. Nishimura. 1996b. Field survey report for Saanich Inlet eelgrass, July, 1995. Can. Data Rep. Fish. Aquat. Sci. 975. 29 p.
- Levings, C.D. 1995. Natural factors to be considered in restoration of marine and estuarine ecosystems supporting fisheries. Proceedings of the Osaka-Wan Symposium, Kobe, Japan, June 5-7, 1995. p. 65-68 (English); p. 69-70 (Japanese).
- Levings, C.D. 1996. Compensation and mitigation techniques used to assist fish habitat management in British Columbia estuaries. Proceedings of the Sumoto City International Marine Symposium, July 18-20, 1996. p. 81-85 (English); p.87-90 (Japanese).
- Levings, C.D., and R.M. Thom. 1994. Habitat changes in Georgia Basin: implications for resource management and restoration, p. 330-351. In R.C.H. Wilson, R.J. Beamish, F. Aitkens, and J. Bell [ed.]. Review of the Marine Environment and Biota of Strait of Georgia, Puget Sound and Juan de Fuca Strait. Can. Tech. Rep. Fish. Aquat. Sci. 1948.
- North, M.S. 1996. Intertidal fish habitat classification studies undertaken as part of the DFO marine foreshore fish habitat assessment project, p. 36-40. In T. Curran [ad.]. Proceedings of the Ocean Feature Classification Workshop, Institute of Ocean Sciences, Sidney, British Columbia, May 3, 1996.
- Odum, W.E. 1970. Insidious alteration of the estuarine environment. Trans. Amer. Fish. Soc. 99: 836-847.
- Resource Inventory Committee. 1995. Standards for Terrestrial Ecosystems Mapping in British Columbia. Prepared for the Ecosystems Working Group of the Terrestrial Ecosystems Task Force. 840 Cormorant Street, Victoria, B.C. Canada V8W 1 R1. 190 p. (draft).
- Simenstad, C.A., M. Diether, C.D. Levings, and D.E. Hay. 1997. The terrestrial/Marine Interface. p. 149-187. In P.K Schoonmaker, B. van Hagen, and E.C. Wolf, [ed.]. Proc. Conference on The Environment and People of the Coastal Temperate Rain Forest, Whistler, B.C. August 28-30 1994. Island Press, Washington, D.C.
- Thomson, R.E. 1981. Oceanography of the British Columbia coast. Can. Spec. Pub. Fish. Aquat. Sci. 56. 291 p.
- Waldichuk, M. 1990. Industrial and domestic pollution in the North Pacific. Trans. Royal Society Canada, Series 1, Volume 1 (1990): 387-433.

The NOAA Trajectory Analysis Planner: TAP 11

Christopher H. Barker
Hazardous Materials Response Division
Office of Response & Restoration
National Ocean Service, NOAA
7600 Sand Point Way NE
Seattle WA 98115-0070

Abstract

Trajectory Analysis Planner (TAP 11) is a computer-based tool designed to investigate the probabilities that spilled oil will move and spread in particular ways within a particular area, such as a large bay or inlet with substantial ship traffic. By graphically presenting the results of thousands of oil-spill trajectory simulations, TAP 11 helps emergency planners understand and anticipate many possible outcomes when developing local-area contingency plans for oil spill response.

TAP 11 assists in the following planning tasks:

- assessing potential threats from possible spill sites to a given sensitive location
- determining which shoreline areas are likely to be threatened by a spill originating from a given location
- calculating the probability that a certain amount of oil will reach a given site within a given time-period
- estimating the levels of impact on a given resource from a spill
- analyzing shortfalls in response personnel and equipment

I. Introduction

Community oil-spill response is a complex business that typically brings together stakeholders from a wide range of disciplines, including engineers, natural resource trustees, property owners, government managers, emergency responders, maritime industry representatives, fish and wildlife experts, etc. To even begin developing a unified plan, these groups must share a common understanding of oil spills and the likely impacts of a spill in their local area. Many members of community response planning teams have little or no background in physical oceanography or trajectory analysis. The task for oil-spill modelers in support of these planning groups is to present a practical ensemble of information on potential spills and their probable consequences in relation to the various stakeholder interests represented on the planning team. A more detailed

discussion of this complex task is given in Galt & Payton (1999).

Oil spill response planners must have a basic understanding of what is likely to happen.

- 1 What (and how much) oil might spill?
- 2 Where might the oil spill?
- 3 Where might it go? and how much?
- 4 Who or what might get hurt?

The first two questions can be answered by looking at the kinds and sizes of vessels that normally travel in an area, their cargo, and the types and amounts of oil they carry, as well as onshore oil handling facilities. TAP 11 is a tool that provides information to answer the last two questions: Given a specific spill location and type, where might it go and what might it harm?

II. Why TAP 11?

The current state of the practice is *scenario-based* spill response planning, whereby a response is planned for a so-called "worst case scenario" or, in some cases, a small set of scenarios. To generate these scenarios, sets of oceanographic and meteorologic conditions are selected based on a set of assumptions about what constitutes the worst possible outcome from a given spill at a given location.

There are limitations to this approach. For example, although a particular worst case may pose the worst possible outcome from the perspective of one stakeholder, this may not be true from another perspective. Fig. 1 is a schematic of a hypothetical bay where an oil spill could occur. Depending on the conditions at the time of the spill, the oil could threaten a wildlife preserve (Scenario A), a beach with many tourist hotels (Scenario B), or a nuclear power plant with a cooling water intake (Scenario C). Different stakeholders would give very different answers as to which is the worst case. Another difficulty with worst-case scenario planning is that even if a worst case is agreed

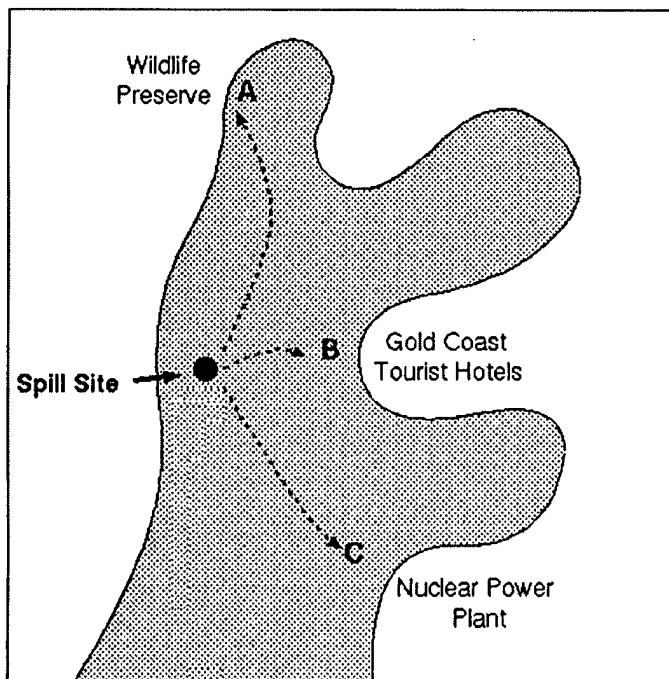


Fig. 1. Three possible worst-case scenarios of an oil spill in a hypothetical bay

upon and planned for, the likelihood of that particular scenario is often unknown. Also, a response plan formulated for a particular worst case may be inappropriate for other scenarios that would require a completely different response.

TAP II provides an alternative approach: *statistics-based planning*. *Statistical analysis* is an analysis of data derived from a sample in order to predict the characteristics of the population under study (Morris 1992). In the case of oil-spill response planning, the *population* under study is the set of all possible oil spills in a region. TAP II is the interface to a database of thousands of modeled spills, a *sample* of the *population* of all possible spills. The TAP II interface helps response planners understand characteristics of the possible oil spills in a given region. Understanding these characteristics allows responders to plan not only for *one or a few* possible high-impact events, but to determine the best overall plan for *many* events, across the entire spectrum of probabilities and levels of impact.

A. History of TAP and TAP II

The Trajectory Analysis Planner (TAP), a user-friendly tool to support spill-response planning, was developed in 1998 by the Hazardous Materials Response Division (HAZMAT) of the National Oceanic and Atmospheric Administration (NOAA). Initially developed as a pilot study for Delaware Bay and San Francisco Bay, TAP is an application and viewing engine for an area-specific database that allows the user to view graphically the probabilities that a specific oil will move from a specified spill site to a designated target location. After completing the TAP pilot project, HAZMAT (now a division of the Office of Response

& Restoration) worked with response planners to evaluate their receptiveness to the product and to observe how they interpreted the information given. We also began an in-depth analysis of the statistical methods used in TAP so that we could better understand uncertainty of the information presented and the potential spatial gaps in the initial geophysical data used to generate a specific scenario set (Barker & Gait 1999, Lehr et al. 1999).

The results of this usability testing lead to the realization that TAP's configuration failed to provide some statistical analyses that would be highly useful to planners. These include distinguishing between 1) locations very likely to be oiled with a small amount of oil, and 2) locations, although less likely to be oiled, that would be hit with a large amount of oil. We also found that users often misinterpreted the information that TAP did provide. The results of these studies have led to the reformulation of the TAP analysis procedures. The new version, known as TAP II, provides a greatly expanded and more powerful spill-trajectory database that specifically addresses major areas of concern to spill-response planners.

B. Methodology of TAP II

To provide statistics of oil spill movement, TAP II must process data from a large number of trajectories. Each trajectory is a function of the physical processes of oil movement, including the dynamics of wind, ocean currents, and turbulent diffusion. Each trajectory is calculated using a unique set of data of hydrologic, oceanographic, and meteorologic conditions. For each location chosen (e.g., San Francisco Bay), historical wind records are examined to determine the wind field for as long a time-period as possible. Typically, at least 10 years of continuous wind records are available. In many locations, weather patterns vary substantially among seasons. To accommodate these variations, temporal parameters of the data are broken down by season, with wind and ocean patterns specific to each season. Data on historic tidal currents, river flows, and wind-driven current patterns are also computed by season to complete the geophysical dataset that defines the physical processes that move the oil.

Once the physical processes have been defined, the entire shoreline of the bay is divided into about 200 separate segments or "receptor sites." About 200 possible spill locations, or "source sites," are defined throughout the bay, covering all likely spill locations. Some 500 "start times" are randomly chosen from the time-period for which adequate meteorological records are available. For each of these start times, and for each source site, OSSM (NOAA's "On-Scene Spill Model") uses the geophysical dataset to compute a complete trajectory of the oil over a period of 5 days. As the simulated oil spill progresses, the amount of oil that passes through each receptor site is calculated. This is a massive computational task, taking about 2 weeks on 12 Macintosh 350-Mhz G3 computers.

The result of this computation is a large database of the amounts of oil from each source site that threaten each receptor site for each of 500 simulated spills. The TAP II interface is a graphical tool designed to display this data in various ways that are of interest to planners. The user interface provides four display modes, each of which summarizes the database in a different way.

III. Display Modes of TAP II

In all of the display modes the user defines the parameters of the potential spill under study.

Oil type: TAP II includes a simple oil evaporation model. The rate of evaporation depends upon the type of oil spilled.

Amount of oil released. (provided by user)

Season: The TAP II dataset is divided into seasons according to similarity of wind patterns. This could be two seasons (as in San Francisco), or up to four seasons. The user may be interested in a different season at different locations, because the environmental sensitivity of some locations may vary by season.

Time post-spill: The TAP II dataset includes data on how much oil reached each receptor site for ten different time-periods (up to 5 days) following the spill. The data for each time period is cumulative, i.e., the amount of oil that passes through each receptor site from the beginning of the spill until the selected end-point in time. By examining the data at different times following the spill, the user can determine how quickly the response must be mobilized.

Level of concern: Different shoreline types have different sensitivities to oil. The level of concern (LOC) depends on the amount of oil that would be expected to significantly impact a particular site. The LOC is the volume of oil that enters the receptor site. All the receptor sites throughout the bay are approximately the same size (~2 km of shoreline in San Francisco Bay), so that the same volume of oil would have a similar density at all sites.

A. Threat Zone Analysis

Threat Zone Analysis (Fig. 2) helps answer the question: Where might a spill occur that could threaten a shoreline location of concern? The user selects a receptor site of interest (perhaps a sensitive wetland), and is provided with a color contour map of the entire bay, indicating the likelihood of oil reaching the selected receptor site from any location in the bay. The map colors correspond to the percentage of modeled spills from each location in the bay from which the movement of oil to the selected receptor site is equal to or exceeds the LOC for that site. By repeating this analysis for a number of different receptor sites, the user can gain an understanding of the geophysical processes that move oil in the entire area.

B. Shoreline Impact Analysis

Shoreline Impact Analysis (Fig. 3) helps answer the question: If oil is spilled at a given spot, what shoreline locations are likely to be impacted? A spill source site in the bay is selected, and a color map is presented that indicates the likelihood that oil from a spill at that location will reach each of the shoreline receptor sites. The colors correspond to the percentage of modeled spills originating at the selected source site that exceed the LOC for all the receptor sites in the bay.

C. Site Oiling Analysis

Site Oiling Analysis (Fig. 4) provides a way to visualize how a particular receptor site is likely to be oiled by a spill originating at a particular location. The user selects a spill site and a receptor site and is presented with a graph showing the percentage of modeled spills that resulted in a given amount or more of oil reaching the site in the selected time-period.

D. Resource Analysis

Resource Analysis (Fig. 5) provides data on the quantity of a given resource impacted by the modeled spills, or the level of response required to adequately address the impacts of those spills. The user specifies a spill site and a resource of interest, and TAP II generates a graph that indicates the total costs of each of the modeled spills in terms of that resource. The values on this graph are the costs of oil impacting each site at greater than its LOC, summed over all the sites for which the LOC is exceeded.

The cost of a site could be the number of nesting birds at that location, or the length of boom required to protect the site, or virtually any resource of interest, in any appropriate units. The user provides data about each resource in a standard text-file format. These data include the quantity of each resource associated with each receptor site, and the LOC for that site and resource. The LOC is expressed as the amount of oil that must reach the site for the resource to be considered impacted. Because the resource data files are in a text-file format, they can be generated in a text editor, spreadsheet, or database software. Because the information required is spatial, the locations of the receptor sites are provided and can be entered into a GIS system to generate resource files from virtually any GIS dataset.

For examples of resource data files, NOAA provides files generated from our Environmental Sensitivity Index (ESI) maps (NOAA 1997). This data includes the quantity (meters) of each type of ESI shoreline found in each receptor site. For example (as shown in Fig. 5), using this data in the resource analysis mode allows the user to determine how many meters of saltmarsh shoreline are impacted by each

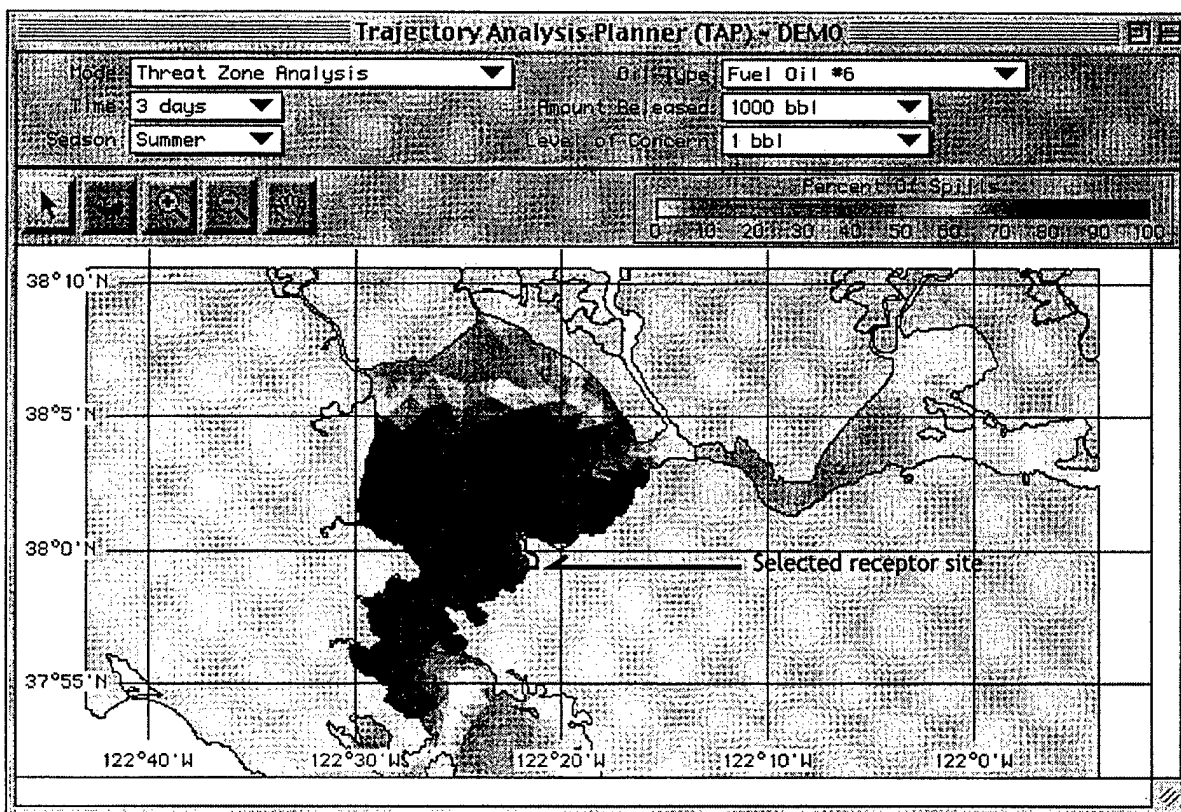


Fig. 2. Example of Threat Zone Analysis for part of San Francisco Bay. Colors indicate the percentage of modeled spills that reached the selected receptor site within 3 days.

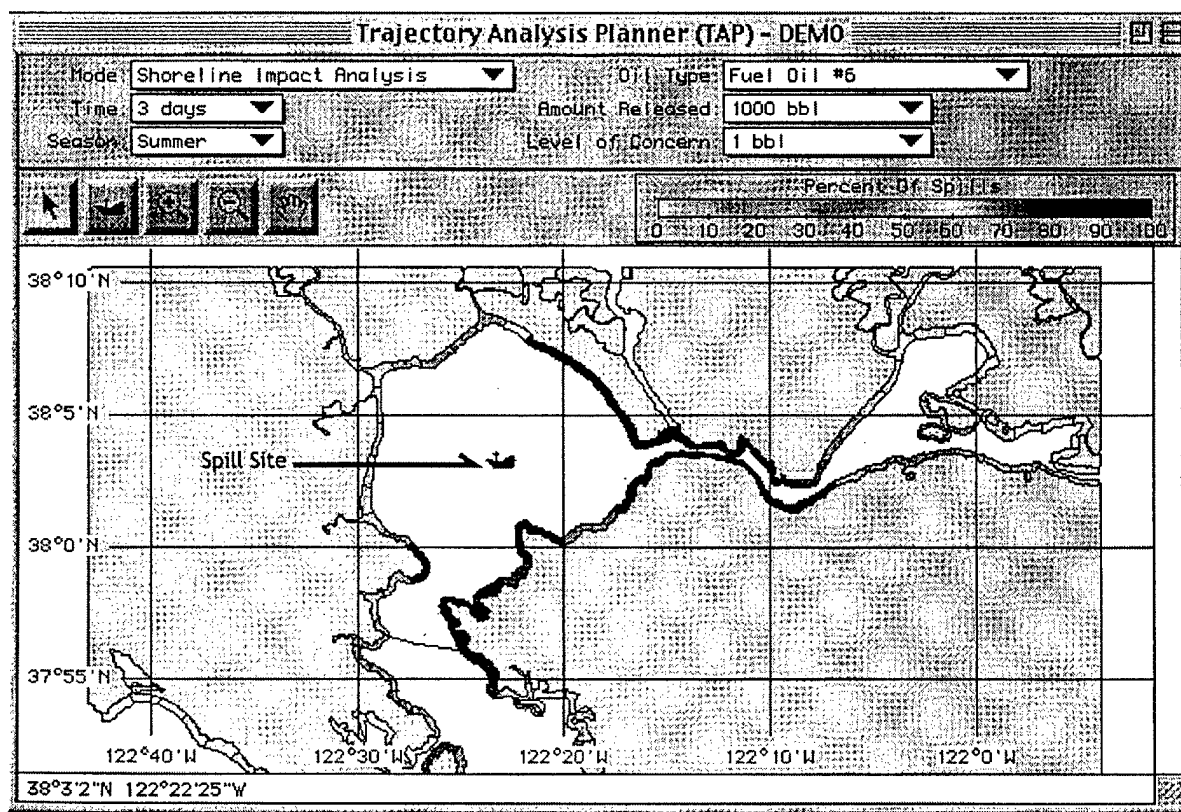


Fig. 3. Example of Shoreline Impact Analysis for part of San Francisco Bay. Colors indicate the percentage of modeled spills that exceeded the Level of Concern (LOC) at each receptor site within 3 days.

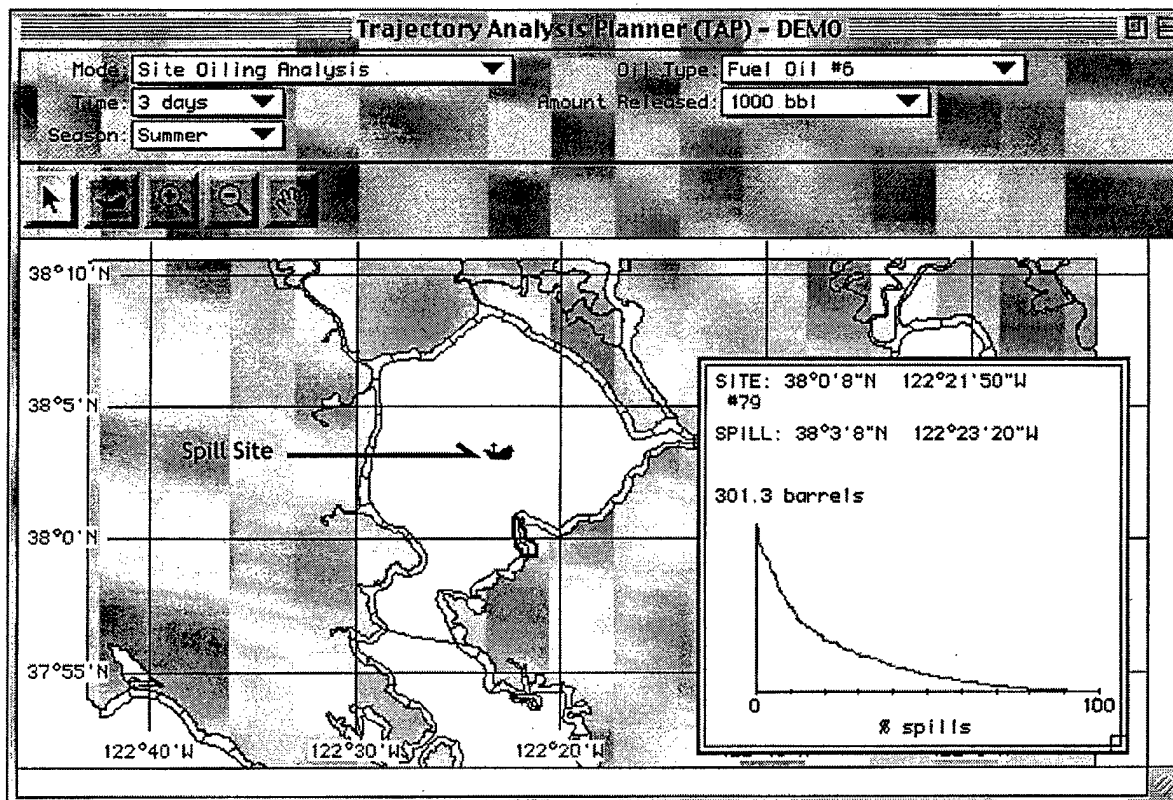


Fig. 4. Example of Site Oiling Analysis for part of San Francisco Bay. The graph plots the percentage of modeled spills in which a given amount or more of oil reached the selected receptor site within 3 days.

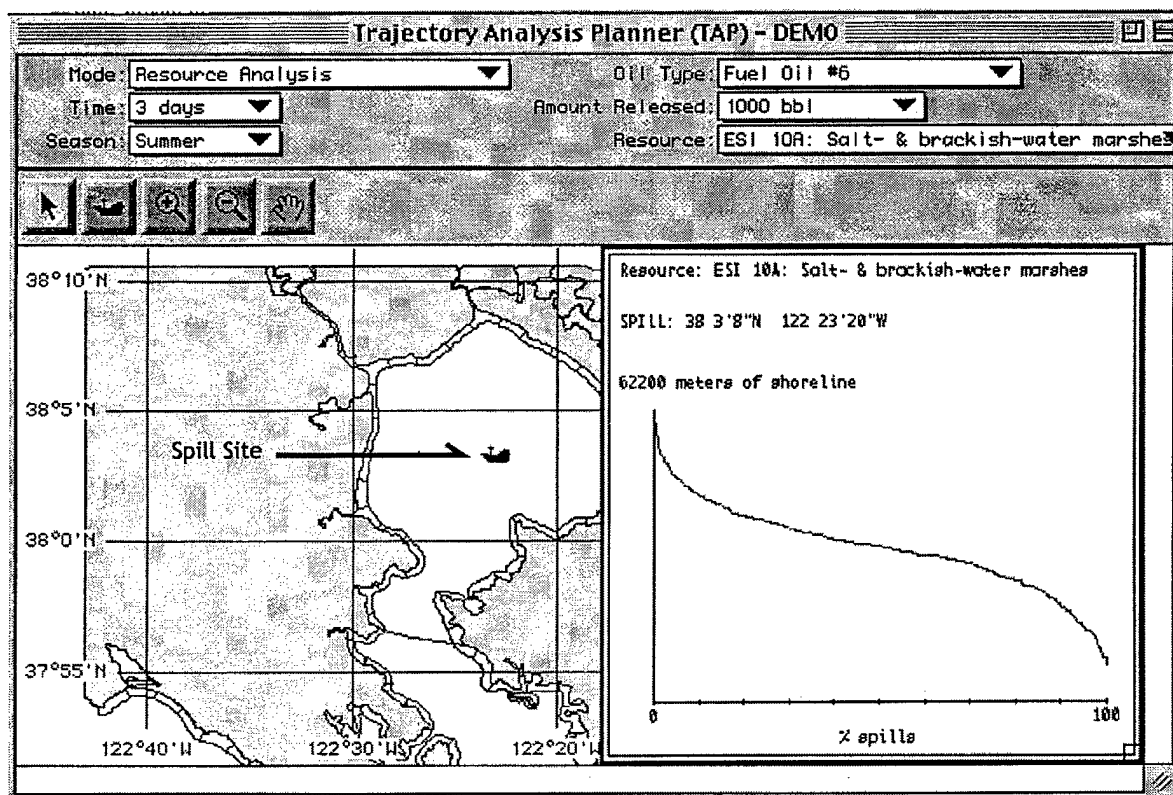


Fig. 5. Example of Resource Analysis for part of San Francisco Bay. Graph indicates total ESI type-10A shoreline (salt/brackish-water marsh) impacted by each of the modeled spills within 3 days. y-axis is meters of shoreline impacted x-axis is percentage of modeled spills in which a given length or more of shoreline has been impacted.

of the modeled spills. The y-axis is the length of shoreline impacted; the x-axis is the percentage of modeled spills for which a given amount or more of shoreline has been impacted. In this case, 0% of spills impacted more than 62,200 meters of shoreline, 50% of spills impacted about 33,000 or more meters, and 100% of spills impacted 6,000 meters or more. (Note: Fig. 5 is from an early prototype of the program. In the final product, the graph will be easier to read.)

Resource Analysis is a powerful tool for response shortfall analysis. Once a response plan for each sensitive location in a bay has been developed, the data from that plan can be entered into a resource data file, indicating, for example, the quantity of boom required to protect each sensitive site. Because it is unlikely that every location included in a plan would need protecting at the same time, Resource Analysis can be used to compute the total quantity of boom required to respond to any of the modeled spills in the database. The total costs can be computed for any of a number of different time frames, so that one could know that one quantity would be needed within 24 hours, and more within 3 days, allowing time for long-distance transport of the equipment to the site.

While, at first glance, Shoreline Impact Analysis and Resource Analysis appear to answer similar questions, they are fundamentally different. Although site A and site B may both be impacted by about 30% of the spills modeled, the two sites are probably not impacted by the same 30% of spills. In fact, it's possible that two given sites are never impacted simultaneously, such that protecting both of them simultaneously would never be required. The Resource Analysis mode computes the total cost of each spill individually, so that these two sites would not simultaneously contribute to the total cost.

IV. Conclusions

TAP II is a graphical tool designed to display localized oil-spill trajectory data in various ways that are of interest to emergency response planners. The dataset is generated using historical wind patterns and both tidal and non-tidal circulation patterns. NOAA's OSSM model uses this information for the next step, generating a series of thousands of individual trajectory analyses, each representing a different potential oil spill scenario. The results are sorted and compressed into a database that TAP II uses to generate its graphic displays. The user interface provides four display modes, each of which summarizes the database in a different way.

TAP II is now under development for the San Francisco Bay and San Diego Bay. Negotiations are underway for additional TAP II implementations. TAP II runs on Macintosh or Microsoft Windows operating systems. For more information, visit our Web site at <http://response.restoration.noaa.gov>, or e-mail tap@hazmat.noaa.gov

V. Acknowledgments

The author wishes to acknowledge the editorial assistance of Nancy Peacock and the graphics assistance of Kristina Worthington.

VI. References

- Barker, C.H., & J.A. Galt. 1999. Analysis of methods used in spill response planning: Trajectory Analysis Planner TAP II. *In* Proceedings of the 1999 International Marine Environmental Modeling Seminar, Lillehammer, Norway. SINTEF Applied Chemistry, Trondheim, Norway.
- Galt, J.A., & D.L. Payton. 1999. Development of quantitative methods for spill response planning: A Trajectory Analysis Planner. *Spill Sci. Technol. Bull.* 5(1).
- Lehr, W., C. Barker, & D. Simecek-Beatty. 1999. New developments in the use of uncertainty in oil spill forecasts, p. 271-284. *In* Proceedings of the Twenty-Second Arctic and Marine Oil Spill Program Technical Seminar, Calgary, Alberta, Canada. Ottawa: Environment Canada.
- Morris, C. (editor). 1992. Academic Press dictionary of science and technology. London: Academic Press.
- NOAA. 1997. Environmental Sensitivity Index Guidelines Version 2.0. NOS ORCA Tech. Memo. 115. Seattle WA: Hazardous Materials Response Division, National Ocean Service, NOAA. Available online at <http://response.restoration.noaa.gov/esi/esiintro.html>

GNOME: NOAA's NEXT-GENERATION SPILL TRAJECTORY MODEL

C. J. Beegle-Krause
Hazardous Materials Response Division
Office of Response & Restoration N/ORR1
National Ocean Service, NOAA
7600 Sand Point Way NE
Seattle, Washington 98115-0070

Abstract

The General NOAA Oil Modeling Environment (GNOME) is a new tool developed by the National Oceanic and Atmospheric Administration (NOAA) for oil-spill response. GNOME generates spill scenarios that support the NOAA standard for trajectory output by providing both "Best Guess" and "Minimum Regret" solutions. GNOME also serves as a tool for novice users, from high school on up, to learn more about oil-spill trajectories and actually run them. The GNOME model, regional location files, documentation, and training materials are available on the internet at <http://response.restoration.noaa.gov/software/gnome/gnome.html>. Training courses are also offered by NOAA HAZMAT. Research is underway on how to effectively use nowcast/forecast models as sources of ocean current fields for the trajectory model. Questions of data size, time-step interpolation, and relevant physics are being investigated to use these models as data fields in GNOME.

I. Introduction

Under the Oil Pollution Act of 1990, the National Oceanic and Atmospheric Administration (NOAA) is mandated to provide scientific support to the U.S. Coast Guard during marine oil spill response. Spill trajectory predictions for use during spill response are one of many kinds of scientific support provided by the Hazardous Materials Response Division (HAZMAT) of the Office of Response and Restoration. These spill trajectories have been generated by the latest version of the On-Scene Spill Model (OSSM) designed and initially implemented by HAZMAT over 20 years ago. A new trajectory model currently under development to replace OSSM is the General NOAA Oil Modeling Environment (GNOME). Both OSSM and GNOME support the NOAA standard for trajectory output by providing both the "Best Guess" and the "Minimum Regret" solutions. The "Best Guess" solution is the trajectory created assuming that all model inputs are correct. The "Minimum Regret" solution is a statistical compilation of trajectories that samples possible forecast errors used to generate an uncertainty boundary that allows planners to examine spill

trajectories that, although less likely, may pose greater risks environmentally or economically.

GNOME is designed to be a multi-purpose trajectory model used by both experts and the public through three different modes: Standard, GIS Output, and Diagnostic. The GNOME model runs trajectories on screen and allows the user to output trajectory images in print, GIS-compatible, and animation formats. The GNOME model, regional location files, documentation, and training materials are available via download from the internet at <http://response.restoration.noaa.gov/software/gnome/gnome.html>. Documentation includes "A Guided Tour of GNOME" and a User's Guide and Example Problems for each Location File. The model is available for Macintosh, Windows NT, and Windows 95 or above. Two types of GNOME training are available through NOAA: GNOME's Standard and GIS Output Modes are covered in a 2-day course; trajectory modeling and GNOME's Diagnostic Mode are covered in a 4-day course. See the HAZMAT website for more information.

This paper will acquaint the reader with the GNOME project design, with the location files, the trajectory model, model uses, and current research and development.

II. Overall GNOME Design

A. Model Modes and Location Files

GNOME is designed to run spill trajectories in three different model modes: Standard, GIS Output, and Diagnostic. The Standard and GIS Output modes use Location Files that incorporate regional hydrographic information coupled with a mini-expert system containing the map, ocean currents, and model parameters, including extensive error checking and help topics. The mini-expert system guides the user in finding and entering relevant oceanographic information, generating spill(s), and running the trajectory model. This system then sets up the trajectory model by converting the user's input into model parameters.

The diagram in Fig. 1 illustrates the flow of information from the user through GNOME. In Standard and

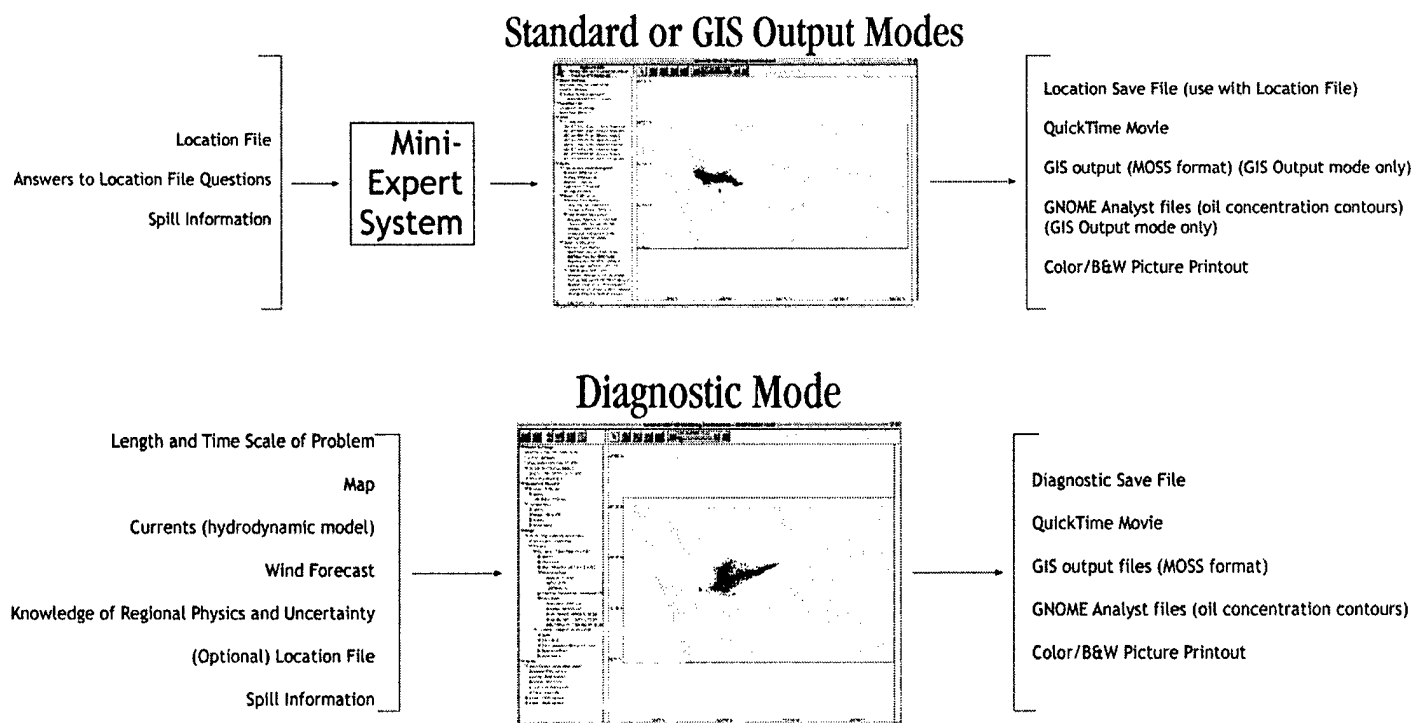


Fig. 1. Diagram of information flow from the user through GNOME and the output options available. In *Standard and GIS-Output modes*, a Location File assists the user in setting up the model and a mini-expert system converts the input into model parameters and setup. In *Diagnostic Mode*, the user is responsible for all model data fields and parameters, and thus the user is expected to have sufficient oceanographic and spill modeling knowledge to create and use the model appropriately.

GIS-Output modes, the user answers questions presented by the Location File. In Diagnostic Mode, the user supplies all the data fields required by the model; thus the user should have a working knowledge of oceanographic processes.

Five Location Files are currently available: central Long Island Sound, Columbia River Estuary, Prince William Sound, Santa Barbara Channel, and Tampa Bay. Initially, NOAA is creating Location Files according to a Coast Guard priority list of 32 Marine Safety Offices. Other Location Files planned for this year include New York City, Boston, Philadelphia, San Diego Bay, and the Strait of Juan de Fuca.

Diagnostic Mode allows the user access to all the model controls. Diagnostic users can create their own regional models by adding their own map, adding and scaling their own currents, and setting model parameters, such as the model time-step. This mode is used in spill response and advanced training in spill modeling.

B. GNOME Trajectory Model

GNOME is a mixed Eulerian/ Lagrangian trajectory model that uses Lagrangian Elements (LEs) or particles to represent spills of oil or other pollutants within Eulerian currents and wind. The model is designed to be

very user-friendly so as to reduce user errors during late-night emergency spill response. Fig. 2 shows the model map window containing the model controls along the toolbar and the model settings and data fields down the left-hand side. The map area presents the visualization of the spill calculation.

Spills also have product information associated with them that is incorporated in a simple weathering model. GNOME simulates six product types: gasoline, diesel, fuel oil #4, medium crude, fuel oil #6, and a non-weathering tracer. Although product weathering is modeled within GNOME, NOAA also offers a separate weathering model, ADIOS™ (Automated Data Inquiry for Oil Spills), for more accurate weathering predictions. An example of the weathering mass balance is shown in Fig. 2 in the lower left-hand corner under the SPILLS heading.

Hazmat current patterns are created by NOAA's CATS (Current Analysis for Trajectory Simulation) application, in which the user selects from three different hydrodynamic models that simulate different combinations of physical processes. Tides are added either with a time-series of tidal currents or tidal coefficients at a reference point. A map is used to create the shoreline to determine product beaching.

GNOME is written using the latest object-oriented methodologies in C++ programming. In this way, maps, pollutants, and movers (e.g., diffusion, winds, currents) are

Diagnostic Mode

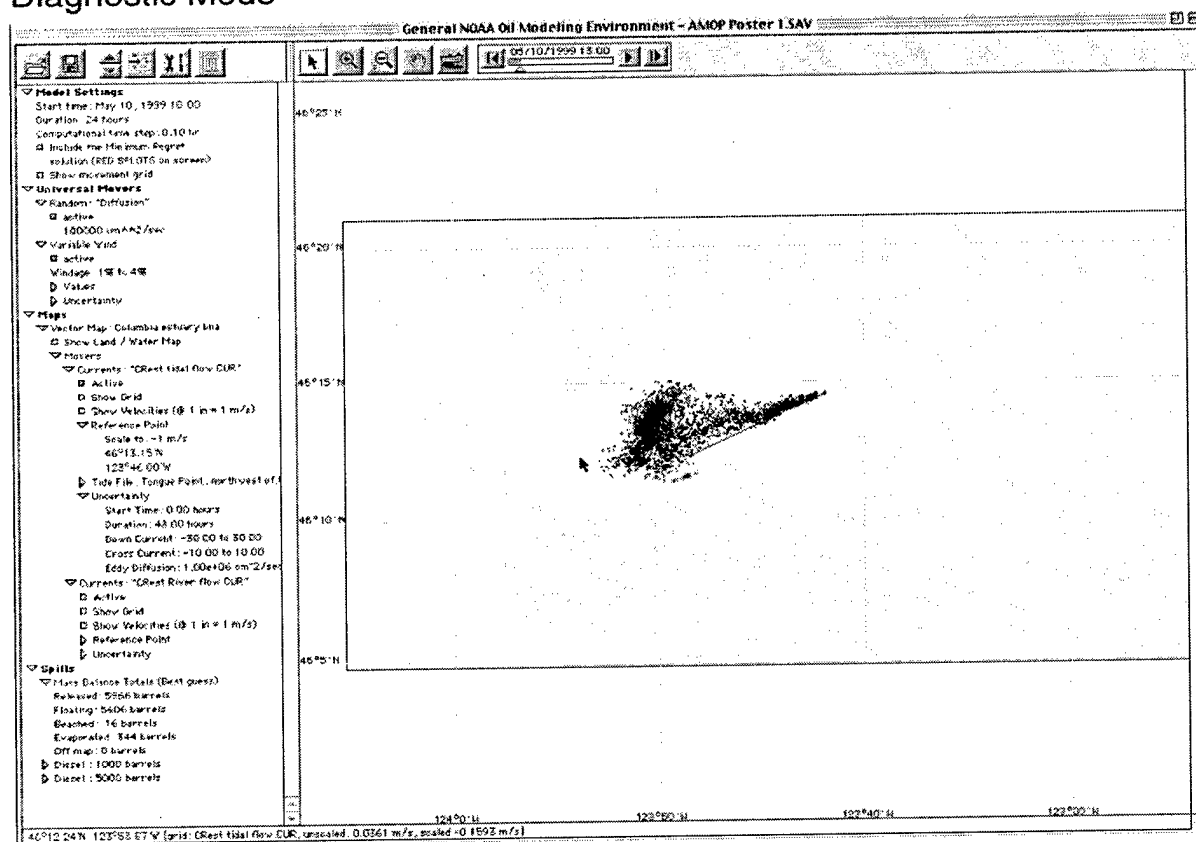


Fig. 2. Screen shot from the GNOME model showing a diesel spill in the Columbia River Estuary. The "Best Guess" solution is indicated by black dots, and the "Minimum Regret" solution by red dots.

all self-contained objects, responsible for their own details such as memory management, data storage, etc. The model simply calls upon (or asks) a list of "mover" objects to move the pollutant, based on their individual hydrodynamic characteristics. New objects can easily be added to the model, such as an additional map type (e.g., a bit map instead of the normal vector format). A new map must answer the same basic questions as the vector-format maps, such as whether a given LE is on land or in the water. A new type of current mover must answer a displacement (or movement) of an LE. Most importantly, new maps, pollutants, and movers can be added to the model without affecting any of the existing objects. This will allow GNOME to interface with third-party models and tools with relatively little effort and modification.

III. Model Uses

GNOME is designed for use by responders during actual spills and to educate others about oil spill trajectories. However, we recommend that only experts in spill-trajectory modeling use GNOME for oil spill response.

For spill-response planning, we recommend using the Trajectory Analysis Planner (TAP), a statistical tool that graphically presents the results of hundreds of oil-spill trajectory simulations in a specified area, enabling emergency planners to understand and anticipate many possible outcomes when developing local-area contingency plans.

A. Spill Response

GNOME is a flexible spill-response model when used in Diagnostic Mode. The model allows the user to quickly load input-data files, set parameters, and run a spill trajectory. GNOME's interface enables the user to examine and alter the model setup, and then rerun the spill. The user can view the results of each time-step on the screen, stop the model at any time during the integration, and scan back through each hour of the current trajectory from the Map Window. The model also incorporates both the "Best Guess" (Forecast) and "Minimum Regret" (Uncertainty) trajectories, so that the "Best Guess" trajectory can be run separately, or both trajectories can be run simultaneously. Uncertainty parameters for movers can be set individually.

B. Creating Scenarios

Spill scenarios can be generated, tested, and revised using either a regional model setup in Diagnostic Mode or a NOAA Location File in any mode. The variety of output options—saved files of the model setup for later use, picture printout, movie animation, and GIS-compatible output—allows the user to customize products for reports or table-top exercises. The TAT application (soon to be renamed GNOME Analyst) utilizes Thessian analysis to convert GNOME output into oil-concentration contours and uncertainty bounds.

Fig. 3 illustrates a second type of GNOME output for the Columbia River Estuary, in which the LE distributions have been converted to concentration contours and an uncertainty bound by the TAT application using Thessian analysis. In contrast, Fig. 2 uses spots to indicate LE distributions and the “Best Guess” and “Minimum Regret” solutions.

C. Intuition Building

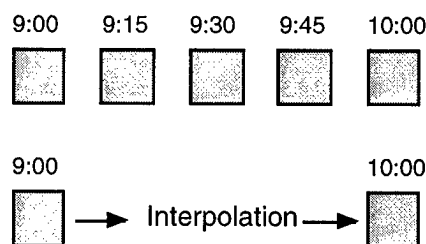
GNOME's design allows the user to isolate particular dynamic forcings in the Diagnostic Mode. By examining how different forcings affect spill trajectories, the user can develop greater intuition regarding trajectory forecasts under a variety of conditions. Standard Mode allows the user to run the same spill under different climate conditions. For example, the user can change the winds or the spill timing to alter the tidal phase. Diagnostic Mode also offers a number of tools for visualizing the dynamics of different model physics. An example is the movement grid, which shows where an LE would move in one time-step, sampled evenly over the model domain. The user can also turn the different movers (e.g., diffusion, wind, or individual current patterns) on and off to gain an understanding of how individual physical forcings move the spill.

IV. Current Research and Development

Development of new LE “movers” continues to expand the range of physics that GNOME can simulate. We are just completing testing of a mover that improves the tie between variable wind and the water-current pattern used. Expanding from 2- to 3- and 4-dimensional modeling is a high priority for development. Besides adding our own vertical parameterization, we also plan to allow users to import current fields from finite-difference circulation models. Eventually we want to be able to use the data fields from external nowcast/forecast models in GNOME to compare with our own hydrographic model results to see how these external models can be used in spill response.

Research has just begun to develop tools for using time-dependent 3-dimensional models in GNOME. We want to be able to run GNOME without having to import data for every time-step of a circulation model. Thus, we

need to define the trajectory error caused by interpolating individual time-steps between data files that are output at intervals longer than one time-step.



These types of criteria—such as the longest allowable time between model output files for a given trajectory error—will vary according to the numerical model, the region where the model is implemented, and the conditions simulated. As part of this research, comparison runs are being done between GNOME and the Southern Puget Sound Model (SPASM) of the Washington State Department of Ecology.

Some models include representations of stochastic phenomena that give the simulation a more realistic look, but are inappropriate for spill-response trajectory modeling. For example, eddy-resolving models can create realistic eddy fields that evolve both spatially and temporally within the model. Although these phenomena exist within the ocean, a trajectory prediction with an eddy field that does not represent real conditions would be more inaccurate than a prediction using the mean field with an uncertainty estimate. For this reason, NOAA HAZMAT has adopted a standard for trajectory information that includes a “Best Guess” scenario based on deterministic physics with a “Minimum Regret” error bound created by statistical trajectories that take into account stochastic physics and errors in data fields and forecasts.

To utilize offsite nowcast/forecast models for spill response trajectories, an estimate of their uncertainty and its temporal development through the forecasted time period is required. NOAA/HAZMAT is just beginning research on how to best use these external models to improve our response trajectory modeling.

V. Summary

GNOME is a spill trajectory model designed for a variety of users ranging from spill responders to individuals who want to model spill scenarios and build their spill modeling intuition. The model, regional location files and documentation are available currently from <http://response.restoration.noaa.gov/software/gnome/gnome.html>. As model development continues, we plan to implement tools to allow external nowcast/forecast circulation models to be used to supply the water current fields. We are currently beginning research into how to effectively use these models within GNOME.

VI. Acknowledgments

The author wishes to thank the entire GNOME team at NOAA/HAZMAT for their efforts and dedication, and Nancy Peacock and Kristina Worthington for editorial and layout assistance.

PROJECT OCEANOGRAPHY: BRINGING OCEANOGRAPHY FROM THE OCEAN, THE LABORATORY, AND SPACE TO STUDENTS IN THE MIDDLE SCHOOL CLASSROOM

P.G. Coble and J.A. Rasure
University of South Florida, Department of Marine science
St. Petersburg, FL

What is *Project Oceanography*? It is a Marine Science educational outreach program designed for active participation of middle school students. Kids are being turned onto science by researchers at the University of South Florida (USF) Department of Marine Sciences through this hands-on learning experience. Technology provides researchers the ability to share equipment and real-world science problems and solutions that students can not otherwise experience in their classrooms. *Project Oceanography* expects to continue to grow and expand through a new initiative to build an interactive teaching center with laboratory and studio facilities.

MISSION STATEMENT

The mission of *Project Oceanography* is to broadcast affordable, age-appropriate educational programming to middle school students, incorporating current topics in marine science to teach basic concepts and promote active learning, thereby enhancing the traditional classroom experience.

WHY IS IT IMPORTANT?

Educators have found that exposing students to research science and allowing them to participate alongside the scientist is the premier way to excite students about science. *Project Oceanography* is unique in that it brings actual scientists *into* the classroom. The Consortium for Oceanographic Research and Education (1996) cites ocean science as providing an ideal framework for teaching the disciplines of geology, physics, biology, chemistry, english, and mathematics. Using technology and innovative thinking, the program successfully accomplishes its goal: to bring marine science research and its technologies into the middle school classroom.

WHO WATCHES PROJECT OCEANOGRAPHY?

As of June 1999, *Project Oceanography* had satellite downlinks in 27 states, with over 247 registered participants. More than 65 of these participants are instructional television stations, which rebroadcast *Project Oceanography* via cable TV stations or directly into schools. The estimated viewing community consists

of over 1.8 million students in public, private, and in-home schools. The programming is a successful teaching tool for all types of students, including magnet, at-risk, handicapped, and those with specific learning disabilities. Participation by members of the live studio audience helps maintain the attention of classroom students.

WHAT IS TAUGHT?

World-class oceanography is used to enhance understanding of basic science concepts. Broadcast during the school year, the 28 weekly programs cover 3-5 topics, organized into learning modules of 3-6 programs per module. Each module is designed by a staff writer under the direction of the lead scientist. In the 1998-99 season, a module on the Marine Reserve at Weedon Island, FL, taught students about coastal habitats, salinity, and effects of pollution on the marine environment. Experts used live plants, screech owls, red-tailed hawks, snakes, and a mini wetland re-created

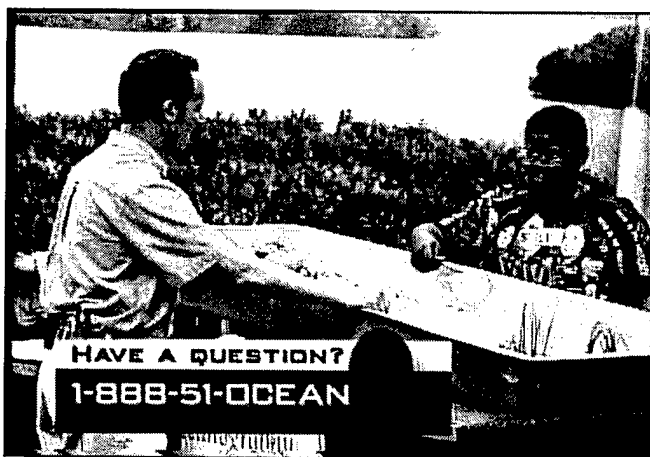


Figure 1. Presenter Howard Rutherford and student volunteer build a model coastal wetland during the Weedon Island module.

in a 4 x 12 tub! Another module, Fish Ecology, centers on fish adaptation to ecological niche, but also includes lessons on ocean geography, water zonation, light, diffusion and osmosis. The students can receive real 'mystery fish' in the mail – making it possible for them to work 'alongside' the TV presenter in their remote classrooms.

Materials and programs are distributed at no charge to registered participants. A highly detailed packet of materials is mailed to each registered site prior to the start of a new broadcast module. The materials include background information that the teacher may use for teaching, hands-on activities, a series of fun facts and trivia, vocabulary words and references for further study.

"Boy, what a great show. My kids have never been so attentive....(*Project Oceanography*) is turning out to be the highlight of our year." -J. Chittenden, 8th Grade Science Teacher

HOW WE DO IT

The distance learning classroom is located at the University of South Florida, in St. Petersburg, FL. The scientist and student audience in the television studio are linked real-time with students at distant locations via television, telephone and computer links. The modern studio includes slide-to-video-projector, fiber optic transmitters and receivers, tape playback, studio cameras, ELMO, chromakey (superposition of the instructor into the picture), PictureTel (two-way video), and a Trinity Graphics System. The Trinity System is used to generate and enhance graphics, edit video, and provide stills from video. Two-way audio connectivity (via telephone or PictureTel) makes interaction between studio and remote sites possible.

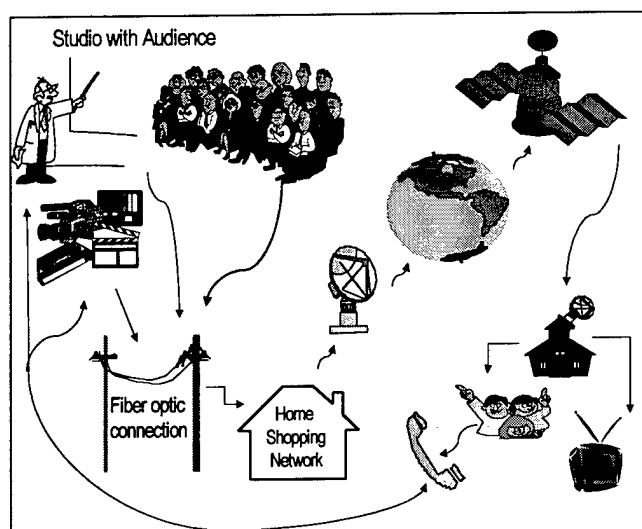


Figure 2. Simplified schematic of how technology connects the *Project Oceanography* studio to the students in their classrooms nationwide.

Technology allows students to view and experience hands-on research equipment like video-enhanced microscopes, satellite mock-ups, and a real Year of the Ocean drifter buoy. In the upcoming year, satellite transmissions will link scientists at work in the Antarctic to the distance learning classrooms via video and the internet.

Live broadcasts are distributed in Florida, Idaho, Vermont, Wisconsin, and North Carolina. Some sites have schedule conflicts, or time zone offsets, and have delayed broadcast. Sites without satellite downlink equipment can request videotapes, either for broadcast or for classroom use. Some elementary and high school teachers have requested tapes and materials which they adapt to appropriate grade levels for their classrooms.

STUDENT INVOLVEMENT

Presenters are encouraged to present their research materials in a way such that the students can actively participate as volunteers. In the past, student volunteers have completed chemistry experiments, held live animals such as lizards, snakes and fish, dressed in fire garb, and interviewed with people involved in marine-related careers. Other students are positively boosted to ask questions of the presenter about the equipment or experiment they are displaying, the materials that they are talking about, or just if they need to gain better comprehension of the topic.

Students, local and nationwide, are able to call in questions during the show using the toll-free number, or send questions via mail or email. The instructor's answers are part of the total learning experience, giving the students access to the science professional.

"*Project Oceanography* is a good idea because we actually get to see what is going on instead of just reading it out of the textbook. I like to 'see' the science. The only downside to this project is that it only lasts for half an hour." -Moya Burgess -8th Grade from Seminole Middle, FL

FUNDING AND PARTNERSHIPS

Project Oceanography is a collaborative effort of the University of South Florida (USF) Department of Marine Science, the National Ocean Partnership Program (NOPP), the Pinellas County School system, the National Geographic Society, the U.S. Geological Survey (U.S.G.S) and the Florida Department of Environmental Protection. Support for the program comes from USF, the National Ocean Partnership Program and the State of Florida.

PROGRESSING INTO THE FUTURE

Project Oceanography has grown faster and larger than was initially dreamed. Our goal of making the programming available to all students, regardless of ability to pay, requires that we search for corporate sponsors, or other philanthropic dollars, to continue this project. Teachers also may need support to purchase the technology needed to receive the signal real-time, or for telephones in their classroom. Additional training for teachers during summers would help them better utilize

the materials, at the same time giving them a chance to share their valuable classroom observations and experience with us to improve the program.

Technological advances are also going to make Project Oceanography much more accessible for teachers and students around the country. Use of MPEG encoders would enable us to transmit our audio and video signal to schools equipped with an MPEG decoder or via the internet. The MPEG system is still beyond the financial means of most schools, but will see expanded usage in the future.

Future plans for Project Oceanography include live broadcasts from a remote location, including simultaneous web casts and chat rooms, increased involvement of students in laboratory settings, and involvement of scientists in other locations as program hosts.

Lastly, we hope to eventually have a home of our own. With our partners at USGS, DEP, the Florida Institute of Oceanography, the Pier Aquarium and the City of St. Petersburg, we are proposing a collaborative initiative, Port Discovery, which would create a marine education and research facility on Bayboro Harbor adjacent to USF's Department of Marine Science. Students and teachers would have access to state-of-the-art teaching laboratories, a computer lab with real-time oceanographic data, and a research vessel. All these facilities would be linked with the television studio for live broadcasts of oceanographic research missions.

REFERENCES:

Report from Education Workshop on Ocean Sciences and K-12 Education, June 20-21, 1996, Consortium for Oceanographic Research and Education (CORE), Washington, D.C., 15, 1996.

Tebbens, S.F., Coble, P.G., and Greely, T. Innovative Programs for 6th-8th Graders Gain Momentum. *Eos Trans.*, AGU 79, 11, 1998.

World Wide Website: www.marine.edu/pjocean

EDUCATION FOR A MARINE TECHNICAL WORKFORCE: THE MARINE ADVANCED TECHNOLOGY EDUCATION CENTER

Nicole L. Crane and Deidre E. Sullivan

Monterey Peninsula College
Monterey, California

Abstract

This paper highlights the major efforts and achievements of the Marine Advanced Technology Education (MATE) Center since its founding in September 1997. The MATE Center was developed through a multi-year grant (DUE-ATE #9752028) from the national Science Foundation's Advanced Technological Education program

A major goal of the MATE Center is to work closely with industry and educational organizations to build strong collaborations that will improve marine technology education. The MATE Center has designed and implemented methods to gather information from stakeholders in the marine community. The process has led to collaborations, partnerships, internship opportunities, industry guidelines for technical jobs in 5 occupational clusters, and the development of a model degree and certificate program in marine technology at Monterey Peninsula College. Five partner high schools have strengthened relationships with local community colleges, and begun development of a curricular framework for pathways from high school to college. Industry/government and university partnerships have been initiated to steer program development regionally.

The MATE Center has taken effective steps to create and distribute information and outreach materials for increasing the Center's impact on major stakeholders in marine science and technology. These include: brochures and informational materials, a web site, quarterly and bi-weekly newsletters, visits to high schools, seminars, and displays at national meetings.

I. INTRODUCTION

The Marine Advanced Technology Education Center is one of 11 Centers funded by the National Science Foundation's Advanced Technological Education (ATE) program. ATE Centers serve to develop and support educational programs in today's key industries with a focus on preparing technicians for the rapidly changing, technologically advanced work environments. This is considered essential for the nation to remain internationally competitive in these fields. The MATE Center's focus is on the fields of marine technology and the education of technicians to work in those fields. These fields and related occupational clusters include ocean resource extraction, aquaculture, ocean exploration and research, ship operations, remote operated vehicle technology, marine related communications technology, marine transportation, coastal engineering, and marine habitat protection and monitoring. The Center's goals include development of programs at the community college level, with strong connections to high school and university programs, and establishing collaborations between educational institutions and industry, military, government, and labor organizations.

The MATE Center is located at Monterey Peninsula College (MPC) in Monterey, California, where a new Marine Science and Technology Associates Degree and Certificate program will begin in Fall of 1999. Although located at MPC, the Center has numerous educational partners throughout the country. These partners are also interacting with industry to collect data regarding employer needs, core skills needed, and job trends. This information is being used to develop new or modify existing marine technology programs. These efforts are leading to improved

marine technology education at the technical level across the United States.

Despite the wealth of new information produced by recent advances in technology, the seas remain the major unexplored region of our globe. Recent attention on a national level to our oceans has provided an important spotlight on the role the oceans play in research, climate, the economy, resource procurement, ecosystem sustainability, pollution abatement, and culture. All of these roles, and others not listed, offer new opportunities for meaningful careers. However, appropriate preparation and education are essential for achieving these career goals. The MATE Center is an important catalyst for this effort. Center goals are not only to create communication links between existing marine education programs and to develop new programs in collaboration with industry, but to make available knowledge of career and educational opportunities to people and workers seeking professional development or career changes.

II. INTERACTIONS WITH EMPLOYERS

A key element of effective curriculum design is knowing the needs of the employers who hire program graduates. In many cases, students emerging from today's education system fall short of employer expectation in several areas, including technical knowledge. An efficient way to address this shortfall in student preparation is to ask employers and currently employed workers what is needed to be successful in their jobs and advance in their profession. With this information, educators can align curricula to real-world needs, and ensure the future success of students in the technologically rich world of work.

The MATE Center has been successful in designing and implementing methods to obtain information and generate support from the marine industry and research community. These include: telephone interviews, written surveys, workshops with employers and technicians, internet searches, partnerships with the Department of Labor and other government agencies, partnerships with professional organizations, and industry site visits.

Establishing industry/research based guidelines for curriculum development

The MATE Center has developed industry guidelines for five marine occupational clusters: Ship-board Marine Technicians, Marine Surveyors, Aquaculture Technicians, Oil Spill Response Technicians and Remote Operated Vehicle Technicians. The guidelines are developed through the use of surveys and workshops, and are designed to help educators understand what types of jobs and job clusters are in highest demand, and how to align curricula with current workforce needs.

Surveys have provided information on workforce trends, job descriptions, skills needed and skills lacking in the workforce, employer interest in hosting interns, and employer interest in supporting educational program development. Survey information is valuable in helping to target specific occupational clusters for further analysis. The MATE Center has taken the next step in developing specific guidelines for occupations by holding directed workshops where technicians and supervisors *currently working in the field* are brought together to discuss and outline the skills, knowledge and abilities needed to be successful at their jobs.

Eight to twelve technicians, selected from appropriate industry/research locations, are invited to participate in the process of establishing guidelines. Participants are sent a survey ahead of time asking them to describe their jobs, and list the skills needed to perform well. These preliminary surveys help to establish the baseline from which the workshop will expand. At the workshop, participants define the job or jobs (job description), the personal qualities needed for the job, instruments/equipment commonly used (current and projected future types), job functions, job tasks, and the knowledge, skills, and abilities needed. They are asked to address the need for both technical skills and basic skills including academic foundations, critical thinking skills, teamwork skills, and interpersonal skills.

This process produces a table outlining the job, and what is needed to do it well. The information is then sent to a wider audience within the field to validate the information collected at the workshop. This validation process allows for critical input and 'fine tuning' of the guidelines from a larger group of stakeholders. The information is then used to develop a core curriculum, and specialty activities, labs, and/or internship experiences. These give students the tool box needed to succeed when looking for jobs.

Faculty and curriculum developers at the MATE Center and partner institutions have found significant overlap in core knowledge, skills and abilities identified from the industry guidelines developed for Ship-board Marine Technicians, Marine Hydrographic Survey Technicians, and Remote Operated Vehicle Technicians. This has provided the foundation for program development emphasizing core skills, with specialty areas of knowledge attainable through specialty courses, activities and/or internships. Identifying the overlap in core skills allows the educational program developers to emphasize broadly transferable skill sets that will prepare students for a variety of related jobs, thus making them more marketable.

Internships give students real-world experience in addition to providing the exposure and training in specialty technical areas. The MATE Center has launched two technical internship programs to respond to this: one is a Monterey regional program in which students are matched with employers for a temporary job experience that emphasizes technical skills; and the other is a national program in partnership with the University National Oceanographic Laboratory System (UNOLS) and the Ocean Drilling Program. In the latter, students are placed for varying lengths of time in paid internships on a research vessel or marine lab. In each, a relationship is established with the host agency, and a supervisor (mentor) is assigned to the intern. An agreement outlining the expectations and scope of the internship is signed by the student and the supervisor.

III. INTERACTIONS WITH EDUCATIONAL ORGANIZATIONS

The development of a Monterey regional program using the process described above has led to collaborations and partnerships between academic institutions. The MATE Center, through Monterey Peninsula College, is a member of a regional consortium of institutions of higher education: the Monterey Bay Crescent Ocean Research Consortium (MBCORC). This consortium allows for the development of collaborative projects, sharing of faculty and students, leveraging of funds, and broadened access to facilities and resources.

Courses for a regional MATE program were developed in partnership with the California State University Monterey Bay's Earth System Science and Policy program. This allows students to exit after a two

year program at the community college, or transfer to the CSUMB program with minimal credit loss. Five regional high schools have participated in curriculum development with the MATE Center. This has improved communication between the high schools and the community colleges, and will help prepare high school students for college programs, particularly in marine science and technology. Critical components of the courses and activities developed are the incorporation of employer guidelines, and an emphasis on basic skills and knowledge.

The MATE Center is committed to involving employers in the educational process to enhance student learning and workforce preparation. A series of curriculum and faculty development workshops for educators and industry partners is being planned to develop a process for incorporating industry guidelines into curricula.

MATE Center partner institutions are implementing many of the processes outlined above, and are key to the success of the Center. Specific projects being conducted by MATE academic partner institutions follows:

- **Cabrillo College** (Aptos, CA) has developed four modular curricula in support of beach monitoring and at sea opportunities for students.
- **Cape Fear Community College** (Wilmington, NC) has developed a new Marine Propulsion program in which 11 students participated, submitted a report for the submersible program, developed a marine electronics course outline, developed an assessment plan for the Marine Technology program, and offered career development opportunities for teachers and students.
- **Clatsop Community College** (Astoria, OR) is planning an institute in coastal/watershed technology related fields for students and educators, to be held in the summer of 1999; announcement cards have been printed, course list has been developed and a list of institutions providing faculty has been published.
- **Harbor Branch Oceanographic Institution** (Fort Pierce, FL) is working on an internship manual for MATE and has developed four career scenarios for users to learn more about career opportunities in the marine environment and to provide problem sets for the classroom.

- **Nunez Community College** (Chalmette, LA) has focused on gathering information on the local marine related industries, disseminating MATE information and recruiting students (on Dec 3, 1998, 22 students from Slidell High School attended an interactive session on marine technology focusing on water quality activities).
- **Hartnell Community College** (Salinas, CA) has participated in the development of a regional workshop for local employers and developed a new course called "Careers in Marine Technology". Additionally, Hartnell has updated its coastal Geology Course and has developed a preliminary outline for an Industrial Technician Program, which will have a thirteen unit core, then branch into a variety of technical areas, including Marine Technology.
- **Southern Maine Technical College** (South Portland, ME) has participated in an Aquaculture DACUM (defined as 'Developing A CUrriculuM) is collecting information on existing Aquaculture education programs and has identified a student internship opportunity.
- **Prince William Sound Community College** (Valdez Alaska) PWSCC's major project is the development of an on-line web based course in oil Spill prevention and response. Vince Kelly of PWSCC also worked with Alyeska pipeline Service Company to develop scholarships to help fund Alaska Natives' tuition in the Spill Response and Safety Management degree program.

IV. INFORMATION AND OUTREACH

The MATE Center has taken steps to create information and outreach materials and to increase its outreach efforts to the major stakeholders in the marine science and technology fields. A web site has been developed that provides information, and serves as a repository for many of the products being developed. Surveys which provide valuable information from employers, students and educators are located on the web site. The web site features a job listing, including internships, and an interactive database with the employer information collected. The Center also produces a bi-weekly news updates (available on the Web) and a quarterly newsletter.

V. SUMMARY

The MATE Center has embarked on a national mission to improve technology education aimed at serving businesses and workers in marine related fields. Although targeted training programs are often necessary in highly technical fields such as Remote Operated Vehicle operations, there are, many skills, knowledge, and abilities that overlap several occupational clusters. Educational programs in these areas can provide the foundation skills which will make students employable in a variety of jobs. Specific training and education targeted to narrow occupations needs to happen in partnership with industry and research organizations who can contribute the expertise and technology required. In part, this training will come from internships and other work-based educational programs. We believe this combination of foundation skills and realworld, workplace based training and experience, achieved through academic/ employer partnerships will provide the toolbox needed for students, workers, and businesses to be most successful, today and tomorrow.

For more information about the MATE center, or to contact our office, see our website at www.marinetech.org, or call 831.645.1393, or write to the MATE Center, Monterey Peninsula College, 980 Fremont St. Monterey CA. 93940.

REFERENCES

Braddock, Douglas J. (1992, February) Scientific and Technical Employment Monthly, Labor Review, Department of Labor, Washington, D.C.

California Department of Education, Industrial and Technology Education Unit, 1995. Industrial and Technology Education Career Path Guide and Model Curriculum Standards

Crane et al. 1998. The Marine Advanced Technology Education Center, Developing an Education Infrastructure for our Nation's Marine Oriented Workforce. Proceedings of the 1998 Symposium, Diving for Science, American Academy of Underwater Sciences.

Crane et al. 1997. Critical Issues in Marine Technology Education. NSF/DUE Report. Heritage Press.

Fenton, Steve, 1994 Developing a Curriculum -The DACUM Process, ATEEC News: Quarterly Review of Education and Career Opportunities in Environmental Science and Technology, Winter 1994 Vol. 1:4

The Oceanography Society for the Department of the Navy Grant N00014-89-J-3125, 1995. Careers and Employment Opportunities in Oceanography and Marine-Related Fields, (1995). Office of Naval Research, Virginia Beach, VA

The Secretary's Commission on Achieving Necessary Skills (SCANS). U.S. Department of Labor, 1991 What work requires of schools: a SCANS report for America 2000.

Synergy Bulletin, National Science Foundation, Directorate for Education and Human Resources. Advancing Technological Education. March 1999. James S. Deits (Ed.) Deborah Shapley, Corby Horvis, Gerhard Salinger, Elizabeth Teles (contributing authors). NSF 99-71.

U.S. Government Printing Office, Washington, D.C. 1992. Science and Technology Act, 1992.

CONSTRUCTION AND VISUALIZATION OF A SEAFLOOR BACKSCATTER DATABASE USING NAVAL "THROUGH THE SENSOR" TECHNOLOGY

W. E. Brown,¹ M. L. Barlett,² and J. F. England²

¹ Naval Oceanographic Office,
1002 Balch Blvd., Stennis Space Center, MS 39522

² Applied Research Laboratories, The University of Texas at Austin,
P. O. Box 8029, Austin, TX 78713

ABSTRACT

This paper describes recent developments in the Sonar Active Boundary Loss Estimation project. The aim of the project is to produce high-resolution bottom backscatter and bottom-loss databases using combatant AN/SQS-53C sonar "through the sensor" data collection. The approach utilizes modified signal processing techniques developed specifically for Naval sonar systems to automatically detect and identify features of interest in the recorded time series of each beam. The current implementation is able to process acoustic returns from a variety of sonar setups. For each ping, all beams are processed. Feature parameters are extracted from the sonar signals, automatically geo-referenced, and stored in a database along with supporting ship and sonar status information. Unique features inherent to the database, analysis tools, and visualization capabilities include use of MATLAB, a commercially available software package; on-the-fly creation of gridded data at arbitrary (user-specified) grid cell resolution; ship's status, navigation, and sonar setup data; the ability to extract, analyze, and display parameters by azimuth of observation; and the ability to generate "images" of the ocean bottom along the ship's track as seen by the actual sonar system. In this paper we present an overview of the signal and data processing from the sonar beamformer output to the production of a gridded geo-referenced database and provide several examples of data visualization and data filtering which are possible with this approach.

I. INTRODUCTION

The Sonar Active Boundary Loss Estimation (SABLE) project is developing the capability to produce high-resolution bottom backscatter and bottom-loss databases using combatant "through the sensor" data

collection. Efforts to obtain this capability are motivated by a variety of factors. In recent years major changes in U.S. Naval doctrine and requirements have taken place during an era of declining defense budgets. Moreover, these changes have had a corresponding impact on requirements for oceanographic and geophysical databases to support fleet operations. Operational requirements for littoral seas and shallow water that are anisotropic in nature and require high-resolution databases to describe them are now taking a higher priority. These requirements, in conjunction with reductions in defense spending, place a premium on efficiency. At the same time, continued advancement of ADP hardware and software promotes the collection and processing of larger data sets. This confluence of changing requirements, decreasing resources, and evolving technology presents both a challenge and an opportunity. Our effort to meet this challenge is the focus of this paper.

Two approaches for estimating seafloor acoustic backscatter are direct measurement techniques^{1,2} and methodologies of systematic comparison between observed reverberation and modeled results.³⁻⁵ Direct measurements have the advantage of reducing degrees-of-freedom and uncertainty in the estimate of scattering coefficients. A primary limitation of this approach has been the large volume of data and corresponding collection resources required when constructing high-resolution databases over large areas (e.g., worldwide). The data-model comparison approach, when coupled with detailed knowledge of seafloor sediments, has the potential to extend databases to regions where measured data are sparse. The intent of the SABLE approach is to utilize the best of both of these approaches. The use of combatant data collections greatly increases the volume of data for direct measurement analysis and creation of high-resolution databases and reduces associated collection costs. In addition, detailed modeling and comparisons of modeled

reverberation and measured reverberation will be used to validate and/or correct derived bottom scattering parameters.

In the following section, we present an overview of the SABLE data processing stream from the recorded outputs of the AN/SQS-53C (53C) beamformer to the extraction of database feature parameters. We also provide a general description of the database, which contains the feature parameters, as well as ship's status, sonar setup, and navigation information. We then present examples of visualization tools available to display parameters of the database and illustrate how these tools may be used to extract, analyze, and display database parameters as a function of constraints on database variables. Finally, we provide a synopsis of planned future extensions and refinements of the SABLE database. We do not intend to present methodologies for deriving bottom loss/backscatter parameters from "through the sensor" sonar measurements in this paper. Rather, the objective of this paper is provide an overview of an innovative database from which such information can be extracted and to illustrate visualization and the filtering capabilities inherent in this approach. These capabilities can, in turn, be used to interpret and validate derived quantities such as bottom scattering parameters.

II. SABLE DATA PROCESSING AND SABLE DATABASE

The processing chain described in this section provides a capability to process "through the sensor" data from the 53C sonar and extract various parameters associated with features identified in the received acoustic time series. All beams are processed, and features and associated parameters are geo-referenced using ship navigation and sonar parameters. Currently, the processing is limited to specific sonar setups, but this is primarily a research decision which was implemented for simplicity; in principle, any sonar setup may be processed via the methods described in this paper.

The input to the SABLE processing chain consists of complex, quadrature demodulated outputs from the 53C beamformer. When available, these inputs are obtained via conversion of tapes from the AN/SQQ-89 System Level Recorder (SLR) system. For those ships not equipped with the SLR system, an adjunct 8 mm recorder (microDRAPS) may be installed to acquire 53C data. The microDRAPS tapes are also used as inputs into the SABLE processing chain. In addition to the 53C acoustic data, these tapes typically contain both ship status and sonar setup information. Ship's navigation information is also fused into the database processing stream to provide ship position at ping initiation.

The 53C sonar system has a variety of operator-selectable transmit waveforms, pulse durations, pulse train structures, and transmitter/receiver spatial beam setups. For transmit structures containing multiple waveforms (e.g., coded pulse (CP) and continuous wave (CW)), returns for the transmitted components are

separable spectrally and are thus individually available for processing. At present, the SABLE processor employs structures derived from a CP waveform to identify regions of interest. Using knowledge of the temporal and spectral separation of the CP-CW pulses, regions of interest identified in the CP transmission are also identified in the CW transmission. Schematic diagrams of the shipboard data acquisition process and SABLE processing chain are given in upper and lower panels of Fig. 1, respectively.

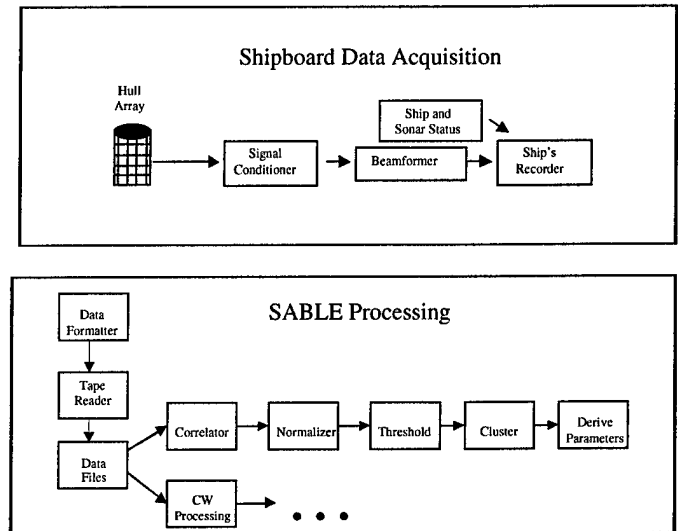


Fig.1. Schematic diagram of shipboard data acquisition (upper panel) and SABLE data processing stream (lower panel).

As discussed above, the initial acoustic inputs are recorded basebanded beamformer outputs from the 53C sonar. For each beam, the CP complex, basebanded time series is replica correlated (match filtered) with the transmit waveform. The correlation provides a degree of "time compression" in the return to improve the temporal localization of structures in the CP return.

Following replica correlation, the correlator output for each beam is then normalized by a local noise estimate. For each correlator output test point, X , a split window spanning the point X is used to estimate the median value, M_X , associated with the test point. The median estimate is then compared with the test point value, A_X , and the test point value is "sheared" if the value exceeds a shear threshold, T_X :

$$T_X = \text{shear constant} * M_X. \quad (1)$$

If $A_X > T_X$, the test point value is replaced by

$$A_X = \text{replacement constant} * M_X \quad (2)$$

Test points not exceeding the shear threshold are left unchanged. The process continues through the entire input sequence ("edge" effects are accommodated by

data wrapping), producing an edited median sequence. The median sequence is then used to make an estimate of the local noise associated with a given test point by combining weighted split window averages for each test point, and the correlator output is normalized by dividing the test point value by the estimated noise mean for the test point. The half windows are "slid" to the next point, and the normalization repeated until the entire correlator data sequence has been normalized. Examples of time series at the beamformer output, correlator output, and normalizer output for a CP pulse are shown in the upper, middle, and lower panels of Fig. 2, respectively.

The normalized CP correlator outputs for each beam are used to identify "regions" of interest in the CP normalizer time series. This is done using a combination threshold/clustering approach. For each beam, a threshold is applied to the normalizer output. Points which exceed the threshold are then grouped into "clusters" (time series segments) according to user-specified rules. The clustering criteria can include a minimum temporal (or range) separation between clusters (i.e., grouping threshold crossings within a minimum time from the previous crossing together), a minimum number of crossings per cluster, and a minimum number of contiguous threshold crossings per cluster.

Once clusters for a given beam have been identified, each cluster is geo-referenced, and features associated with each cluster are extracted. In order to geo-reference each cluster, the amplitude-weighted mean CP normalizer output over the cluster duration is used to compute the mean travel time of the cluster. This time is then converted to the range from the projector using parameters from the sonar system. Using the ship's position and the absolute beam bearing, the latitude and longitude of the cluster are then computed.

In addition to computing the latitude and longitude of each cluster, various other parameters which can be used to characterize the cluster are extracted for each cluster and written to the database. These include the beginning/ending sample numbers, cluster duration, the peak sample number and value, weighted cluster center, and travel time. Other parameters which are more directly related to bottom interactions (e.g., statistical estimators of energy and its moments) are not calculated at the CP normalizer output because the normalization process affects interpretation of these measures. Rather, energy-related parameters are calculated at the beamformer and correlator outputs prior to the normalization process.

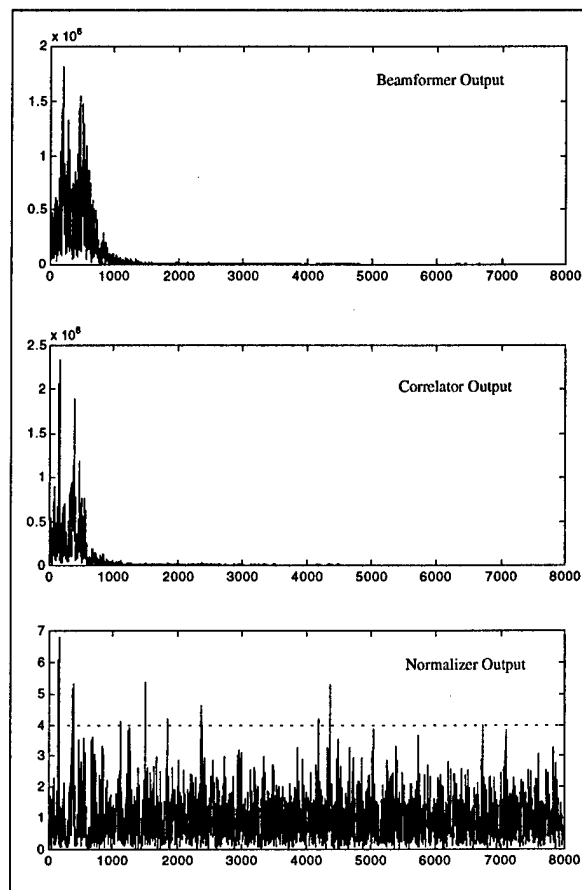


Fig. 2. Representative CP time series at the beamformer output (upper panel), correlator output (middle panel), and normalizer output (lower panel). The x axis is the sample number; the y axis is the received amplitude (linear). The dashed line in the lower panel represents the clustering threshold.

Time segments of the beamformer and correlator outputs corresponding to the travel time interval of each CP normalizer cluster are identified by accounting for temporal shifts in the sonar processing stream due to parameters such as transmitted waveform pulse width and correlator delay. Additional parameters are then extracted from these data segments, associated with each geo-referenced CP normalizer cluster, and written to the database. Information extracted includes characteristics of the "cluster" (endpoints, peak value, duration, etc.) at the beamformer and correlator outputs, as well as the statistical characterizations (mean, median, moments, etc.) of the return amplitudes associated with the cluster at these points in the processing stream. Features are also calculated at the CP beamformer output which are used to characterize phase information contained in the CP return. Finally, for sonar setups in which both CP and CW waveforms are sequentially transmitted, parameters characterizing the amplitude and phase response are derived at the CW beamformer output for travel times corresponding to each cluster and are also recorded in the database.

Thus, at present, there are three (four) points in the 53C processing stream where characteristics of the sonar return are measured for a CP (CP/CW) transmitted waveform. These measures, together with sonar setup, ship navigation information, and dataset descriptors comprise the database entries for each cluster.

III. VISUALIZATION TOOLS AND DATABASE FILTERING

In the previous section, the processing of 53C acoustic data and the construction of the SABLE database were described. The database produced in this process is a point database (as opposed to a gridded database) and contains acoustic information in the form of basic estimators and measures derived from the 53C output time series at various points in the processing chain. Although this approach produces a database containing a large number of parameters, it has the distinct advantage in that it affords great flexibility in producing "end-products." For example, with this approach it is possible to filter or constrain the database parameter(s) used to calculate a bottom scattering parameter, in order to investigate sensitivities of derived parameters to variations in input constraints, etc. In this section, we present illustrations of several ways in which parameters from the SABLE point database can be displayed, and also provide illustrations of how database parameters can be filtered or constrained.

Several different visualization tools have been developed to aid in the display and interpretation of parameters stored in the database. Visualization of data may be performed either as point data or as gridded data at user-specified resolution. Examples of point and gridded visualizations are given in the upper and lower panels of Fig. 3, respectively. In the top panel of the figure, the geo-referenced cluster positions for a series of pings is plotted, with each cluster indicated by a '+'. In the bottom panel of the figure, these data have been gridded with a resolution of 0.01 deg and the data displayed as the logarithm (base 10) of the number of times a cluster fell into each grid cell (i.e., number of hits). Such information and displays are useful for establishing the statistical significance of derived physical parameters, area coverage, etc. In addition, gridded visualizations can be produced with resolutions to match existing environmental or geophysical databases, simplifying displays that combine data from multiple databases.

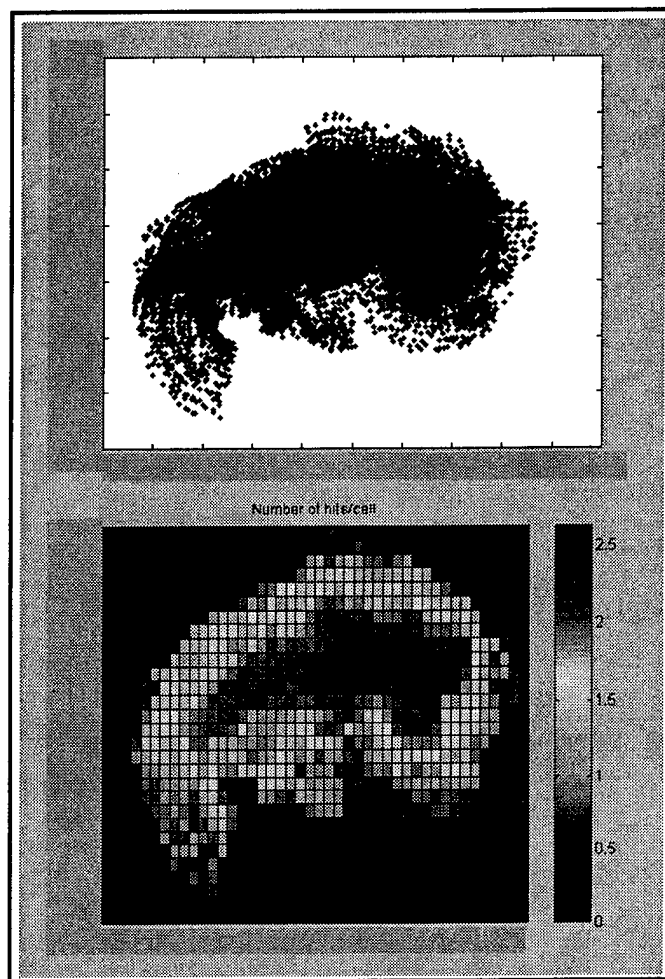


Fig. 3. Illustrations of point (upper panel) and gridded (lower panel) database displays. The grayscale in the bottom panel represents \log_{10} of the number of counts in a grid cell.

Database entries may also be constrained or filtered prior to display or use. For example, the top portion of Fig. 4 shows the geo-referenced cluster distribution for a series of pings. In this case the clustering algorithm grouped all threshold crossings within 65 yards of the previous threshold crossing together into a cluster and required a minimum of 2 threshold crossings per cluster. In the bottom portion of Fig. 3, the average of the mean cluster energy at the CP beamformer output is displayed over a 50 X 50 grid. Similar displays are shown in Fig. 5, except that 10 threshold crossings per cluster were required for the data shown in these displays. The effect of requiring additional threshold crossings per cluster not only reduces the number of clusters over the set of pings being processed, but it also tends to select the clusters with the larger average mean energies out of the original database, as one would expect.

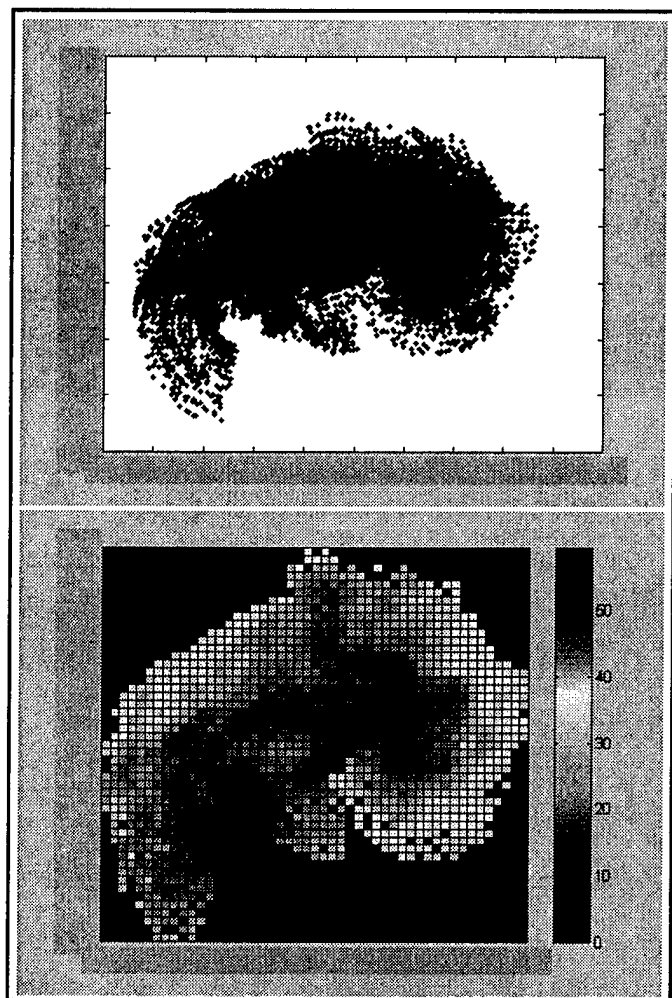


Fig. 4. Geo-referenced cluster positions for a series of pings (upper panel) and corresponding gridded average cluster amplitude for the CW return (lower panel) in dB.

IV. FUTURE DEVELOPMENTS

There are several enhancements to the current processing methodology and corresponding database which are planned for future implementation. A version of the processing stream that will accommodate significantly more sonar setups than are processed with the current version is currently under development. This will provide a corresponding increase in the number of samples that can be incorporated into the database. In addition, a new version of the database is under development which will contain embedded bathymetric and environmental data (sound speed profiles, wind speed/direction, and sea state) when available from other sources. Inclusion of such information in the database will permit additional data filterings based on environmental constraints that are not currently possible for both measured and derived parameters. Finally, a modeling system will be developed that supports propagation path analysis for range



Fig. 5. Geo-referenced cluster position (upper panel) and gridded average CW cluster energy in dB (lower panel) for clusters which are constrained to have a minimum of 10 threshold crossings.

corrections and bottom loss estimation. The modeling system will also be used for comparisons between modeled reverberation levels and measured reverberation data to determine database constraints that will enhance clustering associated with significant bottom interactions while suppressing responses from surface and volume reverberation.

V. SUMMARY AND CONCLUSIONS

A novel point database approach has been developed for use in analyses of recorded "through the sensor" sonar returns. The database incorporates both geo-referenced acoustic measures from structures observed in the sonar returns as well as sonar setup and ship's navigation information. Visualization tools have been developed which permit display of point data parameters, gridding of point data at user

specified resolution, and filtering of displayed data based on database constraints.

The flexibility inherent in the database design provides an advantage over previous approaches for characterization of acoustic bottom properties. The database structure permits examination of dependencies of derived bottom parameters on various characteristics such as observation angle, sonar parameters, etc. In addition, data may be displayed either as cumulative results or as "through the sensor" results along a particular ship's track. It is our belief that this approach will permit better control over the quality of bottom measurements derived from "through the sensor" acoustic measurements.

REFERENCES

1. D. F. NcCammon, "Low grazing angle bottom scattering strength: Survey of unclassified measurements and models and recommendations for LFA use," U. S. Navy J. Underwater Acoust. 43, pp. 33-46 (1993).
2. R. J. Urick, *Principles of Underwater Sound*, 3rd ed. McGraw Hill, New York (1983).
3. G. A. Scanlon, R. H. Bourke, and J. H. Wilson, "Estimation of bottom scattering strength from measured and modeled mid-frequency sonar reverberation levels," IEEE J. Oceanic Eng. 21, No. 4, pp. 440-451 (1996).
4. Gary A. Scanlon, "Estimation of bottom scattering strength from measured and modeled AN/SQS-53C reverberation levels," Masters Thesis, Naval Postgraduate School, Monterey, CA (June, 1995).
5. R. T. Miyamoto, Applied Physics Laboratory, Univ. of Washington (private communication).

Ship to Shore "Digital Status Report" Multimedia Communication

Steven C. Cash
Naval Oceanographic Office, N92
John C. Stennis Space Center, MS 39522

ABSTRACT

A methodology is currently being tested which makes it possible to better inform shore-based managers about shipboard operations. A multimedia software package called a Digital Status Report (DSR) is being developed, and is intended to make it easier for shore-based staff to more clearly visualize remote operations. This highly desirable capability can be achieved through a remote user's ability to view video clips, images, text and data routinely collected at sea and transmitted to the U.S. Naval Oceanographic Office (NAVOCEANO) via the NAVOCEANO Network and then routed through the INMARSAT on a daily basis. This new possibility also makes it feasible for highly trained staff at multiple locations to network ideas and solutions concerning decision-making situations at remote locations where less experienced staff may need additional assistance. This type of multimedia conferencing is certain to have a large impact on resource sharing and troubleshooting problems.

The first page of the DSR contains fields with images concerning the ship position, local meteorologic and oceanographic conditions, as well as video clips of the current shipboard activities. Any type of graphic media (satellite images, sonar images, bathymetric plots, etc.), including video clips as well as images captured from video or other sources, is brought into the software and made accessible to the user with event associated push buttons. A popup text box also appears in which the sender or receiver may type information concerning the recorded event. Subsequent pages contain information specific to the ship and survey operations.

At the end of the survey, each day's DSR will be written onto a CD-ROM, thereby providing a permanent record of the survey. This end product may prove to be a useful resource for future surveys when the mission guidelines remain the same but different personnel are involved. The CDs may also be used in some cases as training for new personnel, public relations tools, or a methodology to familiarize other scientists with NAVOCEANO operations.

The ship to shore multimedia software package, Digital Status Report (DSR) is currently in a state of dynamic development. The current version of the DSR is written in a C++ scripting software package called ToolBook Instructor Ver. 6.5¹. In addition to the software, a digital camera, video camera and video capture card and are all essential items in the overall program concept.

The DSR is intended to be used by regularly capturing video clips and images of shipboard operations. This information is to be sent daily from the ship back to Naval Oceanographic Office headquarters. The video and image data will be captured using a HI8 video camera with 450-lines-per-inch resolution. To minimize the file size, 5-second video clips (avi files) are recorded at a capture rate of 15 frames per second. This translates into 5 MB per video clip, which will then be compressed. The frame grabber can also be used to capture individual images (jpg, bmp, etc.) from the video.

The first page of the DSR consists of event driven push buttons that will give the viewer back at NAVOCEANO pertinent information concerning the ship position, meteorology, sea state condition, and the current shipboard activities. A preprogrammed package is available, however, events are easily programmable and may be reprogrammed easily. Fig. 1 shows is first page of the DSR.

The screenshot displays a complex interface with multiple data fields and buttons. At the top, it shows the date '19 Feb 99' and time '1300'. Below this, there are fields for 'USNS Henson' and 'Atlantic Ocean'. The interface is divided into several sections, each with a title and a list of items. The first section is titled '30.17 N / 90.18 E' and contains 'Cloudy Squalls', 'Secure Equipment', and 'Current Meter Ops'. The second section is titled '3500' and contains 'ENE 176', 'ENE 223', and '1000+ NM'. The third section is titled '20 feet' and contains 'ENE'. To the right of these sections, there are numerical values: '130 meters', 'Very Rough', 'All well', 'AVHRR', '17C', '19C', '997.3', '1013.1', '85%', '77%', '15C', '17C', '17C', '24C', and '150 m/s'. At the bottom, there is a text box with the message 'Deteriorating weather conditions and high seas brought about the retrieval of TOSS and initiated activities to secure all ondeck equipment'. Below this text box are buttons for 'SIS Menu', 'LIS Menu', '<<<', and '>>>'. In the top right corner, there is a button labeled 'Instructions'.

Fig. 1

I. INTRODUCTION

¹ ToolBook II Instructor Ver. 6.5 is a C++ authoring package from Asymetrix.

Notice that the event push buttons are in two colors; the red buttons indicate a video clip, and the blue buttons indicate an image. Images can consist of still frames captured from the video or digital camera, as well as satellite images, acoustic images or graphical output from just about any source. A text box, included in the bottom left-hand corner, allows both the originator as well as the recipient of the package to make any comments they feel necessary. All pages also have push buttons in the bottom right that will allow the user to navigate forward or backward. Subsequent pages of the DSR illustrate detailed presentations of current engineering operations.

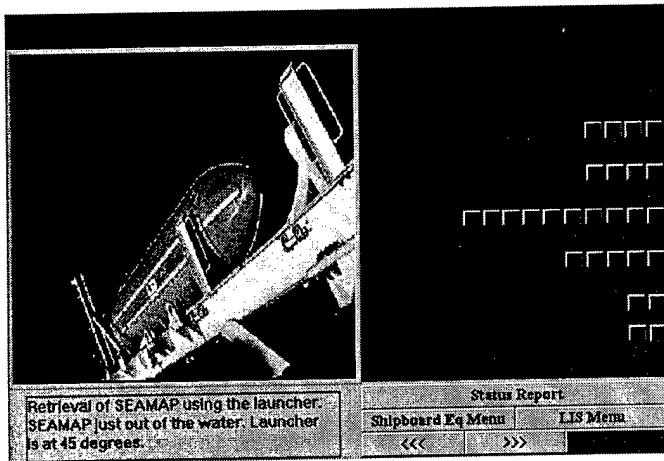


Fig. 2

In this example Fig. 2 provides event push buttons that break down SEAMAP launch and recovery procedures. This type of graphic illustration can be used to replay any type of shipboard engineering operation. One advantage of using this type of graphics software over current conventional methods is that with a push of the button it is possible to visualize any shipboard operations. It is one thing to read a written communication that simply states in black and white that the sea state is too rough to perform any deckwork, and quite another to see an image or a video clip of waves breaking over the ship as in Fig. 3.

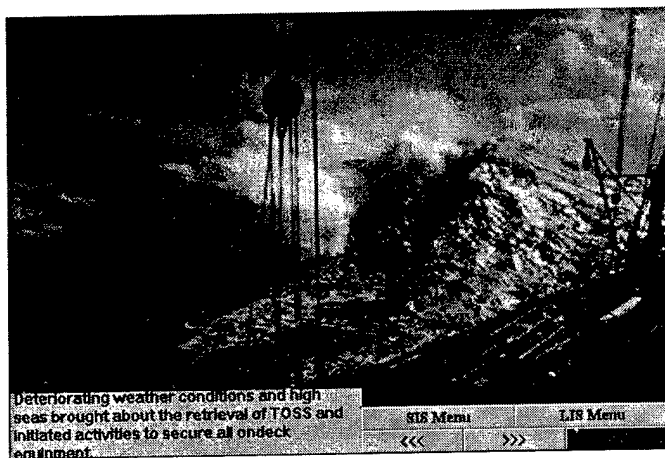
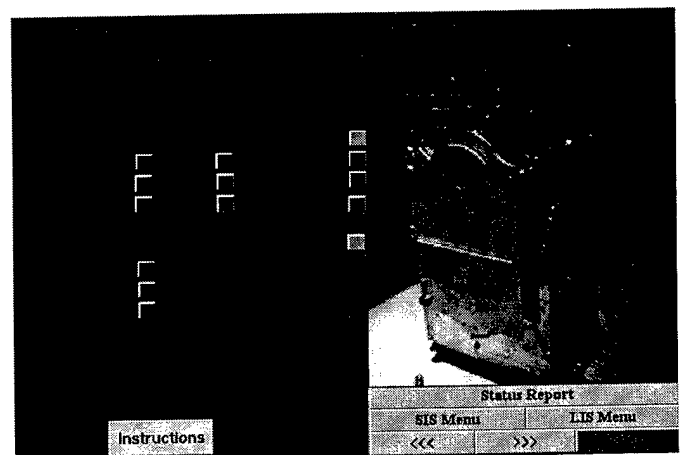


Fig. 3

In addition, there may be occasions when engineering operations onboard the ship could well require the assistance of engineers back at NAVOCEANO. Taking a video clip or images of the equipment and the problem and then sending it back for senior engineers to review will undoubtedly assist in troubleshooting many problems. Even communications between various NAVOCEANO ships could be facilitated by elements of the DSR. Using this type of human resource sharing will enhance the capabilities of all shipboard operations and allow our most valuable human assets to be used to the maximum potential.

II. SHIPBOARD INFORMATION SYSTEM

In its full-featured version, the DSR functions as a part of the OceanVision System. There are numerous components to this package which have large sections devoted to the major shipboard systems. Fig. 4 illustrates a push button selection of those areas. More selections could be added or others removed. In a complete version each image would be tied to a database and would be associated with attribute information about each item. In its current state of development, each image recorded is



stored in a flat file and is not associated with a database.

Fig. 4

Clicking on the red button for shipboard Equipment and Operations will take the viewer to a series of screens which gives the option of navigating to an area of interest with other images and video concerning the ship. Clicking on the red button associated with NAVOCEANO operations will navigate the viewer to a series of screens specifically



concerned with NAVOCEANO personnel and the operations they have performed on this specific survey. (See Fig. 5)

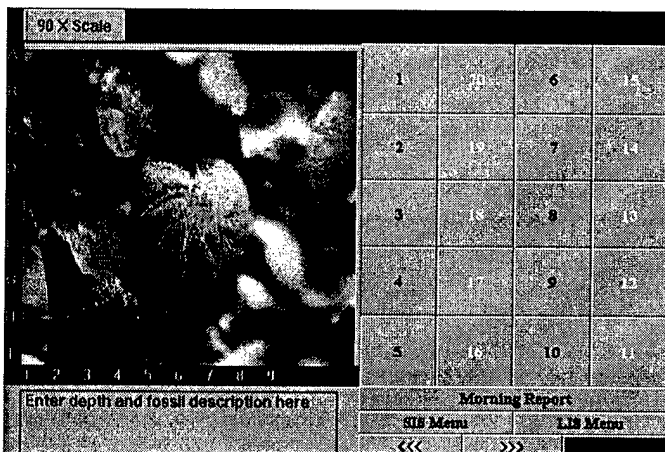
Fig. 5

III. LITHOLOGIC INFORMATION SYSTEM

The entire software package was written around the Lithologic Information System (LIS) module. It has many screens to assist the user in viewing maps, reports, and images of sediments. (See Fig. 6.) It allows the viewer to

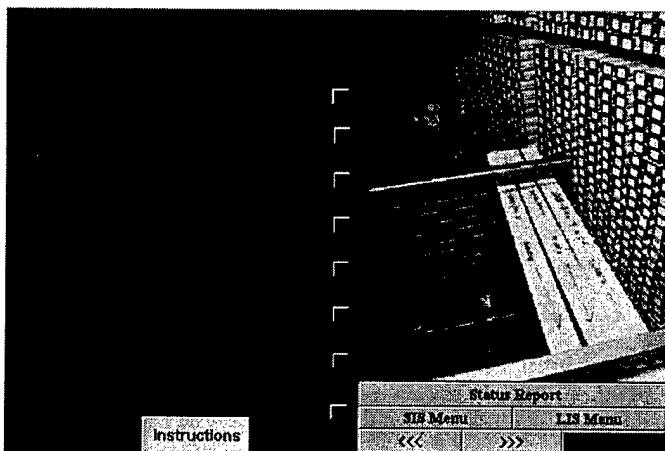
Fig. 6.

access images taken during the coring process as well as detailed lithologic descriptions concerning sediments



examined thru a microscope. The microscope is connected to a video camera that is in turn connected to a frame grabber on the computer. After focusing on the subject under the microscope, an image may be taken at either low or high magnification and stored in an easy-to-use lookup table. The following example uses software and data (Cash, 1997) that were generated from a system the author used prior to working for NAVOCEANO. In Fig. 7 the viewer may examine an image containing a microfossil along with a text box with information concerning the depth and a fossil description.

Fig. 7



IV. CONCLUSION

The DSR will become operational in the very near future. It will be used to collect near real time information that will then be sent back to NAVOCEANO. The most significant drawback to this procedure concerns the bandwidth of the satellite transmissions, and the time it will take to relay the data back to NAVOCEANO. Considering the cost of using INMARSAT (\$5 per minute) it will be an expensive proposition to use the fully developed DSR for routine operations. As the cost of satellite transmission goes down, this procedure will certainly become commonplace.

As a means of keeping permanent records of survey operations it will be easy to make CDs of the individual surveys when this procedure is used. Uses for these CDs will include training new NAVOCEANO oceanographers and engineers, as well as providing the scientific/academic community with a valuable source of information.

It is also under consideration to rewrite the DSR in order to make it more compatible with other NAVOCEANO software. ArcView Ver. 3.1² is the most likely candidate for this change in application software.

Additionally, there is much attention being given to sending operational real time video and data directly from the ship back to NAVOCEANO. Soon it will be possible to send real-time video and data back from ships from all over the world. When this becomes an operational reality, the next big issue will be how to display this information most effectively. Currently the method being investigated for this is to use 3D visualization technology.

REFERENCES

Cash, S. C. 1997 "Abstract – Videomicroscopy and the Corporate Exploration Team" Transactions of the Gulf Coast Association of Geological Sciences.

The inclusion of names of any specific commercial product, commodity, or service mentioned in this paper is for information purposes only and does not imply endorsement by the Navy or NAVOCEANO.

² ArcView is a Geographic Information Systems package from Environmental Systems Research Institute.

RECONSTRUCTION OF SAMPLED AND MODELED OCEANOGRAPHIC INFORMATION USING AN EXPLORATORY ENVIRONMENT

Peter Gruzinskas
David Cole
Naval Oceanographic Office
Stennis Space Center, Mississippi 39522

Andy Haas
Logicon, Inc.
Stennis Space Center, Mississippi 39522

Abstract

The Naval Oceanographic Office (NAVOCEANO) Department of Defense (DoD) Major Shared Resource Center (MSRC) operates as a DoD shared high performance computing (HPC) center, serving over 2000 users nationwide. Scientific visualization is an essential element of HPC that provides the methodology to explore, define, and present the results of computations. Accurate and understandable representation of data impacts a project in several ways: it helps scientists understand the physical phenomena they are studying, it helps communicate this work to their colleagues, and it helps explain the work and its significance to the public. Our scientific visualization team, in conjunction with researchers at our facility and other DoD facilities, have accomplished numerous visualizations of large data sets. In this paper we present examples of the methods, techniques, and results of our efforts to visualize observational data and the output of numeric ocean models.

I. Background

The staff at the Naval Oceanographic Office (NAVOCEANO) Major Shared Resource Center (MSRC) Visualization Lab is tasked with supporting the DoD research community by providing state-of-the-art scientific visualization support involving several Computational Technology Areas (CTA). Our MSRC provides tailored support for Computation Fluid Dynamics, Signal Image Processing, Climate Weather and Ocean Modeling, Environmental Quality Modeling, Computational Electromagnetics and Acoustics. We also work closely with various components of NAVOCEANO's operational community, to assist in the development of new techniques to display, analyze, and quality control some of the measurements and model output which provide critical operational support to the Navy. The common problem that this support must overcome is dealing with large data sets. "Large" is a fluid definition; it changes as technology evolves. In

today's environment we are dealing with datasets that range routinely from hundreds of megabytes to several gigabytes. Service to remote users also poses a challenge to our scientific visualization staff. Remote could be considered anywhere from a room in another building, to another building, in a different state, in a different time zone. Our user base is nationwide.

II. Introduction

The premise of this paper and presentation is to demonstrate the utility of an interactive digital environment to analyze oceanographic data and measurements. In such an environment one can gain insight into physical processes and ensure the quality of both measurements and model output by exploring and interrogating the data in both time and space. In this case we are dealing with environmental processes which are historically difficult to model and measure. Some if not all of these processes have impact on naval weapons and sensors. Our ability to understand, model, predict, and present these phenomena is important to our military. In our study we will analyze ocean bathymetry, circulation, and other ocean climatology over several domains. We will explore both space and time as we interrogate these data sets in 3-D computer space. Each data type has its own unique requirements and must be available to the display routine. The routine involves storage, networking, processing power, memory, and more to achieve this environment. Fortunately, these requirements are becoming readily available at low cost.

Modern oceanographic survey and modeling techniques, coupled with the successes of high performance computing, have begun to overwhelm both scientists and researchers with numerical information. The challenge of scientific visualization is to present the critical, distilled information to a varied client base, but in all cases, maintain the integrity of the data. These data appear to be increasing in resolution at an enormous

pace, both spatially and temporally. The term "large data set" will be continuously redefined.

Our 3-D environment will represent static measured boundary conditions, such as bathymetry, fused with dynamic modeled oceanographic parameters, such as circulation and temperature.

III. The Data

A. Measured

Digital elevation data obtained from a variety of public domain sources form the frame of reference in which to present our time series oceanographic information. It is critical when presenting this type of information to accurately define the surface and geophysical boundary conditions of the modeled environment. For the most part we will define our geophysical boundary with ETOPO5, but have enhanced some enclosed basins with higher resolution bathymetry. Therefore, our topography represents nominally 5-nmi horizontal resolution and our bathymetry anywhere from 5- to 1-nmi resolution. The techniques developed using these grid resolutions can and will be applied to higher resolution data. Work with different components within NAVOCEANO has involved viewing a variety of data types within the context of our terrain visualization. These data types include, but are not limited to, acoustic imagery, bioluminescence, circulation, salinity, sonic layer depth, and temperature.

B. Modeled

The modeled data that we present illustrates 3-D ocean circulation and create a large overhead in storage, memory, and input/output (I/O). Model output comes in a variety of formats, with varying resolutions in both the spatial and temporal domains. Determining the optimal sample rate and display resolution becomes the challenge of scientific visualization. Higher resolutions have larger storage/bandwidth requirements. One timestep of the Miami Isopycnal Coordinate Ocean Model (MICOM), which covers the Atlantic with 16 vertical layers, is approximately ½ GB.

The following describes the modeled output we visualize:

Numerical modelers at the University of Miami have long pursued the goal of studying the ocean circulation using models formulated in density (isopycnal). Because many physical processes in the ocean are rather intimately related to isopycnal surfaces and to the way in which they deviate from the horizontal, isopycnal models must have to contribute in elucidating oceanic circulation features with scales ranging from frontal to global. The association of vertical shear with isopycnal packing and tilting in the ocean makes these models appropriate for studies of strong baroclinic currents, such as the Gulf Stream. However, the fundamental reason for modeling

ocean flow in density coordinates is that this system suppresses the "diapycnal" component of numerically caused dispersion of material and thermodynamic properties. It is this characteristic that allows isopycnal models to keep deep water masses near the freezing level for centuries—in agreement with observation—while surface waters can be as warm as 30 degree Celsius. Models framed in Cartesian coordinates suffer from vertical "heat leakage" which cases the ocean to act as a giant heat sink in climate simulations.

The long-term goals of the modelers at the University of Miami are to perform a realistic, truly eddy-resolving wind- and buoyancy-forced numerical simulation of the North Atlantic Basin with data assimilation capabilities and to assess the nowcast/forecast capabilities of such a high-resolution ocean model. One of the primary research objectives is real-time forecasting of both Lagrangian trajectories and 3-D Eulerian fields associated with such physical parameters as velocity, temperature, salinity, and density. The five major components of the effort will be (1) MICOM, (2) data, (3) an Extended Kalman Filter (EKF) with a Gauss-Markov Random Field (GMRF) model for spatial covariances, (4) a random flight turbulence model for Lagrangian trajectory prediction, and (5) contour-based parameter estimation and assimilation techniques. The computational requirements for basin-scale ocean modeling at the resolutions of interest (less than 10 km) are extreme. Each time that the horizontal resolution is increased by a factor of n , the computational load goes up by a factor n^3 since the n -fold reduction in linear mesh size requires n times more time steps to integrate the model over a given time interval.

The main scientific goal will be to generate optimal estimates of the time-varying ocean state in support of the Navy's needs on synoptic time scales on the order of weeks to months and on spatial scales typically on the order of 100 to 1000 km (mesoscale). Doing this in real time requires interplay between large varied data sets, numerical ocean circulation models, and data assimilation algorithms. Due to the large demand placed by near-optimal assimilation techniques on raw computing power, this work will fit most naturally under the Grand Challenge label.

The project's fine-mesh simulation of the North Atlantic circulation (mesh size 0.08 degree longitude, 6 km on the average) is presently in its eighth year of integration. This simulation has generated considerable interest in both the computing and the oceanographic community. The term "fine-mesh" describes a horizontal grid resolution—typically of order 10 km—which allows barotropic/baroclinic instability, shear instabilities typical for geophysical flows, to be modeled. Since these instabilities cause ocean currents to meander and break up into individual eddies, fine-mesh ocean models are also referred to as "eddy-resolving."

In this configuration, a realistic result for the Gulf Stream separation is achieved. This result supports the view that an inertial boundary layer (which results from the fine resolution) is an important factor in the separation process. It was also the first simulation with a fully thermodynamic basin-scale model to simulate the separation in a realistic fashion. This simulation allows direct and detailed comparisons with observations such as satellite data (sea surface height and sea surface temperature), mooring measurements, inverted echo sounders, and free-floating drogues.

The computational domain is the North and Equatorial Atlantic Ocean Basin from 28°S to 65°N (including the Caribbean Sea and the Gulf of Mexico but excluding the Mediterranean Sea) with a horizontal resolution of 1/12 degree (mesh size on the order of 6 km) and 16 layers in the vertical. The vertical grid was chosen to provide maximum resolution in the upper part of the ocean.

NAVOCEANO has developed an operational capability to forecast ocean currents and thermal structure in semienclosed seas. The Persian Gulf is one of the areas in which a numerical modeling system has been employed. The principal elements of the system are (1) a 3-D primitive equation circulation model, (2) temperature, salinity, and bathymetry data bases, and (3) meteorological forecasts provided by the Fleet Numerical Meteorology and Oceanography Center.

The model uses terrain-following vertical coordinates, where each level is a fixed fraction of the water depth. The spacing of the levels is reduced near the surface and bottom so that top and bottom boundary layers are resolved. The Persian Gulf models uses an along-axis resolution of 4.4 nmi and a cross-axis resolution of 4.6 nmi.

The Persian Gulf is a shallow, semienclosed basin with a mean depth of only 25 to 40 m. The circulation of this basin is driven primarily by the local wind stress and secondarily by thermohaline forcing. The prevailing wind in the Persian Gulf is from the northwest and is called the shamal. A wind-driven generally cyclonic circulation results. The lands surrounding the Persian Gulf are dry so there is strong excess evaporation over the Persian Gulf. This results in a surface inflow of relatively fresh water and an outflow of deeper, more-saline water at the Strait of Hormuz.

Model output shows the generally cyclonic circulation but with more complexity. Some of the highest current speeds are in the inflow through the southern side of the Strait of Hormuz. This inflow feeds the eastward coastal current along the south edge of the Gulf, which is strongest near Qatar. Along the Iranian coast, there is

another eastward current where it terminates and its remnant turns south into the interior.

IV. The Application

There are several generations of explorers built to view uniquely different data sets. Our strategy is to build the application around the data and provide low-cost portable tools which are tuned to the user's data visualization needs. In an interactive computer environment such as the one we describe, one must be able to deal with the geometry which describes the ocean basin before attempting to inject and interact with additional information, such as time-series circulation, temperature, or salinity. Rendering the terrain dynamically is accomplished using Dynamic Surface Generation (DSG). DSG uses layers of varying resolution (mip mapped) to provide optimum resolution vs. interactive performance with the option to view full resolution at any time. We plan to provide NAVOCEANO's Seafloor Data Bases Division a version of this software which will provide them a low-cost, portable means to assist in the exploration and quality control of their gridded data bases. They will push the envelope of our application, applying it to their high-resolution grids, which are nominally .1 arc minutes or approximately 180 m.

DSG is a simplification of the Silicon Graphics, Inc. (SGI) Active Surface Definition (ASD) technique. ASD maximizes terrain quality (both surface texture and geometry) while maintaining high frame-rate interactivity. It is intended for visual/flight simulation and supports real-time texturing of large landscapes. Its ability to roam large textures is based on clipmapping hardware available only on SGI Infinite Reality systems. To maintain portability, DSG does not use clipmapping. DSG builds surface geometry on the fly by computing the extent of longitude and latitude within the user's field of view. Multiple-resolution copies of the bathymetry data exist in a mipmap, which can be thought of as an inverted pyramid with the highest resolution layer on top and progressively smaller resolution layers working downward. The best resolution layer is chosen such that the number of polygons needed to cover the extent of longitudes and latitudes is kept to a minimum. This minimum can be set lower or higher to increase interactivity or resolution, respectively.

DSG is optimal when the view direction is perpendicular (i.e., looking top down) to the surface. As the view direction becomes parallel with the surface, the viewing area increases and drives DSG to use a coarser resolution to cover the increased area of data. Fly-through visual simulations, by their very nature, operate with view direction parallel to the surface. Because of this, ASD optimizes surface resolution by combining high-resolution data closest to the user with lower resolution data farther away. This is an involved process

that contrasts DSG's approach of maintaining a uniform resolution for all data in the field of view. This simpler approach works well in oceanographic applications where it is common to look at the data in a top-down fashion.

The viewing area used by the DSG is not only important for interactive terrain rendering, but for visualizing large data sets. Because the full range of data is often much larger than the memory and graphics can handle, the viewing area limits the amount of data that needs to be read. Data are read at a resolution that matches the terrain. When data are read across a large view area, a coarser version is produced to fit the memory and graphics. As the view area becomes smaller, the application can visualize the data closer to its original resolution. The application interleaves data I/O with its animation and user input. This allows data covering different areas/resolutions to be processed, while allowing the user to interact with the current data.

The data bounded by the topography are dense and curvilinear along one or more dimensions. The data contain velocity information that is visualized via two techniques: glyphs and particles. Glyphs are 3-D arrows that provide the viewer with a general feel of the vector data. They are constructed as cones with a tube body and rendered with OpenGL, which is the standard graphics library for 3-D rendering on PC's and workstations. The length and color of the glyphs map the ocean current speed. The color mapping defaults to speed, but can be mapped to other scalar information throughout the grid. The standard blue, green, red is used, but any table of colors can be supplied. The glyphs can be sampled at full or partial resolution across the data. Even at full resolution, glyphs by themselves are only clues about the flow of information hidden within the data. Particle advection is used to reconstruct the continuous sense of flow by interpolating velocities and grid layer depths (for isopycnal models) in space and time. Integrating particle velocities creates paths lines that are persistent across time. This persistence allows time-varying data to be studied more effectively than glyph animations. Path line colors are mapped the same as glyphs. The color of each path line changes continuously to highlight the particle speed.

The advection is a P-space algorithm which integrates particle velocities in the physical (longitude, latitude, meters) world coordinate system. P-space world coordinates are inverted back to their C-space logical (i, j, k) data coordinates to obtain velocities at each particle. The P-space position of each particle is integrated by its current velocity. Either a first-order (Euler) or second-order (Runge-Kutta) integration method may be used. Integration continues until the particle exits the grid or enters a singular area of the grid (i.e., land) which does not have an inverse from P-space to C-space.

The accuracy of the integration was tested by forming computer-generated velocities with each timestep pointing in a constant compass direction (E, NE, N, NW, W, SW, S, SE) in a counterclockwise order. Particles were advected at the beginning timestep and were allowed to complete several cycles. All paths were observed as purely circular. There was very little or no deviation as the particles made several passes around the circle.

The application does not have a conventional graphical user interface with menus, forms, and text fields. Instead the rendered scenery itself is the interface. For local navigation the user can travel to a point in the scene by holding the mouse at that point. For global navigation a small reference map showing the full topography can be clicked on to travel anywhere. Once in the desired area, the user can drag the mouse to change line-of-sight and to move forward or backward. Glyphs at different depths can be turned on or off by clicking a vertical legend of grid layers. Particles can be placed uniformly across a layer, or individually placed by clicking the desired location in the scene.

The user observes and controls time through a timeline at the top of the scene. The timeline covers all timesteps in the given model output. A marker in the timeline shows the current time which can be changed by clicking a different area in the line. The application maintains a timer that can be toggled on and off. When the timer is on, the application advances the current time by a given increment (default is 1 hour) and interpolates and adjusts all data and graphics to reflect the new time. Fig. 1 shows a typical Micom_Explorer scene with pathlines demonstrating the loop current in the Gulf of Mexico.

V. The Hardware

Our development hardware environment consists of a variety of SGI workstations up to and including ONYX2. The ONYX systems provide the raw power and memory for testing interactive techniques on large data sets. These systems contain up to 8 processors, 4 GB of main memory, and 64 MB of texture memory. This texture memory provides for hardware texture mapping, which outperforms software texture mapping. The Infinite Reality graphics pipe is the industry standard, for producing virtual environments. These servers come equipped with a Graphics to Video Option (GVO), which allows the capture of interactive screen sessions directly to video tape. SGI has historically transitioned their graphics technology from the large graphics servers down to their desktops. The Octane demonstrates this featuring dual processors, hardware texture mapping, and cross-bar switched memory. The INDIGO2 is our most abundant and commonly used platform. They are single-processor systems with high impact graphics and

256 MB of main memory. There are also several O2's which provide multimedia capabilities. Our target hardware is any system or workstation with a C compiler and OPENGL libraries.

VI. The Software

The operating environment at the MSRC Visualization Lab is IRIX UNIX. With the release of IRIX 6.5 we have a common version operating system between all of our SGI platforms. We are investigating, porting, and benchmarking some of these codes to other operating systems such as SOLARIS, LINUX, and NT. Our facility maintains a toolbox of commercial off-the-shelf software to assist in the display and analysis of a wide spectrum of data. These software applications range from a suite of Geographic Information Systems for analyzing geospatial data, to robust application environments such as IBM Data Explorer (DX) and Application Visualization System (AVS), to high-fidelity batch rendering applications that support a wide range of special effects such as Alias/Wavefront (now MAYA). These products provide us with a rapid prototyping environment when undertaking new projects. They provide the means to translate and understand the various data structures and how they map into 2-D and 3-D space. A full range of shareware/freeware visualization utilities available today is also supported. Eventually the application is ported to C code which exploits graphics libraries that are available on virtually every class of workstation.

VII. The People

It requires an interdisciplinary staff to accomplish these tasks. The sophistication of the visualization requires computer scientists and specialists to work closely with oceanographers, ocean modelers, geophysicists, and even warfighters to tune a visualization application to the data. Fig. 2 shows the co-author and developer of these OPENGL applications in front of a large screen projected in stereo, which provides an immersive experience.

VIII. Future Efforts

In the immediate future we want to optimize and transition our DSG surface generator to NAVOCEANO's Seafloor Data Bases Division to help them explore and quality control their gridded datasets. It may be possible to interface this application to a 2-D grid editor rather painlessly. Work continues on the draping of acoustic imagery over DSG-generated 3-D surfaces. The imagery resolutions provide a challenge to create an interactive tool which allows exploration at full resolution. Dynamic paging of textures will be required, but hopefully portability can be maintained. Data correlation in general, will be exploited, but specifically, temperature

and/or salinity will be displayed with circulation in our digital exploratory environment.

IX. Acknowledgements

We would like to acknowledge the work of NAVOCEANO's Modeling and Techniques Division, particularly Dr. Phu Luong, who has subsequently left NAVOCEANO to work at the U.S. Army Corps of Engineers Waterways Experiment Station, and Dr. Eric Chassignet from the University of Miami. Both provided us with data, insight into the data, and a need to explore.

X. References

Chassignet, Eric, R. Bleck, and A. Mariano, "Data Assimilation in High Resolution Numerical Simulations of the Ocean Circulation." DoD Challenge Project Resource Request, 1999.

Horton, C., M. Clifford, D. Cole, J. Schmidt, and L. Kantha, "Operational Modeling: Semienclosed Basin Modeling at the Naval Oceanographic Office." Oceanography, Vol. 5, No. 1, 1992.

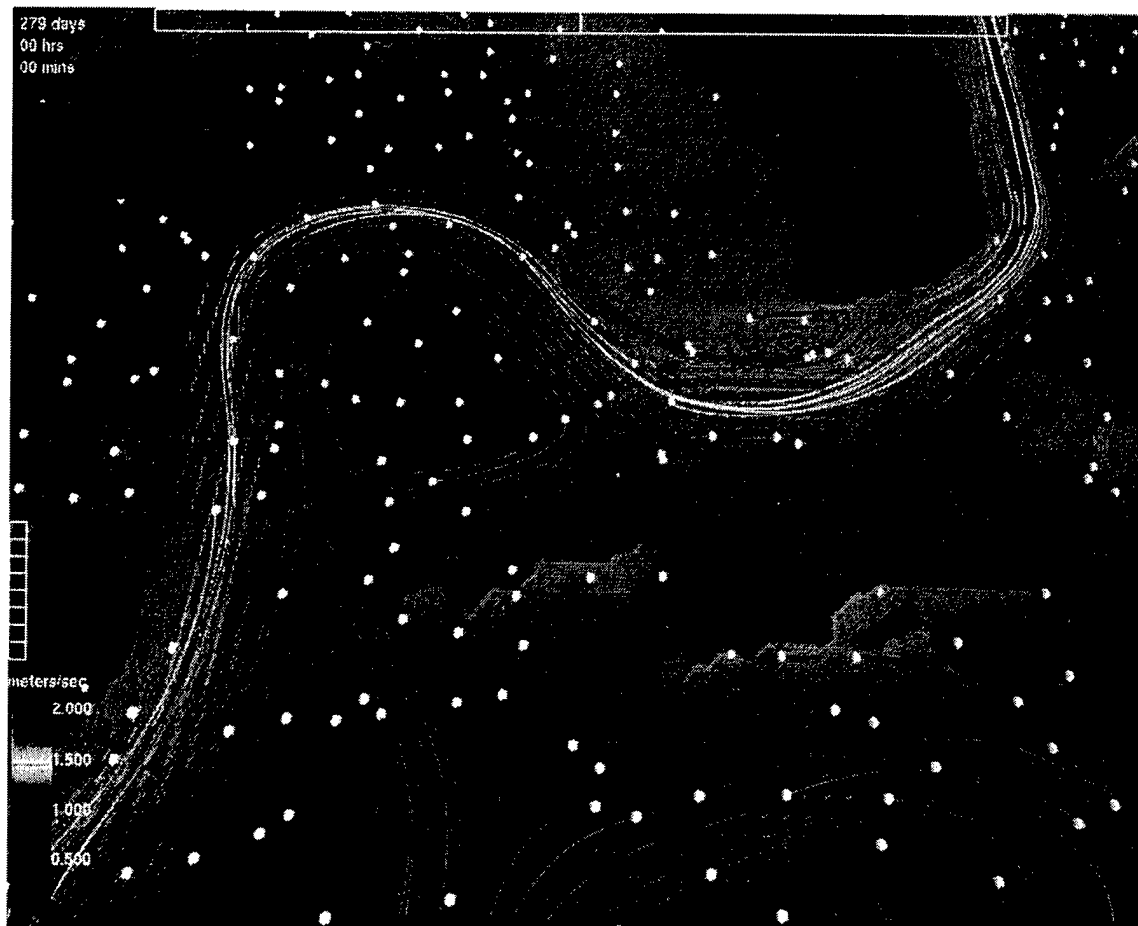


Fig. 1

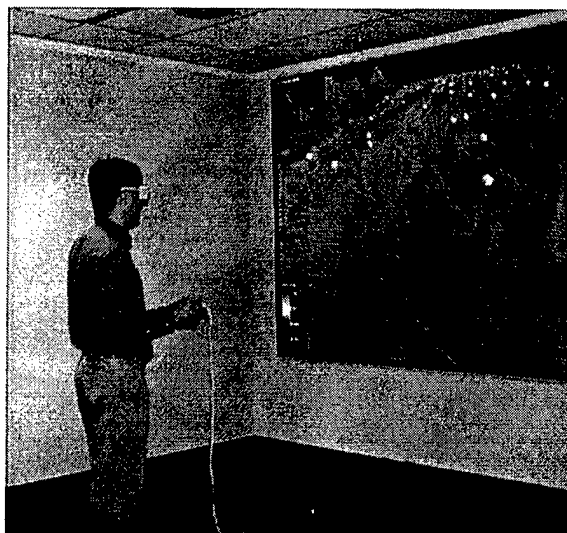


Fig. 2

AIRBORNE LIDAR: A SURVEYING TOOL FOR THE NEW MILLENNIUM

Rebecca A. Smith
Naval Oceanographic Office
Stennis Space Center, Mississippi

Geraint R. West
John Chance and Associates
Lafayette, Louisiana

Joint Airborne Lidar Bathymetry Center of Technical Expertise, Mobile, Alabama¹

I. Abstract

The last few years of the 20th century have witnessed the "coming of age" of Airborne Laser Bathymetry (ALB) and its transition from research and development technology to routine operational use. Despite this transition, the technology is still generally poorly understood in the hydrographic survey community, and in this environment it has been difficult to establish a universally accepted philosophy for its use. This paper explores the strengths and limitations of the technology and relates these characteristics to several scenarios, with particular emphasis on how the use of Airborne Laser Bathymetry systems is likely to impact survey operations of the future.

II. Introduction

There has been a tendency to regard Airborne Laser Bathymetry (ALB) technology as developmental and only an addendum to multibeam echo sounders (MBES). However, as with MBES, several systems have now reached operational maturity, and it is clear that ALB has proven its worth as a survey tool for hydrographic surveys. This paper discusses the characteristics of ALB and how it can be best employed to integrate with existing survey systems.

The attraction of ALB lies in its capability to augment conventional surveys in a cost-effective manner, while operating within relatively clear, shallow-water regions that are the most costly, hazardous, and time-consuming areas for ship and boat operations. This capability is highlighted by the comparison between ALB and multibeam fitted launches which suffer from significantly decreased swath width in very shallow waters, while ALB swath width remains fixed, irrespective of depth (Fig. 1). This is particularly significant in an environment where the US

Navy has vast "brown water" requirements. In addition, ALB has the ability to provide a rapid response to new survey areas measured in weeks, as opposed to months, for typical shipborne operations. In summary, Hydrographic Survey Launches (HSLs) are currently the primary platforms for surveys in depths shallower than 50m, but suffer from the following disadvantages:

- A. Dependence on a Mother ship,
- B. Slow coverage rates,
- C. Vulnerability to damage.

ALB has the potential to overcome all these disadvantages (Guenther, 1985).

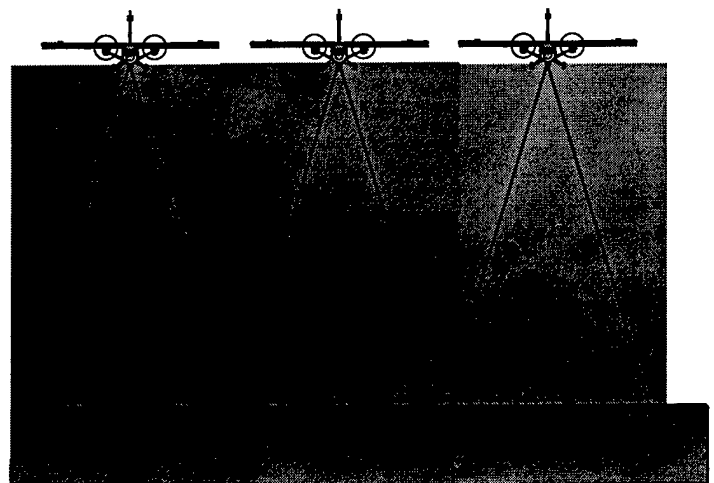


Fig. 1. Comparison of ALB and MBES coverage.

III. Principles of Light Detection and Ranging (Lidar)

All Lidar systems operate on the principle that water depth may be calculated from the time difference of laser returns reflected from the sea surface and seabed. In

¹ The Joint Airborne Lidar Bathymetry Technical Center of Expertise (JALBTCX) was established in May 1998 by the signing of a Memorandum of Agreement between the US Army Corps of Engineers, South Atlantic Division, the Waterways Experiment Station, and the Commander, Naval Meteorology and Oceanography Command.

most systems an infrared channel (1064 nm) is used for surface detection, while bottom detection is from a blue-green channel (532 nm), as shown in Fig. 2. The maximum depth measurable by a system is heavily dependent on water turbidity and can vary considerably from just a few meters in very turbid water to several tens of meters in very clear water. Water clarity is usually expressed as the diffuse attenuation coefficient K_d , which numerically is the distance over which light intensity diminishes to 1/e of its initial value. Consequently, depth performance of ALB systems is generally expressed as the product $K_d D$, where D is the depth.

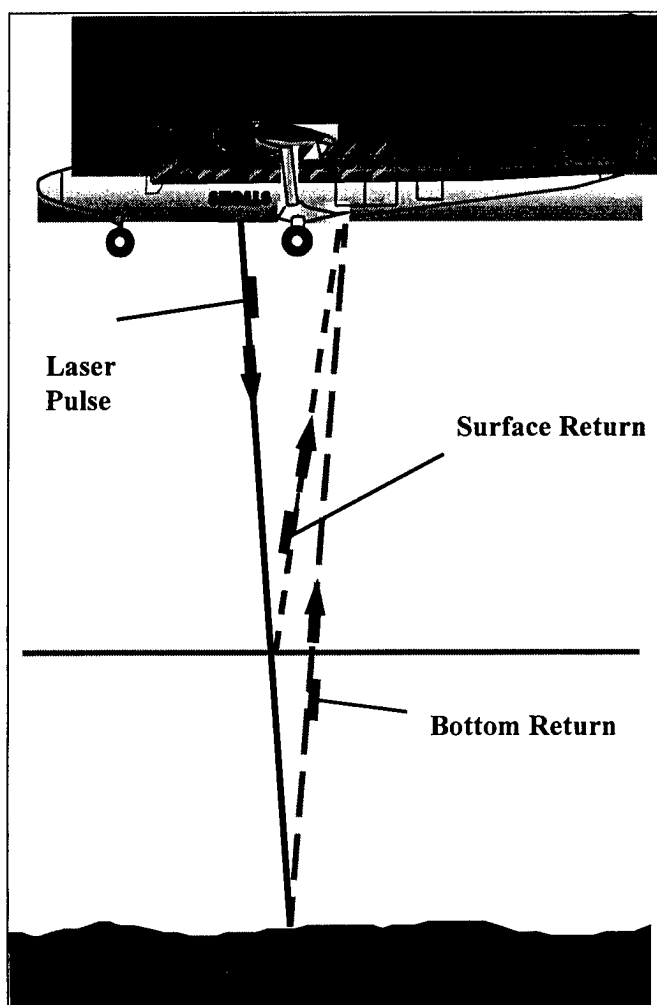


Fig. 2. ALB depth measurement.

The basic geometry of an ALB system is shown in Fig. 3, though it should be noted that the rectilinear scan pattern shown is a generalization, since many systems employ a swept arc pattern. Although source beam divergence is of the order of 12 mrad, producing a spot on the sea surface of about 1.5m diameter, the many spreading and scattering effects mean that 90% of the energy is contained within a footprint of diameter approximately equal to the depth. However, much of this energy is returned with a significant time lag and is insignificant for measurement purposes. The

consequence is that a footprint with a diameter of $\frac{1}{2}$ the water depth (containing 50% of the energy) is normally regarded as the "effective" footprint of an ALB system. It is important, however, to realize that illumination of the bottom does not infer detection of small targets within the footprint. For this to occur, the ratio of illuminated target area to illuminated bottom area has to be sufficiently high to enable both automatic and human recognition. To understand the reasons for this, it is necessary to discuss briefly how bottom detections are made.

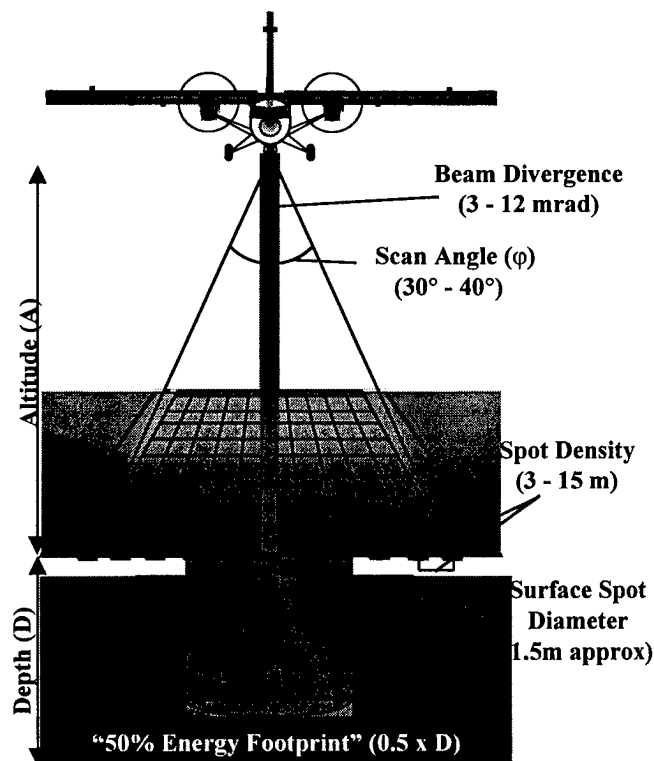


Fig. 3. Basic ALB geometry.

Although surface detection is usually made with the infrared channel, the blue-green channel will also detect the surface. Because of this, the generic ALB waveform is of the type shown in Fig. 4, with two distinct returns from the air/sea interface and the bottom. The asymmetry of the bottom return is a consequence of the large footprint but, as stated above, the "tail" is largely from outside the "50% diameter" footprint. Since the detection is measured on the leading "up" ramp of the waveform, it becomes clear why this scattered energy is irrelevant to the depth calculation. Present ALB systems have demonstrated capability to achieve depth accuracy standards at least as accurate as current acoustic systems (Riley, 1995) and because of this, compliance with current IHO Standards can justifiably be claimed.

Fig. 5 illustrates a typical shallow-water waveform. The bottom is saturated on the deep channel, clearly illustrating that the use of two channels is often preferred. In Fig. 6, a deep return is shown; not only does this fall beyond the maximum depth of the shallow channel, but it has a low

amplitude waveform resulting from considerable spreading of energy, which results in a large "footprint" that may get lost in noise.

Although the examples above describe the majority of cases, it is the determination of target detection capabilities that is fundamental to the characterization of Lidar as a hydrographic survey tool. The distinction between bottom illumination and confident target detection is therefore important to understand. Fig. 7 illustrates the case where there is evidence of a return above the bottom (deep channel); however, the shallow channel shows this to be a distinct and separate return, so the likelihood is that this is fish. In Fig. 8, both the deep and shallow channels show a separate return in midwater column, clearly indicating fish or other suspended material. These cases are just two examples of the problems posed in distinguishing apparent anomalies with real bottom hazards; the technology has changed, but the role of the hydrographer as an interpreter of the data has not. The situation becomes even more difficult in deep water, where a decreasing proportion of the total incident energy will illuminate small objects so they become masked by the "up" ramp of the bottom return.

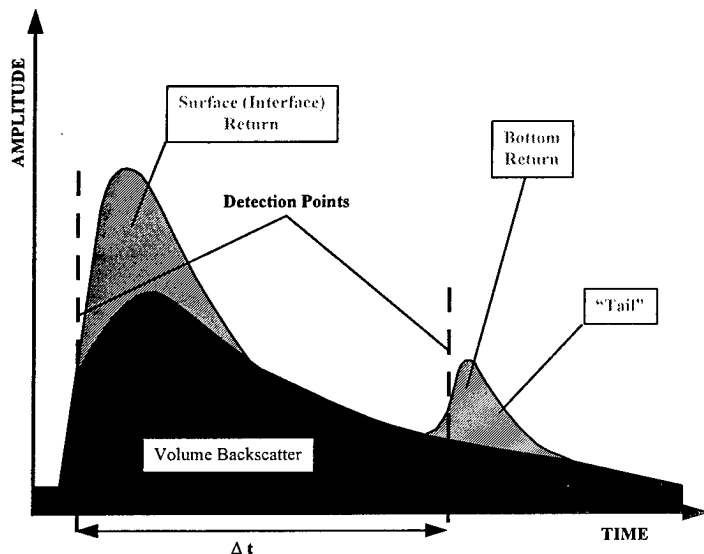


Fig. 4. Generic Lidar waveform.

IV. Hazard Detection

So far, only the single sounding (often known as a "shot") has been considered, and it should be clear by this point that such a situation falls short of the requirements of a hydrographic system, both in coverage and object detection. Current ALB systems employ a mechanical scanning mirror to achieve a swath, which when combined with the PRF of the laser produce a grid pattern of spots. Equally, the need for drawing a clear distinction between 100% bottom illumination and hazard detection confidence should also be recognized. Because of the need to

illuminate a target with sufficient proportion of the laser footprint to result in detection, denser spacing of shots results in higher chances of detection.

This "sounding" spacing is generally referred to as spot density, and considerable debate has occurred over recent years as to optimum spot density required for hydrographic purposes. Guenther et al. (1996) highlighted this issue in a study from which Fig. 9 is developed. This is a stark illustration of the relative effectiveness of different spot densities and underlies his conclusions that "significant gains can be obtained in many cases by decreasing average linear sounding spacing to 3m." It was further concluded, "objects less than 1m high are not frequently detectable." As will be apparent from this paper, the operational benefits of ALB over acoustic systems are so compelling that the desire to replace these older systems with ALB has become extremely powerful. Consequently, the need to define the envelope of ALB capabilities is an important step if it is to replace traditional acoustic systems in legitimate circumstances. It is in this area that the most significant work in proving the efficacy of laser hydrography can be done; and while the work of Guenther et al. (1996) has been a leap ahead in the characterization of Lidar for hydrography, the process of fully characterizing ALB performance is only in its infancy. In parallel with this, we are also challenged to fully define the capabilities of our older technologies and, moreover, to be honest as to whether they actually achieve the capabilities we have so often only assumed. Most importantly for ALB, although its ability to achieve compliance on the basis of depth measurement accuracy with all Orders except "Special" (of the new IHO Standards) is assured, target detection criteria will dominate as the controlling factor over which Order an ALB survey will fall into.

V. Cost Effectiveness

Fig. 10 compares the coverage rates in differing depths of ALB to other shallow-water survey systems. While the vastly superior coverage rates of ALB over most shallow-water survey systems should come as no surprise, the relative effectiveness of ship-mounted multibeam in depths greater than 50m is evident. Consequently, there seems little to be gained from increasing the depth capability of ALB systems at present. Equally, it is worth noting that, while acoustic systems are close to maturity and therefore to their performance limits, ALB has much potential for further development and is only likely to increase its advantages.

Several studies have attempted to analyze the cost benefit of ALB, the most recent of which examined several scenarios including ALB in a multiplatform environment (Axelsson and Alfredsson, 1999). To an extent, the validity of this exercise is questionable since the comparison between a high-resolution sidescan

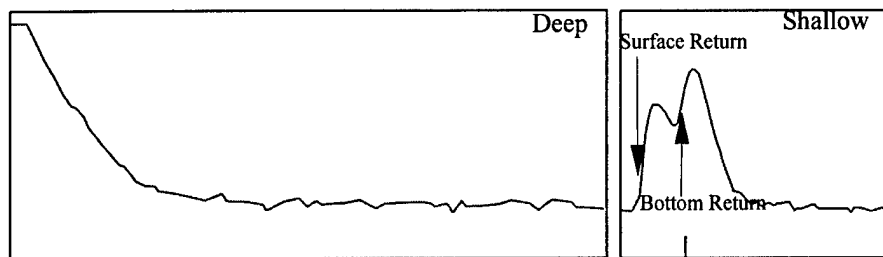


Fig. 5. Shallow-water waveform.

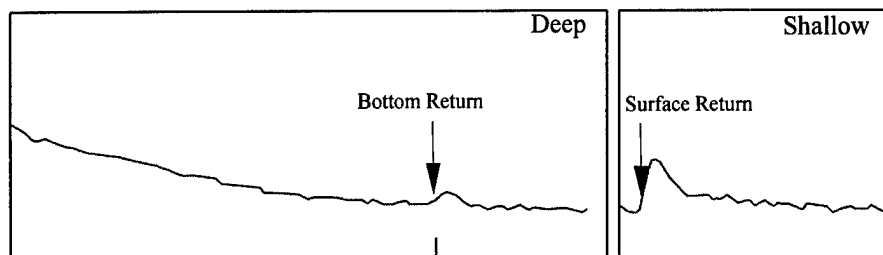


Fig. 6. Deep-water waveform.

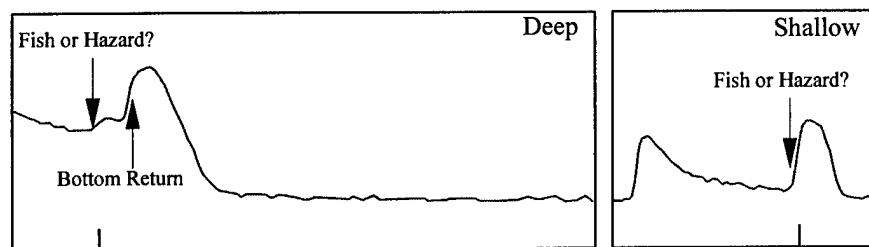


Fig. 7. Waveform showing return close to seabed.

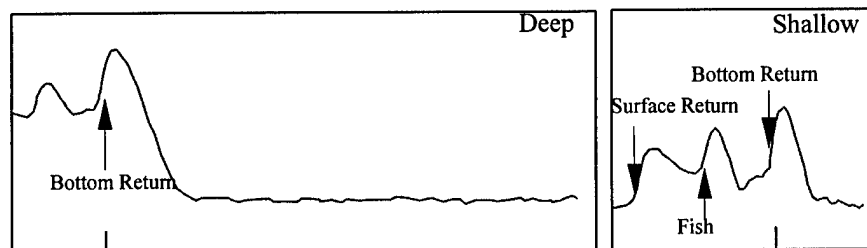


Fig. 8. Waveform showing midwater column return.

survey and ALB, for instance, is not a fair one. However, the utility of this is to indicate where the potential benefits of different systems are most likely to be realized. Indeed, Fig. 10 indicates some startling, if hardly surprising, features. Most notable is that ALB is at least as cost effective to run as conventional systems, while it is most economical in areas where conventional assets are least economic—in very shallow water. When taken in these terms, the new International Hydrographic Organization Standards for Hydrographic Surveys (SP 44) becomes especially significant, as it gives far more latitude for the survey planner/charting authority to choose required resolutions.

VI. Practical Applications

In July 1996, the Airborne Lidar Bathymetry Technical Center of Expertise (ALBTCX) was established by the United States Army Corps of Engineers (USACE). Its missions are to produce quality products using the SHOALS system, promote the commercialization of lidar bathymetry, and foster the evolution of airborne lidar and complimentary technologies. The ALBTCX is comprised of personnel representing the USACE, John E. Chance and Associates, the National Oceanic and Atmospheric

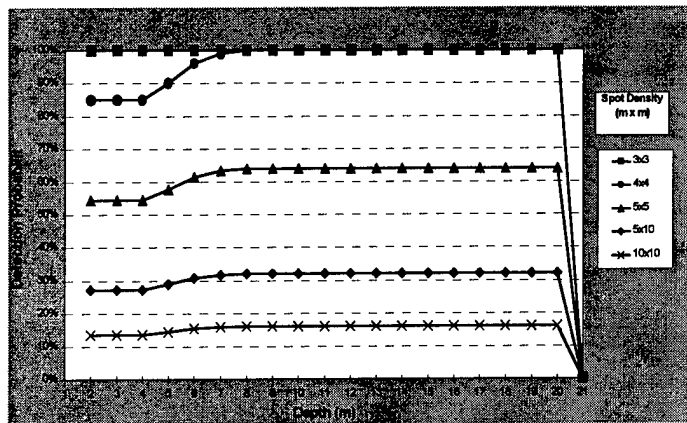


Fig. 9. Probability of detection of a 2m cube by different spot densities (Guenther et al., 1996).

Administration's Aircraft Operations Center (AOC), the National Ocean Service (NOS), and Optech, Inc.

A Memorandum of Agreement (MOA) signed by the Commander, Naval Meteorology and Oceanography Command (COMNAVMETOPCOM) and the USACE in May 1998 expanded the scope of the USACE ALBTCX to a Joint ALBTCX (JALBTCX), incorporating the Naval Oceanographic Office's (NAVOCEANO's) needs into its mission and promoting the mutual leveraging of knowledge, resources, and expertise with respect to ALB and related technologies. It also serves as a vehicle to facilitate the availability of SHOALS to support COMNAVMETOPCOM/NAVOCEANO surveys. One of the primary roles of the JALBTCX is to develop the applications of Lidar technology; this has principally been achieved through operational use of the Scanning Hydrographic Operational Airborne Lidar Survey (SHOALS) system. Probably the most versatile Lidar survey system in use anywhere in the world today, it has recently undergone a major upgrade to enable it to operate from either fixed wing aircraft or helicopter. The system was installed in a Twin Otter (Fig. 12) during the fall of 1998 and has since completed projects in New Zealand, Hawaii, and the Bahamas in addition to the continental USA.

SHOALS incorporates a 400Hz laser, scanning a swath of up to 220m with a selectable spot density of 3 to 15m. Depending on selected scan width and spot density, the system can be flown at speeds up to 120kn. A single operator can operate the airborne system, but due to the extended duration of flights, usually two operators are used. Data are recorded onto Exabyte 8mm dual tape drives, which are also used for loading survey flight planning data. After landing, the data are processed by specialized postflight depth extraction procedures that calculate depths and positions, and correct for tides and waves. Automation is maximized in this part of the software so that the amount of human intervention is reduced, producing a time ratio of 1:1 with data collection. The output from the automated

processor can then be accessed via a manual processor interface, that is the primary method of editing and quality-controlling the data. The final postprocessing product is an ASCII x, y, z file that can be imported into any standard CAD package for mapping.

VII. Regional Coastal Management

One of the main reasons for the development of SHOALS was to conduct USACE channel condition and structure surveys and their impacts to adjacent shorelines. However these surveys have traditionally been small in scale and narrowly focused, which degrades many of the economic benefits of SHOALS. More recently, however, there has been a realization that effective management of the coastline relies on accurate, quantified characterization of a region over time. This approach allows computation of sediment volumes of smaller areas, which can then be monitored over time to establish sediment transport budgets. Traditionally the typical method of collecting survey data in and around coastal projects consists of widely spaced transects or profiles derived from conventional acoustic sounders and land leveling. The need for greater detail on the regional level is typically overlooked and often results in missing associated features that have an effect on surrounding areas. In an effort to redress this situation, the USACE has started to move toward a regionalized approach for sediment management, starting with a demonstration area in the coastal regions of the northern Gulf of Mexico. The objective of the proposed demonstration is to assess the benefits of managing sediment, specifically sand, as a regional-scale resource and to identify the obstacles that may hinder or prevent the realization of such benefits (Parson et al., 1999).

Conceptually, this approach appears to make perfect sense; however, it has become viable only as a result of Lidar technology. Because of its ability to rapidly survey entire regions seamlessly across the land/sea interface, SHOALS has become the tool of choice. The key to this has been the development of Kinematic GPS capability, which has effectively given SHOALS the ability to collect data independently of the sea surface. Consequently, all vertical elevations are directly related to the ellipsoid and are not subject to errors introduced by tidal measurements and changing datums.

As a participant in the USACE sediment management initiative, the Florida Department of Environmental Protection (FLDEP) has been concerned with the fact that almost 40% of the beaches are suffering serious erosion (Green, 1998). Using traditional methods, FLDEP has been able to survey only 4 counties each year quickly. However, in 1998 SHOALS commenced a program that will result in the entire Florida coast being mapped every 2 years, 50% each year. Elevations from 500m landward of the waterline to 750m seaward are

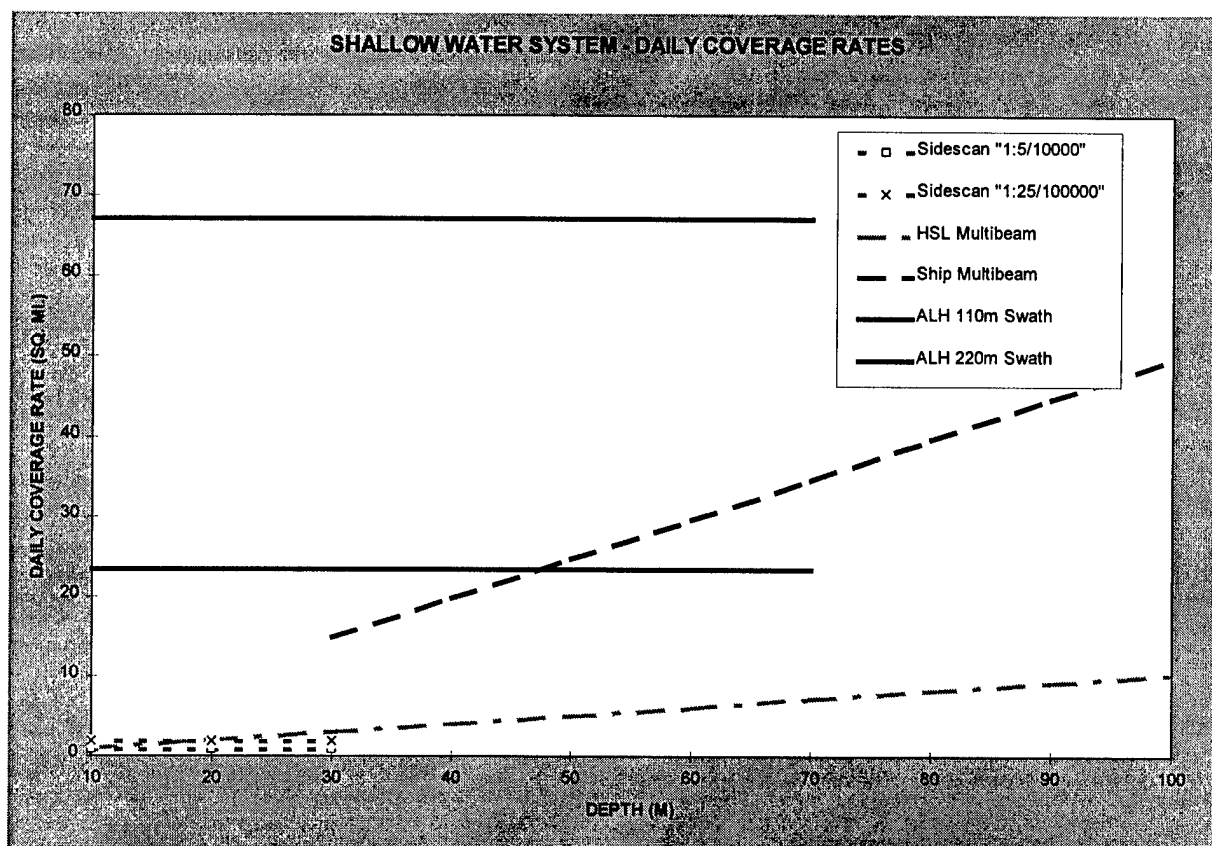


Fig. 10. Comparison of shallow-water system coverage rates (Axelsson and Alfredsson, 1999).

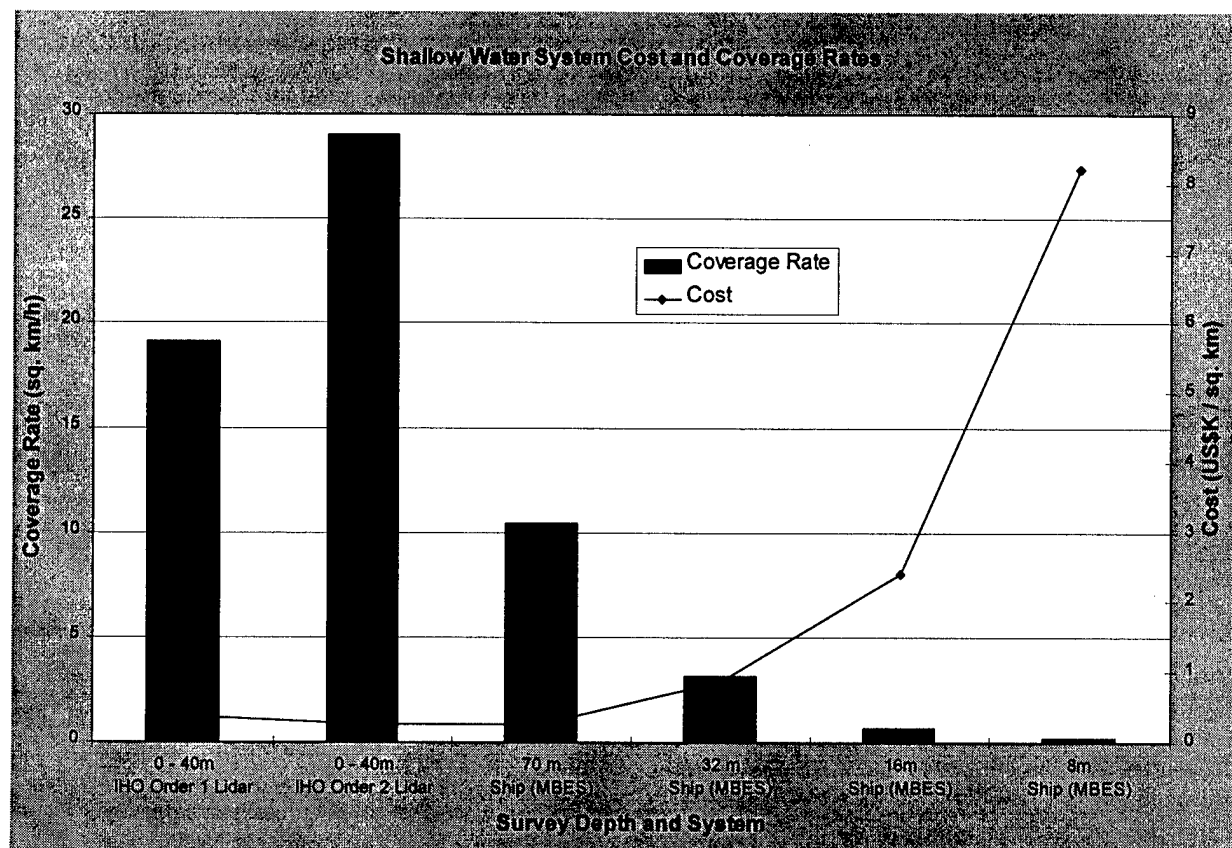


Fig. 11. Comparison of cost and coverage rates (Axelsson and Alfredsson, 1999).

collected at 8m spacing; the data are then fused with aerial photography and overlaid in a GIS for presentation and analysis (Fig. 13). This represents a quantum leap in resource management that has come to fruition only because of the availability of Lidar technology (Watters and Wiggins, 1999).



Fig. 12. SHOALS Twin Otter at Invercargill, New Zealand.

VIII. Nautical Charting

Since becoming operational, SHOALS has completed major nautical charting projects in Mexico (Pope et al., 1997), New Zealand, and the Bahamas. The survey of Snares and Solander Islands (see Fig. 14), lying 60 miles SW and 120 miles south of the New Zealand mainland illustrates the considerable benefits accruing from combining Lidar capability with conventional acoustic platforms. These sub-Antarctic island groups of Snares and Solander Islands are remote, dominated by predominantly foul weather and surrounded by pinnacles that rise unpredictably to form one of the most infamous ship graveyards in the world. In addition, both the islands are wildlife sanctuaries that attract an increasing number of cruise ships, so human impact has to be minimal. The challenge was therefore to mobilize during an extremely short weather window a survey effort that could collect a bathymetric data set in dangerous, uncharted waters and delineate inaccessible coastlines, while also ensuring the safety of survey craft operating around the islands. SHOALS was quickly identified as crucial to such a project, able to meet all the inshore requirements while also providing safe clearance for conventional acoustic platforms to work in the deeper water. The advantage of using SHOALS in an environment as hostile as the Snares and Solander Islands lies in its ability to rapidly chart shallow-water areas close to rocky coasts where conventional ship methods are difficult and dangerous (West et al., 1999).

Delineating and classifying features that are anomalous to the general trend of the seabed is one of

the critical elements of any nautical charting survey; this was a key role for SHOALS and one that it is optimized for. Small pinnacles, only a few meters in cross-sectional area but tens of meters in vertical extent, were commonplace. Although some of these dangers were self-evident, the more dangerous ones rose from depths in excess of 30m to within a few meters of the surface without breaking it (Fig. 14). SHOALS was therefore used to sweep many apparently deep areas with the aim of locating any rocks which posed a danger to surface navigation. Quality control (QC) of the complexes of drying and breaking rocks in the inshore zone required particular attention, as the Lidar waveform characteristics of whitewater and land are extremely similar. Integration of data sets from vastly differing sensors can be a challenge, and the value of powerful QC packages was key to reconciling the datasets. Overall, the New Zealand survey was a model of the innovative solutions that will increasingly be required by the marine community of the future. Close integration of SHOALS with conventional methods was fundamental to this.

IX. Rapid Reaction Surveys

A combination of the SHOALS' features outlined in the preceding paragraphs has made it increasingly attractive as a tool for support of military operations. The ability to quickly chart an area inclusive of topographic elevations and water depths is naturally the prime attraction. However, SHOALS' potential to be significantly less vulnerable than boats to enemy activity may also prove to be important in the future. During the last years of the 20th century, there has been a shift in emphasis of naval warfare to "brown water" activities that has resulted in new shallow-water requirements being generated considerably faster than the ability of routine survey activity to keep up. Consequently, the incidence of short-notice survey requirements has increased dramatically, while at the same time the theatres have become less of a single military arm's problem and more joint in nature.

While conducting surveys in Hawaii during early 1999, two "rapid reaction" demonstration projects to illustrate the concept of Lidar support for the warfighter were undertaken. The area shown in Fig. 15 was one of these areas and comprised 1.8 sq km, which took 10 minutes to fly and one hour to map, and resulted in a data set containing 200,000 points through which profiles could be cut as required. Supporting data from the same flight came from oblique photography and grabs from the vertical video record that is always run during survey operations. Although this survey took place in highly controlled conditions, the potential for Lidar to provide a comprehensive product rapidly is clear, and for this reason the Navy will further develop this proof of concept during a NATO Rapid Environmental Assessment exercise scheduled to take place in 2000.



Fig. 13. SHOALS bathymetry merged with aerial photography.

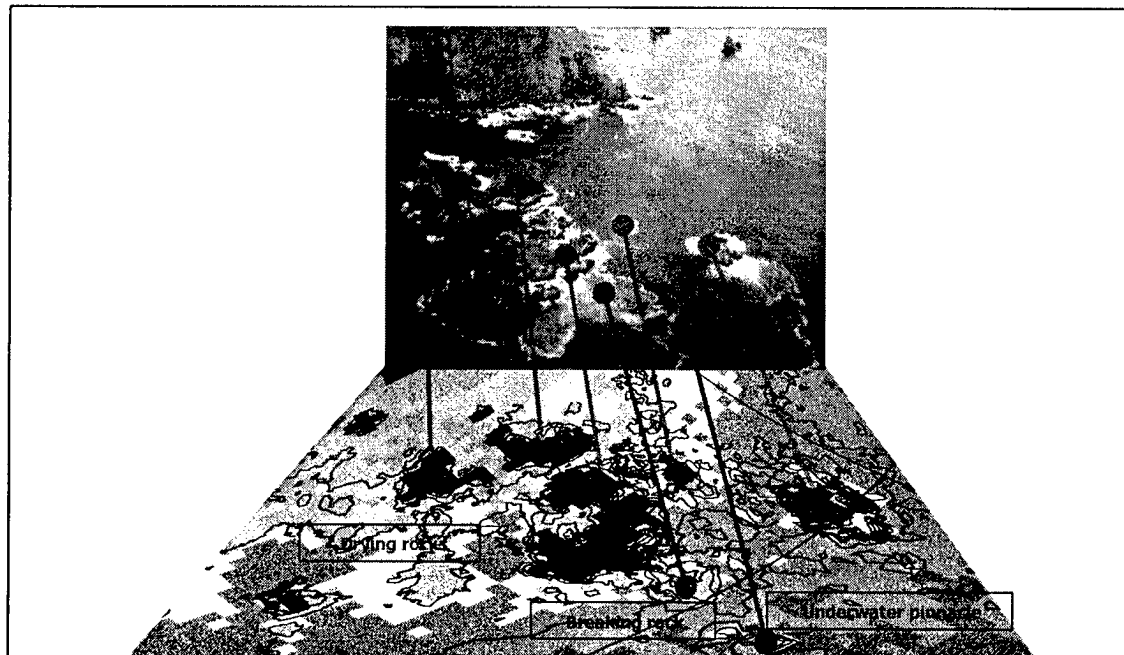


Fig. 14. Rock Complex, Solander Islands, New Zealand.

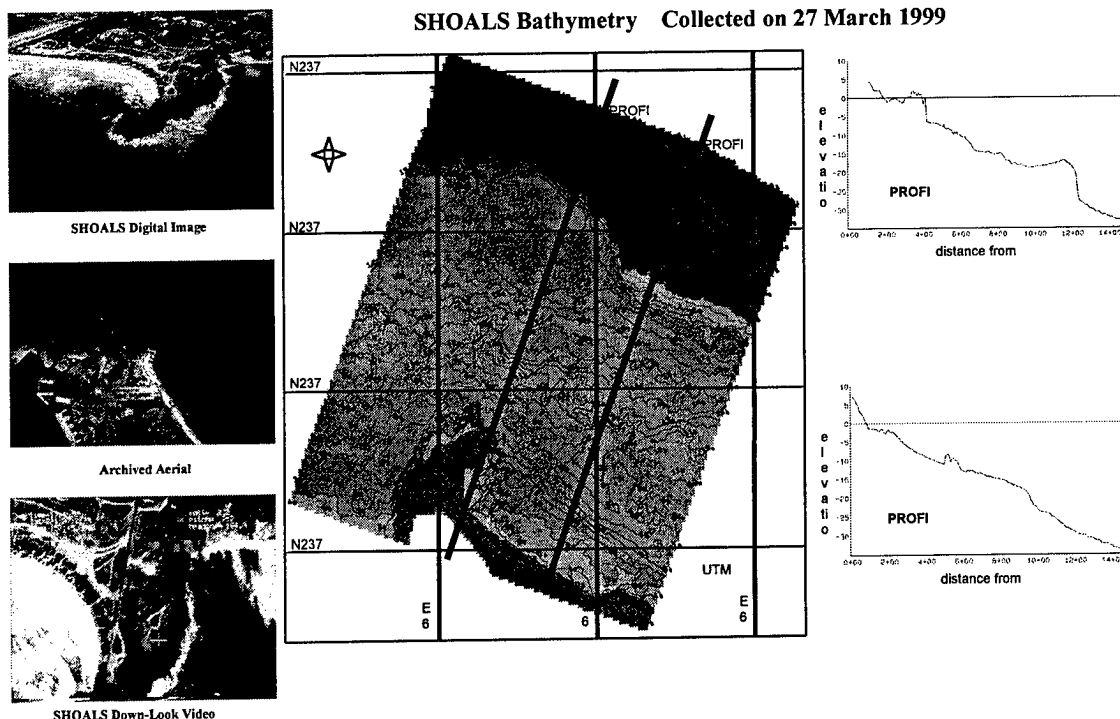


Fig. 15. SHOALS Rapid Amphibious Beach Survey (RABS) product.

The need to respond rapidly to evolving situations is not just the province of the warfighter, though, and SHOALS has now become one of the USACE's primary resources in the aftermath of hurricanes striking the southern USA. For example, in 1995, a Category 3 Hurricane, Opal, struck the Florida panhandle, causing widespread damage and reshaping of coastal features. At the time, SHOALS was engaged in routine surveys in New England but received an immediate call to assess the condition of East Pass Channel at Destin. In response, SHOALS had, by 5 p.m. on the second day after call, flown the survey; maps and volume calculations were generated and delivered less than 6 hours later.

X. Conclusions

The potential benefits of ALB are considerable and will continue to open up new opportunities in fields as diverse as regional sediment management and warfighting support. In the field of conventional hydrographic survey, ALB should become the tool of choice in clear, shallow waters that are noncritical to deep-draught navigation since it will usually achieve coverage rates several orders higher than current launch methods at less cost per square mile. Therefore, deployment of a survey launch in such waters is, by comparison, a waste of an asset and should be confined to high-resolution surveys or where Lidar is ineffective. Conversely, ALB has diminishing benefits in deeper water where multibeam fitted ships become steadily more efficient. Consequently, there are limited gains associated with increasing depth penetration of an ALB beyond 50m, unless there is also an increased swath width and/or speed of operation. Route surveys

where obstruction location is critical will continue to be the domain of high-resolution sidescan and/or mechanical sweep surveys. It still remains to be seen whether we have adequately defined the boundary between ALB capabilities and other surveying tools, but such characterization will to a greater extent be system specific. The result of this determination will not always be a simple and close integration of ALB, and conventional assets such as in New Zealand will often be mutually beneficial.

XI. References

- Axelsson, R., and M. Alfredsson, 1999. "Capacity and Capability for Hydrographic Missions," Proc. 1999 U.S. Hydrographic Conference, April 26-29, Mobile, AL.
- Green, K.G., 1998. "Florida's Beach and Inlet Management Program," Proceedings of the 67th Coastal Engineering Research Board, Fort Lauderdale, FL.
- Guenther, G.C., 1985. "Airborne Laser Hydrography: System Design and Performance Factors," NOAA Professional Paper Series, National Ocean Service 1, National Oceanic and Atmospheric Administration, Rockville, MD.
- Guenther, G.C., T.J. Eisler, J.L. Riley, and S.W. Perez, 1996. "Obstruction detection and data decimation for airborne laser hydrography," Proc. 1996 Canadian Hydro. Conf., June 3-5, Halifax, N.S.
- International Hydrographic Bureau. "Standards for Hydrographic Surveys," International Hydrographic Organization Spec. Pub. No. 44.

Parson, L.E., W.J. Lillycrop, and J.K. McClung, 1999. "Regional sediment management using high density Lidar data," Proc. Coastal Sediments '99, June 21-23, Long Island, NY.

Pope, R.W., B.A. Reed, G.R. West, and W.J. Lillycrop, 1997. "Use of an airborne laser depth sounding system in a complex shallow-water environment," Proc. Hydrographic Symposium XVth Int'l Hydro Conference, April 21-22, 1997, Monaco.

Riley, J.L., 1995. "Evaluating SHOALS bathymetry using NOAA hydrographic survey data," Proc. 24th Joint Mtg. of UJNR Sea-Bottom Surveys Panel, Nov. 13-17, 1995, Tokyo, Japan.

Watters, T., and C.E. Wiggins, 1999. "Utilization of Remote Sensing Methods for Management of Florida's Coastal Zone," Proc. 1999 U.S. Hydrographic Conference, April 26-29, Mobile, AL.

West, G.R., T. Graham, K. Smith, and J. Spittal, 1999. "Improving the efficiency, safety and economy of the New Zealand National Charting Programme through the integrated use of Lidar in a multi-sensor surveys," Proc. 1999 U.S. Hydrographic Conference, April 26-29, Mobile, AL.

BEACH AND NEAR-SHORE CRAWLING UUV FOR OCEANOGRAPHIC MEASUREMENTS

J.C. Evans, J.S. Smith, P. Martin, Y.S. Wong

Department of Electrical Engineering & Electronics
The University of Liverpool
Liverpool L69 3GJ, United Kingdom
E-Mail: evansjon@liv.ac.uk

Abstract

This paper gives an overview of the design and operational details of a Beach and Seabed Crawler UUV (Unmanned Underwater Vehicle) constructed to make oceanographic measurements in tidal shore environments. Currently, there is no established way of rapidly collecting data in near-shore and surf zone environments. The ability to move instruments quickly to a series of known locations within a single tidal cycle (7 or 13 hours), and to accurately repeat / return to known locations on a shore, hugely increases the value of such oceanographic measurements.

To meet this need, a twin-tracked crawling vehicle with a range of standard vehicle and oceanographic instruments has been constructed. The vehicle was recently used in Portugal as part of the two month fieldwork programme of the INDIA (Inlet Dynamics Initiative Algarve) project. The focus of INDIA is the oceanographic study of a small, tidal, highly dynamic, multiple-inlet system in southern Portugal, and includes partners from the UK, France, Netherlands, Portugal, USA, Australia, Korea, and Poland. This paper describes the electrical and mechanical features of the crawler, and the measurements taken as part of the fieldwork trials.

I Introduction

Seabed crawling vehicles make up only a small minority of the underwater vehicles in operation today. Most UUVs (Unmanned Underwater Vehicles) are free swimming and are used extensively in offshore oil and gas production, and increasing in marine environment studies. The crawling vehicles that are in use are typically work-class vehicles (weighing many tonnes) used for seabed trenching and cable burying.

Oceanographic scientists working in shore environments currently mount instruments on poles buried or fixed on the beach at low tide, or (in deeper water) on platforms dropped to the seabed. As most, the beach-deployed instruments can be moved every tidal cycle (13 hours), though more typically every few days. With submerged platforms, instruments are deployed to a single location for perhaps months at a time.

Ideally, the scientists would like to move the instruments

to several locations during the same tidal cycle, perhaps returning to each location two or three times in the cycle. By repeating the whole process at a different location the following day, a complete survey of the environment can be assembled, allowing them to investigate the effects of sediment transport and wave-current interaction.

The BSC vehicle is a unique design, with the aim of providing a mobile deployment platform for oceanographic instruments. It incorporates several novel features that facilitated rapid construction and minimised costs. Fig. 1 shows a photograph of the BSC during field trials in March 1999 and gives some idea of scale. Fig. 2 shows a close up of the vehicle.

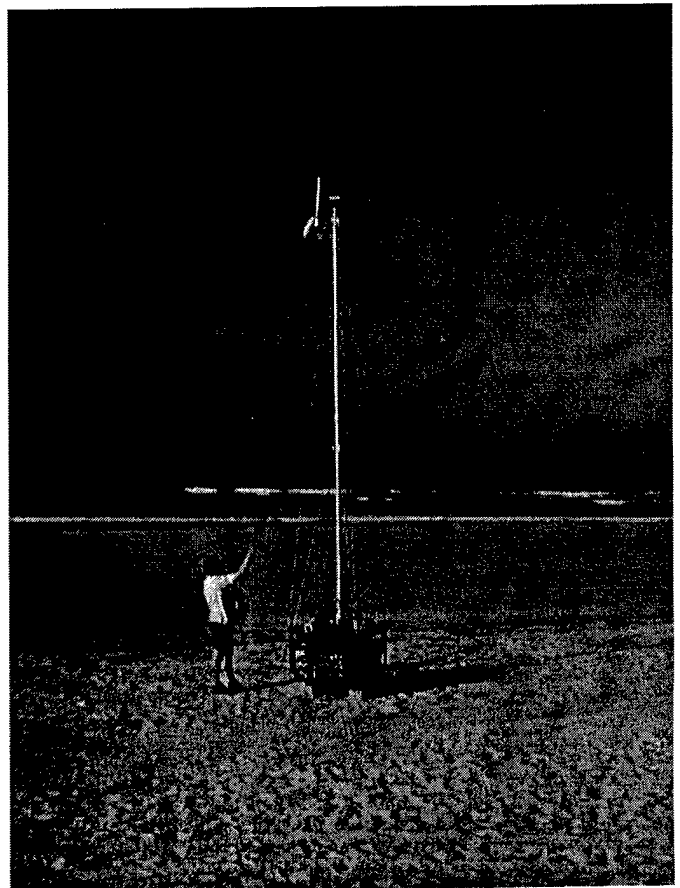


Fig. 1: BSC (Beach and Sea-bed Crawler) with 6m GPS Mast on Field Trials in Portugal

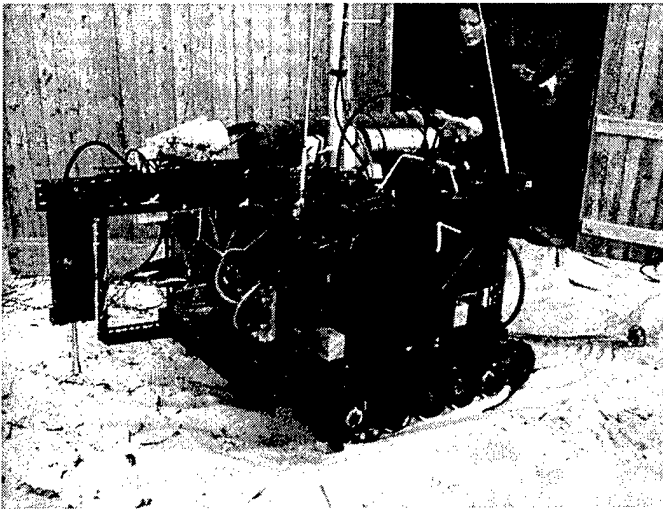


Fig. 2: Close up of the BSC Vehicle

II Vehicle Sub-Systems

A Overview

The focus of the INDIA (Inlet Dynamic Initiative Algarve) project is the oceanographic study of a small, tidal, highly dynamic, multiple-inlet system in southern Portugal. An overview of the whole INDIA project can be found in [1]. As part of the INDIA project, the design of BSC Vehicle (Beach and Seabed Crawler) was constrained by the budget and time-scales set out in the overall project. This is important since the 12 months and UK £60K (approx. US \$100K) had a strong influence on the design and the choice of both off-the-shelf mechanical and electronic components. This has led to a dual PC design incorporating an embedded PC on the vehicle, and standard PC workstation as the pilot's top station. The vehicle is linked to the surface via a 500 metre umbilical cable carrying: 2 independent 240V AC circuits; a 10 Mbit/s Ethernet link; 2 video channels for onboard video cameras; and 3 bi-directional RS422 differential serial communications links. A standard Honda 4.5KW, 240VAC petrol generator powers the entire system. The vehicle and the supporting hardware can be deployed without the need for heavy lifting equipment, and can be easily managed with a team of three.

The following sections provide a description of the various aspects of the BSC vehicle.

B Mechanical

After an initial study to determine the time and costs of manufacturing a completely new tracked suspension unit, the decision was made to use a Honda "Power-carrier". This could then be "cannibalised" to form a basic starting point for the mechanical design (see Fig. 3). The "Power-Carrier" is a petrol driven horticultural vehicle, twin tracked with a frame strong enough to carry

>500Kg up steep (>25%) slopes. Its tracked design gives it good traction, even on the softest sand, and will survive extended periods of submersion if washed down with fresh water after removal from the sea. This approach gave the advantage of an off-the-shelf solution for the tracks and drive train, and allowed the mechanical design to concentrate on conversion to a precision controlled electric drive and suitable watertight enclosures.



Fig. 3: Basic vehicle chassis at early stage of assembly

The space requirements of the electric drive (see section C), and stability considerations, required the vehicle to be widened from 0.55m to 1.0m. On top of this base is a metal frame designed to safely distribute the load of the 6 metre aluminium mast (with GPS antenna). The frame is designed to withstand the maximum loading (approximately 11 tonnes) from the mast when then rigging wires are fully tensioned.

The electronics are contained within three watertight enclosures: two cylinders containing the embedded PC, interface electronics, internal sensors, and power electronics for the electric drive; and a third custom enclosure designed to house the stepper motors and gearboxes. The pressure rating of all the watertight enclosures is in excess of 100 metres.

C Drive System

The design of the electrical drive system is a compromise between power consumption, load carrying capability and the maximum speed of the vehicle. The lack of mains electricity at the fieldwork site and cost, meant that a hydraulic or 3-phase solution was infeasible. Brushless DC servomotors were considered, but the final design used two relatively small stepper motors (Pacific Scientific K33HLFL-LNK-NS-00) with 15:1 reduction gearboxes (Bayside right-angle gearboxes RA90-15). The output shafts of the gearboxes are coupled to the drive sprockets of the left and right tracks (see Fig. 4). The arrangement will generate about 1hp per track.

The drive system uses Parker Automation Ministep

CD80M drivers connected to an I/O card frequency generator controlled by the embedded PC. This allows precision control of the drive system using software running on the onboard PC, or from the top-station PC via the 10 Mbit/s Ethernet communications link (see section D). Each track can be controlled independently, both forwards and backwards, giving a zero turning cycle (i.e. the vehicle can rotate to any heading on the spot).

Typically vehicle speeds are in 0.1 m/s to 0.5 m/s, however absolute top speed is less important than many underwater vehicles since the oceanographic instruments require the vehicle to be stationary while sampling. In addition, the drive system has been optimised to provide low speed torque at the expense of top end speed. This is essential on soft sand beaches.

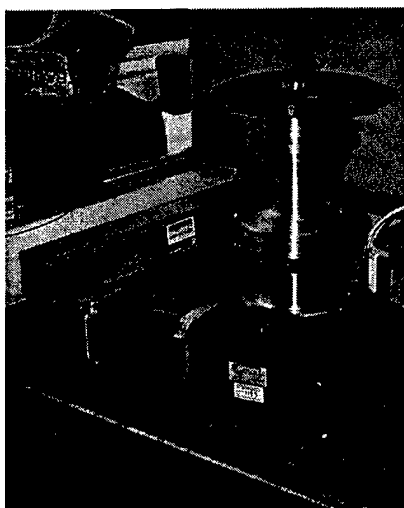


Fig. 4: Single Motor Unit with Right-Angle Gearbox and Drive Sprocket

D Electronic and Computer Systems

A schematic of the electronic systems is shown in Fig. 5. The vehicle and its top station essentially form a two PC LAN linked via the 500-metre umbilical.

Standard embedded PC components were used to build the Intel P-233 MHz based machine. The PC runs Windows NT to allow standard PCI-based I/O, video capture and network cards to be used. The choice of Windows NT for an embedded design is unusual. It was chosen because NT driver support is now standard for almost all card manufacturers, and allows industry standard development tools such as Visual C++ to be used. This use of standard hardware and development tools, resulted in rapid prototyping and testing of the BSC's computer systems.

Communications between the top station and vehicle uses standard TCP/IP protocols. By using standard high-level OS functions calls, the software design can assume that all low-level error detection / correction / retransmission is handled by the OS (with various exceptions raised if certain quality measures are not

met). Again, this leaves the software design to concentrate on data validation (i.e. does the received data make logical sense), and speeded the development process.

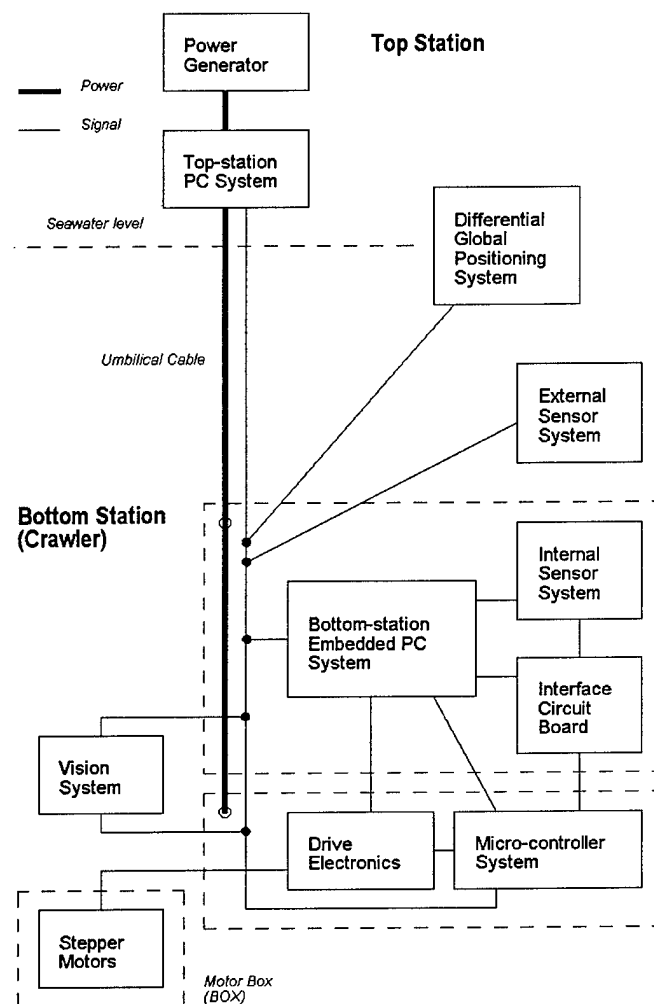


Fig. 5: System Diagram

The vehicle is fitted with various sensors that help provide real-time feedback to pilot, as well as essential information when post-processing the data logs for use with the external oceanographic instruments. The internal sensors include: KVH C100 flux gate compass; two Lucas Control Clinometers (for pitch and roll); water pressure transducer (for depth and wave turbulence); temperature; internal humidity sensor (acting as water ingress alarm). All these sensors are connected to the onboard PC, and their readings passed to the top station PC for logging, and display on the Pilot Console.

The top station is a standard PC workstation running Windows NT. The Pilot Console software (Fig. 6) allows the operator to monitor the vehicle's various systems, and drive the vehicle using the joystick. The Console software also allows the operator to start and stop the various data loggers, and control the external instruments that require an external timing trigger.

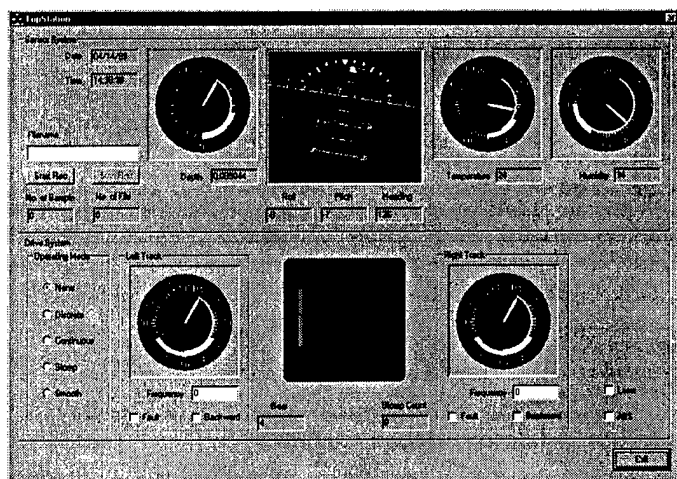


Fig. 6: Screenshot of Pilot Console running on Top Station PC

E RTK GPS System

One of special features of the BSC is its navigation system. When deploying instruments conventionally, perhaps to securely fixed poles, they are surveyed in. This may involve a conventional theodolite survey, or perhaps DGPS fix. The aim to the BSC vehicle within the INDIA was to investigate the use of a mobile deployment platform. It was an essential requirement of the oceanographers that the position of all the measurements were known as accurately as possible, ideally. This is not possible using standard DGPS, which has a positional accuracy between 1m and 5m.

The latest state-of-the-art differential based GPS equipment support dual-band L1 / L2 phase-based corrections. Commonly known as RTK (Real Time Kinematic), this equipment provides a 3D fix to centimetre accuracy, up to 5Hz. Since it is a differential based system, a base station must be established within a few kilometres at a known position, and a communication path to transfer the RTCM-104 correction data established (see Fig. 7).

The BSC vehicle is fitted with a Trimble 7400 RTK receiver, and can be configured to receive the RTCM correction messages via the umbilical cable, or via a UHF radio modem. The waterproof UHF antenna is mounted with the L1 / L2 GPS antenna on top of the 6 metre mast. The unique mast and rig design supports the antenna clear of the water, and provides ultra-accurate positioning of the vehicle in water up to 6 metres deep.

Standard GPS navigation software was used to navigate the vehicle around the field site. In addition, the 3D positional fix was logged, along with the data from the other sensors and instruments for detailed analysis. The accuracy of the fix is such that the roll and pitch of the vehicle can be corrected for to give the absolute position of the instruments.

The ability to rapidly deploy oceanographic instruments to several locations (included those below the low water mark) and move them with such accuracy to several locations within a tidal cycle is, we believe, unique.

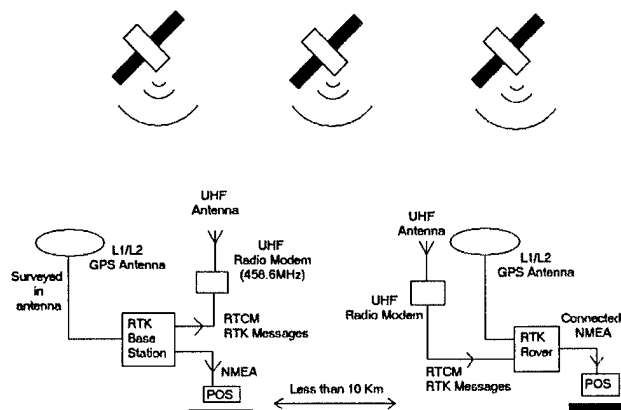


Fig. 7: RTK system diagram

III External Sensors Systems

Since the mid 1980s, interest in sediment movement has focused on quantifying the effects of turbulent currents and wave action, and their combined effect on the transport of sedimentary material. To measure the effects of these processes requires techniques that have sufficient resolution to resolve the fine scale processes involved. To achieve this, it is necessary to measure both the 3-dimensional flow characteristics of the water, and to quantify the amount of material in suspension.

The BSC was fitted with instruments to measure both of these properties: Acoustic Back-Scatter (ABS) and Optical Back-Scatter (OBS) systems to measure the suspended sediment; together with an Acoustic Doppler Velocimeter (ADV) to measure the flow characteristics. The philosophy of the BSC design means little or no modification is needed to external instruments, or their software, for deployment on the BSC vehicle.

A ABS: Acoustic Back-Scatter

ABS instruments have become established as a way of obtaining high quality measurements of the sediment in suspension. Excellent papers covering the acoustic properties of the instrument, and its use in oceanography can be found in [2] and [3].

The typical mode of operation of ABS systems is to mount a downward looking transceiver, between 1m and 2m above the bed. The transducer typically operates in the range 1 - 5 MHz, and the transmitted pulse is in the order of several microseconds in duration. As the sound propagates from the transceiver to the bed, the envelope of the back-scattered signal is recorded. This record is used to obtain information on the material in suspension.

The great advantage of acoustic measurement is that it provides suspended sediment profiles unobtrusively and remotely. The temporal and spatial resolution of the instrument allows examination of "within wave" and turbulent sediment processes.

The BSC vehicle was fitted with three ABS transceivers, operating at 1MHz, 2MHz and 4MHz. All three were mounted as close as possible (to measure the same column of water), and in a known (close) configuration to the OBS and ADV. The trigger for the ABS data-logging cycle could be synchronised with the other instruments from the Pilot Console software. However, other than providing DC power and the trigger signal, no modifications to the ABS were needed. This is part of the BSC philosophy, i.e. that conventional instruments can be deployed using the BSC with little or no modification.

B OBS: Optical Back-Scatter

Miniature Optical Back-Scatter instruments are another established method of quantifying the amount of suspended sediment. The BSC was fitted with three OBS sensors arranged in a vertical log-spaced profile, connected to a Marine Data System data-logger. Data acquisition was synchronised using the GPS time signal. Except for DC power, no modifications to the OBS was needed for deployment. After the vehicle's return, the recorded data can be downloaded and later correlated to the data from the other instruments.

C ADV: Acoustic Doppler Velocimeter

ADV is a relatively new instrument that offers highly accurate three-dimensional flow measurements at high sampling rates, with a small sample volume. An excellent evaluation of the ADV in field experiments can be found in [4].

The ADV was originally developed for use in physical model facilities [5]. It operates using the Doppler shift effect, implemented as a bistatic (focal point) acoustic Doppler system. It consists of a 10MHz transmitter and three receivers positioned at 120° intervals, 30° from the vertical axis of the transmitter. This focuses the sampled volume approximately 10.8 cm from the probe.

The probe is submerged in the flow, and the transmitter gives short acoustic pulses along the transmit beam. As the pulses propagate through the water column, a fraction of the acoustic energy is scattered back by small particles suspended in the water. The phase data from successive coherent acoustic returns are converted into velocity estimates in each of the three directions.

The BSC was fitted with a Nortek ADV. Its serial communications interface was wired onto one of the umbilical's bi-directional twisted pairs. This allowed the ADV's standard PC-based data acquisition software to be run without modification on a laptop back at the pilot's control cabin. The ADV software gives an instant, real-

time display of the water velocity and is very useful in monitoring the status of the vehicle with respect to the current.

D LBS: Laser Bedform Scanner

This is a new instrument being developed at Liverpool. It uses the principle of "laser line deformation" to measure small (a few centimetres) differences in seabed height. The principle is illustrated in Fig. 8. The laser line is projected about 50cm in front of the vehicle. A CCD camera in a separate watertight housing observes the scene from a slightly offset viewpoint. This difference in viewpoints causes a perceived vertical displacement of the laser line as it passes over the non-uniform surface. Since the amount of displacement is proportional to the difference in height, the relative height of every point in the line can be calculated. As the vehicle moves forward, changes in the line's profile reflect the changing bedforms. Conventional image processing techniques are used to threshold and identify the position of laser line. This can be done at full video rates (25Hz), and the resulting data when combined with the RTK-GPS position, can be used to build large-scale 3D maps of seabed. A detailed discussion of the principles behind laser line deformation can be found in [6].

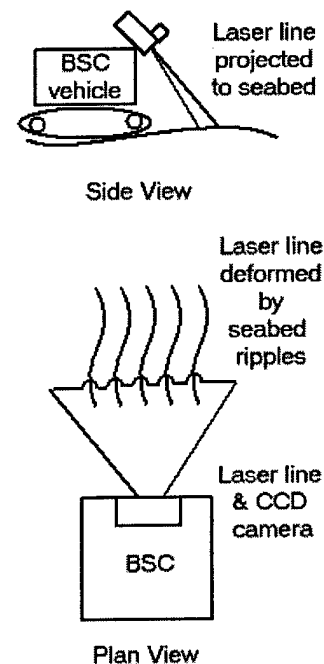


Fig. 8: Diagram of Laser Scanner Assembly

Problems with the video system in Portugal meant no data from the LBS was recorded. However, further fieldwork trials in the UK are planned for Summer 1999 to help us evaluate the performance of the LBS system. We are also experimenting with building Virtual Reality (VR) models of the data sets, to aid the visualisation of the seabed data.

IV Field Trials: Ancão Inlet, Faro, Portugal

The INDIA project is focused on a large, tidal, highly dynamic, multiple-inlet system in southern Portugal, and includes partners from the UK, France, Netherlands, Portugal, USA, Australia, Korea, and Poland.

As part of the INDIA project, the BSC vehicle was deployed at the Ancão Inlet, near Faro. This inlet was artificially opened in June 1997. The INDIA project has been studying its development, and modelling the coastal processes at work. The overall aim is to better understand the general processes at work on this type of coastline, typically of main places in Europe, North America, and Asia.

Over the 2 years since the Ancão Inlet was opening, natural sediment transport process have widened the inlet to 350 metres, and are now causing its migration eastwards along the coast. There is a typical tidal range of 4 metres, with peak currents in the inlet over 5 knots (10 m/s).

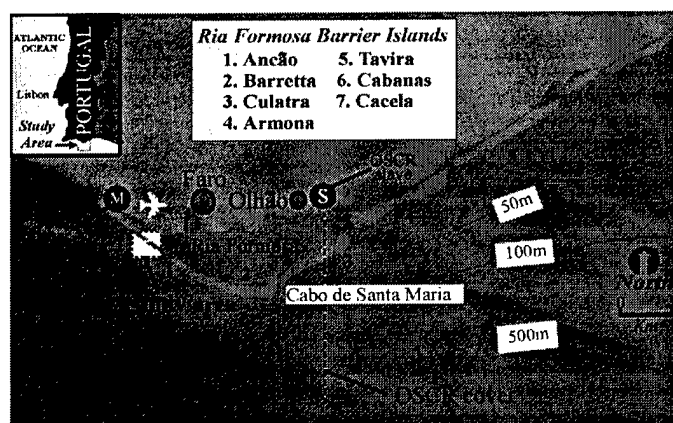


Fig. 9: Map of the Ria Formosa Inlet System, Southern Portugal



Fig. 10: Aerial Photograph of the Ancão Inlet

During the INDIA fieldwork period of January to March 1999, the BSC vehicle performed field trials to evaluate its performance as a mobile platform for instrument

deployment. The BSC fieldwork team worked out of fixed base (fieldwork hut), and were able to perform sample transects in the lagoon, across the inlet and in the surf / swash zone on the seaward beach.

The instrument sampling regime was 20 minutes of data collection, on the hour and half-hour. This left 10 minutes to move the crawler to the next sampling location. This was achieved using the RTK GPS equipment, with some visual adjustment via radio from spotters on the beach to the pilot. Sampling was over half (7 hours) and full (13 hours) tidal cycles, with the crawler returning to the same locations to make several readings over the cycle.

With a rigid mast (3m or 6m), and 1.0 m x 1.3m footprint, stability was always going to be an important issue. The BSC performed well in both the lagoon and inlet, in currents up to 4 knots (2 m/s). Traction was good both on the beach and in the water (with very soft, saturated sand sea floor), with the vehicle remaining stable on slopes up to 30°. Much greater problems were encountered in the surf, because of the huge shock force experienced by the waves breaking. It was impossible to launch in breaking wave heights greater than 0.5m with mast. In tests without the mast and rig (i.e without the GPS antenna), it was still too difficult to travel the 150m plus to get the crawler beyond the (more typical) 1m - 2m high breakers. This goes to emphasise the extreme forces exerted by breaking waves. Performance in the lagoon and inlet leads us to believe that if the crawler could have got beyond the surf zone, it would have had fewer problems moving about the sea floor at greater depths. However, with breaking surf of any significant size the simple approach of "driving through the waves" will not work, especially with the GPS mast attached.

In addition, a problem with drive assembly and tracks became apparent during the field trials. Our design estimates of the power output of the vehicle had predicted that, although not overpowered, the low-speed torque (via the reduction gearbox) should have been sufficient to turn the track under most conditions. However in the field, the vehicle seemed under-powered especially compared to a petrol driven (but similarly rated) "Power Carrier" being used to move equipment around the fieldwork site.

Both tracks, but particularly the right track seemed to jam under quite modest conditions (for instance, climbing soft shallow slopes). This was worse in the dry compared to in the water, but still below our exceptions. This was eventually traced to an error that was made during final assembly. A small misalignment of the rear motor and gearbox assembly had led to a metal-on-metal friction contact between the gearbox housing and one of the track's guide wheels. As sand was thrown up from the beach, it increased dramatically the energy wasted in turning the track wheel against the gearbox housing. Inevitably, this caused the track to stall under demanding conditions. We estimate that more than 30%

of the available power was being lost. Unfortunately, to correct this problem would have required a workshop to strip down the vehicle. This was not possible, but since the stalling was less of a problem in the water (due to the sand being washed out more quickly) it did not interfere too much.

Since our return, the logged data from both the on-board sensors and external instruments has now error checked and has gone through the first stages of quality exception tests. An example of this is shown in Fig. 11. This graph shows the recorded value of the pressure transducer (depth sensor) over a full tidal cycle. The 20 minutes of stationary data collection, followed by 10 minutes of vehicle movement to new location can easily be seen in the general form of the graph. The arc of the graph during the 20-minute sampling periods is caused by the incoming, and then outgoing tide.

All the data has now been entered into the INDIA project database, together with the data collected by the other groups. It is hoped that it will contribute to the models of the inlet system, and help predict how it will evolve in the future.

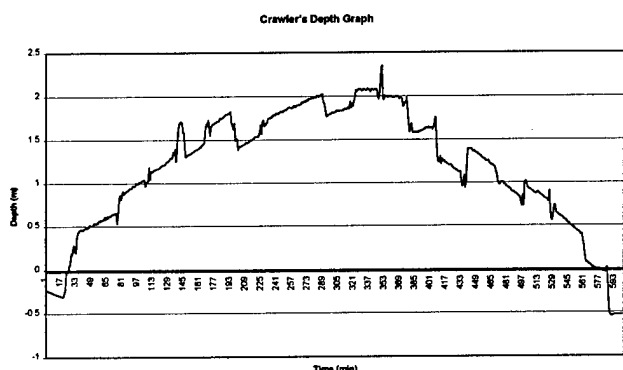


Fig. 11: Graph of Recorded Pressure (Depth) over a 13-hour Tidal Cycle

V Conclusions and Future Work

Although the BSC vehicle was successfully deployed during the INDIA fieldwork campaign, certain problems did become apparent. The metal-on-metal contact that causing significant power loss from the drive system has now been rectified. Interference problems on the video signals, which prevented the use the LBS in Portugal, have also been resolved. There are still issues of stability, particularly in the surf zone when operating with the mast. We are considering the use of ballast and stabilising "out-riggers" in such conditions. However, we were pleased with the vehicle's stability in high current conditions (experienced at peak flow in the inlet), and on slopes up to 30°.

As to future work, in the short term the BSC is being prepared for some field trials in a large estuarine environment in the UK. The aim is to evaluate improvements to vehicle's control software, and in obtain

some real field data with the Laser Bedform Scanner (LBS).

In the medium term, we are looking into semi-autonomous and autonomous navigation for the BSC. The aim would be to allow the vehicle automatically navigate its way to sites for data collection. The pilot would be able to specify locations the vehicle should move to, describe the sampling regime, how often it should return to a particular location. Autonomous navigation would also be very useful in systematic seabed surveys with the LBS system.

In the longer term, we are looking into umbilical-less operation using on-board batteries and a high-speed radio data link. We are also considering the problem of accurately positioning the vehicle at greater depths without a mast, perhaps using a floating GPS buoy, or a Sonar Positioning Net (SPN).

Although the BSC vehicle was designed to meet the needs of the scientists working on INDIA project, it was always a specific design goal to create a vehicle with enough flexibility be used in different situations in the future. We have already had some enquiries from other oceanographic and marine engineering groups in Europe and the USA. We would be happy to hear from any groups who would be interested in making use of the BSC as mobile deployment platform.

References

- [1] Williams, J. et al, "Inlet Dynamic Initiative: Algarve (INDIA)", Coastal Sediments '99, New York, Jun 1999, pp 612-627.
- [2] Thorne Peter D. and Hardcastle Peter J, "Acoustic measurements of suspended sediments in turbulent currents and comparison with in-situ samples", J. Acoust Soc. Am., 101 (5), Pt. 1, May 1997, pp 2603-2614.
- [3] Thorne Peter D. et al, "Analysis of Acoustic Measurements of Suspended Sediments", J. Geophysical Research, Vol. 98, No. C1, Jan 1993, pp 899-910.
- [4] Voulgaris G. and Trowbridge J. H., "Evaluation of the Acoustic Doppler Velocimeter (ADV) for Turbulence Measurements", Journal of Atmospheric and Oceanic Technology, Vol. 15, Feb 1998, pp 272-289.
- [5] Kraus N. C. A. et al, "New acoustic meter for measuring 3D laboratory flows", J. Hydraul. Eng., 120, 1994, pp 406-412.
- [6] White R.A., Smith J.S. and Lucas J., "A vision based gauge for on-line weld profile metrology", Proc. IEE Science, Measurement and Technology Vol. 141 No 6, 1994 521-526

Acknowledgements

The INDIA project is supported in part by The Commission of the European Directorate General for Science, Research and Development under Contract **MAS3-CT97-0106**.

We would like to thank **everyone** who provided help and invaluable advice both during construction and in Portugal. Our special thanks go to Jon Williams, Kevin Keller, Zoe Hughes, Steve Mack, Ian Kelly and Ian Edwards.

Development of Deep Sea Free Swimming ROV "UROV7K"

Taro Aoki, Takashi Murashima, Satoshi Tsukioka,
Hidehiko Nakajoh, Masahiko Ida

Japan Marine Science and Technology Center(JAMSTEC)
2-15 Natsushirna, Yokosuka, 237 Japan

Abstract

A free-swimming vehicle UROV7K has been developed since 1996. This vehicle is equipped with a high quality and high-speed communication system for wide frequency band devices such like TV cameras, obstacle avoidance sonar and manipulator. Using with the expendable optical fiber cable, the cable is one millimeter in diameter and stored in a spooler such like a fishing reel. The lithium-ion battery which is rechargeable and immersed in oil, has been developed for this vehicle. Its capacity is 100V 60Ah. The big cable store winch, traction winch and high voltage power source are not necessary for this system.

The vehicle was able to dive to more than 2000 meters in depth and swim for 90 minutes December 1998. We have a plan to dive this vehicle up to 7,000meters in depth July 1999.

I. INTRODUCTION

ROVs (Remotely operated vehicles) which have received a power supply and have data communications through tether cables linked the vehicles with the support ships, are generally used at present.

The tether cables are valuable in both supplying sufficient power to ROVs and which enable them to making high speed communication such as video signal transmissions between support ships and underwater vehicles. However, because activity of the vehicles must be reduced, and the cable handing onboard equipment such like a cable store winch or traction winch are big.

On the other hand, cableless under water vehicles (AUVs), which could move freely without restriction. However, these vehicles cannot make effective investigations by means of real time moving pictures of the sea floor, because of their inability to transmit high speed signals such as videos, and are weak in works using with manipulators.

In addition AUVs can only perform limited operations, and are unable to respond with precision and flexibility to all the users' needs. Given these limitations, AUVs cannot

take the place of ROVs.

The authors have been developing ROV "UROV" (development code name) system using with the expendable optical fiber cable. This system can provide both high maneuverability and high speed communication. In other words, it can simultaneously provide advantages of both cabled ROVs and uncable ROVs (or AUVs).

Since 1987, the UROV2000, which could descend to 2000m from the sea surface, had been developed as a prototype, and had been used for the study of creating an evolutionary system corresponding to various needs. UROV500 was the first UROV system developed for practical use, investigation for fishes or crabs in Japan Sea. Since 1996, we have been developing a 7,000meter class UROV.

II. OUTLINE OF UROV SYSTEM

The vehicle has a single optical fiber whose diameter is smaller than 1mm. This single optical fiber is the sole link between the vehicle and the support ship, and high speed data communications are possible through this optical fiber. The operator controls the vehicle on the support ship by observing video pictures. It is unnecessary to supply any power from the support ship because the vehicle has secondary batteries as energy source. .

This UROV system has three spoolers. The two of them are put on the vehicle, and another one is overboard on the support vessel. In one spooler, the optical fiber is wound 10,000meter. The fiber is smoothly loosen out from the spooler in its axial direction with slight tension. The two spoolers on the vehicle connected in series, are connected one on the support vessel. During operation, the vehicle moves around leaving the optical fiber loosen out from the spooler, enabling the vehicle to carry out long distance cruising of over 30,000m away from the support ship with high maneuverability, because of little cable drag. Accordingly, it is possible to investigate a submarine-volcano or a bomb, above which support ship can not stay with safety.

At the beginning of the operation, the vehicle is launched

from the support ship loaded with two kinds of ballast. The vehicle descends from the weight of these two ballast weights and after reaching the destination depth, it releases one of them. By adjusting the weights, the vehicle can achieve neutral buoyancy without the left ballast while surveying at the destination. After cruising, the vehicle releases another one to get positive buoyancy, and ascends to the surface where it is recovered. At the same time, the optical fiber can be cut with an optical fiber cutter placed at the top of the spooler on the vehicle. In this system the optical fiber is expendable, so fiber troubles cannot do any damage to the whole system. This means the vehicle can make its way even through the complicated structures.

3. SPECIFICATION OF UROV SYSTEM

Table 1 shows the major features of UROV7K. The system can be operated with a small ship because the system does not need large on-board equipment such as a cable store winch or a power supplier.

The onboard system consists of an optical data transmission unit, two computer units, a joy-stick controller box, acoustic positioning CRT, obstacle avoidance sonar CRT, video monitors, VTR sets and status indicator units.

4. SYSTEM COMPONENTS OF UROV7K

4-1. OPTICAL FIBER SPOOLER

The optical fiber is broken down at a tension of about 5kgf, and is also easily broken down by bending or kinking. The equipment is necessary for the UROV system to allow the optical fiber to be drawn out smoothly under lower tension.

When using a rotary type drum, the momentum and friction will create huge tension. Moreover, in that case, to use a rotary connector is necessary and this increases the optical loss.

To solve this problem, a non-rotary type optical fiber supplier "spooler" has been developed and is used in the UROV system. The spooler is designed to avoid applying a high level of friction on the optical fiber. The tension needed to draw the fiber out of the spooler is about 10gf, as measured in a free fall test in a pool.

During operation, to avoid the optical fiber being overdrawn, a braking device is placed on the spooler to adjust the tension needed to draw out the fiber. The spoolers are located on both the vehicle and the ship to reduce the possibility of the fiber being severed even if it is caught by something on the sea floor.

An optical fiber cutter is also located at the top of the spooler, so that the operator can cut from a remote distance.

4-2. OPTICAL DATA TRANSMISSION SYSTEM

Water pressure, tension and bending affect the optical power loss. Therefore, the transmission method must be one that can work under variable optical loss.

In order to send all the data through a single optical fiber, there must be no more than two optical channels (uplink and downlink), due to the wavelength division multiplexing method.

Uplink data consists of three channels of video signal and other sensor signals, such as a depth sensor and a direction sensor. The pulse coded modulation (PCM) method has been adopted to send the signals because of its simple construction and high endurance against change in optical loss. The sensor signals are multiplexed electrically with the video signal. Using this method, the number of uplink optical channels is reduced to one.

On the other hand, control signals are sent to the vehicle as one channel (downlink) using the pulse code modulation (PCM), time division multiplex (TDM) method because of the easy interface with the CPU unit and high endurance against change in optical loss. Measurements show that loss change allowed with the system is about 10dB, which reveals there would be no problem for practical use.

4-3. CONTROL AND DATA PROCESSING SYSTEM

UROV7K has a control and data processing system using micro computers on board. This system processes the joystick controller data and controls the rotation of the motors of the thrusters, and it can also perform automatic depth and direction hold operations. Uplink data such as depth, water temperature, and direction are indicated by seven segment LEDs, although battery power.

As a self-diagnosis function, this system informs the operator with an alarm lamp when optical or electrical signals cease. Moreover, when water leakage into the pressure housing is detected, this system not only inform but also releases the ballast automatically, to enable the vehicle to surface quickly before it loses sufficient buoyancy.

When the optical fiber is accidentally cut, the vehicle loses control and it is impossible to draw the vehicle up because no tension member exists. To ensure the vehicle can be retrieved even in such an event, the vehicle is designed to automatically switch off all of the equipment

and release the ballast five seconds after the optical signal from the ship ceases.

4-4. POWER SOURCE

The power source is one of the most important in providing practical UUVs or AUVs without power cables. The types and capacities of power sources should be determined according to the operational conditions of the systems. A pressure-balanced secondary battery is a suitable energy source for the UROV7K system because it is rechargeable, light and safe. Among these types of batteries, Li-ion battery is used because of its long life, ease of handling, and high energy density. These batteries supply 100V of power for the thrusters and halogen lights, and converted to several voltage level power sources for the control unit, cameras, and other sensors. Necessary capacity to carry out a three hour operation on sea floor are appraised at less than 60Ah.

4-5. THRUSTERS

The vehicle has two vertical thrusters (600W each) and two horizontal thrusters (600W each) oilfilled, pressure-compensated DC brushless motors are used because of their small size and high reliability. Their rotation speeds are controlled with the onboard computer using the pulse width modulation (PWM) method.

4-6. BALLAST DEVICES

The vehicle has two kinds of ballast devices. One is loaded to put weight on the vehicle for descent, and by releasing this ballast, the vehicle achieves neutral buoyancy. The other is loaded to keep the buoyancy neutral while cruising the sea floor, and releasing this ballast gives the vehicle positive buoyancy to ascend. In the UROV7K system, descent weighs about 200kg and the other for ascent weighs about 150kg. Small steel balls (2~3mm in diameter) can be used. for the ballast weights. The ballast balls are contained in hoppers and it is released by opening the bottom lid. This method is relatively safe the ballast should be released accidentally on board, and the weight is easily adjustable. Electromagnets are used to take on and release the ballast. In this case, residual magnetism acts to prevent the ballast from being released, so the magnetism eraser circuit, which reverses the direction of current repeatedly, is used to ensure the release.

5. SEAGOING TESTS AND PRACTICAL OPERATIONS

Seagoing tests were carried out in December 1998, with JAMSTEC's "YOKOSUKA" as the support vessel at Sagami Bay and Suruga Bay. The Li-ion batteries fast charging capability allowed a operations per day, so four test dives of about two or three four each could be carried out in five days. The vehicle reached the maximum depth of 2,111m.

It was shown that the automatic direction holding system could hold the vehicle's heading direction. Distinct

color video pictures of the sea floor proved its ability to make effective investigations.

In one test, the optical fiber was broken to examine the security functions for vehicle recovery. As soon as the optical fiber was cut, the vehicle released the ballast and ascended to the surface automatically. It showed that the system worked reliably, in accordance with its design.

After some adjustment in improving the system, next operations will be carried out in July 1999 at Japan Trench.

6. CONCLUSIONS

UROV system has developed as a easy-use, high performance submarine robot system, applying an optical data transmission technique. It shall be available not only for simple investigations of marine resource, but also for various studies or work in the marine field.

In the future, UROV7K will be examined to consider the feasibility of equipping with a autonomous abilities or some sensors for underwater science, and to study improvement to create a more evolutionary system.

REFERENCE

1. T.Aoki, S.Tsukioka, M.Hattori, N.Ietsugu, T.Itoh, T.Nakae, (1992) OCEANS92 : *Development of Expendable Optical Fiber Cable ROV "UROV"*, pp 813-818.
2. T.Aoki, S.Tsukioka, M.Hattori, T.Adachi, N.Ietsugu, T.Itoh, T.Nakae, (1994) Techno Ocean94 : *Development of a ROV Using with a Small Diameter Umbilical Cable, VI*, pp319-324.
3. T.Murashima, T.Aoki, S.Tsukioka, H.Nakajyoh, (1998) Underwater Intervention 98 : *7,000m, Class Expendable Fiber Optics ROV "UROV7K"*, New Orleans, pp8-18.
4. H.Nakajyoh, T.Aoki, T.Murashima, S.Tsukioka, (1998) OMAE98 : *7,000m Class Expendable Optical Cable ROV (UROV7K) System*, Lisboa, Portugal, OMAE-98-4344(CDROM).

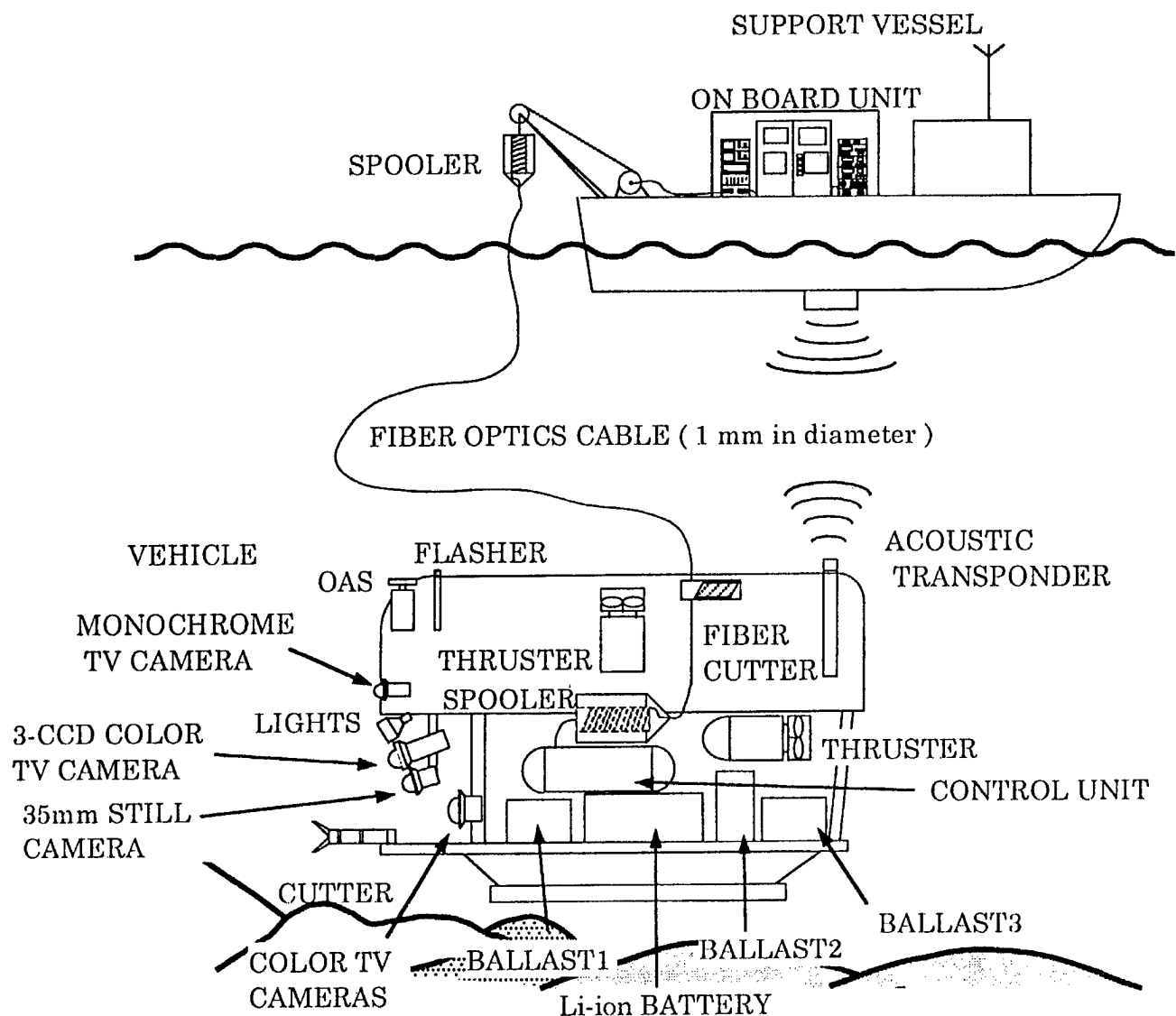


Fig. 1 UROV7K System

Table. 1 Specification

Weight	About 2700 kg
Dimensions	About 2.8 (L) × 1.8 (W) × 2.0 (H) m
Max. operating depth	About 7,000 m
Power	Lithium-Ion Rechargeable Battery 108V60Ah (Oilfilled and Pressure-compensated)
Propulsion	2 horizontal thrusters, 2 vertical thrusters DC brushless motors 800W (Oilfilled and Pressure-compensated)
Equipment	<ul style="list-style-type: none"> · Wide color TV cameras (× 2) · Monochrome TV camera · Altitude sonar · Ring laser gyro · Obstacle avoidance sonar · 3-CCD color TV camera · Still camera & strobe light · Depth meter · Flasher · Acoustic transponder

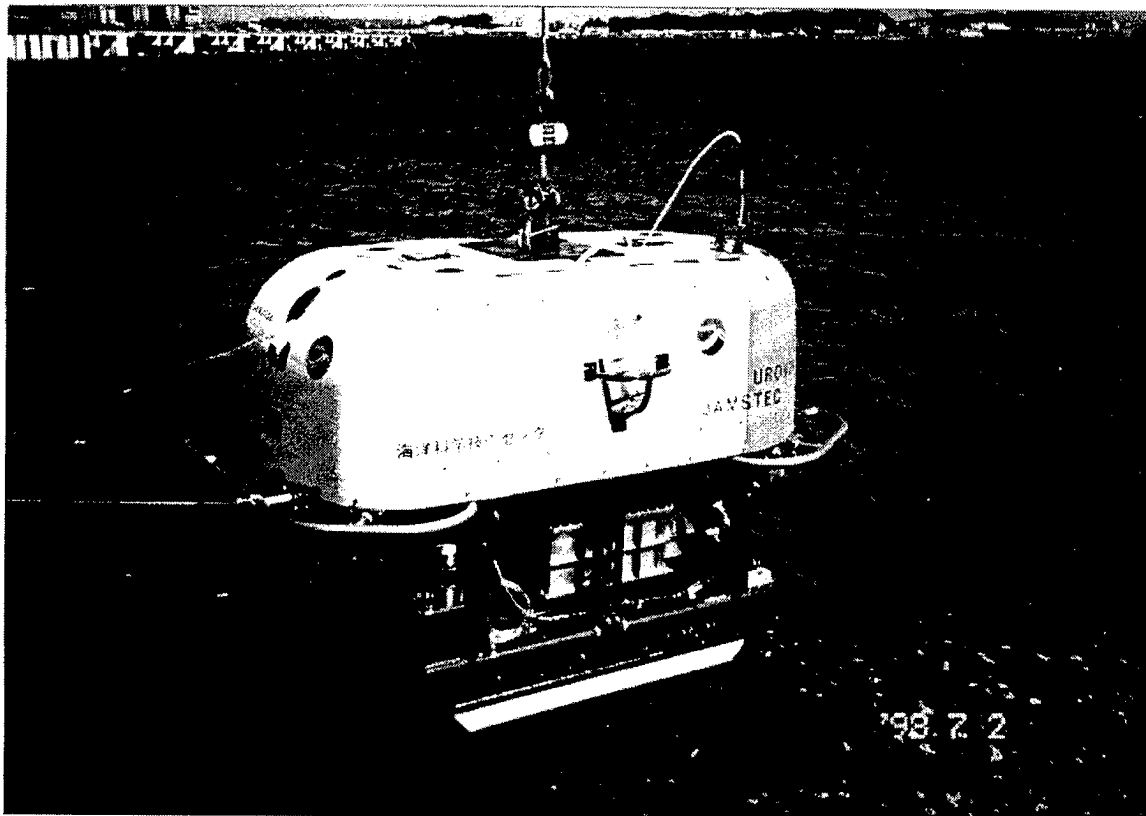
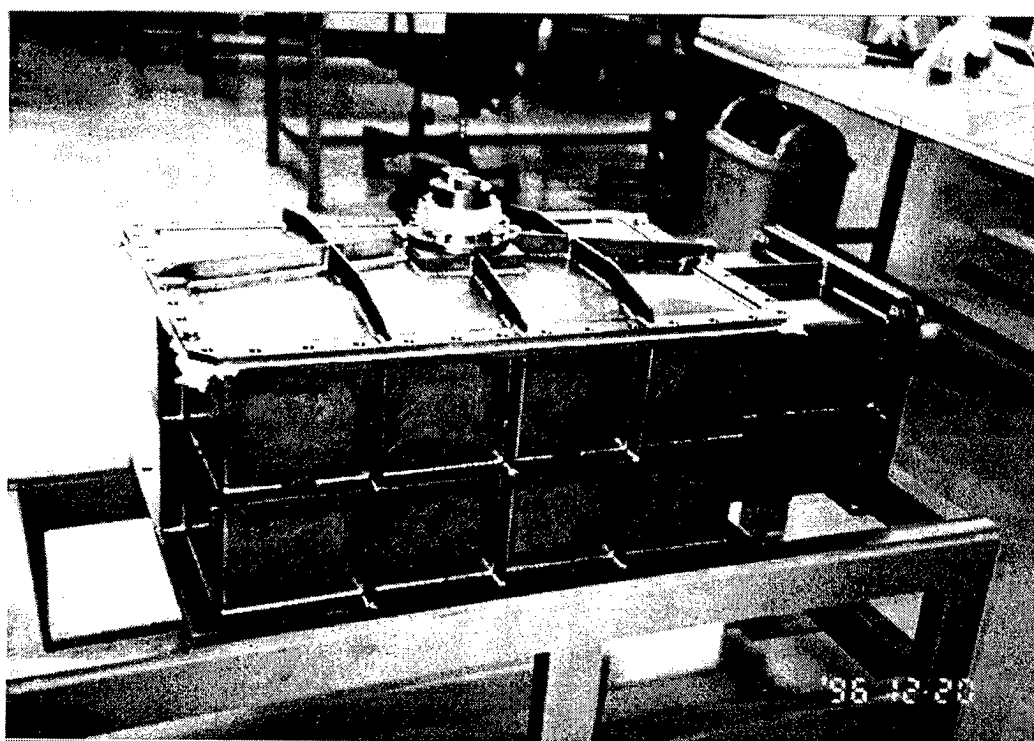


Fig. 2 UROV7K

Fig. 3 Oil Filled Li-ion Rechargeable Battery



MISSION COMMAND MACROS FOR AUTONOMOUS UNDERWATER VEHICLE

Xiaohong Yuan*, K. Ganesan***, Scott Snowden**, Samuel M. Smith**, Matthew Evett*

*Department of Computer Science & Engineering, Florida Atlantic University

**Department of Ocean Engineering, Florida Atlantic University

777 Glades Road, Boca Raton, FL 33431

xhyuan@cse.fau.edu, smith@oe.fau.edu

***Microsoft Corporation

Abstract – The software system on the Ocean Explorer (OEX) at Florida Atlantic University provides a mission command language (MCL) for the user to program missions. Recently, MCL was augmented to permit the definition and use of high-level macros in mission plans. This paper describes the syntax of MCL macro definition and use, and the implementation of the macro mechanism. It also illustrates how mission command macros are used in programming practical AUV missions and in communicating with the OEX through its acoustic modem.

I. Introduction

In autonomous underwater vehicle (AUV) or robotics research, one important area is to make AUV missions highly configurable by end users ([4], [5], [6]). Similar to ISER's AUV control system, which gives users the ability to create and change critical mission parameters through a simple script editor, the OEX control system provides a simple, special purpose scripting language, called mission command language (MCL) for the user to program missions. Because MCL contains very few flow-of-control constructs (i.e., no loops), the scripts for complex missions, such as those involving lawnmower-pattern surveys, can be quite large, with sections of code repeated many times. As the plan size increases, so does the potential for errors, and the cost of modifying plans for future missions.

Recently, we have augmented MCL to permit the definition and use of high-level macros in the mission plans. The benefits of the macros are similar to those derived by the use of macros in modern programming languages, including parsimony and modularity. The macros greatly increase the parsimony of the mission plans by substituting simple macro invocations for

repeated blocks of code. The modularity provided by the macros tends to localize errors in mission plans to a single macro, instead of having that error repeated many times throughout a plan.

Another important benefit of the parsimony induced by the macros is that it facilitates the communication of the OEX with the surface. The communications capabilities of the OEX make it possible for on-surface human operators to transmit commands to the OEX remotely in real time via its on-board acoustic modem, but because of the noisy environment, the modem's throughput is very low. The macros decrease the size of these transmissions, increasing the efficiency of operator control of the OEX.

This paper describes the syntax of MCL macro definition and use, and the implementation of the macro mechanism. Finally, we illustrate how mission command macros are used in programming OEX missions, and in communicating with the OEX through its acoustic modem.

II. Mission Command Language

The MCL in which mission plans are written has the following syntax [1]:

1) Set <what> <value(s)>

To set the value of a specific item indicated in <what>, which can be heading, rudder, speed, criteria, combination-type etc.

2) Start <what> <value(s)>

To start the item indicated in <what>, e.g., managers, motor, etc.

3) Stop <what> <values>

To stop the item indicated in <what>

4) Need <what>

To select specific features of a behavior tree, that is, to configure an arbiter. <what> can be simplealtitude, complexaltitude, auvsimspeed, etc.

5) *Clear* <what>

To clear the item mentioned in <what>, e.g., criteria.

6) *Go* <label>

To execute a set of setpoints/waypoints given so far, where <label> is an optional command label.

7) *Gohome*

Return the OEX to the HomePosition coordinates in shared memory.

A mission plan written in the above MCL is as below:

```
Set Origin 30 10.05 N 88 44.7 W 0.0
Set HomPos 30 10.1 N 88 44.76 W
Start Mgr StateMgr      100
...
Need SimpleAltitude
...
Clear criteria
Set Criteria Plane -2
Set TimeOut 800
Set Depth 3.0
Set Speed 2.5k
Set WaypointNE -100 -450
Go
...
Stop Motor
Stop Mission
```

The MCL syntax and the above mission plan example show that MCL contains very few flow-of-control constructs (i.e., no loops). The scripts for complex missions, such as those involving lawnmower-pattern surveys, could therefore be quite large, with sections of code repeated many times, especially when patterns only change slightly from mission to mission. As the plan size increases, so does the potential for errors, and the cost of modifying plans for future missions. A solution to this problem is to add the capability for the user to define command macros in the mission plan, and use the macros to simplify and avoid repetition of commands. Mission command macros allow the user to specify tasks in pieces of reasonable size. The pieces can be combined hierarchically to create large plans.

III. Mission Command Macros

The mission command macro feature added to the current OEX MCL greatly simplifies mission programming. The user defines mission command macros using existing mission commands illustrated above, and then uses these macros in the mission command file. A macro can also be defined using an already defined macro. A special macro "repeat" command is provided, so that a macro command can be repeated many times. This is similar to adding a loop

control construct to the current MCL. The syntax of macro definition, macro use and the repeat command is illustrated below.

A. The Syntax of Macro Definition

```
macro <macroName> <parameter(s)>
<command(s)>
endmacro
```

macro: MCL keyword that starts a macro definition.

<macroName>: The name of the macro

<parameter(s)>: MacroName is followed by 0 or more parameters for the macro.

<command(s)>: One or more lines of mission commands, or macro commands that have already been defined, or a repeat command.

endmacro: Keyword that ends the definition of a macro.

An example of a macro definition would be:

```
macro mac1 x y
Set wayPointDeltaNE x y
Go
Set wayPointDeltaNE 0 y
Go
Set wayPointDeltaNE -x 0
Go
Set wayPointDeltaNE 0 y
Go
endmacro
```

B. The Syntax of Macro Use (A Macro Command)

```
<macroName> <parameter value(s)>
```

An example macro command is:

```
mac1 100 100
```

When the mission is run, this command will be replaced with the definition of macro mac1, with x, y being replaced with 100, 100 respectively.

C. The Syntax of Repeat Command

```
repeat <count> <command>
```

<count>: A positive integer that specifies how many times to repeat the macro command.

<command>: A mission command or user defined macro command.

An example would be:

```
repeat 5 mac1 100 100
```

which means to repeat "mac1 100 100" 5 times. Obviously this does a lawnmower-pattern survey since waypoints are specified relative to current location.

IV. Implementation of Mission Command Macros

The OEX software systems ([1], [2], [3]) consist of several supporting tools, including a shared memory management system, a data logger, a monitor, various types of arbiters, and several managers to handle scheduling. The managers are: PlannerMgr, NavMgr, PositionMgr, SpeedMgr, etc. Mission planning and navigation are implemented by PlannerMgr and NavMgr. The Planner is responsible for interpreting the mission command file "mis_plan", and generating navigation commands to be executed by the navigator. The planner parses the mission plan in MCL, converts the commands to navigation commands, and sends them to the navigator via the navigation command queue (NavQueue). There are three command queues: NavQueue, ModemQueue, and ErrorQueue. Navigation commands from the mission plan file are processed through the NavQueue, commands sent by the operator through the acoustic modem are placed in the ModemQueue, and commands for exception handling are stored in the ErrorQueue. Each command queue has a priority, and the navigator executes the command from the queue with highest priority. A single navigator command may consist of one, or a group of planner commands.

To augment MCL to permit the definition and use of high-level macros in the mission plans, there could be two strategies: 1) Add a preprocessing module to compile the mission plan with macros into a mission plan without macros and give it to the planner; 2) Make changes to the Planner so that it could parse macro definitions and macro commands. We adopted the second strategy in implementing macro commands. The planner stores macro definitions in shared memory when parsing macro definitions, and when parsing macro commands, it replaces the macro with the mission commands from the macro definition. Therefore, the planner parses the macro definitions and commands together with other mission commands. The advantage of such an implementation is that it facilitates communication of the OEX with the surface. The communications capabilities of the OEX make it possible for on-surface human operators to transmit commands to the OEX remotely in real time via its on-board acoustic modem, but because of the noisy environment, the modem throughput is very low. Since the planner is able to parse macro commands dynamically, we can send shorter macro commands to the AUV remotely through the acoustic modem, thus improving efficiency. It should be noted that macro definitions should be included in the mission plan file, since it would be very inefficient to send lengthy macro definitions through acoustic modem.

V. Programming Missions with Command Macros

A. A Practical Mission Plan Example with Macros

The following is an example of mission plan file with mission command macros (a line starting with "//" is a comment):

```
// Macro definitions
macro GetGpsFix DELAY HEADING
  // set depth to 0
  clear criteria
  set criteria depth 0.0 1.2
  set depth 0.0
  go S surface
  // stop the motor
  clear criteria
  set rpm 0
  set torque 0
  set direction 0
  go SM stop motor
  // Cycle power on the gps
  clear criteria
  set payload MHPowerCtrlOut 2
  go S1 Turn off gps
  // Put up the antenna
  clear criteria
  set criteria GPSfix 2
  set timeout DELAY
  set payload MHPowerCtrlOut 3
  set payload gpsAntennaeCmdOut 1
  go S3 Get fix
  // put the antenna down
  set criteria duration 30
  set payload gpsAntennaeCmdOut 2
  set payload MHPowerCtrlOut 2
  go S10 turn off gps power
endmacro
// End of GetGpsFix -----

macro HfssNSLeg L S E
  clear criteria
  Need Tracking
  set criteria plane -15
  set speed 2.5k
  set depth 10.0m
  set waypointDeltaNE 0 S
  go OFF1 east S
  // Go a little way before turning on the HFSS
  set waypointDeltaNE -E 0
  go OFF1 North -E
  // ----- South bound leg 1 -----
  // Start collecting HFSS data
  set payload startHFSSScanOut 1
  set waypointDeltaNE -L 0
  go L2 North -L hfss data on
  set payload startHFSSScanOut 0
  set waypointDeltaNE -E 0
  go L3 North -E hfss data off
```



```

set waypointDeltaNE 0 S
go L4 east S
set waypointDeltaNE E 0
go L5 north E
// ----- North bound leg 2 -----
set payload startHFSScanOut 1
set waypointDeltaNE L 0
go L6 north L hfss data on
set payload startHFSScanOut 0
set waypointDeltaNE E 0
go SP1 north E hfss data off
endmacro
// End of HfssNSLeg Macro

// HfssNSLawn L S E CNT PLANE SPD DEP TMOUT
macro HfssNSLawn L S E CNT PLANE SPD DEP
TMOUT
  clear criteria
  Need Tracking
  set criteria plane PLANE
  set speed SPD
  set depth DEP
  repeat CNT HfssNSLeg L S E
endmacro
//***** END OF MACRO DEFINITIONS *****

//***** MISSION BEGINS HERE *****
Set Origin 26 18.153 N 80 3.788 W
Set HomePos 26 18.153 N 80 3.788 W 0.0
Start Mgr StateMgr 100
Start Mgr FSHeadingMgr 100
Start Mgr FSPitchMgr 100
Start Mgr FSDepthAltMgr 100
Start Mgr SpeedMgr 100
Start Mgr GuidanceMgr 100
Start Mgr SimMgr 100
Need SimSpeed
Need SimDepth
Need SimAlt
Need SimRpm
Need SimHeading
Need SimMotion
Need NoSurfaceSafety
// to execute the feature selections
go N1
//start motor
// Turn the HFSS payload on
clear criteria
set payload turnHFSScanCpuOnOut 1
go S2Turn on sidescan power
// Start the camera
clear criteria
set payload videoCmdOut 1
go S8 Power the camera
// Get a GPS fix
// GetGpsFix <timeout> <heading>
GetGpsFix 30 0
// power up the fish
clear criteria

```

```

set criteria duration 3
set payload turnHFSScanPowerOnOut 1
// Go to the NW corner of grid 1
clear criteria
set criteria plane -15
Need Tracking
set timeout 600
set speed 2.5k
set depth 10.0
set waypointLL 26 18.153 N 80 3.778 W
go W1 Go to the NW corner of grid 1
// Do 6 legs (3 north/south cycles)
// HfssNSLawn <length> <space> <end zone>
<count> <plane> <speed> <depth> <timeout>
HfssNSLawn 200m 25m 20m 3 -15m 2.5k 10.0m
600
GetGpsFix 30 0
set rpm 0
set torque 0
set direction 0
go STP0
stop Mission

```

In the mission plan, three command macros are defined: GetGpsFix, HfssNSLeg and HfssNSLawn. The GetGpsFix macro contains steps for getting a GPS fix, for example, to set the depth to 0, stop the motor, turn off the GPS, put up the antenna, etc. The HfssNSLeg macro does one north south cycle of a lawnmower pattern for the HFSS payload. Fig. 5.1 illustrates the path of HfssNSLeg macro and its three parameters: L, S, E. It first goes south distance E before turning on the HFSS (bc), then turns on HFSS and collects data as it goes south distance L (cd), then turns off HFSS (de) for distance E, then goes east for distance S (ef), and north distance E (fg) with HFSS off, and then north distance L (gh) with HFSS on, then north S with HFSS off, and so on. Macro HfssNSLawn does a lawnmower pattern survey with HFSS by repeating HfssNSLeg. The path and the parameters are illustrated in Fig. 5.2.

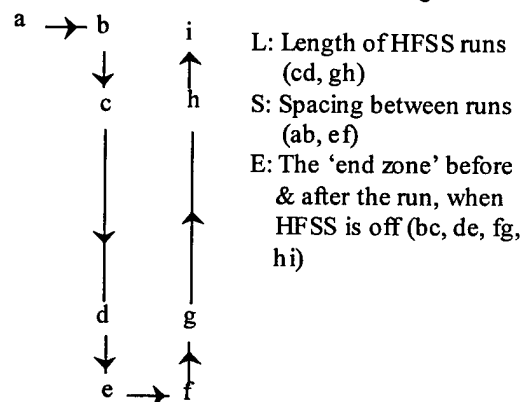


Fig. 5.1 Survey path of macro HfssNSLeg

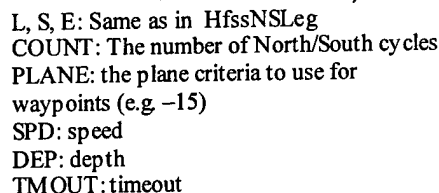


Fig. 5.2 Survey path of macro HfssNSLawn

B. Acoustic Communication with Command Macros

The implementation of the command macro mechanism makes it possible to send shorter command macros to AUV through acoustic modem to control mission in real time. This greatly improves the practical ability to control the AUV remotely since acoustic communications have inherently low throughput. For example, we could download the above mission plan to the AUV, and make the vehicle perform the lawnmower-pattern HFSS survey. While the AUV is in the mission, the AUV transmits data back to surface through the acoustic modem. Based on this data, we might want the vehicle to concentrate on a spot and do a lawnmower survey in that specific small area. We could send the HfssNSLawn macro with parameters changed to small values through the acoustic modem. In this way we are able to control the vehicle on line to do adaptive sampling and other complex missions.

VI. Conclusion

Mission command macros have significantly improved the capability of the OEX AUV to execute complex missions that are increasingly required as the OEX is used. The modularity and repeat features have aided users in creating error-free missions. Also, the time required to create error-free mission plans has been greatly reduced by reusing macros. Finally, the ability to control the AUV remotely via the acoustic modem has been enhanced both by allowing complex command sequences to be sent efficiently, and by allowing the remote control interface to be quickly modified by defining new macros rather than changing the modem communications protocol.

REFERENCES

- [1] OEX Software Manual, Version 2.0. Advanced Marine Systems, Florida Atlantic University, May 1, 1998.
- [2] Ganesan, K., Smith, S. M., White, K. and Flanigan, T. A pragmatic software architecture for UUVs. *IEEE Symposium on Autonomous Underwater Vehicle Technology*, 1996.
- [3] Yuan, X., Ganesan, K., Evett, M. and Smith, S. M. Providing real-time data trajectory access in autonomous underwater vehicles. *Ocean'99 MTS/IEEE Conference*, Sept. 12-16, Seattle, Washington, 1999.
- [4] Kao, M., Weitzel G. and Zheng, X. A simple approach to planning and executing complex AUV missions. *Proceedings of the Symposium on AUV Technology, (AUV'92)*. June, 1992.
- [5] Bellingham, J. G. and Leonard, J. J. Task configuration with layered control. *Proceedings of IARP 2nd Workshop on Mobile Robots for Subsea Environment*, p193-302, Monterey, CA, USA, May, 1994.
- [6] Bellingham, J. G., Consi, T. R., Beaton, R. M. and Hall, W. Keeping layered control simple. *Proceedings of the Symposium on AUV Technology, (AUV' 90)*. June, 1990. Washington DC.

Restoration of Maritime Navigation Systems in Central American Ports

Alan R. Beam

Volpe National Transportation Systems Center

55 Broadway, Kendall Square

Cambridge, MA 02142-1093

arbeam@aol.com

Senora Liana de Cáceres

Executive Secretary

Central American Commission of

Maritime Transportation

COCATRAM

Cine Cabrera 2c. Este 2½c. al Sur

Apartado Postal 2423

Managua, Nicaragua, C.A.

Maurice J. Moroney, Jr.

Chief, Center for navigation

Volpe National Transportation

Systems Center

55 Broadway, Kendall Square

Cambridge, MA 02142-1093

E-mail: moroney@volpe.dot.gov

ABSTRACT

This paper describes the project that was conducted early this year to reinstate maritime navigation in Central American (CA) ports that were devastated by the hurricane that occurred in November 1998. The project objectives, which were accomplished, were to install navigation facilities rapidly, and to use advanced technologies in the renovation to insure that the capabilities of the new systems would exceed those which existed before the hurricane. The damage to the ports and their installations and facilities was severe; but the ruination of their navigation systems also had far reaching effects. For instance, ships carrying relief supplies and medicine to countries such as Honduras, often found it extremely hazardous to enter ports that had greatly diminished aids to navigation. Recognizing the plight of neighboring countries as a result of the hurricane, U. S. Secretary of Transportation, Rodney E. Slater, initiated a program to reconstruct the maritime navigation infrastructure in Central American ports. The Research and Special Programs Administration of the US/DOT, with technical support from the Volpe Center, was given the lead role in the CA Navigation Systems Revivification project. Working with the CA

Commission of Maritime Transportation (COCATRAM), damage assessment was performed and a relief priority list was drawn up. The ports of Cortez and San Lorenzo in Honduras were hardest hit by the hurricane and consequently they were designated for the first replacements. The execution of the project required demanding logistics and acquisition planning that will be detailed in the paper. In the spirit of turning a disaster into an opportunity, it was decided to optimize the use of satellite technology where possible rather than revert only to the use of conventional aids to navigation. The Center for Navigation at the Volpe Center, capitalized on experience gained in navigation development projects for the Panama Canal and the Saint Lawrence Seaway to design and implement navigation and buoy positioning systems in CA. The Differential Global Positioning Satellite System was selected as the primary signal source in order to provide highly accurate navigation in ports recovering from the hurricane. In cooperation with COCATRAM, the rapid response navigation system will be integrated into a comprehensive navigation complex for all major ports in Central America.

ROV actuator fault diagnosis through servo-amplifiers' monitoring: an operational experience

R. Bono, Ga. Bruzzone, Gi. Bruzzone, M. Caccia

Consiglio Nazionale delle Ricerche

Istituto Automazione Navale

Via De Marini, 6

16149 Genova, Italy

E-mail: {ric, gabry, gio, max}@ian.ge.cnr.it

Abstract

A system for ROV actuator fault detection, diagnosis and accommodation through servo-amplifiers' monitoring and dedicated steady-state maneuvers has been designed on the basis of real data recorded during operating missions of Romeo, the ROV prototype developed by CNR-IAN. In particular, an actuator fault during at sea operations of Romeo enabled the validation with real data of the developed system.

1. Introduction

Currently, unmanned underwater vehicles (UUVs) can satisfactorily perform a large amount of scientific missions: autonomous underwater vehicles (AUVs) can navigate through a set of way points with sufficient precision for a large set of oceanographic surveys (Singh et al., 1995; Bellingham et al., 1994; Smith et al., 1995), while remotely operated vehicles (ROVs) can be tele-operated to execute tasks requiring strong interactions with the operating environment, e.g. exploration of an unknown area and operations in the proximity of the seabed or man-made underwater structures (Ballard, 1993; Nokin, 1998; Kirwood, 1998; Dawe et al., 1998; Bono et al., 1998). As discussed in (Healey, 1998), at this stage the main technical issue is to improve the system reliability in order to guarantee the mission is accomplished even in the presence of some variations from the nominal conditions, i.e. faults. In this sense, fault management systems for UUVs able to detect, isolate and accommodate faults, have been investigated and designed in order to improve the vehicle degree of autonomy, reliability and capability of performing missions in harsh environments. These systems also play the role of interface between the robot and the human operator for performance monitoring in the case of tele-operation.

UUVs' operations can be affected by two kinds of faults: failures in the hardware and software subsystems of the vehicle, such as thruster seizing or sensor breaking, and unforeseen environmental conditions, which could jeopardize the working mode of the sensors measuring the vehicle-environment interactions, such as multi-path

phenomena affecting echo-sounders' performances. In the past, attention focused on the vehicle faults, distinguishing between actuator and sensor faults, and trying to classify the expected system failures on the basis of their probable response as reported in (Rae and Dunn, 1994), where zero-response breaking, permanent offset jamming, intermittent slipping, decreasing response creeping failure and random control failure damages have been listed.

In the nineties, theoretical advancements in fault diagnostics obtained in various fields of applications, from aeronautical and aerospace systems to nuclear and chemical plants, have been transferred to underwater robotics. Since unmanned underwater vehicles can be modeled by a small number of state variables (Fossen, 1994), model-based techniques for fault detection have been preferred to model-free ones. In particular, fault detection techniques based on parameter estimation and analytical redundancy, i.e. the same quantity can be calculated by combining data from different sensors or model-based predictors, have been developed. An example of black-box identification combined with gradient filtering to generate failure events is given in (Rae and Dunn, 1994), while a technique to manage analytical redundancy through expert systems' rules is presented in (Orrick et al., 1994). In (Healey, 1998), a model-based observer is used to generate a residual between the sensor measured values and that predicted from the model in order to detect dynamic faults. A fault is detected when the residual magnitude is higher than a suitable threshold for more than a fixed length of time. The same method to avoid false alarms, after processing residuals generated through analytical redundancy, is used in (Yang et al., 1998), where an accommodation technique for thruster failures is also presented in the case of an over-actuated vehicle. Modeled actuator faults can be detected and isolated through a bank of extended Kalman filters as discussed in (Alessandri et al., 1999). Due to the difficulties of having available recorded telemetry data of UUV actual faults, the above mentioned investigations are based on simulations of plant damages of the types classified in (Rae and Dunn, 1994). In particular, in (Orrick et al., 1994) failure detection is performed on the heading and depth control surfaces and sensors of a simulated torpedo-like AUV. The Rae and Dunn's failure detection system has been tested and

evaluated on the simulator of the Ocean Voyager AUV in the case of speed sensor slipping and jamming, depth-meter breaking and compass jamming (Rae and Dunn, 1994). In the same way, the model-based observer approach presented in (Healey, 1998) has been tested by simulating a stern plane fault in the presence of wave disturbances using a model of the US Navy DSRV vehicle. On the other hand, Yang et al. and Alessandri et al. simulated thruster and sensor failures suitably programming the actuation and acquisition system of actual vehicles, Odin and Roby2 respectively, operating in water. Anyway, only time-invariant actuator faults have been considered.

In the following, research focusing on the design of fault detection, isolation and accommodation system based on operationally experienced faults in ROV actuators is presented. The main goal is to design a fault management system for unmanned underwater vehicles, able to satisfy the basic requirement of "handling experienced faults", and conventional zero output failures treated in the literature. In addition, the fault management system has to be easily integrated in the hierarchical control architectures, which characterize a large number of advanced UUVs such as the NPS Phoenix (Brutman et al., 1998), IFREMER Vortex (Le Rest et al., 1994) and Romeo. This requirement involves the development of fault detection and isolation modules at the various levels of the control architecture, such as servo-amplifiers, model-based dynamics and steady-state monitoring, resulting in a reliable diagnostics system based on information redundancy. Operational experience, ripened during the under-ice missions of the Romeo ROV during the XIII Italian expedition to Antarctica in 1997-98 (Bono et al., 1998), revealed the permanent time-varying multiplicative effects of flooded thruster failures. The time-varying multiplicative nature of flooded thruster faults, combined with the vehicle model uncertainty and the unavailability of linear velocity and acceleration measurements, e.g. in the case of the ROV heave motion only noisy depth measurements were available, has made it difficult to generate robust observer-based residual during closed-loop operations and suggested the execution of pre-defined steady-state maneuvers specifically designed to solve ambiguities in the presence of position measurements only.

A short description of Romeo, is given in section 2, while the faults occurred in the course of the vehicle operations are reported in section 3, where failure models are defined, and detection, isolation and accommodation techniques are evaluated on actual mission recorded data and discussed. In particular, the effects of the flood of a vertical thruster are reported. The behavior of servo-amplifiers, and steady-state residual generators is discussed, and a reliable procedure for actuator fault detection and isolation is proposed. Fault accommodation through the reconfiguration of the Romeo Thruster Control Matrix is presented in section 4.

II. Romeo

The Romeo ROV has been designed and developed by the Robotics Dept. of the Institute for Ship Automation of the Italian National Research Council for scientific applications and research in the field of intelligent vehicles. Its mechanical design follows the structure of the last generation scientific ROVs, such as Tiburon (Kirkwood, 1998) and Victor (Nokin, 1998). The vehicle is constituted by three sections: on the bottom an interchangeable toolshed for scientific devices is connected to the basic frame, the foam for buoyancy is positioned on the top, while in the middle section, the basic frame carries on control and communication electronics, sensors and actuators as shown in Figure 1. The resulting ROV is about 1 m in height, 0.9 m in width and 1.3 m in length, weighs about 450 kg in air and is intrinsically stable in pitch and roll.

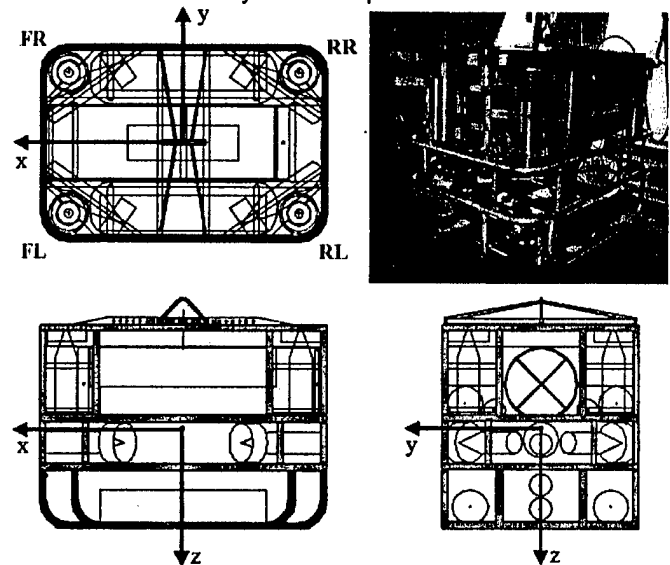


Fig. 1. Romeo mechanical design

As shown in Figure 1, the thrusters are arranged two by two in the corners, with the horizontal ones parallel to the diagonals of the xy section. This redundant thruster configuration uncouples the horizontal control of surge, sway and yaw, from the vertical control of roll, pitch and heave. Calling θ the module of the angle between the horizontal thrusters and the vehicle's longitudinal axis, b , c and d the thruster arms with respect to the vehicle center of mass respectively for yaw, roll and pitch motion, the horizontal and vertical Thrust Control Matrixes, relating the thruster forces

$$\tau_H = [\tau_{HFL} \quad \tau_{HFR} \quad \tau_{HRL} \quad \tau_{HRR}]^T \quad \text{and}$$

$$\tau_V = [\tau_{VFL} \quad \tau_{VFR} \quad \tau_{VRL} \quad \tau_{VRR}]^T \quad \text{to the 6 DOFs force}$$

$$\text{and torque } \phi_H = [F_u \quad F_v \quad T_r]^T \text{ AND } \phi_V = [T_p \quad T_q \quad F_w]^T,$$

are
$$B_H = \begin{bmatrix} \cos \alpha & \cos \alpha & -\cos \alpha & -\cos \alpha \\ \sin \alpha & -\sin \alpha & \sin \alpha & -\sin \alpha \\ b & -b & -b & b \end{bmatrix} \quad \text{and}$$

$$B_V = \begin{bmatrix} -c & c & -c & c \\ -d & -d & d & d \\ 1 & 1 & 1 & 1 \end{bmatrix} \quad \text{respectively.}$$

A general purpose "optimal" distribution of the control actions consists in minimizing the quadratic energy cost function

$$J = \frac{1}{2} \tau^T P \tau, \quad \text{which, in the case all inputs are}$$

equally weighed, has the solution $B^\# = B^T (BB^T)^{-1}$, known as Moore-Penrose pseudo-inverse (Fossen, 1994). For the square case, as when one faulted actuator is disabled, $B^\#$ is simply equal to B^{-1} , and the unique solution is computed. More detailed information about Romeo computer and software design can be found in (Caccia et al., 1999).

III. Actuator faults: blooded thruster

During the execution of at-sea trials for the identification of Romeo vertical dynamic model, see (Caccia et al., 1999) for details, the pilot revealed anomalous values of the current of the vertical front left thruster. The mission was immediately suspended, the ROV was recovered and the faulted thruster dismantled.

A. Blooded thruster: fault model

Investigations carried out in the Italian station lab revealed that the water inside the thruster modified the internal electrical connections. In particular, the salt water caused a dispersion, which reduced the feed-back signal n_m , of the motor revolution rate n from the tachometer to the servo-amplifier, i.e. $n_m = \lambda n, 0 \leq \lambda < 1$. In these conditions, when the servo-controller forced the feed-back signal n_m to track the desired speed n^* , the actual speed n was higher than the desired one, i.e. $n \rightarrow \frac{1}{\lambda} n^*$.

Since at bollard conditions, the thrust τ delivered by a propeller is $c = a n |n|$, the magnitude of the actual force of the blooded thruster

$$\tau = \frac{1}{\lambda^2} a n^* |n^*| = \frac{1}{\lambda^2} \tau^*$$

is higher than the desired one.

In addition, the thruster fault affected the motor armature current i_a too. The torque exerted by a rotating propeller at bollard conditions is $Q(n) = Q_{|n|} |n|$, while the DC motor dynamics is described by equations:

$$L_a \frac{di_a}{dt} = -R_a i_a - 2\pi K_M n + u_a$$

$$2\pi J_m \frac{dn}{dt} = K_M i_a - Q(n)$$

where L_a, R_a, u_a and are the armature inductance resistance and voltage, K_M is the motor torque constant, J_m is the moment of inertia of motor and thruster, and $Q(n)$ is the load from the propeller. In steady-state conditions:

$$K_M i_a = Q(n, v_a), \quad \text{i.e. } i_a \propto |n|n, \quad \frac{i_a}{|n|n} = k,$$

the armature current is proportional to the signed square of the propeller revolution rate, i.e. to the propeller thrust. In the case of Romeo, the motor current i_{mot} , has been acquired and recorded, and the current-thrust coefficient

$$k = \frac{i_{mot}}{|n|n} \quad \text{has been identified on the basis of}$$

experimental tests. The vertical thrusters have been excited with a square wave signal of the reference propeller revolution rate and the corresponding motor currents of the four vertical thrusters have been measured, as shown in Figure 2.

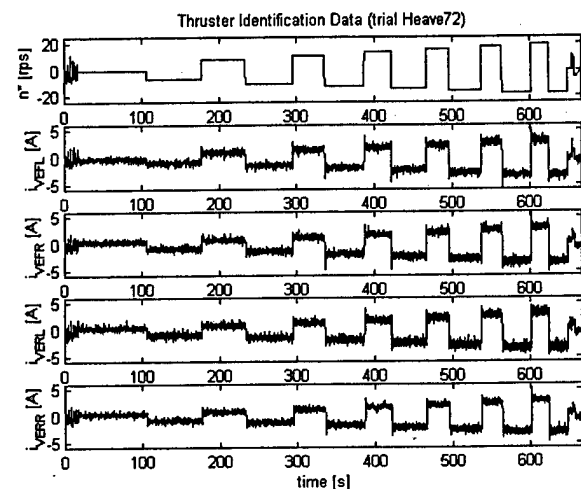


Figure 2. Reference propeller revolution rate and vertical motor currents during identification tests

A Least Square procedure has been applied to the steady-state data, estimating the current-thrust coefficient $\hat{k} = 0.0094 \text{ As}^2$. As shown in Figure 3, where the inverse of the current-thrust coefficients computed for the Romeo vertical thrusters in correspondence of the fault of the front-left actuator is shown, the effects of the flooding are time-varying (see the vertical front-left computed coefficient in the top-left plot). Anyway, k_{VEFL}^{-1} is minor than \hat{k}^{-1} indicating that the actual propeller revolution rate is higher than the nominal one.

B. Blooded vertical thruster: fault detection and isolation

While a single residual is sufficient to detect a fault, a set of evaluated residuals is, in general required for fault isolation. In order to solve this ambiguity, monitoring of other residuals at the various level of the control architecture is required.

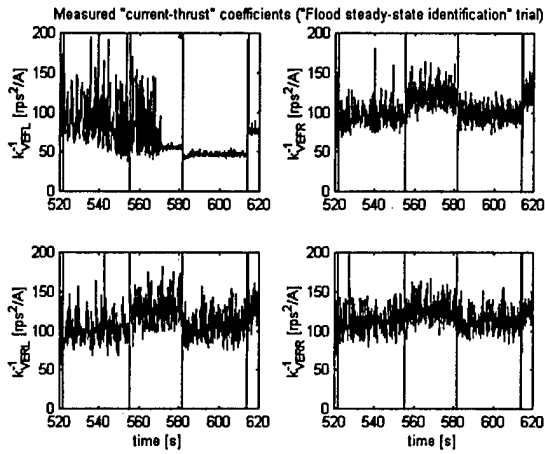


Figure 3. Computed current-thrust coefficients in fault case (trial Heave50)

For instance, a motor current higher, in magnitude, than the expected one can be a symptom both of a flood or seizing thruster and a fault in the corresponding A/D channel. Monitoring the innovation of the model-based depth estimator in nominal plant conditions can allow the detection of some failure in the vertical thrust system. Since, in many operational conditions, the force disturbance induced by a flood thruster fault is of the same order of size of the model uncertainty and only noisy depth measurements are available, this method too generates false alarms, and more reliable residuals have to be monitored. This is the case of pitch and roll displacements from the equilibrium point in steady-state conditions when the system is excited with a constant vertical thrust. The corresponding Incidence Matrix for vertical thruster faults is reported in Table 1, where also the progressive seizing of an actuator has been considered. Fault detection is performed by monitoring the servo-amplifiers residuals, while fault isolation requires the vehicle to execute steady-state maneuvers. This means that the fault management system has to interact with the robot mission controller, asking for the execution of dedicated maneuvers to isolate failures. After fault accommodation, the robot can continue the mission or scheduling a "gracefully" degraded one.

A detailed description of servo-amplifiers, and steady-state residuals generation and evaluation follows.

1) Servo-amplifiers residual generation and evaluation

Given the required propeller revolution rate, for each thruster the expected motor current and the corresponding residual at time t are computed as:

$$\hat{i}_{mot}^j(t) = \hat{k} n_j^* |n_j^*|$$

and

$$|\varepsilon_{i_{mot}}^j(t)| = |i_{mot}^j(t) - \hat{i}_{mot}^j(t)|,$$

where j is the thruster index.

Then the symptoms are computed as

$$S_j(t) = \begin{cases} 1, & \text{if } |\varepsilon_{i_{mot}}^j(t)| > \varepsilon_{mot}^{thr} \\ 0, & \text{otherwise} \end{cases}$$

Since the measurements $i_{mot}^j(t)$ are quite noisy, persistence degrees p_j of the symptoms S_j in a sliding window of width $N \Delta t$ are computed as:

$$p_j(t) = \frac{\sum_{i=0}^{N-1} S_j(t - i \Delta t)}{N}$$

and a fault alarm $f_i(t)$ at time t is given if $p_i(t)$ higher than a threshold p_{mot}^{thr} (Theilliol et al, 1997).

2) Steady-state maneuvers residual generation and evaluation

In the case the UUV is excited with a nominal constant vertical force and no pitch and roll torque, the residuals $|\varepsilon_\phi(t)| = |\phi(t) - \phi_0|$ and $|\varepsilon_\theta(t)| = |\theta(t) - \theta_0|$ are considered, where ϕ_0 and θ_0 are the equilibrium points for the vehicle's roll and pitch when a null vertical thrust is applied.

The steady-state roll and pitch symptoms are computed on the basis of the tests $|\varepsilon_\phi(t)| > \varepsilon_\phi^{thr}$ and $|\varepsilon_\theta(t)| > \varepsilon_\theta^{thr}$ respectively and the corresponding persistence degree indexes are computed in order to reduce the number of fault alarms $f_\phi(t)$ and $f_\theta(t)$.

C. Flooded vertical thruster: experimental results of fault detection and isolation

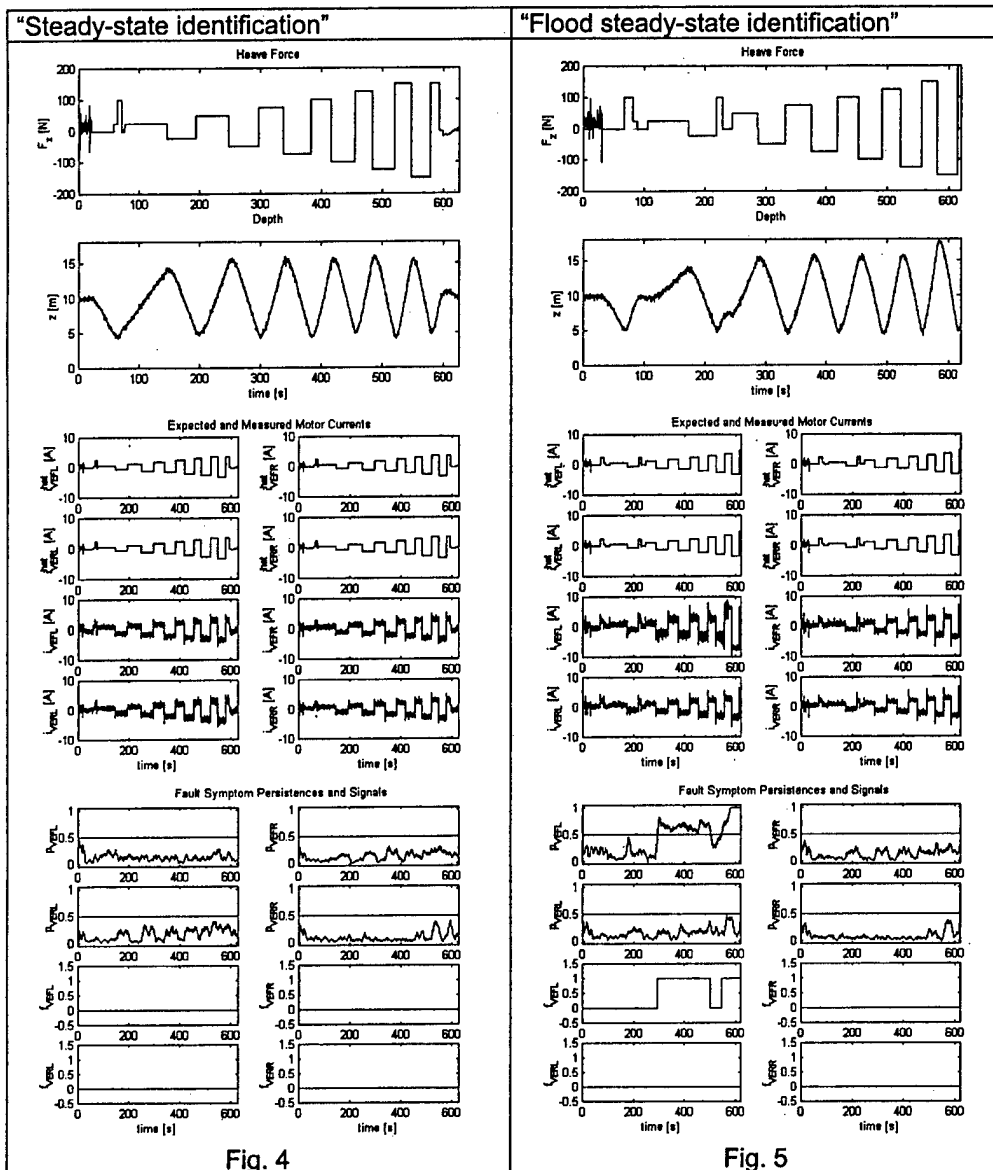
The above described algorithms for fault detection and isolation have been tested on a large amount of data recorded during Romeo campaign in Antarctica. In this paper two prototype trials are examined:

- "Steady-state identification": Romeo was excited with open-loop square wave vertical thrust to identify its vertical drag and thruster installation coefficients and work in nominal conditions;
- "Flood steady-state identification": Romeo was excited with open-loop square wave vertical thrust to identify its vertical drag and thruster installation coefficients and the vertical front-left thruster was flood.

In the case of Romeo operating at sea, the motor current residuals have been computed and evaluated with the

values $\varepsilon_{mot}^{thr} = 0.65$ A and $p_{mot}^{thr} = 0.5$. The results of the servo-amplifier fault detection processing for the examined trials are plotted in Figures 4 and 5 together with the applied nominal vertical force and measured depth.

The symptom of a vertical front-left thruster failure is detected in the case "Flood steady-state identification" trials, while no false alarms are generated.



The considered trials also enable the evaluation of dedicated steady-state maneuvers for fault isolation. The threshold values $\varepsilon_{\phi}^{\text{thr}} = \varepsilon_{\theta}^{\text{thr}} = 0.9\text{deg}$ and $p_{\phi}^{\text{thr}} = p_{\theta}^{\text{thr}} = 0.5$ have been chosen for residual evaluation and persistency degree tests respectively. Results are plotted in Figure 6.

In the case of the "Flood steady-state identification" trial, the combination of the fault alarms, according to the Vertical Thruster Fault Incidence Matrix reported in Table 1, enables the isolation of a flood vertical front-left thruster fault as shown in Figure 8, about at time 570 s.

IV. Fault accommodation:

Actuator fault accommodation is performed by inhibiting the faulted thrust and by reconfiguring the distribution of the control actions canceling the corresponding column in

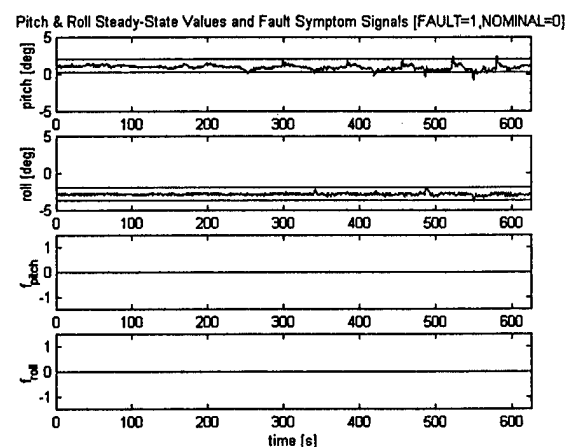


Figure 6. From top to bottom: pitch and roll measurements, and steady-state fault symptom signals: "Steady-state identification" trial

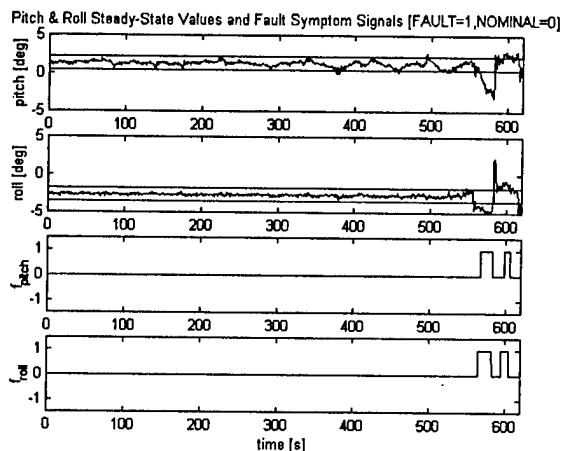


Figure 7. From top to bottom: pitch and roll measurements, and steady-state fault symptom signals "Flood steady-state identification" trial.

the Thrust Control Matrix. As discussed in (Caccia and Veruggio, 1999), Romeo tracking performances are not affected by the fault of one horizontal and one vertical thruster. Of course, the maximum force and torque the vehicle can exert are reduced.

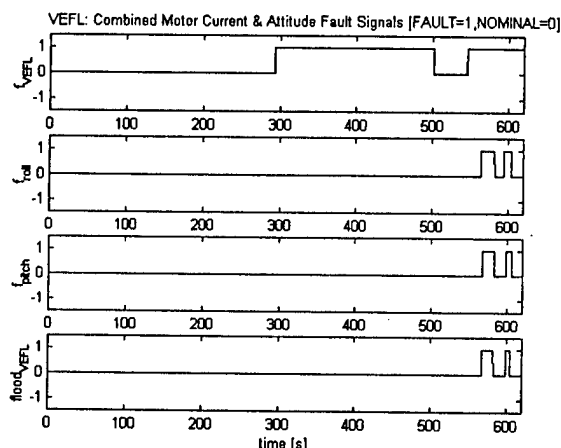


Figure 8. From top to bottom: motor current, steady-state fault symptom signals, and flood thruster signal for the vertical front-left thruster during the "Flood steady-state identification" trial.

V. Acknowledgments

This work has partially been funded by PNRA (Programma Nazionale di Ricerche in Antartide), Project 5.a.5 - Robotica e Telescienza in Ambiente Estremo.

VI. References

Alessandri, A., M. Caccia and G. Veruggio (1999). Fault detection of actuator faults in unmanned underwater vehicles. *Control Engineering Practice*, Vol. 7, No. 3, pp. 357-368, Elsevier Science Ltd.

Ballard, R.D. (1993). The MEDEA/JASON remotely operated vehicle system", *Deep-Sea Research*, vol. 408, pp. 1673-1687

Bellingham, J.G., C.A. Goudey, T.R. Consi, J.W. Bales, D. K. Atwood, J.J. Leonard, C. Chrysostomidis (1994). A second generation survey AUV. *IEEE 1994 Symposium on Autonomous Underwater Vehicle Technology*, pp. 148-156, Cambridge, USA.

Bono, R., Ga. Bruzzone, Gi. Bruzzone, M. Caccia, E. Spirandelli, G. Veruggio (1998). ROMEO goes to Antarctica. *Proc. of Oceans'98*, vol. 3, pp. 1568-1572, Nice, France.

Brutzman, D., A.J. Healey, D. Marco and R.B. McGhee (1998). The Phoenix Autonomous Underwater Vehicle. *AI-Based Mobile Robots*, chapter 13, editors David Kortenkamp, Pete Bonasso and Robin Murphy, MIT/AAAI Press, Cambridge, USA

Caccia, M., R. Bono, G. Bruzzone, G. Veruggio (1999). Variable Configuration UUVs for Marine Science Applications. *IEEE Robotics and Automation Magazine*, Special Issue on Autonomous Underwater Vehicle Technologies, vol. 6, no. 2).

Caccia, M., and G. Veruggio (1999). Guidance and control of a reconfigurable unmanned underwater vehicle. *Control Engineering Practice*. Elsevier Science Ltd. (to appear).

Dawe, T.C., D.S. Stakes, P.R. McGill, J. Barry, S. Etchemendy (1998). Subsea instrument deployments: methodology and techniques using a work class remotely operated vehicle (ROV). *Proc. of Oceans'98*, vol. 3, pp. 1589-1593, Nice, France.

Fossen, T.I.. (1994). *Guidance and Control of Ocean Vehicles*, John Wiley & Sons, England.

Healey, A.J. (1998). Analytical redundancy and fuzzy inference in AUV fault detection and compensation. *Proc. of Oceanology*, pp. 45-50, Brighton, UK

Kirkwood, W.J. (1998). Tiburon: Science and Technical Results from MBARI's New ROV Integrated to a SWATH Platform. *Proc. of Oceans'98*, pp. 1578-1583. Nice, France.

Le Rest, E., L. Marce, V. Rigaud (1994). VORTEXPILOT: a top-down approach for AUV's mission telerobotics language. *Proc. of Oceans 94*, vol. 11, pp. 102-107, Brest, France.

Nokin, M. (1998). Sea trials of the deep scientific system Victor 6000. *Proc. of Oceans'98*, pp. 1573-1577. Nice, France.

Orrick, A. and M. McDermott (1994). Failure detection in an autonomous underwater vehicle. *Proc. of the 1994 Symposium on Autonomous Underwater Vehicle Technology*, pp. 377-382, Cambridge, USA

Rae, G.J.S. and S.E. Dunn (1994). On-line damage detection for autonomous underwater vehicles. *Proc. of the 1994 Symposium on Autonomous Underwater Vehicle Technology*, pp. 383-392, Cambridge, USA

Singh, H., D.R. Yoerger, R. Bachmayer, A.M. Bradley, W. K. Stewart (1995). Sonar mapping with the autonomous benthic explorer (ABE). *9th International*

Symposium on Unmanned Untethered Submersible Technology, pp. 367-375, Durham, USA.

Smith, S.M., K. Heeb, N. Frolund, T. Pantelakis (1995). The Ocean Explorer AUV: A modular platform for coastal oceanography. 9th International Symposium on Unmanned Submersible Technology, pp. 67-76, Durham, USA

Theilliol, D., D. Sauter and L.G. Vela Valdes (1997). Integration of qualitative and quantitative methods for

fault detection and isolation. Proc. of Safeprocess'97, vol. 2, pp. 687-692, Hull, UK

Yang, K.C., J. Yuh and S.K. Choi (1998). Experimental study of fault-tolerant system design for underwater robots. Proc. of the 1998 IEEE International Conference on Robotics and Automation, pp. 1051-1056, Leuven, Belgium

	symptoms	actuator fault				D/A fault			
		flood thruster				increased D/A gain			
		VEFL	VEFR	VERL	VERR	VEFL	VEFR	VERL	VERR
s e r v o	$ \varepsilon_{i_{mot}}^{VEFL} > \varepsilon_{mot}^{thr}$	1	0	0	0	1	0	0	0
	$ \varepsilon_{i_{mot}}^{VEFR} > \varepsilon_{mot}^{thr}$	0	1	0	0	0	1	0	0
	$ \varepsilon_{i_{mot}}^{VERL} > \varepsilon_{mot}^{thr}$	0	0	1	0	0	0	1	0
	$ \varepsilon_{i_{mot}}^{VERR} > \varepsilon_{mot}^{thr}$	0	0	0	1	0	0	0	1
s t e a d y s t a t e	$F_z > 0, \Delta\varphi > 0$	0	1	0	1	0	0	0	0
	$F_z > 0, \Delta\varphi < 0$	1	0	1	0	0	0	0	0
	$F_z < 0, \Delta\varphi > 0$	1	0	1	0	0	0	0	0
	$F_z < 0, \Delta\varphi < 0$	0	1	0	1	0	0	0	0
	$F_z > 0, \Delta\theta > 0$	0	0	1	1	0	0	0	0
	$F_z > 0, \Delta\theta < 0$	1	1	0	0	0	0	0	0
	$F_z < 0, \Delta\theta > 0$	1	1	0	0	0	0	0	0
	$F_z < 0, \Delta\theta < 0$	0	1	0	1	0	0	0	0

Table 1. Vertical Thruster Fault Incidence Matrix

AN ACCURACY ASSESSMENT OF SHORELINE DATA FOR CASTLE BAY ALASKA COMPILED FROM SYNTHETIC APERTURE RADAR

CDR Grady H. Tuell, NOAA
Remote Sensing Research Engineer

James R. Lucas
Chief Photogrammetrist

Douglas B. Graham
Cartographer

National Oceanic and Atmospheric Administration (NOAA)
National Ocean Service (NOS)
National Geodetic Survey (NGS)

Abstract: It is widely recognized that Synthetic Aperture Radar (SAR) technology holds great promise for shoreline mapping applications. Because SAR offers flexibility over weather and time of day restrictions, it may be especially valuable when mapping remote areas such as southwest Alaska. We have mapped a five nautical mile stretch of the coast of Castle Bay Alaska using both 1-meter airborne SAR and RADARSAT fine mode imagery. We have compared the resulting shoreline manuscripts with shoreline data produced using our conventional photogrammetric process. Although the different data sets are separated temporally by several months, and tidal differences exist, the resulting comparisons yield an opportunity to quantify the performance of SAR for this application. As part of our work, we have developed a semi-automated approach to remove positional biases from SAR imagery, and we use the residual vector from this approach as a metric for evaluating accuracy. We present results to date in the analysis of RADARSAT data.

I. Introduction

The shoreline of the United States is the planimetric position of the land/ water interface at a specific stage of tide: Mean High Water (MHW). NOAA navigational charts show the shoreline as a solid line at the land/sea boundary (U.S. Dept. of Commerce, 1997). Similarly, charts show the position of Mean Lower Low Water (MLLW) as a dotted line. This dotted line is the coastline. It is the vertical datum for hydrographic surveys and the horizontal reference for the determination of the seaward

boundaries of the nation (Hicks, 1986). Clearly, these two cartographic features are important to marine navigation. But, they are also key elements of the United States National Spatial Reference System (NSRS). Within NOAA and the National Ocean Service (NOS), the National Geodetic Survey (NGS) establishes and maintains the NSRS. We conduct extensive survey operations designed to map the shoreline and coastline of the nation. For more than 50 years, we have conducted this work using photogrammetry. Our production system, which is based on metric photography, softcopy work stations, and Global Positioning System (GPS) technologies, is both highly refined and accurate. We typically achieve shoreline accuracies of about 3 meters on the open coast, and better than 1 meter on hard targets such as piers and bulkheads. These results easily meet most requirements arising in NOAA's nautical charting program. Our production system is economical and reliable. But there are instances where tide-coordinated aerial photographs are difficult to get, and in these cases shoreline mapping with photogrammetry becomes difficult and expensive. In this paper we present results of ongoing experiments designed to evaluate the usefulness of an alternate technology, Synthetic Aperture Radar (SAR).

NGS has long recognized the potential of SAR. Because it is largely unaffected by the presence of dense cloud cover, SAR delivers flexibility over weather constraints, and introduces the possibility of nighttime operations. Initial investigations by personnel in our research group questioned whether SAR systems deliver the necessary geometric

resolution and reliability for this demanding application (Malhotra, 1985). However, in the past decade the capabilities of both airborne and spaceborne SAR systems have improved dramatically. For example, the best resolution achieved with commercial satellites is about 8 meters (RADARSAT International, 1998); the typical resolution achieved by commercial airborne SAR vendors is about 2.5 meters (Bullock et al, 1997); and several research-level airborne systems have resolutions better than 1 meter (DiMango, et al, 1994). In 1997, we began a series of experiments with SAR technology. Because positional accuracy is important, we have concentrated on this issue in our research. We have recently completed our first estimates as to accuracies achievable with Fine Mode RADARSAT imagery, and we present these results here.

II. Methodology

We purchased a single 8-meter RADARSAT fine mode scene over a test site in southwest Alaska. We also flew panchromatic, 1:50,000 scale, reconnaissance quality aerial mapping imagery of the same area. Our strategy has been to map the shoreline from both sets of imagery and to compare the results from the SAR imagery to the shoreline manuscript produced using photogrammetric techniques. It is important to note that we are, therefore, comparing the SAR-derived shoreline to another estimate, and not to an absolute definition. In this experiment, we define the shoreline mapped from the aerial photographs to be the *reference shoreline*, and the shoreline measured on the SAR imagery to be the *test shoreline*.

Radar and optical imaging are very different processes. We expect the shoreline data mapped from the two sources to differ. Our goal is to understand these differences and to evaluate when RADARSAT imagery can be used for NOAA's nautical charting requirements. There are several aspects of our methodology that may influence the results: (1) factors arising from the geomorphology and the interaction of the SAR signals with the environment; (2) differences introduced because the two sets of images were acquired at different heights of tide; and (3) differences that arise from the mensuration procedures. In this work we define such differences to be errors, and we attempt to associate errors with causes.

A. Project Area

The area mapped in this experiment covers a 5 nautical mile stretch of Castle Bay in southwest Alaska. Castle Bay is a prominent geographic feature located 250 miles southwest of Kodiak and 5 miles south of the village of Chignik, on the Shelikof Strait side of the Alaska

Peninsula. The region is one of the most rugged and remote areas of the nation's shoreline, yet it is important to the Alaska commercial fisheries industry. Chignik's fishery is one of the richest and busiest in western Alaska (Rennick, 1994).

B. Geomorphology and Radar Phenomenology

The geomorphology of Castle Bay must be considered when analyzing our results. The area is fjord-like in structure, with steep, rocky cliffs rising to mountains of 3000 feet over a horizontal distance of 1 mile. The shoreline is a mixture of: rocky beaches backed by high bluffs; sand beaches backed by lower bluffs; and rocky headlands with no beach at all. Because of the well-known layover effect in SAR imagery, it is possible that the bluffs obscure the shoreline in some parts of the RADARSAT image (Tuell, 1998). Radar shadowing also occurs in topographic regions that slope away from the SAR sensor, creating dark areas that are difficult to interpret. When the reference shoreline and test shoreline differ because of these two effects, we label the differences *phenomenology - induced errors*.

C. Image Acquisition

The photography was flown at a slightly higher level than usual, 25,000 feet, and with significant cloud cover. For this reason, we classify the images to be of reconnaissance quality. The photo mission was executed by NOAA personnel in the NOAA Cessna Citation aircraft on August 27, 1997. The predicted stage of the tide at time of photography was 6.0 feet above MLLW. The MHHW level for the area is 8.5 feet (NOAA Chart 16566). The film was processed under contract and scanned into digital files using a pixel size of 12.5 μ m. The resolution in the digital photographs is about 0.6 meters per pixel.

We worked with NOAA colleagues at NESDIS, and through personnel at the University of Alaska, Alaska SAR Facility to acquire the RADARSAT image specifically for this experiment. The scene was acquired on May 22, 1998, when the satellite was in the ascending orbit. The predicted height of tide at the time of image acquisition was 1.3 feet. The imaging mode for the satellite was SAR Fine 5 FAR Beam, and the image resolution is nominally 8 meters. The product delivered to NGS was a Path Image Plus, on a CDrom.

The resolution in the aerial photographs is almost an order of magnitude better than in the SAR image. Previous research published by our group has suggested that in order to achieve accuracies that are competitive with photogrammetry, 1 -meter or better resolution SAR



Fig. 1. 1-Meter Orthophotograph of Project Area

imagery is required (Tuell, 1999). The reader can gain some measure of appreciation for this issue by comparing a detail from the 2 types of images as presented in Fig. 1 and Fig. 2. We show a 1-meter resolution orthophotograph constructed from the original aerial photographs in Fig. 1, and the same area from the RADARSAT image in Fig. 2.

In the 8-meter RADARSAT images, we can not say inside a pixel where the shoreline exists. In comparison with the aerial photographs, we expect *resolution-induced errors* to be as large as 7 meters at any one pixel. However, over a large number of shoreline pixels this effect should tend to zero.

The two sets of image data were acquired eight months apart, and were obtained with a 4.7 foot difference in predicted tides. We define errors in the shoreline comparison associated with the tidal differences to be *tide-induced errors*. Simple trigonometric relationships show that these errors are a function of the beach morphology. Over the extent of the shoreline covered in this experiment, we expect that the magnitude of tide-induced errors will range from zero, on the rocky headlands, to as much as 8 or 9 meters on gently sloping beaches. Here we note that this error range may lie within the area covered by a single pixel in the SAR image.

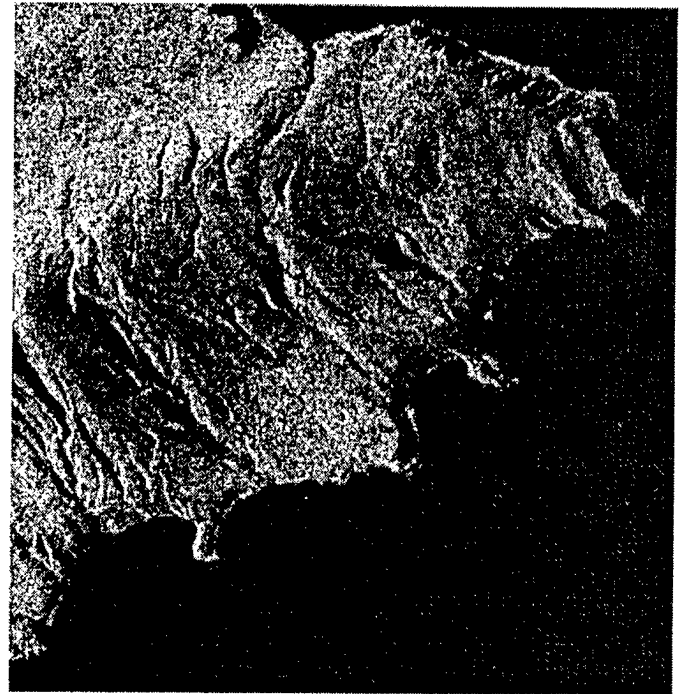


Fig.2 8-meter RADARSAT Image

D. Shoreline Mapping Procedures

The reference shoreline was mapped from the aerial photographs by an experienced photogrammetrist using a softcopy workstation. The aerotriangulation solution was performed using airborne GPS data to compute the positional elements of the exterior orientation, and by making photogrammetric observations of tie points to estimate the rotational elements. The mensuration of the shoreline was performed in the stereo models, and the shoreline was stored as a digital file. This file was imported into ERDAS Imagine as a GIS vector layer. The shoreline file was projected onto the Alaska State Plane Coordinate System.

The test shoreline was mapped from the RADARSAT imagery by the same photogrammetrist. The scene was imported into ERDAS Imagine and the geographic coordinates were projected onto the Alaska State Plane System. Mensuration of the shoreline was performed in the mono mode and consisted of manually tracing the land/water interface. The RADARSAT image was not manipulated in any way other than to occasionally alter the contrast in order to better interpret the land/water interface. Because we have not had previous experience in mapping from RADARSAT data, we expect the test shoreline contains interpretation-induced errors. As an example, we noted areas where the interpreted location of the shoreline could be shifted by one or two pixels. This uncertainty in interpretation typically occurred where there

were areas of pronounced radar shadowing at the shoreline. We expect the magnitude of interpretation-induced errors to be on the order of 8 to 16 meters, particularly in areas of radar shadow.

III. Georeferencing the SAR Imagery

Early in our experiment, we discovered that the RADARSAT image was not rigorously georeferenced. The magnitude of the error is clearly visible in the display of the initial results of the shoreline mapping operations shown in Fig. 3. Here we can see a prominent positional bias in both coordinates of the RADARSAT data. In this image, the RADARSAT - derived shoreline is positioned approximately 100 meters to the south and west of the photogrammetrically mapped shoreline. Without correction, *georeferencing-induced errors* dominate all other differences in the two depictions of the shoreline. In order to proceed with a mapping application of the SAR data, we must bring the SAR image into closer positional agreement with the aerial photographs. We have explored several procedures that can be used for this purpose. We elaborate on this issue in this section, and detail the development of a solution that can be used to remove the positional biases and provide a foundation for the accuracy analysis.

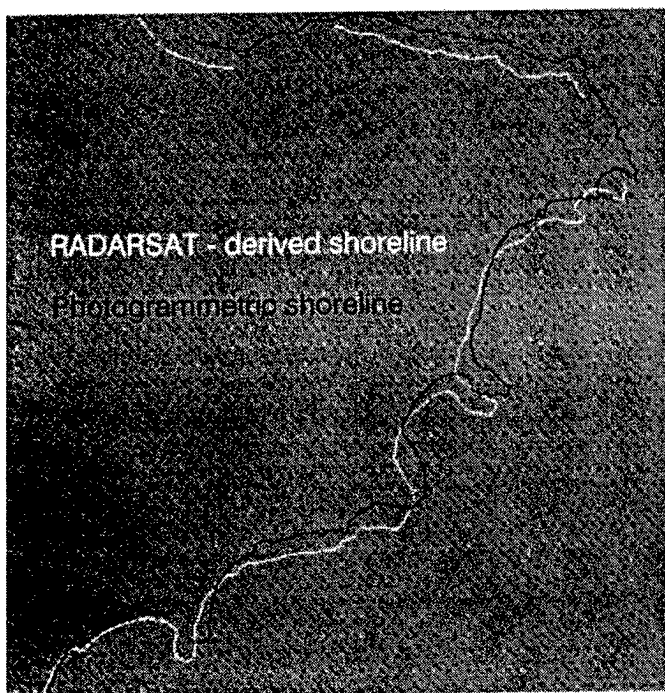


Fig.3. Positional Bias in RADARSAT

A. The Conjugate Point Approach

The usual approach to the georeferencing problem is to solve for a 3 parameter transformation based on the identification of conjugate points in the two sets of data. This computation is shown in (1), where one might choose

to treat the RADARSAT coordinates as observations (primed notation) and the photograph coordinates as fixed. The parameters are the two translations, and the trigonometric functions of the rotation required to bring the RADARSAT data into agreement with the photograph (after a change in algebraic sign).

$$\begin{aligned} X' &= X \cos\theta + Y \sin\theta + T_x \\ Y' &= -X \sin\theta + Y \cos\theta + T_y \end{aligned} \quad (1)$$

In the mapping sciences, (1) is typically solved by measuring a large number of conjugate points, and then casting the solution as a least squares adjustment for the translations (T_x and T_y) and the Rotation (θ). This was our initial approach. However, the procedure proved to be tedious and the results unimpressive. Using 12 conjugate points, we achieved estimates of a 70 meter translation in X, a 121 meter translation in Y, and a rotation of zero. Although a graphical application of these corrections applied to the RADARSAT data indicated that these estimates were believable, we were disturbed by the very large residuals associated with our solution (some more than 50 meters). It was clear that the poor solution resulted from the difficulty of identifying the conjugate points themselves.

One way to increase the reliability of the estimates is to measure a very large number of conjugate points. However, this is not an appealing solution because it requires a human operator to attempt the process when he has the differences in resolution and phenomenology working against him. Furthermore, the results would differ among individual operators. We decided to reject this approach in favor of one that was based on comparing the measured shoreline rather than the images themselves. This approach amounts to comparing two lines, and allows us to treat the problem as a correlation.

B. The Correlation Approach

In the correlation-based approach, we adopt the definitions given in Section II: the shoreline measured on the photographs is defined as the *reference shoreline* and the shoreline measured on the RADARSAT image is the *test shoreline*. The two shorelines have very different sampling intervals that were inherited from the imagery from which they were mapped. So, for this experiment we also characterize the reference shoreline as the *high resolution shoreline* (HiRes) and the test shoreline as the *low resolution shoreline* (LoRes).

We developed a solution based on matching distinctly-shaped segments of the reference shoreline to the test shoreline, and using correlation as the similarity measure. We implemented this approach as a

1-dimensional correlation in which we stepped the reference segment along the test shoreline with the lag coincident with the X-axis. By interpolating the LoRes shoreline to the same resolution as the HiRes shoreline, we were able to generate a solution containing more than 10,000 points, and this is a clear improvement over the manual method. But, even though the solution yielded believable results, it failed when the trend of the test shoreline ran more generally

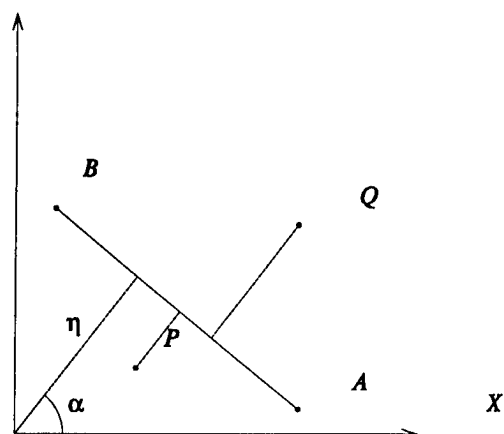


Fig.3 Distance of Points from Line Segment

along the Y-axis. These failures required an error analysis to remove false matches from the solution, and then an iteration of the computation (Graham et al, 1999). We concluded that a 1-dimensional correlation was not sufficiently objective for our applications.

C. An Approach Based on Minimizing the Residuals

We have developed a new technique that simultaneously addresses the goal of high dimensionality and objectivity. It is based on the widely accepted principles of least squares mathematics. In this approach we compute a shift (systematic error) in X (easting) and Y (northing) required to bring the test shoreline into the position of best average fit to the reference shoreline. In contrast to our previous correlation-based approach, we interpolate the HiRes shoreline to a regular grid, and compute distances from the interpolated points along a direction perpendicular to the line connecting the two nearest points on the LoRes shoreline. These distances are signed according to whether they are landward or seaward, and their standard deviations are used as the statistic to quantify the random error in the LoRes shoreline.

In the first step, we re-sample the HiRes shoreline at a fixed interval of one unit (one foot in this case) along its length. This technique differs from that used in the correlation approach where the re-sampling was at unit

intervals along the X-axis. (That process resulted in very sparse sampling along shoreline running approximately north and south.) Although sampling along the length of line required more computation, it resulted in a more reasonably spaced set of points with which to work.

Our technique requires a priori knowledge of the approximate transformation. As a second step, we estimate and apply the shift required to bring the test shoreline into close correlation with the reference shoreline. In our experiment we used the approximate shift estimated from the conjugate point method discussed in Section III, A. We found that the translations computed from several points well distributed over the lengths of the data sets brought the two representations of the shoreline into position for our iterative procedure to converge. In the following paragraphs we describe the procedure used to generate the *observations* for the least squares adjustment (Lucas, 1999).

Let A and B be two consecutive nodes on the LoRes shoreline and P and Q two points on the HiRes shoreline as shown in Fig. 1. (Recall that in this example the LoRes shoreline is also the test shoreline). The normal form of the equation of a line through the points A and B is

$$X \cos \alpha + Y \sin \alpha - \eta = 0 \quad (2)$$

where η is the length of the line segment from the origin perpendicular to the line and α is the positive angle it makes with the positive X-axis. The perpendicular distance from point P to the segment AB is given by

$$D = X_p \cos \alpha + Y_p \sin \alpha - \eta \quad (3)$$

and a substitution of the coordinates of Q will provide the distance of this point to the segment. This equation provides a signed distance. If the segment is considered to be a directed distance from A to B, then distances of points to the right will be positive and those of points to the left will be negative.

Because of its signed nature, the distance equation (3) can serve as an observation equation for a least squares adjustment to remove systematic errors from the positions of the LoRes nodes. Each point on the HiRes shoreline generates an observation of the distance (and direction) that the particular LoRes segment must shift in order to coincide with that point. The least squares adjustment of all of these observations provides a single shift that, when applied to all LoRes nodes, minimizes the sum-of-squares of the perpendicular distances between the HiRes points and the corresponding LoRes segments.

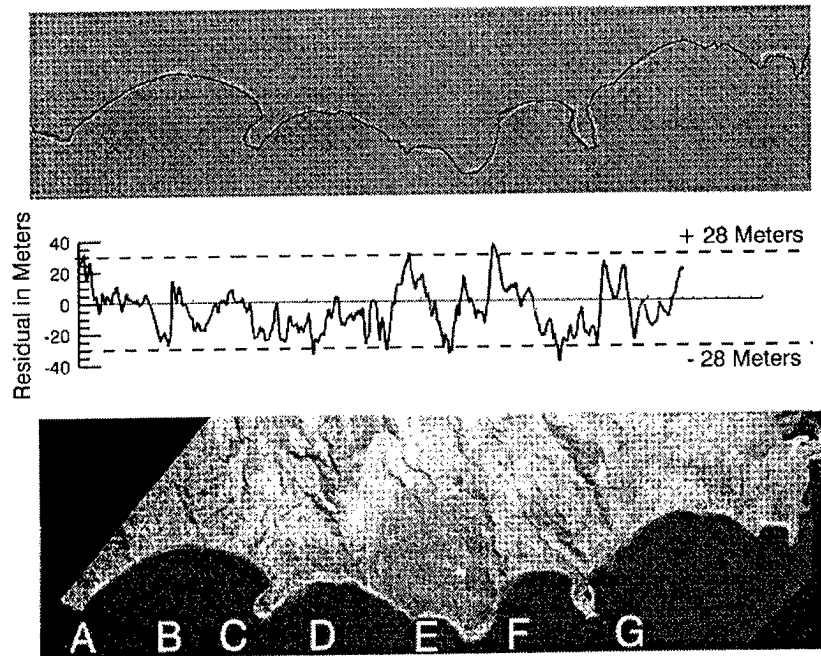


Fig.5. Analysis of Residuals

While the observation equations are linear in the unknown shift parameters, the adjustment does not behave as a linear adjustment. Once the computed shift is applied, some points may be beyond the terminus of the line segment to which they were being compared and must now have their distances from a different segment evaluated. This situation creates the need to iterate the adjustment until the computed shifts become sufficiently small as to be disregarded.

IV. Discussion

In our experiment, we used the *minimized residuals* approach to compute and remove the following positional biases from the RADARSAT imagery: $T_x = 74.9$ meters and $T_y = 134$ meters. The computation used about 9500 points. The standard deviation of the residuals is 14.2 meters, and the residuals are less than or equal to 28 meters in 95% of our data.

We can interpret the residual vector as a description of the separation between the reference and test shorelines at one foot spacing along the length of the data sets. One can imagine walking, one foot in front of the other, along the length of the reference shoreline and looking left and right at the incorrectly positioned test shoreline. The residuals are caused by interaction of the error sources discussed in Section II. Our goal is to understand the residuals within the framework of these errors.

As an aid in the analysis, we have found it useful to study the residual vector in a geographic context. The upper part of Fig. 5 shows the RADARSAT shoreline plotted on top of the photogrammetric shoreline after we applied the translations. This plot can be compared to Fig 3., where the reference shoreline (photogrammetric shoreline) is also depicted with the black line. The center illustration in Fig. 5 shows the residual vector from the least squares solution placed in its proper geographic orientation. The bottom part of the figure shows the orthophotograph.

Although the average error shown in the residual plot is zero, there are varying segments where the RADARSAT shoreline is too far landward and others where it is too far seaward. (Here, a positive residual corresponds to the RADARSAT shoreline being located too far seaward). The data points used in our analysis lie between point A and point G (about 5000 points over a distance of about 1.5 nautical miles). The area corresponding to A is composed of a steep cliff, with no beach. Here, the RADARSAT shoreline is seaward of the reference shoreline by as much as 33 meters. This error appears to be induced by a combination of resolution difference and shadowing, which are manifested in interpretation errors.

Between A and B, the agreement between the two shorelines is very good. This area is composed of a low, sandy beach backed by a low, grassy bluff. The residuals are on the order of 10 meters. We expect to encounter tide-induced errors in this situation. The low residuals

appear to validate the prediction that tide-induced errors are on the order of one pixel in the RADARSAT scene.

At *B* there is a zone in which the RADARSAT shoreline is too far landward by 25 meters. This error results from a combination of shadowing, and interpretation errors. Inspection of the RADARSAT image reveals that the shoreline is not visible in this area.

At *C*, there is a broad area of good agreement along a rocky beach backed by a low bluff, but at *D* there is a larger area where the SAR shoreline is too landward. The area at *D* is a small sandy beach backed by a low bluff. The residuals here result from a combination of tide-induced, resolution-induced, and shadow-induced errors.

At *E* and *F* there are interpretation-induced errors resulting from radar shadowing. There is a 35 meter error at *F* clearly arising from shadowing.

Between *F* and *G*, on the left side of the thumbshaped peninsula, the SAR shoreline is too far landward by as much as 30 meters. Because of the steep topography on this peninsula, we believe that these errors are generated by layover. We can see a crisp edge in the SAR image, but this edge is probably not the beach/water interface but rather the apparent interface between the cliff top and the water.

At *G*, there is another area where the SAR shoreline is too far landward. This error arises from shadowing and interpretation errors.

The observations in the preceding paragraphs appear to support a few generalizations.

(1) In this scene, radar shadowing generated more interpretation errors than did the inherent difference in the image resolutions.

(2) The tide-induced errors appear to be within the predicted range of one to two pixels in the RADARSAT image.

(3) Layover-induced errors did occur when steep bluffs faced the direction of satellite illumination. These errors were on the order of 20 meters.

(4) In this example, most of the interpretation-induced errors resulted in a landward shift of the RADARSAT shoreline.

(5) In this very complicated topography, the overall agreement between the two shorelines was better than 30 meters at the 2 sigma level.

V. Conclusions and Further Work

We have shown that differences in shoreline data mapped from RADARSAT Fine Mode images and aerial photographs are caused by numerous factors. In this case, the predominant error source was the misregistration of the RADARSAT image. We have shown that a positional bias (in this case 70 meters in one coordinate and 130 meters in the other) can be removed using a semi-automated technique. Our technique is based on registering the two shoreline vectors to each other using the least squares criterion. We achieve both high dimensionality and objectivity. The residual vector from the solution provides a natural mechanism for analysis of errors.

In this experiment, the georeferencing error was a first order effect. Phenomenology-induced errors (layover and shadowing) were tightly coupled with interpretation-induced errors. These two classes are second order effects, and in this case, they interacted to generate mapping errors less than 28 meters in 95% of our data. Tide-induced errors did not appear to be significant, and we have classified them as a third order effect.

One can argue that the results of this experiment represent a worst-case scenario. There are few areas of the U.S. coast that have more rugged and forbidding terrain than Castle Bay. In other areas phenomenology-induced errors are likely to be smaller and tide-induced errors larger. Also, we expect interpretation-induced errors to decrease as our experience with SAR technology increases.

We believe the results of this experiment are encouraging, and we have entered into active discussions with our NOAA colleagues in the Office of the Coast Survey to explore the application of RADARSAT shoreline to the nautical charts. To facilitate further work, we intend to increase the level of automation in our georeferencing approach. We also intend to apply this technique to other sources of data, for example to 1-meter airborne SAR data.

VII. Acknowledgements

The authors wish to thank Mr. Charles Challstrom, Director, NGS, and CDR Jon Bailey, Chief, Remote Sensing Division for their continued support and encouragement. We also thank CDR George Leigh (ret.) and CAPT Lew Lapine (ret.) for their vision in anticipating the potential use of SAR for the shoreline mapping application. We offer our gratitude to Mr. Bob Winokur, Director, NOAA NESDIS (ret.) and Mr. Bill Pichel, NESDIS, for their assistance in procuring the RADARSAT image. We also thank the NOAA flight crew (CDR Bob McCann, LCDR Brad Kearse, and Mr. Bill Stone) for their hard work in acquiring the reconnaissance photography, and Mr. Tim Blackford, Remote Sensing Division for processing the kinematic GPS solution for the photo mission.

VII. References

Bullock, M., Lawrence, G., and Tenant, K., 1997. "Commercial Applications of the Intermap IFSARE System". Proceedings of the Third International Airborne Remote Sensing Conference and Exhibition, Copenhagen, Denmark, Vol. 1, pp 34-41.

DiMango, M., Hanna, W., and Andersen, L., 1994. "The Data Collection System (DCS) Airborne Platform". Proceedings of the First International Airborne remote Sensing Conference and Exhibition, Strasbourg, France. pp 22-31.

Hicks, Steacy D., 1986. "Tidal datums and Their Uses - A Summary", The Hydrographic Journal, January 1986. pp 17-20.

Graham, D. G., Lucas, J. R., and Tuell, G. H., 1999. "Accuracy Assessment of RADARSAT-derived Shoreline, Preliminary Results", NOAA Internal Briefings (NGS/OCS/NOS) presented March 22, 1999.

Lucas, J.R., 1999. "A Least Squares Method for Comparing Two Shoreline Vectors", NGS Internal Report, 1999.

Malhotra, R.C., 1985. Preliminary Evaluation of STAR-1 Radar Imagery for NOS' Nautical charts. National Ocean Service, Office of Charting and Geodetic Services, NCRDL, Rockville, MD.

Radarsat International, 1998, Corporate data published on the World Wide Web: <http://www.rsi.ca> May 22, 1998.

Rennick, 1994. "Communities of the Alaska Peninsula", The Alaska Peninsula, Alaska Geographic, Volume 21, No. 1, 1994.

Tuell, 1998. "The Use of High Resolution Airborne Synthetic Aperture Radar (SAR) For Shoreline Mapping", ISPRS Commission III Symposium, Columbus, Ohio, July, 1998.

U.S. Department of Commerce and Department of Defense, 1997. Chart No. 1, United States of America Nautical Chart Symbols Abbreviations and Terms, Tenth Addition, November, 1997.

W-BAND RADAR MEASUREMENTS OF LABORATORY WATER WAVES

G. Connan¹, H.D. Griffiths², P.V. Brennan²
and R. Garelli¹

¹ENST-Bretagne, ITI Dept., France

²University College London, EE Dept., UK

ABSTRACT

The paper presents results on millimetre wave radar backscattering from laboratory water waves. Firstly, in a linear wave-tank, the radar has sensed mechanically generated surface waves of varying frequency (1 to 4Hz) and amplitude (0.5 to 10cm). Finally, in a 13m diameter wave-tank, scaled versions of particular internal wave phenomena have been set-up under mechanically generated surface waves, and the resulting wave-field has been sensed by the radar in SAR mode. Both series of experiments have been carried out at the Laboratoire des Écoulements Géophysiques et Industriels, Grenoble, France, within the EC project Mesoscale Ocean Radar Signature Experiments. First, the role of the radar and its operating mode are briefly presented, and the experiments are described. Then, the paper focuses on the data analysis and draws some conclusions on the backscattering mechanisms.

I. INTRODUCTION

In the frame of the European MAST project MORSE [1], an experimental W-band radar has been designed and developed at University College London Department of Electronic and Electrical Engineering, as part of an effort to improve the understanding of internal wave SAR imaging [2]. The idea was to obtain high resolution images of the water surface in the presence of internal waves, under laboratory conditions. The original design of the radar is based on two techniques: Synthetic Aperture Radar (SAR) and Frequency Modulation Continuous Wave (FMCW) [3].

The centre frequency is 94GHz corresponding to a 3.2mm electromagnetic wavelength. The radar bandwidth is 3GHz, which provides a slant range resolution of 5cm. A Pulse Repetition Frequency (PRF) of 625Hz or 2500Hz is used. Table 1 summarises the main radar parameters and Fig. I-1 shows a picture of the radar front-end, with separate dual polarization capability transmit and receive antennas.

The FMCW transmitted signal is linearly frequency modulated and radiated by a W-band antenna. A similar antenna receives the echo which is a delayed version of the transmitted signal. The mixing of both signals (intermediate Frequency signal) results in an instantaneous frequency difference between the echo and transmitted signal and this beat frequency is proportional to the target range. Hence, a variation in range is equivalent to a variation in frequency.

Therefore, the range information can be recovered by spectral analysis of the beat frequency. Thus, the simplicity of this radar system is that the downconversion of the IF signal is direct to base-band, which is convenient for signal processing, and gives a much lower bandwidth of the signal to be processed.

High resolution in cross-range implies the use of aperture synthesis techniques with the radar front-end moving along a circular arc in the wave-tank. The synthetic antenna provides a bigger aperture and consequently a better resolution.

Table 1: MORSE radar parameters

centre frequency	94GHz
wavelength	3.2mm
sweep bandwidth	3GHz
Pulse Repetition Frequency	625/2500Hz
sweep duration	1.6/0.4ms
IF bandwidth	100-400kHz
antenna beamwidth	32°
slant range resolution	5cm
azimuth resolution	0.5 to 1cm

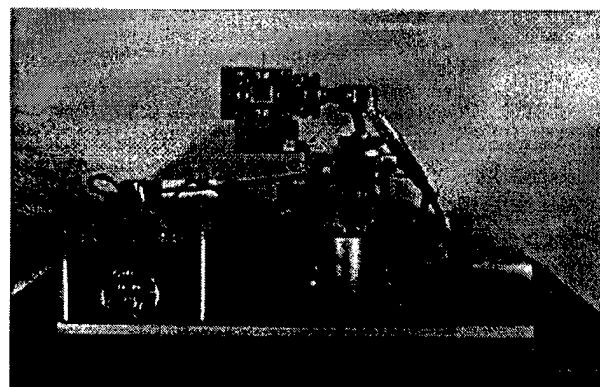


Figure I-1: MORSE radar front-end

A schematic view of these experiments is provided in [4].

A. Flume measurements

In static measurements, the radar is looking at the water surface at a height of 1.5 m and with an incidence angle of 35°. Over 1s, 625 (or 2500) FMCW chirps are transmitted and the received signal is recorded as a function of time. For each chirp, the Fourier transform of the echo yields the range information. Then, for each range bin, the Fourier intensity over 1s provides the time variation of signal intensity, at that particular range. To extract the frequency of the modulations appearing in the time variations of a given range, a Fourier transform of the time variation is performed, providing Doppler information.

The linear wave-tank is 55cm wide and it is filled with a fresh water column 25cm high. The water surface in this flume is modulated by a wedge-wave generator

B. Coriolis wave-tank measurements

In SAR measurements, the synthetic aperture is performed with a platform speed of 1m/s along a circular arc of 1 m, which corresponds to an integration time of 1s. The radar front-end is placed at a height of 1.7m, looking at the water surface with a 35° incidence angle.

In the circular wave-tank, a 4cm high fresh water column is lying above an 80cm salt water. An internal wave is generated by the rapid release of 100l of fresh water in the wave-tank. The internal wave, of a few millimetres amplitude at surface level, propagates just below a mechanically generated surface wave field of 3cm amplitude and the surface wave frequency varies from 2 to 5Hz.

C. Comments on the radar signal strength

In both experiments, the measurements are made for a VV-polarization since other polarization set-ups provide a significantly weaker radar signal.

A stronger radar echo is found for larger wave amplitude. But in the circular wave-tank experiments, the surface wave amplitude is limited by the fresh water layer height. It must therefore be kept small enough to maintain a good interface between the two layers.

The signal is also stronger for lower PRF, which is easily explained by the radar equation. But a higher PRF system exhibits less low-frequency noise so it is interesting to have both types of measurements.

The time variations of interest are those corresponding to the closest ranges, i.e. to the smallest incidence angle. Beyond 30° incidence, the signal cannot be properly analysed because of a weaker echo amplitude.

III. DATA ANALYSIS

A. Doppler information

From mechanically generated surface wave measurements, slow modulations as well as rapid ones are observed in the intensity of the echo, in both types of experiments. Fig. III.1 and Fig. III.2 illustrate these signal modulations in a flume experiment, for waves of 6 cm amplitude. To extract the frequency of the modulations, a Fourier transform of the time variation is performed, hence providing Doppler information. The idea is to try and discriminate the respective contributions of the dominant surface wave, free and bound capillary waves, Bragg waves, to the radar backscattering. Theoretical Bragg scattering occurs for a hydrodynamic wavelength such that:

$$\Lambda_{\text{wave}} = \frac{\lambda_{\text{radar}}}{2 \sin \theta} \quad (\text{III.1})$$

These time variations show that the mm-wave backscattering occurs in discrete bursts typically lasting 0.25s, which has also been observed from water wave experiments at other radar frequencies [5] in which they were thought to be related to small-scale events. But the peaks in the plot do not correspond to wave crests, as proved by the theoretical wave speed and average spacing of these

gravity waves. Using Eq. III.2 and Eq. III.3, in the flume, a 1 Hz wave has a wavelength of 1.4m and a speed of 1.3m/s while for a 2.5Hz wave, we have respectively 25cm and 0.6m/s.

The difference in the Doppler shift sign between Fig. III-1 and Fig. III-2 is due to the look direction of the radar. It can distinguish between a wave coming toward its front-end (Fig. III-1) and a wave moving away from it (Fig. III-2).

In the flume, by watching the surface wave profile carefully, one can easily see small capillary waves generated at the wave crests. They mainly propagate in the dominant surface wave direction, but a small portion generated on the back side of the wave, propagates in the opposite direction. This last observation is confirmed by the Doppler spectra of the lower plot of Fig. III-3, where a small peak appears at 40Hz, while the main energy lies in the negative part of the spectrum.

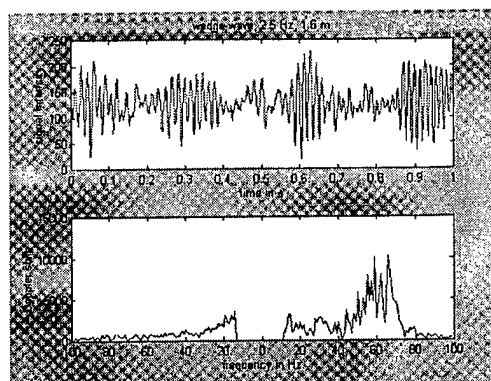


Figure III-1: Time variations and Doppler shift of a 2.5Hz wave

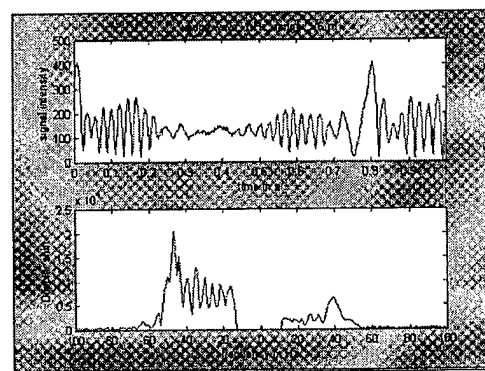


Figure III-2 Time variations and Doppler shift of a 1 Hz wave

We now try to relate the theoretical Doppler shift to the Doppler information we have extracted. The theoretical surface wave phase velocity is given by:

$$c = \sqrt{gh \frac{th(kh)}{kh}} \quad (\text{III.2})$$

$k = 2\pi/\lambda$ is the hydrodynamic wave-number, where λ is the average spacing between two wave fronts and h is the water column height. For a surface wave frequency ω , λ is found using:

$$\frac{\omega^2}{g} = kth(kh) \quad (III.3)$$

Then, the Doppler shift f_D is related to the phase velocity c by Eq. III.4, where θ is the incidence angle and λ is the radar wavelength:

$$c = \frac{f_D \lambda}{2 \sin \theta} \quad (III.4)$$

Fig. III-3 shows the theoretical Doppler shift of wave of wavelength varying from 0.1 to 10cm, when sensed by a mm-wave radar at different incidence angles. It can be deduced from this graph that the Doppler shift and hence the wave speed, increases with the average spacing between two crests and decreases with the radar incidence angle.

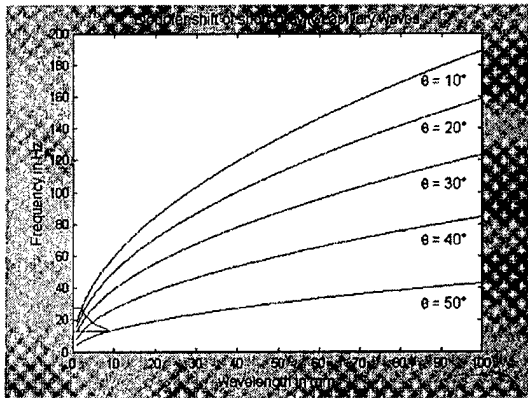


Figure III-3: Theoretical Doppler shift as a function of incidence angle and hydrodynamic wavelength

Let us now compare the experimental and theoretical values of the 1 Hz and 2.5Hz surface gravity wave. First, we can see that the experimental spectrum is made up of several peaks, which shows that scatterers of various wavelengths are detected. Both time variations correspond to the same range, i.e. an incidence angle of 25°. At this angle, the theoretical Doppler shift of the dominant surface waves is respectively 343Hz for 1Hz, and 158Hz for 2.5Hz. These values are well above the values we find in the experimental data. For the 2.5Hz wave, the Doppler shift main energy varies from 40 to 70Hz, while for a 1Hz wave it varies from 10 to 45Hz.

These observations clearly show that the mm-wave energy collected by the radar is mainly due to very small wavelength scatterers (slow scatterers). They correspond to the region 0.2 to 2cm wavelength in Fig. III-3, which includes the Bragg wavelength (3.8mm at 25°). It could be seen in the flume that the capillary waves generated on the wave crests were very small for a low frequency wave, while they were more numerous and of various wavelengths for a higher frequency, which explains the difference between both experimental Doppler shifts.

B. SAR reflectivity of surface waves

The SAR processing had to be adjusted to Coriolis experiment, for the geometry of the experiments required a particular processing, Fig. III-4. The resulting images are shown in Fig.III-5 and Fig. III.6, with a 5cm x 1cm imaging resolution. In the corresponding measurements, no internal wave is generated but the water wave is sensed for two surface wave frequencies. The white lines represent the theoretical average spacing between the crests of the surface wave for each frequency. The distance is respectively 28cm for 2Hz surface wave, and 14cm for 3Hz.

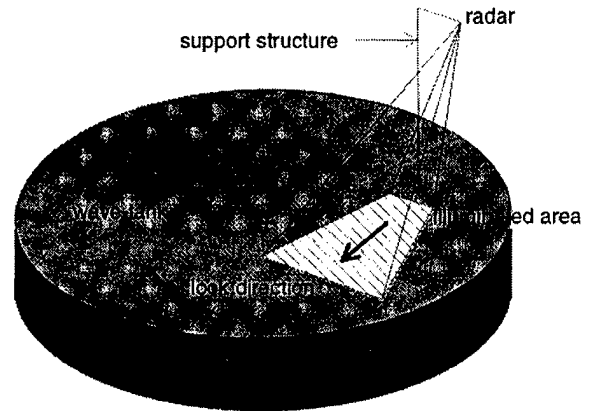


Figure III-4: SAR experiment geometry

The look direction (arrow on the illuminated area), as shown in Fig. III-4, corresponds to the arrow appearing on both Fig. III-5 and Fig. III-6. It has to be noted that the colouring of the images is artificial, the intensity increases with the electromagnetic reflectivity.

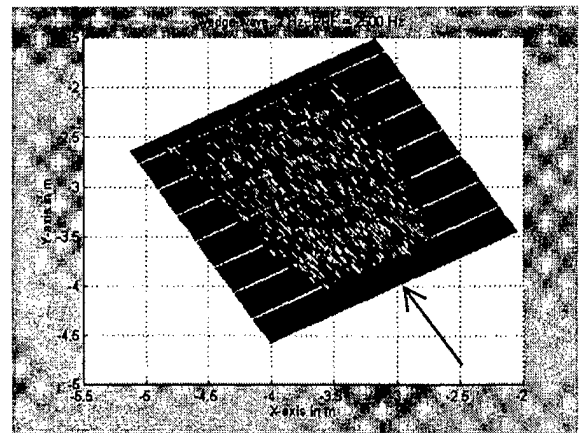


Figure III-5: 2Hz surface wave SAR image

We can see from these images that, although no precise surface wave field feature can be detected, the image reflectivity increases with the surface wave frequency. This can be explained by the fact that a higher surface wave frequency generates more different waves, i.e. more scatterers, to which the radar is sensitive.

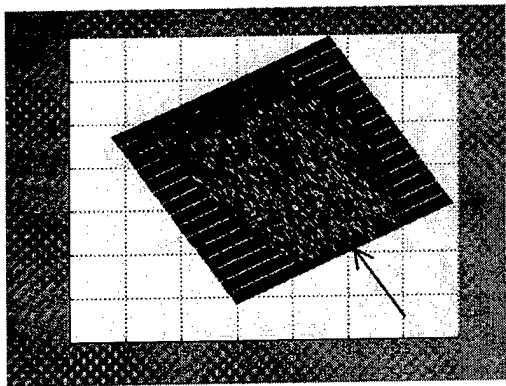


Figure III-6: 3Hz surface wave SAR image

C. Internal wave interaction with surface wave

In experiments where an internal wave propagates simultaneously with a surface wave, for ranges close to the radar, an interesting observation is made. It seems that the effect of the internal wave on the water surface is to modulate the surface wave field very finely in both time and distance. This can be seen at a fixed range in Fig. III-7, where the upper plot time variation seems to be modulated in the bottom plot when an internal wave is present.

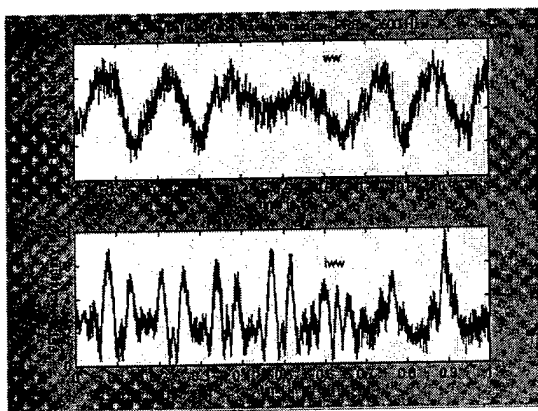


Figure III-7: Internal/surface wave interaction
Upper plot: surface wave
Bottom plot: surface wave and internal wave

These modulations in the echo intensity prove that the mm-wave radar is sensitive to very fine hydrodynamic modulations such as the interaction of an internal wave of very small amplitude with the surface wave-field.

IV. CONCLUSION

The MORSE radar is original because it combines the FMCW and SAR techniques, at 94GHz, in a simple design. The overall results show that the MORSE radar is capable of detecting fine hydrodynamic modulations: small capillary waves and small amplitude internal waves interacting with a surface wave field.

The Doppler analysis presented here attempt to take

into account the nature of the various scatterers detected by the radar. In particular, the radar wavelength (3.2mm) is very close to the actual wavelength of the detected scatterers.

It has been observed that the signal was stronger for ranges closest to the normal, therefore the main echo energy might be due to quasi-specular reflections from the water surface at small incidence angles. From this, we conclude that the backscattering probably originates from the specular reflections of the radar signal on small facets of various small-scale scatterers.

Future work includes a series of experiments, with the MORSE radar, in a wind-wave tank with optical measurement of wave profile, at the Institute of Oceanography, Hamburg University [6]. This will certainly be of great interest to better understand the mm-wave backscattering mechanisms.

ACKNOWLEDGEMENTS

The authors wish to thank the LEGI team of the Coriolis wave-tank and of the linear flume site, for their support and collaboration throughout these experiments. The authors also wish to thank the mm-wave laboratory team of the Microwave Department, ENSTB, for their help in characterising the radar mm-wave components.

This work forms part of that carried out under the CEC MAST III Contract MAS3 CT95-0027 (DG12-ESCY). The authors wish to acknowledge with thanks the support provided by the EU contribution to the funding of the project.

REFERENCES

- [1] L. Leviandier, E. Barthélèmy, P. Brandt, P.V. Brennan, G. Connan, A.C. Edwards, R. Garello, J. Rodenas, H.D. Griffiths, D. Renouard, R. Romeiser, A. Rubino, J.O. Thomas, and K. Woodbridge, "Mesoscale Ocean Radar Signature Experiments: MORSE", Proc. Third European Marine Science and Technology Conference, Lisbon, Vol. II, pp. 883-900, 23-27 May 1998.
- [2] W. Alpers and E. Salusti, "Scylla and Charybdis observed from space", J. Geophys. Res. Vol.88, No.C3, pp. 1800-1808, February 1983.
- [3] G. Connan and P.V. Brennan, "FMCW-SAR Development for internal wave imaging", MTS/IEEE Oceans'97 Conference, Halifax, October 1997.
- [4] G. Connan, H.D. Griffiths, P.V. Brennan, D. Renouard, E. Barthélèmy, R. Garello, "Experimental imaging of internal waves by a mm-wave radar", IEEE Oceans'98 Conference, Nice, September 1998, Vol. 2, pp. 619-623

[5] S.W. Daniel, W. Kwok and B.M. Lake, 'A deterministic, coherent and dual-polarised laboratory study of microwave backscattering from water waves, part 1: Short gravity waves without wind', IEEE Transactions of Oceanic Engineering Vol. OE-9, No. 5, pp. 291-308, 1994.

[6] M. Gade, W. Alpers, S.A. Ermakov, H. Hohnerfuss and P.A. Lange, 'Wind-wave tank measurements of bound and freely propagating short gravity-capillary waves', J. Geophys. Res. Vol. 103, No. C10, pp. 21,697-21,710, September 1998.

POLARIMETRIC RADIOMETER SENSING OF SEA SURFACE FRICTION VELOCITY

David E. Weissman

Department of Engineering

Hofstra University

Hempstead, New York 11549

Tel: (516) 463-5546; FAX: (516) 269-5920; E-mail: eggdew@hofstra.edu

Vladimir G. Irisov

Environmental Research Laboratories/NOAA

Boulder, CO 80303

William J. Plant and William Keller

Applied Physics Laboratory

University of Washington

Seattle, WA 98195

Abstract

The coincident measurements of the X-band radar scatterometer and the 37 GHz polarimetric radiometer during the COPE Experiment (Sept - Oct'95) and the Labrador Sea Experiment (which was coincident with NSCAT measurements during the Winter of 1997) were used to determine the dependence of the radiometers' azimuthal signature on friction velocity (and incidence angle). The radar cross section measurement provides the in-situ sensing of surface winds and stress (friction velocity). The scatterometer radar cross section can be converted into friction velocity using algorithms for Kuband, X-band and C-band measurements. The azimuthal signatures of the 37 GHz Stokes vectors are being analyzed to study the dependence of the 2nd and 3rd harmonic coefficients on incidence angle, wind speed and friction velocity.

I. Introduction

This study seeks to apply the measured anisotropy of the polarimetric microwave brightness to the estimation of sea surface wind stress. Coincident measurements with both radiometers and radars from airborne platforms have provided a unique opportunity to gauge the azimuthal parameters of the radiometer measurement in terms of surface wind stress, as sensed by the radar, with additional support from surface meteorological sensors.

The capability of airborne polarimetric microwave radiometers for the measurement of sea surface winds is being extended to include the estimation of sea surface friction velocity. This development is being advanced using microwave radar scatterometers operating

coincidentally with polarimetric radiometers during aircraft experimental operations. The in-situ data is supplemented with meteorological instruments on board ships (flux measurements collected on board the R.V. Knorr), by using dropsondes and with coincident NSCAT data.

The long term goal is to develop the capability of polarimetric microwave radiometers to estimate the sea surface wind stress, both the magnitude and direction, and to better understand the physical causes of the azimuthal variation of the sea surface brightness temperature, and its dependence on the air-sea parameters. Future plans are to demonstrate the benefits of the integration of active and passive remote sensing to advance our physical knowledge and the skills of radiometry for measuring the air-sea interface. This will add to the scientific foundation for sensors, applications and operational space-based systems, such as the proposed WindSAT passive being developed by NPOESS.

II. Approach

In the COPE-95 field experiment, the radar instrument on board the blimp is a coherent real aperture radar (CORAR) developed by APL/UW that operates at X-band (H-pol) in either of two modes: rotating for wind, wave and current measurements or fixed-azimuth for imaging. In the rotating mode, range gating enables the radar to measure the normalized radar cross section at incidence angles from 25 to 60 degrees in steps of 5 degrees. The azimuthally averaged NRCS at 40 and 50 degrees are most useful for conversion to friction velocity.

The polarimetric radiometer is capable of rotating azimuthally and determining the wind speed and direction at a variety of incidence angles. Data collected with dual polarizations and +45 and -45 degree measurements enable the calculation of the second and third Stokes parameters.

The instrument characteristics, flight operations, measurements and initial data analysis is presented in the paper by Irisov and Trokhimovski [1]. The algorithm for friction velocity that will be used to convert the radar cross section data is discussed in [2] and the application of this method is discussed in [3].

At each data run (which usually lasts between 10 to 15 minutes) the radiometer scan is at a constant incidence angle, and the radar observes numerous incidence angles simultaneously (from 35° to 60° in steps of 5°) using a new range-gating approach. The polarimetric radiometer data is processed to yield the 2nd and 3rd Stokes parameters, from which their Fourier coefficients (Q_1 , Q_2 , U_1 and U_2) are computed. A tabulation of the dependence of each of these items on incidence angle and friction velocity will be followed by their interpolation to create a geophysical model function for this instrument with higher resolution.

During the LABSEA Experiment, measurements coincident with NSCAT orbits were selected to utilize the u^* estimates derived from the NSCAT observations. The 37 GHz radiometer was one of many radiometers and other instruments on the NASA Wallops Flight Facility P-3 aircraft that participated in the Ocean Winds Imaging experiment in the Winter of 1997. [4] The aircraft rotation during descent in a spiral pattern enables the radiometer to have a variable azimuth observation.

III. Results

A sample of the azimuthal measurement of the 3rd Stokes coefficient, "U", at 32 degrees incidence is shown in Fig. 1. This was collected during the COPE Experiment from the BLIMP platform. It represents an azimuthal scan duration of 10 minutes. The wind speed was 6.6 m/s and the $u^*=0.31$. The individual radiometer measurements are 1-second averages, which are binned in 10-degrees increments, and the error bars represent the standard deviation in each bin. The wind direction was approximately from the North, where we can see that "U" is zero.

Scans such as this one in COPE and others in LABSEA, during a wide variety of wind conditions enables the collection of numerous data points for Q_1 , Q_2 , U_1 and U_2 , with which a u^* dependence can be studied. Fig. 2 below displays a preliminary assemblage of these observations. There is a clear strong

dependence of Q_2 and U_2 on wind stress, but Q_1 and U_1 display rather irregular, noisy variations without a clear signature.

Studies of the LABSEA data are still in progress and a more complete analysis of the available data will be available in the near future.

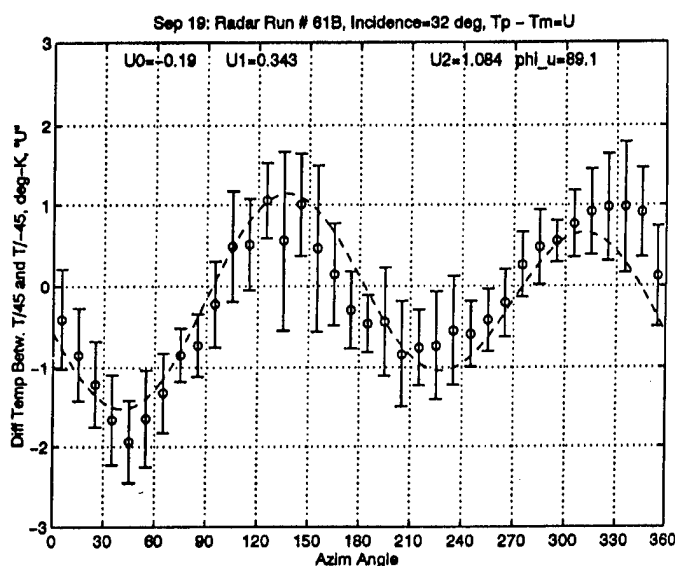


Fig. 1 Means and standard deviations of the binned groupings of the measured azimuthal dependence of "U" for a flight segment during COPE 95. Harmonic coefficients, U_0 , U_1 and U_2 , are also labeled.

IV. Acknowledgment

The support of this work by the Office of Naval Research Remote Sensing and Space Program is gratefully acknowledged. The authors would to acknowledge the assistance of Dr. A.J. Gasiewski of NOAA/Environmental Technology Laboratory in providing access to the Ocean Winds Imaging Experiment data and Dr. Peter Guest of the U.S. Naval Postgraduate School for providing his meteorological measurements onboard the R.V. Knorr

References

- [1] V.G. Irisov and Y.G. Trokhimovsky, "Observations of the Ocean Brightness Temperature Anisotropy during the Coastal Ocean Probe Experiment", IGARSS 96 Proceedings (IEEE International Geoscience and Remote Sensing Society), May 27-31, 1996, Lincoln, Nebraska
- [2] D.E. Weissman, K.L. Davidson, R.A. Brown, C.A. Friehe and F. Li, 1994: The relationship between the microwave radar cross section and both wind speed and stress: model function studies using FASINEX data, J. Geophys. Res., 99, C5, 10,087-10,108
- [3] D.E. Weissman, F. Li, S. Lou, S. Nghiem, G. Neumann, R. McIntosh, S. Carson, J. Carswell, H.

37 GHz Polarimetric Radiometer, Incidence Angle Range: 10 to 19 degrees

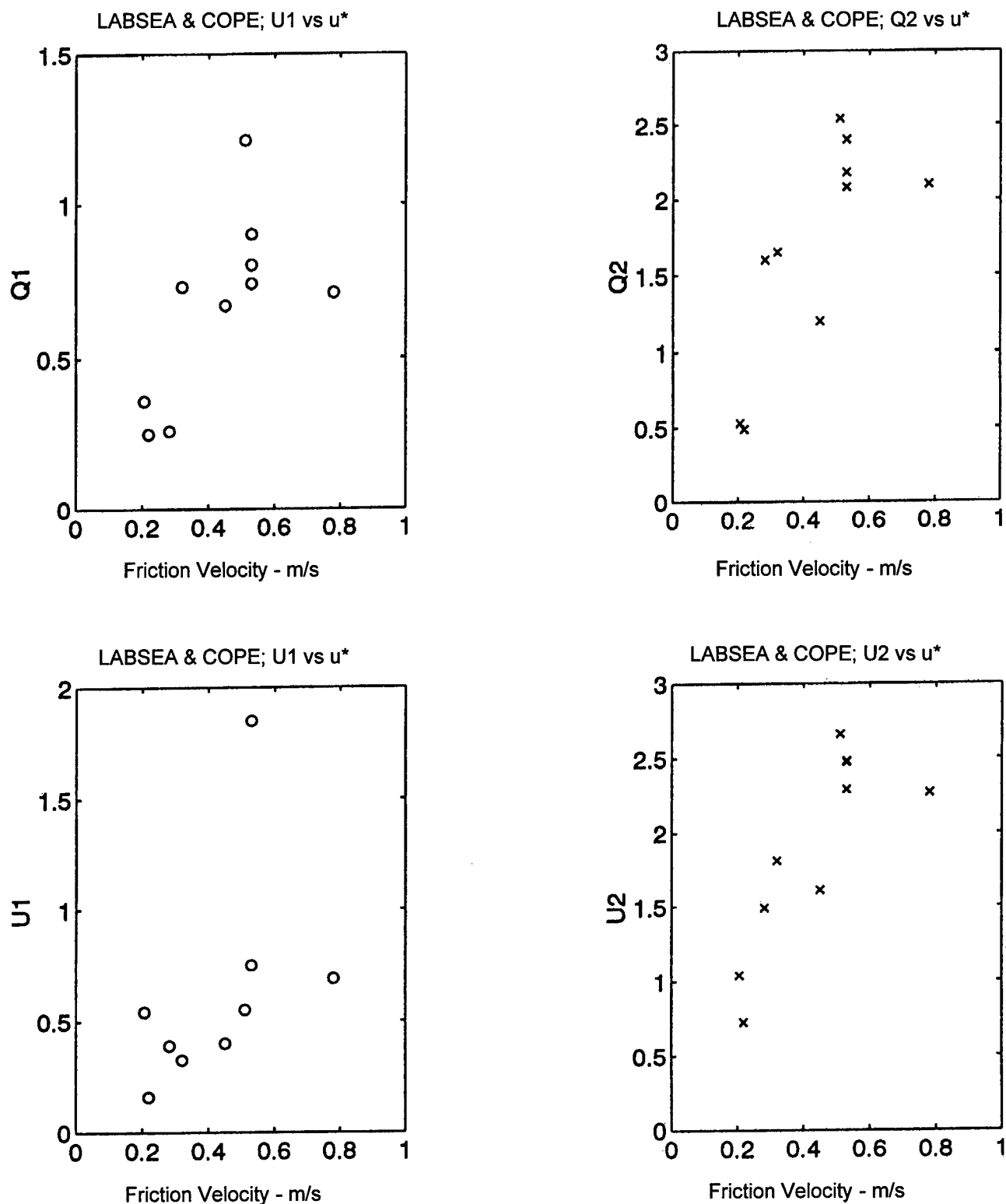


Fig. 2 Friction velocity dependence of the 37 GHz harmonic coefficients for the 2nd and 3rd Stokes parameters using combined measurements of the COPE Experiment for low winds and the LABSEA Experiment for high winds.

Acoustical Remote Sensing of Ocean Internal Waves: Progress and Remaining Challenges

Daniel Rouseff, Terry E. Ewart, and Stephen A. Reynolds

Applied Physics Laboratory
College of Ocean and Fishery Sciences
University of Washington Box 355640
Seattle, WA 98105 U.S.A.

Abstract

The state of the art for using acoustics to characterize ocean internal waves is reviewed. Results are presented for several experiments that span a wide range of oceanographic conditions. The inclusion of the proper physics in the model for acoustic propagation is shown to be crucial. Examples of remaining challenges include developing techniques to handle steeply turning ray paths, and generalizing Rytov theory to calculate two-point statistics in the presence of a sound speed gradient.

I. Introduction

Internal waves are ubiquitous in the ocean. As a basic research topic, they are of interest to oceanographers. Internal waves cause fluctuations in the sound speed and so are also of interest to ocean acousticians. Models for internal wave fluctuations come in two general flavors: for deep water, where there may be many different uncorrelated sources for the waves, a statistical representation is appropriate; for shallow water, where a distinct local bathymetric feature may excite discrete packets of internal waves, an additional more deterministic representation may have to be included. In either case, it is natural to propose using acoustics as a remote sensing tool to characterize internal waves. Acoustic measurements provide the versatility to probe the ocean over a range of temporal and spatial scales not easily accessible with conventional oceanographic instrumentation.

In this paper, the state of the art for using acoustics to characterize ocean internal waves is reviewed. Observations from several field experiments are summarized. These include the Mid-Ocean Acoustic Experiment (MATE), the AIWEX Acoustic Transmission Experiment (AATE), the recent Volume Scattering Primer Experiment, and the Shallow Water Acoustics in a Random Medium Experiment (SWARM). Together, these experiments encompass a variety of oceanographic situations (deep water, shallow water, the Arctic), acoustic frequencies (224 Hz to 150 kHz) and ranges (800 m to 40 km). In each case, direct environmental measurements were made concurrent with the acoustic transmissions and are critical to providing a baseline for the acoustic inversions. The remaining technical challenges are outlined.

II. Deep Water

By studying several deep water oceanographic data sets, Garrett and Munk developed a "universal" spectral model for

ocean internal waves [Munk, 1981]. Nominal values for some of the parameters of the model have been estimated, but oceanographers are interested in cases that deviate from the norm. The goal of an acoustic inversion would be to quantify the parameters of the internal wave model.

Like other waves, internal waves satisfy a dispersion relationship that relates their spatial and temporal properties. Using an approximate dispersion relationship, Flatté et al. [1979] gave alternative forms for the internal wave spectrum in terms of different combinations of the spatial and temporal transform variables, and the internal wave modes. It will prove useful in the context of solving the inverse problem to use a mixed representation that includes both the wavenumber $\mathbf{k} = (k_x, k_y, k_z)$ and the time separation τ . The index of refraction spectrum Φ is written as:

$$\Phi(\mathbf{k}; \tau) = F(\mathbf{k}) \cos(\omega_0 \tau), \quad (1)$$

$$F(\mathbf{k}) = \frac{\phi_g \kappa |k_z|}{(\kappa^2 + (\omega_i/N)^2 k_z^2)^q (k_z^2 + k_g^2)^{d/2}}, \quad (2)$$

where the fact that the spectrum is a function of k_x and k_y only through $\kappa^2 = k_x^2 + k_y^2$ ensures horizontal isotropy. The buoyancy frequency N is a function of depth while the inertial frequency ω_i is a known constant for a given latitude. The vertical part of the spectrum rolls off at wavenumber $k_g = j_* \pi N / (b N_0)$, where j_* is the internal wave modal bandwidth, N_0 is the reference buoyancy frequency, and b is the reference depth. An approximate dispersion relationship sets ω_0 :

$$\omega_0(\mathbf{k}) = \left(\frac{\kappa^2 N^2 + k_z^2 \omega_i^2}{\kappa^2 + k_z^2} \right)^{1/2} \quad (3)$$

It remains to fix the spectral level ϕ_g . In general, the index of refraction variance for internal waves is a function of depth that scales approximately like N^3 in deep water. Accordingly, the variance $\langle \mu_0^2 \rangle$ at the reference depth is defined by

$$\langle \mu_0^2 \rangle (N/N_0)^3 = \int d\mathbf{k} F(\mathbf{k}). \quad (4)$$

Substituting (2) into (4), the integrals can be evaluated exactly [Rouseff et al., 1997]. Solving for the spectral level yields an

Work supported by Office of Naval Research Code 321OA.

expression in terms of the remaining free parameters in the model. Assuming the buoyancy frequency is known from direct measurement, there are up to four free parameters in the model: the variance $\langle \mu_0^2 \rangle$, the mode bandwidth, j_* , and the power law exponents p and q . Within the standard Garrett-Munk model, the exponents are $p=q=2$. A typical deep water value is $j_* = 3$. In the above derivation, the WKB result is given. Methodology based on a more general formulation are also available.

One of the first systematic efforts where observed acoustic fluctuations were related to internal wave activity was the 1977 Mid-ocean Acoustic Transmission Experiment (MATE) [Ewart and Reynolds, 1984]. MATE was designed as a careful study in wave propagation in random media (WPRM) of the effects on acoustic intensity and phase induced by a variety of ocean phenomena including internal waves. Transmissions took place over an 18 km path between fixed towers placed on seamounts. Simultaneous oceanographic measurements of the intervening field were made so that ocean model statistics were determined [Levine, et al., 1986]. The original experiment was designed as a forward problem to test the ability of theory to explain acoustic phase and intensity statistics. Using a determined environmental internal wave model, the phase statistics were well explained by existing theory while the intensity fluctuations were not. MATE demonstrated that weak fluctuation theories (e.g. Born or Rytov [Ishimaru, 1978]) could be used to explain the phase fluctuations even though multiple scattering theory was needed to explain the intensity fluctuations. Having both environmental and acoustic phase measurements, the MATE data sets were later used to show that using Rytov theory, an ocean spectral model could be determined using inversion techniques. The results of this inversion are shown in Fig. 1 where both environmental (moored isopycnal displacement statistics) and acoustic phase statistics have been converted to common index-of-refraction units. The region between the inertial and buoyancy frequency is the internal wave band and the moored and travel time curves are related through the model in (2) with $q=1.85$.

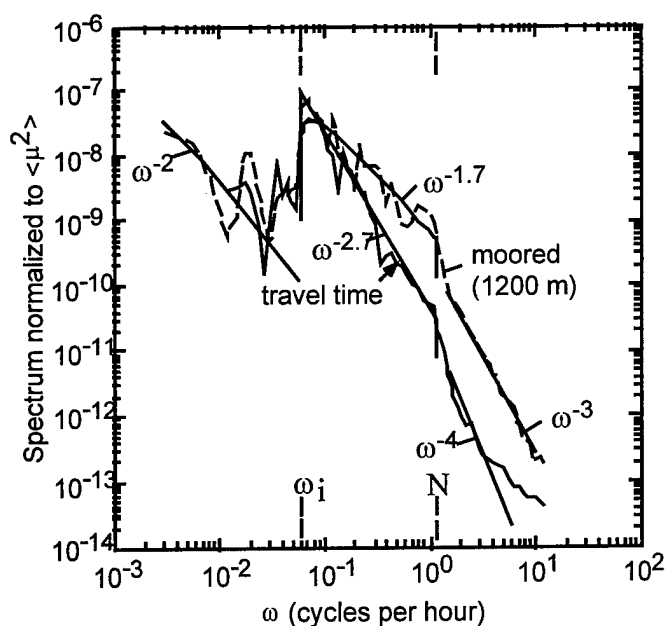


Figure 1. MATE phase and moored temperature sensor data converted to normalized units. [From Ewart and Reynolds, 1993]

The MATE intensity requires multiple scattering theory. In this scattering regime, inversion methods using intensity are problematic as the relationship between the acoustic observation and the environmental model is not simple. Another difficult case is when the acoustic ray path is steeply turning. The measurements in Fig. 1 were made over a deep, nearly straight acoustic ray path. A second MATE ray, with an upward trajectory, sampled fluctuations nearer the surface. These so-called "upper paths" remain a challenge for theorists [Heney and Macaskill, 1996].

Taking measurements with bottom mounted equipment is complicated and expensive. Using moored instrumentation reduces complexity and cost while making it possible to take measurements over a larger vertical aperture. In the very weak internal wave environment found under Arctic Ice, another set of acoustic measurements were obtained during the 1984 AATE (AIWEX Acoustic Transmission Experiment) [Ewart and Reynolds, 1990; 1993]. Acoustic energy propagated over a 6.4 km path between sources and receivers suspended below the ice. With AATE there has not been a successful inversion for the field. Motion in the array made use of the phase statistics problematic and although the weak scattering field produced small amplitude fluctuations, no theory exists for use with the ray paths encountered where there is significant curvature over the AATE paths. However, the concept of using amplitude measurements made using suspended receivers was later demonstrated in numerical studies [Ewart, et al. 1998]. The level of scattering in these studies was comparable to that encountered during AATE.

Internal waves are ubiquitous in the deep ocean. At very long ranges, internal waves are a primary noise-process in tomographic measurements of large scale ocean processes. The "noise" induced in these measurements has been used by investigators to infer the strength of the internal wave field as well as study the more deterministic baroclinic internal tides

also found in the internal wave band [Colosi, et al. 1999, Dushaw et al. 1995].

III. Shallow Water

In deep water, internal waves are typically propagating in many different directions. They are uncorrelated making it appropriate to model internal waves as a random process represented by a spectrum. The acknowledged success of the Garrett-Munk approach has lead to speculation that a similar model might be developed for shallow water. At a minimum, certain modifications to the model are known to be required [Heney et al., 1997]. Shallow water internal waves are dominated by lower order modes; j_* might be one, or even zero. Consequently, some approximations used to produce (1), particularly those derived from the WKB technique, might be invalid. The internal waves may also have a preferred direction.

In addition to a random background internal wave field, there is frequently another type of internal wave present in shallow water. Driven by tides and propagating from distinct bathymetric features, discrete packets of internal waves are often present. Satellite images have shown that these waves can retain their coherence over multiple tidal cycles [Liu, 1988]. Because of the bore-like nature of these waves, the term "solibore" has been coined [Heney and Hoering, 1997].

Despite these complications, acoustics offers a promising technique for studying both types of shallow water internal waves. At the very least, acoustic measurements can provide a range-averaged, integral constraint on an oceanographic model that might be developed. The specific inverse technique used will depend on the acoustic frequency and range, as well as the type of internal wave being studied.

A. Short Range/High Frequency

At sufficiently short ranges, the interaction of sound with the seabed can be neglected. This fact drives the inversion strategy and permits a rough partitioning between the effects of solibores and the effects of background processes. A ray-based model for the acoustics, similar to that used in deep water, remains appropriate

As an example, consider Fig. 2. On the left is a sound speed profile. The profile was obtained by averaging measurements made during the summer for a site off the Massachusetts coast. The sound speed is nearly constant near the surface with the thermocline causing a steep gradient between 10 and 25 meters depth. To the right are the two associated eigenrays connecting source and receiver separated by 815 m. The one ray path is nearly horizontal while the other is bent by the steep sound speed gradient and samples more of the water column.

Near the site where the profile in Fig. 2 was measured, an acoustic transmission experiment was performed in August 1996 [Williams et al., 1999]. As part of the Synthetic Aperture Sonar Primer Experiment, transmissions were at center frequencies 6, 20, 75 and 129 kHz. Source and receiver arrays were mounted on towers 815 m apart, with both at least 10 m above the seafloor. The goal was to measure the effects of internal waves on acoustic propagation when there were at least two distinct ray paths as suggested by Fig. 2.

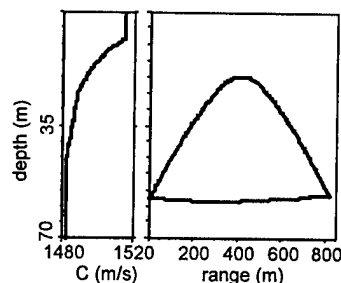


Figure 2. Shallow water sound speed profile and associated eigenrays connecting source and receiver. Note for the 815 m separation shown, two paths are permitted.

Figure 3 shows the travel time measured along the two paths over the course of nearly one day. Typical of shallow water, the upper path is seen to arrive after the lower path. Note how the time lag between the two paths is substantially reduced beginning around day 235.6. Concurrent oceanographic measurements show that this is when a solibore entered the acoustic propagation regime. The effect of the solibore was to depress the depth of the maximum sound speed gradient by about 10 m. The depressed sound speed profile caused the upper path to take a shallower trajectory closer to the lower path thereby reducing the time lag. Note also the increased fluctuations on both paths during the solibore. When the acoustic transmissions resumed at day 235.9, the solibore had passed and the paths again became more widely separated.

The detailed analysis of data from the Volume Scattering Primer remains an on-going effort [Heney et al., 1997; Williams et al., 1999]. Two distinct approaches are being taken. When no solibores are present, such as before day 235.6 in Fig. 3, the fluctuations in the acoustics are being attributed to background internal waves. The goal is to relate the statistics of the acoustics to the statistics of the internal waves. A different approach is needed when solibores are present. The distinct, event-like nature of the solibores makes a statistical approach unwarranted. Rather, a deterministic approach is taken. One goal is to relate the changes in the travel time to the rising and falling of the thermocline.

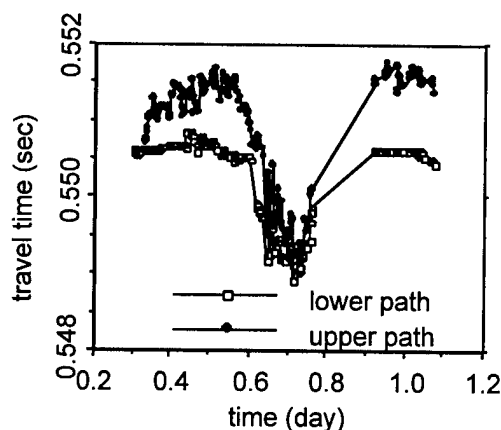


Figure 3. Results from the Synthetic Aperture Sonar Primer Experiment. Travel time measurements are shown for the two ray paths suggested by Fig. 2.

Unlike in deep water, where experiments are typically in the strong scattering regime, one could imagine designing a shallow water experiment where the weak-scattering Rytov theory applies. A typical criterion for the validity of Rytov theory is that the variance of the acoustic log-amplitude be less than 0.3 [Ishimaru, 1978]. Calculations suggest that this might be satisfied along the lower path in Fig. 2 at 6 kHz when no solibores are present.

There are significant practical advantages to basing an inversion strategy on the Rytov approach. When the background sound speed profile can be neglected, Rytov theory gives expressions for the two point statistics for both the log-amplitude and phase of the acoustic field. The log-amplitude and the phase are sensitive to different parts of the internal wave spectrum, a useful feature in doing an inversion.

The way in which Rytov theory would be applied is highly dependent on the specific experimental geometry. At one extreme, consider a rigid vertical receiving array. If the positions of the receiving elements were known precisely, it would be possible to use both the acoustic log amplitude and the phase in the inversion. If the array were fully populated, it would be possible to also estimate the vertical wave number spectra for both the log amplitude and the phase from the measurements. Together with the frequency spectra, this would be a comprehensive acoustic data set that could be used in an inversion. At the other extreme, consider a single moored receiver. Here, there is no vertical aperture and it would likely prove difficult to separate sensor motion from acoustic phase fluctuations. The only quantity that might be used in the inverse is the temporal spectrum of the log-amplitude.

In a numerical study, Ewart et al. [1998] considered a hierarchy of acoustic inversion strategies based on Rytov theory. An ocean model was used to simulate realizations of a time-evolving, three-dimensional internal wave field [Winters and D'Asaro, 1997]. Acoustic propagation through the realization was modeled using the parabolic equation method. The various synthesized acoustic spectra were then used as input to a least-squares inversion algorithm. Various combinations of the free parameters in the ocean model (1)-(4) were fit and compared to theory. For the most complicated experimental configuration consisting of a fixed vertical receiving array, all four free parameters of the model could be recovered. For the simplest scenario of a single moored receiver, two parameters could still be fit with reasonable accuracy. This has important implications for field experiments. Because precise tracking of the source and receiver positions is not required to measure the log-amplitude, such measurements would be simple to implement. The measurements could provide an important and inexpensive adjunct to oceanographic experiments.

Rytov theory is well-established, but certain extensions would prove useful for solving inverse problems. A priority is developing a theory for the two-point statistics when there is a background sound speed profile. Munk and Zachariasen [1976] included a profile in their calculations, but considered only the variance of the field at a single point and not the two-point vertical autocorrelation.

B. Long Range/Moderate Frequency

For acoustic propagation in shallow water to distant receivers, interaction with the bottom cannot be ignored. A convenient representation for the acoustic pressure is in terms of normal modes. A forward problem model based on normal modes requires different strategies for solving the inverse problem.

To illustrate normal modes in a simple setting, consider first the range-independent problem. Assume a time-harmonic point source is located at depth $z = z_s$. Neglecting certain scaling terms, the familiar expression for the pressure as a function of depth and range x is [Jensen et al. 1994]

$$p(x, z) = \sum_m (\xi_m x)^{-1/2} \Psi_m(z_s) \Psi_m(z) e^{i\xi_m x}. \quad (5)$$

Here, Ψ_m is the eigenfunction (normal mode) and ξ_m is the eigenvalue (horizontal wavenumber) associated with the discrete mode m .

If the medium varies in range, such as it will when internal waves are present, (5) no longer applies. The simplest generalization is the so-called adiabatic approximation. In this approach, the horizontal wavenumber is modified by adding a range-dependent perturbation term. This perturbation term can be directly related to the range dependence in the medium. The phase $\xi_m x$ in (5) is replaced by the integration of the now range-dependent ξ_m over range. Lynch et al. [1996] used this approach to study internal wave effects in an experiment conducted in the Barents Sea.

If the medium is strongly range-dependent, as might be the case when solibores are present, the adiabatic approximation will fail. The next level of sophistication in the acoustic modeling is to assume one-way coupled modes. In this approach, energy is allowed to be interchanged between modes as the wavefront propagates. As an example, consider the situation shown in Fig. 4. The heavy line shows a contour of constant sound speed. At time $\tau=0$, the region $x_1 < x < x_f$ contains a solibore. Over the time scales of interest, the solibore does not change shape; it simply propagates towards the shore at velocity u . Rouseff and Turgut [1998] showed that the pressure measured along the array as a function of time is

$$p(x_f, z; \tau) = \sum_m \Psi_m(z) \exp[i\xi_m(x_f - x_j + u\tau)] \times \sum_n (\xi_n x_f)^{-1/2} P_{mn} \Psi_n(z_s) \exp[i\xi_n(x_1 - u\tau)]. \quad (6)$$

The result has a simple interpretation. The energy in mode m propagates to the leading edge of the packet at range $x_1 - u\tau$. The transmission matrix with elements P_{mn} describes how the packet causes mode coupling; input mode m maps into output mode n . The field then propagates without mode coupling from the trailing edge of the packet at $x_f - u\tau$ to the receiving array.

The Shallow Water Acoustics in a Random Medium (SWARM) Experiment was performed in 1995 [Apel et al., 1997]. Analysis of the fluctuations in both the travel time and the intensity is continuing [Headrick, 1997; Pasewark et al. 1998]. The acoustic model (6) was developed to describe the

rapid decorrelation of the acoustic modes. For a more complete discussion of this effort, see the paper by Turgut, Wolf and Rouseff [1999] in these proceedings.



Figure 4. Model for propagation through solibore. The solibore position is a function of ut , where u is the group velocity and t is time.

For the SWARM experiment, the long propagation paths mean that solitary waves are always present somewhere. This can be shown by a simple calculation. Suppose the solitary waves are driven by the M_2 tide, and that the waves travel shoreward toward the acoustic source. Then the distance between packets equals the M_2 tide period times the packet group velocity. For $M_2=12.421$ hours and the 0.62 m/s packet velocity observed in the SWARM experiment, the distance between packets is 28 km. For the receiving array located at range 42 km, there were always at least one packet between the source and the array. Consequently, there is never a period where the acoustic fluctuations can be ascribed solely to the background internal waves. The model (6) neglects background internal waves. From the observed data, then, it is difficult to know how much of the acoustic fluctuation is due to solitary waves, and how much is due to the larger scale background processes. Developing techniques that would separate the two is the subject of current research

IV. Discussion and Conclusions

The experiments reviewed in this work encompass a wide variety of oceanographic conditions. The results emphasize that before the acoustic inverse problem can be solved, it is crucial that the forward problem be properly modeled. Ray-based techniques, the Rytov approach, multiple scattering theory, and both adiabatic and coupled modes can all be useful methods, but they must be applied in the proper context. In the MATE experiment, the Rytov approach was inadequate for the intensity and it was necessary to use multiple scattering theory. In the SWARM experiment, the adiabatic approximation was inadequate and it was necessary to include mode coupling.

The use of acoustics as a remote sensing tool to determine properties of ocean internal waves is in its infancy. The work has largely concentrated on verifying that the correct forward model has been used for a given oceanographic scenario. This verification has been accomplished by comparing acoustic results with concurrent oceanographic measurements and demonstrating consistency. The fact that this consistency has been achieved in multiple scenarios lends credibility to the notion that acoustic inversion can be a feasible approach to studying internal waves.

References

- J. R. Apel, et al., "An overview of the 1995 SWARM shallow-water internal wave acoustic scattering experiment," *IEEE J. Oceanic Eng.* 22, 465-500, 1997.
- J. A. Colosi and the ATOC Group, "A review of recent results on ocean acoustic wave propagation in random media: basin scales", *IEEE J. of Ocean. Eng.*, 24, 138-155, 1999.
- B. D. Dushaw, B. D. Cornuelle, B. M. Howe, and D. S. Luther, "Barotropic and baroclinic tides in the central North Pacific Ocean determined from long-range reciprocal acoustic transmissions" *J. Physic. Oceanog.* 25(4), 631-47, 1995.
- T. E. Ewart and S. A. Reynolds, "The Mid-ocean Acoustic Transmission Experiment - MATE", *J. Acous. Soc. Am.*, 75, 785-802, 1984.
- T. E. Ewart and S. A. Reynolds, "Instrumentation to measure the depth/time fluctuations in acoustic pulses propagated through arctic internal waves", *J. Atmos. and Ocean. Tech.*, 7(1), 129-139, 1990.
- T. E. Ewart, S. A. Reynolds, "Ocean acoustic propagation measurements and wave propagation in random media," in *Wave Propagation in Random Media (Scintillation)*, edited by V. I. Tatarskii et al., (IOP Publishing, Philadelphia) 100-123, 1993.
- T. E. Ewart, S. A. Reynolds and D. Rouseff, "Determining an ocean internal wave model using acoustic log-amplitude and phase--A Rytov inverse" *J. Acoust. Soc. Am.* 104, 146-155, 1998.
- S. M. Flatte' (Editor), R. Dashen, W. H. Munk, K. M. Watson, F. Zachariasen, *Sound Transmission through a Fluctuating Ocean*, (Cambridge University Press, Cambridge, MA), 1979.
- R. H. Headrick, "Analysis of internal wave induced mode coupling effects on the 1995 SWARM experiment acoustic transmission," Ph.D. dissertation, MIT/WHOI Joint Program in Oceanography and Oceanographic Engineering, 1997.
- F. S. Henyey and C. Macaskill, "Sound through the internal wave field", in *Stochastic Modeling in Physical Oceanography*, R. Adler, P. Müller, and B. Rozovskii (eds), 141-184, 1996.
- F. S. Henyey and A. Hoering, "Energetics of borelike internal waves," *J. Geophys. Res.*, 102, 3323-3330, 1997.
- F. S. Henyey, D. Rouseff, J. M. Grochocinski, S. A. Reynolds, K. L. Williams, and T. E. Ewart, "Effect of internal waves and turbulence on a horizontal aperture sonar," *IEEE J. Ocean Eng.* 22, 270-280, 1997.
- A. Ishimaru, *Wave Propagation and Scattering in Random Media*, Vol. 2, (Academic Press), 1978.
- F. B. Jensen, W. A. Kuperman, M. B. Porter, and H. Schmidt, *Computational Ocean Acoustics*, (American Institute of Physics, New York) 1994.
- J. F. Lynch, et al., "Acoustic travel-time perturbations due to shallow-water internal waves and internal tides in the Barents

Sea Polar Front: theory and experiment," *J. Acoust. Soc. Am.* 99, 803-21, 1996.

J. F. Lynch, "Report on ONR Shallow-Water Acoustic Workshop, 1-3 Oct. 1996," *WHOI-97-12*, 1998.

M. D. Levine, J. D. Irish, T. E. Ewart, and S. A. Reynolds, "Simultaneous spatial and temporal measurements of the internal wave field during MATE", *J. Geophys. Res.* 91(C8), 9709-9719, 1986.

A. K. Liu, "Analysis of nonlinear internal waves in the New York Bight," *J. Geophys. Res.*, 93, 12317-12329, 1988.

W. H. Munk and F. Zachariasen, "Sound propagation through a fluctuating, stratified ocean: Theory and observation," *J. Acoust. Soc. Am.*, 59, 818-838, 1976.

W. H. Munk, "Internal waves and small-scale processes," in *Evolution of Physical Oceanography*, edited by B. A. Warren and C. Wunsch, (MIT Press, Cambridge, MA) 264-291, 1981.

B. H. Pasewark, S. N. Wolf, M. H. Orr and J. F. Lynch, "Fluctuations in acoustic propagation seen in the SWARM 95 experiment," *J. Acoust. Soc. Am.* 104, 1765, 1998.

D. Rouseff, T. E. Ewart and S. A. Reynolds, "Obtaining the ocean index of refraction spectrum from the acoustic amplitude fluctuations," in *High Frequency Acoustics in Shallow Water*, edited by N. G. Pace, et al., (NATO SACLANT Undersea Research Centre, La Spezia, Italy) 467-474, 1997.

D. Rouseff and A. Turgut, "Coherence of acoustic modes propagating through shallow water internal waves," *J. Acoust. Soc. Am.* 104, 1765, 1998.

A. Turgut, S. N. Wolf and D. Rouseff, "Broad-band acoustic propagation through moving internal solitary wave packets in shallow water." To appear in these proceedings.

K. B. Winters and E. D'Asaro, "Direct simulation of internal wave energy transfer," *J. Phys. Oceanog.* 27, 270-280, 1997.

K. L. Williams, F. S. Henyey, D. Rouseff, S. A. Reynolds and T. E. Ewart, "Internal wave effects on high frequency propagation to horizontal arrays: Experiment and implications to acoustic imaging." Submitted to *J. Acoust. Soc. Am.* 1999.

DOUBLE DIFFUSION IN THE MODE OF «SALT FINGERS» IN THE OCEAN: NEW IN METHODOLOGY OF LABORATORY STUDIES.

Valery V. Kobylansky, Leonid S. Vilentchik, Mikhail M. Domanov, Dmitry L. Lushnikov, Ilgiz G. Ahmetsafin.

Federal Research Center MCB «Electron».

I. Abstract.

Studying of convective processes regularities, occurred under different physical and geographical conditions of World Ocean, is a traditional problem of physical oceanology. The laboratory experiments, which allow simulating the real physical processes of various scales – being one of conventional methods of the ocean physics investigations. The aim of this work is the creation of physical-mathematical model for heat- and mass- exchange in self-organizing structure of «salt fingers». The similar processes are characteristic for thin termohalin structures formed in the ocean by the double diffusion.

Experiments with model solutions (NaCl) and natural seawater were performed. The process of development of convective motion in two-layer nonstable system was initiated by double diffusion in the bath experiment. To measure the parameters of the process the special automatic installation with the termoprobe was designed and used, that allows to obtain good spatial-temporary resolution for the temperature. Dynamics (in time and space) and parameters of the 3-dimension complicated structure were studied. The fluxes of heat and salt between the structural elements were determined and compared with theoretical calculations. The experimental and theoretical results are discussed.

II. Introduction.

Interest to laboratory phenomena studies of double diffusion are kept in spite of the fact that the first laboratory experiments were executed by known authors sufficiently long ago (Turner, 1967; Stern and Turner,

1969; Linden, 1971). The theoretical and laboratory investigations of those years have allowed to define integral flows of heat and salts between layers of seawater in exchange processes for the mechanism of double diffusion and to evaluate their value for the ocean (Williams, 1974).

Number of problems, which one can to solve by only laboratory modeling, however is kept (Chashechkin, 1994).

We have considered expedient to execute a series of experimental work for more detailed study of the dynamics of «salt fingers» process formation, and determination of parameters a heat and salt exchange in the structure of «salt fingers». Assumed to get additional data about physico-chemical processes in thin termohalin structure and, in the end total, create a complete physico-mathematical phenomena model. In the present work the results of the first stage of researches are stated.

III. The experimental method.

Shaping of "salt fingers" simulated in the two-layer system: cold salty under - warm more-salty upper layer. Experiments were executed in the glass tank $9.5 \times 9.5 \times 20$ cm. As a main medium the solution of NaCl (35‰) is used. Temperature of the lower cold layer was equal to room temperature to exclude heat exchange through walls of container. In two series of experiments salinity of an added solution was differed from base salinity solution on $\Delta S = 1.4\text{‰}$ and $\Delta S = 0.5\text{‰}$. For visualizations of shaping process of "salt fingers" added solution was coloured by the known amount of dye

KMnO₄. Fixed volume (10ml) of the salty dyed solution heated up and was cautiously poured atop of cold layer.

Temperature sensing (vertical and horizontal) realized by means of the probe (detector element - thermistor CT1-19). Results of sensing were fixed by the grapher. Characteristic of experimental installation allowed reliably registering fluctuations of temperature in 0.01°C. The process of formation a spatial structure was shot by a camera.

Thickness of the upper painted layer at the beginning of experiment, as a rule, was 1cm. Using the volume ratio of upper painted layer and amounts of added warmed solution, the salinity of upper layer at the beginning of experiment was calculated, and initial difference of salinity layer was evaluated. Subject to possible mistakes by the visual determination of layer thickness (0.2 cm) the salinity of upper warmed layer can be accepted equal $\Delta S = 35.06 \pm 0.03\text{‰}$ for $\Delta S = 0.5\text{‰}$ and $\Delta S = 35.16 \pm 0.03\text{‰}$ for $\Delta S = 1.4\text{‰}$.

Main parameters, which characterized the simulated system for $\Delta S = 0.5\text{‰}$ are indicated in the Table 1. For the typical spatial scale d was accepted thickness layer of maximum temperature gradient (2cm). Obtained numbers Rs (salinity) and Ra (temperature) corresponds areas of "salt fingers" on the diagram of stability of liquid, stratified on the temperature and salinity (Turner, 1973).

Table 1.

Parameters describing simulating process	Value
$Rs = \frac{g\beta \Delta S d^3}{\nu k}$	$\sim 2.5 \times 10^4$
$Ra = \frac{g\alpha \Delta T d^3}{\nu k}$	$\sim 5 \times 10^4$
$\frac{\alpha \Delta T}{\beta \Delta S}$	~ 2
$Re = \frac{VD}{\nu}$	~ 3
$Pr = \frac{\nu}{k}$	~ 10
$\tau = \frac{k_S}{k}$	$\sim 10^{-2}$

In the table and below are accepted:

g (cm/sec²)- acceleration of gravity;

β (°/°°)⁻¹- corresponding coefficient for salt;

α (°C)⁻¹- coefficient of volume expansion;

ν (cm²/sec)- coefficient of kinematic viscosity;

k (cm²/sec)- coefficient temperature conductivity;

V (cm/sec)- mean velocity of streams falling;

k_S (cm²/sec)- coefficient of salt diffusion;

D (cm)-diameter of main part of "salt finger";

Re - Reynolds number;

Pr - Prandtl number;

IV. Results.

Process of "salt fingers" structure development is shown in Fig.1. Cellular structure, as a rule, consisted of the periodically located falling streams. Mean diameter of streams was 7 mm, but average of falling velocity was 0.06 cm/c for $\Delta S = 1.4\text{‰}$ and 0.04 cm/c for $\Delta S = 0.5\text{‰}$. On each side of container was observed 9-10 streams. Total number of forming steams was 80-100.

Changing of vertical temperature profiles in the heat and salt exchange process between layers in the mode of "salt fingers" are shown in Fig.2. In Fig.3 are shown temperature profiles in the heat exchange without "salt fingers" forming (blank experiment with the same salinity ($\Delta S = 0$), but different initial temperature in identical conditions). Results of temperature measurements for horizontal crossing through a structure "salt fingers" are shown in Fig.4.

The maximum amplitude of temperature fluctuation through horizontal crossing of "salt fingers" was 0.037°C.

V. Discussion.

Using plots of temperature changing in time for simulated two-layer system, effective temperature conductivity coefficient k_z through area with a "salt fingers" was calculated. Value of coefficient is defined from expression

$$k_z = \left(\frac{\partial T}{\partial t} \right) / \left(\frac{\partial^2 T}{\partial z^2} \right). \quad (1)$$

The time and directional derivatives were determined from experimental plots $T(t)$ and $T(z)$. Here and below t -time, z -vertical coordinate. The obtained thus mean value of effective temperature conductivity coefficient was equal 1.1×10^{-2} cm²/sec, which on the order exceeds

a temperature conductivity coefficient for seawater $1.49 \times 10^{-3} \text{cm}^2/\text{sec}$ (under 20°C).

On the ground of measurements of "salt fingers" growing rate and geometric sizes of their main part were calculated values of density in fingers on different horizons. For calculation used balance equation in Stokes approximation of the form

$$\Delta\rho = 18 \frac{\nu\rho V}{gD^2}, \quad (2)$$

where $\Delta\rho$ (g/cm^3) is difference of density in the buoyancy element and in the medium ρ .

Using data of the buoyancy element temperature and its density values of salinity exchanging in "salt fingers" on different horizons were found. For the temperature of buoyancy element was taken a maximum absolute value of temperature fluctuation through horizontal. Results of experimental and calculation data are shown in Fig.5.

Obtained data show that with moving away the interface of layers, salinity gradients between «salt fingers» and interfinger medium decrease. Line approximation shows that decrease of gradient is $\sim 0.002^\circ/\text{cm}$. One may to note that under line approximations a maximum salinity value of «salt finger» near interface layers is evaluated of $35.04^\circ/\text{oo}$. Calculated value of upper layer salinity is $35.06 \pm 0.03^\circ/\text{oo}$.

Using the found values allows make principle evaluations of heat and salt fluxes directly in layer of «salt fingers».

Obtained experimental and calculating material will be elaborated and used for getting the constants of transport equations in mathematical models describing heat and salt exchange in the mode of «salt fingers».

References.

Turner J.S. 1967, Salt fingers across a density interface. - «Deep-Sea Res.», vol.14, p.599-611.

Stern M.E., Turner J.S. 1969, Salt fingers and convecting layers. - "Deep-Sea Res.», vol. 16, p.497-511.

Linden P.F. 1971, Salt fingers in the presence of grid-generated turbulence. - "J. Fluid Mech.», vol.49, part 3, p.611-624.

Williams A. 1974, Salt fingers in the Mediaterranean outflow. - "Science», 185, N4155, p.941-943.

Turner J.S. 1973, Buoyancy effects in fluids. - Cambridge Univ. Press, 367p.

Chashechkin U.D. 1994, Double diffusion (termohaline) convection. - (Chapman-conference of American Geophysical Unity. (Scottsdale, Arizona, 1993), Oceanology, vol. 34,N6, p. 931-933.

Fedorov K.N. 1976, Thin termohaline structure of the ocean waters. - Leningrad, Gidrometeoizdat, 184p.

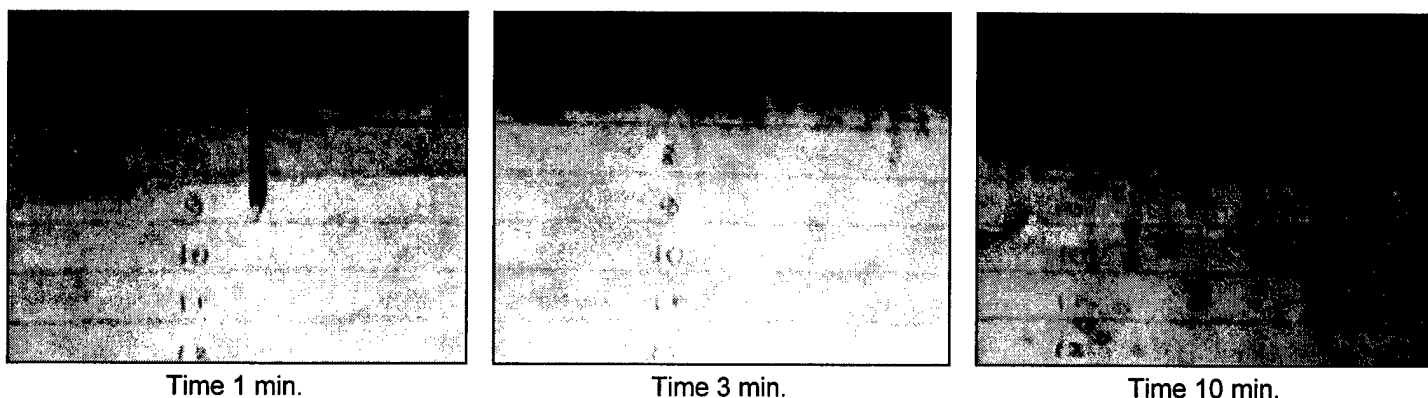


Fig.1. Development of «salt fingers» structure.

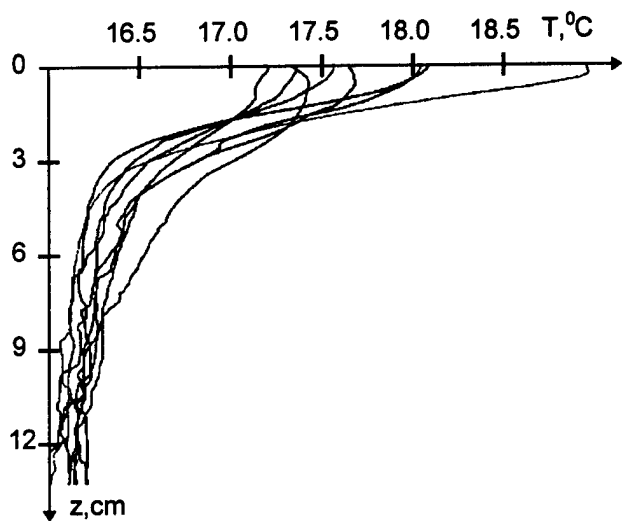


Fig. 2. Series of temperature vertical profiling (upwards-downwards) when forming «salt fingers». Interval of profiling is 3 min. $\Delta S = 0.5\text{‰}$.

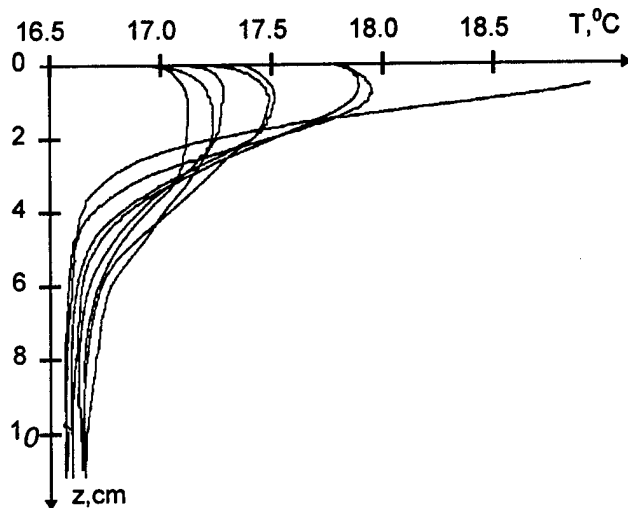


Fig. 3. Series of temperature vertical profiling (upwards-downwards) without forming «salt fingers». Interval of profiling is 8 min. $\Delta S = 0$.

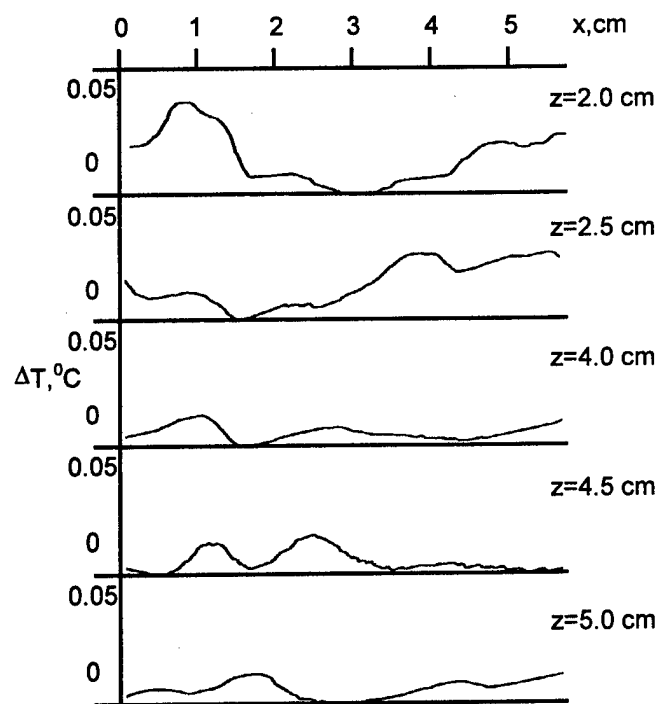


Fig. 4. Spatial temperature fluctuation on different distances from the interface of layers. Axis x distance of horizontal displacing a sensor. $\Delta S = 0.5\text{‰}$.

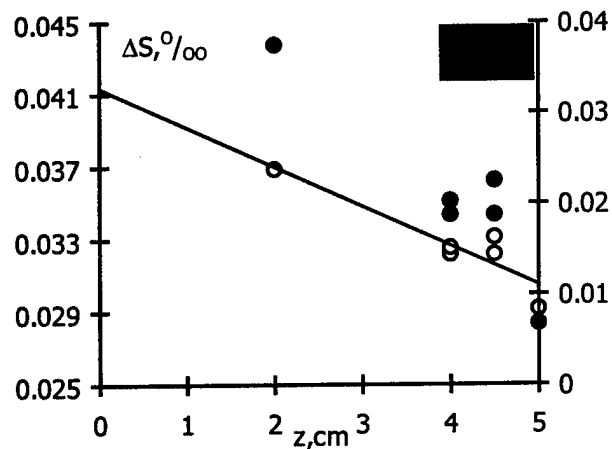


Fig. 5. Difference of «salt fingers» temperature and salinity and interfinger medium on different distances z from the interface. • - temperature (experiment), ○ - salinity (calculation). $\Delta S = 0.5\text{‰}$.

TIDAL ZONING and VERTICAL REFERENCE MEASURING COOK INLET, ALASKA 1999

**John Oswald,
LCMF
Doug Lockhart, Robert Richards,
Racal Pelagos, CA**

Abstract:

The U.S. Department Of Commerce, National Oceanic And Atmospheric Administration National Ocean Service, Office Of Coast Survey, Hydrographic Survey Division (NOS) is in the process of obtaining basic nautical charting of 160 square nautical miles (136,000 acres) of Upper Cook Inlet shipping lanes during the summers of 1999 and 2000. Multibeam surveying techniques will be required meeting the International Hydrographic Organization (IHO) specifications.

Racal Pelagos (RPI) and its subcontractors, LCMF Incorporated (LCMF) and Terra Surveys LLC (Terra), conducted an extensive vertical reference measurement and tidal study in upper Cook Inlet during the fall of 1998 and throughout the survey period in the summer of 1999. The primary task was to establish a tidal zoning scheme suitable for supporting the accuracy requirements of multibeam hydrographic surveys. The tidal regime for this area is the most complex in the United States, as the tidal range is large, sites are remote, extensive mud flats are prevalent, high currents are the norm, and the weather is severe. The tide correction can exceed thirty feet and constitutes by far the largest part of the error budget.

The project included the installation of multiple tide stations, operating for the duration of the summer field season from early May through September 1999. During the preliminary surveys of 1998, a tidal reduction method was developed and implemented during the multibeam surveys during 1999-2000.

SIMULATION AND CONTROL TECHNIQUES UTILISED FOR GENERIC ASSESSMENT OF A FULLY REELABLE SUBMARINE TOWED ARRAY HANDLING SYSTEM

Dr S P Tomlinson, Mr. D Cowling and Mr.J.S.Baker

Underwater Systems Integration
Defence Evaluation & Research Agency
Winfrith Technology Centre
Dorchester DT2 8XJ
United Kingdom

1 Introduction

The traditional design of in-service Towed Array Sonar within the Royal Navy has, in the main, employed equipments of relatively short acoustic aperture and 'clip-on' technology. However, as the role of the submarine has changed to meet the perceived threat, so the technology has adapted to meet the naval requirement. Hence, certain classes of submarine are required to have fully reelable towed arrays that provide long acoustic apertures and are stowed on the platform, a procedure entailing both deploy and recover operations.

The handling and control of a fully reelable array transmission system presents a severe technical challenge to the designer. Operational difficulties have been observed in many systems required to recover and deploy such lengthy arrays, which are of a combined plastic and elastic composition. The plastic properties of the external hose give rise to material failure, which manifests itself either as rucking or stripping of the array modules. In addition, the physical characteristics of these systems vary dramatically during different phases of the deploy and recover operations, due to variations in both

platform speed and sea temperature. Reelable arrays require carefully designed handling transmission systems, which avoid both the occurrence of slack cable (with consequent loss of control) and the tendency of the array to 'ruck' (a distortion associated with the natural modal shape) when placed in compression. Array rucking is associated with the hose material strength properties and the complexity of the guidance path, being particularly prone to occur at bends and the passage through the deployer.

In order to reduce the high risk associated with the design of a fully reelable array handling system, it is necessary to acquire a thorough understanding of both the complex properties of arrays and the transient performance of deployment and recovery equipment over a wide range of operational conditions. To this end, DERA Winfrith have engaged in Applied Research activities to further the understanding of these systems. This research involves both theoretical modelling and experimental activities. The latter makes use of a DERA Platform Integration and Cable/Array Handling Test Facility, capable of assessing a wide range of submarine and ship Reelable Array and associated systems. The principal activities include:

- Development of Control System strategies
- Development of Array and Cable Handling and Guidance Systems

These aspects are assessed with the following complementary activities:

- Mathematical modelling
- Experimental testing

Generic mathematical models of a range of towed array handling systems have been developed, capable of predicting the behaviour of complex electro-hydraulic systems comprising winches, deployers and guidance routes with electronic feedback control systems. The term Rapid Control Prototyping (RCP) is used to describe the process whereby a system model is used to develop and optimise a control system. This control system is subsequently downloaded to produce a real time control for use in the loop with the real hardware (reelable array system). RCP (real time model) has been used for on-line control experimental applications and non real-time models used to perform sensitivity case studies and assess the effects of alternative circuit configurations or control strategies. The two approaches are complementary and combine together to enhance the understanding of the sub-systems and hence determine how these are best integrated to obtain optimum performance.

The design and development of a fully reelable array system presents difficult control and handling system requirements, necessitating evaluation by means of the detailed computer model. The real-time model has therefore been used for the assessment of 'robust' feedback control systems, capable of meeting the diverse

performance requirements over the required operating envelope. The behaviour of this type of system changes considerably during different phases of the deploy and recover operations, due to variations in both platform speed and sea temperature, the latter affecting the properties of the external hose. This can give rise to material failure, which manifests itself either as rucking or stripping of the array modules. When deploying the array, the control system ensures that the deployer unit maintains a positive back tension at the winch until the in-water drag on the array is sufficient to provide this back tension. However, the motion of the drum winch required to store the array presents a severe problem. When initiating deploy, the transmission system is required to provide a precise control of the tension, whilst overcoming very large frictional forces and high inertia transients. Both these effects require careful consideration in order to ensure smooth motion with no likelihood of either an array ruck or zero tension, these being conditions that would result in a total malfunction of the handling system.

In order to overcome this type of operational problem, a Modern Control approach is required and Fuzzy logic has features ideally suited to the solution. Fuzzy logic is based on the interpretation of expert human experience and is implemented by defining linguistic rules which allow for partial rather than discrete membership of logic sets, a feature that is the kernel to its power. When the model has been developed, the fuzzy logic controller is added to ensure parameter boundaries for safe handling are not exceeded. The combined discrete/continuous software, which incorporates the features of MATLAB-Simulink and DSPACE, is then used to generate real-time control system code and this is used for the supervisory fuzzy control of the array handling system.

The control strategy for deployment and recovery therefore comprises numerous operational modes, based on discrete-event handling. Finite state transition theory is used in a supervisory manner to send set-point commands to the sub-layer controllers. These consist of classical PID feedback terms, used to control the winch and deployer so that they can track set-point demands from the supervisory logic. The safe operating envelope of the deployer and array can only be determined experimentally, due to the high level of uncertainty resulting from its markedly non-linear and discontinuous characteristics. Fuzzy logic is ideally suited to the control of this type of system and the linguistic membership rules for this are readily determined from experimental results.

To fully ascertain the key parameters critical to safe handling of a Fully Reelable Towed Array Outboard System (TAOS), DERA Winfrith have developed a generic non real-time mathematical system model. The elements represented in the model include the storage winch, transfer unit (for deployment and recovery), guidance system, spooling and control system. The model library infrastructure includes a broad range of hydraulic and associated equipments such as motors, pumps and valves, transmission devices such as winches, deployers, pulleys and bends and various types of array such as 'bulkhead' and 'crustacean'. The physical details of the array sub-model are outlined in this paper, giving considerable detail in its representation of the interactions between hose and strength member/devices. A detailed test programme was undertaken in order to fully quantify these strength and damping parameters. The component sub-models are connected together to form an overall system model, which is used to predict the system behaviour and explore the effects of parameter changes. As the system model is generic, it can be rearranged to examine the behaviour of alternative

handling system configurations or control strategies.

In practice, a typical handling system may have a number of devices of various sizes around which the array must be passed. The expression 'guidance path' is used to refer to the path taken by the array between the winch and the transfer unit. Figure 1 illustrates a much-simplified handling system guidance path, in which an array passes from a winch, through a flaking system, around a rudder stock and on to the transfer unit or deployer.

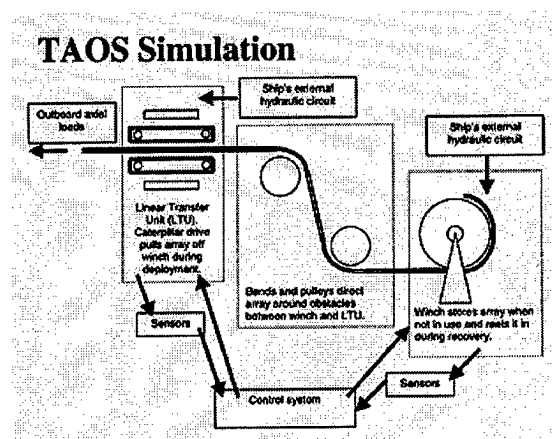


Figure.1 Towed Array Outboard System

1.1 Array Failure within the Handling System

During array deployment or recovery, one intuitively expects the array between the deployer and winch to be in tension, simply because the deployer is being used to pull the array off the winch. Given that array failure by the rucking mechanism noted above occurs when the hose is placed in compression, one might expect that the handling system should not be problematic in this respect.

The situation is in practice more complex than this, because one must consider separately the forces in the inner load bearing core, and the outer PVC hose, and the combined effects of bulkheads and module end-connectors, described in more detail in Section 3. It is then possible for the core to be in tension, bearing the

majority of the overall array load, whilst the hose is in compression and therefore susceptible to failure by the rucking mechanism.

In the simplest terms, this suggests that a well-designed handling system should minimise the size of compressive forces arising in the array hose. In practice, compressive strain is likely to be impossible to eliminate entirely, and the adoption of a more sophisticated failure condition based on a buckling criterion will be required. The principle of column buckling [1] is well understood. In effect, a column deforms into a modal shape, resulting in severe material deformation. Reelable arrays are conceptually plastic columns of variable length, which can deform longitudinally, laterally and torsionally in a variety of modes. Considerable analysis has been devoted to the understanding of the phenomena of array rucking under Applied Research by DERA Winfrith. The computer model of an array described in this paper incorporates stress-strain relationships derived from the material stiffness, damping, creep and stress relaxation characteristics. These are very much dependent on the type of hose material and its temperature. The model is currently being validated by comparison with experimental data over the observed range of operational behaviour, including conditions that lead to rucking. For the purposes of this paper, it is proposed that the simplest possible 'metric' be adopted so that the design of a handling system can be quantified: namely that reduced compressive deformation of the array within the handling system is better.

2 Non Real-time TAOS Model for sensitivity studies and assessment of alternative circuit configurations and control strategies.

The TAOS Model comprises a number of subsystems of mechanical, hydraulic and electrical nature. There are key components described in detail below include:

- The Array
- The Handling System (Guidance Route)
- The Winch and Associated Hydraulics
- The Deployer and Associated Hydraulics
- The Control System

2.1 The Array

The array itself comprises a stiff load bearing core and an outer hose. The core, made of kevlar, is considered as a spring with high stiffness that can support no load in compression. The hose, made of PVC, is intended to offer physical protection to the sensitive transducers contained within it. In practice, the hose also bears a proportion of the total load in the array, and by the nature of its construction, may support a small compressive load. Failure by 'rucking' occurs when compressive loads are induced that are in excess of the load bearing capacity of the hose.

Acoustic transducers and electrical cabling are contained within the hose, which must therefore be acoustically transparent over the frequency range of interest. Overall, the array must be neutrally buoyant. The schematic of Figure 2 indicates the general construction.

In the arrays in use at present, rigid 'bulkheads' are distributed along the core. Their purpose is to prevent damage to the sensitive acoustic transducers as the array is stored on the winch and enabling it to pass safely around bends in the guidance path and through the transfer unit during deployment / recovery. The bulkheads are fixed to the load-bearing core, but not to the hose. In the absence of laterally applied forces there is no mechanism for

the transfer of load between hose and core and the hose can slide over the bulkheads. When lateral forces are applied to the hose, friction at the hose / bulkhead boundary permits the transfer of axial load from hose to core, and *vice versa*. If there is sufficient lateral load, then the hose will be constrained to move at the same speed as the core (this situation occurs within the array stored on the winch, when the hose and core are effectively locked together by forces acting radially to the winch). More generally, around bends within the guidance path or within the transfer unit, load is transferred between hose and core, but the hose may also slip with respect to the core, and the two may therefore have different velocities. This condition can lead to a ruck.

A complete array is constructed from a number of 'modules' linked by end connectors. These are the only points at which the motion of the hose is constrained to exactly match that of the core at all times, regardless of position within the guidance path. The presence of end connectors has a very significant effect of overall array dynamics and requires careful consideration within the simulation. At any intermediate point between end connectors, the motion of the hose relative to the core depends on the

loads applied to the array along its length, and on the creep / stress relaxation behaviour of the hose material.

The PVC hose is highly significant, because it displays complex dynamical behaviour when subjected to applied forces and deformations. When a constant stress is applied to a length of this material, it displays creep behaviour, where its extension increases with time. When a constant strain is applied, the material displays stress relaxation behaviour where the force required to maintain the constant strain reduces with time. Mathematically, the two phenomena of creep and stress relaxation are well described by the Standard Linear Solid (SLS) model, comprising a spring-dashpot combination (known as a Maxwell unit) with an additional spring element in parallel with it, as shown in Figure 3. The SLS unit is characterised by the values of the glassy modulus E_m , rubbery modulus E_a and viscous dashpot coefficient N_m . Large variations in physical properties occur with temperature [2] and this is mainly due to the change of dashpot coefficient N_m . It is also necessary to account for variations in E_m and E_a due to the very non-linear temperature dependence of PVC material.

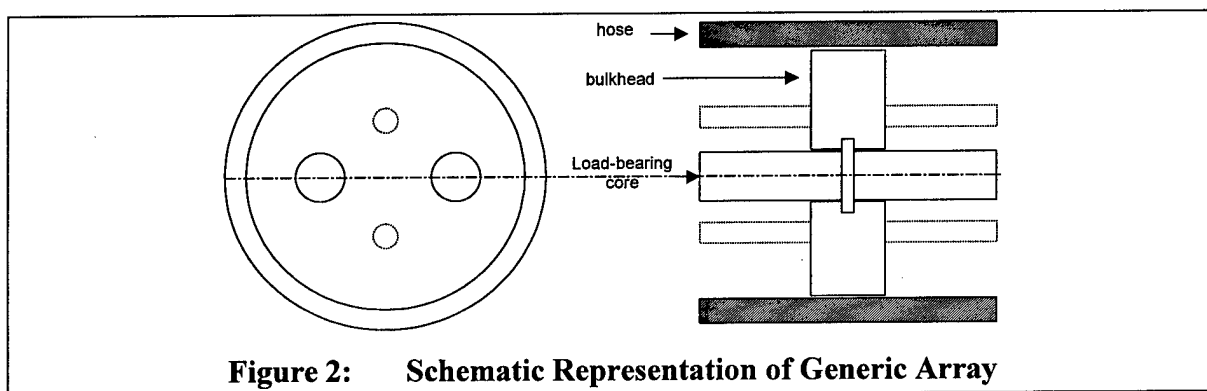
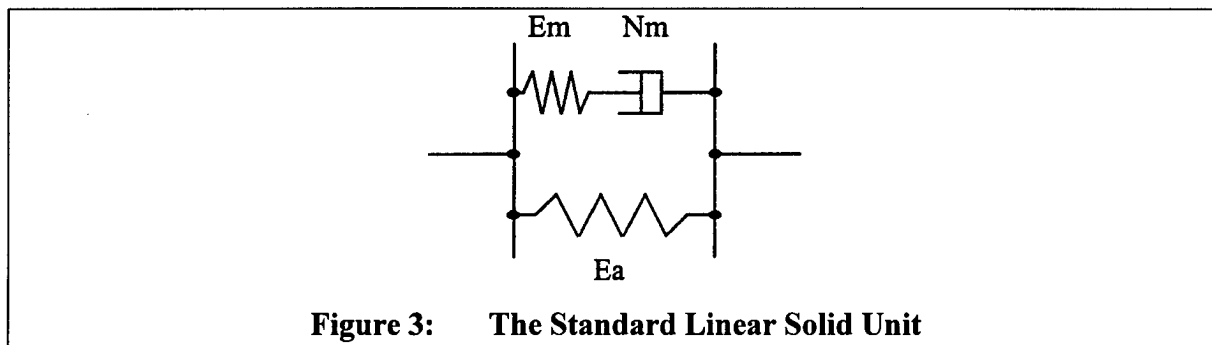


Figure 2: Schematic Representation of Generic Array



The portion of the array within the handling system at any time is treated as a collection of SLS units connected in series, each modelled as indicated in Figure 3. The deformation of each unit is calculated as it passes through the handling system, enabling the state of the array hose at any point in time and space to be determined throughout the deployment or recovery processes.

2.2 The Handling System

The handling system comprises an arrangement of passive mechanical 'devices' in the form either of pulleys or fixed bends, enabling the array to be guided around the various devices between winch and deployer. These devices are connected by lengths of straight guidetube, within which the array is essentially unrestrained.

The devices that make up the handling system are highly significant because they provide sites along the guidance path at which lateral load may be applied to the array. These loads arise from the normal reaction force applied to the array by each device as the path of the array deviates from a straight line. The combination of applied lateral loads and friction effects enables these devices to modify the forces acting on the array in the axial direction. Passive devices (i.e. components such as fixed bends or pulleys that are not driven by an externally applied torque) act in such a way as to oppose the motion of the array through the handling system.

The guidance path geometry and the axial forces in the array enable the friction forces arising and the amount of slip to be determined at each of the device / hose contacting surfaces and also at the hose / bulkhead contacting surfaces within the array itself. In this way, the velocity of the hose relative to the core is determined and this is integrated to yield the deformation of the array hose at any time and at any point within the handling system.

As soon as any significant length of array has been deployed, it is necessary to consider the effect of outboard drag on the system. This results in an additional load being applied to the array within the guidance path. The total outboard drag is represented using the well-established Munn's formula [ref], based on empirical measurements of a number of towed arrays. The drag associated with completely deployed modules within the array is distributed between the core and hose in proportion to their relative stiffnesses. Thus the vast majority of this component is transferred to the core. The remaining component of the total drag, attributable to the length of array hose of the incompletely deployed module nearest to the submarine, is transferred entirely to the hose in the handling system.

2.3 The Winch and Associated Hydraulics

The winch drum, coupled directly to a hydraulic motor, may be considered as another of the handling system devices described above, in the sense that it provides a location at which lateral force

are applied to the array. In this case however, the device represents the winch drum, which is 'active', being driven by the torque imparted by a hydraulic motor. This torque provides a link between the model of the winch hydraulic circuit and the handling system model.

Dynamic system models are vital when assessing the behaviour of electro-hydraulic control systems. Hydraulic and associated equipment models are developed as sets of differential and algebraic equations representing the behaviour of components in isolation. The hydraulic component models are developed as stand-alone elements in a library [3], which can be connected to form an overall system model. The differential equation set representing the system behaviour is solved using numerical integration techniques [4]. SimulinkTM provides an ideal package with which these techniques can be applied, not least because the mechanical, hydraulic and control elements of the problem can be modelled together in a single fully integrated simulation environment.

2.4 The Deployer and Associated Hydraulics

The deployer, also known as the transfer unit or caterpillar, may also be considered as a special kind of 'active' device, driven by a hydraulic motor. In this case however, the array does not pass around a bend but is pulled by a rubber belt, with a lateral load applied by an hydraulic press. The load is profiled along the length of the deployer, as one would expect it to be of reduced magnitude, close to the edges of the 'gripping length' of the device. It is the operation of this device that requires the presence of bulkheads in the array design, if it is to successfully assist in the deployment of the array, without crushing the acoustic transducers.

2.5 The Control System

The principal requirements of an efficient reelable array system are:

- Array rucking or damage due to excessive tensions is avoided
- The system deploys and recovers at the required speeds
- The system operates at the required platform speeds
- The system is stable
- Array tension is maintained at the winch
- The desired tension increment across the deployer can be controlled accurately.
- The system is fail-safe
- The system can be manually operated if automatic modes fail or need to be overridden.
- The system is viable under all expected environmental conditions

A control system is used to maintain these requirements during array deployment and recovery procedures. The difficult problems of controlling an array in a fully reelable system arise principally from the tendency of the hose to manifest significant compressive forces and hence ruck. Factors that are likely to increase hose compression include increased temperature, increased platform speed, increased guide tube friction and increased differential tension setting across the caterpillar. The array is thus a difficult component to deploy and recover under all circumstances and may be best controlled using an 'intelligent' system to identify when compressive hose forces (and hence high likelihood of a ruck) will be large. PID (Proportional-Integral-Derivative) may therefore be inadequate to cope with the complexity required for reliable control of an array. Modern robust control

systems such as 'adaptive', 'fuzzy set', 'neural net' are able to cope with wide ranging plant characteristics and may well be applicable to the fully reelable array problem.

In essence, PID fulfils three fundamental control functions. The proportional (P) term governs the speed with which the output (tension or speed) reaches steady-state. The integral (I) term governs the accuracy, the theoretical steady-state error being zero if this is functioning correctly. The derivative (D) governs the stability of the system and can take the form of a lead/lag network. The essential problem with PID is its poor robustness. If parameters in the plant vary significantly throughout the operating envelope, the P, I and D terms may be unable to maintain their independent functions. Modern Control systems overcome such problems by incorporating a 'degree of intelligence' to account for the effects of plant variations and uncertainty. Modern controllers are necessarily more complex than classical controllers as they require computational facilities that implement the required algorithms. If, however the system characteristics do not change significantly over the operating range, then classical control can be used.

3 Simulation case study

3.1 *Effect of changing deployer differential tension setting*

It is necessary to determine a suitable control strategy for the transfer unit that ensures a successful deployment and recovery of the array. It is also important to note when developing a simulation that any closed loop control strategy must employ signals that can realistically be measured in the actual system when fitted to a submerged submarine. In this case study, the simulation model is used to examine an existing configuration,

whereby differential tension across the transfer unit is under PID control. This is done using load cells located in the transfer unit mounting arrangement combined with suitable electronic amplification and correction for submarine pitch. The controller output is used to drive the deployer hydraulics proportional flow directional control valve (DCV) in order to pressurise the hydraulic motor line, thereby ensuring the appropriate torque (hence line tension) is achieved.

A simple PID controller has been adopted to give precise closed loop speed control of the winch. A typical demand speed of 1 m/s is taken and the winch hydraulics adjust the opening of the proportional flow control valve (DCV) to deliver the flow rate required for this deployment speed.

The simulation is used to compare the behaviour of the system for different demanded deployer differential tension settings. For clarity, two values of 600 and 1200 N are presented. An identical handling system is used throughout.

3.2 *Model Output*

Figure 4(a and b) is a surface plot of array hose strain, as a function of distance along the guidance path, comprising winch, flaking system, rudder stock guidetube and deployer (measured from 0 m at the deployer to nearly 15 m at the winch). These strains must be considered in the context of the SLS 'units' that comprise the array hose – the length of each is equal to the bulkhead spacing in the array. It is apparent from this single surface plot that along portions of the guidance path, the array hose can be placed in compression (negative values). This is despite the fact that the *total* array load remains in tension throughout the deployment.

Figures 4(a) and 4(b) respectively show the hose strain for the 600N and 1200 N deployer demand cases. The figures

indicate the benefit of reduced differential tension, as this yields a significant decrease in compressive deformation within the array. The maximum array element compression appears to decrease approximately in proportion to the reduction in differential tension. Thus, the simulation is able to identify a simple control strategy that gives a significant reduction in hose compressive force and hence likelihood of a ruck occurring. It is of course necessary to ensure that low tension conditions do not result in a slack cable condition.

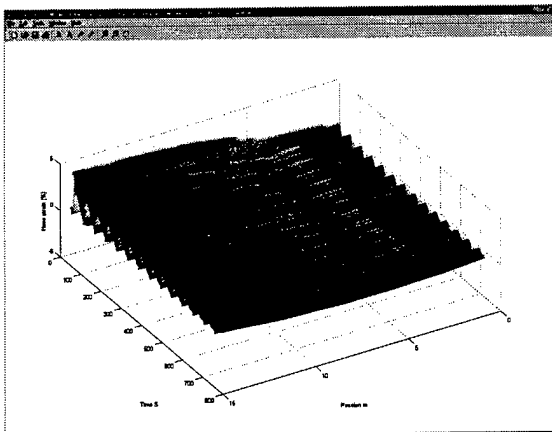


Figure 4a Differential tension setting 600N

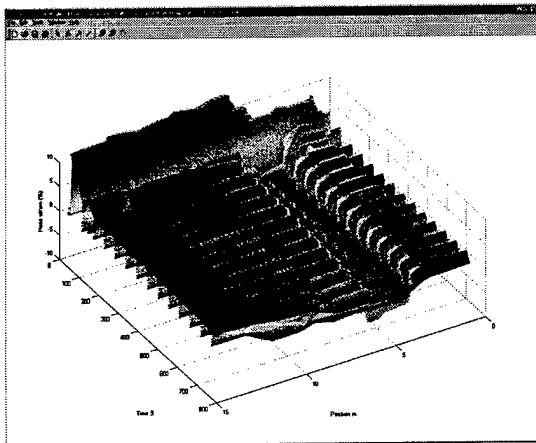


Figure 4b Differential tension setting 1200N

The simulation was also used to show the effects of variations in array temperature, platform and array speeds and fiction levels throughout the system in addition to a range of control and guidance route options. These provided valuable design

information but are not addressed in this paper due to space limitations.

4 Control System Development using Real-time Modelling

4.1 Problems associated with Array Deployment and Recovery

The design and development of a fully reelable array system presents difficult control and handling system requirements, necessitating evaluation using experimental testing, supported by a detailed real-time computer model. The model is therefore being used for the assessment of 'robust' feedback control systems, capable of meeting the diverse performance requirements over the complete operating envelope. The behavior of this type of system changes considerably during different phases of the deploy and recover operations, due to variations in both platform speed and sea temperature, the latter affecting the properties of the external hose.

The reliable behavior of the deployer is of prime importance to the viability of the overall handling system. It is vital to measure (characterise) the safe operating envelope of the deployer for ranges of speed, line tension and array clamping force. Adverse settings for these cause the array to slip with respect to the gripping pads and if this becomes excessive, then a ruck will occur in the array. Characterisation gives a three dimensional envelope of safe deployer operation, which forms part of the real-time model in the form of a 'look-up' table. This type of data is particularly suited to 'fuzzy' control, whereby linguistic rules can be applied to various regions of operation. These enable changes to be made to the discrete setting

of hydraulic valves, which, in conjunction with classical PID, provide reliable robust control for this type of system.

The array tensions during deploy and recover are quite different and the control system likewise will quite different. When deploying the array, the control system ensures that the deployer unit maintains a positive back tension at the winch until the in-water hydrodynamic drag on the array is sufficient to provide this back tension. However, the motion of the drum winch required to store the array presents a severe problem. When initiating deploy, the transmission system is required to provide a precise control of the tension, whilst overcoming very large frictional forces and high inertia transients. The deployer creates a pull force in order to overcome the losses in the winch and provide sufficient tension to deploy the array at the required speed. Storage winches are large inertia dominated systems and the transiently generated torque ($I \cdot d\omega/dt$) is appreciable, compared to the torque required to generate line tension. This effect is particularly significant in the initial stage of deployment, when the line tension is comparatively low.

Careful consideration of the controller design is required in order to ensure smooth motion with no likelihood of either an array ruck or zero tension, these being conditions that would result in a total malfunction of the handling system. The experimental programme indicates that to maintain positive array tension at the winch, it is necessary, particularly during the initial phases of deployment, for the winch drive to be accurately tension controlled. At the start of deployment, the deployer tension setting will initially be low and in the order of 500N to 1000N. To maintain controllability the minimum back tension must be capable of maintaining the levels of tension at a value lower than the minimum drag force.

On recovery, the array tensions will initially be highest and the primary requirement is to prevent array damage due to over-stressing. The load tension is proportional to the length deployed and the square of the tow speed (approximately). During recovery, it is important to ensure a minimum positive back tension at the winch as this is necessary to prevent slack array occurring. This would result in loss of control and 'loose turns' appearing.

The experimental programme has shown the suitability of a control strategy whereby the deployer is driven in constant speed mode and the winch in constant tension mode. Both hydraulic systems use a novel electro-hydraulic concept termed 'differential pressure control'. Using appropriate pressure control valves, this allows bi-directional rotation of the motor in a variety of speed or pressure control modes. This technique prevents slack cable ('nesting' the array) which is known to occur if the winch were in speed control and the deployer in tension control mode. This control strategy has therefore been proposed for both the deployment and recovery phases.

4.2 Characterisation of Safe Operating Envelope for the Deployer

The deployer in the system under test is a linear transfer unit (LTU) in which two padded belts are driven (electrically or hydraulically) in unison in order to pull the array from inboard to outboard. A hydraulic actuator is used to exert a clamping load on the belt and this load is under automatic feedback control. It is necessary to obtain the 'safe operating envelope' of the LTU in order to define its closed loop requirements. This is determined by a series of open loop test in which line tension and speed and clamping force are varied throughout the overall operating range and safe conditions, in which there is no appreciable slip between belt and array, are determined. These

conditions correspond to those where array rucking does not occur. The measured three-dimensional relationship for safe operation is shown in figure 5. This forms part of the real-time model and the fuzzy controller ensures that for any line tension and speed, the clamping force always lies within this envelope.

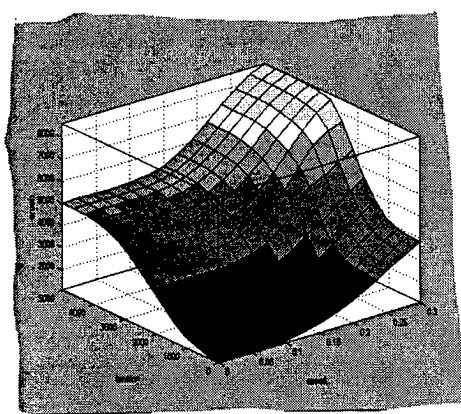


Figure 5 LTU safe operation envelope

4.3 Control strategy for Deploy and Recovery Operations

The control procedure incorporates the following sequence of operations for the input drive:

4.4 Deployment Phase

- (1) Deployment is initiated by pulling the deployer off the winch and through the guidance route using the LTU.
- (2) Following an initial phase of deployment using the LTU, the hydrodynamic drag is continuously monitored until there is sufficient drag to overcome the losses and frictional effects of the handling system (hydrodynamic drag algorithm is a function of deployed length and array speed through the

water). If this is the case the LTU is no longer required.

- (3) The LTU speed is set to zero and the winch brake is activated. The LTU clamp force is now set to completely unclamp the array. Once this is initiated the winch brake is unactivated. At this juncture the supervisory logic ascertains whether the winch under tension control continuous to stream the array as would be the case if there is sufficient outboard drag or hauls the array back if there is not. In the latter case the supervisory logic will stop the system, clamp the array again and deploy for a further 500N increment of array drag. The procedure is repeated again until full deployment is achieved.
- (4) Deployment now continues under tension control at the winch. The winch speed increases linearly until the set line tension is achieved. For safety reasons, an override (outer loop speed controller) ensures that array speed does not exceed a defined maximum.
- (5) At the end of deployment, a signal derived from a shaft encoder initiates slowing down and stopping of the winch at which point the system is locked

4.5 Recovery Phase

- (1) The winch recovers the tow cable at a set line tension. The speed is limited to a maximum (outer loop speed controller).
- (2) The end of the tow cable phase is sensed and the speed decreased linearly. The line tension for the array is set, and in order to prevent the outer layers from crushing the inner layer bulkheads stored on the

winch drum, this setting varies. This feature reduces the winch speed when the measured array tension exceeds the set level and therefore provides a natural means of tension limiting.

- (3) In the final stages of recovery when outboard drag is of a low value the system is stopped and the array is clamped. The LTU is driven at low speed, which aids in the final stages of recovery by creating a back tension in the system.

4.6 AUTOMATIC DEPLOY/RECOVER

4.6 Overall Supervisory Control System

The hierarchy of the overall supervisory control system is shown in figure 6. This features a strong supervisory monitoring of device controllers, which in themselves use linguistic rule-based logic to determine the actions of classical PID feedback systems. The supervisory capability embodies a number of checks including safety/damage limits, watchdog and diagnostic monitoring. These allow the acquisition of valuable information that can be used both in real time and post-processing analysis.

As an example of information transfer, the set point for the LTU clamp force demand is calculated using fuzzy logic, based on the array tension and the speed of the array. This setting is fed to a closed loop PID controller which senses a feedback clamp force hydraulic pressure (hence force) and 'closes this loop' and ensures that the fuzzy clamp force demand is met.

Supervisory logic plays a major role in the action of the LTU, which is fully automated for deployment and recover. The following actions are required:

- (1) Continually monitor the system to determine the system operational mode
- (2) Determine belt clamp/unclamp actions
- (3) Set LTU belt speed commands

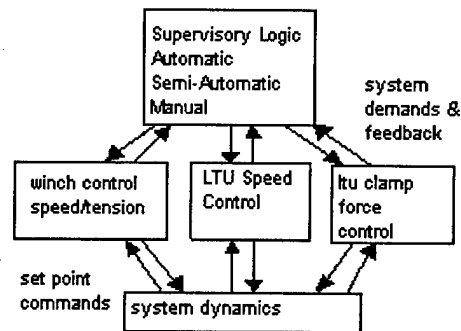


Figure 6 Supervisory Control Structure

4.7 Experimental Recordings of System Response

To test the control system when the LTU decouples, during both insufficient and sufficient outboard hydrodynamic DERA Cable/Array Handling Test Facility was used in back to back winching. The rig set-up consists of two winches, the LTU and guidance route. Two winches are required, one to act as the tension controlling winch (8kN) and the other to act as the sea drag inducing winch (50kN). In this mode of operation the 50kN winch is under manually speed control. This allows the operator to dictate whether the outboard tension is low or high). A typical automated trial deployment evolution is shown in figure 7. To assist in the understanding of the logged data a typical dSPACE deployment run with the event marks is indicated.

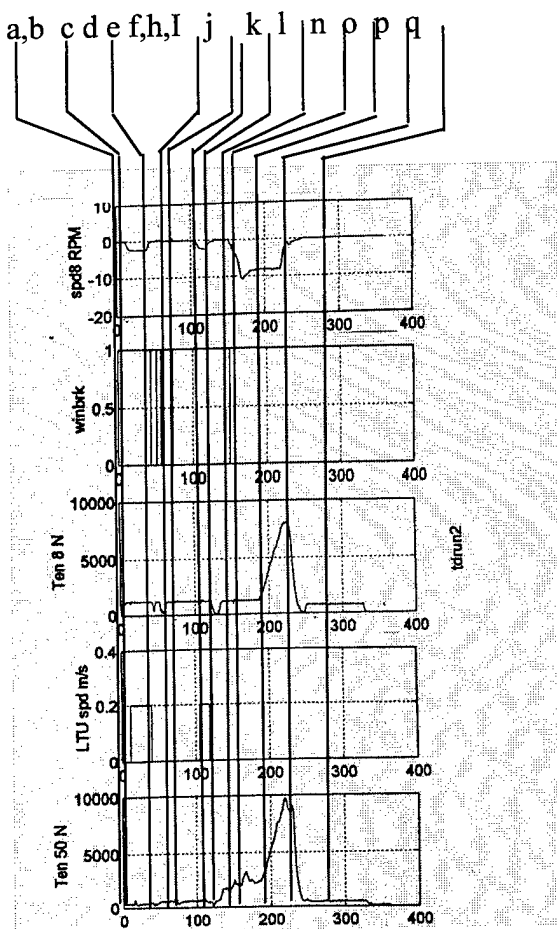


Figure 7 time response auto deployment

- a If not already applied the LTU is clamped down onto the array to start deployment sequence
- b The brake on the storage winch is released and a minimum back tension is manually set and applied to the array.
- c Once the storage winch brake has released the automatic deployer sequence is initiated and the LTU starts to deploy.

- d. The 50kN winch is manually adjusted in speed to take up the array deployed but without applying a "drag induced" tension.
- e At an appropriate deployed length (dependant upon boat speed) the LTU stops deploying.
- f Once the LTU has stopped moving the storage winch brake is applied.
- g The LTU unclamps fully.
- h The storage winch brake is released and because there is insufficient "drag induced" tension the winch hauls.
- i As soon as the control notes the storage winch is hauling then the storage winch brake is applied.
- j The LTU is clamped onto the array and the storage winch brake is released.
- k An additional defined length of array is deployed and the LTU stops.
- l Once the LTU has stopped moving the storage winch brake is applied.
- m The LTU unclamps fully.
- n The 50kN winch is manually adjusted to provide sufficient "drag" and when the storage winch brake is released the storage winch deploys.
- o As the winch deploys the speed is increased to the maximum.
- p When the speed reaches the maximum pre-set limit the

tension is increases up to the full system drag.

- q As soon as the tow cable termination has left the guide path bellmouth it is assumed that full deployment has occurred and the speed is reduced.
- r Once the storage winch has stopped the storage winch brake can be applied.

From the time response data, the control system (8kN winch) can be seen to control the line tension to a satisfactory degree as it follows the outboard drag (50kN winch).

5 Summary and Conclusions

Generic mathematical models of a range of fully reelable towed array handling systems have been developed, capable of predicting the behavior of complex electro-hydraulic systems comprising winches, deployers and guidance routes with electronic feedback control systems. The models are both *real-time* for on-line control experimental applications and *non real-time* to perform sensitivity case studies and assess the effects of alternative circuit configurations or control strategies. Thus, two allied but substantially different approaches have been applied to the problem of controlling fully reelable array systems.

The real-time model has been used successfully for the development of 'robust' Modern feedback control systems, capable of meeting the diverse performance requirements over the required operating envelope. The behavior of this type of system changes, often unpredictably, during different phases of the deploy and recover operations, due to variations in both platform speed and sea temperature, the latter affecting the properties of the external hose.

In order to overcome this type of operational problem, a Modern Control approach has been investigated required and Fuzzy logic has features ideally suited to the solution. Supervisory Control is also used to ensure that the independent device controllers operate satisfactorily. The control system strategy, developed as a result of this programme, addresses the fundamental problems associated with the deploy and recover phases of fully reelable array handling systems. The controller design described in the paper ensures that provided a suitable array and guidance route are chosen, then smooth motion can be obtained during deploy and recover. Thus, the likelihood of an array ruck or zero tension condition occurring is minimised, these being conditions that would result in a total malfunction of the handling system.

The programme has demonstrated the power of developing the real-time model and adding the fuzzy logic controller to ensure parameter boundaries for safe handling are not exceeded. The combined discrete/continuous software, which incorporates the features of MATLAB-Simulink and DSPACE, has been used to generate real-time control system code and this is used for the supervisory fuzzy control of the array handling system.

The determination of safe operating envelopes for the deployer and array is done experimentally, due to the high level of uncertainty resulting from its markedly non-linear and discontinuous characteristics. Fuzzy logic is ideally suited to the control of this type of system and the linguistic membership rules for this are readily determined from the mathematical model.

The non real-time TAOS model has been developed to perform sensitivity case studies and assess the effects of alternative circuit configurations or control strategies. The model includes all the significant features that govern the dynamical behavior of the real system but particular

emphasis has been given to the development of a detailed array sub-model, embodying the practical features of this type of equipment. The system model is generic and is readily reconfigured to enable a comparison to be made between various design options.

Results have been presented in this paper for one particular aspect of the total range of array designs, handling system configuration, and operational and environmental conditions that can be investigated using this model. The effect of the control strategy applied to the handling system has been demonstrated. An investigation into the variation of compressive deformation in the array hose with demanded differential tension across the deployer has indicated that the lower the tension difference the better, from the point of view of this array failure mechanism alone. The objective of this paper is not to propose an 'optimum' handling system design, but rather to demonstrate the power and flexibility of the tool by giving an indication of the results that can be generated. The simulations procedures described in this paper provide a means of making significant design decisions based on quantitative analysis early in the overall design cycle, reducing risk and consequently saving the customer time and money.

The research has involved the development of novel and realistic solutions to counter the inherent problems associated with the design of a fully

reelable towed array system. This paper summarises the methodology and results of two complementary approaches, which are offered as a design solution to the problem of automatic array handling. Application of the models and control techniques to more complex handling system geometries will provide valuable tools to support the challenging problem of automatic array handling system design and assessment.

6 REFERENCES

- [1] Warren C Young, 'Roark's Formulas for Stress and Strain', 6th Edition, McGraw-Hill Book Company 1989
- [2] I. M. Ward and D. W. Hadley, 'An Introduction to the Mechanical Properties of Solid Polymers', John Wiley and Sons, 1993
- [3] Richards CW, Tilley DG, Tomlinson SP and Burrows CR. 'Bathfp - A Second Generation package for Fluid Power Systems', *Proc BHRA 9th International Symposium on Fluid Power*. 9th International Fluid Power Symposium, Cambridge, UK. April 1990. 315 - 322.
- [4] Shampine, L. F. and M. W. Reichelt, 'The MATLAB ODE Suite', *SIAM Journal on Scientific Computing*, Vol. 18-1, 1997.

THE DEVELOPMENT OF A SONOBUOY USING SPARKER ACOUSTIC SOURCES AS AN ALTERNATIVE TO EXPLOSIVE SUS DEVICES

Authors:

Dr. Raymond B. Schaefer
Phoenix Science & Technology, Inc.

Dan Flynn
Acoustics Technology Branch
Naval Air Warfare Center

Abstract

This paper is on the development and testing of sparker acoustic sources deployed in a sonobuoy for environmental measurements. Currently, Signal Underwater Sound (SUS) explosive acoustic source devices are used in the measurement of acoustic transmission loss and reverberation. Sparker acoustic sources are an alternative to explosives that offer potential as a cost-effective method of obtaining controllable, multiple, broadband acoustic pulses at various depths. Aircraft deployment constrains the design to a sonobuoy package, which limits the size of the electrical driver. Consequently, sparker efficiency of converting electrical into acoustic energy determines the source level. We report on development of high efficiency sparker acoustic sources, integration of the sparkers into a sonobuoy, and on sea tests characterizing the acoustic source level and spectrum from the sparker based sonobuoy.

Sparker operation in ocean water typically has a low efficiency of converting electrical energy into acoustic energy. In order to maximize the source level produced by the sonobuoy, we investigated how the acoustic efficiency changes with sparker parameters, including geometry, electrode gap and electrical driver design. Based on test results we selected the most promising candidates for sonobuoy deployment. This led to the design and fabrication of a sonobuoy that operates at high efficiency and accommodates small sparker arrays. We plan to report results of sea tests to characterize the acoustic energy and spectrum produced by the

sonobuoy for operation as a function of depth, number of sparkers and electrical driver energy.

I. Introduction

Signal Underwater Source (SUS) explosive devices provide impulsive acoustic waveforms for applications including measurement of acoustic transmission loss and reverberation, deep and shallow water sonar and gathering oceanographic data. Use of explosives has environmental and safety implications that restrict use and impact fleet operations. Also, since explosive sources must be replaced after each use, testing with a field of explosive sources is time consuming and costly.

Sparker acoustic sources are an electrically driven alternative to explosives that offer potential as a cost-effective method of obtaining controllable, multiple, broadband acoustic pulses at various depths. Sparker acoustic sources produce an acoustic waveform similar to explosives, but sparkers are safer. Also, sparkers can be used many times and can be packaged in a multi-use sonobuoy with other sensor systems. Sparker technology also has application in geophysical exploration (e.g. seismic profiling), mine countermeasures, minesweeping and sonar.

In applications requiring aircraft deployment, the sparker design is constrained to a sonobuoy package, which limits the size of the electrical driver. Consequently, sparker efficiency of converting electrical into acoustic energy determines the source level and number of pings.

We've undertaken the development of high-efficiency sparker acoustic sources, packaged sparkers in a sonobuoy, and plan to conduct sea tests characterizing the acoustic source level and spectrum for a small array of sparkers.

Sparker operation in ocean water typically has a low efficiency of converting electrical energy into acoustic energy. In order to maximize the source level produced by the sonobuoy, we investigated how the acoustic efficiency changes with sparker parameters, including geometry, electrode gap and electrical driver design. Based on test results we selected the most promising candidates for sonobuoy deployment. This led to the design and fabrication of a sonobuoy that accommodates small sparker arrays. Sea tests are planned to characterize the acoustic energy and spectrum produced by the sonobuoy for operation as a function of depth, numbers of sparkers and electrical driver energy. We hope to report the results of these tests at Oceans '99.

II. SUS Acoustic Sources

II.A. Description

The Signals Underwater Sound (SUS) device is a small bomb-shaped expendable device three inches in diameter and up to twenty-six inches long. There are two versions of the SUS, one an explosive and the other electronic. The original purpose of the explosive SUS was for simulating a weapons attack in place of much larger depth charges or depth bombs. Presently, it is used operationally as a signaling device from an aircraft to submerged submarines and is used by the acoustic research community as an omni-directional sound source for acoustic characterization of ocean environments. The explosive SUS uses a spring-loaded piston and rupture disc to sense the water depth and to operate the arming and firing systems. The primary role of the electronic version is as a signaling device from an aircraft to a submerged submarine. Powered by a sea water battery, the electronic SUS transmits coded tones into the water using a vibrating ceramic ring.

II.B. Applications

The Naval air research community uses explosive SUS in the collection of ocean environmental acoustic data. This data is analyzed to make calibrated measurements of reverberation and transmission loss. These measurements are further reduced to extract bottom loss versus angle and bottom scattering strength, which are important parameters for acoustic performance modeling. Present data collection methods utilize AN/SSQ-57, attenuated (-20dB, -40dB, -60dB, -70dB) AN/SSQ-57 sonobuoys and MK61 SUS charges. Each (attenuated and non-attenuated) sonobuoy contains a calibrated omni-directional hydrophone. These hydrophones are deployed in pods (5 buoys per pod) at 5, 10 and 15-mile spacing. For transmission loss data collection, the aircraft proceeds in a straight line dropping one SUS every nautical mile. For the reverberation analysis, the aircraft drops SUS devices only at the pod locations collecting both monostatic and bistatic reverberation data.

II.C. Limitations

The explosive family of SUS is limited to a single detonation per unit and is subject to operational area restrictions. To achieve multiple detonations at the same location the aircraft must return to the location and deploy a second unit. The uses of explosive devices are restricted within a specified distance of land and within a specified water depth. Malfunctioned SUS pose a threat to fishing operations, sea mining operations, and future offshore construction.

The electronic SUS is usually not used for ocean characterization due to its severely limited frequency response and low source level. The frequencies are

limited to 2.95 kHz and 3.5kHz while the maximum sound pressure level is 160 dB/1uPa at 1 meter.

II.D. Emerging Naval Air Requirements

As undersea warfare transitions to littoral environments, the lack of historical data, and the large spatial variability of many environmental parameters such as bottom loss, and bottom scattering strength, dictate the need for in-situ data collection to be input into tactical decision aids in order to update tactical predictions. Presently, the Navy is exploring sparker technology as a potential candidate for a safe, economical broadband source that would be incorporated into an aircraft deployable, acoustic measurement sonobuoy. This multi-sensor sonobuoy potentially would combine the AN/SSQ-57 omni-directional calibrated hydrophone sonobuoy, the AN/SSQ-36 bathythermograph sonobuoy and additional sensors to measure wave characteristics, surface currents, wind speed, air temperature, acoustic bottom properties, bottom composition, salinity, turbidity and transmission loss.

III. Sparker Acoustic Sources as an Alternative to SUS Sources

Sparker acoustic sources have the same characteristic pressure waveform and acoustic spectrum as SUS devices. Both sparkers and SUS devices are impulsive acoustic sources in which energy is deposited rapidly into the water. Pulses of electrical energy drive the sparker, in contrast to the chemical detonation of the SUS. The impulsive driver produces a strong initial pressure peak and leaves behind a high-pressure bubble (or "cavity"). The bubble expands, producing a low-level rarefaction, and then collapses, emitting another strong pressure peak. This cycle repeats until the energy in the bubble dissipates and the bubble breaks up. The pressure waveform and acoustic spectrum from a sparker, shown in Fig. 1, have the same characteristics as a SUS. Fig. 1(a) shows the first three peaks of the pressure waveform. Most of the acoustic energy (and thus "source level") is contained in the first two pressure peaks. The acoustic spectrum in Fig. 1(b) is broadband, providing significant source level over several octaves.

Because the explosive driving SUS devices have such high energy density, the source level is greater than a sparker acoustic source with the same volume. However, sparkers have advantages in terms of safety, the ability to provide multiple pings, the control of the acoustic spectrum and in the integration with other sensor packages in a multi-use sonobuoy.

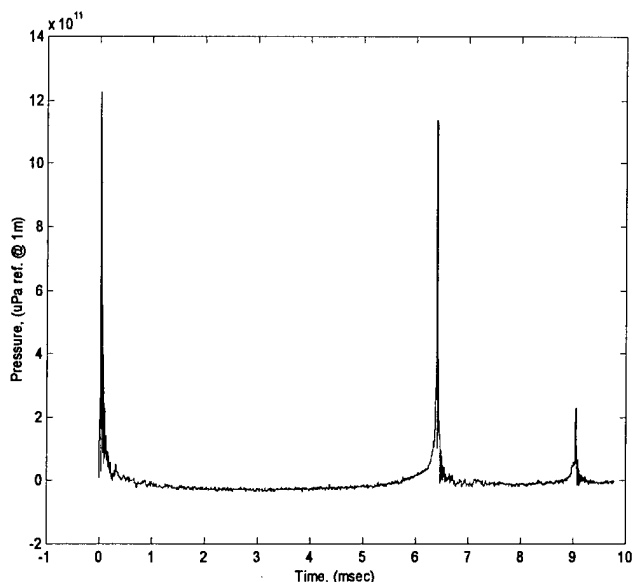


Fig.1(a) Sparker Pressure Pulse

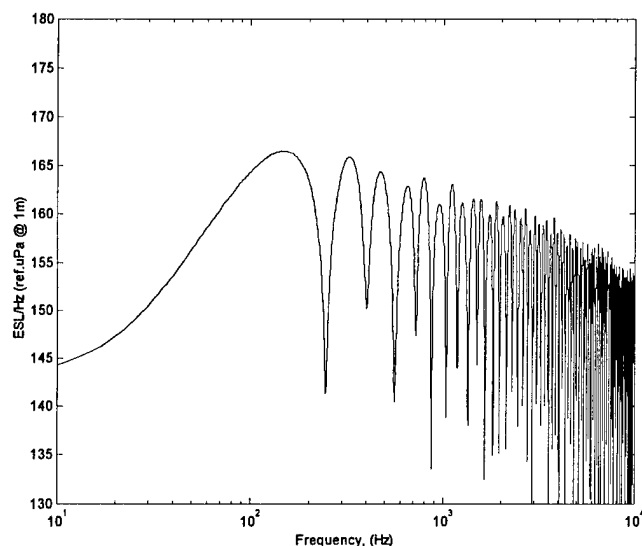


Fig.1(b) Acoustic Spectrum

Sparkers are powered by capacitors that operate at voltages similar to that encountered in existing sonobuoys, with source levels in a similar range. Consequently, sparker acoustic sources can be packaged in sonobuoys with other subsystems. As in any multi-use sonobuoy, care must be taken to electrically isolate each subsystem from one another.

Sparker acoustic sources also can produce multiple pings, unlike SUS devices. This provides flexibility in designing sparker systems for different applications. For a sparker system, the number of pings and the source level of each ping are determined by the application, the available volume for the sparker and the efficiency of the sparker in converting electrical energy into acoustic energy. For a given size sonobuoy, the system can be

designed to have relatively high source level with a small number of pings, or a lower source level with a larger number of pings⁽¹⁾. The sparker can operate a single ping at a time or be repetitively pulsed to produce a pulse train. Furthermore, because the sparker projector head is small, several sparkers can be packaged in a sonobuoy, allowing for the possibility of small arrays and rapid-fire pulse trains.

The acoustic spectrum of a sparker also can be partially controlled⁽²⁾. Although the pressure waveform of a sparker is impulsive with a broadband spectrum as in Fig. 1, both the source level and shape of the spectrum can be varied. For instance, the source level from a single sparker can be varied by changing the charging voltage. Thus a series of pings could be programmed (or controlled remotely) to produce different source levels. Furthermore by arranging sparker pulses in specific time sequences, the source level can be increased and decreased in specific spectral regions. Similarly, small arrays of sparkers can provide directionality.

The possibilities for using sparker acoustic source systems for different applications are largely unexplored. In the application reported here, the objective is to produce a small number of pings with high source level, using an "A" size sonobuoy (4.875" diameter by 36" long). A key parameter in achieving high source level is the efficiency of converting electrical into acoustic energy, discussed in the next section.

IV. Development of Sparkers for Use in Sonobuoys

IV.A. Summary

Just as for a SUS device, where the source level increases with the weight of the explosive, the source level of a sparker increases with the electrical energy stored in the electrical driver. For a system with a limited volume, the maximum stored electrical energy is determined in part by the energy density capability of capacitor technology. Over the past two decades capacitor energy density has increased more than an order of magnitude, making it practical to consider sparker-based sonobuoys. Recently, we demonstrated for the first time the feasibility of packaging and operating a sparker housed in a sonobuoy-like system⁽³⁾, pictured in Fig. 2. The sonobuoy was packaged in a PVC tube and tested in a fresh water quarry. This initial demonstration set the stage for further development of sparkers for sonobuoys that operate in ocean water with higher source level.

Sparkers operating in ocean water typically have had low efficiencies on the order of a few percent or less. However, we showed in tests at Seneca Lake⁽⁴⁾ that

sparkers operating in fresh water can have an efficiency exceeding forty per cent. SUS devices also convert approximately forty percent of the chemical energy of the explosive into acoustic energy⁽⁵⁾. Consequently, we have been investigating the means to increase acoustic efficiency of sparkers in ocean water.



Fig. 2 Sparker Sonobuoy-like System

For sparkers, the primary difference between "fresh" and "ocean" water operation is due to the different electric discharge mechanisms due to the different electrical conductivity of the water. In high-efficiency fresh-water sparkers the initiation is by means of an electrical breakdown in which plasma streamers arc between electrodes. This "plasma breakdown" process is very fast (on the order of microseconds) and requires little energy. In ocean water, on the other hand, initiation occurs by means of the evaporation of water and the growth of a steam bubble. This "thermal breakdown"

process is relatively slow (typically hundreds to thousands of microseconds) and requires much more energy than a "plasma breakdown". The efficiency of generating acoustics in ocean water is less than in fresh water in part because of the greater energy lost to initiation. In addition, since the generation of acoustics is proportional to the volume acceleration of the water⁽⁶⁾, the relative slowness of the initiation in ocean water also results in lower efficiency. Thus, the initiation process is key in determining efficiency.

The key to improving sparker efficiency in ocean water is to understand how sparker operation depends on the inter-relationship of many variables. We report here on initial efforts to improve the efficiency of sparker operation in ocean water. The investigation includes effects of water salinity, separation between electrodes, charging voltage, parallel and series sparker arrangements, electrical circuit design and sparker geometry.

The experimental results reported in this paper are from a series of trade-off tests conducted in the laboratory, that provide basic information on the scaling of acoustic performance with operating parameters. The acoustic measurements in the lab tests are "semi-quantitative" due to tank reflections. Conducting tests in the lab allowed control of test parameters and allowed a large number of tests to be made (over 1500 experimental points analyzed). This provided the basis to select a small number of sparker system parameters for incorporation into a sonobuoy and quantitative evaluation in free-field tests at sea. The sonobuoy design and plans for sea tests are discussed in section 5. We expect the sea tests to demonstrate a marked improvement in acoustic efficiency over previous ocean sparkers, but still to be less than the efficiency achieved in fresh water. Additional increases in efficiency may be achieved both by improving initiation techniques as well as the utilization of "enclosed" sparkers⁽²⁾. The next sections are an overview of the tests conducted, the experimental set-up and key results

IV.B. Experimental Set-up

A schematic for the experiment is shown in Fig. 3. The set-up consisted of a test tank, electrical drivers for the sparkers, digital data acquisition and a digital delay pulse generator to control the timing of sparker operation and data acquisition. The test tank contained water, one or more sparkers and a hydrophone for measuring the pressure of the sparker(s). Tests were conducted in two test tanks, a small one at low electrical energy (less than fifty joules) and a larger one at higher energy (up to about five thousand joules). The water salinity was measured for each test series, and was changed for different tests using Synthetic Ocean. The separation between hydrophone and sparkers was chosen to be as small as possible without saturating the pressure signal

for a given test series. Subject to that condition, the sparker and hydrophone were positioned both horizontally and vertically to maximize the time that the measured pressure was free of reflections. Also, for each sparker set-up we measured the electrical resistance between the electrodes of the sparker, an important parameter in sparker initiation in electrolytic liquids such as ocean water. Additional test variables included the gap between electrodes of the sparker, the sparker geometry, and number of sparkers and electrical arrangement.

One or more electrical drivers were employed in each experiment. The schematic of a single sparker circuit in Fig. 4 shows the key components: the electrical driver, sparker and diagnostic probes. A high voltage power supply charges a bank of energy storage capacitors. The charging voltage, determined by a setting on the power supply, is measured separately with a high voltage probe. The sparker is isolated electrically from the capacitors by a switch. After the capacitors are charged, a pulse from the digital delay pulse generator (see Fig. 3) initiates the trigger circuit for the switch, and the electrical discharge into the sparker commences. The time dependent voltage across the sparker and the current through the sparker are measured and recorded on a digital oscilloscope.

Electrical driver set-up parameters included charging voltage and capacitance and, in some cases, the use of two electrical drivers (one low energy, the other high energy).

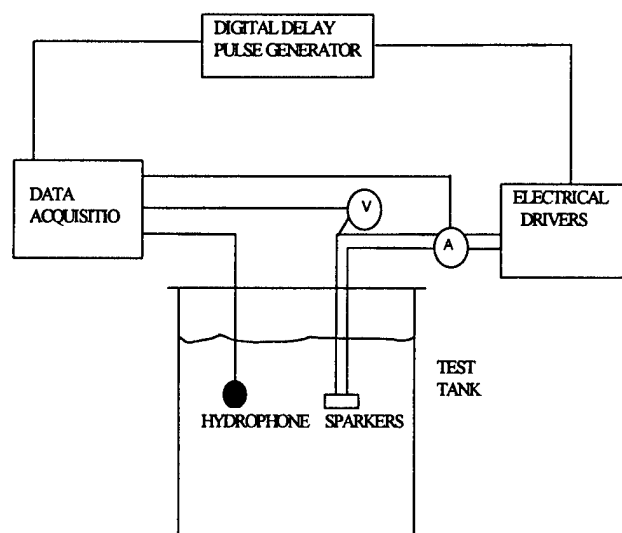


Fig. 3 Set-up Schematic of Laboratory Tests

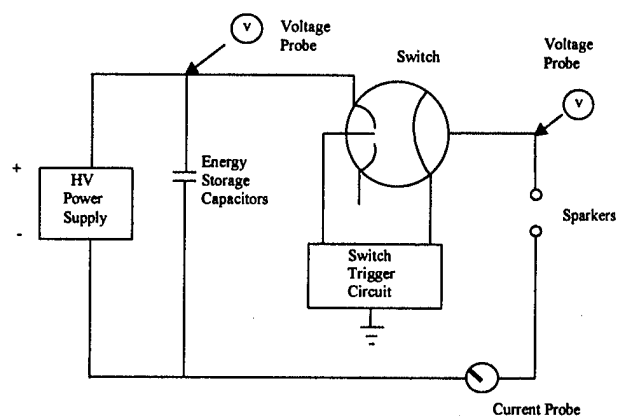


Fig. 4 Schematic of a Sparker Circuit

For each electrical discharge, digital recordings were made of the pressure pulse, the charge voltage, the sparker current and the sparker voltage. Three repeat tests were made at each operation point. All data was logged, hard copies made of the pressure and electrical traces, and the digital data compressed and archived for possible future use.

Both the electrical and acoustic data were analyzed and the results summarized in tables. Due to tank reflections only the acoustic energy in the first and second pressure peaks could be measured. The two-peak efficiency ignores acoustic energy in the rarefactions and in the third and subsequent peaks. However, the two-peak efficiency provides means for evaluating how changes in system parameters effects acoustic efficiency.

IV.C. Laboratory Test Results Summary

This section contains a summary of the key results of the laboratory tests. Example results are presented exhibiting the effects of water salinity, electrode gap and charging voltage. Also, we discuss the effects of multiple sparkers driven by a single electrical driver, different sparker geometries and the use of two electrical drivers and multiple electrode sparkers.

IV.C.1) Salinity Effects

Tests of the effect of salinity showed that the acoustic efficiency decreases as salinity increases. Fig. 5 shows the results of an example test series in which all test variables remain the same except for salinity. The two-peak acoustic efficiency (ratio of acoustic energy in the first two peaks to the electrical energy) is shown as a function of water salinity. This data shows how the efficiency decreases from about forty percent at the lowest salinity to about five percent at ocean salinity. This trend was observed for a wide range of capacitances, electrode gaps and charging voltages.

The effect of salinity also was evident in the electrical discharge measurements. At low salinity, once the switch was closed both the sparker voltage and current increased rapidly. This is evidence of the prompt initiation characteristic of plasma streamers. However, at high salinity, once the switch closed, the sparker voltage increased rapidly but the current remained low for a "delay time" before finally increasing rapidly. This delay is characteristic of thermal initiation, during which electrical energy evaporates water, creating an expanding vapor cloud. Once the vapor cloud spans the electrode gap, the electrical resistance drops quickly and the current rises rapidly. During the initiation phase energy is lost to producing the vapor cloud, thereby reducing efficiency.

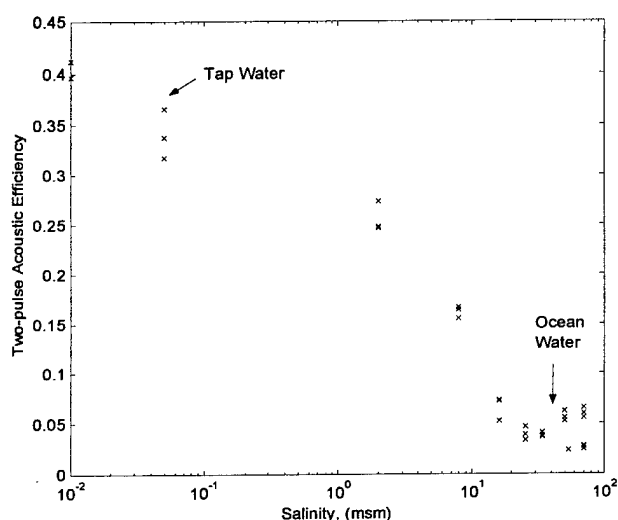


Fig. 5 Water Salinity Effect on Acoustic Efficiency

IV.C.2) Electrode Gap Length Effects

For ocean water the effect of gap length has two regions. In the first, for short gaps (up to on the order of a couple centimeters) increasing the gap between electrodes decreases acoustic efficiency because of increases in electrical energy expended while the vapor cloud spans the gap. In the second region, for longer gaps, the acoustic efficiency remains about constant because the ocean water acts as the second electrode. Moving the metal electrode further away does not change the measured resistance between the cathode and anode because of the volumetric conductivity of the ocean water. The spark generated is localized near the anode, and does not bridge the gap between electrodes. Early commercial sparker systems had electrode gaps of several inches and system efficiency was low.

The gap length effect in ocean water is evident in Fig. 6, which shows the two-pulse acoustic efficiency as a

function of gap length for a low energy discharge (7.2 joules, with 0.05 μ F, 17kV) between two #22 wires serving as the electrodes. For short gap lengths up to about two centimeters the acoustic efficiency falls off rapidly from about seven percent to less than two percent. For longer gaps the efficiency transitions to a constant efficiency of about 1.2 percent from about seven to the longest gap tested, thirty centimeters. In this example, by choosing the shortest gap tested, the acoustic efficiency is almost six times higher than when the gap length is seven centimeters or more.

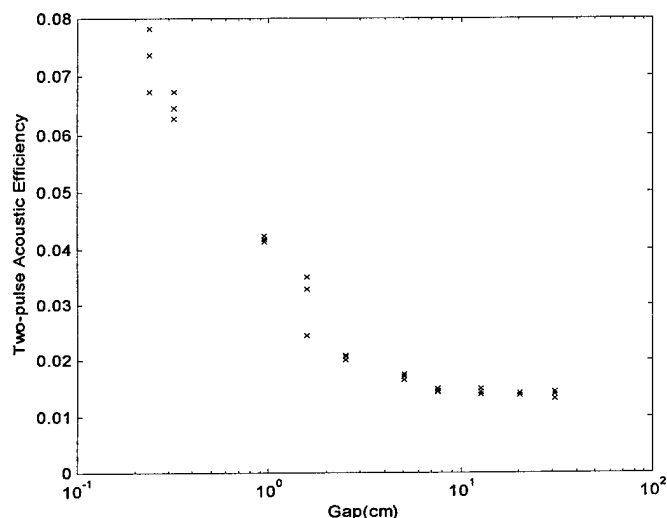


Fig. 6 Electrode Gap Length Effect on Efficiency

Generally, each sparker set-up (e.g., electrical driver, charging voltage, geometry and water salinity) has a different optimum gap length. In the limit of zero gap the circuit shorts itself, producing no acoustic energy. For short gaps the initiation energy is relatively small, so acoustic energy is generated efficiently. However, the acoustic efficiency has a complicated dependence on salinity, gap length, charging voltage, capacitance and sparker geometry. Consequently, testing is used to evaluate acoustic performance. The next section addresses another key sparker operating parameter, the charging voltage.

IV.C.3) Charging Voltage Effects

For a given sparker set-up the acoustic efficiency has an optimum charge voltage. For voltages below the optimum voltage, initiation energy losses are large whereas for voltages above the optimum voltage capacitor circuit losses become important. These effects

are evident in Fig. 7, which shows the two-pulse acoustic efficiency in ocean water as a function of charging voltage, for a gap length of 1.27 cm and capacitance of 142 μF . At the lowest voltage tested (1.5 kV), which is just above threshold for thermal initiation, the efficiency is less than four percent. The highest efficiency, more than nine percent, is at 3.0 kV, and the efficiency decreases at higher voltages, falling to less than four percent at 5.5 kV. The capacitors in the sea tests will have smaller electrical losses, so that the optimum voltage is expected to be higher.

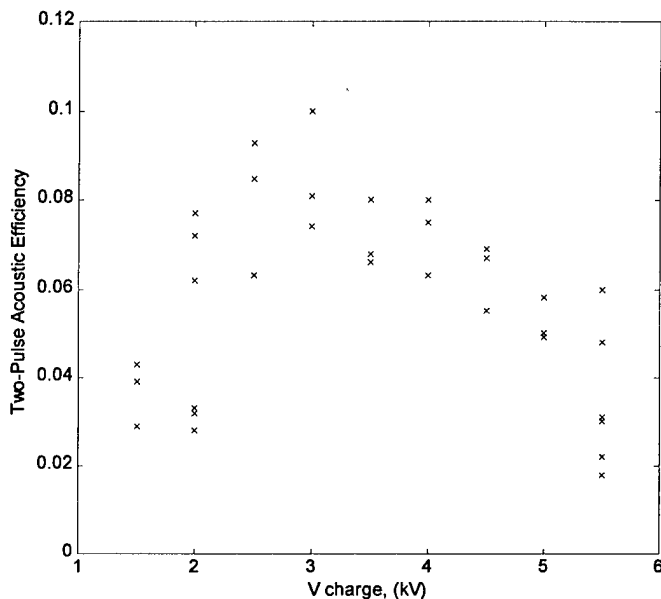


Fig. 7 Charging Voltage Effect on Acoustic Efficiency

IV.C.4) Additional Sparker Testing Results

Sparker testing also included investigation of sparker arrays, possible means for improving sparker initiation, and sparker geometry effects.

The use of a small array of sparkers with the sonobuoy has the potential to increase source level through directionality. In the lab tests we found that a single electrical circuit can drive several sparkers in parallel. The directionality and effects of operating multiple sparkers on acoustic efficiency could not be measured because of the combination of multiple sparks and reflections. Quantitative far-field measurements are planned in upcoming sea tests.

We also tested an alternative initiation technique that uses two electrical circuits. One circuit is at low energy, intended to provide a high conductivity path for the second, high-energy sparker. Tests were conducted with

both a standard two-electrode sparker and a three-electrode sparker. Experimental implementation of the two circuits required electrical isolation that turned out to be costly and would add significant weight and volume to the sonobuoy. Consequently, this initiation technique was not pursued further. In the small number of tests that were conducted the two electrical circuits generated sparks that functioned almost independent of one another.

The arrangement of the electrodes defines the sparker geometry. Different geometries include simple opposing electrodes, cylindrical (i.e., along the surface of a cylinder), annular (i.e., coaxial), and a "toaster" geometry in which the gap between electrodes is maintained constant. Tests of these geometries did not show a clear advantage of any geometry for acoustic efficiency. The "toaster" geometry was chosen for the sonobuoy because of its low cost and ease of implementation with a sonobuoy.

V. Sparker-Sonobuoy Demonstration

The results of the tests described above were used to select parameters for testing at sea, and lead to the design of the sonobuoy shown in Fig. 8. The testing at sea, shown schematically in Fig. 9, will provide quantitative far-field measurements of the pressure waveform, acoustic spectrum and efficiency.

The sonobuoy has three electrical drivers, for testing one, two and three sparkers. The capacitors are low loss, for efficient electrical operation, and have an annular geometry so that the electrical wires are fed down the center of the sonobuoy. Three high voltage power supplies located on the ship charge the capacitors. Controls (e.g., trigger pulses for the switches) and data acquisition also are located on the ship. The capacitance for a single sparker can be changed by connecting the capacitors from different drivers in series and parallel. A small array allowing up to six sparkers will be attached to the bottom of the sonobuoy, as indicated in Fig. 9.

The sparker-based sonobuoy system was designed to facilitate trade-off testing and to acquire spectral source level data for a range of system parameters. Consequently, this sonobuoy provides flexibility in operation parameters and of necessity is much larger than the "A" size of the intended application. The objective of the tests is to provide acoustic source information that will lead to a specific sparker design for integration and testing in an "A" size sonobuoy.

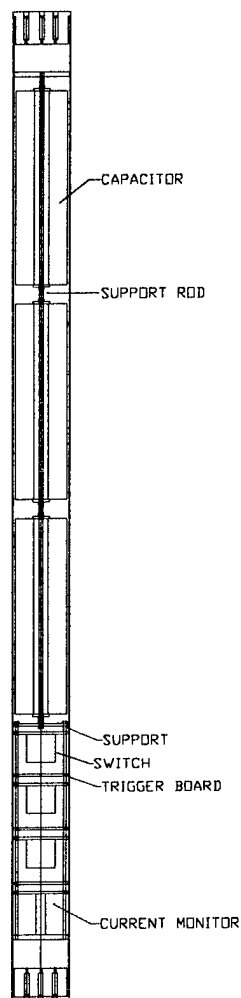


Fig. 8 Sonobuoy Design

In the sea tests, pictured in Fig. 9, the sonobuoy and hydrophone are deployed over the side of the ship, approximately seventy feet apart. The electrical driver(s) are charged and triggered electronically from the control room on the ship. The hydrophone measures the pressure from the sparker(s) and a current monitor in the sonobuoy measures the sparker(s) electrical current. The data is acquired and recorded digitally on the ship.

At the time this paper was written, the sparker based sonobuoy system pictured in Fig 8 was being built, with the sea tests planned for late summer. Further details will be included in the talk.

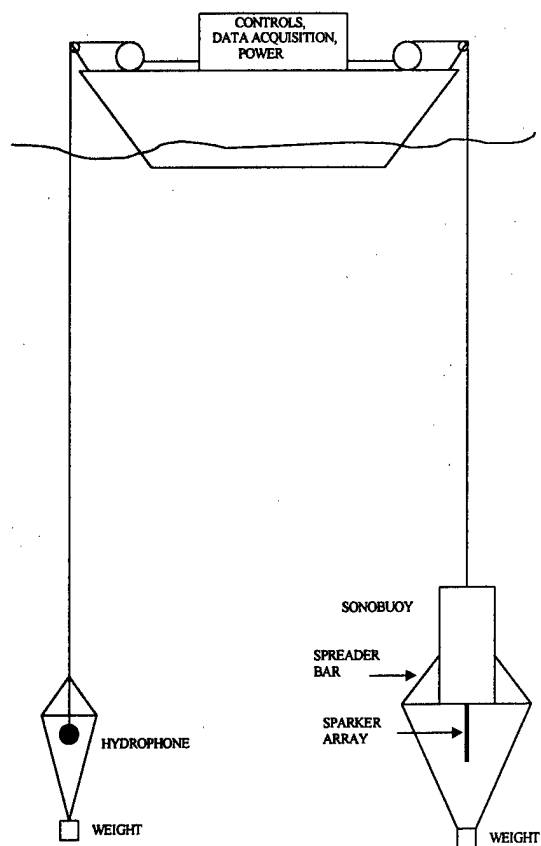


Fig. 9 Sea Test Schematic

References

1. Schaefer, Raymond B., "Evaluation of a Controllable Impulsive Surface Discharge Acoustic Source for "A" Size Sonobuoy Application", Fin. Rpt., Con. No. N62269-95-C-0142, Prepared for Naval Air Warfare Center, (1996).
2. Schaefer, Raymond B., "Spectral Control of Sparker Acoustic Sources", IEEE Oceans '97, 9 October, 1997, Halifax, Nova Scotia.
3. Schaefer, Raymond B., "Insertion of Surface Discharge sparker Acoustic Sources into Submarine Countermeasures", Fin.Rpt., Con. No. N00024-97-C-4133, prepared for Naval Sea Systems Command (1997).
4. Schaefer, Raymond B., "Surface Discharge Acoustic Source Development." Fin. Rpt, Con. No. SDIO84-89-C-0034, (1991) ; Surface Discharge Light and Acoustic Source for Maritime Environmental Applications", Fall 1992 Maritime Environmental Symp., ASNE; "Surface Discharge Acoustic Source Development", Fin. Rpt., Con. No. SDIO 84-92-C-0008, SPAWAR (1993).
5. Willis, H.F., Underwater Explosions, Time Interval Between Successive Explosions, Brit. Rpt WA-47-21 (1941); Urick, Robert J., "Principles of Underwater Sound", 3rd edition (1983).and Cole, Robert H., Underwater Explosions, Dover Publications, (1948).

SIREM: AN INSTRUMENT TO EVALUATE SUPERDIRECTIVE AND INTENSITY RECEIVER ARRAYS

Paul C. Hines and Daniel L. Hutt

Defence Research Establishment Atlantic,
P.O.Box 1012, Dartmouth, NS, Canada, B2Y3Z7
e-mail: hines@drea.dnd.ca, hutt@drea.dnd.ca

Abstract - Pressure gradient arrays have been in use within the acoustic community for several decades. Historically most underwater acoustics measurements employing pressure gradient arrays have used the superdirective array whereas air applications have relied on the intensity array approach. Intensity arrays based on pressure sensors require the same hardware (and equally rigorous hardware tolerances) as superdirective arrays. The difference between the two methods lies in how one processes the received signals. One obtains the intensity by *multiplying* pressure and pressure gradient signals; The superdirective solution is obtained by *summing* the pressure and the pressure gradient signals. The measurement objective dictates which solution is better for a given experiment. The Defence Research Establishment Atlantic (DREA), in collaboration with Guigné International Ltd., has developed a 6-channel hydrophone array which will be used to explore the processing advantages of both methods. Two configurations of the system will be examined: a tri-axial array of dipoles enabling measurements along the x, y, and z axis, and a 6-channel linear array configuration enabling measurement of gradients up to 5th order along a single axis. In this paper, the array configurations will be outlined and the impact of system noise on the processing methods will be described.

I. INTRODUCTION

Pressure gradient arrays have been in use within the acoustics community for several decades. As the name implies, these arrays compute the gradient of the pressure field rather than just its magnitude and this offers two advantages: First and foremost, computing the pressure gradient allows one to obtain the direction of propagation of a pressure wave. Secondly, estimating the gradient requires inter-element spacings that are a small fraction of an acoustic wavelength; Thus by its nature, the array is much more compact than a conventional array.

Two realizations of the pressure gradient array shall be examined in this paper. The first is the intensity array and the second is the superdirective array. Both devices require the same hardware and equally rigorous hardware tolerances. The difference between the two lies in how one processes the received signals. One obtains the intensity by *multiplying* pressure and pressure gradient

signals; The superdirective solution is obtained by *summing* the pressure and the pressure gradient signals.

The Defence Research Establishment Atlantic (DREA), in collaboration with Guigné International Ltd., has developed a 6-channel hydrophone array known as SIREM (Superdirective/Intensity Receiver Evaluation Module). The device will be used to explore the processing advantages of superdirective and intensity receivers in a variety of acoustical environments. Moreover, two configurations of the system will be examined: a tri-axial array of dipoles enabling intensity and superdirective measurements along the x, y, and z axis, and a 6-channel linear array configuration enabling measurement of gradients from 0th to 5th order along a single axis. In this paper, the array configurations will be outlined and the impact of system noise on the processing methods will be described.

II. THE SUPERDIRECTIVE/INTENSITY RECEIVER EVALUATION MODULE (SIREM)

Conventional line arrays form acoustic beams using the principle of time-delay-and-sum [1] to align the signal received at each sensor. This causes the (coherent) signal to reinforce and the (incoherent) ambient noise to average out. This design benefits from large inter-element spacings since the signal tends to have a greater coherency length than does the noise. In contrast, superdirective and intensity hydrophone arrays estimate pressure gradients of various order by taking the difference between signals received at pairs of sensors and normalizing by the sensor spacing. Since this latter technique approximates the gradient, the inter-element spacing must be much less than a wavelength. Thus, by its very nature the superdirective/intensity array is much more compact than the conventional array. Superdirective and intensity arrays based on pressure sensors require essentially the same hardware specifications; The difference between them lies in how one processes the received signals [2]. One obtains the intensity by *multiplying* pressure and pressure gradient signals; The superdirective solution is obtained by *summing* the pressure and the pressure gradient. The measurement application dictates which solution is better for a given experiment. It is interesting to note that in a conventional array, gain occurs against ambient noise if the noise is *incoherent* since it will then average out; However, in a

difference array, gain occurs only against *coherent* noise. One achieves gain against ambient noise with the difference array because at small inter-element spacings the ambient noise is coherent.

The principle disadvantage of these "difference arrays" is that theoretical gains are difficult to achieve due to their susceptibility to uncorrelated noise. That is to say, the very process of taking the difference between the acoustic signals at two sensors means that the signal to noise ratio (SNR) must degrade. Noise sources include pre-amplifier voltage noise, inter-channel imbalance in gain and/or phase, sensor spacing errors, acoustic scatter and hydrophone self-noise due to hydrodynamic flow past the sensors. Voltage noise and inter-channel imbalance can be minimized through careful design of pre-amplifiers and modern digitization techniques. Sensor position errors are reduced by compliantly mounting the hydrophones to stiff mounting rods. Flow noise can be reduced by enclosing the hydrophones in an acoustically transparent shroud such as open-cell foam. Finally, noise resulting from scatter can be minimized by ensuring that hardware in the vicinity of the hydrophones is sufficiently low-profile in design. This last constraint is perhaps the most difficult to quantify and it is oftentimes the quality of the data which determines if the design requirement has been met. Modeling[3] indicates that in the absence of sensor noise, a six-hydrophone array with an aperture of 0.8 m will provide approximately 15 dB gain against three-dimensionally isotropic ambient noise.

III. THE SIREM HARDWARE

There are two configurations for the SIREM hardware: A three-dimensional (volume array) arrangement in which 3 pairs of hydrophones are arranged symmetrically along the Cartesian axis, and a linear arrangement in which all six hydrophones are aligned with a single axis. Both of these configurations are described below.

A. The Volume Array Configuration

Fig. 1 shows a schematic of the sensor layout for the volume array configuration. Horizontal rods (not shown) are used to set the transverse spacing to either 8 cm or 19 cm depending on the frequency band of interest. Each hydrophone pair is aligned with its respective Cartesian axis and the geometric center of the array corresponds to the point $(x, y, z) = 0$. The hydrophones, denoted $(X1, X2)$, $(Y1, Y2)$, and $(Z1, Z2)$, are compliantly coupled to stiff stainless steel mounting rods which sets the vertical alignment. Wires run from the hydrophones to a set of preamplifiers approximately 2 m away. The pre-amplifier container is physically separated from the hydrophones to reduce acoustic scatter and diffraction effects. Care must be taken to ensure that the wires are immobilized to prevent electronic pick-up from contaminating the signals.

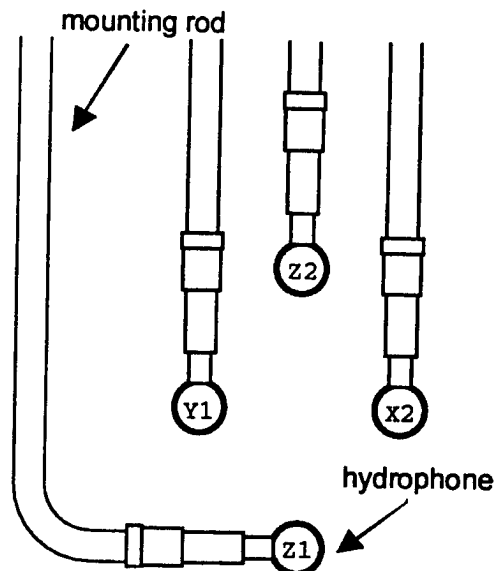


Fig. 1: Cross-section of sensor layout for volume array. Hydrophones Z1 and Y1 block the view of Y2 and Z2, because the section is taken at 45°.

B. The Linear Array Configuration

Fig. 2 shows a schematic of the linear array configuration. Inter-element spacing is maintained by mounting the hydrophones to a pair of wire-rope strength-members held in tension. This assembly is wrapped in open-celled foam and encased in a polyurethane hose. The foam serves to compliantly couple the sensors to the hose wall, which in turn maintains the axial symmetry of the array and provides mechanical protection. The hose is open-ended to eliminate scatter from the endcaps. The entire assembly

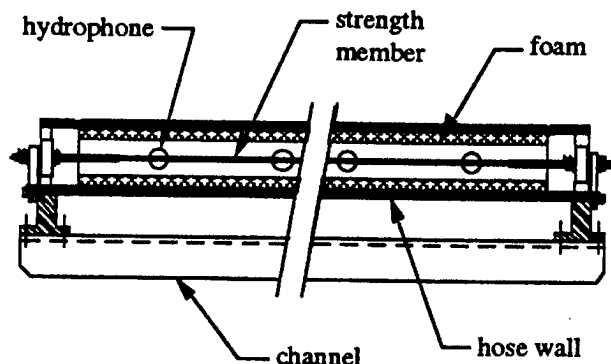


Fig. 2: Cross-section sensor layout for linear array. Only four of the six sensors are shown.

is connected via metal stand-offs to a length of aluminum channel which allows the array to be attached to a variety of structures. The hydrophone wires run along the wire-rope to a pre-amplifier can located outside the hose. As with the volume array, care must be taken to ensure that the wires are immobilized to prevent electronic pick-up from contaminating the signals.

C. The Pre-amplifiers

The SIREM is a six channel difference array receiver used in DREA's Wide Band Sonar (WBS) system [1]. The hydrophones have a nominal acoustic sensitivity of -200 dB re $1\text{V}/\mu\text{Pa}$. The pre-amplifiers were custom-built. The pre-amplifiers have a 12 dB fixed gain at the input stage with 60 dB additional gain selectable in 12 dB increments. The dynamic range of the pre-amplifier varies from a high of 150 dB at the 12 dB gain setting to a low of 100 dB at the 72 dB gain setting. At 1 kHz, the pre-amplifier noise (referred back to the input) is less than -165 dBV/ $\sqrt{\text{Hz}}$ all gain settings. Fig. 3 shows the inter-channel relative phase matching of the pre-amplifiers as a function of frequency. The five curves represents the relative phase of 5 of the pre-amplifiers to the 6th (the Z2 pre-amplifier). A phase difference of 0° means that the channels are perfectly phase matched. Phase matching between all six pre-amplifiers is better than $\pm 3^\circ$ across the frequency band. For the volume array configuration, the pre-amplifiers were paired to minimize the phase mismatch along each axis. For example, the dashed curve shows the relative phase of the (Z1, Z2) pair. The two solid curves are the (X1, X2) pair and the dash-dot curves are the (Y1, Y2) pair. Phase matching between pairs is better than $\pm 0.05^\circ$ across the frequency band.

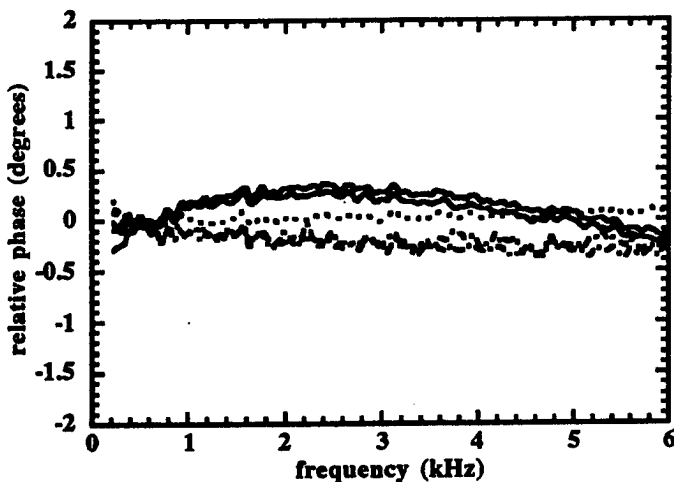


Fig. 3: Phase matching of five of the pre-amplifiers relative to the sixth.

Fig. 4 shows the inter-channel relative gain matching of the pre-amplifiers as a function of frequency. The five curves represents the relative gain of 5 of the pre-amplifiers to the 6th (the Z2 pre-amplifier). A gain difference of 0 dB means that the channels are perfectly matched in gain. The dashed curve shows the gain of the (Z1, Z2) pair. Gain matching between all six pre-amplifiers is better than ± 0.3 dB and matching between two co-axial pre-amplifiers is better than ± 0.1 dB. The line designations are the same as in Fig. 3.

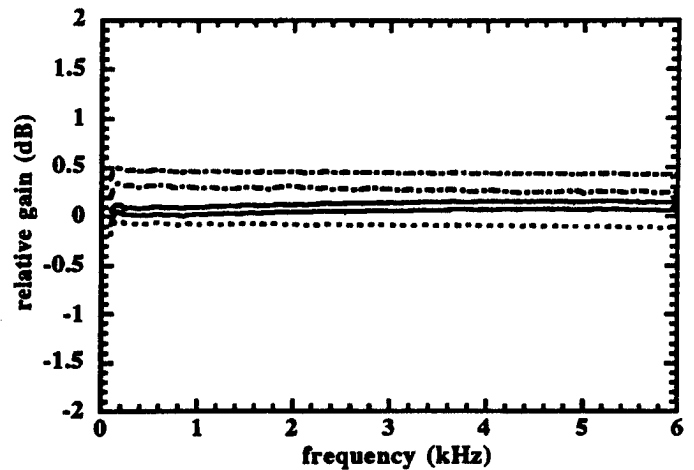


Fig. 4: Gain matching of five of the pre-amplifiers relative to the sixth.

IV. SYSTEM NOISE AND ITS IMPACT ON ARRAY GAIN

In this section we examine the effect of system noise on array gain for the linear array and for one axis of the volume configuration. The degradation occurs because forming the gradient reduces signal amplitude while leaving uncorrelated system noise unchanged. System noise includes pre-amplifier voltage noise, inter-channel imbalance in gain and/or phase, sensor spacing errors, acoustic scatter and hydrophone self-noise due to hydrodynamic flow past the sensors. In SIREM, voltage noise limits the array's performance. Since the superdirective and intensity arrays both employ the gradient approach, the impact of system noise will be similar for the two processing techniques. For brevity, remarks will be limited to the superdirective configuration.

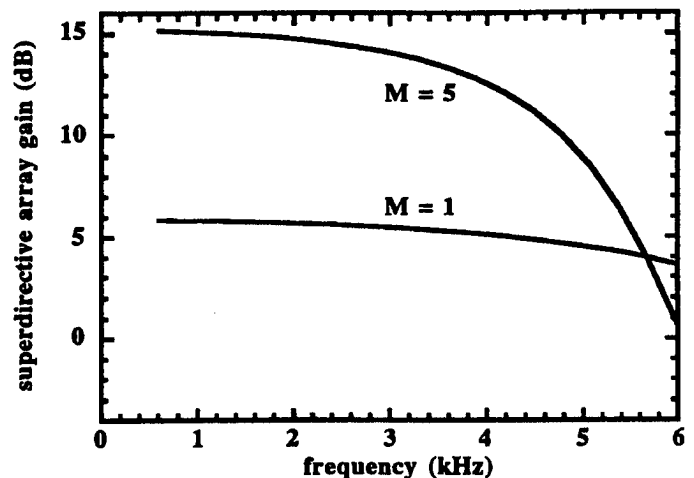


Fig. 5: Ideal gain for a 2-hydrophone ($M = 1$) and for a 6-hydrophone ($M = 5$) superdirective array.

Figure 5 shows the array gain (AG) in decibels for a 1st order (2-element) and a 5th order (6-element) superdirective array [3]. The model assumes a three-dimensionally isotropic ambient noise field, an inter-element spacing of $d=0.16$ m, and zero system noise [5]. The array gain decreases with increasing frequency because the approximation to the gradient degrades; This defines the high frequency operating limit of the superdirective array. The low frequency limit of the superdirective array arises when one includes the effects of uncorrelated system noise. To quantify its effect we note from [3] that the degradation in array gain AD due to uncorrelated noise can be written as:

$$AD = 1 + \frac{N_m AG}{N_o} \quad (1)$$

where N_o is the ambient noise power and N_m is the system noise and we have normalized to unity signal gain. The system noise at the output of a superdirective line array is given by:

$$N_m = N_s \left\{ \left[\sum_{i=1}^{M/2} \frac{w_{2i-1} C_i}{W(-p^2)^i} \right]^2 + 2 \left[\sum_{i=1}^{M/2} \frac{w_{2i-1} C_{i+1}}{W(-p^2)^i} \right]^2 \right\} + \dots \quad (2)$$

$$N_s \left\{ 2 \left[\sum_{i=1}^{M/2} \frac{w_{2i-1} C_i}{W(-1)^{i-1} p^{2i-1}} \right]^2 + 2 \left[\sum_{i=2}^{M/2} \frac{w_{2i-1} C_{i-1}}{W(-1)^{i-1} p^{2i-1}} \right]^2 \right\} + \dots$$

where N_s is the system noise power of an individual pre-amplifier, ${}_a C_b$ is the binomial coefficient for the $(b+1)^{st}$ term, $W = \sum_{n=0}^M w_n$, is the sum of the gradient weights, w_n , and $M/2$ and $\overline{M/2}$ represent the summation taken to the floor or ceiling of the fraction, respectively.

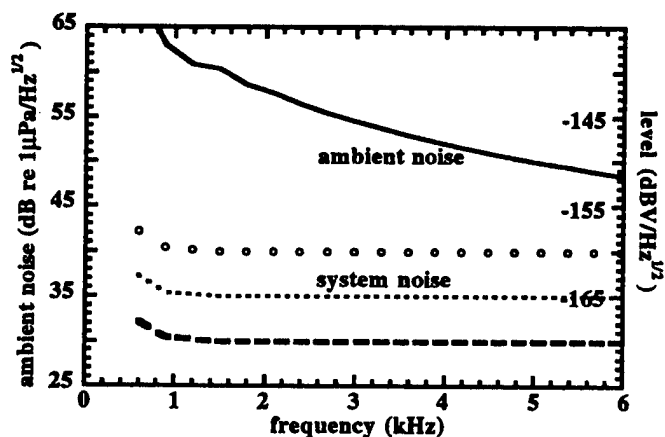


Fig. 6: Sample noise floor for pre-amplifier (dotted line) and noise floor 5 dB quieter (dash line) and 5 dB noisier (open circles). The noise curves are compared to the pre-amplifier response to ambient noise (solid line).

In order to quantify the effect of voltage noise on array performance, one must first compute the voltage response of the hydrophone/pre-amplifier for a specific ambient noise data set. This is compared to the voltage noise of the pre-amplifier. By way of example Fig. 6 shows ambient noise collected on Western Bank off the coast of Nova Scotia (solid line) [1]. The data were collected in water 60 m deep during winds of 20 knots. The measured data are limited to below 2 kHz; The data have been extrapolated to 6 kHz by assuming a roll-off of 6 dB/octave. The left vertical axis shows the data in units of dB re $1 \mu Pa / \sqrt{Hz}$ whereas the right vertical axis provides the conversion to dBV/√Hz using the SIREM hydrophone sensitivity. Also plotted in the figure is the voltage noise background (N_s) of an individual SIREM pre-amplifier (dotted line) and curves representing a 5 dB reduction in pre-amplifier noise (dash line) and a 5 dB increase in pre-amplifier noise (open circles). Using Fig. 6, and Equations (1) and (2) one can estimate the array degradation as a function of frequency and from that, adjust the theoretical array gains shown in Fig. 5 to obtain the corrected receiver array gain.

Figs. 7 and 8 show the array gain in decibels for a 6-element and a 2-element array, respectively, for the ambient noise and pre-amplifier noise of Fig. 6. The line conventions for array gain correspond to the line conventions for pre-amplifier noise in Fig. 6. For comparison, the ideal gain curves are re-plotted from Fig. 5. The four curves are well separated for the 6-element array but all four curves overlay one another for the 2-element array. Clearly, system noise has a much more severe impact on higher-order difference arrays. This occurs because the finite-difference method of computing higher order gradients successively reduces the signal (in this case ambient noise) while maintaining the same system noise background.

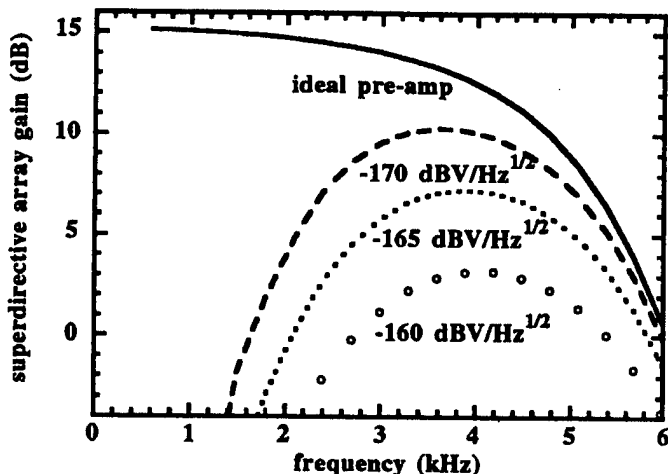


Fig. 7: Array gain for 5th order superdirective array for three pre-amplifier noise floors with the ambient noise conditions given in Fig. 6. The solid line is the ideal gain re-printed from Fig. 5. The other three curves correspond to the pre-amplifier noise curves shown in Fig. 6.

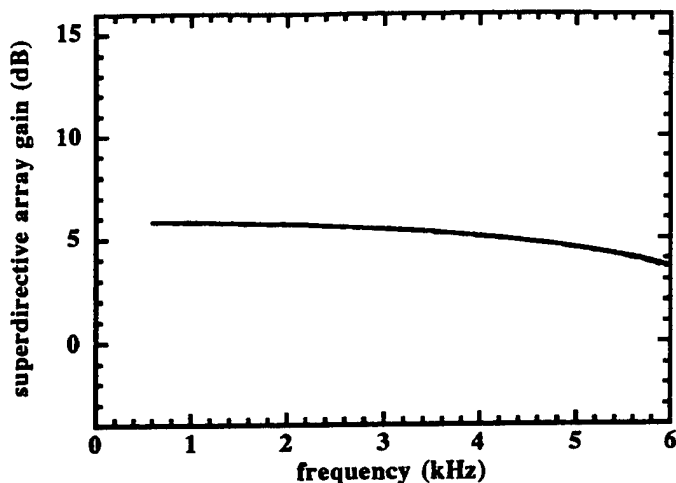


Fig. 8: Array gain for 1st order superdirective array for three pre-amplifier noise floors and the ideal gain reprinted from Fig. 5. Note that all four gain curves overlay one another. The four gain curves were computed using the ambient noise conditions given in Fig. 6.

V. CONCLUSIONS

SIREM is a 6-element receive array designed to examine the processing gains of two pressure-gradient processing techniques in the superdirective array and the intensity array. The system can be configured as either a 6-element linear array or a tri-axial array of dipoles. The array was designed to operate from approximately 1 kHz to 5 kHz.

The principle disadvantage of pressure-gradient arrays is that theoretical gains are difficult to achieve due to their susceptibility to uncorrelated noise. This problem becomes more pronounced as one calculates higher-order gradients. For example, with the present hardware specifications, the 6-element linear array achieves a maximum gain of approximately 7 dB, some 8 dB below the theoretical limit. Improving pre-amplifier noise performance by $5 \text{ dBV}/(\text{Hz})^{1/2}$ results in a maximum gain of approximately 10 dB. In contrast, the dipole array reaches its theoretical gain of 6 dB not only using the current pre-amplifier specification but also using a pre-amplifier that is $5 \text{ dBV}/(\text{Hz})^{1/2}$ noisier.

VI. REFERENCES

- 1 Robert J. Urick, *Principles of Underwater Sound*, 2nd ed. (McGraw-Hill, 1975), pp. 51.
- 2 J. Barrie Franklin, "Intensity Measurements and Optimum Beamforming Using a Crossed Dipoles Array," Defence Research Establishment Atlantic, DREA CR/97/443, (1997).
- 3 Barrie Franklin, "Superdirective Receiving Arrays for Underwater Acoustic Application," Defence Research Establishment Atlantic, DREA CR/97/444, (1997).
- 4 Paul C. Hines, W. Cary Risley, and Martin P. O'Connor, "A Wide-Band Sonar for Underwater Acoustics Measurements in Shallow Water," Proceedings: Oceans'98, Nice, France, Sept. 29-Nov. 1, 1998.
- 5 To obtain Fig. 5, a gradient weighting scheme optimized for 2-dimensionally (i.e., horizontally) isotropic noise was chosen due to its robustness in the presence of self-noise and channel imbalance. As it happens, optimizing the weights for a 2-D isotropic noise field, and employing them in a 3-D isotropic noise field results in less than a 0.5 dB reduction in array gain.
- 6 Mark Hazen and Francine Desharnais, "The Eastern Canadian Shallow Water Ambient Noise Experiment", Conference Proceedings, Oceans'97, Vol. 1, pp. 471-476, (1997).

THE SOUND IS CLEANER: A CENTURY OF CONTAMINANT TRENDS OBSERVED FROM DATED CORES

E. A. Crecelius, L. F. Lefkowitz, and V. I. Cullinan
Battelle Marine Sciences Laboratory
1529 West Sequim Bay Road
Sequim, Washington 98382

I. SUMMARY

Human activity in and around Puget Sound is reflected in the discharge of concentrated organic and inorganic contaminants into the sound's sediments. As industrial-age human activity increased, so did the contaminant levels in the sediment. Age-dated sediment cores collected in 1982 showed that the input of chemicals to the Sound, including lead (Pb), mercury (Hg), silver (Ag), copper (Cu), and hydrocarbons, began to increase above background in the late 1800s. The maximum concentration of these chemicals appears to have been discharged into sediments between 1945 and 1965. Synthetic organic compounds, such as polychlorinated biphenyls (PCBs), dichlorodiphenyltrichlorethane (DDT), and chlorinated butadienes, first appeared in sediments deposited in the 1930s and reached a maximum in the 1960s. The presence of the subsurface maximum concentrations in fine-grained, deep-water sediments suggests that pollution-control strategies have improved the sediment quality of central Puget Sound.

The purpose of this study is to: 1) continue monitoring historical trends in the concentration of contaminants in Puget Sound sediments, and 2) quantify recent trends in the recovery of contaminated sediments. Results from this study can be compared with those obtained in the 1982 study to determine whether sediment quality is still improving and to estimate the rate of recovery. A statistically significant reduction in sediment contamination over the past 20 years would provide empirical evidence that environmental regulation has had a positive impact on the water quality in Puget Sound.

Chemical trends were evaluated from six age-dated sediment cores collected from the main basin of Puget Sound. Chemical analyses included metals, polynuclear aromatic hydrocarbons (PAHs), PCBs and chlorinated pesticides, nutrients (total nitrogen [N], and phosphorus [P]), butyltins, and total organic carbon (TOC). Sedimentation (cm/yr) and deposition rates (g/cm²/yr) were estimated using a steady-state ²¹⁰Pb dating technique (Lavelle et al. 1985, 1986; Nevissi et al. 1989).

The results of this study were in agreement with the earlier study by Bloom and Crecelius (1987). Trace metal

contamination including Ag, arsenic (As), Cu, Hg, Pb, antimony (Sb), tin (Sn), and zinc (Zn) began in the late 1800s, reached a maximum in the mid-1900s, and began to decline in the mid-1970s. Statistically significant average recovery rates estimated from the slope between the maximum and surface concentrations were observed for Cu, Hg, Pb, Sb, and Sn. Recovery rates for Ag, As, and Zn showed only a trend toward recovery. Concentrations of Cu, Pb, Sb, and Zn declined at a statistically significant rate in the last 20 years (which is generally after the maximum concentration was observed), lending support to our hypothesis that the strengthening of environmental regulation since 1970 has influenced the water quality of Puget Sound.

Trends in organic chemicals in the sediments over time also show a subsurface maximum. Hydrocarbon contamination appears to parallel that of heavy metals. Only DDT, however, showed a statistically significant average recovery rate. PAH concentrations, although decreased over four-fold from maximum concentrations, appear to be relatively constant over the past several decades. Significant decreases in sediment concentrations of synthetic organic contaminants were also observed with two- to four-fold decreases in surficial sediment concentrations. Concentrations of PCBs and DDT appear to be continuing to decrease.

Nutrients (P and N), linear alkyl benzenes (LABs), and biomarkers (hopane and total terpanes) were the only contaminants not showing a clear decrease in concentration. The nutrients show an extremely slight, but statistically significant, increase. Since the concentrations of LABs and biomarkers fluctuate in the near surface sediments, a plateau cannot be substantiated. Nutrients and LABs are associated with municipal sewage. Hopane and total terpanes are associated with petroleum products. Both sources of contaminants are expected to increase with an increasing population. However, despite the population growth of over one million people in the Seattle/Tacoma region in the past several decades, there has not been a substantial increase in these contaminants. Thus, the effect of strengthening environmental regulations on water quality cannot be negated.

II. INTRODUCTION

Human activity in and around Puget Sound is reflected in the discharge of concentrated organic and inorganic contaminants into the Sound's sediments. As industrial-age human activity increased, so did the contaminant levels in the sediment. Age-dated sediment cores collected in 1982 (Bloom and Crecelius 1987) showed that the input of chemicals to the Sound, including lead (Pb), mercury (Hg), silver (Ag), copper (Cu), and hydrocarbons, began to increase above background in the late 1800s. The maximum concentration of these chemicals appears to have been discharged into sediments between 1945 and 1965. Synthetic organic compounds, such as polychlorinated biphenyls (PCBs), dichlorophenyltrichlorethane (DDT), and chlorinated butadienes, first appeared in sediments deposited in the 1930s and reached a maximum in the 1960s. The presence of the subsurface maximum concentrations in fine-grained, deep-water sediments suggests that pollution-control strategies have improved the sediment quality of central Puget Sound.

The purpose of this study is to: 1) continue monitoring historical trends in the concentration of contaminants in Puget Sound sediments, and 2) quantify recent trends in the recovery of contaminated sediments. It is hypothesized that changes recorded in the cores reflect changes in the sediment contaminant loading and are a result of changes in industrial practices and in laws restricting disposal of contaminants. In the mid-1980s, two federal laws, the Safe Drinking Water Act (enacted 1974) and the Clean Water Act (enacted 1972), were amended by the Water Quality Act (1987) to provide greater enforcement and stricter regulatory standards to reduce chemical discharges from industrial waste into fresh surface waters, underground aquifers, and marine waters. Before 1980, regulations in Puget Sound were established for only 23 contaminants or groups of contaminants (Arbuckle et al. 1993). The relatively recent monitoring activities of the Puget Sound Water Quality Authority, established in 1985 by the Washington State legislature, puts greater political pressure on point-source polluters to further reduce chemical concentrations from their waste discharge. Results from this study can be compared with those obtained approximately 10 years ago by Bloom and Crecelius (1987) to determine whether sediment quality is still improving and if so, to estimate the rate of recovery. A statistically significant reduction in sediment contamination over the past 20 years would provide empirical evidence that regulation has had a positive impact on the water quality in Puget Sound.

III. METHODS

A. Field Sampling

Sediment cores were collected from six locations in the main basin of Puget Sound during September, 1991 by scientists from the Battelle/Marine Sciences Laboratory (MSL). These sites were chosen because an earlier study (Bloom and Crecelius 1987) showed that little natural or anthropogenic disturbance occurred in these areas. The mixing of sediments from bioturbation takes place mainly within the top 2 cm but can occur down to 200 cm in depth from activity of crustaceans (e.g., *Axiopsis spinacauda*), bivalves (e.g., *Panope generosa*), sea urchins (e.g., *Brissaster latifrons*), sea cucumbers (e.g., *Molpadia intermedia*), and echiuroid worms (MacGinitie and MacGinitie 1949). These species are all known to occur at the sampling depth of 200 m (Wennekens 1959). Coring locations were determined using a Global Positioning System and a Loran C radio navigation system.

Samples were collected from the *RV Kittiwake* using a stainless steel, open-barrel gravity corer (Kasten corer), 2.5 m long, with a square cross section of 15 x 15 cm (Zangger and McCave 1990). Both a Kasten corer and a 7.6-cm-diameter open-barrel gravity corer, 1.5 m long, with a clear plastic liner, were used in the 1982 study (Bloom and Crecelius 1987). The Kasten corer, however, tended to provide more intact cores with less core shortening (Nevissi et al. 1989). Core shortening, an artifact of the coring process, is when the cored material is not pushed upwards within the core barrel.

Sediment cores were processed on board the research vessel. The core barrel was opened by removing screws along the entire length. Sediment smeared during the coring was removed by scraping the exposed surface with a clean stainless steel spatula. An acceptable core was approximately 1.5 m in length and had no visible disturbance of surface sediments. Color photographs were taken, and visible changes in color, structure, and texture were recorded. The core was then sectioned into 2-cm intervals with a clean, stainless steel spatula. Sectioned samples were stored in precleaned jars, either glass or polystyrene, depending on the corresponding analysis. The coring equipment was rinsed with ambient seawater between stations and scrubbed and acetone rinsed after each cruise day to remove possible contamination. The 300-kg-weight corer stand was wrapped in a polyethylene film to further reduce possible contamination.

At the time of collection, a chain-of-custody form was initiated and then maintained with each sample through the life of the sample (i.e., through storage, analytical analysis, and disposal). Samples were stored on ice in a cooler for no more than 2 days while in transit to the MSL, where they were logged into the laboratory database system.

(FOXBASE). Samples were then stored approximately 1 month either frozen (-22 ± 2 C) or cold (4 ± 2 C) until analysis.

B. Analytical Methods

Approximately 25 2-cm sections were analyzed from each core. Sediment concentrations of metals and the radionuclide lead-210 (^{210}Pb) were analyzed from equally spaced intervals from all six cores. Cesium-137 (^{137}Cs) was analyzed from equally spaced intervals from Cores 2 through 6. For Cores 3, 5, and 6, sediments from the adjoining 2-cm sections were analyzed for polynuclear aromatic hydrocarbons (PAHs), PCBs, chlorinated pesticides, nutrients (phosphorous [P] and nitrogen [N]), and butyltins. In addition, adjoining sections from Cores 3, 5, and 6 were analyzed for grain size and total organic carbon (TOC).

Analyses for most of the chemicals measured followed methods used for the National Oceanic and Atmospheric Administration (NOAA) National Status and Trends Program (Lauenstein and Cantillo 1993). Measurements of analytical precision were based on the variance from individually processed standard reference materials.

1) Metals

A total of 16 metals were analyzed at the MSL in Sequim, Washington. They were: silver (Ag), aluminum (Al), arsenic (As), cadmium (Cd), chromium (Cr), copper (Cu), iron (Fe), mercury (Hg), manganese (Mn), nickel (Ni), lead (Pb), antimony (Sb), selenium (Se), silica (Si), tin (Sn) and zinc (Zn). Three metals, Ag, Cd, Se, were analyzed by graphite furnace atomic absorption (GFAA) spectrometry using Zeeman background correction following the method of Bloom (1983). Two metals, Sb and Sn, were analyzed by inductively coupled plasma mass spectrometry (ICP/MS). Mercury was analyzed using cold-vapor atomic absorption (CVAA) spectroscopy (Bloom and Crecelius 1983). The remaining 10 metals were analyzed using energy-dispersive x-ray fluorescence (XRF). All metal concentrations are presented in $\mu\text{g/g}$ dry weight.

To prepare sediments for analysis, samples were freeze-dried and blended in a ceramic Spex mixer-mill. Approximately 5 g of mixed sample was ground in the ceramic ball mill. The XRF analysis was performed on a 0.5-g aliquot of dried, ground material pressed into a pellet with a diameter of 2 cm. For ICP/MS, GFAA, and CVAA analyses, 0.2-g aliquots of dried homogenous sample were totally digested using a 4:1 nitric:perchloric acid solution and concentrated hydrofluoric acid in a Teflon pressure vessel placed in a 130 C oven for a period of 16 h.

2) Radionuclide Analysis ^{210}Pb and ^{137}Cs

The activity of ^{210}Pb in sediment was determined at the MSL by counting the alpha particles from the granddaughter polonium-210 (^{210}Po), similar to the method of Koide et al. (1973). Sediment samples were spiked with ^{208}Po and digested with nitric acid. The Po isotopes were plated on a silver disk and then counted using silicon barrier diode detectors. The excess ^{210}Pb was determined by subtracting supported ^{210}Pb from the measured ^{210}Pb activity. Activity of ^{210}Pb is reported in disintegrations per minute per gram (dpm/g) on a dry weight basis.

The activity of ^{137}Cs was determined at the MSL by gamma counting sediment on a lithium drifted germanium diode [Ge (Li)] detector; it is reported in dpm/g on a dry weight basis. The diode was calibrated with certified reference soil in the same geometry.

3) Polynuclear Aromatic Hydrocarbons (PAH)

Polynuclear aromatic hydrocarbons analyses were performed at the Battelle Ocean Sciences (BOS) Laboratory in Duxbury, Massachusetts, following the method of NOAA Status and Trends Program (Lauenstein and Cantillo 1993). Samples were solvent extracted with dichloromethane (CH_2Cl_2) using Soxhlet extraction. Extracts were cleaned using a combination of Al/Si column chromatography, followed by additional cleanup using high-performance liquid chromatography (HPLC). Extracts were then analyzed using gas chromatography/mass spectrometry (GC/MS) operated in the selective ion mode (SIM). A total of 20 specific PAH compounds and a number of alkylated PAH compounds were reported. In addition, linear alkylbenzenes, hopanes, and terpanes were also analyzed. Results are reported in $\mu\text{g/kg}$ dry weight.

4) Polychlorinated Biphenyl (PCB) and Chlorinated Pesticides

PCB and chlorinated pesticide analyses were performed at BOS. Samples were extracted simultaneously with the PAHs, as described above, and analyzed by gas chromatography/electron capture detection. Eighteen individual PCB congeners and 16 chlorinated pesticides were reported without second column confirmation in $\mu\text{g/kg}$ dry weight.

5) Total Nitrogen and Phosphorus

Nitrogen was analyzed by Huffman Laboratories, Inc. of Golden, Colorado. Analysis was performed using a Carlo-Erba 1106 combustion instrument using The American Society for Testing and Materials (ASTM) D5291 (ASTM 1992 guide). Phosphorus was analyzed at Battelle/Pacific Northwest Laboratories in Richland, Washington,

using wavelength-dispersive XRF. Both nutrients are presented as a percentage of the total dry weight.

6) Butyltins

Butyltin compounds were analyzed at the MSL using gas chromatography/flame photometric detection (GC/FPD) following the methods of Unger et al. (1986). Samples were extracted with methylene chloride and tropolone. Propyltin was added before extraction as a surrogate compound to assess extraction efficiency. The mono-, di- and tributyltin compounds extracted from the sediment were derivatized to a less volatile, more thermally stable form (nonionic *n*-pentyl derivatives). Extracts were passed through a Florisil liquid chromatography column for cleanup, and butyltins were quantified by GC/FPD. Butyltin results are presented in $\mu\text{g/kg}$ dry weight.

7) Grain Size

Sediment grain size was determined at the MSL using a combination of sieve and pipette. The grain-size intervals measured were gravel (<2 mm), sand (2 mm to 0.063 mm), silt (0.063 mm to 0.004 mm), and clay (<0.004 mm). Results are presented in percentage by weight.

8) Total Organic Carbon (TOC)

Total organic carbon was analyzed at Global Geochemistry in Canoga Park, California. Dried, ground samples were sent to the lab, where the inorganic carbon was driven off and the remaining sample was analyzed for organic carbon using a combustion method, with a Leco WR-12 induction furnace. Results are presented as a percentage of the total dry weight.

9) Sediment Dry Weight

The dry weight of each sediment section was determined by freeze-drying known amounts of sediment for a minimum of 96 h. Results are reported in percentage by weight.

C. DATA ANALYSIS

1) Sedimentation and Deposition Rates

Sedimentation (cm/yr) and deposition rates ($\text{g/cm}^2/\text{yr}$) were estimated using a steady-state ^{210}Pb dating technique (Lavelle et al. 1985, 1986; Nevissi et al. 1989). This method assumes: 1) sedimentation rate is constant, 2) loss of ^{210}Pb from sediment layers occurs only by radioactive decay, 3) mixing is confined to the surface mixed layer, and 4) intervals of sediment used for analysis have well defined depositional times that are short compared to the overall dating period.

Only data from below the surface mixed layer was used to calculate the sedimentation rate. Mixing can be a result of human activities and/or can occur naturally from bioturbation and currents. The thickness of the surface mixed layer is elucidated (albeit subjectively) by a plot of the natural log ^{210}Pb activity (dpm/g) of dry sediment versus sediment depth (cm). The depth at which the natural log ^{210}Pb activity indicates steady-state decay behavior and no longer fluctuates erratically marks the end of the mixed layer. The mixed layer within Puget Sound has been observed to vary in thickness from depths of 2 cm to 30 cm (Carpenter et al. 1984, 1985).

Excess ^{210}Pb was determined by subtracting supported ^{210}Pb , which is generally assumed to be the average concentration of ^{210}Pb measured in the lower section of the cores displaying a constant ^{210}Pb activity. However, if a core was not long enough to reach background, a value for supported ^{210}Pb associated with cores taken in close proximity from earlier studies (Bloom and Crecelius 1987; Lavelle et al. 1985) was used. Previous studies in Puget Sound sediment have reported excess ^{210}Pb activities in the surface sediment of approximately 10 dpm/g and supported ^{210}Pb ranging from 0.5 to 1 dpm/g (Bloom and Crecelius 1987; Carpenter et al. 1985; Lavelle et al. 1985, 1986).

If cores did not reach background ^{210}Pb activity, a second evaluation on the supported ^{210}Pb activity was conducted. Using the current value of supported ^{210}Pb activity (i.e., from neighboring cores that did reach background), the resulting stable Pb time series was evaluated, since this time series is well documented for Puget Sound (Romberg et al. 1984). Romberg et al. (1984) determined that the background levels (prior to 1890) of stable Pb range from approximately 4 $\mu\text{g/g}$ in sandy sediment to 7 $\mu\text{g/g}$ in mud. By 1890 (± 5 yr) stable Pb concentrations equaled two times the background concentration. This was most likely due to the Tacoma smelter, which began operating as a Pb smelter in 1890. If the resulting stable Pb time series showed increases of Pb beyond approximately 10 $\mu\text{g/g}$ before 1900, then the supported ^{210}Pb was decreased in a step-wise fashion until the resulting elemental Pb time series matched historical knowledge.

2) Trend Analysis

A trend analysis, following Bloom and Crecelius (1987), was conducted on metal, PCBs, and DDT concentrations, which displayed a potential decline after obtaining a maximum value. In order to determine the correlation between the strengthening of environmental laws with sediment contaminant loadings, the linear correlation coefficient (*r*) was used to evaluate the significance of the relationship between the concentrations of Ag, As, Cu, Hg, Pb, Sb, Zn, total PCBs, and DDT against year from 1970 to 1991 individually for Cores 3, 5, and 6. A least squares

analysis would be inappropriate since neither axis can be assumed to be known without error. A significant negative correlation (i.e., a decrease in concentration of these contaminants with increasing year) provides empirical evidence that the strengthening of environmental legislation in the past 20 years has had an influence on the water quality in Puget Sound.

3) Sediment Recovery Rates

Sediment recovery rates are defined as the rate at which contaminant loadings in the sediment are reduced. Ideally, one would be interested in the year that sediment contaminant loadings return to background conditions. However, this estimation problem requires an unrealistic assumption that recovery rates remain constant beyond the bounds of the observed data.

Recovery rates were estimated by calculating the slope between the subsurface maximum and the surface concentration for contaminants indicating a decrease (e.g., Ag, As, Cu, Hg, Pb, Sb, Zn, total PCBs, and DDT). The slope was calculated using only these two observations per contaminant to provide greater weight to the current recovery pattern. Alternatively, the least squares solution, using all of the data between the maximum and surface concentrations, could be used to estimate recovery rates. However, observations with the steepest gradient (generally deeper in the core) would have much greater influence on the slope estimate than would the data near the surface, which generally show a slowing of recovery. An average recovery rate for the region based on the combined rates estimated from Cores 3, 5, and 6, and with 95% confidence limits were calculated. Even though contaminant loadings and deposition rates are different for each site, it might be expected that the rate of recovery within the region might be consistent for any given contaminant.

IV. RESULTS AND DISCUSSION

The following is a summary of results. National Oceanic and Atmospheric Administration Technical Memorandum, NOS ORCA 111 (1997) is a full report and contains tables, figures, and appendices of data.

A. Sedimentation Rates

In this study, the mixed layers ranged from 10 cm to 40 cm in depth based on observed fluctuations in the concentrations of ^{210}Pb . Core 5, taken northeast of Vashon Island, showed the deepest mixed zone of approximately 39 cm, and Cores 1 and 6, the northern- and southernmost cores, had the smallest, at approximately 10 cm. Table 3.1 presents the location, supported ^{210}Pb , mixing depth,

sedimentation rates, porosity, and deposition rates for all six cores, assuming a seawater density of 1.0229 g/cm^3 and a salinity of 30‰ (Lavelle et al. 1985).

Initially it appeared that background was reached in Core 6, based upon a leveling of the ^{210}Pb activity, which decreased to an average $0.78 (\pm 0.07) \text{ dpm/g}$. However, the resulting time series for stable Pb was not consistent with established background concentrations (Romberg et al. 1984). A supported level of $0.4 \text{ }^{210}\text{Pb} \text{ dpm/g}$, however, did approximate the expected stable Pb time series and was used in the final calculations. A supported ^{210}Pb concentration of 1 dpm/g was sufficient for Cores 3 and 5 and a supported ^{210}Pb concentration of 0.3 dpm/g was needed for Cores 2 and 4. Activities of excess ^{210}Pb ranged from approximately 0.6 dpm/g to 12 dpm/g .

Our results indicate a sedimentation rate of approximately 1 to 2 cm/yr in the deep region of central Puget Sound, which agrees with the results found in an earlier study by Lavelle et al. (1985, 1986). The mean porosity ranged from 0.72 to 0.82, which is consistent with the mean porosities calculated by Lavelle et al. (1985, 1986), which ranged from 0.66 to 0.83. Deposition rates ranged from 480 to $1000 \text{ mg/cm}^2/\text{yr}$, with the lowest accumulation found in Core 6, which was located just north of Tacoma. These rates agree well with data from past studies within the same region and water depth of Puget Sound, where mass accumulation rates ranged from 98 to $790 \text{ mg/cm}^2/\text{yr}$ (Carpenter et al. 1985), 340 to $1400 \text{ mg/cm}^2/\text{yr}$ (Bloom and Crecelius 1987), and 260 to $1200 \text{ mg/cm}^2/\text{yr}$ (Lavelle et al. 1985, 1986).

1) Cesium-137 Dating

Activity of ^{137}Cs (dpm/g) in the sediment was measured to provide a second means of determining the age of a sediment layer. During the last 30 years, ^{137}Cs has been entering the oceans from the atmospheric testing of nuclear weapons. The major input occurred between 1957 and 1965, producing a maximum of ^{137}Cs activity in the ocean surface water in approximately 1965. Since then, the ^{137}Cs level in surface water has decreased slowly due to mixing with the deep ocean and radioactive decay (Livingston and Bowen 1979). Marine sediments in contact with seawater exchange stable Cs and ^{137}Cs ; thus, the levels of ^{137}Cs in the seawater and the sediments are related. Once these sediments are removed from interaction with seawater through burial, the ^{137}Cs activity could change. The presence of a subsurface maximum would suggest that both mixing and migration have not been intense enough to distort this feature (Romberg et al. 1984). A distinct subsurface maximum is evident in the 1960s for Cores 2, 3, and 6. Cores 4 and 5 reached a maximum in the early 1970s. Assuming that the ^{137}Cs maximum was introduced in roughly 1965, the ^{137}Cs profile compares well to the sedimentation rate determined from the ^{210}Pb data.

TABLE 3.1. Station Data and Best-Fit Model Results

Core No.	Latitude (N)/ Longitude (W)	Water Depth (m)	Core Depth (cm)	Supported ²¹⁰ Pb Activity (dpm/g)	Number of Samples ^(a)	Mixing Depth (cm)	Sedimen- tation Rate ^(b) (cm/yr)	Mean Porosity	Average Deposition Rate ^(c) (g/cm ² /yr)
1	47°47.59' N 122°25.97' W	189	100	0.5	7	9	0.90±0.37	0.725±0.020	0.65±0.05
2	47°42.09' N 122°26.58' W	203	170	0.3	15	19	1.70±0.20	0.774±0.008	1.00±0.04
3	47°36.90' N 122°26.80' W	201	188	1.0	14	19	1.88±0.14	0.803±0.006	0.94±0.04
4	47°33.41' N 122°26.26' W	238	170	0.3	9	19	1.11±0.49	0.794±0.010	0.58±0.03
5	47°28.68' N 122°24.28' W	194	170	1.0	10	39	2.01±0.47	0.819±0.009	0.90±0.06
6	47°21.00' N 122°24.59' W	178	190	0.4	9	9	1.05±0.31	0.816±0.006	0.48±0.02

^(a) Below the mixed layer and above background.^(b) Confidence limits are at the 95% level.^(c) The deposition rate is calculated using Equation 4 assuming a seawater density of 1.0229 g/cm³, and a salinity of 30‰ (Lavelle et al. 1985).

2) Ancillary Analysis

Grain size was analyzed in approximately 20 samples from Cores 3, 5 and 6. Greater than 95% of the particles from Core 3 were <0.0625 mm in diameter, with approximately 51% silt (0.0625 mm to 0.004 mm) and 45% clay (<0.004mm). Core 5 was approximately 5% sand, 46% silt, and 49% clay. Sediment from Core 6, however, contained slightly higher percentages of sand, ranging from 4% to 18%, especially in the upper half of the core. The average percentages of silt and clay for Core 6, the southernmost station, were 42% and 49%, respectively. Overall, the ranges of sand, silt, and clay content did not vary greatly with depth. This supports the assumption of a constant sedimentation rate in the ^{210}Pb -dating model.

Total solids were measured in all intervals from all cores. Percentage total solids ranged from approximately 30% to 45% and increased slightly with depth in all cores. Total organic carbon was measured from equally spaced intervals from Cores 3, 5, and 6; it ranged from 1.37% to 2.26%, reported as a percentage of TOC on a dry weight basis. In general, a decrease in TOC can be correlated with an increase in percent sand; thus, TOC was measured to confirm changes in sediment type. The range of TOC for these cores suggests that no natural or other disturbances that would affect sediment type occurred within the 200-year time frame encompassed by the cores.

C. Nutrients

Nutrients (percentage of P and percentage of total N) were measured from equally spaced 2-cm intervals from Cores 3, 5, and 6. There was a general increase in concentration of nutrients over time. The concentration of P ranged from 0.09% at the surface to 0.06% in the deepest sections of the cores and increased an average of 0.0002% ($\pm 7 \times 10^{-5}$) per year, whereas that of N ranged from 0.26% at the surface to 0.16% at the bottom of Core 6, and increased an average of 0.0005% (± 0.0001) per year. The increases in both nutrients are statistically significant ($\alpha = 0.05$). The slight increase in total N is probably a result of increased sewage entering the system. In closed systems, peaks in a core profile indicate over-nutrication, which can often be associated with a point-source, such as a sewage outfall. However, in the nutrient rich waters of the Pacific Ocean and Puget Sound, these measurements may be too coarse to determine anthropogenic influences. Specific nitrogen compounds (e.g., nitrites) might provide more information associated with anthropogenic sources of contamination.

D. Metals Concentrations and Trends

Ten metals were analyzed by XRF in all cores. An additional six metals, for a total of 16, were analyzed at equally spaced intervals from Cores 3, 5, and 6. The level

of many of these metals has decreased steadily since the study by Bloom and Crecelius (1987).

The profile of Pb concentration versus year is similar for all cores. In general, each profile depicts a steep rise in Pb concentration to a series of peaks spanning from 1920 to 1960 and then declining from 1960 to the present. The maximum value of Pb was $69.4 (\pm 0.276) \mu\text{g/g}$ obtained in approximately 1922 from Core 6. Cores 3, 5, and 6 produced an average 38% drop from the maximum to the surface concentration (Table 3.3). The concentration of Pb in the central basin of Puget Sound was determined to be significantly ($\alpha = 0.05$) decreasing by $0.57 (\pm 0.31) \mu\text{g/g}$ per year. Significant ($\alpha = 0.05$) negative correlations between year and concentration for sediments deposited after 1970 lends support for the effectiveness of current environmental regulation.

Concentrations of the crustal elements, Al, Fe, and Si, were at background levels in all cores and showed little or no change in concentration with depth. These profiles are consistent with the assumption that sediment mineralogy (a mixture of feldspars, quartz, and clay minerals) in the deep basin of Puget Sound has not changed in the recent past as a result of either natural or human causes. The profiles of Mn show a slight to a nearly twofold increase in concentration in the upper intervals of the core. We suggest that this is due to reducing conditions at depth and post-depositional migration (Riley and Chester 1976) rather than to anthropogenic influences. The extent to which elements are mobilized prior to migration is dependent on the redox potential, pH, and organic content of the sediment. Iron has been predicted to be slightly more stable than Mn (Riley and Chester 1976). With one possible exception (Core 6), the profile for Fe does not indicate that post-depositional migration is occurring, even though the profiles for TOC for Cores 3, 5 and 6 are nearly identical. This result is consistent with the findings of other studies (Carpenter 1985; Romberg et al. 1984).

Concentrations of a number of other metals analyzed (Ni, Cd, Cr, and Se) did not show any consistent changes in concentrations with depth; instead, they showed erratic fluctuations throughout the core. Concentrations in the top five surficial sediment intervals of Cr, Ni, and Se were not significantly different from the sediment concentrations found in the five deepest sections of the cores, based on a t-test with $\alpha = 0.05$. Cadmium was found to be significantly different ($\alpha = 0.05$). However, in Core 3, Cd increased with time, and in Cores 5 and 6 a general decrease was observed. In all three cores, Cd fluctuated continuously; therefore, any observed relationship is probably spurious. Temporal trends for some metals showed a reproducible pattern of increasing concentrations to a maximum, then of decreasing concentrations through the present. This trend has been detailed in a number of other studies from sediment cores taken from Puget Sound (Bloom and Crecelius 1987; Romberg et al. 1984). Metal showing this

trend are Pb, Ag, As, Cu, Hg, Sb, Sn and Zn. Bloom and Crecelius (1987) tested the apparent trend of decreasing metal concentrations of Pb, Ag, Cu, and Hg in Puget Sound sediment deposited between 1955 and 1982 for a significant negative correlation. The trends established in 1987 indicated mean concentrations of Pb, Ag, and Hg decreased significantly ($\alpha = 0.05$), approximately 7% to 17% since the 1960s. No statistically significant decreases in Cu concentrations were observed (Bloom and Crecelius 1987).

Arsenic concentrations reached a maximum concentration of $28 (\pm 0.68) \mu\text{g/g}$ between the early 1950s and 1960s. The highest levels of As were found in Cores 5 and 6, the southernmost cores and closest to the ASARCO smelter, which operated in Tacoma from approximately 1889 to the 1980s. Crecelius et al. (1975) suggest that the ASARCO smelter was a major source of As to Puget Sound sediments. Antimony concentrations, a byproduct of smelter operations at ASARCO, followed a similar pattern, reaching a maximum concentration of between 2 and $4 \mu\text{g/g}$ between the 1950s and 1960s. Both metals have shown a greater than 25% decrease from the maximum to the surface concentration in all cores (Table 3.2). Only Sb, however, had a significant ($\alpha = 0.05$) recovery rate of $0.039 (\pm 0.035) \mu\text{g/g}$ per year. Antimony also produced a consistent significant ($\alpha = 0.05$) negative correlation between year and concentration in sediments deposited after 1970. In contrast, concentrations of As in deposited sediments have remained fairly constant over this time period.

Mercury reached a maximum concentration of $0.5 (\pm 0.01) \mu\text{g/g}$ in the late 1940s. An average 50% drop from the maximum to the surface concentration was observed in Cores 3, 5, and 6 (Table 3.2) with a significant ($\alpha = 0.05$) average sediment recovery of $0.006 (\pm 0.005) \mu\text{g/g}$ per year. However, the concentrations of Hg over the last 20 years remained fairly constant and did not produce a statistically significant negative correlation.

Silver, Cu, and Zn all appear to have reached maximum concentrations in the early 1960s followed by decreasing concentrations in the late 1960s. Silver reached a maximum of $0.91 (\pm 0.004) \mu\text{g/g}$ in mid-1960; however, it displayed an average drop of only 17% from the maximum to the surface concentration (Table 3.2). Except in Core 3, there was no statistically significant negative correlation between year and concentration for Ag in sediments deposited after 1970. Copper and Zn, however, had maximum values of $70 (\pm 0.34)$ and $167.7 (\pm 1.26) \mu\text{g/g}$ respectively, dropped an average of 23% and 18%, and had significant ($\alpha = 0.05$) negative correlations between year and concentration. Only Cu produced a significant ($\alpha = 0.05$) sediment recovery rate of $0.437 (\pm 0.076) \mu\text{g/g}$ per year.

Tin may have reached a maximum concentration in the 1960s; however, concentrations have not steadily declined since wide fluctuations in concentration are still evident in surficial sediments. Despite the wide fluctuations, all three

cores displayed an average 24.2% drop from the subsurface maximum to the surface concentration and produced a significant ($\alpha = 0.05$) regional recovery rate of $0.041 (\pm 0.025) \mu\text{g/g}$ per year (Table 3.2).

Except for Ag and Hg reductions in Core 3, the largest percentage of reductions was observed in Core 5, which is located near several sewage treatment plant outfalls. Secondary treatment of sewage discharged into the Sound did not begin until the late 1950s. Therefore, the initiation of primary treatment and changes to industrial practices must account for the decrease in metals observed at the site.

E. Organic Concentrations and Trends

Organic compounds were analyzed in equally spaced intervals from Cores 3, 5 and 6. Analytes of interest were PAHs, PCB congeners, and chlorinated pesticides. Consistent with the Puget Sound Protocols (Tetra Tech, Inc. 1986), total PAHs consist of the sum of 16 anthropogenically derived PAH compounds. The PAHs that are primarily derived from combustion processes, such as the burning of automobile fuels, coal, and wood, are defined as combustible PAHs; they have four, five, and six rings. In addition, linear alkylbenzenes (LABs), indicators of municipal waste, and biomarkers hopane and total terpanes, hydrocarbons associated with petroleum products, were analyzed.

1) PAHs

Total PAH concentrations ranged from approximately $100 (\pm 21.6) \mu\text{g/kg}$ in the deepest sections of the cores to a maximum of up to $6788 \mu\text{g/kg}$ in the early 1940s, and then declined to an average of $1300 \mu\text{g/kg}$ in the surface sediments. An average 59% decrease in concentration of total PAHs was observed between the maximum and surface concentrations (Table 3.3); however, a statistically significant negative correlation between year and concentration was not obtained for sediments deposited after 1970 for any of the cores. The sediment recovery for total PAHs was estimated as $56.5 (\pm 106) \mu\text{g/kg}$ per year, which was not significant. The sedimentary history of these hydrocarbons appears to parallel the initial urbanization of the Seattle/Tacoma area, which coincides with an increased use of fossil fuels. Sources of PAHs to the Puget Sound are postulated to be primarily sewage and atmospheric dustfall (Barrick 1982).

2) Combustible PAHs

Combustible PAHs are the higher molecular weight PAH compounds, consisting of the four-, five-, and six-benzenering compounds. These compounds are produced

by the as wood. The concentrations of combustible PAHs generally parallel the total PAH concentrations in the sediment cores. An average 60% reduction in concentration between the maximum and surface concentrations was observed; however, sediments deposited after 1970 did not produce a significant negative correlation between year and concentration. Average sediment recovery estimated at 49.6 (± 95) $\mu\text{g/kg}$ per year was not significant.

Prior to 1900, the relative contribution of combustible PAHs to total PAHs averaged about 50%. As the use of fossil fuels increased, this ratio also increased to a maximum of approximately 85% in the 1940s, which corresponds to the increased number of households in the Seattle/Tacoma area using coal as their heat source. Since the 1920s, this ratio has remained approximately 80%. The near-surface proportions of combustible PAHs does not appear to be decreasing in Cores 5 and 6, and shows only a slight decrease in Core 3.

The maximum concentrations of both total and combustible PAHs occurred in sediments deposited between 1930 and 1950. These patterns were observed in cores collected in 1981, as part of a study on the distribution of toxicants in Puget Sound (Romberg et al. 1984). Comparison of PAH levels measured from cores in the same vicinity as the 1981 study reveal similar concentrations in both surface and subsurface sediments. This would be expected, based on the assumption that the source of these elements to Puget Sound during the last century has been consistent over the entire region.

3. Linear Alkyl Benzenes

LABs are used in the production of linear alkyl sulfonates (LAS), which are widely used anionic surfactants in detergents. These products became commercially available in the early 1960s and their use rapidly became widespread. The source of LABs to the environment is exclusively anthropogenic, primarily from municipal sewage. A dramatic increase in concentrations occurred in the early 1980s in all cores to a maximum of 184 $\mu\text{g/kg}$, which corresponds to the rapid increase in population in the Seattle/Tacoma region. The actual concentrations vary among the different coring locations and may be due to differences in the volumes of effluent discharged near each site. In general, concentrations do not appear to be decreasing in surficial sediments, and there is no negative correlation between year and concentration for sediments deposited after 1970. The average sediment recovery rate for LABs was 11.4 (± 34.3) $\mu\text{g/kg}$ per year and was not statistically significant. Core 5 showed an 84% decrease in LABs between the maximum and surficial concentrations. Although this result may be spurious, this core also had the greatest decreases in metals, which we hypothesize to be due to changes in sewage treatment. Regionally,

however, a decreasing trend in LAB concentrations is not evident, which suggests that sources of these compounds are still being actively discharged.

4) Biomarkers: Hopane and Total Terpanes

Biomarkers such as hopane and total terpanes are biomolecules that are naturally derived from organic compounds and are found in petroleum materials, such as oils and coals. These compounds are resistant to both physical and biological degradation, and can be used to characterize petroleum contamination. The distribution of these biomarkers within oil deposits (i.e., oil fields and oiled sediments) can be used to distinguish among possible sources of oil or to evaluate weathering (or degradation) of the deposit.

In Cores 5 and 6, the concentrations of both hopane and the total terpanes show little variation with depth after 1920, averaging approximately 200 and 2000 $\mu\text{g/kg}$, respectively. Core 3, in contrast, displayed a 30% reduction between the maximum and surficial concentrations of both biomarkers (Table 3.3), and there were significant ($\alpha = 0.05$) negative correlations between year and concentration for sediments deposited after 1970. Neither biomarker, however, produced a statistically significant average recovery rate.

5) Polychlorinated Biphenyls (PCB) and Dichlorodiphenyltrichloroethane (DDT)

Temporal trends in the contamination of central Puget Sound with synthetic organic chemicals, such as PCB and DDT, are similar to those of metals and hydrocarbons, except these chemicals did not appear until about the 1930s. Since these compounds are anthropogenic in origin, no background levels occurred in sediments prior to their introduction in the mid- 1930s (values less than 5 $\mu\text{g/kg}$ should be regarded as analytical noise). A rapid increase in concentrations occurred until the mid-1970s when environmental regulations, such as the Toxic Substance Control Act (enacted 1976), limited their use and greatly reduced the amount of PCBs getting into the environment. Maximum concentrations observed in the sediments during this period reached over 35 (± 0.523) $\mu\text{g/kg}$. Concentrations found in the surface sediments of the cores average about 8 $\mu\text{g/kg}$. Even though an average 68% reduction between the maximum and surface concentrations of PCBs was observed (Table 3.3), only Core 3 had a significant ($\alpha = 0.05$) negative correlation between years and concentration for sediments deposited after 1970. The average sediment recovery rate estimated as 0.649 (± 0.653) $\mu\text{g/kg}$ per year was not statistically significant.

DDT concentrations for Cores 3 and 6 showed a depositional pattern similar to that of PCBs, increasing in

TABLE 3.2. Maximum and Surface Concentrations (µg/g) of Selected Metals for Three Cores Collected from Puget Sound During Summer 1991

	<u>Ag</u>	<u>As</u>	<u>Cu</u>	<u>Hg</u>	<u>Pb</u>	<u>Sb</u>	<u>Sn</u>	<u>Zn</u>
Core 3:								
Max Year	1965	1965	1960	1949	1965	1960	1965	1965
Max	0.91	19.5	54.6	0.479	48.9	2.05	4.9	134.6
Surface	0.68	12.5	42.7	0.179	30.3	1.28	3.94	114.7
% change	25.3%	35.9%	21.8%	62.6%	38.0%	37.6%	19.6%	14.8%
Recovery Rate	0.009	0.280	0.397	0.007	0.744	0.026	0.038	0.796
Core 5:								
Max Year	1982	1964	1947	1947	1922	1952	1962	1962
Max	0.84	28.3	70	0.505	69.4	3.9	4.85	167.7
Surface	0.69	13.1	49.3	0.213	36.7	1.6	3.96	119.2
%change	17.9%	53.7%	29.6%	57.8%	47.1%	59.0%	18.4%	28.9%
Recovery Rate	0.017	0.563	0.470	0.007	0.474	0.059	0.031	1.672
Core 6:								
Max Year	1965	1950	1963	1950	1954	1963	1963	1954
Max	0.65	23.5	64.7	0.403	62.3	2.43	4.25	128.8
Surface	0.59	17.3	52.7	0.277	44.7	1.52	2.78	115.5
%change	9.2%	26.4%	18.5%	31.3%	28.3%	37.4%	34.6%	10.3%
Recovery Rate	0.002	0.155	0.444	0.003	0.489	0.034	0.054	0.369
Average Recovery Rate µg/g/y	0.009	0.333	0.437	0.006	0.569	0.039	0.041	0.946
95% CL ±	0.014	0.424	0.076	0.005	0.308	0.035	0.025	1.348

TABLE 3.3. Maximum and Surface Concentrations (µg/kg) of Selected Organic Compounds for Three Cores Collected from Puget Sound During Summer 1991

	<u>PCB</u>	<u>DDT</u>	<u>Total PAH</u>	<u>Combustible PAH</u>	<u>LABS</u>	<u>Terpanes</u>	<u>Hopane</u>
Core 3:							
Max Year	1960	1960	1943	1943	1983	1943	1953
Max	34.5	4.71	6788	5917	101	2260	235
Surface	9.00	1.19	1434	1162	80.7	1570	158
% Change	73.9%	74.8%	78.9%	80.4%	19.8%	30.5%	32.8%
Recovery Rate	0.851	0.117	114	101	2.85	14.7	2.09
Core 5:							
Max Year	1966	1984	1942	1942	1986	1990	1962
Max	25.8	5.76	3430	2898	184	2360	227
Surface	5.33	4.77	1303	1050	29.3	2360	224
% Change	79.3%	17.2%	62.0%	63.8%	84.0%	0.0%	1.1%
Recovery Rate	0.819	0.142	43.412	37.706	30.878	0.000	0.087
Core 6:							
Max Year	1961	1961	1935	1935	1977	1923	1965
Max	15.5	4.25	1883	1516	69.4	2290	203
Surface	7.39	2.80	1212	977	63.9	1860	183
% Change	52.2%	34.2%	35.6%	35.5%	7.9%	18.8%	9.5%
Recovery Rate	0.278	0.050	12.198	9.793	0.421	6.418	0.768
Average Recovery Rate µg/kg/y							
	0.649	0.103	56.5	49.6	11.4	7.03	0.980
95% CL ±							
	0.653	0.096	106	95	34.3	14.9	2.061

the 1930s and producing a maximum in the 1960s. Core 5, however, reached its maximum concentration in the 1980s. Over all, concentrations of DDT are low and do not vary dramatically in relation to the analytical error. Maximum levels of DDT reached $5.7 (\pm 1.0) \mu\text{g/kg}$ compared to undetected at 1 g/kg of in the early 1920s. Regulations have resulted in decreasing use of this pesticide and current surficial sediment concentrations vary, ranging from 1 to $2.8 \mu\text{g/kg}$. Despite a 42% reduction between the maximum and surface concentrations of DDT (Table 3.3), only in Core 3 was there a potentially significant ($\alpha = 0.05$) negative correlation between year and concentration for sediments deposited after 1970. DDT, however, did show a potentially significant ($\alpha = 0.05$) average recovery rate of $0.103 (\pm 0.096) \mu\text{g/kg}$ per year. The words "potentially significant" were used in association with the DDT results because the analytical error was large in relation to the observed concentrations. These data should be used only to suggest a possible trend.

6) Trends in Organic Contaminants

Overall trends show subsurface maxima and a steady decrease in concentrations to the present for all organic constituents except LABs, hopane, and total terpanes. Unlike the metals, which showed the greatest decreases in contaminant concentrations in Core 5, organic contaminants showed the greatest declines in Core 3, taken west of Elliott Bay. Surface total PAH concentrations of approximately $1400 \mu\text{g/kg}$ represent a two-fold decrease over the maximum concentrations observed earlier this century. Decreases in total PAH ranged from 36% to 79% for the three cores, but concentrations from sediments deposited after 1970 did not suggest that the strengthening of environmental laws in the past 20 years had much of an influence on this decline. Decreases in other organic contaminants, such as PCBs and DDT, also decreased significantly, but not within the last 20 years. Total PCB concentrations decreased on the average of 68% from the early 1960s to present. DDT concentrations decreased an average of 42%.

F. Butyltins

Four sediment core samples (two from the upper 10 cm top, one from the middle of the core, and one from near the bottom of the core), from Cores 3, 5, and 6 were analyzed for butyltins. All observations were less than detection ($1 \mu\text{g/kg}$) and were not considered productive for a profile analysis. Thus, no further analyses were conducted.

V. CONCLUSIONS

The temporal trends in central Puget Sound described

in this report were based on the chemical composition of age-dated sediment cores. The sedimentation rates used to estimate the dates of the various sediment fractions ranged from 1 to 2 cm/yr . This range is consistent with sedimentation rates obtained from similar locations in other studies (Bloom and Crecelius 1987; Carpenter et al. 1985; Lavelle et al. 1985, 1986).

Trace metal contamination (Ag, As, Cu, Hg, Pb, Sb, Sn, and Zn) began in the late 1800s, reached a maximum in the mid-1900s, and began to decrease in the last two decades. Average recovery rates, estimated from the slope between the maximum and surface concentrations, were observed for Cu, Hg, Pb, Sb, and Sn. Recovery rates for Ag, As, and Zn were too variable to be declared significantly different from zero. However, all three showed a trend toward recovery. Concentrations of Cu, Pb, Sb, and Zn declined at a significant rate in the last 20 years, lending support to our hypothesis that the strengthening of environmental regulation since 1970 has influenced the water quality of Puget Sound.

Trends in organic chemicals in the sediments over time also show a subsurface maximum. Hydrocarbon contamination appears to parallel that of heavy metals. Only DDT, however, showed a statistically significant average recovery rate. The recovery rates for PCB, total PAH, and combustible PAH were too variable to be called significant, but these contaminants did show a trend toward recovery. PAH concentrations, although decreased over four-fold from maximum concentrations, appear to be relatively constant over the past several decades. Synthetic organic contaminants appear in sediments deposited more recently, in the mid-1930s and 1940s, and reached a maximum in the mid-1960s. Statistically significant decreases in sediment concentrations of these contaminants were also observed with two- to four-fold decreases in surficial sediment concentrations. Concentrations of compounds such as PCBs and DDT appear to be continuing to decrease.

Nutrients (P and N), LABs, and biomarkers (hopane and total terpanes) were the only contaminants not showing a clear decrease in concentration. The nutrients show an extremely slight, but statistically significant, increase. The concentrations of LABs and biomarkers fluctuate in the near-surface sediments so that a plateau cannot be substantiated. Nutrients and LABs are associated with municipal sewage. Hopane and total terpanes are associated with petroleum products. Both sources of contaminants are expected to increase with an increasing population. However, despite the population growth of over one million people in the Seattle/Tacoma region in the past several decades, there has not been a substantial increase in these contaminants. Thus, the effect of strengthening environmental regulations on water quality cannot be negated.

VI. REFERENCES

- Arbuckle J. G., M. L. Miller, F. W. Brownell, K. J. Nardi, D. R. Case, A. P. Olney, W. T. Halbleib, D. G. Sarvadi, L. J. Jensen, J. W. Spensley, S. W. Landfair, D. M. Steinway, R. T. Lee, and T. F. P. Sullivan. 1993. *Environmental Law Handbook*. 12th ed., Government Institutes, Inc., Rockville, Maryland, 550 pp.
- ASTM (American Society for Testing and Materials). 1992. *Standard Test Methods for Instrumental Determination of Carbon, Hydrogen, and Nitrogen in Petroleum Products and Lubricants*. ASTM Designation D5291-92. American Society for Testing and Materials, Philadelphia, Pennsylvania.
- Barrick, R. C. 1982. "Flux of Aliphatic and Polycyclic Aromatic Hydrocarbons to Central Puget Sound from Seattle (West Point) Primary Sewage Effluent." *Environmental Science and Technology*. 16:682-692.
- Bloom, N. S. 1983. "Determination of Silver in Marine Sediments by Zeeman-Corrected Graphite Furnace Atomic Absorption Spectroscopy." *At. Spectrosc.* 4:204-208.
- Bloom, N. S., and E. A. Crecelius. 1983. "Determination of Mercury in Seawater at Sub-Nanogram per Liter Levels." *Marine Chemistry*. 144:49-59.
- Bloom, N. S., and E. A. Crecelius. 1987. "Distribution of Silver, Mercury, Lead, Copper and Cadmium in Central Puget Sound Sediments." *Marine Chemistry*. 21:377-390.
- Carpenter, R., M. L. Peterson, J. T. Bennett, and B. L. K. Somayajulu. 1984. "Mixing and Cycling of Uranium, Thorium and ^{210}Pb in Puget Sound Sediments." *Geochimica et Cosmochimica Acta*. 48:1949-1963.
- Carpenter, R., M. L. Peterson, and J. T. Bennett. 1985. " ^{210}Pb -Derived Sediment Accumulation and Mixing Rates for the Greater Puget Sound Region." *Marine Geology*. 64:291-312.
- Crecelius, E. A., M. Bothner, and R. Carpenter. 1975. "Geochemistries of Arsenic, Antimony, Mercury, and Related Elements in Sediments of Puget Sound." *Environmental Science and Technology*. 9:325-333.
- Koide, M. K., E. Bruland, and E. D. Goldberg. 1973. "Th-228/Th-232 and Pb-210 Geochronologies in Marine and Lake Sediments." *Geochimica et Cosmochimica Acta*. 37:1171-1183.
- Lauenstein, G. G. and A. Y. Cantillo. 1993. *Sampling and Analytical Methods of the National Status and Trends Program National Benthic Surveillance and Mussel Watch Projects 1984-1992*, Volumes I - IV, NOAA Technical Memorandum NOS ORCA 71, Silver Spring, Maryland.
- Lavelle, J. W., G. J. Massoth, and E. A. Crecelius. 1985. *Sedimentation Rates in Puget Sound from ^{210}Pb Measurements*. NOAA Technical Memorandum ERL PMEL-61. Prepared by Pacific Marine Environmental Laboratory, Seattle, Washington, for National Oceanic and Atmospheric Administration, Environmental Laboratories, Seattle, Washington.
- Lavelle, J. W., G. J. Massoth, and E. A. Crecelius. 1986. "Accumulation Rates of Recent Sediments in Puget Sound, Washington." *Marine Geology*. 72:59-70.
- Livingston, H. D., and V. T. Bowen. 1979. "Pu and ^{137}Cs in Coastal Sediments." *Earth and Planetary Science Letters* 43:29-45.
- MacGinitie, G. E., and N. MacGinitie. 1949. *Natural History of Marine Animals*. McGraw-Hill Book Company, Inc., 473 pp.
- National Oceanic and Atmospheric Administration (NOAA). 1997. *Historical Trends in the Accumulation of Chemicals in Puget Sound*. NOAA Technical Memorandum NOS ORCA 111. Silver Spring, Maryland.
- Nevissi, A. E., G. J. Shott, and E. A. Crecelius. 1989. "Comparison of Two Gravity Coring Devices for Sedimentation Rate Measurement by ^{210}Pb Dating Techniques." *Hydrobiologia*. 179:261-269.
- Riley, J. P., and R. Chester. 1976. *Chemical Oceanography*. Vol. 5. Academic Press, London, England.
- Romberg, G. P., S. P. Pavlou, R. F. Shokes, W. Hom, E. A. Crecelius, P. Hamilton, J. T. Gunn, R. D. Muench, and J. Vinelli. 1984. *Toxicant Pretreatment Planning Study Technical Report C1: Presence, Distribution and Fate of Toxicants in Puget Sound and Lake Washington*. Metro Toxicant Program Report No. 6A, Water Quality Division. Prepared for Municipality of Metropolitan Seattle (Metro), Seattle, Washington.
- Tetra Tech, Inc. 1986. *Recommended Protocols For Measuring Selected Environmental Variables in Puget Sound*. TC-3991-04. Prepared for Puget Sound Estuary Program by Tetra Tech, Inc., Bellevue, Washington.

Unger M. A., W. G. MacIntyre, J. Greaves, and R. J. Huggett. 1986. "GC Determination of Butyltins in Natural Waters by Flame Photometric Detection of Hexyl Derivatives with Mass Spectrometric Confirmation." *Chemosphere*. 15:461-470.

Wennekens, P. M. 1959. *Marine Environment and Macro - Benthos of the Waters of Puget Sound, San Juan Archipelago, Southern Georgia Strait, and Strait of Juan*

OCEANOGRAPHIC DATALINK

K.A. Gamache & P.E. Fogel
ViaSat, Inc.
Acton, Ma. 01720

Abstract

There has always been interest in the impact of the ocean on the global environment, but the devastating effects of recent El Nino and La Nina events have increased global efforts to understand this relationship. As a result, there have been significant advances in sensors and systems to monitor the ocean environment over the last few years. These sensors and systems are becoming increasingly complex. AOSN (autonomous ocean sampling network) is a good example, with a network of cooperating autonomous underwater vehicles sampling a volume rather than a single plane of the ocean. In addition, these sensors and systems are being placed in increasingly remote regions of our world's oceans.

This combination of increased complexity and increasingly remote operation limits the options for data telemetry. Systems such as INMARSAT, MSAT/AMSC, and GOES are either too costly, provide only limited ocean coverage, or support limited throughput. ARGOS provides the necessary coverage, but it is one-way with very limited throughput. It is considered in many cases to be the primary bottleneck in today's oceanographic systems and is inadequate to support the next generation of sensors and systems. Therefore, without significant advances in oceanographic telemetry, it will not be possible to take advantage of the benefits of these new sensors and systems.

Help is on the horizon. There is considerable excitement and interest in new and planned satellite systems, especially low earth orbit (LEO) systems. Systems such as Iridium and Orbcomm appear to be the best thing since sliced bread. However, this paper discusses the disadvantages of these systems for oceanographic applications and describes an alternative based on existing geosynchronous satellites, the Oceanographic DataLink (ODL).

ODL is based on existing geosynchronous satellites and is not dependent on the financial success of a

complex network of satellites. It provides the lowest cost, lowest risk solution for remote environmental data collection required for the next generation of sensors and systems. This paper describes the system, the underlying technology, and possible applications including moored and drifting buoys and long endurance autonomous underwater vehicle applications it compares this system to current and planned systems and describes its benefits for global environmental data collection.

What is ODL?

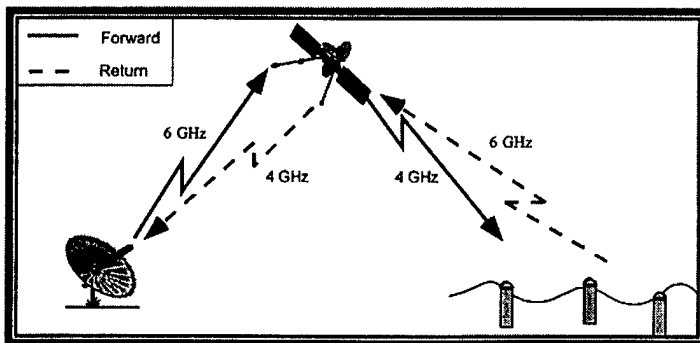
The Oceanographic Data Link (ODL) is a datalink capable of providing worldwide¹ telemetry for a wide variety of applications. It is unique because it takes advantage of existing C-band geosynchronous satellites.

ODL is a hub and spoke architecture with remote terminals communicating with a central hub using existing INTELSAT satellites. Specifically, for oceanographic applications, ODL uses global beam transponders on these satellites. Each of these transponders covers 41% of the earth's surface allowing coverage of all of the world's oceans with as few as three satellites.

ODL consists of a two-way link, a forward link (hub to terminal) and return link (terminal to hub). This two-way capability will support dynamic experimentation as well as monitoring and control of remote sensor systems.

ODL is small. Using C-band patch antenna technology, antennas as small as a quarter are possible resulting in remote terminals no larger than a VCR tape.

ODL is designed to be battery operated. It takes advantage of advanced digital signal processing, M-ary modulation, state-of-the-art coding, and interleaving



¹ Nonpolar, 75° N to 75° S.

to provide throughput 10 to 100 times ARGOS at an energy cost at least an order of magnitude less. However, with an effective rate 10 to 100 times ARGOS, depending on the application, ODL can dissipate more power to support these increased rates. So, with ODL there is a tradeoff between performance and power. Yet, in all but the most stringent applications, ODL is competitive with ARGOS and supports a number of applications not currently possible.

These features are attractive; however, cost is what makes this system truly unique. Cost consists of two components, equipment costs and service fees.

Service fees quickly outweigh equipment cost in overall cost of these systems and ODL provides the lowest services fees of any planned system.

Service fees are a function of recurring and fixed costs amortized over the life cycle of the product. This system is based on existing satellites and requires as few as three hubs to provide global coverage. Therefore, the capital cost required to develop and maintain it is an order of magnitude smaller than planned systems, resulting in services fees that are a small fraction of the costs expected for these new systems.

Why ODL?

The Office of Naval Research (ONR) for oceanographic applications is developing ODL. C-band geosynchronous satellites were not ONR's first choice for this next generation oceanographic datalink. It expressed interest in the use of the planned Low Earth Orbit (LEO) systems, specifically Iridium for this datalink.

The Navy understood the limitations of ARGOS and GOES, the cost, power, and size constraints of INMARSAT C and saw these next generation LEOs as the potential solution for their

oceanographic needs. ViaSat, with considerable knowledge of satellite systems and no predisposition for any particular solution, evaluated current and planned systems objectively. The result of this analysis indicate that using existing C-band geosynchronous satellites provides the lowest cost, lowest risk solution for a wide variety of applications, including oceanographic applications.

This analysis was conducted several years ago.

However, ViaSat continues to monitor existing, new, and planned systems and believes even more strongly in the use of existing C band systems for oceanographic applications. An update of this analysis is presented here.

	Coverage	Capacity	Cost Use/Equip	Energy Cost
LEOs				
ARGOS	Global		Low/Low	Low
"Little" LEOs ¹	Global	Medium		Low
"Big" LEOs ²	Global	High		Low
GEOs				
GOES	Coastal		Low/Med	
L-band ³	Coastal	Medium	Med?/Med?	Med?
C-band (ODL)		Medium	Low/Low	
Ku-band ⁴	Coastal	Medium		Med

1. OrbComin used as an example.

2. Iridium used as an example.

3. MSAT, AMSC, ACES, and INMARSAT 3 are examples.

4. OmniTracs used as an example.

Traditional Systems

Traditionally, the oceanographic community has relied on ARGOS, and to some extent GOES, to support its telemetry needs. ARGOS is a low earth orbit (LEO) system (500-900 mi. orbit) that provides a global, one way, store-and-forward capability. Its limited throughput (roughly 1 Kbyte/day) has frustrated oceanographers for a long time. However, its wide coverage, low cost (equipment and usage fees), and low power have made it the system of choice for remote telemetry needs².

GOES is a government sponsored geosynchronous (~23,000 mi. orbit) satellite system. It, too, is one-way with limited capacity (~20 Kbytes/day). In addition, its coverage is limited to the continental United States and the immediate coast. The usage price is right if you

² Not all applications require a satellite link. Applications where line-of-sight is possible can use wireless systems that provide two way capability at rates considerably higher than satellite systems. Though, their range is very limited (5 to 10 miles).

are a government agency (free), but its limited coverage, limited capacity, and large, power hungry equipment has restricted its use to remote land based environmental monitoring and large off shore buoys (NDBC).

A third system rarely mentioned for oceanographic applications is INMARSAT C. INMARSAT was developed for maritime applications, but specifically for boats. It uses L-band geosynchronous satellites and provides a global, two-way store-and-forward capability. Equipment size, cost, and power are considerably more than ARGOS, but the main limitation to the use of INMARSAT for oceanographic applications is the usage fees. At $\sim 1\text{¢}/\text{bit}$, the cost to use INMARSAT C isn't too restrictive at low data rates (roughly the same yearly cost as ARGOS (\$4k/PTT) at 1 Kbyte/day), but at higher rates the cost becomes prohibitive, i.e., at 100 Kbytes/day it would cost \$400K/year! As a result, INMARSAT's utility for environmental oceanographic applications is questionable even given a two way, higher throughput capability.

Recent Developments - Recently, AMSC/MSAT, INMARSAT³, and ACeS launched new mobile satellite services using next generation L-band geosynchronous satellites. These satellites take advantage of spatial reuse (spot beams) to provide additional capacity in the crowded L-band frequency spectrum resulting in lower service fees than past systems.

This technology also supports smaller, lower power terminals for both voice and data applications. However, these systems provide limited ocean coverage (coastal) and focus primarily on voice services. There are, to date, no small, low cost, low power terminals for data applications. As a result, such systems can not be seriously considered for widespread oceanographic use.

ARGOS is limited. Are the LEOs the answer for oceanographic telemetry?

In addition to these geosynchronous systems, Iridium and Orbcomm have launched LEO systems aimed at voice and data services respectively. A number of other similar systems have been proposed and are under development. These systems can be characterized as "little" LEOs, "big" LEOs⁴ and broadband LEOs. The focus of this paper will be on the "little" and "big" LEOs since the broadband LEOs are designed for fixed site, very large bandwidth applications. Iridium is a "big" LEO, Orbcomm is a "little" LEO.

These systems, and others like them⁵, promise to provide global connectivity using small, low cost, low power handsets and terminals. Therefore, ever since Iridium announced its plans in 1990, oceanographers have been wondering whether this system, or something like it, was the telemetry "silver bullet."

The answer is unclear. For certain applications, LEOs might make sense, however, there are a number of disadvantages that need to be considered. These can be summarized as coverage, capacity, and cost.

Many of these systems provide limited coverage of ocean areas, only Orbcomm⁶ and Iridium provide truly global coverage.

Capacity is a major issue for oceanographic applications since LEO systems are not designed to handle the typical quantities of data. Many are fooled by the instantaneous data rates supported by these systems. These rates range from 2400 to 4800 bps and beyond. However, this has no correlation with throughput. The throughput is considerably less.

⁴ Originally satellite size determined if a system was "big" or "little", but this distinction has become blurred and the difference can be best described by system operating frequency. "Big" LEOs operate at L-band, "little" LEOs at VHF/UHF.

⁵ Other "little" LEOs include Final Analysis and LeoOne. Other "big" LEOs include GlobalStar and ICO.

⁶ 48 satellite constellation, current 36 satellite constellation has significant coverage gaps. LeoOne has minimal coverage gaps and does not include the poles.

³ AMSC/MSAT covers North America, INMARSAT the rest of the world.

As an example, based on Orbcomm's figures for gateway downlink capacity, the 15 gateway system under development today supports a worldwide aggregate capacity of roughly 210 Kbps! Therefore, if there were 20,000 active daily users, each would average ~100Kbytes/day or 100 times what ARGOS can do today. Not bad, but significantly less than 4800 bps one might assume. However, Orbcomm needs several million users to break even and as the number of active users increases, individual throughput decreases (200,000 active daily users equates to 10K bytes/day).

This isn't a problem for most applications supported by Orbcomm. Their system is designed around short, intermittent data applications⁷ such as asset tracking, electric utility meter reading, etc. But, for oceanographic applications where tens or hundreds of kilobytes or more per day are necessary, such an application could bring this system to its knees.

LEOs are attractive, but service cost is a real concern.

Iridium and the other "big" LEOs may have more capacity, but at what cost?? These systems cost an order of magnitude more than the "little" LEO systems, and the "little" LEO systems aren't cheap. Therefore, even if all the "big" and "little" LEOs provided global coverage and they all had unlimited capacity, the cost of these systems would result in unacceptable service fees for most oceanographic applications.

A large number of satellites are required at low earth orbit to provide global coverage. As an example, Iridium requires 66 satellites with several in-orbit spares. Orbcomm is a 48 satellite constellation when fully configured. Such a large number of satellites results in high system capital costs.

The type of service to be offered also has a big influence on the cost of the system. "Big" LEOs such as Iridium were designed for voice and data. These systems require large, complex satellites and ground stations resulting in system costs of

several billions of dollars!⁸ "Little" LEOs support short, random data messaging. These satellites and ground stations are less complex, but still result in system costs of several hundred million dollars!⁹

So, can these systems attract enough users to justify attractive service fees? Many of these systems are still in the development stage. Only Iridium and Orbcomm can be analyzed to date.

Iridium has failed to attract subscribers. But, it is unclear whether this is due to the high service fees (\$7/min) or the lack of a market? Consensus in the financial community is, it is a little of both. There is concern amongst analysts that predictions of a 42 million subscriber market was very optimistic. And, there is consensus that Iridium's pricing was too high, especially considering the proposed rates for the other "big" LEO competitors.

Iridium's future is uncertain. It is currently in the process of restructuring its bank debt and there is talk of bankruptcy. There is some discussion about expanding its markets towards data applications. However, without considerable debt relief, given Iridium's high cost, it is doubtful it could ever compete with "little" LEOs for data telemetry applications.

Orbcomm has been more successful. It had 60,000 units on order or installed by the end of the first quarter (March 31, 1999) and expected 200,000 by year's end¹⁰. Its equipment costs (\$150-\$995) and service fees vary depending on application, but it needs quite a subscriber base to keep service fees attractive.

Orbcomm is offering its services for oceanographic applications at 1¢/byte and \$30/month. 1¢/byte equates to roughly \$4K per year¹¹ at 1 Kbyte per day, but \$40K and \$400K per year at 10 and 100 Kbytes per day respectively.

⁸ Iridium costs are estimated between 5 and 7 billion dollars.

⁹ Orbcomm costs roughly \$500M.

¹⁰ Only 10% of the 60,000 units are currently revenue bearing. By year's end, 50% of the 200,000 are expected to be revenue bearing.

¹¹ Typical daily ARGOS throughput.

⁷ Orbcomm can only support 180 simultaneous users worldwide.

This is similar to the cost of INMARSAT C. This high cost has been one of the key reasons INMARSAT C hasn't been used more widely in the oceanographic community. In addition, there is the monthly service fee as long as the Orbcomm transceiver is registered, regardless of usage.

Is Orbcomm a better solution than what exists today for oceanographic applications? It is two way and equipment is smaller, lower power, and lower cost than INMARSAT C. Orbcomm is global and does provide increased throughput over ARGOS, but at a corresponding increase in service fees. Therefore, for most applications service fees are still too high to support any significant increase in throughput.

Cost is a constant concern with these LEO systems. However, ViaSat believes there is an alternative.

An Alternative - ViaSat believes a system based on existing C-band geosynchronous satellites

can support oceanographic and a wide variety of other global data applications. More importantly, with costs an order of magnitude less than the current and planned LEO systems, service fees a small fraction of these systems are possible. In addition, this system would not be dependent on the technical and financial success of a complex network of satellites, greatly reducing the risk of developing such a system.

C-band satellites were chosen for a number of reasons including; capacity, coverage, and cost. Existing C-band satellites do not have the spectrum limitations of the LEO systems. A single C-band geosynchronous satellite has 500 MHz of spectrum to provide its services and using simple reuse techniques supports an effective capacity of roughly 3 GHz!! This is more effective capacity than the entire Iridium network. In addition, a single satellite provides coverage of 41% of the globe! Therefore, as few as 3 satellites could provide global coverage.

The cost of this system, like the LEO systems, is based on capital cost. However, in this case,

the satellites already exist and recurring cost to use these satellites is a small fraction of the total yearly cost. Recurring costs are low because these satellites have long life spans and considerable capacity. Therefore, the cost of these systems can be amortized over a number of years and a wide variety of users¹². As a result lease costs are quite inexpensive and fixed costs are limited to ground facilities. This cost is estimated to be tens of millions of dollars for ODL versus several hundred million for the planned "little" LEO systems.

Given these differences in cost, and a market size similar to LEO systems, ViaSat estimates service fees for ODL to be a small fraction of those being charged by Orbcomm, ARGOS, and proposed by the other "little" LEOs. Much like Orbcomm, the service fee will vary depending on the application and will consist of either a cost/bit,

a flat rate, or a combination of both. Assuming a cost/bit charge for oceanographic

Is there a better alternative than LEOs for oceanographic applications?

applications, then a cost of 10¢/kbyte or less is expected. This results in a yearly cost of roughly \$4K assuming 100kbytes/day.

Status - ViaSat is under contract with the Air Force and the Navy (ONR) to develop and demonstrate this datalink technology. The Air Force effort, Global Location and Tracking System (GLTS), is aimed at demonstrating this technology for global asset tagging and tracking. A demonstration is planned for spring of 2000. This demonstration will verify the ability to track a vehicle using a prototype tag the size of three VCR tapes.

The Navy effort, ODL, focuses on demonstrating this datalink technology for oceanographic applications. Specifically, the datalink will be demonstrated on a solar powered Autonomous Underwater Vehicle (SAUV) and a conventional AUV. The goal of this effort is to confirm that the

¹² These satellites provide video services, high speed telephone circuits and occasional data services all on a single satellite.

datalink can be used to monitor and control oceanographic equipment using a satellite.

Two demonstrations are planned. The first in November, will integrate the datalink into the Autonomous Undersea System Institute¹³ (AUSI) SAUV. This demonstration will verify the feasibility of using the datalink for long endurance AUV missions. The intent is to transmit data collected during the evening while the AUV is on the surface during the day recharging.

The second demonstration will be held in the spring of 2000. This demonstration will integrate the datalink into the MIT Odyssey AUV. This will verify satellite control and monitoring of the Odyssey AUV when it is on the surface. This effort is being conducted in concert with Woods Hole Oceanographic Institute (WHOI)¹⁴ at their facility in Woods Hole, Massachusetts.

The AUV datalink is interesting because it uses a directional C-band patch antenna that is positioned towards the satellite by the AUV. The AUV steers towards the equator to position the antenna for communication with the satellite. These are broadbeam antennas so positioning accuracy isn't a big issue.

The focal point of the ODL effort is AUVs, however testing will include over-the-air testing in the lab and on a buoy at WHOI as part of the system test and integration. As a result, upon completion of the test and demonstration the datalink will have been evaluated on land, and at sea in a variety of applications.

ViaSat is in system test and integration of the prototype datalink. There were a number of challenges, but ViaSat has identified and addressed each of these challenges. The main issues were power, size, and equipment cost. These were conflicting requirements because as size was decreased, antenna size was reduced. As a result, power had to be increased to support the same data rate. Yet, increased power meant

increased cost and decreased battery life. So, there was a delicate balance necessary when designing to these requirements. In the past,

geosynchronous systems were not considered for low power applications

because too much power was required to support communication with the satellite. These applications typically used an omni-directional antenna with very low gain (0-3dB). This, coupled with the free space loss to a C-band geosynchronous satellite (~200 dB), suggested too much power for battery operated applications.

However, ODL is unique. Unlike the LEO systems¹⁵, ODL uses "dumb" satellites. As a result, all processing is done on the ground and ViaSat is able to take advantage of the latest signal processing technology to reduce transmitted power. In addition, ViaSat is using advanced antenna technology to provide remote terminal antenna gain through the use of small C-band patch antennas. And finally, ViaSat takes advantage of the gain provided by the hub antenna to support communication with the satellite at an energy cost/bit that is at least an order of magnitude lower than ARGOS!

The ability to transfer data over any wireless link is a function of the received signal and noise. The higher the ratio of signal to noise, the more robust a given datalink will be. Typically, datalinks are characterized by the bit error rate (BER). The type of modulation and coding determines the signal to noise ratio necessary to achieve a given BER. ViaSat chose a power efficient modulation for this effort. Such modulations require a lower signal to noise ratio allowing robust communication at low power levels. ViaSat chose an M-ary FSK modulation¹⁶.

The required signal to noise ratio can be further reduced through coding. Coding

ODL is the lowest cost, lowest risk solution for most oceanographic applications.

¹³ AUSI is a partner in a NICOP sponsored effort to demonstrate this datalink on the SAUV.

¹⁴ WHOI is subcontractor to ViaSat on the ONR ODL effort.

¹⁵ LEO systems are based on processing satellites with technology that is several years old and upgrades are very limited over the life span of the satellites (5-8 yrs).

¹⁶ M-ary FSK modulation sends a frequency tone for every M transmitted symbols.

provides redundancy, allowing recovery of the transmitted signal with errors. Initially, ViaSat chose standard Viterbi encoding and decoding, supporting communication with the satellite at 5W or less. Recently, a major break-through in coding technology has been reported. Turbo Codes claim to provide significant improvement in required signal to noise. Depending on the modulation and required BER, this improvement can be 3 dB or greater. 3 dB improvement results in a factor of 2 reduction in transmit power given the same transmitted data rate.

Turbo Codes are so named because they feed back the output of standard decoders to provide incremental improvement through iterative decoding. I.e., they pass the same information through the decoders a number of times to improve error performance. It requires a complex interleaving and multiplexing of this feedback data to achieve the improved performance. As a result, developing a practical implementation of this new technology has been a challenge. Several software models of these decoders have been implemented and demonstrated, but a practical hardware solution is still to be developed.

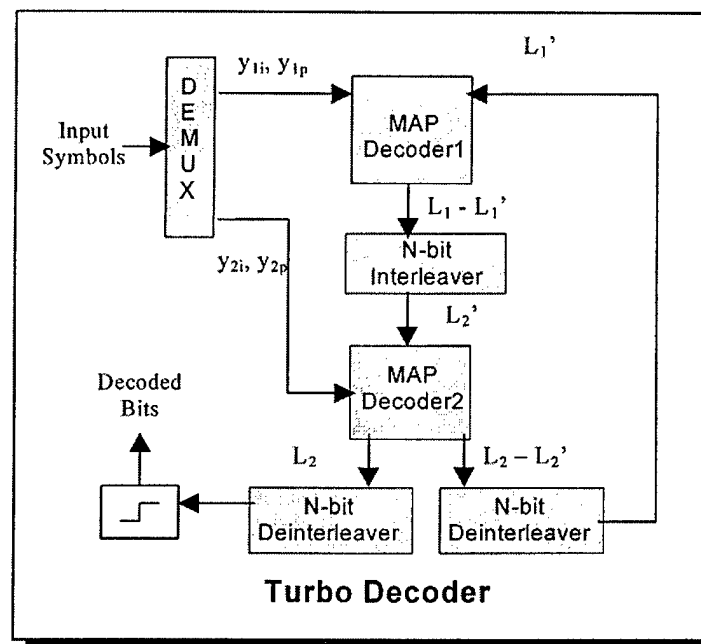
ODL can take advantage of this technology because ODL is a software-based design. This design supports throughputs 10 to several thousand times ARGOS in a variety of configurations and applications. Modulation, demodulation, acquisition, coding and decoding are all preformed in software on a Texas Instrument (TI) Digital Signal Processor. This approach was possible due to recent advances in processing performance of these DSPs.

Another advantage of the software implementation is the reduction in power over a hardware implementation. Additional processing

is necessary only at the decoder for Turbo Codes and only on the return link¹⁷. This requires more processing, and therefore, more power. Unlike the remote terminal, power isn't an issue at the hub. Therefore, implementing a Turbo Code

decoder at the hub to support the return link is possible. ViaSat has chosen to implement the Turbo Codes on the next generation TI DSPs, the TMS5000 series of DSPs.

The addition of Turbo Codes to the return link is expected to provide a 3dB improvement allowing communication with the satellite at 2.5W or less. This transmit power is also made possible through the



transmit and receive antenna gains of the return link. At the remote terminal ViaSat has developed small, low cost C-band patch antennas that provide 6-dB omni-directional type coverage to 17 dB asymmetric antennas for more directional applications.

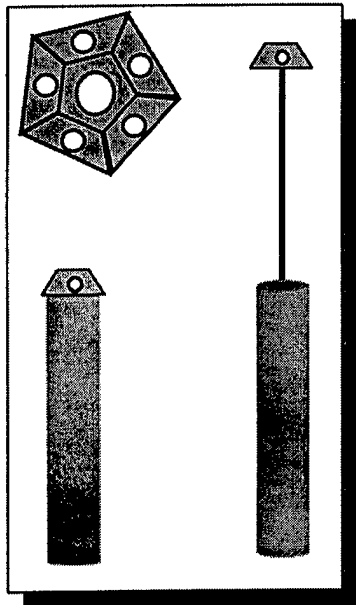
These antennas consist of individual elements no large than a quarter. For the 6-dB application, 5 of these antennas are arranged in a pentagon no larger than the diameter of a RAFOS buoy. This arrangement, along with a indication of heading, allows the remote terminal to use the appropriate antenna to communicate with the satellite in any direction.

The more directional antennas consist of a passive array of these elements arranged to provide symmetric or asymmetric beam patterns. These antennas can be used for fixed site oceanographic applications, in AUVs with surface positioning capability, or on moored buoys with simple, single axis positioners. These antennas can

¹⁷ The advantages on the forward link are much subtler and do not outweigh the additional power required at the remote terminal to implement Turbo Codes on the forward link.

either support increased throughput at equivalent transmit power, or support similar throughput with significantly less power. The energy cost/bit remains the same. These antennas will be used for the AUV demonstrations in November and in the spring of 2000.

The hub receive antenna gain is another key component in the return link design. The ODL is a hub and spoke architecture. All data from remote terminals is received at the hub. Using a large hub antenna, it is possible to receive very small signals from remote terminals. The production hub is a 13m antenna¹⁸. This is typical of hub antennas for other low



power applications and these antennas are produced by a number of vendors. Such an antenna provides a receive gain of 53 dB. This receive antenna gain in concert with the remote terminal transmit gain and the state-of-the-art coding supports communication from remote terminals transmitting at 2.5W from anywhere on the globe.

Size was another concern in developing ODL. Antenna size was the first issue. There was no market for small C-band antennas, so none existed. ViaSat, working with Seavey Engineering Associates developed a number of small prototype C-band patch antennas. Single element antennas were developed for an asset tracking demonstration and more directional (14 and 17 dB) antennas were developed for several oceanographic demonstrations. The single element antennas are roughly the size of a Susan B. Anthony dollar and the directional flat plate

antennas are roughly 2/3 the size of a sheet of paper.

Next, there was concern about the size of the Radio Frequency (RF) electronics. ODL is essentially a radio and includes a C-band transceiver. Again, no market existed for such equipment and initial transceivers were big and expensive. However, there have been great strides in this technology in the past five years. This equipment, including a 5W power amplifier and the modem can be housed in a package roughly the size of three VCR tapes stacked on top of one another. A 2.5W design will decrease this size considerably and the goal of the production design is a package the size of a VCR tape.

Equipment cost was the last major concern. The remote terminal consists of a C-band transceiver, a modem, a GPS receiver, antennas, batteries, and packaging. The cost of the transceiver easily outweighs the cost of all the other items combined.

The current transceiver design consists of five components and in small quantities this equipment costs close to \$6000. However, the production design is a single unit and cost estimates for production quantities is a small fraction of this cost.

There is precedent for such cost reductions at C-band. As an example, consider C-band Low Noise Block (LNB) converters. The converters include a Low Noise Amplifier (LNA) and an L-band downconverter. These are made in very large quantities for backyard satellite television applications. For this design, a LNA is necessary, but not the L-band downconverter. The LNB goes for roughly \$80 in small quantities while the LNA by itself costs \$2000 in small quantities! Given similar cost reductions, ViaSat believes that remote terminals priced between \$500 and \$1000 will be possible, depending on the application.

Who Would Use ODL?

The Oceanographic Data Link (ODL) is designed to support applications similar to those being considered for the "little" LEO systems. Given the coverage, capacity, and cost of this system as compared with LEOs, significant market share should

¹⁸ The demonstration hub antenna is 4.5m supporting 1/2 the data rate using hemispheric beams on an INTELSAT VIII series satellite.

be possible even given the late entry into the market.¹⁹

The size of the market is uncertain. Independent analysis indicates an addressable market of 50 to 150 million users in several different market segments. These include asset monitoring (i.e., oil and gas pipeline monitoring), shipping asset tracking and monitoring (i.e., trucks, truck trailers, rail cars, shipping containers, etc.), utility monitoring (i.e., remote electric utility meter reading), and oceanographic applications.

The ODL datalink technology provides the lowest risk, lowest cost approach for each of these applications and in addition, provides the broad coverage necessary to support coastal and deep ocean oceanographic applications. It is unclear what level of market penetration is possible with ODL technology, but even 2% of the 50 million addressable market results in 1 million subscribers.

Application	Market	Comment
Oceanography	20K	Environmental
Marine Data/FAX	20K	INMARSAT C apps
Fixed Data	10-15M	Environmental SCADA – 15K exist Utilities – 10-15M
Asset Tracking & Recovery	20-30M	Newer Autos – 15-20M Trucks – 100K Rail/Shipping – 5-10M

Summary

This paper describes a global oceanographic telemetry system that provides the lowest cost, lowest risk solution for remote oceanographic data applications. It is based on existing geosynchronous satellites and is not dependent on the technical and financial success of a complex network of satellites. As a result, capital costs are greatly reduced and service fees an order of magnitude lower than planned low earth orbit (LEO) systems are possible. In addition, this system provides two way communication and supports throughput 10 to 100 times ARGOS.

Equipment cost between \$500-\$1000 is

expected in a package about the size of a VCR tape. Service fees of 10¢/kbyte are planned for oceanographic applications with energy cost per bit at least an order of magnitude lower than ARGOS.

This paper also describes a market of between 50 and 150 million users for oceanographic and related applications. This is important because the oceanographic market is small. Yet, ViaSat's datalink technology can be used in a wide variety of remote data applications, greatly reducing the cost of this system for all users.

Finally, this paper discusses the various state-of-the-art techniques used in this datalink design. However, there are other potential improvements that could reduce power required to communicate with the satellite even further. Transmit power on the order of 1W, or less, may be possible and ViaSat is evaluating this technology for potential incorporation into the production design.

ODL is a unique alternative to existing and planned satellite systems. No other system can provide the coverage and throughput at such low cost. ODL is under development with demonstrations planned in November and next spring (2000). Production development will follow with initial units expected in late 2001.

¹⁹ Production units expected late calendar year 2001.

Performance Analysis of the Real-Time Motion Compensation System Controlling a Directional Antenna Aboard the OceanNet Buoy

Michael O. Mathewson, Seatex Incorporated
Wes Covell, Harris Corporation

Michael Mathewson
Seatex Incorporated
911 Western Avenue, Suite 302, Seattle, WA 98101
Tel: +1 206 903 8393
Fax: +1 206 903 8394
michaelo@seatexinc.com

Abstract:

A recent experiment demonstrating the capabilities of the OceanNet buoy, a self-contained instrument platform with high-bandwidth satellite data communications, was conducted in the Bahamas. The buoy communicates in real-time via Intelsat at 1 Mb/sec using a specially designed directional antenna from Harris Corporation and an antenna controller from Mantra Marconi Ltd. The motion and heading of the buoy is measured by a Seatex Seapath 200 and sent to the controller in order to orient the antenna for maximum data transmission.

By analyzing the data throughput with respect to the motion of the buoy, we are able to evaluate the effectiveness of the antenna controller system in varied sea-states. Since the motion of a buoy platform of this size is of general interest, we will also discuss and evaluate the nature of the buoy movement as reported by the motion measurement system.

Michael O. Mathewson
1111 Third Avenue
Suite 2500
Seattle, WA 98101

michaelo@seatexinc.com
Tel: +1 206 583 8358
Fax: +1 206 583 8356
<http://www.seatex.no/>

BI-DIRECTIONAL COMMUNICATION INTO THE DEEP OCEAN BASED ON ORBCOMM

SATELLITE TRANSMISSION AND ACOUSTIC UNDERWATER COMMUNICATION

G. Meinecke, V. Ratmeyer and G. Wefer

Dept. of Geosciences, University of Bremen, Klagenfurter Str.,
28359 Bremen, Fed. Rep. Germany

Abstract

In the end of 1997 the DOMEST projects started. The aim of this project was the development of a moored sensor network in the deep ocean near the Canary Islands. With the implementation of an bi-directional satellite link and underwater acoustic modems, a data-link from land into the deep sea should be established on a daily base.

With DOMEST, a remotely controlled measurement of element and particle transport in the deep sea will be possible. Remote control includes access on a variety of data without recovering sensors from the deep ocean. Data access will be possible at any time via Internet and satellite communication. Sampling intervals can be changed interactively from land, status data from the instruments can be checked and it is possible to download the data subsequently. These possibilities allows an advanced sampling and probing of parameters depending on various environmental parameters, such as satellite derived ocean colour or particle input during dust storms.

Communication underwater is based on 4 independent acoustic modem clients, combined with different sensors. Bi-directional data transmission between these modems is possible up to 2.400 baud. Each sensor package and acoustic modem is controlled by an integrated digital controller, responsible for hand-shaking and data-management. At the sea surface, a permanent surface buoy is moored in 3.600 m water depth. Above water, the OrbComm based satellite network will establish the data transport between the moored systems and the land based ground station in Italy. At the ground station, messages are routed via SMTP into the Internet.

During a scientific cruise of RV METEOR in May 1999, the first close-loop test - with data request from ship via satellite into the deep sea and back via satellite to the ship - have been performed successfully, within less than 8 minutes. The final configuration of the complete DOMEST mooring will be deployed at 3.600 m water depth over a maximum duration of one year. New sensors will provide high-resolution data on particle fluxes and element concentrations in the deep ocean.

1. Introduction

For the pending problems of our world climate it is a need to give necessarily predictions about a possible climatic development. Our climate is however a combination from many, itself mutually influencing factors. The ocean as large reservoir for organic carbon and carbon dioxide is one of the most important factors in the atmospheric system. Planktonic organisms live in the uppermost parts of the water column, building up their organic tissues and carbonate shells with carbon, which is dissolved in the surrounding waters. Amounts of this carbon derives from carbon dioxide of the overlying atmosphere which is in equilibrium with the surface water. Enhanced biological productivity in surface water will utilize more carbon from the surrounding water - thus the water is in the state of undersaturation. This effect leads to an enhanced carbon dioxide transport from the atmosphere into the surface water of the ocean, a process generally called the "biological pump". For this reason it is necessary to determine the transport fluxes of particles and chemical components in the ocean on a high temporal resolution base.

Standard instruments for this monitoring are Sediment traps, still in use since more than 20 years, taking particle samples or multipump systems for chemical component sampling. In recent time also still cameras or digital video cameras are used for monitoring the particle fluxes in the ocean. In most cases, these devices are operating autonomously, i.e. they are programmed on the ship and deployed in the ocean afterwards. Despite the pre-checking onboard the ships, failures occur. Still, sometimes the devices did not work in the way they should or the environmental situation would have made a remote control necessary. Establishing a direct data link to the deployed devices is not possible in most cases, because the mooring ends approx. 500 m below the oceans surface.

For this reason, there is a substantial demand for bi-directional data communication with the deployed devices. With an innovative technology like this, the user would be able to check the correct operation of the devices and to get data from the deployed instruments. On the other hand,

the user could change the current configuration without recovering the instruments.

This was the initial idea for the project DOMEST, which deals with "Data communication in the ocean and measuring techniques for high-resolution material transport into the deep sea". The project DOMEST is national funded by the Minister for Research and Technology (BMBF, Germany). The SME technology companies OHB Teledata and OHB System (Bremen, Germany) are cooperating partners in this project. They are responsible for the interface development and for the operation of data communication as well.

II. Basic programme

A combination of new methods and innovative technologies should enhance the knowledge of particulate material transport mechanisms from surface waters into the deep sea. The most innovative technology is the implementation of a bi-directional data communication system based on a combination of acoustic underwater modems and the OrbComm satellite telemetry. With this design, data from the moored instruments can be transmitted through the water column by acoustic communication and from the water surface via satellite into the research institutes - and vice versa. In order to fit into this link, the devices moored in the ocean were modified with respect to a serial standard interface (RS 232). In combination with the integrated digital controller, each acoustic underwater modem can be addressed separately. At the water surface the acoustic signals are converted and transferred via OrbComm satellites to the groundstation Lario (Italy). From here the messages are routed via Internet to the institutes - or vice versa. As relay station at the water surface, a surface buoy was deployed in October 1998 north of Gran Canaria (Canary Island) in 3.600 m water depth.

III. System description

The complete system consist of three units (Fig. 1) - the *Surface Buoy Unit* (SBU), the *Moored Sensor Unit* (MSU) and the *Deep Ocean Unit* (DOU). Each unit consist of one or two communication system - the digital controller (BC1) and the acoustic underwater modem (ORCA).

A. Digital Controller (BC1)

For controlling the data exchange between the underwater clients, the digital controller do not have to be really fast. For this reason, the standard BC1 based on an 80c652 CPU with 8bit technology and the ability of code-

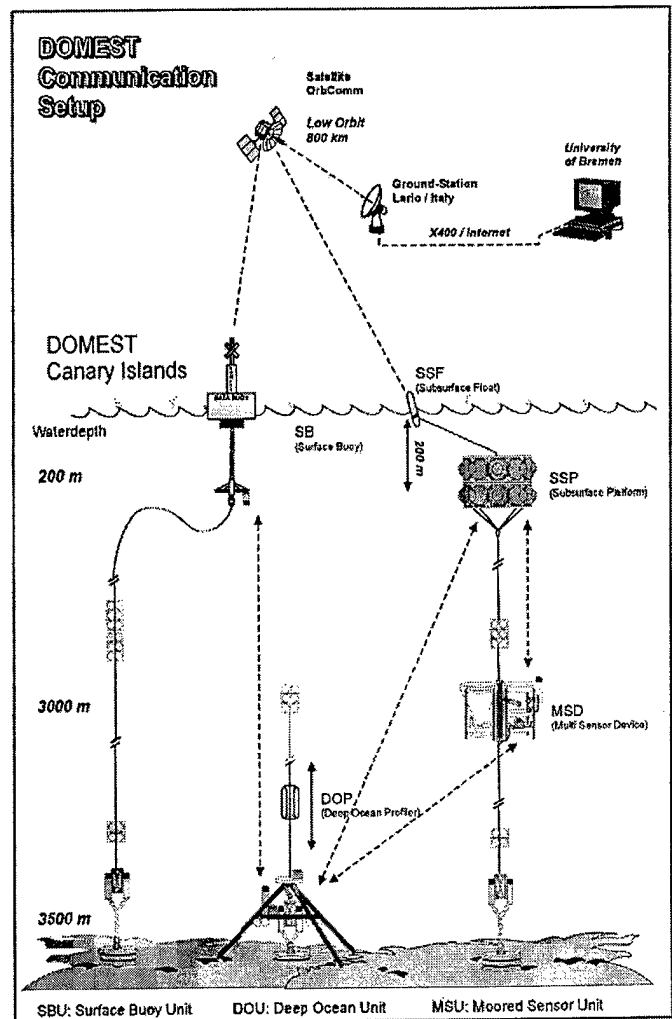


Fig. 1: System setup and communication lines of the DOMEST mooring, located near the Canary Island "Gran Canaria". Dotted lines showing the underwater acoustic and atmospheric satellite transmission pathways.

banking. The BC1 provide 512 kb ROM and 1 mb of Static RAM. In addition to this, 512 kb of EEPROM is available. The controller offers 5 COM-Ports, 4 of these are used as User-Interface and one COM port still is used for communication (GSM, OrbComm, Modacom, X-25). The digital controller is equipped with hardware Watchdog, RTC, Alarm functions, Powersave-Mode (with 0 mAmp external Power) and the ability of software downloading. The BC1 is able to run with a power supply from 12 to 24 Volts DC under temperature conditions from -40° to +80° Celsius.

B. The acoustic underwater modem (ORCA)

Based on its experience in high baud rate transmission, the French company ORCA instrumentation has developed

the MATS (Multimodulation acoustic telemetry system), a two way acoustic telemetry system (i.e. acoustic modem). According to each encountered acoustic environment, the MATS allows the digital controller BC1 to optimize its data link by choosing the adequate modulation (CHIRP, FSK, PSK 2 / PSK 4) and baud rate (between 20 and 2.400 bit/s). The DSP based modem has a frequency band from 10 - 14 kHz and separate Transducer-Heads. An error correction is possible by using the VITERBI coding. All modems have been modified to Standard RS 232 ComPorts and still uses external power supply of 24 Volts DC.

C. Surface Buoy Unit (SBU)

In order to establish the data link from the atmosphere into the ocean as fast as possible, the SBU mooring was placed 0.5 nm beneath the MSU mooring. The surface buoy operates as a relay station for the coupling of acoustic underwater link and satellite based atmospheric link. Technology installed on the buoy includes acoustic underwater modem, on-board digital controller (BC1), OrbComm satellite telemetry, and a small weather station (Fig. 2). In addition, a low range pocket radio link is installed for remote

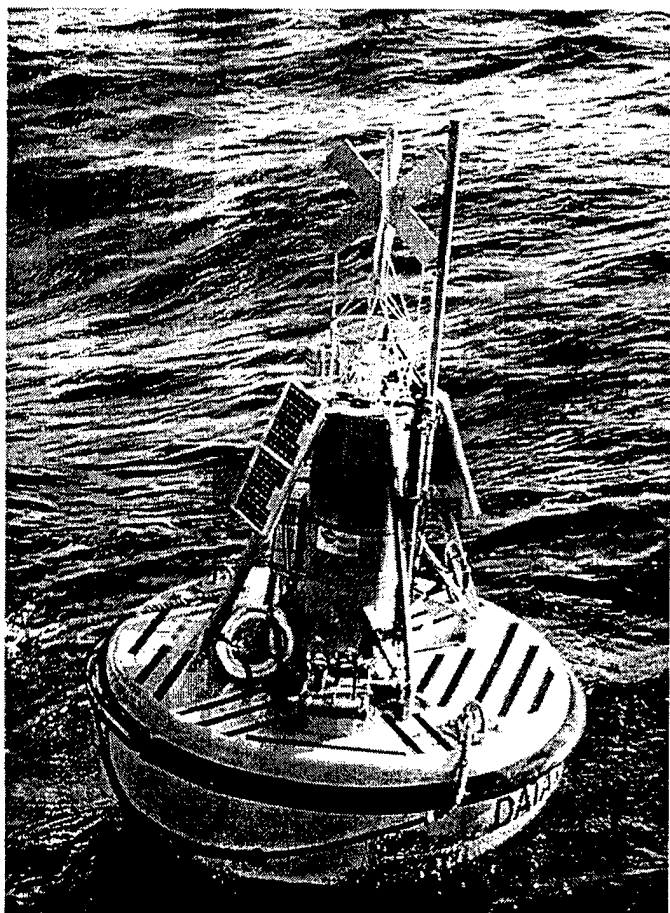


Fig. 2: Surface buoy (SB) equipped with OrbComm telemetry and acoustic modem.

control of the buoy's electronics. Acoustic data from the deep-sea units were received by the separate buoy transducer head, attached 30 m below the buoy. On board the buoy, the signals were converted inside the BC1 and passed on over the OrbComm satellite telemetry to Italy. On the other hand, feedback messages can be send via satellite from Italy to the buoy, where they are converted to an acoustic data stream which is being transmitted into the deep sea by passing several acoustic modems.

D. The Moored Sensor Unit (MSU)

The Moored Sensor Unit (MSU) is the central mooring in the Domest project. This mooring consist of two major components, the *Sub Surface Platform* (SSP) at the top of the mooring line (Fig. 3), 200 m below the surface and the *Moored Sensor Device* (MSD) in 2.500 m waterdepth. In addition to the digital controller, acoustic modem and batteries, a small underwater winch is installed on the sub surface platform, also. With assistance of this underwater winch, a small profiler can be ascended to the surface and drawn in again. The profiler itself is equipped with the same communication unit as the surface buoy. It is planned to run all the communication through this small profiler and to replace the buoy unit at the end of the project. All devices are connected to the digital controller which itself is connected to the acoustic modem of the SSP.

The multi-sensor device MSD is an integrated sensor package (Fig. 4), consisting of a new designed sediment trap with enhanced sample capacities, an acoustic currentmeter with CTD and backscatter sensors, a multi-

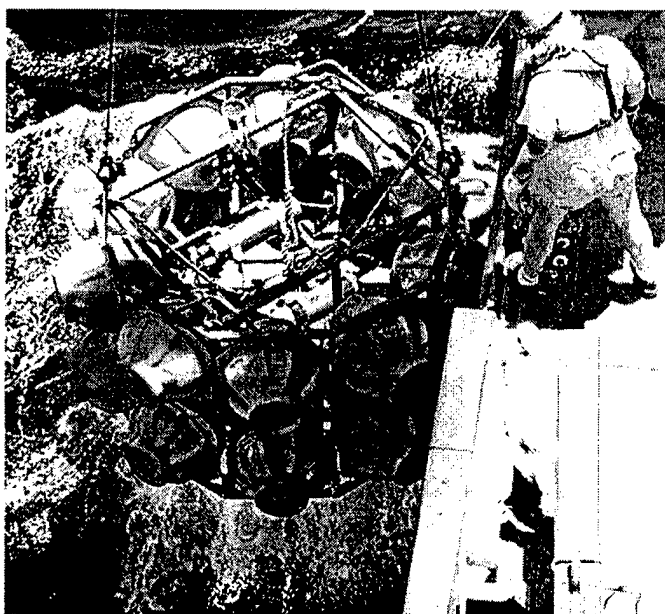


Fig. 3: Subsurface Platform (SSP) equipped with acoustic modem, digital Controller and batteries.

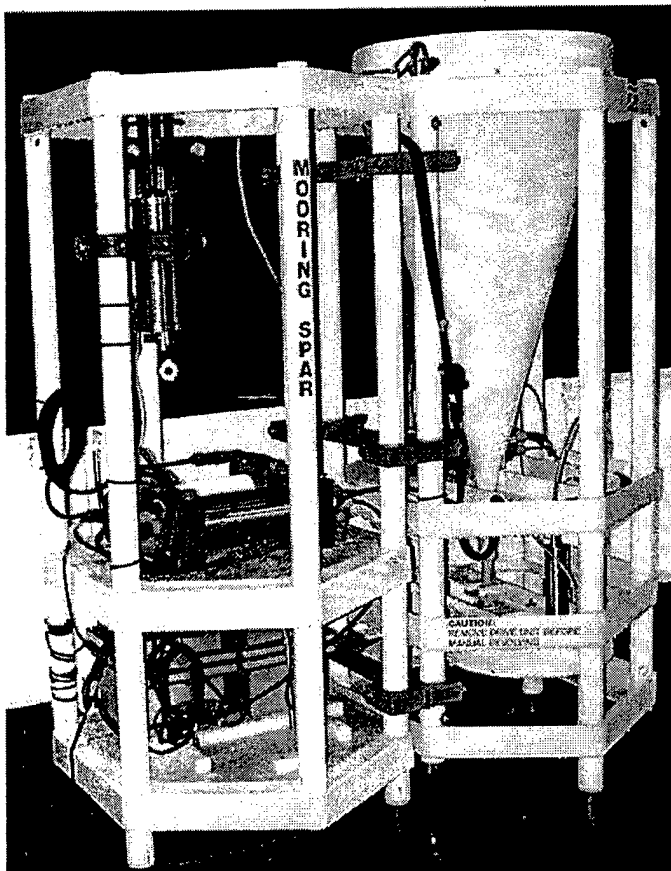


Fig. 4: The coupled frames of the Multi-Sensor-Device MSD. Integrated system of Sedimenttrap, currentmeter with CTD, acoustic modem and digital controller.

pump system for the measurement of chemical components and a digital video camera system in combination with an image processing software. The aim of the image processing software is to analyse separate digital frames in order to reduce the image information to ASCII data strings and to minimize the data rate. Again, all devices are connected to the digital controller which itself is connected to the acoustic modem of the MSD.

E. The Deep Ocean Unit (DOU)

The Deep Ocean Unit (DOU) is a bottom station in 3.600 m waterdepth, approximately 0.5 nm apart from the MSU mooring. Down here, the same batteries, video camera and image processing system are installed. Additionally, an upward looking bluewater ADCP is integrated. For data access, these devices are connected via the digital controller to the acoustic modem of the DOU. Mounted at the bottom station, the platform itself is the basic frame for the *Deep Ocean Profiler* (DOP, Fig. 5), a profiling deep-sea YoYo system. This buoyancy driven autonomous profiling carrier system ascends and descends

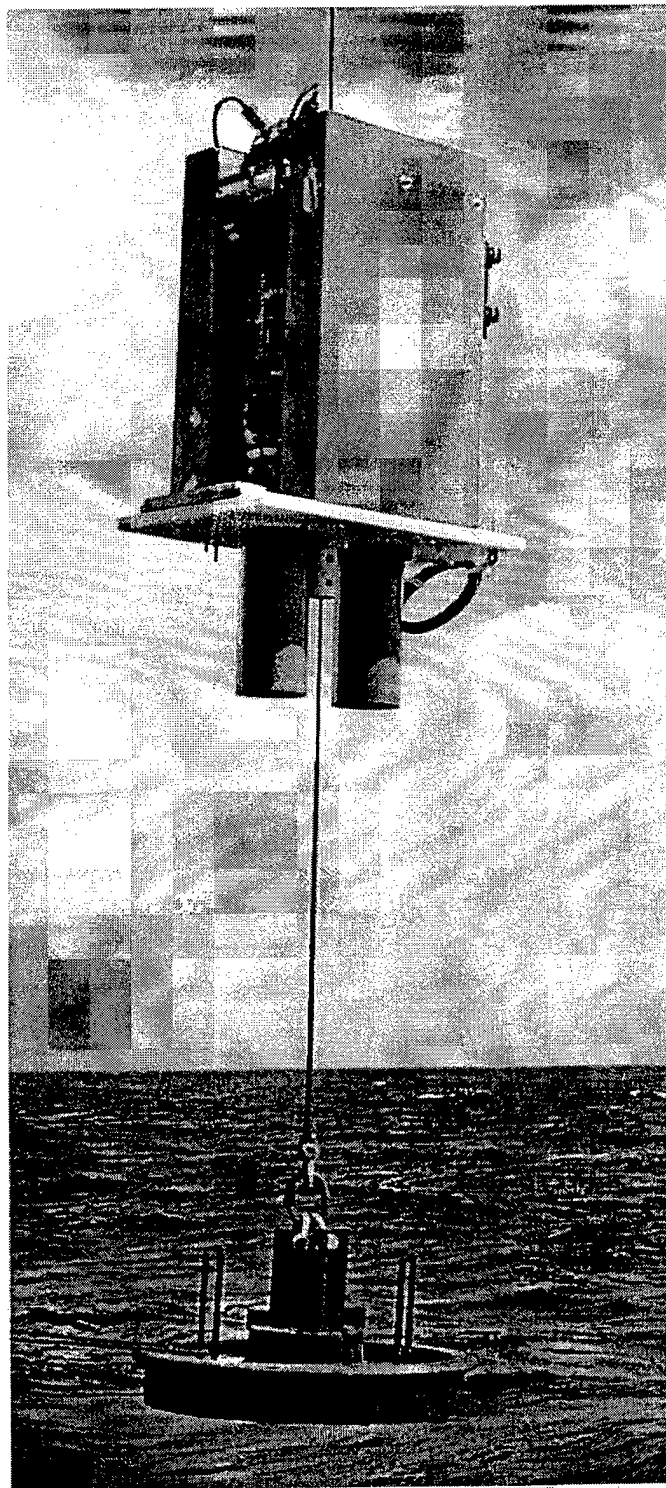


Fig. 5: Deep Ocean Profiler (DOP). Autonomous profiling YoYo system. The system descends and ascends guided by a rope between 3.500 m and 3.000 m waterdepth.

- led by a rope - over a range of 500 m within the deepest 500 m of the ocean. The attached CTD performs continuous measurements.

All major units are connected acoustically to the surface buoy unit and each client can be addressed separately without any "master and slave" philosophy. On this base, a remote control and data retrieval from the deployed instruments is possible.

IV. Project status and Results

The project was started in May 1997 and will last till the end of April 2000. The permanent surface buoy unit is moored since October 1998. Several expeditions with intense field testing have been done. The underwater acoustic telemetry system works very reliable with data communication rates up to 2.400 baud.

During the past field tests, the satellite transmission system have had some failures, due to the new created European ground center. Now, the OrbComm ground center in Lario (Italy) is in operational mode and it is possible to establish the bi-directional satellite link on an reliable base.

During a scientific cruise in May 1999 with the German Research Vessel METEOR, the buoy's electronic has been modified and the newest OrbComm transceiver was implemented. Several field tests were performed on this cruise with great success. In addition, it was the first successful "close loop" test of the coupled underwater-atmospheric communication lines.

For this close loop test, the communication started on the mobile OrbComm satellite transceiver onboard the RV METEOR with an request for underwater CTD-Data (deployed in 3.000 m water depth, attached to the MultiSensor-Device / MSD). This request was send via OrbComm satellites to Lario (Italy), from there routed back via satellite to the Surface buoy (SB) near the Canaries. Here the message was transferred from the OrbComm transceiver via the digital controller BC1 to the acoustic modem and transmitted into the deep sea, afterwards. The first underwater client (the Deep Ocean Unit, DOU) has routed the request to the MSD modem. The digital controller from the MSD started the request for CTD-data. After retrieving of the CTD-data, the MSD-modem have sent these data back to the surface buoy. From here the data were sent via satellite to Italy and routed back via satellite to the mobile OrbComm satellite transceiver onboard the RV METEOR. The overall transmission time for this complete loop was less than 8 minutes.

Despite this request for data, the buoy still is sending data from the weather station on hourly base since May 1999 via OrbComm. For safety reasons, a second and complete independent OrbComm transceiver still is sending tracking data of the buoy on a daily base.

V. Perspectives

It is planned to build up an operational DOMEST test bed in the year 2001. This mooring should be open for scientific colleagues on an international basis. DOMEST will provide an open ocean mooring with routine support, bi-directional satellite and acoustic link with standard interfaces (RS 232) and download protocols. The communication is based on OrbComm Services with access via Internet.

Acknowledgement

The DOMEST project is funded by the "Bundesministerium für Bildung, Wissenschaft, Forschung und Technologie, BMBF", Federal Republic Germany.

USING SMALL AUV FOR OCEANOGRAPHIC MEASUREMENTS

Manhar Dhanak, Edgar An, Ken Holappa and Samuel Smith
Department of Ocean Engineering,
Florida Atlantic University, Boca Raton, Florida 33431.

Abstract

The use of Florida Atlantic University's the Ocean Explorer, a small autonomous underwater vehicle, as a mobile platform for oceanographic measurements will be described. The OEX is a 2.4m long versatile, Gertler body which can perform pre-programmed underwater missions to a depth of 300m. At a speed of 1-2 m/s, it can perform missions over a period of several hours, collecting in-situ oceanographic data and storing it on an on-board data-logger. Three missions are described, two in shallow waters off the coast of South Florida during December, 1997, and one in the Gulf Stream during July 1997 at depths of up to 130m. During the missions, the AUV was equipped with a 1200kHz broad band ADCP, a CTD package and, on the Gulf Stream mission, a small-scale turbulence measurement package. The vehicle may also carry a side-scan sonar or other instruments for subsidiary measurements. The versatility of the AUV allows measurement of oceanographic data over a substantial region, the motion of the platform being largely decoupled from that of the sea surface. In the missions of Dec. 5 and 11, 1997, 'lawn-mower pattern' AUV surveys were conducted over 1 km² regions on the east coast of Florida, north of Fort Lauderdale, at depths of 7m and 3m respectively in a water column where depth ranged from 10 - 32m. During Dec. 5, the region was subjected to a cold front from the northwest. Local wind measurements show presence of up to 10m/s winds at temperatures of up to 10-15°C below normal for the time of the year. Measurements are compared with those of a fixed ADCP. In the Gulf Stream missions, significant shear layers were encountered. Bathymetry, current, CTD and small - scale turbulence measurements obtained during the missions will be presented and the problems associated with making such measurements and choosing sampling strategies will be discussed. The data collected using the mobile AUV have been utilized to develop maps of the bottom topography, the local distributions of current, temperature and density variations and variations in rate of energy dissipation in the context of background flow features.

1. Introduction.

Using one or more small, mobile, autonomous underwater vehicles (AUVs) as platforms for appropriate measurement instruments for continuous oceanographic surveys of a region is now possible. The small AUVs are versatile and can be low cost both in terms of hardware and operations, the latter being partly due to the fact that the vehicles can be launched from a small research vessel. Here, we describe the use of a small AUV, one of the *Ocean Explorer*

(*OEX*) series autonomous underwater vehicles built at Florida Atlantic University, as a platform for ADCP, CTD and side-scan sonar measurements in two regions off the coast of Florida. In section 2, we describe the *OEX* and the instruments used. In section 3, we describe a mission in the Gulf Stream during July 1997 and two missions in December 1997 on the East Coast of Florida.

2. The Ocean Explorer Series Vehicle.

An *OEX* series AUV, designed and built at Florida Atlantic University (Smith et al., 1995), is typically 2.4m long (Figure 1) with a modified Gertler's Series 58 Model 4154 fiber-glass hull of 0.53m maximum diameter. The *OEX* is designed to support multiple in-situ sensor payloads for performing search and mapping operations in coastal shallow-water environments. Its unique feature is a modular bayonet-mount interface between its payload and tail-section, allowing easy switching between payloads. The 1.2m tail-section houses navigation, control and propulsion components, including a 1200kHz ADCP, a CTD, a GPS receiver unit, a Watson-Block self-motion sensor, whereas a nominal 1.2m payload section, which may be extended to 2.4m, is dedicated to housing mission-specific instruments. In air, the *OEX* weighs approximately 181kg, and is designed to be neutrally buoyant. Its maximum depth rating is 300m. Using its onboard rechargeable NiCad batteries, which can provide up to 2kWh total energy approximately, the *OEX* can maintain a cruising speed of 3 knots (a speed range of 2-5 knots) for approximately 10 hours continuously between the recharge cycles. A Motorola 68060 CPU with a VX operating system and 1 Gbyte disk storage capacity allows logging significant amount of navigation and environmental data. The autonomous submarine carries out pre-programmed missions defined using ascii text files which can be downloaded to the *OEX* underwater via an Ethernet cable or remotely on

surface via RF connection, thereby increasing the operational efficiency. The submarine has several safety features which allow it to surface in case of difficulty. The AUV location is also continuously tracked acoustically via an USBL transponder from a research vessel, which is also used to launch and recover the AUV. During the mission, 113 different variables are recorded on the on-board computer, including its depth, velocity through the water, and, where bottom-lock is possible, its ground velocity and altitude, its position in latitude and longitude, and in-situ conductivity and temperature.

3. Oceanographic Measurement Missions.

Mission of July 1997. The mission of 7/16/97 was carried out in the Gulf Stream off the coast of Boca Raton, Florida, where the water depth is 150m. During the mission, the AUV traveled in a general southerly direction, against the current, at a relative water speed of 1.4m/s for 48 minutes, diving, in steps, to a depth of 126m and returning to the surface. A horizontal distance of 1200m was covered over the mission.

The depth, salinity and temperature determined from the recorded CTD data are shown in figure 2 a-d. The salinity data indicate occurrence of a broad salt layer at around 80m. There is good correspondence between salinity and temperature variations, the latter varying, across the seasonal thermocline, by 15°C over the depth covered. The speed of the vehicle through the water is shown in figure 2e, measured using the on-board ADCP.

For this mission, only the shear probes and the accelerometers were utilized. Only one of the two shear probes deployed functioned properly. However, analysis of the recorded turbulence data have shown that they are of very good quality data, being over the dissipation range $O(10^{-7} - 10^{-8} \text{ W/kg})$. Sample spectra are shown in figure 3. The dissipation rates are high

in the vicinity of the salt layer apparent in figure 2b at around 80m depth. Significant information from the measurements will be reported elsewhere.

Missions of December 1997. During a passage of a cold front (December 5 - 9, 1997) over sub-tropical waters of South Florida, 1km square region off the coast of Fort Lauderdale, on the edge of the Gulf Stream between two along shore reefs, were surveyed. The water depth here varies between 12m and 36m. In this region, currents are frequently induced by large eddies which spin off the Gulf Stream. During the winter, the region is subjected to cold fronts when winds of highly variable speeds and with temperatures 10°C or more below ambient blow offshore from the northeast and are favorable to upwelling. Available background information recorded by NOAA's C-MAN buoys north and south of the region during the mission is shown in figure 4. Station LKWF1 is at Lake Worth ($26^{\circ} 37'\text{N}$, $80^{\circ} 2'\text{W}$) about 32 miles north, while station FWYF1 is at Fowey Rocks ($25^{\circ} 35'\text{N}$, $80^{\circ} 6'\text{W}$), about 39 miles south of the surveyed regions. The wind speed, air and water temperature and the atmospheric pressure at the two station during the period December 1 – 12, 1997 are shown in figure 4 a, b, d, e and f respectively. Figure 4c shows currents recorded by a moored 600 kHz ADCP located at Port Everglades in Fort Lauderdale at a depth of 7.22m for comparison with the currents measured by the AUV at a depth of 7m. The periods of AUV operations are marked on the figure by the two sets of vertical bars. In order to survey the area, the AUV traveled at an average speed of 1m/s repeatedly along "lawn mower pattern" paths at pre-programmed constant depths, surfacing twice to obtain GPS fixes. Based on CTD and currents measured by the on-board sensors, spatial maps of bathymetry, salinity, temperature and currents and density have been developed. A sample is shown in figure 5. Detailed description are given elsewhere (An et. al., 1999).

4. Summary.

Small AUVs are versatile platforms for oceanographic surveys and can be adapted to provide high quality, low platform noise, oceanographic data. Turbulence measurements of superior quality have been made in the Gulf Stream, off the East Coast of Florida, using an AUV over 0.8 - 100 cpm wavenumber range. Other turbulence measurement missions using a small AUV have been reported elsewhere (Dhanak and Holappa, 1999). 'Lawn-mower' type surveys in shallow waters off the Florida Coast have been utilized to develop maps of spatial distributions of salinity, temperature, bathymetry and currents. Full details are given in An et al. (1999). Other recent missions include continuous surveys of the water column over extended periods and surveys to monitor the influence of adverse weather on the water column.

Acknowledgement. This work is supported by the Office of Naval Research under Grant No: N00014-96-1-5023 (Program Manager: Dr Thomas B. Curtin).

References.

- An, E., M. R. Dhanak, L. K. Shay, S. Smith, J. Van Leer. Coastal Oceanography Using a Small AUV. 1999. Submitted to J. Atmos. Ocean Tech.
- Dhanak, M. R. and K. Holappa. 1999. An Autonomous Ocean Turbulence Measurement Platform. To appear in J. Atmos. Ocean Tech.

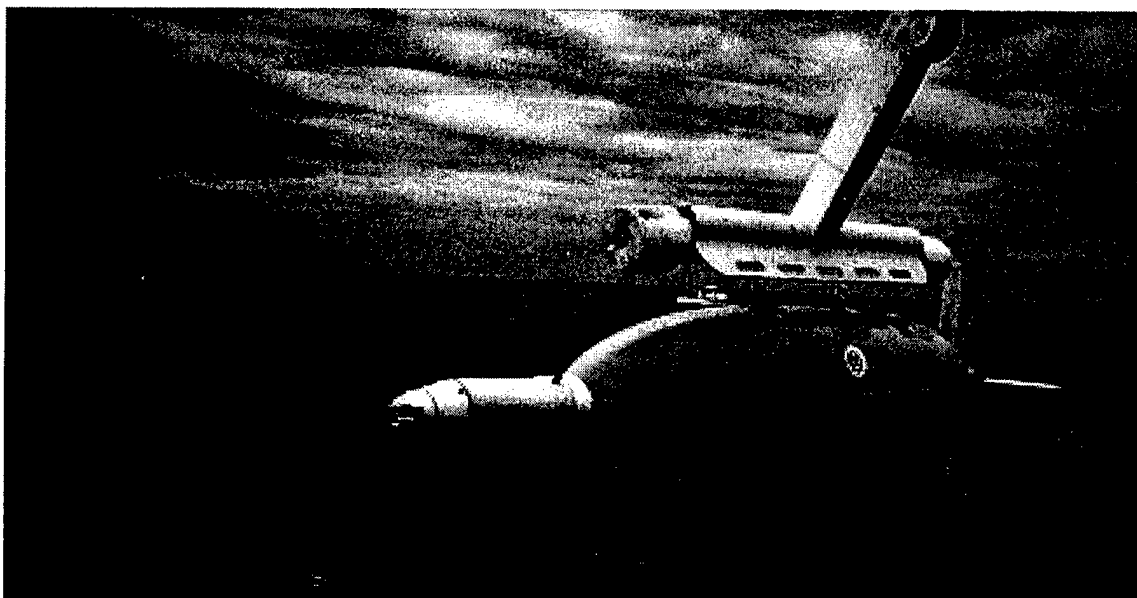


Figure 1. The Ocean Explorer AUV, shown with a turbulence package mounted on its nose.

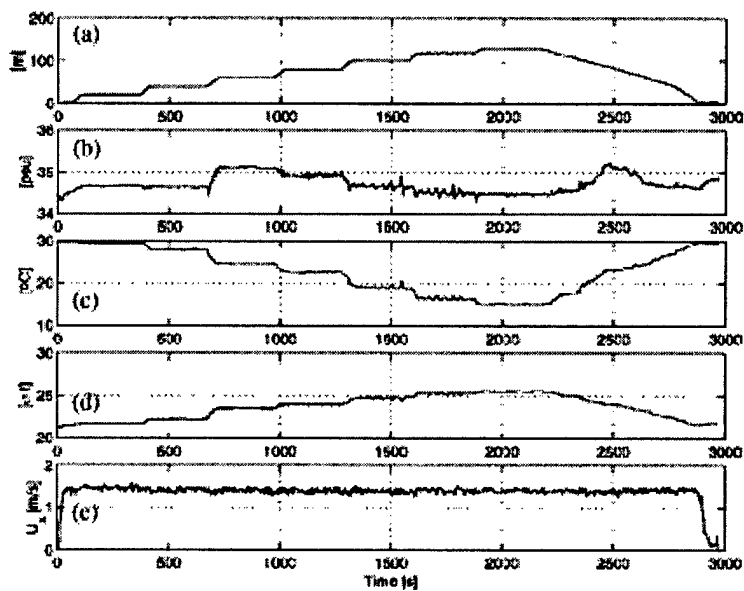


Figure 2. Time series of the mean data for 7/16/96 mission determined from the CTD and mean velocity measurements: (a) Vehicle depth, (b) salinity, (c) temperature, (d) density, (e) streamwise (x) component of velocity.

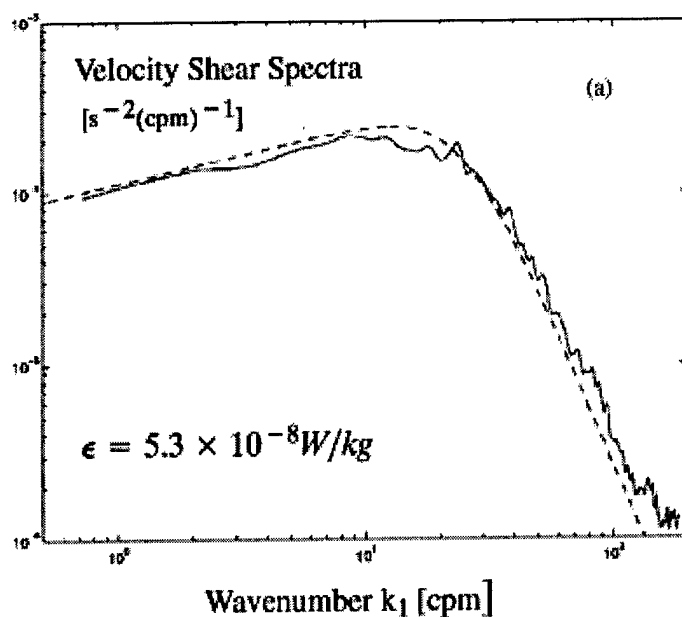


Figure 3. Averaged shear spectra over the region traversed during the Gulf stream mission of 7/16/97. ---: Nasmyth spectrum for the corresponding average dissipation rate.

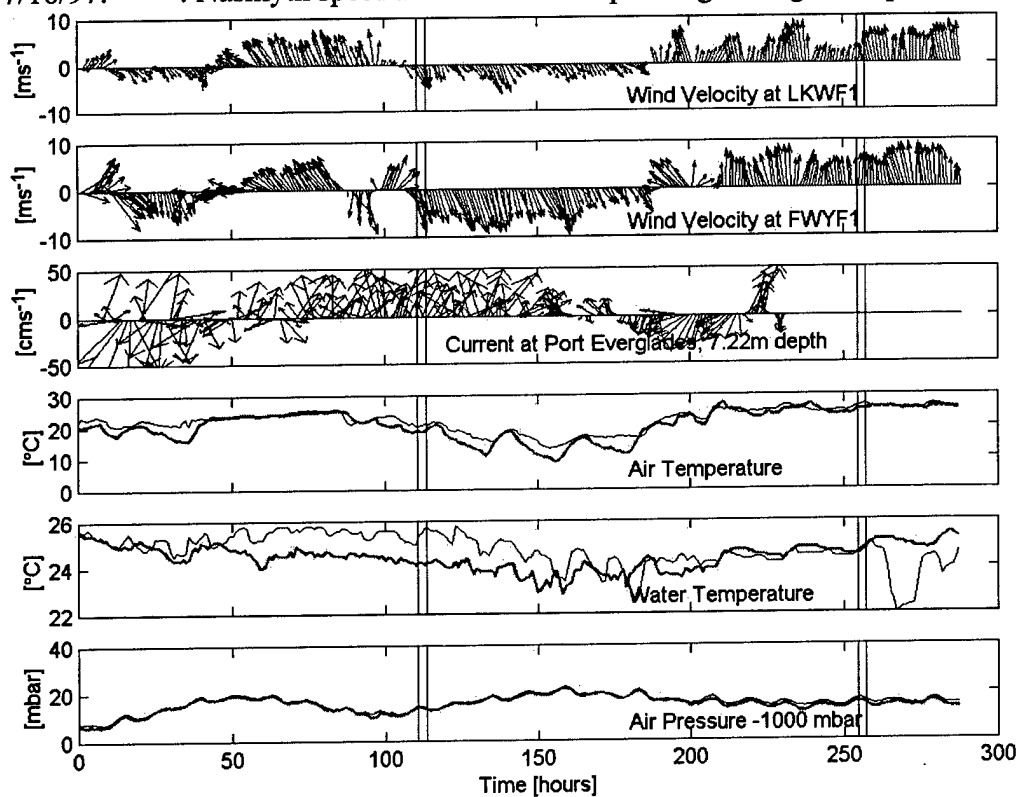


Figure 4. Buoy data at FWYF1 (thin line) and LKWF1 (thick line) Dec 1-12, 1997

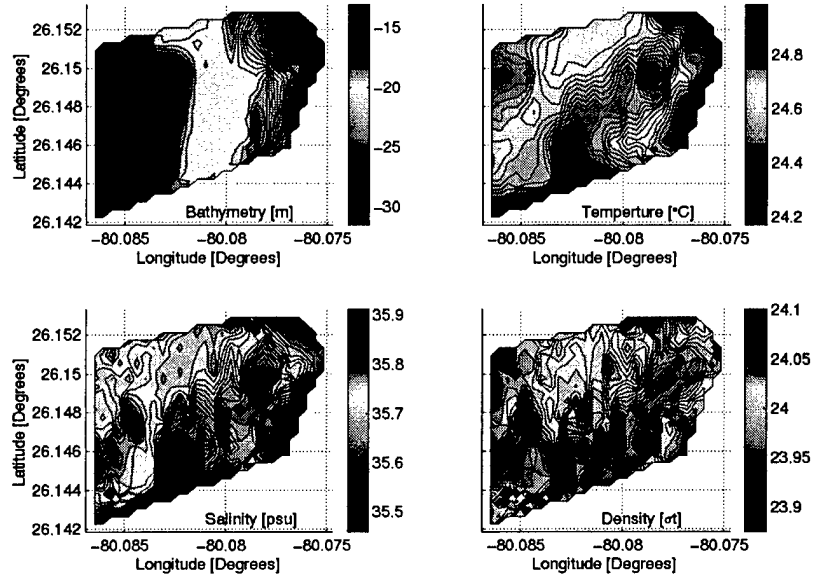


Figure 5. Spatial maps of bathymetry, temperature, salinity and density developed from data recorded from on-board sensors during AUV surveys.

APPLICATION OF SWIMMING FUNCTIONS OF AQUATIC ANIMALS TO AUTONOMOUS UNDERWATER VEHICLES

Naomi Kato

Tokai University, 3-20-1, Orido, Shimizu, Shizuoka, Japan

Abstract – This paper focuses on AUVs with the types of accelerators and maneuvers in the category of fish gaits to perform precise maneuver such as hovering and turning at a certain point not only in survey of an intricate seabed, but also in dexterous manipulation in their floating condition. This paper summarizes on-going project on mechanical pectoral fin from the following three aspects. (1) Maneuver of fish robot with a pair of two-motor-driven mechanical pectoral fins in horizontal plane, (2) Control of interaction of forces and moment between an underwater vehicle in a free swimming condition and a manipulator by a pair of mechanical pectoral fins in horizontal plane and (3) Hydrodynamic characteristics of a pair of three-motor-driven mechanical pectoral fins which enables the fish robot to swim not only in horizontal plane, but also in vertical plane.

I. INTRODUCTION

Studying the locomotion mechanisms and the autonomous systems of aquatic animals through surrounding fluid is significant in that they have adapted to their various living circumstances since the birth of life on earth. This paper is aimed at applying the swimming functions of the aquatic animals to development of a new type of autonomous underwater vehicle (AUV). It is necessary to make sure if these functions can overcome the present technologies on AUV. The key technologies on AUV are power sources, propulsion and maneuver performance, autonomous control system, sensor system, information transmission system and so on. This study focuses on propulsion and maneuver performance of aquatic animals to AUV.

According to the category of fish gaits, there are three types: cruiser/sprinters, accelerators and maneuvers. Previous studies have focused on the fish fin motion as an oscillating foil for propulsion [1,2,3,4]. The fish fin motion belongs to the type of cruiser/sprinters propelling themselves with thrust maximizing propulsors. However, application of the oscillating foil to underwater vehicles as the main thruster is not straightforward, because of strong

competition with screw type thrusters. The advantages of the oscillating foil are that the emitted noise level will be lower and its characteristics will approach the natural ones if the propulsion mechanism can approach the muscle system of aquatic animals, and that the oscillating foil is friendly to nature because it does not catch sea plants on the seabed. On the other hand, screw-type thrusters have a drawback in the sudden generation of the thrust force in the hovering condition of underwater vehicle, which leads to imprecise control of position and attitude of the vehicle and manipulators. Few researchers considered the utilization of fish fin motion to maneuver and stabilize underwater vehicle[5].

This paper focuses on AUVs with the type of maneuvers to perform precise maneuvering such as hovering and turning at a certain point. The high maneuverability enables the underwater vehicles not only to survey an intricate seabed, but also to perform a dexterous work using multiple manipulators in their floating condition [6]. Because many fishes use oscillating pectoral fins for their maneuvers at low swimming speeds [7], the utilization of the pectoral fin motion has the possibility of overcoming the drawback of the screw type thrusters.

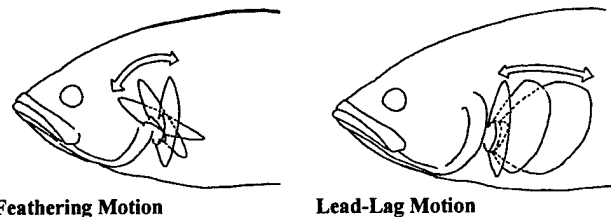


Fig.1 Illustration of feathering motion and lead-lag motion

The author developed a pair of two-motor driven mechanical pectoral fins for maneuver of underwater robots based on observation and experimental analysis of pectoral fin motion of Black Bass (*Micropterus salmoides*) [8,9,10]. The work revealed (1) that the pectoral fin motion in the condition of the fish swimming in the horizontal plane mainly consists

of the feathering motion, that is characterized by a rotational motion along a horizontal fin ray, and the lead-lag motion, that is characterized by a posterior and anterior motion in the horizontal plane (see Fig.1), (2) that the combination of those motions on both sides dominantly generates the fish motions of forward swimming, backward swimming, hovering and turning in the horizontal plane, (3) that a mechanical pectoral fin making the feathering motion and the lead-lag motion generates thrust force in a certain range of phase difference between both motions, and (4) that the fish robot composed of rigid fish body and a pair of the mechanical pectoral fins on both sides can perform forward swimming, backward swimming, and turning in horizontal plane.

This paper summarizes on-going project on mechanical pectoral fin from the following three aspects.

- (1) Maneuver of fish robot with a pair of two-motor-driven mechanical pectoral fins[11,12].
- (2) Control of interaction of forces and moment between an underwater vehicle in a free swimming condition and a manipulator by a pair of mechanical pectoral fins in horizontal plane.
- (3) Development of a pair of three-motor-driven mechanical pectoral fins to apply to an AUV with high maneuverability.

II. MANEUVER CONTROL OF FISH ROBOT WITH TWO-MOTOR-DRIVEN MECHANICAL PECTORAL FINS IN HORIZONTAL PLANE

This chapter discusses the performance of guidance and control of the fish robot with a pair of the two-motor-driven mechanical pectoral fins in horizontal plane for rendezvous and docking with an underwater post in water currents.

The variables for the motion control of the fish robot in the horizontal plane are basically (i) each phase difference between the lead-lag motion and the feathering motion on each side, (ii) each angle of central axis of the lead-lag motion on each side, (iii) each angle of central axis of the feathering motion on each side, (iv) phase difference between the feathering motions on both sides, (v) each amplitude of lead-lag motion on each side, (vi) each amplitude of feathering motion on each side and (vii) motion frequency, in total 12. The input variables are X-axis component of the position, Y-axis component of the position and yaw angle. Because the motion of the fish robot is highly non-linear about the control variables and it is not possible to express the equations of the motion explicitly in terms of the control variables, we employ fuzzy control algorithm which is applicable to such ill problems.

A. Two-Motor-Driven Mechanical Pectoral Fin

Fig.2 shows a pair of two-motor-driven mechanical pectoral fins. Each fin system has two servo motors of which angles are sensed by potentiometers and are controlled by a personal computer by use of PD control. Two servo motors generate the lead-lag motion and the feathering motion of the pectoral fin. Although the fin system can generate any kind of programmed motion within the performance of the motors, sinusoidal were used. The pectoral fin model is a flat plate which is made of stainless steel of thickness of 0.6 mm and of chord length of 0.155 m.

B. Fish Robot with a Pair of Two-Motor-Driven Mechanical Pectoral Fins

Fig.3 shows the photograph of the fish robot "Bass II" with a pair of two-motor-driven mechanical pectoral fins (2MDMPFs). The fish body is made of Fiber Reinforced Plastic. Its dimensions are as follows: Length \times width \times height = 1.08m \times 0.28m \times 0.39m. A pair of 2MDMPFs were installed at a quarter length of the fish body from the head.

We define the lead-lag angle ϕ_L , the feathering angle ϕ_{FE} and flapping angle ϕ_{FL} on the right hand side as shown in Fig.4. We set ϕ_{FL} as zero and X-axis parallel to the longitudinal axis of the fish body, positive direction of which points to the head of the fish body. We make Y'-axis lie in the plane of X-Y axis.

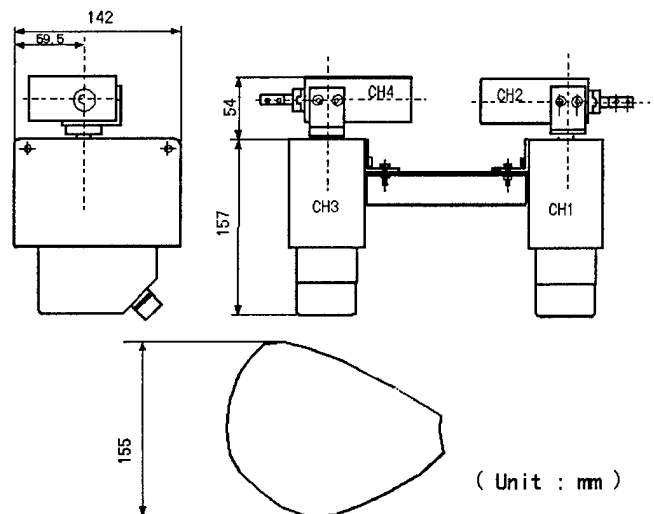


Fig.2 Two-Motor-Driven Mechanical pectoral fins

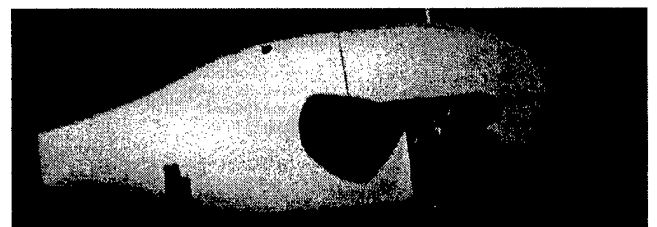


Fig.3 Photograph of "Bass II"

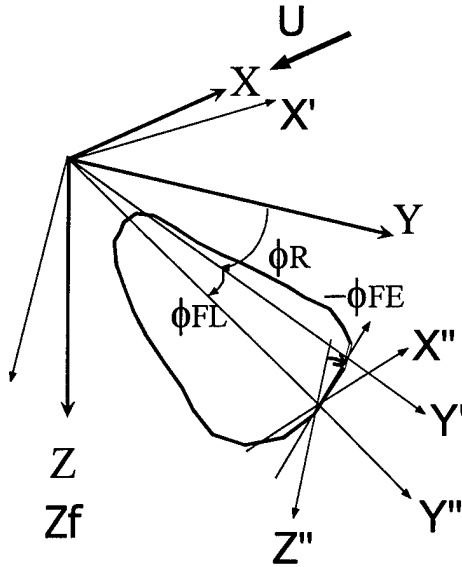


Fig.4 Definition of Coordinate System and Notation

C. Setup of Experiment

The carriage for the measurement of motion of the fish robot in horizontal plane was mounted on a water circulation tank having the measurement section of 2.2 (m) long, 1.4 (m) wide and 0.9 (m) deep. The fish robot was immersed in water at half depth of the tank. The fish robot and the carriage was rigidly connected by a support rod which is located at a quarter length of the fish body from the head. X_0 -axis component and Y_0 -axis component of the position of the fish robot were measured by use of two rotary encoders and yaw angle ϕ was measured by use of potentiometer. The mass of a pair of mechanical pectoral fins motion is 8.42 (kg), volume of fish body is 0.0494 (m^3) mass of fish body is 15.74 (kg), mass of the carriage is 7.0 (kg), and friction force between the carriage and the rails on the tank is 0.49 (N). A pipe of length of 0.1 (m) and of diameter of 0.02 (m) was attached to the front of the fish robot to perform rendezvous and docking test with an underwater post which has a hole of diameter of 0.08 m. The weight of the fish robot including the support rod in water was set as almost zero. The control frequency was set as 10 [Hz].

D. Control Laws for Rendezvous and Docking with an Underwater Post in Water Currents

Pre-arranged course from point O to point C was given as shown in Fig. 5. The underwater post was arranged at point C.

The control laws consist of (i) a fuzzy control law for forward swimming from point O to point A and from point B to point C, (ii) a fuzzy control law for decrease of swimming velocity around point A and point B, (iii) lateral swimming from point A to point B and (iv) switch of control laws.

We define here O' - x - y coordinate system. We take the origin O' at a target point chosen from points O, A, B and C according to the position of the fish robot. We set x -axis parallel to X_0 -axis and y -axis parallel to Y_0 -axis.

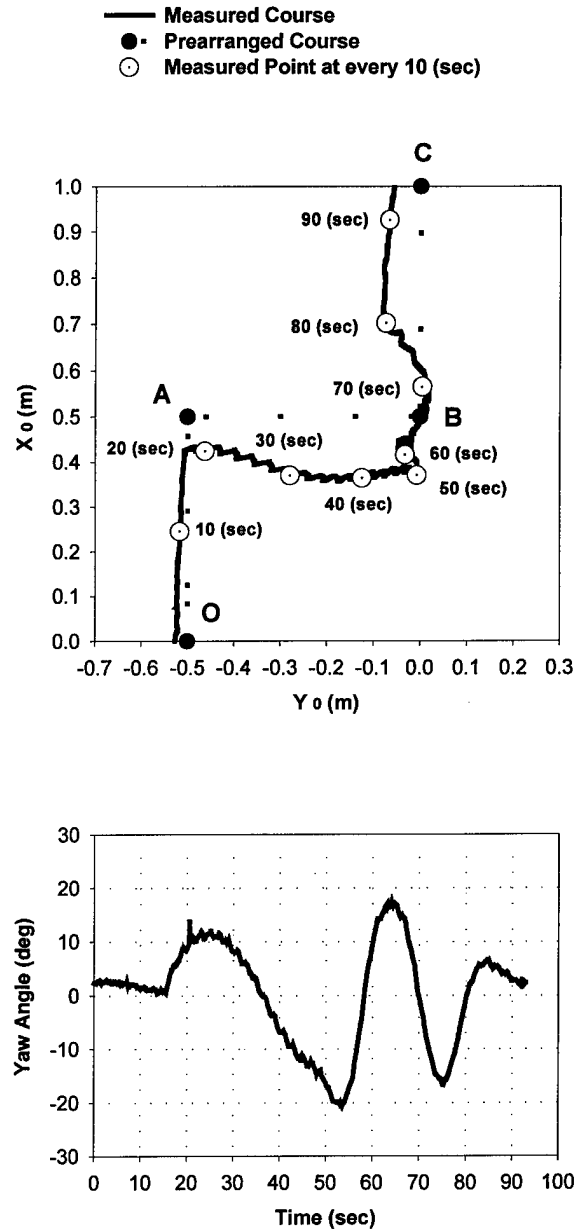


Fig.5 Loci and yaw angle of fish robot in water current of 0.05 m/s

E. Experimental Results

Fig.5 show loci of the fish robot and its yaw angle in water current of 0.05 m/s in negative direction of X_0 axis, respectively. Although some amount of offset from the prearranged course at the start point was given, the fish robot swims forward, stops swimming forward around point A, swims laterally toward point B

with small yaw angle, stops swimming laterally to swim forward and finally docks with the underwater post. We found it takes more time to reach the underwater post, amount of drift to the direction of the water current between point A to point B becomes larger and the yaw angle becomes more oscillatory as the velocity of water current increases.

III. COORDINATED CONTROL OF AN UNDERWATER VEHICLE IN A FREE SWIMMING CONDITION AND A MANIPULATOR BY A PAIR OF TWO-MOTOR-DRIVEN MECHANICAL PECTORAL FINS IN HORIZONTAL PLANE

The interaction of forces and moments between vehicle and manipulator(s) forms a complex time varying, non-linear, multivariable dynamic system, with a large number of degrees of freedom (DOF), the control of which is not straightforward. However, the additional DOF made available by the manipulator(s) can be used usefully in the design of the vehicle at an early stage, to achieve more precise motion control. For example, if only one arm is required to execute the mission, other arms can be used to assist in stabilizing the vehicle, either by attaching to a structure or by moving, to dynamically counterbalance the reaction forces and moments from the mission arm on the vehicle. Thus, the redundant degrees of freedom are used usefully in controlling the robot.

Thus far, the majority of research on such use of underwater manipulators has been limited to the condition where a manipulator is attached to a structure [13]. However, several research have focused on the problem with the vehicle in a free swimming condition [6,14,15,16,17,18].

The previous paper of the author [6] reported analysis and simulation studies for the coordinated control of multiple manipulators on a free swimming underwater robot. The control objective was to perform an open loop control of the end effector position of one of the arms. A formulation was derived for both the inverse dynamics and inverse kinematics of an underwater robot with multiple manipulators, having a redundancy in degrees of freedom of motion, in the presence of external generalized forces. The method was applied to a model of an underwater robot comprising a 6 DOF mission arm and a further pair of 2 DOF paddling arms used for stabilization in a free swimming condition. The numerical simulation results showed the effectiveness of the coordinated control method with the assistance of the stabilizing arms.

This chapter shows the experimental results in horizontal plane on the stabilization of motion of model of an underwater robot equipped with a manipulator with assistance of the pair of 2MDMPFs instead of the paddling arms used in the simulation.

A. Model of Underwater Robot with a Manipulator

Fig.6 shows the model of the underwater robot with a manipulator. The dimensions of the model are as follows: Length \times width \times height = $0.9\text{m} \times 0.6\text{m} \times 0.5\text{m}$. The mass of the model is 25.95 Kg. The manipulator consists of 3 links where 3 DC motors and 3 potentiometers are installed. The dimensions of the manipulator are as follows: Length \times width \times height = $0.651\text{m} \times 0.040\text{m} \times 0.095\text{m}$. The distance between each link is 0.2 m. The mass of the manipulator is 2.55 (kg). The pair of 2MDMPFs were installed at 0.34 m behind from the root of the manipulator.

B Setup of Experiment

The model of an underwater model and the carriage for the measurement of the motion in the horizontal plane was rigidly connected by a support rod which is located at 0.34 m behind from the root of the manipulator. The fish robot was immersed in water at half depth of the water circulating tank.

C Control Algorithm

Fuzzy algorithm was used for the control of yaw motion of the model of an underwater robot with a manipulator. The control variables were a pair of phase differences between the lead-lag motion and the feathering motion on both sides. The amplitudes of both motions were fixed.

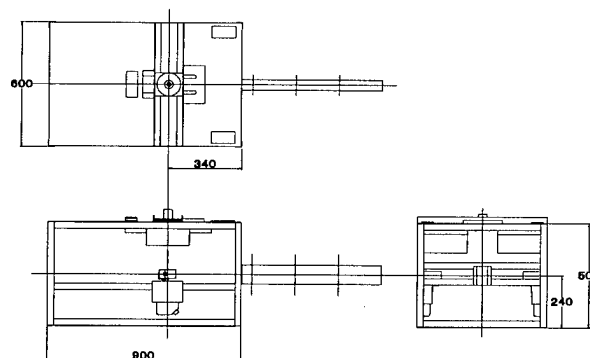


Fig.6 Model of Underwater Robot with a Manipulator

D Experimental Results

Fig.7 shows an example of experimental results of yaw motion of the model during a period (11.1 s) of oscillatory motion of manipulator. The position and the posture of the model with a manipulator is illustrated each 0.6 s. We find that the strong interaction of motion occurs between the model and the manipulator.

Fig.8 shows the ratio of root-mean-square of yaw motion of the model without control to with control during 5 periods of sinusoidal motion of the manipulator against the variables of period of manipulator from 5.5 s to 11 s and that of pectoral fin from 1.0 s to 2.0 s. We can see that slower motion of

manipulator produces better performance of control that is hardly dependent of period of motion of fin, and that the control performance increases as the fin moves faster with faster motion of the manipulator.

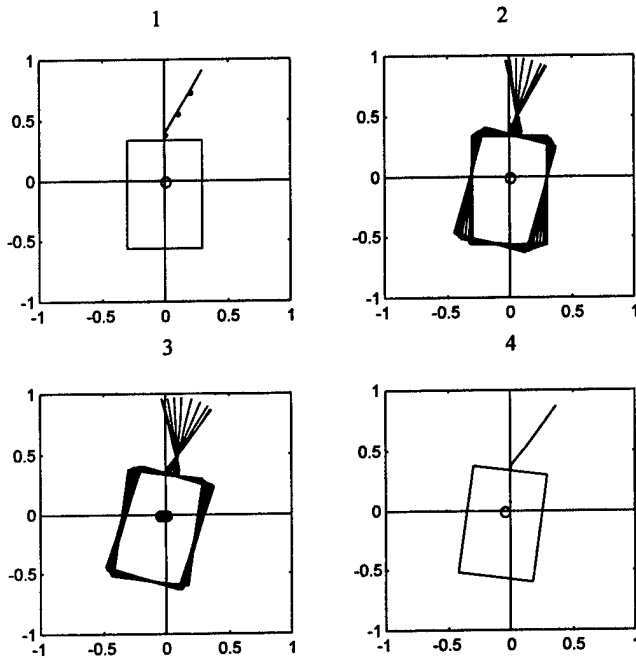


Fig.7 Motion of Model of an Underwater Robot induced by an Oscillatory Motion of a Manipulator

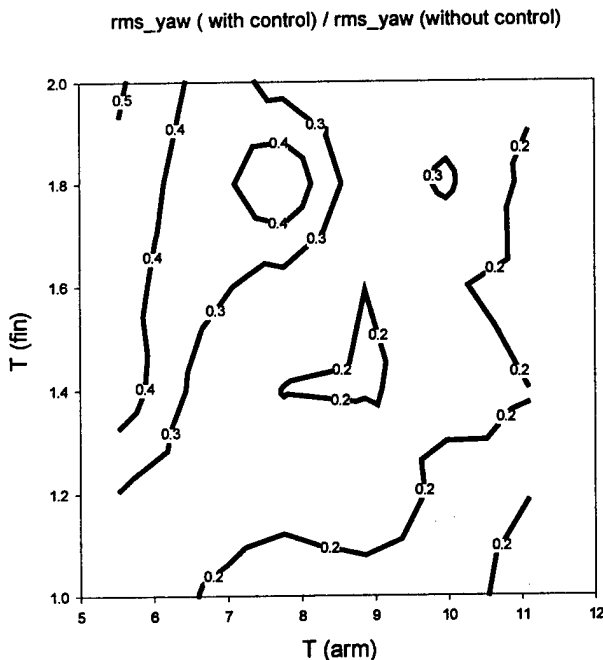


Fig.8 Ratio of Yaw Motion of Model with Control to without Control

IV. HYDRODYNAMIC CHARACTERISTICS OF TREE-MOTOR-DRIVEN MECHANICAL PECTORAL FIN

We have developed a pair of three-motor-driven mechanical pectoral fins (3MDMPFs) where gimbal structures are incorporated to allow three DC servo motors to independently generate the lead-lag motion, the feathering motion and the flapping motion producing vertical motion of fin as well as to be housed in a compact pressure vessel (see Fig.9). The addition of the flapping motion to 2MDMPF produces vertical force. It enables a fish robot equipped with a pair of 3MDMPFs to swim not only in horizontal plane, but also in vertical plane.

We analyzed the hydrodynamic characteristics of 3MDMPF theoretically using unsteady vortex lattice method including the effect of vortex diffusion [10]. Figs.10 and 11 show the comparison between numerical simulation and the experimental results for the coefficient of mean thrust of 2MDMPF and for its propeller efficiency, respectively, versus the phase difference between the lead-lag motion and the feathering motion. We can see that the simulation method can reasonably express the experimentally measured unsteady forces acting on a 2MDMPF and that the thrust force and the propeller efficiency become maximum in the range of the phase difference from 60° to 90° .

Based on the comparisons between the numerical simulation and the experimental results, we carried out the numerical simulation to analyze the hydrodynamic characteristics of 3MDMPF. Fig.12 shows the computed results for the coefficient of mean thrust of 3MDMPF versus the phase difference between the lead-lag motion and the flapping motion, where the phase difference between the lead-lag motion and the feathering motion was taken as 90° and the amplitude of the flapping motion was set

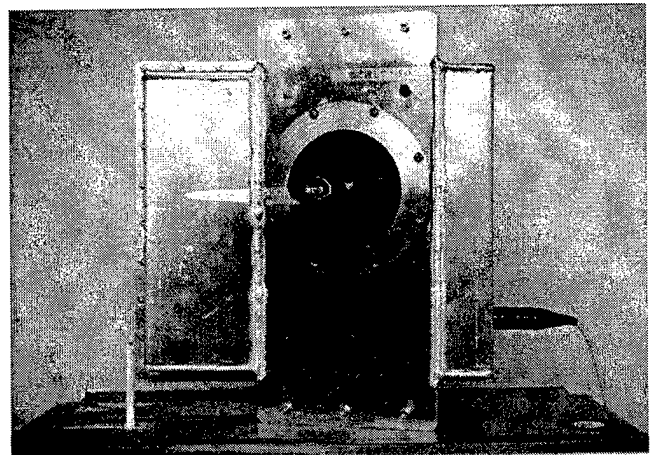


Fig.9 Three-Motor-Driven Mechanical Pectoral Fin

as 20° . Fig.13 shows the computed results for the propeller efficiency. We can see that both the coefficient of mean thrust of 3MDMPF and the propeller efficiency at those maximum values are about 1.5 times as large as those of 2MDMPF.

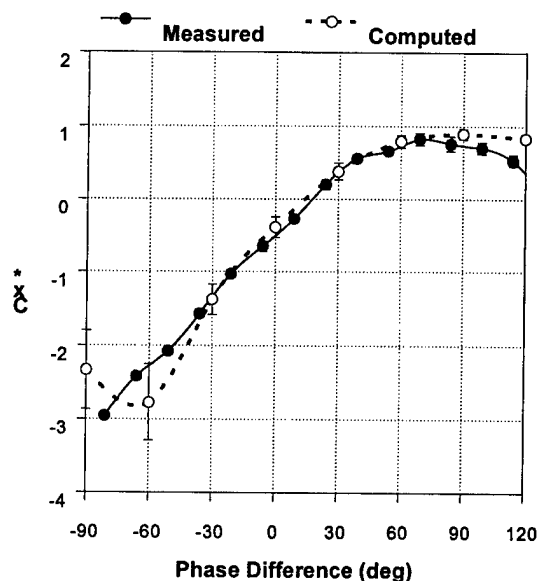


Fig.10 Comparison between a Numerical Simulation and the Experimental Results for the Coefficient of Mean Thrust C_{x^*} of 2MDMPF

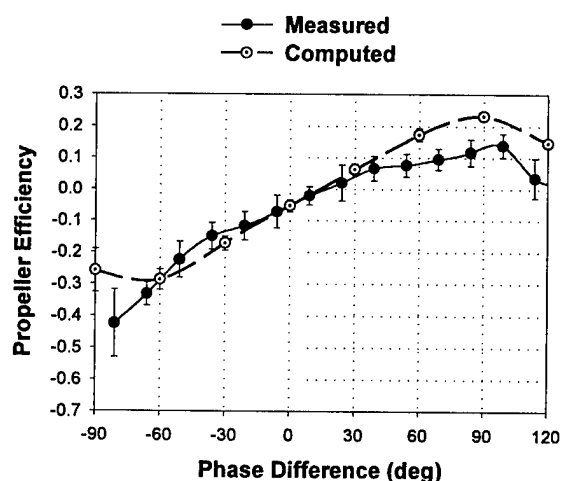


Fig.11 Comparison between a Numerical Simulation and the Experimental Results for the Propeller Efficiency of 2MDMPF

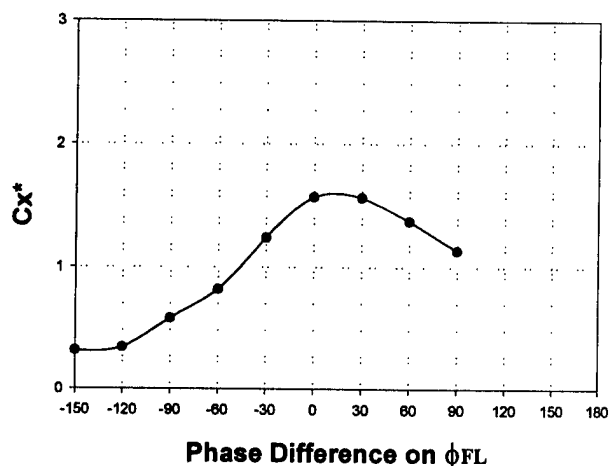


Fig.12 Computed Results for the Coefficient of Mean Thrust C_{x^*} of 3MDMPF

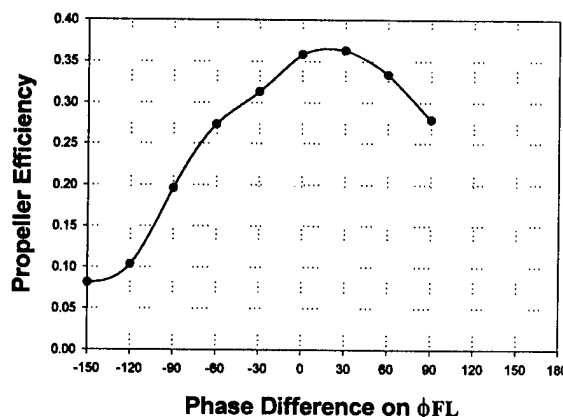


Fig.13 Computed Results for the Propeller Efficiency of 3MDMPF

V. CONCLUSION

On-going project on mechanical pectoral fin has been presented from the viewpoint of its application to AUVs with the types of accelerators and maneuvers in the category of fish gates. This paper has demonstrated that the fish robot equipped with a pair of two-motor-driven mechanical pectoral fins has a high maneuverability in the horizontal plane, an induced yaw motion of a model of an underwater robot in the horizontal plane caused by a forced motion of a manipulator can be largely decreased with the assistance of a pair of two-motor-driven

mechanical pectoral fins and that three-motor-driven mechanical pectoral fin has a higher performance on thrust and propeller efficiency than two-motor-driven mechanical pectoral fin. We are now under developing a testbed of fish-like AUV equipped with a pair of three-motor-driven mechanical pectoral fins to test its swimming performance.

REFERENCES

- [1] Hertel, H., 1966, *Structure-Form-Movement*, Reinholds, New York
- [2] Isshiki, N. and H. Morikawa, 1982, "Study on Dolphin-Style Fin Ship," (in Japanese), *Bulletin of Society of Naval Architects of Japan*, No. 642, pp.2-9
- [3] Barrett, D.S. and M.S. Triantafyllou, 1995, "The Design of Flexible Hull Undersea Vehicle Propelled by an Oscillating Foil," *Proceedings of 9th International Symposium on Unmanned, Untethered Submersible Technology(AUSI)*, pp.111-123, Durham, NH, September 25-27
- [4] Tanaka, I. and M. Nagai, 1996, *Hydrodynamics of Drag and Propulsion -Learning from High Speed Swimming Performance of Aquatic Animals* (in Japanese), Ship and Ocean Foundation, Japan, August, ISBN 4-916148-00-2 (Not for sale)
- [5] P.B., Bandyopadhyay, J.M. Castano, J.Q. Rice, R.B. Philips, W.H. Nedderman, and W.K. Macy, "Low-Speed Maneuvering Hydrodynamics of Fish and Small Underwater Vehicles," *Journal of Fluids Engineering, Transactions of the ASME*, 1997, Vol.119, pp.136-144
- [6] Kato, N. and D.M. Lane, 1996, "Co-ordinated Control of Multiple Manipulators in Underwater Robots," *Proceedings of the 1996 IEEE International Conference on Robotics and Automation*, pp.2505-2510, Minneapolis, MN, April 22-28
- [7] Lindsey, C.C., 1978, "Form, Function and Locomotion Habits in Fish," in *Locomotion Fish Physiology VII* edited by Hoar, W.S. and , D.J. Randall, Academic Press, pp.239-313
- [8] Kato, N. and M. Furushima, 1996, "Pectoral Fin Model for Maneuver of Underwater Vehicles," *Proceedings of 1996 IEEE Symp. On Autonomous Underwater Vehicle Technology*, pp.49-56, Monterey, CA, June 2-6
- [9] Kato, N., 1998, "Locomotion by Mechanical Pectoral Fins," *J. of Marine Science and Technology(SNAJ)*, Vol.3, No.3, pp.113-121
- [10] Kato, N., 1999, "Hydrodynamic Characteristics of Mechanical Pectoral Fin," *Trans. of ASME, J. of Fluids Engineering*, Vol.121, No.3 1999 in Press
- [11] Kato, N. and Inaba, T., 1998, "Guidance and Control of Fish Robot with Apparatus of Pectoral Fin Motion," *Proc. of 1998 IEEE International Conference on Robotics and Automation*, pp.446-451
- [12] Kato, N. and Inaba, T., 1998, "Control Performance of Fish Robot with Pectoral Fins in Horizontal Plane," *Proc. of 1998 International Conference on Underwater Technology*, pp.357-362
- [13] Ioi, K. and K. Itoh, 1990, "Modelling and Simulation of an Underwater Manipulator," *Advanced Robotics*, Vol.4, No.4, pp.303-317
- [14] H. Mahesh, J. Yuh and R. Kakshimi, 1991, "A Coordinated Control of an Underwater Vehicle and Robotic Manipulator," *J. Robotic Systems*, Vol.8, No.3, pp.339-370
- [15] S. McMillan, D.E. Orin and R.B. McGhee, "DynaMechs, 1995," An Object Oriented Software Package for Efficient Dynamic Simulation of URVs, "Underwater Robotic Vehicles Design and Control (Editor: J. Yuh), pp.73-98
- [16] Leabourne, K.N. and S.M. Rock, 1998, "Model Development of An Underwater Manipulator For Coordinated Arm-Vehicle Control," *OCEANS'98(IEEE)*
- [17] Lapiere, L., P. Fraisse and N.K. M'Sirdi, 1998, "Hybrid Position/Force Control of a ROV with a Manipulator," *OCEANS'98(IEEE)*
- [18] Diaz, E.O., C.C.d., Wit and M. Perrier, 1998, "A Comparative Study of Neglected Dynamics on an Underwater Vehicle/Manipulator System under Nonlinear Robust Control," *OCEANS'98(IEEE)*

The optical refractometer Project OPRA- A further development of an in situ going optical density measuring sensor

Christoph Waldmann

MARUM-Center for Marine Environmental Sciences
University of Bremen, Klagenfurter Str., 28359 Bremen, Germany

Abstract- Currently there are several initiatives to look for alternative methods to determine the salinity or density of seawater especially for long term unattended measurements. EUROGOOS, the European initiative of the world-wide observation program GOOS, has established a working group devoted to evaluate different approaches. One way that has been considered is the refractometer principle. The attractive feature of this principle lies in the fact that there is no direct interaction like in the case of conductivity measurements of the sensing elements with the surrounding fluid and the sensor head can be streamline shaped. This allows for a better flushing of the measuring volume. On the other hand due to the high demands in the design of the optical imaging system and the photodetector module most designs are still in an experimental phase or just exist as an idea. Furthermore a new equation of state has to be developed as there are up to now no reliable reference data. Facing this problems a redesign of an existing in situ going refractometer has been started that shows new solutions to the above mentioned problems. The basic principle that has been described in earlier OCEANS papers is still the same. But the redesign of the sensor head has gone through some major changes. The new geometry allows measurements in water and in air without replacing any components. This is of utmost importance for the calibration procedure. Furthermore dedicated modules as for example a hybrid photodetection unit has been developed to ease a production of the sensor by a company. In this paper the performance in laboratory and under field conditions of the redesigned sensor will be described

I. Introduction

The potential of the refractometer method as a powerful tool for salinity and density measurements has been well known in the past. But still there are now systematic investigations of the properties of the parameter available. The main reason lies in the technological implementation of the method. There has been many attempts to get access to this parameter. But laboratory investigations as has been

started 30 years ago did not show the path to the design of a dedicated set of in situ and laboratory instruments. Furthermore there are still open problems that has to be solved as for example the fundamental measurement of the pressure dependence of the refractive index. This means that there are no reference liquids available for calibrating the instrument in refractive index units as a function of pressure.

What is needed to convince different groups to take up such an investigations is first of all an in situ going instrument that will stimulate new interest to this parameter. But getting an in situ system on track has been a task with overwhelming technical detail problems. Every component has to be designed individually for this task and has to fulfill high requirements concerning to ruggedness and precision. To have control over surface effects between the interface of glass and water is also of paramount importance.

What is known about this parameter up to now ? It has a closer relationship to density or salinity than conductivity. The explicit temperature dependence is at least less by a factor of 100 compared to conductivity. Therefore the matching of time constants between different sensors is less stringent. Additionally the basic principle allows to design a fast responding sensor. Both properties makes this principle ideal for turbulence measurements. The design of high accuracy salinity or density measurements looks very promising based on measurements taken in the laboratory. But the in situ performance of systems that are under development right now are still unknown.

In this paper a further development of an existing system will be discussed that addresses some of these problems.

II. Sensor description

The basic principle has been described in earlier publications [1,2,4]. It relies on the refraction of a light beam at the interface between water and a reference glass body. The angle of refraction as a measure of the refractive index is measured with a high precision analog position photodetector. The critical elements of the design that has been reconsidered within this project has been:

- The mechanical mount of the optical fiber to achieve easier adjustment
- A new reference body design to achieve better flushing

- Reduction of the overall length of the sensor- optical bench
- A compact design of the photodetector unit
- A data acquisition unit for high speed in situ measurements

These improvements are described in the following:

A. Redesign of fiber optical launch

The sensor head determines the temporal and spatial response of the sensor. It has to be optimized accordingly but at the same time one has to simplify the construction to make a future production of the system possible. Past designs were suffering from delicate adjustment procedures at the sensor head. Therefore a systematic calculation of the optical propagation conditions has been undertaken and ended up with a design that is shown in Fig.1. The fiber has been soldered into a capillary tube which an easy way to seal the capillary end. As it is shown there is just one degree of freedom needed for the adjustment of the fibers. As one can see the fiber end has been retreated from the glass surface to allow for a better flushing. Additionally there is a second strut that allows the mounting of a high speed thermistor. The next step in the design will be to fix the fiber permanently into the metallic structure of the sensor head.

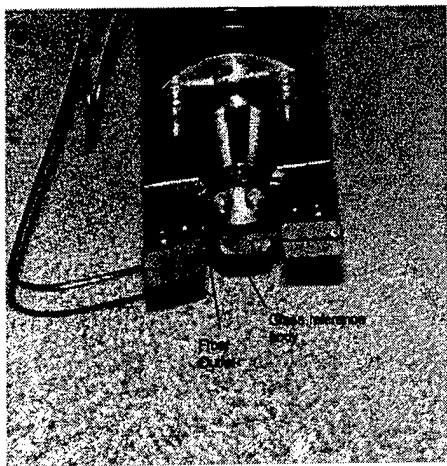


Fig. 1: The redesigned optical sensor head that allows for better flushing of the measuring volume

B. Redesign of glass reference body

Together with the optical fiber output a redesign of the prism has been undertaken. The design goal was to put the sensitive surface on the tip of the glass prism. This calls for a reflection of the launched light rays with an additional mirror surface on one side of the glass body. At this point it was found out that an additional mirror surface would allow taking measurements in air without any readjustments in the optics. This means that an additional reference measurement is possible. As the refractive index of air is known with high

accuracy even at high pressures this will allow an independent check of the pressure dependence of the mechanical structure of the sensor. By this one could circumvent the lack of high accuracy data of the refractive index at high pressures.

C. Redesign of the optical bench

The redesign was necessary because of the changes in the optical design of the sensor head. The goal was to achieve the same optical transfer function with an even shorter design. The resolution of the system is determined by the focal length of the front lens and the magnification of the following microscopic system. By changing these parameters it is possible to reduce the length by a factor of two. The tradeoff lies in the increased sensitivity of the optical elements to displacement. The demands on the optical bench as such stay the same.

D. Redesign of the photodetector unit

Beside the sensor head design there are great demands on the mechanical design of the photodetector unit. To achieve a resolution of $5.1 \cdot 10^{-7}$ in refractive index one has to reach a position resolution of 0.2 μm . Therefore it was decided to build a hybrid module that incorporates the detector with the preamplifier electronics on a ceramic disc. This leads to a compact and easy reproducible unit

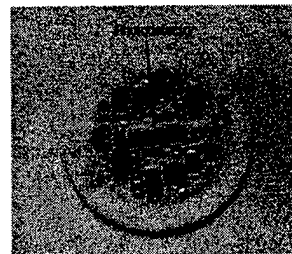


Fig 2: The front side of the photodetector unit.

There are several advantages of this design:

- Fixation of photodetector improved
- Less noise introduction through shorter wiring
- Less space needed
- Easier fixation on optical bench
- Lesser cost by standardization of production
- Better control on heat distribution by using thermal conductive ceramic

This design results in a lower temperature dependence of the complete unit.

E. High speed data acquisition

The high speed data acquisition unit consists of an 4 channel multiplexed, 16 bit A/D converter with 30 kHz sample rate and a PC/104 board for data storage and read out. The parallel port in ESP mode is used for the high speed data transfer from the A/D- converter to the hard disk. Typically one gets 240 Mbyte of data within 2 hours of measurement time. Therefore the integrated Etherlink is used as a fast method to read out the data. Due to the large amount of data the evaluations of the data is done Offline. This unit is put into a separate pressure housing.

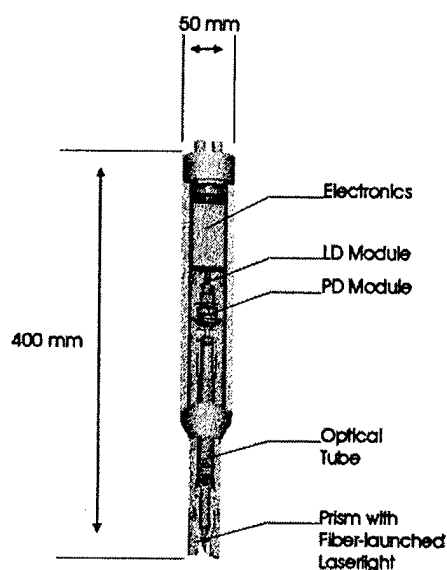


Fig. 3: The outline of the refractometer OPRA

Fig. 3 shows the sensor unit without the separate data acquisition module but including all analog driver and signal conditioning modules.

III. Laboratory tests

The first goal of the laboratory measurements were to determine the resolution and the time behavior of this system. As has been expected the flushing of the sensor head has been improved significantly while at the same time the resolution was comparable to the earlier design ($\Delta n = 6 \cdot 10^{-7}$)

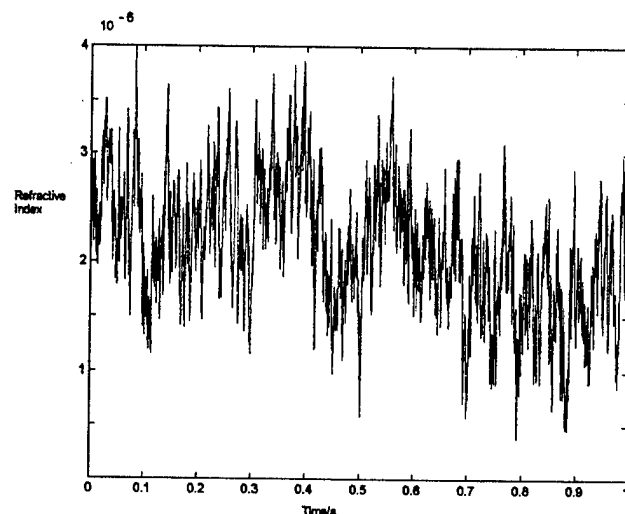


Fig.5: Resolution in refractive index units at 1 KHz sample rate

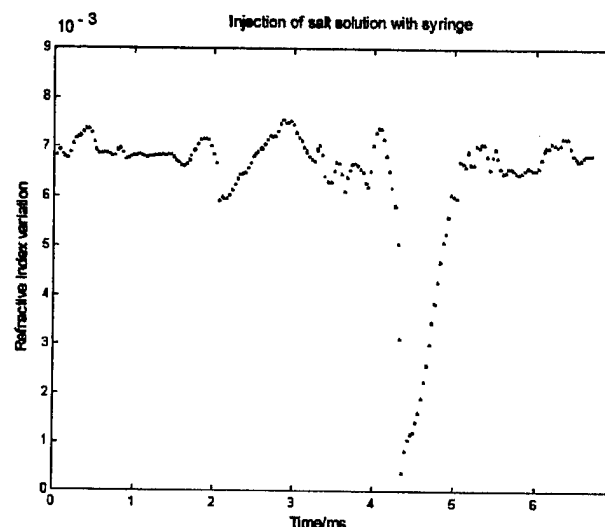


Fig.6: Test of time response by injected a salt solution into the measuring volume

Furthermore for the planned in situ tests a calibration measurement was done. For this purpose one of the temperature calibration tanks of the Institut für Meereskunde, Kiel was used. It had a volume of 80 l and a homogeneity of better than 0.01 K. The accuracy of the temperature measurement was 0.01 K (Pt-100 sensor with ASL Kelvimat indicator instrument). This allows an accuracy of the refractive index measurement of $1 \cdot 10^{-6}$. To translate this to a density variation one has to multiply by approximately a factor of 3 [3]. A FP07 fast thermistor tip was brought into close proximity to the refractive index sensor head. This allows for estimating the temperature homogeneity of the bath as well as a supporting measurement of the reproducibility of the refractometer. The result of this measurement is shown in Fig 6. The overall change in density produced by heating up and cooling down the bath was about $1.8 \cdot 10^{-3}$. The deviations between the density calculated from

the temperature data compared to the density calculated from the refractive index data is displayed as a difference expressed in density units. This measurement proves that the reproducibility of the sensor is $2 \cdot 10^{-6}$ in refractive index and $6 \cdot 10^{-6}$ in density.

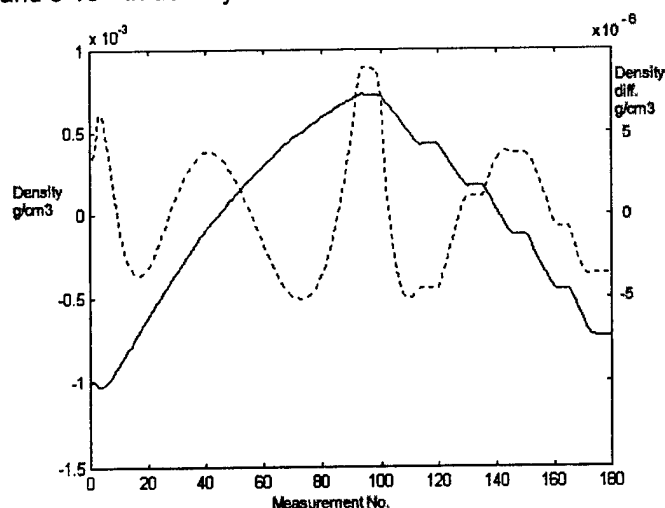


Fig.6: Reproducibility measurement in temperature controlled bath

Due to the large amount of data the results of the evaluation of the field measurements will be presented during the conference.

IV. Conclusions

The further development of the in situ going refractometer OPRA has lead to a significant improvement in the dynamical properties of the sensor. At the same time the improvement of decisive modules of the systems brings a commercial production closer to realization.

V. Acknowledgment

This work has been supported by the Senator für Umwelt of the City of Bremen. The support is gratefully acknowledged. I am indebted to J. Langhof of the Institut für Meereskunde, Kiel, who is in charge of the CTD-calibration. His competent support in preparing the calibration measurements has been of great help.

REFERENCES

- [1] K.-H. Mahrt, H.-C. Waidmann, "Field proven high speed micro optical density profiler sampling 1000 times per second with 10^{-6} precision," *OCEANS88*, IEEE publ. no. 88CH2585-8, Baltimore MD, p. 497-504, 1988
- [2] K.-H. Mahrt, H.-C. Waldmann, "Extrinsic fiber optical point refractometer for top to bottom optical density profiling in the ocean with 10^{-6} precision," *Oceanology International*, Brighton (UK), 1990
- [3] R. C. Millard, G. Seaver, "An index of refraction algorithm for seawater over temperature, pressure, salinity and wavelength", *Deep Sea Research*, vol. 37, No. 12, 1990
- [4] H.-C. Waldmann, S. Thiele, "Results of the dynamical tests of a special designed optical microstructure density probe based on the measurement of the refractive index", *OCEANS96*, IEEE publ, Ft. Lauderdale, FL, 1996

Location and Recovery of Lost Instruments Using Acoustic Targets

Archie T. Morrison 111^{1,2} and Albert J. Williams 3rd²

¹McLane Research Laboratories, Inc.
Falmouth Technology Park
121 Bernard E. Saint Jean Drive
East Falmouth, MA 02536 USA

²Department of Applied Ocean Physics
and Engineering, Bigelow I 10, MS 12
Woods Hole Oceanographic Institution
Woods Hole, MA 02543 USA

Abstract - Despite the increasingly reliable techniques and technologies developed by the oceanographic community, the all too frequent failures of instruments and moorings to surface on command remains a problem. The loss of both equipment and data is costly to the community. In our experience, the effort to locate and recover lost equipment, even in shallow water, has often been futile and costly. In this paper we describe a low-tech, approach that we have developed and used to recover two lost instruments. Our approach utilizes passive acoustic targets, side scan sonar, and divers. A large research vessel is not required, the targets can be readily manufactured from stock material, and, in deeper waters, ROVs can replace the divers.

I. BACKGROUND

In 1994 we were involved in several overlapping research programs taking place off the Outer Banks of North Carolina. We had deployed a large (6m), instrumented BASS (Benthic Acoustic Stress Sensor) tripod in 20m of water approximately 5km offshore of the Army Corps of Engineers Research Facility in Duck, NC. Colleagues had deployed a bottom mounted ADCP (Acoustic Doppler Current Profiler) in a 3mx2mx1m trawl resistant frame a further 10km offshore in 25m of water. The ADCP system was a one of a kind prototype. The cost to replace either instrument was approximately \$100,000 (US).

The BASS tripod was equipped with two independent recovery systems. Each system employed a bum wire to release a rigid float string on receipt of a coded acoustic command. The floats carried lift lines to the surface that could be used to recover the tripod. The ADCP frame included compressed air cylinders and inflatable lift bags that could raise the entire platform to the surface for recovery. Bag inflation was triggered acoustically by sending a signal to a commercial release. Triggering the release freed a heavy spring, mounted in a plastic tube, to open a valve and inflate the bag.

During the first of several recovery cruises for the tripod, both recovery systems were triggered multiple times. Neither float string appeared on the surface. This may be a familiar

scenario to more than one reader. The authors dove on the known GPS position of the instrument and swept out a portion of a 30m (radius) circle around an anchor pivot before dwindling air supplies forced the abandonment of the search.

On a subsequent cruise, several hours after multiple acoustic triggers were sent, one float reached the surface at dusk. Recovery was postponed until morning because of deteriorating visibility. By morning the float had vanished and one of us (Morrison) and a colleague again dove on the GPS position, sweeping out another circular search pattern with a rope. Dwindling air supplies again forced the abandonment of the search.

Attempts to improve on the GPS position by triggering the release mechanism's transponder with a pinger on the ship's inflatable, while triangulating on the response at the research vessel, failed because of uncontrolled ship drift. Detection with the vessel's depth sounder was similarly unsuccessful. We chose to forego the use of a grapple, because of the difficulty involved and the risk of damage to the equipment.

The ADCP suffered a similar, if somewhat less dramatic, fate. While the acoustic release was responsive to the deck unit, the platform did not return to the surface after multiple attempts. No divers were present on the cruise and no immediate search or follow-up recovery cruises were conducted.

II. UNDERSTANDING THE PROBLEM

After the frustrating failed attempts to recover the tripod in 20m of water we came to the realization that the problem was not so much the localization of the equipment nor its physical recovery, but the link between those operations. Put another way, we were unable to translate the information we had at the surface to information useful to divers on the bottom. Bottom time is limited and can easily be exhausted if it is necessary to search even a small area.

Consider that the GPS position of the tripod was fairly well established, optical visibility while diving was as high as 3m to 4m, the bottom was sand and mud, free of growth and rocks, and the depth was well inside diver limits. We dove several times from ships of opportunity and searched large circles, pivoting around an anchor with a sweep line. The anchor was placed from the ship based on the GPS position. Yet, although

we knew almost precisely where the tripod lay (localization), we were unable to attach a lift line (recovery).

At face value the situation seemed absurdly simple, thus our frustration. The tripod was only 20m down and we had a GPS fix from the deployment. Recovery should have been a straightforward exercise, yet we were unable to even find the equipment. Of course, those readers with long experience will recognize and appreciate the actual difficulty of this seemingly simple task.

More realistically, the actual accuracy of the original differential GPS fix, acquired when the tripod was deployed, was inherently no better than 10m; the reference station for the differential signal was more than 30km away. The error was probably larger given the distance and variable bearing from the GPS antenna to the launch point on the starboard side of the vessel. Further error was introduced by the time difference between the GPS fix logged on the bridge and the actual release of the tripod from the crane. Similar errors are associated with the placement of the pivot anchor.

Diver disorientation and drift, ship's drift, and the finite time between location fixes and diver actions, while trying to carry the imprecise surface information to the bottom, also contribute, particularly if the divers place the pivot. For example, during one brief dive in these waters one of us (Morrison) and a diving safety officer entered 20m of water directly from the starboard side of a moderately large research vessel. They descended straight 'to the bottom to compare some gauges with the ship's depth sounder. They ascended "straight" to the surface less than five minutes later, approximately 500m from the port side of the vessel. The larger the area that has to be searched, the more unlikely it is that divers with limited-bottom time will be able to complete the search. The reliability and repeatability of such a search is also in question.

The critical points to be made here are, first, that surface information is probably not as precise as we would like to believe. Second, and more importantly, even with precise surface knowledge, the problem of transferring that knowledge to a bottom system that could then reliably attach a lift line remains. The search burden placed on the bottom system has to be reduced to some realistic level. Note that all of these problems exist, in varying degrees, if GPS is replaced by ship mounted or towed sonar or if the divers are replaced by ROVs or grapples.

Obviously both problems could be avoided by using a 'high-tech' search system such as an ROV or manned submersible with its own sonar and possibly an acoustic navigation network on the bottom. However, the cost of such a system, particularly compared to the cost of the lost instrument, is often prohibitive. This was certainly so in our case. After the first recovery attempt failed we were essentially dependent on ships of opportunity to pursue our recovery efforts.

We needed a system based on inexpensive and readily

available or easily manufactured components that could realistically address the localization and linkage problems as outlined above.

A portable, towed, side scan system was available, at nominal cost, from a pool of instruments maintained by the Coastal Research Center (CRL) of the Woods Hole Oceanographic Institution (WHOI). The side scan could almost certainly locate the instrument, but that position information was relative to the tow fish. The position of the fish relative to the ship at any given moment would not be well known. Side scan alone would provide little or no improvement over the GPS information, which we already knew to be inadequate.

However, by using acoustic targets in conjunction with the side scan we were able to solve both problems.

III. LOCALIZATION AND LINKAGE WITH ACOUSTIC TARGETS

Our method uses a pair of sonar reflecting anchors, each attached to a surface float by a light line sized for minimal scope. The anchors were fabricated in the WHOI welding shop from 3/8" mild steel plate. One of the anchors is shown on the deck of the recovery vessel in Fig. 1. The anchors are the acoustic equivalent of the corner-cube radar reflectors found on most small and large vessels. Geometrically they are simply the top half of such a reflector.

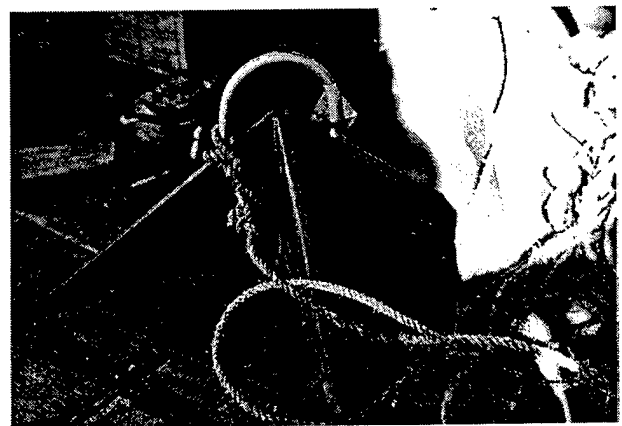


Fig. 1: SONAR REFLECTING ANCHOR - The material is 3/8" mild steel plate. The anchors are approximately 40cm along each side and 21cm tall at the peak below the lift point. Each one weighs 48lbs (22kg). The dimensions reflect a balance between signal return strength and directionality.

We chose the dimensions with attention to several competing factors. Maximizing the strength of the return echo makes the anchors easier to image and is therefore desirable. Increasing the size of the reflector increases the echo strength, but it also increases the directionality or focus of the echo beam. This is simply a result of the antenna equation, which says main lobe width decreases

with increasing aperture [1]. The practical consideration here is manufacturing tolerance; if the focus is narrow and the planes of the reflector are not orthogonal, the return echo will miss or only graze the transducer on the tow fish. This would reduce the strength of the return echo and make it difficult to detect at any distance, just as the wide, weak return of a small target would be difficult to detect. The anchor also needs to be sized for handling.

The sonar could be operated at either 100KHz or 500KHz, acoustic wavelengths of 1.5cm and 0.3cm. Patently only a reflector that was "many" wavelengths wide would provide sufficient signal return strength to stand out clearly on the sonar record. Therefore the angles between the planes of the anchor would have to be fairly precise. The WHOI welding shop was able to manufacture both anchors in the space of a few hours to an angular precision better than 1^0 . In practice we found that the anchors were clearly visible at both 100KHz and 500KHz. However, they were easier to distinguish from natural objects (e.g., rocks) at 500KHz. At the higher frequency the return echo was more focused and produced a clear hyperbola on the side scan record, a characteristic of a strong point source [1]. (As the tow fish travels in a straight line past a point target, the finite angular width of the main lobe, oriented at a right angle to the line of travel, passes over the target. The slant range from the transducer is largest when the edge of the main lobe first encounters the target. The range decreases to a minimum as the center of the main lobe paints the target and then increases again. The geometry is such that the range curve is a hyperbola. Distributed targets, such as our tripod, do not generally exhibit an obvious curve because of the interference of returns from several different parts of the structure.)

Using the anchors to locate and recover a lost instrument is an iterative process. An initial side scan tow past the site images the lost equipment and produces a rough GPS position. That position is obtained by estimating (guessing) the location of the tow fish relative to the ship's antenna. That offset is combined with the measured side scan range offset and applied to the GPS fix obtained as the instrument was imaged. Accuracy of a few tens of meters is sufficient, although increased accuracy will shorten the process. If desired, the GPS to tow fish offset can be measured by making side scan passes in opposite directions and differencing. In practice, we did not find this to be necessary. In either case, estimation is easier if the side scan passes are made along north-south or east-west tracks.

Proceed to the estimated GPS position and deploy one of the anchors. A second side scan pass will now show both the instrument and the first anchor. The location of the instrument is now known relative to the anchor and the divers can reach the anchor simply by following the line from the surface float. Significantly, this relative error is completely

independent of all the previous localization errors. In fact, the absolute and relative locations of the ship, the GPS antenna, the tow fish, and the instrument are no longer relevant.

Now use the offset between the first anchor and the instrument, as measured by the side scan, to make a relative placement of the second anchor. The placement is simply done by hand and eye relative to the first surface float. Recall that the scope of the line has been kept small. The anchor can be placed from the research vessel, but the process will be faster if the ship's boat can be used.

A further side scan pass will show the instrument and both anchors. The second anchor will presumably be much closer to the instrument. An iterative cycle of leapfrogging anchor movements and side scan passes is then followed until the acoustic images of the instrument and one of the anchors converge. Again, note that the errors making localization difficult have all been rendered harmless. They affected only the "initial guess" that started the iterative process and were irrelevant thereafter.

Finally, divers with a lift line descend to the anchor along the float line, a physical link carrying the now precise surface information provided by the side scan to the divers in a form that is useful at the bottom.

IV. YES, BUT DOES IT WORK?

We applied this approach to the location and recovery of the BASS tripod and the trawl resistant ADCP in early November of 1994. On November 2 we departed Norfolk, VA on board the R/V Cape Hatteras for the transit to the 20m site where the tripod lay. The ship's schedule would allow us only one day on site. We arrived on station at 0400 on November 3 and began operations. Given our inexperience operating side scan sonars, we made several initial passes along both north-south and east-west tracks, imaging the tripod on each pass and estimating the position from the ship's GPS. The positions varied, but all fell inside a circle of radius 50m. We were very fortunate in having a flat, nearly featureless bottom with no other strong targets in the vicinity of the tripod. The multiple passes also allowed us to refine our communication procedures with the bridge as we waited for first light. The refinements improved the timing, and therefore the accuracy, of the GPS fix. Fig. 2 is a copy of the hand annotated side scan record from one of these passes. At dawn we placed the first anchor at $36^{\circ}11.875'N$ $75^{\circ}42.40'W$ from the deck of the R/V Cape Hatteras. We then made another set of side scan passes, trying to image both the tripod and the anchor. These passes were made operating the side scan at 100KHz with a cross track range of 100m to either side. The results were somewhat ambiguous with several false returns. We attribute this entirely to our inexperience. We assumed, incorrectly,

that one of these was the anchor. The eastbound pass is shown in Fig. 3.

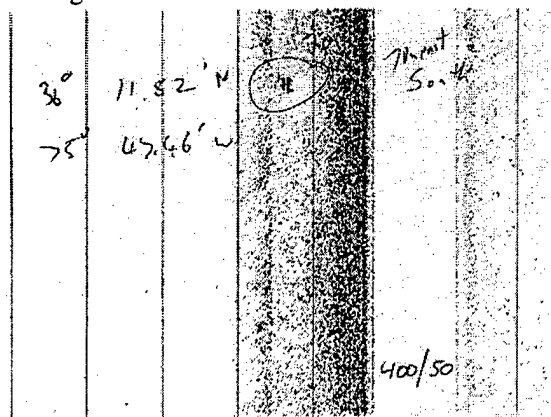


Fig. 2: SIDE SCAN PASS IMAGING THE TRIPOD - This is a copy of the hand annotated side scan record (thermal paper strip chart) of one of the initial imaging passes. The ship was on a southward track (towards the top of the figure). The ship track is centered on the vertical white strip with the "400/50" notation. Sonar returns appear to both the left (port, east) and right (starboard, west) of the track. The 400/50 notation indicates the full-scale range to either side was set to 400m and the distance between range lines was 50m. The range lines are the equally spaced vertical lines to either side of the track. The full extent of the record to left and right is not shown and the cropping was done asymmetrically. The tow fish cable was positioned off the starboard side of the fantail with the crane. Bubbles and turbulence in the wake of the RN Cape Hatteras cause the strong (dark) return on the port side. The tripod is circled and lies ~70m to the east of the ship's track. The GPS position is marked. The strong returns may be from the air filled pressure housings. There were no other strong targets near the tripod.

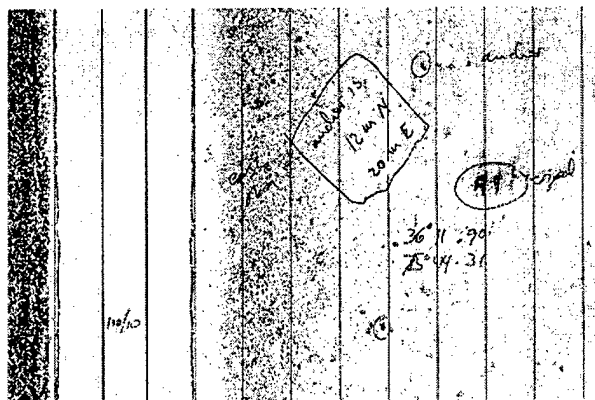


Fig. 3: IMAGING THE TRIPOD AND THE FIRST ANCHOR - The ship is on an eastward track and the range lines are spaced 10m apart. The tripod is circled and labeled. Two false anchor returns are also circled. The one we assumed was the real anchor, 23m ENE of the tripod, is also labeled.

We later determined that the ambiguity arose because the ship track was too far from the targets. Only the tripod was within the 100m range for which the side scan had been set;

none of the returns was the anchor, which was actually about 30m WSW of the tripod.

We placed the second anchor about 20m WSW of the first, judging the distance and direction essentially by eye. This placement was made from the inflatable launch of the RN Cape Hatteras with some assistance from a spotter on the bridge of the larger vessel.

The next side scan pass was made eastbound and closer to the targets. The acoustic frequency was still set at 100KHz, but we had extended the range to 150m on each side of the track line. This pass is shown in Fig. 4.

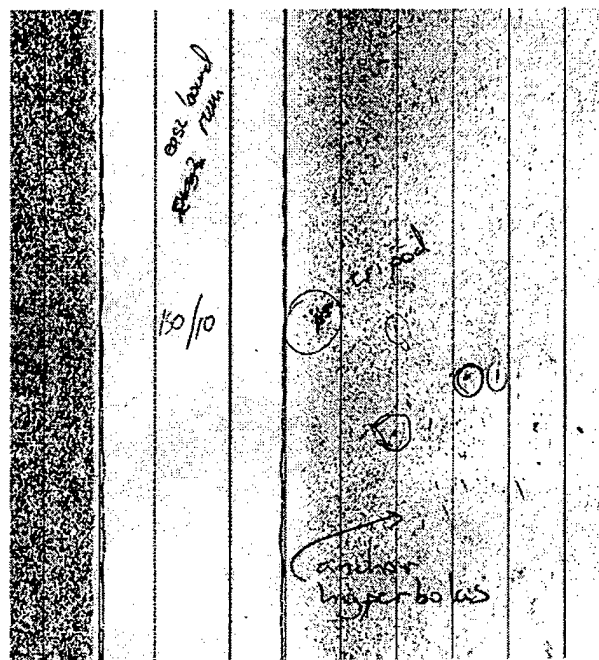


Fig. 4: TRIPOD AND BOTH ANCHORS AT 100KHz - The ship is on an eastward track and the range lines are spaced 10m apart. The tripod is circled and labeled. The anchors are visible SW of the tripod. Note the faintly visible hyperbolas. This time there was no ambiguity about the location.

This time there was no ambiguity about the anchors. Although faint, each anchor produced a clear hyperbola in the side scan record. The anchors were actually SW of the tripod. We changed the side scan frequency to 500KHz, hoping for a clearer picture, and were rewarded on the next pass. The westbound track is shown in Fig. 5. While the anchors are more apparent at this frequency, the tripod is somewhat fainter. There are benefits to having more than one frequency available.

The misplacement of the second anchor was now clear and also easily correctable. It was also apparent that we were learning and improving with practice. Using the inflatable, we moved the second anchor, which was somewhat further from the tripod, using the surface float of the first anchor as a reference. The second anchor was moved to a position approximately 25m NE of the first anchor. Again, this was done by eye from the launch with assistance from a spotter

on the R/V Cape Hatteras. The side scan pass that followed is shown in Fig. 6.

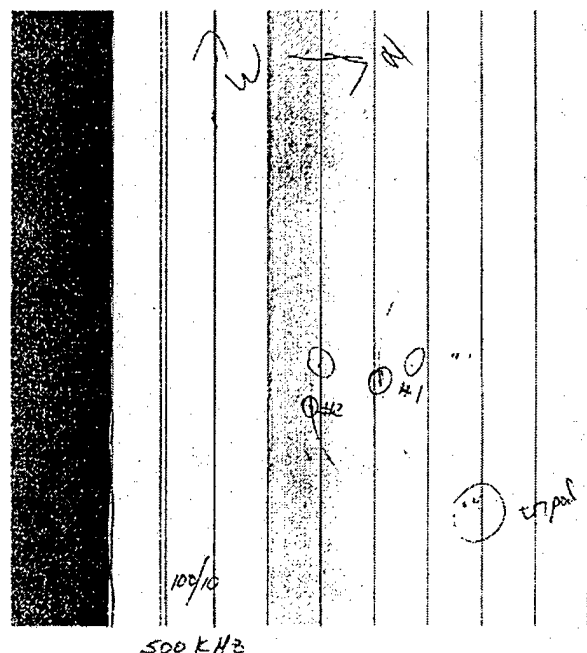


Fig. 5: TRIPOD AND BOTH ANCHORS AT 500KHz - The ship is on a westward track and the range lines are spaced 10m apart. The tripod and anchors are circled and labeled. Note the clear, unambiguous, hyperbolas produced by the echoes from the anchors. Note also that the tripod is fainter at this frequency and that the bubbles in the wake of the ship are brighter.

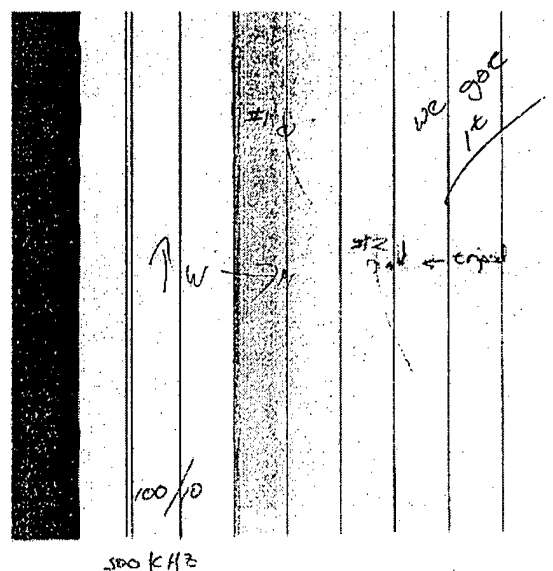


Fig. 6: CONVERGENCE - The ship is on a westward track and the range lines are spaced 10m apart. Both anchors are clearly identified by hyperbolas. The second anchor appears to have converged with the tripod. The notation to the upper right says it all.

The echoes of the second anchor and the tripod had converged, essentially on the first iteration (the first iteration after we figured out what we were doing).

The authors dove from the inflatable, following the line from the surface float down to the second anchor. We trailed a lift line and carried a shackle and a wrench with us. At the bottom the lifting bail of the tripod was easily located only 40cm from the anchor. We attached the lift line and proceeded to inspect the instrument.

The tripod was lying on its side, trapping one of the recovery floats against the bottom. The line from the float that had been seen on the surface during the earlier cruise was present right up to the eyebolt that attached it to the float. The bolt had been sheared cleanly off. We assume the propeller of one of the research vessels then in the area struck it during the night or early in the morning. The float might have been below the surface at that time, pulled under by the drag of the flood tide on the lift line. The cradle from which the float had released was at an angle that might have trapped the float even after the bum wire released it. This was due to the resting position of the fallen tripod. From other angles it could have released cleanly. The right combination of currents, perhaps during a particular direction of tidal flood, could have subsequently freed it. This would explain sighting the float on the surface some hours after the release signals were sent. From other damage to the frame it was apparent that a fishing trawler, or something similar, had struck the tripod and tipped it over.

We ascended the lift line to the inflatable, recovered the anchors, and returned to the R/V Cape Hatteras. From there we recovered the tripod without further difficulty. It was now mid morning on November 3, less than six hours after our early morning arrival on station.

The transit to the 25m site, 10km distant, occupied the next hour. The recovery of the ADCP can only be described as a text book example of this approach. We located the instrument on the first pass, based on the GPS position from the deployment cruise. We used the 100KHz acoustic frequency and a large cross-track range. The ADCP, like the tripod, was a stronger target at the longer wavelength. The extended range improved the chance of imaging the target. We placed the first anchor and achieved convergence in two iterative steps. The divers located the ADCP about 1m from the anchor and attached a lift line. The instrument was recovered without farther difficulty.

Examination showed that several fittings in the inflation lines had pinhole leaks due to localized corrosion. This may have been due to spot impurities in the brass. By the time the release was triggered there was no air left in the system. The release itself had fired, but bivalve larvae and a considerable sediment load had settled inside the spring tube. The larvae had grown larger and had developed hard shells over the months of the deployment, jamming the spring and preventing it from turning the inflation valve.

With both instruments secured on deck we headed towards Beaufort, NC, the R/V Cape Hatteras' home port, and broke for lunch. It was 1300 on November 3. We had trained ourselves in the technique, located the targets at sites 10km apart, attached lift lines, and recovered both instruments in less than nine hours.

V. OBSERVATIONS AND LESSONS LEARNED

Several caveats and observations are in order here. We were more than a little fortunate to have lost the tripod and the ADCP in such uncluttered terrain. The nearly complete absence of strong false returns aided us significantly and we freely concede that the recovery cruise would probably not have been as smooth or as successful if the bottom morphology had been more complex. However, that does not mean this method is inappropriate over more complex terrain, only that a more experienced side scan operator may be required to separate the true targets from the false in the record.

It should be noted that, while we were working in favorable terrain, we had no prior experience operating side scan sonars or interpreting their output. Further, we had no prior experience applying the new approach. We were still completely successful. Note as well that there are a number of active, shallow water experimental programs intentionally located in uncomplicated terrain. There will be lost instruments to recover from similar circumstances in the future.

The addition of a passive reflector to an instrument package would greatly improve its visibility at minimal cost. The reflector would be particularly helpful in cluttered terrain because the target, like the anchors, would stand out from other targets by exhibiting a hyperbola in the sonar return.

This approach would probably be difficult to apply in continental slope and deeper waters. In those cases remedies involving more costly, sonar equipped ROVs or manned submersibles may be necessary. However, we think our approach will suffice for continental shelf waters, with low-cost, video-only ROVs replacing divers below 40m depth. Placing anchors on either side of a target instrument might also facilitate grappling since the surface floats could provide some terminal guidance to the vessel.

Lost instrument recovery is not an inexpensive operation and those costs need to be weighed against the potential benefits. One obvious cost associated with our approach is the side scan sonar. Side scan systems are readily available today. Some portable units can be purchased for as little as \$10,000 (US). Units are also available for rent. Even the fairly advanced unit we had access to could be operated successfully, at least at a basic level, with relatively little training and experience.

Another obvious cost is ship time, which varies depending on the situation and requirements of the recovery. Our

approach reduces search time, making much more efficient use of the research vessel. It is also quite easy to operate the side scan system from a small boat. We were able to run it successfully from a 25' dive boat charter at one point. All of the work of locating the target and attaching a lift line and marker could be accomplished from such a craft very inexpensively. A large research vessel would only be required for the actual recovery, a relatively fast operation when lift lines are already in place.

There are several important benefits to recovering a lost instrument. First there is the instrument itself, which is generally expensive and often irreplaceable. Then there is the data set, which can be enormously valuable and can never be replaced if lost.

A more subtle benefit, one with long term ramifications for future instruments, is the knowledge gained about the mode of failure. In the case of the ADCP, a prototype, our colleagues were able to identify the weaknesses in their recovery system and improve their design. This will prevent multiple expensive losses in the future. We have added greater redundancy to our recovery system, with an improved float system that is generally not dragged under water by currents and that can release cleanly from the tripod over a much greater range of angles [2]. This approach has already saved us from undertaking several search and recovery cruises.

Finally, we do not wish to claim that our method is the only answer or even the best answer in all situations. We think it is a good answer and one that we feel confident recommending. The approach falls into the broad category we call "nickel knowledge". Nickel knowledge is the sort of information that is derived from experience and shared among practitioners, often simply by word of mouth. It is seldom codified in a textbook, but once learned it can make a job easier or more likely to be successful. Oceanographic engineering is a field particularly rife with nickel knowledge. This is just one more piece.

ACKNOWLEDGMENTS

Our thanks to the other divers, Fred Thwaites, Steve Liberatore, Alan Hinton, Lisa Garland, and Woody Sutherland. Thanks also to Allan Gordon of WHOI, the WHOI Welding Shop, and the crew of the R/V Cape Hatteras.

REFERENCES

- [1] Mazel C, *Side Scan Sonar Training Manual*, Klein Associates, Inc., Klein Drive, Salem, NH 03079, USA, 1985.
- [2] Williams, A. J., 3rd, Morrison, A. T., III, "Shallow Water Messenger-Line Recovery System", *Proceedings OCEANS '96, MTS/IEEE/OES*, September 1995, Vol. 11, pp. 646-649.

PRECISE HEADING AND DGPS MEASUREMENTS OF VESSEL MOTION IMPROVE VM-ADCP CURRENT MEASUREMENTS SIGNIFICANTLY

John-Morten Godhavn^{\$} and Pierre Jaccard[&]

^{\$}Navia Maritime AS, Division Seatex, Pirsenteret, 7462 Trondheim, Norway

[&]Geophysical Institute, University of Bergen, 5007 Bergen, Norway.

Abstract

This paper describes how Vessel Mounted Acoustic Doppler Current Profiler (VM-ADCP) measurements are improved when accurate navigation data are available. Quality of vessel velocity, position and attitude are required for determining absolute current measurements. While the ship's position and attitude data are necessary to transform measurements made in the vessel fixed coordinate system into Earth fixed coordinates, vessel speed is required for correcting measured acoustic velocities. Experimental data presented in this paper result from a narrowband ADCP interfaced with the accurate integrated navigation system Seapath. Seapath integrates strapdown inertial motion sensor technology with satellite position measurement technology (GPS). Several comparison tests have been carried out to verify improved current measurements obtained with an ADCP-Seapath system.

I. INTRODUCTION

Acoustic Doppler Current Profilers (ADCP) measure Doppler frequency shift from reflected acoustic pulses. Reflections occurring mainly on passive particles, this shift can be used to resolve water current profiles. Applications in which ADCP instruments are used include oceanography, hydrology, circulation modeling, and both open and closed channel discharge measurements.

When mounted on a vessel (VM-ADCP), ocean currents are measured relative to a reference system moving along with the vessel. If the vessel's navigation parameters are known, one can compensate for this motion in software to resolve absolute current velocities. However, good quality data rely on an accurate navigation system providing position and velocity measurements relative to an Earth fixed frame as well as attitude, i.e. heading, roll and pitch, to compensate for changes of instrument orientation.

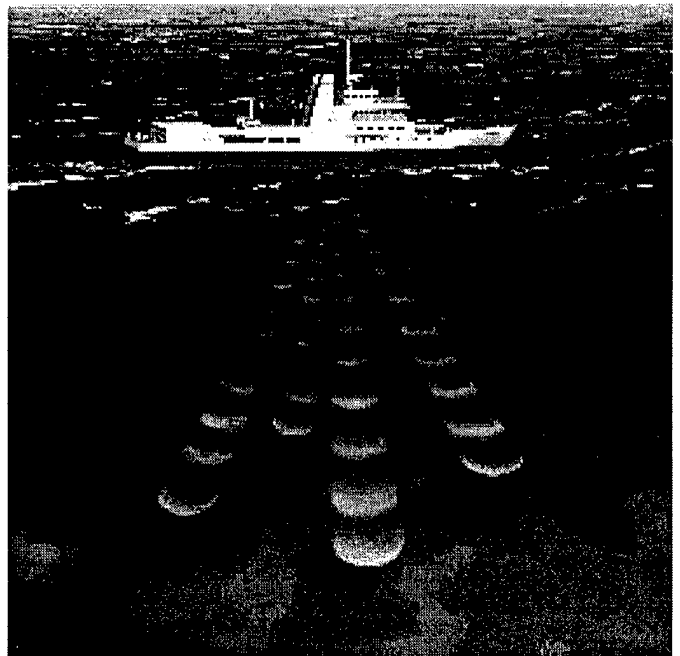


Figure 1: ADCP survey

Typically, VM-ADCP consists of four beams, their directions varying with the ship's orientation. If not compensated for, oscillations in roll and pitch due to vessel wave motion will be seen in the measured data. Averaging of measurements over a period of time reduces these errors. However, precise heading, roll and pitch data available at a high rate are important for measuring ocean currents with high accuracy in rough sea conditions. Accurate heading information is essential to transform measured velocities into an Earth fixed coordinate system. The heading accuracy of a gyro compass is not sufficient for providing high quality ADCP measurements. Another important navigation parameter is vessel velocity. Before DGPS was available, best results were obtained by measuring the vessel velocity from bottom reflections. In such a case, accurate measurements can only be performed where acoustic

pulses can reach the sea floor, that is in shallow areas. Deep-water layers can also be used as reference over deeper waters; however, this technique is less accurate. Differential corrections are necessary to provide sufficiently accurate GPS velocity measurements.

Seapath is a navigation system that integrates inertial technology (gyroscopes and accelerometers) with differential GPS. The result is precise navigation data with high update rate (100 Hz). A carrier phase solution for heading with two antennas combined with gyroscope measurements gives a very accurate heading. Precise measurements of attitude and vertical motion (heave) are also available from Seapath.

Seapath navigation measurements can be entered into the ADCP for compensation of ship motion. The result is high quality profiles. This integration of VM-ADCP and Seapath has been tested on board R/V Håkon Mosby in the Norwegian Sea since early 1998. A Seapath 200 has been installed and interfaced to the ADCP in order to provide navigation data to the underlying electronics. Technical comparisons of ADCP measurements with and without Seapath 200 were carried out. Significant improvements with Seapath 200 navigation data were qualified.

Section II presents an overview of ADCP technology. Section III presents an overview of Seapath 200 technology and in Section IV the improvements of integrating VM-ADCP with Seapath are discussed. Comparison tests from sea trials in the Norwegian Sea are discussed in Section V. The paper ends with a few concluding remarks in Section VI.

II. ADCP

An ADCP is a profile current meter. It measures speed-through-water, i.e. the speed of the water relative to the speed of the vessel (for VM-ADCP) the ADCP instrument is mounted on. Its predecessor was the Doppler speed log that measures the speed of ships through the water or over the sea bottom at shallow waters. A redesign of the speed log to measure more accurate velocity over a depth profile resulted in the first VM-ADCP in the 1970s. ADCP technology developed further in the 1980s with different ADCP models (self-contained, vessel mounted, and direct reading). Doppler signal processing has evolved over the years. Relatively simple processing algorithms with phase locked loops have been used in speed logs. RDI [5] developed in their first generation of ADCP a narrow-bandwidth, single-pulse, autocorrelation method. RDI began shipping its first production prototype Broadband ADCPs in 1991. Broadband ADCP is an even more accurate method that enables ADCPs to take advantage of the full signal bandwidth available for measuring velocity. The result with 100 times as much bandwidth is velocity

measurements with 10 times better accuracy than with narrowband ADCP. The accuracy of the current velocity measurements is typically a few centimeters/second. ADCP is now a standard, indispensable oceanographic instrument.

The Doppler shift is a change of frequency of a sound wave when reflected from an object moving with a relative speed to the sound source. ADCPs use the Doppler effect by transmitting sound at a fixed frequency and listening to echoes returned from scatterers present in the water (small particles or zoo-plankton). It is assumed that these particles, in average, move with the same horizontal velocity as the water.

Narrowband ADCPs measure frequency shifts of single sound pulses. Broadband ADCPs measure phase shift of multiple echoes, i.e. over a broad range of frequencies. Each broadband sound pulse contains many shorter coded pulses. The phase ambiguity is resolved by autocorrelation methods. Broadband Doppler phase processing is equivalent mathematically to the Doppler shift of frequency.

Depth cells can be compared to single current meters. They are regularly spread in a grid covering the volume that is measured with the ADCP. ADCP gives the average velocity vector over each cell. A weight function is applied, so that the signal in the centre of each diamond shaped cell has more weight. The following data are produced by a broadband ADCP: current velocity in Earth coordinates, echo intensity (depends on sound absorption, beam spreading, transmitted power and scatters), correlation coefficient (depends on data quality), and percent good parameter (depends on correlation coefficient and vertical error velocity). The length and range of the pulses (pings) are limited by the operating frequency. The pulse length determines the minimum cell size. Single-ping random errors are relatively large. Hence, averaging over time is hence necessary to get reliable measurements. Typically an averaging period lasts 5 minutes. During this period, ADCP data are logged along with navigation data. Conversion of ADCP measurements to absolute current velocities are typically performed afterwards with post-processing, but they can also be processed on-line. Systematic errors like bias cannot be removed with averaging. More details about ADCP can be found in the RDI primer [5].

III. SEAPATH 200

The Seapath 200 provides a real-time heading, attitude, position and velocity solution by integrating the best signal characteristics of two technologies: Inertial Measurement Units (IMUs) and the Global Positioning System (GPS). It is a well-proven integrated navigation system used extensively in the offshore and

hydrographic industry. Three standard ship navigation instruments (gyro compass, speed log and GPS receiver) can be replaced by one product (see Figures 2 and 3). Seapath is a stand alone system which does not require data from any other sensors in order to provide accurate navigation data. However, DGPS corrections are required in order to achieve optimal position and velocity performance. True heading is available anywhere on Earth, and the heading accuracy is not a function of the latitude location. There is no scheduled maintenance or calibration needed, which is necessary for both conventional gyro compasses and speed logs. Seapath is robust against GPS dropouts. Accurate dead reckoning navigation is performed with motion measurements up to 20 seconds after loss of GPS data. The accuracy is not affected by vessel turns and maneuvers. Seapath offers flexible configuration of output variables and interface set-up.

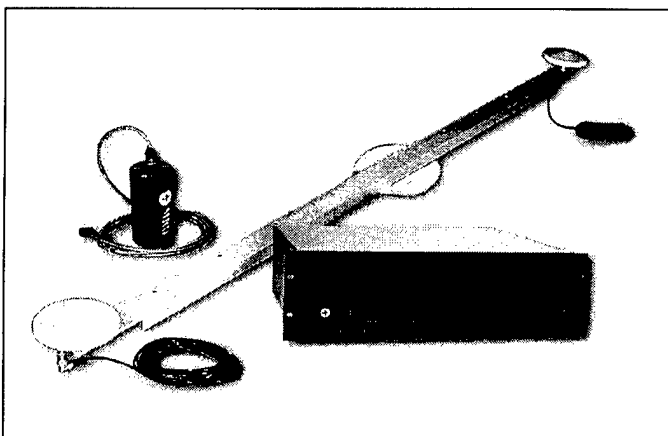


Figure 2: The figure shows the configuration of the integrated navigation system Seapath. An MRU-5, the Motion Reference Unit, is connected to a processing unit containing 2 GPS receivers with antennas mounted 2 - 4 meters apart on a antenna rack.

Standard data formats used by ADCP systems (the RDI data format, NMEA GGA, and others) are available from Seapath. It is easy to operate, install and calibrate. A position accuracy of 1 meter RMS is available with DGPS supported by inertial sensors. Velocity (speed over ground) measurements with an accuracy of 0.03 meters/second are also available. The two antenna GPS heading solution provides heading with an accuracy level (RMS) of 0.05 degrees (with 4 meters antenna separation). The proven and reliable MRU-5 from Seatex is a motion sensor including 3 low-cost rate gyros and 3 military grade linear accelerometers. An MRU can provide accurate measurements (100 Hz) of roll, pitch, and heave. The MRU outputs are used to support the measurements from the GPS receivers between GPS samples (1 Hz) and during GPS dropouts. A Kalman Filter in the Seapath processing unit blends data from GPS and the MRU and outputs all navigation data in real time. The measurements from the MRU are also used to

compute position, velocity, heading and attitude in real time. GPS measurements alone are delayed relative to real time. Data integrity within Seapath is evaluated by monitoring the characteristics of GPS dropouts, the PDOP GPS constellation parameter, and the difference between GPS and MRU measurements. This monitoring is not possible in a single sensor system. The ability to interface and use proprietary differential signals gives Seapath the ability to become a highly accurate positioning tool in its own right. The differential GPS corrections are available worldwide for Seapath. More details about Seapath can be found in the manual [6].

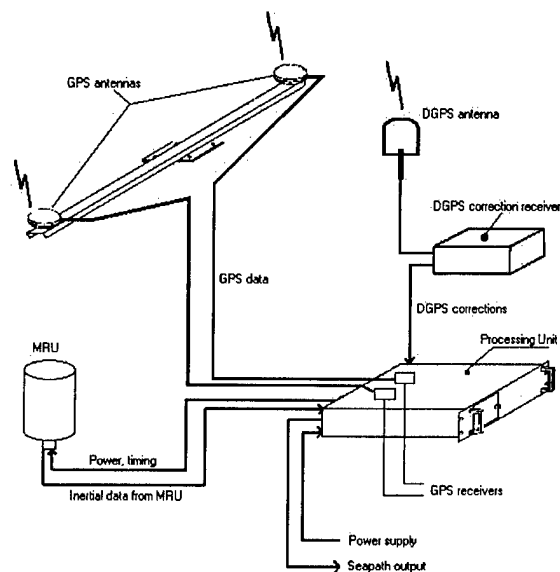


Figure 3: The figure shows the Seapath configuration. Measurements from GPS are sent to a processing unit together with motion data sent from the MRU.

An alternative without a motion sensor to Seapath is a 3-antenna GPS system (see e.g. Griffiths [3]) offering position, velocity, heading, roll, and pitch. However, with this alternative post-processing is necessary, whereas real-time processing is possible when integrated with Seapath. Also, Seapath eliminates long dropout periods currently experienced by attitude GPS users. The vessel velocity measurements are also less accurate and reliable without the motion sensor support that Seapath has.

IV. IMPROVEMENTS

Griffiths et. al. [2] introduced the idea of using multiple GPS antenna phase measurements to compute accurate attitude for ships with ADCP. The importance of accurate heading measurements, i.e. better than possible with a conventional gyro compass, was discussed by Griffiths ([1] and [3]). The following navigation data will improve ADCP measurements:

A. Vessel heading accuracy - gyro vs GPS compass

A gyro compass is the traditional heading sensor on vessels with hull-mounted ADCPs. An alternative is a fluxgate compass. Both these are able to provide heading with about 1 degree RMS accuracy. When rotating the current velocity in ship coordinates to Earth fixed coordinates with a heading error $\Delta\psi$, the horizontal current velocity error Δv is given by

$$\Delta v = u \Delta\psi$$

where u is the velocity of the ship. Hence, crossing a current of the order of 0.30 meters/second with a speed of 8 knots will result in a 12% error in the current measurement if the heading accuracy is not better than 0.5 degrees. The precision obtained by gyro compasses is typically 1-2 degrees in comparison. Heading errors are also introduced with transducer misalignments.

B. Vessel position accuracy: - GPS vs DGPS

Accurate position measurements are required to put the current velocities on the correct position on the map. Also, in some systems, mean ship velocity is computed by the change of position during the averaging period (divided by the length of the period). Then, accurate position measurements are very important in order to compute an accurate mean velocity. The accuracy of DGPS (1 meter RMS) vs non-differential GPS with SA (50 meters RMS) is indeed required to produce high quality VM-ADCP measurements.

C. Vessel speed - Bottom Tracking vs DGPS

The typical Bottom Tracking (BT) accuracy is 0.02-0.05 meters/second. Absolute values of BT velocities are often biased towards even larger values (0.1-0.2 meters/second). BT is restricted to shallow waters. Deepwater layer tracking can also be used, however, this method is less accurate. In comparison will a DGPS Navigation system (NAV) be able to provide vessel speed with an accuracy of 0.03 meters/second, which is independent of environmental conditions at any depth.

D. Vessel Pitch and Roll - Attitude measurements

Reference systems like motion sensors or inclinometers (vertical gyros) can be used to measure the vessel's roll and pitch angles. In Figure 4 the rotations from ship fixed coordinates to Earth fixed coordinates are shown in two steps.

Large ships with small angular motion may not require this information if the weather conditions are good enough. Furthermore, the influence of ship's roll and pitch motion on current measurements is mostly removed by averaging. However, in rough sea with

severe wave conditions, better results can be achieved if each ping is corrected with roll and pitch angles from a motion sensor. Especially will the vertical current velocity accuracy depend more on available roll and pitch measurements than the horizontal velocities do. Kosro [4] reported from a sea trial that horizontal currents were about 0.01 meters/second different when compensating for roll and pitch, whereas the vertical currents were about 0.05 meters/second different.

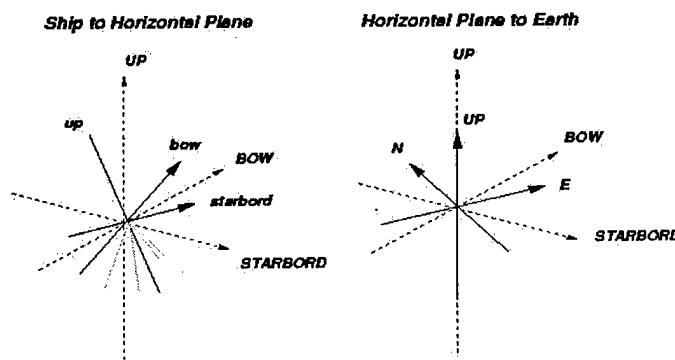


Figure 4: In the first step one rotates with roll and pitch angles from ship fixed coordinates to an horizontal plane (azimuth or heading frame). In the next step one rotates to Earth fixed coordinates (North-East-Down) by the measured heading angle.

E. Timing of signals - Real time vs delayed data

Seapath outputs navigation data at 100 Hz in real time whereas GPS measurements are usually delayed with up to 1 second. Data in real time are important for compensation of ADCP measurements made in rough sea with high vessel dynamics. A high update rate on the navigation data makes it possible to compensate the ADCP measurements with navigation data with the same time stamp.

V. EXPERIMENTAL RESULTS

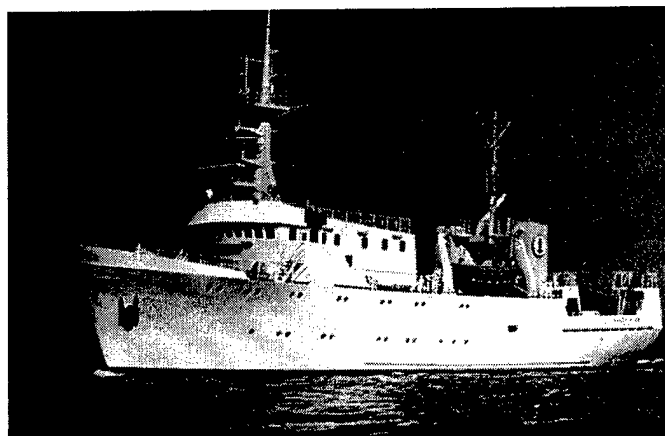


Figure 5: R/V Håkon Mosby

The integration of VM-ADCP and Seapath 200 has been tested on board R/V Håkon Mosby (see Figure 5) in the Norwegian Sea. Tests were carried out during several cruises by Geophysical Institute, University of Bergen, along a line extending from (62°N22', 5°E12'), to (64°N40', 0°E0').

The system consisted of a 150 kHz narrowband ADCP and a Seapath 200. A special interface has been built to transmit attitude parameters from Seapath directly to the ADCP. Data were averaged on 5 minutes interval in 8 meters depth bins ranging from 16 - 450 meters depth.

A. Comparison of gyro compass and Seapath heading

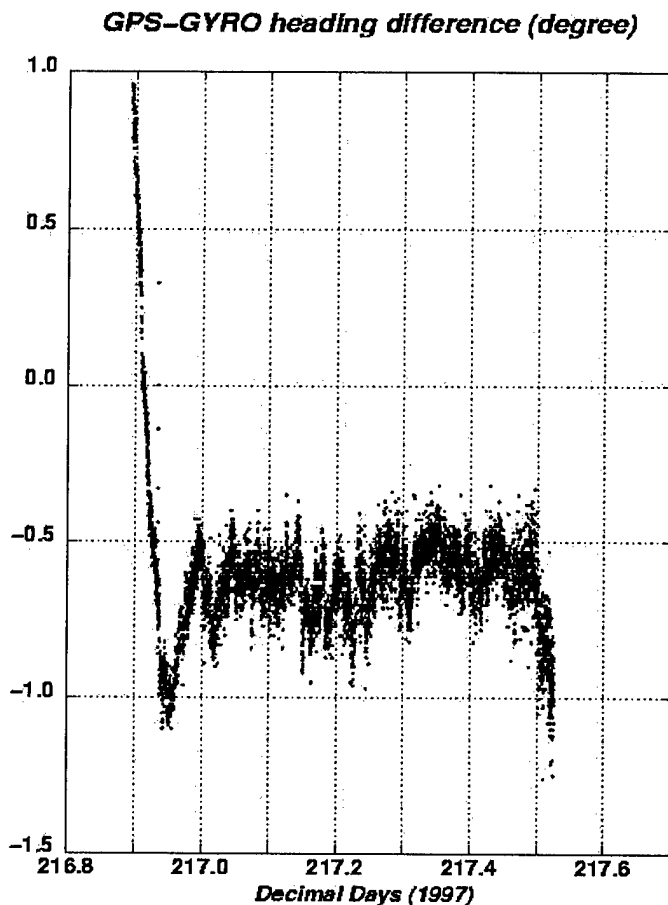


Figure 6: The figure shows the difference between GPS heading from Seapath and a gyro compass. Large gyro compass errors initially reflect the case where the ship makes a turn of 180 degrees.

Even if a gyro compass provides heading information that is sufficient for navigation at sea, it is not sufficiently accurate for transforming measured currents into an Earth fixed coordinate system. Because ADCP data are averaged over a certain time interval, errors due to bad heading are unrecoverable. Another important criterion is the instant availability of heading information. Gyro compasses are subject to oscillations and inertia. This is not the case for Seapath. This is clearly shown in Figure

6, where the gyro compass needs more than one hour to stabilize after a 180 degrees vessel turn.

B. Comparison of bottom tracking and Seapath speed

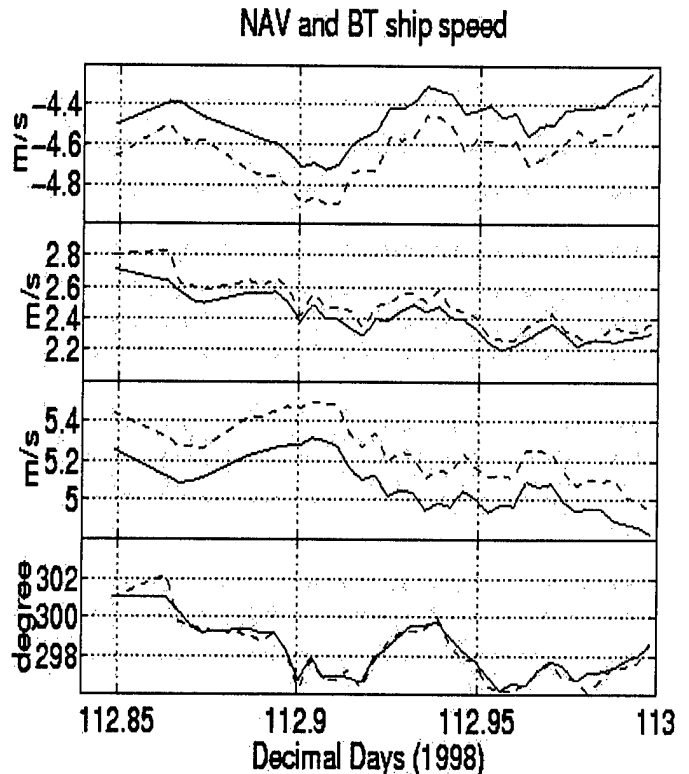


Figure 7: Ship velocity obtained from bottom tracking (BT for dashed line) and navigation (NAV for continuous line) as a function of time. The upper plot shows a comparison of forward velocity (surge) from BT and NAV. The second plot compares sway velocity and the third compares total horizontal speed (magnitude of velocity vector with surge and sway). The lower plot shows a comparison of heading measurements from a gyro compass and Seapath.

Resolving absolute currents from both echoes from bottom and the navigation device showed that ship speed from bottom tracking was always larger in amplitude, but similar in direction (see Figure 7). Absolute currents are obtained by adding the ship's velocity to relative currents. Consequently, if the measured ship speed is too large, the along track component of the measured absolute current will be larger than its true value (see Figure 8). Hence, in the case of the data sets considered here, absolute currents in bottom tracking mode will be rotated towards the ship's course, when compared to those derived from the navigation. Note that differences on absolute currents become larger for weaker currents. Note also that if bottom tracking shall be used as a reference for ship velocity, then the measurements must be calibrated.

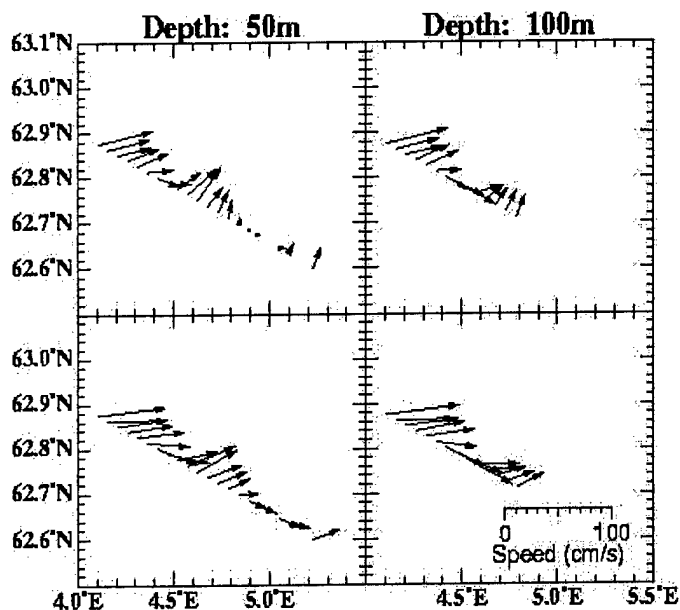


Figure 8: Effect of ship velocity errors on absolute currents. The upper plots show the result with bottom tracking, and the lower plots are ADCP with Seapath as velocity reference.

C. On station measurements

The stability and precision of the Seapath navigation system was tested on station, that is several measurements at the same position, to reveal accuracy and stability. The duration of the measurements was long enough to have a sufficient number of profiles, and short enough to consider the current to be constant. Absolute currents were resolved using information from the navigation device. Because the ship is slightly drifting, the navigation device must be able to sense this change of position in order to measure the same current during each profiling interval. The results are shown in Figure 9 and confirm the good quality navigation data.

V. CONCLUSION

In this paper it has been shown that Seapath navigation data can improve ADCP measurements significantly. Heading errors from gyro compasses being typically up to one degree are too large to provide the accuracy required for high quality VM-ADCP measurements. Using bottom velocity as a reference for the ship speed has the disadvantage of being limited to shallow areas. This is not the case with a navigation system providing an accurate vessel speed independent of vessel dynamics, weather, and depth. Furthermore, availability of accurate ship attitude parameters at a high frequency make it possible to carry out good quality measurements in rough sea conditions, or at a higher ship speed than has been the case before. Seapath offers all the

measurements required to achieve accurate ADCP measurements for all depths and even during bad weather conditions.

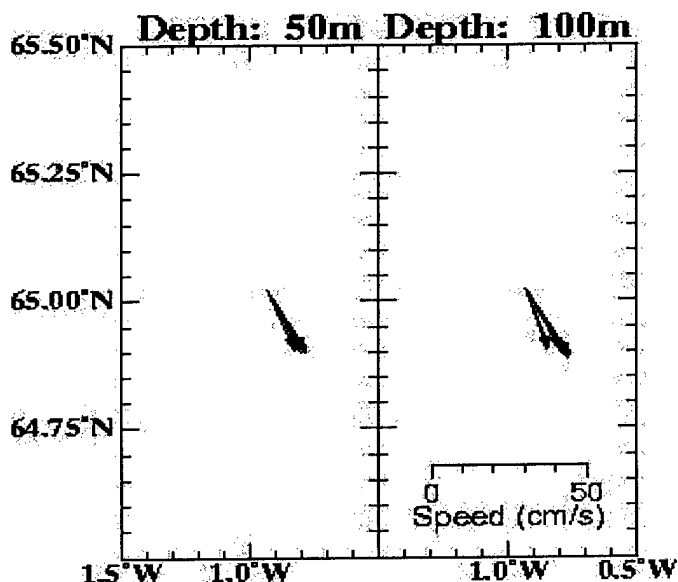


Figure 9: The figure shows absolute currents at different depths using data from Seapath for ship speed corrections of ADCP measurements. Data were collected while the ship was on station. It is seen that the current measurements are stable and reliable.

REFERENCES

- [1] Griffiths, G. (1993), *Improved underway ADCP data quality through precise heading measurement*, IEEE Oceans '93 conference, Victoria, Canada, October 1993. Also in the UK WOCE newsletter, No. 11, 4-5, 1993.
- [2] Griffiths, G., B. A. King, and E. B. Cooper (1994), *Precise measurements of ship's attitude using satellite Navigation*, Electronic Engineering in Oceanography, Sixth International Conference, Cambridge, UK, July 1994. Also in Journal of Naval Science, Vol. 21, No. 2.
- [3] Griffiths, G. (1994), *Using 3D GPS heading for improving underway ADCP data*, J Atmospheric and Oceanic Technology, Vol. 11, No.4, pp 1135-1143.
- [4] Kosro, P.M. (1985), *Shipboard acoustic current profiling during the Coastal Oceanic Dynamics Experiment*. Scripps Institution of Oceanography (SIO) reference 85-8.
- [5] RD Instruments (1996), *Acoustic Doppler Current Profiler, Principles of Operation, A Practical Primer*, 2nd Edition.
- [6] Navia Maritime AS, Division Seatex (1998), *Seapath 200, Product Manuals*.

Performance Data Of A Buoyancy Driven Deep Sea YOYO- Profiler For Long Term Moored Deployment

Christoph Waldmann

MARUM-Center for Marine Environmental Sciences
University of Bremen, Klagenfurter Str., 28359 Bremen, Germany

Abstract— Within the framework of the national funded project DOMEST a deep sea YOYO profiler is to be developed at the University of Bremen, MARUM (Germany). The goal of this system is to take continuous CTD-measurements over a depth range of 500 m above the ocean bottom. The system is designed to withstand a maximum pressure of 400 bar and is supposed to take one profile each day within one year. The system is also well suited to accommodate additional sensors as for example current meters or fluorometers. The basic instrument carrier contains a hydraulic propulsion unit similar to the well known ALACE floats. The hydraulic system is built to produce a buoyancy change of up to 3 kg to enable free profiling motion along a taut mooring line. The electronic unit contains a new PC-based microcontroller that is expected to have a superior performance compared to the well known TATTLETALE systems. The development of a deep sea version calls for a special design of the whole instrument of smallest achievable volume. Therefore the applicability of now pressure housing materials as for example ceramics is going to be tested.

I. Introduction

The aim of ongoing global research programs like GOOS or CLIVAR is to get real time data of relevant ocean parameters and to incorporate these in operational models to forecast the circulation patterns of major current systems. The only tool that presently achieves global coverage is satellite remote sensing. To obtain the necessary data for the modeling process these measurements of ocean surface parameters have to be complemented by subsurface measurements as for example with data from fixed buoy arrays. The success of the TOGA/TAO array to predict the occurrence and the intensity of the EL NINO events shows the importance and practicability of this concept. Therefore one should look at possibilities to extend the scope of continuous subsurface measurements to other areas of the ocean and also to the full water column. At this point it is necessary to reconsider current methods and develop new

methods that deliver data from greater depths and of higher quality than current available techniques. The development of floats like ALACE and derivatives like PALACE or PROVOR gives the due for an innovative approach to subsurface measurements. They are built for long term deployment and are well suited for profiling measurements of the water column. The main drawback of these profiler's are that their usage is ruled out in areas of high currents, as for example the Antarctic Circumpolar Current. In those areas moored profilers are more advantageous and they use could be supplemented by the deployment of free floating profilers. Basically the technology of floats can be as well used for moored profilers. Additionally the development of moored systems has to take into account that more energy is needed to move the carrier along the mooring line due to friction and the action of strong currents. The two basic design criteria are to optimize the energy usage and to enhance the overall reliability of the system.

Moored profiling systems has been well known as a method to obtain upper-ocean time-series data since the '70s. (van Leer et al. [4], 1974, Eriksen et al [3]. 1982). Recently there has been several efforts to extend the depth range of these instruments from 1000 m (Provost et al.[2], 1996) down to full ocean depth (Doherty et al [5]., 1998). The main advantage of these instruments lies in the fact that with one set of sensors the predetermined depth range can be continuously sampled. This allows for a better spatial resolution of the measurements compared to fixed instrument chains with a separation of about 50 m, as they are used with fixed buoy stations (TOGA/TAO or PIRATA arrays). Additionally with multiple sensors the drift and the offsets of the individual sensors are unknown so that interpolated profiles from fixed sensor chains are questionable. Therefore employing a single profiling instrument carder will allow new insight in the study of mixing processes in the sea.

The development of the described profiler is part of a national funded project called DOMEST ([6],[7]). This project aims at designing a communication network from underwater stations to achieve real time data transmission from deployed instruments to the laboratory. The complete system is essential for the usefulness of the profiler as complementary observational tool for satellite measurements.

II. Technical description of the developed system

The development of the current deep sea profiler (DOP Deep Ocean Profiler) is based on experiences that has been collected with a shallow water system developed by the University of Copenhagen called TRAMP [1]. The system has been designed as a pure instrument carrier to incorporate multiple sensors. The deep sea version has been modified in some mechanical and electrical aspects but the basic principle is the same. It is a buoyancy driven system that consist of two tubes containing the hydraulic and the electronic unit. (See Fig. 1) By using two tubes it is possible to balance the weight distribution of the system so that it does not move tilted. The hydraulic system is a closed system where oil is pumped back and forth between an external and an internal bladder. The system in its basic test configuration is completely autonomous. The profiler contains a battery pack and all data are stored on a hard disk. These can be read out after recovery via a serial interface.

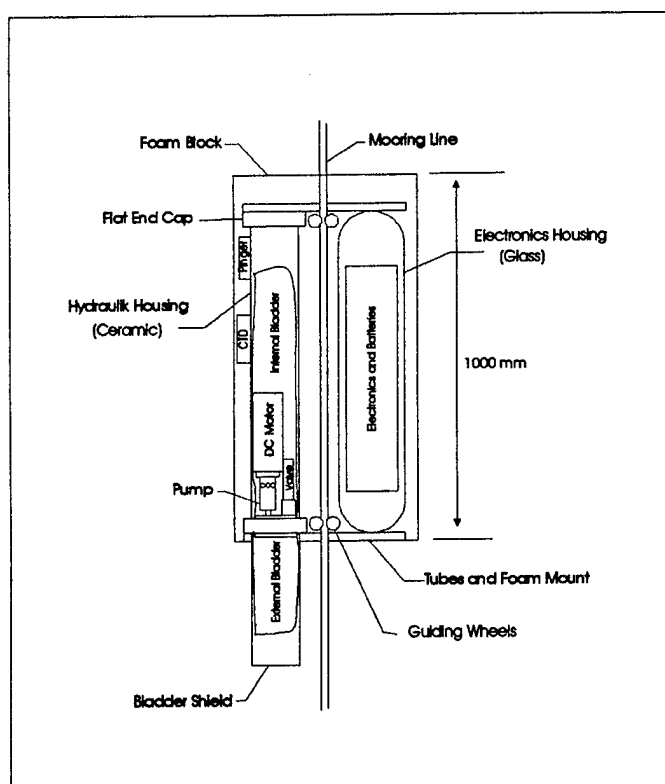


Fig. 1: Basic Elements of the realized Deep Ocean Profiler DOP

In the development phase of the deep sea profiler several items have been reconsidered:

A. Buoyancy control

It has been considered to use a piston type of buoyancy control. This allows for a simpler mechanical design of the

hydraulic unit. But this concept calls for extra volume that has to be hold out. The other problem is that the piston pushes out the oil to fast even if one uses a gear unit. As it is disadvantageous for batteries to deliver large amount of energy in a short time and the gear box takes a lot away of the overall efficiency this idea has not been pursued. With a special pump it is possible to pump small amounts of fluid against a large pressure gradient. At the same time the pump rotation speed fits perfectly with the optimum motor rotation rate. Therefore there is no gear box needed and we end up with an efficiency of the pump system including the electric motor of about 60 %. The calculated efficiency agrees very well with measurements that has been taken in our large pressure tank facility. The pump used has a pump rate of 0.15 l/min and works up to 1000 bar.

B. Energy calculation:

The most part of the needed energy is spent for the pumping process. Therefore to give an estimate of the needed energy the following numbers apply:

Pressure: 400 bar
 Pumped Volume : 3 l → 33 Wh
 Energy content of a Lithium- Batterypack
 Weight 15 kg
 Volume 8 l → 3000 Wh
 Total No. of Profiles achievable → 90

For this application a depth range of 500 m at a minimum depth of 3500 m is necessary. To make the most out of the energy it would be advantageous to pressurize the system with an inside pressure of at least 300 bar. With this prepressure the number of profiles would increase by a factor of 4.

The aim of the development is to have a system of 1001 (100 kg air weight) including CTD- probe and current meter. With a pumped volume of 3 l and an average density gradient of 0.004 kg/m³ per meter depth change one could achieve a maximum speed of 50 cm/s and a depth range of 7600 m.

C. Pressure Housing

To achieve the best performance and handling of the system it is necessary to evaluate different materials according to their weight and stiffness. Four different materials had been compared: Aluminum, Titanium, Glass and Ceramics. With a standard housing of 110 mm inner dia and 800 mm length we end up with the following numbers:

	Weight in air	Weight in water
Aluminum(6061T6)	16 kg	2 kg
Titanium(6Al-4V)	10 kg	0.3 kg
Glass(Pyrex)	6 kg	- 4.5 kg
Ceramic	6 kg	- 4 kg

This means that there is a real advantage of employing glass or ceramics for this application. As the central part of the system, the hydraulic unit, needs a solid base as a mechanical construction platform and has to be rugged in the handling it was decided to test the applicability of ceramics. The basic unknown is the repeatability of the production process. The material has to be homogeneous and the geometry needs to be tight tolerated. Both could be achieved by using a commercial available tube from a specialized company. The tube thickness is well above the needed wall thickness (10 mm compared to 6 mm needed). Therefore we do not expect any problems with the present tube. The titanium endplates that have similar properties to the chosen ceramic are used to built up the mechanical parts into the housing. As ceramics have a larger range of elasticity compared to glass the danger of cracking is diminished.

The glass housing on the other hand is well suited to incorporate the electronic unit with the batteries. It has the lowest weight at the given dimensions. On the other hand the handling is very delicate.

D. Electronics

As the central microcontroller the ELAN system of AMD is used. It is based on the usual PC-processor structure but has similar power down modi as comparable microcontrollers. To enhance the reliability of the system it was decided to use a real time kernel. This system allows for parallel execution of different tasks. This contributes to a higher reliability of the system and minimizes the risk of data loss. Using a PC based system also means lower cost for development tools and easy interfacing to additional units.

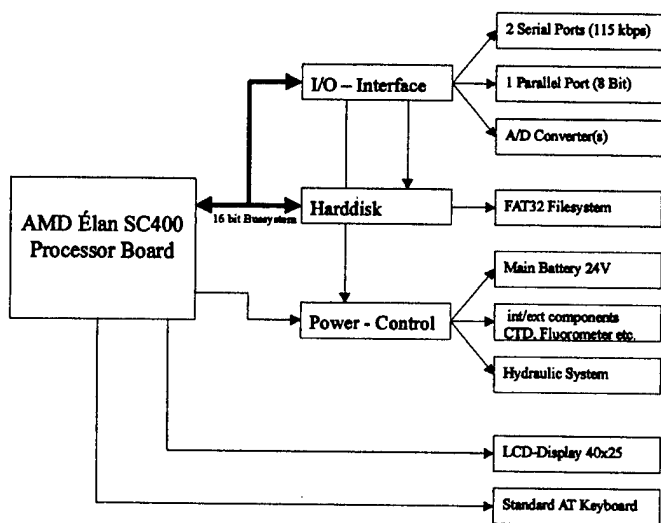


Fig.2: The basic microcontroller architecture of DOP

III. First field tests

The prototype system was tested on board the German research vessel METEOR in May '99. The aim was to prove the viability of the concept. As the prototype system has an overall volume of 180 l it has a weight change of about 5 kg going from freshwater to seawater. As the amount of the pumped volume is limited to 3 l the system has to be adjusted to at least 200g to be able predict the profiling speed reliably. The present weight is much higher compared to what we can achieve. Our design goal is to come down to less than 100 kg weight in air.



Fig.3: Deployment of DOP from board F.S. METEOR, cruise M45/1

The critical performance parameters of the system that has to be determined are:

- Time interval for one complete depth cycle
- Power consumption
- Maximum profiling speed
- Performance of the hydraulic system under high pressure

Therefore the focus of the tests lies in the propulsion unit with the hydraulic system and the according sensors. We made a total number of eight deployments where the last delivered the data shown in the figures 4 and 5. The system was fixed to the ship's winch and lengths of up to 2500 m rope were paid out. The depth interval was limited by two

stopper that were fixed to the rope. During the last deployment the system was programmed to do two profiles over a depth interval of 200 m. The final depth of 2000 m was chosen because of the limited time at the end of the cruise. The profiler worked without any faults and delivered a complete dataset of internal housekeeping data and external CTD- data. The following numbers show the results:

Pumping time	2500 s
Pumped Volume	21
Electrical power consumption during pumping	16 W (22.5 V, 0.7 A)
Valve opening time	60 s
Time for complete cycle (Including Timeouts of 720 s)	85 min
Speed	18 cm/s

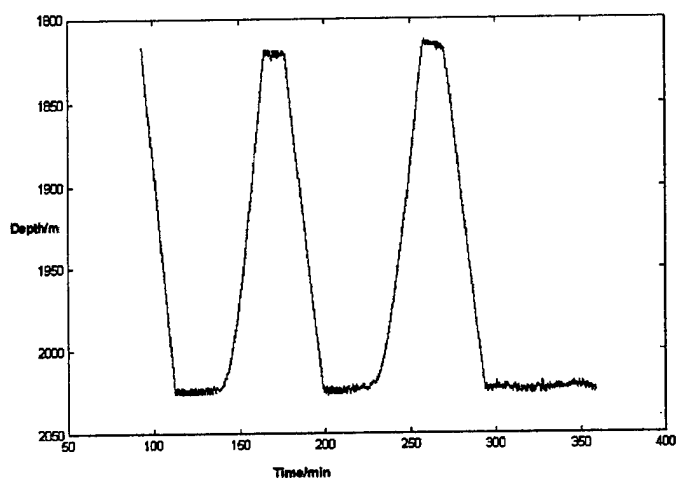
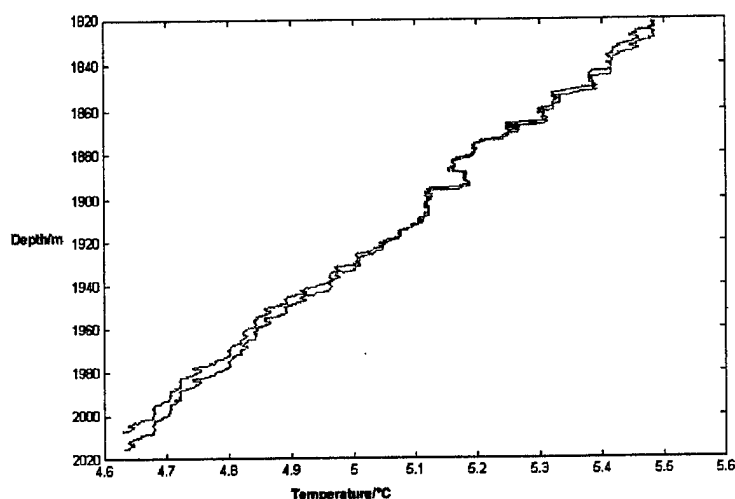


Fig. 4 : Pressure plot of the profiler test at the final test depth

Fig. 4 shows the time series plot of the pressure. The first leg is due to the settling of the profiler after the complete payout of the rope. After a predetermined resting phase the hydraulic pump starts to increase the buoyancy by pressing out the oil. After a slow start the profiler reaches its final speed of about 18 cm/s. As the oil is pressed back by the high pressure the final speed of 16 cm/s for the down cast is reached much faster. The speed numbers agree very well with the calculated values. The final resting phase shows that the profiler has finished its program as expected. One special feature of the profiler is its smooth motion through the water column. Therefore the CTD- data show a high reproducibility which is shown in Fig. 5. In the depth range of 1900 m the repeatability of the temperature structure is good enough to check the CTD sensors. This feature is special to buoyancy driven moored profilers that makes them ideal for continuous current velocity measurements complementary to for example ADCP observations.

IV. Conclusions:

A newly designed deep ocean profiler has been designed and tested in deep water on board F.S. METEOR in May '99. Beside the fact that the handling of the system i.e. the adjustment of buoyancy has to be improved the system looks very promising as a tool for long term observations in deep water. The design proves to be a viable concept. The main limitation in the performance results from the limited amount of power that is available for the complete autonomous system. Keeping in mind the relation between needed power and overall volume of the buoyancy driven system one has to look for new materials that can be used for pressure housings. The combination of ceramics and titanium looks very promising. But other housing materials should be evaluated as well.



For example the application of composite materials like Fig. 5: Successive temperature profiles taken with the deep sea profiler DOP

carbon fiber composites should be considered. There is a chance to compensate for the pressure change in the density. This would mean less amount of oil to be pumped to achieve the same speed.

The idea of using fixed profilers to collect relevant oceanic parameters in real time is very encouraging. The cost effectiveness of such systems lies in the fact that a single device covers a large depth range. On the other hand it has to be proved that the reliability of such a technique is comparable to current methods.

Currently there are groups in the US (Toole, Doherty, WHOI), France (Provost, Université Paris) and Germany (Waldmann, University of Bremen, Budeus, Alfred Wegener Institute, Bremerhaven) engaged in pursuing deep sea profiling YOYO instruments.

The first successful tests have been accomplished but it is still questionable which concept will survive over deployment times of 6 months and more.

V. Acknowledgment

This work has been funded by the German Ministry of Education, Research and Technology as part of the project DOMEST. The help is gratefully acknowledged.

VI. References:

- [1] Skoglund, S.: The shallow water profiler TRAMP, *Internal Report*, 1998
- [2] Provost, C.: YOYO Profiler: An Autonomous Multisensor, *SEA Technology*, Vol. 10, 1996
- [3] Eriksen, C.C.: An Upper Ocean Moored Current and Density Profiler Applied to Winter Conditions near Bermuda, *JGR*, Vol.87 NO. C10, 7879-7902, 1982
- [4] Van Leer, J.: The Cyclesonde: an unattended vertical profiler for scalar and vector quantities in the upper ocean, *Deep-Sea Research*, Vol. 21, 385-400, 1974
- [5] Doherty, K.W.: A Moored Profiling Instrument submitted to *Journal of Atmospheric and Oceanic Technology*, 1998
- [6] Waldmann, C.: A newly designed deep sea YOYO- profiler for long term moored deployment, *SECOND INTERNATIONAL Conference on EUROGOOS*, Rome, 10-13 March 1999
- [7] Meinecke, G., Ratmeyer, V.: A Bi-directional Link into the Deep Sea - The DOMEST Project, *Second International Conference on EuroGOOS*, Rome, 10-13 March 1999

SIGNAL RECEIVED BY AN AIRBORNE POLARIMETRIC BISTATIC RADAR OBSERVING THE SEA SURFACE

O. AIRIAU, & A. KHENCHAF

Laboratory S.E.I. - EP CNRS 63, IRESTE - University of Nantes,
Rue Christian Pauc, La Chantrerie, BP 60601, 44306 NANTES Cedex 3, FRANCE,
Tel. (33) 2 40 68 32 60, Télécopie (33) 2 40 68 32 33
email: oairiau@ireste.fr, akhencha@ireste.fr

ABSTRACT

This paper deals with the simulation of the signal received by a polarimetric bistatic radar observing the sea surface. The radar is considered installed on aircraft or helicopters flying over the sea at a constant velocity. We present in this paper the modeling of the received signal as a function of time.

We model completely the bistatic moving radiolink by taking into account the antennas radiation, the polarimetric behavior of the target and the mobiles velocity effect.

In this application where the sea surface is considered as the target, its scattering behavior is calculated by using the two-scale model.

I. INTRODUCTION

Most current radars are scalar radars working in monostatic configuration. Nevertheless this kind of radars presents limitations in particular when it is used to detect or to classify targets involving in a natural media, or for detection of stealthy targets.

Consequently the use of polarimetric radars using fully the vectorial aspect of the electromagnetic waves permits to increase the information on the target by analysing the polarization of the received wave compared with the transmitted one [1]. Then, it will be possible to classify the target more easily. The detection of targets will be improved by using polarization states for which the clutter echo is low; and particularly for radiolinks in the maritime environment. In addition a bistatic configuration permits, by separating the transmitting antenna and the receiving antenna, to improve the information on the target and to reduce the furtivity efficiency.

Furthermore, the technological advances allow to realize more complex radar systems which can be more easily installed on mobiles such as ships, aircraft, helicopters, ...

In this context, the development of polarimetric bistatic radars presents great advantages. And then the necessity to model the signal received by this kind of radars in the general

case where the transmitter, the target and the receiver are moving, is clearly appeared in order to develop and to test new classification methods.

We give in this paper the expression of the received signal as a function of time, by taking into account the antennas radiation (*transmitting antenna and receiving antenna*), the effect of the target on the polarization of the transmitted wave, and the influence of mobiles velocity.

In this paper where the sea surface is considered as the target, its scattering behavior is simulated by using the two-scale model.

A simulation is finally presented for the case where the sea surface is observed by a polarimetric bistatic radar for which the transmitter is mounted on a helicopter whereas the receiver is fixed on a hill.

II. RECEIVED SIGNAL MODEL

II.1. ANTENNAS RADIATION

The performances of a radar system or a radiocommunication system depends on the radiation characteristics of the transmitting antenna and of the receiving antenna. Consequently it is necessary to use radiation features optimized to the application. Thus, the antennas of a radar system are generally chosen to have a maximum radiation in the direction of the target and a radiation very small in the other directions in order to reduce the contribution of the undesirable echos.

Most important features of an antenna are its radiation pattern, its gain, and its polarization. The latter characteristic is defined as the polarization of the wave radiated in the direction of the maximum radiation.

Many antennas used by radar systems are reflectors which can have diverse geometries. These antennas can be considered as aperture antennas. In particular the paraboloidal reflector can be modelled by a circular aperture.

The radiation pattern of an aperture antenna is calculated in the far-field zone by applying the Huygens' principle associated to the image theory. The electrical field

radiated by the antenna in any \hat{r} direction is given by the following expression [2][3]:

$$\vec{E}(\hat{r}) = jk \frac{e^{-jkr}}{2\pi r} (\hat{n} \wedge \vec{P}) \wedge \hat{r} \quad (1)$$

with

$\vec{P} = \iint_{S_a} \vec{E}_a e^{jk(\hat{r} \cdot \hat{r}')} dS'$: the bidimensionnal Fourier transform of the electrical field \vec{E}_a in the aperture surface S_a ,

\hat{r} : the unit vector orthogonal to the aperture,

k : the wave number.

We note according to (1) that the electromagnetic field radiated by an aperture antenna in the far-field zone is plane because the E_r component of the electrical field in the direction of the propagation is null.

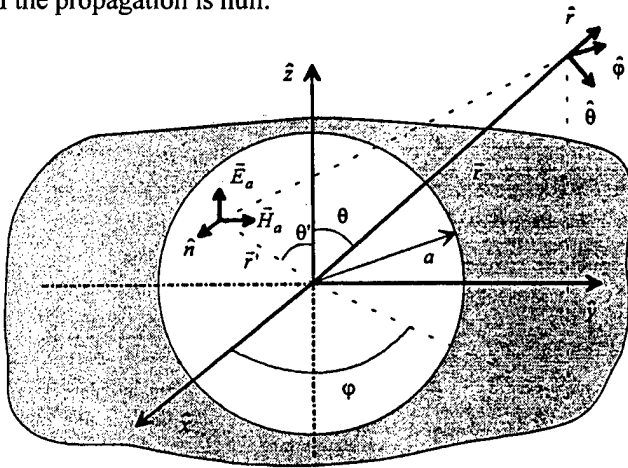


Fig. 1: Circular aperture geometry.

The use of antennas focusing the radiated energy in the main beam permits to reduce the contribution of echos returned from bodies neighboring the detected target.

The sidelobes level decrease is obtained by weighting the electrical field across the aperture by using a suitable distribution law. In that case the reduction of the electrical field discontinuity on the boundary of the aperture contributes to the sidelobes attenuation but in the same way to the main lobe expansion.

Let consider a circular aperture which is placed in the (Oyz) plane and illuminated with the distribution law $f(r')$ defined by:

$$f(r') = A + (1-A) \cos^2 \left(\frac{\pi r'}{2a} \right) \quad (2)$$

where A represents the electrical field attenuation on the boundary of the aperture, and a is the radius of the circular aperture.

The electrical field distribution is written as a vectorial expression by:

$$\vec{E}_a(r') = \vec{E}_0 f(r') \quad (3)$$

Then, the components of the electrical field radiated by the antenna in the far-field zone are given by the following relations:

$$\begin{cases} E_r = 0 \\ E_\theta = -jk \frac{e^{-jkr}}{2\pi r} P_z \cos \varphi \\ E_\varphi = jk \frac{e^{-jkr}}{2\pi r} (P_z \cos \theta \sin \varphi + P_y \sin \theta) \end{cases} \quad (4)$$

where P_x , P_y , and P_z are the components of the bidimensionnal Fourier transform of the electrical field across the aperture, expressed in the $(\hat{x}, \hat{y}, \hat{z})$ antenna coordinate system.

The antenna power gain in the direction of maximum radiation is given by (5) by assuming that the losses are insignificant.

$$G_{\max} = \frac{4\pi}{\lambda} \frac{\left| \int_0^a \int_0^{2\pi} f(r') r' dr' d\theta \right|^2}{\int_0^a \int_0^{2\pi} |f(r')|^2 r' dr' d\theta} \quad (5)$$

The components E_θ and E_φ of the normalized radiated electrical field are drawn on fig. 2 and fig. 3 for a circular aperture vertically polarized, and illuminated using the distribution law (2). These two figures show that the sidelobes level is about $-28dB$ whereas for a uniformly illuminated circular aperture it is about $-17dB$ [2].

In order to simplify the expression of the received signal we express, as a 2×2 matrix noted $[g]$ the radiation characteristics of the antenna polarized either horizontally or vertically. The coefficients of this matrix are written as a function of the maximum power gain and the components E_θ and E_φ of the far-field radiated electrical field.

$$[g] = \begin{bmatrix} g_{hh}(\theta, \varphi) & g_{hv}(\theta, \varphi) \\ g_{vh}(\theta, \varphi) & g_{vv}(\theta, \varphi) \end{bmatrix} \quad (6)$$

When the antenna is vertically polarized, the coefficients g_{hv} and g_{vv} define respectively the radiation in the horizontally polarized channel and in the vertically polarized channel and are given by

$$\begin{aligned} g_{hv}(\theta, \varphi) &= \sqrt{G_{\max}} \frac{E_\varphi(\theta, \varphi)}{\sqrt{|E_{\varphi\max}|^2 + |E_{\theta\max}|^2}} \\ g_{vv}(\theta, \varphi) &= \sqrt{G_{\max}} \frac{E_\theta(\theta, \varphi)}{\sqrt{|E_{\varphi\max}|^2 + |E_{\theta\max}|^2}} \end{aligned} \quad (7)$$

We obtain in a similar way the coefficients g_{hh} and g_{vh} characterizing respectively the antenna radiation in the co-polarized channel and in the cross-polarized channel when the antenna is horizontally polarized.

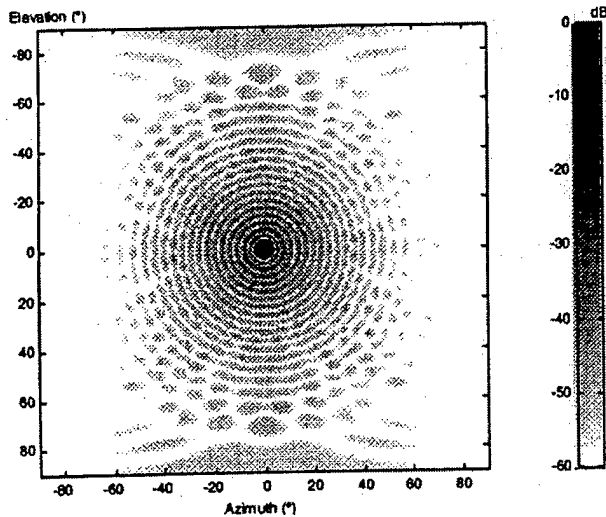


Fig. 2: E_θ component of the radiated electrical field
($a = 30\text{cm}$, $A = -10\text{dB}$, $\lambda = 3\text{cm}$).

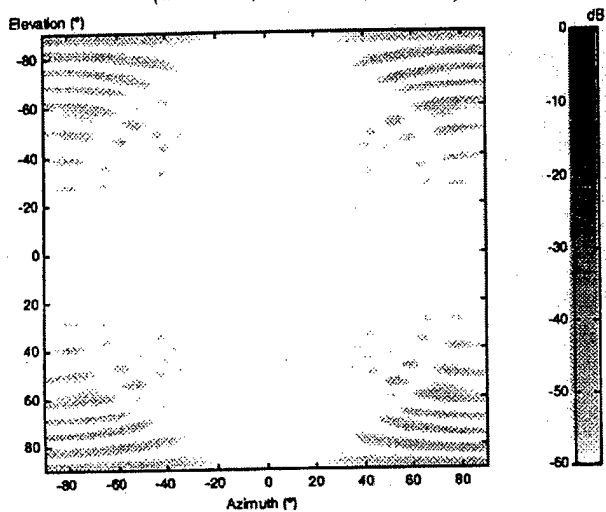


Fig. 3: E_ϕ component of the radiated electrical field
($a = 30\text{cm}$, $A = -10\text{dB}$, $\lambda = 3\text{cm}$).

II.2. TRANSMITTED WAVEFORM

The choice of the transmitted waveform has a great influence on the radar detection performances. The radar resolution in range or in radial velocity is directly related to the transmitted waveform. The radial velocity depends on the target illumination duration. So, a burst of pulses transmission permits to observe the target on a relatively long duration, and to improve the resolution by realizing a coherent integration on many pulses of the received signal [3].

The resolution in range is improved using a large bandwidth signal. Then we must transmit a burst of very short pulses if we wish to have a good resolution [3]. Nevertheless it is necessary to increase the transmitted peak power in order to keep a transmitted mean power sufficient to satisfy the detection threshold. But transmitted peak power increasing is limited by technological constraints. Consequently, pulse compression techniques permitting to increase the transmitted signal

bandwidth are generally used [3]. These techniques are based on a phase modulation of the carrier signal.

Typically, the detection performances of a pulse-radar are improved by transmitting a burst of rectangular pulses linearly modulated in frequency. For this kind of waveform which is also called a «chirp» the frequency is linearly swept from

$$f(t) = f_0 + \frac{\Delta f}{T} \left(t - \frac{T}{2} \right) \quad (8)$$

with

f_0 the carrier frequency,

Δf the bandwidth,

T : the pulse duration.

This waveform is given as a function of time by

$$S_e(t) = \sum_{n=0}^{\infty} \Pi_{[0,T]}(t - nT_r) e^{j2\pi(t-nT_r) \left[f_0 + \frac{\Delta f}{2T}(t - (n+\alpha)T_r) \right]} \quad (9)$$

where T_r is the repetition period, $\alpha = T/T_r$ the duty cycle and $\Pi_{[0,T]}(t)$ is the unity if $0 \leq t \leq T$ and null elsewhere.

The signal radiated by the transmitting antenna is written as a vectorial formulation in the transmitting antenna coordinate system by the following expression

$$\vec{E}^e(t) = \begin{bmatrix} E_h^e(t) \\ E_v^e(t) \end{bmatrix} = E_0 S_e(t) [g^e(\theta(t), \varphi(t))] \hat{e}(t) \quad (10)$$

where the matrix $[g^e]$ characterizes the transmitting antenna radiation, $S_e(t)$ is the transmitted waveform expressed by (9), \hat{e} is the transmitting Jones vector which is respectively equal to $[1 \ 0]^T$ or $[0 \ 1]^T$ if the antenna is respectively horizontally polarized or vertically polarized. The superscript T represents the transpose operator.

II.3. SEA SURFACE SCATTERING

The polarization of the wave scattered by the sea surface is generally different from the incident. This state polarization change depends on the physical features (*permittivity, permeability*) and on the geometrical features of the sea surface. It also depends on the observing angles of the surface ($\theta, \varphi, \theta_s, \varphi_s$ as indicated in fig. 4). The scattered wave polarization change is modeled by a complex 2×2 matrix $[S]$ called the scattering matrix [5].

The calculus of the scattering coefficients consists in solving a random rough surface scattering problem. The classical analytic approaches based on the Kirchhoff approximation and small perturbation method are restricted in domain of validity [6].

For the two-scale model the surface can be modeled as having only two average sizes of roughness where one is large compared with the incident wavelength and the other small.

The incident field \vec{E}^i is written in the (\hat{h}, \hat{v}) basis like where

$$\bar{E}^i = E_0 \hat{a} \text{ with } E_0 = |E_0| e^{-jk\hat{a} \cdot \vec{r}} \quad (11)$$

\hat{a} is the incident wave Jones vector, k the wavenumber of the transmitted wave, and \hat{a} , the unit vector in the incident direction.

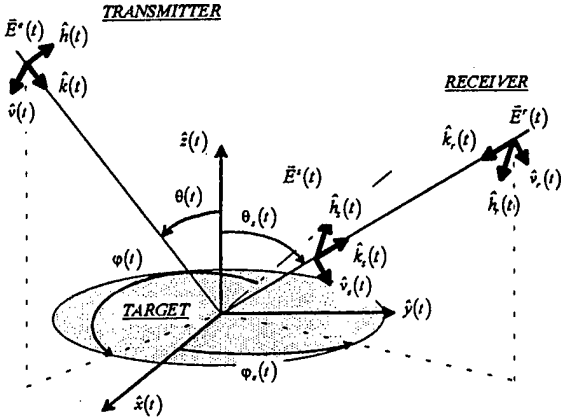


Fig. 4: Bistatic scattering configuration.

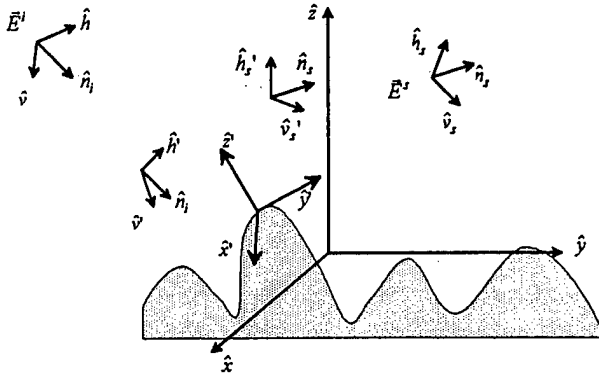


Fig. 5: Bistatic scattering configuration of the two-scale model.

In the local reference (Cf. fig. 5) the incident field can be rewritten as

$$\bar{E}^i = E_{v'}^i \hat{v}' + E_{h'}^i \hat{h}' = ((\hat{a} \cdot \hat{v}') \hat{v}' + (\hat{a} \cdot \hat{h}') \hat{h}') E_0 \quad (12)$$

and the scattering field is expressed in the (\hat{h}_s', \hat{v}_s') basis by

$$\bar{E}^s = \begin{bmatrix} E_{h_s'}^s \\ E_{v_s'}^s \end{bmatrix} = \begin{bmatrix} S_{h_s'h'} & S_{h_s'v'} \\ S_{v_s'h'} & S_{v_s'v'} \end{bmatrix} \begin{bmatrix} E_{h'}^i \\ E_{v'}^i \end{bmatrix} \quad (13)$$

The scattered field can be rewritten in the (\hat{h}_s, \hat{v}_s) as

$$\bar{E}^s = \begin{bmatrix} E_{h_s}^s \\ E_{v_s}^s \end{bmatrix} = [S] \bar{E}^i \quad (14)$$

where the scattering matrix $[S]$ is given by

$$[S] = \begin{bmatrix} \hat{h}_s' \cdot \hat{h}_s & \hat{v}_s' \cdot \hat{h}_s \\ \hat{h}_s' \cdot \hat{v}_s & \hat{v}_s' \cdot \hat{v}_s \end{bmatrix} \begin{bmatrix} S_{h_s'h'} & S_{h_s'v'} \\ S_{v_s'h'} & S_{v_s'v'} \end{bmatrix} \begin{bmatrix} \hat{h}' \cdot \hat{h} & \hat{h}' \cdot \hat{v} \\ \hat{v}' \cdot \hat{h} & \hat{v}' \cdot \hat{v} \end{bmatrix} \quad (15)$$

Putting p (h_s or v_s) the received polarization and q (h or v) the transmitted polarization, the components of the scattered field are obtained in the co-polarized channel and the cross-polarized channel from

$$E_{pq}^s = (\hat{v}_s' \cdot \hat{p}) \{ (\hat{q} \cdot \hat{v}') S_{v_s'v'} + (\hat{q} \cdot \hat{h}') S_{v_s'h'} \} + (\hat{h}_s' \cdot \hat{p}) \{ (\hat{q} \cdot \hat{v}') S_{h_s'v'} + (\hat{q} \cdot \hat{h}') S_{h_s'h'} \} E_0 \quad (16)$$

Then the average $\langle E_{pq}^s E_{pq}^{s*} \rangle$ with respect to the large scale roughness can be calculated and rewritten in terms of the scattering coefficients σ_{pq}^s as

$$\begin{aligned} \sigma_{pq}^s = & \left((\hat{p} \cdot \hat{v}_s')^2 (\hat{q} \cdot \hat{v}')^2 \sigma_{v_s'v'}^2 + (\hat{p} \cdot \hat{v}_s')^2 (\hat{q} \cdot \hat{h}')^2 \sigma_{v_s'h'}^2 \right. \\ & + (\hat{p} \cdot \hat{h}_s')^2 (\hat{q} \cdot \hat{v}')^2 \sigma_{h_s'v'}^2 + (\hat{p} \cdot \hat{h}_s')^2 (\hat{q} \cdot \hat{h}')^2 \sigma_{h_s'h'}^2 \\ & + (\hat{p} \cdot \hat{h}_s')^2 (\hat{q} \cdot \hat{v}') (\hat{q} \cdot \hat{h}') \sigma_{h_s'h_s'v'}^1 \\ & + (\hat{p} \cdot \hat{v}_s') (\hat{p} \cdot \hat{h}_s') (\hat{q} \cdot \hat{h}')^2 \sigma_{h_s'h_s'v_h'}^1 \\ & + (\hat{p} \cdot \hat{v}_s') (\hat{p} \cdot \hat{h}_s') (\hat{q} \cdot \hat{v}') (\hat{q} \cdot \hat{h}') \sigma_{v_s'v_h'h_s'}^1 \\ & + (\hat{p} \cdot \hat{v}_s') (\hat{p} \cdot \hat{h}_s') (\hat{q} \cdot \hat{h}') (\hat{q} \cdot \hat{v}') \sigma_{h_s'v_h'h_s'}^1 \\ & + (\hat{p} \cdot \hat{v}_s') (\hat{p} \cdot \hat{h}_s') (\hat{q} \cdot \hat{v}')^2 \sigma_{h_s'v_h'v_h'}^1 \\ & \left. + (\hat{p} \cdot \hat{v}_s')^2 (\hat{q} \cdot \hat{v}') (\hat{q} \cdot \hat{h}') \sigma_{v_s'v_h'h_s'}^1 \right) |E_0|^2 \end{aligned} \quad (17)$$

where

$$\sigma_{pqmn}^1 = 16 \times \left| k^2 \sigma \cos \theta' \cos \theta_s' \right|^2 \text{Re}(\alpha_{pq} \alpha_{mn}^*) W(k_x + k \sin \theta', k_y) \quad (18)$$

$$\sigma_{pq} = 8 \times \left| k^2 \sigma \cos \theta' \cos \theta_s' \right|^2 |\alpha_{pq}|^2 W(k_x + k \sin \theta', k_y) \quad (19)$$

σ is the standard deviation of the surface height; and $*$ denotes the complex conjugate. The average $\langle \cdot \rangle$ in the scattering coefficients may then be calculated by using any model of surface slopes distribution. The α_{pq} 's that appear in σ_{pqmn}^1 and σ_{pq} are the polarization dependent factors given in [7] [8].

II.4. RECEIVED SIGNAL

The received signal waveform is written from the waveform of the transmitted signal delayed in time. This delay is the wave propagation time between the transmitter and the receiver. In the case for which the transmitter, the target and the receiver are moving this delay is a function of time. For a bistatic configuration the delay depends on the projection of the velocities of the transmitter and the target on the transmitter-target axis and also on the projection of the velocities of the target and the receiver on the target-receiver axis.

This delay function of time introduces on a the received signal a phenomenon well known as Doppler effect and gives

rise to a phase modulation of the received signal. So, this phenomenon is characterized respectively by a frequency positive shift or a negative shift of the received power spectrum depending on whether the mobiles are moving closer or farther.

The transmitter-target propagation delay $\delta t_{EC}(t)$ and the target-receiver propagation delay $\delta t_{CR}(t)$ are respectively given by relations (20) and (21) assuming that the mobiles velocity is constant during a pulse duration transmission.

$$\delta t_{EC}(t) = \frac{\bar{r}(0) \cdot \hat{k}(0)}{c + \bar{v}_c(t) \cdot \hat{k}(t)} - \frac{[\bar{v}_e(t) - \bar{v}_c(t)] \cdot \hat{k}(t)}{c + \bar{v}_c(t) \cdot \hat{k}(t)} [t - \delta t_{CR}(t)] \quad (20)$$

$$\delta t_{CR}(t) = \frac{\bar{R}(0) \cdot \hat{k}_r(0)}{c - \bar{v}_r(t) \cdot \hat{k}_r(t)} - \frac{[\bar{v}_r(t) - \bar{v}_c(t)] \cdot \hat{k}_r(t)}{c - \bar{v}_r(t) \cdot \hat{k}_r(t)} t \quad (21)$$

where $\bar{r}(t)$ and $\bar{R}(t)$ are the instantaneous distances transmitter-target and target-receiver respectively; and \bar{v}_e , \bar{v}_c and \bar{v}_r are the velocities of the transmitter, the target, and the receiver respectively.

The transmitter-receiver total propagation delay is obtained by adding (20) and (21), such as

$$\delta t_{ER}(t) = \delta t_{EC}(t) + \delta t_{CR}(t) \quad (22)$$

The received signal waveform is then given as a function of time by [9] [10]

$$S_r(t) = \sum_{n=0}^{\infty} \Pi_{[0,T]}(t - nT_r - \delta t_{ER}) \cdot e^{j2\pi f_0(t - nT_r)} \cdot e^{j\pi \frac{\Delta f}{T}(t - nT_r)[t - (n+\alpha)T_r]} \cdot e^{-j2\pi \delta t_{ER} \left[f_0 + \frac{\Delta f}{2T}(2t - (2n+\alpha)T_r - \delta t_{ER}) \right]} \quad (23)$$

The received signal is written as a vectorial formulation expressed in the receiving antenna coordinate system

$(\hat{k}_r, \hat{v}_r, \hat{h}_r)$ like

$$\bar{E}^r(t) = \begin{bmatrix} E_h^r \\ E_v^r \end{bmatrix} = E_0 \frac{e^{-jk[c\delta t_{EC}(t) + c\delta t_{CR}(t)]}}{c^2 \delta t_{EC}(t) \delta t_{CR}(t)} S_r(t) \cdot \begin{bmatrix} g_{h,h}^r(t) & g_{h,v}^r(t) \\ g_{v,h}^r(t) & g_{v,v}^r(t) \end{bmatrix}^T \cdot \begin{bmatrix} -1 & 0 \\ 0 & 1 \end{bmatrix} \quad (24)$$

$$\begin{bmatrix} S_{h,h}(t) & S_{h,v}(t) \\ S_{v,h}(t) & S_{v,v}(t) \end{bmatrix} \cdot \begin{bmatrix} g_{hh}^e(t) & g_{hv}^e(t) \\ g_{vh}^e(t) & g_{vv}^e(t) \end{bmatrix} \cdot \begin{bmatrix} a_h \\ a_v \end{bmatrix}$$

with $S_r(t)$: the waveform of the received signal, $[g^e]$ and $[g^r]$: the matrices characterizing the radiation of the transmitting

antenna and of the receiving antenna respectively, $[S]$: the target scattering matrix, \hat{a} : the transmitted Jones vector.

III. NUMERICAL RESULTS

This section presents the simulation of the signal received from the sea surface by a bistatic radar for which the transmitter is mounted on a helicopter flying in the east direction, (Cf. fig. 6) at constant altitude ($h_e = 1000m$) and at constant velocity ($V_e = 180km/h$). The receiver is fixed on the ground at an altitude equal to 300m over the sea surface. At the initial simulation instant, the distances between the transmitter and the observed sea surface area and between the observed area and the receiver are above 1300m and 550m. And then the location of the transmitter and of the receiver from the observed sea area are defined by the angles $\theta = 41.3^\circ$, $\varphi = 118.1^\circ$, $\theta_s = 56.9^\circ$, $\varphi_s = 90^\circ$. The parameters of the transmitted waveform are chosen such as $T_r = 100\mu s$, $\alpha = 10\%$, $\Delta f = 5MHz$, and $f_0 = 10GHz$. The sea surface is characterized by a 35ppm salinity, 20°C temperature and a 6.85m/s ($\approx 13kt$ sea at 10m) wind speed. The modulus of the scattering coefficients are calculated using the two-scale model, and their phase is assumed to be a uniformly distributed random variable.

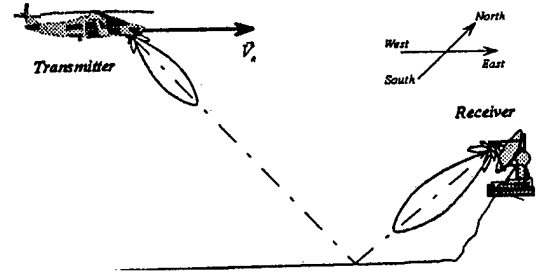


Fig. 6: Geometrical configuration of the simulation.

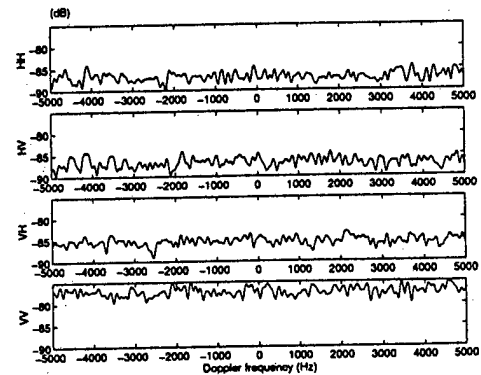


Fig. 7: Power spectrum of the received signal.

Figure 7 represents, for each polarization channel, the power spectral density of the signal received from the sea surface. It appears that the sea echo looks like a noise reducing the detection of bodies placed in the observed area.

Figures 8(a)-(d) represent the distribution of the received power in various transmitting and receiving polarization channels. Thus, histogram 8(b) illustrates the distribution law of the signal received when the transmitting antenna and the receiving antenna are respectively vertically polarized and horizontally polarized. Figure 8(d) shows that the signal received from the sea surface is maximum when the polarization of the transmitting antenna and of the receiving antenna is linear vertical.

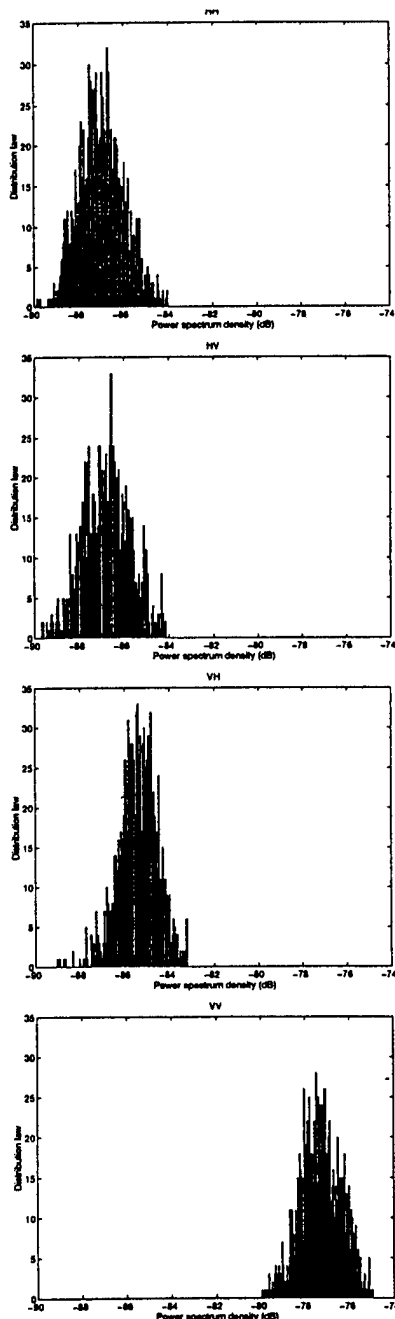


Fig. 8: Distribution of the received power spectrum
(a) HH, (b) HV, (c) VH, (d) VV

IV. CONCLUSION

The expression of the signal received by a polarimetric radar is developed in a bistatic configuration for the general case where the transmitter, the target and the receiver are moving. The presented model can be used for any target by the only knowledge of the target scattering matrix. Like that, a simulation is realized to the sea surface observation by taking the sea surface as the target. The scattering coefficients of the sea surface are calculated using the two-scale model, and assuming that the phase of these coefficients is a uniformly random variable. This modeling permits to simulate the signal received by a polarimetric bistatic radar for a wide range of radar scenarios and to be useful for target classification algorithms development and test.

REFERENCES

- [1] W.M. Boerner, «Recent Advances in Polarimetric Tomographic (Multi-Interferometric) SAR POL-IN/TOMO-SAR Theory & Technology and its Application», 5th International Conference on Radar Systems, BREST, FRANCE, May 18-20, 1999.
- [2] W.L. Stutzman, G.A. Thiele, Antenna Theory and Design, John Wiley, 1981.
- [3] M.I. Skolnik, Radar Handbook, Mac-Graw Hill Book Company New-York, 1980.
- [4] D.K. Barton, C.E. Cook, P. Hamilton, Radar Evaluation Handbook, Artech House Inc, 1991.
- [5] W.M. Boerner, W.L. Yan, «Introduction to Radar Polarimetry», Journées Internationales de la Polarimétrie Radar, NANTES, Mars 1990.
- [6] A. Khenchaf, F. Daout, and J. Saillard, «The twoscale model for random rough surface scattering», IEEE Supp. Proc. Oceans'96, pp. 50-54, Ft Lauderdale, Florida, USA, 1996.
- [7] Donald E. Barrick, «A review of scattering from surfaces with different roughness scales», Radio Science, vol. 3, No 8, August 1968.
- [8] F.T. Ulaby, R.K. Moore, and A.K. Fung, Microwave remote sensing: Active and Passive, volume 2. Addison-Wesley Publishing Company, 1982.
- [9] O. Airiau, A. Khenchaf, J. Saillard, «Signal Received by a Bistatic Radar from a Moving Target Applied to a Canonical Target», Proc. of the 4th International Workshop on Radar Polarimetry, NANTES, FRANCE, July 13-17, 1998, pp. 141-149.
- [10] O. Airiau, A. Khenchaf, J. Saillard, «Signal Received from a Moving Target by a Moving Polarimetric Bistatic Radar», 5th International Conference on Radar Systems, BREST, FRANCE, May 18-20, 1999.

SEA SURFACE SCATTERING FOR NEAR-GRAZING INCIDENCE

A. KBENCHAF

*Lab. SEI / EP CIVRS 63, IRESTE, University of Nantes,
Rue Christian Pauc, La Chantrerie, BP 60601, 44306, Nantes Cedex 03, FRANCE,
Tel. 33 02 40 68 30 43, Fax 33 02 40 68 32 33, Email akhencha@ireste.fr*

ABSTRACT

The radar cross section of sea clutter at (or near) the horizon is a critical parameter in naval radar system performance evaluation. At the low grazing angles and ranges involved, the existing data base is quite limited. At near-grazing illumination, the radar receives an echo from the sea surface which is characterized by short bursts of power. These are significantly stronger than the random average scattering. The problem of developing a model for rough surfaces is a very difficult one, since, at best, the scattering coefficient σ^0 is dependent upon (at least) radar frequency, geometrical and physical parameters, incident and observation angles, as well as polarization. In this paper the development of a theoretical two-scale model describing bistatic reflectivity is presented as well as the numerical results computed for the bistatic radar cross-section from random rough surfaces especially from the sea surface. The numerical results for the bistatic scattering coefficient for the sea surface are used to show the brewster angle effect on near-grazing angles.

1- INTRODUCTION

The scattering of waves by random rough surfaces at low-grazing angles has important applications in remote sensing of ocean and land. For a bistatic link over the sea surface, it is necessary to combat multipath fading caused by sea reflection that can disrupt an electromagnetic system near the sea surface, understanding the effect of the scattering by this natural surface is an absolute necessity. In this paper the bistatic scattering properties of the sea surface is explained in terms of a two-scale roughness model where the small-scale waves are assumed to satisfy the small perturbation assumptions, while the large-scale waves are assumed to satisfy the Kirchhoff approximation. The two-scale composite model uses the result of the small perturbation model to compute the scattering coefficient due to small-scale waves and to account for the tilting effect of the large-scale waves by averaging this scattering coefficient over the slope distribution of the large-scale waves.

The geometry of the surface scattering reflection is shown in Fig. 1.

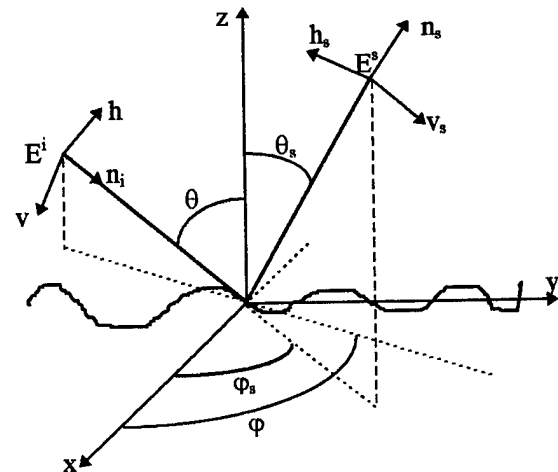


Fig.1 : Geometry of the surface bistatic scattering problem

2- TWO-SCALE MODEL

The classical analytic approaches of solving random rough surface scattering problems based on the Kirchhoff approximation and small perturbation method are restricted in domain of validity [1] [2] [3]. For the two-scale model the surface can be modeled as having only two average sizes of roughness with one large and the other small compared with the incident wavelength. Fig.2 shows the geometry of the surface scattering problem. The transmitter and the receiver are located in a reference (X,Y,Z) by the angles θ , ϕ , θ_s , and ϕ_s .

The 2×1 complex element vectors E^i and E^s describe the polarizations of the incident and scattered electric fields, respectively.

Assume the incident wave E^i to be :

$$E^i = E_0 a \text{ with } E_0 = |E_0| e^{-jk n_i \cdot r} \quad (1)$$

where a is the unit polarization vector (vertical polarization v or horizontal polarization h), k is the wave-number of the illuminating wave, and n_i is the unit vector in the incident direction.

in the local reference

$$E^i = E_{v'}^i v' + E_{h'}^i h' = ((a \cdot v')v' + (a \cdot h')h')E_0 \quad (2)$$

and the locally scattered field due to incident waves are:

$$E^s = E_{v_s'}^s v_s' + E_{h_s'}^s h_s' = [S]E^i = \begin{bmatrix} S_{v_s'v'} E_{v'}^i + S_{v_s'h'} E_{h'}^i \\ S_{h_s'v'} E_{v'}^i + S_{h_s'h'} E_{h'}^i \end{bmatrix} \quad (3)$$

where $S_{p'q'}$ is the scattered field for unit incident fields.

Then the scattered fields can be written as

$$E^s = E_{v_s'}^s v_s + E_{h_s'}^s h_s = [S]E^i \quad (4)$$

where the scattering-matrix $[S]$ is given by

$$[S] = \begin{bmatrix} v_s' \cdot v_s & h_s' \cdot v_s \\ v_s' \cdot h_s & h_s' \cdot h_s \end{bmatrix} \begin{bmatrix} S_{v_s'v'} & S_{v_s'h'} \\ S_{h_s'v'} & S_{h_s'h'} \end{bmatrix} \begin{bmatrix} v' \cdot v & v' \cdot h \\ h' \cdot v & h' \cdot h \end{bmatrix} \quad (5)$$

For the received polarization p (v_s or h_s) and the transmitted polarization q (v or h), the scattered polarized and depolarized fields are obtained from

$$E_{pq}^s = (v_s' \cdot p) \left\{ (q \cdot v') S_{v_s'v'} + (q \cdot h') S_{v_s'h'} \right\} + (h_s' \cdot p) \left\{ (q \cdot v') S_{h_s'v'} + (q \cdot h') S_{h_s'h'} \right\} E_0 \quad (6)$$

Then the average $\langle E_{pq}^s E_{p'q'}^{s*} \rangle$ with respect to the large-scale roughness can be calculated and rewritten in terms of the scattering coefficients as [8] as a function of the σ_{pq}^s transmitter polarization q and the receiver polarization p

$$\begin{aligned} \sigma_{pq}^s = & \left\langle (p \cdot v_s')^2 (q \cdot v')^2 \sigma_{v_s'v'}^2 + (p \cdot v_s')^2 (q \cdot h')^2 \sigma_{v_s'h'}^2 + \right. \\ & (p \cdot h_s')^2 (q \cdot v')^2 \sigma_{h_s'v'}^2 + (p \cdot h_s')^2 (q \cdot h')^2 \sigma_{h_s'h'}^2 + \\ & (p \cdot h_s')^2 (q \cdot v') (q \cdot h') \sigma_{h_s'h'v_s'}^1 + (p \cdot v_s') (p \cdot h_s') (q \cdot h')^2 \sigma_{h_s'h'v_s'}^1 + \\ & (p \cdot v_s') (p \cdot h_s') (q \cdot v') (q \cdot h') \sigma_{v_s'v'h_s'}^1 + \\ & (p \cdot v_s') (p \cdot h_s') (q \cdot h') (q \cdot v') \sigma_{h_s'v_s'v_h'}^1 + \\ & (p \cdot v_s') (p \cdot h_s') (q \cdot v')^2 \sigma_{v_s'v_s'v_h'}^1 + \\ & \left. (p \cdot v_s')^2 (q \cdot v') (q \cdot h') \sigma_{v_s'v_s'v_h'}^1 \right\rangle E_0^2 \quad (7) \end{aligned}$$

where

$$\sigma_{pq}^1 = 16 \times$$

$$|k^2 \sigma \cos \theta' \cos \theta_s|^2 \operatorname{Re}(\alpha_{pq} \alpha_{p'q'}^*) W(k_x + k \sin \theta', k_y)$$

$$\sigma_{pq} = 8 \times |k^2 \sigma \cos \theta' \cos \theta_s|^2 |\alpha_{pq}|^2 W(k_x + k \sin \theta', k_y)$$

σ is the standard deviation of the surface height, θ' is a local incidence angle, θ_s is a local scattering angle and $*$ denotes the complex conjugate.

The average $\langle \cdot \rangle$ in the scattering coefficients may then be calculated by using any model of surface slopes distribution.

The α_{pq} 's that appear in σ_{pq}^1 and σ_{pq} are the polarization dependent factors given in [4] [5]. For near grazing angles ($\theta \approx \theta_s \approx 90^\circ$) these coefficients are reduced to the following forms

$$\begin{aligned} \alpha_{hh} & \approx -\cos \varphi_s, \quad \alpha_{vh} \approx -\sqrt{\epsilon_r - 1} \sin \varphi_s, \\ \alpha_{hv} & \approx \sqrt{\epsilon_r - 1} \sin \varphi_s \text{ and } \alpha_{vv} \approx (\epsilon_r - 1) \cos \varphi_s - \epsilon_r \end{aligned} \quad (8)$$

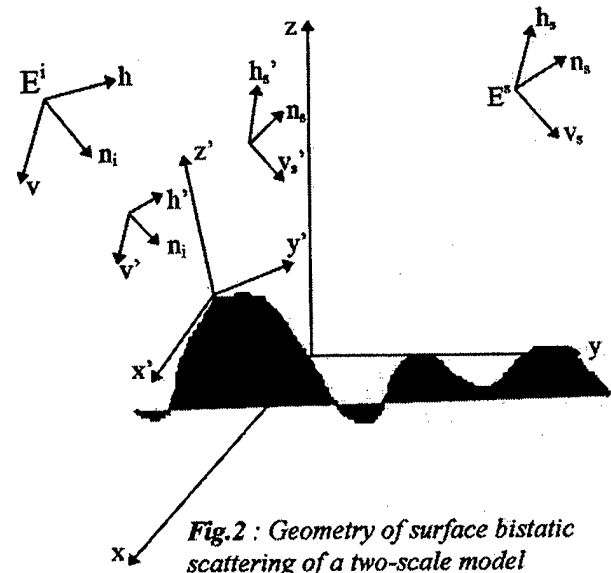


Fig.2 : Geometry of surface bistatic scattering of a two-scale model

3- APPLICATION TO THE OCEANIC SURFACE

The application is realized using the sea surface as a composite surface.

The scattering from composite surfaces is composed of a specular component and a diffuse component. The specular component is calculated from the Kirchhoff approximation (Geometrical Optics) and the diffuse component is given by the two-scale model as described in section 2. The bistatic scattering coefficients $\sigma_{v_s'v'}^s$, $\sigma_{h_s'h'}^s$, $\sigma_{v_s'h'}^s$ and $\sigma_{h_s'v_s'}^s$ are plotted in the forward scatter case in figures (3-4-7-8 with gaussian model) and (5-6-9-10 with directional spectrum). Note that the composite component $\sigma_{h_s'h'}^s$ is not affected by the Brewster angle effect.

The bistatic RCS of sea surface is plotted in figures 12 and 13, using the Gaussian roughness spectrum, as a function of the bistatic angles β (Cf Fig. 11), where β is calculated from the direction vectors in Fig. 1 and given by $\cos(\beta) = (n_s - n_i) \cdot z / \|n_s - n_i\|$. Figures 12, 13, 14 and 15 show the curves of the scattering coefficient $\sigma_{v_s'v'}^s$, which is strongly affected by the Brewster angle effect. As the bistatic angle increases (between 60 and 90°) for different values of φ_s , the $\sigma_{v_s'v'}^s$ RCS increases above 80° in Fig. 12 (without shadowing condition) and decreases in Fig. 13 (with shadowing condition).

Figure 14 shows the bistatic radar scattering coefficients $\sigma_{v,v}^s$ with the modified Pierson-Moscowitz's spectrum [6] and the slope distribution given by Cox and Munk [7]. This variation is confirmed by the Fig. 15 where both the diffuse component (2-4-6) and the sum of components (1-35) are plotted in the forward scatter case. This figure shows clearly the Brewster angle effect on the diffuse component (*without shadowing condition Fig 15 (2-6)*) and on the total component (*with or without shadowing condition Fig. 15 (13-5)*).

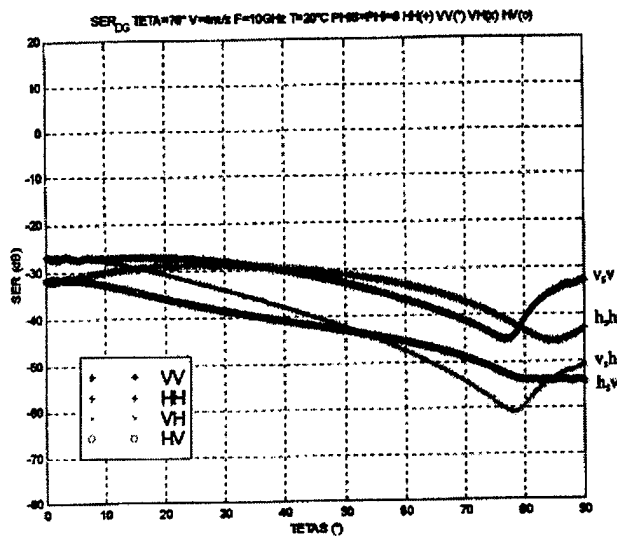


Fig.3 : Bistatic scattering coefficients (diffuse component) $\sigma_{v,v}^s$, $\sigma_{h,h}^s$, $\sigma_{v,h}^s$ and $\sigma_{h,v}^s$ with $F=9.9$ GHz, $\theta=70^\circ$, $T=20^\circ\text{C}$, $S=35\text{ppm}$, and wind speed $\sim 12\text{-kt}$ sea (at 10m) (Gaussian model)

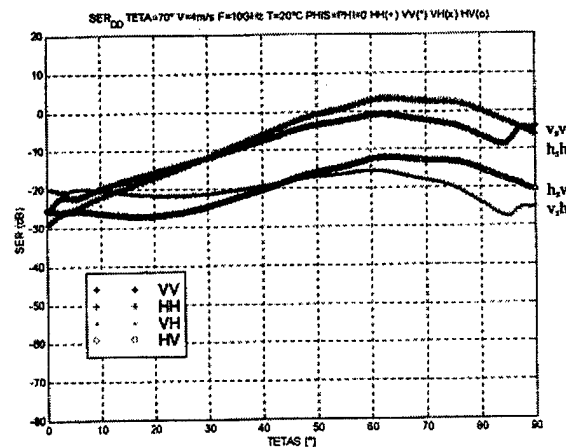


Fig.5 : Bistatic scattering coefficients (diffuse component) $\sigma_{v,v}^s$, $\sigma_{h,h}^s$, $\sigma_{v,h}^s$ and $\sigma_{h,v}^s$ with $F=9.9$ GHz, $\theta=85^\circ$, $T=20^\circ\text{C}$, $S=35\text{ppm}$, and wind speed $\sim 12\text{-kt}$ sea (at 10m) (directional spectrum)

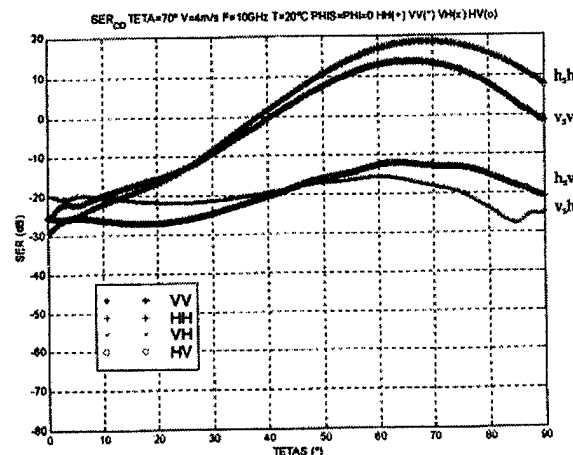


Fig.6 : Bistatic scattering coefficients (composite component) $\sigma_{v,v}^s$, $\sigma_{h,h}^s$, $\sigma_{v,h}^s$ and $\sigma_{h,v}^s$ with $F=9.9$ GHz, $\theta=70^\circ$, $T=20^\circ\text{C}$, $S=35\text{ppm}$, and wind speed $\sim 12\text{-kt}$ sea (at 10m) (directional spectrum)

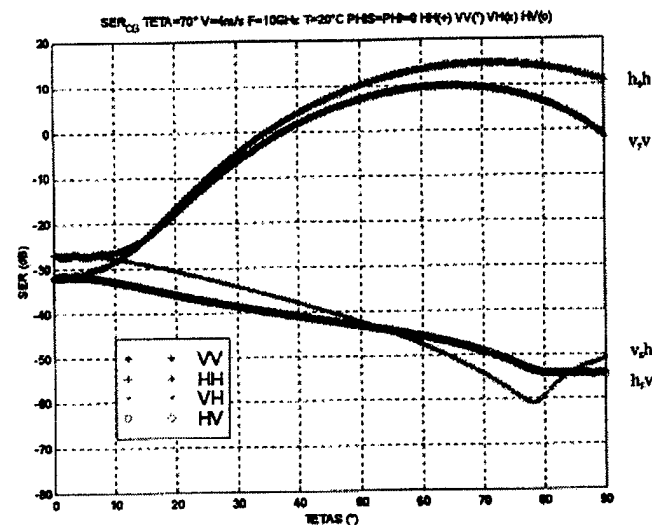


Fig.4 : Bistatic scattering coefficients (composite component) $\sigma_{v,v}^s$, $\sigma_{h,h}^s$, $\sigma_{v,h}^s$ and $\sigma_{h,v}^s$ with $F=9.9$ GHz, $\theta=70^\circ$, $T=20^\circ\text{C}$, $S=35\text{ppm}$, and wind speed $\sim 12\text{-kt}$ sea (at 10m) (Gaussian model)

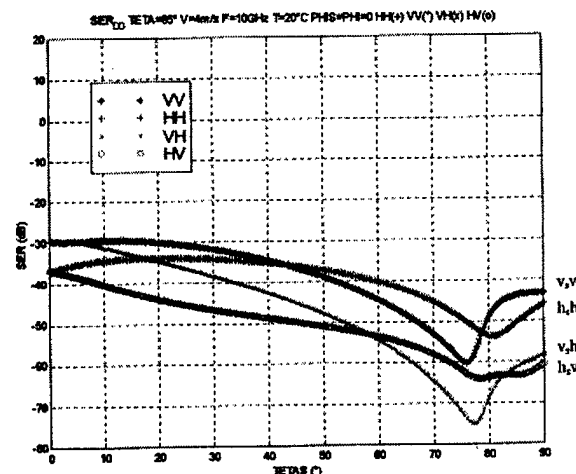


Fig.7 : Bistatic scattering coefficients (diffuse component) $\sigma_{v,v}^s$, $\sigma_{h,h}^s$, $\sigma_{v,h}^s$ and $\sigma_{h,v}^s$ with $F=9.9$ GHz, $\theta=85^\circ$, $T=20^\circ\text{C}$, $S=35\text{ppm}$, and wind speed $\sim 12\text{-kt}$ sea (at 10m) (Gaussian model)

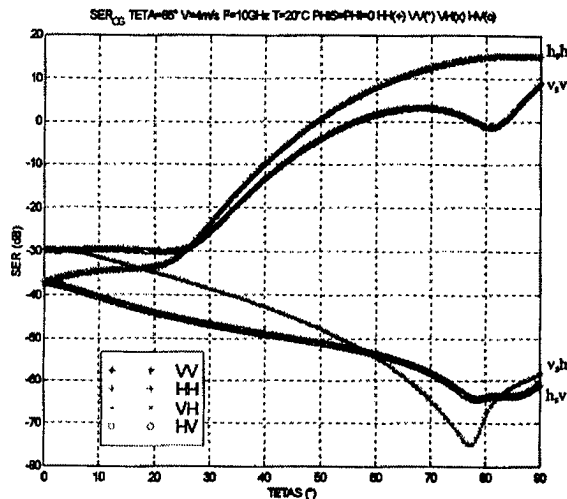


Fig. 8 : Bistatic scattering coefficients (composite component) $\sigma_{v,v}^s$, $\sigma_{h,h}^s$, $\sigma_{v,h}^s$ and $\sigma_{h,v}^s$ with $F=9.9$ GHz, $\theta=85^\circ$, $T=20^\circ\text{C}$, $S=35\text{ppm}$, and wind speed $\sim 12\text{-kt}$ sea (at 10m) (Gaussian model)

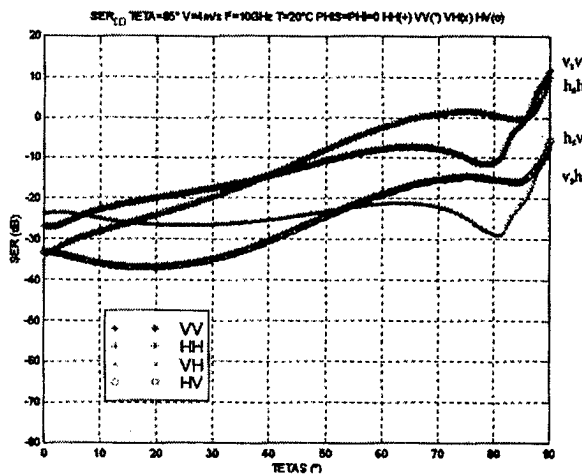


Fig. 9 : Bistatic scattering coefficients (diffuse component) $\sigma_{v,v}^d$, $\sigma_{h,h}^d$, $\sigma_{v,h}^d$ and $\sigma_{h,v}^d$ with $F=9.9$ GHz, $\theta=85^\circ$, $T=20^\circ\text{C}$, $S=35\text{ppm}$, and wind speed $\sim 12\text{-kt}$ sea (at 10m) (directional spectrum)

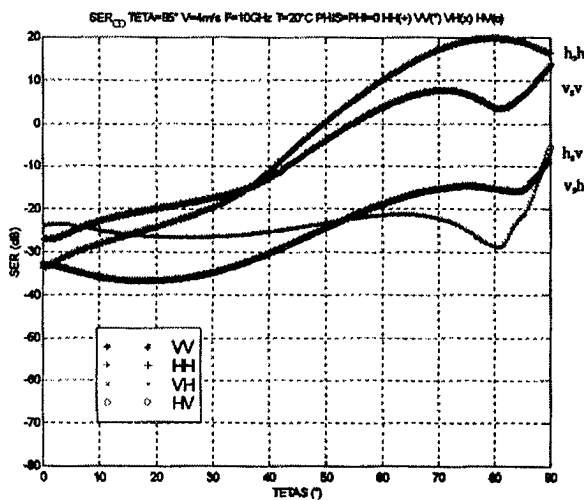


Fig. 10 : Bistatic scattering coefficients (composite component) $\sigma_{v,v}^s$, $\sigma_{h,h}^s$, $\sigma_{v,h}^s$ and $\sigma_{h,v}^s$ with $F=9.9$ GHz, $\theta=85^\circ$, $T=20^\circ\text{C}$, $S=35\text{ppm}$, and wind speed $\sim 12\text{-kt}$ sea (at 10m) (directional spectrum)

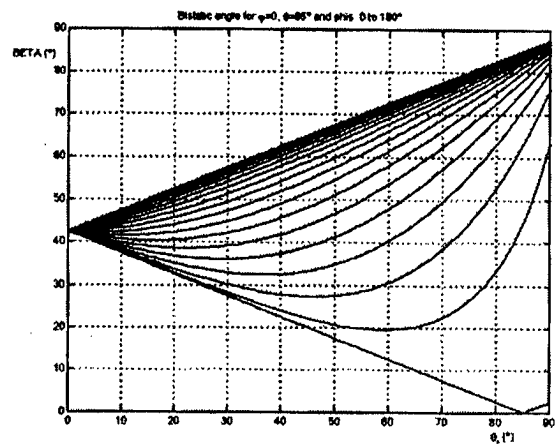


Fig. 11: The bistatic angle β for $\varphi=0^\circ$, $\theta=85^\circ$ and φ_r ranging from 0 to 180°

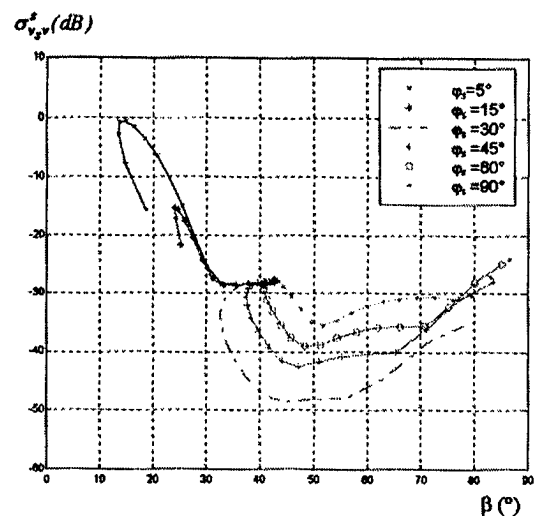


Fig. 12 : $\sigma_{v,v}^s$ with $F=9.9$ GHz, $\theta=85^\circ$, $T=18^\circ\text{C}$, $S=35\text{ppm}$, and wind speed $6\text{m/s} \sim 12\text{-kt}$ sea (at 10m) (Gaussian model)

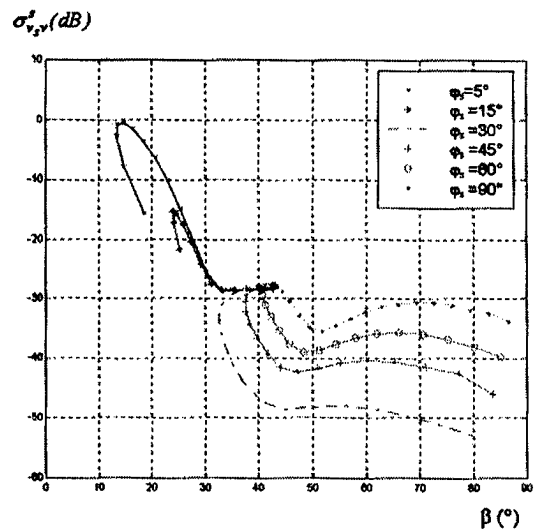


Fig. 13 : $\sigma_{v,v}^s$ with $F=9.9$ GHz, $\theta=85^\circ$, $T=18^\circ\text{C}$, $S=35\text{ppm}$, and wind speed $6\text{m/s} \sim 12\text{-kt}$ sea (at 10m) (Gaussian model)

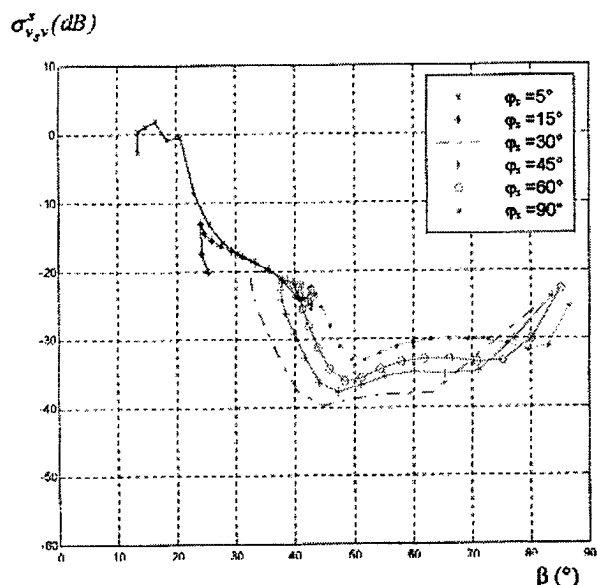


Fig.14 : $\sigma_{v,v}^s$ with $F=9.9$ GHz, $\theta=85^\circ$, $T=18^\circ\text{C}$, $S=35\text{ppm}$, and wind speed 6m/s -12-kt sea (at 10m) (directional model)

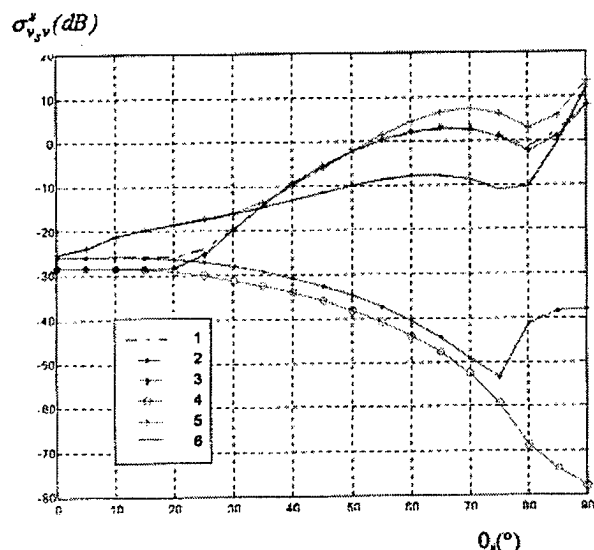


Fig.15 : $\sigma_{v,v}^s$ with $F=9.9$ GHz, $\theta=85^\circ$, $T=18^\circ\text{C}$, $S=35\text{ppm}$, and wind speed 6m/s -12-kt sea (at 10m)

4- CONCLUSION

The development of a theoretical composite model describing bistatic; reflectivity is presented as well as the numerical results computed for the bistatic radar cross-section from rough surfaces especially from the sea surface using the Gaussian Model and the Pierson-Moscowitz's spectrum. The scattering coefficients are calculated from the incoherent summation of echoes projected by each surface element and rewritten as a function of the transmitter and the receiver polarization. The numerical results are used to show the Brewster angle effect on near-grazing angle scattering. At larger grazing angles the diffuse component is usually larger for the vertical polarization than for horizontal. Notice that for the composite component $\sigma_{h,h}^s$ exceeds $\sigma_{v,v}^s$.

ACKNOWLEDGMENTS

This work was partially supported by the « Centre d'Electronique de L'Altmement », Thomson-CSF and DCN Toulon.

REFERENCES

- [1] P. Beckman and A. Spizzichino, « *The Scattering of Electromagnetic waves from Rough Surfaces* » Oxford: Pergamon, 1963.
- [2] A. Khenchaf, F. Daout, and J. Saillard, « *Polarization degradation in the sea surface environment* », IEEE Proc. Oceans 95, vol.3, San Diego, California, 1995, pp.1517-1522.
- [3] A. Khenchaf, F. Daout, and J. Saillard, « *The two-scale model for random rough surface scattering* » - IEEE Supp. Proc. Oceans 96, Ft. Lauderdale, Florida, 1996, pp, 50-54.
- [4] F.T. Ulaby, R.K. Moore, and A.K. Fung - « *Microwave remote sensing: Active and Passive* », volume 2. Addison-Wesley Publishing Company, 1982.
- [5] Donald E. Barrick, « *(A review of scattering from surfaces with different roughness scales* », Radio Science, vol. 3, No 8, August 1968.
- [6] A.K. Fung, K.K. Lee, « *A semi-empirical sea-spectrum model for scattering coefficient estimation* », IEEE Journal of oceanic Engineering, vol. OE.7, No 4, pp. 166176, October 1982.
- [7] C. Cox and W. Munk, « *Measurement of the roughness of the sea surface from photographs of sun glitter* », J. Opt. Soc. Amer., vol. 44, No 11, pp. 838-850, 1954.
- [8] A. Khenchaf, « *The Brewster Angle Effect on Sea Surface Scattering for Near-Grazing Incidence* », IGARSS'99, 28 June - 2 July 1999, Hamburg, Germany.

USE OF IN-SITU BURNING AS PART OF THE OIL SPILL RESPONSE TOOLBOX

Nir Barnea
Office of Response & Restoration N/ORRx1
National Ocean Service, NOAA
7600 Sand Point Way NE
Seattle, Washington 98115-0070

Abstract

In-situ burning of spilled oil has some distinct advantages as a response option. Throughout the United States over the last decade, research, field tests, and development of guidelines have advanced the understanding and use of in-situ burning. The lessons learned from past spill incidents about the effectiveness of in-situ burning can facilitate its consideration at future spills. To that end, I describe four case studies of in-situ burning, each representing a different scenario: on the open sea, in a river, in a wetland, and inside a stranded vessel. Although the circumstances of these burns differ, it is evident that in-situ burning can effectively remove spilled oil from the environment. In-situ burning is not suitable for all spill situations, and there are issues that need to be resolved.

I. Introduction

Over the last decade, considerable research on in-situ burning has been conducted on several fronts: Scientists and spill responders have 1) conducted test burns to study the feasibility of burning oil on water under various conditions, 2) investigated smoke plumes and characterized their components, and 3) developed computer programs to predict burn smoke-plume trajectories. Federal and state agencies have prepared guidelines to incorporate in-situ burning into spill response efforts around the nation, and monitoring plans are in place to assess particulate concentrations at sensitive locations downwind of the burn.

Another way to assist decision makers in evaluating in-situ burning as a spill response option is to examine specific incidents where in-situ burning was used on-scene and discuss the lessons learned.

The purpose of this paper is to 1) provide a brief overview of in-situ burning and its benefits and tradeoffs, 2) describe and discuss four case studies representative of in-situ burning in different spill environments, and 4) evaluate the effectiveness of these burns based on accumulated experience and current understanding.

II. Overview of In-Situ Burning

A. What is In-Situ Burning?

"In-situ" is Latin for "in-place." In-situ burning is the controlled burning of oil that is contained in, or has spilled from, a grounded vessel, a ruptured pipeline, or fuel storage or other facilities. On the open seas, the oil to be burned may be contained within a floating boom or sometimes within a stranded vessel, as in Fig. 1.

Inland, the oil may be contained in a marsh, wetland, or collected within a fire boom on a river. The oil is [it using a hand-held igniter or an igniter suspended from a helicopter, and the fire burns as long as the oil is thick enough to support combustion-usually about 1/10 of an inch (23 mm) thick. When conducted properly, in-situ burning can significantly decrease the amount of oil and minimize its adverse effects on the nearby environment.

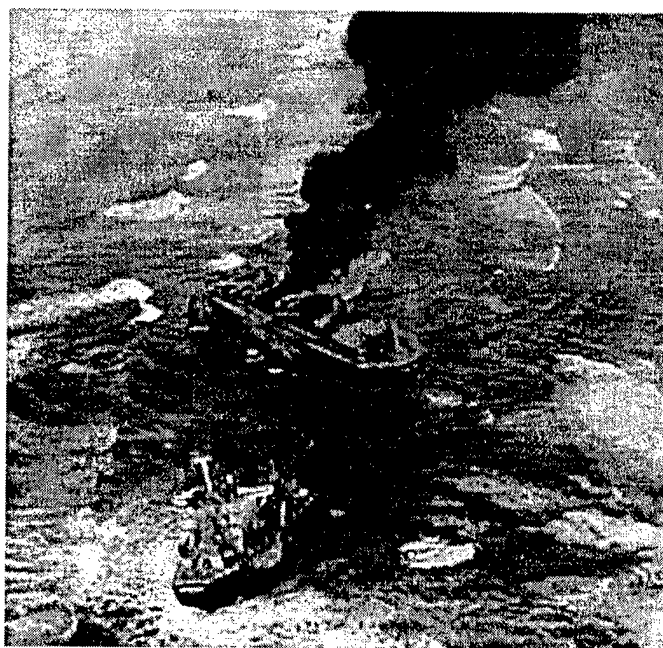


Fig. 1. Burning of fuel oil in the *New Carissa*, Coos Bay, Oregon, February 1999

B. Pros and Cons

Minimizing the spread of the oil slick and removing as much of the oil as possible is the major objective of oil spill response. In-situ burning is a response option that, when used alone or with other methods, can optimize the spill-response effort. Under the right conditions, in-situ burning is a fast, efficient, and relatively simple way of removing spilled oil from the water or from within the vessel. It also greatly reduces the amount of collected oil that must be stored and disposed, as well as the amount of waste generated. When oil spills onto ice-covered water or into a marsh, in-situ burning may be the only feasible spill response method (Buist et al. 1994). Because only the oily layer on the water surface is burned, the roots of marsh vegetation are left intact, and regrowth is rapid. In contrast, mechanical cleaning may be disruptive to fragile marshland, both from equipment and human trampling, and recovery is slower.

On the other hand, in-situ burning is not feasible under all circumstances. Wind and water conditions can preclude burning; for example, when winds are greater than 20 knots, waves are higher than 3 feet, and water current is swifter than 1 knot. Most oil will not ignite when emulsification is greater than 25-30%, unless treated with an emulsion breaker. In addition, a special fire boom is required during a burn that can withstand the intensive heat as well as the usual mechanical stresses associated with wave action and maneuvering of the boom (Buist et al. 1994). In-situ burning also requires strict safety precautions for the personnel conducting the burn.

When burning oil in a marsh, the oil must be floating on the water; otherwise burning may drive the oil down into the soil and the roots of plant life, possibly exacerbating rather than minimizing the oil's damage. Finally, because in-situ burning produces copious amounts of black smoke, concerns about human health impacts may either preclude an otherwise feasible burn or require monitoring at sensitive locations such as downwind population centers (Barnea & Laferriere 1999).

III. Case Studies

The following four case studies represent different scenarios in which in-situ burning have taken place. Table 1 summarizes the statistics for type and amount of oil spilled and burned for each case study.

A. Exxon Valdez Oil Spill, Alaska

On the evening of March 25, 1989-nearly two days after the *Exxon Valdez* spilled 11 million gallons of Alaska North Slope crude oil into Prince William Sound-two fishing vessels from the Port of Valdez, with a crew of fishermen and oil spill experts, conducted in-situ burning of an estimated 15,000-30,000 gallons of spilled oil about 10 miles south of the *Exxon Valdez* grounding site (Allen 1990). The crew

collected the oil for approximately 30 minutes by towing a fire boom in a U configuration through patches of Alaska North Slope crude oil, which at this point was somewhat emulsified and varied in thickness from an estimated 1/10 mm to several mm.

When it was estimated that enough oil had been collected in the apex of the fire boom, an igniter made of gelled gasoline in a plastic bag was released from one of the boats, floated toward the oil, and ignited it. The burn lasted for about 70 minutes, with flames reaching an altitude of 150-200 feet. When the fire was out, a taffy-like residue totaling about 300 gallons remained.

Close monitoring of the burn was hindered by darkness. However, when the amount of oil collected, the total burn time, and the amount of residue was calculated, an estimated 15,000 to 30,000 gallons of oil were burned, with an efficiency of 98-99% removal of the oil contained in the boom (Allen 1990). Although the boom sustained some damage, it was still operational at the end of the burn. Unfortunately, a massive storm the next day caused extensive emulsification of the oil, rendering it unburnable and spreading the oil over a larger area.

To date, this is the only in-situ burning on record in which a fire boom was used to burn accidentally spilled oil on the high seas. Assuming that 30,000 gallons of oil were burned in the boom, this amounts to less than 0.3% of the total oil spilled by the *Exxon Valdez*. However, this successful operation provided a significant boost to promote in-situ burning of oil as a feasible spill response option.

Table 1. Summary of amounts and types of oil at four in-situ burns.

Description of spill	Est. gals. and type of oil before burning	Est. gals. of oil burned
March 1989 <i>Exxon Valdez</i> Alaska	11 million Alaska North Slope Crude	15,000– 30,000
October 1994 Pipeline spill San Jacinto R., Texas	546,000–840,000 ¹ Mixed diesel, Arabian Light Crude	323,000– 590,000 ²
April 1993 Naval Storage Facility Brunswick, Maine	23,500 JP-5 aviation fuel	23,000
February 1999 <i>New Carissa</i> Coos Bay, Oregon	320,000 IFO, diesel	200,000

¹ Rough mass balance (NOAA 1994).

² Est. composite amount of oil burned, beached, and dispersed. No separate estimate available for amount of oil burned (NOAA 1994).

B. San Jacinto River, Texas

Following massive rainfalls in southeastern Texas in mid-October 1994, the San Jacinto River flooded, causing extensive damage in its path. Four pipelines crossing the river east of Houston were damaged by the flood and began releasing petroleum products: liquefied petroleum gas (LPG), gasoline, diesel fuel, and Light Arabian crude oil (NTSB 1996). The LPG and gasoline pipelines ruptured around 9:50 a.m. on October 20, 1994, followed by a series of explosions and a massive fire on the San Jacinto River. The crude oil and diesel pipelines ruptured later that day, adding their contents to the ongoing burn. Not all the product caught fire, however; some escaped unburned and floated down the river, contaminating the shoreline and triggering a massive cleanup operation (Leonard 1997).

The fire burned for 4 days, diminishing gradually over time. On the morning of October 23, only several small fire points remained. At that time, the FOSC approved a burn enhancement plan that called for using a fire boom across the San Jacinto River downstream of the ruptured pipelines to "contain and remove by burning additional crude oil and products." In essence, this was an in-situ burning plan designed to minimize potential shoreline impacts by taking advantage of the river current transporting floating oil into a fire boom stretched across the river channel where the oil would be ignited.

The plan was carried out as outlined. A fire boom was stretched across the river channel and anchored to the shoreline. At 6 p.m. that evening the product that had accumulated in the boom was ignited using flares set on a trash-can lid that was sent floating down the river and into the fire boom. At that point it was estimated that the 500-foot boom contained about 40,000 gallons of product (NTSB 1996). The mixture of gasoline, diesel, and light crude oil ignited readily and burned throughout the night and next day, self-extinguishing 28 hours later.

Although in its investigation report, the National Transportation Safety Board (NTSB 1996) identified safety and communication problems in the execution of the burn, the burn was deemed very successful in eliminating the released oil. The NTSB stated that, "In hindsight, the in-situ burn was likely the most effective remedy measure that could have been undertaken; however, risk to workers and the public were increased significantly when the unified command conducted an in-situ burn without having in place appropriate checks and balances to ensure that approved procedures and requirements were followed explicitly" (NTSB 1996).

C. Brunswick Naval Air Station, Maine

When considering the frequency of in-situ burning over the last decade, one fact immediately stands out: In situ burning was conducted for landborne spills far more often than for spills on open water or rivers. This is not

surprising because few spills are amenable to burning in the open ocean. While confining factors such as containment, weather conditions, and a narrow window of opportunity (mostly due to rapid emulsification) can prevent burning at sea, these factors play a much smaller role on land. The burning operation near Brunswick, Maine is a case in point.

On March 29, 1993, personnel of Brunswick Naval Air Station detected a spill of about 63,500 gallons of JP-5 aviation fuel. The fuel leaked from a storage facility on base, and made its way, through a storm sewer system, into a freshwater wetland where it was contained by ice, snow, and other natural barriers. The wetland is not easily accessible at the best of times; and the snow and ice still covering most of its surface made access difficult for cleanup personnel and machinery. Also, hauling in cleanup equipment and personnel could have harmed the fragile wetland ecosystem and driven the oil deeper into the ground. A compromise was reached: Mechanical means would be used to the extent feasible, followed by in-situ burning to hopefully eliminate as much of the remaining oil as possible (Eufemia 1994).

Mechanical recovery of the spilled JP-5 fuel took place over several days, using containment booms, underflow dams, sorbent pads, and vacuum trucks. When mechanical recovery reached the limit of its effectiveness after collecting about 40,000 gallons of product, a successful trial burn was conducted. Then, on April 6, more than a week after the spill was discovered, the remaining fuel in the wetland was ignited by wicks at the end of poles, and a full-scale in-situ burn ensued for about 5 hours. Smaller burns were conducted during the next 2 days to burn the remaining oil emerging from beneath the ice cover.

When the burn was completed, it was estimated that less than 450 gallons of fuel product remained in the wetland. Visual inspection of the wetland the following spring and summer indicated little impact from the spill or the burn, and long-term follow-up confirmed these observations.

The successful combination of mechanical removal and in-situ burning at this spill highlights several points. First, several spill response methods can work in combination, either simultaneously or in tandem, as was the case here. Second, the emphasis on evaluating tradeoffs and identifying the best methods to address a specific situation was proven effective. The goal in this case was to clean up the wetland with maximum efficiency and minimum damage to the environment. As long as mechanical means were adequate, they were used. However when vacuuming and absorbing the oil were no longer effective and continuing them threatened to cause more damage than good to the wetland, in-situ burning was used. Third, after considering all the options, burning was accepted both by the spill responders and by the general public. Despite the fact that nearby homes were less than half a mile away, there was no opposition to the burn or complaints after it was done. Burning was done only when

the winds were favorable, and local officials and agencies were involved and informed. When burning is done in this fashion, it is viewed as a necessary alternative and is accepted as such, as in Brunswick, Maine and, nearly six years later, in Coos Bay County, Oregon during the New Carissa incident.

D. New Carissa, Oregon

On Thursday, February 4, 1999 the MV *New Carissa*, a wood-chip freighter with 400,000 gallons of fuel onboard, was pushed toward shore by a gale-force wind and became stranded on the Oregon Coast 2.7 miles north of the entrance to Coos Bay. Several attempts to free the ship from the sandy beach using its own power failed, and a series of powerful winter storms prevented tugboats from coming to the rescue. Lightering the ship was also impossible due to severe logistical problems and the continuing stormy weather.

After a week of being battered by a series of winter storms, the *New Carissa's* structural integrity was compromised and fuel (IFO and diesel) began spilling from its fuel tanks and impacting the nearby shoreline. The National Weather Service was forecasting more severe winter storms, threatening an even larger spill. On Wednesday, February 10, the Unified Command decided to burn the fuel aboard the *New Carissa*.

Burning ships in-situ to prevent an oil spill and environmental damage has been done before, but with smaller ships and far from population centers (Allen 1999). The circumstances may have been different, but the main reasoning is similar: A vessel becomes hopelessly stranded, cannot be salvaged, and poses a risk to the environment-in which case burning the vessel, or at least its fuel, is deemed the least damaging option.

Following the decision to burn the fuel on the ship, a Navy ordnance team, working closely with the US Coast Guard, placed explosives on the ship and by the evening of February 10 attempted to breach the fuel tanks and ignite the fuel. The first attempt was unsuccessful; a second attempt the next day utilized more explosives. Around 5:45 p.m. on February 11, the charges were set off, the fuel ignited, and the ensuing in-situ burning continued for over 30 hours, with the intensity of the burn gradually diminishing over time.

Less than two hours after the burn began, the ship broke in two. Fortunately this event did not result in significant additional spillage, although it presented a major problem later when the time came to tow and scuttle the ship. The bow section was towed on March 2, broke loose 50 miles offshore, and was beached 60 miles north of Coos Bay, near Waldsport, Oregon. On March 8 the bow of the *New Carissa* was freed again, towed out to sea, and 3 days later was sunk by explosives, then canon fire from a destroyer, and finally by a submarine-fired torpedo, 280 miles west of the Oregon Coast.

Public health was an issue in this burn. Because the ship was only a few miles from the nearby towns of Empire, North Bend and Coos Bay, the burn raised concerns about possible impacts of the smoke. Of particular concern were the effects of small particulates in the smoke plume on sensitive members of the general public, such as the elderly, the very young, and persons with respiratory problems. Exposure to the smoke plume was possible 1) if the wind were to blow from the west, sending the smoke over these towns, or 2) if the plume-which usually tends to rise and stabilize at several hundred feet, thus blowing overhead-were to stay low and actually come in contact with people at ground level.

To predict the path and behavior of the smoke plume and its possible impacts, modeling trajectories of the smoke plume were done before the burn was initiated. These trajectories estimated that given the predicted southerly wind, the smoke plume would rise to several hundred feet, stabilize at this elevation, and be carried toward the north, parallel to the shoreline.

In addition to the modeling, the Federal On-Scene Coordinator (FOSC) requested that the smoke plume be monitored at ground level, at the population centers near the burn. The Special Monitoring of Advanced Response Technologies (SMART) program was implemented for this incident. Small and flexible monitoring teams were deployed before the burn at several population centers in the vicinity of the ship. Particulate concentrations were monitored, both before the burn (to ascertain background levels) and later during the duration of the burn. Data were recorded automatically by the instruments' data logger and manually by the monitoring personnel.

Monitoring results confirmed that at no time during the initial burn of the ship (about 30 hours) were particulate concentrations at any of the population centers above the level of concern. Most of the time during the first 16 hours of the burn, the wind carried the smoke out to sea. Both the fire and the smoke had both greatly diminished by the time the wind changed direction and blew the smoke northeasterly toward shore. Particulate levels recorded under these conditions were still much below the level of concern.

Approximately 200,000 gallons of the 380,000 gallons of IFO and diesel fuel originally onboard the *New Carissa* are estimated to have burned. An estimated 80,000 gallons spilled, mostly before the burn, and the remainder is still trapped in the vessel-a solid paste in the cold, near-freezing waters where the bow was sunk.

IV. Discussion

A. In-Situ Burning as a Response Option

When considering the effectiveness of in-situ burning as a response option, we conclude that, under favorable conditions, it has proven to be very effective. In some cases, burning would have been more effective had it been

implemented on a broader scale.

In the case of the *Exxon Valdez*, for example, one team using 500 feet of fire boom was able to burn between 15,000 and 30,000 gallons of oil in one evening. Let's assume that 1) there had been three teams, each using 500 feet of fire boom and conducting three burns per day over two days (until the storm emulsified the oil, rendering it unburnable) and 2) the same efficiency in operation and oil collection. In this hypothetical scenario, the total amount of oil that could have been burned is between 270,000 and 540,000 gallons. Although this would have burned only 2.5% to 5% of the total 11 million gallons spilled, it is a significant quantity given that the estimated oil recovered after two weeks of skimming by dozens of skimmers was only 600,000 gallons (Skinner & Reilley 1989).

Experience with in-situ burning elsewhere shows similar trends. Although uncertainty remains about the amount of oil spilled during the San Jacinto incident, it is generally agreed that the initial fire greatly reduced shoreline impacts, and that the in-situ burning conducted later further reduced the amount of oil that could have impacted down-river shorelines.

The same can be said for marsh and wetland burns. When the burning was initiated near Brunswick Naval Air Station in Maine, around 25,000 gallons were still present in the wetland and could not be recovered by mechanical means. When the burning was completed, less than 500 gallons remained. Similar results have been achieved elsewhere. A March 1995 burn conducted at the Rockefeller Wildlife Refuge in Louisiana, following a pipeline spill of gas condensate, removed a large portion of the remaining product (Henry 1996). A follow-up study conducted 3 years later indicated that, despite the high toxicity of the spilled gas condensate, eliminating the product by burning promoted recovery of the marsh to its pre-burn condition (Pahl & Mendelson 1999).

The burn conducted during the *New Carissa* incident confirmed what spill response planners greatly emphasize: The need to select the response method that will best address the situation at hand. Because of the adverse circumstances specific to the *New Carissa* spill, other response methods were not feasible. The options were to do nothing, or conduct in-situ burning of the fuel in the vessel to reduce the potential for shoreline contamination from a ship that had already begun spilling oil. It was clear to the Unified Command and to public health officials that the burn would generate a significant amount of smoke. However, the components of the smoke plume were well known, weather predictions and modeling data indicated that the smoke plume would be carried northward, away from population centers, and field monitoring provided real-time particulate concentrations to the Unified Command. Because public health officials were brought into the process and were provided the information they needed, they were ready with contingency plans to protect the public in case the smoke were to blow inland.

The *New Carissa* burn was not a complete success. Initially it was hoped that most, if not all, the fuel onboard the vessel could be ignited and burned. However, considering the fact that no other response option was possible at that time, and the possible adverse implications of doing nothing--i.e., a large spill impacting many miles of environmentally sensitive shoreline--the decision to conduct the burn proved not only courageous, but wise.

B. Problems

In-situ burning, as shown by the cases above, may be a highly effective spill response tool in some cases, but not in all. When in-situ burning was conducted in the Komi Republic in Northern Russia following massive multiple spills from a pipeline, the burn eliminated a significant portion of the spilled oil (which in some places formed a layer 1-meter thick). However, there was no standing surface water on which the oil could float--a layer that would have also served to insulate the soil from the heat. Thus the heat generated by the burn drove the oil deep into the ground, and the residue layer on top of the peat moss substrate was viscous and difficult to remove. This suggests, in this case, that in-situ burning may not have been the best response option (Hartley 1996). Similarly, burning may not be suitable if the fire can damage the vegetative habitat in a specific environment (Zengel et al. 1999). When considering in-situ burning, the tradeoffs should be evaluated carefully, and the burn conducted only if it provides a net environmental benefit and enhanced recovery.

Another factor that may render in-situ burning undesirable is concern for human safety. In most burns safety has been suitably addressed and has not been a problem. During the San Jacinto burn, however, several factors converged to create a situation that put human safety at risk (NTSB 1996). Recommendations to correct the safety deficiencies have been made and should be closely followed whenever in-situ burning is conducted, to protect the safety of personnel conducting the burn.

Potential public exposure to the smoke plume particularly to the small particulate matter in the plume has been a concern for a long time, and has been addressed on several fronts. Burns are pre-approved only when they are at a minimum distance from population centers, with case-by-case approval required when a burn is requested at a closer proximity. Smoke trajectory models have been developed that can provide a relatively accurate prediction of plume behavior; and a monitoring program has been developed to measure particulate concentrations at sensitive locations and provide this data, almost real-time, to the Unified Command. Close cooperation with public health officials is recommended for burns where there is the potential for public exposure to the smoke plume, such as the *New Carissa*.

Lastly, it seems that one of the main impediments to the use of in-situ burning (when it is feasible and appropriate) are not lack of technical capabilities or

environmental limitations, but lack of support from public officials and citizens (McKenzie & Lukins 1998). Local, state, and federal decision-makers may be apprehensive about using in-situ burning. Some members of the general public may be against it, environmental groups may oppose it, and public health officials may not welcome in-situ burning for concerns that water pollution is traded for air pollution. The unwillingness to use spill response method, despite its effectiveness, means that it may be passed over even if it offers distinct advantages. In-situ burning should be part of the repertoire of response tools that are available, all of which are evaluated at the scene on the basis of their specific benefits and limitations and within the context of the specific spill conditions.

References

- Allen, A.A. 1990. Contained controlled burning of spilled oil during the *Exxon Valdez* oil spill, p. 305-313. *In* Proceedings of the Thirteenth Arctic and Marine Oil Spill Program Technical Seminar, June 6-8, 1990, Edmonton, Alberta.
- Allen, A.A. 1999. Personal communication, Feb. 9, 1999. Spilltec, Woodinville, Washington.
- Barnea, N. & R. Laferriere. 1999. SMART- Special Monitoring of Advanced Response Technologies. Paper #069 presented at International Oil Spill Conference, Seattle WA, March 8-11, 1999.
- Buist, I.A., S.L. Ross, B.K. Trudel, E. Taylor, T.G. Campbell, P.A. Westphal, M.R. Meyers, G.S. Ronzio, A.A. Allen, & A.B. Nordvik. 1994. The science, technology, and effects of controlled burning of oil spills at sea. MSRC Tech. Rep. Ser. 94-013, Marine Spill Response Corp., Wash. DC, 382 P.
- Eufemia, S.F. 1994. Brunswick Naval Air Station JP-5 aviation fuel discharge. In-situ burn of fuel remaining in freshwater marsh, April 1993, p. 87-90. *In* Proceedings, In-Situ Burning Oil Spill Workshop, Orlando FL, January 1994.
- Hartley, A. E. 1996. Overview of the Kolva River Basin 1995 oil recovery and mitigation project, p. 1301-1308. *In* Proceedings of the Nineteenth Arctic and Marine Oil Spill Program Technical Seminar, June 12-14, Calgary, Alberta, Canada.
- Henry, C.B. 1996. Fate of spilled oil following application of in situ burning as a spill mitigation technique at Louisiana's Rockefeller Refuge: Chemistry results from year-one monitoring study. Tech. Rep. IES/RCAT96-23, Inst. for Environ. Studies, Louisiana State Univ., Baton Rouge LA, 48 p.
- Leonard, J.J. 1997. San Jacinto River incident: Armageddon visits Houston, p. 972. *In* Proceedings, International Oil Spill Conference, Fort Lauderdale FL, April 7-10, 1997.
- McKenzie, B. & J. Lukins. 1998. Preparedness for in situ burning operation: An Alaskan perspective, p. 47-54. *In* In Situ Burning of Oil Spill Workshop, New Orleans LA, Nov. 2-4, 1998.
- NTSB (National Transportation Safety Board). 1996. Evaluation of pipeline failures during flooding and of spill response actions, San Jacinto River near Houston, Texas, October 1994. Pipeline Special Invest. Rep., Notation 6734. Wash. DC, 50 p.
- NOAA (National Oceanic and Atmospheric Administration). 1994. Draft Mass Balance, 26 Oct. 94. San Jacinto River Spill Information Management Report. NOAA-HAZMAT, Seattle, WA.
- Pahl, J.W. & L.A. Mendelson. 1999. Recovery of a Louisiana Coastal Marsh 3 Years After In Situ Burning of a Hydrocarbon Product Spill. Paper ID #268 presented at International Oil Spill Conference, Seattle WA, March 8-11, 1999.
- Skinner, S.K. & W.K. Reilley. 1989. The *Exxon Valdez* spill. A report to the President. National Response Team, 68 p.
- Zengel, S.A., J.A. Dahlin, C. Headley, & J. Michel. 1999. Environmental effects of in situ burning in inland and upland environments. Paper #376 presented at International Oil Spill Conference, Seattle WA, March 8-11, 1999.

BALLAST WATER TREATMENT DURING EMERGENCY RESPONSE: THE CASE OF THE M/T *IGLOO MOON*

Alan J. Mearns
Hazardous Materials Response Division
Office of Response & Restoration
National Ocean Service, NOAA
7600 Sand Point Way NE
Seattle, Washington 98115-0070

LCDR Brad Benggio
Office of Response & Restoration
National Ocean Service, NOAA
Commander USCGD7 (m-SSC)
Brickell Plaza Federal Building
Miami, Florida 33131

Thomas D. Waite
College of Engineering
243 MacArthur Building
University of Miami
1251 Memorial Drive
Coral Gables, Florida 33145

Abstract

This paper describes an emergency ballast-water response incident aboard a liquid petroleum gas tanker stranded on a coral reef near Miami, Florida in November 1996. Ballast water from the stricken tanker had to be offloaded in order to move the ship off the reef. Because of the origins of the ballast water and the vessel's proximity to the sensitive environment of Biscayne Bay National Park, concerns were raised over the potential risk of introducing non-indigenous biota via the ballast water that could harm the reef's natural biota. Twelve days after the stranding, 1.1 million gals. (4.3 million L) of water in the ballast tanks were treated with a biocide, calcium hypochlorite, $\text{Ca}(\text{OCI})_2$, at dosages of 50 or 100 ppn chlorine. The treated ballast water was then discharged overboard, after which assisting vessels safely towed the stricken freighter off the reef without incident or spillage (other than the discharge of the chlorinated ballast water).

The primary considerations that led to the decision to treat the ballast water were confounded by many explicit and implicit uncertainties about the actual presence or absence of non-indigenous species, the holding times and sources of water in each tank, and minimum effective treatment levels. Had there been more accurate shipboard records of the vessel's ballast-water exchanges throughout its voyage, these response actions may not have been necessary. Thus, to expedite emergency ballastwater responses in the future, vessel owners need to maintain and provide accurate ballast-water records. Other lessons learned from this experience include the need for trustee-acceptable sampling and monitoring strategies before and during

treatment, accurate data on biocide effectiveness (including required concentrations and contact times), and the recommendation that ships avoid taking on ballast water over foreign reefs.

I. Introduction

Ballast is any solid or liquid placed in a ship to alter the draft and trim during voyages and for port entry, to regulate transverse stability at sea, improve maneuverability and propulsion efficiency, to control trim and heel during cargo handling and keep the vessel within hull-loading limits, etc. The discharge of ballast water from foreign locations is considered a major pathway for introduction of nonindigenous aquatic species to new ports and coastal regions. Some nonindigenous species, such as the zebra mussel (*Dreissena polymorpha*) and an Asian clam (*Portamocorbula amurensis*), have significantly altered some aquatic ecosystems of the United States (NRC 1996). As a result, local, state, provincial, national, and international authorities have been passing legislation and agreements to control introductions, including voluntary and involuntary ballast-water management actions (NRC 1996, Cohen 1998). These actions include high-seas ballast water exchange and physical and chemical shipboard treatments of ballast water.

This paper explores issues associated with ballast-water treatment during emergency response to a ship's grounding or oil spill. In the case of the grounded *Igloo Moon*, its ballast water had to be offloaded to allow the ship to be safely removed from the reef. Yet the origins of its ballast water, and the vessel's proximity to an environmentally sensitive area, raised concerns

about introduction of unwanted species. The ultimate question is: Should the treatment of ballast water be integral to an emergency response? We hope that this paper will promote discussion of the need for emergency treatment of ballast water and will stimulate planning and preparing for future responses. This paper describes a specific emergency-response incident and the decision and implementation processes that led to the treatment and discharge of ballast water from a grounded ship, all within the context of the overall incident response. The paper discusses implications for future ballast-water responses and recommends research and management initiatives.

II. Background and Methods

On the morning of November 6, 1996 the LPG (liquid petroleum gas) tanker MIT *Igloo Moon* stranded hard aground on a coral reef 5.5 km south-southeast of Cape Florida on the boundary of Biscayne Bay National Park (Fig. 1). The vessel's cargo was 6589 metric tons (t) of butadiene; the ship also carried 205,000 liters (L) of intermediate fuel oil (IFO 380), 108,000 L of diesel fuel, and 22,000 L of lubrication oil. The worst-case scenario of a spill from the vessel would have been disastrous for the sensitive reef environment and nearby urban areas. The overall response was well organized and culminated 16 days later on November 21 in successfully refloating the ship without any oil spillage. In fact, this incident response served as an example of the successful implementation of the U.S. Coast Guard's newly established Incident Command System (Benggio et al. 1998).

All three authors were involved in the response: LCDR Brad Benggio served as the NOAA Scientific Support Coordinator (SSC) to the Federal On-Scene Coordinator (FOSC), i.e., the U.S. Coast Guard. Dr. Thomas Waite had recently served on a National Research Council (NRC) Marine Board Committee on controlling non-indigenous species introductions from ballast water (NRC 1996) and was familiar with ballast issues and treatment options. Dr.

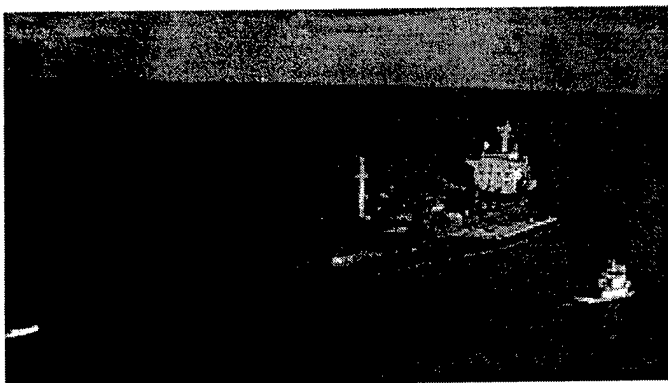


Fig. 1. The M/T *Igloo Moon* stranded on a coral reef near Miami, Florida, November 1996. Barge is offloading fuel.

Alan Mearns was with NOAA's Biological Assessment Team as part of the SSC support.

Background research for this report included collecting and reviewing historical "hot lines" transmitted from the scene, U.S. Coast Guard reports, daily incident reports, other notes on file at the Marine Safety Office (MSO) in Miami, and personal notes and recollections. A pre-stranding history of the ship's ballast water activity during its voyage was compiled from ship records.

III. Initial Status of the MIT *Igloo Moon* and Response Objectives

After the ship's stranding, the highly explosive butadiene remained in the undamaged refrigerated tanks. The double-bottom fuel tanks in the hull were ruptured, but no fuel was being released. The overall goal of the response was to refloat the vessel without any spillage and safely move it, and its hazardous cargo, to a nearby port. To do this, it was necessary to offload most of the ship's fuel, an estimated 400-700 t of butadiene, and most of its ballast water. The response objectives focused on the safety of the public and responders and the protection of sensitive marine resources and habitats. Incident actions included securing the site, lightering the fuel and cargo, chemical inhibitor recertification, hydrographic surveys for safe exit, assessing resources at risk, detailed planning for refloating, and possible evacuation. As described in Benggio et al. (1998), weather conditions and rough seas greatly influenced the timing of response activities (Fig. 2).

The many challenges to implementing these objectives are described in detail in Benggio et al. (1998). It is important to place the issue of ballast-water treatment within the overall perspective of the potential hazards of this stranded vessel. The chemical cargo, butadiene, is a colorless gas used to make plastics and other chemicals, and is shipped as a refrigerated liquified gas. Refrigeration must be maintained by an onboard fuel supply. Butadiene must also be shipped "inhibited" to prevent polymerization that would rupture the tanks. The chemical inhibitor must be periodically certified and replaced when certification expires. Butadiene is an easily ignited gas, heavier than air. If escaping vapor is ignited, it can very easily flash back to the source leak. Butadiene is also a suspected carcinogen.

Inhibitor certification was about to expire when the *Igloo Moon* went aground. Several fuel tanks were ruptured. Although there were no fuel spills, fuel had to be lightered off except for an amount necessary to maintain ship operations, especially refrigeration. In the event that neither of those actions could be undertaken, a safety zone and evacuation plan had to be developed and ready for implementation. Yet several response objectives and actions necessary to maintain the integrity of the cargo and fuel were delayed by several episodes of threatening weather and sea conditions (Benggio et al. 1998).

MT Igloo Moon Grounding

Salvage Operations Map
prepared by NOAA

Date/Time: 18 November 1996

1 inch = 2.40 miles

USE ONLY AS A GENERAL REFERENCE

Graphic does not show precise location of vessel.

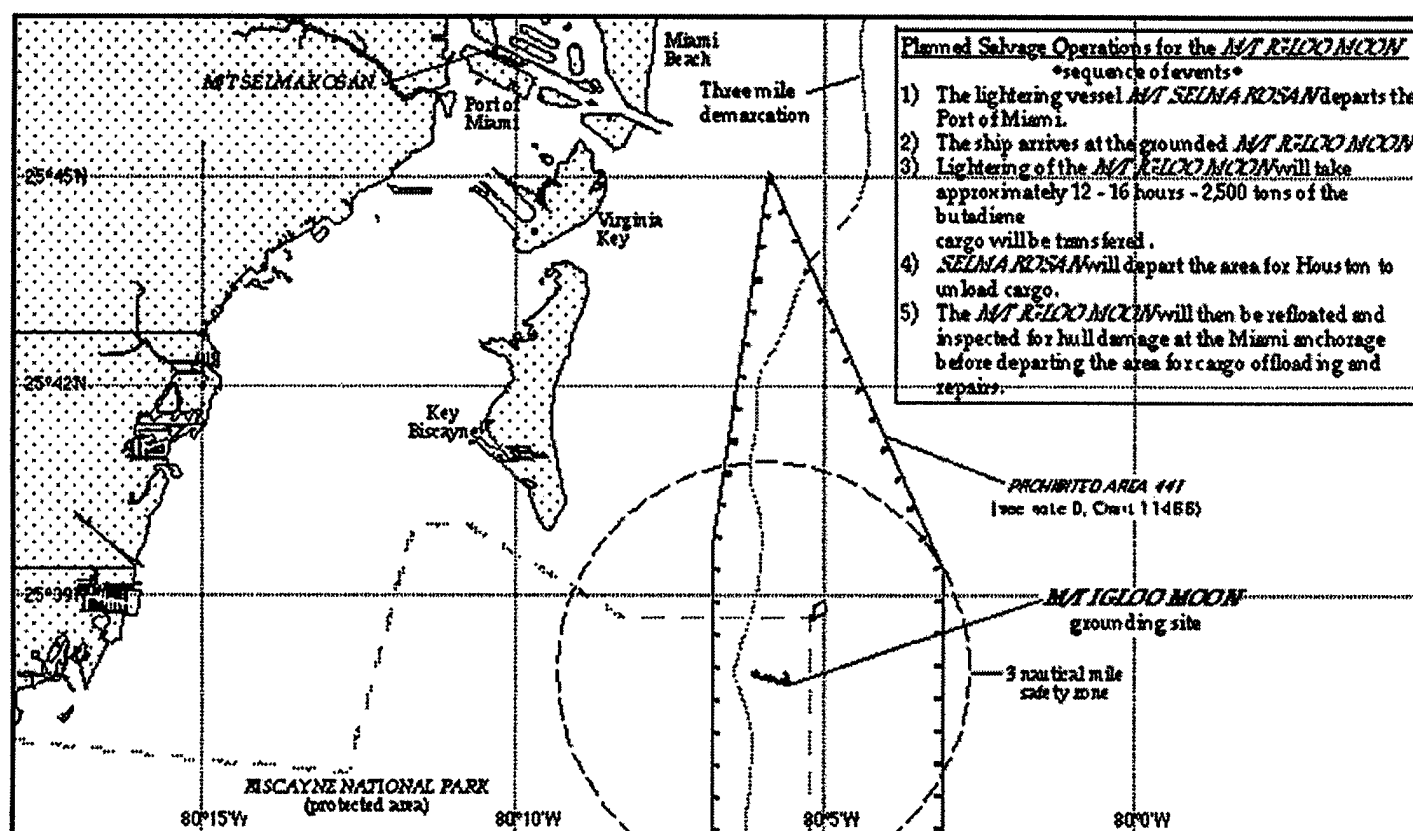


Fig. 2. Salvage Operations Map of the MT Igloo Moon grounding, prepared by NOAA.

IV. Ballast Water: What Were the Actual Risks?

Deballasting was the final step necessary to refloat the stricken vessel. The *MT Igloo Moon* had 11 ballast water tanks with a total capacity of 4144 t, or 1.24 million gals. Some of the tanks were not full when the vessel stranded, and water was exchanged during the course of the response to maintain stability, as needed. A pre-stranding history of the ship's ballast water exchanges during its voyage was compiled from ship records, although these records were incomplete and inconsistent. Attempts to calculate a "mass balance" of filling and discharge (Table 1) resulted in a mass balance inconsistent with the apparent mass onboard during the stranding. It eventually became evident, however, that at least some of the ballast water was from foreign coastal waters, notably western Africa (Dakar) and the Indian Ocean (Bandla, India; Table 1). The National Park Service (NPS), trustee of the reef, was concerned that release of the ballast water could introduce foreign marine life hazardous to the Biscayne Bay coral reef community. On November 15, during the closing days of the response, the NPS requested an assessment of the

threat posed by releasing the ballast water near the reef. A science committee was convened to review ballast-water treatment alternatives. Regardless of the sources of the ballast water, the committee was concerned that ballast tank sediments may have harbored nuisance species (such as predatory crabs or echinoderms). Thus, it was necessary to consider treatment of all the tanks, regardless of the most recent ballast-water source available. The committee agreed to treat all the tanks with chlorine before deballasting.

A. Assessing Risks and Ballast-Water Treatment Alternatives

Sampling protocols and treatment alternatives for ballast water discharge are reviewed in NRC (1996). The NRC recommends biological sampling to determine the presence or absence of nonindigenous biota. Ideally, water and sediment samples would have been taken from the ballast tanks of the *Igloo Moon* to assess the risk of exotic reef species being released onto the Biscayne Bay coral reefs. However, because of safety concerns, it was not possible during the waning days of the response to sample

Table 1. History of ballast-water exchange and emergency response actions for MIT *Igloo Moon*, July to November 1996. (See Benggio et al. 1998 for overall emergency response, e.g., cargo management, air monitoring, evacuation scenarios, etc.). t = metric tons

Day	Ship location	Event and/or ballast-water action.
7/10	Venice, Italy	Port & starboard side ballast tanks filled (+ 178.4 t)
7/13	Brindisi, Italy	6WD DB and port and starboard side ballast tanks discharged (max. -2892.6 t)
7/31	Altimira, Mexico	Takes on 788 t ballast (tanks unspec.)
8/14	Atlantic Ocean 29.27°N, 52.23°W	6WD DB ballast tanks filled (+2714.2 t)
8/21	Algericas, Spain	Forepeak ballast tank filled (+270.6 t)
8/26	Dakar, Senegal	Forepeak ballast tank discharged (-270.6 t). All ballast discharged (max. -4144.1 t). No ballast taken on.
8/28	Dakar, Senegal	Aftpeak tank filled (+418.2 t)
9/10	Al Yubail	Forward deep tank discharged (-562.7 t)
9/15	Red Sea (southern) 13.34°N, 41.51°E	Aftpeak tank discharged (-418.2 t)
9/28	Kandla, India	Forward deep tank filled (+562.7 t).
9/29		Takes on 1020 t at pier (discharged at sea because visibly dirty).
10/10	Al Jubail, Saudi Arabia	Takes on 800 t at pier (tanks unspec.)
11/6	Biscayne Bay FIL	Vessel hard aground.
11/8		Fuel lightering completed (some fuel left onboard for power).
11/9		3 anchors deployed to stabilize vessel.
11/12		Ballast added (tanks unspec.); notified of pending tropical storm.
11/13		Ballast added to forepeak tank at high tide; removed at low tide.
11/14		Approval to take on 450 t ballast to empty fuel tanks. Request to evaluate trade-offs of sanitizing ballast water in tanks.
11/15		Storm surge, vessel in motion; ambient ballast water added to fuel tanks.
11/16		Starboard list, small crack in engine room; vessel stable.
11/17		Wind and seas moderating; better conditions predicted. Decision to treat ballast water in tanks. Ca(OCl) ₂ brought on-scene. Two tanks treated to 100 ppm Cl. 2-hour hold planned, but discharge postponed.
11/18		Treated ballast from forepeak and #1 port wing tanks discharged (1108,000 gals.). Remaining tanks treated to 50 ppm Cl. Pre-approval to discharge ambient ballast from fuel tanks.
11/19		Vessel extraction channel identified and marked. Cargo (butadiene) lightering vessel delayed. Remaining treated ballast in tanks remains onboard.
11/20		Cargo lightering completed.
11/21		All ballast discharged; vessel refloated at 1447L. Vessel departs via extraction channel; enters deep water at 1527L.

the ship's ballast water in order to satisfy the trustee's concerns. Also, there was no information from the shipboard records to confirm whether or not ballast water had in fact been taken on or near foreign coral reefs. In the face of these uncertainties, it was quickly decided that all the ship's ballast water needed to be treated in order to adequately address the trustee's concerns.

B. Decision to Treat with HTH Calcium Hypochlorite

The ballast-water treatment alternatives considered by the science committee included 1) no response, 2) physical treatment (e.g., heat or UV irradiation), and 3) chemical treatment (sanitizing with chemicals). Following a brief review of the alternatives, chemical treatment was quickly deemed to be the only realistic option to insure that nonindigenous biota, if present, would not be released alive. The chemical alternatives were quickly narrowed down to chlorination. Chlorine destroys bacteria, pathogens, and other organisms by oxidizing or "burning" cell walls. It reacts vigorously with anything organic and, once it has reacted, is used up (i.e., breaks down into a less toxic form). This is why chlorine disinfection in swimming pools and water supplies is a continuous process requiring a continuous supply of chlorine.

Alternatives for chlorination included sodium hypochlorite (a liquid) and calcium hypochlorite (a solid). Calcium and sodium hypochlorites are commonly used as disinfectants and bleaching agents. The most available and workable reagent for this response was calcium hypochlorite, $\text{Ca}(\text{OCl})_2$: a whitish powder containing about 65% available chlorine (the active ingredient) and the remainder made up of calcium and impurities. In reaction with water, calcium hypochlorite forms calcium hydroxide and hypochlorous acid, the active killing agent. However, calcium hypochlorite is extremely reactive when mixed with anything organic--skin, grass clippings, paper, oil and petroleum products--becoming intensely hot and sometimes exploding.

C. Dosage

The effective disinfection concentrations for swimming pools is about 1 to 3 mg/L (or parts per million, ppm) as chlorine. However, higher concentrations are needed to insure that marine organisms are killed. In the experience of one of the authors, chlorine concentrations sufficient to kill all marine organisms in all life stages had to be in the range of 25-100 ppm (as chlorine) with a "soak" time of several hours, during which the chlorine concentrations would decline. It was then estimated that at the time and points of deballasting, chlorine concentrations would be no greater than 10 ppm, quickly diluting to nonhazardous concentrations near the ship's discharge.

Calculations were made for treating each tank at 25, 50, and 100 ppm chlorine. The maximum dosage (100 ppm) for all tanks required purchasing and transporting to

the ship about 1600 pounds of HTH calcium hypochlorite.

This was completed on November 17 and 18. Instructions and cautions were provided to the USCG Strike Team for diluting $\text{Ca}(\text{OCl})_2$ powder in stock solutions and then feeding that through tubes into each tank.

D. Treatment, Deballasting, and Completion of Response

Because of the concern by the ship's engineers and salvors that the *Igloo Moon* could be sifting on a reef pinnacle, and under increasing stress, the decision was immediately made (November 17) to treat two ballast tanks with 100 ppm chlorine with HTH calcium hypochlorite for 2 hours and then discharge those tanks. The remaining ballast tanks were to be treated the next day at a dosage of 50 ppm for a minimum of 6 hours.

On November 18, ballast water in the previously treated forepeak and #1 port wing tanks were discharged after soaking for 12 hours. The total volume released from the two tanks was 107,000 gallons. All remaining tanks were then treated with 50 ppm calcium hypochlorite. The combined volume was over 1.13 million gallons. However, deballasting could not begin until 1000 t of butadiene were successfully lightered to another LPG tanker brought alongside on November 20. This and operational problems delayed deballasting until the morning of November 21 (3-day soak time) when all remaining tanks were finally discharged. The *Igloo Moon* was then towed out by tugs on the afternoon flood tide and safely transferred to Miami for inspection and repair.

V. Discussion and Future Implications

By any measure--health, safety, environmental pollution--the response to the grounding of the *Igloo Moon* was a complete success. No one was injured, nothing was spilled other than treated ballast water, and the vessel was safely removed from peril. Essentially, only the ship's footprint on the corals directly under the hull remained at the end of the response.

On reflection, however, we wonder to what extent ballast-water treatment was necessary. In part, our concern stems from the potential risks to both the response workers and the coral reef of bringing on-scene a highly toxic oxidizing agent--calcium hypochlorite--and the extent to which that risk is weighed against the uncertainties associated with potential hazards to the coral reef from possible nonindigenous marine life in the ballast tanks. Obviously, the intent of ballast treatment during the *Igloo Moon* response was to prevent nonindigenous marine life from invading and possibly colonizing the coral reef. We had to act under the assumption that organisms hazardous to the reef were present in either the water or sediments of the ballast tanks. For purposes of response planning in areas with sensitive natural resources--i.e., where the "window of opportunity" for ballast treatment may be unusually narrow, or the chemical

reactivity/health and safety risk is higher--it is fair to ask whether more reliable evidence of potential harm from onboard ballast water should be required to justify the risks associated with emergency treatment. Are there specific criteria that could be used to justify sampling? How many negative samples should it take to result in a "no threat" call? What evidence of "low risk" potential should be used in prioritizing and selecting ballast treatment options?

An even larger question looms. It will soon become international policy for vessels to undertake and record mid-ocean ballast water exchange. There was no evidence that the *Igloo Moon* undertook high-seas ballast water exchange during its final Atlantic crossing. How should we have responded had there been clear evidence of complete mid-ocean ballast-water exchange? Should we have been concerned about biota or cysts in tank sediments that likely had not been thoroughly flushed during highseas exchange? If treatment was nonetheless required, how might this encourage (or discourage) adherence to implementing voluntary ballast-water exchange?

The last nonindigenous coastal water taken on by the *Igloo Moon* was 800 t at Al Jubail, Saudi Arabia, in the Persian Gulf. Although this was a fraction of the ballast capacity, we had no specific information on which tanks were filled at Al Jubail and, thus, could not give higher treatment priority to these tanks. By contrast, and as noted above, other tanks had contained no foreign coastal water for many months. If specific information had been available to us on the source history of each tank, would that have allowed us to prioritize treatment, focusing on the "highest-risk" tanks? Complicating the case of the *Igloo Moon* is the fact that the ship's ballast-water management data (Table 1) reveals that at least several tanks had exchanged ballast at the scene of the grounding before treatment even, became an issue. Nonetheless, it was determined that all the tanks had to be treated, including several that arrived empty and were subsequently filled during the course of the response.

In a recent review, Cohen (1998) identifies studies suggesting that entrained biota suffer considerable mortality after several weeks in ballast tanks. This implies that the risk of releasing hazardous biota decreases substantially with time. At the time of treatment of the *Igloo Moon* ballast tanks (November 18), the Al Jubail water had been in the ballast tanks for 39 days. The uptake of ballast water previous to Al Jubail was 1020 t taken aboard on September 28-29 in the Indian Ocean coastal port of Kendla. That water was in ballast for 50 days before treatment. In addition, the initial ballast uptake at Kendla was exchanged offshore. In both cases, it is likely that many organisms suffered substantial mortality during the subsequent weeks of transit. Can or should that probable mortality be taken into account when prioritizing treatment?

There are other on-scene considerations as well. For example, the *Igloo Moon* response was underway while many ships passed nearby presumably discharging ballast water or releasing exotic biota from fouling organisms. This

raises the question: How far must a vessel be from a sensitive resource, such as a coral reef, to consider ballast water discharge a non-issue? What if the *Igloo Moon* had stranded 1, 5, or 10 km from the reef?

Perhaps the most serious impediment during the *Igloo Moon* response to minimizing the risk of introducing unwanted species, via the ships ballast water, into the sensitive Biscayne Bay area was the lack of knowledge by the responders of a variety of ballast-water treatment scenarios. For example, little is known about the inactivation kinetics of various marine organisms by biocides. If values for required biocide doses, contact times, and decay rates had been known, the ballast water could have been quickly rendered acceptable for discharge.

These are just a few of many questions that need to be addressed as management options are developed to address the issues raised by aquatic nonindigenous species and as ballast water treatment is increasingly incorporated into response planning. We hope that this paper stimulates provocative discussion and contributes to the critical planning process relative to ballast water treatment during emergency operations.

VI. Acknowledgments

The authors wish to acknowledge the editorial and layout assistance of Nancy Peacock and Kristina Worthington, Office of Response & Restoration, NOAA; and proofing by intern Jennifer Nafzgar, California Polytechnic University, San Luis Obispo.

VII. References

- Benggio, B., N. Barnea, J.K. Farr, M. Evans, D. Miller, R. Sperry, W. O'Brien, and T. Edwards. 1998. The M/T *Igloo Moon* incident: A case study of a successful response, p. 1-14. In *Proceedings, Fifteenth Technical Seminar on Chemical Spills*, June 1998, Edmonton, Alberta, Canada. Ottawa: Environment Canada.
- Cohen, A. 1998. Ships' ballast water and the introduction of exotic organisms into the San Francisco Estuary: Current status of the problem and options for management. Richmond CA: San Francisco Estuary Institute, 81 p.
- NRC (National Research Council). 1996. *Stemming the tide: Controlling introductions of nonindigenous species by ships' ballast water*. Marine Board Committee on Ships' Ballast Operations. Wash. DC: National Academy Press.

RESOLVING ALASKA AND WEST COAST OIL DISPERSANT ISSUES

Alan J. Mearns
Hazardous Materials Assessment Division
Office of Response & Restoration
National Ocean Service, NOAA
7600 Sand Point Way NE
Seattle, Washington 98115-0070

Abstract

Agencies and spill responders are currently deliberating about the efficacy of pre-approving the use of dispersants to treat oil slicks in nearshore and shallow waters of the U.S. West Coast and Alaska. The decisions rest on understanding the effectiveness of dispersant operations, the long-term fate and effects of dispersed oil, and the effects of oil slicks and shoreline oiling on critical fisheries and marine species. Processes and knowledge leading to this critical decision point are briefly reviewed.

I. Introduction

Dispersants are chemicals used to mix floating oil into the water. Dispersing oil slicks helps protect birds, mammals, and intertidal marine life from injury or contamination caused by contact with floating oil (NRC 1989). The primary concerns about dispersing oil are (1) effects of dispersants and dispersed oil on life in the water and on the sea floor, and (2) the effectiveness of dispersant applications in reducing adverse impacts.

Despite extensive international experience, dispersants have rarely been used to combat oil spills in the United States. In the 1990s, however, this has changed dramatically. Virtually all U.S. regions or states now include dispersants in their response plans, and several recent (relatively small) spills off Texas have been treated with dispersants. Generally, dispersant use has been preapproved only for offshore oil slicks (1-3 miles), or beyond the 10-m (30-ft) depth contour, whichever is closer. However, many spills occur closer to shore, inside these limits, and in many bays and estuaries. Some states approve nearshore use of oil dispersants, although only on a case-by-case basis. This means that approval must be obtained quickly because oil becomes more viscous, and thus less dispersable, as it weathers. This situation is leading response authorities to consider pre-approving use of dispersants nearshore and in shallow-water areas. These proposals to pre-approve (or "quick-approve") nearshore dispersal are being challenged, however, by citizens and resource trustees who are concerned that the dispersed oil will injure water-column and subtidal marine resources in shallow or even deep nearshore waters.

These concerns are especially critical along the U.S. Pacific Coast and Alaska. Many believe that the resources of these shorelines and near-coastal waters are sufficiently unique to merit special emphasis and concern. For example, unlike the U.S. East and Gulf coasts, the West Coast, from San Francisco Bay northward to Alaska, is bathed by highly productive cold waters of the southward-flowing California Current and northward flowing Alaska Gyre. In this region, intertidal bay and estuarine shorelines provide extensive spawning habitat for herring and pink and chum salmon, and juvenile habitat for all six species of Pacific salmon. In Prince William Sound, Alaska, both groups of commercially-important fishes were severely impacted over several years by the *Exxon Valdez* oil spill (e.g., see Heintz et al. 1999). Also, many coastal stocks of salmon in California, Oregon, and Washington have now been "listed" under the Endangered Species Act, prompting any and all action necessary to protect and restore their stocks. There are numerous oyster and salmon aquaculture facilities and hatcheries along this coast, and a considerable amount of rocky intertidal and subtidal reef and kelp-bed habitats that harbor populations of oil-sensitive sea otters. Alaskan shores are home to several major and threatened populations of fur seals, also highly vulnerable to oiling.

On the other hand, many of these oil-sensitive species live in close proximity to nearshore deep water (10's to 100's of meters), unlike the East or Gulf Coasts. Intentionally dispersed oil does not penetrate the water



Fig. 1. Helicopter spraying fine dispersant mist on an oil slick.

column much deeper than about 10 meters (NRC 1989). However, these deepwater inlets—such as the Strait of Juan de Fuca, the Strait of Georgia, many Alaskan inlets, and even the central portion of San Francisco Bay—are moderately exposed to wind and strong tidal currents, offering numerous possibilities for fast dispersal and flushing. Thus depth, together with large tidal amplitudes and strong circulation patterns, creates a situation conducive to rapid mixing and flushing.

These factors—i.e., oil-sensitive coldwater species with sensitive shorelines, and pelagic life stages in proximity to well-flushed bays and channels—prompt protection concerns and response opportunities that may be different than those along the East or Gulf coasts. Indeed, the decision to disperse or not to disperse a major oil spill near shore sometimes becomes a battle between different groups wishing to protect different nearshore life stages of the same species.

This paper explores, within a historical context, some of the most controversial issues surrounding nearshore oil dispersal along the U.S. West Coast and Alaska: 1) how dispersant decisions are evolving, 2) how the controversies are being resolved, 3) new cooperative research and development efforts, and 4) the emerging role of comparative risk assessment to quantify response tradeoffs.

II. Methods

The author gathered information on the major dispersant issues as part of his participation in recent workshops and conferences, and during actual spill responses and major oil-spill drills. Examples include a technical review of dispersant applications in Alaska compiled by Trudell et al. (1998), a two-day conference sponsored by the Oil Spill Recovery Institute (Trudell 1998) in Alaska, a 1998 "Spill of National Significance" (SONS) drill in Anchorage, and dispersant risk-assessment workshops in Washington and California. The author also participated in recent oil spill conferences at which new reports were presented on the successes and concerns with dispersed oil operations in other countries. To place current issues in perspective, a re-review of major (now historical) reviews and syntheses on oil-spill dispersants (Allen 1984, NRC 1989) was conducted as well as a review of recent assessment and planning documents, published reports on the ecological effects of specific oil spills, and selected peer-reviewed literature on the effectiveness and effects of dispersed and untreated oil. The author drew on recent and continuing modeling, simulation, and research activities conducted by colleagues in the Hazardous Materials Assessment Division of NOAA's Office of Response & Restoration in support of ongoing dispersant risk-assessment workshops.

III. Historical Perspective and Basics of Dispersants

The history of dispersant use and research through the late 1980s is well documented by the National Research Council (NRC) report, *Using Oil Spill Dispersants on the*

Sea (NRC 1989). As noted in their report, the term "dispersant" became a common word in spill response following the 1-million barrel (bbl) *Torrey Canyon* crude oil spill off the English coast in 1967. About 10,000 bbl of various chemicals, largely degreasing solvents, were sprayed on the water and along the shoreline. The use of these chemicals caused mortality of shoreline marine life, greatly worsening the effects of the oil alone. The lessons from this single experience lead to great skepticism and caution about using dispersants. More importantly, it generated over 30 years of product development, physical-chemical studies, ocean modeling and simulation research, acute and chronic sediment and water toxicity testing, laboratory and mesocosm experiments, experimental oil spills, and spill-of-opportunity measurements of the fate and effects of dispersed oil. The NRC (1989) report cites nearly 700 papers on these developments.

Before responders became interested in using oil dispersants nearshore, we knew that a series of processes takes place in a matter of minutes or hours, and these and other factors define temporal/spatial "windows-of-opportunity." Within these windows, oil is dispersible; outside the windows, dispersability is unlikely.

1) The new generation of dispersants is considerably less toxic to marine life than chemicals used in the 1960s.

2) Dispersants reduce the surface tension of oil, but only when properly applied as a mist and *not* sprayed or poured onto oil or the adjacent water surface.

3) Specific oils and fuels are less dispersible than others, due to high or increasing viscosity and formation of water-in-oil emulsions.

4) Wave energy is absolutely required for effective dispersion, by breaking the oil into tiny droplets that mix into the upper water column as a "cloud" of tiny, neutrally-buoyant droplets.

5) This cloud of droplets is mixed laterally and deeper into the water column via Langmuir circulation, current shear, and other natural mixing processes.

6) Tidal and other currents transport the continually-diluting material out of the spill area.

7) Dispersed oil does not "sink." In fact, the maximum sea depth at which intentionally-dispersed oil has been measured, or predicted in model simulations, is on the order of 10 meters. This means, however, that in shallow waters (<10 m), dispersed oil may indeed contact the sea floor and bottom sediments.

8) Oil dispersability decreases with time due to weathering processes.

9) Newer dispersants are generally less toxic to marine life than the oils being dispersed.

10) Acute toxicity of dispersed oil decreases with decreasing concentrations in the dispersing plumes.

During the 1990s, as reviewed in documents such as Trudell (1998), our understanding of these processes has been strengthened by numerous field, mesocosm and laboratory studies, and by a major oil spill (the *Sea Empress*) during which dispersants were successfully used to reduce environmental impacts (SEEEC 1998, Lunel 1998). More importantly, continued studies and product

development have widened the "windows-of-opportunity," the types of fuels and oils amenable to dispersant use, and the temporal and physical conditions (esp. salinity) under which dispersion is possible, at the same time reducing acute toxicity. Cooperative efforts by Federal/state/ industry have resulted in standardized effectiveness and toxicity testing (Aurand 1995). Also, recent research--building on past observations--suggests that dispersed oil may biodegrade at rates perhaps ten times faster than non-dispersed oil (Swannell & Daniel 1999).

IV. Current Dispersant Issues

By the mid 1990s, after years of numerous planning exercises, workshops, and training activities, there were still no pre-approvals for dispersant use in U.S. bays and estuaries, and only reluctant, case-by-case approval (with requests often rejected) for use on west coast and Alaska nearshore areas. The three most common categories of issues and concerns dominating dispersant planning workshops were 1) *effectiveness* of dispersant operations; 2) short-term (hours to days) *toxicity* of dispersed oil to water-column and benthic organisms, and 3) longterm (days to weeks) *fate and effects* of dispersed oil.

It is not immediately apparent, given the existing knowledge about dispersant use, what has been holding back the decision process. One reason has emerged in a unique decision-maker survey conducted by Bostrom et al. (1997). The authors found, through interviews, that much of the research over the previous decades was not effectively communicated to decision-makers or the public. Decision-makers were operating with information that was several decades old. These authors also revealed that few decision-makers were looking at the problem in the context of tradeoffs; i.e., comparing the risks of not dispersing oil with the risks associated with oil dispersion.

Much new information about the consequences of *not* treating oil slicks has come to light in just the past several years (e.g., the growing literature on the *Exxon Valdez* oil spill). It is abundantly clear that unless oil is dispersed, or otherwise removed or treated, spreading slicks and tar-ball fields will continue to contaminate sea birds and marine mammals (such as sea otters and fur seals) and will wash ashore, possibly killing wading and shorebirds and contaminating mud flats, marshes, aquaculture operations, etc. Data on the long-term effects of shoreline oiling and shoreline cleanup, the multi-year effects of residual shoreline oiling, and new data on the effectiveness of shoreline cleanup methods all support concerns about long-term effects of shoreline oiling.

Recently, Heintz et al. (1999) reported that dissolved total PAH (polycyclic aromatic hydrocarbon) concentrations as low as 1 ppb (1 part per billion) may damage or kill developing pink salmon embryos; further, that direct contact of embryos with oiled gravel is not necessary for this effect; and that water percolating through gravel berms contaminated with weathered crude oil contains enough PAH to damage salmon embryos over several spawning seasons. Similar observations have been made for herring, an intertidal spawning fish (R. Heintz, NMFS Auke Bay Lab., pers.

commun.). In a related review, Mearns (1996) estimated that, at most, about 20% of the oil contaminating Prince William Sound shorelines was actually removed by an aggressive multi-year shoreline cleanup program. The first-year cleanup campaign-involving the use of high-pressure, hot-water washing-killed much of the marine life that survived the initial oiling. About half the oil has been removed naturally each year by winter storms. In 1999, small deposits of nearly-fresh oil remain buried under (and are leaching from) the armor of boulder-cobble beaches of Prince William Sound. Oil has remained, apparently enough to impact salmon and herring a decade after the cleanup.

The significance of these studies is that these effects from residual oiling can occur even in areas subjected to aggressive shoreline cleanup. This means that shoreline cleanup itself cannot be relied upon to protect sensitive species. At a recent workshop, questions were raised such as "Should we disperse or not? What about the effects of dispersed oil on planktonic and larval stages of commercial fishes?" Heintz and his colleagues, knowledgeable about dispersed oil concentrations and toxicity, responded emphatically: "By all means, disperse the oil before it contaminates spawning beds!"

In summary, recent shoreline oiling and cleanup studies, highly relevant to the West Coast and Alaska, are revealing that not only can shoreline cleanup itself be damaging to the shoreline marine environment, but that even small amounts of residual oil after the cleanup can injure key life stages of shoreline marine life. Such studies should provide additional rationale for resource trustees to consider pre-approving the use of dispersants in nearshore shallow waters to minimize shoreline oiling.

V. Resolutions

As a result of their study, Bostrorn et al. (1997) recommended that agencies develop a new series of nontechnical papers focused on seven subjects:

1. *Fate and Transport of Dispersed Oil in Marine Waters*: Decision-makers have an oversimplified understanding and need to grasp the "big picture," especially of long-term fate and effects of dispersed oil.

2. *Dispersability of Oil in Marine Waters*: "Windows of opportunity" are wider than currently being considered in contingency planning.

3. *Links between Processes of Fate and Transport and Exposure and Effects*: There are considerable misconceptions about the extent and duration of toxic concentrations in oil and how current and past toxicity testing applies to decisions about dispersant use.

4. *Acute and Chronic Effects of Exposure in the Upper Water Column Relative to the Use of Dispersants*: The research and literature on dispersants have been remiss in providing direct comparisons of the consequences of treatment vs. non-treatment.

5. *Natural Processes of Biodegradation, Evaporation, Photo-Oxidation, and Sedimentation of Oil in Marine Waters*: Dispersion is only one of several natural oil-degrading processes and may enhance or inhibit these others.

6. *Logistics of Dispersant Use*: Decision-makers perceive a critical lack of information about our ability and preparedness to effectively treat oil.

7. *Monitoring*: There is considerable disagreement on the need to monitor and what to monitor, including lack of appreciation for testing and confirming predictions.

It is not yet clear if any agency is taking on the challenge of commissioning these "white" papers. However, D. Aurand of Environmental Management Associates, Inc. (EMA, Purcellville VA, pers. commun.) took these a step further by stimulating and initiating a series of "risk assessment" workshops now underway in Washington and California, Galveston Bay, Texas, and Long Island Sound. The workshops, most conducted by EMA, are designed to acquaint decision-makers and resource trustees with current information on the effects and effectiveness of alternative oil-response strategies, including dispersing, burning, mechanical cleanup (skimming), and the "no response" alternative. Workshop panelists are asked to identify spill-scenario criteria (oil type, weather, season, effectiveness of response method, etc.) for specific bays. This information is used by NOAA HAZMAT's Modeling and Simulation Studies group and NOAAs Scientific Support Coordinators (SSCs) to simulate oil budgets (evaporation, natural dispersion, dissolution, weathering) and generate maps of spreading and transport of surface slicks and submerged plumes and in-situ burn atmospheric plume transport. NOAA HAZMAT biologists convert this information to oil concentration isopleths. Participants are then provided summaries of the available literature on oil and dispersed oil toxicity and encouraged to develop and apply, by consensus, exposure concentration criteria of concern. Participating resource biologists then evaluate specific resources that may be exposed to surface oil, subsurface oil, and shoreline oiling under all alternative response scenarios. This results in a cooperative evaluation of near-real tradeoffs.

This "comparative risk-assessment approach" is not new. It has been used for years in other environmental management venues, such as for coastal wastewater management actions (NRC 1993). Indeed, a similar approach was proposed and quantitatively explored for dispersant decision making many years ago by Trudel (1984). If the "first round" of workshops is successful, more will be conducted throughout the U.S.

VI. The Immediate Future

At the time of this writing, the regional workshops described above are continuing and no results are yet available. However, the procedure is already providing benefits

by allowing resource trustees to clearly understand what is at risk, the effectiveness or ineffectiveness of various response strategies, the uncertainties under all response scenarios, and the information gaps. It remains to be seen if these workshop efforts can be completed and result in well-supported decisions.

VII. Acknowledgments

The author greatly acknowledges constructive interactions with Glen Watabayashi and editorial assistance from Nancy Peacock, Kristina Worthington, and Rebecca Hoff, all from NOAAs OR&R.

VIII. References

- Allen, T.E. (ed). 1984. Oil spill chemical dispersants: Research, experience and recommendations. A Symposium by ASTM Committee F-20 on Hazardous Substances and Oil Spill Response, October 1982. ASTM Publ. 04-840000-24. Philadelphia: American Society for Testing and Materials, 465 p.
- Aurand, D. 1995. A research program to facilitate resolution of ecological issues affecting the use of dispersants in marine spill response, p. 172-190. In Lane, P. (ed.), The use of chemicals in oil spill response. ASTM Publ. 1252. Philadelphia: American Society for Testing of Materials.
- Bostrom, A., P. Fischbeck, J.H. Kucklik, R. Pond, & A.H. Walker. 1997. Ecological issues in dispersant use: Decision-makers and information needs. Prepared for Marine Preservation Assoc., Scottsdale, AZ. Alexandria VA: Scientific and Environmental Associates, Inc., 86 p.
- Heintz, R.A., J.W. Short, & S.D. Rice. 1999. Sensitivity of fish embryos to weathered crude oil. Part II: Increased mortality of pink salmon (*Oncorhynchus gorbuscha*) embryos incubating downstream from weathered Exxon Valdez crude oil. Environ. Toxicol. Chem. 18 (3):494-503.
- Lunel, T. 1998. Sea Empress spill: Dispersant operations, effectiveness and effectiveness monitoring, p. 59- 77. In Trudel, B.K. (ed.), Proceedings, Conference on Dispersant Use in Alaska: A Technical Update, Anchorage, March 1998. Cordova AK Prince William Sound Oil Spill Recovery Institute (OSRI).
- Mearns, A.J. 1996. Exxon Valdez shoreline treatment and operations: Implications for response, assessment, monitoring, and research. In Rice, S., & B. Wright (eds.), Proceedings, Exxon Valdez Oil Spill Symposium, February 1993, Anchorage. Bethesda MD: American Fisheries Society Symposium Series.

NRC (National Research Council. 1989. Using oil spill dispersants on the sea. Wash., DC: National Academy Press, 335 p.

SEEEEC (*Sea Empress* Environmental Evaluation Committee). 1998. The environmental impact of the *Sea Empress* oil spill. ISBN 0 11 702156 3. London: The Stationary Office, 135 p.

Swannell, R.P.J., & F. Daniel. 1999. Effect of dispersants on oil biodegradation under simulated marine conditions. Paper #212 presented at 1999 International Oil Spill Conference, Seattle, Washington, March 1999. American Petroleum Inst. (CD only).

Trudel, B.K. (editor). 1998. Proceedings, Conference on Dispersant Application in Alaska: A Technical Update, Anchorage, March 1998. Cordova AK Prince William Sound Oil Spill Recovery Institute, 341 p.

Undersea Object Detection and Recognition: The Use of Spatially and Temporally Varying Coherent Illumination

Frank M. Caimi¹

Department of Electrical Engineering
Florida Institute of Technology
150 W University Blvd.
Melbourne, Florida 32901

Bernard C. Bailey and Joel H. Blatt

Department of Physics and Space Sciences
Florida Institute of Technology
150 W University Blvd.
Melbourne, Florida 32901

Abstract: Increased optical range of target detection and recognition is always a problem in the marine environment. The inherent optical properties of light absorption and scattering in water limit both radiative and information transfer for image formation. These limits are further restricted by suspended particulate matter scattering. Near the surface in peak daylight conditions, the intense background scattered light makes for an extremely difficult job of object detection due to contrast washout. In any conventional underwater imaging system design, these limitations are either difficult or seemingly impossible to surmount. Methods for the formation of images in scattering media generally rely upon temporal or spatial methodologies. Some interesting designs have been developed in an attempt to circumvent or overcome the scattering problem. Time gating is a temporal example of image formation whereby a light source is time pulse projected toward a target and the detector is time gated to accept image-forming illumination from a specific range. To be successful at eliminating much of the backscatter, this method requires exacting range information and loses the simplicity of a continuous light source. Holography is one example of an image formation method requiring specific spatial relationships, i.e. mutual coherence between a reference beam and a signal beam. The coherence allows the formation of an interference pattern that carries the signal information on a "spatial carrier". In order for the method to be of use, the medium in which the beams are carried must preserve the coherence or phase spatially across the beams and in relation to the reference beam. In water, the distance over which the phase may be preserved is dependent upon many factors, including turbulence induced refractive index variations, thermal gradient structure, and relative motion. If pathlength differences exceed the temporal coherence length of the beam, interference is not obtained and the method breaks down. Generally, the demands of maintaining a spatially coherent beam at optical frequencies is difficult over long range thereby limiting the usefulness of the technique for image formation in turbid media. A paper submitted by the authors at the OCEANS '98 Conference describes a variation of the spatial interferometric technique that relies upon projected spatial

gratings with subsequent detection against a quasi-coherent return signal. The method is advantageous in not requiring temporal coherence between reference and signal beams and may use a continuous illumination source. Coherency of the spatial beam allows detection of the direct return, while scattered light appears as a noncoherent noise term. The theoretical foundation of the method and the initial results for turbid media were developed. This paper will present the latest ongoing research results.

I. INTRODUCTION

Most laser imaging systems are designed to reduce the effects of scattering on the produced image improving image visibility in near shore water conditions. Synchronous scan systems minimize the common volume occupied by laser illumination and the detector field-of-view [1]. LIDAR systems time gate the receiver aperture to eliminate relatively intense backscatter originating from the water while allowing the return from the target to be detected [2]. Both systems provide a specific set of advantages, but neither normally utilize coherent detection techniques to improve performance. In addition, the systems produce reflectance maps of the scene being illuminated and are not particularly sensitive to object contour, shape, or surface texture.

Recently, several laboratories have demonstrated the use of temporal modulation and subsequent synchronous detection to improve imaging of subsurface objects in shallow water environments [11]. The technique allows for the extraction of the signal reflected from the target/object via a synchronous detection technique that is well known in signal detection theory. The advantage of the approach is that the signal return from the target is coherent with the transmitted waveform while the return produced from scattering is quasicohherent and represents noise. The idea is to achieve "processing gain" via correlation of the transmitted and received signals against a "noise" background.

¹ Author is also affiliated with Harbor Branch Oceanographic Institution, Ft. Pierce, Fl.

This technique was proposed by the authors as well, and may provide needed improvement in the detection of low contract targets.

Unfortunately, real world scenes often exhibit nearly identical reflectance over a two dimensional cross section especially if the target reflectivity matches the background, making difficult the task of interpreting depth cues, especially in turbid water at maximum range where the signal-to-noise ratio is low. Observation of undersea objects with 2-D imaging devices requires sufficient contrast at spatial frequencies corresponding to the characteristic features on the object surface or, at a minimum, shape information consistent with a feature database. Features distributed in the range or depth dimension are often subject to misinterpretation since reflectance information alone does not necessarily provide an adequate feature set for reliable detection or identification. Additional information useful for object identification and characterization can be obtained by creating a range map or depth contours, and methods have been devised to obtain shape, velocity, and position information using intensity gradient cues observed in the scene as a result of illumination from natural or artificial light sources [3, 4].

Range or depth information is available from LIDAR, structured illumination (e.g. via triangulation), and interferometric system approaches. The resolution achievable is dependent upon the laser pulsewidth, system geometry, and environmental parameters in each case. Although LIDAR and triangulation [5] methods have received a significant amount of attention, they do not offer the potential advantages of an interferometric approach. Interferometric systems [6, 7] can be classified as temporally or spatially modulated types. There are several recent reports using temporal modulation to improve image quality and to acquire range information, but few using spatial coherency (modulation). Holography has also been tried and functions over very short distances where both temporal and spatial coherency remains relatively unperturbed by the properties of the medium.

An alternative approach using spatially modulated or coded waveforms has been proposed [7, 8] offering an intermediate solution to obtaining additional feature information, and utilizing novel optical techniques and signal processing algorithms for object classification, feature extraction, and image restoration with minimum a-priori information.

In an earlier paper [8], the background, definitions, theoretical development and implementation methodologies were introduced. In this paper, some of the theoretical computer modeling and an early qualitative experiment are introduced.

II. TRANSMISSION MODEL

Much of the transmission model used has been previously derived by other authors. According to Mertens [9], the spread function due to refractive deterioration along the transmission path closely resembles the Gaussian curve.

The standard deviation σ is used as a measure of spreading and the rms value of observed spreading is set equal to σ . The modulation transfer function (MTF) corresponding to the refractive deterioration on the direct image is given as and exponential dependence related to σ and the angular frequency. Recent models [10] suggest MTF remains relatively constant over a large angular frequency range above some low frequency limit. These models are in agreement with the suggestion and results in this paper showing that high spatial frequency content can be used for detection against the scattered light field even if large angular frequencies are used.

Using the conventional model of Mertens, the resulting MTF can be approximated as

$$T_P = 1 \quad \omega \cong 0$$

$$= C \exp(-0.5 \cdot \sigma^2 \cdot \omega^2) \quad \omega > 0, \quad (1)$$

where C represents direct image scattering attenuation. Experimental values of σ are:

$$\sigma \cong 1.9 \times 10^{-4} \text{ rad, giving}$$

$$T_R = \exp(-0.692 \times 10^{-6} f^2), \quad (2)$$

where f is the spatial frequency in cycles per radian. This model initially addresses only the effect of the refractive deterioration or transmittance T_R .

Target illumination from a monochromatic source at normal incidence and distance r is considered to be a sum of a direct component, E_D , and a forward-scattered component, E_S . We assume that the target is illuminated by vertical light fringes emanating from a Michaelson Interferometer and that they are essentially parallel as in Fig. 12. After a beam expander, the fringes maintain a uniform separation and appear slightly divergent. However, for the distances being studied, this model assumes parallel illumination and simplifies the illuminance calculations by disregarding all terms in $E_S(r)$ involving the scattering phase function. To simulate vertical fringes, the intensity I is modified by a cosine function which allows a normalized intensity to range from 0 to 1. To affect forward scattering in each transmission fringe, the refractive deterioration MTF factor is applied directly to the cosine function in the E_S term. The total illuminance at the target is the sum of the terms:

$$E(r) = E_D(r) + E_S(r). \quad (3)$$

The difference between the target illuminance and the background illuminance at the detector a distance r from the target can be represented by a luminance (or radiance) term

$$B_d = E(r) (R_t - R_b) e^{-\sigma/\pi}, \quad (4)$$

where R_t and R_b are target and background reflectivity.

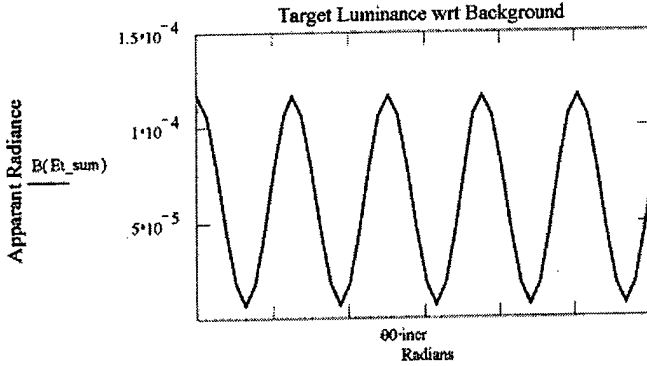


Fig. 1: Structured Illumination Transmission model example.

The above graph is a representative result of the transmission model in Mathcad with $r = 4.5$ meters, $c = 0.33$, a target illuminated spatial frequency of 1 cm/cycle, and source intensity normalized.

III. BACKSCATTER MODEL

A MTF backscatter model modified for spatially modulated illumination (SMI) has been recently developed also using the standard model as outlined by Mertens, integrating over the common volume intersected by source, target and detector.

The total illuminance is the sum of direct and backscatter terms:

$$E(r) = E_D(r) + E_{BS}(r) \quad (5)$$

where

$$E_D(r) := \frac{I \cdot e^{-\sigma r}}{r^2}$$

$$E_{BS}(r) := \frac{2.5 \cdot I \cdot k \cdot e^{-k r}}{4 \pi r} \quad (6)$$

The apparent radiance is an integral between r_i and r_t the two end points of the common volume along the line of sight:

$$B(r) := \int_{r_i}^{r_t} s \cdot E(r) \cdot e^{-k r} dr \quad (7)$$

where s is the average backscatter coefficient at the detector to illuminator offset angle.

In all figures in this section and in the next, w is the spatial frequency of the SMI, r is distance between source and target,

and c is the average backscatter coefficient at detector to illuminator offset angle.

Figures 2 and 3 below show comparative results between SMI and conventional lighting using the same parameters as in the transmission model. The figures indicate a backscatter apparent radiance relative to source output. There are two important features to note: 1) SMI backscatter is significantly less than from a conventional source; 2) There is little to no structure within the SMI backscatter, especially as spatial frequency increases.

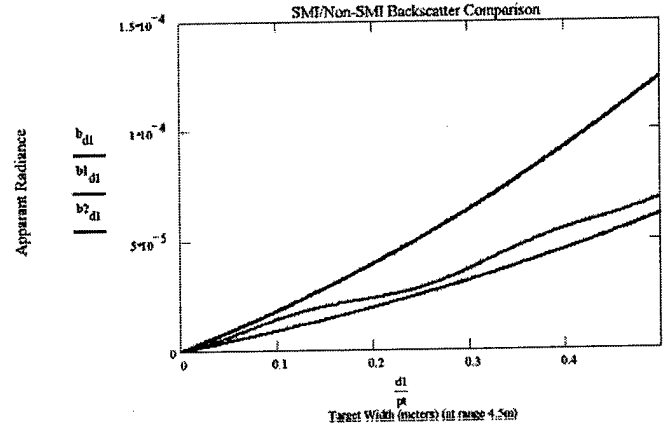


Fig. 2: b_{d1} = SAH Backscatter; b_{l1} = Conventional Backscatter; $b_{2d1} = 1/2$ Conventional Backscatter; $w = 0.25$ m/cycle, $r = 4.5$ meters, $c = 0.33$

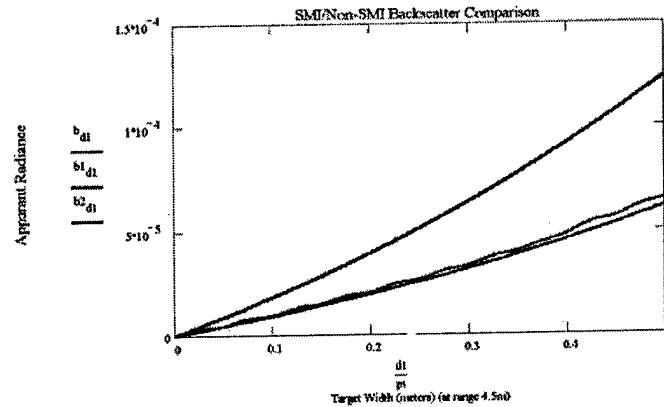


Fig. 3: b_{d1} = SMI Backscatter; b_{l1} = Conventional Backscatter; $b_{2d1} = 1/2$ Conventional Backscatter; $w = 0.05$ m/cycle, $r = 4.5$ meters, $c = 0.33$

IV. COMBINED SMI MODEL

Figures 4 through 6 show a comparison of transmitted and backscattered apparent radiance at varying spatial frequency and target range. The lack of structure in the backscatter as compared to the SMI is quite evident. Figures 7 through 11 show the sum of transmitted and backscattered apparent

radiance at varying spatial frequency and target range. The most important feature to note in these figures is that the modulation remains in the received transmission to the edge of detection.

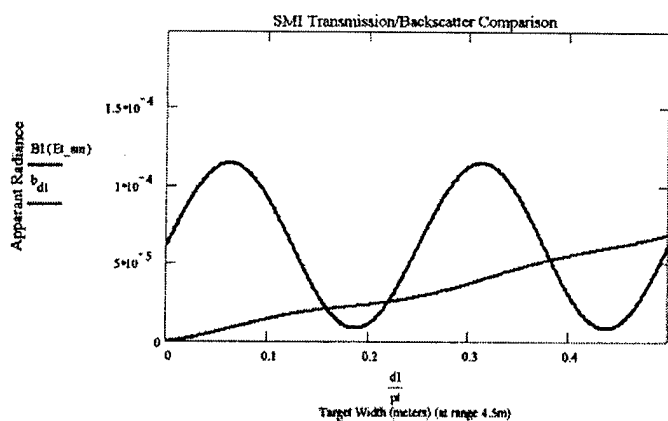


Fig. 4: b_{d1} = SMI Backscatter; $B1(Et_sm)$ = SMI Transmission; b_{d1} = SMI Backscatter; $w = 0.25$ m/cycle, $r = 4.5$ meters, $c = 0.33$

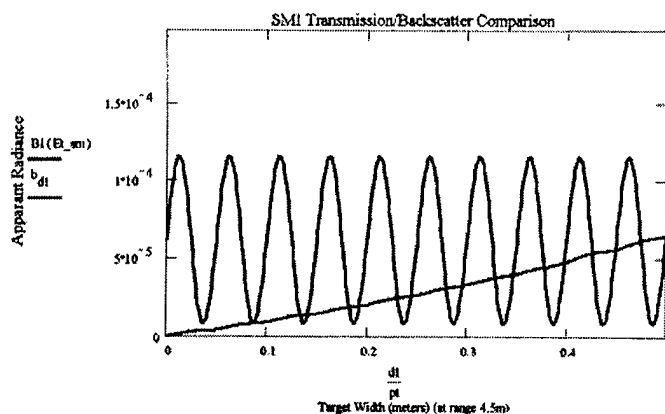


Fig. 5: b_{d1} = SMI Backscatter; $B1(Et_sm)$ = SMI Transmission; b_{d1} = SMI Backscatter; $w = 0.05$ m/cycle, $r = 4.5$ meters, $c = 0.33$

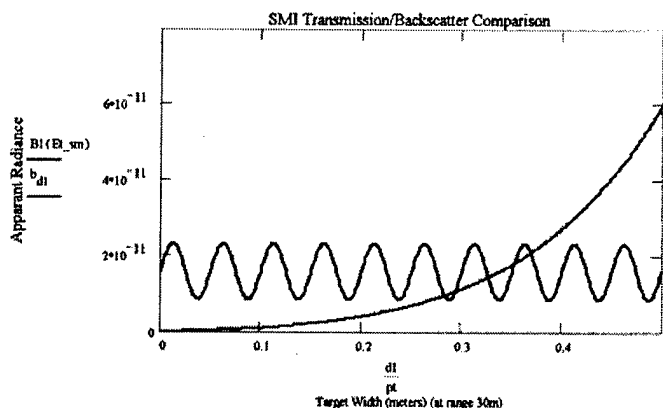


Fig. 6: b_{d1} = SMI Backscatter; $B1(Et_sm)$ = SMI Transmission; b_{d1} = SMI Backscatter; $w = 0.05$ m/cycle, $r = 30$ meters, $c = 0.33$

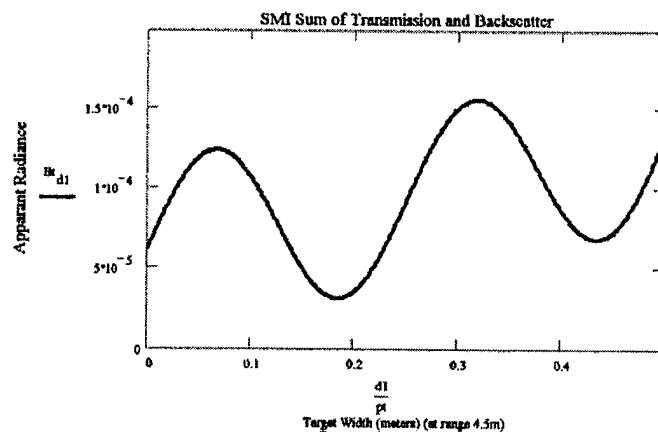


Fig. 7: Bt_{d1} = SMI Sum of Transmission and Backscatter; $w = 0.25$ m/cycle, $r = 4.5$ meters, $c = 0.33$

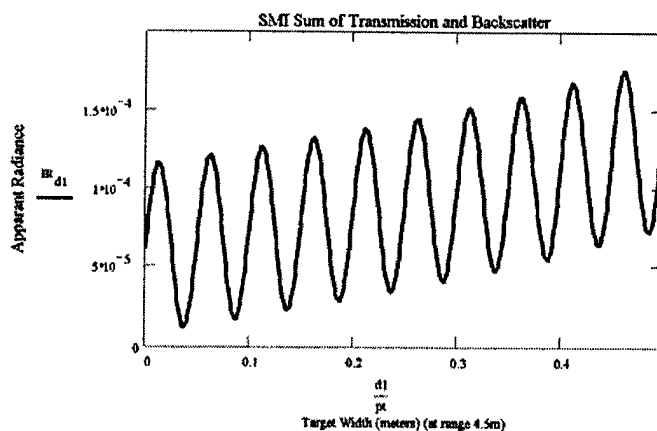


Fig. 8: Bt_{d1} = SMI Sum of Transmission and Backscatter; $w = 0.05$ m/cycle, $r = 4.5$ meters, $c = 0.33$

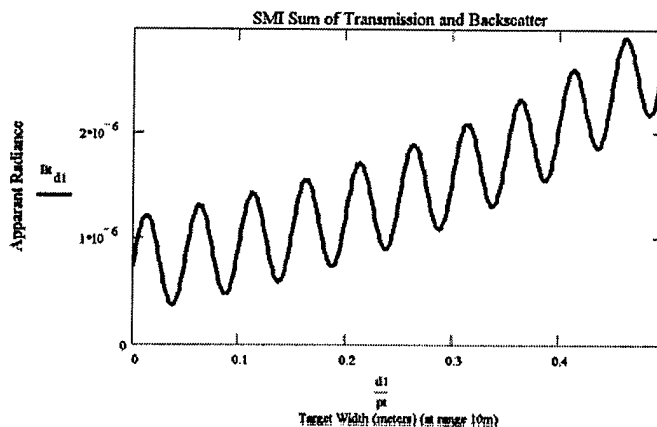


Fig. 9: Bt_{d1} = SMI Sum of Transmission and Backscatter; $w = 0.05$ m/cycle, $r = 10$ meters, $c = 0.33$

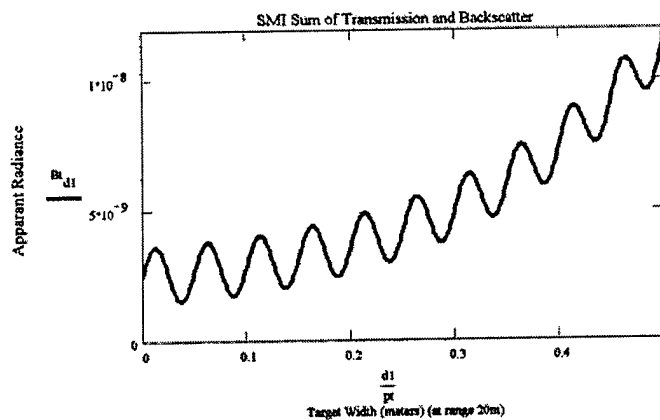


Fig. 10: $B_{t_{d1}}$ = SMI Sum of Transmission and Backscatter; $w = 0.05$ m/cycle, $r = 20$ meters, $c = 0.33$

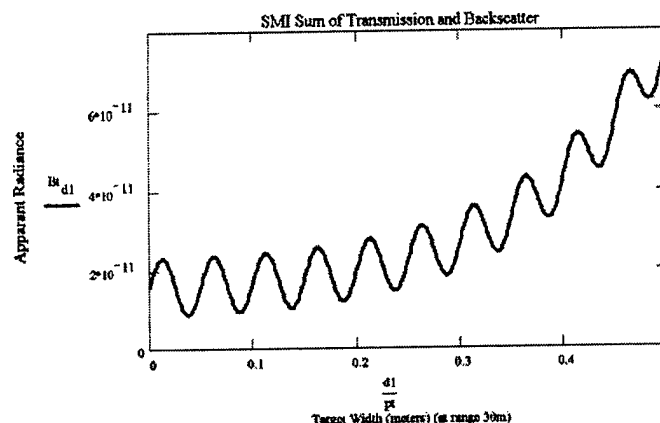


Fig. 11: $B_{t_{d1}}$ = SMI Sum of Transmission and Backscatter; $w = 0.05$ m/cycle, $r = 30$ meters, $c = 0.33$

V. INITIAL EXPERIMENT

An experiment was devised using a variable frequency illumination source and highly turbid medium to investigate the presence of spatially modulated backscattered light at various angular frequencies (Figure 12).

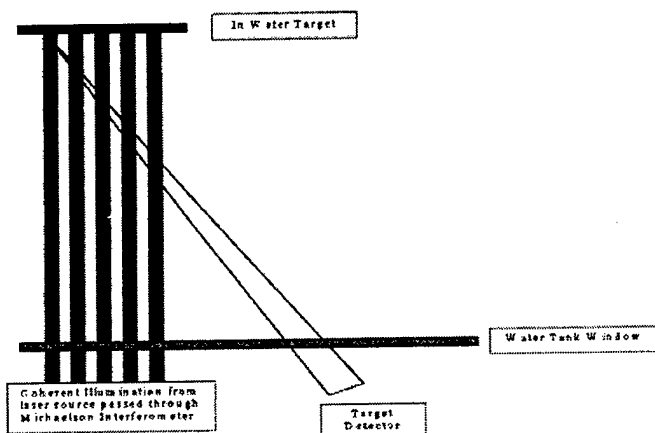


Figure 12. Experimental setup for proof of principle.

The proposed detection method for discriminating the spatially modulated returns from the target against the veiling illumination due to scatter requires the scattered light field to exhibit little or no observable modulation. The experiment was designed to observe the transmission and backscatter of a spatially variant (structured) illumination source created by a portable Michelson interferometer and 1 to 2 watt argon ion laser operating at 514 nm. The interferometer was adjusted to provide adjustable spatial frequency vertical fringes at the side entrance window of a 4.5-meter diameter tank of water.

Figures 13-15 are photographs of the modulated beam from different vantage points. As the model predicts, there is no observable structure evident in the backscatter (left side of Fig. 13) when viewing the beam fringes from the side. The fringes are lost as the viewing angle is changed slightly from a look direction parallel to beam propagation direction. The fringes are observed, however, at the rear wall of the tank (i.e. at the target plane). Figs. 14 and 15 show a low contrast image produced by a target illuminated with low and high spatial frequency structure, respectively. Only the shadows provide an indication of the presence of a raised surface against the tank wall. Fringe structure is observable however, and is modulated spatially by the variation of object profile in the beam propagation direction. Detection of these variations via spatial correlation methods can then provide a means of detection for otherwise featureless images in high turbidity environments.

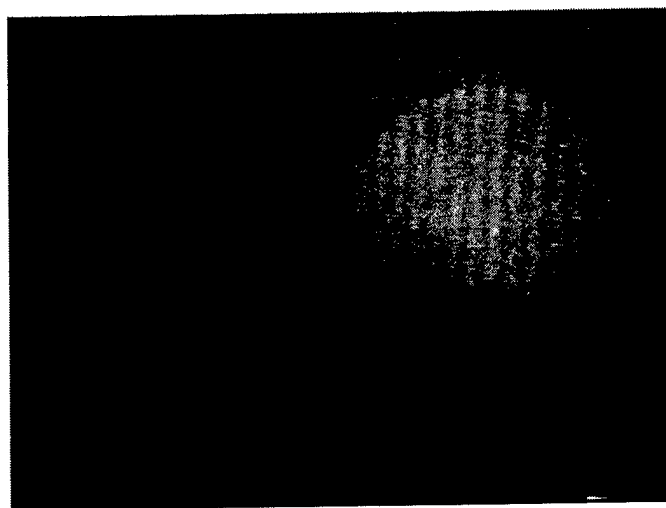


Fig. 13: View of reflection from rear of tank as well as crossbeam backscatter in foreground. Structure is not visible in scatter normal to fringes.

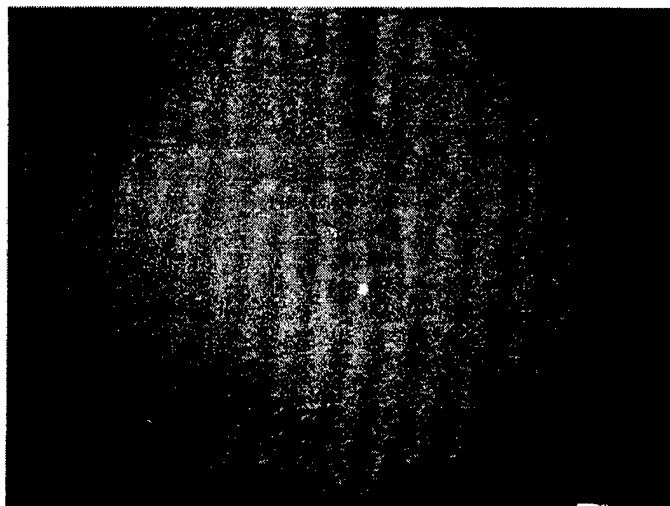


Fig. 14: View of low contrast target against tank wall with low spatial frequency illumination.

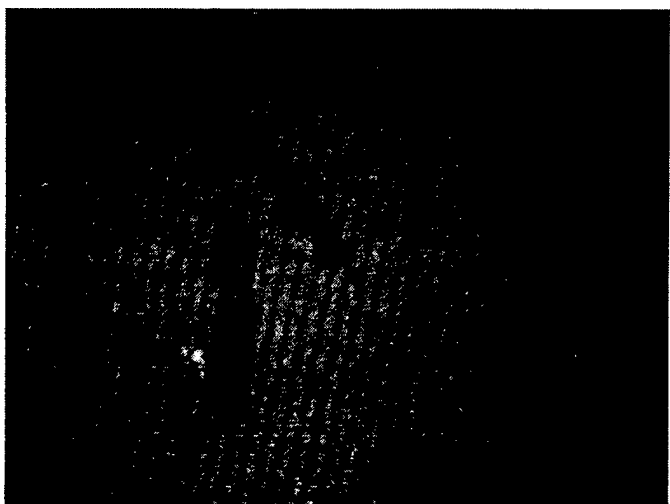


Fig. 15: View of low contrast target slightly away from tank wall with high spatial frequency illumination.

V. CONCLUSIONS

A spatially variant modulation method using a laser has been proposed and demonstrated for use in detection of low contrast targets in turbid water conditions. The method has the advantage of using pulsed illumination (range gating) in conjunction with a spatial profiling method that may also be synchronously demodulated against the veiling luminance due to scattering. The viability of the physical approach has been verified to first order by experiment and by model results.

The design and implementation of discriminant detection methodology is a subject of current work. It is expected that specific signatures due to target shape may be detected or identified by standard methods used for target recognition once the spatial profile is converted to an electrical signal.

Direct optical methods for correlation are more difficult to implement. A combined technique for converting the spatial profile to a temporally variant signature is being investigated. Wide/Narrow and Narrow/Wide techniques are possible for source/detector fields-of-view. Additional work is required to assess the advantages gained in relation to existing imaging methods.

ACKNOWLEDGMENTS

The authors wish to thank the Atlantic Foundation for partial support of this work. This is HBOI contribution number 1309.

REFERENCES

1. Funk, C. J., Bryant, S. B., and Heckman, P., *Handbook of Underwater Imaging System design*, Ocean Technology Dept., NUSC, 1972.
2. Heckman, P., and Hodgson, "Underwater Optical Range Gating", *IEEE Journal of Quantum Electronics*, QE-3, 11, Nov. 1967
3. Horn, B. K. P., *Robot Vision*, MIT Press, 1986.
4. Yu, C., and F. M. Caimi, "Determination of Horizontal Motion through Optical Flow Computations", submitted *IEEE J Ocean Engineering*, 1994.
5. Caimi, F. M., J. H. Blatt, B. G. Grossman, et al., "Advanced Underwater Laser Systems for Ranging, Size Estimation, and Profiling", *MTS Journal* 27 (1): 31-41, 1993.
6. Swanson, N. L., "Coherence Loss of Laser Light Propagated through Simulated Coastal Waters", *Proceedings of Ocean Optics XI*, 1750, 1992.
7. Blatt, J. H., F. M. Caimi, and J. Hooker, "Adaptation of Video Moire Techniques to Undersea Mapping and Surface Shape Determination", *Optics and Lasers in Engineering*, March 1991.
8. Caimi, F. M., B. C. Bailey and J. H. Blatt, "Spatial Coherence Methods in Undersea Image Formation and Detection", *OCEANS '96 MTS/IEEE Supplementary Conference Proceedings*, pp. 40-46, 1996
9. Mertens, L. E., *IN-WATER PHOTOGRAPHY Theory and Practice*, Wiley-Interscience Series, 1970.
10. Fournier, G. R., M. Jonasz, "Computer Based Imaging Analysis," *Proc. SPIE*, Denver, July 1999. Paper 3761-09
11. Mullen, V. M., M. Strand, B. Coles, "Modulated Laser Line Scanner for Enhanced Underwater Imaging", *Proc. SPIE*, Denver, July 1999. Paper 3761-01.

PI Controller for Visual Tracking: Further Results

B. CHAOUKE, H. TAIRI, Lh. MASMOUDI and L. RADOUANE

LESSI Département De Physique Faculté Des Sciences

B.P. 1796 Fès Atlas 30000, Maroc

Tel. (212) 5 64 23 89, Fax (212) 5 64 25 00

Email: chaouki_bk@hotmail.com

Abstract:

The problem we want to address here is to track line segments in a sequence of time varying images acquired by a camera on a robot moving in an indoor environment. Two representations for the line segments are presented and discussed, and an appropriate representation is derived. In order to achieve our objective, we combine computer vision that detect and measure motion with simple control strategies. A mathematical formulation for the model of the dynamic system is given for each parameter of line segments, and we propose to use a discrete PI controller to compute the desired motion of the robot system. The selection of the controller is based on the vision technique used for the computation of the successful visual tracking. Computer simulations evaluated the reliability and precision of the technique.

Key-Words: Robotics, Computer Vision, Visual Servoing, Target Tracking.

I-Introduction

This work interests in the use of vision to ensure robotic tasks, especially for target tracking by visual servoing. The goal is to track line segments in a sequence of time varying images acquired by a camera on a robot moving in an indoor environment. These lines are corresponding to the edges extracted from the image being analyzed [2], [5]. The sensory information can be obtained through a variety of sensors such as position, velocity and acceleration of each parameter of line segment [4], [1], [12].

Some work has been reported toward the use of vision information for tracking. Hunt and Sanderson [7] presented algorithms for visual tracking based on mathematical prediction of the position of the object's centroid. Their algorithm needed the computation of the coordinates of the centroid and could only track slowly moving objects. Lee and Wohn [9] used image differencing techniques to track the system that incorporates a combination of visual and acoustic sensing. Dickmanns and Zapp [3] presented several methods (Kalman filters) for the integration of vision information in the feedback loop of various mechanical

systems. Weiss et. al. [14] proposed solutions to the problem of the robotic visual tracking under the framework of model reference adaptive control. Koivo and Houshangi [8] used adaptive control techniques in conjunction with the information provided by the stationary camera in order to control the robotic device. Papanikolopoulos et al. [10-11], have used the sum of squared differences (SSD) algorithm in order to compute the displacement vector. The best measurement is based on the confidence measure of each window. Tairi [13] have proposed the mean of squared difference (AMSD) algorithm to select an appropriate window in order to improve the accuracy of the vision measurements. These measurements are fed to an appropriate control scheme to calculate the requirement motion of the robotic system.

In this paper, two representations for the line segment are presented and discussed, and an appropriate representation is derived (midpoint, length, and orientation). A mathematical formulation for the model of the system is given for each parameter of line segment and we propose a complete control scheme (proportional integer PI controller) which explicitly enables to track a moving object. The simulation results show the effectiveness of the proposed method.

The organization of this paper is as follows: section II describes line segment representation. The mathematical formulation of the model of the dynamic system is described in section III. The selection of the appropriate control law is discussed in section IV. The simulation results are presented in section V. The last section concludes the paper.

II- Representation For Line Segment in the 2-D model:

An important subproblem is to choose an appropriate representation for the line segment, since the tracking will be based on this representation. It is clear, for example, that tracking both endpoints of each segment will be very difficult, since they are not at all reliable due to the fact that segments can be broken from one frame to another. For this reason, two types of representation have been considered.

• Representation c, d, θ, ℓ

In this representation a line segment having endpoints at point $P_1(x_1, y_1)$ and $P_2(x_2, y_2)$ is characterized by the vector $v_1 = [c, d, \theta, \ell]^T$. The components of v_1 are derived from the endpoints as follows:

The orientation θ of the line segment:

$$\theta = \arctan\left(\frac{y_2 - y_1}{x_2 - x_1}\right) \quad (1)$$

The length ℓ of the line segment:

$$\ell = \sqrt{(x_2 - x_1)^2 + (y_2 - y_1)^2} \quad (2)$$

The distance of the origin to the line segment denoted by the parameter c :

$$c = \frac{(x_2 y_1 - x_1 y_2)}{\ell} \quad (3)$$

The distance d , along the line from the perpendicular intersection to the midpoint of the segment

$$d = \frac{(x_2 - x_1)(x_2 + x_1) + (y_2 - y_1)(y_2 + y_1)}{2\ell} \quad (4)$$

• Representation x_m, y_m, θ, ℓ

The representation characterizes a line segment by the vector $v_2 = [x_m, y_m, \theta, \ell]^T$ where the point $P_m(x_m, y_m)$ defines the coordinates of the midpoint P_m of the segment and are given by

$$x_m = \frac{(x_1 + x_2)}{2} \quad \text{and} \quad y_m = \frac{(y_1 + y_2)}{2} \quad (5)$$

To find what representation is more appropriate for our tracking algorithm, we have to calculate the covariance matrices associated to the vectors v_1 and v_2 that defines both representations from those of the endpoints. We use the nonlinear relations that give these vectors function of the vector $P = [x_1, y_1, x_2, y_2]^T$ and the following relation:

$$\Lambda_v = \frac{\partial v}{\partial P} \Sigma \frac{\partial v'}{\partial P} \quad (6)$$

where $\frac{\partial v}{\partial P}$ is the 4x4 Jacobian matrix and Σ is the 4x4

covariance matrix of the vector $P = [x_1, y_1, x_2, y_2]^T$. Assuming no correlation between the endpoints and the same covariance matrix Λ for both endpoints leads to the following 4x4 covariance matrix Σ :

$$\Sigma = \begin{pmatrix} \Lambda & 0 \\ 0 & \Lambda \end{pmatrix} \quad (7)$$

where Λ is the 2x2 matrix associated to each endpoint:

$$\Lambda = \begin{pmatrix} \sigma_x^2 & \sigma_{xy}^2 \\ \sigma_{xy}^2 & \sigma_y^2 \end{pmatrix} \quad (8)$$

Due to the fact that the line segments may be broken differently from one image to another, an endpoint is not reliable. We model this segmentation noise introduced

by the polygonal approximation, as follows: assume that Λ is diagonal in the coordinate system defined by $u_{||}$ and u_{\perp} two units vectors parallel and perpendicular to the line segment, respectively. In this coordinate system, Λ is written:

$$\Lambda = \begin{pmatrix} \sigma_{||}^2 & 0 \\ 0 & \sigma_{\perp}^2 \end{pmatrix} \quad (9)$$

It should be noted that in general Λ is not diagonal except when $\sigma_{||}^2$ and σ_{\perp}^2 are from independent error source as, for example, when $\sigma_{||}^2$ is due to uncertainty in the position of the end of an edge chain by output the edge detector and the σ_{\perp}^2 is due to the residual in the polygonal approximation to the chain. In this case, which is most common in practice, we have $\sigma_{||}^2$ much greater than σ_{\perp}^2 expect for very short segments.

Noting that the coordinate system defined by $u_{||}$ and u_{\perp} is obtained using a rotation of an angle θ around the origin leads to the following relations for the covariance matrix Λ

$$\begin{cases} \sigma_x^2 = \sigma_{||}^2 \cos^2(\theta) + \sigma_{\perp}^2 \sin^2(\theta) \\ \sigma_y^2 = \sigma_{\perp}^2 \cos^2(\theta) + \sigma_{||}^2 \sin^2(\theta) \\ \sigma_{xy}^2 = (\sigma_{||}^2 - \sigma_{\perp}^2) \sin(\theta) \cos(\theta) \end{cases} \quad (10)$$

Applying these results to the vectors $v_1 = (c, d, \theta, \ell)^T$ and $v_2 = (x_c, y_c, \theta, \ell)^T$. We find after some algebra that the covariance matrix Λ_{v_1} and Λ_{v_2} respectively are given as follows:

$$\Lambda_{v_1} = \begin{bmatrix} \frac{\sigma_{||}^2}{2} + \frac{2d^2\sigma_{\perp}^2}{\ell^2} & \frac{-2cd\sigma_{\perp}^2}{\ell^2} & \frac{-2d\sigma_{\perp}^2}{\ell^2} & 0 \\ \frac{-2cd\sigma_{\perp}^2}{\ell^2} & \frac{\sigma_{||}^2}{2} + \frac{2c^2\sigma_{\perp}^2}{\ell^2} & \frac{2c\sigma_{\perp}^2}{\ell^2} & 0 \\ \frac{-2d\sigma_{\perp}^2}{\ell^2} & \frac{2c\sigma_{\perp}^2}{\ell^2} & \frac{-2\sigma_{\perp}^2}{\ell^2} & 0 \\ 0 & 0 & 0 & 2\sigma_{||}^2 \end{bmatrix} \quad (11)$$

$$\Lambda_{v_2} = \begin{bmatrix} \frac{\sigma_{||}^2 \cos^2(\theta) + \sigma_{\perp}^2 \sin^2(\theta)}{2} & \frac{(\sigma_{||}^2 - \sigma_{\perp}^2) \cos(\theta) \sin(\theta)}{2} & 0 & 0 \\ \frac{(\sigma_{||}^2 - \sigma_{\perp}^2) \cos(\theta) \sin(\theta)}{2} & \frac{\sigma_{\perp}^2 \cos^2(\theta) + \sigma_{||}^2 \sin^2(\theta)}{2} & 0 & 0 \\ 0 & 0 & \frac{2\sigma_{\perp}^2}{\ell^2} & 0 \\ 0 & 0 & 0 & 2\sigma_{||}^2 \end{bmatrix} \quad (12)$$

From these results, three important points need to be noted and discussed:

1-The c, d, θ, ℓ representation leads to a covariance matrix that depends strongly on the position of the associated line segment into the image through the parameters c and d that appear on the covariance matrix Λ_{v_1} . Therefore, two given line segments with the same length and orientation will have their uncertainty on the (c, d) parameters completely different depending on their position within the image. This is a real drawback since a large value for c (resp. d) will lead a large uncertainty for d (resp. c). This is not the case for the midpoint representation since the uncertainty to the midpoint (x_m, y_m) depends only on the uncertainty of the endpoints.

2-The mid-point representation leads to a lack of correlation between the parameters (x_m, y_m) and the parameters θ and ℓ . This lack of correlation between the parameters does not exist for the representation c, d, θ, ℓ since the parameters c, d and θ are correlated through the non-null terms Λ_{v_1} and Λ_{v_2} .

3- For the particular case where $\sigma_{||}^2 = \sigma_{\perp}^2$ the four parameters x_m, y_m, θ, ℓ are not correlated, while it is not the case for the c, d, θ, ℓ representation, where we have assume that σ_{\perp}^2 is equal to zero or at least $\sigma_{||}^2$ is much more greater than σ_{\perp}^2 in order to deal with parameters no correlated.

From these remarks, it appears clearly that the best representation is the midpoint since in general case the parameters x_m, y_m are much more reliable to track than the c and d parameters and since we only have to deals with two correlated parameters x_m, y_m instead for the c, d, θ, ℓ representation. In the simulation, our tracking algorithm deals with line segments represented by four points in a 1 dimensional space: the x_m and y_m position information and the length and the orientation information. When a given segment moves in the image, these four points follow a trajectory in the 1D space. The kinematics of the motion of the given line segment is the kinematics of the four points, i.e., trajectory, velocity and acceleration. Therefore, we will run four tracking algorithms independently on each parameter. In the general or exact implementation, we have taken account the correlation between x_m and y_m . Thus when a given segment moves in the images, the point x_m, y_m follows a 2D trajectory in the 2D space while the length and the orientation follow a 1D trajectory in the 1D space. The kinematics of the motion of the given line segment is the Kinematics of the three points, i.e. trajectory, velocity and acceleration.

III-Mathematical Formulation of the Dynamic System's Model.

Based on the mathematical model for the visual tracking of the feature point, we will develop the mathematical model for the 2-D visual tracking of the line segment. In this model, the 2-D visual tracking is realized by visually tracking multiple parameters that belong to the line segment. Consider a target that moves on a plane perpendicular to the optical axis of the camera. The projection of the target on the image plane is the area Ω in the image plane. It is assumed that the target rotates around an axis Z, which at $k=0$ coincide with the optical axis of the camera. Line segments are obtained by using the edge detector technique followed by the polygonal approximation [6]. The problem of 2-D visual tracking is fundamentally the same as the problem of tracking several parameters of the line segment. Consequently, a mathematical model for the task can be derived based on the derivation (for a single feature point) as in [11]. In this work, we applied the mathematical model for each parameter x_m, y_m, θ , and ℓ of the line segment. Each state vector is of dimension three and composed just by the position of the given parameter, its velocity and its acceleration. Therefore, we deal with the following state vector $[x_m, \dot{x}_m, \ddot{x}_m], [y_m, \dot{y}_m, \ddot{y}_m], [\theta, \dot{\theta}, \ddot{\theta}]$ and $[\ell, \dot{\ell}, \ddot{\ell}]$ the notation used for the state vector at the k^{th} time step $X^T = [x, \dot{x}, \ddot{x}]$

• The state-space representation of this model is:

$$X(k+1) = A_{\Delta t} X(k) + BU_c(k) + Ed(k) + Hw(k) \quad (13)$$

It is easy to verify that assuming a motion with constant acceleration and a state vector of dimension 3 leads to the following matrix $A_{\Delta t}$:

$$A_{\Delta t} = \begin{pmatrix} 1 & \Delta t & \frac{(\Delta t)^2}{2} \\ 0 & 1 & \Delta t \\ 0 & 0 & 1 \end{pmatrix} \quad (14)$$

and $B = E = \Delta T \cdot I_3$, $H = I_3$. $U_c(k) = (u_i(k), 0, 0)^T$ is the control input vector. $d(k) = (u_{oi}(k), 0, 0)^T$ is the exogenous disturbance vector and $w(k) = (w_i(k), 0, 0)^T$ is vector of random disturbance of the dynamic system and is usually modeled as white noise. $w_i(k) \sim N(0, W)$. With $i = x, y, \theta, \ell$.

• The measurement model used is:

$$Y(k) = CX(k) + \eta(k) \quad (15)$$

The measurement model $Y(k)$ assumes that the position x is measurable from the matching process while the velocity \dot{x} and the acceleration \ddot{x} are not. Therefore C is in our application defined by the following vector: $C = [1 \ 0 \ 0]$. $\eta(k)$ is the noise vector of the new measurement. $E[\eta_i] = 0$ and $E[\eta_i \eta_j^T] = R_i \delta_{ij}$.

In the exact application, we take into account the correlation between x_m and y_m and therefore the metastate vector X_m are $[x_m, \dot{x}_m, \ddot{x}_m, y_m, \dot{y}_m, \ddot{y}_m]^T$

The state of the model (6) and (8) can be rewritten as

$$X_m(k+1) = A_m X_m(k) + B_m U_c(k) + E_m d_m(k) + H_m w_m(k) \quad (16)$$

$$Y(k) = C_m X_m(k) + \eta(k) \quad (17)$$

where $B_m = E_m = \Delta t I_6$, $H_m = I_6$,

$$C_m = [1 \ 0 \ 0 \ 1 \ 0 \ 0]$$

$$U_c(k) = (u_i(k), 0, 0, v_i(k), 0, 0)^T,$$

$$d_m(k) = [u_{oi}(k), 0, 0, v_{oi}(k), 0, 0]^T.$$

$$\text{and } A_m = \begin{bmatrix} 1 & \Delta T & (\Delta T)^2/2 & 0 & 0 & 0 \\ 0 & 1 & \Delta T & 0 & 0 & 0 \\ 0 & 0 & 1 & 0 & 0 & 0 \\ 0 & 0 & 0 & 1 & \Delta T & (\Delta T)^2/2 \\ 0 & 0 & 0 & 0 & 1 & \Delta T \\ 0 & 0 & 0 & 0 & 0 & 1 \end{bmatrix}$$

IV- PI Controller for the Visual Tracking Problem

The control objective is to minimize at each instant of time the error vector between the feature position and the desired feature position:

$$e(k) = (x_m(k) - x_{md}(k), y_m(k) - y_{md}(k), \theta(k) - \theta_d(k), \ell(k) - \ell_d(k))^T \quad (18)$$

by choosing an appropriate control input vector $U_c(k) = (u_x(k), u_y(k), u_\theta(k), u_\ell(k))^T$. One simple technique for the elimination of the disturbances is the proportional-integral control technique (PI controller). This linear control law is given by:

$$U_c(k) = \left[G_p e(k) + G_i T \sum_{i=1}^k e(i) \right] T^{-1} \quad (19)$$

where G_p and G_i are constant proportional and integral gain matrices, respectively. There are several techniques for the calculation of the G_p and G_i matrices. One obvious effect of proportional control is that it increases the type of the system by one. Thus, the steady-state error is reduced and the disturbances are suppressed. On the other hand, the new system can be less stable than the original or even become unstable if the matrices G_p and G_i are not properly selected.

V-Simulation

Computer simulations were performed to test the proposed feature prediction model and control law. The goal is to track line segments in a sequence of time varying images. The objects used in the tracking examples are geometrical 3-D solid objects such as

cubes, cylinders, and prisms. These objects are moving with constant acceleration motion. Each pixel's intensity is corrupted with white noise. If we considered a synthetic sequence formed by 3-D cubes, the algorithms perform satisfactory with white noise in the range 10% and 20%. With higher noise, the results degenerate. The PI controller is done with the help of the of MATLAB software package. The matrices G_p and G_i are chosen in a way that keeps the closed-loop system stable [11]. The simulation are done with the matrices $G_p = -I_5$ and $G_i = -0.1I_5$. Thus, all the results shown in Fig (1-4) are done by using a steady state discrete of each parameters of line segments (midpoint, length, and orientation). The (PI) controller camera's trajectories are shown together with the parameters of line segments.

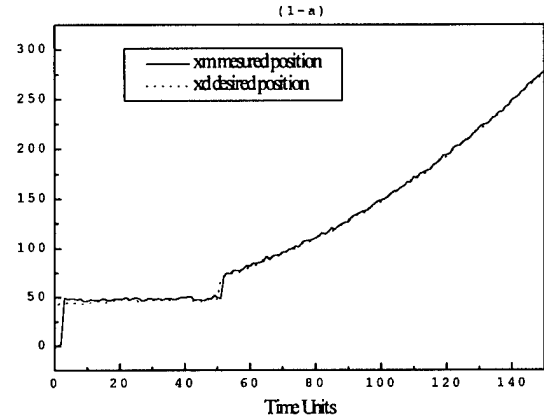


Fig (1-a): Tracking Result of x_m parameter

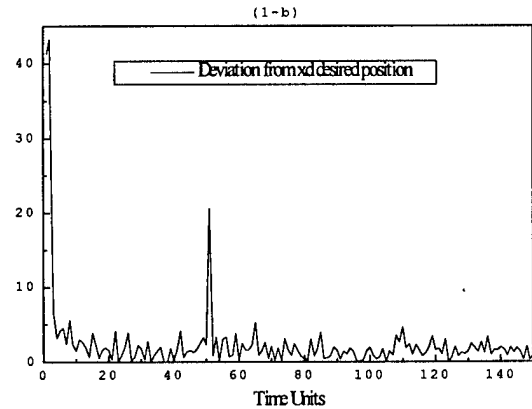


Fig (1-b): Deviation from the desired x_m parameter

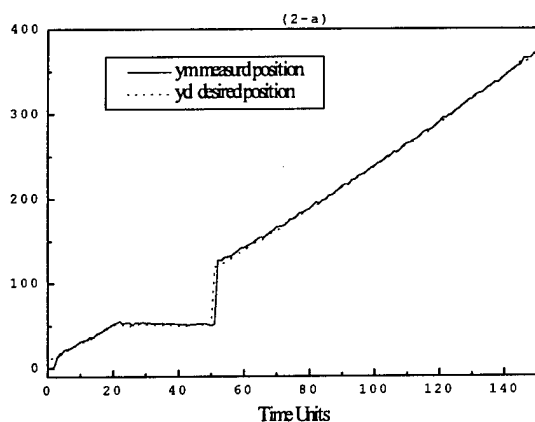


Fig (2-a): Tracking Result of y_m parameter

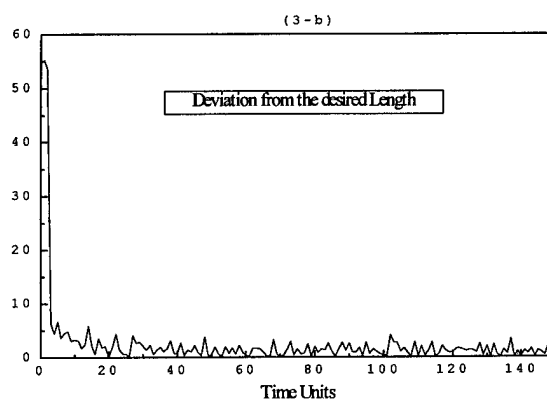


Fig (3-b): Deviation from the desired ℓ parameter

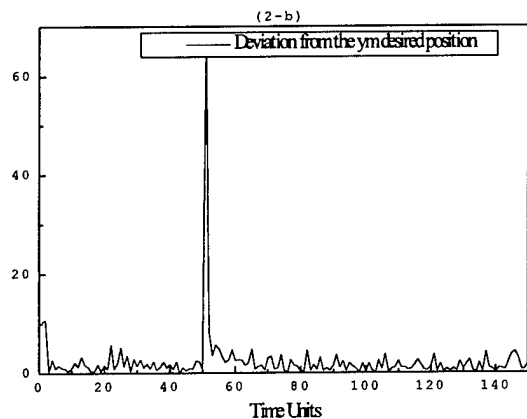


Fig (2-b): Deviation from the desired y_m parameter

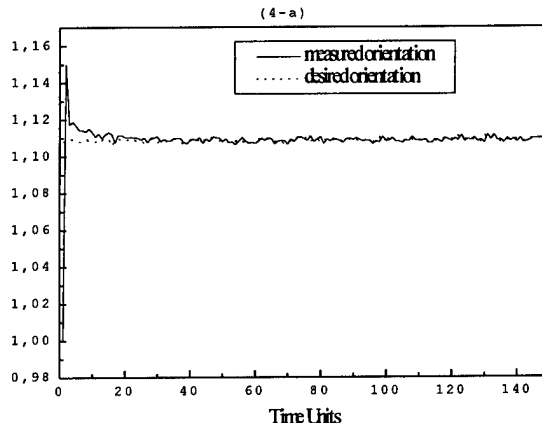


Fig (4-a): Tracking Result of θ parameter

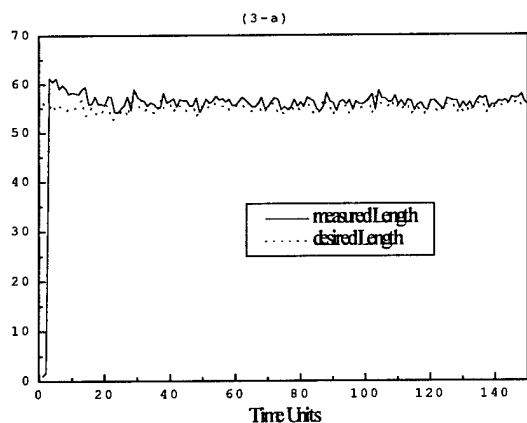


Fig (3-a): Tracking Result of ℓ parameter

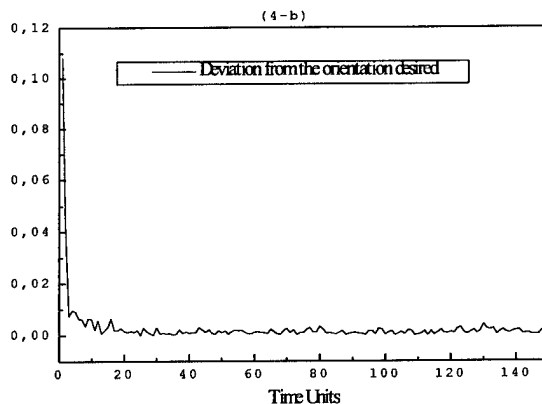


Fig (4-b): Deviation from the desired θ parameter

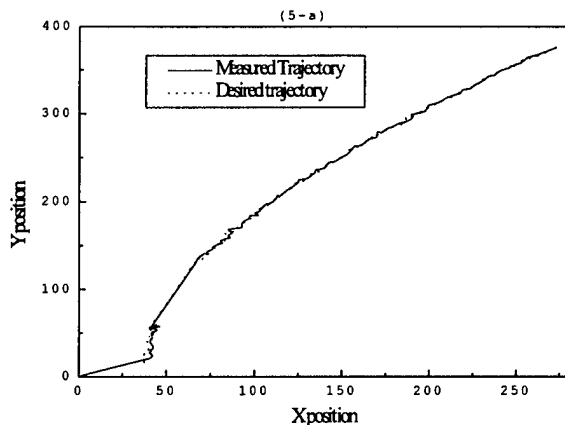


Fig 5: Tracking result of the trajectory x-y

VI. Conclusion

In this paper, we considered the robotic visual tracking problem. Specifically, we addressed to track line segments corresponding to the edges extracted from the image being analyzed. We first proposed an adequate representation for the line segment (midpoint, length, and orientation); thereafter we have presented a mathematical formulation for the model of the dynamic system for each parameter of line segments. The next step was to show the effectiveness of the introduced idea of combination of control (PI controller) with vision for an efficient solution to the tracking problem. Generally, this controller is tuned easily and deals satisfactorily with the tracking constraints and with the noisy type of the measurements. The simulation results show the reliability and the validity of the proposed approach.

References

- [1] Crowley. J.L, Stelmaszyk. P, Skordas. T, & Puget. P, "Measurements and integration of 3-D structures by tracking edges lines," *International Journal of computer. Vision* Vol.8, No.1, pp. 29-51. 1992.
- [2] Deriche. R & Faugeras. O., "Tracking line segments," *Image and vision computing*. Vol. 8, No.4, pp. 261-270. November. 1990.
- [3] Dickmanns. E. D & Zapp. A, "Autonomous high speed road vehicle guidance by computer vision," in *Proc. 10th IFAC World Congr*, July. 1987.
- [4] Faugeras. O, Deriche. R, Ayache. N, Lustman. N, & Giuliano. E, "Depth and Motion Analysis": *The Machine Being Developed within Esprit Project P940. Proceeding IAPR Workshop on Computer Vision, Special Hardware and Industrial Applications*, Oct 12-14, Tokyo, Japan. 1988.
- [5] Faugeras. O, Deriche. R. & Navab. N, "Optical flow of lines to 3-D motion and structure," *Proc. IEEE Int.*

Work. Intell. Syst. Tsukuba, September . Japan. 1989.

- [6] Giraudon. G "Chainage efficace des contours," INRIA Report, INRIA, France, May. 1987.
- [7] Hunt. A. E & Sanderson .A. C, "Vision-based predictive tracking of a moving target," *Carnegie Mellon Univ, The Robotics Inst, Tech. Rep. CMU-RI-TR-82-15*, Jan. 1982.
- [8] Koivo. A. J. & Houshangi .N, "Real-time vision feedback for servoing of the robotic manipulator with self-tuning controller," *IEEE. Trans. Syst. Man Cyber*, Vol. 21., No. 1, pp. 134-142. 1991.
- [9] Lee. S. W & Wahn. K, "Tracking moving objects by a mobile camera," *Dep. Comput.and Info. Sci., Univ. Pennsylvania*, Tech. Rep. MS-CIS-88-97. Nov. 1988.
- [10] Papanikolopoulos. N, Khosla. P K & Kanade. T, "Visual Tracking of a moving target by a camera mounted on a robot: A combination of control and vision," *IEEE Trans. Robotics and . Automation*, Vol. 9, No.1, pp. 14-34, Feb. 1993.
- [11] Papanikolopoulos .N & Khosla .P K, "Adaptive Robotic Visual Tracking: Theory and Experiments," *IEEE Trans automat contr*, Vol. 38, march. 1993.
- [12] Skordas. T, Puget. P, Zigmann. P & Ayache. N., "3-D edge- lines tracked in an image sequence," *Proc. 2nd Conf. Intell. Auton. Sys.* Amsterdam. December 1989
- [13] Tairi. H, El Ansari. M, Masmoudi. L & Radouane. L, "A combination of control and vision," *2nd IMACS International Multiconference CESA'98 Computational Engineering in Systems-Applications*, Tunisia. 1998.
- [14] Weiss. L. E., Sanderson. A. C & Neuman. C. P, "Dynamic sensor-based control of robots with visual feedback," *IEEE. J. Robotic Automation*. Vol. RA-3, No. 5, pp. 404-417. October. 1987.

FANBEAM HYPERSPECTRAL ACQUISITION FOR UNDERWATER APPLICATIONS

Eiji Yafuso, Robert Anderson and Ron Seiple
Science and Technology International

ABSTRACT

The Fanbeam Spectral Imager (FSI) system provides high area coverage rate acquisition of 3-D spatospectral data for use in underwater remote sensing. The FSI system is designed around a modular approach which utilizes separated illumination and detector units for reduction in common volume backscatter. The desired modularity and sensitivity have required novel optical and system design solutions. This paper will detail aspects of the FSI intended mission relevant to determination of system requirements, along with a description of the selected design approach and its expected performance.

I. Introduction

Underwater imaging instrumentation is used for the monitoring of a variety of ocean floor targets and for applications ranging from military to environmental in nature. The Fanbeam Spectral Imaging (FSI) system falls into a class of such instruments in which the imaging system is deployed in either an unmanned underwater vehicle (UUV) or underwater towed body. An illustration of a UUV-deployed FSI system is provided in Figure 1.

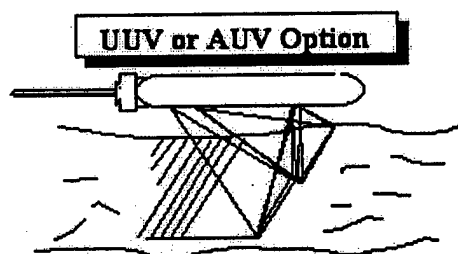


Figure 1: UUV-Deployed FSI System

The instrument packages typically acquire a lateral field of regard with longitudinal scanning provided by vehicle forward motion. The goals of these systems is to provide maximum area coverage rate while maintaining high discrimination capability for the targets of interest. State of the art optical systems in this class presently use laser line scan (LLS) configurations, in which

monochromatic laser illumination is combined with common path point imaging using "flying spot" scanning to provide the lateral field of regard. By contrast the FSI system provides ultrawide swath width "fanbeam" illumination, reduced common path imaging, and hyperspectral visible and fluorescence acquisition.

II. Design Concept

The FSI system is intended to be useful for a variety of acquisition needs. Thus the targets of interest fall into multiple categories. A common characteristic among the varied targets is that they are mostly man made and located on the sea floor. That the targets are man made introduces the likelihood that spatial pattern recognition algorithms will be helpful in discriminating a real target from naturally occurring bottom objects. The FSI system augments the spatial acquisition using both white light and fluorescent hyperspectral acquisition. To reliably provide hyperspectral acquisition while also maintaining ultrawide swath field of regard, a decision was made to invoke a modular system design approach. Thus, the illumination system is made up of two identical fanbeam illuminators aligned side-by-side, while the receiver is composed of four wide-angle spectrographic line imagers.

A. Illumination System

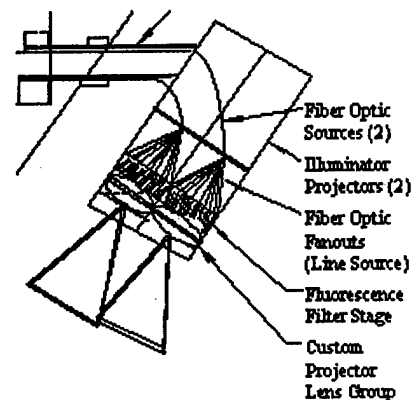


Figure 2 is a schematic of the illumination scheme.

Figure 2: Fanbeam Illuminator

As stated earlier, the fanbeam illuminator is made of two identical sub-illuminators aligned to form one wide line illumination. Each sub-illuminator consists of a line source made up of multiple optical fibers arranged to form a line, which is then projected through anamorphic projection optics onto the sea floor. Light to the fiber optic is supplied by a high-intensity arc source, which provides both white light and ultraviolet (UV) illumination.

The illumination is used in one of two possible modes, depending on the target of interest: reflectance hyperspectral, in which the source is unfiltered, or fluorescence hyperspectral, in which the source is filtered to output only the UV excitation light.

B. Spectrograph Receivers

Figure 3 illustrates the optical layout of the spectrograph receivers.

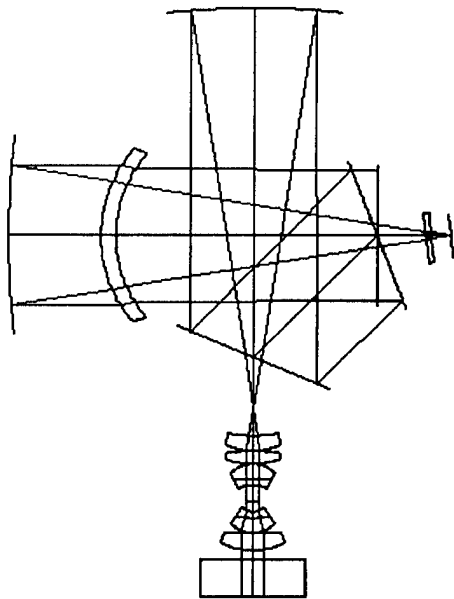


Figure 3: Spectrograph Receiver Layout

Light from the target is input to the system via a sevenelement modified double-gauss foreoptic. Prior to the foreoptic (bottom of Figure 3) is the pressure window, which is provided to give the spectrograph a dry and controlled operating environment within the vehicle. After passing through the foreoptic, light is imaged through a slit, which forms the input to the spectrograph. The spectrograph is basically a folded asymmetric, all reflective grating design, providing low F/# radiometric performance, while maintaining a reasonably small overall package. The fold mirrors, as well as the grating are centrally obscured, allowing the design to be optically axial, and obviating the necessity for off-axis aspherics. For simplicity in both manufacture and alignment, the collimating and focusing mirrors are both spherical. Reduction in coma is provided by the only refractive element in the spectrograph, a double-pass BK7 lens (middle left of Figure 3). Light enters the spectrograph through the slit, proceeds to the collimating mirror (top of Figure 3), reflects collimated directly back down to a fold mirror, which then folds the beam to the right and onto the grating. The grating is blazed for the first-order, diffracting the light in the plane of the figure through the coma reducing element and onto the focusing mirror. Finally,

the focusing mirror focuses the beam through a hole in the grating and onto a high sensitivity, low noise CCD.

The sub-field of regard provided by a single spectrograph is defined by the relationship between the slit, foreoptic and ocean floor. The system has an overall swath width on the order of 100 degrees, such that the required swath of each of the four spectrograph receivers is approximately 25 degrees.

A useful and alternative way to view this design is as a projector of the spectrometer's slit onto the sea floor through the foreoptic. This perspective is useful to prevent oversight of the fact that, since this is a modular design, each spectrograph will see an angled aspect of the line scan. This condition is schematically illustrated in Figure 4.

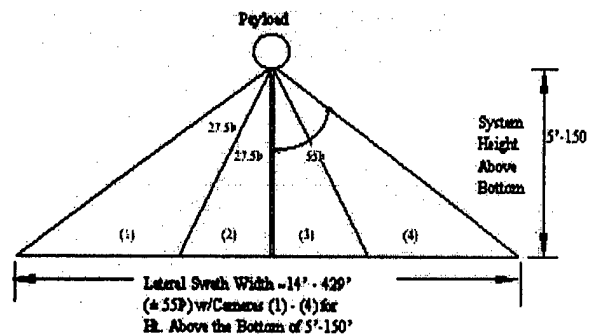


Figure 4: Modular Field of Regard

In the figure four separate receivers are aligned to form one continuous field of regard, which will then be scanned along the sea floor as the vehicle moves forward. Each swath is the projection of a spectrograph slit through the foreoptic and onto the area to be scanned. Using this perspective it is clear that the image of the slit must be projected differently by each receiver in order to map properly along the flat target area. In fact the slit must generally be projected such that the image plane is tilted from normal relative to the optical axis, and the amount of tilt depends on which part of the swath the particular receiver is projecting. To provide the needed versatility, the opto-mechanical design makes use of the Scheimpflug¹ condition. The foreoptic can be adjustably tilted relative to the slit in such a way as to render the image of the slit properly mapped to the non-normal sea floor.

C. Common Volume Reduction

The final advantage in design modularity is the ability to reduce the common path volume shared by the illuminator and receiver. Thorough treatises in making spectral irradiance measurements² as well as the general study of light propagation through water³ have

been performed, and are readily available in the literature. The issue as it pertains to the FSI system is that ocean water is a highly scattering medium. Light from the illumination is forward scattered toward the target, spreading the illumination footprint, and backscattered toward the illuminator reducing illumination intensity at the target. Once the beam is incident at the target, it is then reflected from the target toward the receiver optics. This light emanating from the target is then backscattered toward the target, reducing the relative luminosity, and forward scattered toward the receiver, blurring the imagery. Multiply forward scattered light from the target is a major cause of reduction in receiver modulation transfer function capability (MTF). Because the illumination and receiver are separate units, they can be projected through separate columns of water. As seen in Figure 1, the FSI illuminator projects from the back of the vehicle forward, illuminating a linear swath directly below the receiver optical system. The altitude above the sea floor at which the system is used for surveying, along with the linear separation of illumination and receiver units provides the angle between the two. The scheme is illustrated schematically in Figure 5.

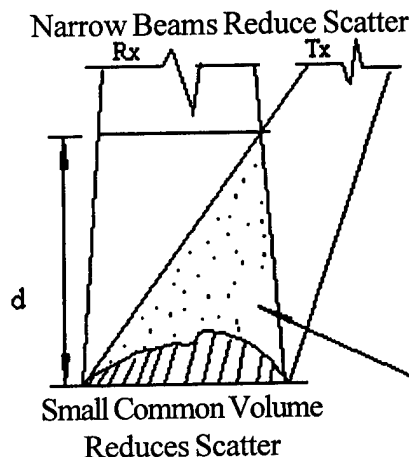


Figure 5: Common Volume Reduction

In the figure "Rx" is the path seen by the receiver optics, while "Tx" is the illumination beam. The angle between them reduces the common volume which contributes to forward scatter into the receiver (dotted area).

III. Utility

As previously noted, underwater line-scan systems are already in existence, and provide high area coverage rate and good discrimination for the limited targets of interest. The LLS systems are among the most highly regarded, but are limited to monochromatic acquisition. The FSI system is intended to enhance detection and especially characterization by providing hyperspectral detection and

white light as well as fluorescence illumination. In so doing, the FSI system shall be able to widen the acquisition utility of line scan underwater imaging to new areas of military, scientific, and environmental interests. By enabling spectral discrimination, the FSI system will provide greater capability in such areas as hazardous materials (HAZMAT) container monitoring, underwater habitat assessment, sunken vessel exploration, geological mapping, and other environmental conditions. The addition of fluorescence excitation with hyperspectral acquisition extends the capability to monitoring of oceanic biota, oil and gas exploration, and assessment of coral health.

IV. Future Work

The FSI system design would be a precarious undertaking without quantitative accounting for the scattering and absorbing effects which will be seen in the ocean environment. Accurate analytical approaches to predicting performance are difficult to perform and sometimes imprecise. As a result accurate models of optical propagation in ocean environments have relied heavily on empirical data. Nevertheless, preliminary performance models were developed for the FSI system utilizing Jerlov Water Types (JWT) to approximate the effects of ocean water. Effects of biological scattering were also estimated with the overall objective of simplifying the forward propagation problem to one including mostly Beer's law attenuation with spherical expansion.

$$P(\lambda) = \frac{M_0 \eta p r^2 e^{-(c+K)R}}{4R^2} \quad (1)$$

In equation 1, $P(\lambda)$ is the wavelength dependent power emanating from the target. M_0 is the source radiant exitance in watts per square meter, r is the radius of the system pupil, R the distance from pupil to target, c is the beam attenuation coefficient, K is the diffuse attenuation coefficient, p is the object albedo, and finally, η is a constant to account for the various system-related radiometric losses and gains. To predict the FSI system performance, this model was employed at narrow wavelength intervals, covering the continuous operating spectral range from 400 - 700 nm. System characteristics specific to the actual optical design for both illumination and receiver spectrographic systems were input, as well as responsivity figures for the intended focal plane CCD. All this in mind and given the nature of the simplifications previously mentioned, these performance models are understood to be non-rigorous in approach, and are only intended as rough guidelines to aid in system design. What the models do furnish is the prediction that at operating altitudes of 50 feet, where the present FSI system is destined for duty, the

receiver SNR will provide sufficient capability for hyperspectral detection and discrimination. There remains the issue of accurately modeling the fluorescence excitation propagation, along with the resulting hyperspectral return. The return itself is an identical problem to white light hyperspectral acquisition, since the fluorescence will fall within the same wavelength boundaries. The differences arise primarily in the approximation of forward illumination propagation, with ultraviolet more highly impeded through water, and the assumed target albedo, which must be replaced with fluorescence conversion efficiencies.

V. Summary

The intent of the FSI program has been to provide an underwater scanning system, augmented by both white light and fluorescence hyperspectral data acquisition. An additional goal of the endeavor was to provide this with extremely high area coverage rate while simultaneously minimizing the effects of common volume forward scatter. The approach taken has been to design modular illumination and spectrographic receiver systems which each provide sub-area coverage, but which could be combined to form a system with greater overall capability. The targets of interest in the initial FSI study are military in nature, however, the FSI system has been designed for broad applicability in underwater remote sensing.

Acknowledgments

This work was funded by the National Defense Center of Excellence for Research in Ocean Sciences (CEROS). CEROS is a part of the Natural Energy Laboratory of Hawaii Authority (NELHA), an agency of the Department of Business, Economic Development & Tourism, State of Hawaii. CEROS is funded by the Defense Advanced Research Projects Agency (DARPA) through grants to and agreements with NELHA. This report does not necessarily reflect the position or policy of the Government, and no official endorsement should be inferred.

References

1. W.J. Smith, *Modern Optical Engineering*, 2nd Edition, McGraw Hill, New York, pp.52 - 53, 1990.
2. J.E. Tyler and R.C. Smith, *Measurement of Spectral Irradiance Underwater*, Gordon and Breach, New York, 1970.
3. R.E. Walker, *Marine Light Field Statistics*, John Wiley and Sons, New York, 1994.

Author Biographical Data

Eiji Yafuso is a consulting Senior Scientist on the FSI program. He received a B.S. in Physics from the University of California, and M.S. and Ph.D. in Optical Sciences from the University of Arizona's Optical Sciences Center. Dr. Yafuso has a combined 12 years experience in development of advanced electro-optical systems and interfaces.

Robert Anderson is the program manager of the Fanbeam Spectral Imager program at Science and Technology International. Prior to STI, Robert has worked with Hughes Aircraft, developing test equipment for infrared missile systems, and eventually with the Hughes Santa Barbara Research laboratories, developing state-of-the-art infrared focal planes and associated electronics technology. Prior to this he worked with NASA on development of Lunar Television Video Transmission. Robert holds a B.S. in Electronic Technology from the Capital Radio Engineering Institute, and an M.S.E.E. from the University of Arizona.

Ron Seiple is the Vice President for Programs at Science and Technology International. He has been in the Navy R & D community for over thirty years. He was the Science Advisor for the Commander in Chief of the Pacific Fleet, retired Captain in the Navy and a decorated Navy Seal who served two tours in Vietnam. Ron worked for Space and Naval Warfare Center as a Senior Scientist and was responsible for numerous Programs including, Submersible Training Platform for the Seals, Diver Decompression Computer, numerous Swimmer Delivery Vehicle Systems, Fiber Optic Air Deployment Systems, Marine Mammal Hardware Development, Mobile Inshore Undersea Warfare Upgrade System, Remote Unmanned Work System, was the Craft Master of the Navy's first SWATH Ship, Kaimalino and managed numerous other programs. Ron was the Commanding Officer of a Diving and Salvage Unit and was responsible for numerous salvage operations including assisting in the Enewetok Clean-up Operation.

A DIGITAL PROGRAMMABLE HIGH RESOLUTION 200KHZ WATER COLUMN PROFILER.

Ward W. Cartier and David D. Lemon

ASL Environmental Sciences Inc.
1986 Mills Rd., Sidney, B.C. V8L 5Y3
Canada

Abstract

Acoustical instrumentation for imaging the water column has traditionally been ship mounted and configured to work in a downward looking orientation. Until recently, data acquisition for these acoustic instruments has used an analog strip chart recorder tended by an operator on board a surface vessel. With the advent of digital electronics, digital echo sounders have begun to appear. However, these instruments have followed the traditional configuration and, for the most part, have remained shipboard mounted. The past five years has seen unprecedented growth in the development of low power digital microprocessor, storage and data acquisition technologies.

An acoustical 200kHz high resolution, digital, programmable Water Column Profiler (WCP) has been developed incorporating these new technologies. The WCP offers unprecedented flexibility for the user and, except for the analog front end, is completely digital, fully programmable and is housed in a pressure case capable of bottom (upward looking), mooring or shipboard (downward looking) mounting configurations. The aluminum pressure case is capable of deployments to 200m with connectors for telemetry and power if real time data are required. The WCP can ping at up to 2 Hz with an acoustic range resolution of 3 cm and is capable of digitizing four samples per acoustic range bin. The maximum probing depth, depending on the water column properties, is 200 m and the WCP is capable of storing data internally for up to 3 weeks at maximum ping and sampling rates. Data can be transferred realtime via a 10 Mbit/s 10Base2 Ethernet link to a surface system or local area network for viewing and/or data storage.

The system can also be controlled remotely over the local area network. For self-contained autonomous insitu deployments, internally recorded data can be recovered from the WCP at very high rates to a storage system over a high speed Ethernet connection. The WCP is designed to work with other acoustic instruments

like the RDI Sentinel series ADCPs. The high resolution WCP sonar data complements the ADCPs velocity data creating a very powerful analytical acoustic profiling tool. In September 1998, a prototype of the instrument was deployed near Istanbul in the Bosphorus (Istanbul Bogazi) strait. The WCP was co-deployed, in roughly 62m of water, with an RDI 300kHz Sentinel Workhorse ADCP to image the two layered stratified flow in the Bosphorus.

I. Introduction

A. Overview

In the past acoustical instrumentation for imaging the water column have for the most part consisted of large, heavy instruments requiring large amounts of power and operator attention to make them work. They were manufactured with virtually all analog parts and have used the same basic design methodology for many years. Until recently, data acquisition for these acoustic instruments has been with an analog strip chart recorder. This technology, which has come to be known as the "echo-sounder", has undergone a significant technological transformation over the past 5 years. This has been largely due to advancements in low power digital electronics and display technologies which have been incorporated into modern Water Column Profilers (WCPs). However most commercially available WCPs are still quite large and are still based on the same functionality as the original echo sounders. For this reason most modern WCPs, although they incorporate many of the new technologies, follow the traditional configuration, being ship mounted and configured to work in a downward looking orientation.

B. A New Design Approach

With the recent explosion in digital, low power, microprocessor, storage, data acquisition and communications technologies it is finally possible to reduce the WCP to a size where it can be deployed remotely in a non-conventional manner. An acoustical 200kHz high resolution, digital, programmable Water

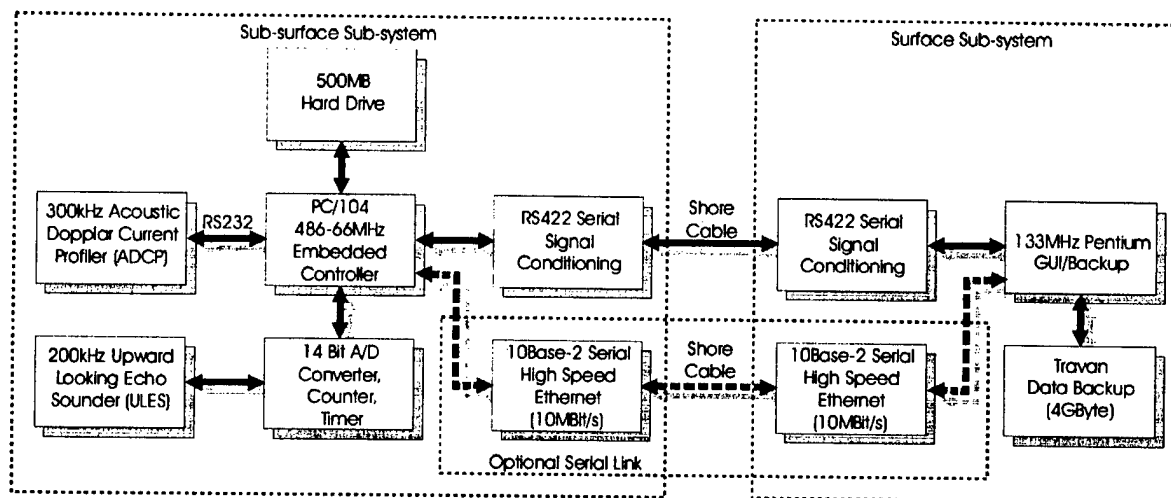


Figure 1: Upward looking water column profiler block diagram

Column Profiler (WCP) has been developed incorporating these new technologies and, except for the analog front end, is completely digital, fully programmable and is housed in a pressure case capable of bottom (upward looking), mooring or shipboard (downward looking) mounting configurations. The aluminum pressure case is capable of deployments to 200m with connectors for telemetry and power if real time data is required.

II. Implementation

The Upward Looking WCP comprises two sub-systems; a sub-surface section and a surface section (see Figure 1). The sub-surface sub-system resides in a pressure case capable of deployments to 225 m and can be deployed in either bottom-mounted, moored or surface-mounted configurations for use in either upward or downward modes of operation. The surface sub-system, connected to the sub-surface sub-system via cable, is a station where an operator can control the sub-surface sub-system and view data in real time. It also serves as a mass storage station enabling the overall system to have very long deployment periods. The sub-surface sub-system receives power from either the surface subsystem, for real time deployments or from batteries for autonomous deployments. The surface sub-system can be either ship- or shore- mounted.

The WCP is based on a 200 kHz analog sonar transceiver card capable of pulse repetition (ping) rates of up to 2 Hz with an acoustic range resolution of 3 cm. The transceiver card compensates for geometric spreading loss with Time Varying Gain (TVG) ranging from 10.3 to 90.3 dB and has a 3 dB bandwidth of roughly 6 kHz. The card is capable of producing 40Wrms which yields an effective range of approximately 200 m, depending on the conditions in the water column. The sonar card output is digitized at 14 bit resolution and the

data is sent to a PC/104 66 MHz 486 embedded controller. The digitizer is capable of digitizing four samples per acoustic range bin resulting in about 133 samples/m. This sampling density gives the WCP the ability to produce high resolution images. The data can be stored internally to a 500MB hard drive, if the system is to be deployed in a self-contained autonomous in-situ mode. The drive capacity allows 3 weeks of internal data storage at maximum ping and sampling rates. For an insitu real-time deployment, data from the sub-surface sub-system may be sent via a suitable serial communication link to the surface sub-system for real time display and storage. The serial communication link can be either RS422 or high speed (10 Mbit/sec) 10Base-2 Ethernet through a suitable shore cable. In this configuration the system is controlled remotely over a local area network formed with the serial high speed Ethernet link or through serial commands through the RS422 serial link.

The WCP is designed to work with the 300kHz RDI Workhorse series Acoustic Doppler Current Profilers (ADCPs). The ADCP interfaces directly to the 486 embedded PC/104 controller through the RS232 serial port (Figure 1). In the in-situ autonomous deployment mode its data is written to its own internal memory, 80 Mbytes total, but can also be sent to the embedded controller to be stored on the local hard drive or sent up to the surface sub-system for display and storage. The ADCP can be programmed either before the deployment, for in-situ autonomous deployments, or can be programmed while the system is deployed during real time deployments. It is possible to communicate directly with the ADCP from the surface sub-system through the Graphic User Interface (GUI). Once the WCP and the ADCP are running the two systems operate independently and, because of the difference in operating frequencies, do not interfere with each other. If the ADCP is programmed to pass data to the embedded

controller, the controller takes the ADCP data, along with each ping of WCP data, and puts it in packet form. Along with header and checksum information, the packet is sent up to the surface sub-system via the serial communication link. The surface sub-system then checks for transmission errors, unpacks the data, displays the WCP data and stores both the WCP and ADCP data to hard drive. For self-contained autonomous in-situ deployments, internally recorded data can be recovered from the WCP at very high rates to a storage system over a high speed Ethernet connection.

III. Sample Results

In September 1998, a prototype of the instrument was deployed near Istanbul in the Bosphorus (Istanbul Bogazi) Strait (see Figure 2). The WCP was co-deployed, in 62m of water, with an RDI 300kHz Sentinel Workhorse ADCP to image the two layered stratified flow in the Bosphorus. The Bosphorus provides an extremely challenging and interesting site to image. A multi layered flow exists, principally driven by the prevailing north winds, which force the fresh Black Sea water to flow south into the Sea of Marmara. This, in turn, sets up a counter flow where the dense salty Mediterranean Sea water flows north, underneath the less dense fresh Black Sea water, into the Black Sea. This multi layered flow exchange is responsible, in part, for the transport of salt out of the Mediterranean Basin [1].

Figure 3 shows the deployment configuration in the Bosphorus. At the deployment site the Bosphorus is 825m wide and about 65m deep with the deepest part of the channel being on the west side. A 700m cable was run from the instrument package to the surface sub-system on the east shore, near the Anadolu Hisari (an old fortress). The WCP was configured with a 68.08 m range, a ping rate of 0.5 Hz and a digitization rate of 10 kHz.

Figures 4 and 5 show an 8 minute, 55 second section of ADCP and WCP data, respectively. Figure 5 also shows a plot of both sound speed and sigma-t vs. depth. Sigma-t varies from 11.5 in the upper layer (Black Sea water) to 28

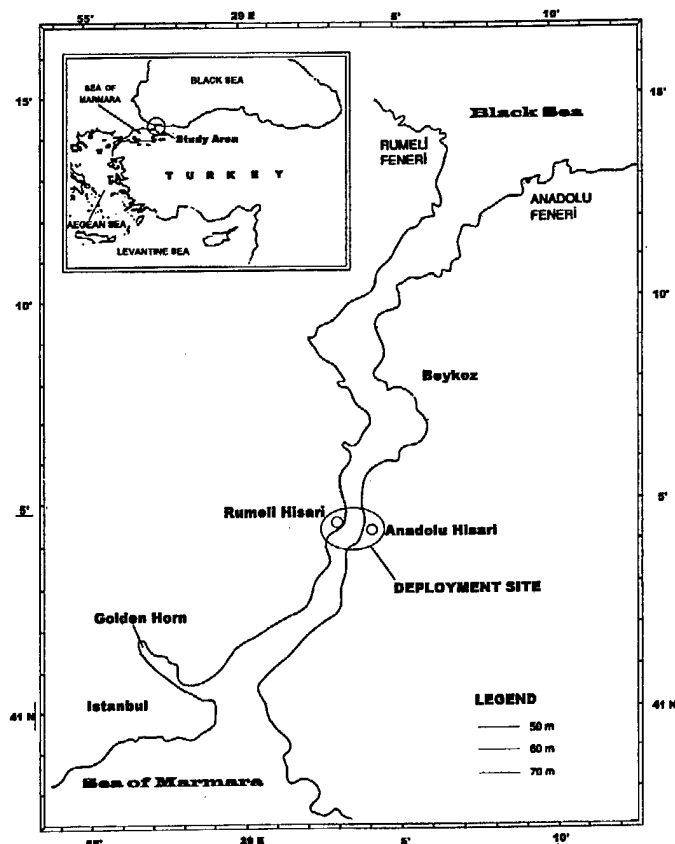


Figure 2: Map showing the deployment site near Istanbul in the Bosphorus (Istanbul Bogazi).

in the lower layer's Mediterranean Sea water. There is a significant sound channel in the interface region between the two layers. Figure 4 displays data from the ADCP, illustrating the strong shear in the flow. Current speeds in the upper layer reach nearly 1m/s to the south and in the lower layer exceed 1m/s to the north (bottom right image). The interface region can be discerned in the intensity image on the left of Figure 4 although the detail is poor. In contrast, details of the interface region can clearly be seen in the high resolution WCP image shown in Figure 5. Here details of the fine structure that exists in the interface region are clearly evident. One interesting note is that the last part of the record shows a wave-like structure starting on the interface.

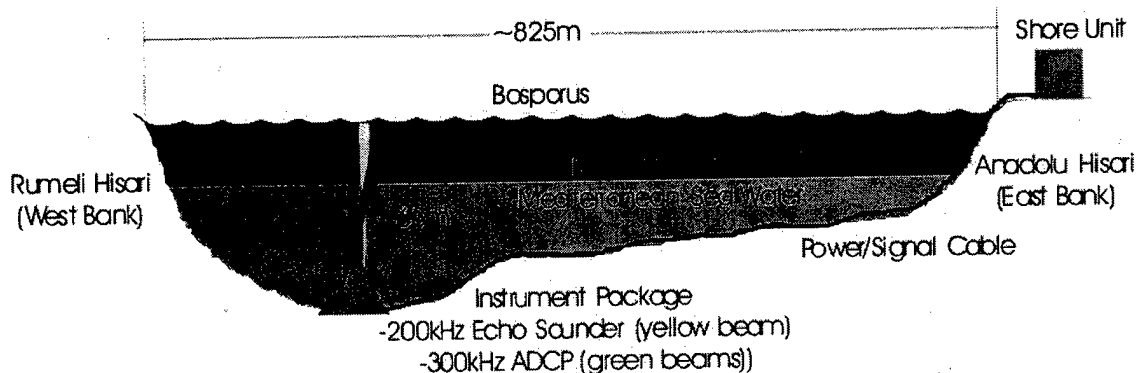


Figure 3: Prototype WCP deployment in the Bosphorus.

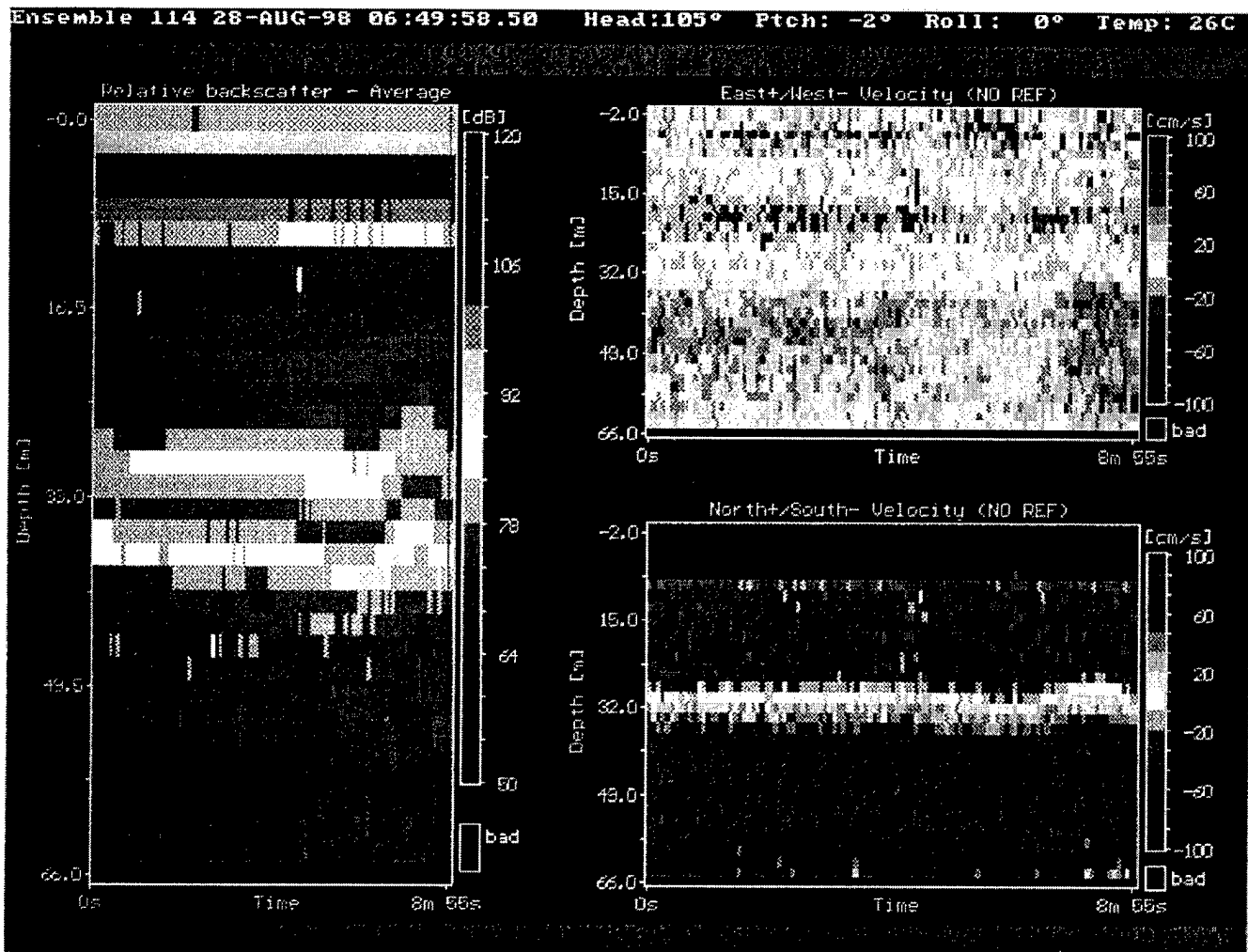


Fig. 2: ADCP data record for 8 minutes, 55 seconds at the Bosphorus site.

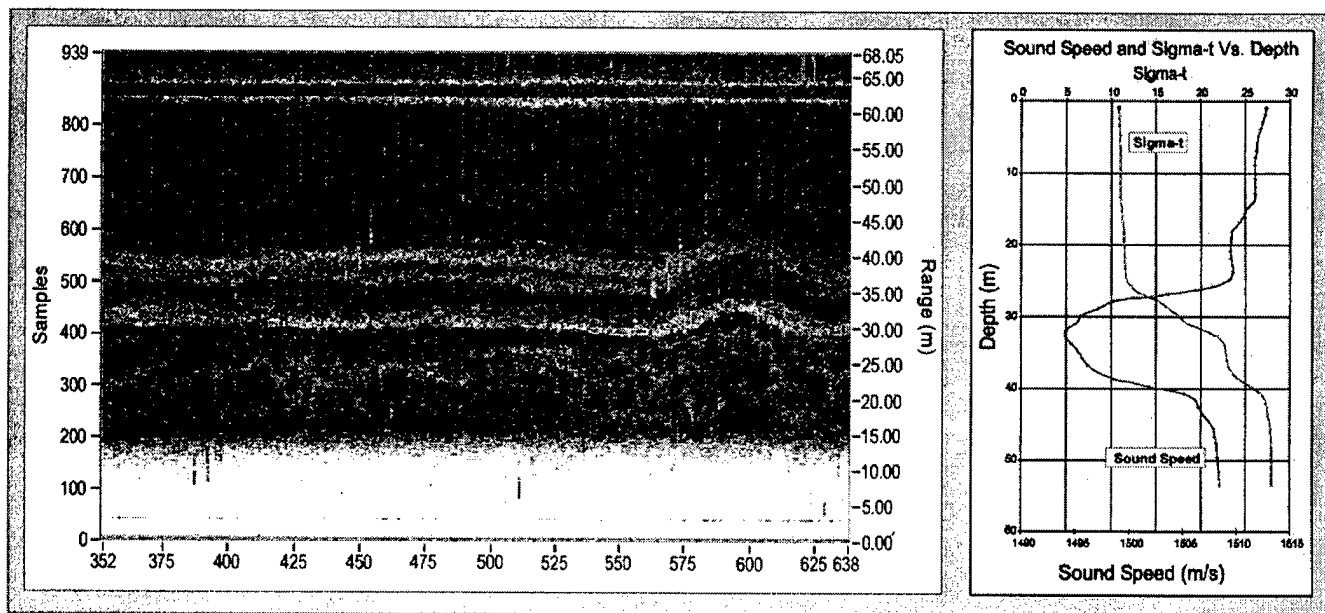


Figure 3: WCP data record for the same 8 minute, 55 second period as the ADCP data in Fig. 4.

This corresponds to a bow wave being impressed on the interface during the passage of a large tanker. Short sections of vertical lines are seen at intervals in the image which the authors believe originate from the ship's sounder as it was passing overhead. These are not evident in the rest of the record before or after the passage of the tanker.

IV. Conclusions

With the tremendous burst of technology improvements over the past 5 years it is now possible for a new highly flexible, fully digital, low power, compact Water Column Profiler to be constructed. This high resolution acoustic imaging instrument is capable of operating in new modes and deployment schemes impossible only a few years ago. The high resolution WCP sonar data complements the ADCP's velocity data creating a very powerful analytical acoustic profiling tool.

References

- [1] U. Unluata, T. Oguz, M. A. Latif, E. Ozsoy, "On the physical oceanography of the Turkish straits", L. J. Pratt (ed.), *The Physical Oceanography of Sea Straits*, pp. 25-60, Kluwer Academic Publishers (Neth), 1990.

BEAMFORMING AND IMAGING WITH ACOUSTIC LENSES IN SMALL, HIGH-FREQUENCY SONARS

Edward O. Belcher
Applied Physics Laboratory
University of Washington, Seattle, WA

Hien Q. Dinh
Naval Explosive Ordnance Disposal
Technology Division, Indian Head, MD

Dana C. Lynn
Code 6410, Naval Surface Warfare Center,
Carderock Division, West Bethesda, MD

Thomas J. Laughlin
Naval Surface Warfare Center, Crane Division,
Glendora Lake Facility, Sullivan, IN

Abstract - A high-resolution acoustic imaging system is an important aid in turbid water where optical systems fail. Applications include inspecting structures, searching for and identifying mines or contraband on hulls of ships, monitoring work of divers or remotely operated vehicles (ROVs), and monitoring tests in low-visibility water. The three sonars described in this paper use acoustic lenses to form near-video-quality images. The first sonar, Limpet Mine Imaging Sonar (LIMIS), is diver-held, forms 64 beams, each with a beamwidth of 0.35° in the horizontal axis by 7° in the vertical axis. This sonar has a 20° field-of-view, operates at 2 MHz, has a practical range of 10 m, and forms between 5 and 12 images/second. The second sonar, Glendora Lake Acoustic Imaging System, (GLACIS), is used to monitor underwater tests and pans and tilts on a platform that can change depth. This sonar forms 64 beams, each with a beamwidth of 0.55° horizontal and 10° vertical. It has a 32° field of view, operates at 750 kHz, and forms 5 or 9 images/second at an operating range of 60 or 30 m, respectively. The third sonar, Acoustic Barnacle Imaging Sonar (ABIS), mounts on an ROV and forms 128 beams, each with a beamwidth of 0.25° horizontal by 10° vertical. This sonar has a 32° field-of-view, operates at 3 MHz, has a range between 1.8 m and 2.4 m, and forms 6 images/second. All three sonars use a set of thin, acoustic lenses made of polymethylpentene to focus sound on a 1-3 composite linear array. The acoustic lenses form beams at the speed of sound with no circuitry and thus eliminate the complexity and power consumption of conventional beamforming electronics. Two disadvantages are (1) the lenses and the spaces between the lenses add volume in front of the transducer array, and (2) multiple reflections between lens surfaces cause internal reverberation. The reverberation inside these sonars is about 40 dB down from the target echoes and scatters to form a slightly brighter background. No range-shifted "ghosts" of target images are seen.

I. INTRODUCTION

In clear water and with appropriate lighting, optical cameras can image out to 5 m. With increasing fre-

quency, underwater work that would require optical systems is situated in water where optical systems fail. In many rivers, lakes, harbors, bays, and other coastal areas visibility is a fraction of a meter. There, optical systems have white screens, and divers resort to tactile means. The three sonars discussed here use acoustic lenses and bridge the gap between existing sonars and optical systems. Their maximum ranges are relatively small (60 m, 10 m, and 3 m) but their resolutions (0.55° , 0.35° , and 0.25°) allow them to form near-video-quality images. High resolution and a fast frame rate allow them to substitute for optical systems in turbid water. These sonars have a low power consumption (25-30 W), which makes them useful for diver-held operations or on platforms with a power budget.

II. LENS TECHNOLOGY

Acoustic lenses allow both transmission and reception of narrow beams. The lenses operate at the speed of sound, form multiple beams in parallel, and consume no power. Two disadvantages of acoustic lenses are (1) the lenses and the spaces between them add volume in front of the transducer array and (2) multiple reflections between the lens surfaces cause reverberation.

Acoustic lenses are made of plastic, epoxy, rubber, or liquid and refract sound using the same basic laws as optical lenses. The lenses discussed here have a rectangular aperture with curvature only in the horizontal direction. As illustrated in Figure 1, the lenses form a narrow beam of sound in the horizontal plane, and the curved transducer array forms a wide beam in the vertical plane. Each element in the transducer array transmits a short pulse and receives echoes confined within a narrow horizontal direction. The amplitudes and time delays of the echoes are mapped into pixel colors and positions on the sonar display.

A. Lens Design

A lens design must consider beamwidth, sidelobe amplitudes, field of view, and lens efficiency. Designing an acoustic lens begins with optical lens design techniques. There are many optical lens design computer

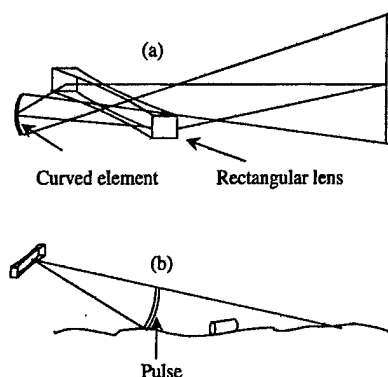


Fig. 1(a). The lens systems use a rectangular lens and curved element to form a focused narrow beam of sound. (b). When a sound pulse exits the lens, and is directed toward a slanted object plane, it interrogates a narrow line on the object plane as a function of time. The echo response is mapped on the display.

programs. Two such programs^{1,2} that run on PCs were used as part of the design of the acoustic lenses described here. A candidate design is found with these programs, which primarily use ray models. Next, a wave analysis model^{3,4} predicts the beamwidth, sidelobes, and lens loss for each of the beams formed by the candidate design, and how these beams would change with changes in the salinity and temperature of the ambient water. The wave analysis often indicates that the beam patterns need improvement. If so, new candidates with different lens prescriptions and sometimes different lens materials are designed and analyzed. After several iterations between candidate designs and wave analysis, a successful design prescription is found, and the lenses are fabricated.

B. Lens Transducer Array

The three sonars discussed in this paper all use linear transducer arrays with one element designated for each beam formed in the sonar. The horizontal width of the element is small compared to its height. For example the array on the diver-held sonar consists of 64 elements with a pitch of 1.37 mm and a height of 46 mm. The elements in all three arrays are made with PZT 1-3 composite constructed by the dice-and-fill method. The 1-3 composite allows us to have a wide bandwidth, shape the transducers without much concern about unwanted resonances, and curve the element surfaces to control the vertical beamwidth in each beam. A quarter-wave layer on the array face further increases the array's efficiency and bandwidth.

C. Internal Reflections

We chose a plastic, polymethylpentene (TPX RT-18), for the major component of lens materials in part because its acoustic impedance is close to that of water. Less than 1% of acoustic energy is reflected as sound passes through each water/plastic interface. This is im-

portant from the viewpoint of efficiency but even more important from the viewpoint of reverberation within the lens. To measure internal reflections, we transmitted 10- μ s acoustic pulses into the sonars. The transducer arrays first received the focused pulse, and then they received a series of pulses that were delayed because of multiple reflections in the lens set. The amplitudes of the first set of reflected pulses were down 40 dB or more from those of the focused pulses. Reflected pulses with exponentially decaying amplitudes continued to arrive for 0.3 ms after the first pulse arrived. Ghosting is a potential problem but has not been seen in the displayed images. The lens reverberation scatters and blurs any potential ghosts, so they manifest as a slightly brighter noise floor, not as a range-shifted image of the object.

III. THREE ACOUSTIC LENS SONARS

A. Limpet Mine Imaging Sonar (LIMIS)

The Limpet Mine Imaging Sonar⁵ (Figure 2) was developed, as the name implies, to detect mines attached to hulls of ships. It allows a diver or the operator of a remotely operated vehicle (ROV) to identify mines at distances up to 5 m and to detect mines up to 10 m from the sonar. The sonar display⁶ mounts on the diver's mask and, with the help of optical lenses, a virtual image



Fig. 2. A diver views images from the LIMIS diver-held sonar through a mask-mounted color video display.

appears a comfortable distance in front of the diver even in zero visibility water. The high resolution and rapid update rate of LIMIS make it a viable replacement for a video system on underwater vehicles in turbid water.

LIMIS measures 17.8 cm wide, 20 cm high, and 36 cm long, including a 10-cm handle. It weighs 7.7 kg in air and is 100 g buoyant in seawater. A set of acoustic lenses (Figure 3) occupies the upper, rectangular region of the sonar, and electronics occupy the lower region. LIMIS operates at 2 MHz, forms 64 beams with beamwidths of 0.35° in the horizontal axis by 7° in the vertical

axis, and consumes 25 W. Figure 4 shows three LIMIS images. Their near-video quality is very important because divers and ROV operators want to positively identify the objects they are imaging. LIMIS provides a smooth display of dynamic scenes with updates of at

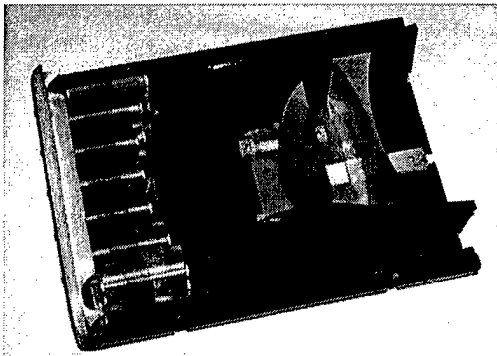


Fig.3. The lens set begins with a triplet plastic-liquid-plastic lens (left side of the photo) followed by two plastic lenses. The transducer array (not shown) fits in the rectangular opening on the right side of the housing. When the sonar is submerged, ambient water fills the spaces between the lenses and the transducer array.

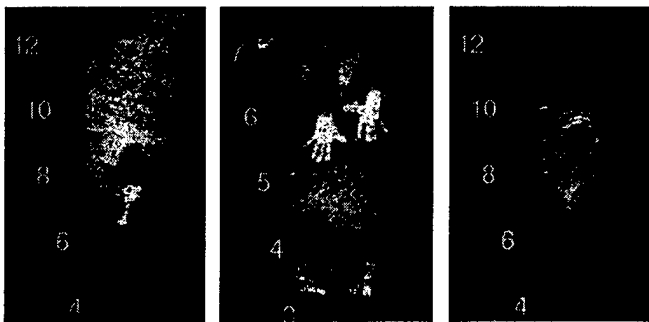


Fig. 4. Three sample images taken with LIMIS. The left image shows a limpet mine on the hull of a ship 7 feet from the sonar. The center image shows two hands. The right image shows an intake on the hull of a ship. The intake is approximately 46 cm in diameter and is 9 feet from the sonar. The left and right images were taken in Chesapeake Bay in water with 15-cm visibility.

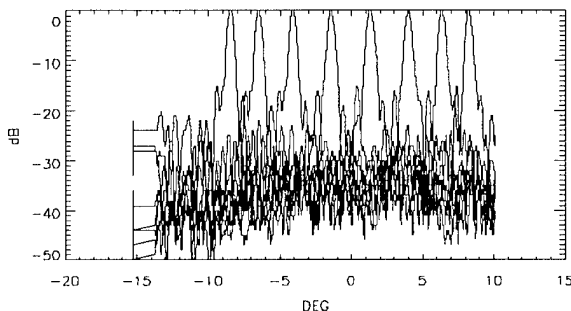


Fig.5. Eight of 64 beam patterns of LIMIS collected at APL's Acoustic Measurements Facility. Beamwidths are 0.35° and sidelobes are down between 16 dB and 18 dB.

least 11 images/second for targets 8 m or less from the sonar. Figure 5 shows one set of eight of the 64 beam patterns.

B. Glendora Lake Acoustic Imaging System (GLACIS)

The Naval Surface Warfare Center's Glendora Lake Facility (GLF) in Sullivan, Indiana, monitors and measures the motions and configurations of objects under test with GLACIS (pronounced "glasses"). GLACIS consists of a sonar mounted on an underwater platform (Figure 6) and a control and display station separated from the platform by 500 ft of cable. The operator in the control room can pan and tilt the sonar on its platform and raise and lower the platform in the 100-ft water column. The sonar operates at 750 kHz and forms 64 beams, each 0.55° horizontal by 10° vertical. GLACIS updates images with ranges out to 60 m five times per second and images with ranges out to 30 m nine times per second. The field-of-view is 32° . Figure 7 shows the horizontal beam patterns of the 32 even-numbered beams. Note that the sidelobes are down almost 30 dB. The GLACIS lens set (Figure 8) uses an epoxy lens (L1) to reduce the sidelobes. The other lenses are made from polymethylpentene. Figure 9 shows the GLACIS shore display that gives the platform and sonar parameters (such as depth, heading, pitch and roll) as well as an acoustic image. The resolution of GLACIS is demonstrated in Figure 10, which shows the image of an Air Deployed Active Receiver (ADAR) sonobuoy. The image indicates that the five arms have deployed and the bright spots on the arms indicate the locations and separations of the articulated joints.

C. Acoustic, Barnacle Imaging Sonar (ABIS II)

At the time of this writing, ABIS II is beginning in-water tests. ABIS II will image fouling, damage, and foreign objects on hulls of ships. The sonar will mount on an ROV and will be used to determine what sections of the hull need to be cleaned, initially with an operator in the loop and ultimately only with pattern classification methods. The system will work in zero visibility water. The sonar operates at 3 MHz and has 128 beams, each measuring 0.25° horizontal by 10° vertical. The sonar has a 32° field-of-view and updates at the rate of 6 images/second. Figure 11 shows the soundhead and electronics module. The division into two modules gives more flexibility in placement on a submersible. Figure 12 shows the ray diagram of the lens set for beams spaced between 0° and 16° off-axis. The predecessor⁷ of ABIS II has four mechanically scanning elements and updates images at the rate of 2 images/second. ABIS II has no moving parts and three times the update rate. The quicker updates will improve feedback needed for navigation and pattern recognition.



Fig. 6. Glendora Lake Acoustic Imaging System. The sonar mounts on a platform that is 27-kg positive. It moves up and down the water column by reeling out and in three weights resting on the lake bottom.

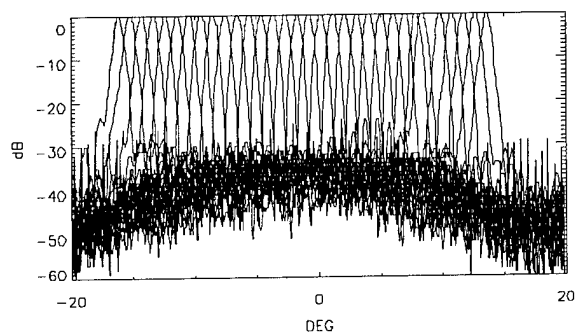


Fig. 7. Beam patterns of 32 even-numbered beams from the 64-beam GLACIS sonar. The beamwidths are 0.55° and the sidelobes are down 30 dB.

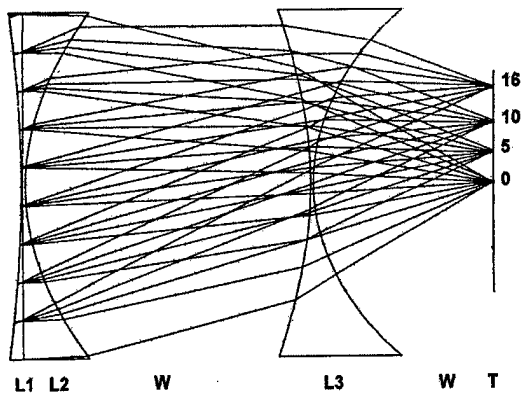


Fig. 8. A diagram of the GLACIS lens system. L1 is an epoxy lens used primarily for reducing the sidelobes. L2 and L3 are lenses made from polymethylpentene. Four wavefronts, arriving 0° , 5° , 10° , and 16° off-axis are traced to the transducer array, T, where they focus in four unique locations. Water, W, fills the spaces between the lenses and the transducer.

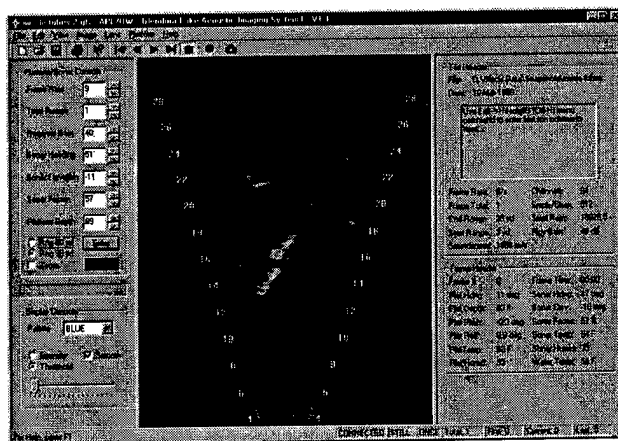


Fig. 9. The shore display for GLACIS allows the operator to control the platform and sonar, read their status, and observe and store sonar images. In this case, the image is of two missile tubes on the bottom of the lake.

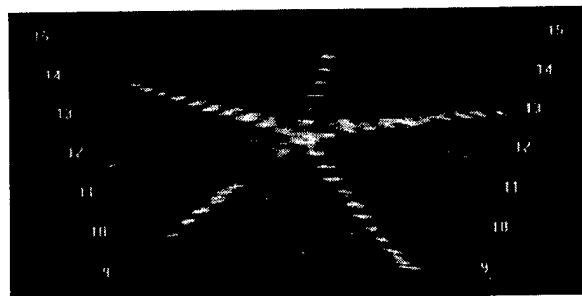


Fig. 10. GLACIS image of an ADAR sonobuoy showing five arms that hold an array of transducers. The bright returns reflect off joints in the articulated arms and allow detailed analysis of proper extension.

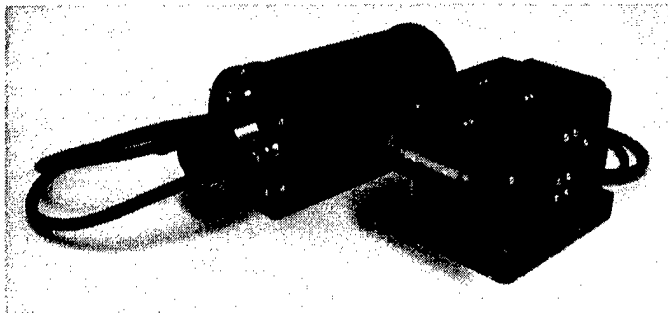


Fig. 11. The ABIS soundhead and electronics module form a forward-looking sonar that mounts on an ROV. The ROV will inspect hulls for fouling and clean selected sections. The images will update 6 times/second and provide 1-cm resolution at 3-m range.

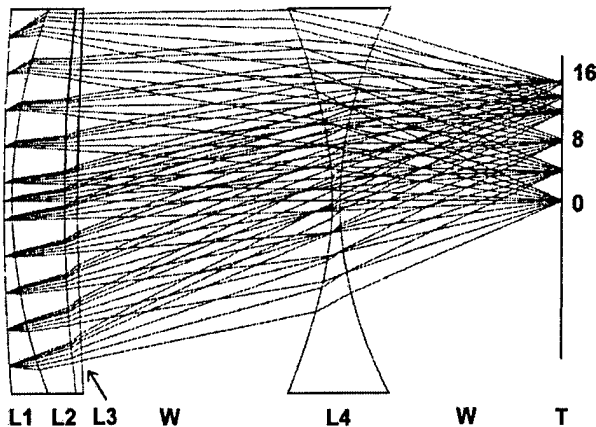


Fig. 12. A diagram of the ABIS lens system. L1, L2, and L3 form a lens triplet. L1, L3, and L4 are made from polymethylpentene. L2 is a fluid, FS-5. Six wavefronts 0° to 16° off-axis are traced to the transducer array, T, and focus at unique locations. Water, W, fills the spaces between the lenses and the transducer array. ABIS forms 128 beams over a 32° field-of-view.

IV. CONCLUSIONS

Acoustic lenses make very good beamformers. They require no power and can transmit or receive many beams simultaneously. They simplify the electronics because they eliminate the high-speed sampling and signal processing required in digital beamformers. The lenses described here have all been machined. If lens sonars

were mass-produced, lenses could be injection molded for additional savings in fabrication costs.

ACKNOWLEDGMENTS

Don Folds, Ultra-Acoustics, Inc. (Woodstock, GA), provided the prescriptions for the acoustic lens designs. John Siegel, American Medical Design (Paso Robles, CA), fabricated the transducer arrays. Dennis Gallagher, Coastal Systems Station, Diving and Life Support Division (Panama City, FL), provided the mask-mounted display for LIMIS. Bill Hanot, Applied Physics Laboratory, University of Washington (APL-UW), developed the electronics and software for all three systems. Joe Burch, APL-UW, created the mechanical designs and assembled the systems. The Office of Special Technology (Fort Washington, MD) and the Naval Explosive Ordnance Disposal Technology Division (Indian Head, MD) sponsored the sonar development that led to these applications. Dr. H. Guard, Code 331, Office of Naval Research sponsored the ABIS I & II ROV imaging systems.

REFERENCES

1. BEAM3 Optical Ray Tracer, Stellar Software, P.O. Box 10183, Berkeley, California 94709.
2. ZEMAX Optical Design Program, Focus Software, Incorporated, P.O. Box 18228, Tucson, Arizona 85731.
3. D. Folds, "Acoustic Lens Performance Analysis," Technical Report, ARINC Research Corporation, Panama City Beach, Florida, December 1993.
4. K. Fink, "Computer simulation of pressure fields generated by acoustic lens beamformers," M.S. Thesis, University of Washington, 1994.
5. E.O. Belcher, "Limpet mine imaging sonar," Proceedings of SPIE, Vol. 3711, 13th Annual International Symposium on AeroSense, Orlando FL, April 1999. In Press.
6. D.G. Gallagher, "Development of miniature virtual image displays for Navy divers using state-of-the-industry microdisplay technologies," Proceedings of SPIE, Vol. 3711, 13th Annual International Symposium on AeroSense, Orlando FL, April 1999. In Press.
7. E.O. Belcher and D.C. Lynn, "An application of tapered, PZT composite lenses in an acoustic imaging sonar with 1-cm resolution," Proceedings of Oceans '97 MTS/IEEE, October 1997, Halifax, Nova Scotia, pp. 1043-1047.

**How to Succeed at Hydrographic Surveying
and related services for multiple sheets
in the Upper Cook Inlet, Alaska:
Planning, Testing, Training and Attention to Detail**

**Robert Richards, Doug Lockhart, William Gilmour,
Carol MacKenzie, Edward Saade**

Racal Pelagos, CA

Abstract:

RPI conducted Hydrographic Surveying and related services for multiple sheets in the Upper Cook Inlet, Alaska, Spring/Summer of 1999. This Task included the mobilization and testing of the multibeam system and all peripheral devices in the San Diego, CA area and eventually in Seattle, WA, prior to departure for operations in the Upper Cook Inlet. The mobilization included transformation of the fishing vessel Quicksilver into a survey launch, and the rigging of the mother ship, R/V Davidson. The Quicksilver was converted from its fishing configuration to a state-of-the-art high speed multibeam data acquisition platform. The multibeam system consisted of a RESON-8101, integrated with a TSS HDMS via an RPI WinFrog multibeam software system. All phases of development and testing including accuracy verifications and procedures were continuously documented and recorded. Extensive training was conducted at RPI prior to the mobilization period beginning. The mothership was outfitted with multiple UNIX based processors integrated with a UNIX server operating CARIS Hydrographic processing and cleaning software with another team of highly trained personnel. The processing procedures were also extensively developed and documented. The vessels transited to Alaska and operations were commenced in a timely manner once the ice had moved out of the Upper Cook Inlet. In addition, RPI subcontractors LCMF and Terra Surveys have conducted tide monitoring and RTK data collection, respectively.

EXPLORING 3-DIMENSIONAL OCEANOGRAPHIC DATA SETS ON THE WEB USING VIRTUAL REALITY MODELING LANGUAGE

C. W. Moore¹, D. C. McClurg¹, N. N. Soreide², A. J. Hermann²,
C. M. Lascara³, and G. H. Wheless³

¹Joint Institute for the Study of Ocean and Atmosphere,
University of Washington, Seattle, WA

²NOAA/Pacific Marine Environmental Laboratory, Seattle, WA

³Center for Coastal Physical Oceanography, Old Dominion University, Norfolk, VA

I. ABSTRACT

Newly emerging Virtual Reality technologies are giving scientists new ways to analyze data that bend the imagination. In fact, the power of Virtual Reality is the ability to immerse in and interact with data. This new experience gives the scientist a chance to gain intuition and insight into complex physical processes. Virtual Reality Modeling Language (VRML) is a file format which allows users to access, navigate, explore, and interact with environmental data in 3-D on the Web, and to share this multidimensional experience with colleagues in remote locations. VRML is platform independent, available to PC users as well as those working on high-end workstations, and viewers or plug-ins are freely available for popular Web browsers, such as Netscape or Internet Explorer.

We will present web-based interfaces that support interactive, 3-D visualizations of oceanographic data drawing on such diverse oceanographic studies as hydrothermal vents, ocean circulation, air-sea interactions, and El Niño studies. The techniques available for scientific data visualization using VRML will be enumerated, and resources for those interested will be given. Demonstrations include real-time El Niño/La Niña data from the TAO (Fig. 1, [1]) network of El Niño monitoring buoys in the tropical Pacific Ocean, Fisheries Oceanography model output animations, hydrothermal plumes from sea floor volcanic eruptions, and global gridded data sets.

II. METHODOLOGY

A. Virtual Reality Modeling Language

Virtual Reality Modeling Language (VRML) is a scene description language which describes three-dimensional environments and allows users to access, navigate, explore and interact with environmental data in three dimensions on the Web. VRML is scaleable across platforms ranging from PCs to high-end workstations, and viewers or plug-ins are freely available for (and now included with) popular Web browsers. A VRML world typically consists of polygonal surfaces that mimic the real

environment. In oceanographic terms this includes contoured "slices," vector fields, bathymetry or topography, and textured surfaces. These objects can be touched, rotated, or animated using controls that the browser provides. This relatively new technology has been developed only over the last few years, and an international open standard has been accepted as of December 1997 [2].

VRML objects can be primitive (cubes, spheres, etc.), or user-defined (elevation grids, polygonal surfaces, lines), and can be given traits such as color, texture, sound, and video. Animations can be created by swapping surfaces of arbitrary shape using cached memory or morphing a surface by changing its defining coordinates over time. VRML can interact with Java to create a myriad of 3-D and 2-D user interfaces. A typical geophysical application might create a gridded surface of bathymetry, and animate surfaces of water properties or tracers. One of the authors (Wheless) has created such a world with much success¹. It allows a user to "fly" through the Chesapeake Bay, viewing any of a selection of standard hydrographic variables as sections that the user may turn on, raise to inspect, or turn off. A comprehensive view of bay properties is quickly attained in this way. The Chesapeake Bay application was created using an IDL² toolkit that the Virtual Reality/Visualization group at Old Dominion University developed utilizing on-the-fly scene generation³. A similar toolkit has been created for Matlab by Dr. Craig Sayers at WHOI to enable simple 3-D plotting and animation⁴.

While many software packages export VRML including ARC/INFO, Iris Explorer, Matlab, and Cosmo Worlds, no single package seems to produce animated, file-size limited VRML code from arbitrary scientific data formats.

¹ODU Java/VRML, <http://www.ccpo.odu.edu/~ties/Atlas/VRML/Bay/atlas.html>

²Interactive Data language (IDL), <http://www.rsinc.com>

³ODU's Virtual Environments Laboratory, <http://www.ccpo.odu.edu/~vel>

⁴VRMLplot, <http://www.dsl.whoi.edu/DSU/sayers/VRMLplot>

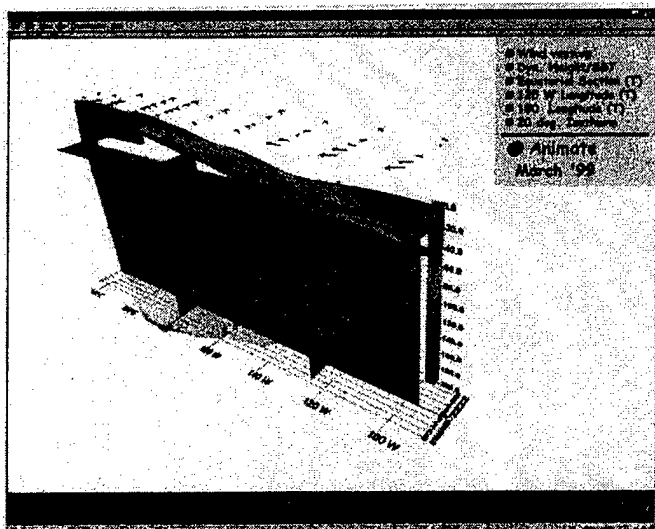


Fig. 1. Screen snapshot of VRML Tropical Atmosphere Ocean (TAO) demonstration showing temperature sections, dynamic height, sea surface temperature, winds, and 200 isotherm. The user can navigate through the world using the VRML controls at the bottom, and choose surfaces to animate from the control panel (upper right).

One software package worth mentioning is known as the Visualization Toolkit or VTK⁵. Frequently used in the health sciences for MRI imaging analysis, this package is a library of visualization algorithms written in object-oriented C++, and comes with wrapper code for Java as well as interpreted languages like Python and Tcl/Tk. The power of VTK is in its advanced 3-D visualization graphics (based on the OpenGL standard), its well-designed pipeline architecture, and the advanced algorithms for polygonal surface decimation. Since oceanography tends to produce huge data sets, and the web tends to balk at transferring large files, many of the surfaces in the demonstrations to follow were decimated using VTK to take advantage of these and other visualization algorithms.

B. VRML Representations of Oceanographic Data

We have developed a prototype, three-dimensional VRML visualization and animation of data from nearrealtime NOAA's Tropical Atmosphere Ocean (TAO) buoy network in the tropical Pacific (Fig. 1). With the recent strong El Niño and the strong La Niña now developing, we believe that many Web users will welcome the opportunity to interact with a three-dimensional representation of data from one component of NOAA's El Niño Southern Oscillation (ENSO) observing system. The VRML world consists of five polygonal surfaces for each month: three depth sections of temperature (at the equator, the dateline, and 125°W), the 20° isotherm, and dynamic height, as well as a grid of wind vectors at the surface. The user can use the panel (upper, right) to turn surfaces on or off, and to animate the monthly surfaces through the last 18 months of data. The controls located in a dashboard at the bottom allow the user to rotate and zoom in on the object of interest.

⁵Visualization Toolkit (VTK), <http://www.kitware.com>

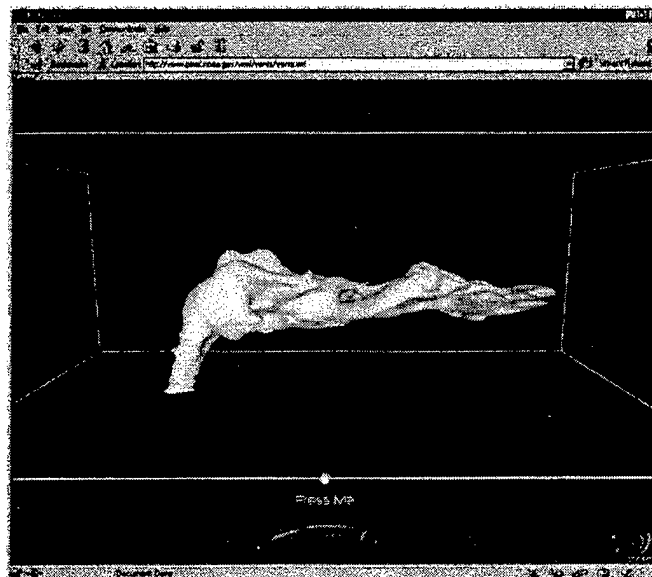


Fig. 2. Screen snapshot of NOAA's Vents program model output of a hydrothermal plume. Red plume is a Gouraud-shaded polygonal surface of the 150° isotherm.

A "work-in-progress" VRML world depicting a hydrothermal vent plume uses animated model output from NOAA's Vents Program (Fig. 2). Polygonal surfaces representing isotherms are rendered in succession to show the development of a plume. This highly amorphous shape is rendered taking advantage of a technique known as Gouraud shading in order to eliminate the faceted look of the polygonal surface. VRML output was obtained using the VTK visualization software.

An animated representation of fisheries-ocean data from NOAA's Fisheries Oceanography Coordinated Investigations (FOCI) program shows model bathymetry and fish larvae drift paths for the Shelikof Strait pollock spawning grounds (Fig. 3). Work is in progress to use the VRML output to tune model parameters as the model runs (a method known as "parallel rendering"). Al Hermann and Chris Moore have written Ferret and Matlab scripts to generate VRML from model output, as well as Java code to generate VRML from netCDF files. These scripts, and all VRML worlds are accessible through NOAA's VRML web page⁶.

⁶NOAA's VRML web page, <http://www.pmel.noaa.gov/vrml>

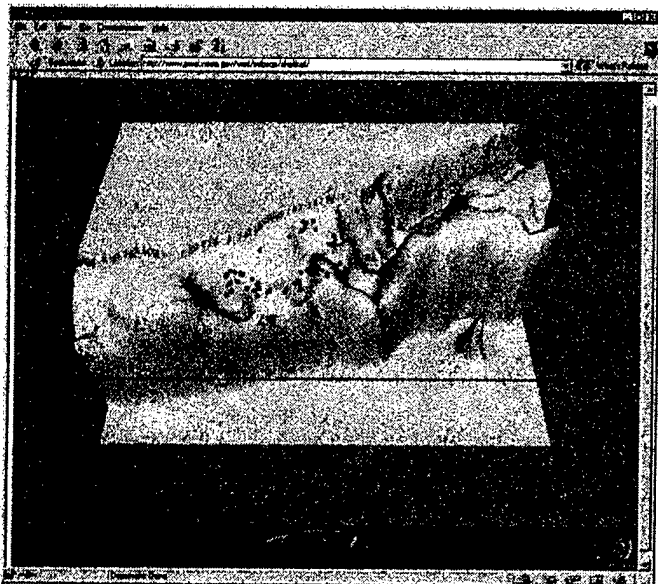


Fig. 3. Screen snapshot of Southeast Bering Sea Carrying Capacity (SEBSCC) VRML demonstration showing Shelikof Strait bathymetry, fish-larvae advection animation, and Netscape/Cosmo Player VRML browser controls.

III. FUTURE DIRECTIONS

Virtual Reality is useful for the layperson and the scientist. Immersive technology has shown how powerful a tool Virtual Reality can be: by viewing multidimensional fields in context, and by the ease of changing viewpoints and variables viewed, a 3-D representation of data can give the scientist a heightened sense of presence, and greatly improve the ability to gain insight into complex dynamics.

Web-based virtual reality (VRML) can do this and more. The 3-D experience can be shared. The VRML specification [2] allows for the sharing of worlds with other people, including interactions between multiple users across the network. People sharing a virtual world can see, talk, and interact with one another in the form of "avatars" - human representations in the virtual world. The Sony Corporation, Blaxxun and Oz Interactive have teamed up to build a standard that allows for multi-user VRML interaction. The implications for this are quite impressive. Two (or more)

scientists at institutions that span the globe can view a data set in 3-D. The standards body Web3D has instantiated a working group called Core Living Worlds to standardize the interaction of users in a virtual "world." With the increase in data transmission speed from the recent installation of the Next Generation Internet (NGI), we hope to prove the concept of shared worlds, for observed data and model outputs from projects such as the TAO network of El Niño monitoring buoys in the Pacific Ocean and the Southeast Bering Sea Carrying Capacity (SEBSCC) fisheries-oceanography program.

We also plan to develop toolkits in parallel with the IDL toolkit to allow the scientist to simply create VRML objects and worlds using current standard data formats (netCDF, EPIC, etc.). Since VRML is scalable across platforms, a natural choice for toolkit development is Java, as it is also platform independent, and events can be passed back and forth between Java and VRML, allowing for dynamic interaction, and on-the-fly VRML creation.

IV. CONCLUSION

We present here the results of our efforts to make environmental data, specifically oceanographic data, available as interactive 3-D worlds via the web using the modern, standards-based Virtual Reality Modeling Language. Our first efforts involve interactive, 3-D visualizations and animations of the present El Niño and La Niña as monitored with the TAO network of buoys in the tropical Pacific Ocean. Results are available on the web at

<http://www.pmel.noaa.gov/vrmi/>.

V. REFERENCES

- [1] Soreide, N.N., D.C. McClurg, W.H. Zhu, D.W. Denbo, and M.J. McPhaden (1998): Web access to real time data from the TAO buoy network in the Tropical Pacific Ocean. Ocean Community Conference '98, Marine Technology Society, 16-19 November 1998, Baltimore, MD.
- [2] Virtual Reality Markup Language (VRML) standard: VRML97, ISO/IEC 14772.

ACOUSTIC COMMUNICATION CHANNEL MODELING FOR THE BALTIC SEA

Paul A. Baxley, Homer Bucker, and Joseph A. Rice
Space and Naval Warfare Systems Center, San Diego
Acoustic Branch, Code D881
San Diego, California 92152-5001

Maurice D. Green
Datasonics, Inc.
P.O. Box 8
Cataumet, Massachusetts 02534

Jonas Woxstroem
Defense Material Administration
Underwater Weapons Directorate
Underwater Surveillance Division
SE-115 88 Stockholm, Sweden

Abstract

A physics-based numerical propagation model which includes the effects of multipath spread and Doppler spread is currently being developed as a prediction and analysis tool for underwater acoustic communication problems. The model uses three-dimensional Gaussian beams and quadrature detection to obtain the channel response for finite-duration constant-wavelength tones. By using a very short pulse, the output of the quadrature detector represents an estimate of the band-limited channel impulse response, which may be used to determine the multipath spread. In addition, the Doppler shifts associated with source/receiver motion can be accumulated from the individual beams, providing Doppler spread. The usefulness of the model for experiment planning is demonstrated for a shallow-water Baltic Sea test site. The fidelity of the model is tested via a comparison of simulated channel responses with those measured in the Baltic Sea test.

I. Introduction

Acoustic communication signals propagating through a shallow-water environment may be adversely affected by the phenomena of multipath spread and Doppler spread. The multipath spread is caused by the complex multipath propagation

characteristic of shallow-water waveguides, including such effects as refraction, multiple reflections from boundaries, and scattering from inhomogeneities. The Doppler spread results from the time-variability of the acoustic medium, arising primarily from source/receiver motion or surface boundary motion. These phenomena can significantly disperse and distort the signal as it propagates through the channel [1].

A physics-based numerical propagation model that attempts to account for these effects is currently being developed as a prediction and analysis tool for underwater acoustic communication problems [2]. Currently, the model includes multipath spread associated with propagation through a refractive medium and the reflection and scattering of energy from arbitrarily-rough boundaries and a depth-varying seafloor. Doppler spread resulting from source-receiver motion is only included at present, although future implementations will include the effects of a time-varying sea surface.

In this paper, the application of the model to experimental scenarios and its use as a prediction and analysis tool is demonstrated. In particular, a shallow-water region in the Baltic Sea is analyzed. Experimental data from both a stationary and moving source recorded in this region facilitates a

comparison between simulated and measured impulse responses. A brief discussion of the modeling approach is presented in Section II. Section III describes the shallow-water Baltic Sea environment analyzed. Simulated impulse responses, providing a measure of the multipath spread, for this environment are next presented in Section IV. In Section V, measured impulse responses are presented and compared to the model predictions. Section VI summarizes the results and discusses future plans and implementations.

II. 3-D Gaussian Beam/Quadrature Detector (GBQD) Modeling Approach

Computationally intensive broadband simulations of time series (via Fourier synthesis) are often not necessary for determining how a pulse propagates through a medium. This is because the complex Fourier coefficients of a pulse at a receiver can be computed via a knowledge of the propagation characteristics of the signal (level, travel time, phase shifts, and Doppler shifts) and the use of a quadrature detector (QD). The QD is an analog version of the discrete Fourier transform, and provides a convenient means of obtaining the complex Fourier coefficients as a function of time for a given pulse. This is especially true for a finite-duration constant-wavelength (CW) pulse, since the QD response is simply a triangle-modulated version of a CW signal. Since finite-duration CW pulses are common signals in communication schemes, the modeling of such signals is appropriate, although other pulse types can also be implemented.

Assume that a continuous sinusoidal signal $A \cos(\omega t + \phi)$ arrives at a receiver, where ω is the frequency, t is the time, and ϕ is a phase shift associated with boundary interactions. If the signal is processed by a quadrature detector, as diagrammed in Fig. 1, the signal is split with one part being multiplied by $2 \cos(\omega_0 t)$ and the other part being multiplied by $-2 \sin(\omega_0 t)$. ω_0 is the reference frequency, which should be approximately equal to ω . Both parts are then passed through a low-pass filter to obtain the quadrature components $A \cos[(\omega - \omega_0)t + \phi]$ and $A \sin[(\omega - \omega_0)t + \phi]$, respectively. The complex output R_{QD} of the QD is then simply

$$R_{QD} = A \exp[i(\omega - \omega_0)t + \phi]. \quad (1)$$

This is basically an analog form of the discrete Fourier transform. If $\omega_0 \neq \omega$, R_{QD} will experience a rotation of $\omega - \omega_0$ radians per second.

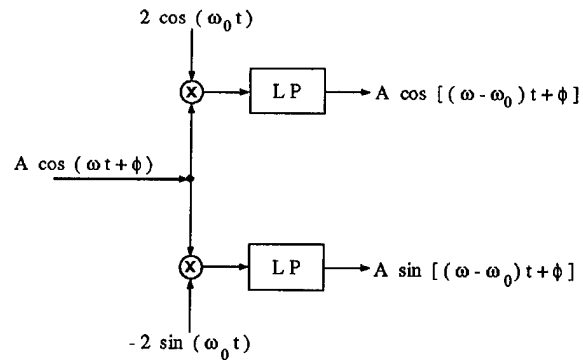


Fig. 1. Quadrature detector algorithm for a continuous sinusoidal signal.

Now assume that the incoming signal is a finite sinusoidal pulse of duration τ seconds and frequency ω . Assume also that the travel time from the source to the receiver along path p is t_p and that the time constant t_c (effective integration time) of the low-pass filters in the QD is τ seconds. For this case, R_{QD} is modulated by a triangle function $T(t)$ that is zero for $t < t_p$, increases linearly from zero to a value of unity at $t = t_p + \tau$, and then decreases linearly back to zero at $t = t_p + 2\tau$. Therefore, the quadrature response for a beam travelling along path p is

$$R_{QD} = AT(t) \exp[i(\omega - \omega_0)t + \phi]. \quad (2)$$

If the time constant t_c is larger than the pulse duration τ , R_{QD} remains at the value of the apex until $t > t_p + t_c$. In either case, R_{QD} still experiences the rotation $\omega - \omega_0$ if $\omega_0 \neq \omega$. The only way that ω_0 cannot equal ω in the above scenario is for a Doppler shift to have occurred somewhere along the path p . Therefore, source/receiver motion or sea-surface motion results in a rotation of R_{QD} for a path influenced by that motion.

The 3-D Gaussian Beam/Quadrature Detector (GBQD) modeling approach is to trace, in three-dimensions, closely-spaced microbeams of a finite-duration CW pulse from source to receiver, accumulating travel-time, level, phase-shift, and Doppler-shift information for each microbeam. This information is used to construct the QD response for each microbeam. The total QD response is then obtained by summing the QD responses of all component microbeams. By using a very short pulse, the output of the quadrature detector represents an estimate of the channel impulse response, which may be used to determine the multipath spread. Three-

dimensional Gaussian beam tracing is used so that out-of-plane reflections from rough surfaces or sloping bathymetry can be adequately modeled. The use of a dense fan of Gaussian microbeams allows direct modeling of scattering from arbitrarily rough surfaces.

For a more detailed description of the 3-D Gaussian beam propagation model, the reader is referred to Appendix A and Ref. [3].

III. Baltic Sea Environment

Datasonics, Inc. and the Defense Material Administration of Sweden conducted a series of demonstrations/experiments in a shallow-water region in the Baltic Sea in March 1999. The area possesses variable bathymetry with water depths ranging from 50 to 100 m. The present analysis only considers test events in which a receiving ship was moored in 55-m water, while a source ship transited along a constant course with a closest-point-of-approach (CPA) of 400 m. A receiving hydrophone was deployed over the side of the receiving ship at a depth of 30 m. A source hydrophone was attached to a towbody deployed by the source ship. The source depth was nominally 30 m, however, the actual value varies with the speed of the source ship. The nominal source level was approximately 180dB/ μ Pa (reference to transmission of a single CW tonal). Transmission types included frequency-hopped, M-ary frequency-shift-keying (FH/MFSK) signals, direct sequence, differential M-ary phase shift keying (DS/DMPSK) signals, MPSK, and LFM and CW channel probe signals.

The source ship positioned itself at an initial range of 1000 m and set a course to achieve CPA at a range of 400 m and a speed of 8 kts. Figure 2 shows the water depth along a portion of the source track, along with the position of transmission events. The origin is placed at the approximate CPA point. The water depth at the receiver is also indicated, but it should be remembered that the receiver position is not in the same plane as the depth profile shown, since the track passed through CPA. Note that the water depth at the receiver is close to the depth of the plateau to the right of CPA, suggesting that the shallower water at the receiver may be associated with this feature. While not shown in Fig.2, the water depth remains constant at about 55 m for another 6 min past the end of the plot, after which it drops to a constant level of 90 m. Transmission events occurred approximately every 3 minutes. Events 084-088 occur to the right of the times shown in Fig. 2. Source range and speed

and the water depth at the source and receiver for each event are summarized in Table 1.

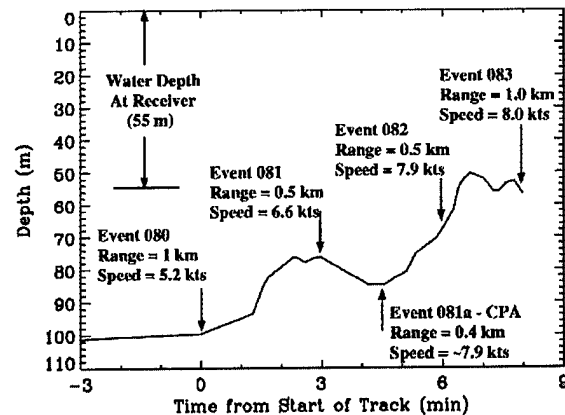


Fig. 2. Water-depth profile along source-tow track and location of events.

Table 1. Source-Tow Event Summary

Event	Range (km)	Speed (kts)	Water Depth at Source (m)	Water Depth at Rec. (m)
080	1.0	5.2	99.7	55.0
081	0.5	6.6	77.3	55.0
081a	0.4	7.9	84.8	55.0
082	0.5	7.9	69.9	55.0
083	1.0	8.0	56.7	55.0
084	1.5	7.9	53.6	55.0
085	2.0	7.9	68.2	55.0
086	2.5	7.9	91.1	55.0
087	3.0	8.1	90.9	55.0
088	3.5	5.0	63.0	55.0

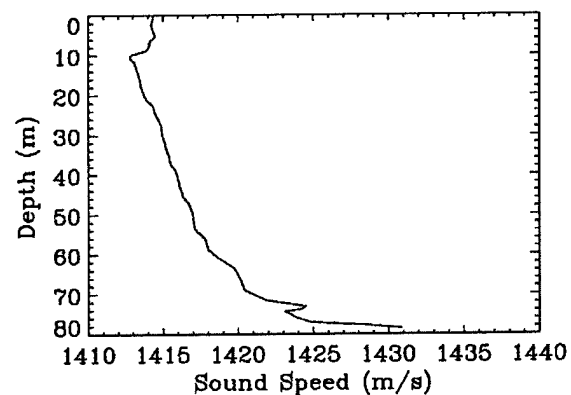


Fig. 3. Representative Baltic Sea sound speed profile measured during source-tow.

CTD (Conductivity, Temperature, and Depth) measurements were made at both ships during the events. The resulting sound speed profiles were observed to be stable over space and time. Figure 3 presents a sound speed profile representative of the conditions during the source-tow. The channel is seen to be upward refracting. This fact, combined with the low attenuation in the Baltic, accounts for the relatively long-range propagation observed during the experiment.

Geoacoustic bottom properties were not measured during the experiment and suitable archived data has not yet been identified. A sediment sample taken in the region suggests that the sediment is largely composed of silt. Therefore, values indicative of silt provided by Jensen et. al.[4] are assumed for the bottom; namely, a density of 1.7 g/cm^3 , a compressional sound speed of 1575 m/s , and a compressional wave attenuation of $1.0 \text{ dB}/\lambda$. The actual geoacoustic parameters may be quite different, and further analysis will be required for a more accurate determination of these properties.

IV. 3-D GBQD Simulation Results

Simulated impulse responses obtained via the 3-D GBQD approach are presented for several of the events during the source-tow in Fig. 4, which plots the magnitude of the output of the quadrature detector. These results were obtained with a very short (0.2 ms) 12-kHz CW pulse so that the output of the quadrature detector approximates a band-limited impulse response. Since the bathymetry in the direction perpendicular to the depth profile in Fig. 2 is not known at present, a linear interpolation between the water depth at the source and the water depth at the receiver was used. While this restriction precludes exact comparison between modeled and measured results, it still allows for qualitative comparisons of gross features. In all simulations, the source and receiver depths were assumed to be 30 m . The time constant (averaging time) was set equal to the pulse length to produce the triangle modulation discussed in Section II. Figure 4a presents results for Event 080, Fig. 4b for Event 081a (CPA), Fig. 4c for Event 083, Fig. 4c for Event 085, and Fig. 4d for Event 087.

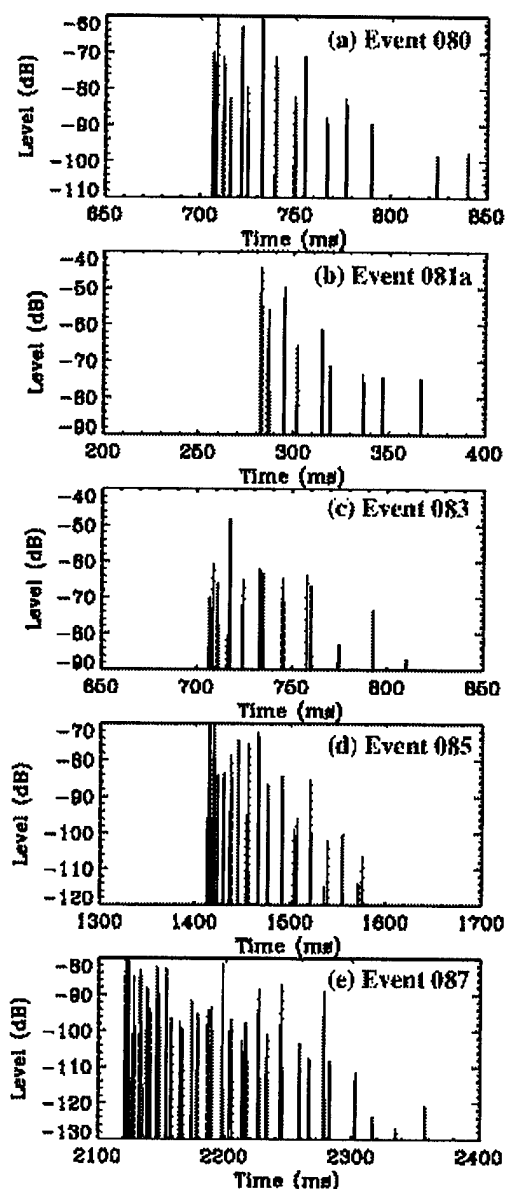


Fig. 4. Magnitude of simulated quadrature detector output, representing an estimate of the channel impulse response, for several events during source-tow. Finite-duration 12-kHz CW pulse. Pulse length = time constant (averaging time) = 0.2 ms . Source depth = receiver depth = 30 m . (a) Event 080; (b) Event 081a (CPA); (c) Event 083; (d) Event 085; (e) Event 087.

The impulse responses in Fig. 4 provide a description of the multipath arrival structure, and hence also of the multipath spread. Each peak can be shown to correspond to a particular eigenpath connecting the source and the receiver. As source range increases, the multipath spread increases, since

more eigenpaths become possible as source range increases. However, the levels for the longer ranges are much lower and would likely be masked by noise in real scenarios. Information like that contained in Fig. 4 has been successfully used to help design experimental configurations for sea tests in both the Baltic and shallow-water regions in the Pacific near San Diego, California.

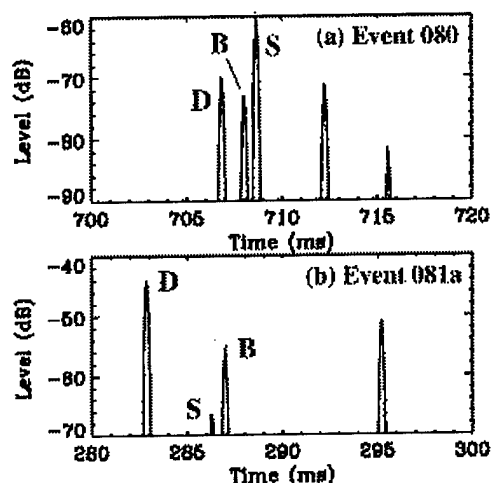


Fig. 5. Close-up view of impulse responses for (a) Event 080 and (b) Event 081a (CPA). Finite-duration 12-kHz CW pulse. Pulse length = time constant (averaging time) = 0.2 ms. Source depth = receiver depth = 30 m.

A close-up look at Events 080 and 081a, focusing on the first group of arrivals, is presented in Figs. 5a and 5b, respectively. The various multipaths can be identified with the help of the eigenray diagrams in Fig. 6, for Event 080, and Fig. 7, for Event 081a. For Event 080, the direct path is followed by a slightly lower-level bottom-reflected path, and then a stronger surface-reflected path. The later paths are those for the higher-order reflected paths. The high level for the surface reflected path may be the result of energy being focussed by refraction. For Event 081a, the sequence is the direct path followed by a weak surface-reflected path, a stronger bottom-reflected path, and then the higher-order reflected paths. The relative levels of the peaks will likely vary in real data because of fluctuations in the water column.

It is often useful to plot predicted impulse response as a function of source range so that the expected variation in the multipath spread caused by changes in source position can be observed. Fig. 8 illustrates this type of diagram for a source range increasing from 200 m to 400 m at a source depth of

30 m and a constant water depth of 55 m. This scenario approximates that in which the source is moving over the plateau at the later times in Fig. 2. For this case the pulse length and time constant were set equal to 2 ms.

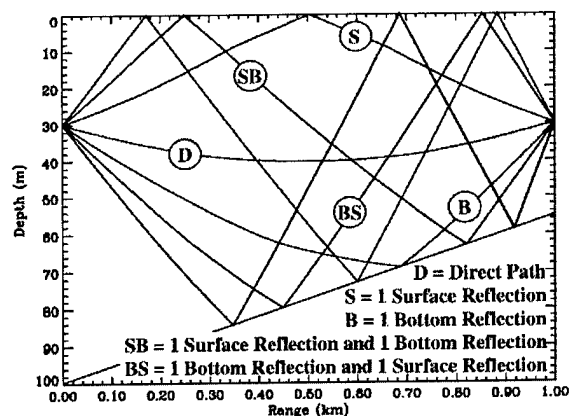


Fig. 6. Eigenray diagram for Event 080.

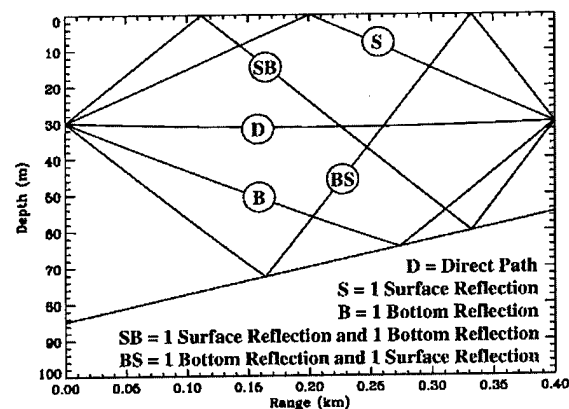


Fig. 7. Eigenray diagram for Event 081a (CPA).

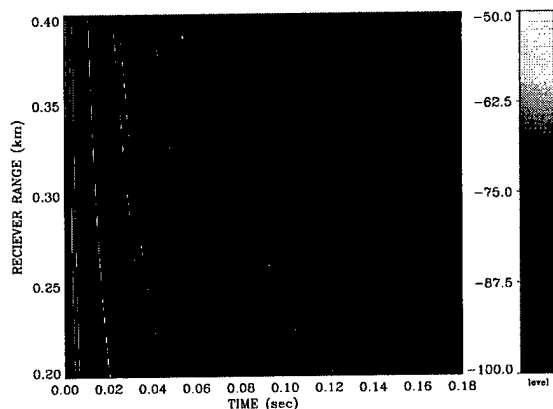


Fig. 8. Simulated impulse response versus source range. Finite-duration 12-kHz CW pulse. Pulse length = time constant = 2.0 ms. Source depth = receiver depth = 30 m.

V. Experimental Results

Experimental estimates of the impulse response were obtained by correlating received LFM pulses with the transmitted LFM pulse. Figures 9-11 present the results for three transmissions under conditions similar to Event 080, when the source range was 1.0 km. These data, however, were recorded at the initial position of the source ship before it began the track. Note the significant variation in the arrival structure over time at a stationary position. The multipath spread is seen to be on the order of 1.5 to 2 ms. Considering only the first three arrivals in the predicted impulse response of Fig. 5a, the predicted multipath spread is about 2.5 ms, and the three-path arrival structure is similar to that in Fig. 9. The lack of later arrivals in the data suggests that the model is assuming a bottom that is too reflective. A fine-tuning of the model parameters is required to eliminate these features.

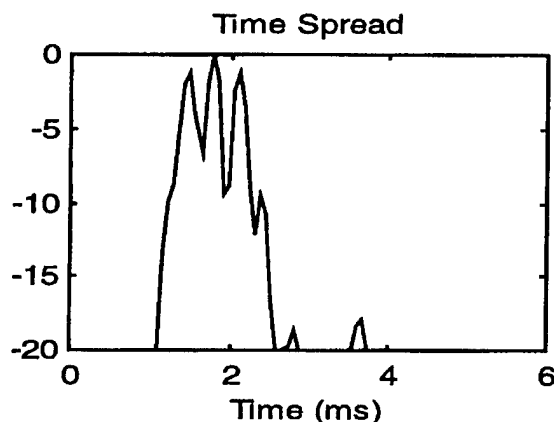


Fig. 9. Data impulse response No. 1 measured at position of Event 080. Source range = 1.0 km. Vertical axis is level in decibels.

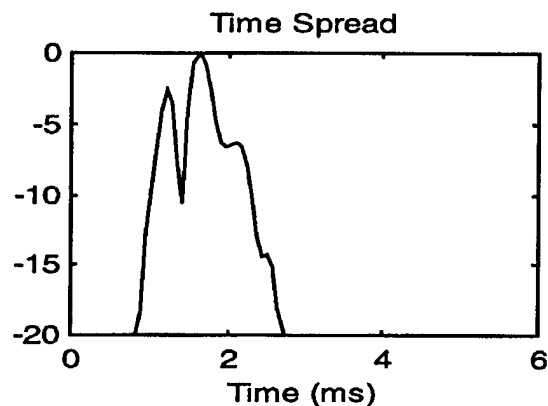


Fig. 10. Data impulse response No. 2 measured at position of Event 080. Source range = 1.0 km. Vertical axis is level in decibels.

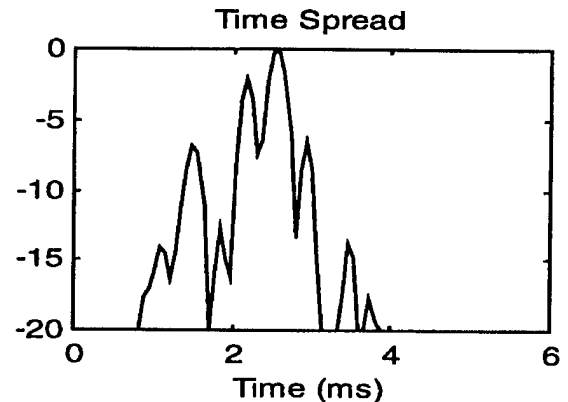


Fig. 11. Data impulse response No. 3 measured at position of Event 080. Source range = 1.0 km. Vertical axis is level in decibels.

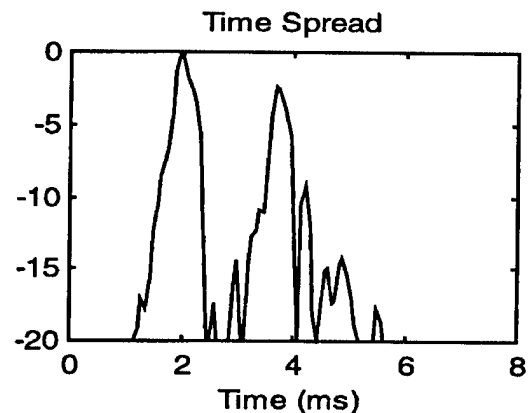


Fig. 12. Data impulse response measured at position of Event 081a (CPA). Source range = 0.4 km.

Figure 12 presents the measured impulse response for an LFM transmission when the source was at CPA (Event 081a). Two distinct paths are observed, consistent with the prediction in Fig. 5b. However, the time separation between the two paths is larger in the predicted impulse response (4 ms compared to 1.8 ms).

While a detailed comparison between modeled and experimental results is not possible because of a lack of knowledge of important environmental information (3-D bathymetry, bottom properties, actual source depth, etc.), the comparisons presented illustrate the usefulness of a physics-based model for underwater acoustic communications problems. It is expected that a better knowledge of the environment will improve the agreement between the data and the model. Preliminary data/model comparisons for a

well-characterized shallow-water environment in the Pacific near San Diego have shown excellent agreement. It is also expected that a fine-tuning of model parameters could help characterize the unknown environment.

VI. Summary and Future Work

The 3-D Gaussian Beam/Quadrature Detector approach to channel modeling provides an efficient means for the study of important underwater acoustic communications effects such as multipath spread and Doppler. Its usefulness as a prediction and analysis tool has been demonstrated for a Baltic Sea test site. While the model predictions do not agree exactly with data, the model does predict the general character of the channel.

An analysis of data collected in a Pacific shallow-water environment near San Diego, for which the environment is well known, has shown excellent agreement to date. Since the model is currently able to predict the spectral spread caused by a moving source, a comparison of model predictions of this effect with data is planned for both the Pacific and Baltic environments.

The Baltic Sea data set, with its variable bathymetry and good propagation characteristics, provides an excellent opportunity to investigate the 3-D features of the model. The effect of bathymetric features on the channel response, via the reflection of energy out of the plane containing the source and the receiver, deserves further investigation.

Finally, modeled impulse responses are currently being supplied as input to a statistics-based real-time channel emulator being developed by Datasonics, Inc. The use of realistic physics-based impulse-response predictions results in a tool which can augment at-sea measurements for the testing and development of underwater acoustic modems and sonar systems.

Appendix A: 3-D Gaussian Beam Propagation Model

The 3-D Gaussian beam model is a modified version of that presented by Bucker [3]. For a specified sound-speed profile and seafloor, beams are traced from a source in three dimensions following the laws of ray acoustics and boundary interactions. Ray theory requires the determination of eigenrays, which can be computationally intensive, particularly in three

dimensions. Determination of eigenrays is unnecessary in the Gaussian beam formulation. The sound field at a receiver is obtained by combining the coherent contributions of each beam as determined by the closest point of approach (CPA) of the beam path to the receiver. Consider an arbitrary beam path p that travels from a source S and passes close to a receiver X , as shown schematically in Fig. 1a. The point x represents the CPA of the beam to the receiver and ρ is the CPA distance. The actual path length (arc length) from S to x is designated S_x , and is shown linearized in Fig. 1b. The pressure at the receiver X associated with this beam path is then given by

$$p = C_n B[\exp(-a\theta^2 + i\omega t)] / S_x, \quad (A.1)$$

where C_n is a normalization constant, a is an empirical constant, $\theta = \tan^{-1}(\rho / S_x)$, ω is the angular frequency, and t is the travel time to point x . A spherical wave-front correction equal to $(L - S_x)/c_x$, where $L^2 = S_x^2 + \rho^2$ and c_x is the sound speed at x , is included in the travel time t . B accounts for energy loss and phase shifts resulting from surface and bottom reflections. See [3] for fuller explanation of the constants a and C_n .

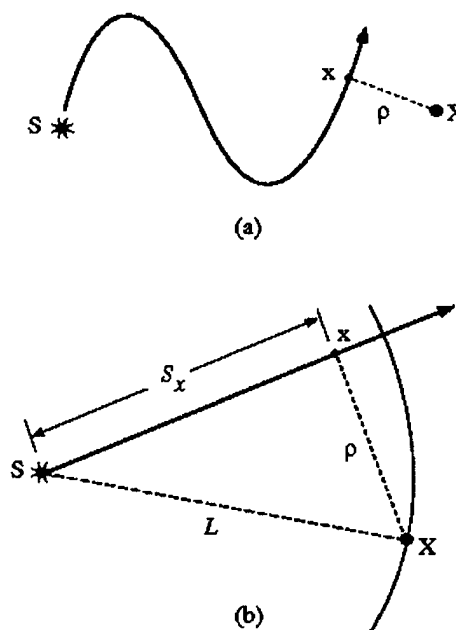


Fig. A.1. Geometry used to determine pressure contribution of a Gaussian beam at CPA to sensor X.

Acknowledgement

The Office of Naval Research via the Space and Naval Warfare Systems Center, San Diego Independent Research Program sponsored this work.

References

- [1] J. A. Rice, "Acoustic signal dispersion and distortion by shallow undersea transmission channels," *Proceedings of the NATO SACLANT Undersea Research Centre Conference on High-Frequency Acoustics in Shallow Water*, Lercici, Italy, pp. 425-442, July 1997.
- [2] P. A. Baxley, H. P. Bucker and J. A. Rice, "Shallow-water acoustic communications channel modeling using three-dimensional Gaussian beams," *Proceedings of the MTS Ocean Community Conference '98*, 16-19 Nov. 1998, Baltimore, MD, Vol.2, 1022-1026].
- [3] H. P. Bucker, "A simple 3-D Gaussian beam sound propagation model for shallow water," *J. Acoust. Soc. Am.*, vol. 95, no. 5, pp. 2437-2440, May 1994.
- [4] F. B. Jensen, W. A. Kuperman, M. B. Porter, and H. Schmidt, *Computational Ocean Acoustics*, American Institute of Physics Press, New York, p. 41, 1994

FSK and PSK Performance of the Utility Acoustic Modem

Mark Johnson, James Preisig, Lee Freitag

Woods Hole Oceanographic Institution

majohnson@whoi.edu

Milica Stojanovic

Northeastern University

Abstract

The Utility Acoustic Modem (UAM) is a high performance and compact digital signal processing system for acoustic communications, designed at Woods Hole Oceanographic Institution. The UAM is fully integrated, containing 4 hydrophone input channels, a switching power amplifier, and non-volatile memory. The device consumes 3W when receiving and up to 30W when transmitting with a source level of about 185dB re microPascal. At the heart of the UAM is a 30MFLOP (million floating point operations per second) DSP chip capable of implementing a wide range of acoustic communication signalling and receiving algorithms in real-time. To date, two communications links, have been implemented on the UAM and evaluated. The first is a low-rate incoherent system using frequency-hopped FSK signalling and strong error-correction coding to provide robust

communications in channels with rapidly-varying multipath. The second link is a high-rate coherent method using QPSK signalling and a Doppler-tolerant multi-channel adaptive equalizer. The two communications methods have been tested individually, and against each other, in a variety of shallow water channels. The proposed paper will review the design and capabilities of the UAM and describe in detail the FSK and QPSK implementations. Performance results for both schemes from at-sea experiments will then be presented. The ultimate aim of the UAM development is to produce a robust communications link able to adapt modulation type and rate to the channel conditions. Some preliminary steps towards this will be discussed in the light of the at-sea results. [Funding for this work came from ONR 322OM]

EXPERIENCE OF WORKING OUT AND MODERNIZATION OF MULTIBEAM ECHOSOUNDERS

S.Dremoutchev, V.Iourytsin, V.Kuznetsov, A.Nosov, G.Postnov
P.P.Shirshov Oceanology Institute, Moscow, Russia

The Laboratory of sound reflection and scattering during many years worked out, built and used in ocean expeditions the towed multibeam sonars. The primary aim was to develop the device for direct measurement of bottom reverberation of sound and to study its characteristics for regions with different geomorphology. This task determines the configuration and processing method of the device - installation on towed body for measuring near the bottom, using of nonequidistant array for diminishing the number of independent receiving channels, simultaneous beamforming in the vertical plane parallel to direction of towing, statistical signal processing. The beamforming in receiving antenna included Fourier-transform of signal spatial correlation function (FT) calculation; the correlation function's estimation was the result of averaging of sound pulses [1]. It was experimentally established that for definite relations between vessel's speed and ocean depth the averaging doesn't lead to sufficient diminishing of spatial resolution if spatial correlation function converges rapidly, and mentioned way of beamforming may be used for bathymetric measurements.

The experience in working out of towed multibeam sonars was used for restoration of multibeam echosounder ECHOS-XD installed at R/V "Akademik Ioffe" in 1988. The receiving and transmitting matrices, power amplifier and multichannel receiving amplifier of this echosounder were in working state, but beamformer and processing system for depth measuring were ruined. The main idea of echosounder's modernization was to incorporate the new system of beamforming and control into existing matrices and amplifiers. It was possible because the transmitter and multichannel receiving amplifier are practically autonomous with simple digital control interface; the control was fulfilled by standard personal computer through the plate of universal parallel port ADVANTECH PCL-720. The method of signal bringing into computer included synchronous detecting from 14 independent channels, simultaneous remembering of instant values of 28 quadrature components in sample-and-hold tracks with discretisation frequency 1 kHz, sequent reading by ADC. This method proved its reliability in towed sonars. For beamforming were used elements of vessel's equidistant receiving matrix with numbers 1, 8, 15, 22, 29, 36, 43, 50, 51, 52, 53, 54, 55, 56. All possible pairs of these elements provide the evaluation

of 55 equidistant samples of spatial correlation function. Its FT calculation permits to double the angular resolution comparatively with primary processing method (beamformer summed element signals with proper delays). Besides the acoustical data the echosounder registered pitch and roll angles, course direction and data from satellite navigation receiver NT200D. All necessary conditions for bathymetric measurements were fulfilled.

We registered the raw data - sine and cosine samples of acoustical signals and auxiliary information. That was done to provide the possibility to choose the best real time beamforming and representative algorithm. One of processing results is the range-angle dependence of backscattered sound intensity. It is showed that for regions with even profile of bottom (slope less than 10 degrees) good convergence of correlation function took place (number of samples 5-10, time averaging instead of ensemble averaging). The reradiated sound intensity may be reliably measured in angular interval ± 60 deg. and limited by presence of twice scattered sound pulses.

Mentioned registration procedure allowed to modify the bathymetry. We found out the depth measurement algorithm using a priori assumption that exist only two imaginary sound sources under bottom (when its slope isn't too large), their angular sizes are less than array angular resolution. Besides that, the reradiated sound's intensity may be visualised in a manner similar to one of side-scan sonar. The supplementary advantage of described beamforming method is the possibility to get the valid evaluation of scattered sound field's angular spectrum, when some array elements are disrepaired. Our experience showed that it is possible to perfect the obsolete sonar by means of modern software and technology. This work was supported by the RFBR, grant 98-05-64779.

REFERENCE

1. V.Kuznetsov et al. Use of multibeam towed sonars for acoustic investigation in the ocean//Journal of Technical Acoustics, 1994, V, 1, # 2, P.61-64

An Integrated Approach to Improving Tsunami Warning and Mitigation

F. I. Gonzalez, E. N. Bernard, H. B. Milburn, V. V. Titov,
H. O. Mofjeld, M. C. Eble, J. C. Newman, R. A. Kamphaus, C. L. Hadden
NOAA/Pacific Marine Environmental Laboratory, Seattle, WA

ABSTRACT:

NOAA has a goal to mitigate the tsunami hazard to Hawaii, California, Oregon, Washington, Alaska, and U.S. possessions in the Pacific Region. Fulfilling this goal requires research, development and implementation of tsunami forecasts (with increased accuracy and speed) and the creation of state-of-the-art inundation maps. The strategy is to focus research and development on advanced technologies for: (a) field measurements using a real-time tsunami warning network and (b) numerical modeling — pre-computed databases of tsunami simulations for rapid forecasting of tsunami heights (tuned to particular tsunami events using data assimilation from the real-time buoy network)

and inundation maps for threatened coastal communities (generated in cooperation with various institutions and agencies). The Project has also taken the lead in the creation of Web-based Tsunami Community Modeling Activities to share software, data, simulations, and expertise among institutions and agencies involved in tsunami modeling. This broad approach to tsunami mitigation is both necessary and a challenge since it requires the coordination and integration of instrument development, numerical modeling and Web-based implementation. In the paper, we present examples of this work for Pacific tsunamis that are incident on Hawaii and the Oregon Coast.

ENVIRONMENT OF RUSSIAN MARGINS – THE INTERPLAY FIELD OF OCEANOLOGY AND INDUSTRY INTERESTS

Lev R. Merklin, Leopold I. Lobkovsky, and Sergey A. Kovachev

Shirshov Institute of Oceanology, RAS

Russia, 117851, Moscow,

Nahimovsky prospekt 36;

Tel.: 7 (095) 1248547; Fax: 7 (095) 1245983;

E-mail: lmerklin@sio.rssi.ru]

Anatoly N. Dmitrievsky

Institute of Oil and Gas Technologies, RAS

63 Leninsky Prospekt, Moscow 117917,

Tel.Ⓜ095) 1358076, Fax: (095) 1358876

Closer to the end of XX the activity of resource industry and international investment were strongly increased for Russian margin seas (Barents Sea oil&gas fields, Caspy-to-Black sea pipelines, Okhotsk Sea oil fields, etc.). Here the industry faced into poorly studied problems of severe environment including high seismicity and tsunamy, neotectonic movements and sediment slides, nearbottom currents and turbidite flows, ice cover and permafrost, clathrates and gase seepage, and etc. All these processes are subjects of investigation for oceanology and oceanological technologies, so only oceanologists can resolve these multidisciplinary problems.

We started seeking the interconnection of modern geodynamic, geological and oceanological processes to answer on engineering requirements of oil&gas industry. For example, last year the microseismicity measurements by using ocean bottom seismic stations (OBS) together with high-resolution seismic data superimposed on revised picture of Black Sea hydrological regime helped to correct the *Bluestream* deep-sea pipeline route.

In April-June, 1998 Shirshov Institute of Oceanology received new seismicity data on the Caucasus and Anatolian shelves and slopes of the Black Sea. Our OBSs were installed on the water depths 80-2000 m for the time from half to one month and recorded the strong distant deep eathquakes (Fig. 1) alongside the very weak seismic events (Fig. 2), located in the upper sediment layer (zeroth depth of focuses). During one month of seismological measurements on Caucasus slope we determined 61 earthquake epicenters by magnitude less than 2

(Fig. 3). The earthquake focuses were distributed in the wide depth range from upper mantle up to nearbottom sediments. As illustrated (in Fig. 3), near projected pipeline route it was discovered a seismicity active fracture.

During 15 days of bottom seismological measurements in Samsun region (Anatolian shelf and slope) it was determined the coordinates of 44 earthquake epicenters by magnitude up to 4. More than half of regional events happened under Western and Eastern Pont Ridges. At the Black Sea we determined 17 events which sites were both in upper earth crust and in mantle on the depth more than 100 km.

At the Black Sea shelf and slope there is a combination high microseismicity produced plate geodynamic undertrusting with nearbottom gase-bearing sediments (Fig. 4A), gase "seeping" (4B) sediment slides (Fig. 4C) and turbidite flows (Fig. 5). Sediment flows on the shelf and continental slope control by nearshore anticyclonic gyres (Fig. 6) and bottom currents.

Gravitational disruption of the big sediment slide from a side of underwater canyon is preceded by fracturing along a decollement surface. There is appeared the cluster of microearthquakes with specific distribution of focuses in the space and time (really with zeroth depth and fit to disruption line). This process can be preceded by strong earthquake near fracture zone which acts as cock for sediment slide moving down. Considering that such weak events with zeroth depth fall on steep sides of sediment ridges on the continental slope, its have

sliding non-tectonic origin.

We propose to monitor such processes by special system of bottom seismic (geoecological) monitoring in which OBSs and tiltmeters can fix the beginning of sliding and complete process of sediment moving down. Really, high sensitivity of OBS allows to record many microearthquakes during short time lapse (15-30 days). Based on usual regional land stations the representative seismological information may be obtained only during 10 years and more. The second advantage of OBS observations is the capability for thereof direct installation onto geodynamic active area of sea floor for seismic hazard estimation of engineering constructions in low seismicity regions.

Underwater monitoring system (Fig. 7) can be designed as bottom cable network the size of 15x60 km, connecting local bottom multisensor stations spaced on 3-20 km in accordance with a level of local geoecological risk. OBSs, connected to local cable, can include next sensors: 4C seismic detectors, thermometers, pH, current meters, resistivimeters, and etc. Optical and radiofrequency spectrometers may be included top OBSs for measurements of nearbottom water and gase composition. The merits of such underwater monitoring system lie in the possibility of fast repairment and regular modernization by using of relative cheap vessel 1000-1500 t, equipped with trawl winch.

Combination of seismological, hydrophysical and hydrochemical sensors in ocean bottom oceanological station (OBOS) together with swath high-resolution geophysics enhance the implementation of oceanology from traditional engineering (for platforms, terminals, pipelines and bottom cable telecommunication) to general environment monitoring and catastrophe prediction-precasting.

References

1. Lev R. Merklin and Lev L. Utyakov, "Russia: Ocean Monitoring through Intellectual Multisensor Nets". – *Sea Technology*, August 1998, V.39, No.8, 49-53

Fig. 1. The record of distant earthquake by $M=4,1$ on the Black Sea shelf.

Fig. 2. The record of weak nearbottom event by $M<2$ on the Caucasus continental slope.

Fig. 3. Seismicity data of 1998 measurements near the Dzgubga (Black Sea).

Fig. 4. High-resolution seismic records at the Black Sea region:

4A. Gase-bearing sediments on Caucasus shelf.

4B. Gase «seepage» on Anatolian shelf.

4C. Sediment slides on Caucasus continental slope.

Fig. 5. The main turbidite flows along bottom valleys on the Black Sea continental slope (Dzgubga).

Fig. 6. Black Sea mesoscale anticyclonic gyres (1), convergence zone (2) and divergence zone (3) plotted on the scheme of currents for average annual wind conditions [Bogatko et al., 1979; Ovchinnikov, Titov, 1990].

Fig. 7. Proposed system of bottom cable monitoring along underwater pipeline.

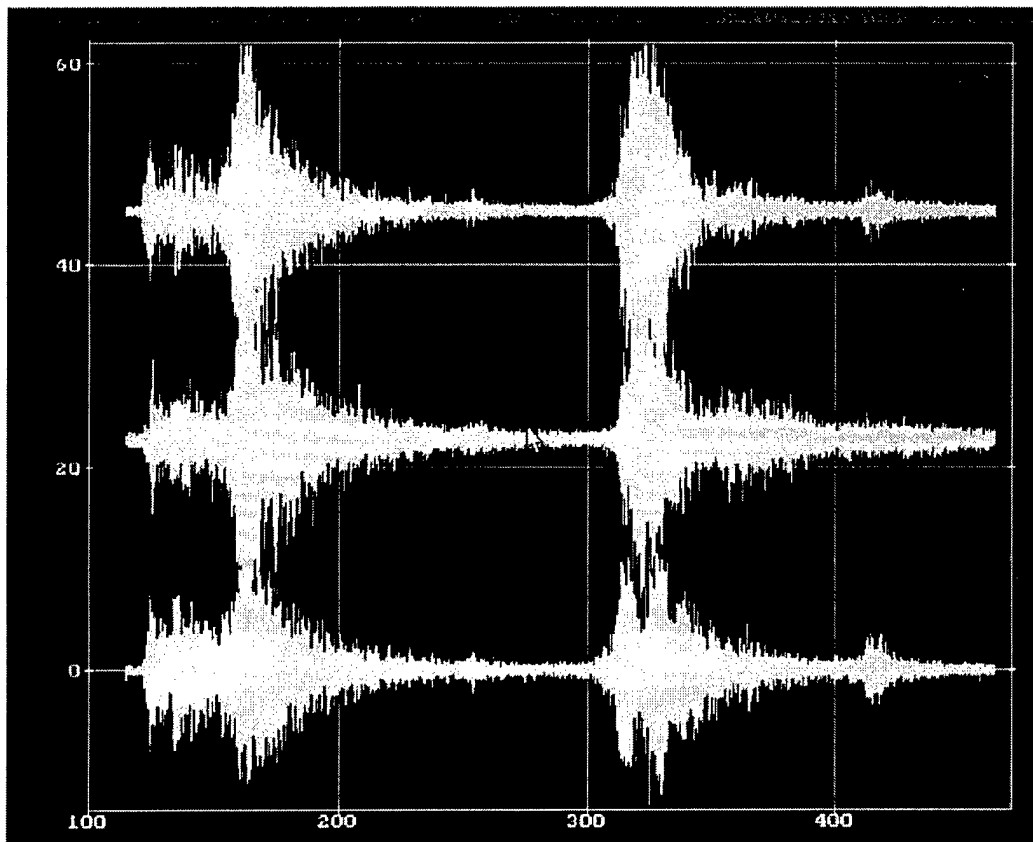


Fig. 1. The record of distant earthquake by $M=4,1$ (Black Sea shelf).

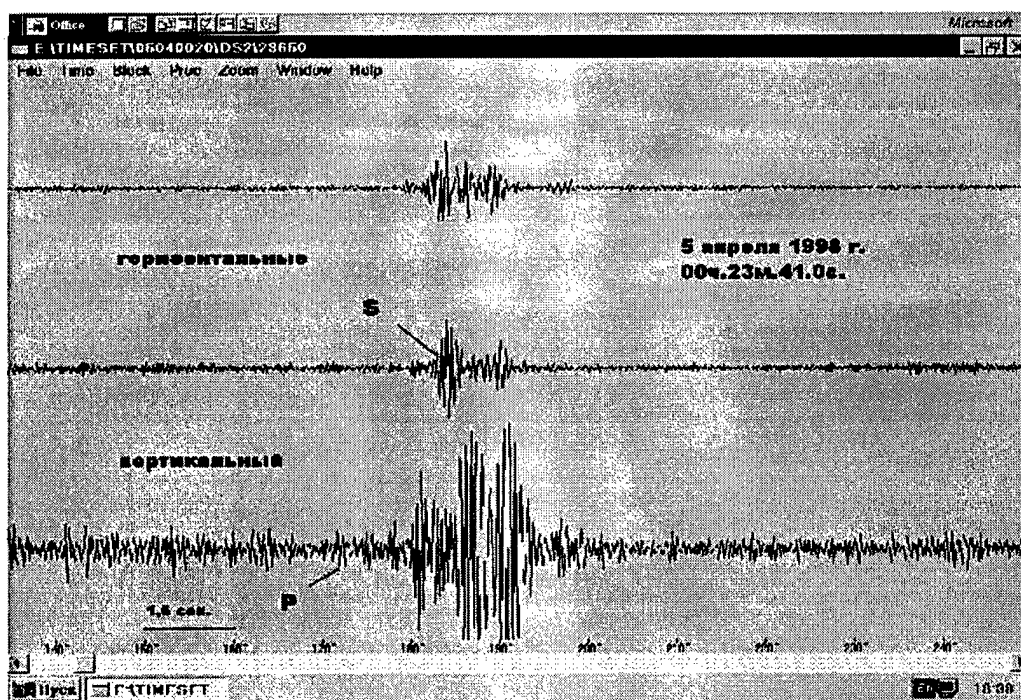
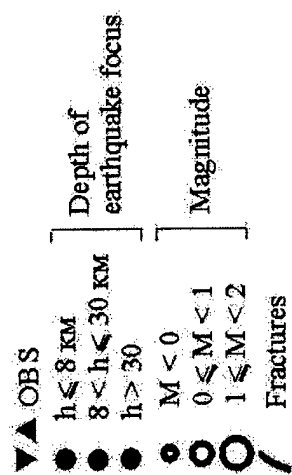
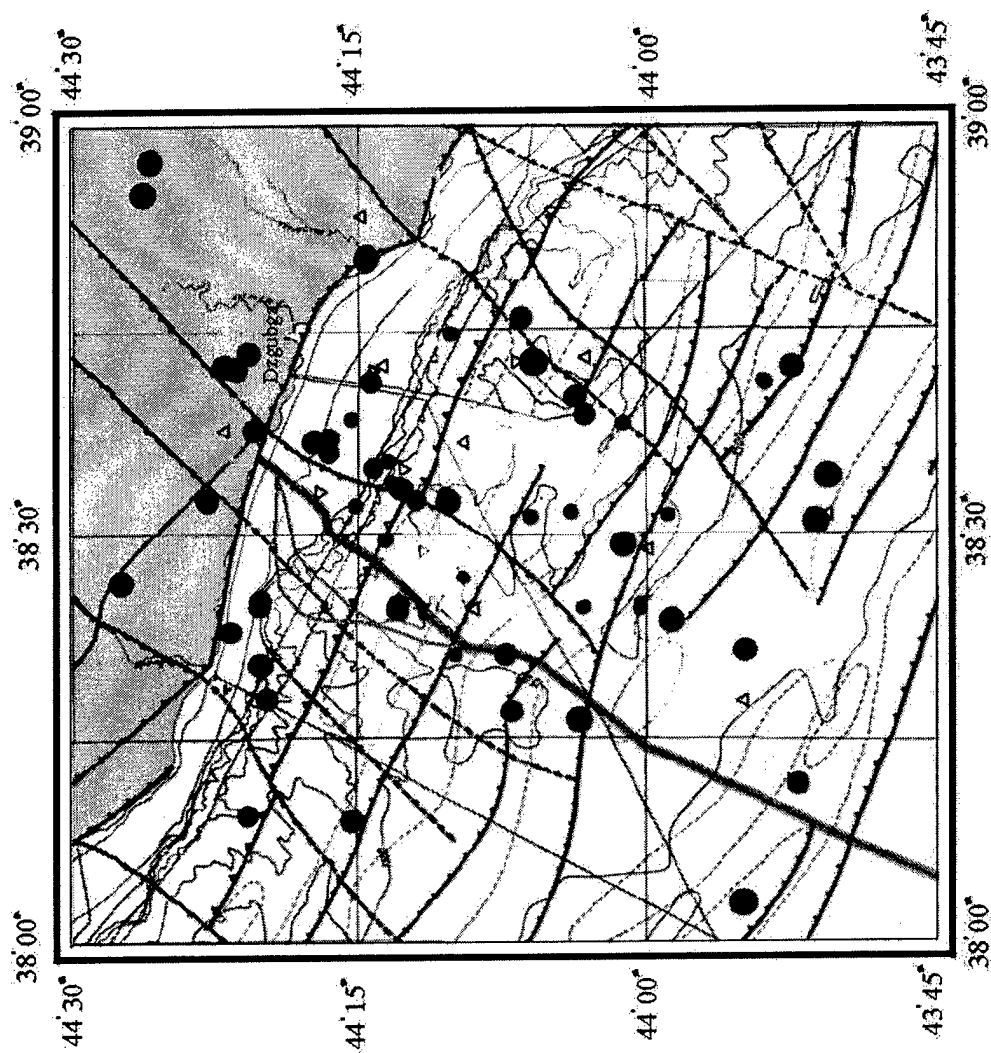


Fig. 2. The record of weak nearbottom event by $M<1$ (Caucasus continental slope, Black Sea).



Proposed Bluestream pipeline routes



Fig. 3. Seismicity data of 1998 measurements near Dzgubga (Black Sea)

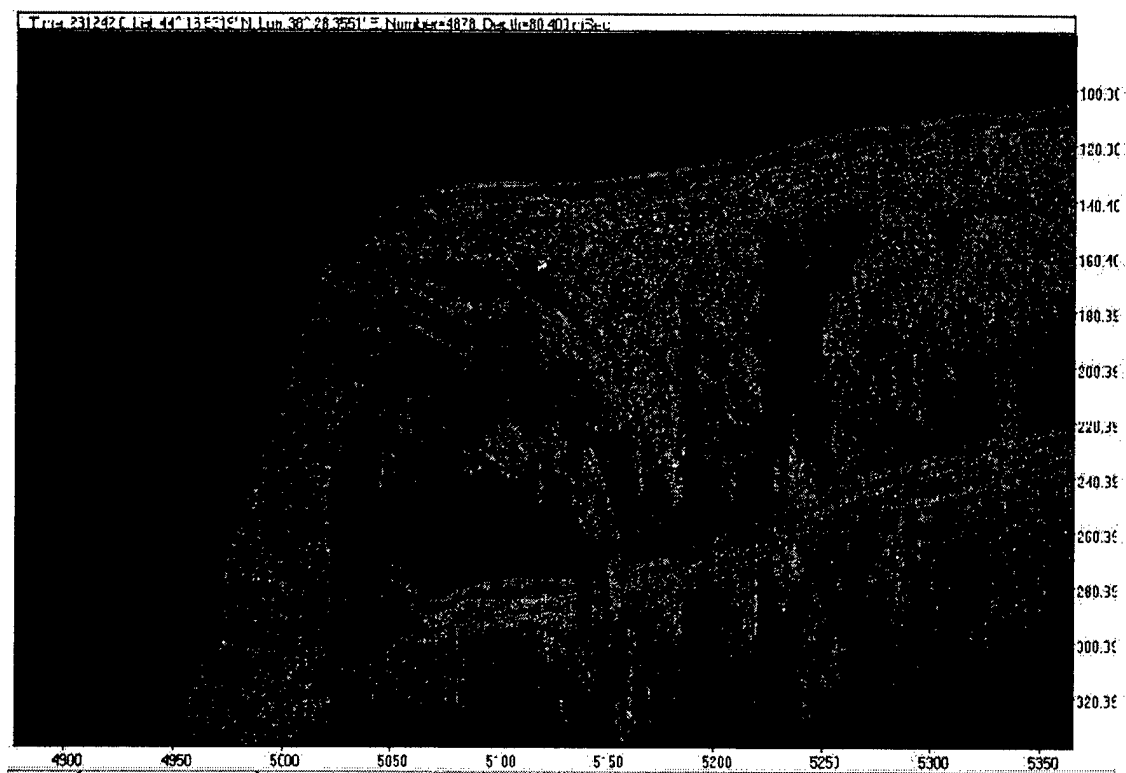


Fig. 4A. Gase bearing sediments on Caucasus shelf.

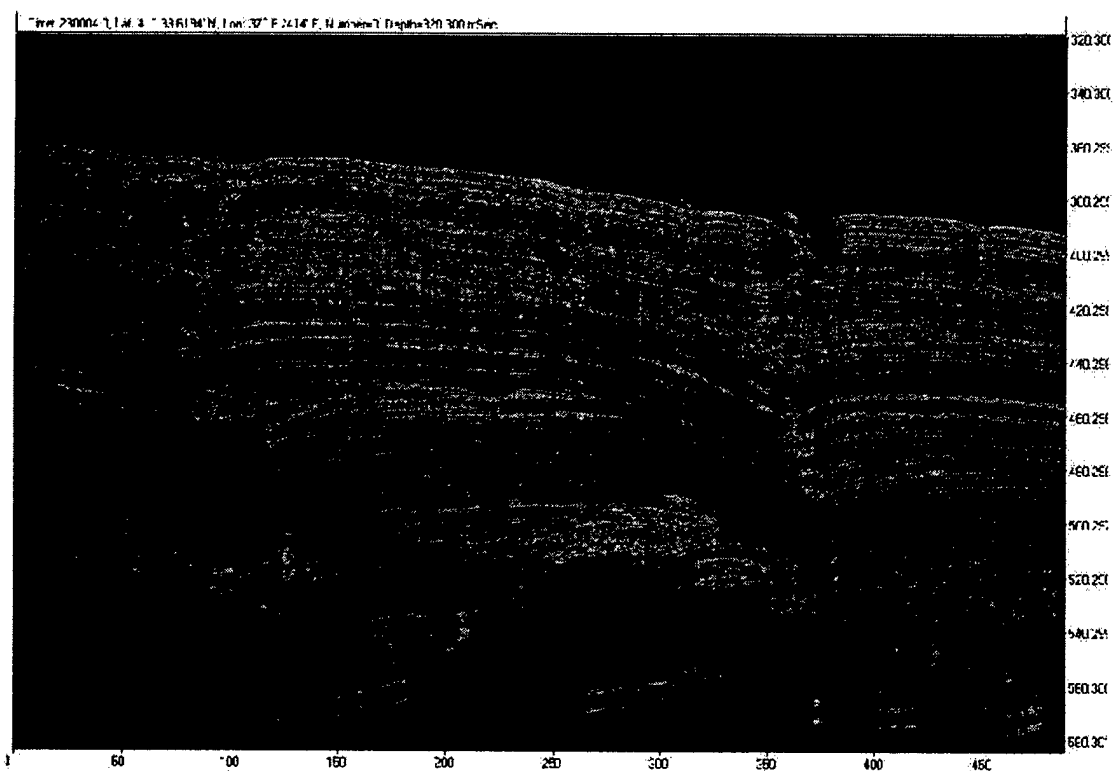


Fig. 4B. Gase "seepage" on Anatolian shelf.



Fig. 4C. Sediment slides on Caucasus continental slope.

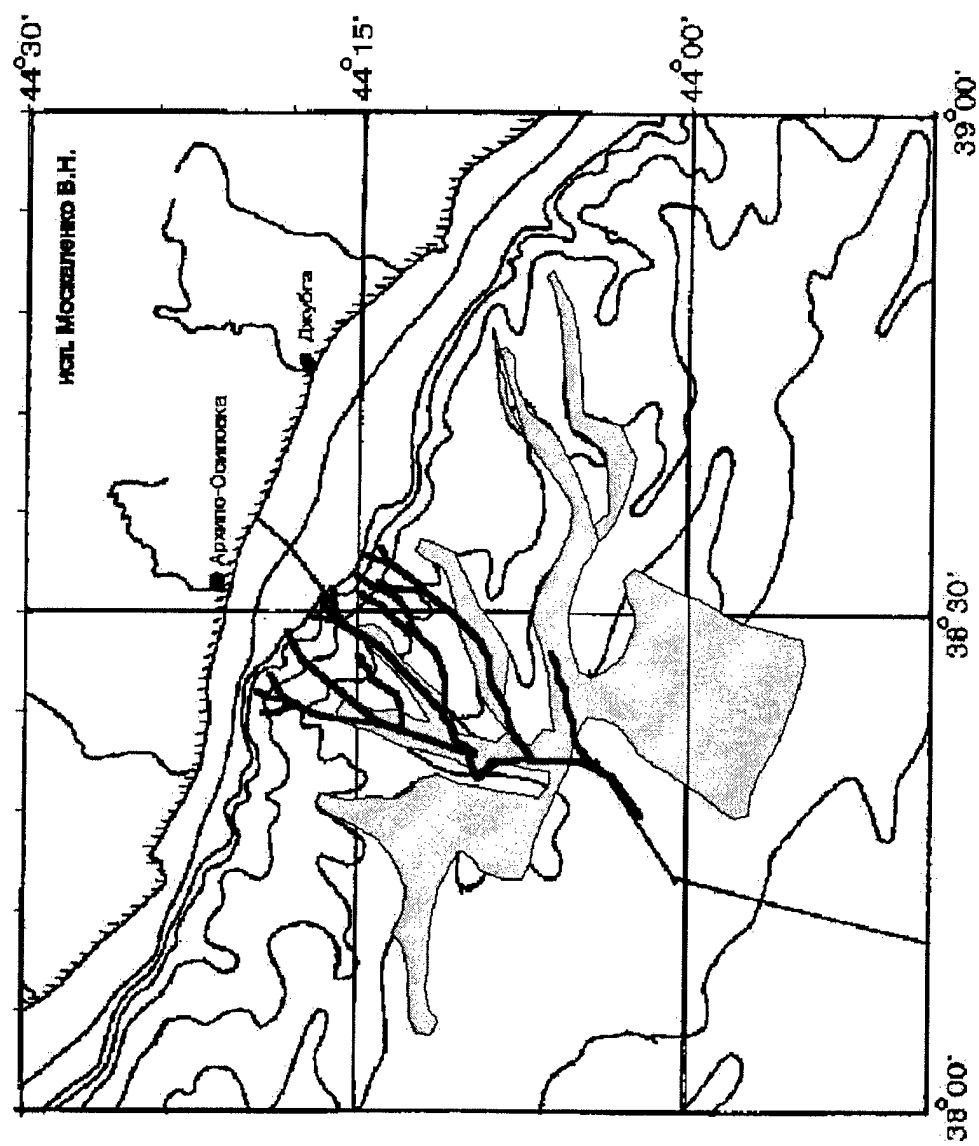


Fig. 5. The main turbidite flows along bottom valleys on the Black Sea continental slope (Dzhubga).

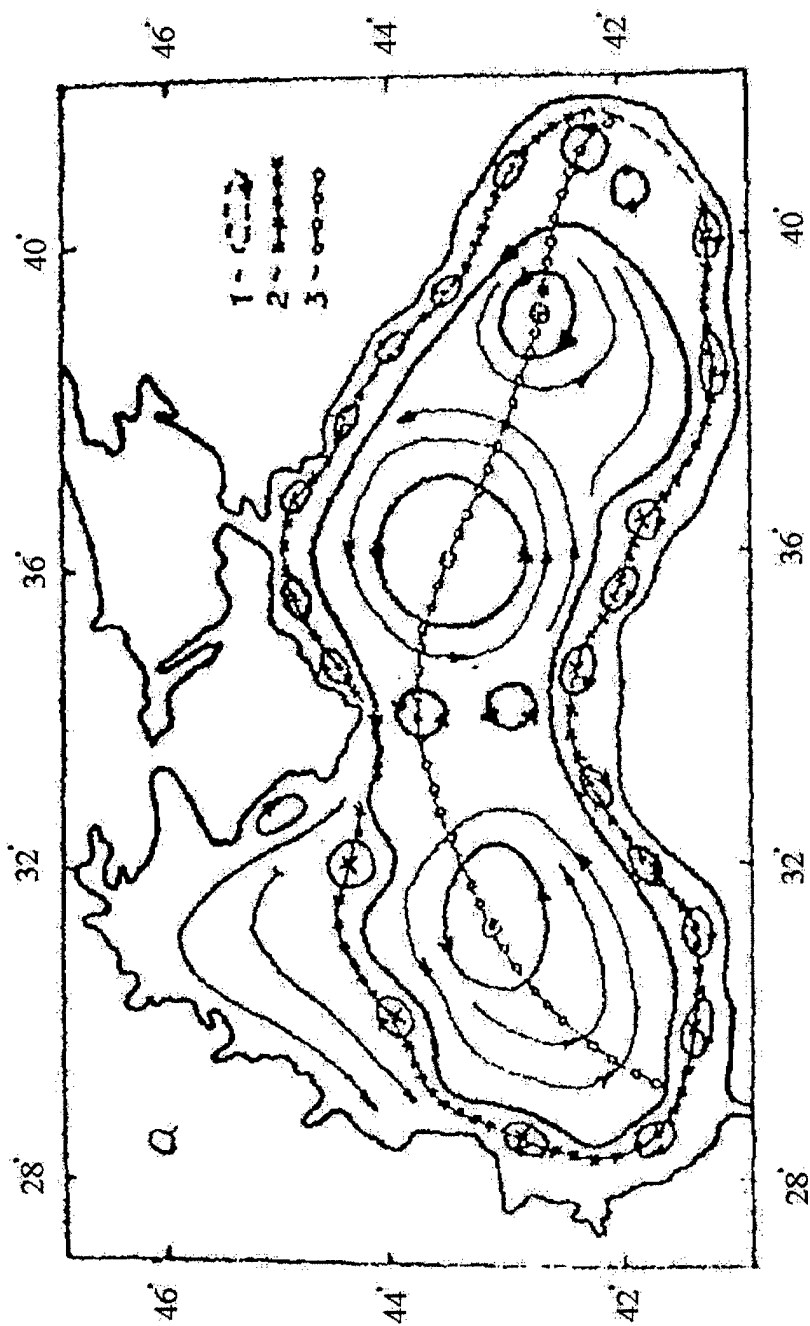


Fig. 6. Black Sea mesoscale anticyclonic gyres (1), convergence zone (2) and divergence zone (3) plotted on the scheme of currents for average annual wind conditions [Bogatko et al., 1979; Ovchinikov, Titov, 1990].

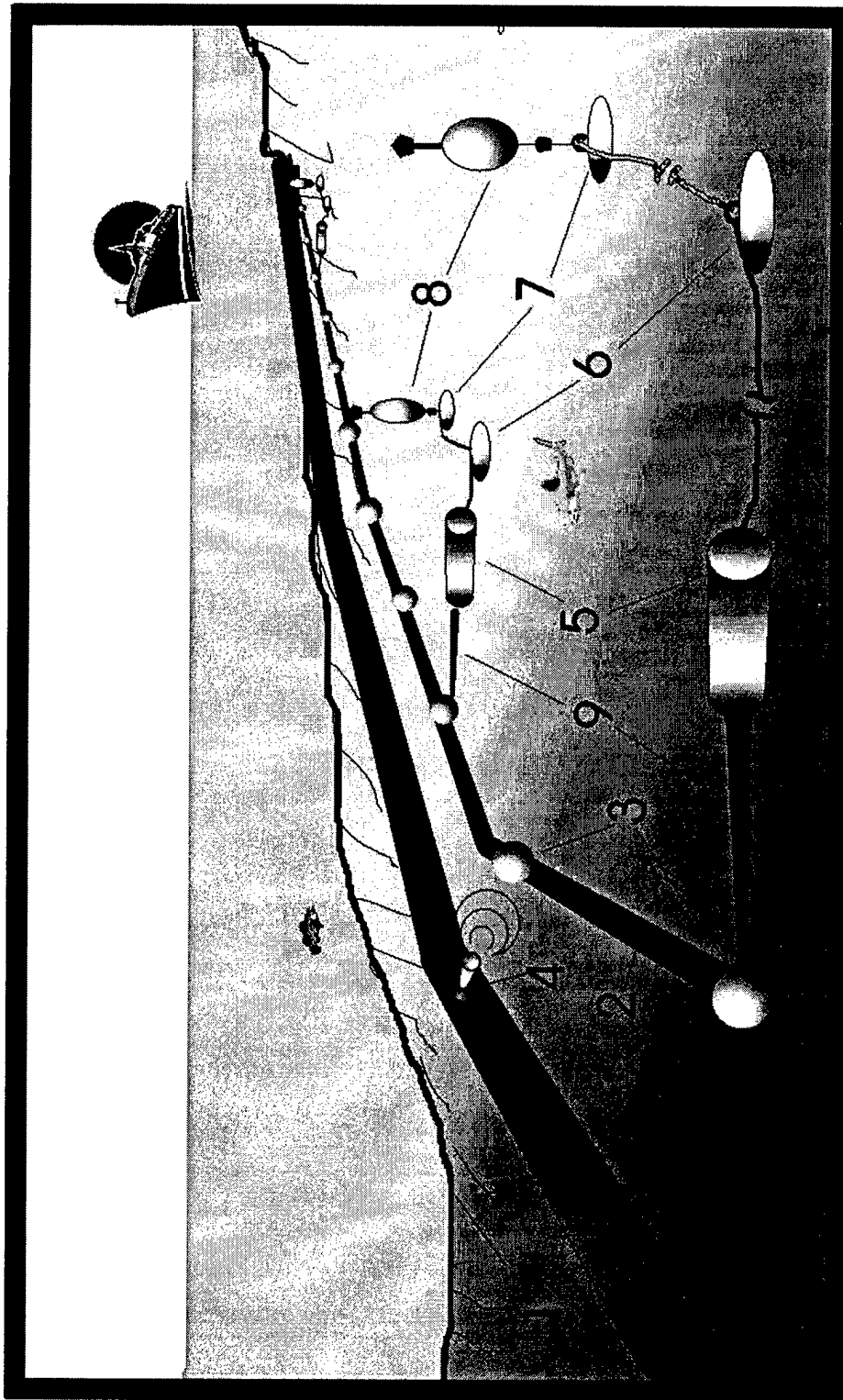


Fig. 7. Proposed system of bottom cable monitoring along underwater pipeline

- | | |
|---|-----------------------|
| 1 - pipeline | 6 - anchors |
| 2 - fiber-optic telecommunication cable | 7 - ballast |
| 3 - local cable bottom station | 8 - pop-up buoy |
| 4 - pipeline sensor with acoustical transceiver | 9 - local cable lines |
| 5 - sensor on local cables | |

Seafloor Characterization And Mapping Pods (SCAMP): submarine-mounted geophysical mapping

Dale N. Chayes, Lamont-Doherty Earth Observatory of Columbia University
E-mail: dale@ldeo.columbia.edu

Robert M. Anderson, Arctic Submarine Laboratory, US Navy

Stuart Goemmer, Johns Hopkins Applied Physics Laboratory

Jose L. Ardai, Lamont-Doherty Earth Observatory of Columbia University

Bernard J. Coakley, Tulane University

Mark R. Rognstad, Roger B. Davis, Margo Edwards, University of Hawaii

Abstract:

In 1998 the Seafloor Characterization and Mapping Pods (SCAMP) were deployed on the US Navy nuclear attack submarine USS HAWKIBILL (SSN666) for unclassified swath mapping and subbottom profiling under the Arctic ice canopy. Data was collected under the SCICEX program which is guided by the terms of a memorandum of agreement between the Navy, the Office of Naval Research, the National Science Foundation (NSF), the U.S. Geological Survey and the National Oceanic and Atmospheric Administration. SCAMP consists of a Sidescan Swath Bathymetric Sonar (SSBS) and a High-Resolution Subbottom Profiler (HRSP), and a marine gravity meter that are integrated with a physically compact Data Acquisition and Quality Control System (DAQCS). The transducers for each of the sonars are mounted in purpose built hydrodynamic pods that are temporarily fastened to special purpose threaded weldments along the boat's keel. The weldments were installed in drydock but the pods, transducers and junction boxes were installed and can be serviced by divers at the pier. The inboard electronics for the system are packaged for submarine installation and

mounted in the torpedo room. The SSBS is a 12 kiloHertz SeaMARC design adapted for under-ice mapping by adding transmit and receive beam forming and shading to suppress spurious returns from the ice canopy. Transducers are housed in a keel-mounted pod with electronics mounted outside the pressure hull but above the water line when surfaced. Swath image data is produced over a 135 to 140 degree swath centered at nadir while high quality bathymetry covers a 120 degree swath. The HRSP is a Bathy-2000P FM modulated subbottom profiler adapted for submarine installation and operation. It produces high quality subbottom data using an array of 9 DT-109 transducers driven by a 2 kilowatt transmitter. Seafloor penetration in excess of 100 meters with a resolution of 10s of centimeters is common in sediment filled areas of the Arctic basins. Initial at-sea tests on the submarine were conducted out of Pearl Harbor, Hawaii in May 1998. The first deployment in the Arctic took place during SCICEX-98 during which more than 30 days of data were collected in the data release area. Substantial improvements to the system were completed and tested in January and February 1999. The second deployment in the Arctic is scheduled for April and May of 1999.

INVESTIGATIONS OF HYDROACOUSTIC PARAMETRIC SUB-BOTTOM PROFILER CHARACTERISTICS

V.A. Voroiun, S.S. Konovalova,
T.N.Kutsenko, S.P.Tarasov, V.I.Timosheiibo
Taganrog State University of Radioengineering, RUSSIA

ABSTRACT:

The problem of sub-bottom profiling with large accuracy is urgent and reasonably difficult. The purpose demands the use of high directivity low-frequency wide band acoustic source. As such source the most expedient is using a parametric acoustic array. Research by specific property of parametrical array permits one to create bottom profiler for shelf, which can be established on small-sized vessels for fulfillment of works on geology, marine archeology, ecology, oceanology and etc. The account of the power characteristics of parametric systems has a little differences from account of conventional sonars. The differences are stipulated by features of parametric arrays. The transmission of energy from pump waves to difference frequency waves is executed within the zone of nonlinear interaction. Model of the bottom we consider consisting from similar layers with flat horizontal borders. Duration of signals is shorter

than time of propagating of sound inside of layer and it is possible to select the signals from bottom and surface of layer. The factors of reflection and passade can be determined for each layer. The received expression permits us to calculate capacity on each frequency pump, necessary to determine bottom sediments in view of their characteristics. The dependence of signal-noise ratio from sediment layer depth and different frequency were calculated. The result permits us to determine the profiler potential possibility for determination of bottom sediment in various conditions.

The received calculated results are confirmed by conducting investigations in real conditions. The parametric profiler developed in Taganrog State University of Radio-engineering, is used for the investigation. The results of our investigation of parametric profiler show the real possibility and perspective of parametric array use.

A VERSATILE, PORTABLE AND LOW COST COMPUTERIZED DATA LOGGING AND CHARTING SYSTEM COMPATIBLE WITH ELECTRONIC NAUTICAL CHARTS

Peter Pirillo, P.E.*

I. Introduction

FDA's Division of Cooperative Programs (DCP) has used non-computerized instrumentation extensively and proficiently for its specialized coastal water pollution studies that assist state management of shellfish harvest waters. This paper summarizes the instrumentation development portion of a September 1998 fluorometric study in coastal Connecticut. Fluorometry was used to study estuarine dispersion, travel time, and dilution of wastewater treatment plant discharge, yet the computerized hydrography system (CHS) can be used with any instrument that supports real-time ASCII (or NMEA 0183) output. The CHS is illustrated in Figure 1.

Leading up to this instrumentation development were technology advancements for geographical positioning systems (GPS), fluorometers, portable PC's, electronic nautical charts, and navigation and hydrographic software. Prior to this study, only one off-the-shelf software application (*Chartview Pro*) was found that had a feature intended to computer log and display instrument data correlated to a plot of the vessel track on electronic nautical charts, both real-time and after the study. Yet this hydrographic feature had not been implemented by an end-user, until FDA-DCP staff developed a computerized hydrography system (CHS) that included *Chartview Pro*, and the software developer responded to feedback from FDA-DCP instrumentation trials. Stability as well as the responsiveness of the software company were some criteria for the CHS software, as was low cost, and therefore the off-the-shelf appeal. Versatility was also important. For example, FDA-DCP hydrography typically includes salinity and temperature studies and this instrumentation may be added to the CHS in the future.

A purpose of developing the CHS was to update the hydrography instrumentation used by FDA-DCP and its cooperative program partners. As with most hydrographic studies, the data from instruments needed to be accurately correlated with time and position data to be most useful and credible. Prior to developing this CHS, paper NOAA nautical charts were used for planning, data

collection, analyses, and reporting. Manual reconstruction of vessel tracks and data points on paper nautical charts provided a formidable challenge to accuracy when based on manually recorded GPS data, and especially when based on manually recorded position data without use of a GPS. Paper nautical charts have also been used for a wide range of purposes in addition to navigation by state programs, making *ChartView Pro's* compatibility with nautical charts ideal for a FDA-DCP computerized hydrography system.

II. System Overview

This phase of the computerized hydrography system (CHS) used for data collection consisted mainly of a Turner Designs digital field fluorometer, Differential GPS, notebook PC, *Chartview Pro* software, NOAA electronic nautical charts, Noland Engineering's serial multiplexer, 12-volt batteries, and electrical and mechanical apparatus. Table 1 lists the main components of the CHS, including vendor information when there were not many alternative sources to choose from. Usually, either a multiplexer or a serial I/O card would be used, as explained below.

Table 1: Computerized hydrography system components

Component	Source
10-AU Fluorometer	Turner Designs
<i>ChartView Pro</i> software	Nautical Software
N183-41 Multiplexer	Noland Engineering
Or, Serial I/O card	Many
Elec. nautical charts	Many (e.g., BSB, NDI, Maptech)
Differential GPS	Many
Portable PC	Many
Liquid pumps	Many
Mech. apparatus	Custom
Electronic apparatus	Custom
Batteries, 12 volt	Many
Spreadsheet software	Many
Graphics software	Many
Color printer	Many

*Peter Pirillo, P.E., FDA, CFSAN, Division of Cooperative Programs, HFS-628, 200 C Street SW, Washington, DC 20204; Phone: 202-690-5771; Email: pcp@cfsan.fda.gov

Reference to any specific commercial product, service, or company does not constitute its endorsement or recommendation by FDA or its representatives.

Figure 1 is an illustration of the CHS that also points out some features of the system, for example, versatility. The CHS is compatible with different and multiple scientific instruments and devices that support real-time ASCII or NMEA 0183 output. Figure 1 indicates that the CHS logs the data from scientific instruments simultaneously with time and position (latitude and longitude). These data can be seen real-time at any point along the vessel track, using *ChartView Pro's* "Track Console," or later within *ChartView Pro* using two options: (1) By pointing and clicking along the vessel track plotted onto the nautical chart; and (2) Opening a table of all the data recorded, at 2 second or slower intervals. The vessel tracks on nautical charts and the related data tables can be viewed either within *Chartview Pro* or with other software using the *Chartview Pro* images (see Figure 2) or data tables (see Table 2). After importing into other software, the data tables and colored vessel tracks on nautical charts can be enhanced and viewed on a PC screen, or on color prints, such as Table 2 and Figure 2.

Table 2: Sample of *ChartView Pro* ASCII output, with background correction from a spreadsheet application.

Time	Latitude	Longitude	Concentration (ppb)	
			Field	Corrected
13:30:51	41° 01.884' N	073° 32.218' W	4.017	3.85
13:30:57	41° 01.878' N	073° 32.220' W	4.720	4.55
13:31:03	41° 01.872' N	073° 32.221' W	5.577	5.41
13:31:08	41° 01.867' N	073° 32.223' W	5.764	5.59
13:31:15	41° 01.861' N	073° 32.224' W	4.729	4.56
13:31:21	41° 01.855' N	073° 32.226' W	4.122	3.95
13:31:27	41° 01.850' N	073° 32.227' W	4.315	4.15
13:31:33	41° 01.844' N	073° 32.228' W	4.584	4.41
13:31:38	41° 01.839' N	073° 32.229' W	4.012	3.84
13:31:45	41° 01.833' N	073° 32.230' W	3.294	3.12
13:31:51	41° 01.827' N	073° 32.230' W	2.735	2.57
13:31:57	41° 01.821' N	073° 32.231' W	2.759	2.59
13:32:03	41° 01.815' N	073° 32.233' W	2.707	2.54
13:32:08	41° 01.811' N	073° 32.234' W	2.830	2.66
13:32:15	41° 01.804' N	073° 32.236' W	2.861	2.69
13:32:21	41° 01.798' N	073° 32.238' W	2.990	2.82
13:32:28	41° 01.792' N	073° 32.240' W	3.581	3.41
13:32:33	41° 01.786' N	073° 32.241' W	3.718	3.55
13:32:40	41° 01.779' N	073° 32.241' W	3.490	3.32
13:32:46	41° 01.773' N	073° 32.241' W	3.839	3.67

Chartview Pro can be used for logging separate data collection tracks, as compared to continuous logging. Two computer files are created for each data collection track. One file stores proprietary information to plot the vessel track onto nautical charts, and to display a formatted data table within *Chartview Pro*. The second file is an ASCII file of the data table. It is this latter file

that is imported into spreadsheet software for further processing (see Table 2). The method used for calibration determines whether background needs to be subtracted from data. Additional files can be created, including marks that can be dropped at the vessel position and related to data typed into the PC.

A serial multiplexer is needed when the number of instruments connecting to the PC is greater than the number of PC serial ports. A PC with a built in pointing device is needed so that a single serial port is available for a multiplexer, rather than a mouse. With two serial ports, for example, a multiplexer could be avoided if only one scientific instrument is being used in addition to a GPS. Even if a portable PC has only one serial port, a second serial port can be added if the PC will accept a Serial I/O Card, e.g., a PCMCIA card. Avoiding the use of a serial multiplexer simplifies the electrical apparatus required for the CHS, thereby minimizing malfunction of the portable CHS on board a survey vessel.

III. Results

This project included the successful first implementation of a computerized hydrography system (CHS) for data logging and charting that used *ChartView Pro* software. The software was user friendly, as was seen by independent operation of the CHS by study participants new to the software, for data collection.

The CHS allows one investigator to collect magnitudes more data at magnitudes shorter logging intervals, in corrected and final units, with all data being exactly correlated upon real-time computer recording. A six-second logging interval was selected from a wide choice of intervals. The CHS required no manual processing for the real-time computer plots of vessel tracks with their correlated instrument data onto NOAA electronic nautical charts, with the maximum available accuracy of corrected GPS. These plots and others were also used for analyses and printed for reporting (see Figure 2). The CHS made it possible and simple to include all of the data in a report (see Table 2). These instrumentation developments improved accuracy, efficiency, and objectivity beyond the realm of possibility with any number of investigators conducting non-computerized studies.

Since *Chartview Pro* is compatible with any scientific instrument supporting real-time ASCII (or NMEA 0183) output, not just a fluorometer, other applications for the CHS are unlimited and include petroleum pollutant studies and chlorophyll *a* fluorometry. More specific to FDA-DCP, salinity and temperature studies using a CTD probe along with a fluorometer is an objective for future use of the CHS. Also, the improvements in fluorometry instrumentation could lead to improvements in model calibration and verification, by FDA-DCP and others.

In summary, *ChartView Pro* was the software found prior to this project offering the following hydrography improvements:

- Computer plots of the data collection vessel tracks, with their correlated instrument data, onto NOAA electronic nautical charts, with the maximum available accuracy of corrected GPS, real-time and later for analyses and printing (see Figure 2).
- Tide and current predictions and animations overlaid onto electronic nautical charts, for planning, analyses, and report printing.
- Hydrographic software that also was used for navigation, to conduct data collection traverses and to avoid shallow water and obstructions. Previous vessel tracks can optionally remain on the PC screen and nautical chart during the study.
- Tools such as marks and electronic dividers, together with the electronic nautical charts, were also used for planning, analyses, and report printing of various information (e.g., profile studies and conclusions) in addition to the vessel tracks.

To summarize, the computerized hydrography system developed for data logging and charting improved FDA-DCP hydrography in *additional* ways, including:

- Location, time, and scientific instrument data were simultaneously computer logged during the study.
- Magnitudes more data were collected, and logging can be conducted at two second intervals or slower.
- No manual or even computer post processing of data was found necessary, for both computer plots of data collection vessel tracks onto nautical charts, and for their correlated data tables.
- All the data was included in the FDA-DCP report.
- Report graphics were created and delivered in color, as originally shown on the paper NOAA nautical charts that all parties are accustomed to.
- The CHS development made possible a future addition of a CTD probe, to complete the computerization of data typically logged for FDA-DCP hydrography, yet other instruments may be added as well. All the above reported features will then apply to salinity and temperature as well as fluorometric studies.

These CHS instrumentation improvements better allowed unplanned vessel courses for data collection, an important part of studying estuarine and marine dispersion of tracer dye injected into a pollution discharge, or released instantaneously into seawater. The CHS development and its elimination of the need for manual data logging results in improved accuracy, efficiency, and objectivity of FDA-DCP hydrography. Additionally, these technological improvements give the hydrographer much more time for strategizing during data collection because s/he no longer has to manually interpret and record location, time and data from other instruments on board the survey vessel.

Acknowledgements

This project would not have been possible without contributions from several people, all of whom are sincerely appreciated. These people are too numerous to mention, but the author would like to thank the following groups and people: (1) The Connecticut DA, Bureau of Aquaculture personnel for participating in estuarine fluorometry, and for providing a digital fluorometer; (2) Greg Goblick, RI DEM, Office of Water Resources for participating in equipment preparation and testing, and for providing a digital fluorometer. He and his colleagues have been and continue to be valued collaborators for estuarine fluorometry; (3) The NY DEC, Bureau of Marine Resources personnel for participating in estuarine fluorometry; (4) The FDA Regional Shellfish Specialists, Jerry Mulnick and Marty Dowgert, for their participation in and facilitation of FDA - State collaborative projects; (5) Malcolm Field, Ph.D., EPA, for both providing a digital fluorometer and for participating in estuarine fluorometry; (6) Gia Lamela, US Navy Research Laboratory, also for providing a digital fluorometer, and for participating in software testing; (6) Captain Fred Pease, the crew of CT1, and URI Ocean Engineering for providing a research vessel for estuarine fluorometry; (7) Last and especially, Aaron Bowman, Nautical Software, for the many phone conversations in which he responded to FDA-DCP feedback for part of his timely improvements to *ChartView Pro's* data logging features.

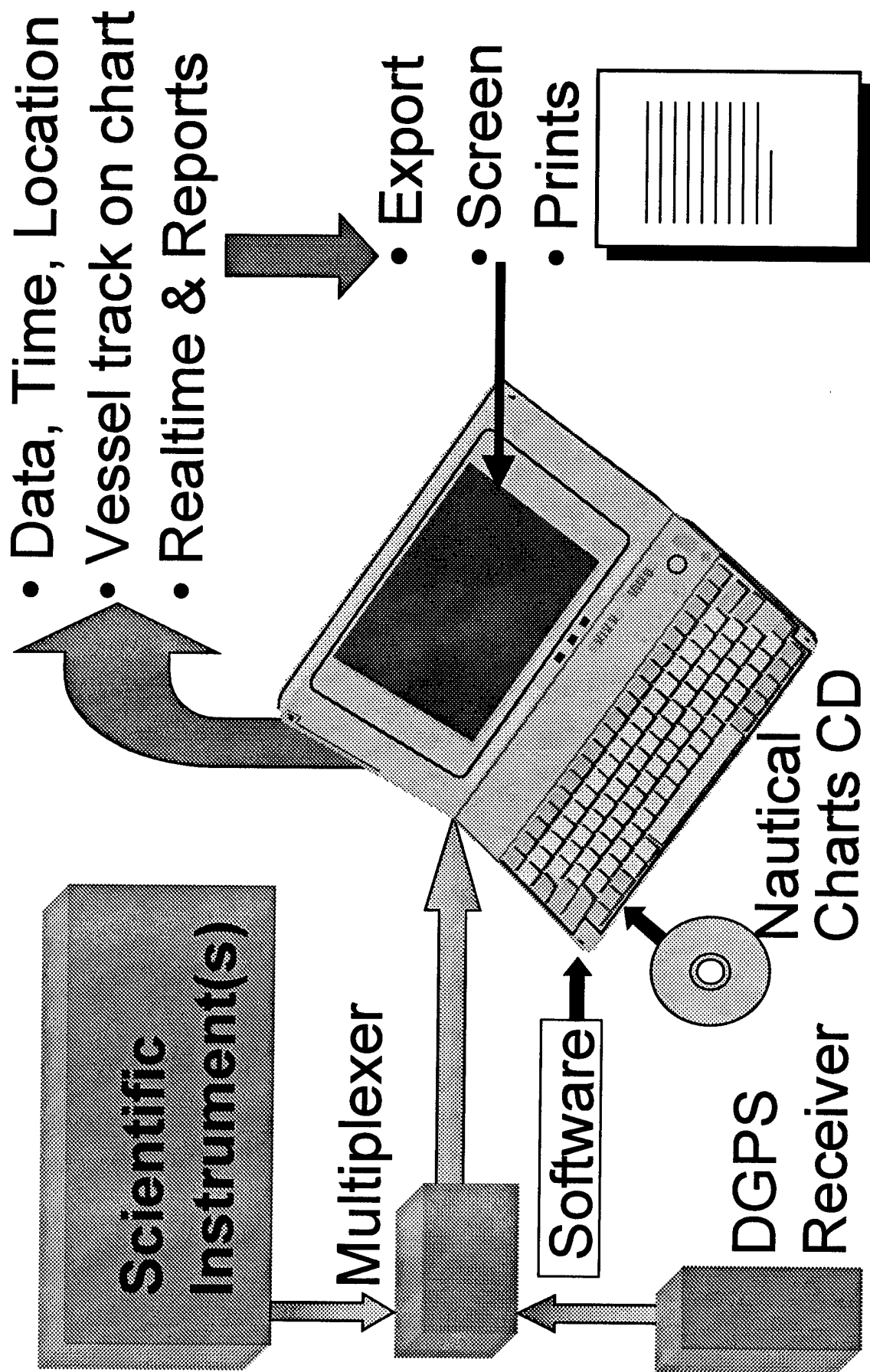


Figure 1 A computerized data logging and charting system implemented for FDA-DCP 9-16-98 estuarine fluorometry near Stamford, CT. *Chartview Pro* software plotted the data and vessel tracks on NOAA electric nautical charts, real-time and later for analyses and printing.

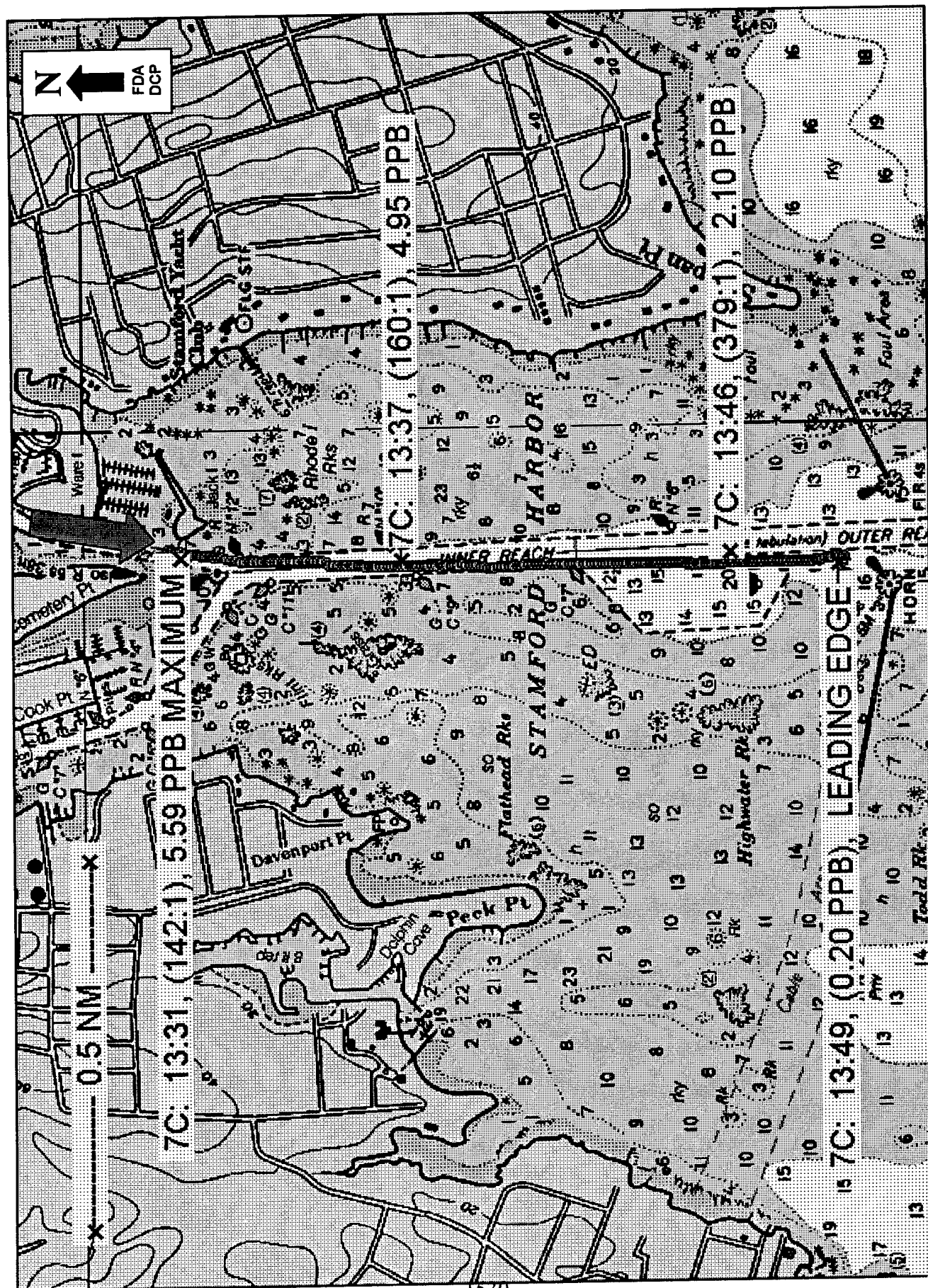


Figure 2 Track 7C (dotted line) of Connecticut vessel, 11:31-11:49. Time (24 hour), dilution, and tracer dye concentration (near surface) are labeled. Report contains complete data, computer logged at six-second intervals, for the 9/16/98 ebb tide hydrography of Stamford, CT wastewater discharge.

Design considerations and Peculiarities for Hyperbaric Manned Submersibles Life Support Systems

Eugeniy I. Trushliakov, Ph.D., Associate Professor, Ukrainian
State Maritime Technical University, Visiting Scientist at University of Michigan
E-mail teug@engin.umich.edu

Abstract

Possibility of the prolonged staying of aquanauts in the hyperbaric environment is conditioned by the Life Support System (LSS) functioning. Creation and support of the physiology needed and comfort conditions of the living environment is provided by the work of the primary LSS, and the survival of people in the extreme or emergency situations - with the help of the complex of emergency systems rescue units. The selection of LSS rational decisions for perspective hyperbaric manned submersibles on the base of imitative models is too complicated and many-sided problem. Although the final goal of LSS design is clear - to create optimal conditions for comfortable and safe human activity in hyperbaric atmosphere, to provide the habitability of living compartment, but there are many aspects and peculiarities of this design: necessity to secure human safety and comfort at three working regimes - compressions, isopressions and decompressions. These regimes differ by duration, pressure values, compositions of mixed gas, and, consequently, comfortable and safe parameters of breathing gas atmosphere; possibility of various breathing gas mixtures using; possibility of various working regimes for mixed gas conditioning system - heating, cooling, humidifying or dehumidifying and their combinations; lots of indeterminate original data; complexity of a rational effective criteria selection and calculation; necessity of imitative models elaboration and calculation methods

choosing for definition of mixed gas thermo-physical properties, which change and depend on pressure values and composition of gas mixture, distribution of mixed gas in pressure chambers, optimization of LSS design parameters. The design algorithm for LSS, which has the following peculiarities, is proposed: LSS is closed system, that's why it requires equipment for removal of carbon dioxide and monoxide, odor and other human life waste; increased and changing during the system's work mixed gas pressure requires application of equipment in pressure hulls; big diapason of mixed gas thermo-physical properties changes requires equipment keeping and supporting the given conditions under the various changes; narrow diapason of supporting comfort temperatures leads to bigger requirements to the accuracy of the mixed gas temperature control and regulation support; dependence of the comfort temperature of the mixed gas pressure complicates the system of the automatic temperature regulations; dependence of aquanauts health from the mixed gas parameters leads to the increased requirements to the reliability of the LSS and the obligatory duplication of the equipment; insignificant time of the system usage on the ultimate pressures and accordingly increasingly on the variable regimes with partial usage of the heat and electrical energy.

APPLICATION OF MAGNETIC SIGNATURE PROCESSING TO MAGNETIC CENTER PINPOINTING IN MARINE VEHICLES

A. V. Kildishev and J. A. Nyenhuis

Purdue University, School of ECE, West Lafayette, IN 47907-1285, U.S.A., a.v.kildishev@ieee.org

D. L. Boyko, P. N. Dobrodeyev and S. A. Volokhov

Magnetism Division, IED, NASU, 310106, PO Box 72, Kharkov, Ukraine, itl34@online.kharkov.ua

Abstract - This work improves measuring techniques and predictive capabilities in naval magnetic silencing. Enhanced investigations of measuring procedures, which analyze external magnetic fields, can lead to concepts and methods for controlling those fields in marine vehicles. This necessitates the development and use of improved analysis and imaging techniques to satisfy demanding requirements in magnetic silencing. This report is aimed at investigation of high-precision measurement techniques to be used in the design of a land- or marine-based magnetic test range. Modeling of the dynamic measuring procedures receives our special attention. We use standard field sources and sense coils to simulate magnetic signatures of marine vehicles. A standard field source consists of an array of suitably placed circular coils that carry stabilized currents. Sense coils are cylindrical in shape and detect the magnetic signature (magnetic flux) from the standard source when the source and sensors are moved relative to one another. These signatures are analyzed further for the identification of a magnetic center with our original integral transforms. We simulate four different multipole magnetic sources to calculate magnetic signatures. The standard magnetic field source, which is used in the experiment, includes coils with external diameter of 0.1 m and length 0.02 m. The magnetic moment of each coil is 10 A·m². The estimated error of the magnetic center location with the magnetic signature analysis does not exceed 10% for the 61-point grid. The measurement procedure illustrated could be used to determine the locations of major on-board magnetic sources and identify how to compensate them.

Index terms - magnetic center, magnetic multipole, magnetic signature, magnetic silencing, naval electromagnetics, spherical harmonic analysis.

I. INTRODUCTION

A marine vehicle, such as a ship or a submarine, can produce an external magnetic field by magnetized parts, and from on-board electrical equipment. In military and civilian applications, it is often desired to reduce the external field. Magnetic silencing is the process of reducing the external generated magnetic field. The magnetic signature is the set of magnetic field data obtained when the source (marine vehicle) and sensors move relative to each other [1], [2]. Nowadays magnetic silencing requirements are extremely demanding for a variety of ship classes, since new propulsion systems (including full electric and MHD propulsion) are becoming of increasing relevance for future naval applications. At the same time, a low magnetic signature is a significant factor in the design of future marine vehicles. Improvement of measuring procedures, which use spatial harmonic analysis of magnetic signatures, lead to methods for maintaining low magnetic signatures in ships, subma-

rines and UUV. To retrieve and process data with an adequate precision requires new concepts, which we discuss in the report.

The classical Schmidt approach [3] defines the MC as the location of co-ordinate system origin that causes the zonal and two tesseral quadrupole coefficients of a spherical harmonic expansion of the magnetic scalar potential to vanish. By placement of an appropriate compensating dipole and quadrupole at the MC, the first eight coefficients of the magnetic potential could be experimentally nulled.

For determination for the magnetic center, the first eight coefficients (M_{g10} , M_{g11} , M_{h11} , M_{g20} , M_{g21} , M_{g22} , M_{h21} , M_{h22}) of a spherical harmonic expansion of the magnetic potential are determined. The MC co-ordinates (x_m , y_m , z_m) are calculated according to (1):

$$\begin{aligned} x_m &= (L_0 - M_{g10}D)/(3M^2), \quad y_m = (L_1 - M_{g11}D)/(3M^2), \\ z_m &= (L_2 - M_{h11}D)/(3M^2) \end{aligned} \quad (1)$$

where $L_0 = 2M_{g10}M_{g20} + 3(M_{g11}M_{g21} + M_{h11}M_{h21})$

$$L_1 = -M_{g11}M_{g20} + 3(M_{g10}M_{g21} + 2M_{g11}M_{g22} + 2M_{h11}M_{h22})$$

$$L_2 = -M_{h11}M_{g20} + 3(M_{g10}M_{h21} - 2M_{h11}M_{g22} + 2M_{g11}M_{h22})$$

$$D = (L_0M_{g10} + L_1M_{g11} + L_2M_{h11})/(4M^2)$$

$$M^2 = M_{g10}^2 + M_{g11}^2 + M_{h11}^2$$

The objective of this work is to show how to use magnetic signature analysis to determine the location of an effective magnetic center (MC). A compensating magnetic field source may be placed at the MC to make a vehicle more magnetically silent. The magnetic signatures considered are obtained by a set of measuring coils coaxial with a straight-line trace of the magnetic source. It is known that using the spherical coefficients from the harmonic expansion of the external magnetic field, we can determine the strength and the location of the magnetic dipole source, which is the best fit for the dipole-quadrupole spherical coefficients. This technique is successfully applied to the determination of the MC in geomagnetism [3], [4].

II. METHODS

A. Measurements

Experiments were made at the Facility for Magnetic Measurements of the Magnetism Division, which was designed for magnetic silencing in shipboard type equipment.

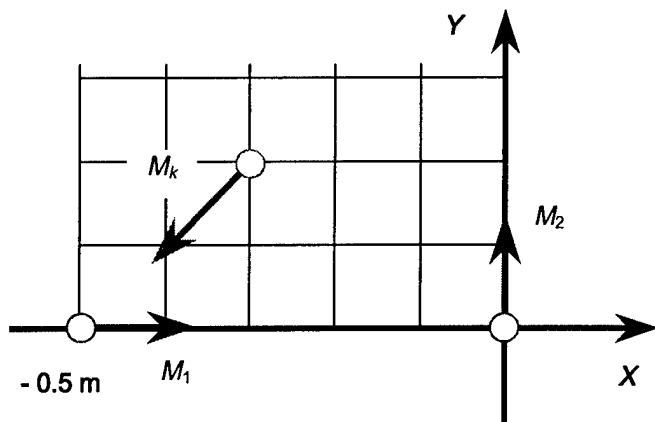


Fig. 1. The standard source No 1 with two equal dipolar coils M_1 and M_2 . M_k represents a compensating dipole at the magnetic center.

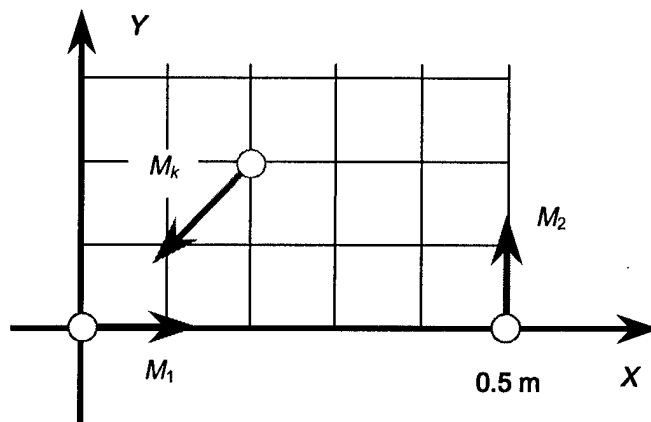


Fig. 2. The standard source No 2 with two equal dipolar coils M_1 and M_2 . This source is created from the source of Fig. 1 by the 0.5-m offset in the x-axis direction.

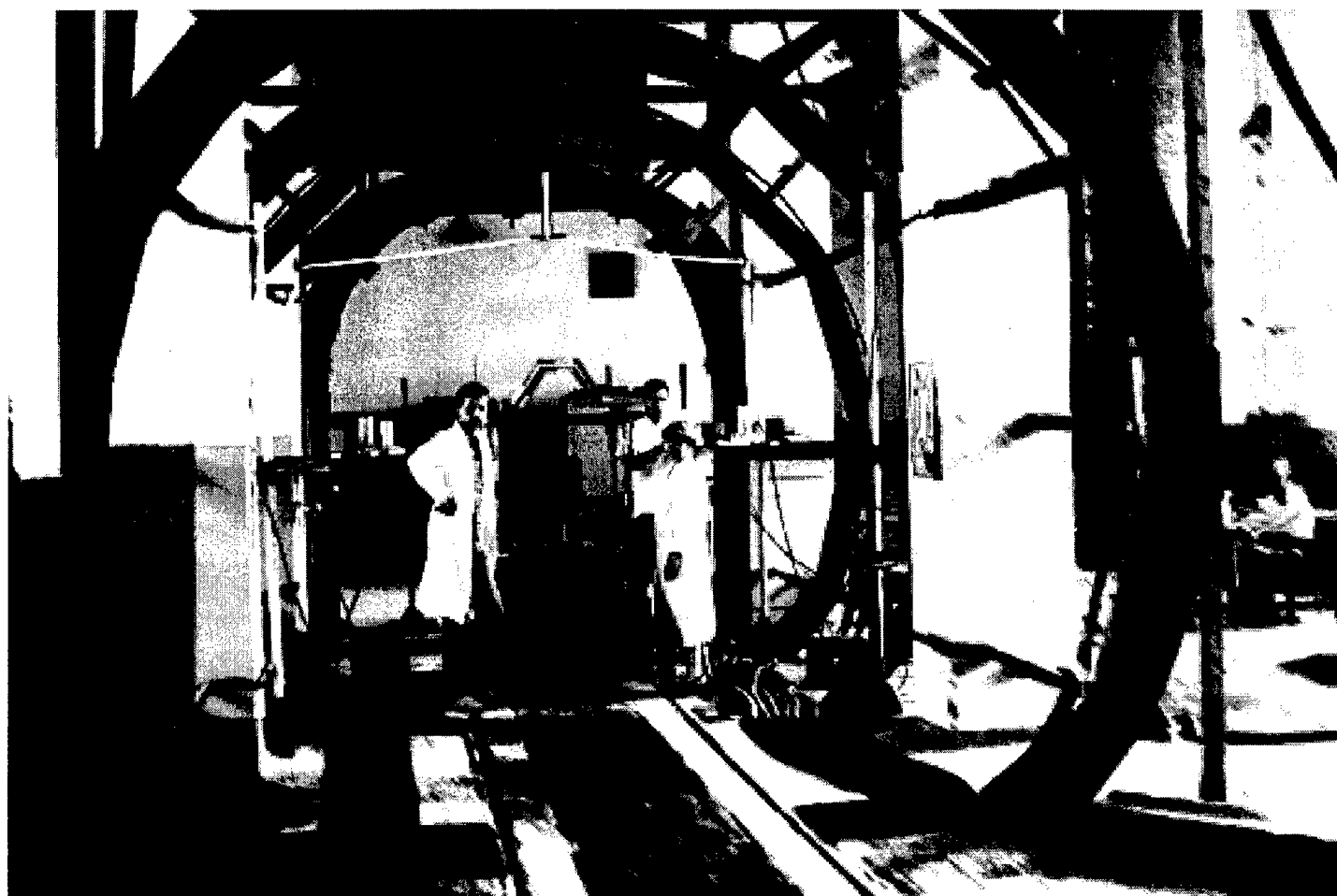


Fig. 3. One of the magnetic measuring systems in the Facility for Magnetic Measurements, Magnetism Division, Kharkov, Ukraine.

The apparatus consists of sense coils on the surface of a 5-m radius cylinder and shares a single polar axis and a single geometric center (the center of the measuring system). This instrumentation includes Helmholtz coils, gradient Maxwell coils and Boev-Ostrovershenko saddle coils [5]. Different types of sense coils used in experimental work are the large circular structures in Fig.

5. Each of these coils is sensitive to a single coefficient of the spherical harmonic expansion of the magnetic field. Thus, we used Helmholtz coils to measure the zonal dipole component M_{g10} and Maxwell coils for the zonal quadrupole M_{g20} . The tesseral and sectorial multipoles were measured by Boev-Ostrovershenko coils. A standard field source consists of an array of suitably

placed circular coils that carry appropriate currents from stabilized generators. Fig. 1 illustrates Source 1 with two dipole coils. Each coil has a radius of 0.18 m and a length of 0.02 m. The current is adjusted so that the magnetic moment ($M = I \times N \times A$: current \times number of turns \times coil area) for each coil is $M_1 = M_2 = 10 \text{ A} \cdot \text{m}^2$.

According to [6] the first eight spherical multipole coefficients of a dipole with coordinates (x, y, z) and magnetic moment $\vec{M} = (M_x, M_y, M_z)$ can be calculated in the following manner:

$$\begin{aligned} M_{g10} &= M_x, M_{g11} = M_y, M_{h11} = M_z \\ M_{g20} &= 2xM_x - yM_y - zM_z \\ M_{g21} &= yM_x + xM_y, M_{h21} = xM_z + zM_x \\ M_{g22} &= (yM_y - zM_z)/2, M_{h22} = (yM_z + zM_y)/2 \end{aligned} \quad (2)$$

Using (2) we can determine that the standard source of Fig. 1 generates the multipoles $M_{g10} = M_{g11} = 10 \text{ A} \cdot \text{m}^2$, and $M_{g20} = -10 \text{ A} \cdot \text{m}^3$, where M_{g10} and M_{g11} are dipole moments and M_{g20} is a zonal quadrupole. The exact location of the compensating dipole M_k that cancels the magnetic field in the remote region was calculated by (1). This dipole with a strength of $14.1 \text{ A} \cdot \text{m}^2$ should be located at the MC ($x_m = -0.3125 \text{ m}$, $y_m = 0.1875 \text{ m}$). Source 2 of Fig. 2 generates a multipole set of $M_{g10} = M_{g11} = 10 \text{ A} \cdot \text{m}^2$, and $M_{g21} = 5 \text{ A} \cdot \text{m}^3$. The compensating dipole ($14.1 \text{ A} \cdot \text{m}^2$) now should be located at the MC ($x_m = y_m = 0.1875 \text{ m}$).

Measurements were made by a precision integrating fluxmeter, when the DC current in the standard source was switched on and off. The sense coil constants were $K_{g10} = 19 \cdot \text{Wb/A} \cdot \text{m}^2$; $K_{g11} = 13 \cdot \text{Wb/A} \cdot \text{m}^2$; $K_{g20} = 4.5 \cdot \text{Wb/A} \cdot \text{m}^3$; $K_{g21} = 2.7 \cdot \text{Wb/A} \cdot \text{m}^3$; $K_{g22} = 3 \cdot \text{Wb/A} \cdot \text{m}^3$. The relative error of the magnetic multipole measurement was less than 5%.

The multipole coefficients for the standard sources were determined using a static technique. That is, the flux generated in the coils described above was measured with the source at a single fixed location relative to the sense coils. From the measured multipole coefficients, the magnetic center was determined according to (1). This experimentally determined magnetic center was compared with the actual value. A compensating dipole of strength M_k was then placed at the experimentally determined magnetic center and the quadrupole coefficients were again measured. This confirmation proved the validity of the magnetic center concept.

B. Digital simulations

A schematic representation of the dynamic measuring system we are modeling [7] is shown in Fig. 4. A marine vehicle moves on the axis of a set of coaxial cylindrical magnetic sensors. A distance meter determines the exact position of the vehicle. A data acquisition system records a magnetic flux through each magnetic sensor vs. distance. A real-time computer program restores the multipole coefficients and the MC of the vehicle.

Computer modeling was used to calculate the magnetic signatures that would be obtained if the standard field source of Fig. 1 or Fig. 2, which simulated the magnetic field of a vehicle, were moved relative to the sensors.

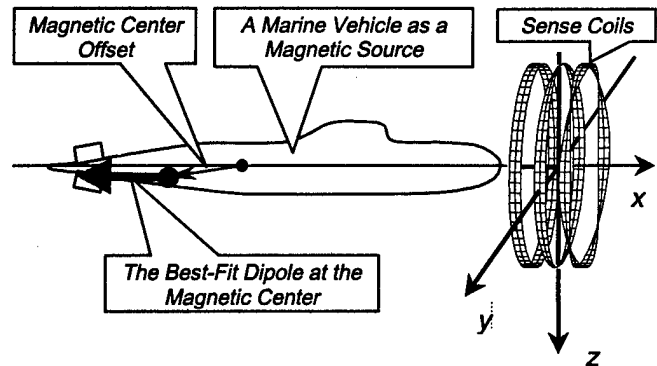


Fig. 4. A measuring procedure for the MC pinpointing.

In addition to the experimental study, two new standard sources (3 and 4) were examined. Source 3 was modeled by two dipoles $M_1 = (-10, 0, 0)$ and $M_2 = (0, 10, 0)$ with Cartesian co-ordinates $(0, 0, 0)$ and $(0, 0.5, 0)$. Source 4 had the same components of its dipole pair, but the co-ordinates of the dipoles were $(0, -0.5, 0)$ and $(0, 0, 0)$.

Fig. 5 shows three types of sense coils, which were simulated in our work. These cylindrical coils detect the magnetic flux from the field source when the field source and sensors are moved relative to one another. In Fig. 5, coil (a) is a gradient coil for detection of zonal multipoles (M_{g10} and M_{g20}) and coils (b) and (c) sense the tesseral M_{g21} , and the sectorial M_{g11} multipoles.

The angular dependence of coil width follows the equations: $x_0 = x_m$, $x_1 = x_m \cdot \cos\phi$, and $x_2 = x_m \cdot \cos 2\phi$. The maximal coil width x_m is 5% of the coil radius r_c , and ϕ is the angle with respect to a fixed direction in the coil.

Fig. 6 shows the calculated magnetic flux vs. distance (magnetic signature) when Source 1 of Fig. 1 is moved relative to coil (a) and (b) of Fig. 5. Fig. 7 displays the magnetic signature when Source 2 is moved relative to coils (a) and (b). Fig. 8 shows magnetic signatures generated by Source 4 in coils (a), (b) and (c) of Fig. 5.

All these signatures use a normalized relative distance t [7], [8]. The actual distance x from the source center to the coil of radius r_c is connected with t at an equidistant grid of $t \in [-1, 1]$, with the following relation

$$x = r_c \cdot t / \sqrt{1 - t^2} \quad (3)$$

To fit the range $[-1, 1]$, each calculated magnetic flux is also normalized relative to its maximal value.

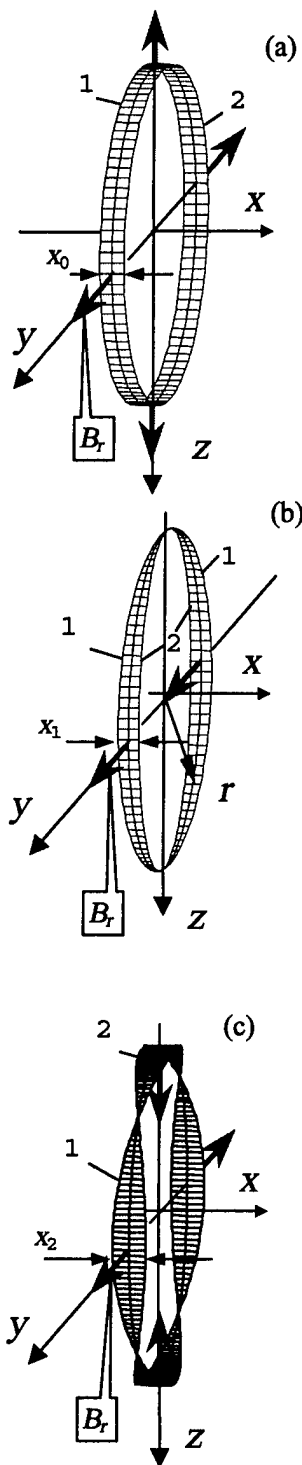


Fig. 5. General geometry of sense coils which have an angle-dependant sensitivity to the radial component of the magnetic field. Arrows indicate polarity of sensitivity.

III. RESULTS

A. Experimental determination of the MC

Our experimental study with Source 1 and Source 2 proves that measuring the multipole coefficients provides an acceptable accuracy for the MC localization.

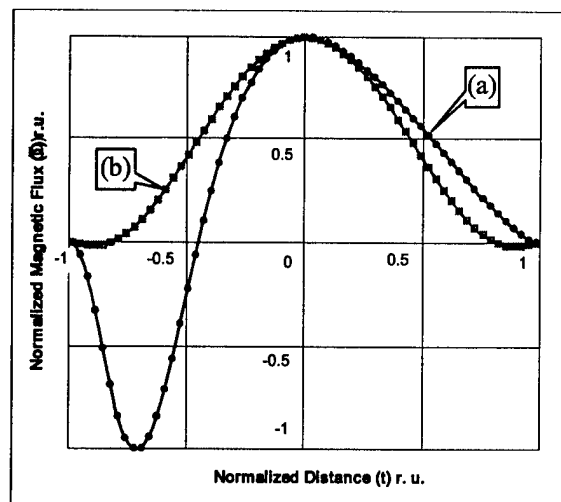


Fig. 6. Calculated magnetic signature generated by Source 1 in coil (a) and coil (b) of Fig. 5.

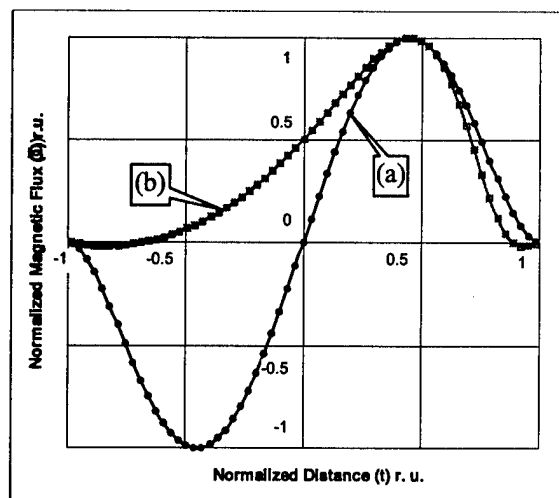


Fig. 7. Calculated magnetic signature generated by Source 2 in coil (a) and coil (b) of Fig. 5.

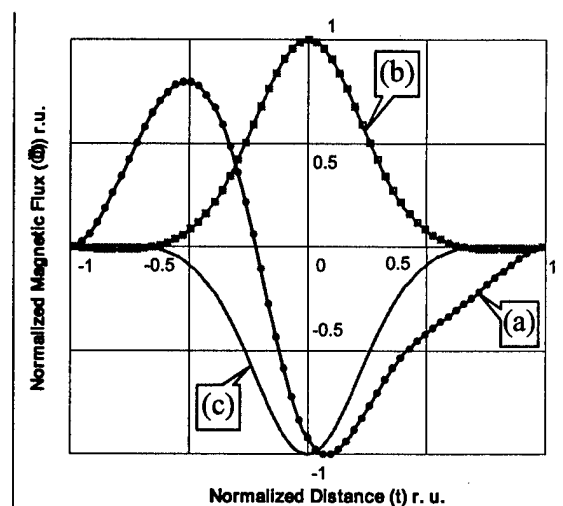


Fig. 8. Calculated magnetic signature generated by Source 4 in coils (a), (b) and (c) of Fig. 5.

Table 1 - Relative error of the digital simulation for the MC pinpointing in the standard sources

Source	Magnetic Multipole			Magnetic Center			Error
	Component	Exact	Modeled	Co-ordinate	Exact	Modeled	
1	M_{g10}^2 (A·m ²)	10	9.937	x_m	0.3125	-0.3357	7.12 %
	M_{g11}^2 (A·m ²)	10	9.927	y_m	0.1875	0.2013	
	M_{g20}^3 (A·m ³)	-10	-10.667	r_m	0.365	0.391	
2	M_{g10}^2 (A·m ²)	10	10.036	x_m	0.1875	0.1842	1.66 %
	M_{g11}^2 (A·m ²)	10	10.027	y_m	0.1875	0.1844	
	M_{g21}^3 (A·m ³)	5	4.93	r_m	0.265	0.2606	
3	M_{g10}^2 (A·m ²)	-10	10.039	x_m	0.1875	-0.1845	1.3 %
	M_{g11}^2 (A·m ²)	10	10.004	y_m	0.1875	0.1855	
	M_{g21}^3 (A·m ³)	-5	-4.944	r_m	0.265	0.2616	
4	M_{g10}^2 (A·m ²)	-10	9.998	x_m	0.1875	-0.161	7.7 %
	M_{g11}^2 (A·m ²)	10	9.935	y_m	-0.3125	-0.296	
	M_{g20}^3 (A·m ³)	5	4.129	r_m	0.365	0.337	
	M_{g22}^3 (A·m ³)	-2.5	2.494				

For Source 1, the measured MC coordinates are $x_m = -0.304$ m, $y_m = 0.184$ m, which are consistent with the actual values ($x_m = -0.3125$ m, $y_m = 0.1875$ m).

For Source 2, the measured co-ordinates of the MC are $x_m = y_m = 0.18$ m, while the actual values, which are given by (1), are both equal to $x_m = y_m = 0.1875$ m.

B. Digital simulations

Table 1 contains the experimental results for four standard sources that simulate magnetic signatures in different coils of Fig. 5. We used the 61-point grid, which was normalized according to (3). The resultant signatures were processed using the digital transforms of [2] and [8]. Thus, valid multipole components were measured. Default values of all other components not mentioned in Table 1 were considered equal to zero.

To evaluate the relative error, the exact values for the multipole co-ordinates were determined using (1). The Cartesian co-ordinates (x_m , y_m) and a resultant offset of the MC $\bar{r}_m = \sqrt{x_m^2 + y_m^2}$ were obtained with (2). The relative error equals $\delta = |1 - r_m / \bar{r}_m| \cdot 100\%$.

Table 1 indicates that with the 61-point grid our method gives a relative error of 8 %, when a zonal quadrupole M_{g20} is generated by the standard source and is less than 2 % without a zonal quadrupole.

There are many directions in which this analysis might be extended, some of which are in progress. One extension would be to design the axial sense coils rather than radial (transverse) sense coils of this report. Another is to develop enhanced signal processing techniques for magnetic signature analysis and as a result, to improve accuracy in pinpointing of the MC. In addition, the prolate spheroidal analysis [7] could be applied to the same problem providing, as expected, better efficacy for axially elongated objects.

ACKNOWLEDGMENT

Support for this work was partially provided by National Academy of Sciences, Ukraine. Computer equipment was donated by Intel Corporation. Dr. Kildishev is supported by a NATO-NSF Grant #DGE 9804545.

REFERENCES

- [1] E. Radoi and A. Quinquis, "A robust discriminant parameter set for the underwater object classification", *OCEANS '97 Proceedings*, vol. 2, pp. 789-794, 1997.
- [2] A. Kildishev, L. Silayeva, and S. Volokhov, "Measuring instrumentation in magnetic silencing: Orthonormal discrete transforms of magnetic signatures," *OCEANS'98 Proceedings*, vol. 1, pp. 522-526, 1998.
- [3] A. Schmidt, "Der magnetische Mittelpunkt der Erde und seine Bedeutung," *Gerlands Beil. Geophys.*, Bd. 41, pp. 346-358, 1934.
- [4] Y. Sano, "A Best-fit eccentric dipole and the invariance of the earth dipole moment," *Journal of Geomagnetism and Geoelectricity*, vol.43, No 10, pp. 825-837, 1991.
- [5] V. M. Boyev and V. T. Ostrovershenko, *USSR Patent No 577 485*, BI No 39, 1977.
- [6] L. D. Landau and E. M. Lifshitz ; "The Classical Theory of Fields," Oxford - New York: Pergamon Press, 1975.
- [7] A. V. Kildishev, J. A. Nyenhuis and A. V. Hetman, "Zonal magnetic signatures in spherical and prolate spheroidal analysis," to be presented at the *MARELEC-99*, 5 - 7 July 1999.
- [8] D. Bojko, A. Kildishev, and S. Volokhov, "An Advanced Technique for the Multipole Imaging of a Magnetic Source: Discrete Transforms in High-Precision Magnetic Signature Processing," *CPEM'98 Digest*, pp. 260-261, 1998.

Analysis of a Multi-Element Multi-User receiver for a Shallow Water Acoustic Network (SWAN) based on Recursive Successive Interference Cancellation (RSIC) Technique

H. K. Yeo, Bayan S. Sharif, Oliver Hinton, A. E. Adams

University of Newcastle Upon Tyne, Newcastle Upon Tyne, England.

Abstracts - A novel technique based on Recursive Successive Interference Cancellation (RSIC) is proposed for cancelling intersymbol interference (ISI) and multiple access interference (MAI), which adversely affect the performance of Shallow Water Acoustic Networks (SWAN). Conventional structures employing decision feedback equalisation (DFE) are known to be effective for intersymbol interference reduction. However, if there are one or more interfering users, the DFE performs inadequately in extracting the useful signal for the weaker user. The performance is further degraded due to power control inefficiency. The simulation results presented in this paper demonstrate the ability of the RSIC structure in mitigating the effect of MAI, ISI and power control inefficiency.

I. Introduction

The multi-element single user receiver structure with decision feedback equalization (DFE) has been shown to be effective in a single user communication, [1],[2] for compensating against Doppler effect, multipath fading propagation, attenuation and intersymbol interference (ISI), etc. In addition to these problems, a shallow water acoustic network (SWAN) exhibits multiple access co-channel interference (MAI). Power control inefficiency is another problem present in a SWAN. Due to the time-varying property of the channel, power control may be difficult to realize. Therefore, the receiver has to cope with the suppression of ISI, MAI and power control inefficiency.

Although the single user DFE is effective against ISI cancellation, it exhibits poor performance in a multiuser scenario. Several types of multiuser detection strategies have been introduced. The multi-user structure described in [3] employs "cross-over" feedback filtering to suppress co-channel interference. The multistage receiver described in [4] was observed to be more effective when the received powers are equal. The

multistage structure based on successive interference cancellation (SIC) [5],[6] was observed to be effective if the received powers are widely variable. However, it is common that the received power in a network communication may be equal, widely variable or slightly variable. Therefore, the design of a receiver structure capable of coping with these problems is desirable. The multi-element multi-user (MEMU) structure based on recursive successive interference cancellation (RSIC) described in this paper combines the features from [4],[5].

The purpose of this paper is threefold. First, we describe a system model which we worked towards for in the simulation. Second, the MEMU structure based on RSIC for tackling MAI, ISI and power control inefficiency is described. Thirdly, we present the simulated results for both the multi-element single user DFE and MEMU based on RSIC.

II. System Model

The channel transfer function for user K , $h_K(f)$, in the context of a direct path with a single interfering path can be expressed as,

$$h'_K(\omega) = (1 + k(t)e^{-j\omega t})h_K(\omega) \quad (1)$$

where $k(t)$ is the time-varying gain-factor for the multipath channel and t is the multipath excess delay, by which (1) can be easily extended to include multipath interfering signals. The receiver equalizer therefore needs to establish a transfer function,

$$G(\omega) = (1 + k(t)e^{-j\omega t})^{-1} \quad (2)$$

Apart from performing the inverse equalization of the channel, the receiver structure has to take into account the effect of co-channel interference from other users. A

simple representation of the received signal can be expressed as

$$y(t) = \sum_{k=1}^K \sum_{\ell=1}^L A_{k\ell} \cdot h_{k\ell}(t - \tau_k) \cdot b_{k\ell}(t - \tau_{k\ell}) \cdot \cos(w_c t + \theta_{k\ell}) + n(t) \quad (3)$$

where K is the number of users, L is the number of elements in the receiving array, $A_{k\ell}$ denotes the amplitude of K^{th} user received signal, b_k denotes the bit sequence of K^{th} user, τ_k , θ_k are the time delay and phase of K^{th} user, $n(t)$ is the background noise and $h(t)$ the multipath channel.

In asynchronous network communication, apart from performing ISI cancellation, the receiver also needs to define when MAI cancellation starts, as shown in Fig. 1.

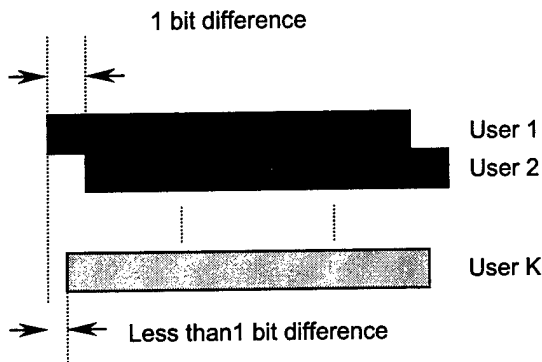


Fig. 1 Asynchronous reception in a network communication.

In block processing, the received signals for each user are grouped into a cancellation window, where the timing between the first bit and last bit of each users is acquired. MAI cancellation starts only when the first bit of the interfering user is detected and ends when the interfering user is absent from the block.

III. RSIC receiver structure

Although the SIC, [4],[5] was observed to be effective in a widely variable received power for users, a major problem occurs when user's signals are received with the same amplitude,

$$A_1 = A_2 = A_3 = \dots = A_k \quad (4)$$

The SIC structure encounters another problem when the received power are varied slightly. For simplicity, we treat user 1 as the strongest user with descending order of powers to user k ,

$$A_1^2 > A_2^2 > A_3^2 > \dots > A_k^2 \quad (5)$$

If the power in $A_1^2 > A_2^2$ is 1 dB, then user 1, although being the strongest user, suffers significantly in the presence of the summed interference of other users.

The improved method proposed in this paper adopts a multistage adaptive DFE decoding receiver structure based on Recursive Successive Interference Cancellation (RSIC), shown in Fig 2.

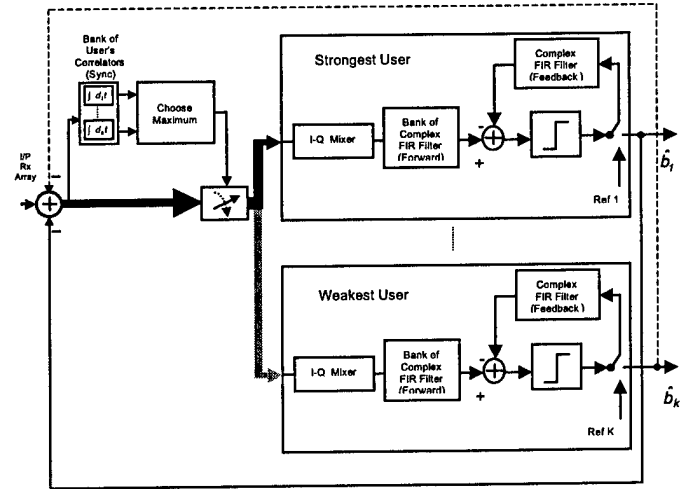


Fig. 2 System model of a multistage adaptive DFE structure base on Recursive Successive Interference Cancellation (RSIC).

The RSIC structure works by first detecting the strongest user from the received signals. Symbols of the strongest user are then decoded and subsequently cancelled from the received signal. Subsequent weaker users are then decoded from the subtracted received signals. This process is repeated until the last or weakest user has been decoded, which is similar to the SIC structure. However, what makes this structure distinctive is the loop-back (dotted line in Fig 2) to the strongest user to cancel out the summed effects from other users. The estimated decision from all the weak users are summed, cancelled from the received signals and the strong user is decoded again with the assumption that only background noise is present. Decoding for weak users are then performed again for a predefined number of loops.

The advantages of implementing this structure are threefold. First, it works as an adaptive multistage DFE parallel interference cancellation (PIC). For users with equal received power, the recursive loop back will eliminate the effects of MAI from each user. Secondly, it also works as an adaptive multistage DFE SIC for users with unequal powers. Observations made from simulation results shows that the loop back feature yields a better performance compared to that of the adaptive DFE "cross-over" feedback equalization

structure, multistage PIC and multistage SIC structure. Finally, by implementing this structure, power control inefficiency in a SWAN can be effectively tackled.

The detector of this form can be described in the following algorithmic form:

- i) Obtain sufficient statistics from the received signal to rank users in descending power.
- ii) Perform adaptive DFE symbol estimation of strongest user.
- iii) Estimated result is cancelled from received signal.
- iv) Subtracted signal is passed to next weaker user for decoding.
- v) Decisions of all subsequent users are summed, fed back to the next stronger user for MAI cancellation.
- vi) Return to ii), repeat ii) to v) where cancellation is perform for the next weaker user for a pre-defined iteration, $u = 2, 3, 4, \dots K$.

In the case when equal power are received between, the process of cancellation is quite identical to the described algorithm: -

- i) Obtain sufficient statistics for the received signal to determine users, if received powers are equal, switch to the first available user. Return to ii), repeat ii) to v) where cancellation is perform for the next weaker user for a pre-defined iteration, $u = 2, 3, 4, \dots K$.

IV. Simulation Results

A. Network setting

The channel model used for the simulation adopts a geometrical multipath propagation which consists of the main or direct path, surface rebound path, bottom rebound path, surface-bottom rebound path and bottom-surface rebound path [7]. Both users uses a common bandwidth from 8 – 12 KHz, with a carrier frequency of 10 KHz. The power spectrum for the signal prior to transmission is shown in Fig. 3, (user 1) and the combined received power spectrum is shown in Fig. 4.

The network setting used in the simulations presented in this paper assumed the following parameters:-

Table 1 Simulation Parameters

Parameters	User 1	User 2
Tx Distance (m)	200	2000
Tx Depth (m)	5	5
Rx Array	6 elements vertical alignment with $\lambda/2$ spacing. Depth of first element : (10 m)	
Channel Depth (m)	20	

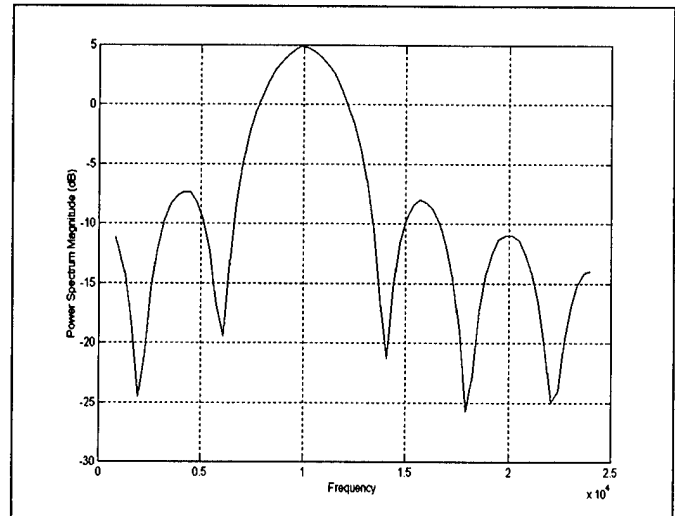


Fig. 3 Power spectrum for user 1 prior to transmission.

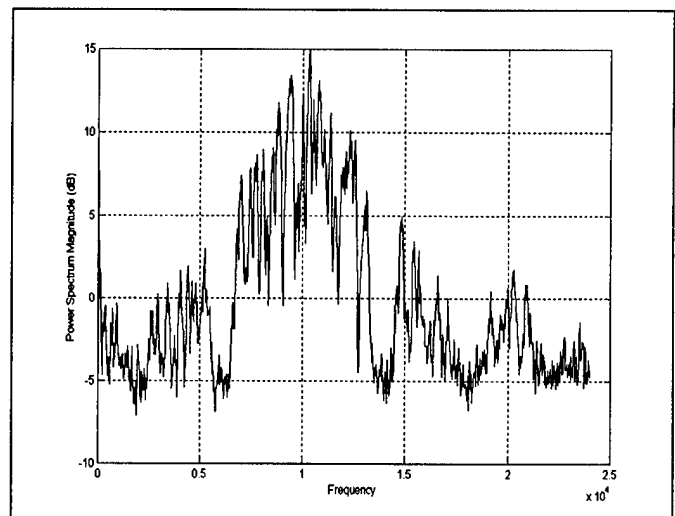


Fig. 4 Power spectrum for combined received signal packet for both user 1 and user 2.

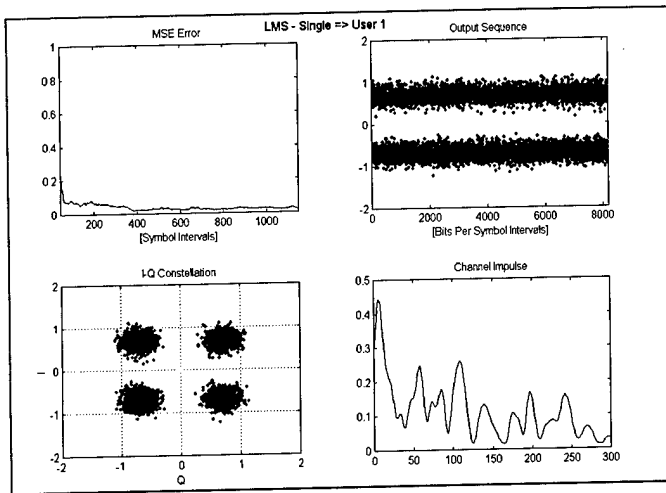


Fig. 5 Graphical output of adaptive DFE single user detection – User 1

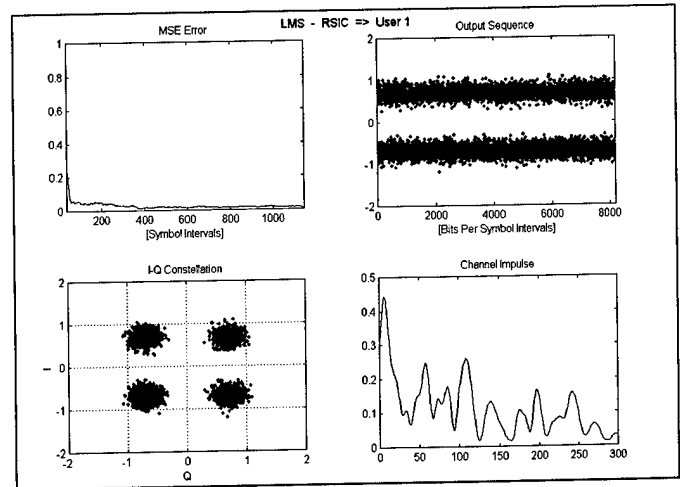


Fig. 7 Graphical output of adaptive DFE RSIC detection – User 1

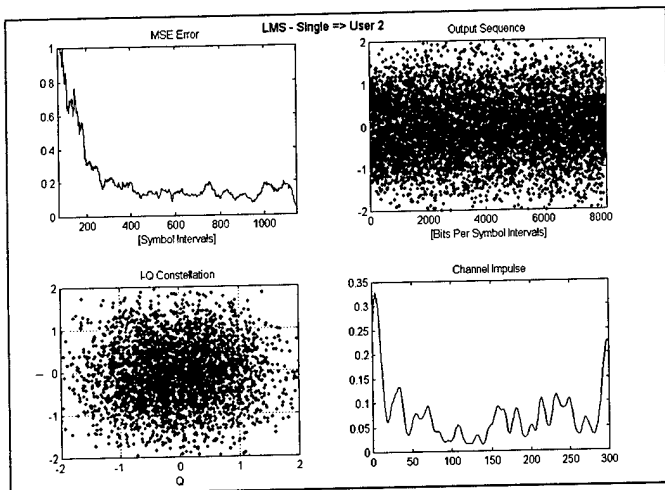


Fig. 6 Graphical output of adaptive DFE single user detection – User 2

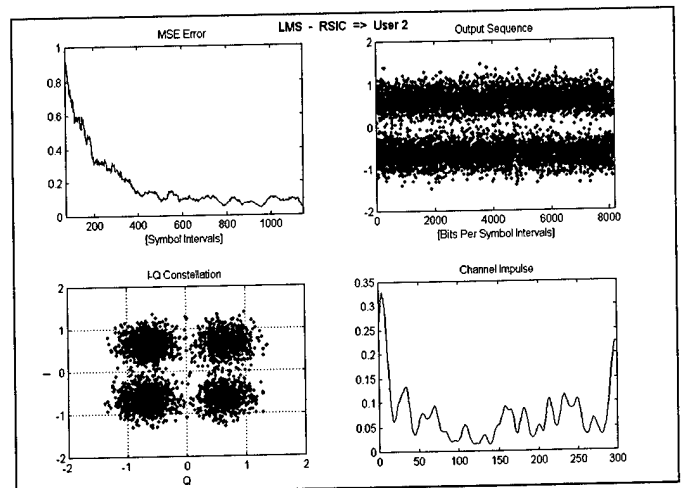


Fig. 8 Graphical output of adaptive DFE RSIC detection – User 2

For both DFE structures, a filter length of 20 and 40 is used for the forward and feedback filters respectively. The input SNRs for user 1 and user 2 are 5 dB and -1 dB respectively. Several adaptive algorithms were employed in the simulation. The results presented in this paper are based on the canonical complex Least Mean Square (LMS) algorithm.

Fig. 5 shows the graphical output (user 1) for the single user DFE structure. Since user 1 has a higher SINR output of 14.331 dB (BER = 0), it was not affected significantly by the interference from user 2. However, the weak user (user 2) was affected by strong MAI from the strong user. The convergence for user 2 shown in Fig 6, was observed to be slow, not being able to extract useful information from the received data. The SINR of user 2 is 4.053 dB with BER of 0.36 (2956 / 8192) where the data packet is of length 8192.

By performing a loop back from the weak user to the stronger user, the output SINR of user 1 shown in Fig. 7,

was improved by another 0.95 dB, resulting to 15.282 dB with BER = 0.

Significant improvement was observed in the weak user when the RSIC structure is used. The output SINR for user 2 shown in Fig. 8, was observed to be 9.106 dB, a 5.053 dB leap jump from the results obtained the single user DFE structure, with BER = 74 / 8192, which is 0.009 of error.

The output SNR is shown in Fig. 9 as a function of the number of elements or diversity order which ranges from $L = 1$ to 6 for user 1. Naturally, the receiver's output SINR improves with the increase of elements. Although suffering negligibly from the interfering weaker user, the SNR output for user 1 was observed to improve with the introduction of the RSIC structure. As for the case of user 2, which suffers from the strong interference from user 1, the single user DFE structure performs poorly even in the presence of diversity order, shown in Fig 10.

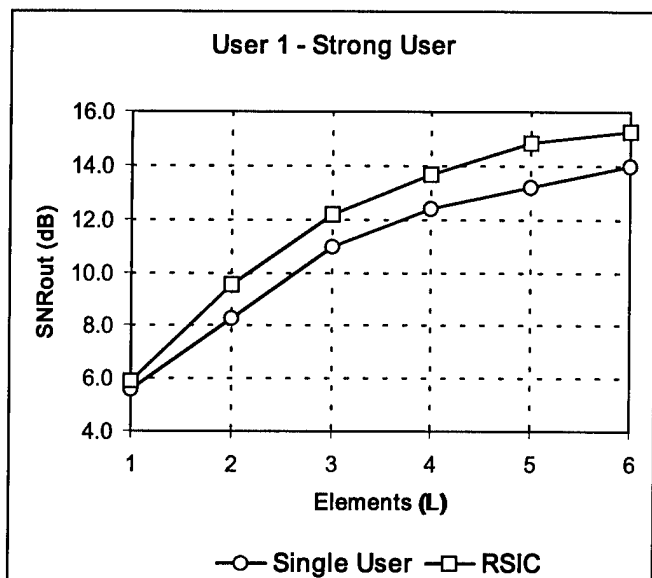


Fig. 9 Comparison of the output SINR, user 1 strong user, as a function of diversity order.

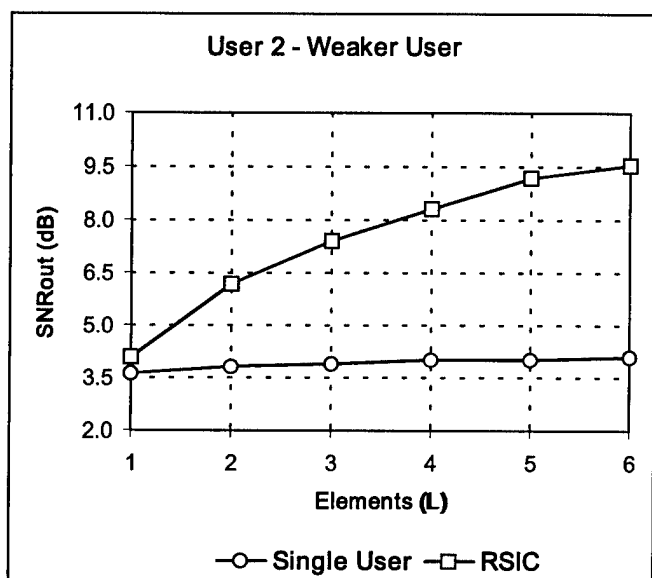


Fig. 10 Comparison of the output SINR, user 2 weak user, as a function of diversity order.

As the strong interfering signal from the received signal had been eliminated, the RSIC structure is able to extract useful information for the weak user.

With $L > 2$, the results obtained by the RSIC gives a better result than that of the single user DFE structure. At $L = 6$, the RSIC structure exhibits a 5.053 dB improvement as compared to that obtained by the single user DFE. Therefore the simulation results suggests that the RSIC structure is a potential candidate for ISI and MAI cancellation under inefficient power control scenarios.

IV. Conclusions

This paper presented a multistage MEMU adaptive decision feedback equalization receiver structure based on recursive successive interference cancellation (RSIC).

The simulation results suggest that the RSIC structure is suitable for a wide range variation of received power. The results also suggest that in the absence or inefficiency of power control in a shallow water acoustic network (SWAN), the RSIC structure is robust in extracting useful from the received data.

Reference

- [1] Shahid U. H. Qureshi, "Adaptive Equalization", Proc. IEEE. Vol 73, No 9, Pg 1349 – 1387, 1985.
- [2] Milica Stojavonic, Josko A Catipovic, John G. Proakis – "Phase-coherent digital communications for underwater acoustic channels." IEEE Journal of Oceanic Engineering, Vol. 19, No 1, pg100, January 1994.
- [3] Milica Stojavonic, Zoran Zvonar, "Multichannel processing of broad-band multiuser communications signals in shallow water acoustic channels." IEEE Journal of Oceanic Engineering, Vol. 21, No. 2, pg156, April 1996.
- [4] Behnaam Aazhang, majesh K. Varanasi, "Multistage Detection in Asynchronous Code-Division Multiple Access Communications." IEEE Transactions on Communications, Vol 38. No 4, pg 509, April 1990.
- [5] Pulin Patel and Jack Holtzman, "Analysis of a simple successive cancellation scheme in a DS/CDMA system." IEEE Journal on selected areas in Comms, pp 798 – 807, June 1994.
- [6] Y. Cho, J. H. Lee, "Analysis of an Adaptive SIC for Near-Far Resistant DS-CDMA." IEEE Transactions on Communications, pp1429 – 1433, November 1998.
- [7] Adam Zielinski, Young-Hoon Yoon and Lixue Wu, "Performance Analysis of Digital Acoustic Communication in a Shallow Water Channel." IEEE Journal of Oceanic Engineering, vol 20, No. 4. Oct 1995.

MICRO ROV FOR UNDERWATER OBSERVATIONS

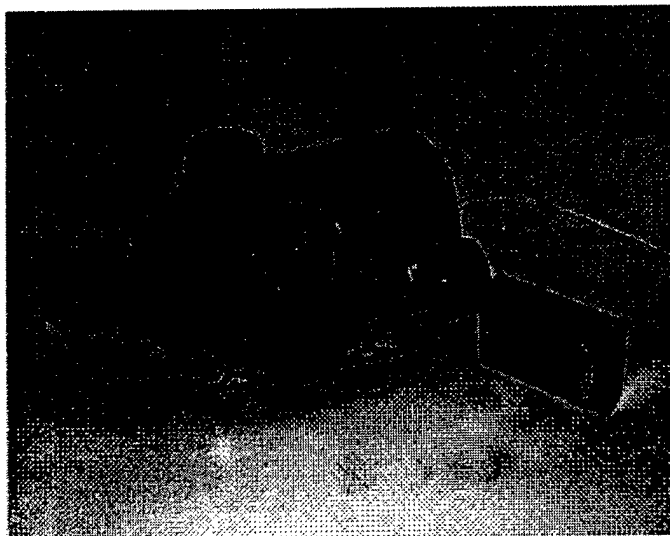
Boris J. Rozman, Lev L. Utyakov

P.P. Shirshov Institute of Oceanology of Russian Academy of Sciences,
Moscow, Russia

Abstract. In 1999 P.P. Shirshov Institute of Oceanology RAS together with Industrial electronics (Indel) company, Moscow, designed and tested a small sized microROV «GNOM» intended for underwater investigations and observations. It contains video camera, thrusters, lights and sensors. GNOM operates from on board console by joystick or computer's keyboard via coaxial cable and video picture displays on TV or monitor.

Technical parameters

- max depth - 100m
(up to 6000m in a development)
- length of cable max - 100m
- type of cable - coaxial - 2 wire
- volume - 1...3dm³
- videocamera b/w 420lines, 72-90grad, 0.1 lux
- supply voltage - 100V DC.
- max current - 1.5A
- max speed (horizontal) - 0.5m/s
- number of thrusters - 4



One of applications are surveys and investigations of sunk ships and other objects. It is a very important problem a penetration inside spaces via small sized wrecks and holes for translation video from there. Existing ROVs [1,2,3] allow to do this but have limitation connected with their size and powered tether and problems with remote control. Such ROVs request big power for thrusters as well. It is very critical when ROV penetrates inside and begins to turn to other sides. At that moment they must pull the tether with increased force. And sometimes occur situation when the tether ravel and blocks movement. As a result of that is losing of ROV. The risk of losing becomes much more if ROV moves further and further inside. It is also problem to return it back. Besides, such ROVs are expensive (tenth and hundred of thousands dollars).

Another important problem is bringing the ROVs into those objects. This problem becomes very complex when those objects are at big depth.

Realizing all mentioned problems we decided to design a new generation of small size ROVs for survey and inspection of internal spaces of submerged objects. We named it "GNOM" (abbreviation of 4 Russian words meaning: Deep-sea unmanned observing microRov).

In collaboration with the company INDEL, Moscow, we have made few modifications of submersible vehicles and different modifications of operational terminals. These GNOMs are electronically identical, but each of them is equipped with different kind of thrusters, video-cameras, lights and sensors.

In the nearest future we intend to install several GNOMS on each of manned submersible research vehicles "MIR-1" and "MIR-2" capable to dive up to 6000 m. GNOM is simple, low-cost, small size vehicle. Due to small size (near 1.5dm³) and thin tether (d=1.2mm, length 100m) it can penetrate inside sunk ships and other underwater objects. Two marsh thrusters ensure horizontal movement forward and backward with max. speed of 0.5 m/s and rotation in both directions, two vertical thrusters ensure movement up and down with speed near 0.2 m/s. Lights based on 6 LEDs ensure visibility up to 5m in full darkness in clear water. Power supply (100 V DC), controlling commands from the joystick or keyboard and a video signal from the camera are transmitted via coaxial tether. We made on table equipment including all power supplies and electronics in one monoblock. This box (size LxWxH = 300x300x150 mm) with galvanic isolation is connected to joystick, TV (RF input) and to GNOM, its input power is equal to 220/110 VAC. This block has a built-in microcomputer which processes signals from the joystick and transmits the digital data via modem and coaxial cable to GNOM. It also receives digital signal from GNOM's sensors, processes them and indicates the information at the front panel of the box. Such power and information transmission is ensured by half duplex data channel between on board equipment and GNOM. The modem provides modulation and demodulation of video and control signals. Maximum operational depth of existing sample is 100m. We also develop samples able to operate at a depth of 6000 m, and we plan to test it this year on board the submersible MIR.

One of the possible applications of the GNOM are common works with submersible vehicles such as manned vehicles and unmanned ROVs. We plan to develop such research systems using the GNOMS for scientific and industrial aims.

References.

1. Remotely Operated Vehicles of the World 96/97, Edition, 404p.
2. Sea lion AUV/ROV Review 1991-92. Fourth Edition. Proceedings. P.O. Box 261149, San Diego, California 92196, USA, June 10-12,1992, p.134.
3. D. Wettergreen, C. Gaskett, A. Zelinsky. Development of a Visually-Guided Autonomous Underwater Vehicles. OCEANS'98 IEEE/OES Conference Proceedings. Nice, France. Volume 2.

NEW GENERATION OF TECHNICAL MEANS AND METHODS FOR OCEAN MONITORING SYSTEMS

L.L. Utyakov, D.G. Levchenko, I.S. Kovchin

P.P. Shirshov Institute of Oceanology of Russian Academy of Sciences, Moscow, Russia

A.A. Paramonov

Experimental Design Bureau of Oceanology Techniques, Moscow, Russia

M.A. Shakhramanian

Ministry of Extreme Situations RF, Moscow, Russia

Abstract. P.P. Shirshov Institute of Oceanology and Experimental Design Bureau of Oceanology Techniques of Russian Academy of Sciences have achieved certain progress in creation of new research equipment for long-term monitoring of marine areas. There are autonomous bottom stations of new generation, Shipboard equipment for research vessels and Computing centers. This equipment has designed for solution of the modern tasks: ecological monitoring, prediction of the strong earthquakes, investigation of large ocean whirlwinds, and another goals.

Specialists of P.P. Shirshov Institute of Oceanology of Russian Academy of Sciences (IO RAS) and Experimental Design Bureau of Oceanology Techniques (EDBOT) have achieved certain progress in creation of new generation of technical means and methods of highly effective long-term monitoring of large marine areas. They have designed autonomous bottom stations (ABS) which measure parameters of near bottom water layers (velocity and direction of currents, temperature, pressure, optic and other parameters). The operational principles of the devices is based on acoustic or inclination registration method of float deviation caused by current. The use of original technical diagrams and design solutions allowed to increase their efficiency reliability, prolong the autonomous of their operation, decrease the energy consumption, their weight and size, the price of their manufacture, to make

their installation and exploitation. The stations contain hydroacoustic digital channel, which allows remote record of measurement results. Such channel provides a considerable decrease of the exploitation cost of the distributed net composed of these stations. There is no more need in lifting the stations for receiving records and their further reinstallation. First samples of near bottom current meters were made in 1994 and were tested at the NS "Komsomolets" in Barents Sea.

The installation of distributed nets ABS for long term (for several years) hydrophysical monitoring of large areas (for example in the Arctic Basin) is very perspective for the study of both hydrophysical processes and transport and exchange processes. There are following advantages of their use: possibility of the stations exploitation in ice regions; small energy consumption of ABS, which are equipped with energy independent numerical solid storage of information, and availability of adaptation working regime, which ensure their reliable functioning during 3-5 years without changing the energy piles; small Weight and size of ABS make the transportation of the stations much easier and reduce troubles connected with their installation; distant record of data simplify considerable their exploitation.

It is observed the some development the modern vessel technologies of the Oceanology researching in IO RAS. By the economic conditions and the activity in the marine

management in Russia the development of the technologies of the present-day experimental Oceanology went along the path of higher information ability and representativeness of the observation techniques followed with ship underway. This, in practice, is implemented as follows:

integration in one shipborne measuring - information system based on the computer network of towed hydrophysical, seismic and hydrochemical complexes, XVT - zonds, shipborne acoustic Doppler profiler, side scan and multibeam sonar, bottom seismic acoustic profilers together with satellite navigation and communication systems;

equipping the stand - alone mooring measuring system with data - logger acoustical retranslators for ships passing by;

extension of express analysis of sea water and development mini - ROV operation with the ship under way;

organization on ships of reception of data from satellite information on currents, swell, and level fluctuations, cloudiness and condition of the ice cover for monitoring and prediction of the hydrometeorological and ice situations.

Following these trends in the development of the science consuming technologies the Shirshov Institute of Oceanology has been performing work on instrumental refitting of research vessels: "Academic Sergei Vavilov"; "Academic Ioffe", "Professor Shtockman" making specimens of new equipment and elaboration of procedures for implementation of measurements and interpretation data obtained.

UNDERWATER RESEARCH OBSERVATORY

This project is carrying out by EDBOT and 10 RAS under State contract with Ministry of

Science and Technology of Russian Federation.
Date of project finish is December of 2000.

Project description

Project intended to creation of bottom research multifunction observatory as a complex of unique oceanology measurement instruments, which are united in structure and system modular unit for research of geophysical and geochemical processes in near-bottom stratum of the World Ocean, continental shelf and inland basins to carry out researches of nature and man-made ecology disaster situations in sea areas and coastal zones (earthquakes, tsunami).

Geophysical networks in the ocean may be deployed in the base of this complex. Observatory will have special value to solve the tasks of Earth crust researches and to estimate the level of seismic and ecology emergency of some regions.

Observatory is based on autonomous bottom hydrophysical station with enhanced possibilities in measured parameters, capacity of information to be write, process and transfer. It has features for receiving and transfer large arrays of information to computer center.

Observatory allows uninterrupted data registration and transfer via cable during not less than 1 year, in autonomous mode not less than 2 months.

Configuration of underwater research observatory

- I. Underwater complex (UC);
- II. Computing Center (CC);
- III. Shipboard Set (SS).

UC - stationary unmanned measuring system, which is intended to long-term data acquisition and transfer of data via communication to CC. UC communicated to cable communication line with length of 10 km to CC as it has cable communication unit.

Underwater Complex (UC)

UC carrying out such functions as:
measuring of geophysical and geochemical parameters;
magnification and filtration of signals from sensors and hydroacoustic antennas;
analog-to-digital conversion of analog input signals;
data lock-on precise timing;
digital data processing and acquisition in capacity not less than 2 Gb;
holding of registered and processed information and transfer of it via communications;
testing and diagnostics;
changing of working modes by remote control commands from CC;
working with cable during not less than 1 year, in autonomous mode not less than 2 months;
availability equipment on depth to 6000 m.

Configuration of UC

- 1 - registration and control unit;
- 2 - hydrophysical unit with sensors of temperature, static pressure, current vector and conductivity;
- 3 - underwater spectrum analyzer;
- 4 - three-component bottom seismometer with vertical orientation system and azimuth meter;
- 5 - sensor of magnetic field;
- 6 - hydroacoustic communication and navigation unit;
- 7 - radioactive contamination monitoring unit;
- 8 - radio satellite communication unit;
- 9 - hydroacoustic ballast releaser;
- 10 - power supply unit.

Computing Center (CC)

CC carrying out such functions as: data processing computer with operational system Windows control; time-signal service based on GPS or atom time via global network INTERNET; module of the cable communication line to underwater complex; Internet-server based on

specialized computer for wide-range access to the received information, also in a real time scale.

Shipboard Set of equipment (SS)

SS carrying out such functions as: computer for testing of UC and data processing of the information; time-signal service based on GPS for synchronization and binding of the data with uniform time; hydroacoustic communication and navigation unit; launch and rising facilities;

Area of application

Fundamental problems

- Study of a Earth crust structure in some areas of the World Ocean;
- The research of ensemble of geophysical fields in tectonic ruptured zones directly at ocean bottom;
- Research of a condition of sea environment in near-bottom zone and its interaction with tectonic processes;
- Geophysical monitoring of complex hydraulic engineering structures;
- The generalized modeling of a seismic and ecological condition of area, factor analysis with data accumulation and generalization for expert estimations.
- Operative estimation of seismic and hydrodynamical conditions of areas both forecasts of probable seismic and ecological consequences.
- The early warning of earthquakes and tsunami.

Applied tasks

- Revealing of harbingers seismic, geochemical, hydrophysical sightings of catastrophic earthquakes, which sources are under ocean bottom, the realization of the intermediate term and short-term forecast of earthquakes with magnitude 5.5 and higher;

- Essential increase of accuracy of the tsunami forecast;
- The control of changes of the stressdeformed condition of Earth crust sites of shelf zones next to developed deposits of petroleum and gas caused by extraction of carbohydrates, edge waterflooding and other artificial influences on a petroleum layer;
- Choice of ecologically safe modes of operation in deposits,
- The forecast of propagation of Earth crust deformations and induced seismicity.
- The forecast of small local earthquakes, dangerous damages of boreholes, petroleum platforms or underwater pipelines.

References

1. Levchenko D.G., Soloviev S.L., Son`kin A.V., Voronina E.V. Recording of ocean-bottom seismic noise and of a strong earthquake in the Himalayas by broadband digital OBS installed on the Mid-Atlantic ridge. *Physics Earth and Planetary Interiors*, 1994, v.84, p.305-320.

2. Levchenko D.G., Rozman B.Ya-, Utiakov L.L., Shahramanian M.A. The Bottom Stations for geophysical monitoring and warning of Earthquake and Tsunami. Abstracts of the Oceanology International Conference 01-96. Brighton, United Kingdom, V.3, 1996, p.341-344.

3. Levchenko D.G., Zhdanov M.A. Some Theoretical and Experimental Results of the Sea Bottom Microseisms Research for Broadband Frequency Range. Abstracts. XXV General Assembly ESC. September 914, 1996. Reykjavik, Iceland. P.39.

4. Levchenko D.G., Kuzin I.P., Kovachov S.A. Kamchatka project of the bottom monitoring sistem. Extending Abstract of the International Workshop on Scientific Use of Submarine Cables. Okinawa, Feb. 2528, Japan. 1997.

5. Levchenko D.G., Rozman B.Ya., Utyakov L.L. The Complex Bottom Station for Registration Geophysical and Hydrochemical Forecastings in the Epicenter Area of the Expected Strong Earthquake on subductive Zone. Abstracts of the Oceanology International Conference 01-97. Pacific Rim. Singapore, 1997, p.41-48.

6. Merklin L.R., Utyakov L.L. Russian Oceanology Goes to Ocean Monitoring Through Intellectual Multisensors Nets. *Sea Technology*. August, 1998, p.49-53.

7. Utyakov L.L., Donev V.S., Shekhvatov B.V., Slabakov Kh.D. ShoreBased Telemetry System for Oceanologic Studies. *Oceanology*. Vol.28, N21, 1988, p.135-137, Moscow, Russia.

ACOUSTIC TOMOGRAPHY OF EDDY IN THE WESTERN MEDITERRANEAN SEA.

Y.A.Chepurin, V.V.Goncharov, D.L. Aleynik

P.P.Shirshov Institute of Oceanology of Russian Academy of Sciences, Moscow, Russia

Abstract Acoustic tomography experiment THETIS-2 was conducted in 1994 in the Western Mediterranean. Seven moored transceivers formed the tomography network. Our acoustic measurements were carried out with a single hydrophone deployed from drifting research vessel "Akademik S.Vavilov" (IORAS, Russia). A CTD survey was also made. An interthermocline eddy with a cold core was found during this experiment. Acoustic signals from the transceivers were recorded at 16 points within and around the eddy to study the feasibility of reconstruction of such mesoscale inhomogeneities by acoustic tomography means. The result of such reconstruction was presented.

A tomography network of seven moored transceivers was deployed in the Western Mediterranean Basin in early 1994 by IfM (Kiel, Germany), IFREMER (Brest, France) and WHOI (Woods Hole, U.S.A.) in the framework of the European project THETIS-2. The locations of the THETIS-2 transceivers are shown in Fig.1.

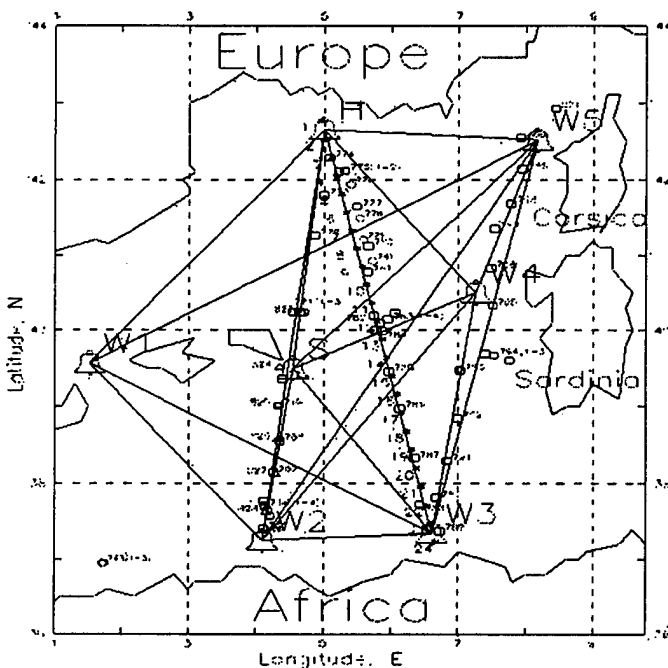


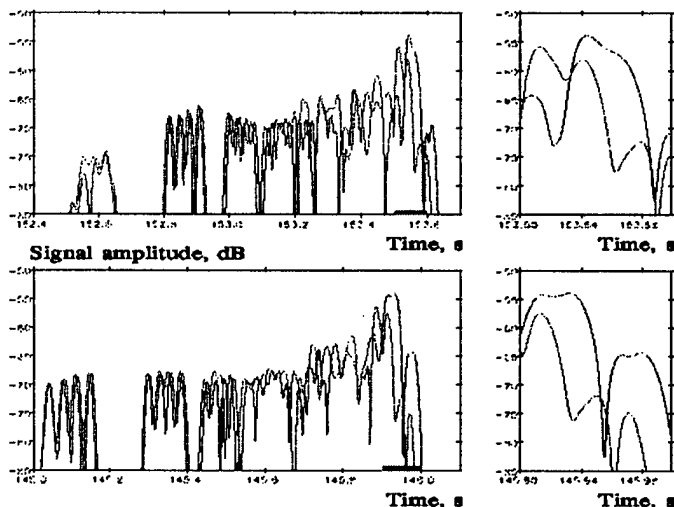
Fig.1 The general View of experiment

They are labeled according to the notation accepted by THETIS-2 participants. These devices were moored

near the sound channel axis approximately at a 150 m depth. Transceiver H had the central frequency of 250Hz, all the others operated at a central frequency of 400 Hz. The emitted signals were M-sequences. These signals were also utilised in the Moving Ship Tomography (MOST) experiment [1,2]. It was fulfilled by the research group from IORAS and MIPT during the expedition on-board of R/V "Akademik S.Vavilov" of the Russian Academy of Sciences. Simultaneous operation of the traditional tomographic network and a specialised acoustic R/V in the same area created a unique opportunity to assemble the experimental data for adequate comparison of traditional and dynamic tomography under the well-controlled environmental conditions. The single receiving hydrophone was deployed from the R/V drifted with engines turned off to decrease the ship's noise. The receiver depth was 270-300 m. The hydrophone position of 150-200 m off the sound channel axis was chosen to maximise the number of resolvable ray arrivals. Each acoustic reception was accompanied by the CTD measurements to a depth of at least 700 m. In addition to our CTD measurements a series of XBT casts was fulfilled in the framework of the THETIS-2 project. The recorded acoustic signals were complex demodulated and correlated against the transmitted replica. For coherent averaging of the received signals a special computer algorithm was developed to measure and remove the Doppler frequency shift due to the R/V drift [3]. Hence for each point of measurement we have a set of arrival patterns of acoustic signals through the different eigenrays from different transceivers. The time resolution was 10 ms and 16 ms respectively. Thus, R/V motion inside this region sufficiently increased the number of tomographic traces in comparison with the traditional approach.

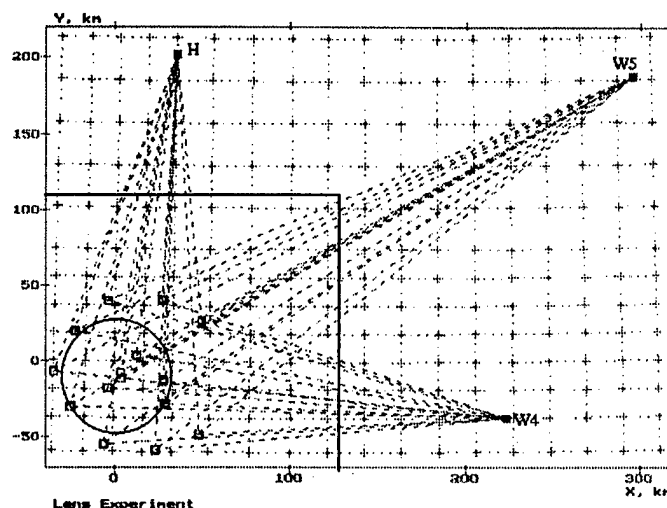
Our CTD survey in the North-Western part of the Algeria-Provensal Basin revealed a cold low-saline interthermocline eddy. T and S contours of the eddy were ellipsoidal in plane and had the axes of about 45 and 85 km. The vertical extent of the eddy was about 400 m. The core situated at depths of 150-200m. It differed from the surrounding waters at the same depths by 0.8°C in temperature and 0.4 psu in salinity. The observed structure is not typical for the summer period in the surveyed region. The data of our CTD and independent XBT measurements (Dr. C. Millot, COM-CNRS) were compared with the climatic fields from NODC-94 monthly Atlas averaged for July. 3D fields of temperature, salinity, density, heat and salt anomalies,

The main effect of eddy onto the arrival pattern is the prolongation of the received acoustic signal [4]. Acoustic rays propagated near the axis of the sound channel intersect the eddy with angles which are less than those for the other rays. Thus the influence of the cold eddy on such rays was more significant. Their arrival times were increased greater with respect to other rays. It is very important for us, because we use the dynamic tomography approach. The absolute propagation times of the emitted signals were measured with errors, which were due to GPS navigation inaccuracy. This was essential for our tasks. In Fig.3, one can see the effect of increasing the time duration of received signal with respect to the adiabatic normal mode theory prediction.



under the presence of the inhomogeneity. The receiver was located within the eddy (lower plot) and behind the eddy with respect to the source (upper plot). The final parts of the arrival patterns (underlined with brown on the left plots) are reproduced on the right on a large scale.

The scheme of our experiment in the horizontal plane was presented in Fig.4.



Points H, W4, W5 correspond to the appropriate sound sources, marks “□” corresponds to the reception points which were already processed and whose data are valid. The dashed lines are the acoustic traces. The other 4 sources (W1,W2,W3,S) have not been used in our postprocessing yet due to there weak signals. The position of eddy is presented in the lower left corner of this figure. The sound speed profiles (ssp) at points marked “+” belong to background sound speed field, that was constructed from the Levitus data bank. The same “background” ssp were taken at the points of sources and receivers locations. We interpolate linearly the ssp for the points of intersections of sound traces with the dashed lines according to:

where only 2 or 3 of A_{ij} are nonzero. According to Munk's the liner scheme [5] each vertical plane including acoustic trace contains all parameters of eigenrays between the source and the receiver. All coefficients of linear equations associated with the ssp variations versus time delays are found as:

$$\sum_{ijk} B_{ijk}^l \cdot \Delta C_{ijk} = \Delta T_l = T_{le} - T_{lo}, \quad (2)$$

T_{le} and T_{lo} are the measured and calculated times along the l -th ray. In the case of dynamic tomography we used the differential scheme. So we looking for the difference of equations (2) with one of this set (the reference rays are exists). Thus, we can obtain the system of linear equations, where ΔC_{ijk} are unknown.

The number of these equations are too large and it is equal to the number of the ssp multiple the number of horizons. We can reduce this number sufficiently by taking into account only the active layer of water (0 - 500m) and only the region where the eddy can be found. The next step is to make our tomography scheme been horizontal only. For this purpose let us sum (2) trough vertical. As a result, we obtain the system:

$$\sum_{ij} \overline{B}_{ij}^l \cdot \Delta C_{ij} = \Delta T_l = T_{le} - T_{lo}, \quad (3)$$

which contains sufficiently smaller number of unknown variables and can be solved by the standard tomography methods [6]. At the first step this scheme was tested via model experiments. The results seem good. The real experiment, as usual, provide us a set of difficulties associated with rays' identification. To avoid them we changed slightly the receiver location (depth and distance to the source). We also calculated the correct time delays (arrival pattern) using the real (measured) sound speed field with the eddy. This way we identified some rays and found necessary time delays which were within the of experimental errors. The results of such reconstruction of the eddy are presented in Fig. 5.

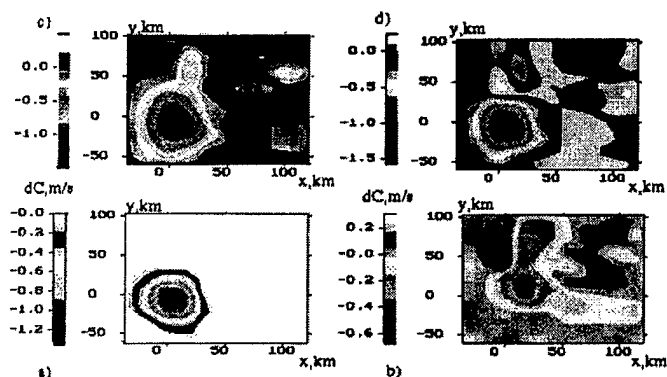


Fig.5 The results of the tomography reconstruction
a.) original eddy, b.) 9 traces, c.) 15 traces, d.) 28 traces

The different plots correspond to the different number of points of receptions taken into account. So one can see that the result becomes better when these number becomes larger. When the number of processed traces becomes more then 20, the result of tomography reconstruction of the eddy became better a little. This is the effect of saturation.

As a conclusion we can say that the proposed tomography scheme may resolve eddies in the horizontal plane. The results of the horizontal 2D inversion can be used for the reconstruction of the eddy in the vertical planes to investigate the structure of the eddy in more details.

This work was supported by the grant of Russian Academy of Sciences.

References

1. O.A. Godin, S.V. Burenkov, D. Yu. Mikhin, S. Ya. Molchanov, V.G. Selivanov, Yu. A. Chepurin, and D.L. Aleynik, "An experiment on dynamic acoustic tomography in the Western Mediterranean" // *Doklady Akademii Nauk*, 1996, v.349, N3, pp.398-403
2. D.Yu. Mikhin, O.A. Godin, Yu.A. Chepurin, S.V. Burenkov, V.V. Goncharov, V.M. Kurtepov. An experiment on acoustic tomography of Western Mediterranean from a moving ship. *Proc. 3d European Conference on Underwater Acoustics*, ed. by J. S. Papadakis Heraklion: FORTH- IACM, 1996, v.2, pp.821-826
3. Aleynik D.L., Burenkov S.V., Chepurin Yu.A., Godin O.A., Mikhin D.Yu., Molchanov S.Ya., Selivanov V.G. 1994 moving ship tomography experiment in the Western Mediterranean. *JASA*, V.97, N5, Pt.2, p.3264, 1995
4. Aleynik D.L., Burenkov S.V., Chepurin Yu.A., Godin O.A., Mikhin D.Yu., Molchanov S.Ya., Selivanov V.G. Acoustic footprints of an in thermocline eddy: Field experiment and numerical simulation. *JASA*, V.97, N5, Pt.2, p.p.3264-3265, 1995
5. Munk, W., P. Worcester, and C. Wunsch. *Ocean Acoustic Tomography*, Cambridge Univ. Press, 1995.
6. Goncharov V.V., Zaytsev V.Yu., Kurtepov V.M., Nechaev A.G., Khilko A. 1. "Akusticheskaya tomografiya okeana", 1997, IPF RAN, N. Novgorod. russ.

Implementing a 4000 meter HDTV Camera System

Mark Chaffey

MBARI
7700 Sandholdt Rd., PO Box 628
Moss Landing,
CA 95039-0628

Email: chma@mbari.org

Abstract - The video systems on MBARI's Remotely Operated Vehicles (ROV's), Ventana and Tiburon, are the single most important data source. Real-time images are uplinked for scientific observation, used as data for post mission processing, and provide visual information for the pilots operating the vehicles. The technical standard used to define television equipment -and the maximum resolution - used throughout North America has been little changed since the development of color television in 1949. Advances in digital electronics and data compression algorithms combined with the United States Governments desire to remain competitive in the international television market has resulted in the approval in 1996 of a new television format, the Digital Television (DTV) standard, that provides a five times increase in video image resolution. The MBARI High Definition Television (HDTV) project is a development effort that is implementing this emerging technology on our ROV's. In order to use DTV 1920 X 1080 standard HDTV equipment on an ROV several technical problems had to be

addressed. The major design challenges were uplinking the very high data rate video signal, maintaining the extremely high resolution imaging though the camera housing optical dome correction optics, and repackaging a commercially available camera for 4000 meter ocean depths. The development of the optical uplink for the 1.485 Gb/sec HDTV serial data was constrained by the requirement of having all camera related functions use a maximum of one optical fiber, which provides a direct link from the camera housing itself to the ship based ROV control room. The original camera image quality is preserved to the digital HDTV recorder by conforming to the SMPTE 292M digital video standard for the entire transport and recording system and remaining in the optical domain as much as possible. This is accomplished by placing the optical transceivers within the remote camera housing. The high quality video image that results significantly improves our ability to resolve the details of biological and geological targets at all size scales and allows the capture of publication quality still frames.

A NEW WAY OF IDENTIFYING BURIED OBJECTS

David BOULINGUEZ, André QUINQUIS

EIA Dpt, ENSIETA, 29806 BREST Cedex 09, FRANCE

Tel: +33 2 98 34 87 82 Fax: +33 2 98 34 87 50

Email: boulinda@ensieta.fr quinquis@ensieta.fr

Abstract - Underwater object identification is of great interest for a few years to acousticians (detection of boulders), marines (detection of buried mines), or archaeologists (detection of wreckage). Image and Signal processing succeed in identifying objects lying on the sea bottom, however identification of an object buried in sediment remains complex.

The purpose of this work is to propose a complete identification of objects embedded in the sediment using an adapted technology. We use a parametric source, which properties are based on the water nonlinear propagation characteristics; it has many advantages as an acoustic source (high relative bandwidth, narrow beam) which are useful for object detection and classification. This paper presents a procedure which computes discriminant parameters from images to classify these objects.

I. INTRODUCTION

The purpose of this research is to study new kinds of processing for detection and classification of underwater objects (simply immersed, or buried) in normal incidence. For a long time, pingers have been used for the detection of buried targets like pipelines; however this does not perform good results for localization and classification.

Our method uses a parametric array (presented in the first part) in the self demodulation regime and in normal incidence, in order to obtain sub-bottom profilers. Thanks to this system, we can store three-dimensional data (x,y,z) of a sub-bottom zone and perform a precise detection [1].

We present then the most important development of this research concerning a classification using several methods.

II. DATA ACQUISITION

A. Parametric Array

The parametric array has many advantages as an acoustic source: high relative bandwidth, narrow beam with no sidelobes using a small transducer surface. All these features imply high relative spatial and temporal resolutions which are very useful in application such as object detection and classification [2].

Briefly, a carrier frequency is generated and mixed in a double balance mixer with a raised cosine bell envelope created from

a function generator. The modulation is sent to a power amplifier and then to a transducer. Due to the water nonlinear propagation characteristics, a low frequency self-demodulated pulse is generated, which corresponds to the second derivative of the square envelope of the created signal [3]. In the following example the signal is a Ricker pulse which temporal and spectral features are described in Fig.1. The generated pulse center frequency is around 50 kHz and its beamwidth is about 3 degrees. During the experiment, the sonar is

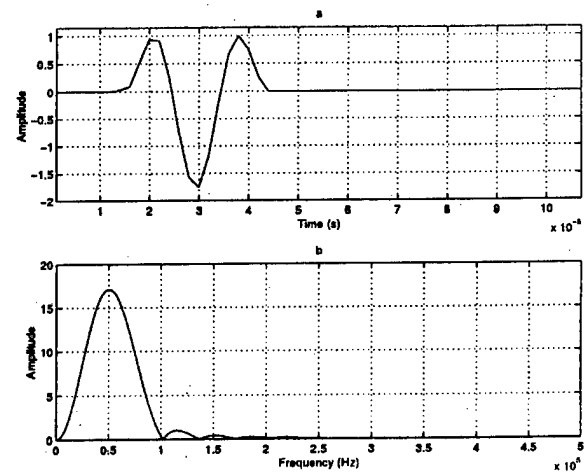


Fig. 1. a: Ricker - b: Fourier Transform of the analytic ricker

moved, step by step in both horizontal directions (x,y), near over the water/sediment interface. Signal frequencies are low enough to penetrate the sediment and the object without important attenuation. Thanks to the narrow beamwidth, a small surface of the object is insonified: we can therefore realize multi-line vertical scans over the object as shown in Fig. 2 and obtain a 3D information of the target.

B. Target Description

Following processing are based on simulated data and on real data collapsed during trials made in a pool. Fig.2 shows a cross section of a water-filled cylinder target buried in sandy sediment. One can clearly notice the water/sediment interface, and the two interfaces of the object. Three kinds of immersed objects have been used: cylinders, spheres and truncated

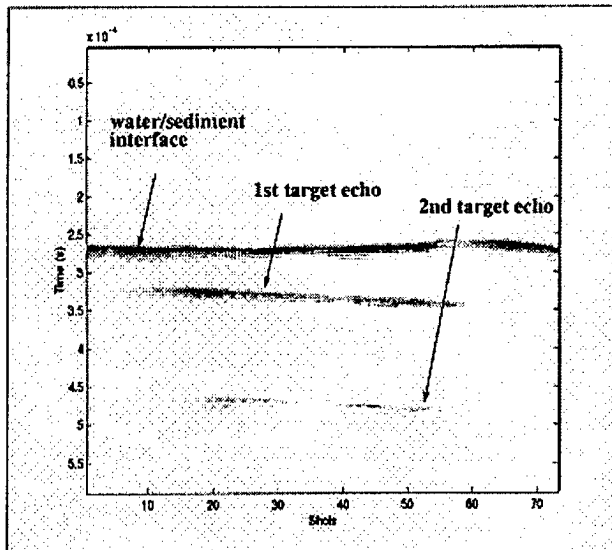


Fig. 2. Experimental result: water filled cylinder

cones (these shapes are currently used for mines). However, in order to test classification algorithms, we need to have a large data base, so a simulated target data base has been created. The simulated targets have been generated in three dimensions and, in order to have many different objects in the same class, we have simulated objects with different dimensions, and the shape details are different for each target.

III. CLASSIFICATION PROCESSING

The main purpose is to separate natural objects (boulders,...) with manufactured objects (mines, pipe-lines,...) and then to separate different kinds of manufactured objects thanks to their shape, their material, ...

A. Denoising

As we can see, real data can be severely noised and it necessary to introduce a denoising processing: we propose here to use a method based on a wavelet packet decomposition.

Several works have been realized for few years based on wavelet packets (WP) to denoise 1-D or 2-D signals. WP analysis has been developed by Coifman and Wickerhauser as a generalization of the multiresolution analysis [4]. The principle of the WP decomposition is shown in Fig.3, where x is the temporal signal. Each row is computed from the row above, by filtering it with a low-pass filter (h) for approximation coefficients and a high-pass filter (g) for detail coefficients, and decimating it by 2. Consequently, the coefficients in each table location (subband), generate after filtering, two coefficients subsets in the adjacent table locations below. Hence, this matrix presents the wave packet coefficients of the function x . The row number indexes the scale of the wavelet packet listed therein and the column number indexes both frequency and position parameters. We

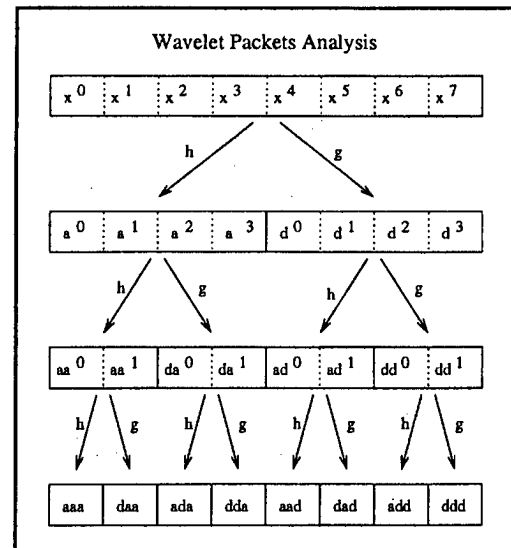


Fig. 3. The principle of Wavelet Packets Analysis

use then the best basis search algorithm proposed in [4] which minimizes the entropy cost-function. This function is defined for a sequence $x = \{x_j\}$ in (1).

$$\mathcal{H}(x) = - \sum_j p_j \log p_j \text{ where } p_j = \frac{|x_j|^2}{\|x\|^2} \quad (1)$$

Thus, a minimum entropy configuration is obtained, which is characteristic for the regularity degree of the signal structure. In order to denoise the signal, it is necessary to represent it with fewer coefficients, as a linear combination of elements of wave packet library. The idea is to discard components with insignificant amplitude (that correspond to the noise contribution) according to some criterion, and we will try to arrange that the resulting approximation differs minimally from the original. We sort the coefficients of any optimal representation in decreasing order of absolute value and then keep only as many of the largest as we can afford, discarding the rest.

B. First Classification Step

1) Higher Order Spectra Analysis

The first idea to separate objects into two classes (natural/manufactured) is to determine the presence of a hull at the surface of the object: indeed it can only be detected on man-made objects. On received signals, this hull is characterized by two reflections of the acoustic wave (sediment/shell and shell/water interfaces for a water filled object). In spite of the good resolution of the beam, the wavelength is necessarily higher than dimensions of the shell of the objects and one is faced to a temporal resolution problem. Moreover classical methods (matched filter, wavelet packets,...) do not succeed in separating both echoes due to the presence of the shell. A first processing [5] based on Higher Spectra Analysis is proposed here to improve the temporal resolution of signals.

One of the Higher-Order Spectra usual application is the time delay estimation between two sensors. The idea is to use the same processing by considering an observation signal and a reference signal (the emitted ricker).

A complete description of Higher-Order Analysis is given by [6].

The signal bispectrum is defined as the bi-dimensional Fourier transform of the third-order cumulant sequence. The main problem of this analysis concerns the estimation of spectra: indeed a way of estimating polyspectra is to use higher-order periodogram. Equation (2) gives the definition of the biperiodogram:

$$P_x(\omega_1, \omega_2) = \frac{1}{NT_e} X(\omega_1)X(\omega_2)X(\omega_1 + \omega_2) \quad (2)$$

where $x(k)$, $k = 0, 1, \dots, N-1$ is a real-valued stationary time series with zero-mean, $X(\omega_\lambda)$ is the Fourier transform of $x(k)$, $\omega_\lambda = \frac{2\pi}{N}\lambda$ for $\lambda = 0, 1, \dots, N-1$, and T_e is the sampling period.

In order to reduce the estimation variance, we can smooth the higher-order periodogram over neighboring frequencies, or average periodogram estimates over disjoint time blocks, or combine the aforementioned two approaches (Welch method). This estimation method is similar to the one used for the second order (estimation of the power spectrum), but the estimation qualities are different.

As explained in [7], the averaged biperiodogram variance decreases faster than the averaged periodogram variance when the number of segments used for the average increases. Following results will compare their performances.

In our problem, the signal received by the transducer (defined in (3)) can be written as a sum of shifted copies of the emitted signal $S(k)$ (ricker) and a noise source $W(k)$, supposed to be Gaussian and not correlated with the emitted signal.

$$y(k) = \sum_{i=1}^n s(k - D_i) + w(k) \quad (3)$$

Since w and s are not correlated, their cross-bispectrum is equal to zero; we can therefore write the crossbispectrum between y and s as described in (4):

$$P_{syy}(\omega_1, \omega_2) = P_s(\omega_1, \omega_2) \cdot \sum_{i=1}^n e^{-j\omega_2 D_i} \quad (4)$$

We can then compute the ratio $\mathcal{R} = \frac{P_{syy}(\omega_1, \omega_2)}{P_s(\omega_1, \omega_2)}$ and then define the function $h(\tau)$ [6] by

$$h(\tau) = \int d\omega_1 \int \mathcal{R} e^{j\omega_2 \tau} d\omega_2 = \sum_{i=1}^n \delta(\tau - D_i)$$

This function should display strong peaks at the location of true delays. In practice, we estimate D_i as index τ which maximizes $|h(\tau)|$. In the same way, at the second order, we can compute the ratio of the cross-power spectrum between S and Y to the power spectrum of S .

2) Results

First results have been obtained on simulated data without noise (two rickers shifted by two samples). In this case the matched filter does not allow to separate echoes (Fig.4.b). Record length is 128 samples which corresponds to a signal duration of $256\mu s$; Fig.4 compares the results of Bispectrum and Power Spectrum methods which performances are equal; this result proves that these methods can separate both echoes. Then gaussian noise is added to signals. One noticed if noise and signal are correlated, performances of this method are severely degraded. So the introduction of denoising processing beforehand is really necessary.

Fig.5 presents the results of both methods for two signal to noise ratio; in Fig. 5.a and Fig. 5.b, $S/N = 1dB$, and thanks to the denoising, it is now easy to separate the two rickers for both methods. Fig. 5.c and Fig. 5.d present results for $S/N = -6dB$: the Bispectrum method is still efficient; however, with the Power Spectrum method, it becomes difficult to extract the two echoes. It just proves that the Bispectrum estimator quality is better than the Power Spectrum.

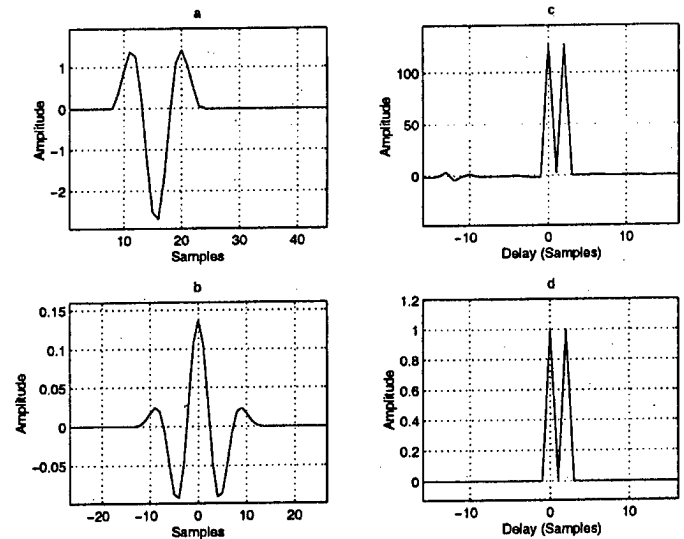


Fig. 4. (a) Observed Signal - Echoes Separation using: (b) Matched Filter - (c) Bispectrum method - (d) Power Spectrum method

Finally we have tested the method on several real data collected on a water-filled aluminum cylinder that had been immersed into water: the thickness of the shell is about 8 mm; the sampling frequency is 500 kHz and the dilatational wave speed is about 6300 m/s. The last figure (Fig. 6) shows the result of the higher order analysis

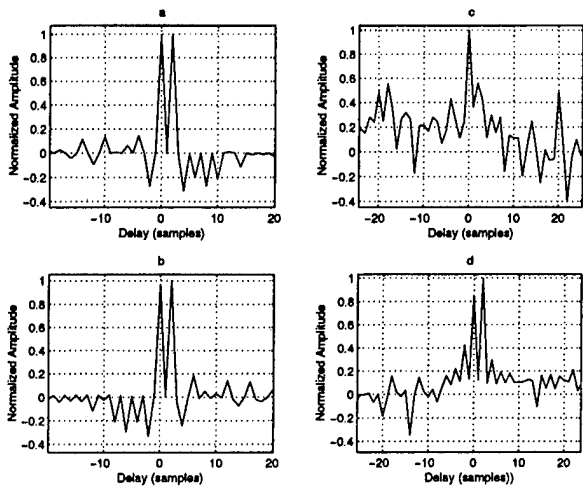


Fig. 5. Echoes separation after denoising: Power Spectrum method [(a) S / N = 1dB - (c) S / N = -6dB] Bispectrum method [(b) S / N = 1dB - (d) S / N = -6dB]

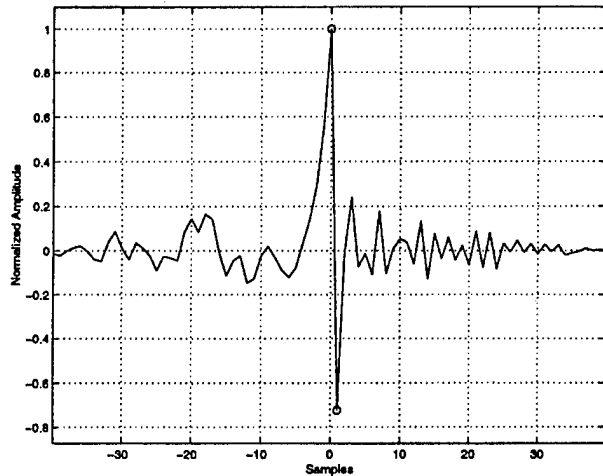


Fig. 6. Estimation of a shell thickness

after denoising: two peaks, separated by one sample (e.g. 2, μs), can be detected which means that a good approximation of the shell thickness is about 6 mm. The second peak is reversed because the reflection coefficient between the material and water is negative. It is a real improvement in comparison with matched filter usually applied for that kind of problem.

C. An Improved Classification

1) Feature Extraction

Now, inside the class **Manufactured Object**, we would like to recognize several kinds of targets according to their shape.

Since we have 2D view of the objects in cross sectional images, we decided to develop a pattern recognition. The purpose is to extract some parameters from these images that could discriminate the different kinds of objects. We propose to compute Fourier descriptors [8] that has been already used so as to describe the silhouette of an object: it consists in a decomposition of an edge into a Fourier series. Its main advantage is the possibility to make these descriptors rotation, translation and homothetic invariant. A same kind of object is nearly described by the same descriptors whatever its size, its orientation or its position in the image are. A closed edge can be considered as a list of uniformly spaced pixels with complex coordinates or as a discrete complex signal U_m . The Fourier coefficients of this signal are given by (5) where N is the number of samples of this signal. These terms are called Fourier descriptors.

$$C_n = \frac{1}{N} \sum_{m=0}^{N-1} U_m e^{-j2\pi \frac{nm}{N}} \quad (5)$$

With the inverse transformation written in (6), the edge can be built again from Fourier descriptors.

$$U_m = \sum_{n=0}^{N-1} C_n e^{j2\pi \frac{nm}{N}} \quad (6)$$

With an edge following algorithm and a maxima extraction applied on cross sectional images, we succeed in visualizing a binary shape describing the object (Fig. 7). Then we compute Fourier descriptors and we can notice that only few descriptors are enough to recognize an object. Indeed Fourier descriptors associated with high frequencies correspond to edge details. These details are not useful to recognize the shape: as we can see on figure 8, only the first 20 descriptors are enough for a correct recognition. Each target will be represented by a feature vector composed by these descriptors.

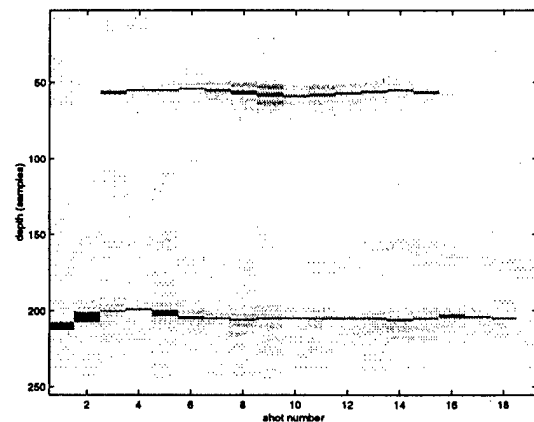


Fig. 7. Processed image and original image

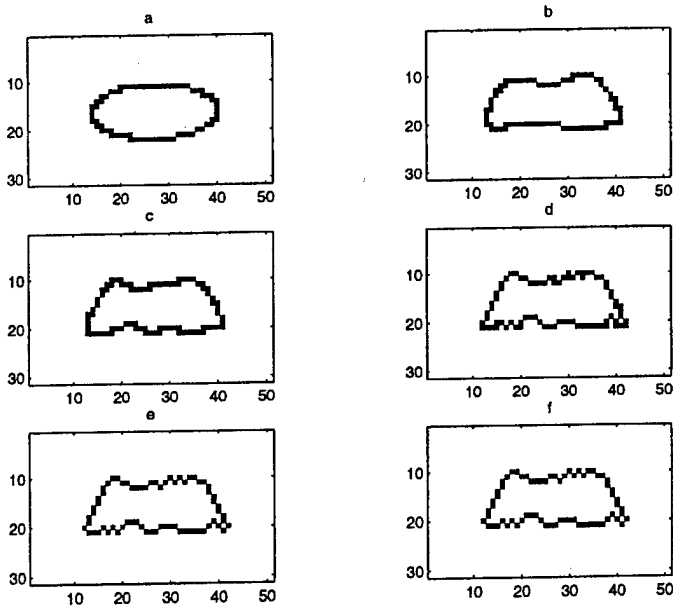


Fig. 8. Reconstruction of a truncated cone with the first 2, 10, 20, 64, 128 coefficients, and original (f)

2) Results

Since we do not know the class distribution, we have chosen a non-parametric method to classify targets. We need to create two data sets: the simulated data base is divided into two parts in order to realize the classifier learning and to test the algorithm. The training base is composed by 72 feature vectors in each class (cylinder, sphere and truncated cone) and the test base is composed by 90 feature vectors in each class.

The error rate due to misclassification is around 3% for the class *cylinder*, 2% for the class *truncated cone*, 3% for the class *sphere*.

To validate the procedure in a real environment, we have made a second series of tests by using the real data set composed by 40 feature vectors in each class. Correct classification rates appear in the table 1; the misclassification rate is always less than 8%. We proved the relevance of Fourier descriptors as discriminating parameters. However the limits appear when the shape of the object becomes complex: indeed only one cross sectional image can not represent the whole target shape.

Classes	Cylinder	Truncated Cone	Sphere
Cylinder	97,5%	2,5%	0
Truncated Cone	2,5%	95%	2,5%
Sphere	2,5%	5%	92,5%

Table I
Classification results using real data base

3) Towards a complete classification...

We are now working on the computation of discriminant parameters from the whole 3D information; these parameters will be rotation, translation and homothetic invariant too and they will describe the whole 3D target shape. With this more general approach, we are expecting to reach good classification rate.

IV. CONCLUSION

In conclusion, this work succeeded in improving the temporal resolution of acoustic signals thanks to the introduction of the Higher-Order Spectra Analysis. The principal application is an original geometrical way of classifying a buried, or immersed object. To improve this classification, we propose to compute discriminant parameters called *Fourier Descriptors* from target 2D view: this method is really efficient and allows to obtain some good classification rates. However to achieve a complete recognition, we are now computing some 3D discriminant parameters.

Many underwater applications can be associated: for instance the search for pipe-line or buried cables, the recognition of mines and their neutralization. The differentiation between manufactured objects and natural objects (like boulders) makes ecological applications possible too: for instance, cleaning the sea floor.

REFERENCES

- [1] J. Y. GUIGNE, "Technical introduction to benthic drums and company description," tech. rep., GUIGNE International LTD'S, Apr. 1995.
- [2] O. BERGEM and N. G. PACE, "Installation and calibration of a parametric array for shallow water backscatter measurements," *IEEE*, 1996.
- [3] P. CERVENKA, *Contribution théorique et expérimentale à l'étude de l'émission et de la réception paramétriques*. PhD thesis, Université Pierre et Marie CURIE (Paris VI), 1988.
- [4] R. R. COIFMAN and M. V. WICKERHAUSER, "Entropy-based algorithms for best basis selection," *IEEE Transactions on Information Theory*, vol. 38, pp. 713-718, Mar. 1992.
- [5] D. BOULINGUEZ, A. QUINQUIS, and M. BRUSSIEUX, "Classification of buried objects using a parametric sonar," in *OCEANS'98 MTS/IEEE*, pp. 1264-1268, Sept. 1998.
- [6] C. L. NIKIAS and A. P. PETROPULU, *Higher-Order Spectra Analysis*. Englewood Cliffs, nj: prenticehall ed., 1993.
- [7] C. SERVIERE, J. L. LACOUME, and C. JUTTEN, *De l'ordre 2... aux ordres supérieurs en traitement du signal*. INPG, June 1996.
- [8] C. T. ZAHN and R. Z. ROSKIES, "Fourier descriptors for plane closed curves," *IEEE Trans. on Computers*, vol. C-21, no. 3, pp. 269-281, 1972.

CONVERSION OF THE *OCEAN CLIPPER* TO DPS-3 CLASSIFICATION

Joshua D. Carter, Christopher P. Scott, Hunter M. Taylor
Ocean Engineering Program / Civil Engineering Department
Texas A&M University
College Station, Texas 77843

I. Abstract

The Texas A&M Ocean Engineering senior design project for 1999 was to design the upgrade of Diamond Offshore's dynamically positioned drillship, *Ocean Clipper*, from a DPS-1 classed vessel to a DPS-2 and DPS-3 classed vessel. The objective of this paper is to describe the results of this design.

A dynamically positioned drillship has the capability to maintain a fixed position and heading in any environment up to the maximum design environment. The Dynamic Positioning System (DPS) classification status (DPS-1, DPS-2, and DPS3) defines the redundancy necessary to withstand specified failures on the drilling vessel while maintaining station. During drilling operations, failures such as the loss of an electrical bus, generator, engine, or thruster are considered. In addition, the complete loss of a compartment, including its contents, due to fire or flood while maintaining station in the maximum design environment is evaluated. Four environments are considered for the operation of the upgraded *Ocean Clipper*. These environments are the Gulf of Mexico, the North Sea, the South China Sea, and West Africa.

The modifications suggested for the *Ocean Clipper* to operate under a DPS-3 classification differed for each environment. For the West Africa environment, the recommended modifications are the addition of a third electrical bus, the division of the SCR room into three compartments, the separation of the transformer room and air conditioning (AC) condensers, the addition of a door and back-up differential global positioning systems (DGPS) in the dynamic positioning (DP) room, and the addition of another thruster control system. These modifications are also recommended for operation in each of the other environments as well other modifications specific to the environment. To operate in the South China Sea, the addition of a third bulkhead is recommended to further subdivide the engine room. The recommended modifications for the Gulf of Mexico are the addition of three new engines and upgraded thruster capabilities. For the North Sea, the modifications recommended are upgrading the main screws and azimuthing thruster capabilities, the addition

of an azimuthing thruster in the bow, replacing the seven current engines with five more powerful engines, and the necessary electrical modifications to compensate for the upgraded power.

II. Background

A. Ocean Clipper Configuration

Diamond Offshore Drilling Company's *Ocean Clipper* is currently a DPS-1 classified drilling vessel operating in the Gulf of Mexico, and is designed to drill to depths of up to 7500 ft. It is approximately 570 ft long with a 107 ft beam and an average draft of 24 ft. Fully loaded with its risers, the *Ocean Clipper* displaces 900,895 ft³, which gives her a tonnage of 28,840 tons. The *Clipper* is equipped with two main screws, five tunnel thrusters, and one azimuthing thruster, as shown in Fig. 1.

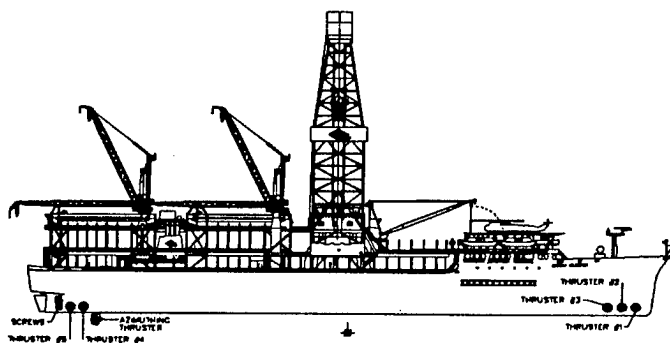


Fig. 1: *Ocean Clipper*'s Current Configuration

B. DPS Classification Requirements

A DPS-1 classed vessel has a dynamic positioning system that automatically maintains the position and heading of the vessel against a maximum environmental condition (ABS, 1994). This system includes a manual position control and an automatic heading control. To upgrade from DPS-1 to DPS-2 the vessel must be able to survive any single point failure. A single point failure is the failure of any single system on the vessel but does not include the loss of a compartment due to fire or flood.

With regards to the electrical system, a single point failure may include the loss of one of the electrical bus-tie breaker's or the loss of a transformer. Other single point failures may be the loss of an engine, thruster, air conditioning condenser, or fuel line. To upgrade to DPS-3, the vessel must be able to survive any single point failure as well as the complete loss of a compartment due to fire or flood. Because the *Ocean Clipper* is currently designed with several key components located in the same compartment, bulkheads must be added to limit the effect of a single compartment catching on fire or becoming flooded. The compartments that are of main concern are: the engine room, Silicone Control Rectifier (SCR) room, transformer room, aft winch room, and the auxiliary machinery room.

C. Objective

The objective of the 1999 Texas A&M Ocean Engineering senior design project was to design the upgrade of Diamond Offshore's dynamically positioned drillship, *Ocean Clipper*, from a DPS-1 classed drilling vessel to a DPS-2 and DPS-3 classed drilling vessel (Applequist, et.al., 1999). The capability of the *Clipper* to operate off of the coast of West Africa, in the South China Sea, the Gulf of Mexico, and in the North Sea are to be considered for each classification. The purpose of this paper is to discuss the results of the design for the *Ocean Clipper* upgrade.

D. Environmental Conditions

Maximum operating environmental conditions for each drilling location are shown in Table 1 (Webb, 1999). As can be seen in Table 1, the North Sea has the most severe overall environmental conditions, that include a significant wave height (H_s) of 32.2 feet and on minute mean wind speed of 66 knots. West Africa has the least severe overall environmental conditions with a significant wave height of 12.8 feet and a one minute mean wind speed of 22.9 knots.

Table 1: Operating Environmental Conditions

	Gulf of Mexico	North Sea
1 min. Mean Wind (knots)	43.7	66
Surface Current (knots)	0.7	1.9
H_s (feet)	20	32.2
Period (seconds)	10.9	10.2
	South China	West Africa
1 min. Mean Wind (knots)	40	22.9
Surface Current (knots)	1.8	1.9
H_s (feet)	15	12.8
Period (seconds)	10	16.2

E. Environmental Forces

Three different methods were used to compute the maximum environmental forces applied to the vessel in each environment. These are the American Petroleum Institute recommended practices (API, 1993), the wind tunnel test data collected from the Texas A&M University low-speed wind tunnel, and the SponClip software developed by Diamond Offshore (Webb, 1999). First, the API formulas were used to gain a general feel for the magnitude of the environmental forces on the vessel. Next, the data from the wind tunnel tests were supplied to the senior design groups by Diamond Offshore. The design groups were then able to analyze these data and determine the wind and current forces acting on the vessel in each environment. Finally, the SponClip software, developed specifically for the *Ocean Clipper*, was used to evaluate the environmental forces on the vessel from any direction. The results obtained from the SponClip program are displayed in Table 2.

Table 2: Ocean Clipper Forces in Maximum Operating Environment

	West Africa			South China Sea		
Force (kips)	Bow	Quarter	Beam	Bow	Quarter	Beam
Wind	22	54.5	54.8	67	150	168
Wave	74.7	132.5	135.8	55	86	118
Current	4.4	48.3	50.8	4	32	48
	Gulf of Mexico			North Sea		
Force (kips)	Bow	Quarter	Beam	Bow	Quarter	Beam
Wind	80.3	180	201	183	410	459
Wave	143	209	268	246	339	426
Current	0.6	4.9	7.21	4	36	53

When comparing the results obtained from the wind tunnel test data and the SponClip software it was evident that the two were very similar (Applequist et.al., 1999). Due to this similarity the values obtained from SponClip were used to compute the maximum environmental forces.

F. Capability Plots

To determine the *Ocean Clipper's* capability to maintain station while drilling in each environment several capability plots were generated using the SponClip program. The wave height and current velocities are input along with the required (design) wind speed, and the capability plot, Fig. 2, shows the maximum wind speed in any direction that the *Clipper* can withstand without drifting off station. Each circle represents a wind speed, that increases in multiples of 10 knots, with the center at 0 knots and the outer most circle at 100 knots. The solid black line is the capability line and represents the wind speed the *Ocean Clipper* can withstand for the input wave and current conditions. The dashed circle represents the required wind speed

that the *Clipper* must withstand in order to maintain station during the given environmental conditions. The design criteria for the *Ocean Clipper* requires that the vessel be capable of withstanding the design wind speed in each environment when the design environment is acting 30° to either side of the bow. The 30° lines shown in Fig. 2 represent this design window. For this study the wind, current, and wave forces are assumed to be concurrent. Also, the thruster's and main screws are only allowed to operate up to 80% of their total power to ensure no thrusters are overworked.

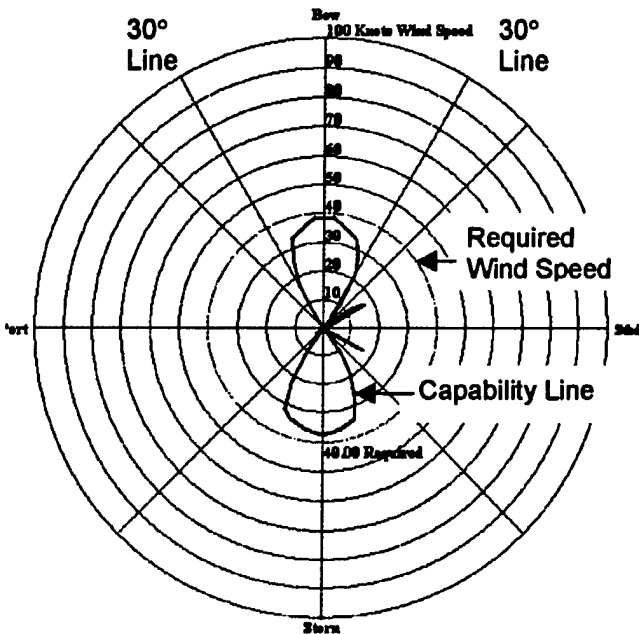


Fig. 2: Typical Capability Plot

III. West Africa

A. DPS-1

To determine the capability of the *Ocean Clipper* to maintain position under each DPS classification, several capability plots were generated. First, the capability of the *Clipper* under a DPS-1 classification was determined. Under a DPS-1 classification, no loss of power or equipment is considered, only the ability of the vessel to maintain position while subjected to the environmental forces typical for the drilling location. Fig. 3 shows that while drilling off the coast of West Africa, the *Ocean Clipper* can withstand a wind speed of approximately 60 knots in the design window, 30° either side of the bow, when subjected to the design wave height of 12.8 ft and surface current of 1.9 knots. This is well above the required wind speed of 22.9 knots under these conditions; therefore, the *Clipper* is able to drill in this location under a DPS-1 classification with no modifications.

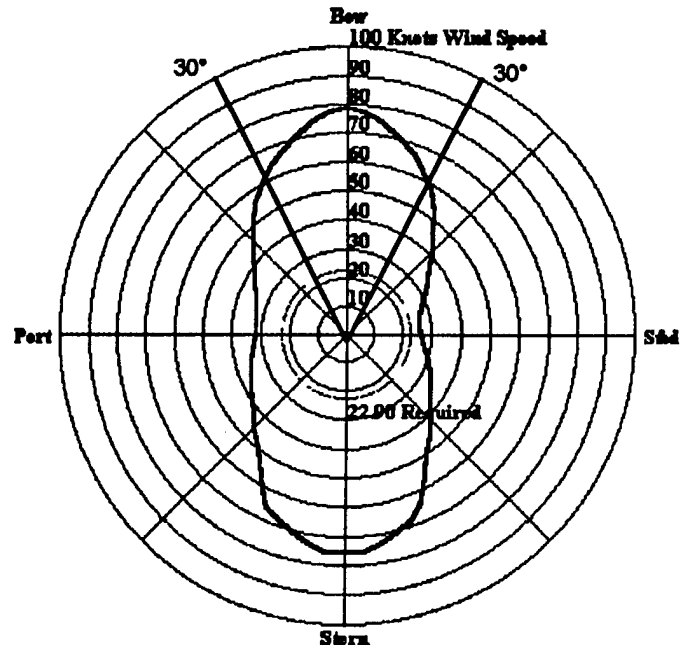


Fig. 3: DPS-I Capability of the *Ocean Clipper* with its Current Configuration in West Africa

B. DPS-2

To upgrade to a DPS-2 classification the *Clipper* must be able to maintain station while losing any single system on the ship. The most critical single point failure on the *Clipper* is the loss of one of the two electrical buses that route power from the engines to the thrusters and screws. Table 3 shows the arrangement of the components currently on each bus. Two capability plots were generated to determine the vessel's capability with the loss of buses A and B. As expected, the more critical of the two is the loss of bus A, shown in Fig. 4, due to the fact that the majority of the vessels power and thrust capabilities are located here. However, even with the loss of bus A, the *Clipper* can withstand a wind speed of approximately 40 knots along with the design current and wave forces in the 300 design window, which exceeds the required wind speed by almost 20 knots.

Table 3: Current Two Bus Arrangement

BUS A	BUS B
4 Engines	3 Engines
Starboard Main Screw	Port Main Screw
Azimuthing Thruster	Thruster 1
Thruster 2	Thruster 5
Thruster 3	
Thruster 4	

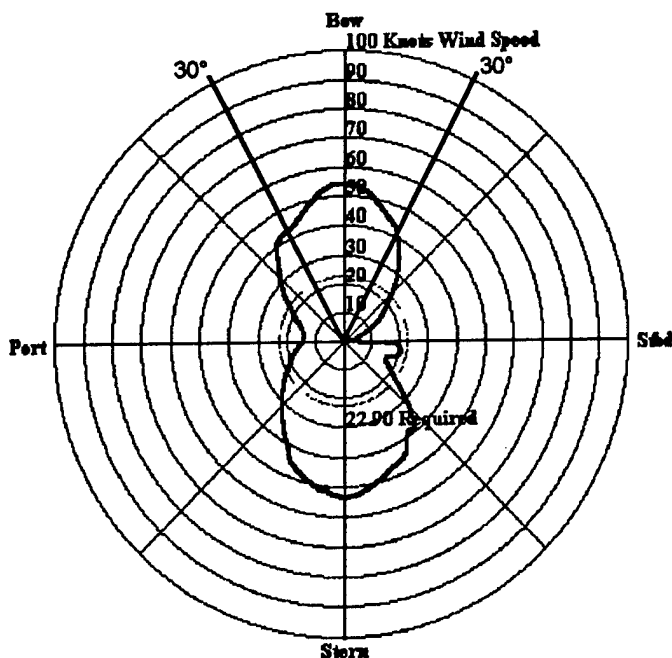


Fig. 4: DPS-2 Capability of the *Ocean Clipper* with the Loss of Bus A in West Africa

To upgrade to a DPS-2 classification no major structural modifications are recommended. The only modifications necessary are to the start air and fuel lines located in the auxiliary machinery room. Currently, there is only one set of fuel lines connecting the day tanks to the engines, and if these lines are lost no fuel can be distributed to power the ship. To correct this, it is recommended that an additional set of fuel lines be installed to ensure that even under a single point failure of the fuel lines all seven engines can receive fuel. A similar modification is recommended for the start air lines. An additional start-air line connecting the emergency pumps to the engines is recommended, due to the fact that a break in this line causes the *Clipper* to lose the ability to start any of the engines on the ship. With these two modifications any significant single point failure is eliminated, and a DPS-2 classification is attained.

C. DPS-3

To upgrade to a DPS-3 classification the *Clipper* must not only withstand a single point failure, but the loss of a single compartment due to fire or flood as well. To meet the ABS requirements for a DPS-3 classed vessel, the following modifications are recommended. New A60 watertight bulkheads are to be installed in several compartments to ensure that a fire or flood is contained and to ensure that the systems in the compartment have a back-up system. First, it is recommended that the engine room be separated into two compartments with one containing three engines and the other containing the remaining four engines as shown in Fig. 5. This is to ensure that at least three engines are available for operation even if one engine room is lost.

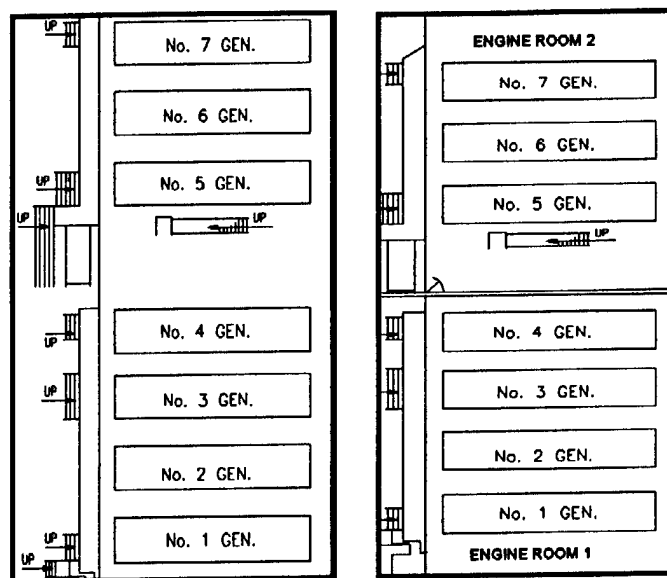


Fig. 5: Existing (left) and Suggested Modifications (right) to the Engine Room for West Africa

The current arrangement of the transformer room is such that all seven transformers are located in one compartment. If this compartment is lost, then all power to the ship is lost; therefore, it is suggested that the transformer room also be split into two separate compartments, similar in fashion to the engine room, using an A60 watertight bulkhead.

The aft winch room is currently an open compartment that houses the air-conditioning condensers. It is suggested that A60 watertight bulkheads be added to separate the air-conditioning condensers to provide redundancy for the air-conditioning system and to prevent the loss of the entire air-conditioning system if the aft winch room were to be lost due to fire or flood as shown in Fig. 6.

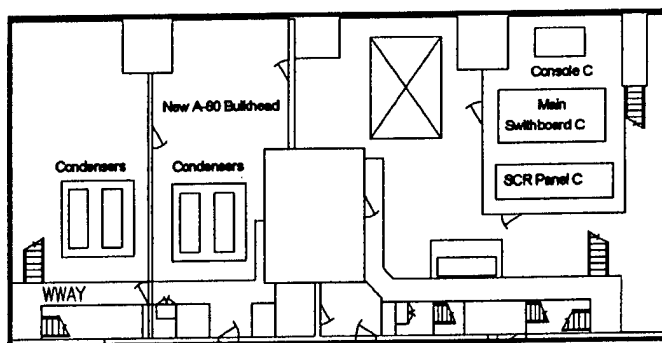


Fig. 6: Modified Aft Winch Room Arrangement for West Africa

The suggested modification to the SCR room is the addition of an A60 watertight bulkhead to separate the existing SCR room in two. This provides the required redundancy for a DPS-3 classification as per ABS. The electrical system requires modifications as well. These

include the rewiring of power and control cables to prevent the loss of a system if a compartment is lost due to fire or flood, separating the air-conditioner units onto two independent electrical busses, adding new uninterruptible power supply (UPS) units, modifying the SCR system, and adding a new bus tie-breaker, bus C. The addition of this bus allows the *Clipper* to spread out failure points so that the loss of a bus affects fewer of the ship's systems. The new bus components and their arrangement are shown below in Table 4. The new bus system is configured such that all three busses can run off either engine room. Therefore, if one compartment is lost to fire or flood the remaining power can still be used by all of the busses.

Table 4: Modified Bus Arrangement Including the Addition of Bus C for West Africa

Bus-A	Bus-B	Bus-C
Engines 1&2	Engines 3&4	Engines 5,6,&7
2 Transformers	2 Transformers	3 Transformers
Fwd Thruster (#3)	Fwd Thruster (#4)	Stern Thruster (#5)
Stern Thruster (#7)	Fwd Thruster (#6)	Az Thruster (#8)
Stbd Screw (#1)	Port Screw (#2)	

To determine the *Clipper's* ability to maintain station with a DPS-3 classification, the most critical loss of a single compartment must be determined as well as the most critical single point failure. With the modifications stated above, the most critical loss of compartment is the loss of the SCR room containing bus A, which is shown in Fig. 7. With this loss the *Ocean Clipper* is able to maintain station with a maximum wind speed of approximately 40 knots with the design current and wave forces acting concurrently with the wind. This exceeds the design wind speed by approximately 20 knots.

D. Cost

To upgrade the *Ocean Clipper* to a DPS-2 classification for the West Africa environment, the estimated cost is \$2.4 million US dollars, and to upgrade to DPS-3 classification it is an additional \$5.75 million US dollars. This includes \$77,000 US dollars in duplicated costs due to set receiving fees at the shipyard and new inspection fees. To upgrade straight to a DPS-3 classification it costs approximately \$8.1 million US dollars. All of these estimates contain a 10% contingency to provide for unforeseen expenses during construction.

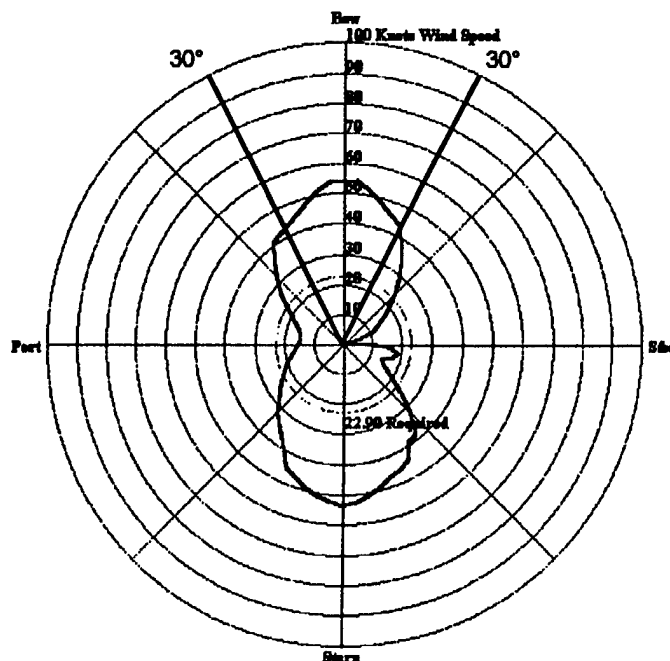


Fig. 7: DPS-3 Capability of the *Ocean Clipper* with the Loss of Bus A in West Africa

IV. South China Sea

A. DPS-1

To begin the upgrade analysis of the *Ocean Clipper* from a DPS-1 classed drilling vessel to a DPS-2 and DPS-3 classed drilling vessel in the South China Sea, the capability of the vessel to maintain station under each classification was analyzed. Currently, the *Ocean Clipper* can maintain position in the South China Sea operating environment as a DPS-1 classed drilling vessel. As can be seen in Fig. 8, the *Clipper* can withstand a wind speed of approximately 60 knots along with the design current and wave conditions 30 degrees off either side of the bow under its current configuration. This more than satisfies the design requirement of a 40 knot wind speed with a 1.8 knot current and 15 ft waves acting in the same direction.

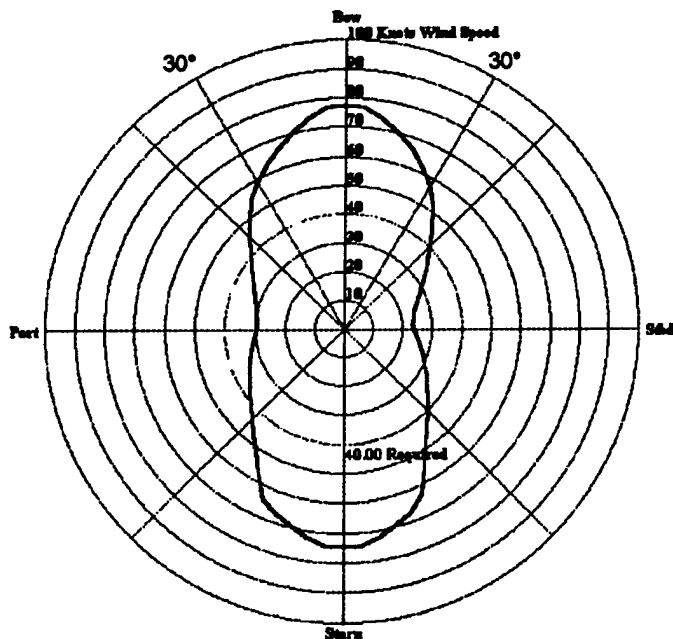


Fig. 8: DPS-1 Capability of the *Ocean Clipper* with its Current Configuration in the South China Sea

B. DPS-2

To upgrade the *Ocean Clipper* to a DPS-2 classification it must be able to withstand the most critical single point failure. With the present two-bus configuration of the *Ocean Clipper*, shown previously in Table 3, the worst case is the loss of bus A. This is because the majority of the vessel's power and thrusters are on this bus. With the loss of the components on bus A only three engines are left to power the vessel, along with two tunnel thrusters and one main screw providing station keeping abilities. It is no surprise that the *Ocean Clipper* cannot maintain position with the loss of bus A while operating in the South China Sea. In fact, the *Clipper* can only withstand a wind speed of approximately 20 knots in the design window, half of the required value, when bus A is no longer operational. The first alternative considered to increase the *Clipper's* capability under a DPS-2 classification was to increase the thrust capabilities of the main screws and thrusters. However, the amount of thrust required to maintain station with the loss of bus A, an additional 97 kips per tunnel thruster, is unfeasible; therefore, the most reasonable solution is to change the current two-bus system to a three-bus system, which is displayed in Table 5. With this change the most critical single point failure becomes the loss of the new bus A. With the loss of bus A, the main components lost are two engines and tunnel thrusters 1 and 5. The port and starboard main screws and the azimuthing thruster are not lost due to the fact that they are also wired onto one of the other buses. The *Clipper* can withstand a wind speed of 40 knots in the

30 degree design window with the loss of bus A while using a three bus system, as is shown in Fig. 9. Therefore, it is recommended that the *Ocean Clipper* change the current two-bus system to a three-bus system to operate under a DPS-2 classification in the South China Sea.

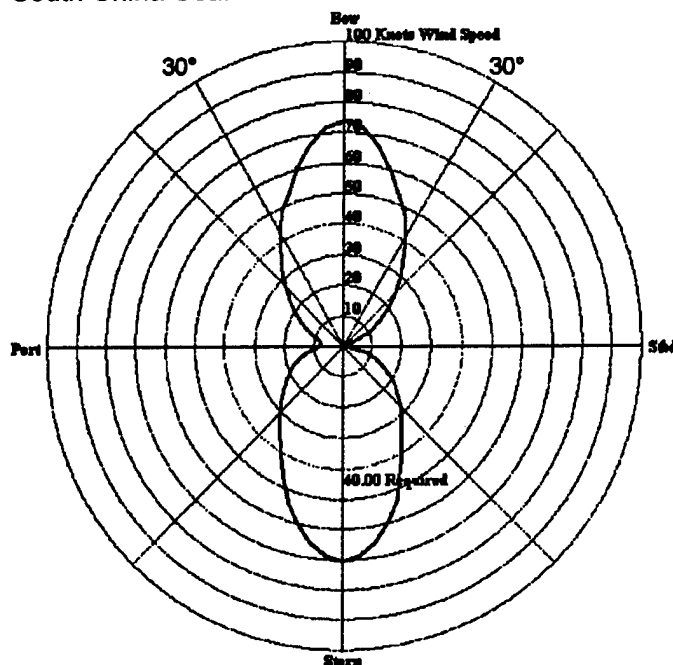


Fig. 9: DPS-2 Modified Capability of the *Ocean Clipper* with the Loss of Bus A in the South China Sea

C. DPS-3

To determine the ability of the *Ocean Clipper* to operate under a DPS-3 classification the most critical loss of one compartment must be known. To determine this, several capability plots were generated that showed the effect of the loss of different key compartments on the ship. For the *Clipper* to operate under a DPS-3 classification, several primary conversions are recommended. As in DPS-2, one of the main conversions is to change the present two-bus system to a three-bus system, which is shown in Table 5.

Table 5: Three-Bus Configuration for the South China Sea

BUS A	BUS B	BUS C
2 Engines	3 Engines	2 Engines
Port Main Screw	Azimuthing Thruster	Port Main Screw
Starboard Main Screw	Thruster 2	Starboard Main Screw
Thruster 1		Thruster 3
Thruster 5		Thruster 4
Azimuthing Thruster		

This configuration eliminates the loss of most of the thrusters when a single bus is lost. Note that each main screw and the azimuthing thruster are connected to two separate busses. This prevents the loss of these components with the loss of a single

bus. With this new bus system, capability plots were produced showing the effects due to the loss of each of the SCR rooms containing the buses, which is essentially only the loss of the bus in the room. In each of these plots the maximum wind speed that the *Clipper* can withstand 30 degrees off either side of the bow is 40 knots, which is the required wind speed. Therefore, the loss of any of the busses does not affect the *Clipper's* ability to maintain station in the South China Sea under the design environmental conditions.

The next key compartment loss that was evaluated was the loss of an engine room. In its current configuration all seven of the engines powering the vessel are in a single room; therefore, the loss of this room due to a fire or flood causes the vessel to lose all of its power. To begin, it was recommended that a bulkhead be added to separate the engines into two engine rooms containing three and four engines each. With the loss of the engine room containing four engines the ship has only three engines remaining to generate power. With only three engines left to generate power, the wind speed that can be withstood in the design window is only approximately 25 knots, which is well under the 40 knot requirement. Next, the capability of the *Clipper* operating with four engines was determined. Fig. 10 shows that four engines generate enough power to maintain station keeping ability with a 40 knot wind speed 30 degrees off either side of the bow in addition to the other operating environmental conditions.

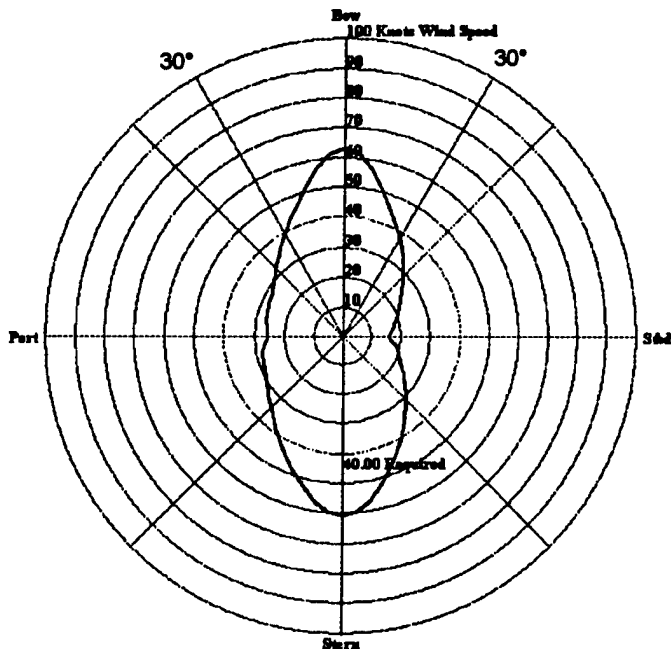


Fig. 10: DPS-3 Capability of the *Ocean Clipper* with Four Engines Operating in the South China Sea

Therefore, four engines are necessary to maintain position in the South China Sea with the three-bus

configuration. In order to achieve the level of redundancy required to maintain a DPS-3 classification, the engine room is split longitudinally into three compartments by two watertight, fire resistant A60 bulkheads. Two of these compartments contain two engines each and the other contains three engines, as shown in Fig. 11. The effect of losing one of these compartments leaves a minimum of four operable engines. The transformer room requires a similar sectioning with watertight A60 bulkheads to provide the proper amount of redundancy. The loss of any one of these compartments leaves a minimum of four functioning transformers.

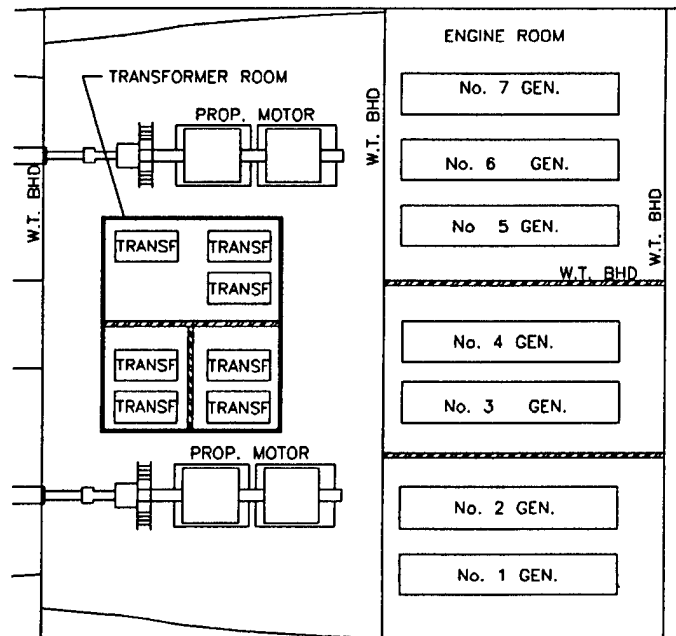


Fig. 11: Modifications to Engine Room and Transformer Compartment for the South China Sea

Forward of the engine room, the auxiliary machinery room requires splitting with another watertight A60 bulkhead so that redundant equipment can be added. A secondary setup of air compressors, dryers and receivers are installed on the port side of this new bulkhead to insure a flow of air to the engines. Also, the fuel and start air line modifications made by the West Africa group are recommended for both a DPS-2 and DPS-3 classification.

To support the three-bus arrangement, supplemental SCR rooms are required. These rooms are created by placing watertight A60 bulkheads on the starboard side of the existing SCR room. The current SCR room is split down the center by a similar bulkhead so that each bus and the operating equipment on that bus is supported in the event of a loss of one of the SCR rooms. Additional SCR equipment is required for the new room. A secondary set of air conditioning units,

attached to a separate bus line, is added to ensure the temperature is controlled in the SCR rooms in the event of a failure of the existing set. These suggestions are shown in Fig. 12.

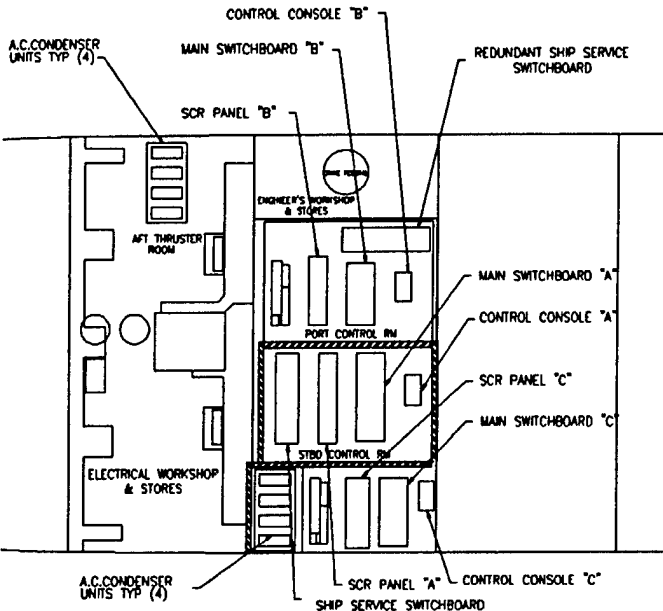


Fig. 12: Recommended Modifications to the SCR Room for the South China Sea

D. Cost

The final task is the cost analysis. Diamond Offshore provided the unit costs for each of the modifications (Baca, 1999). Using these unit prices, the cost to install the needed bulkheads, wiring and equipment, as well as the labor and welding costs were compiled. The cost to complete the upgrade to a DPS-2 or a DPS-3 system was calculated and compared to determine which is more cost effective. The final amounts calculated for conversion of the *Ocean Clipper* are \$5.79 million US dollars to obtain a DPS-2 classification, and \$9.01 million US dollars for a DPS-3 classification. This cost includes a ten-percent contingency for unforeseen expenses during construction.

V. Gulf of Mexico

A. DPS-1

Under a DPS-1 classification no loss of equipment is considered, and with the Gulf of Mexico design environment approaching within 30° of the bow, the vessel can withstand the 43.7 knot design wind speed, as can be seen in Fig. 13.

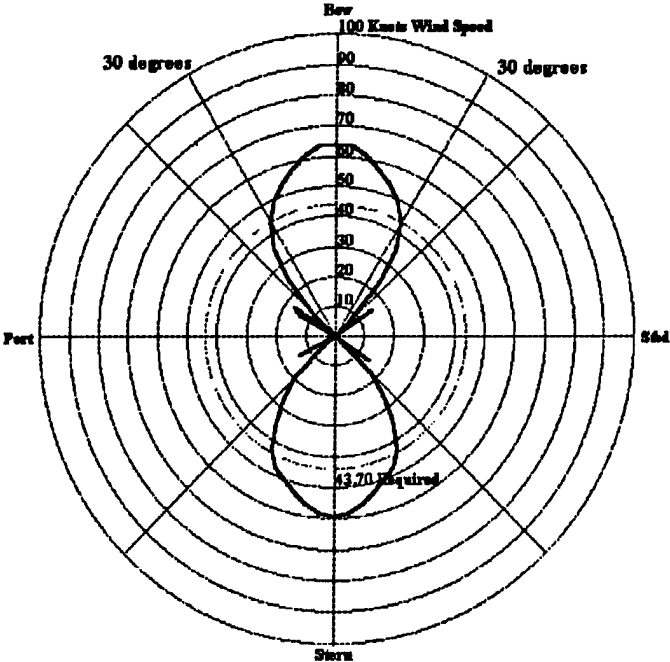


Fig. 13: DPS-1 Station-Keeping Capability in the Gulf of Mexico

B. DPS-2

For a DPS-2 classification the most critical loss of a single component on the ship must be known. This critical failure is the loss of one of the two electrical busses. The original DPS-1 design of the *Ocean Clipper* is configured in such a way that the seven generators, six thrusters, and two propellers are located on two electrical buses. The Gulf of Mexico analysis of the DP capability plots show that the loss of any one of these buses causes station keeping abilities to be lost, and that seven generators must remain online at all times in order to maintain station with all thrusters and screws operating. Therefore, a new bus system is introduced that allows for the loss of a single bus. This new five-bus system, shown in Table 6, is configured in such a way that at least seven generators remain online in the event of the loss of a single bus. Table 6 also shows the addition of two new generators, three new transformers, and eight new thruster motors. The two generators are added for power necessities, and the three transformers are added in order to handle this new power. The thruster motors are added for redundancy.

Table 6: Five-Bus Arrangement for the Gulf of Mexico

A-Bus	B-Bus	C-Bus	D-Bus	E-Bus
2 Generators	2 Generators	1 Generator	2 Generators	2 Generators
Thruster #2	Thruster #3	Thruster #1	Thruster #1	Thruster #3
Thruster #4	Thruster #4	Thruster #2	Thruster #5	Thruster #5
Thruster #6	Thruster #6	Port M. Screw	Port M. Screw	Port M. Screw
Stbd. M. Screw	Stbd. M. Screw			Stbd. M. Screw

With this change in the bus arrangement the loss of any one of the busses was analyzed to determine the DPS-2 capability in the Gulf of Mexico. The loss of any one of the busses containing two generators is the most critical single point failure. This loss results in the loss of the power provided by the generators tied to that bus, and even with the remaining thrusters running at 80% power, the DP system is not able to maintain position for a near bow environment. However, because SponClip allows the user to determine which modifications are necessary to maintain station-keeping capability, the necessary thruster modifications were determined. With the current thruster configuration the vessel can only withstand a wind speed of approximately 40 knots, which is less than the required value of 43.7 knots. With the upgrade to two 10,000 HP main screws and a 4,000 HP azimuthing thruster the *Clipper* can maintain station under the design environment in the Gulf of Mexico. Fig. 14 displays the station keeping capability for a DPS-2 classification. The vessel can withstand a wind speed of approximately 45 knots in addition to the given wave and current forces acting 30° off either side of the bow.

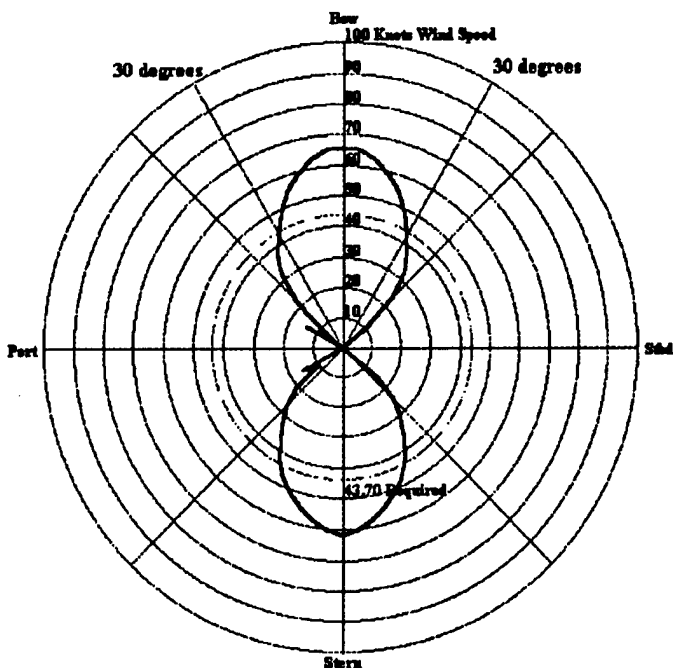


Fig. 14: DPS-2 Capability with the Loss of One Bus (A,B,D, or E) in the Gulf of Mexico

C. DPS-3

The most critical loss of a compartment for a DPS-3 classification is the loss of one of the SCR rooms, which has the same effect as the loss of the bus contained within the room as in DPS-2. An engine room loss also has the same effect because the engine room is modified such that any single room contains at most

two engines. Therefore, the suggested modifications for station keeping ability are roughly the same for the two classifications. The upgrade to a DPS-2 and DPS-3 classification in the Gulf of Mexico requires the addition of a five bus system along with upgrading the propulsion equipment to two 10,000 HP main screws and a 4,000 HP azimuthing thruster. The start air and fuel line modifications made by the West Africa group are also recommended for operation in the Gulf of Mexico with a DPS-2 and DPS-3 classification.

In complying with a DPS-3 classification, the loss of a single compartment must not affect the station keeping ability of the vessel beyond a set value. The capability plot (Fig. 14) shows that the *Clipper* must always have seven engines online. Therefore, the original engine room is partitioned so that the loss of a compartment allows seven engines to remain online. Also, under the five-bus system that was developed, the loss of two engines is equal to losing one bus. Therefore, the engines in each engine room are isolated in order that the ship loses at most two engines with the loss of one compartment. It is recommended that the original engine room be split into four compartments with watertight A60 bulkheads. One additional engine is placed in the original engine room, bringing the total number of engines in the original engine room to eight, with each new compartment containing two engines. The second additional engine required for station keeping ability is placed in the auxiliary machinery room, where other modifications are also necessary, as shown in Fig. 15.

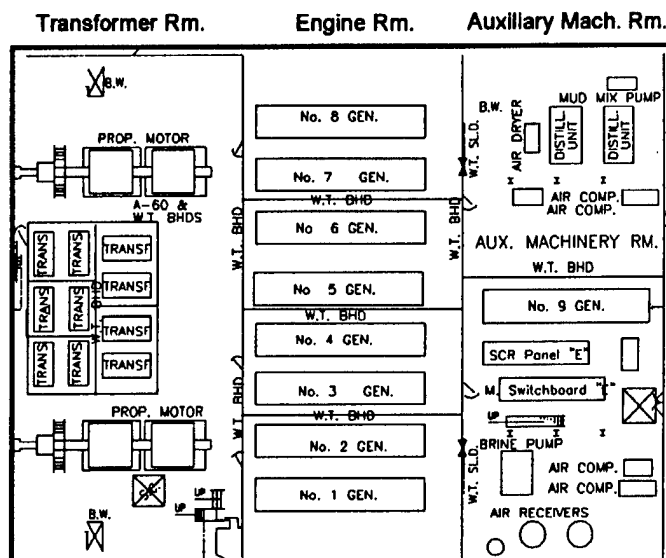


Fig. 15: Engine Room, Auxiliary, and Transformer Room Modifications for the Gulf of Mexico

The auxiliary machinery room (Fig. 15), just forward of the engine room, has several original and redundant

components that are not separated. Therefore, in the event of a fire or flood in this room all capability of these components is lost. Examples of these components include the air compressors, receivers, and distiller units. It is recommended that the auxiliary machinery room be split with a watertight A60 bulkhead to separate original and redundant components. Also, the second additional engine required for station keeping ability is located in the room along with the third additional electrical bus. Due to the fact that both an engine and a bus are located in this same room, extra air conditioning is also added.

It is recommended that the transformer room be partitioned into five different compartments to insure redundancy due to a fire or flood. Loss of the original transformer room results in total shutdown of the power relay from the generators to the buses. Therefore, A60 watertight bulkheads are installed separating the ten transformers. This allows for redundancy, and no power conversion ability is lost with a fire or flood.

A similar situation exists in the SCR room, where a fire or flood disables both original buses. The loss of a single bus with this original system prevents the distribution of electricity to any onboard system, including the thrusters. Thus, major steps are made to modify the SCR room and bus system for DPS-3 requirements. First, the original SCR room is split with an A60 watertight bulkhead, as shown in Fig. 16. Bus A and bus B are already in the original SCR room, and bus C is placed in a split electrical workshop and stores room. Bus D is placed in the aft winch room, and the final bus, bus E, is placed in the auxiliary machinery room.

Because of the high humidity in the Gulf of Mexico, air conditioning for the rooms containing sensitive electrical components is addressed. In the original aft winch room, there are two air conditioning condensers. These air conditioning condensers supply air to the vessel and most importantly to the SCR rooms. The SCR rooms containing the electrical busses must be air conditioned because the loss of the air conditioning condensers leads to condensation forming on this sensitive circuitry and power relays to the thrusters. With the addition of three new buses, more air conditioning capability is added. Two new air conditioning units are added to the aft thruster room, which not only adds more air conditioning capability, it also adds redundancy to the original units. In the case of a loss of the aft winch room, the two new units are still available. Fig. 16 shows the SCR, aft winch, and aft thruster room modifications.

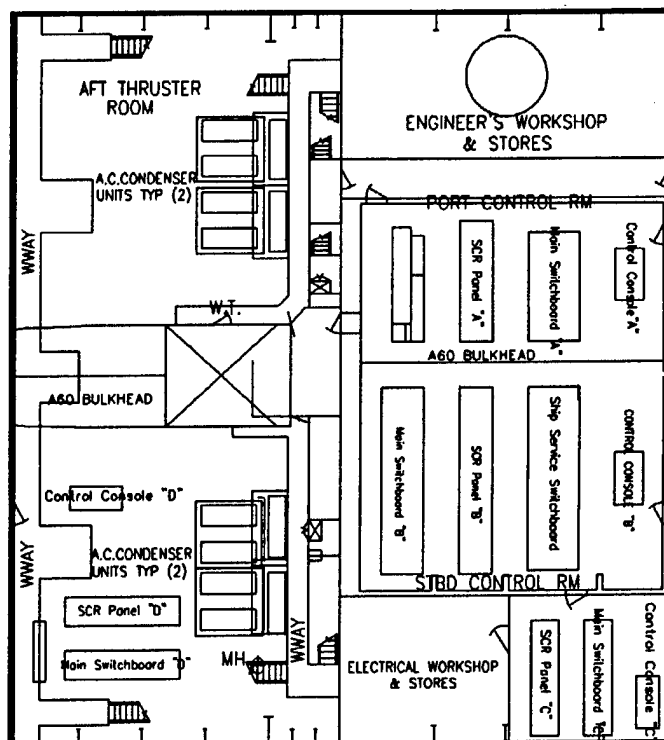


Fig. 16: SCR, Aft Winch, and Aft Thruster Room Modifications for the Gulf of Mexico

D. Cost

The conversion of the *Ocean Clipper* is estimated to require 105 days of work in a dry dock shipyard. To convert from a DPS-1 to a DPS-2 classification, it is estimated to cost \$17.6 million US dollars. This cost includes all shipyard services, personnel services, and electrical and propulsion modifications. Advancing to a DPS-3 classification can be done simultaneously and only takes 75 of the total 105 days to complete because the DPS-3 classification only needs structural modifications when advancing from the DPS-2 classification. The DPS-3 classification requires an additional \$2.8 million US dollars, yielding a total DPS-3 cost of \$20 million US dollars.

VI. North Sea

A. DPS-1

The *Ocean Clipper* can not maintain station when subjected to the operating environmental conditions in the North Sea under its current configuration in a DPS-1 classification. To maintain station while drilling, it is necessary to replace the existing engines that provide 23,468 HP with four 16 CM32 Caterpillar engines and one 8 M32 Caterpillar engine that provide 43,402 HP total. Two new azimuthing thrusters are also needed to maintain station. One replaces the existing thruster, and the other is placed 100 feet forward of midship. With

these conversions, the capability of the *Ocean Clipper* in the North Sea is shown in Fig. 17. The *Clipper* can withstand a wind speed of approximately 66 knots along with the design wave and current forces in the North Sea when these forces are applied in the 30° design window.

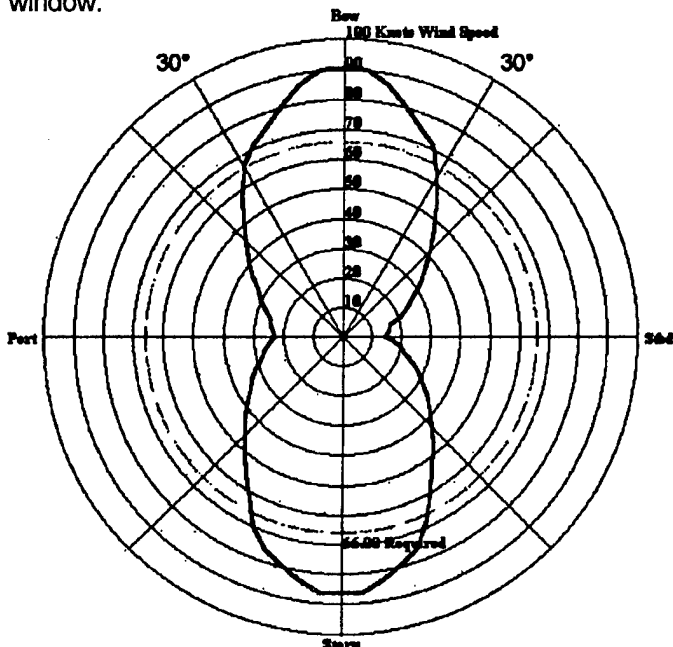


Fig. 17: Capability of the *Ocean Clipper* with Upgraded Thrusters and Engines in the North Sea

With the installation of five upgraded engines and two azimuthing thrusters, several hull modifications were made. The upgraded engines are arranged longitudinally as shown in Fig. 18. Also shown in Fig. 18 is the arrangement of the upgraded transformers. One new transformer is required with the addition of the bow azimuthing thruster and the original seven transformers are upgraded proportionally to match the azimuthing thruster's increased power requirements.

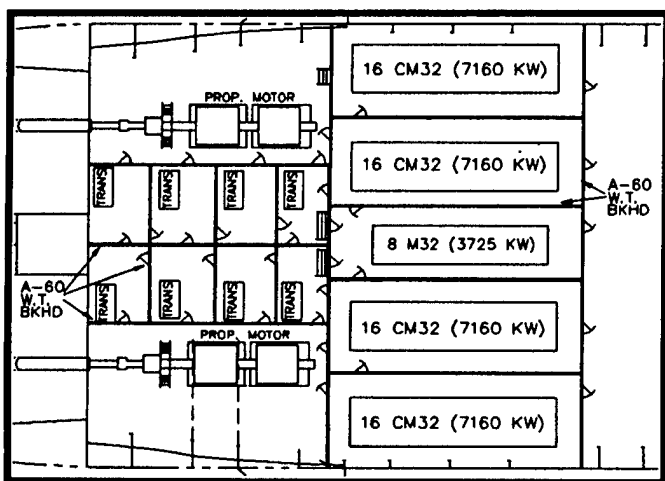


Fig. 18: Modified Engine Room with the Addition of the A60 Watertight Bulkheads for the North Sea

As a result of the upgraded engines, additional SCR capacity is added to convert the AC power from the engines to DC power needed for the thrusters. The additional power provided by the upgraded engines is approximately double the power provided by the existing engines, so the SCR capabilities are also doubled to handle the increased load. To meet these requirements the number of SCR panels are doubled. One new air conditioning unit is added to provide adequate temperature control to the new SCR room. The original air conditioning unit is moved into the engineering workshop, and the new unit is located in the electrical workshop, directly adjacent to the SCR room. Fig. 19 shows the relocation of the air conditioning condensers and the additional SCR capacity located in the aft winch room. Fig. 19 also depicts a new elevated catwalk system located directly above the engine room. Elevation of the catwalks is required because the upgraded engines are 17 feet high and ample space must be left for maintenance and air circulation.

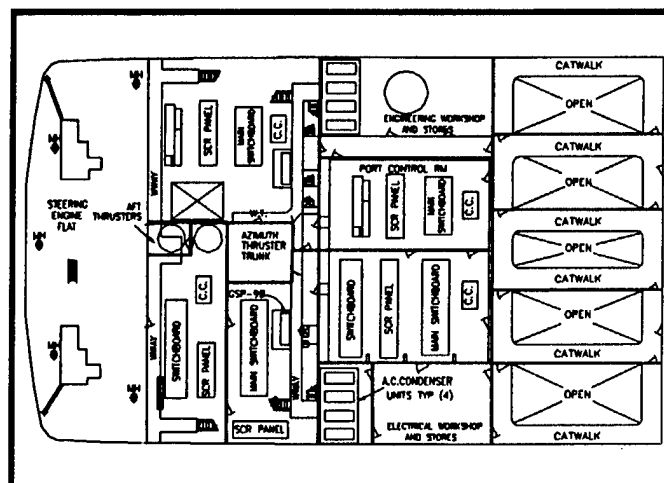


Fig. 19: SCR Room with the Addition of the A60 Watertight Bulkheads for the North Sea

The new azimuthing thruster is located 100 feet forward of midship along the longitudinal centerline. This distance is greater than 6.5 propeller diameters (assumed diameter is 14 feet) away from the riser. This is a sufficient distance so that no flow effects from the thruster will hinder operation of the riser. The new azimuthing thruster is retractable; therefore, a trunk for retraction is cut into the hull.

B. DPS-2

In order to meet a DPS-2 classification, a five bus system, shown in Table 7, is installed to replace the current two bus system. This gives the necessary redundancy to meet failure requirements. Also, the main screws are upgraded to 220 kips so that the *Clipper* can maintain station while sustaining the most critical

single point failure, which is the loss of the aft azimuthing thruster. The SCR panels and transformers are also upgraded to be compatible with the five bus system. The start air and fuel line modifications are also recommended. The capability of the *Clipper* with these modifications under a DPS-2 classification is shown in Fig. 20. Although the *Clipper* cannot withstand the design wind speed of 66 knots in the design window, it can maintain station within a 20° window on the bow, as well as a 77 knot wind speed acting directly on the bow, which is determined to be acceptable.

Table 7: Five Bus Arrangement for the North Sea

A-Bus	B-Bus	C-Bus	D-Bus	E-Bus
1 Generator Thruster #5 Stbd. M.S.	1 Generator Thruster #1 Port M.S.	1 Generator Thruster #2 Az. Thruster #2	1 Generator Thruster #3 Port M.S.	1 Generator Thruster #4 Az. Thruster #1 Stbd. M.S.

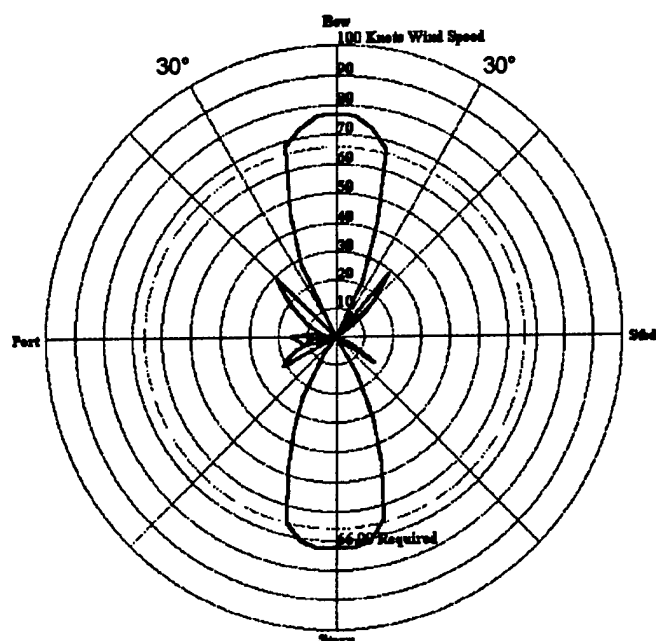


Fig. 20: The Ocean Clippers Capability with Upgraded Main Screws and the Loss of Bus #1 (Aft Azimuthing Thruster) for the North Sea

C. DPS-3

The capability needed to meet DPS-3 requirements is the same as DPS-2; therefore, the only additional modifications that must be made are structural. Compartmentalization of several key components is done to ensure redundancy in case of fire or flood. These components include the engines, SCR panels, transformers, AC condensers, and equipment in the DP room. Fig. 18 and Fig. 19 show the A60 watertight bulkheads added to the engine room (top tank deck) and SCR room (second deck) in order to meet the DPS-3 classification. In the case of a failure in any single compartment due to fire or flood, the addition of these bulkheads prevents the loss of more than one engine, transformer, or SCR panel.

D. Cost

The North Sea cost analysis shows that it costs \$48.7 million US dollar's to convert from a DPS-1 to a DPS-2 classification. To convert from DPS-2 to DPS-3 it will cost \$4.4 million US dollars. The total cost to convert from DPS-1 to DPS-3 is \$53.1 million US dollars. It costs approximately \$290 million US dollars to build a new DPS-3 class drillship for the North Sea environment. The difference between building a new ship and modifying the *Ocean Clipper* is \$237 million US dollars. It is recommended that all of the modifications needed to upgrade from DPS-1 to DPS-3 be accomplished at once since the cost difference is not dramatic.

VII. DIP Room

The current configuration of the dynamic positioning (DP) room, located just aft of the bridge, is shown in Fig. 21. This room is modified in several ways in order to meet DPS-3 classification requirements. The first problem that is addressed concerns fire safety. In the event of a fire breaking out on the bridge, the DP Room must be manned in order to ensure that the ship is able to stay on station. Since there is only one exit from the DP room, that leads onto the bridge, a crew-member in the DP Room is trapped until the fire is brought under control. A more serious concern is the possibility of a fire burning uncontrolled, necessitating the evacuation of the bridge deck. In this case a crew-member cannot escape. In order to rectify this problem a second door is installed in the DP Room as a means of fire escape.

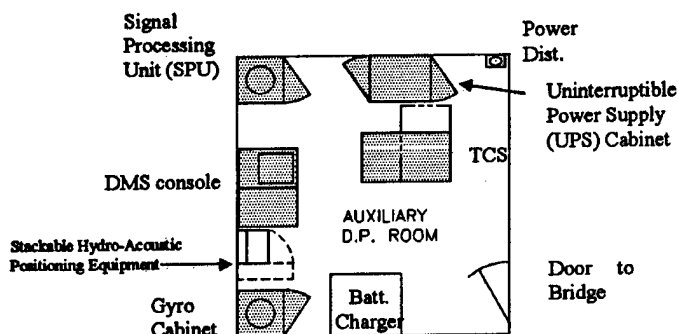


Fig. 21: Current DP Room

Next, equipment is moved out of and into the DP room to gain redundancy for all of the positioning systems. The DP room currently houses two hydro-acoustic positioning systems. These systems are used to position the ship by acoustic beacons placed on the seafloor and give essential information about the riser angle relative to the blowout prevention stack, or BOP. These are the only two acoustic positioning systems

on the ship; therefore, the loss of the DP Room results in loss of all hydro-acoustic positioning capability. Furthermore, the only uninterruptible power supply cabinet (UPS) is located in the DP room. The UPS is designed to provide battery power to the ship in the event of a blackout.

Finally, both of the two differential global positioning system (DGPS) sensors on the ship are located on the bridge. Loss of the bridge results in the loss of all DGPS reference capability. While the loss of either the hydro-acoustic systems or the DGPS systems by themselves do not cause a critical failure in the ship's ability to maintain station, it does leave the ship relying on one system alone. Loss of the UPS is catastrophic in that no power for lighting or essential systems is available to a repair team.

Each of the four design teams developed a modified DP room arrangement to adjust for the problems discussed previously. Next, the merits of each design were evaluated using a weighted objectives analysis as shown in Table 8.

Table 8: DP Room: Weighted Objectives Analysis

Objective	Weight %	WA	Score	SCS	Score
Low Cost	20	2	0.4	1	0.2
Fire Safety	35	4	1.4	4	1.4
Redundancy	35	4	1.4	4	1.4
Space	10	3	0.3	2	0.2
Total Score			3.5		3.2
Objective	Weight %	GOM	Score	NS	Score
Low Cost	20	4	0.8	4	0.8
Fire Safety	35	4	1.4	4	1.4
Redundancy	35	4	1.4	4	1.4
Space	10	2	0.2	2	0.2
Total Score			3.8		3.8

Each objective from the different designs is ranked 1 - 4, with a value of 1 representing a barely passable solution and a score of 4 representing an ideal solution. Each objective is weighted by a percent of importance making the highest possible total score from any group a 4. The highest scores are found in the Gulf of Mexico and North Sea groups. Taking this into consideration,

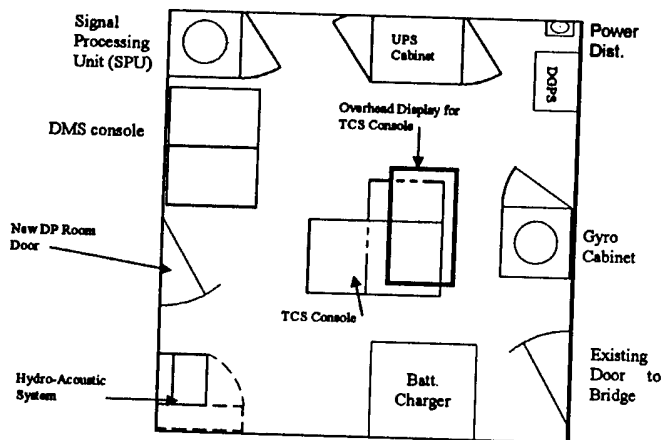


Fig. 22: Combined DP Room Proposal

all of the teams collaborated to propose the configuration shown in Fig. 22.

The combined proposal for the DP room has the essential fire safety measures installed and meets the redundancy requirements stipulated by a DPS-3 classification. The DP room has an additional exit located on the aft wall of the compartment. One DGPS unit is moved from the bridge into the DP room. One hydro-acoustic system is moved from the DP room to the bridge. A new UPS cabinet is placed on the bridge, and a new thruster control system (TCS) overhead display is placed in the DP room.

VIII. Cost Comparison

Table 9 shows a comparison of the costs to convert the *Ocean Clipper* from a DPS-1 to a DPS-2 class for each different environment. West Africa (WA) has the lowest cost (2.2 million) because it does not require any major structural changes. The North Sea (NS) has the highest cost (48.7 million) because all of the current engines must be replaced with more powerful engines, and an additional azimuthing thruster must be added, and other propulsion and electrical systems must be upgraded. The general costs include docking and inspection fees, painting, and any items that do not fall into the remaining categories. The structural costs include the addition and removal of bulkheads, and any hull modifications that were made. The propulsion costs include any additional propulsion equipment as well as any upgrades to the existing equipment. Finally, the electrical costs include any electrical modifications made on the vessel such as the addition of an electrical bus or wiring.

Table 9: Comparison of the Costs for the Different Environments for DPS-1 to DPS-2 in Millions of US Dollars

	Gen.	Struc.	Prop.	Elec.	Total
WA	2.2	None	None	None	2.2
SCS	2.9	0.2	None	2.1	5.2
GOM	8.8	None	4.8	4.1	17.6
NS	13.3	0.2	30.7	4.5	48.7

Table 10 shows a comparison of the costs for the *Ocean Clipper* to be converted from a DPS-1 to a DPS-3 classification. The conversion from DPS-1 to DPS-3 is recommend to be done at once because the difference in cost is not substantial for the conversion (\$3.2 million dollars average for the different groups). The main modification taking place in this conversion is the addition of the A60 watertight bulkheads.

Table 10: Comparison of the Costs for the Different Environments for DPS-1 to DPS-3 in Millions of US Dollars

	Gen.	Struc.	Prop.	Elec.	Total
WA	2.2	0.9	None	2.1	5.2
SCS	4.4	1.7	None	2.1	8.2
GOM	11.1	0.5	4.8	4.1	20.4
NS	17	0.8	30.7	4.5	53.1

IX Conclusions

The recommended changes to upgrade the *Ocean Clipper* from a DPS-1 classed drilling vessel to a DPS-3 classed drilling vessel are as follows. For drilling off the coast of West Africa a third electrical bus must be added to the two existing busses. The SCR room, transformer room, aft winch room, engine room, and A. C. condensers must be split with watertight A60 bulkheads. An additional door, backup hydro-acoustic equipment, and TCS must be added to the auxiliary DP room. These modifications are also recommended for the remaining three environments as well as other changes for each environment. To drill in the South China Sea under a DPS-3 classification it is recommended that two bulkheads be added to separate the engine room into two rooms containing two engines each, and one room containing three engines. To attain a DPS-3 classification in the Gulf of Mexico it is recommended that two engines be added to the engine room, and the azimuthing thruster and main screws be upgraded. Also, eight thruster motors and three electrical busses must be added to the vessel. To be classed as a DPS-3 drilling vessel in the North Sea the seven existing engines must be replaced with five more powerful engines. Also, an azimuthing thruster must be added to the vessel and the current azimuthing thruster must be upgraded. Finally, three new electrical busses must be added to the two existing busses.

X. References

American Bureau of Shipping (ABS). Guide for Thrusters and Dynamic Positioning System
ABS: New York, 1994.

American Petroleum Institute (API). Analysis of Spread Mooring Systems for Floating Drilling Units, 2nd Edition. American Petroleum Institute: Washington D.C., 1993.

Applequist, J., Carter, J., Dickey, R., Kyle, D., Kilgore, P., Lenamond, M., Madigan, C., Martinez, J., Mathews, E., Nelson, V., Noel, P., Olson, J., Phillips, P., Scott, C., Taylor, H., Turney, T., White, A., Conversion of the Ocean Clipper to DPS-3 Classification. Senior Design Project Report, Ocean Engineering Program, Civil Engineering Department, Texas A&M University College Station, TX, 1999

Baca, G., Personal Communication, Diamond Offshore Drilling Co: Houston, TX, 1999.

Webb, D., Personal Communication, Diamond Offshore Drilling Co: Houston, TX 1999.

XI. Acknowledgments

We would like to acknowledge several individuals who helped tremendously with our project. We would like to begin by thanking our professor Dr. Bob Randall who contributed tremendous amounts of time and energy to this project and acted as the course instructor and mentor for the completion of this paper. We also thank our classmates, Jonathan Applequist, Ray Dickey, David Kyle, Patrick Kilgore, Mitchell Lenamond, Chris Madigan, Jose Martinez, Erin Mathews, Virginia Nelson, Paul Noel, Josh Olson, Patrick Phillips, Tracey Turney, and Adam White, for their outstanding work. We would like to thank Diamond Offshore for agreeing to work with the class on the project and for providing data, drawings and software support. Special acknowledgments go to Mr. Dave Webb of Diamond Offshore who served as a visiting instructor. The contributions of Tony Martinez, John Williams, Captain Bamber, Don Howard, and George Baca are also greatly appreciated. We would like to thank everyone at Nautronix for aiding us in understanding the DPS equipment on the vessel. Finally, we thank all those at the Texas A&M Low Speed Wind Tunnel for the tour of their facilities.

FAST INTERPOLATION, SEGMENTATION AND VISUALIZATION OF 3D SONAR SEABOTTOM DATA BY USING TREE STRUCTURES

R.E. Loke and J.M.H. du Buf

Vision Laboratory, Dept. of Electronics and Computer Science

University of Algarve, 8000 Faro, Portugal

email: {loke, dubuf}@ualg.pt

URL: <http://w3.ua1g.pt/~dubuf/vision.html>

Abstract: *We describe an unsupervised processing pipeline for the analysis and visualization of sonar data. Recently developed 3D interpolation and segmentation methods are introduced, as well as a completely new surface construction method. All methods are based on employing quad- and octrees, which results in a fast processing. Accurate results are obtained for complex boundary shapes. Processed seabed data are accurately fused with bathymetric data. The methods enable a fast, highly accurate and interactive seabed analysis.*

I- Introduction

3D processing and visualization extends traditional image analysis, facilitates the detection of structures and objects, and improves analytical accuracy. 3D seabed data are obtained at various sites by using bottom-penetrating sonar (Topas) on a vessel which maneuvers in zigzag patterns. In order to extract continuous surfaces from these data, robust interpolation, segmentation and surface construction methods are required. For the interpolation a method has been developed which takes the nature of the data into account [1]. For the segmentation a 2D method [3, 4] has been extended to 3D. Marching Cubes [21] is a well-known surface construction algorithm. Here, a method is presented which creates efficiently-encoded surfaces. In the methods hierarchical data representations play an important role. Each method consists of an upward pass in which a multi-resolution pyramid is built and a downward pass in which the processed data is refined. Because processing at low resolutions is very fast, initial coarse processed data are quickly obtained whereafter the ROI can be easily adjusted. This improves the interactivity and avoids unnecessary computationally-expensive processing at high resolutions. Hence, this fast user interaction enables a fast analysis of huge data volumes of large survey areas.

II- Volumetric interpolation

The most prominent feature of Topas sonar is that each acoustic signal represents 1 vertical line in the seabed (ping). Therefore,

we can make a map of the ship trajectory, i.e. a pingmap (see, e.g., Fig. 6a). After the selection of a user-defined ROI in the map, the ping data is registered on a regular volume. The empty spaces in the volume are then filled using a 3D interpolation method based on a quadtree of the pingmap. Its basic idea is that by sampling the data in a quadtree the gaps get smaller at higher tree levels. Small gaps can be interpolated at low and big gaps at high levels, both using adjacent information available; see Fig. 1. Below the processing steps are described.

A- Quadtree construction: Let the original pingmap (with gaps) be level 0 of the quadtree. Starting at level 0, the following 3 processing steps are performed for each level l . First, if $l > 0$, a new level is constructed by performing for each position a bottom-up selection at $l - 1$. If a 2×2 block of child positions contains 1 or more pings, one is selected. Second, all gaps between data positions of size l are marked for interpolation. Gaps are marked differently, depending whether $\Delta x = 1$ or $\Delta y = 1$; if $\Delta x = \Delta y = 1$ the gap is marked as $\Delta x = 1$. This facilitates the interpolations because we need only to interpolate between 2 pings. Third, it is determined if a higher level must be added. If all positions are either marked or filled the tree is ready.

B- Interpolation and down-projection: Let the constructed quadtree contain n levels. For each level l , starting at level $n - 1$ and ending at level 0, the following 3 processing steps are performed. First, if $l < n - 1$, an extra marking pass is performed in order to mark new gaps which have been created by down-projecting data from higher levels, see below. Second, pings are determined for all empty positions. At each non-marked position the closest ping is determined in the local 2×2 block using a top-down selection at level 0. This ping is then duplicated. This leads to a blocky effect. In the results section we describe how to perform the interpolation without these duplications. At each marked position (x, y) a ping is interpolated using either the pings

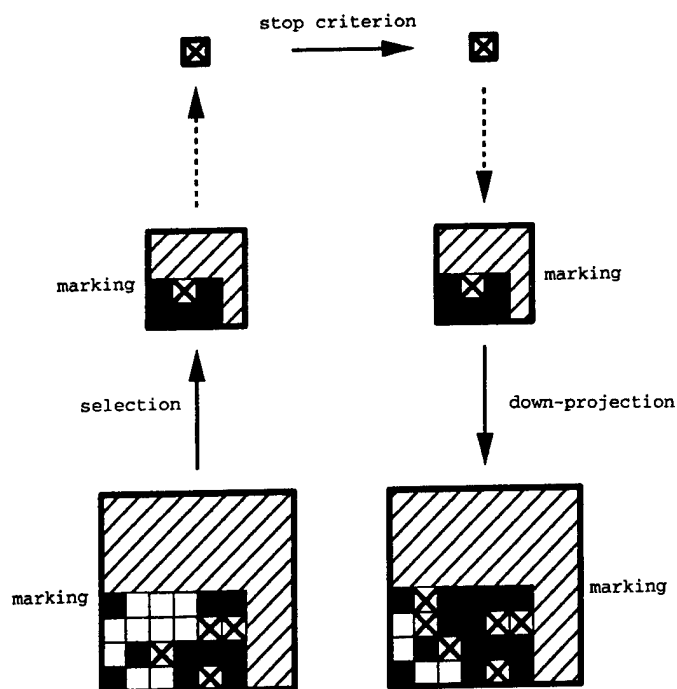


Figure 1: Processing steps in the quadtree of the pingmap which guides the 3D interpolation. Empty positions are denoted as white and filled positions as black squares. A cross in a white square denotes that the position is marked for interpolation. A grey cross indicates that the position is marked in a second pass.

at $(x-1, y)$ and $(x+1, y)$, or $(x, y-1)$ and $(x, y+1)$, depending whether (x, y) is marked as $\Delta x = 1$ or $\Delta y = 1$. The closest pings are used by performing a top-down selection at level 0. Then, an interpolation scheme is used in which boundary orientations at each depth in the data pings are estimated by calculating cross correlations, using a mask of size s . The correlations are obtained by fixing the depth of the mask in one ping (M in $p1$) and changing it in the other ping (M_i in $p2$); see Fig. 2. Totally, N depths are used for each depth z in $p1$. A high correlation indicates a good fit between the data in the masks. Therefore, the depth with the maximum correlation is determined. This defines the orientation for a linear interpolation between the data values in $p1$ and $p2$, and results in a value for ping p . If there are multiple depths with identical absolute maxima, each depth is taken into account. This allows for the interpolation of complex shapes. After performing this interpolation scheme at all $p1$ depths, remaining empty places in the ping p are filled by using linear interpolations, because not necessarily all places are filled. Third, if $l > 0$, the determined pings are down-projected to their child positions at all lower levels.

III- Volumetric segmentation

Regions are automatically detected by using a segmentation method which is very robust to noise in the data. The basic idea is that by spatially smoothing data in an octree

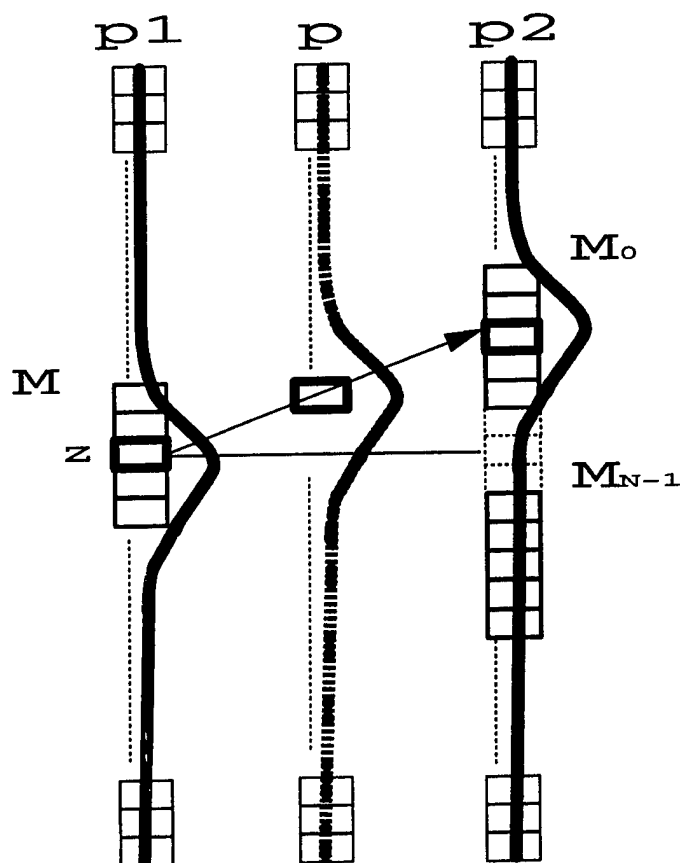


Figure 2: Shape-based interpolation between 2 pings at a depth z . The 2 bold lines ($p1$ and $p2$) denote available signals, solving a simple reflection. The dashed bold line (p) is the interpolation result. M is the fixed mask at $p1$, M_i the variable mask at $p2$. The arrow indicates the determined orientation.

the class separation in the feature space increases. This allows for a good data classification at a high tree level. Then, by employing a noise-robust filter method in the boundary regions, data can be classified at high spatial resolutions. Below the processing steps are described.

A- Octree smoothing and clustering: In the octree construction, voxels at level 1 ($l > 0$) are calculated by averaging non-overlapping voxel blocks of size $2 \times 2 \times 2$ at level $l-1$. The resulting tree contains n levels where level 0 represents the original data. In the special case that level 0 has the size of a cube, level $n-1$ consists of only 1 voxel which is the mean of all data voxels. At a level l_c where the noise in the feature space is sufficiently reduced, an unsupervised clustering method without spatial connectivity constraints is applied in order to determine the data clusters. Local-centroid clustering [4] is used. In this algorithm the histogram is iteratively changed by calculating, for each greyvalue x , a sum of histogram values in a local mask. The sum is weighted depending on the distance to x . This weighted sum indicates another greyvalue to which the histogram value at x is added. The algorithm stops when there are no more changes in the histogram. Then the histogram directly yields the clusters. Furthermore, a

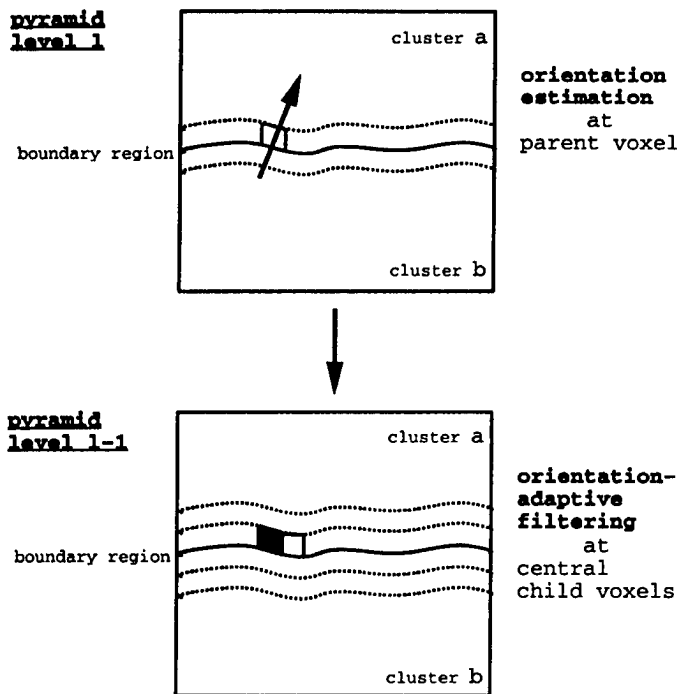


Figure 3: 2D scheme of the 3D boundary-filter method applied to a simply-shaped configuration. It shows a crosssection of 2 corresponding tree levels l and $l-1$. Level l has been expanded. At level l , the boundary region consists of 2 voxel layers; at level $l-1$, of 4. At level l the arrow indicates the orientation perpendicular to the boundary. At level $l-1$ the filled square indicates a child voxel whose neighborhood is filtered.

supervised method has been implemented which allows the user to interactively specify clusters in the histogram. The segmentation at level l_c is obtained by labeling each voxel with the label of its nearest cluster.

B- Down-projection and boundary refinement: In order to obtain the segmentations at lower levels ($0 \leq l < l_c$) for each level l , starting at level l_c and ending at level l , the following 2 steps are performed. First, the label of each non-boundary voxel is down-projected to its 8 children. Also, for the children which are not centrally located, their parent label is directly allocated. Second, for each boundary voxel, an orientation-adaptive refinement is used. It consists of calculations performed at level l and $l-1$; see Fig. 3. At level l , all cluster configurations in the neighborhood of the voxel are determined. For each configuration, the 3D orientation of the vector orthogonal to the boundary is estimated. Then, at level $l-1$, for each child which is centrally located in the boundary region, the local data is convolved with a 2D planar filter which is positioned successively in all determined orientations. The use of this filter, instead of a 3D diaboloid-like filter, highly improves the boundary quality. The label which is allocated to the child is determined by using a smallest distance criterion between the filter responses and the clusters.

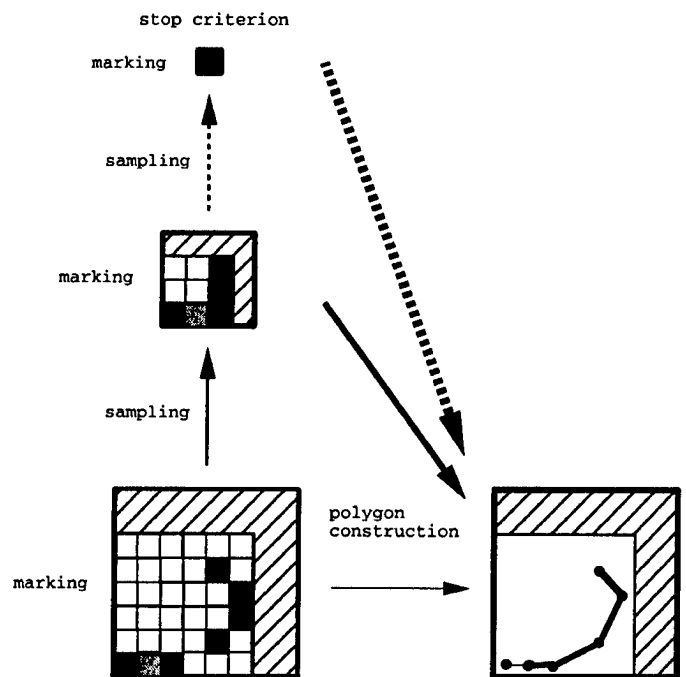


Figure 4: 2D scheme of the processing steps in the octree which guides the surface construction and approximation. On the left an octree is shown and on the right a corresponding continuous space. Squares represent voxels and dots vertices. Filled squares denote boundary voxels, white squares background voxels. A grey square indicates that the spatial continuity of the voxel is marked. Lines denote edges. The thicker the line, the higher in the tree it has been constructed.

IV- Surface construction and visualization

After the segmentation, a connected-component labeling is performed in order to partition each cluster into separate regions, because regions which belong to the same cluster may not be spatially connected. Then the surfaces of each region are extracted by using a new method. Its basic idea is that by sampling the data in an octree the spatial continuity of the boundary voxels increases at higher tree levels. With some restrictions, high-curvature areas can be connected at high and low-curvature ones at low resolutions. Furthermore, separated voxels at a high resolution can be connected at low resolutions; see Fig. 4. In this way it is possible to construct large polygons covering flat boundaries and smaller ones in curved boundaries and intersections. Below the processing steps are described.

A- Octree construction: Let the original data of size $N_x \times N_y \times N_z$ consist of boundary voxels denoted by $I1$ and background voxels denoted by $I0$. This is octree level 0. Starting at level 0, the following 4 processing steps are performed for each level l . First, if $l > 0$, a higher level is constructed by performing for each voxel a top-down search in the $2 \times 2 \times 2$ non-overlapping block of child voxels at $l-1$. If at least 1 of the 8 children is equal to $I1$ or is marked (see below), the parent is set to $I1$. Second, for each $I1$ voxel the spatial continuity in its neighborhood is

determined. A simple model is used which only takes into account the 6 closest voxels: $x0, x1, y0, y1, z0$ and $z1$. Let $j01$ denote $j0 \neq I0 \wedge j1 \neq I0$, and X, Y, Z, XY, XZ and YZ denote $x01, y01, z01, x01 \wedge y01, x01 \wedge z01$ and $y01 \wedge z01$, respectively. Hence, X denotes a voxel with continuity in x ($I1$ in $x0$ and $x1$), and XY denotes a voxel with continuity in x and y (diagonal). Then, continuities are marked differently, depending on the boolean values X, Y, Z, XY, XZ and YZ ; if $X \wedge Y \wedge Z$, it is left unmarked because we want only to construct polygons for region surfaces, and not for region interiors. This facilitates the 2D polygon construction. Third, if $l > 0$, for each marked voxel it is determined whether it is also valid at higher resolutions. A marked voxel is valid if it is equal to or higher than ($XY > X, XY > Y, XZ > X, XZ > Z, YZ > Y$ and $YZ > Z$), and not contradicting (according to 3 orthogonal groups: $\{X, Y, XY\}$, $\{X, Z, XZ\}$ and $\{Y, Z, YZ\}$) its marked child voxels at all lower levels. Fourth, it is determined whether a higher tree level must be added. If $N_x < 2, N_y < 2$ or $N_z < 2$ the tree is ready. Only when $N_x \geq 6, N_y \geq 6$ or $N_z \geq 6$ an extra level is built.

B- Polygon construction: Let the constructed octree contain n levels. Then n surfaces can be built, independently of each other, at the different resolutions. Let s ($0 \leq s < n$) be the desired resolution level. Then, for each level l , starting at level $n - 1$ and ending at level s , a polygon construction scheme is performed for each marked voxel. If $l > s$, it is performed only for voxels which are valid at s . In this scheme, vertices are determined for the relevant voxels by performing a top-down selection in the tree. Thereafter, a polygon is constructed by connecting the vertices in a, for XY, XZ and YZ differently defined, clockwise order.

V- Results and discussion

The methods were applied to both artificial data volumes and 3D sonar data. Underwater acoustic data were obtained with Topas sonar at a Norwegian site *Horten*. A part of the pingmap, can be seen in Fig. 6a. The positions were obtained after linear interpolation between GPS coordinates using an independent ping timer. Each ping was preprocessed performing a gain correction (different pings can have different gain values), a time-variable gain modification, an averaging filter and rectification. See Fig. 6b for a traditional 2D dataplot of the 8 "linear" trajectories. After the selection of a 3D ROI, a volume was created by mapping the pings to a regular grid of size $64 \times 128 \times 128$. Thereafter, 16.46% of the *Horten* volume was filled; see Fig. 8a.

A- Complex shapes: Both the interpolation and segmentation allow for the processing of complex-shaped boundaries. In the ping interpolation scheme multiple orientations are calculated. Then, for each orientation an interpolation is performed. In the boundary refinement of the segmentation, multiple cluster configurations in the local voxel neighborhood are determined. Then, for each configuration the boundary is filtered, and the allocated label is determined by taking

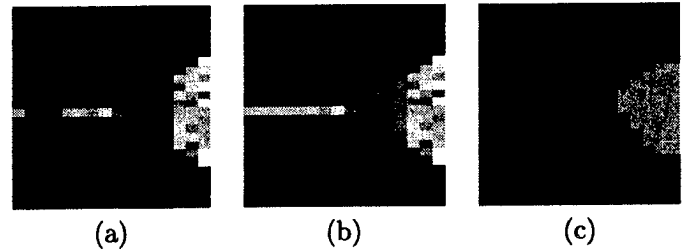
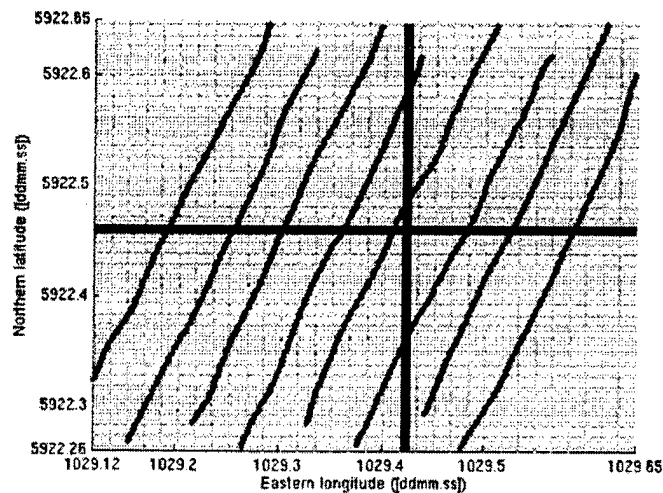


Figure 5: A slice of an artificial noisy volume with gaps (a), and the same slice after 3D interpolation (b) and segmentation (c).

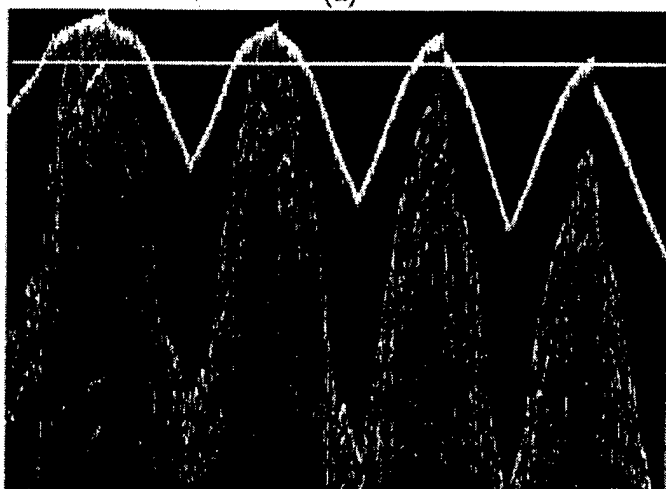
all the filter responses and clusters into account. See Fig. 5 for the interpolation and segmentation of a complex-shaped boundary. The boundary was accurately processed. The size of the volume was $16 \times 16 \times 16$. The greyvalues were 0 and 255. Zero-mean Gaussian white noise with $\sigma = 32$ was added. In the interpolation, the correlation mask size s and correlation neighborhood size N were set to 9. In the segmentation the clustering was performed at level 2. The local-centroid clustering algorithm, performed with a mask size of 29, found 3 clusters after 9 iterations. In the boundary refinement the size of the planar filter was 5×5 . At level 2 and 1, the percentage of boundary voxels in complex neighborhoods was 33 and 12, respectively.

B- 3D interpolation: Interpolation results on *Horten* can be seen in Figs. 7 and 8. The 3D interpolation was performed by using only shape-based interpolations and no duplications. Therefore, the gaps which are normally filled by duplication, were marked by performing iterations of the method on x and y shifted data. In each iteration interpolations were performed for gaps which could not be marked before. Totally, 9 shifts, covering all possible configurations of a 2×2 subblock in a 4×4 block, and iterations were performed. Only in a tenth iteration duplications were allowed to fill in gaps on the borders of the volume. This highly increased the smoothness of the final result. The highest pyramid consisted of 6 levels. The parameters s and N were set to 51 and 31, respectively. Both small and big gaps have been adequately interpolated and the boundaries are smooth; see Fig. 7. In 3D the data is coherent; see Fig. 8. A blocky appearance on the borders, in both the slices as in the volume, can still be seen. Here, only very few pings were available. We note that the visibility of the data in Fig. 8 is highly improved by interactively rotating the volume on the screen.

C- 3D segmentation: Slices of the segmented *Horten* volume can be seen in the third column of Fig. 7. The local-centroid clustering was performed at tree level 1 with a mask size of 19. The algorithm found 9 clusters after 10 iterations. For the boundary refinement, the size of the planar filter was set to 7×7 . At level 1, 44% of the voxels were in the boundary region, from which 42% in complexshaped neighborhoods. At level 0, 68% of the child voxels were located in the center of the boundary region. As



(a)



(b)

Figure 6: Raw 3D seabed data of *Horten*. In (a) and (b) the vertical and horizontal bars denote slices shown in Fig. 7.

can be seen, the boundaries are very smooth and there are only few isolated regions. The boundary filtering effectively smoothes the jaggies introduced by the interpolation. Below, we visualize the boundaries between the regions in the segmented volume with VRML.

D- Data fusion: At *Horten* bathymetric data were obtained using multibeam echosounder. In order to evaluate the volumetric processing, these data were gridded to the interpolated *Horten* volume. Fig. 7 shows fusion results. The boundary shape of both data is corresponding accurately.

E- Surface visualization: Surfaces are visualized in VRML (Virtual Reality Modeling Language). This allows for an interactive 3D analysis by “flying” through and around the ROI data. In the future we plan to use OpenGL which allows to perform 3D measurements, e.g., the interactive calculation of distances and angles. Results of the surface construction method (at the highest resolution) can be seen in Fig. 9. The visibility on the screen is much better by the use of color attributes and rotations. Figure 9a shows the polygons built for an artificial solid

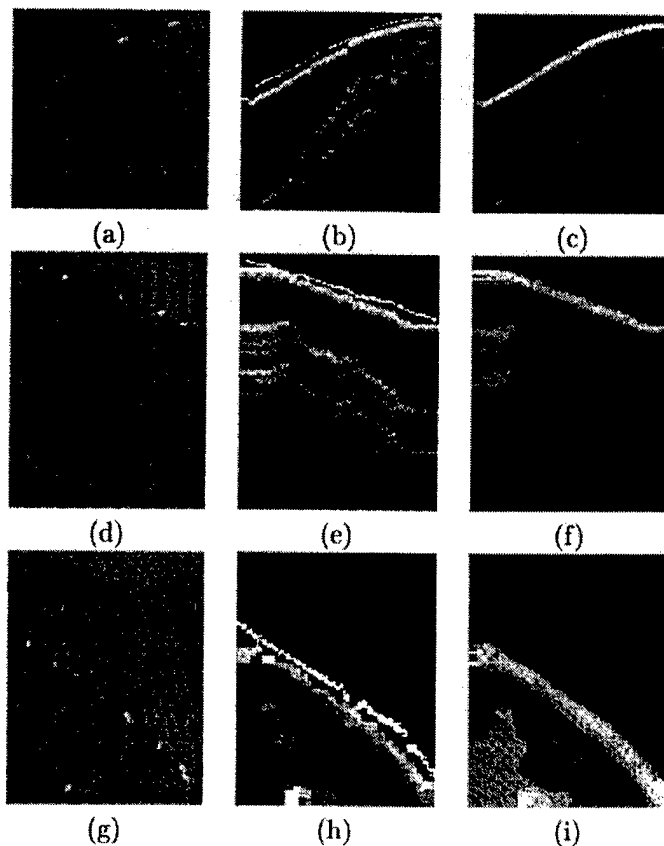


Figure 7: Slices of *Horten*, after 3D registration (a,d,g), interpolation (b,e,h) and segmentation (c,f,i). The first row shows the slice indicated by the vertical bar in Fig. 6a, the second the slice indicated by the horizontal bar in Fig. 6a, and the third the slice indicated by the horizontal bar in Fig. 6b. In (b), (e) and (h) white denotes fused bathymetric data.

cube. The surfaces are efficiently encoded with big polygons in the center of the faces and smaller ones at the edges. Figure 9b shows the surfaces built for the regions of I cluster in the segmented *Horten* volume. The method was performed on a selected ROI of $28 \times 48 \times 128$ in the original volume. The tree consisted of 3 levels. As can be seen, the cluster consists of 3 regions, of which only one is small and isolated (on the right). Small polygons were created for high-curvature areas and big ones for low-curvature areas. The surfaces of the cube are completely connected, whereas the surfaces of the more irregular *Horten* data still contain many gaps. Furthermore, in the *Horten* data, there are still some incorrect polygons created at low resolutions which connect the 2 deepest surfaces. This is due to the simple spatial continuity model used. We intend to develop a more elaborate model which incorporates all the voxels in the local $3 \times 3 \times 3$ neighborhood, and not only the closest. Figure 10 shows the extracted surfaces of all regions in the ROI of the segmented *Horten* volume when a simple method is used. The boundaries are coherent, very smooth and there exist almost no small isolated regions. The seabed consists of 4 sediment layers. See Tab. I for the computation times

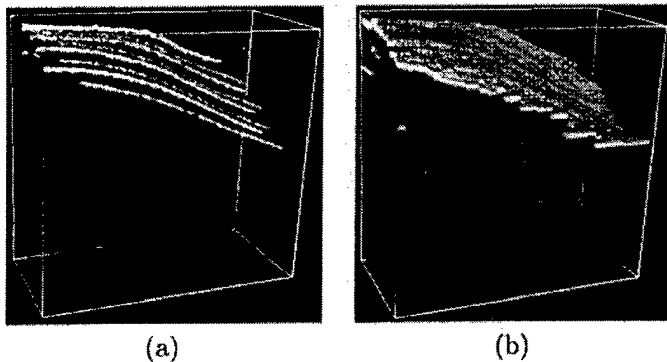


Figure 8: Volumetric visualization (with Bob) of *Horten* before (a) and after (b) 3D interpolation.

Table 1: Processing data of *Horten*.

size of raw Topas data	
number of pings	5899
MBytes	92.2
ROI volume size	
number of voxels	64×128×128
MBytes	4
voxel size (m)	
longitude	6.29
latitude	5.60
depth	0.24
CPU time (seconds)	
registration	4
interpolation	189
segmentation	485
surface construction	
simple method	129
fast method	24

of the developed methods on *Horten* and further information of the *Horten* data. CPU times refer to the execution on a SGI Origin 200QC server, using only one of the 4 processors. Future parallelized versions we expect to be at least a factor 3 faster. Furthermore, for the segmentation we expect a significant speedup, because the filter method is still performed in 3D, not taking into account the 2D planar filter. More experimental results, of this and other sites, including movies, VRML and OpenGL worlds, as well as raytraced animations, can be interactively visualized at our webpages of the ISACS project.

V1- Acknowledgements

This work was supported by the European MAST-III ISACS Project, contract MAS3-CT95-0046.

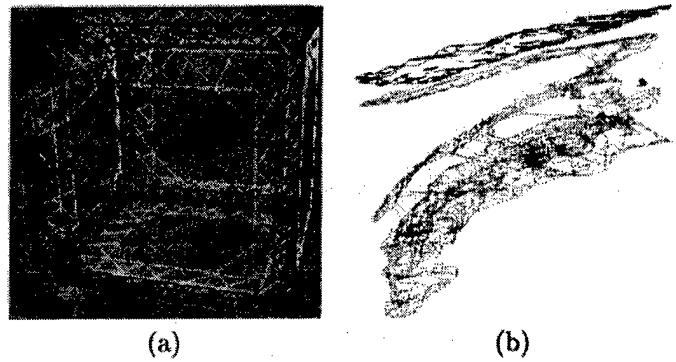


Figure 9: Polygon visualization in VRML.

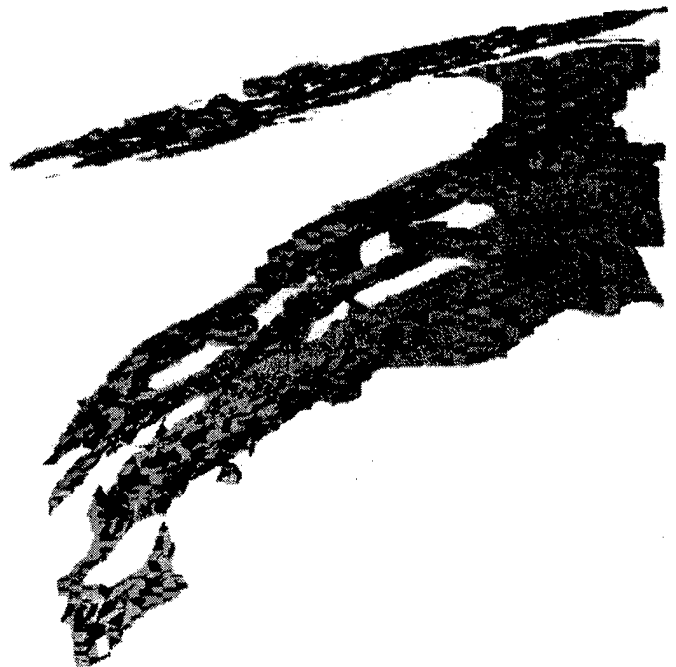


Figure 10: Surface visualization in VRML of a ROI in *Horten*.

VII- *

- [1] R.E. Loke and J.M.H. du Buf. Hierarchical 3D shapebased interpolation of irregularly-spaced sonar data. Tech. report: UALG-ISACS-TRO6, 1999.
- [2] W.E. Lorensen and H.E. Cline. Marching cubes: A high resolution 3D surface construction algorithm. *Computer Graphics*, 21 (4):163-169, 1987.
- [3] P. Schroeter and J. Bigiin. Hierarchical image segmentation by multi-dimensional clustering and orientation-adaptive boundary refinement. *Pattern Recognition*, 28 (5):695-709, 1995.
- [4] R. Wilson and M. Spann. *Image Segmentation and Uncertainty*. Research Studies Press Ltd., Letchworth, England, 1988.

MATCHED ARRIVAL PROCESSING FOR EFFICIENT INVERSION IN UNDERWATER ACOUSTICS

Xiaoqun Ma and Zoi-Heleni Michalopoulou

Department of Mathematical Sciences,
New Jersey Institute of Technology,
Newark, NJ 07102

ABSTRACT

The focus of this paper is on the linearization of the inverse problem in underwater acoustics. We develop a simple inversion method for source range and depth estimation. The method identifies the time arrivals of the direct and first surface reflected ray paths in the true ocean impulse response and compares them to corresponding arrivals in a replica impulse response. Through the linearization of the relationship between time arrival difference and source location parameters, the source location is estimated efficiently and accurately.

I. INTRODUCTION

A popular approach for inversion in underwater acoustics is matched-field processing [1]. Inversion of the acoustic field using matched-field processing techniques requires a combination of wave propagation modeling for the generation of replica fields at receiving phones and a decision rule that estimates the unknown parameters, based on which values of these parameters maximize the similarity between replica and true acoustic fields. When the number of the unknown parameters is large and the signal carries broadband information, the computational load of matched-field inversion methods is substantial, because many replicas need to be computed and compared to the true field. In order to reduce this load without compromising the quality of the estimates, we implement a linearization inversion method that can be applied for the estimation of source location coordinates. This linearized inversion takes into account two ray paths: the direct path connecting source and receiver and a path that undergoes a single surface bounce. The paths are identified in the impulse response of the ocean estimated from data and their times of arrival are compared to those of corresponding paths in replica impulse responses.

Linearization is a method frequently used in inverse problems [2] and has been successfully implemented in several aspects of inversion in underwater acoustics. Recently, linearized inversion comparing direct path time arrivals at spatially separated phones was demonstrated in [3] with excellent results in array element localization. Linearization for source localization and bottom depth estimation using time arrivals of several paths was suggested in [4]. The approach proposed in [4], however, would require identification of the nature of each arrival observed in the ocean impulse response (that is, how many bounces each path has gone through and with which interfaces it has interacted). Such identification is not always straightforward, especially when only limited prior information is available on the propagation environment.

The novel element of this paper is the implementation of a linearization approach that employs two paths, the direct and first surface bounce, for source localization. The specific paths were selected in this work, because they are typically simple to identify. Usually, the direct path is the first detected arrival, whereas the first surface bounce, following the direct arrival, can be easily identified because of its sign difference from the direct path, a result of the reflection at the surface; this sign/phase difference is illustrated in Fig. 1. In essence, the proposed method is a localization approach through model-based time-delay estimation.

II. ENVIRONMENT DESCRIPTION

We consider a shallow water environment and a broadband, high-frequency source. Ray theory is used to model propagation between source and receivers [5]. Only relatively short range propagation is considered, in order for the direct and surface paths to be resolvable [6]. The sound-speed profile is assumed known. The received fields are measured at several, vertically separated receiving phones (the importance of the number of phones will be addressed later in the

This work was supported by ONR Ocean Acoustics, through grant number N00014-97-1-0600.

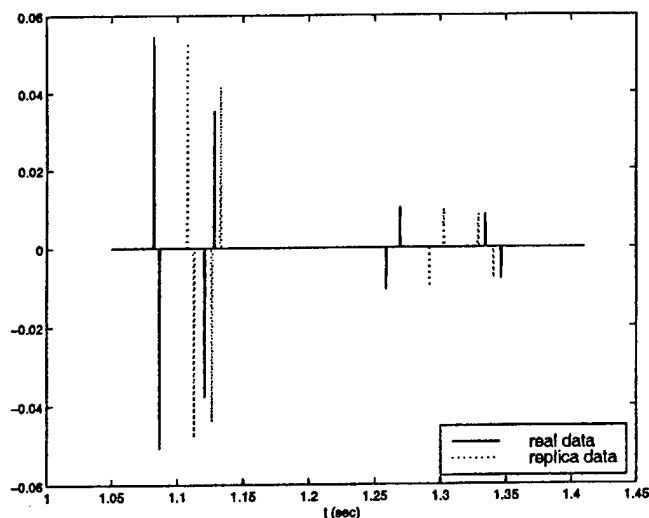


Figure 1: Arrivals in the ocean impulse responses.

paper). A sketch of the problem geometry is shown in Fig. 2.

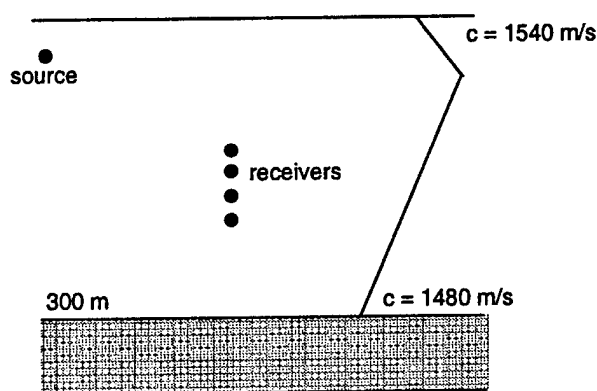


Figure 2: The propagation environment.

III. RAY TRAVEL TIME DERIVATIVES

The linearization approach requires the computation of ray travel derivatives with respect to the unknown parameters, source range and depth. The derivation of the time derivatives for the direct ray path is presented analytically in [3]. The approach of [3] can be extended for the time derivative calculation for the first surface bounce, considering rays connecting the source to the ocean surface and the surface to the receiving phone. Calculations involving ray paths require the ray parameter $p = \cos(\theta(z))/c(z)$ characterizing eigenrays connecting source and receiver, where $\theta(z)$ is the path grazing angle and $c(z)$ is the sound speed at depth z . Parameter p is usually assigned an initial value which is then updated using Newton's method [3].

IV. THE LINEAR SYSTEM

The arrival times of the different paths depend on the geometry parameters in the underwater problem of interest:

source range, source depth, bottom (water column) depth, and receiving phone depth. We assume that the phone depths are precisely known. Although bottom depth is a significant factor determining time arrivals of paths that have been reflected off the seafloor, it does not affect the inversion process of this work, since the two selected paths do not interact with the sea-bottom.

We assume a linear relationship between time arrivals and the geometry parameters. We then select a set of initial conditions for the unknown geometry parameters (r_0 and s_0 for range and depth) and generate replica signals corresponding to the selected initial conditions. The time differences are measured between path arrivals in the real and replica signals. Under the assumption of linearity, these time differences can be written as:

$$\Delta\tau_{ij} = \alpha_{ij}\Delta r + \beta_{ij}\Delta s, \quad (1)$$

where $i = 1, \dots, n$, the number of receiving phones, and $j = 1, 2$; when $j = 1$, the arrivals of the direct path are considered and when $j = 2$ the arrivals of the first surface reflected path are compared. Parameters r and s are the unknowns of the problem, namely the source range and depth. Parameters Δr and Δs are the "corrections" required in the assumptions r_0 and s_0 for range and depth for a better match between replica and real time arrivals. Coefficients α_{ij} and β_{ij} are the time derivatives with respect to source range and depth respectively, calculated for path j and receiver i for the assumed initial conditions r_0 and s_0 .

Equation 1 leads to an overdetermined linear system when all paths and receivers are combined. Depending on the proximity between initial values r_0 and s_0 and true range and depth and noise in the arrival times, the system might need to be solved several times before convergence; each time, replicas are generated for the "corrected" source range and depth. The "correction" is the result of the addition of Δr and Δs to the initial conditions of the previous iteration. The overdetermined linear systems can be solved with the least-squares approach [7]. Replicas here are generated using BELLHOP [8].

V. THE ROLE OF TIME INFORMATION IN INVERSION

We initially assume that source and receiver are synchronized leading to a known absolute time for the arrivals at the receiving phones. Table 1 presents the localization results obtained when the time arrivals of

Table 1: Source localization results using the linearized approach.

number of receivers	number of iteration steps	r	s
3	3	800.00	15.01
5	3	800.01	15.00
10	3	800.00	15.01

Table 2: Source localization results using the linearized approach with uncertain time arrivals.

number of receivers	number of iteration steps	r	s
3	4	799.78	14.25
5	4	799.99	14.39
10	3	800.00	15.13

the direct path and first surface reflection can be measured with no error. The initial conditions are 1200 in and 50 in for source range and depth, whereas the true source location is at a range of 800 in and depth of 15 m. The table shows results from three different configurations involving three, five, and ten phones. The results are excellent, the source location being estimated accurately only after three iterations.

Table 2 shows the localization results when time arrivals are uncertain. The uncertainty is taken into account through the addition of random noise to the time arrivals. The noise is drawn from a zero-mean Gaussian distribution with a standard deviation of 0.5 ins (Table 2 presents results from a single realization with uncertain arrivals). The source localization results are slightly degraded because of the uncertainty in the time arrivals, but the source is still located accurately.

In practice, absolute time is not always known in underwater acoustics problems. In such cases, the linearization approach described above becomes more complex.

Here, we address the problem of unknown time by comparing the differences between the direct and first surface reflection arrival time from real and replica signals. Additionally, considering the time series at one of the receivers as a reference, we compare the time differences between the first surface reflection paths across hydrophones between real and replica signals.

Comparison of Tables 3 and 1 shows that, when no temporal uncertainty is present, localization is accurate

Table 3: Source localization results using the linearized approach using relative travel times.

number of receivers	number of iteration steps	r	s
3	5	799.99	15.04
5	5	800.13	15.02
10	4	800.00	15.01

Table 4: Source localization results using the linearized approach with uncertain time arrivals using relative travel times.

number of receivers	number of iteration steps	r	s
3	9	769.49	13.56
5	7	783.05	14.07
10	8	800.00	16.00

no temporal uncertainty is present, localization is accurate and fast whether absolute or relative time is used. With time arrival noise involved, the error of the estimation is increased, however, as the results of Table 4 illustrate. Noise in the time arrivals is actually magnified in the relative arrival time approach, since it is present in both direct and surface arrivals, the difference between which is measured and matched to the difference between direct and surface path arrivals of a replica signal. It can be seen from a comparison of Table 4 to Tables 1, 2 and 3 that, when only relative time information is available and noise is present in the time arrivals, the linearization approach requires more iterations for convergence-, the number of total iterations is still manageable, however, and the process is efficient and accurate under those circumstances as well. Table 4 also shows that the estimation process is assisted through the presence of a large number of receiving phones; data collection at ten phones improves the source localization results obtained with only three phones.

VI. DISCUSSION

A linearized approach to source localization employing time arrivals of two ray paths, direct and first surface reflection, was presented in this work. The method was tested on synthetic data and gave successful result seven in cases of time arrival measurement uncertainty. It was observed that knowledge of

absolute time offers an advantage to the localization process and such information should be used when available. When the source instant is unknown, however, successful localization (with only a minor performance degradation) can still be achieved using relative time information; more iterations and phones are, then, needed for convergence.

It is our goal to use the linearized inversion scheme either for active source localization in the ocean or as a preprocessing tool for active, broadband geoacoustic inversion. In the first application, the linearization approach is expected to give excellent results without inverting for parameters of the ocean environment that are unknown but have no impact on the direct and surface paths. The method would, thus, not suffer from poor bathymetry and/or lack of sediment property knowledge and would be more computationally efficient than a model-based matched-filter [9, 10].

In geoacoustic inversion the method can be used to find estimates of the source location that would refine prior knowledge. As seen in [3, 10] accurate knowledge of source location is crucial for successful geoacoustic inversion. The proposed linearization approach can, thus, provide useful information at a minimal computational cost. Once the source location is estimated with the proposed scheme, matched-field inversion can be subsequently implemented for the estimation of environmental parameters.

The linearization approach can be also used for sound speed estimation in the ocean and for array element localization extending the approach of [3].

V11. REFERENCES

- [1] A. Tolstoy, *Matched Field Processing for Underwater Acoustics*. Singapore: World Scientific, 1993.
- [2] A. Tarantola, *Inverse Problem Theory*. Elsevier, 1987.
- [3] S. E. Dosso, M. R. Fallat, B. J. Sotirin, and J. L. Newton, "Array element localization for horizontal arrays via Occam's inversion," *J. Acoust. Soc. Am.*, pp. 846-859, 1998.
- [4] Z.-H. Michalopoulou and M. B. Porter, "Focalization in the Gulf of Mexico," in *IEEE Workshop on Underwater Acoustics Signal Processing*, (University of Rhode Island), October 1995.
- [5] F. Jensen, W. Kuperman, M. Porter, and H. Schmidt, *Computational Ocean Acoustics*. New York: American Institute of Physics, 1994.
- [6] E. K. Westwood and D. P. Knobles, "Source track localization via multipath correlation matching," *J. Acoust. Soc. Am.*, vol. 102, no. 5, pp. 2645-2654, 1997.
- [7] G. Strang, *Linear Algebra and its Applications*. Harcourt, Brace, Jovanovich, 3rd ed., 1988.
- [8] M. B. Porter, "The KRAKEN normal mode program." SACLANT Undersea Research Centre Memorandum (SM-245) and Naval Research Laboratory Mem. Rep. 6920, 1991.
- [9] J.-P. Hermand, "Broadband geoacoustic inversion in shallow water from waveguide impulse response measurements on a single hydrophone; theory and experimental results," *IEEE Journal of Oceanic Engineering*, vol. 24, no. 1, pp. 41-66, 1998.
- [10] Z.-H. Michalopoulou, "Matched impulse response processing for shallow water localization and geoacoustic inversion," tech. rep., Dept. of Math. Sciences, New Jersey Institute of Technology, 1999.

DIVER NAVIGATION AND TRACKING SYSTEM

D. Newborough and B. Woodward

Loughborough University, Electronic and Electrical Engineering Department, U.K.

E-mail: D.Newborough@lboro.ac.uk

Abstract - This paper describes an intelligent underwater acoustic system that allows the positions of several divers to be tracked in three-dimensional space and to telemeter each diver's co-ordinates to a remote receiver at the surface. The positions of the divers are fixed using three randomly deployed seabed transponders that may be described as 'intelligent'. The transponders fix their own relative positions and the position of the surface receiver, usually a vessel, by an exchange of coded acoustic pulses. These positions can be related to a differential GPS system at the surface if absolute co-ordinates are required. The divers each know their own position from a wrist-worn computer with a backlit graphical/numerical display. As well as the current position, the display can show the track from the beginning of the dive, the location of the surface vessel and the instantaneous position of the other divers. Also, a transponder can be attached to Remotely Operated Vehicle (ROV) or Autonomous Underwater Vehicle (AUV) to allow the position and data of the vehicle to be tracked by the surface vessel and by any divers in the vicinity.

1. Introduction

An 'intelligent' system to track the position and to allow divers to find positions underwater in three-dimensional space is of significant importance when the underwater operating time is limited due to the diver's air supply. Not only would the system reduce the time for the diver to orientate himself with his surroundings, it would allow consecutive dives to start at the exact point at which the previous dive finished. Also, the safety and progression of the diver can be monitored from a surface vessel. The main applications are seen to be for commercial and military operations and in scientific expeditions, for example archaeological surveys. A through-water acoustic communication link between the transponders and the vessel allows a surface computer to track the position of each diver in real time. Vital information about the divers' safety, such as their remaining air capacities and decompression times, may be calculated because the computer and the divers' wrist-worn units monitor the depth profiles. The data encoding technique employed is Phase Shift Keying (PSK), which gives high data rates, allowing short communication packet lengths. The communication protocols adapt to the surrounding environment and transponder positions. During the calibration of the transponder's positions, communication time windows are assigned to each

transponder. These windows devised depend on the arrival of reverberations of sufficient magnitude to affect the transmitted signal arriving at the destination transponder. This allows the transponder to transmit again before the previous transmission has had time to subside. Having short packet lengths reduces the problem of inter-symbol interference due to reverberation and minimises the need for error correction algorithms. However a Cyclic Redundancy Check (CRC) is encoded into the transmitted signal. The basic system arrangement is shown in Fig. 1

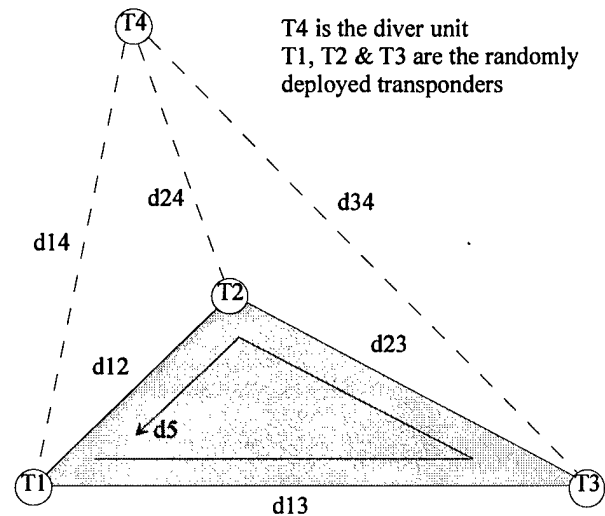


Fig. 1. Basic Transponder Arrangement

Distances d_{12} , d_{13} , d_{23} are determined by measuring the time of flight of a signal transmitted from one transponder to another and back. When the initiating transponder receives the reply it can measure the time for the two-way path plus the response dead time. The distance corresponding to the one-way time is calculated by subtracting the response dead time, dividing the result by two as it is a two-way path, and multiply the resulting time by the velocity of sound in water.

$$d_{12} = \frac{t_{12} - \text{deadtime}}{2} \times c \quad (1)$$

where c = velocity of sound.

2. System Design

The system is designed around an AMD 186 embedded microcontroller, which offers lower development costs than many Digital Signal Processors (DSP). Some software routines for the device can be evaluated on a normal desktop Personal Computer (PC) as software code for the 186 is upward compatible and hence will run on a 486 or Pentium microprocessor, this speeds up the debugging process. There are also significant power saving, interfacing and cost advantages.

A disadvantage with the AMD186 is that it does not have a Math Co-processor incorporated, which slows down the mathematical computation of the divers position. This was assessed and deemed unimportant, because after a signal is received a dead time has to be incorporated before the next transmission to allow the reverberations to subside. Also, there are four processors, including the diver worn unit, which if required can share the mathematical calculations, so in effect parallel processing is employed.

If there is more than one diver in the water then the transponders can effectively share out the control of each diver, e.g. if four divers are in the water, T_1 controls diver 1 and 4, T_2 controls diver 2, T_3 controls diver 3. This is one of the reasons why each transponder has been designed exactly the same, instead of making one a Master and the other two Slaves. This also simplifies the design and construction of each unit as each is just a replication of the original. The basic system shows the peripheral components with the AMD 186 at the heart of the system, Fig. 2.1. The hydrophone used is a one-inch ball (HS/70), which is resonant at around 80kHz and is used to ensure the system is as omi-directional as possible. The mechanical design, Fig. 3., shows how the hydrophone is mount/connected to allow data to be down-or-up loaded and the battery recharged without having to opening the transponder pod. The hydrophone is isolated from the input circuit and connected to the output circuit during the transmission by a mechanical relay. The relay ensures the input noise performance is retained when the contacts are closed and the input circuitry is totally isolated during the output waveform transmission. The source code of the program is stored in the FLASH memory that allows the program to be altered by unplugging the hydrophone and connecting a special serial lead to the 8-way micro-subconn. This has proved very useful during the development of the system, as the software can be changed using a PC in trial situations. The diver-worn wrist unit is similar to the transponder pods that are placed on the seabed, but to relay information to the diver a graphical backlit display is interfaced to the AMD 186. The diver unit also has sealed optical switches to allow the diver to control and input information like the marking of way-points whilst underwater. The menu-driven display software allows

data to be efficiently entered and Short Text Messages (STM) between the surface and diver or between divers to be relayed easily.

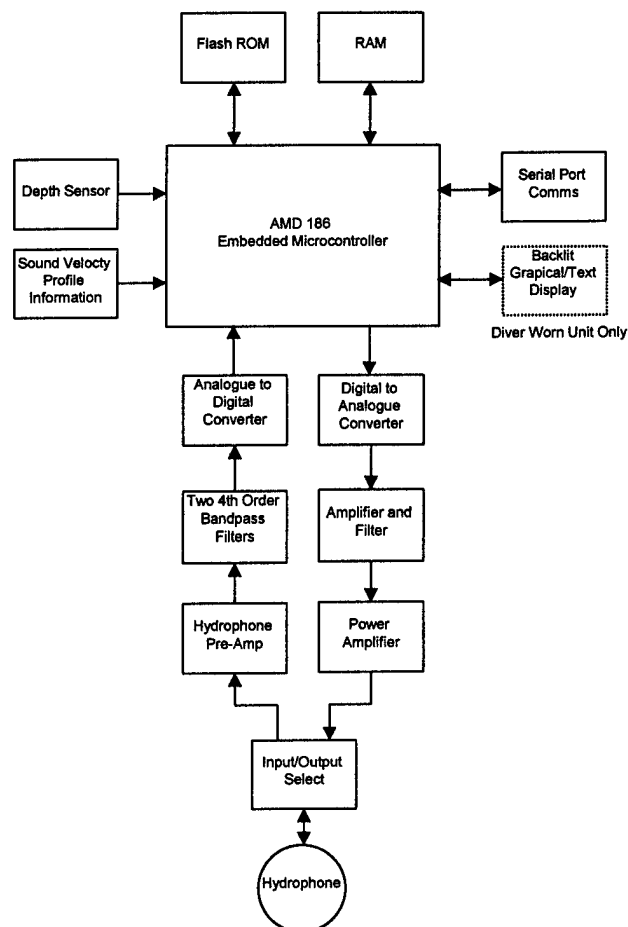


Fig. 2. Basic System Design

3. Mechanical Design

The transponder pods are constructed from a thick walled PVC tube with a screw on the base cap that seals with a single 'o' ring. Access to the battery pack is gained by unscrewing the end cap as this is the only entry point. The electronics are protected behind a double 'o' ring piston sealed bulkhead. A pictorial view of the transponder housing is shown in Fig. 3. The conical section is to minimise the masking of the hydrophone caused by the body of the housing. The hydrophone is plugged onto a bulkhead-mounted micro 8-way subconn connector. The hydrophone is specially made with an 8 way micro subconn connector moulded very close to the active part of the hydrophone, which makes the assembly a semi-rigid hydrophone that stands 150mm high. The pressure sensor is fitted in the conical section a fixed distance away from the hydrophone so that the actual depth of the active element can be corrected for in software.

The output of the pressure sensor is digitised and fed to the AMD 186 data bus.

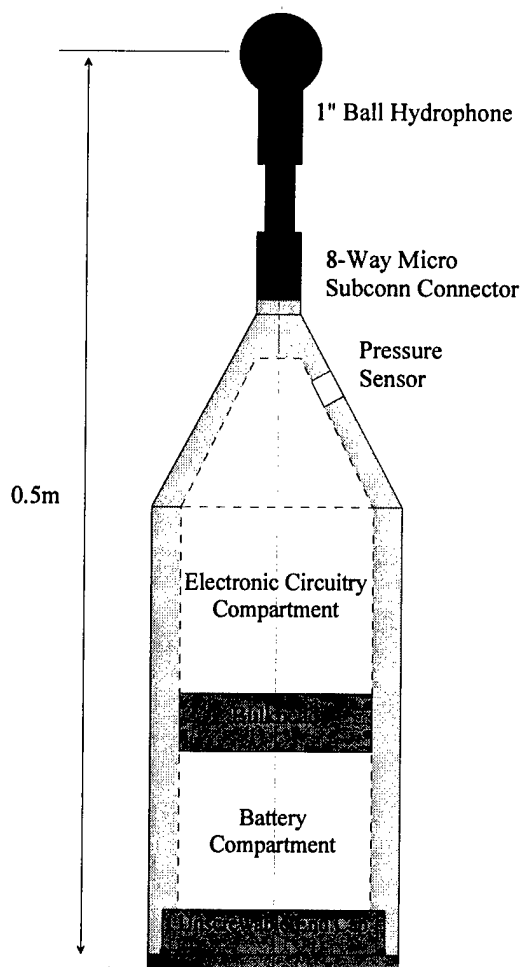


Fig. 3. Mechanical design of the Transponder Pod

4. Communications

There are numerous types of communication technique employed in underwater communication e.g., Amplitude Shift Keying (ASK), Frequency Shift Keying (FSK), Phase Shift Keying (PSK) and Pulse Position Modulation (PPM). For this system, PSK is adopted. Some of the constraints regarding the system are explained below. However, this paper is mainly based around the three-dimensional positioning algorithms and not the communications.

The one-inch ball hydrophone (HS/70) is used because the system has to be omi-directional. The resonant frequency of the hydrophone is around 80kHz, hence giving the best electro-acoustic efficiency at this frequency. Also, an added advantage is that the sea state noise is at its lowest around 70kHz. At lower frequencies, precipitation and shipping noise cause problems and the data packet

length would become too long. At high frequencies, thermal noise and attenuation due to absorption starts to cause problems due to the operating range. The maximum working range of the system has been specified as a radius of 200 metres from the cluster of transponders. The maximum absorption and transmission losses at the 80kHz can be calculated. The other major constraint is the physical height of the hydrophone off the seabed; the height is kept to a minimum to prevent currents from moving the hydrophones. The maximum time of the data packet has to be less than the two-way interference path. The minimum path length is twice the height of the transponder, hence one metre, which gives a maximum data packet duration of $666\mu\text{s}$ (assuming the velocity of sound in water is 1500m/s). Using a communication frequency at the resonance of the hydrophone gives the maximum electro-acoustic efficiency. At 80kHz one cycle is $12.5\mu\text{s}$ in duration, which gives only 53 cycles to encode the minimum of 61 bits of data. Fig. 4. Shows the ideal data packet design. This equates to a data rate of nearly 100Kbit/s, which is very high when using a low damped ball hydrophone. The minimum number of data bits to communicate the position of the diver is 48, that is a 16-bit number for each axis (x,y,z). With 65536 steps, and assuming a maximum operating range of $\pm 200\text{m}$, this gives a position resolution of 6.1mm in the x and y planes. In the vertical (depth plane z) the resolution could be a lot greater as the maximum depth the system is design to operate to is 200m; in this case the depth resolution would be 3mm. To reduce the number of bits transmitted the system only transmits position data if it has changed. The information that fronts the position data packet indicates which diver or transponder pod the packet is intended for; these are called the Identification (ID) bits. Each unit is assigned an ID upon initial communication with the seabed transponders, the new unit indicates what it is, i.e. a diver, surface vessel, ROV or AUV. At present the system has been designed to handle a maximum of 32 units, hence the 5 bit ID. To check that transmission reverberations and natural or man-made sounds have not corrupted the received data, an 8-bit Cyclic Redundancy Checksum (CRC) is calculated and attached to the back of the transmitted data packet. However, because the information data rate is fast, there is no reason to request a send again instruction, hence the received data with errors is just ignored unless it persists. If the position data of a diver has not been up-dated within a pre-determined period, an alarm sounds to inform the diver of transmission problems. These may be because the diver is out of operating range of the system (the diver is warned when he begins to approach the operating range of the system) or acoustically masked from the transponders.

To allow the processor to detect the incoming signal a synchronisation pulse at the beginning of the packet allows the processor to lock on to the communication

frequency. That is to detect the peaks and troughs of the synchronisation pulse, then the incoming data can be sampled at a relatively slow rate, depending on the PSK technique employed. The maximum bandwidth has been calculated to allow the ideal data packet in Fig. 4. to be transmitted in a single time-window. The refresh rate will change depending on the number of divers in the water at any one time. The normal refresh rate is limited to a maximum of once a second because of the maximum distance a diver or ROV can move in a second is small.

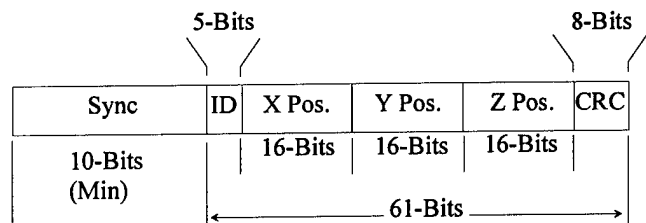


Fig. 4. Idea Data Packet Design

The intelligent transmission time-window protocol (ITTWP) is designed to overcome the problem of having to wait a pre-determined time after a transmission for the reverberation to subside. The idea is that during initialisation the transponder not only logs and communicates the time of arrival of the direct signal, but also the time of arrival of the surface, bottom and other interfering reverberations. The transponders then allocate communication time-windows to enable reverberation-free transmission times, which depending on the surrounding environment. The transponder can then transmit several packets of data so that data via the direct transmission path arrives in between the reverberations and inter-symbol interference is avoided. This increases the transmission data rate.

5. Positioning Algorithm

The three-dimensional positioning of a diver relative to the plane of three transponder T_1, T_2 and T_3 with known positions is relatively easy. However, knowing the precise position of a transponder on the seabed relative to another is not a simply task. For this reason the navigation system is designed to work with randomly deployed transponders. Although, 'randomly deployed' for the system to work with greater accuracy they should be sensibly positioned to form a triangle and not a line. The transponders then "calibrate" themselves so that distance between each transponder is known. As only three transponders are used to calculate the diver's position an ambiguity occurs with the position of transponder T_3 .

Considering the problem in two-dimensional space, transponder T_1 is considered to be at position (0,0) and

T_2 is positioned along the x-axis and hence at position ($d_{12}, 0$). The position of T_3 is calculated by finding the angle ϕ , which is calculated using the cosine rule (2).

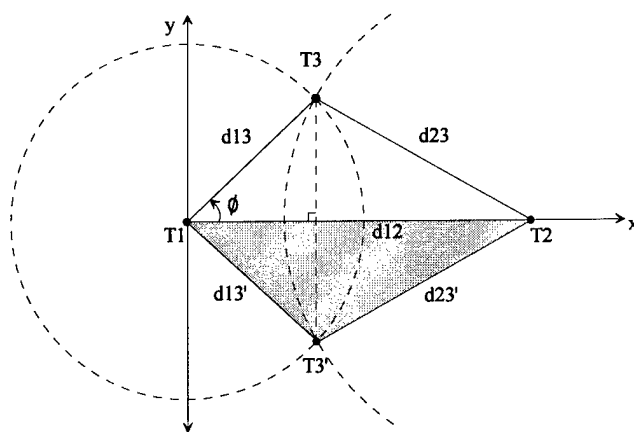


Fig. 5. Calibration ambiguity

$$\phi = \cos^{-1} \left(\frac{d_{12}^2 + d_{13}^2 - d_{23}^2}{2 \times d_{12} \times d_{13}} \right) \quad (2)$$

Once ϕ is known then the (x,y) position of T_3 is calculated:

$$x = d_{13} \cos \phi$$

$$y = d_{13} \sin \phi \quad (3)$$

Fig. 4. shows that two possible positions for T_3 exist, either the y-position is in the positive or negative half of the coordinate set. This ambiguity can be eliminated by the addition of a fourth transponder. However, this is not desirable as these transponders sit on the seabed and once the calibration procedure has been carried out the divers position ambiguity can be ruled out as the second position is below the seabed.

If there is no Global Positioning System (GPS) interfaced with the surface unit then the x,y position of the diver is only relative to the transponder positions. In this case the third transponder, T_3 can always be assumed to be in a positive y-position. If interfaced to a GPS system then the coordinates of the GPS in two different positions would allow the transponder to calculate the bearings of the diver relative to compass North. Once the positions of the three deployed transponders are established the position of a diver in three-dimensional space can be calculated, assuming the diver cannot go below the transponders. This ambiguity, if it occurs, can easily be removed if a surface vessel is present as this then acts as a fourth transponder, with a known z-position. Fig. 5. shows a

typical location of a diver above three randomly deployed transponders.

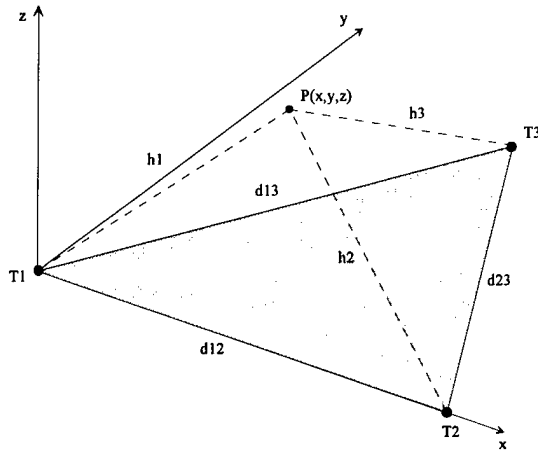


Fig. 5. Three Dimensional Position

All of the distances d_{12} , d_{13} , d_{23} , h_1 , h_2 and h_3 can be calculated by measuring the time of flight of the two-way path between the transponders and the diver. As all the distances are known the problem can be visualised in two-dimensions, as in Fig. 5. and described in detail elsewhere [3].

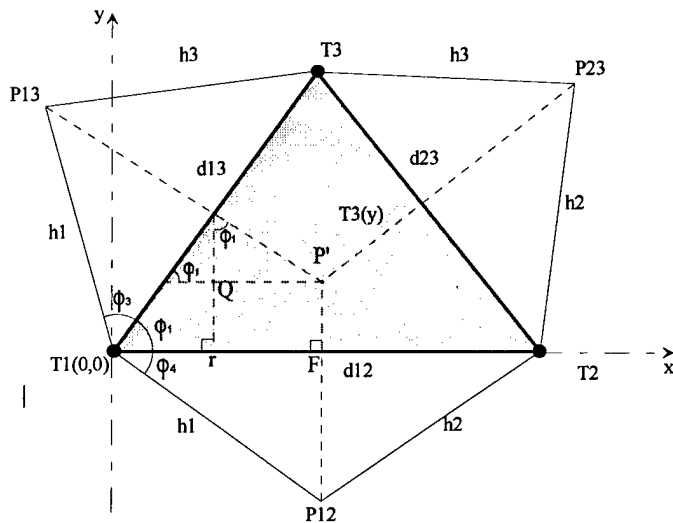


Fig. 6. Two dimensional representation

The position $P(x,y,z)$ obtained is relative to the plane of the transponders and not relative to a horizontal plane, unless by chance the seabed is exactly level. Each transponder is fitted with a pressure sensor to measure the depth, which allows the angle of the plane relative to the horizontal plane to be calculated. If the transponder plane is then rotated into the normal plane, the diver's position can also be rotated by the same amount. The result is that the

divers position is relative to the surface. This make more sense as the diver's depth profile will relative to the surface and not to his position in the x,y plane.

$$\alpha = \frac{(h_1^2 + d_{13}^2 - h_3^2)}{2.d_{13}} \quad (4)$$

$$P(x) = \left(\frac{h_1^2 + d_{12}^2 - h_2^2}{2.d_{12}} \right) \quad (5)$$

$$P(y) = \alpha.\sin \phi - \left(\frac{P(x) - \cos \phi}{\tan \phi} \right) \quad (6)$$

$$P(z) = \sqrt{h_1^2 - P(x)^2 - P(y)^2} \quad (7)$$

The (x,y,z) positions calculated using eqns 4-7 are relative to the transponder plane and the derivation of these equations and the accuracy obtainable is explain in [3].

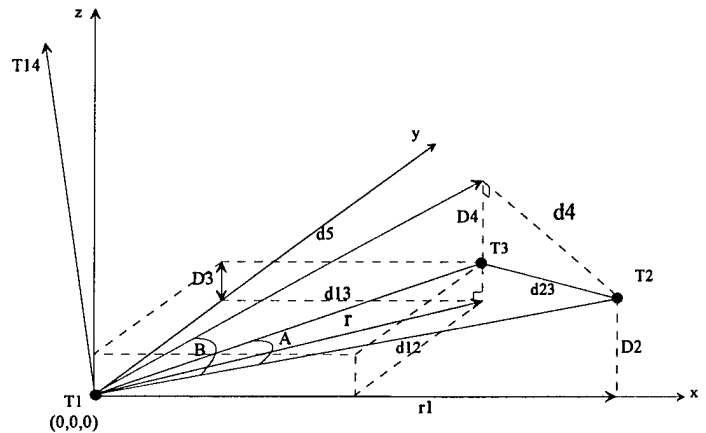


Fig 7. Transponder plane in an orthogonal set

To rotate the plane of the transponders into a plane were T_1 , T_2 and T_3 are all at the same depth z , T_1 is assumed fixed at depth z . The other two transponders are then rotated about the position T_1 so that their depths are also z . Finding the vector product of T_{12} and T_{13} gives a vector T_{14} acting in a direction perpendicular to the two vector T_{12} and T_{13} , with a magnitude of $T_{12} \cdot T_{13} \sin A$, where A is the angle between the two given vectors. From the resulting vector T_{14} the angles of rotation to eliminate the x and y components of the vector can be calculated.

Vector T_{12} in unit vector terms is:

$$T_{12} = r_1 i + 0 j + D_2 k \quad (8)$$

Where r_1 is calculated using pythagarus:

$$r_1 = \sqrt{d_{12}^2 - D_2^2} \quad (9)$$

Vector T_{13} in unit vector terms is calculated as follows:

$$D_4 = D_2 - D_3 \quad (10)$$

$$r = \sqrt{d_{13}^2 - D_3^2} \quad (11)$$

$$d_4 = \sqrt{d_{23}^2 - D_4^2} \quad (12)$$

$$d_5 = \sqrt{r^2 + D_2^2} \quad (13)$$

$$B = \cos^{-1} \left(\frac{d_{12}^2 + d_5^2 - d_4^2}{2 \cdot d_{12} \cdot d_5} \right) \quad (14)$$

$$T_{13} = r \cdot \cos B i + r \cdot \sin B j + D_3 k \quad (15)$$

Thus $T_{12} \times T_{13}$ yields: (16)

$$T_{14} = r \cdot \sin B \cdot D_2 i + r_1 \cdot D_3 - r \cdot \cos B \cdot D_2 j + r_1 \cdot r \cdot \sin B k$$

The resultant vector T_{14} is then rotated by an angle of θ and the resulting vector is then rotated by an angle ϕ . However, as the only known reference is that the vector T_{12} is along the x-axis, the vector must not be rotated about the z-axis. Rotating around the z-axis would shift the x,y plane, giving no physical datum point. The rotation matrix to rotate the vector T_{14} by θ degrees about the y-axis is as follows:

$$\begin{bmatrix} x_1 \\ y_1 \\ z_1 \end{bmatrix} = \begin{bmatrix} \cos \theta & 0 & -\sin \theta \\ 0 & 1 & 0 \\ \sin \theta & 0 & \cos \theta \end{bmatrix} \begin{bmatrix} x \\ y \\ z \end{bmatrix} \quad (17)$$

Rotate the resulting vector ϕ degrees about the x-axis gives.

$$\begin{bmatrix} X \\ Y \\ Z \end{bmatrix} = \begin{bmatrix} 1 & 0 & 0 \\ 0 & \cos \phi & -\sin \phi \\ \sin \phi & 0 & \cos \phi \end{bmatrix} \begin{bmatrix} x_1 \\ y_1 \\ z_1 \end{bmatrix} \quad (18)$$

Multiplying the two-rotation matrices (17) and (18) together gives a three-dimension rotation matrix (19) to allow the diver's position to be rotated into the new coordinate set. The diver's position is calculated in the plane of the transponders, then rotated into the new horizontal plane by multiplying the (x,y,z) coordinates by the matrix (19).

The three-dimensional rotation matrix is

$$\begin{bmatrix} X \\ Y \\ Z \end{bmatrix} = \begin{bmatrix} \cos \theta & 0 & -\sin \theta \\ -\sin \phi \sin \theta & \cos \phi & -\sin \phi \cos \theta \\ \cos \phi \sin \theta & \sin \phi & \cos \phi \cos \theta \end{bmatrix} \begin{bmatrix} x \\ y \\ z \end{bmatrix} \quad (19)$$

The vector T_{14} is evaluated with X and Y equal to zero, hence it has only a Z component. The angles of rotation θ and ϕ are calculated as shown.

$$\theta = \tan^{-1} \left(\frac{x}{y} \right) \quad (20)$$

$$\phi = \sin^{-1} \left(\frac{y}{r_2} \right) \quad (21)$$

$$r_2 = \sqrt{x^2 + y^2 + z^2} \quad (22)$$

Once the diver's position in the new coordinate set is found, the position is relayed to the diver and to the surface vessel. If a GPS system is connected to the surface unit the rotation matrix can also include a z-axis rotation to allow the y or x-axis to be align with North.

6. Conclusion

The development of the underwater navigation and tracking system described here is still continuing as the circuitry and processing power allows the testing and evaluation of new positioning algorithms to be developed. The development and evaluation of a three-dimensional positioning algorithm that incorporates the sound velocity profile of the water channel to give greater accuracy is also being tested. The rotation of the diver's position in to a horizontal plane offers more sensible tracks and depth profile and also simplifies the integration of a GPS system.

7. References

- [1] B. Woodward and H. Sharp, 'Portable real time diver navigation system, Ultrasonics, 29, 381-388, (1991).
- [2] B. Woodward, D.A. Joyce and L. Niazi, 'Diver Navigation with a programmable dive computer and an intelligent transponder array' Acoustics Letters, Vol. 16, No. 3, 1992.
- [3] T.M. Hodder and B. Woodward, 'Algorithms for underwater position fixing' Int. J. Math. Educ. Sci. Technol., 1986, VOL. 17, No. 4, pp407-417
- [4] P.H. Milne, 'Diver and submersible tracking using 3-D computer graphics', S.U.T. Int. Conf. On Diving Technology, London, 24-26 November (1981).
- [5] P.A. Hardman and B. Woodward, 'Underwater location-fixing by a diver-operated acoustic telemetry system, Acustica, 55, 34-44, (1984).

Multipath Time-Delay Detection and Estimation for Ocean Acoustic Tomography: a Bayesian Approach

Fabienne Porée*, Thierry Chonavel*, Thierry Terre**

*ENST de Bretagne, 29285 Brest Cedex, France

**IFREMER, 29285 Brest Cedex, France

Abstract

In this paper a new method for multipath channel time delay estimation is proposed. We present a bayesian approach which takes into account the attenuations and noise distributions at the output of the receiver. This leads to a simple criterion which can be written as the l_1 norm of an affine function of the desired attenuations. The good behaviour of this algorithm is shown on synthetic and real acoustic oceanic tomographic data.

I. Introduction

Oceanic Acoustic Tomography (OAT) is based on the transmission underwater of an acoustic wave [1]. The propagation follows several paths. In order to recover some physical parameters of the ocean (temperature, salinity, ...), the propagation parameters (delays and attenuations) are searched for.

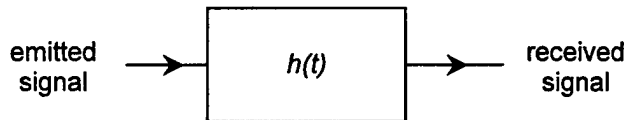


Figure 1: underwater propagation.

The transmission of an acoustic wave through the propagating oceanic acoustic channel leads to the observation of several copies of the transmitted signal, with distinct time delays and attenuations.

Let $e(t)$ denote the transmitted signal, P the number of propagation paths, and $r(t)$ the signal at the receiver input. Accounting for the presence of an additive white gaussian noise $b(t)$ (uncorellated with $e(t)$), we get

$$r(t) = \sum_{p=1}^P \alpha_p e(t - \tau_p) + b(t), \quad (1)$$

where α_p and τ_p respectively represent the attenuation and the time delay of the p th path. The problem that we address here is that of estimating the time delays τ_p and the number P of delays.

II. A brief review of existing techniques

Time delay estimation is a classical problem, and many solutions have already been proposed. Mainly, one can use matched filter techniques or maximum likelihood approaches.

Using the celebrated EM algorithm enables to make the estimation more simple thanks to a decoupling of the parameters associated with distinct paths [2]. Maximum likelihood estimation methods appear to perform better than matched filter techniques, but they require correct initialisation, and prior knowledge of the number P of paths. Two methods have been proposed recently that permit to overcome these limitations. In [3], a gaussian maximum likelihood criterion is proposed that allows a good detection and estimation of the time delays. In [4], the number of paths is estimated by means of a statistical test.

Here, we propose a new approach, of the bayesian kind, that accounts for the particular structure of the non coherent receiver. We will see that this approach permits to incorporate prior knowledge about the noise and paths amplitudes, and that it yields a very simple optimization problem. Also, we will see that the solution of this problem allows good detection and efficient estimation of time delays.

III. Presentation of the method

A. The demodulation scheme

The emitted signal $e(t)$ is a phase modulated pseudorandom sequence. The received signal is in the form

$$\begin{cases} r(t) = \sum_{p=1}^P \alpha_p e(t - \tau_p) + b(t), \\ \text{with } e(t) = s(t) \cos \omega t. \end{cases} \quad (2)$$

$r(t)$ is demodulated by means of two outhogonal carriers. In order to improve the signal to noise ratio, a matched filter $s^*(t)=s(-t)$ is applied on both channels, and square-law detection of the signals is performed according to figure 2, in order to suppress possible

phase errors and possible Doppler effects along the paths.

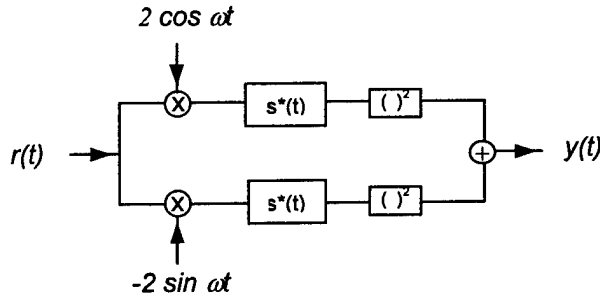


Figure 2: structure of the receiver.

With a view to getting a simple expression for the signal $y(t)$ at the output of the receiver, we are going to consider two approximations. First, the product terms between the signal of interest and the noise are neglected. On another hand, the product terms associated with two distinct paths are supposed to be zero. The first approximation is justified for high SNR at the output of the matched filter, and the second one is generally satisfied for signals with narrow autocorrelation function such as Maximum Length pseudo-random Sequences (MLS - see e.g. [5] p. 831) and for applications such as long range OAT. Then, at the output of the square-law detector, the signal is in the form

$$y(t) = \sum_{p=1}^P a_p z(t - \tau_p) + n(t), \quad (3)$$

where :

$$\begin{cases} z(t) = (s * s^*)(t), \\ \text{with } a_p = |\alpha_p|^2. \end{cases}$$

As the noise $b(t)$ is gaussian, the noise $n(t)$ is obviously exponentially distributed.

B. The bayesian criterion

We usually assume [5] that the amplitudes a_p are gaussian and complex circular. Then, the demodulated signals can be written in the form:

$$r_d(t) = \sum \begin{pmatrix} \alpha_{p_1} \\ \alpha_{p_2} \end{pmatrix} (s * s^*)(t - \tau_p) + \begin{pmatrix} b_1(t) \\ b_2(t) \end{pmatrix}, \quad (4)$$

where $(\alpha_{p_1}, \alpha_{p_2})^T \sim N(0, \sigma_a^2 I_2)$, and I_k is the identity matrix of size k . $N(m, \sigma^2)$ represents a gaussian distribution with mean m and variance σ^2 . Similarly, $(b_1, b_2)^T \sim N(0, \sigma^2 I_2)$.

Thus, a_k is exponentially distributed, with mean $\mu^{-1} = \sigma_a^2 / 2$ ($a_k \sim \mathcal{E}(\mu)$), and $n(t) \sim \mathcal{E}(2\sigma^2)$. Moreover, $\tau_k \sim U_{[0, T]}$.

The posterior maximum likelihood criterion leads to minimising

$$\|Y - Z(\tau)a\|_1 + \lambda \|a\|_1, \quad (5)$$

where $\lambda = 2\sigma^2 \mu$. Let us note that equation (5) doesn't account for the noise correlation for different values of t . This approximation allows the derivation of a very simple criterion.

In order to optimize criterion (5), the time scale is discretised in the same way as in [3][4]. Finally, we get the problem in the form

$$\min_w \|Y - Sw\|_1 + \lambda \|w\|_1, \quad (6)$$

which can be written as

$$\min_w \|B - Aw\|_1, \quad (7)$$

with

$$A = \begin{pmatrix} S \\ \lambda I_M \end{pmatrix} \quad \text{and} \quad B = \begin{pmatrix} Y \\ 0 \end{pmatrix}. \quad (8)$$

In this criterion, S contains shifted versions of the sampled $(s * s^*)(t)$, Y is the data vector and w is the vector of the amplitudes on the sampled time scale.

C. Optimisation of the criterion

The convex criterion $\|B - Aw\|_1$ can be minimized by means of a very simple gradient algorithm:

- initialize $w_0, \varepsilon_0 = \text{sign}(B - Aw_0)$
- for $k = 1, 2, \dots$

$$w_k = w_{k-1} - \rho_k A^T \varepsilon_{k-1} \quad (9)$$

$$\varepsilon_k = \text{sign}(B - Aw_k) \quad (10)$$

with the notation $\text{sign}(x) = +1$ si $x > 0$, et $\text{sign}(x) = -1$ si $x < 0$. If $x = 0$, $\text{sign}(x)$ is chosen randomly in $\{-1, +1\}$. ρ_k can be chosen equal to $1/k$. Also, (7) can be rewritten as a linear programming program using the simplex algorithm [6].

IV. Numerical data

We simulate a set of acoustic oceanic tomographic records. Let $s(t)$ be a MLS of length $2^9=511$. The observation sampling step is $\theta=30$ samples per symbol. In order to get accurate estimates for the time delays, the time resolution is set equal to $T_s/90$, where T_s is the duration of one symbol. The SNR is chosen

equal to 20 dB. The figure 3 shows the evolution of two simulated paths (fig. 3a) and the receiver output signal $y(t)$ (fig 3b) for 100 successive data tracks. Figure 4b represents the results supplied by our method, which are compared to those obtained under gaussian noise assumption (fig. 4a). This method amounts to choosing $\|Y - Sw\|_2$ instead of $\|Y - Sw\|_1$ in (6), as proposed in [3].

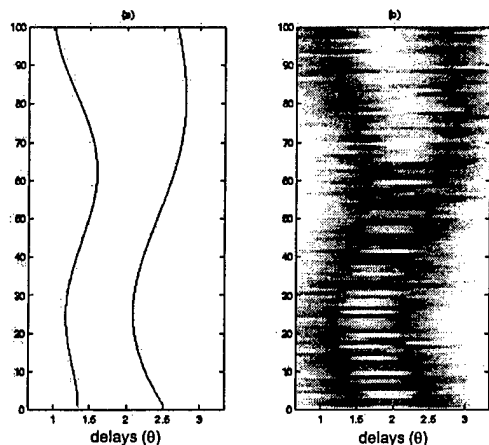


Figure 3: (a) True paths ; (b) Matched-filter output.

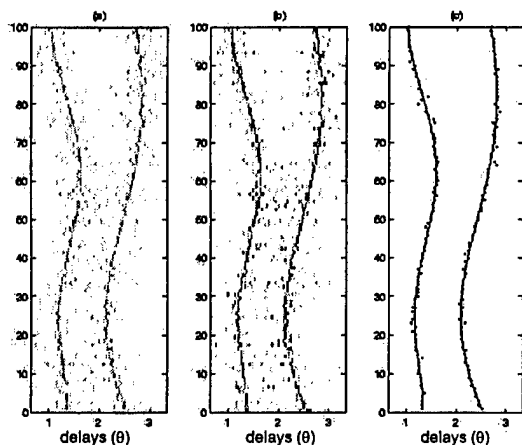


Figure 4: (a) Gaussian noise assumption ; (b) Exponential noise assumption ; (c) Result after tracking.

We observe that the results obtained under exponential noise assumption are better than under gaussian noise assumption. Indeed we distinguish better both delays in the second case (fig. 4b).

In order to eliminate part of the parasite peaks, we use the regular evolution of the delays associated with the trajectories [7]. To make the decision faster, we first apply a threshold to remove less significant peaks.

The figure 4c represents the evolution of the values decided for τ_1 and τ_2 , together with the true evolutions of these parameters.

V. Real data processing

We apply the method to data displayed on figure 5. These data come from the Thetis 2 experience directed by IfM Kiel, Ifremer and FORTH/IACM [9][10], in occidental Mediterranean in 1994. These data are provided by the output $y(t)$ of the circuit receiver. The results of the criterion (7) applied to these data are shown on figure 6. In fact, this image is obtained by performing an additional smoothing which eliminates the parasite peaks close to the main peaks [3].

The first and the last paths are now better localised. Also, it now clearly appears that there are two tracks in the middle part of the data record. However, these tracks are not yet correctly separated. A reason for this lack of resolution is that we didn't take into account the transmitter and receiver transducer filters influence, which distort the transmitted signals. Figure 7 points out the existence of such a distortion, estimated by averaging data around estimated delays of paths 1 and 4.

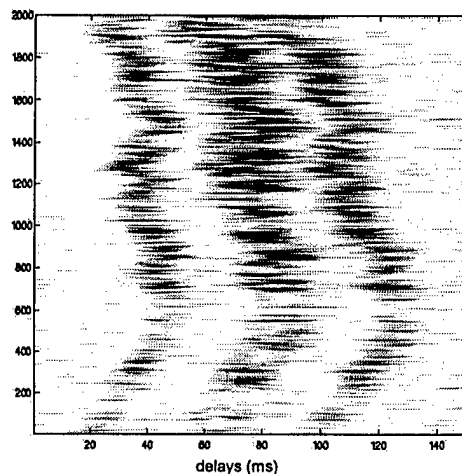


Figure 5: Real data.

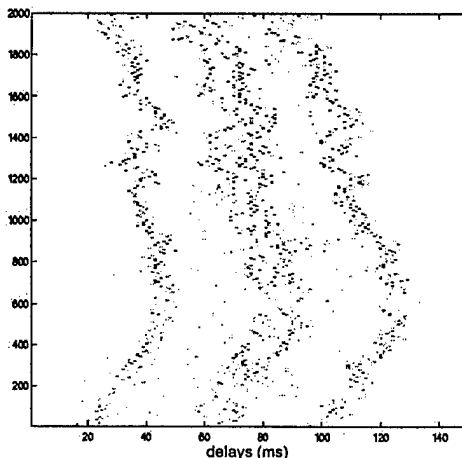


Figure 6: Processed data.

Moreover, let us note that the mean gap between the paths 2 and 3 is rather small, since it is equal to about one third of the MLS autocorrelation function.

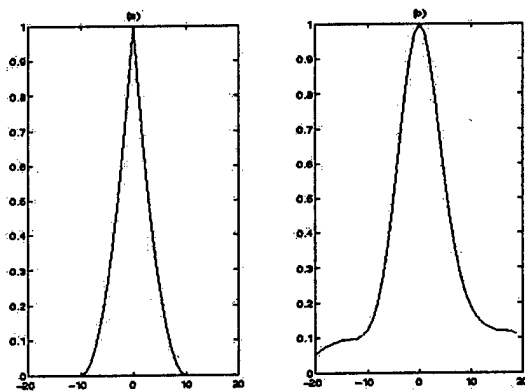


Figure 7: Square of the autocorrelation function of $s(t)$
(a) theoretical ; (b) estimated.

Using an adaptive smoothing method [8], we may easily obtain a good estimation of the mean trajectory of the paths. With this method, it is possible to adjust the desired smoothness of the curve.

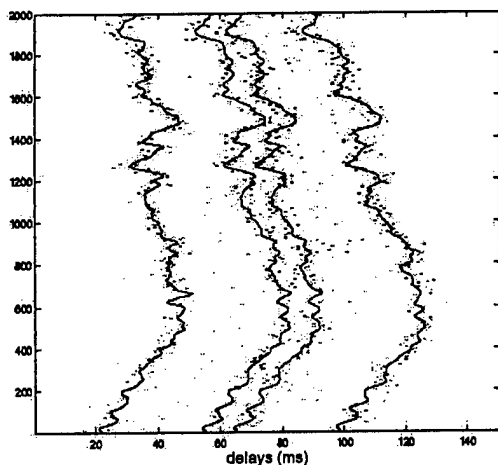


Figure 8: Smoothed trajectories.

In order to obtain a good separation of paths 2 and 3, let us note that smoothed trajectories 1 and 4 are quite similar. By averaging both of them, we obtain a new trajectory which presents a good estimate of trajectories 2 and 3. Then, we try to position it by means of a mean square technique. The figure 9 shows the final result.

VI. Conclusion

In this article the multipath time-delay estimation problem was addressed. We proposed a bayesian approach that accounts for prior statistic information

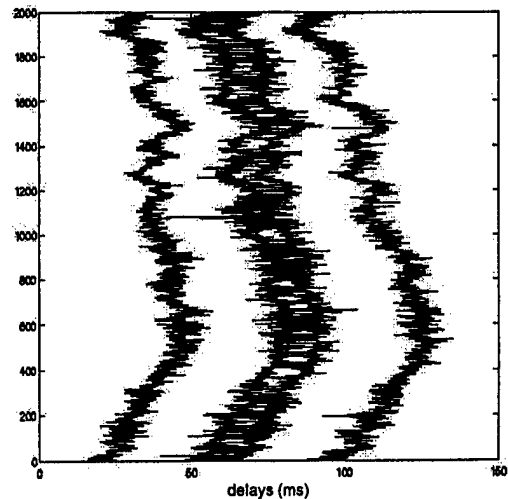


Figure 9: Final result.

upon noise and paths amplitudes, and leads to a simple estimation procedure for detecting and estimating the time delays. We also discussed the possibility of tracking the time delay evolution.

References

- [1] C. Wunsch W. Munk, P. Worcester. *Tomography Acoustic Oceanic*. University Press, 1995.
- [2] M. Feder and E. Weinstein. Parameter estimation of superimposed signals using the EM algorithm. *IEEE Trans. on A.S. S. P.*, 36(4):477-489, 1988.
- [3] J-J. Fuchs. Multipath time-delay detection and estimation. *IEEE Trans. S.P.*, 47(1):237-243, Janv. 1999.
- [4] Tze Fen ILL Multipath time delay estimation using regression stepwise procedure. *IEEE Trans. S.P.*, 46(1):191-195, January 1998.
- [5] J. G. Proakis. *Digital Communications*. Mac Graw Hill, second edition, 1989.
- [6] 1. Barrodale and F.D.K. Roberts. An improved algorithm for discrete l1 linear approximation. *SIAM Numer. Anal.*, 10(5):839-848, Oct. 1973.
- [7] V. Nimier et G. Jourdain. Active estimation of a multipath propagation channel with a bayesian strategy. *Traitement du signal*, 10(3):201-213, 1993.
- [8] J. Lemoine S. Djeziri, E. Petit. An adaptative method for the smothing of curves edge detection application. *Traitement du Signal*, 14(1):3-13, 1997.
- [9] Send U. G. Krahman, D. Mauuary, Y. Desaubies, F. Gaillard, T. Terre, J. Papadakis, M. Taroudakis, E. Skarsoulis and C. Millot. Acoustic observations of heat content accross the Mediterranean, *Nature*, 385, 1997.
- [10] Thetis Group. *Thetis 2: A pilot tomography system for monitoring the western mediterranean bassin*. Final report MAST2-CT91-0006C.

Side Scan Sonar and Interferometric Noise

Christophe SINTES and Bassel SOLAIMAN

GESMA, B.P 42, 29240 Brest-Naval, FRANCE

ENST-Bretagne, B.P 832, 29285 Brest cedex, France

Email {Sintes@gesma.fr, Basel.solaiman@enst-bretagne.fr}

Abstract

This paper concerns the description of different noise sources encountered as well as the impact of each of these sources through the sonar interferometric data acquisition. In fact, these noise sources can generally be classified into two categories : a. environmental noise category (variable celerity, parasite echoes, sonar motion, etc.), and, b. interferometric process related noise (decorrelation baseline, decorrelation of wave train, propagation). In this study, each noise source (considered separately) is first modeled in terms of Signal to Noise Ratio (SNR) as a function of range. This modeling is conducted analytically as well as using computer simulations. The obtained information is, then, converted in order to obtain an altitude error precision scheme. Obtained results clearly show that these different noise sources have not the same altitude error impact. In fact, the decorrelation of wave-train and the parasite echoes are shown to be the most significant. Finally, an error data fusion process is studied in order to evaluate the altitude precision degradation through the integration of several noise phenomena. The main conclusion of this paper concerns the theoretical interest of the conducted approach in terms of the obtained results as well as in order to reduce the impact of these noise sources through the physical and the analytical comprehension of the data acquisition process.

I. Introduction

Side-scan sonars produce ocean bottom realistic images by periodically transmitting acoustic pulses orthogonal to the direction of the sensor motion. Nevertheless, understanding the bathymetry information of an observed scene, in terms of generating important shadows of bottom objects, implies that the sonar needs to be close to the bottom, compared to the sensor range. Recent sonars produce bathymetric information through the use of interferometric methods. These methods are based on the detection of the angular arrival of the plane wave reflected from the bottom. The knowledge of the sonar altitude, the signal arrival time and its angular direction, then, it is possible to compute the bathymetry of each point present in the observed scene. These methods constitute a real improvement when compared to the fusion methods of the bathymetry and the image recorded in two dates and issued from two different sensors. The main drawback of the interferometric methods concerns their weak robustness in a noisy environment. This paper is organized as follow: next section deals with the physical interferometry concepts and its application to the sonar. Section III studies the impact the environmental noise. The impact of the interferometric intrinsic noise is then detailed in section IV. Section V presents the joint effect of noise sources on the precision and the theoretical robustness of the vernier method. Conclusions and further comments are given in section VI.

II. Interferometry Basic Concepts

The traditional experiment to illustrate the interferometry effect is the Young slot [1]. A monochromatic light (i.e. a single carrier frequency) is diffracted through two slots and creates a figure of light consisting in an alternance of high-lighted lines and of shadowed lines on a white paper sheet placed behind. This can be explained by the superposition of two coherent lights. The intensity at each point is given by [1] :

$$I = \langle E_1^2 \rangle + \langle E_2^2 \rangle + 2E_1E_2 \langle \cos(\varphi_1 - \varphi_2) \rangle \quad (1)$$

where, E_1 and E_2 denote the electromagnetic fields amplitude, φ_1 and φ_2 their corresponding phases, and the symbol $\langle . \rangle$ denotes the temporal mean through a wave train length time. The resulting intensity depends, hence, on the phase difference (i.e. the difference of length of the two paths of light). The connection to the interferometric sonar is straightforward, figure 1. The slots are two

acoustic arrays and the paper sheet effect (i.e. superposition of two waves) is computed by $S_a S_b^*$ where S_a , S_b are the complex signals received on each array and (*) denotes the complex conjugate.

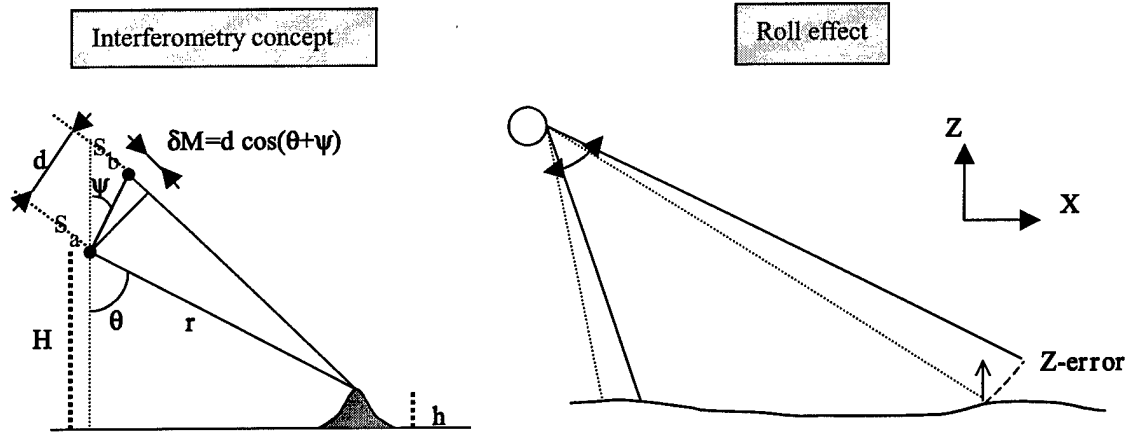


Figure 1, the phase difference and the incidence angle θ

In this figure, δM denotes the path length difference. The link between the phase difference and θ is given by [2,3] :

$$\Delta\varphi = \frac{2\pi d \cos(\theta + \psi)}{\lambda} \quad (2)$$

where "d" is the baseline and λ the wavelength. Finally, the altitude "h" of an observed cell is simply computed by :

$$h = H - r \cos(\theta) \quad (3)$$

III. Environment noise

Several noise sources affect the exact computation of the altitude measure. Some of these sources are related to the environment (parasite motion, water celerity fluctuation and multipath interference). Other intrinsic noise sources are those related to the physical information acquisition process (wave propagation, speckle noise and the length of the wave train). In this section, the environmental sources will be briefly discussed.

III.1 Parasite Motion

The sonar acquisition system is generally towed by a boat. Even if the sonar is far from the surface, the acquired signals suffer the boat motion effects transmitted through the connecting cable. For example, a roll error of 1° , figure 1, can induce an error of 1.7m on the bathymetry at the end of the swath [2].

III.2 Celerity fluctuation

The celerity acts as a prism for optical rays. As the water propagation index is not a constant through Z, the ray trajectories are curved. Indeed, when a ray is received, its propagation time and its arrival angle are known; the ray is assumed to be straight in order to determine the position of the reflecting point. In this study, the following assumptions are made in order to conduct the simulation results : *a.* a celerity gradient of 1m/s per meter depth is assumed, *b.* the celerity stratification is horizontal, *c.* the sea bottom is flat and horizontal, and, *d.* the sonar altitude is 10 meters above the sea bottom.

As will be shown in section V, the results obtained through the simulations, using these assumptions, prove that the Z-error at the end of the swath corresponds to 60 cm [2].

III.3 Multipath interference

Multipath interference constitutes an important noise source through the interferometry process. In fact, the received signal is formed by the composition of a direct path and, eventually, of an interfering signal issued from a secondary reflecting path. The interfering path constitutes a parasite signal contributing to noise the wave front of the main signal.

Generally the direct path (i.e. specular) level is superior to the parasite signal, but, the direction measure of the wave front can be disturbed. This perturbation can be modeled through the use of a statistical approach. In this study, the following assumptions are made : a. a Rayleigh amplitude distribution, b. uniform phase distribution over the interval $[0, 2\pi]$, c. the specular as well as the interfering multipath components are assumed to be statistically independent and the power ratio between these two signals is fixed through out the swath (13 dB higher for the direct signal), and, d. the emission pulse is a narrow band.

In fact, we examine the probability density functions (p.d.f) of four Gaussian variables which correspond to the imaginary and real parts of the two signals. The different coefficients of the autocorrelation matrix are determined by the integration on the angular direction of the distribution of the inphase and the quadratic components. This leads to a p.d.f of the phase difference [1],[2],[3],[4].

$$p(\Phi) = \frac{D^2}{2\pi\sigma_1\sigma_2} \left[\frac{1}{1-X^2} - \frac{X}{(1-X^2)^{3/2}} \left(\frac{\pi}{2} - \text{Arcsin}(X) \right) \right] \quad (4)$$

with $X = \frac{\eta \sin(\Phi) - \rho \cos(\Phi)}{\sigma_1\sigma_2}$, $D^2 = \sigma_1^2\sigma_2^2 - \rho^2 - \eta^2$, $\Phi = \text{phase sensor1} - \text{phase sensor2}$

$$\sigma_i^2 = \langle x_i^2 \rangle = \langle y_i^2 \rangle = \int [S(\alpha) + I(\alpha)] B_i^2(\alpha) d\alpha = P_i + P_s$$

$$\rho = \langle x_1 x_2 \rangle = \langle y_1 y_2 \rangle = \int [S(\alpha) + I(\alpha)] B_1(\alpha) B_2(\alpha) \cos(f_2(\alpha) - f_1(\alpha)) d\alpha = P_s \cos(\phi_s) + P_i \cos(\phi_i)$$

$$\eta = \langle x_1 y_2 \rangle = -\langle y_1 x_2 \rangle = \int [S(\alpha) + I(\alpha)] B_1(\alpha) B_2(\alpha) \sin(f_2(\alpha) - f_1(\alpha)) d\alpha = -(P_s \sin(\phi_s) + P_i \sin(\phi_i))$$

where, $\alpha \in [-\pi, \pi]$, B (res. $f_i(\alpha)$) the amplitude (res. sensor i phase) transfert function within the direction α , S and I are the power distribution of the specular and the interfering multipath signals.

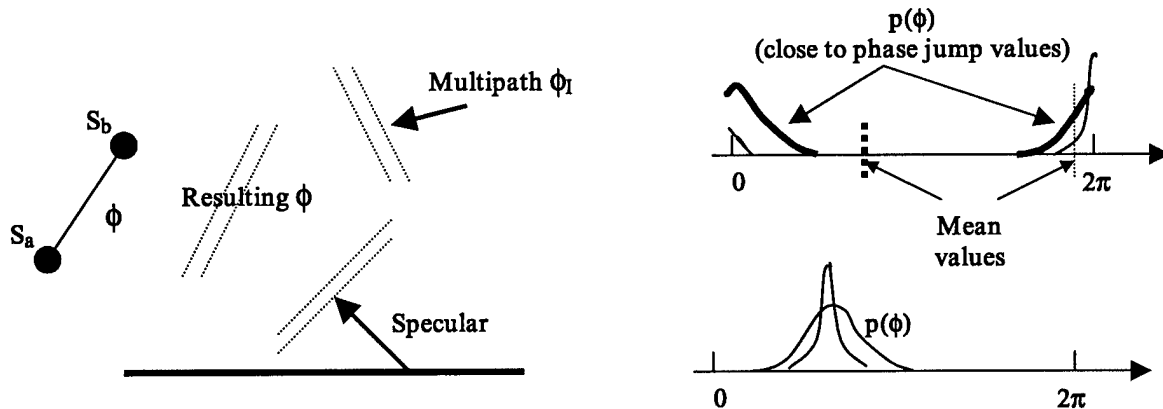


Figure 2, Physical Principle – PDF of ϕ

The shape of ϕ -p.d.f is plotted in figure 2. The resulting phase increases with the range and progresses along the interval $[0; 2\pi]$. When it reaches 2π , it returns to zero. The standard deviation of the p.d.f is small if ϕ_s and ϕ_i are close enough : for example, they are equal if the arriving directions are the same. The more these phase differences are far, the more the standard deviation is high. The drawback of a high standard deviation can be particularly observed near a phase jump because this

mono hill p.d.f becomes a two hills one. In this case, the mean value of this p.d.f does not correspond to the maximum of the p.d.f but to the center of gravity of the two hill surfaces. If the standard deviation is small, then, the mean value follows the maximum of the p.d.f and the bias is small.

The mean value of the p.d.f (for different angles θ s corresponding to the range [0,100]meter and angles $\theta_i \in [0, \pi]$) is plotted in figure 3.

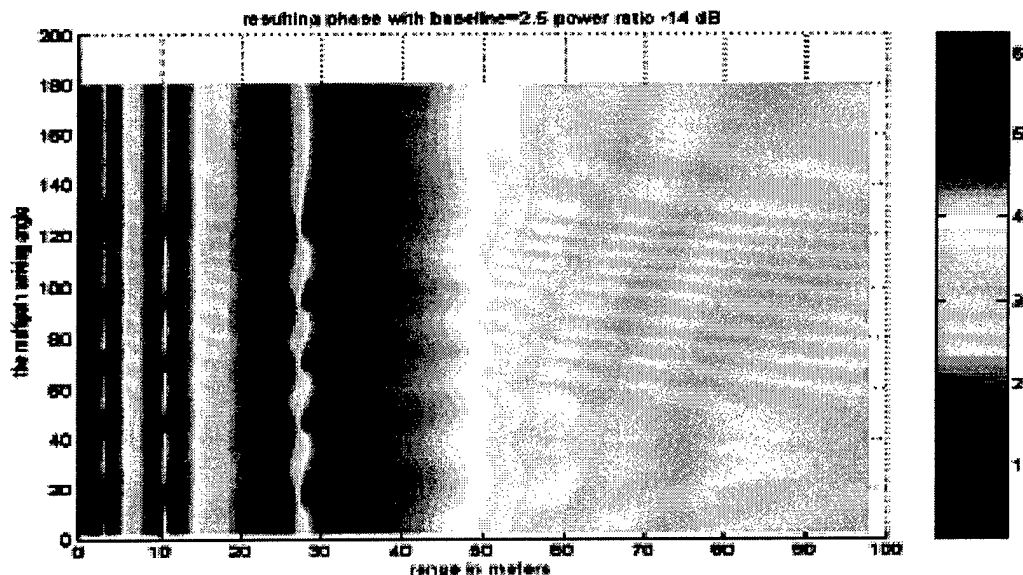


Figure 3, Mean value of the resulting phase difference

In this figure, the undulations and the fluctuations appearing near the phase jump areas are due to the presence of the parasite interfering signal, which introduces the bias on the mean value described above. The most significant zones are located near the phase jumps.

IV. Physical Noise

IV.1. Baseline Decorrelation

The measured gray level value concerning a given pixel on the sonar image, is obtained by the additive power summation of several microscopic backscatters contained within the resolution cell. The backscattered energy by each of these microscopic items can interfere and the power reflected can be null and the received phase difference is random variable: it is the speckle phenomena. The impact of this noise has been computed in terms of Signal to Noise Ratio (SNR) as follows [5],[1]:

$$\gamma = \frac{|\langle S_A S_B^* \rangle|}{\sqrt{\langle S_A S_A^* \rangle \langle S_B S_B^* \rangle}} \quad \text{et} \quad \gamma = \sin c\left(\frac{kdc\tau}{\pi h4} \cos(\theta) \cot(\theta) \sin(\theta + \psi)\right) \quad \text{and the SNR} = \gamma/(1-\gamma) \quad (5)$$

Numerical evaluation of this model shows the average impact is weak but that effect must be considered as a high frequency noise.

IV.2. Length of Wave Train

This effect is also called '*sliding foot print*' effect. This source noise can be derived from an optical effect. The figures obtained through the optical Young slots are less and less contrasted from the center to the exterior. This phenomena is linked to the length of wave trains. The more the phase difference is important the less the time of the coherent integration is important, and thus, the weight of the phase difference cosines decreases. This effect is the reason why the monochromatic light is used : it has a very thin spectral occupation so a large time duration which increases the contrast of

the figure. For the sonar case, the length of the coherent wave train is related to the pulse length and is proportional to [2],[6]:

$$\xi = \frac{c\tau}{2} - \delta M \quad (6)$$

where τ is the time pulse length and c is the wave celerity. ξ corresponds to the time the two arrays have to make the interferometry in common. When converted in terms of SNR, it leads to

$$SNR = \frac{c\tau}{2d \cos(\theta + \psi)} - 1 \quad (7)$$

ξ can be interpreted as the commonly sea bottom surface seen by the two sensors within one sample : the two arrays are not situated at the same distance from the bottom and their footprint on the bottom is lightly shifted. Thus, when the cross product $S_a S_b^*$ is computed, it must take into account this partial superposition.

IV.3. Propagation Lost

The impact of the propagation is important when the frequencies are high because of the resonance of molecules contained in the sea water. The sonar equation is computed as [7]:

$$SNR = SL - TL_1 + TL_2 + RL + GA - NL \quad (8)$$

with, SL :Source Level, TL :Transmission Loss , RL : Reflecting Level, GA : Gain Array, NL : Noise Level

V. Global error

It is of great interest to make the bridge between different SNR's of simulated noise sources and the Z-error concerning the estimated altitude. This conversion is governed by the following equation [2],[6]:

$$\delta z = \frac{H\lambda \tan(\theta)}{\pi \sqrt{SNR} d \sin(\theta + \psi)} \quad (9)$$

This equation takes into account the Rayleigh characteristic of the channel. The sum of errors is computed in terms of the quadratic error sum as :

$$Err = \sqrt{\sum_i \sigma_i^2} \quad (10)$$

Obtained results are given in figure 4. In this figure, two baselines are used : 1.5λ (figure 4.a) and 2.5λ (figure 4.b). For each baseline, Z-errors of different noise sources as well as the quadratic error sum are plotted as a function of the range. These results highlight the most influencing parameters : the wave train effect and the multipath propagation. The first parameter has a physical origin and it can logically be reduced by delaying the arriving data between both interferometric arrays. On the other hand, the interference effect is related to the environment (sea surface, altitude and immersion of the sonar, etc.). This phenomena can be avoid by using several arrays (3 for example) because the main anomalies appear at the phase jumps, so if the sonar uses different pairs of acoustic arrays with different baselines, the jumps will be located differently.

VI. Conclusion and further comments

The interest of studying interferometric noise sources different from the propagation loss is to highlight their great impact on the results. The second point is to divide the noise into two classes : some are intrinsic and predictable (the wave train effect) and other depend on the environment. Their signatures are very different : the wave train effect is important at the end of swath, the interference noise will be significant near the phase jump. On the other hand when an other baseline is used that effect is translated because the two baselines are different. We can imagine it is possible to reduce

that noise by a cooperating system for a given segment of the swath using the more well-suited baseline. In the same way the physical origin of the sliding foot print gives a solution to reduce it by time-shifting the two signals.

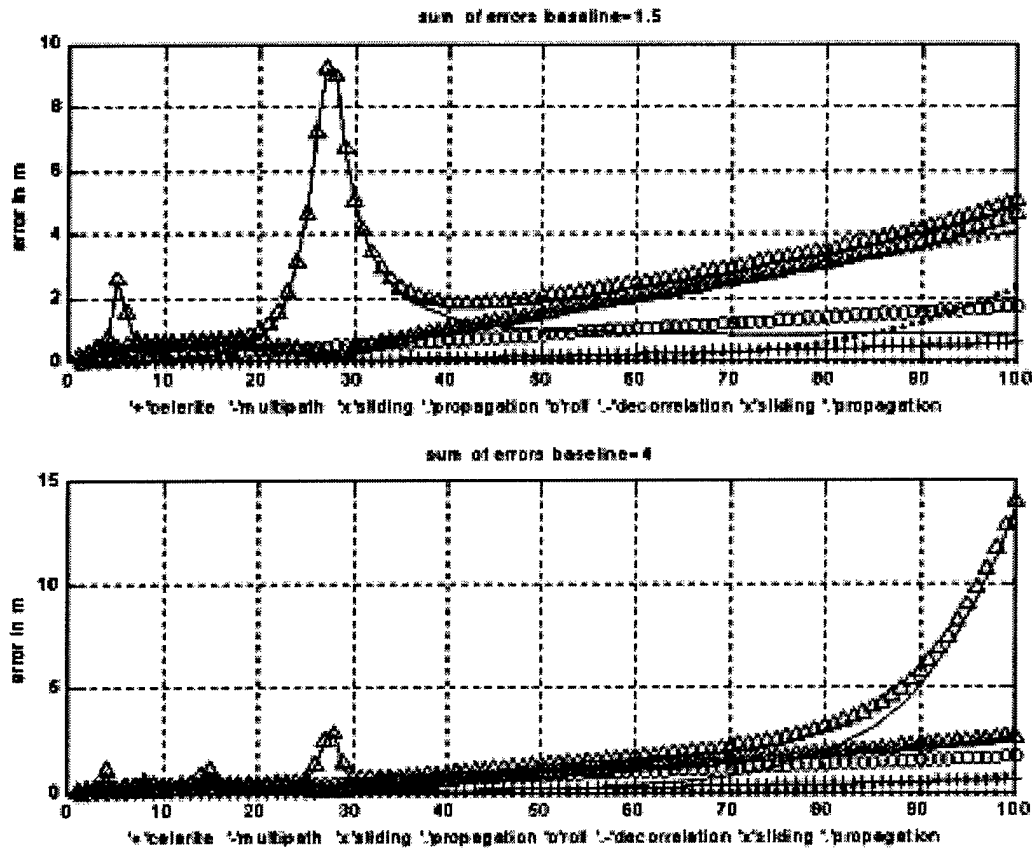


Figure 4, Z-global errors in terms of meters

References :

- [1] J.W. Goodman, 'Laser Speckle and Related Phenomena', in Statistical Properties of Laser Speckle Patterns, J.C. Dainty, Ed. New York: Springer, 1985
- [2] C. SINTES, 'Bruit interferometrique pour sonars lateraux', internal report 4336 GESMA.
- [3] Philip N.DENBIGH, 'Swath Bathymetry : Principles of Operation and an Analysis of Errors', IEEE Journal of Oceanic Engineering, Vol 14, No 4, October 1989.
- [4] D.C. Cooper and B.A. Wyndham, 'Comparison of Monopulse Techniques for Direction Finding in the Presence', IEE, Savoy Place, London, Eng. IEE Conf. Publ. 105, 1973, pp.154-159.
- [5] G. Jin and D. Tang, 'Uncertainties of Differential Phase Estimation Associated with Interferometric Sonars', IEEE Journal Of Oceanic Engineering, Vol. 21, No 1, January 1996.
- [6] Xavier Lurton, 'Precision Analysis of Bathymetry measurements using Phase Difference' OCEANS98
- [7] Urlick, 'Principles of Underwater Sound', 1983 Ed McGraw-Hill

MATCHED FIELD PROCESSING: ENVIRONMENTAL FOCUSING AND SOURCE TRACKING WITH APPLICATION TO THE NORTH ELBA DATA SET

Cristiano Soares¹, Andreas Waldhorst² and S. M. Jesus¹

¹UCEH - Universidade do Algarve, Campus de Gambelas,
PT-8000 Faro, Portugal.

²Fakultät für Elektrotechnik und Informationstechnik,
Ruhr-Universität Bochum, D-44780 Bochum, Germany

Abstract: *Experimental results on the localization of a moving sound source in shallow water are presented. Genetic algorithms (GA) are used to first intensively estimate the environment from a fixed source part of the data. Then, assuming the stationarity of the environment, localization is carried out in the moving source part of the data. Comparison with results obtained previously on the same data set shows that the source range error is reduced by 75%, while the source depth error is reduced by approximately instead of a single frequency conducts to more stable source location estimates.*

I- Introduction

The SACLANT Undersea Research Centre has conducted a sea trial on North of Elba Island in October 1993. The objective of that sea trial was to collect data to verify the performance of geoacoustic and geometric parameter estimation methods based on the inversion of acoustic field observations received on a vertical array of sensors. The data set made available to the authors comprises one period of time where the source is being held fixed and another period where the source is moving away from the receiving array. In a first publication Gingras *et al.* [11] have obtained simultaneous estimates of environmental and geometric parameters using a single frequency Bartlett processor in the stationary source data. A global search procedure based on genetic algorithms (GA) was used for parameter optimization. Source tracking was then carried out in the moving source data using the previously estimated environmental parameters. Later on, on a second publication [21], the same scheme has been followed using two frequency bands. A range-dependent adiabatic normal mode code was used as forward model and it could be shown that at lower frequencies range dependence was not required while a better model fit was obtained at higher frequencies when range dependence was included. The same data set was used by Krolik [31] to test various Minimum Variance (MV) adaptive beamformers. Single frequency data was used and the environmental parameters were assumed

to be within the same interval as in [1]. Among the proposed processors, the MV-EPC†¹ achieved the best source tracking performance and similar to that obtained in [1] with, however, a much less intensive computation load, since no environmental search was performed.

The goal of the present work is to estimate the position of a moving source and demonstrate that the accurateness to which that estimate can be obtained mainly depends on the environmental parameter set used in the forward model processor. The novelty of the work presented in this paper is that the estimation of that environmental parameter set is performed through an intensive GA search - mainly by increasing the population size. It is also shown that using a broadband processor, in a 20 Hz band around 170 Hz, the variance of the source location estimator is reduced, when compared to the single frequency processor. In order to make a fair comparison, a single frequency source tracker was used and the results compared to those of Gingras *et al.* [1]. It is shown that the source range error is reduced by 75% while the source depth error is reduced by approximately 50%.

II- Environmental Parameter Estimation

A- Theoretical Background Matched-field processing (MFP) can be briefly reviewed as follows. The acoustic pressure is measured in an array of sensors. Then, an accurate acoustic model, fed with an appropriate environmental and geometrical model candidate, is used to compute the predicted acoustic pressure replica field. Then a variety of methods is available which, in general, involve some kind of correlation and serves the purpose of comparing the measured and replica fields. Each comparison may be called the MFP response to the environmental and geometric model candidate, and finally the parameter set with the best response is selected. This is an inverse problem, and may be posed as an optimization where the objective function is the MFP response to be maximized.

†¹Minimum Variance with environmental perturbation constraint

In this case the goal is to find a model vector ϑ that maximizes the objective function, which may be written as the Maximum Likelihood estimator:

$$L(\vartheta) = - \sum_{j=1}^J \ln \text{tr}[(\mathbf{I} - \mathbf{P}(\omega_j, \vartheta)) \hat{\mathbf{C}}_X(\omega_j)], \quad (1)$$

where $\mathbf{P}(\omega_j, \vartheta) = \mathbf{H}(\mathbf{H}^H \mathbf{H})^{-1} \mathbf{H}^H$ is a projection matrix of the measured data into the subspace spanned by \mathbf{H} at the frequency ω_j , $\mathbf{H} = \mathbf{H}(\omega_j, \vartheta)$ is a vector with the replica field predicted by the forward model, and $\hat{\mathbf{C}}_X(\omega_j) = \frac{1}{N} \sum_{n=0}^{N-1} \mathbf{X}_n(\omega_j) \mathbf{X}_n(\omega_j)^H$ is the sample spectral density matrix at frequency ω_j .

B- The Baseline Model The baseline model used for

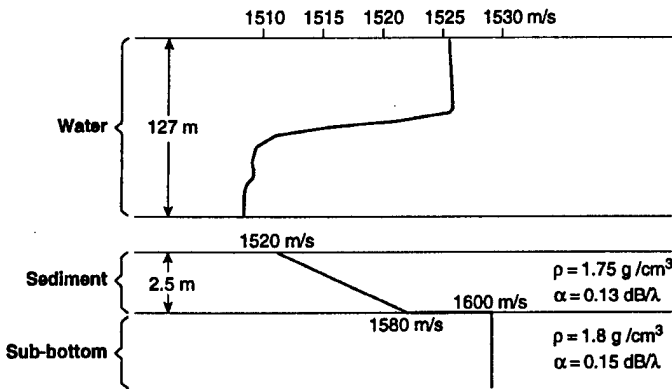


Figure 1: Measured sound speed profile and historical geoacoustic parameters for the North Elba experiment site.

simulations is depicted in Fig. 1 and corresponds to that used by Gingras [4]. It consists of a 127 m depth ocean layer overlying a 2.5 m thick sediment over a half space subbottom. The parameters to be estimated were subdivided into three subsets: the geometric subset (source depth, source range, water depth, array depth), the sediment subset (upper compressional speed, lower compressional speed, density, thickness, attenuation), and the subbottom subset (compressional speed, density, attenuation). The environment was considered range independent.

C- Model parameter estimation The goal is to obtain estimates of the source locations in the moving source portion of the data. For this purpose the environment is first estimated from the fixed source data and then supposed stationary during the moving source part of the data. The sampling frequency was 1 KHz and the FFT block-size was 1024. The sample spectral density matrices were computed in the frequency interval 161.1 to 179.7 Hz, as the average of 10 cross-spectral matrices computed from a time epoch of approximately 1 second each. This procedure was repeated every minute of data. Before starting optimization with the GA a few parameters have to be adjusted: the population size was 270, the number of iterations to 100, the crossover probability was 0.7 and the mutation probability was equal to 0.00875. The final environmental parameter vector estimate over the

10 minutes of data was taken as the mean of the best GA candidates from 5 independent runs on each 1 minute data segment. For comparison purposes the whole procedure was done for a single frequency (169.9 Hz) and in a 20 Hz bandwidth centered in 170 Hz as explained above. The parameter search space was the same as that of Gingras *et al.* [1], except for the source range interval that was much larger in our case, ranging from 5 to 8 km. Another difference is that, instead of estimating sediment and subbottom compressional speeds directly, as done in [1], the water-sediment interface compressional speed is taken as reference and then only the differences between that value and the sediment subbottom interface and subbottom half-space velocities are estimated. Also, those differences are assumed to be always positive, which puts an additional constraint into the search. To give an idea of the computational effort involved in the search procedure, it is sufficient to say that the total search space contains about 10^{24} points, while for each inversion only about 10^6 of those points were explored.

Table 1 shows the results of the narrowband (NB) and broadband (BB) processors. The results given by those two processors are only slightly different. The two last lines of table 1 show the normalized Bartlett peak powers in dB, for the NB and the BB estimated models. These four numbers represent the adjustment - or misadjustment - of the estimated NB and BB models to the data. As it can be noticed, the model adjustment is poorer when measured at one single frequency with the BB model than with the NB model. Similarly, the model adjustment in a frequency band - taken as the mean of the Bartlett peak powers at each frequency in the band - is poorer with the NB model than with the BB model. Strict interpretation of those numbers would indicate that model adjustment is always better in the frequency band on which the environmental parameters were estimated. However, model adjustment is not all in the MFP process since, as it will be seen in the next section, the localization of the moving source gave similar results in narrow and broadband while much stable in the later.

Another way to illustrate the model adjustment dependency on frequency is shown in figure 2. That figure represents the mean square error (mse) between the predicted and measured acoustic fields along the receiving array for each frequency within the considered band. It can be seen that in the neighborhood of the central frequency of 170 Hz the mse is lower for the narrowband model than for the broadband model. When moving away from the central frequency the mse of the narrowband model increases while the mse of the broadband model decreases. The reason for this is that in the narrowband case a good match is forced only for one frequency, while in the broadband case the field has to be matched for the whole band of frequencies.

When comparing the results shown in table I with those of [1], substantial differences can be noticed, specially for the

Model parameter	NB	BB
Geometric		
source range (m)	5602	5593
source depth (m)	76.0	76.3
receiver depth (m)	112.6	113.4
water depth (m)	129.4	129.4
Sediment		
comp. speed upper (m/s)	1486	1477
comp. speed lower (m/s)	1534	1538
density (g/cm ³)	2.3	2.3
attenuation (dB/λ)	0.08	0.09
thickness (m)	3.3	3.7
Bottom		
comp. speed (m/s)	1572	1571
density (g/cm ³)	1.87	1.82
attenuation (dB/λ)	0.11	0.11
NB Bartlett Power (dB)	-0.23	-0.26
BB Bartlett Power (dB)	-0.40	-0.35

Table 1: Estimation results for the narrowband and broadband processors

source location: those obtained here are in all cases closer to the expected values. One reason for that is the number of iterations and the population size chosen by Gingras, that seem to be too low for the optimum of the surface to be attained. In reality the number of forward iterations used here is of the order of $1.5 \cdot 10^6$ while in [1] it was $2 \cdot 10^5$ which represents less than a factor 10 increase and irrelevant when compared to the search space size of 10^{24} .

III- Moving source tracking

Assuming that the environment is stationary, the parameters estimated above are used for estimating the source position during the set of data in which the source is moving away from the receiver. Again, both the single-frequency and multi-frequency cases were considered. The procedure for estimating the cross-spectral matrices was identical as for the fixed source part. In the GA optimization procedure both the population size and the number of iterations were considerably reduced to 40 and 20, respectively. The crossover probability was adjusted to 0.7 and the mutation probability to 0.041. Figure 3 shows the results obtained for the source range and depth in the single frequency case. For comparison purposes the true source range/depth position and the results obtained by [1] are shown in the same figure. It can be easily noticed that the approximately constant 400 m bias in range obtained

by Gingras was considerably reduced to 100 m - which is within the GPS accuracy used for the true range curve [4].

Source depth estimation during has also been improved with an error of approximately 3 m against 5 or 6 m for Gingras *et al.* For the broadband case the source range estimation results, Fig. 4, are very similar to those obtained in the single

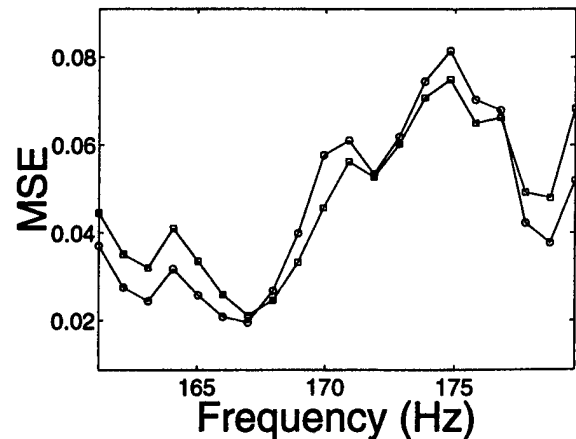


Figure 2: Error between the measured acoustic field and predicted field using: the narrowband environmental estimates (squares) and the broadband environmental estimates (circles).

Time	NB	BB
1	88	85
2	97	123
3	106	100
4	94	100
5	82	88
6	111	100
7	173	120
8	82	103
9	85	117
mean	102	104
std	29	14

Table 2: Estimated source speed in m/minute during source tracking for the narrowband (NB) and the broadband (BB) cases; bottom lines are mean speed and standard deviation

frequency case with, however, considerably less oscillations. In order to quantify those oscillations, table 2 shows the estimated source speed, *i.e.* the slope of the curve range vs. time, in m/minute for the narrowband and the broadband cases. That source speed should be relatively constant and as close as possible to the surface ship speed of 108 m/minute. Both the narrowband and the broadband processors provided a mean speed close to the expected surface ship speed with, however, a much smaller standard deviation of 14 m / minute in the broadband case than the 29 m / minute in the narrowband case.

Finally, a comparison of the normalized Bartlett peak power for the narrowband and the broadband MF processors is shown in Fig. 5 together with equivalent results obtained by Gingras [1]. Assuming that the Bartlett peak power is an indicator of model adjustment, it can be noticed

that the model estimated in this paper offers, in general, and specially for the broadband case, a much better fit than that provided by the model estimated by Gingras.

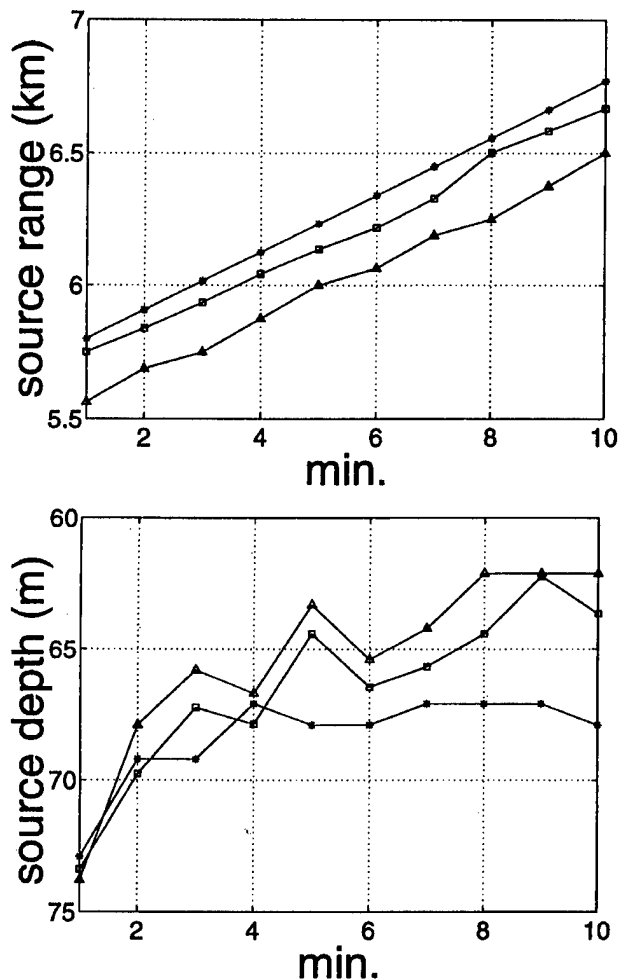


Figure 3: Comparison of source tracking results in the single frequency case: source range (a) and source depth (b); GPS estimated location (asterisks), narrowband tracking (squares), racking in [11] (triangles)

One more interesting point is that, considering the bandwidth in this example, the computation of a broadband model is not significantly more expensive than that of a single frequency. On an DEC4100 AlphaServer (I processor), CSNAP needs 86 ms to compute a model for the single frequency and the 126 ms for the 20 Hz band, which is only a 50% increase in computation time.

IV- Conclusion

MFP was applied to the North Elba data for locating a moving sound source. First the acoustic channel environmental parameters were estimated using an intensive genetic algorithm based search procedure in a portion of the data where the source was stationary. Then, holding the environmental parameters fixed, the moving source part of the data set was processed to test the source tracking

capabilities of the algorithm. Both the environmental parameter estimation and the source tracking were performed at a single frequency of 170 Hz - in order to facilitate comparison with previous results - and in a band of 20 Hz around that single frequency. The results have not only shown

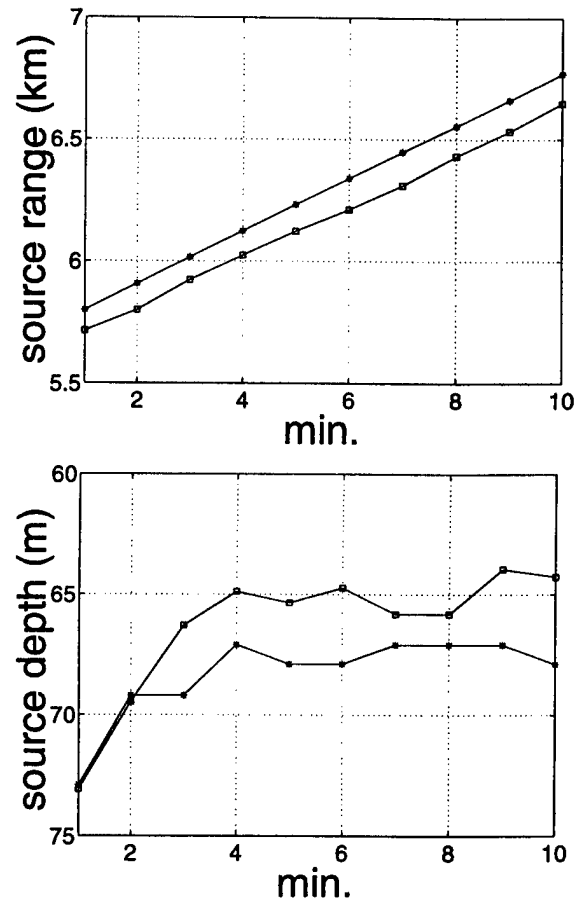


Figure 4: Broadband tracking results: source range (a) and source depth (b); GPS estimated location (asterisks), broadband tracking (circles)

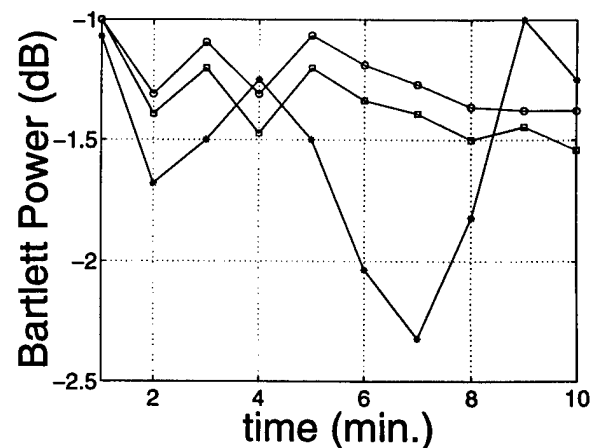


Figure 5: Normalized Bartlett peak power during source tracking in the narrowband case (squares), broadband case (circles), and form [1] (triangles)

that the environment stationarity assumption is valid, but also that broadband algorithm can give a real improvement to the source tracking. This result has been obtained due to a more intensive optimization search during the environmental inversion than that in previous studies. This shows that joint estimation of the environment and source location along time - generally known as focusing [5] - can be advantageously replaced by a computationally more expensive inversion of the environment on part of the data followed by a much less intensive algorithm for source location estimation.

V- References

- [1] Gingras, D. F. and Gerstoft, P. "Inversion for geometric parameters in shallow water: Experimental results", *J. Acoust. Soc. of Amer.*, vol. 97, pp. 3589-3598, 1995.
- [2] Gingras, D. F. and Gerstoft, P. "Parameter estimation using multifrequency range-dependent acoustic data in shallow water", *J. Acoust. Soc. of Amer.*, vol. 99, pp. 2839-2850, 1996.
- [3] Krolik, J. L. "The Performance of Matched-Field Beamformers with Mediterranean Vertical Array Data" *IEEE Transactions on Signal Processing*, vol. 44, pp. 2605-2611, 1996.
- [4] Gingras, D. F. "North Elba Sea Trial Summary", spib.rice.edu/spib/saclant.html, 1994.
- [5] Collins, M. D. and Kupperman, W. A. "Focalization: Environmental focusing and source localization", *J. Acoust. Soc. of Amer.*, vol. 90, pp. 1410-1420, 1991.